Geologica Acta, Vol.9, Nos 3-4, September-December 2011, 217-224
DOI: 10.1344/105.000001745
Available online at www.geologica-acta.com

geologica acta

Subduction Zones of the Caribbean: the sedimentary, magmatic, metamorphic and ore-deposit records

UNESCO/IUGS IGCP Project 546 Subduction Zones of the Caribbean

A. GARCÍA-CASCO [1] [2] [*] **J.A. PROENZA** [3] **M.A. ITURRALDE-VINENT** [4]

[1] **Departamento de Mineralogía y Petrología, Universidad de Granada**
Fuentenueva s/n, 18002-Granada, Spain

[2] **Instituto Andaluz de Ciencias de la Tierra (CSIC-UGR)**
Fuentenueva s/n, 18002-Granada, Spain

[3] **Departament de Cristal·lografia, Mineralogia i Dipòsits Minerals, Facultat de Geologia, Universitat de Barcelona (UB)**
Martí i Franquès s/n, 08028-Barcelona, Spain

[4] **Museo Nacional de Historia Natural**
Obispo no. 61, Plaza de Armas, La Habana 10100, Cuba

* Corresponding author. Email: agcasco@ugr.es. Tel.: +34 958 246 613; Fax: +34 958 243 368

The International Union of Geosciences (IUGS) and UNESCO IGCP project 546 *Subduction Zones of the Caribbean* (http://www.ugr.es/~agcasco/igcp546/) was launched in 2007 and scheduled to be completed by the end of the current year 2011. It was set up with the aim of gathering researchers interested in the geological evolution of the Caribbean realm. The development of this region is largely controlled by a number of subduction zones that formed along its margins from the break-up of Pangea during the Jurassic until Present. The current setting is characterized by a very complex plate-tectonic configuration dominated by subduction zones, large-scale strike-slip faults, volcanic arcs and collision belts (Figure 1). The project was built upon previous developments of IGCP project 433 *Caribbean Plate Tectonics* (2000-2005), of which the Special Volume 4 (Issue 1-2) of Geologica Acta *Caribbean Plate Tectonics. Stratigraphic, Magmatic, Metamorphic and Tectonic Events* (Iturralde Vinent and Lidiak, 2006) deserves mentioning.

Since 2007, Project IGCP 546 *Subduction Zones of the Caribbean* has set up or participated in the organization of several events together with other institutions and agencies, such as field trips, seminars for students, and workshops in Cuba (2007, 2009), Guatemala (2007, 2010), San Francisco (2007, 2009), Dominican Republic (2008), Spain (2008, 2010), Houston (2008), Stanford (2009), United Kingdom (2009), Panama (2010), Venezuela (2010) and Colombia (2009, 2011). This has attracted the interest of researchers and students from a large number of countries including Australia, Austria, Canada, Chile, China, Colombia, Costa Rica, Cuba, France, Germany, Guatemala, Italy, Jamaica, Japan, Malaysia, Mexico, Netherlands, Nicaragua, Panama, Puerto Rico, Spain, Switzerland, United Kingdom, USA and Venezuela, who have produced field-trip guides, abstracts, papers and books dealing with different aspects of the Geology of the whole Caribbean region (see http://www.ugr.es/~agcasco/igcp546/ for details).

This special issue of Geologica Acta, containing fourteen papers, is representative of the aims of IGCP 546, for it covers most of the cutting-edge topics pertaining to the Caribbean's geological development from the Jurassic to the Neogene in the whole Caribbean region (Guatemala, Cuba, Hispaniola, Puerto Rico, Venezuela, Colombia, the isthmus of Panama, Costa Rica, and the offshore Nicaraguan rise). The issue was conceived during the workshop *Subduction Zones of the Caribbean* and associated field trip *Subduction and arc complexes of central Cuba* organized by IGCP 546 in the III Cuban Convention in Earth Sciences, held in Havana, Cuba, during March 2009. The study cases presented in the workshop and contained in this volume are indicated in Figure 1 and briefly commented below.

Both the 2009 Havana workshop and this volume are dedicated to Wayne Travis Jolly, who passed away on February 9, 2008. As noted in his **memorial** (Edward Lidiak, this issue), **Wayne Jolly** was an enthusiastic and valuable petrologist of the Caribbean community. He devoted much of his career to studying the petrogenesis of Puerto Rican, Virgin Islands and other northeastern Antilles ancient island arc volcanic rocks, associated peridotite sources, and subducted sediments (see the references listed by Edward Lidiak in the memorial). Based on firm stratigraphic, regional and geochemical constraints, his work enabled the refining of the tectonic evolution of the northeastern Caribbean, with special emphasis on the evolution of the Mesozoic-Tertiary subduction systems. In his contributions, he suggested a persistent southwest-dipping Cretaceous convergence in the northeast Antilles and a subduction flip (from NE-dipping to SW-dipping) by the Aptian or even earlier (e.g., Pindell and Kennan, 2009; Pindell et al., in press, and references therein), challenging those

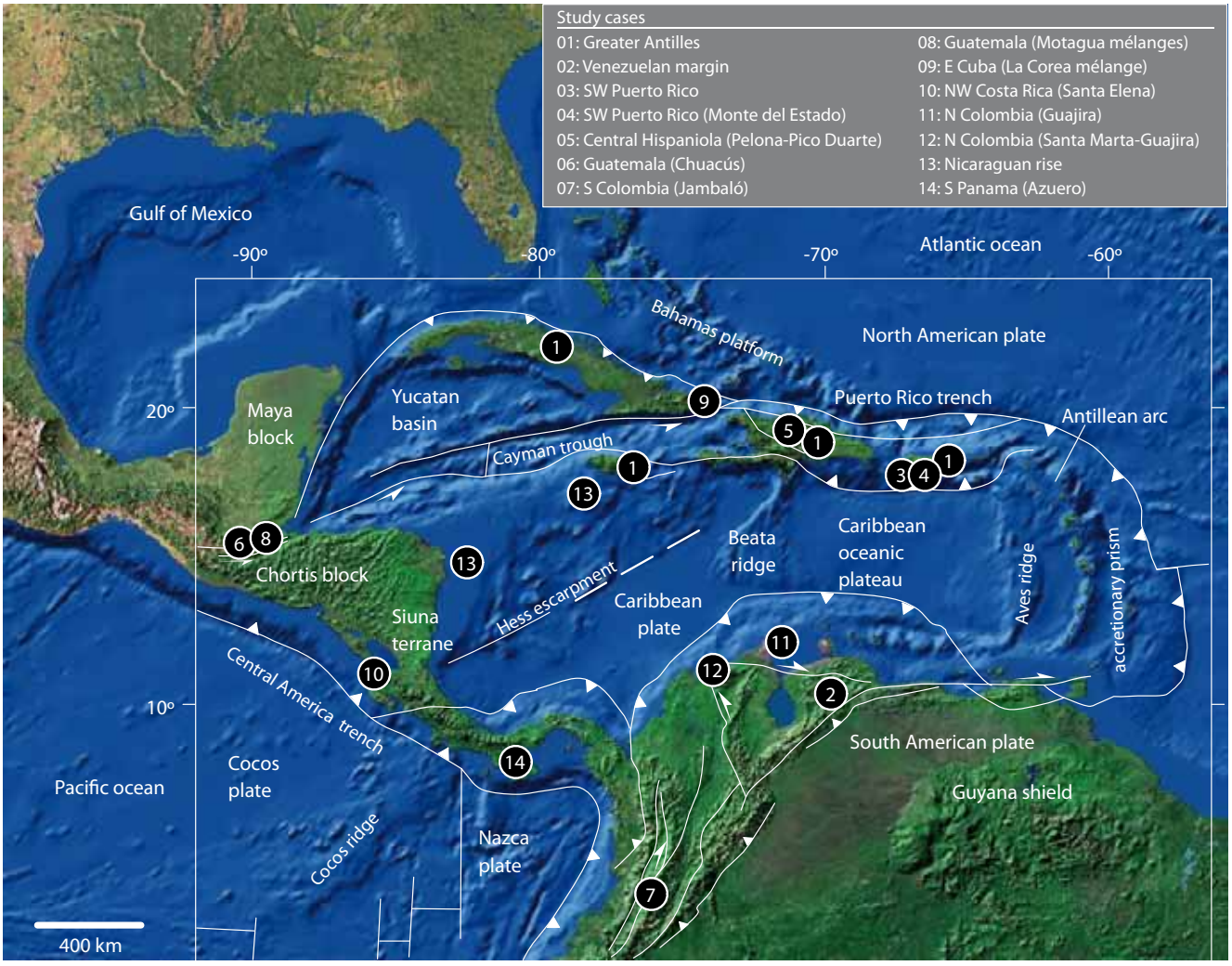

FIGURE 1 | **Plate tectonic configuration of the Caribbean region showing the location of the study cases presented in this issue (numbers refer to papers, arranged as in the issue), and other important geological features of the region (compiled from several sources).**

portraying a subduction flip during the Late Cretaceous (e.g., Kerr et al., 2003, and references therein) .

ORE DEPOSITS OF THE GREATER ANTILLES AND THEIR PLATE TECTONIC SETTINGS OF FORMATION

The first paper of this issue (C.E. Nelson, J.A. Proenza, J.F. Lewis and J. López-Kramer) presents a different approach to that suggested by W. Jolly for evaluating plate tectonic models. This article offers comprehensive maps and descriptions of ore deposits and evaluates **the record of metallogenesis in the Greater Antilles** in relation to the tectonic environment of formation of ore deposits, including (from Jurassic to Recent): rift, platform, volcanic arc, fore-arc and back-arc, syn-orogenic (subduction/collision) and post-orogenic environments. These authors consider that ore formation in the Greater Antilles can be reconciled with plate tectonic models of SW-dipping subduction of the Atlantic since -at least- the Aptian, and in particular with the model proposed by García-Casco et al. (2008) for the Greater Antilles.

PASSIVE MARGINS

Mesozoic passive margins developed in the northern and southern margins of South and North America respectively upon the Jurassic rifting of Pangea. The zircon **provenance study of Early Cretaceous platform sediments of northern Venezuela** by M.I. Noguera, J.E. Wright, F. Urbani and J. Pindell confirms the Guyana shield provenance of Archean, Paleoproterozoic and early Mesoproterozoic detrital zircon grains, though a prominent age population (ca. 0.95-1.2Ga) suggests a western source (Venezuelan and/or northern Colombian Andes). In addition to previous zircon provenance studies (e.g., Rojas-Agramonte et al., 2008), these data allow for the constraint of the paleogeography of the Caribbean region prior to the breakup of Pangea and the longevity of continental scale river systems.

OCEANIC BASINS

The nature of **pre-volcanic arc basement rocks and volcanic arc rocks of western Puerto Rico**, by E.G. Lidiak, W.T. Jolly and A.P. Dickin, help to constrain the nature of the oceanic basement of the Cretaceous-Tertiary volcanic arc crust in Puerto Rico. This basement is formed by serpentinized peridotites, a sequence of Jurassic to mid-Cretaceous pelagic chert, blocks of N-MORB-type amphibolites, and tholeiite and associated trondhjemite fractionates also of N-MORB affinity. The basement is overlain by a younger sequence of pre-arc plateau basaltic and andesitic lava flows having E-MORB and OIB geochemical characteristics. A geochemical analysis of the arc lavas overlying these geologic units was carried out considering the potential effects of subducted pelagic and chert deposits from the Pacific/Caribbean and of pelagic sediments from the Atlantic/Proto-Caribbean on the enrichment of the ultramafic source. This analysis allowed the authors to conclude that the formation of the Late Cretaceous to Eocene (85 to 45Ma) island arc strata was related to the N-dipping subduction of the Caribbean, and not to the earlier (from 125Ma) SW-dipping subduction system that formed the volcanic arc of central Puerto Rico. Such a complex evolution of the Antillean arc, with multiple subduction zones of -possibly- limited lateral extent, are to be expected in the highly mobile/dynamic tectonic environment of oceanic volcanic arc systems. Similar complex histories, with the formation and consumption of back-arc basins, double arcs, reversals of arc polarity and episodic subduction are recorded in other oceanic arc regions, such as the Tertiary-Present arcs of the western Pacific (e.g., Honza, 1991). As a corollary, it could be added that rapid changes (in space and time) of tectonic arrangements should be the rule, rather than the exception in the Mesozoic-Tertiary oceanic evolution of the Caribbean arc. In a related paper, C. Marchesi, W.T. Jolly, J.F. Lewis, C.J. Garrido, J.A. Proenza and E.G. Lidiak give insight on the **origin and evolution of mantle peridotites from the Monte del Estado massif of southwest Puerto Rico**. They are interpreted as a section of lithospheric mantle which underwent several stages of partial melting in the garnet and spinel stability fields, probably during the Jurassic-Early Cretaceous spreading of the Atlantic/Proto-Caribbean oceanic basin. This conclusion is important for it follows that this fragment of the Atlantic/Proto-Caribbean lithosphere should have been tectonically incorporated to the fore-arc region of the Greater Antilles arc within a tectonic scenario of subduction polarity reversal during the Aptian-Albian as proposed by Mattson (1979).

J. Escuder-Viruete, A. Pérez-Estaún, M. Joubert and D. Weis examine the volcanism related to the Late Cretaceous **Caribbean large igneous province** emplaced in the Caribbean volcanic arc. Based on new geological, geochemical and geochronologic data from the **Pelona-Pico Duarte basalts Formation of Central Hispaniola**, these authors find fundamental changes in the mantle sources of Late Cretaceous lavas that fed the volcanic-arc region. This suggests that the Late Cretaceous Caribbean plume flowed toward the mantle wedge region of the Caribbean island-arc in response to back-arc opening induced by the rollback of the SW-directed subduction of the proto-Caribbean slab.

SUBDUCTION ZONE-RELATED COMPLEXES

The nature and age of **metamorphic complexes** documenting the deep tectonic evolution of the convergent margins of the Caribbean realm is considered in detail by L.A. Solari, A. Gómez-Tuena, F. Ortega-Gutiérrez and C. Ortega-Obregón. These authors provide new geochemical and zircon-age data of the **Chuacús Metamorphic Complex of central Guatemala**. They describe a long-lasting evolution which includes three stages of metamorphism of Paleozoic (post-Ordovician/pre-Triassic), Late Triassic, and Late Cretaceous ages, in line with recent developments in the complex North American–Caribbean Plate boundary region of Mexico–Guatemala–Honduras (Ratschbacher et al., 2009). Subduction-related eclogite facies conditions (perhaps reaching ultra-high pressure conditions) were reached during the Paleozoic stage, and a high-P/low-T event -at eclogite-amphibolite facies conditions- also occurred in a Late Cretaceous stage. Such a history, not shared by adjacent continental blocks (e.g., Maya and Chortís blocks) points to an allochthonous character of the Chuacús complex. That is, rather than being a fragment of the Maya block, the Chuacús evolved independently from the Paleozoic until the Late Cretaceous, when it was accreted to the former. In any case, the latest Cretaceous high-pressure event indicates subduction and collision of the Caribbean arc with the margin of the Maya block, followed by accretion and exhumation. This is similar to what has been inferred from other high-pressure rocks of Guatemala (e.g., Brueckner et al., 2009) and the Yucatan basin-Cuba-Dominican Republic-Puerto Rico-Virgin Islands belt (García-Casco et al., 2008). It may not be causal, but the oceanic subduction-related **blueschists of Jambaló, Central cordillera of Colombia** were also exhumed during the latest Cretaceous-earliest Tertiary, as documented by the first Ar-age data available for these rocks provided by A. Bustamante, C. Juliani, C.M. Hall and E.J. Essene. Though the history of the Central Cordillera of Colombia is rather complex (Villagómez et al., 2011a), the data provided suggest that exhumation was caused by the collision of an intra-oceanic arc (rather than the Caribbean plateau; e.g., Kerr and Tarney, 2005) with the continental margin of South America. This collisional event is considered unrelated to synchronous arc-continent collisions in the Northern Andes (and the Antilles and Guatemala) and provides evidence for the possible existence of multiple arc-continent collisions along the margins of the Caribbean plate.

Petrological-geochemical processes occurring in the subduction environment do not only generate blueschists and eclogites. Locally, hydrothermal/metasomatic jadeitite and related rocks such as those from Guatemala are produced, as reported by G.E. Harlow, V.B. Sisson and S.S. Sorensen. These authors provide textural and mineral data of **jadeitite blocks in serpentinite mélanges from distinct settings on opposite sides of the Motagua fault**, and conclude that a contrasting petrologic nature of jadeitite characterize the two districts. Such contrast has to do with different thermal, mechanical and geochemical conditions during slab subduction and development of the subduction channel. It is also related to the ensuing tectonic history, which may include metamorphic reworking, likely related to the complex Cretaceous evolution of the margin of the Caribbean plate and adjacent blocks (*sensu* Brueckner et al., 2009; Pindell et al., in press). The complexities of long-lasting subduction channels are also attested by ultramafic rocks of the related mélanges. I. Blanco-Quintero, J.A. Proenza, A. García-Casco E. Tauler and S. Galí provide petrological and geochemical data of **serpentinite-matrix and -blocks from the Antillean subduction channel, Eastern Cuba**. Antigorite-serpentinites correspond to upper plate peridotites serpentinized at depth in the subduction channel due to dehydration of the subducting slab, whereas antigorite-lizardite serpentinites are lower plate abyssal serpentinized peridotites accreted to the channel, in what seems a regular picture of subduction-related serpentinite-melanges (e.g., Saumur et al., 2010). The authors emphasize that hydration of the upper plate mantle wedge is critical for exhumation of subducted material (e.g., Guillot et al., 2009). The geodynamic settings of formation of these serpentinites and their ultramafic protoliths, however, contrast with that of variably chromitite-bearing serpentinized ultramafic rocks of obducted ophiolitic sheets. In Eastern Cuba these ophiolites (i.e., Mayarí-Baracoa ophiolite belt) have been interpreted as formed in a back-arc/arc region (Marchesi et al., 2006, 2007). Similarly, F. Zaccarini, G. Garuti, J.A. Proenza, L. Campos, O.A.R. Thalhammer, T. Aiglsperger and J.F. Lewis conclude that the **Santa Elena ultramafic nappe of Costa Rica** formed in a suprasubduction zone environment, as indicated by the first systematic geochemical description of chromite and platinum group minerals from Santa Elena chromitites. This work suggests formation of chromitite due to fractional crystallization of boninitic magma and strengthens the view that the ultramafic nappe was formed in a suprasubduction environment (e.g., Geldmacher et al., 2008) rather than at a mid-ocean rift or a hotspot setting. It also illustrates the use of ophiolitic chromitite as a petrogenetic and geodynamic indicator, which is particularly useful when related ultramafic-mafic rocks are moderately to strongly altered.

VOLCANIC ARCS

Ocasionally, suprasubduction zone rocks formed far away from oceanic trenches enter a subduction zone. Complex tectonic scenarios, involving subduction erosion and/or the interplay of several subduction zones

are commonly envisaged to explain these occurrences, as described by M. Weber, A. Cardona, V. Valencia, U. Altenberger, M. López-Martinez, M. Tobón, S. Zapata, G. Zapata and E. Concha for the **eclogites of the Guajira Peninsula, northern Colombia**. The geochemistry of these rocks is similar to that of the Early-to-Late Cretaceous basalts and basaltic andesites of the oceanic island arc tholeiitic series of the Caribbean realm and their Late Cretaceous metamorphic ages are comparable to those of other high-pressure rocks of the southern margin of the Caribbean plate from Venezuela. A generalized stage of volcanic-arc subduction in the southern branch of the Caribbean plate margin points to a complex plate tectonic scenario involving the approach of the volcanic arc to the continental margin of South America. A major question left open by the authors is whether the high-pressure belts of northern South America represent a single continuous subduction zone through time or are part of multiple subduction zones that were modified by a strike-slip system during their approach to the margin (Maresch et al., 2009). Collision and accretion of the Caribbean Cretaceous volcanic arc to the northern margin of South America during the latest Cretaceous-early Tertiary caused orogenesis. Further development of topography resulted from the onset of subduction of the Caribbean plate below South America. Renewed magmatism constrains the evolution of exhumation and tectonic stages during the Cenozoic, as exemplified by the paper by A. Cardona, V. Valencia, M. Weber, J. Duque, C. Montes, G. Ojeda, P. Reiners, K. Domanik, S. Nicolescu, and D. Villagómez on **U-Th/He thermochronology and barometry of Eocene plutonic rocks of the Santa Marta massif and the Guajira Peninsula, northern Colombia**. Several major exhumation events from up to ca. 20 km in Santa Marta and 10 km in Serranía de Guajira are identified since the Eocene, though both complexes experienced independent histories since the late Oligocene. The control of exhumation in this active subduction/strike-slip plate margin is considered essentially tectonic, including post-Eocene changes in plate convergence obliquity and rate. These changes caused the South American margin to override the Caribbean plate, in agreement with fission track thermochronology (Villagómez et al., 2011b).

The paper by J. Lewis, G. Kysar Mattietti, M. Perfit and G. Kamenov deals with the geochemistry of **granitoids recovered from the basement of the northern Nicaraguan Rise**. This will certainly attract the scientific community, for the geology of this important part of the Caribbean is poorly known and controversial. According to this study, the elemental and Pb, Nd and Sr isotope systematics of granitoids indicate that basement rocks of the northern Nicaraguan Rise have a mature oceanic arc affinity and show no evidence for a continental component. Furthermore, these granitoids are similar to the possibly related Late Cretaceous-Paleocene oceanic volcanic-arc granitoid intrusions of Above Rocks (Jamaica) and Terre Neuve (Haiti). Hence, the authors propose that the basement of the northern Nicaraguan Rise in the investigated region corresponds to a Caribbean oceanic arc, probably related to the Siuna terrane (or the Mesquito Composite Oceanic Terrane of Baumgartner et al., 2008, which includes the Siuna terrane) rather than to the Paleozoic-Precambrian continental crust of the Chortís block (e.g., Rogers et al., 2007). This oceanic arc was formed during Cretaceous-Paleocene subduction of the Caribbean lithosphere and the subduction could have been active until the thick Caribbean large igneous province arrived at the trench during the Eocene.

Another case of Late Cretaceous-Tertiary arc-derived rocks, though related to a different subduction zone, is that of the Panamá arc. I. Corral, A. Griera, D. Gómez-Gras, M. Corbella, À. Canals, M. Pineda-Falconett and E. Cardellach present a study of the volcaniclastic **Río Quema Formation of the Azuero Peninsula, Panamá, and the associated gold and copper mineralization**. These authors conclude that the volcano-sedimentary rocks of the Cerro Quema area and associated Au-Cu mineralization were formed in the Panama arc/fore-arc basin during the late Cretaceous-Eocene. Rather than an accreted exotic oceanic terrane, the basement is confirmed to be part of the Caribbean large igneous province (in line with Buchs et al., 2010; Wegner et al., 2011) and is considered autochthonous. This allows the characterization of arc development and maturation since the onset of subduction of Farallon below the Caribbean large igneous province.

As shown, the papers presented in this issue cover a wide spectrum of Caribbean rock complexes in terms of space, time and geologic origin, and add new data and far-reaching ideas that will fruitfully contribute to the current debate on the evolution of the Caribbean and adjacent plates.

ACKNOWLEDGMENTS

The Editors wish to thank the reviewers (D. Buchs, A. Camprubí, A. Cardona, J. Escuder-Viruete, E. Gazel, D. Gimeno, T. Grammatikopoulos, S. Guillot, G.E. Harlow, M. Jaramillo, J.F. Lewis, E. Lidiak, C. Marchesi, W. Maresch, M. Grégoire, U. Martens, D. Morata, C. Nelson, Y. Rojas-Agramonte, J.H. Schellekens, R.J. Stern, T. Tsujimori, V. Valencia and J. Wright in addition to reviewers who wish to remain anonymous), Geologica Acta's Chief Editor (M. Liesa), Journal Manager (L. Rincón) and editorial staff (Montserrat Puig, Adriana Currin, Ivan Pineda and Guim Aguadé), who have made this issue possible. We also wish to thank the Cuban Geological Society, for assistance, and UNESCO/IUGS for funding the workshop *Subduction Zones of the Caribbean* and associated Field Trip *Subduction and arc complexes of central Cuba* organized by IGCP 546 in the III Cuban Convention in Earth Sciences (Havana, March, 2009).

REFERENCES

Baumgartner, P.O., Flores, K., Bandini, A.N., Girault, F., Cruz, D., 2008. Upper Triassic to Cretaceous radiolarians from Nicaragua and Northern Costa Rica - The Mesquito Composite Oceanic Terrane. Ofioliti, 33(1), 1-19.

Blanco-Quintero, I., Proenza, J.A., García-Casco, A., Tauler, E., Galí, S., 2011. Serpentinites and serpentinites within a fossil subduction channel: La Corea mélange, eastern Cuba. Geologica Acta, 9 (3-4), 389-405.

Brueckner, H.K., Avé Lallemant, H.G., Sisson, V.B., Harlow, G.E., Hemming, S.R., Sorensen, S.S., Tsujimori, T., Martens, U., 2009. Metamorphic reworking of a high-pressure-low temperature mélange along the Motagua fault, Guatemala: A revised record of Neocomian and Maastrichtian transpressional tectonics. Earth and Planetary Science Letters, 284, 228-235.

Buchs, D.M., Arculus, R.J., Baumgartner, P.O., Baumgartner-Mora, C., Ulianov, A., 2010. Late Cretaceous Arc Development on the SW margin of the Caribbean Plate: Insights from the Golfito (Costa Rica) and Azuero (Panama) Complexes. Geochemistry, Geophysics, Geosystems, 11(7), 35pp.

Bustamante, A., Juliani, C., Hall, C.M., Essene, E.J., 2011. 40Ar/39Ar ages from blueschists of the Jambaló region, central cordillera of Colombia: Implications on the styles of accretion in the Northern Andes. Geologica Acta, 9 (3-4), 351-362.

Cardona, A., Valencia, V., Weber, M., Duque, J., Montes, C., Ojeda, G., Reiners, P., Domanik, K., Nicolescu, S., Villagomez, D., 2011. Transient Cenozoic tectonic stages in the southern margin of the Caribbean plate: U-Th/He thermochronological constraints from Eocene plutonic rocks in the Santa Marta massif and Serraníade Jarara, northern Colombia. Geologica Acta, 9 (3-4), 445-466.

Corral, I., Griera, A., Gómez-Gras, D., Corbella, M., Canals, À., Pineda-Falconett, M., Cardellach, E., 2011. Geology of the Cerro Quema Au-Cu deposit (Azuero Peninsula, Panama). Geologica Acta, 9 (3-4), 481-498.

Escuder-Viruete, J., Pérez-Estaún, A., Joubert, M., Weis, D., 2011. The Pelona-Pico Duarte basalts Formation, Central Hispaniola: An on-land section of Late Cretaceous volcanism related to the Caribbean large igneous province. Geologica Acta, 9 (3-4), 307-328.

García-Casco, A., Iturralde-Vinent, M.A., Pindell, J., 2008. Latest Cretaceous collision/accretion between the Caribbean Plate and Caribeana: origin of metamorphic terranes in the Greater Antilles. International Geology Review, 50, 781-809.

Geldmacher, J., Hoernle, K.A., Bogaard, P.V.D., Hauff, F., Klügel, A., 2008. Age and geochemistry of the Central American forearc basement (DSDP Leg 67 and 84): Insights into Mesozoic arc volcanism and seamount accretion on the fringe of the Caribbean LIP. Journal of Petrology, 49, 1781-1815.

Guillot, S., Hattori, K., Agard, P., Schwartz, S., Vidal, O., 2009. Exhumation processes in oceanic and continental subduction contexts: a review. In: Lallemand, S., Funiciello, F. (eds.). Subduction Zone Dynamics. Springer-Verlag Berlin Heidelberg, 175-204.

Harlow, G.E., Sisson, V.B., Sorensen, S.S, 2011. Jadeitite from Guatemala: New observations and distinctions among multiple occurrences. Geologica Acta, 9 (3-4), XXX-XXX.

Honza, E., 1991. The Tertiary Arc Chain in the Western Pacific. Tectonophysics, 187, 285-303.

Iturralde-Vinent, M.A., Lidiak, E.G., 2006. Caribbean Tectonic, magmatic, metamorphic and stratigraphic events. Foreword. Geologica Acta, 4(1-2), 1-5.

Kerr, A.C., Tarney, J., 2005. Tectonic evolution of the Caribbean and northwestern South America: The case for accretion of two Late Cretaceous oceanic plateaus. Geology, 33, 269-272.

Kerr, A.C., White, R.V., Thompson, P.M.E., Tarney, J., Saunders, A.D., 2003. No oceanic plateau—no Caribbean plate? The seminal role of an oceanic plateau in Caribbean plate evolution. In: Bartolini, C., Buffler, R.T., Blickwede, J. (eds.). The Circum Gulf of Mexico and Caribbean: Hydrocarbon Habitats Basin Formation and Plate Tectonics. American Association of Petroleum Geology Memoir, 79, 126-268.

Lewis, J., Kysar Mattietti, G., Perfit, M., Kamenov, G., 2011. Geochemistry and petrology of three granitoid rock cores from the Nicaraguan Rise, Caribbean Sea: implications for its composition, structure and tectonic evolution. Geologica Acta, 9 (3-4), 467-479.

Lidiak, E.D., 2011. Memorial to Wayne T. Jolly. Geologica Acta, 9 (3-4), 225-227.

Lidiak E.G., Jolly W.T. , Dickin A.P, 2011. Pre-arc basement complex and overlying early island arc strata, Southwestern Puerto Rico: overview, geologic evolution, and revised data bases. Geologica Acta, 9 (3-4), 273-287.

Marchesi, C., Garrido, C.J., Godard, M., Proenza, J.A., Gervilla, F., Blanco-Moreno, J., 2006. Petrogenesis of highly depleted peridotites and gabbroic rocks from the Mayarí-Baracoa Ophiolitic Belt (eastern Cuba). Contributions to Mineralogy and Petrology, 151, 717-736.

Marchesi, C., Garrido, C.J., Bosch, D., Proenza, J.A., Gervilla, F., Monié, P., Rodríguez-Vega, A., 2007. Geochemistry of Cretaceous magmatism in eastern Cuba: recycling of North American continental sediments and implications for subduction polarity in the Greater Antilles Paleo-arc. Journal of Petrology, 48, 1813-1840.

Marchesi C., Jolly W.T., Lewis J.F., Garrido C.J., Proenza J.A. , Lidiak E.G, 2011. Petrogenesis of fertile mantle peridotites from the Monte del Estado massif (Southwest Puerto Rico): a preserved section of Proto-Caribbean lithospheric mantle? Geologica Acta, 9 (3-4), 289-306.

Maresch, W.V., Kluge, R., Baumann, A., Pindell, J.L., Krückhans-Lueder, G., Stanek, K., 2009. The occurrence and timing of high-pressure metamorphism on Margarita Island, Venezuela: a constraint on Caribbean-South America interaction. Geological Society of London, 328 (Special Publications), 705-741.

Mattson, P.H., 1979. Subduction, buoyant breaking, flipping

and strike-slip faulting in the northern Caribbean. Journal of Geology, 87, 293-304.

Nelson, C.E., Proenza, J.A., Lewis J.F., López-Kramer, J., 2011. The metallogenic evolution of the Greater Antilles. Geologica Acta, 9 (3-4), 229-264.

Noguera, M.I., Wright, J.E., Urbani, F., Pindell, J., 2011. U-Pb Geochronology of Detrital Zircons from the Venezuelan Passive Margin: Implications for an Early Cretaceous Proto-Orinoco River System and Proto-Caribbean Ocean Basin Paleogeography. Geologica Acta, 9 (3-4), 265-272.

Pindell, J., Kennan, L., 2009. Tectonic evolution of the Gulf of Mexico, Caribbean and northern South America in the mantle reference frame: an update. In: James, K.H., Lorente, M.A., Pindell, J.L. (eds.). The Origin and Evolution of the Caribbean Plate. Geological Society of London, 328 (Special Publications), 1-55.

Pindell, J., Maresch, W.V., Martens, U., Stanek, K.P., in press. The Greater Antillean Arc: Early Cretaceous origin and proposed relationship to Central American subduction mélanges: implications for models of Caribbean evolution. International Geology Review. doi: 10.1080/00206814.2010.510008.

Ratschbacher, L., Franz, L., Min, M., Bachmenn, R., Martens, U., Stanek, K., Stubner, K., Nelson, B.K., Herrmann, U., Weber, B., López-Martínez, M., Jonckheere, R., Sperner, B., Tichomirowa, M., McWilliams, M.O., Gordon, M., Meschede, M., Bock, P., 2009. The North American–Caribbean plate boundary in México–Guatemala–Honduras. In: James, K.H., Lorente, M.A., Pindell, J.L. (eds.). The origin and Evolution of the Caribbean Plate. Geological Society of London, 328 (Special Publications), 219-293.

Rogers, R., Mann, P, Emmet, P., 2007. Tectonic terranes of the Chortis block based on integration of regional aeromagnetic and geologic data. In: Mann, P. (ed.). Geologic and Tectonic Development of the Caribbean Plate in Northern Central America. Geological Society of America, 428 (Special Paper), 65-88.

Rojas-Agramonte, Y., Kroner, A., Pindell, J., García-Casco, A., García-Delgado, D. Liu, D., Wang, Y., 2008. Detrital zircon geochronology of Jurassic sandstones of western Cuba (San Cayetano Formation): Implications for the Jurassic paleogeography of the NW Proto-Caribbean. American Journal of Science, 308, 639-656.

Saumur, B-M., Hattori, K.H., Guillot, S., 2010. Contrasting origins of serpentinites in a subduction complex, northern Dominican Republic. Geological Society of America Bulletin, 122, 292-304.

Solari, L.A., Gómez-Tuena, A., Ortega-Gutiérrez, F., Ortega-Obregón, C., 2011. The Chuacús Metamorphic Complex, central Guatemala: geochronological and geochemical constraints on its Paleozoic - Mesozoic evolution. Geologica Acta, 9 (3-4), 329-349.

Villagómez, D., Spikings, R., Magna, T., Kammer, A., Winkler, W., Beltrán, A., 2011a. Geochronology, geochemistry and tectonic evolution of the Western and Central cordilleras of Colombia. Lithos, 125, 875-896.

Villagómez, D., Spikings, R., Mora, A., Guzmán, G., Ojeda, G., Cortés, E., van der Lelij, R., 2011b. Vertical tectonics at a continental crust-oceanic plateau plate boundary zone: Fission track thermochronology of the Sierra Nevada de Santa Marta, Colombia. Tectonics, 30, TC4004. doi: 10.1029/2010TC002835.

Weber, M., Cardona, A., Valencia, V., Altenberger, U., López-Martinez, M., Tobón, M., Zapata, S., Zapata, G., Concha, A.E., 2011. Geochemistry and Geochronology of the Guajira Eclogites, northern Colombia–Evidence of a metamorphosed primitive Cretaceous Caribbean Island-arc. Geologica Acta, 9 (3-4), 425-443.

Wegner, W., Wörner, G., Harmon, R.S., Jicha, B.R., 2011. Magmatic history and evolution of the Central American Land Bridge in Panama since Cretaceous times. Geological Society of America Bulletin, 123, 703-724.

Zaccarini, F., Garuti, G., Proenza, J.A., Campos, L., Thalhammer, O.A.R., Aiglsperger, T., Lewis, J.F., 2011. Chromite and platinum-group-elements mineralization in the Santa Elena Ultramafic Nappe (Costa Rica): geodynamic implications. Geologica Acta, 9 (3-4), 407-423.

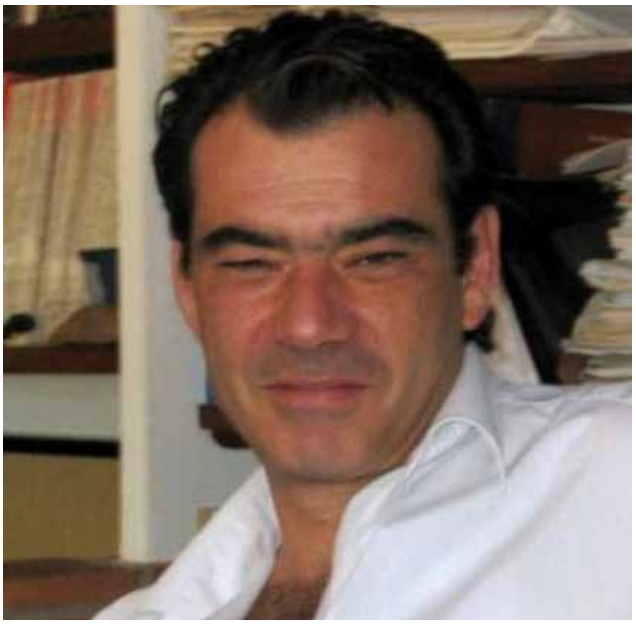

Antonio García-Casco, Ph.D. 1993 (University of Granada), is Full Professor of Petrology and Geochemistry at the University of Granada. His main research interests are metamorphic geology, phase equilibria, P-T-t paths and experimental petrology, with applications to the geodynamic evolution of plate margins (mostly in the Betics, Variscan and Caribbean belts). He has led several research projects in the Caribbean region. More information available in http://www.ugr.es/~agcasco/personal.

Joaquín A. Proenza got his PhD degree in Geology at the University of Barcelona in 1998. He is currently an Associate Professor at the Departament de Cristal·lografia, Mineralogia i Dipòsits Minerals of Barcelona University. His research activities are concerned with mineralogy, petrology and metallogenesis of mafic and ultramafic rocks (mainly in the Caribbean region). His recent projects include the metallogenetic processes of supergene Co-Ni enrichment and platinum group elements in Ni-laterite deposits.

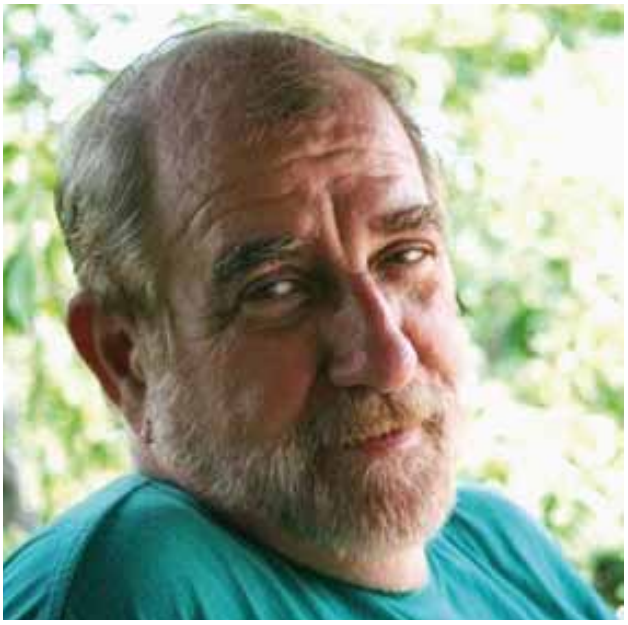

Manuel A. Iturralde-Vinent is the President of the Cuban Geological Society, a member of the Cuban Academy of Sciences, senior professor at the School of Geophysics at the IPSJAE in Havana and at the School of Geology at the University of Pinar del Río, and retired senior researcher of the National Museum of Natural History (Cuba). He has been a member of the scientific board of UNESCO/IUGS Geoscience Program and of several other international organizations. He is author of more than 250 scientific contributions including books, papers, web sites and documentary films about Cuban and Caribbean geology. Lately he is focused on public education to prevent natural disasters derived from extreme geological events. More information available in http://www.redciencia.cu/cdorigen/arca/iturra.html.

Geologica Acta, Vol.9, Nos 3-4, September-December 2011, 225-227
DOI: 10.1344/105.000001712
Available online at www.geologica-acta.com

geologica acta

Memorial to Wayne T. Jolly 1940-2008

Edward G. Lidiak
University of Pittsburgh, Pittsburgh, Pennsylvania 15260, USA

Wayne Travis Jolly passed away on February 9, 2008, in Niagara Falls, Canada, of complications arising from heart surgery and the renewed effects of pneumonia. A memorial was held on February 13 on the campus of Brock University with Wayne's family, the Brock community, and many of his former colleagues and students in attendance. With his death, the Caribbean community lost an enthusiastic and valuable member. Jolly was a prominent petrologist specializing in the petrogenesis of ancient island arc volcanic rocks, associated peridotite sources, and subducted sediments in the northeastern Antilles using major and trace elements and isotope geochemical methods.

As I have been associated with Wayne professionally for the last 20 years, I have been asked to write this memorial. As difficult as I find this, I am honored to write it and hope I do justice to his memory.

Wayne Jolly was born on August 15, 1940, in Jacksonville Texas, a small town in east Texas. He was the first of three brothers. Wayne attended school mainly in Jacksonville and graduated from high school in May of 1957. Wayne then matriculated to the University of Texas at Austin where he majored in Fine Arts (with emphasis in radio and television). He even worked temporarily as a disk jockey during part of the summer months in his hometown. He was initially uninterested in science and waited until his senior year to take a basic science course—Introductory Geology. Totally unexpected perhaps, he became intrigued with the topic and decided that geology was his calling. He completed the Bachelor of Fine Arts degree in 1963 and continued to take geology courses and other science courses with the intent of earning a Bachelor of Arts degree in geology. He completed those requirements and received the Bachelor of Arts degree in geology in 1965. He then continued with an Master of Arts degree in geology in 1966.

I first met Wayne Jolly in the fall of 1962 while he was still an undergraduate at the University of Texas at Austin. We met in one of the X-ray labs where he was working as a volunteer and I was a first-year postdoctoral fellow at the University of Texas making revisions to my Ph.D. dissertation at Rice University. In between experimental X-ray runs, we had numerous discussions about many things geological and specifically about Caribbean geology and research. Wayne was very excited about becoming a geologist. I lost track of Wayne for a short while after I had gone on to the University of Pittsburgh. But then learned that he had applied to the Ph.D. program at Rice to work with Thomas W. (Nick) Donnelly in the Caribbean. Nick, however, had just left Rice and accepted a faculty position at the State University of New York at Binghamton, and Wayne followed him there. For his Ph.D. dissertation that he completed in 1970, Wayne studied the potassic volcanic rocks of the Robles Formation in eastern Puerto Rico. Wayne and I kept in touch for a number of years because of similar interests as I had previously worked on a similar suite of potassic lavas of the Rio Orocovis Group (Puerto Rico).

Wayne Jolly worked briefly as a postdoctoral fellow at Binghamton and at the University of Saskatchewan at Saskatoon before accepting a tenure-stream faculty position in 1971 in the Department of Earth Sciences at Brock University, St. Catharines, Ontario, Canada. At Brock, he progressed from Assistant Professor (1971-1975), to Associate Professor (1975-1980), to Full Professor (1980-2008), serving also as departmental Chairman for 5 years. With regards to research, Wayne spent 20 or so years carrying out petrological and geochemical studies on the meta-volcanic rocks of the Canadian Shield before returning to the Caribbean.

Fast-forwarding to the late 1980s, I received one day somewhat serendipitously, I guess, a letter from Wayne

Jolly asking what I had been doing recently in the Caribbean and stating that he was thinking about resuming work in the Greater Antilles. Well, it was a pleasant coincidence indeed as I had also decided to become active again in the Caribbean. After a few letters and telephone conversations back and forth, we decided instead of competing with each other, to join forces and work together. We thus began a partnership that lasted until his untimely death. A list of Wayne's publications during this period is provided at the end of this memorial.

Wayne Jolly was totally committed to understanding the geology and geochemistry of Puerto Rico and the tectonic evolution of the northeastern Caribbean. He spent at least a month every year for twenty years studying and sampling the volcanogenic strata of the island. In the process, he amassed a reference collection of all of the pre-Oligocene units, which proved to be invaluable in evaluating the sequential development of the island's complex stratigraphy. This collection formed the main basis for the geochemical data, on which the various research papers were based. The data base consists of major and inductively coupled plasma (ICP) trace element analyses of over 800 samples and a total of about 400 individual Sr, Nd, and Pb isotope analyses.

Wayne Jolly was a remarkably productive scientist. Perhaps his greatest talent was his considerable ability to define a specific project quickly and clearly, carry out the research in a timely manner, and then promptly write up the results for publication. He would initially spend countless hours plotting and analyzing elemental and isotopic ratios of specific data sets. Once the evaluation was made, he would then proceed immediately to the writing process. Procrastination was not part of Wayne's vocabulary. He was an excellent but not always a careful writer. Consequently, numerous revisions of an original manuscript typically followed, commonly to the consternation of his co-authors.

In addition to his professional interests, Wayne was a collector of a variety of miscellanea, claiming that his interest in collecting was a genetic thing. He had a large and valuable collection of old Roman coins. He also collected first edition books that included the signature of the author. Among some of the notable signatures he obtained were Neil Armstrong, Henry Kissinger, James A. Baker, and President Ronald Reagan. Wayne had a prized but small collection of glass art. Another collection was an excellent set of books on ancient history. This included complete sets of Homer's *Iliad* and *Odyssey*. The one collection that was his passion for over 20 years was obtaining pristine license plates. His collection totaled about 10,000 plates with specialized interests in Texas, New York, Virginia, Ohio and a near complete collection from Puerto Rico.

Wayne, like most people, was also a complex individual. He readily shared unpublished information with anyone who expressed an interest in Caribbean geology, but would then complain if anyone "borrowed" one of his ideas. We regularly, almost daily, conversed in detail by telephone or e-mail on the geologic topic we were working on at a given time. However, he would also periodically disappear without a trace, only to reappear suddenly beaming with renewed enthusiasm. On the lighter side, Wayne, who was well compensated financially by Brock, at least with respect to university salaries in North America, led a rather frugal life style, except for his collections previously mentioned. He lived in a modest house in St. Catherines that was decorated uniquely with wall-to-wall license plates. One had to see it to believe it. His idea of a gourmet meal was a bowl of Tex-Mex chili and a Dr. Pepper. When in a restaurant in Puerto Rico, he almost invariably ordered a pork chuleta without even bothering to look at a menu. I shall never forget that at one of the geological meetings that we attended, Wayne joined my wife and me at lunch. When we had finished the meal, Wayne reached into a pocket of his one sport coat for his wallet to pay his share of the meal, but instead accidentally pulled out a cold pork chop!

Wayne Jolly was an exceptional and perceptive geologist who made significant contributions to the geology and geochemistry of the Greater Antilles. He will be sorely missed by his colleagues, friends, and by all of those who have a geological interest in the Caribbean region. Rest in peace, Wayne. Wayne Jolly was a confirmed bachelor. His two brothers, Michael and John, and their families survive him.

ACKNOWLEDGMENTS

Mike Jolly graciously provided information on Wayne's early life. I also thank the geological faculty and staff of Brock University, particularly Keith Tinker, Astride Silis, and Mike Lozon, for their help in preparing this memorial.

SELECTED PUBLICATIONS ON ANTILLES GEOCHEMISTRY AND RELATED TOPICS

Jolly, W.T., Lidiak, E.G., Dickin, A.P., 2008. The case for persistent southwest-dipping Cretaceous convergence in the northeast Antilles: Geochemistry, melting models, and tectonic implications. Geological Society of America Bulletin, 120, 1036-1052.

Jolly, W.T., Lidiak, E.G., Dickin, A.P., 2008. Bimodal volcanism in northeast Puerto Rico and the Virgin Islands (Greater Antilles Island Arc): Genetic links with Cretaceous subduction of the mid-Atlantic ridge Caribbean spur. Lithos, 103, 393-414.

Jolly, W.T., Schellekens, J.H., Dickin, A.P., 2007. High-Mg andesites and related lavas from southwest Puerto Rico (Greater Antilles Island Arc): Petrogenetic links with emplacement of the Late Cretaceous Caribbean mantle plume. Lithos, 98, 1-26.

Jolly, W.T., Lidiak, E.G., 2006. Role of crustal melting in petrogenesis of the Cretaceous Water Island Formation (Virgin Islands, northeast Antilles island arc. Geologica Acta, 4(1-2), 7-33.

Jolly, W.T., Lidiak, E.G., Dickin, A.P., 2006. Cretaceous to Mid-Eocene pelagic sediment budget in Puerto Rico and the Virgin Islands (northeast Antilles island arc). Geologica Acta, 4(1-2), 35-62.

Jolly, W.T., Lidiak, E.G., Dickin, A.P., Wu, T.-W., 2002. Recycling in the Puerto Rican mantle wedge, Greater Antilles island arc. The Island Arc, 11, 10-24.

Jolly, W.T., Lidiak, E.G., Dickin, A.P., Wu, T.-W., 2001. Secular geochemistry of central Puerto Rican island arc lavas: Constraints on Mesozoic tectonism in the eastern Greater Antilles. Journal of Petrology, 42, 2197-2214.

Jolly, W.T., Lidiak, E.G., Dickin, A.P., Wu, T.-W., 1998. Geochemical diversity of Mesozoic island arc tectonic blocks in eastern Puerto Rico. In: Lidiak, E.G., Larue, D.K. (eds.). Tectonics and Geochemistry of the Northeastern Caribbean. Boulder (Colorado), Geological Society of America, 322 (Special Paper), 67-98.

Jolly, W.T., Lidiak, E.G., Schellekens, J.H., Santos, H., 1998. Volcanism, tectonics, and stratigraphic correlations in Puerto Rico. In: Lidiak, E.G., Larue, D.K. (eds.). Tectonics and Geochemistry of the Northeastern Caribbean. Boulder (Colorado), Geological Society of America, 322 (Special Paper), 1-34.

Lidiak, E.G., Jolly, W.T., 1998. Geochemistry of intrusive igneous rocks, St. Croix, U.S. Virgin Islands. In: Lidiak, E.G., Larue, D.K. (eds.). Tectonics and Geochemistry of the Northeastern Caribbean. Boulder (Colorado), Geological Society of America, 322 (Special Paper), 133-153.

Lidiak, E.G., Jolly, W.T., 1996. Circum-Caribbean granitoids: Characteristics and origin. International Geology Review, 38, 1098-1133.

Lidiak, E.G., Jolly, W.T., 1996. Rare earth elements in the geological sciences. In: Evans, C.H. (ed.). Episodes from the history of the rare earth elements. Dordrecht (Netherlands), Kluwer Academic Publishers, Chemists and Chemistry, 15, 149-187.

Geologica Acta, Vol.9, Nos 3-4, September-December 2011, 229-264
DOI: 10.1344/105.000001741
Available online at www.geologica-acta.com

geologica acta

The metallogenic evolution of the Greater Antilles

C.E. NELSON [1] **J.A. PROENZA** [2] **J.F. LEWIS** [3] **J. LÓPEZ-KRAMER** [4]

[1] **Consulting Geologist**
2360 23rd St., Boulder, Colorado 80304 USA. E-mail: cnelson945@aol.com

[2] **Departament de Cristal.lografia, Mineralogia i Dipòsits Minerals, Facultat de Geologia, Universitat de Barcelona (UB)**
Martí i Franquès, s/n, 08028 Barcelona, Spain. E-mail: japroenza@ub.edu

[3] **Department of Earth and Environmental Sciences, The George Washington University**
Washington, D.C. 20052, U.S.A. E-mail: lewis@gwu.edu

[4] **Departamento de Geología Ambiental, Geofísica y Riesgos. Instituto de Geofísica y Astronomía AMA-CITMA**
Calle 212/29 y 31, No 2906. La Lisa, Rpto La Coronela, Cuba. E-mail: kramer@iga.cu

ABSTRACT

The Greater Antilles host some of the world's most important deposits of bauxite and lateritic nickel as well as significant resources of gold and silver, copper, zinc, manganese, cobalt and chromium. Beginning in Jurassic time, sedimentary exhalative base metal deposits accumulated in marine sedimentary rift basins as North and South America drifted apart. With the onset of intraoceanic subduction during the Early Cretaceous, a primitive (tholeiitic) island arc formed above a southwesterly-dipping subduction zone. Podiform chromite deposits formed in the mantle portion of the supra-subduction zone, directly above subducted Proto-Caribbean oceanic lithosphere. Within the nascent island arc, bimodal-mafic volcanogenic massive sulfide deposits formed in a fore-arc setting; mafic volcanogenic massive sulfide deposits formed later in mature back-arc basins. The Pueblo Viejo gold district, with five million ounces in production and twenty million ounces in mineable reserves, formed at 108-112Ma, in an apical rift or back-arc setting. By Late Cretaceous time, calc-alkaline volcanism was well established along the entire length of the Greater Antilles. Volcanogenic massive sulfide deposits including shallow submarine deposits characteristic of the primitive island arc gave way to porphyry copper and epithermal precious metal deposits typical of the mature island arc. Oblique collision of the Greater Antilles with North America began in the Late Cretaceous in Cuba and migrated eastward. Orogenic gold and tungsten deposits that formed during the collision event are preserved in ophiolites and in metamorphic core complexes. Since the Eocene, regional tectonism has been dominated by strike-slip motion as the North American continent moved westward relative to the Caribbean Plate. Large nickel-cobalt laterite deposits were formed when serpentinites were exposed to weathering and erosion during the mid-Tertiary. Bauxite deposits were derived from the weathering of volcanic ash within a carbonate platform of Eocene to Miocene age.

KEYWORDS | **Caribbean. Metallogeny. Mineral deposit. Tectonic evolution.**

INTRODUCTION

This paper assembles grade and tonnage information for metallic mineral deposits of the Greater Antilles and relates mineral deposit formation to the tectonic evolution of the northern margin of the Caribbean Plate. Tables are used to compile past production and current (as of 2010) resource information for economically significant examples of each deposit type along with references to the literature. Resource information is from a continually-updated GIS database for mineral occurrences of the Caribbean Basin (CBMap, www.cbmap.net). Other summaries of regional metallogeny for the Greater Antilles include Kesler (1978), Kesler et al. (1990), and Proenza and Melgarejo (1998). Summaries of the tectonic evolution of the Greater Antilles can be found in Lewis et al. (1990, 2000), Mann (2007) and García-Casco et al. (2008). Plate tectonic models are discussed by Pindell and Barrett (1990), Lewis and Draper (1990), Iturralde-Vinent (1998), Meschede and Frisch (1998), Kerr et al. (1999), Pindell et al. (2006) and Pindell and Kennan (2009) among others and will not be reviewed here.

Currently, the mineral endowment (past production plus known resources) of the Greater Antilles totals 36 million ounces (Moz) gold, 277Moz silver, 7 million metric tonnes (Mt) copper, 1Mt lead, 3Mt zinc, 14Mt nickel, 1Mt cobalt, 2Mt chromium, 3.5Mt manganese, and 706Mt aluminium (Tables 1 through 9).

For the purposes of this regional overview, we recognize the following deposit types, each of which is associated with a particular episode in the tectonic evolution of the Greater Antilles volcanic arc. Resource information and references to the literature for deposits with production and/or resources are provided in Tables 1 to 9. Representative examples of each deposit type are described in the text. Readers interested in detailed descriptions for individual deposits should consult the references provided in the text and in the tables.

1. Sediment-hosted deposits formed in extensional basins during the Jurassic and Early Cretaceous separation of North and South America including:
   a. Sedimentary exhalative Cu-Zn-Pb deposits of the Guaniguanico Terrane, western Cuba
   b. Sedimentary exhalative Cu-Zn-Pb deposits of the Escambray Terrane, central Cuba
   c. Stratiform barite deposits and sediment-hosted manganese occurrences
2. Bimodal mafic (Kuroko-type) volcanogenic massive sulfide deposits formed in extensional (fore-arc) basins during the earliest stages of island arc volcanism including:
   a. Cu-Zn-Au-Ag volcanogenic massive sulfide deposits of the Early Cretaceous arc of the central Dominican Republic
   b. Cu-Zn-Au-Ag volcanogenic massive sulfide deposits of the Early Cretaceous arc of the Villa Clara district, central Cuba
   c. Cu-Zn-Au-Ag volcanogenic massive sulfide deposits of the Cretaceous arc of eastern Cuba
   d. Cu-Zn-Au-Ag volcanogenic massive sulfide deposits of the Paleogene arc of the Sierra Maestra, eastern Cuba
3. Mafic (Cyprus-type) volcanogenic massive sulfide deposits formed in mature back-arc basins
4. Epithermal deposits of the Early Cretaceous tholeiitic island arc including:
   a. Au-Ag-Cu deposits of the Pueblo Viejo district, Dominican Republic
   b. Au-Ag-Cu deposits of the Bayaguana district, Dominican Republic
5. Epithermal deposits of the Late Cretaceous to Eocene calc-alkaline island arc including:
   a. Au-Ag-Cu deposits of the Restauración district, Dominican Republic
   b. Au-Ag-Cu deposits of the Massif du Nord, Haiti
   c. Au-Ag-Cu deposits of the Camagüey district, Cuba
6. Porphyry copper and skarn deposits associated with Late Cretaceous to Tertiary calc-alkaline plutons including:
   a. Cu-Au porphyry deposits of the Utuado district, Puerto Rico
   b. Cu-Au porphyry deposits of the Massif du Nord district, Haiti
   c. Cu-Au porphyry deposits of the Restauración district, Dominican Republic
   d. Cu-Au skarn and porphyry deposits of the Terre Neuve district, Haiti
   e. Cu-Au porphyry and iron skarn deposits of the Camagüey and Villa Clara districts, Cuba
   f. Cu-Au porphyry deposits of the Bellas Gate district, Jamaica
   g. Iron skarn deposits of the Hierro Santiago district, Sierra Maestra, Cuba
   h. Iron skarn deposits of the Maimón-Hatillo district, Dominican Republic
7. Volcanogenic (Cuban type) manganese deposits of the Sierra Maestra, Cuba
8. Orogenic deposits formed during collision of the Greater Antilles with North America:
   a. Orogenic gold deposits
   b. Listvenite gold deposits
   c. Tungsten deposits
9. Orthomagmatic (podiform chromite) deposits formed in supra-subduction zones and hosted by ophiolites
10. Bauxite (aluminium) and lateritic nickel-cobalt deposits formed by weathering and supergene enrichment of favorable host rocks:
    a. Bauxite deposits
    b. Lateritic Ni-Co deposits
11. Alluvial and beach placer deposits

The following sections describe each of these tectono-metallogenic events and their associated metallic mineral deposits. Figure 1 shows deposits (with production and/or resources) and mineral occurrences (prospects) on a regional tectonostratigraphic map; additional geologic detail is provided in figures 2 and 3. Figure 4 provides a geologic map for the Pueblo Viejo Au-Ag-Cu district, Dominican Republic. Figure 5 locates each mineral deposit type on a series of cross sections summarizing the tectonic and metallogenic evolution of the northern Caribbean margin.

SEDIMENT-HOSTED DEPOSITS

The oldest metallic mineral deposits to form in the Greater Antilles date to the Jurassic breakup of Pangea. Sedimentary exhalative base metal deposits, stratiform barite deposits and stratiform manganese deposits formed in rift-related terrestrial and marine sedimentary basins that developed along the passive margin of North America as North and South America drifted apart (Proenza and Melgarejo, 1998 and references therein). Host rocks are Jurassic to Cretaceous siliciclastic and carbonate sedimentary rocks exposed in western and central Cuba (Millán, 1996; Iturralde-Vinent, 1998, 2006; Pszczólkowski, 1999; García-Casco et al., 2008). Sedimentary basins of similar age and origin host sedimentary exhalative and Mississippi Valley-type (MVT) ore deposits in northeastern México (González-Sánchez et al., 2009; Camprubí, 2009).

Past production and resource information for sediment-hosted deposits is provided in Table 1; deposit locations are shown on Figs. 1 and 2. The classification of sediment-hosted deposits followed in this paper is that of Leach et al. (2005). Although the Matahambre sedimentary exhalative base metal deposit is an important past producer, no sedimentary exhalative deposits are currently being mined in the Greater Antilles.

Sedimentary exhalative Cu-Zn-Pb deposits of the Guaniguanico Terrane, western Cuba

Sedimentary exhalative deposits are found in Early (?) to Late Jurassic terrestrial syn-rift sedimentary rocks of the San Cayetano basin in western Cuba (Zhidkov et al., 1975; Feoktistov et al., 1983; Lavandero et al., 1988; Kesler et al., 1990; Valdés-Nodarse et al., 1993, 1998; Simón, 1995; Maynard and Morton, 1995; Whitehead et al., 1996; Elswick and Maynard, 1998; Pérez-Vázquez and Melgarejo, 1998; Rojas-Agramonte et al., 2008). The San Cayetano basin (Fig. 2A) belongs to an unmetamorphosed fragment of the Maya Block borderland named the Guaniguanico Terrane by Iturralde-Vinent (1994).

Sedimentary exhalative deposits of the San Cayetano basin are hosted in lenticular black shales interbedded with quartz-feldspar sandstone and siltsone. The main deposits (Table 1) include Matahambre (Cu stockwork with Zn-Pb), La Esperanza (Cu stockwork), Castellanos (Zn-Pb-Ba with Cu stockwork), and Santa Lucía (Zn-Pb-Ba). Some of these deposits (e.g. Mantua and Unión) were interpreted as Besshi-type volcanogenic massive sulfide deposits by Kesler et al. (1996) and by Russell et al. (2000). However, these deposits occur in limestone and calcareous schist, with intercalations of sandstone, mudstone and carbonaceous schist, and could also be tentatively included in the sedimentary exhalative category.

The Matahambre mine (Fig. 2A) reached a depth of 1553 meters on level 45 (Pérez-Vázquez and Melgarejo, 1998). A total of 561,000 tons of copper was produced (Rodríguez-Romero, 2003) during the lifetime of the mine (1916 to 1997). The ore deposit consists of two types of mineralization (Pérez-Vázquez and Melgarejo, 1998). High-grade copper veins up to 10 meters in width cut the sandstone section and are interpreted as hydrothermal conduits. These veins account for the bulk of production to date and for the bulk of the remaining resource. Polymetallic stratiform deposits hosted by black shales (e.g. the Cuerpo 70 ore body) are interpreted as the result of hydrothermal venting on the seafloor (Whitehead et al., 1996) and account for less than 10% of the remaining resource.

Sedimentary exhalative deposits of the Escambray Terrane, central Cuba

Sediment-hosted Cu-Zn-Pb deposits occur within Jurassic metamorphosed carbonate rocks of the Escambray Terrane in central Cuba (Iturralde-Vinent, 1998; Proenza and Melgarejo, 1998; Russell et al., 2000; García-Casco et al., 2008; López-Kramer et al., 2008a). The Escambray Terrane was part of a sedimentary prism that extended southeastward from the Maya Block, named Caribeana by García-Casco et al. (2008). The Escambray and Guaniguanico Terranes represent fragments of the North American passive margin.

Sedimentary exhalative deposits of the Escambray Terrane were interpreted by Russell et al. (2000) as Cyprus-type volcanogenic massive sulfide deposits. However, their occurrence in carbonate rocks, the lack of evidence for volcanism and an extensional setting suggest that they may instead be sedimentary exhalative deposits (Lavandero and Bravo, 1994; Batista-González et al., 1998; Montano-Pérez et al., 1998; Proenza and Melgarejo, 1998). The main deposits are Carlota, Victoria and Guachinango (Table 1, Fig. 2B).

Host rocks for sediment-hosted deposits of the Escambray Terrane include locally graphitic limestone

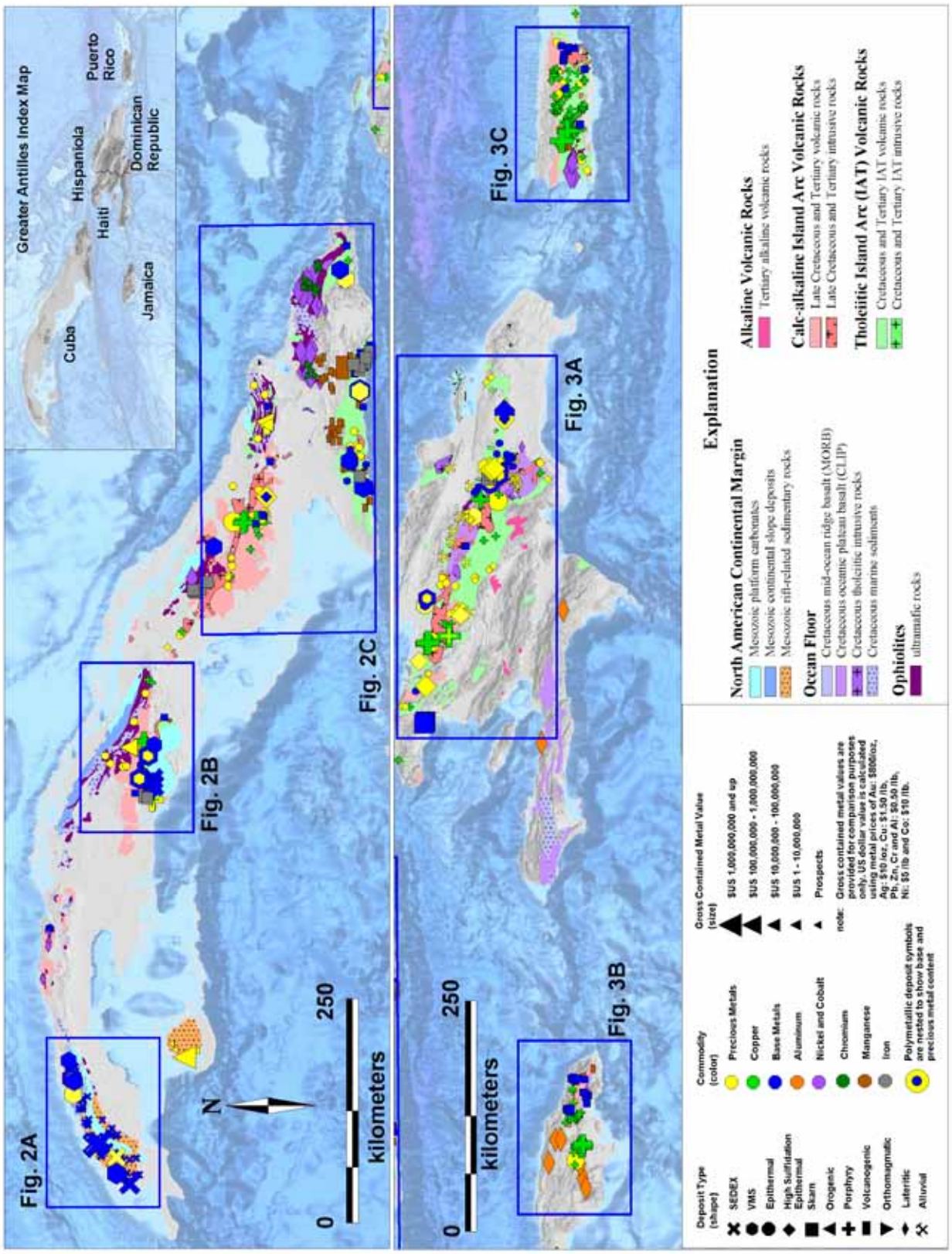

FIGURE 1 | Metallogenic map of the Greater Antilles showing the location of more detailed maps displayed in Figs. 2 and 3. Mineral occurrences are shaped according to deposit type, color coded according to commodity and sized according to gross contained metal value. The geologic base map is from Case and Holcombe (1980), modified to display tectonostratigraphic rock units.

and marble, and lesser limey siltstone and graphitic schist with interbedded, conformable lenses of massive and disseminated sulfide mineralization (Tolkunov et al., 1974a). Locally-colloform pyrite, pyrrhotite and marcasite (80%) are present along with lesser chalcopyrite, sphalerite, quartz and ankerite (Hill, 1958; Cabrera, 1986). Minor galena, melnikovite, bornite, enargite and tennantite are also present (Tolkunov et al., 1974a). Batista-González et al. (1998) and Montano-Pérez et al. (1998) report locally elevated gold and silver.

Stratiform barite deposits and sediment-hosted manganese occurrences

Stratiform barite deposits are found in the San Cayetano basin of western Cuba where they are spatially associated with sedimentary exhalative deposits (Whitehead et al., 1996). The main deposits include Isabel María, El Indio, Santa Gertrudis and Jagua. The barite deposits lack base metals but they are distinctively bedded and are interpreted to have formed in an environment similar to the nearby, barite-bearing, Castellanos, Santa Lucía and Matahambre sedimentary exhalative deposits.

A number of small sediment-hosted manganese mineral occurrences are found in the Guaniguanico and Escambray Terranes. They exhibit short lateral continuity, are thin (<1m), and are composed primarily of Mn oxides (Park, 1942; Simons and Straczek, 1958; Batista-González et al., 1998; Montano-Pérez et al., 1998; Cazañas and Melgarejo, 1998).

BIMODAL MAFIC VOLCANOGENIC MASSIVE SULFIDE DEPOSITS

Southwestward-dipping subduction of Proto-Caribbean lithosphere began in Early Cretaceous time and was responsible for the formation of the Greater Antilles volcanic arc (e.g. Pindell et al., 2006; Pindell and Kennan, 2009). Arc-related volcanism and plutonism extended from Cuba across Jamaica, Hispaniola, Puerto Rico and the Virgin Islands (Iturralde-Vinent, 1998; Kerr et al., 1999; Jolly et al., 2001, 2006; Lewis et al., 2002; Escuder-Viruete et al., 2006, 2007; Proenza et al., 2006; Marchesi et al., 2007). During the Early Cretaceous, the Greater Antilles volcanic arc was dominated by tholeiitic volcanic rocks (e.g. Donnelly and Rogers, 1981; Lewis et al., 1995). Tholeiitic island arc volcanic rocks in the Greater Antilles (Figs. 1, 2, and 3) include the Los Pasos Formation (Fm.) (central Cuba), the Téneme Fm. (eastern Cuba), the Amina, Los Ranchos and Maimón Formations (Hispaniola), and the Water Islands Formation (Virgin Islands). In the Greater Antilles, tholeiitic island arc volcanic rock suites include boninites as well as typical oceanic arc tholeiites.

According to the classification scheme of Franklin et al. (2005), volcanogenic massive sulfide deposits can be divided into five lithostratigraphic types: i) bimodal-mafic, ii) mafic, iii) pelite-mafic, iv) bimodal-felsic, and v) siliciclastic-felsic. Deposits of the first two types are found in the Greater Antilles arc. Bimodal-mafic (also known as Kuroko-type) deposits occur in rifted bimodal volcanic arcs above intraoceanic subduction zones. Mafic (also known as Cyprus-type) deposits form in mature back-arc basins (Franklin et al., 2005 and references therein) and will be discussed separately.

Bimodal-mafic volcanogenic massive sulfide deposits are found in Lower Cretaceous formations of the Dominican Republic (Maimón and Amina Formations, Lewis et al., 2000), central Cuba (Los Pasos Formation) and eastern Cuba (Purial Complex) (Proenza and Melgarejo, 1998; Russell et al., 2000; Bottrill et al., 2000). Another belt of bimodal-mafic volcanogenic massive sulfide deposits occurs in the Paleogene El Cobre Formation (Cazañas et al., 1998a, 2008), part of the Sierra Maestra volcanic arc of eastern Cuba (Fig. 2C). Volcanic host rocks in these belts show the characteristic features of intraoceanic island arc tholeiites (Díaz de Villalvilla, 1997; Cazañas et al., 1998b; Lewis et al., 2000; Kysar-Mattietti, 2001; Proenza et al., 2006). Past production and current resources for volcanogenic massive sulfide deposits of the Greater Antilles are provided in Table 2; deposit locations are shown on figures 1, 2 and 3.

Cu-Zn-Au-Ag volcanogenic massive sulfide deposits of the Early Cretaceous arc of the central Dominican Republic

The principal host rocks for volcanogenic massive sulfide deposits in the Dominican Republic include the Maimón Formation, a northwest-striking belt of low-grade metamorphosed volcanic and volcaniclastic rocks of pre-Albian age (Bowin, 1966; Draper and Lewis, 1991; Lewis et al., 2000; Childe, 2000) and the Amina Formation, a strongly deformed volcanic rock unit of similar composition (Draper and Lewis, 1982; Escuder-Viruete et al., 2007). The Maimón and Amina Formations share the same geochemical, isotopic and petrogenetic signature (Horan, 1995; Escuder-Viruete et al., 2007) suggesting that they were part of the same primitive island arc.

Basaltic rocks of the Maimón Formation range from low-Ti tholeiites with boninitic affinities to typical oceanic island arc tholeiites (Lewis et al., 2000; Escuder-Viruete et al., 2007). Felsic rocks are quartz-feldspar tuffs and porphyries that exhibit a similar depleted trace element signature indicating a common source. The presence of depleted basalts with boninitic affinities in oceanic island arc tholeiites is a characteristic feature of the Izu-Bonin fore-arc in the Western Pacific (Bloomer et al., 1995).

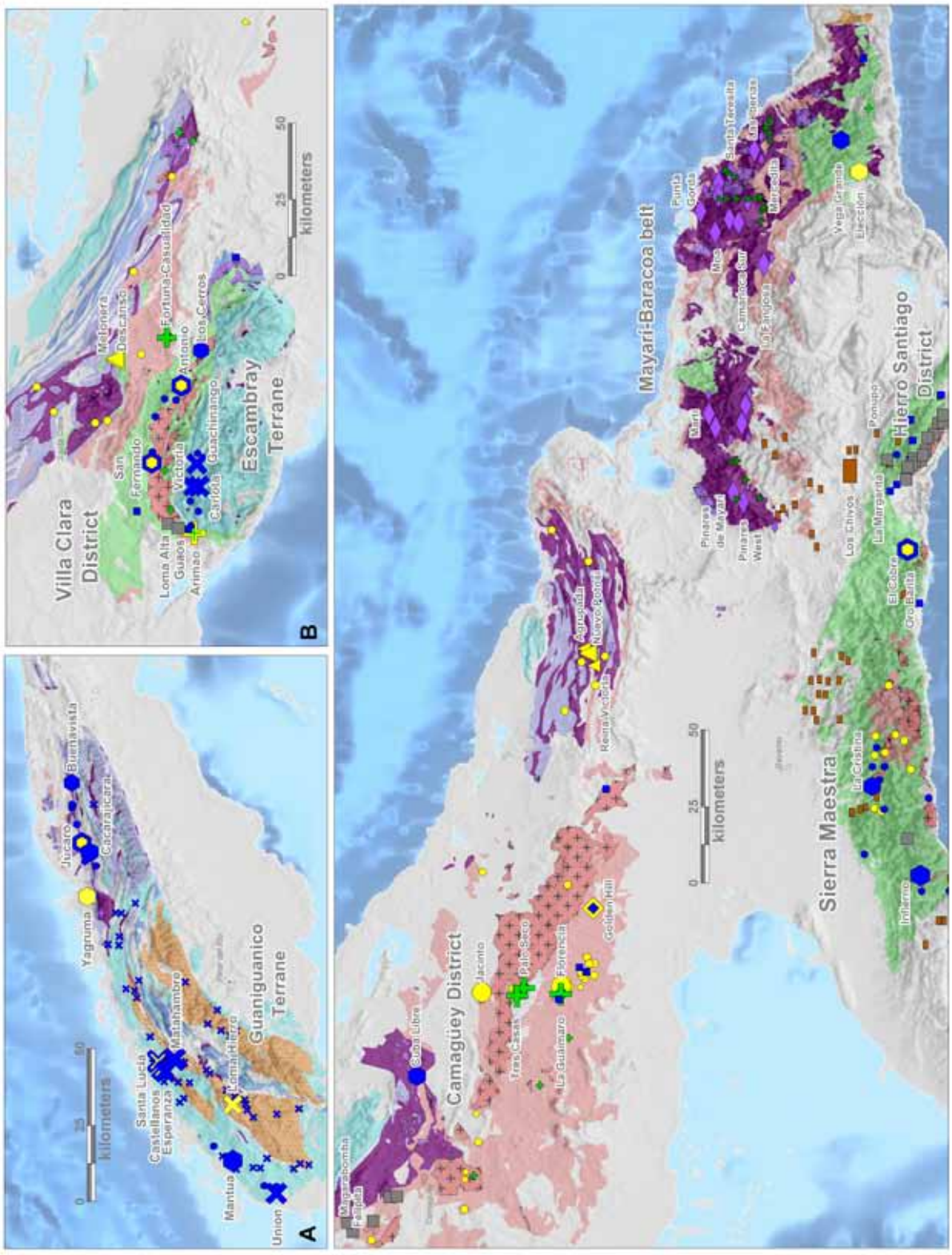

FIGURE 2 | **Detailed metallogenic maps for Cuba. A) Sediment-hosted base metal and volcanogenic massive sulfide deposits of the Guaniguanico Terrane, western Cuba. B) Orogenic gold, porphyry-related copper-gold, sediment-hosted base metal, and volcanogenic massive sulfide deposits of the Villa Clara district and the Escambray Terrane, central Cuba. C) Lateritic nickel-cobalt, orthomagmatic chromite, orogenic gold, porphyry copper, epithermal gold-silver, volcanogenic massive sulfide, volcanogenic manganese and iron skarn deposits of the Camagüey district, the Mayarí-Baracoa belt and the Sierra Maestra, eastern Cuba. The geologic base map for Figure 2 is from Lavandero et al. (1988) modified to display tectonostratigraphic rock units. A legend for rock units and deposit types is provided on Fig. 1.**

TABLE 1 | **Sediment-Hosted Deposits**

Deposit	Past production	Current resource	Observations	References
Matahambre, Cuba	560,938 tons Cu (1916-1997)	13 Mt at 4% Cu	Cu stockwork with Zn and Pb	Rodríguez-Romero (2003), Valdés-Nodarse (1998), Pérez-Vázquez and Melgarejo (1998)
Santa Lucía, Cuba	none	18 Mt at 1 g/t Au, 52 g/t Ag, 0.5% Cu, 1.83% Pb, 5.7 % Zn	Zn, Pb and Ba	Valdés-Nodarse (1998)
Castellanos, Cuba	126,964 ozs (1994-2003)	12 Mt at 2.4% Zn, 43 g/t Ag, 1.28 % Cu, 3.23 % Pb	Zn, Pb, and Ba with Cu stockwork	Whitehead et al. (1996), Valdés-Nodarse (1998), Rabchevsky (1994), Bermudez-Lugo (2004)
Unión, Cuba	none	20 Mt at 0.7% Cu		Russell et al. (2000)
Guachinango, Cuba	none	5.1 Mt at 0.81% Cu, 0.84% Zn	Carbonate hosted	Sherlock and Michaud (2000), Russell et al. (2000)
Mantua, Cuba	none	7.5 Mt at 3.03% Cu	Carbonate hosted, sulfide	Kesler et al. (1996), Russell et al. (2000), Torres (1995, 1999)
Hierro Mantua, Cuba	14,764 ozs Au (1998-2000)	2 Mt at 1.44 g/t Au, 11.65 g/t Ag	Carbonate hosted, oxide cap	Kesler et al. (1996), Russell et al. (2000), Torres (1995, 1999)
Carlota, Cuba	none	2.35 Mt at 1.13% Cu, 3.23% Pb	Carbonate hosted	Sherlock and Michaud (2000)
La Esperanza, Cuba	none	2.5 Mt at 1.55 % Cu	Cu stockwork	Valdés-Nodarse (1998)
Loma Hierro	none	0.8 Mt at 310 g/t Ag	Oxide cap	Krason (1999), Lastra and Lara (1998)
Victoria, Cuba	none	0.536 Mt at 0.86% Cu, 0.19% Pb, 0.2% Zn	Carbonate hosted	Russell et al. (2000)

This observation led Lewis et al. (2000) to suggest that the Maimón Formation and associated volcanogenic massive sulfide deposits formed in a nascent primitive island arc, probably in a fore-arc basin. On the other hand, Horan (1995) concluded that both the Maimón Formation and associated deposits were formed in a back-arc basin, based on geochemical similarity to the Lau Basin in the southwestern Pacific.

Since there is an overlap among some trace elements between the Los Ranchos, Maimón and Amina Formations it has been suggested that these three formations are co-genetic (Escuder-Viruete et al., 2007). However, Lewis (written communication) argues that the mineral deposits in the Maimón and Amina Formations differ strongly in almost all aspects from those in the Los Ranchos and could not have been formed under the same conditions from the same magma system.

Pb isotope ratios help to distinguish among the geochemically similar Maimón-Amina Formations, the Los Ranchos Formation, and the primitive island arc rock units studied so far in Puerto Rico and the Virgin Islands (Cumming et al., 1982; Cumming and Kesler, 1987; Horan, 1995; Frost et al., 1998; Jolly and Lidiak, 2006; Jolly et al., 2008). The $^{206}Pb/^{204}Pb$ ratios for the Maimón and Amina Formations and also the Los Pasos Formation, the volcanogenic massive sulfide-bearing unit of Lower Cretaceous age from central Cuba, cluster at a low value (18.3-18.4) indicating a common source for the host rocks of these three formations (Horan, 1995; Blein et al., 2003). Lead isotope ratios for massive sulfide mineralization exhibit slightly lower $^{206}Pb/^{204}Pb$ ratios (18.2-18.25) than the Maimón Formation host rocks. Maimón Formation lead isotope ratios are lower than those of the Los Ranchos Formation and are also distinct from island arc tholeiites in Puerto Rico where considerably higher $^{206}Pb/^{204}Pb$, $^{207}Pb/^{204}Pb$, and $^{208}Pb/^{204}Pb$ ratios indicate a more evolved source (Cumming and Kesler, 1987; Jolly et al., 2008).

Bimodal-mafic volcanogenic massive sulfide deposits in the Maimón Formation include Cerro de Maimón and Loma Pesada; those in the Amina Formation are Anomaly "B" and Cerro Verde (Table 2, Fig. 3A). Bimodal-mafic

volcanogenic massive sulfide occurrences in the Maimón Formation include Loma Barbuito, Río Sin, Loma la Mina, and San Antonio (Childe, 2000; Lewis et al., 2000; Holbeck and Daubeny, 2000).

The Cerro de Maimón volcanogenic massive sulfide open pit mine (Fig. 3A) went into production in 2008. Ore is drawn from a massive sulfide lens that measures 200 meters in width, 800 to 1000 meters along strike and, near the surface, is up to 40 meters in thickness. The average thickness of the massive sulfide lens is approximately 12 meters and the dip is 30° to the southwest. The orebody, which plunges southeast at 25°, narrows and its dip flattens down plunge. The hanging wall section of intermediate tuffs, mafic flows and thin chert horizons is metamorphosed and exhibits less evidence of hydrothermal alteration than the footwall section. Dominant lithologies in the hanging wall include epidote-chlorite mafic schist intercalated with minor felsic (sericite-pyrite) layers. Exhalites are best developed in the western hanging wall and consist of thin graphitic and hematitic chert horizons (Watkins, 1990; Lewis et al., 2000). Footwall rocks exposed in the western and central part of the deposit are quartz-sericite-pyrite schists, formed by metamorphic recrystallization of pervasively altered host rocks. Alteration in the eastern footwall, where lithologies are mainly mafic to intermediate chlorite schists with minor quartz sericite lenses, is less intense (Watkins, 1990; Astacio, 1997; Lewis et al., 2000).

The Cerro de Maimón orebody is zoned, bottom to top, from primary mineralization, where the Cu:Zn ratio is close to 1:1, through a supergene enrichment zone that contains up to 12% Cu, into a near-surface oxidized zone formed by weathering and leaching of primary mineralization. The primary sulfide mineralogy is pyrite with interstitial chalcopyrite, sphalerite and tennantite (Andreu et al., 2010). Galena and Au-Ag tellurides (altaite, hessite and kernerite) are present as trace minerals (<1%) with a grain size up to 10μm. The supergene sulfide mineralogy is characterized by finely intergrown chalcocite and covellite replacing sphalerite, chalcopyrite and pyrite (Andreu, 2010). Gold in the oxide zone is extremely pure (99% Au). Silver occurs as iodargyrite (AgI) in botryoidal aggregates (Andreu et al., 2010).

Cu-Zn-Au-Ag volcanogenic massive sulfide deposits of the Early Cretaceous arc of the Villa Clara district, central Cuba

The Los Pasos Formation of the Villa Clara district (Fig. 2B) is a bimodal suite of basalt and rhyolite (Díaz de Villalvilla, 1997; Díaz de Villalvilla et al., 2003) with lesser dacite and intercalations of pyroclastic, epiclastic and sedimentary rocks (Iturralde-Vinent, 1998). Chondrite-normalized Rare Earth Element (REE) patterns for both the basalts and the rhyolites are flat with values typical of island arc tholeiites (Díaz de Villalvilla et al., 2003). Bimodal-mafic volcanogenic massive sulfide deposits of the Los Pasos Formation include San Fernando, Antonio and Los Cerros (Table 2, Fig. 2B). Other mineral occurrences include Los Mangos, Independencia, La Ceiba and Minas Ricas (Tolkunov et al., 1974b; Cabrera, 1986; Lavandero et al., 1988; Batista-González et al., 1998; Montano-Pérez et al., 1998; Bottrill et al., 2000; Russell et al., 2000). Alfonso et al. (2007) described stratiform, stratabound and stockwork copper and zinc mineralization at the San Fernando deposit. San Fernando was mined intermittently from its discovery in 1827 to its closure in 1961. Stratiform and stockwork mineralization occur near the contact between basaltic flows and felsic pyroclastic rocks.

Cu-Zn-Au-Ag volcanogenic massive sulfide deposits of the Cretaceous arc of eastern Cuba

Bimodal-mafic volcanogenic massive sulfide deposits in the Cretaceous volcanic arc of eastern Cuba (Fig. 2C) include the Elección deposit and the La Cruzada, Aníbal and Panchita mineral occurrences (Tolkunov et al., 1974b; Lavandero et al., 1988). Host rocks are greenschist facies, volcaniclastic metasedimentary rocks of the Purial Complex (Tolkunov et al., 1974b; Millán, 1996; Iturralde-Vinent, 2006). The occurrences are spatially associated with porphyritic diorite and quartz diorite intrusions. Elección, the most important deposit in the district, went into production in 1938 (Tolkunov et al., 1974b) and produced ore locally in excess of 15% copper from veins that measured up to 30 meters in length and 2.5 meters in width. Ore consists of pyrite, chalcopyrite, quartz with lesser sphalerite, galena, pyrrhotite, cubanite and local gold and silver (Tolkunov et al., 1974b).

Cu-Zn-Au-Ag volcanogenic massive sulfide deposits of the Paleogene arc of the Sierra Maestra, eastern Cuba

Bimodal-mafic volcanogenic massive sulfide deposits are also well developed in the Paleogene (Thanetian to Early Middle Eocene) Sierra Maestra volcanic arc in eastern Cuba. The Sierra Maestra arc is dominated by the El Cobre Group, a volcanic rock sequence more than 4,000m thick (Iturralde-Vinent, 1996; Cazañas et al., 1998a; Kysar-Mattietti, 2001; Rojas-Agramonte et al., 2006b). Volcanic rocks in the lower and middle sequences of the El Cobre Group are low-K island arc tholeiites similar to Early Cretaceous island arc tholeiitic series from elsewhere in the Greater Antilles (Cazañas et al., 1998b). Kysar-Mattietti (2001) suggested that island arc tholeiitic volcanism in the Sierra Maestra represents a very immature intraoceanic arc environment (an "infant arc") that never evolved beyond the first stages of subduction. Pindell et al. (2005) and García-Casco et al. (2008) suggested that arc-related

magmatism in the Sierra Maestra formed as a result of low-angle, intra-arc detachment. The Sierra Maestra volcanic arc was intruded, during the final stages of volcanism, by low- to medium-K tonalites and trondhjemites derived from the same mantle source as the volcanic rocks (Kysar-Mattietti, 2001; Rojas-Agramonte et al., 2006b).

El Cobre (Fig. 2C) is the largest volcanogenic massive sulfide deposit in the Sierra Maestra (Cazañas et al., 1998a, 2008) and the oldest copper mine in the Americas. More than 1 million tons of high grade (>14%) copper ore and over 2 million tons of >3% copper ore has been extracted since the deposit was discovered in 1530 (Tolkunov et al., 1974b). Production began in 1544 and continued intermittently until the most recent mine closure in 2000.

The El Cobre and adjacent Oro Barita deposits are located along the El Cobre fault which extends for over 40 kilometers (Fig. 2C). Three main styles of mineralization are distinguished: i) stratiform manganese, anhydrite and Au-bearing barite deposits; ii) stratabound Zn–Cu–Pb–(Au) mineralization; and iii) Cu-rich veins and stockworks (Cazañas et al., 2008). The deposits are stratigraphically controlled and are underlain by stockworks of disseminated sulphides and quartz (Cazañas et al., 1998a; Russell et al., 2000). Other volcanogenic massive sulfide deposits in the Paleogene Sierra Maestra island arc include El Infierno, La Cristina, El Pino, El Roble, Limoncito, and Precaución.

MAFIC (CYPRUS-TYPE) VOLCANOGENIC MASSIVE SULFIDE DEPOSITS

Extension across the Greater Antilles volcanic arc resulted in the development of back-arc basins and associated mafic volcanogenic massive sulfide deposits. Several of these deposits are preserved in the Northern Cuban Ophiolite Belt (Tolkunov et al., 1974b; Feoktistov et al., 1983; Lavandero et al., 1988; Cruz and Simón, 1994; Russell et al., 2000). The best examples are the Júcaro and Buena Vista deposits of the Bahía Honda region (Fig. 2A). Ore assemblages consist of pyrite, marcasite and chalcopyrite, with minor sphalerite. Other mafic volcanogenic massive sulfide occurrences are located in the Habana-Matanzas region within the Margot Formation (e.g. Margot and America) and near Camagüey (e.g. Cuba Libre deposit, Fig. 2C) (Russell et al., 2000). In addition, the Las Lajas, María Antonieta and La Más Buena mineral occurrences are hosted within Sagua La Chica ophiolitic basalt (Rivero-Manzano, 1998) and can be tentatively classified as mafic volcanogenic massive sulfides.

Sabana Potrero is a mafic volcanogenic massive sulfide mineral occurrence hosted by basaltic rocks including pillow lavas and minor hyaloclastites of the Late Cretaceous Peralvillo Formation, Dominican Republic (Fig. 3A). The basalts show a mid-ocean ridge (MORB) signature with a small negative Nb-Ta anomaly (Espaillat et al., 1989; Lewis et al., 2000) similar to the chemical signature of back-arc basalts in the Lau basin. These data indicate a back-arc basin setting for the Sabana Potrero basalts and associated volcanogenic massive sulfide mineralization.

EPITHERMAL DEPOSITS OF THE EARLY CRETACEOUS THOLEIITIC ISLAND ARC

The Cordillera Central in the Dominican Republic and Massif du Nord in Haiti represent the trace of the Greater Antilles volcanic arc across Hispaniola. Epithermal deposits are known from the entire length of the Greater Antilles volcanic arc and formed throughout its volcanic history. Early Cretaceous tholeiitic volcanic rocks host the Pueblo Viejo and Bayaguana districts in the Dominican Republic. Epithermal deposits characterized by high sulfidation mineral assemblages are best developed in the older, tholeiitic portion of the arc. Deposits characterized by low sulfidation mineral assemblages are much less important economically and are better developed in the younger, calc-alkaline portion of the arc. Epithermal deposits are plotted relative to tholeiitic and calc-alkaline volcanic and intrusive rocks on Figures 1, 2 and 3. Production and resource figures are provided in Table 3.

Au-Ag-Cu deposits of the Pueblo Viejo district, Dominican Republic

The Pueblo Viejo district (Fig. 3A, 4) has produced 5.3Moz of gold and 24.4Moz of silver from oxide ore (1975-1996) and is host to an additional 35Moz of refractory mineralization at a one gram per metric tonne (g/t) gold cutoff grade (Ruiz, 1997). Construction on a new plant facility designed to process the refractory sulfide resource began in 2008. The mine is scheduled to reopen in 2011 at a yearly production rate of one million ounces gold plus by-product silver and copper. Mineable reserves are 20.0Moz gold, 97.9Moz silver, and 388 million pounds (Mlbs) copper (Smith et al., 2008).

The Early Cretaceous Los Ranchos Formation, which hosts mineralization at Pueblo Viejo, is composed of boninites, LREE-depleted tholeiitic island arc basalts, and normal island arc tholeiites with an interval of felsic volcanism dated at 110-118Ma (Kesler et al., 2005a, b; Escuder-Viruete et al., 2007). This felsic volcanic interval which includes volcanic domes is coeval with the extrusion of tholeiitic back-arc basin basalts of the Río Verde Formation (Escuder-Viruete et al., 2010). These felsic domes consist of both intrusive and extrusive facies, both of which are well exposed in the Moore pit (Fig. 4). Field observations reported by Nelson (2000a, b) supporting an intrusive origin for dacite porphyry include: i) cross-cutting contacts between dacite porphyry

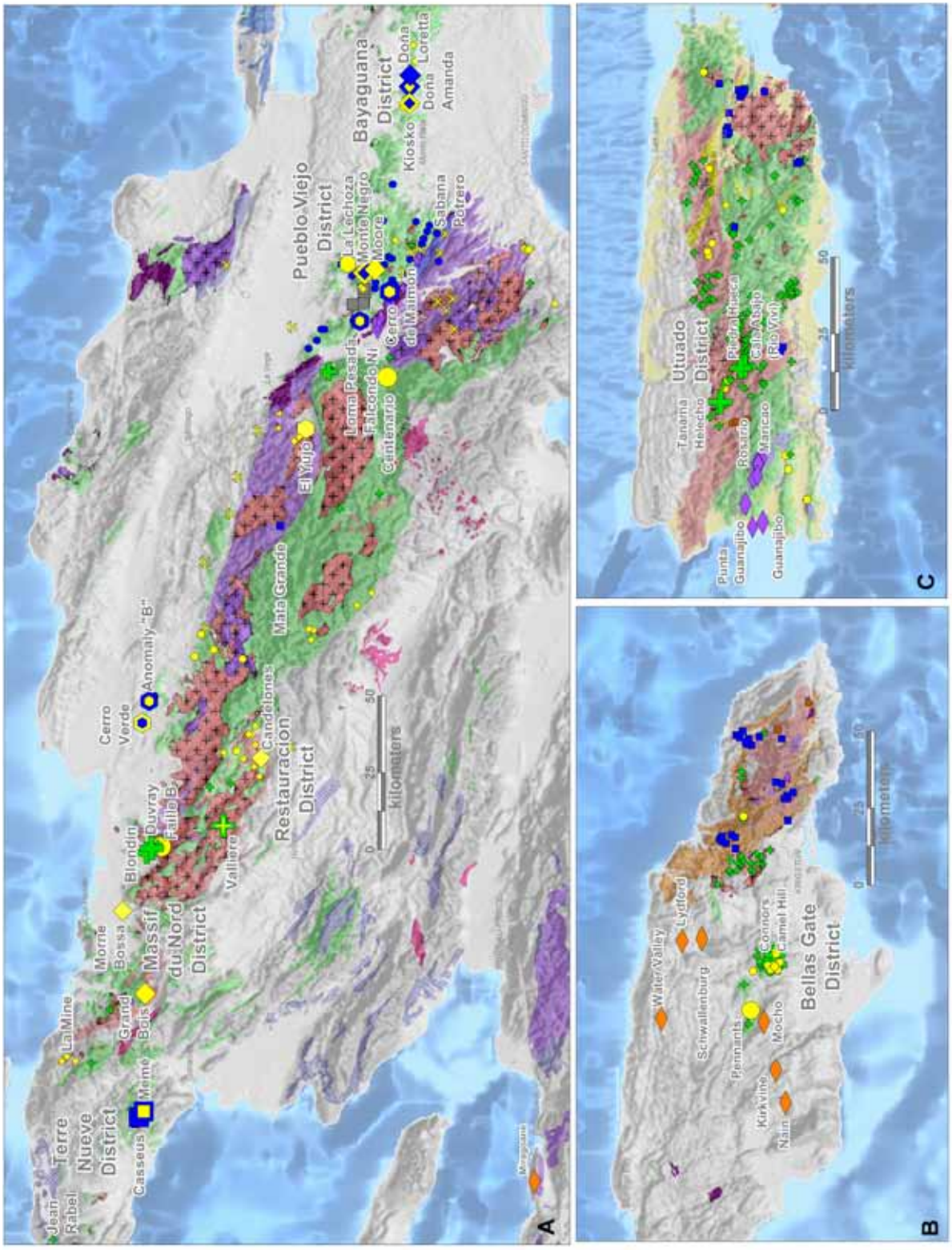

FIGURE 3 | **Detailed metallogenic maps for Hispaniola, Jamaica and Puerto Rico. A) Lateritic nickel-cobalt, volcanogenic massive sulfide, porphyry copper, skarn and epithermal deposits of the Terre Neuve, Massif du Nord and Restauración districts of the Cordillera Central and the Pueblo Viejo and Bayaguana districts of the Dominican Republic. B) Porphyry copper, epithermal gold-silver, sediment-hosted base metal and bauxite deposits of Jamaica. C) Porphyry copper, epithermal gold and lateritic nickel deposits of Puerto Rico. The geologic base map for the Dominican Republic is from Toloczyki and Ramírez (1991) modified to reflect contributions by the ongoing IGME-BGRM Sysmin mapping project. The geologic base maps for Haiti, Jamaica and Puerto Rico are from Vila et al. (1985), McFarlane (1977), and Cox and Briggs (1973), respectively. Each of the geologic maps has been modified to display tectonostratigraphic rock units. A legend for rock units and deposit types is provided on Fig. 1.**

TABLE 2 | **Volcanogenic Massive Sulfide (VMS) Deposits**

Deposit	Past Production	Current resource	Observations	References
El Cobre (Mina Grande), Cuba	300,000 tons Cu (1544 – 1998)	10 Mt at 1.5 g/t Au, 3 g/t Ag, 1.83% Cu	Bimodal mafic type, inactive mine	Krason (1999), Sherlock and Michaud (2000), Russell et al.(2000)
Cerro de Maimón, Dominican Republic	(2008 – present)	4.9 Mt at 1.2 g/t Au, 38 g/t Ag, 2.5 % Cu	Bimodal mafic type, active mine	Lewis et al. (2000)
Antonio, Cuba	50,000 tons Cu at 1.2 to 2.5% Cu (1956-1957)	2.7 Mt at 0.3 g/t Au, 18 g/t Ag, 0.64 % Cu, 3.89 % Zn	Bimodal mafic type	Krason (1999), Russell et al. (2000)
San Fernando, Cuba	38,580 ozs Au, 2,636,444 ozs Ag, 11,000 tons Cu, 28,000 tons Zn (1827 – 1961)	2 Mt at 2.3% Cu, 3.5% Zn	Bimodal mafic type	Childe (2000), Bottrill et al. (2000), Krason (1999), Sherlock and Michaud (2000), Alfonso et al. (2007)
Jucaro, Cuba	62 tons Cu	2.6 Mt at 1 g/t Au, 1.9 % Cu	Mafic type	Russell et al. (2000), Anonymous (1996)
Loma Pesada, Dominican Republic	none	1.09 Mt at 0.16 g/t Au, 4.36 g/t Ag, 2.22 % Cu, 0.77 % Zn	Bimodal mafic type	Lewis et al. (2000), Chenard (2006)
Oro (Zona) Barita, Cuba	none	1.66 Mt at 1.64 g/t Au, 5 g/t Ag, 1.55 % Cu	Bimodal mafic type	Luna (1994), Anonymous (1996)
Yagruma, Cuba	none	1.5 Mt at 2 g/t Au	Mafic type, oxide cap	
La Cristina, Cuba	none	0.8 Mt at 1.15% Cu	Bimodal-mafic type	Russell et al. (2000)
Cacarajicara, Cuba	none	0.6 Mt at 1.2% Cu	Mafic type	Russell et al. (2000)
Cerro Verde (El Anon), Dominican Republic	none	0.23 Mt at 0.15% Cu, 2.18 g/t Au, 3.84 g/t Ag	Bimodal mafic type	Chenard (2006), Childe (2000)
Anomaly "B" (El Anon), Dominican Republic	none	0.3 Mt at 1.81% Cu, 1.34% Zn, 1.1 g/t Au, 12.37 g/t Ag	Bimodal mafic type	Chenard (2006), Childe (2000)
La Lechosa, Dominican Republic	none	0.03 Mt at 2 g/t Au	Bimodal mafic type, oxide cap	unpublished estimate by RosarioResources
Los Cerros, Cuba	750 tons Cu, 2,750 tons Zn (1954-1957)		Bimodal mafic type	Russell et al. (2000)
Buena Vista, Cuba	none	0.1 Mt at 2.58% Cu	Mafic type	Russell et al. (2000)
Infierno, Cuba	none	28 Mt at 2.27% Zn, 0.63% Pb	Bimodal-mafic type	Russell et al. (2000)

and carbonaceous epiclastic sedimentary host rocks, ii) hornfels development adjacent to the dacite porphyry contact, iii) tilting of carbonaceous epiclastic sedimentary host rocks away from the dacite porphyry contact, and iv) a funnel-shaped root in cross section, also documented by Smith et al. (2008). Volcanic domes, by definition, intrude their host rocks but breach the surface and are exposed to erosion. Evidence that the dacite porphyry in the Moore pit breached the paleosurface includes a halo of quartz phenocrysts that appear as clasts in the surrounding epiclastic sedimentary rock section and, adjacent to the dome margin, slump breccias of dacite porphyry that fill channels in the epiclastic sedimentary rock section.

Volcanic domes are also reported (Nelson, 2000a) from the Monte Negro pit. Evidence includes i) development of hornfels at intrusive (dome and dike) margins, ii) multiple intrusive phases within intrusive (dome) facies, and iii) accumulation of unsorted crumble breccia aprons at extrusive (dome) margins. Photos of rock units and their structural relationships in the Moore and Monte Negro pits are provided in Kesler et al. (1981), Nelson (2000a, b) and Mueller et al. (2008).

There is abundant evidence at Pueblo Viejo that mineralization was coeval with volcanic dome emplacement and that dome emplacement was coeval with accumulation of carbonaceous epiclastic sedimentary host rocks. Massive sulfide beds accumulated in carbonaceous epiclastic sedimentary rocks adjacent to the Moore dacite porphyry dome. This same dome contains hydrothermally altered fragments and is itself hydrothermally altered and locally-mineralized (Nelson, 2000a, b). Similarly, in the Monte Negro pit, a hydrothermally altered and locally mineralized andesite dike contains hydrothermally altered and mineralized fragments (Nelson, 2000a; Mueller et al., 2008). Finally, in both pits, hydrothermally altered and mineralized clasts occur in hydrothermally altered and mineralized epiclastic sedimentary host rocks (Kesler et al., 1981; Nelson, 2000a, b).

Detailed U-Pb dating on zircon supports an Early Cretaceous age for mineralization at Pueblo Viejo. Mueller et al. (2008) dated zircon from an inter-mineral dike in the Monte Negro pit at 109±0.6Ma. Inter-mineral intrusions refer to intrusive rocks that contain mineralized fragments and are also mineralized, indicating that intrusion occurred during the mineralization event. Nelson (2000a) assigned this 109Ma inter-mineral dike to the Early Cretaceous Los Ranchos Formation in spite of its much younger K-Ar ages (46.1±1.2Ma on illite and 63.1±1.7Ma on feldspar). Early Cretaceous U-Pb ages (average of 111.56±0.45Ma) are also reported by Kesler et al. (2005a, b) for zircon from an inter-mineral dacite porphyry in the Moore pit. Mueller et al. (2008), reinterpreting the U-Pb data of Kesler et al. (2005a), proposed an age of 108.7±0.6Ma for the Moore dacite porphyry. These U-Pb dates along with the geologic observations summarized above argue for an Early Cretaceous age (108 to 112Ma) for precious metal mineralization in the Pueblo Viejo district, coeval with emplacement of volcanic domes and deposition of epiclastic sedimentary host rocks. The younger K-Ar ages at Pueblo Viejo are best understood as cooling ages reflecting slow uplift and erosion after burial metamorphism (Mueller et al., 2008).

The Pueblo Viejo deposit has long been a subject of debate as far as its origin is concerned. Published models refer to Pueblo Viejo as a Tertiary porphyry copper deposit (Hollister, 1978), a Cretaceous epithermal deposit (Kesler et al., 1981, 2005a), a Cretaceous maar-diatreme (Sillitoe and Bonham, 1984; Russell and Kesler, 1991), a Cretaceous high sulfidation deposit (Sillitoe et al., 1996), a shallow subaqueous epithermal deposit in a Cretaceous volcanic dome field (Nelson, 2000a), and a Tertiary porphyry copper lithocap (Sillitoe et al., 2006). In addition, Hannington (1993), Hannington et al. (1999) and Sillitoe et al. (1996) describe Pueblo Viejo as a high sulfidation volcanogenic massive sulfide deposit. In this review, Pueblo Viejo is interpreted to have formed in an extensional environment, on or immediately adjacent to an Early Cretaceous, tholeiitic, intraoceanic island arc. Pueblo Viejo is best described as a "hybrid deposit", with both epithermal and volcanogenic massive sulfide characteristics, in effect, a volcanogenic massive sulfide deposit that formed at shallow depth.

Mineralized epiclastic carbonaceous sediments at Pueblo Viejo are overlain by carbonate reefs of the Late Lower Albian Hatillo limestone (Myczynski and Iturralde-Vinent, 2005). Russell and Kesler (1991) described the contact as an unconformity. Sillitoe et al. (2006) described the contact as conformable and cited evidence for hydrothermal alteration in the Hatillo limestone that they attributed to the same hydrothermal system that was responsible for mineralization at Pueblo Viejo. If this observation is correct, the Late Lower Albian Hatillo limestone must have been in place during gold mineralization. The unconformity reported by Russell and Kesler (1991) may instead be interpreted as the locally-fragmental base of a fringing reef, offshore of an emerging Early Cretaceous island arc.

Modern analogs to Pueblo Viejo are reported from the western Pacific. Massive sulfide mineralization is accumulating at the Valu Fa ridge in the Lau back-arc basin, behind the Tonga-Kermadec subduction zone (Herzig et al., 1998) and in the PACMANUS hydrothermal field in the Manus back-arc basin, off the east coast of Papua New Guinea (Binns et al., 2007). At PACMANUS, precious metal-bearing massive sulfide mineralization is forming in a series of pull-apart rifts between the inactive Manus trench to the north and the active New Britain trench to the south. Pyrophyllite-bearing acid sulfate alteration and massive sulfide (precious metal-bearing chalcopyrite and sphalerite) chimneys (black smokers) occur in no fewer than five locations along a submarine ridge dominated by dacitic volcanic rocks (Binns et al., 2007). Paulick et al. (2004) interpret some of the dacitic volcanic rocks as originating from a nearby eruption center. Mineralization collected from the seafloor at PACMANUS is remarkably similar in terms of texture, composition and alteration mineralogy to disseminated and massive sulfide mineralization at Pueblo Viejo.

Au-Ag-Cu deposits of the Bayaguana district, Dominican Republic

The Bayaguana District is located approximately 60km east of Pueblo Viejo (Fig. 3A). Epithermal gold, silver and

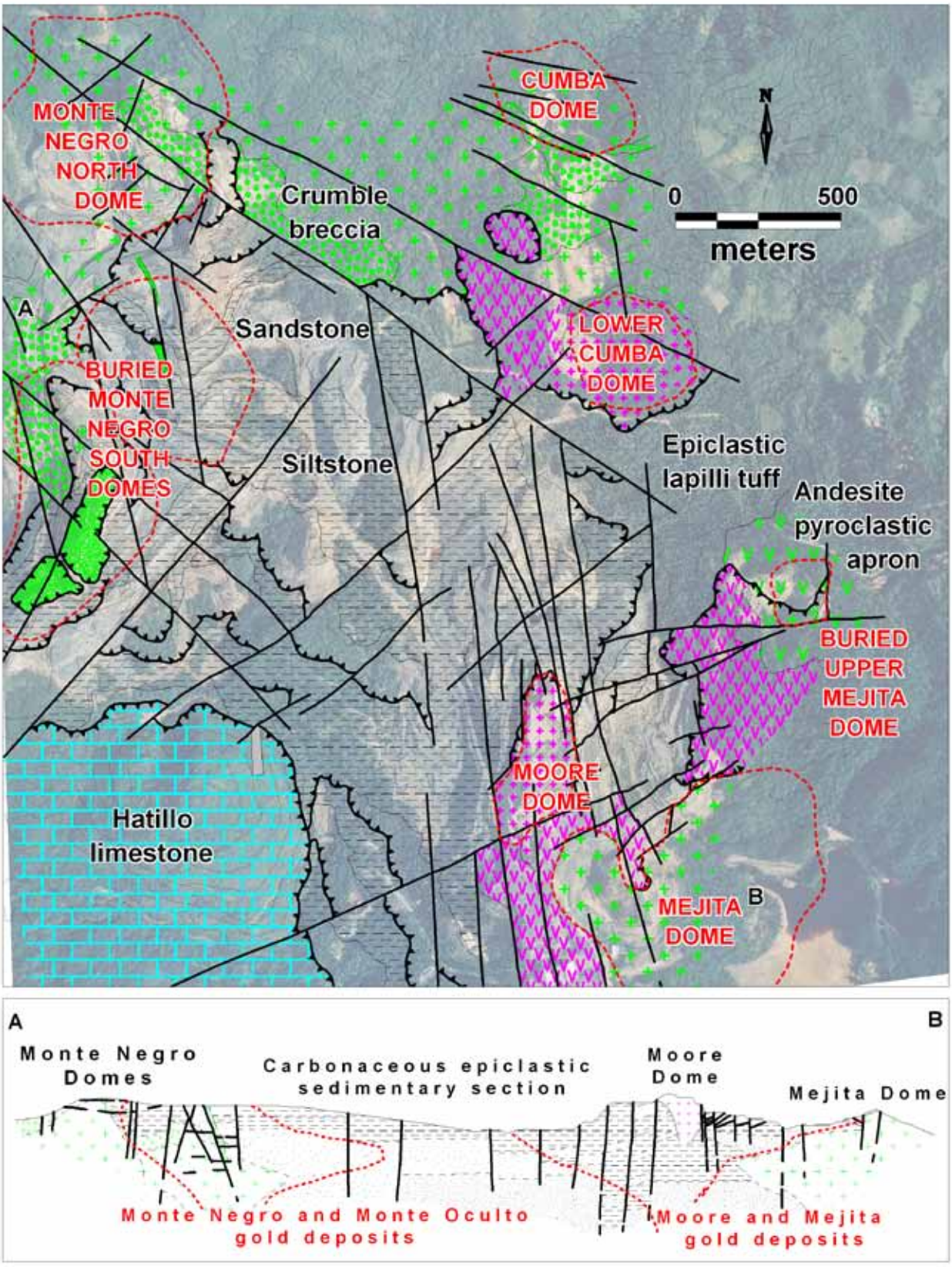

FIGURE 4 | **Simplified geologic map and cross section of the Pueblo Viejo district, Dominican Republic, plotted on an aerial photographic base showing the Moore and Monte Negro pits. Based on 1:2000 scale mapping by Nelson (2000a). Carbonaceous epiclastic sedimentary rocks are shown in grey and labelled as "siltstone" and "sandstone." Basaltic andesite of the Los Ranchos Formation is shown in green; dacite of the Los Ranchos Formation is shown in pink. The Hatillo limestone appears in blue. Volcanic domes are outlined in red.**

copper mineralization is related to a volcanic dome field (Chenard, 2006). A large hydrothermal alteration system, similar in size to the alteration system at Pueblo Viejo, covers over 50 square kilometers and is hosted by the same Early Cretaceous tholeiitic island arc volcanic rocks of the Los Ranchos Formation. Mineralization consists of hydrothermal disseminations and stringers of sulfides dominated by pyrite, chalcopyrite and bornite and locally enriched in gold and silver. Three epithermal deposits (Kiosko, Doña Amanda, and Doña Loretta) have been identified and tested by drilling (Fig. 3A). Resources are listed in Table 3.

Kiosko (Cerro Kiosko) is a silicified, tabular quartz vein swarm hosted by altered mafic volcanics that has been traced for 1.1km along strike. Mineralization consists of disseminations and stringers of pyrite and chalcopyrite with local chalcocite, bornite and enargite. At Doña Amanda, a supergene enrichment blanket (chalcocite and covellite) approximately 100 meters thick overlies strongly silicified and mineralized mafic volcanic rocks that are intruded by porphyritic dacite. Hypogene disseminated and stockwork mineralization at Doña Amanda consists of pyrite and chalcopyrite with local enargite and pyrophyllite (Chenard, 2006). Mineralization at Doña Loretta (also known as Ceja del Coco) consists of a broad zone of hydrothermal alteration associated with silicified and argillized volcanic rocks. At all three deposits, mineralization is associated with volcanic domes of felsic composition (Chenard, 2006). The volcanic domes consist of porphyritic (quartz and feldspar phenocrysts) dacite and/or rhyolite. A U-Pb date on zircon from a dacite dome at Ceja del Coco returned an age of 116 ± 0.8Ma (Escuder-Viruete et al., 2006). Volcanic dome emplacement at Bayaguana apparently occurred a few million years earlier than volcanic dome emplacement at Pueblo Viejo (108 to 112Ma).

Throughout the Bayaguana district, host rocks closely resemble those of the Pueblo Viejo district. Similar sequences of thin- to medium-bedded epiclastic carbonaceous siltstones and sandstones with minor conglomerates accumulated in a basin marginal to a volcanic dome field. As at Pueblo Viejo, terrestrial plant fossils are common. The Hatillo limestone that overlies the epiclastic carbonaceous sedimentary section at Pueblo Viejo also overlies the epiclastic carbonaceous section in the Trinidad area of the eastern Bayaguana district. Although no large metallic mineral deposits have been discovered, hydrothermal alteration and mineralization in the Bayaguana district is similar to that encountered at Pueblo Viejo. High sulfidation mineral assemblages occur with epithermal vein and disseminated Au-Ag-Cu mineralization in both districts. The Bayaguana district indicates that felsic volcanic dome fields and related gold-, silver- and copper-bearing epithermal systems developed at more than one location along the length of the Early Cretaceous tholeiitic island arc rocks of the Los Ranchos Formation.

EPITHERMAL DEPOSITS OF THE LATE CRETACEOUS TO EOCENE CALC-ALKALINE ISLAND ARC

Early Cretaceous tholeiitic volcanism evolved in Late Cretaceous and Paleogene time to calc-alkaline composition (Lewis and Draper, 1990; Lewis et al., 1991, 2000; Escuder-Viruete et al., 2006). Today, the axis of the Late Cretaceous Greater Antilles volcanic arc is marked by a chain of calc-alkaline plutons that extends from Cuba to Puerto Rico (Fig. 1). These plutons have associated porphyry copper mineralization and intrude suites of Late Cretaceous calc-alkaline volcanic arc rocks. Epithermal deposits are strongly developed in these Late Cretaceous volcanic arc rocks in the western Cordillera Central (Restauración district) of the Dominican Republic and its extension into the Massif du Nord district in Haiti, and also in the Late Cretaceous volcanic arc rocks of the Camagüey district of east-central Cuba (Fig. 2 and 3).

Au-Ag-Cu deposits of the Restauración district, Dominican Republic

The Restauración district is located in the western Cordillera Central of the Dominican Republic along the border with Haiti (Fig. 3A). Mineral deposits and prospects in the district have been described by Amarante et al. (1989) and Amarante and Lewis (1996). The mineralization, which is typically polymetallic (Cu-Zn-Pb-Au-Ag), occurs in volcanic and pyroclastic rocks of the Upper Tireo Formation (Jiménez and Lewis, 1989; Louca, 1990; Lewis et al., 1991). Its association with dacitic rocks (quartz-plagioclase porphyries) and the occurrence of barite and massive barite-sulfide mineralization is a characteristic feature of the epithermal mineralization in this district and westwards into Haiti. Barite and sulfides occur together in various mineral associations, textures and proportions, with sulfides forming up to 70% by volume in massive ore. An intimate association of precious metals with barite is a typical feature of the deposits. At Candelones, the largest deposit discovered to date (Fig. 3A, Table 3), vuggy quartz veins containing gold along with pyrite, enargite and barite are surrounded by a gold-bearing vein stockwork and by disseminated mineralization. At shallow levels, gold-barite veins and barite breccias grade into massive, structurally-controlled, barite replacements. Multiple phases of alteration include an early illite-pyrite stockwork accompanied by dickite, kaolinite and alunite within or in close proximity to the orebody. The Savanne La Place prospect, located eight kilometers northwest of Candelones

on the Haitian side of the border shows similar features at the surface and likely belongs to the same hydrothermal system as Candelones.

The Cerro Montazo, Guano and Naranjo prospects are located four to eight kilometers east-northeast of Los Candelones (Fig. 3A). Hydrothermal alteration consists of pyrophyllite-bearing zones of massive chalcedonic silicification, vuggy silica, sulfide stockworks, massive barite and barite veins that grade outwards to dickite and illite at the margins. The hydrothermal system is cut by, at least, two well-defined northwest-striking structures. At Naranjo, gold has been confirmed by trenching across veins and lenses of dense silica-barite alteration. At Guano, gold has also been confirmed by trenching in alteration that consists of vuggy silica, quartz-chalcopyrite veins and massive barite. Gold at Montazo occurs in barite lenses and in argillically altered rock.

Au-Ag-Cu deposits of the Massif du Nord, Haiti

The epithermal mineral deposits in the Massif du Nord (Fig. 3A) have the same general characteristics, particularly the association with barite and barite sulfide mineralization, as seen in the Restauración district described above. Many of the individual deposits and prospects were described by Louca (1990).

Grand Bois is the largest epithermal deposit known to date from the Massif du Nord (Fig. 3A). The resource estimate (Table 3) is based on drilling conducted by the United Nations (1978-1984) which defined a tabular body of mineralized and oxidized volcanic rock with a thickness of approximately 20 meters. In recent years, drilling below the oxide zone has reportedly intersected chalcocite, covellite and chalcopyrite. Morne Bossa (Milot) located south of Cap-Hatien in the Milot-Grande Rivière area is also a gold oxide deposit (Table 3). Louca (1990) states that the mineralization took place on the edge of a dacite porphyry.

Faille B is a low sulfidation epithermal Au-Ag quartz vein deposit (Fig. 3A) that occurs along a major, northwest-striking fault zone. Host rocks include a tabular, wedge-shaped body of micro-tonalite which intrudes a section of metamorphosed mafic to ultramafic rocks (Morne Cabrit Series). Mineralization consists of lenticular veinlets, sheeted veins and five sets of quartz veinlets. Most veins strike northwest, parallel to the regional host fault. Quartz is the principal gangue mineral; the most abundant sulfide is pyrite which is accompanied by smaller amounts of chalcopyrite and sphalerite. Gold occurs as the native metal in quartz as grains that measure 2 to 50 microns in diameter.

La Mine prospect refers to three significant occurrences of epithermal gold, silver and base metal mineralization located in the northernmost exposures the Late Cretaceous volcano-sedimentary sequences of the La Mine Series in the Massif du Nord (Fig. 3A). The principal mineralization is a 3km long northwest trending stockwork vein system consisting of steeply dipping fault strands varying in width from a few meters to 100m wide (Louca, 1990). Polymetallic (Cu, Pb, Zn, Au, Ag) sulfide mineralization, confirmed by trenching, is associated with barite and with barite-sulfide replacements that, locally, cut across the argillically altered fault zone.

Au-Ag-Cu deposits of the Camagüey district, Cuba

Epithermal deposits exhibiting both low (e.g. Jacinto and Florencia) and high sulfidation (e.g. Golden Hill) sulfide mineral assemblages are found in the Camagüey district (Fig. 2C) of Cuba (Lavandero and Bravo, 1994; Barroso et al., 1998; Lugo-Primelles et al., 1998; Simon et al., 1999; Kesler et al., 2004; López-Kramer et al., 2006). The deposits are hosted by calc-alkaline volcanic rocks and surround the Camagüey batholith, a composite intrusion that consists of gabbro-tonalite, syenite, and granodiorite (see section on porphyry copper deposits described below).

Jacinto (Fig. 2C) is a typical epithermal vein deposit with adularia-sericite alteration and a low sulfidation sulfide mineral assemblage. Six crustiform-banded veins measuring up to a kilometer in length contain free gold and gold tellurides in a gangue of quartz, calcite, adularia and minor pyrite. An alteration halo of K-feldspar plus sericite envelops the veins. Host rocks are pillowed basalt, andesite and latite flows of the calc-alkaline Camujiro Formation (Simon et al., 1999; Kesler et al., 2004). Florencia is similar in terms of its gangue mineralogy (quartz, carbonate and chlorite) but is richer in base metal sulfides including chalcopyrite, sphalerite and galena (López-Kramer, 1988).

Golden Hill (Fig. 2C) consists of breccias cemented by two stages of quartz, pyrite and enargite. The first stage is accompanied by kaolinite, zunyite and diaspore. The second stage contains tungsten and bismuth and is accompanied by natroalunite, pyrophyllite and barite (Kesler et al., 2004). Golden Hill demonstrates that epithermal precious metal deposits with high sulfidation mineral assemblages are not restricted to the Early Cretaceous tholeiitic history of the island arc; they also occur in Late Cretaceous calc-alkaline volcanic rocks.

PORPHYRY COPPER AND SKARN DEPOSITS

Porphyry copper deposits of the Greater Antilles are small and, to date, none have been mined. All of the known deposits are associated with calc-alkaline plutons and many are surrounded by clusters of epithermal precious metal occurrences (e.g. Camagüey district of Cuba, Massif

du Nord district of Haiti, Restauración district, Dominican Republic and Bellas Gate district of Jamaica). Porphyry copper and skarn deposits are plotted on Figs. 1, 2 and 3; resource information is provided in Table 4.

Whole rock geochemical data for the associated Late Cretaceous calc-alkaline intrusive rocks of the Greater Antilles exhibit low-K, medium-K and high-K signatures even in a single intrusive complex (Kesler et al., 1975; Lidiak and Jolly, 1996). Most radiometric dates published for plutonic rocks associated with porphyry copper mineralization in the Greater Antilles (Hollister, 1978; Kesler, 1978) are K-Ar dates from the 1970's. As is the case at Pueblo Viejo, K-Ar dates may, in some cases, reflect the age of uplift rather than the age of emplacement and should be interpreted with caution.

Cu-Au porphyry deposits of the Utuado district, Puerto Rico

The Tanamá-Helecho, Piedra Hueca, and Cala Abajo (Río Viví) porphyry copper deposits of Puerto Rico (Fig. 3C) are associated with the Utuado batholith which is zoned from a core of quartz monzonite and granodiorite outward into quartz diorite (Hollister, 1978) and tonalite porphyry (Cox, 1985). The Tanamá-Helecho deposit is associated with tonalite porphyry dikes and stocks that were intruded late in the history of the Maastrichtian Utuado batholith (Cox, 1985) or during a separate Eocene pulse of low-K magmatism (Barabas, 1982). Mineralization consists of stockworks of quartz, chalcopyrite and magnetite with associated potassic alteration, both as K-feldspar and as hydrothermal biotite.

Cala Abajo (Río Viví) and Piedra Hueca are hosted by quartz diorite stocks. The deposits exhibit feldspar-stable hydrothermal alteration along with secondary biotite. Magnetite-bearing quartz stockworks contain chalcopyrite and, locally, molybdenite. Most of the porphyry copper deposits of Puerto Rico were discovered in the late 1950's and drill tested in the early 1960's. None have been developed. Open pit mining has been precluded by law in Puerto Rico since 1996.

Cu-Au porphyry deposits of the Massif du Nord district, Haiti

Porphyry copper mineralization, closely associated with epithermal mineralization of the same Late Cretaceous age, is widespread in the Massif du Nord district of Haiti. Host rocks are plutons of quartz diorite to tonalite composition, the shallow-level expression of the Loma de Cabrera hornblende tonalite batholith that straddles the border between Haiti and the Dominican Republic. As pointed out by Louca (1990), porphyry copper deposits of the Massif du Nord district failed to develop the concentric shells of alteration and mineralization that are typical of porphyry copper deposits and they also lack strong feldspathic alteration. Porphyry copper deposits of the Massif du Nord are characterized by propylitic alteration (epidote, chlorite, albite, quartz and calcite).

The Blondin and Douvray porphyry copper deposits (Fig. 3A) fall on a northwest trending copper-rich zone about 7 kilometers long (Niccolini, 1977). Copper sulfides occur as disseminations and fracture fillings in volcanic rocks and in porphyritic to aplitic quartz diorite intrusive rocks. Sulfides include pyrite, chalcopyrite, bornite, enargite, chalcocite and smaller amounts molybdenite which are preserved beneath an oxide zone that averages about 20 meters in thickness but, locally, reaches 60 meters in thickness.

Two porphyry copper occurrences (Valliere and Mont Organisé) are located in the Massif du Nord, near the western margin of the Restauración district (Fig. 3A). Only the Valliere deposit has a (small) established resource (Table 4). Alteration and sulfide mineralization at the Mont Organisé porphyry copper prospect, 13km east-northeast of Valliere, appears to be confined to the contact zone between a porphyritic tonalite and rocks of the Upper Tireo Group (Louca, 1990). The Treuil porphyry copper prospect, located twelve kilometers south of the La Mine prospect (Fig. 3A), occurs in a quartz diorite stock.

Cu-Au porphyry deposits of the Restauración district, Dominican Republic

Three porphyry copper prospects occur in the northwest Restauración district (Fig. 3). At the El Corozo prospect, situated along the Lebon pluton on the border with Haiti, a multiphase chalcopyrite-pyrite-quartz-magnetite stockwork occurs in silicified granodiorite. Hydrothermal alteration at El Corozo includes secondary biotite and K-feldspar along with (later) epidote and chlorite. The Jiménez occurrence, located 2-3km northeast of the town of Restauración, is centered on three adjoining quartz-feldspar porphyry (dacite) domes (Jiménez, Poco Negro and a third unnamed dome) that intrude basaltic to andesitic flows, andesitic lapilli tuff, accretionary lapilli tuff and a calcareous sedimentary sequence. The mineralization occurs at the base of the domes and is characterized by gold-bearing high-grade chalcopyrite veins. Neita, located about 1km south of Jiménez, is a northwest trending copper-rich zone, the extent of which is based on anomalous values of Cu, Mo and Au in soils.

Several clusters of epithermal gold occurrences are peripheral to these porphyry copper prospects including a NW trending 3km long anomalous As-Ba-Cu-Zn-Au signature in soils located about 1km west of the Neita prospect.

TABLE 3 | **Epithermal Deposits**

Deposit	Past production	Current resource	Observations	References
Moore, Pueblo Viejo District, Dominican Republic	3,521,705 ozs Au, 16,132,220 ozs Ag (1975-1999)	135.1 Mt at 2.9 g/t Au, 14.3 g/t Ag, 0.1 % Cu	High sulfidation, under construction	Ruiz (1997), Smith et al. (2008), Nelson (2000a, b)
Monte Negro, Pueblo Viejo District, Dominican Republic	1,760,852 ozs Au, 8,066,110 ozs Ag (1980-1999)	70.6 Mt at 3 g/t Au, 15.8 g/t Ag, 0.06 % Cu	High sulfidation, under construction	Ruiz (1997), Smith et al. (2008), Nelson (2000a, b)
Grand Bois, Haiti	none	4.5 Mt at 2.3 g/t Au	High sulfidation	Louca (1990), Sillitoe et al. (1996)
Morne Bossa, Haiti	none	2.0 Mt at 2.25 g/t Au	High sulfidation	Louca (1990), Sillitoe et al. (1996)
Candelones, Restauración District, D.R.	none	2.04 Mt at 1.1 g/t Au	High sulfidation	Lamouille et al. (1998), Amarante et al. (1989)
Doña Amanda, Bayaguana District, D.R.	none	43.2 Mt at 0.45% Cu, 0.23 g/t Au, 1.07 g/t Ag	High sulfidation	Chenard (2006)
Golden Hill, Camagüey District, Cuba	none	10.5 Mt at 0.22% Cu, 0.6 g/t Au	High sulfidation	Kesler et al. (2004), López-Kramer et al. (2007)
Centenario (El Higo), Dominican Republic	none	2.5 Mt at 5.5 g/t Au	Low sulfidation	Listin Diario, Santo Domingo, June 21, 1997
(Cerro) Kiosko, Dominican Republic	none	4.92 Mt at 2.01 g/t Au, 5.17 g/t Ag, 0.98 % Cu	High sulfidation	Chenard (2006)
Doña Loretta (Ceja del Coco), Dominican Republic	none	8.2 Mt at 0.5% Cu	High sulfidation	Chenard (2006)
Faille B, Haiti	none	0.5 Mt at 15.5 g/t Au	Low sulfidation	Louca (1990), Espaillat (1996)
Jacinto, Cuba Camagüey District, Cuba	none	1.1 Mt at 4.73 g/t Au	Low sulfidation	López-Kramer et al. (2007)
Florencia, Cuba Camagüey District, Cuba	none	0.837 Mt at 5.37 g/t Au	Low sulfidation	López-Kramer et al. (2006, 2007)
Pennants (Main Ridge), Jamaica	12,000 ozs Au (2001 – 2002)	75,500 tons at 20.4 g/t Au	Low sulfidation	Garrett et al. (2004)

Cu-Au skarn and porphyry deposits of the Terre Neuve district, Haiti

The Memé and Casseus copper-gold skarn deposits of Haiti (Fig. 3A) are found in limestone pendants within the Terre Neuve intrusion, a composite calc-alkaline pluton of medium to high potassium content (Lidiak and Jolly, 1996) with quartz monzonite, granodiorite and quartz diorite phases (Kesler, 1968; Harnish and Brown, 1986). Production dates back to the early 1700's; neither mine is currently active. Gangue minerals consist of garnet, diopside, tremolite, chlorite, wollastonite, epidote, magnetite and hematite. Sulfides include chalcopyrite, pyrite, chalcocite, digenite, covellite, bornite and, locally, molybdenite (Louca, 1990).

Terre Neuve intrusive rocks lie along a northwest trending structure in the Terre Neuve Massif separate from the Massif du Nord to the north. These intrusive rocks are distinctly more K-rich and have a higher content of large-ion lithophile elements (LILE) than those of the western Cordillera Central and Massif du Nord (Lidiak and Jolly, 1996). Their compositions are similar to plutonic rocks from central and eastern Jamaica, central Cuba and the Nicaraguan Rise (Lewis et al., this volume). A single K/Ar date of 66Ma has been published for the Terre Neuve

intrusions (Kesler and Fleck, 1967), younger than most K/Ar and Ar/Ar dates for intrusive rocks in the Massif du Nord and Cordillera Central (Kesler et al., 1991; Escuder-Viruete et al., 2006). This evidence indicates that the magmatism responsible for the Terre Neuve intrusions and Cu-Fe skarn deposits is from a different source than that of the western Cordillera Central-Massif du Nord tonalite plutons, but that it is more evolved and younger in age.

The Jean Rabel (Vert de Gris) porphyry copper-molybdenum prospect is located on the northwest extension of the Terre Neuve massif in an anticlinal structure (Cheilletz, 1976; Cheilletz et al., 1978). Stockwork and disseminated mineralization occur in a complex of porphyritic stocks and dikes. The intrusive rocks include, from oldest to youngest, locally porphyritic hornblende-biotite tonalite, rhyodacite porphyry intrusions and intrusive breccias, and dikes of hornblende andesite porphyry. The sulfide mineral assemblage includes pyrite, bornite, chalcopyrite and minor molybdenite. Copper and molybdenum mineralization occurs with potassic alteration characterized by green to brown secondary biotite, potassium feldspar and apatite at the contact between intrusive rocks and andesite, and, in intrusive rhyodacite breccias. In addition to potassic alteration, phyllic alteration (quartz-sericite-pyrite) and propylitic alteration (chlorite and epidote) are also present. A whole-rock Rb/Sr isochron age of 67.3±4Ma is interpreted as the age of intrusion. A K/Ar isochron age of 57.7±5Ma on four biotite separates is interpreted as the age of mineralization (Cheilletz et al., 1978).

Cu-Au porphyry and iron skarn deposits of the Camagüey and Villa Clara districts, Cuba

Several small porphyry copper deposits are located in the Camagüey district, within a cluster of epithermal precious metal occurrences (Fig. 2C). Examples include the Tres Casas, Palo Seco and Guaimaro Cu-Mo-Au porphyry deposits (Torres et al., 2005), and La Union Au±Cu prospect (Ulloa-Santana et al., 2011). These porphyry deposits (Table 4) are related to a plutonic complex that, as originally defined by Pérez-Rodríguez and Sukar (1997) and modified by Hall et al. (2004), includes three main compositional phases. Recent U/Pb SHRIMP dating on zircons (Rojas-Agramonte, 2006a; Stanek et al., 2009) shows that syenite was the earliest intrusive phase (107-99Ma) followed by granodiorite (~85Ma). Acid magmas of the plagiogranite (trondhjemite) series (81-75Ma) were the last to crystallize. Comparison of the chemistry of the volcanic rocks with those of the plutonic rocks shows that the same magmas were the source of both intrusive and extrusive phases (Piñero et al., 1997; Mari, 1997). Hall et al. (2004) have explained the relatively young Ar/Ar ages, which have a narrow range of ca. 75–70Ma, for both the volcanic and intrusive rocks, as related to rapid cooling and uplift in the Late Cretaceous.

Skarns in the Villa Clara district (Fig. 2B) and in the Camagüey district (Fig. 2C) were formed by the recrystallization of limestone intervals within volcanic and volcaniclastic rocks of Cretaceous age near the contact with calc-alkaline plutons of intermediate composition (see Moreira et al., 2001 for a review). Skarn deposits in the Villa Clara district are found mainly on the western flank of a calc-alkaline batholith (Fig. 2B). Gangue minerals at the Guaos deposit include garnet, pyroxene, chlorite, epidote, wollastonite, calcite, siderite, and magnetite; sulfide minerals include pyrite, chalcopyrite, galena and sphalerite (Tolkunov et al., 1974b; Batista-González et al., 1998). Past producers from the Villa Clara district include Guaos (with up to 11.7g/t Au) and Loma Alta (Fig. 2B). The Felipita and Magarabomba iron deposits (Fig. 2C), in the Camagüey district, are composed of magnetite and hematite plus minor chalcopyrite and covellite with a gangue assemblage that includes epidote, garnet and calcite.

Cu-Au porphyry deposits of the Bellas Gate district, Jamaica

Two small porphyry copper deposits (Connors and Camel Hill) are known from the Central Inlier of Jamaica (Fig. 3B), an erosional window that exposes Cretaceous tholeiitic island arc (IAT) basalts, minor pyroclastic rocks and interbedded volcaniclastic sedimentary rocks. The volcanic rocks are intruded by a Late Early to Early Late Cretaceous suite of diorite, granodiorite and tonalite dikes, sills and stocks (Mitchell, 2003). A hornfels surrounding the granodiorite stock at Ginger Ridge (Porter, 1970) has given a K/Ar isochron age of 85±9Ma (Lewis et al., 1973). At Connors and at Camel Hill, the Ginger Ridge granodiorite stock is partially unroofed and is host to magnetite-bearing quartz veins and stockworks. Mineralization consists of vein and disseminated pyrite, chalcopyrite, and minor sphalerite locally enriched by secondary copper sulfide (chalcocite). The ore bodies occur within a zone of widespread propylitic alteration that surrounds two, northwest-striking, structurally-controlled corridors of phyllic alteration and hydrothermal biotite-bearing potassic alteration. The porphyry copper deposits are surrounded by a cluster of base- and precious metal-bearing quartz veins.

Iron skarn deposits of the Hierro Santiago district, Sierra Maestra, Cuba

Iron oxide deposits classified here as skarns are found in the eastern part of the Sierra Maestra volcanic arc (Lavandero et al., 1988; Cazañas et al., 1989;

TABLE 4 | **Porphyry Copper and Skarn Deposits**

Deposit	Past production	Current resource	Observations	References
Douvray, Haiti	none	180 Mt at 0.59% Cu	Cu-Au Porphyry	Espaillat (1996), Louca (1990)
Tanamá and Helecho, Puerto Rico	none	126 Mt at 0.64 % Cu	Cu-Au Porphyry	Hollister (1978), Cox (1985)
Cala Abajo (Río Viví), Puerto Rico	none	71 Mt at 0.82 % Cu	Cu-Au Porphyry	Hollister (1978), Barabas (1982)
Valliere, Haiti	none	84 Mt at 0.44% Cu, 1.5 g/t Ag	Cu-Au Porphyry	Espaillat (1996)
Blondin, Haiti	none	50 Mt at 0.56 % Cu	Cu-Au Porphyry	Espaillat (1996), Louca (1990)
Piedra Hueca, Puerto Rico	none	33 Mt at 0.82 % Cu	Cu-Au Porphyry	Hollister (1978), Barabas (1982)
Arimao, Cuba	none	60 Mt at 0.3 g/t Au, 18 g/t Ag, 0.31 % Cu	Cu-Au Porphyry	
Camel Hill, Jamaica	none	13.177 Mt at 0.17 g/t Au, 0.35 % Cu	Cu-Au Porphyry	Fenton (1981)
Connors, Jamaica	none	6 Mt at 0.5% Cu	Cu-Au Porphyry	Fenton (1981)
Palo Seco, Cuba	none	42 Mt at 0.15% Cu	Cu-Au Porphyry	
Guaimaro, Cuba	none	103 Mt at 0.1% Cu, 0.011% Mo	Cu-Au Skarn	
Memé, Haiti	97,000 ozs Au, 30,000 ozs Ag (1960-1971)	1.5 Mt at 2 g/t Au, 2 % Cu	Cu-Au Skarn	Louca (1990)
Casseus, Haiti	none	2 Mt at 1.35% Cu	Cu-Au skarn	Harnish and Brown (1986)
Daiquirí (Hierro Santiago) District, Cuba	6,577,457 tons Iron ore (1906-1912)	40 Mt at 40% to 45% Fe	Iron skarn district	Cazañas et al. (1989), Moreira et al. (2001)
Maimón-Hatillo District, Dominican Republic	700,000 tons iron ore (1950-1958)		Iron skarn distict	Bowin (1966)
Mata Grande, Dominican Republic	unknown (minor)		Cu skarn	

Pérez-Rodríguez and Santa Cruz, 1991; Méndez et al., 1994; Sánchez-Cruz et al., 1998; Moreira et al., 2001). Mineralization occurs in volcanic rocks near a contact with plutons of quartz diorite, tonalite and gabbro (Kysar-Mattietti, 2001). The main mining area is the Daiquirí or Hierro Santiago district, where the La Grande, Antoñica, Concordia, Folia, Yuca, El Norte, El Descanso, Vinent, Fausto, Falcón, Falconera, and Chalía mines are located (Fig. 2C). The deposits were mined from 1890 to 1947 with 6,577,457 tons of ore produced between 1906 and 1912 (Moreira et al., 2001); resources are in excess of 40Mt containing 40-45% total iron (Cazañas et al., 1989)

Skarn deposits of the Sierra Maestra have some affinity to iron oxide copper-gold (IOCG) deposits. Sillitoe (2003), Williams et al. (2005) and Pollard (2006) describe iron oxide copper-gold deposits in more detail. In the Sierra Maestra, host rocks are mainly volcanic and volcaniclastic (Pérez-Rodríguez and Santa Cruz, 1991; Moreira et al., 2001) but calc-silicate minerals are present. Iron oxide (magnetite-hematite) is the dominant ore mineral; copper sulfides are present but are uncommon; gold is present as native gold. Calc-silicate minerals include andradite-grossularite with a small amount of pyroxene, calcic amphibole and, in the more distal parts, epidote. Some skarn deposits of the Sierra Maestra contain rare earth minerals.

TABLE 5 | **Volcanogenic ("Cuban-type") Manganese Deposits**

Deposit	Past production	Current resource	Observations	References
Cristo, Ponupo, Los chivos	10 Mt of 35% Mn during the 1940's		Volcanogenic (Cuban-type) Mn	Mosier and Page (1998), Cazañas and Melgarejo (1998), Cazañas et al. (2003)
La Margarita	Included above		Volcanogenic (Cuban-type) Mn	Cazañas and Melgarejo (1998) Cazañas et al. (2003)

Iron skarn deposits of the Maimón-Hatillo district, Dominican Republic

Iron oxide deposits were mined from a dozen small deposits in the Maimón-Hatillo district between 1950 and 1958 (Bowin, 1966). These deposits are located between the Pueblo Viejo district and the Cerro de Maimón deposit (Figs. 1, 3A). In situ mineralization is reported from two deposits, Sabana Grande and Las Lagunas; the others consisted of magnetite boulders (weighing up to twelve tons) embedded in lateritic clay (Bowin, 1966). The in situ deposits consisted of pod-shaped replacements of magnetite (90%) and hematite (10%) in massive limestone. All of the deposits are close to exposures of diorite. At Las Lagunas, magnetite mineralization occurs at the contact between limestone and dikes of diorite. Koschmann and Gordon (1950), Bowin (1966) and Muntean et al. (2007) interpret these deposits as skarns. The age of mineralization is Late Eocene (Kesler et al., 1981) to Early Oligocene (Nelson, 2000a) based on K-Ar dating of associated diorite.

VOLCANOGENIC (CUBAN-TYPE) MANGANESE DEPOSITS

Important manganese deposits formed in the Paleocene to Middle Eocene Sierra Maestra volcanic arc of eastern Cuba (Park and Cox, 1944; Simons and Straczek, 1958; Sokolova et al., 1974; Lavandero et al., 1988; Cazañas and Melgarejo, 1998; Cazañas et al., 2003). Production during the 1940's is estimated at 10Mt at an average grade of 35% Mn (Mosier and Page, 1998; Cazañas et al., 1998, 2003). Manganese deposits of the Sierra Maestra are shown on Fig. 2C; production and resources are listed in Table 5.

Manganese mineralization occurs at several stratigraphic levels in the volcano-sedimentary El Cobre Group, but is best developed at the top of the sequence, near the contact with overlying sedimentary rocks deposited in post-volcanic basins. Manganese ore consists predominantly of botryoidal todorokite and other oxides. According to Cazañas et al. (2003), the mineralization can be interpreted as volcanogenic-exhalative in origin, and was formed in short-lived intra-arc basins. Mosier and Page (1998) use Cuban manganese deposits as a reference model for volcanogenic manganese mineralization. In these deposits, the following lithofacies have been established from the bottom to the top (Cazañas et al., 2003): i) hydrothermal alteration zones at the wall ("green rocks"), ii) jasperoids, iii) massive Mn oxides mineralization ("rich ores"), iv) pyroclastic rocks cemented by Mn mineralization, and v) hematitic hydrothermal alteration bodies.

OROGENIC DEPOSITS

Accretion of the Greater Antilles volcanic arc to the North American margin began in the Late Campanian (García-Casco et al., 2008). Collision may have also triggered the emplacement of metamorphic core complexes (e.g. the Pinos and Escambray terranes). During the suturing process, orogenic deposits formed and were later exposed by erosion. Emplacement of ophiolites in eastern Cuba occured during the latest Cretaceous and Early Danian (Iturralde-Vinent et al., 2006). In western and central Cuba, thrusting of ophiolite onto the Bahamian borderlands took place during the Paleocene to early Late Eocene (Iturralde-Vinent, 1998; Iturralde-Vinent et al., 2008).

Three types of orogenic deposits are recognized: i) orogenic gold deposits, ii) "listvenites" or gold veins deposited in silica-carbonate-altered ultramafic rock, and iii) tungsten deposits. None are in production and only the orogenic gold deposits are known to host substantial resources. Deposits are located on Figs. 1 and 2; past production and resources appear in Table 6.

Orogenic gold deposits

Orogenic gold deposits are known from the entire length of the suture zone that marks the northern margin of the Caribbean Plate. Delita, located in the Pinos Terrane on the Isla de la Juventud off the south coast of western Cuba (Fig. 1) is classified by Bortnikov et al. (1989, 1993)

TABLE 6 | **Orogenic Deposits**

Deposit	Past production	Current resource	Observations	References
Delita, Cuba	unknown (1950's)	18.9 Mt at 2.87 g/t Au, 22.7 g/t Ag	Orogenic Au	López-Kramer et al. (2008a, 2008b), Bermudez-Lugo (2004), Torres (1995), Robertson (1996)
Nuevo Potosí, Cuba	102,724 ozs Au (1904-1990)	83,330 tonnes at 7.8 g/t Au	Listvenite Au	López-Kramer et al. (1998, 2008b), Anonymous (1997)
Melonera, Cuba	none	61,450 tonnes at 28.3 g/t Au, 7.3 g/t Ag	Listvenite Au	López-Kramer et al. (1998, 2008b), Anonymous (1997)
Descanso, Cuba	none	13,840 tonnes at 49.5 g/t Au, 11.8 g/t Ag	Listvenite Au	López-Kramer et al. (1998, 2008b)
Agrupada, Cuba	none	14,200 tonnes at 13 g/t Au	Listvenite Au	López-Kramer et al. (2008b), Anonymous (1997)
Reina Victoria, Cuba	none	1,420 tonnes at 1.42 g/t Au	Listvenite Au	López-Kramer et al. (2008b), Anonymous (1997)
Mina Lela, Cuba	none	0.8 Mt at 0.6% WO_3	orogenic W	Page and McAllister (1944)

as mesothermal. Mineralization consists of quartz veins (0.2-0.5 meters thick) and sulfidic, silicified breccias (Bortnikov et al., 1989) that fill a fault zone within the metamorphic host rocks (López-Kramer et al., 2008a, 2008b). The main gold-bearing mineral is arsenopyrite containing between 5.4 and 56ppm gold (Bortnikov et al., 1993) but native gold is also present. Other sulfides present in minor amounts include sphalerite, tetrahedrite, boulangerite, jamesonite, galena, silver sulfosalts and stibnite (López-Kramer, 1988; López-Kramer et al., 1998).

Listvenite gold deposits

Gold deposits hosted by altered serpentinite in Cuba have been described as listvenites (Cabrera and Tolkunov, 1979; Cabrera, 1986; Lavandero et al., 1988; López-Kramer et al., 1998; Montano-Pérez et al., 1998). These gold deposits have also been referred to as ophiolite-hosted mesothermal gold-quartz veins (Lefebure, 1997). Listvenite is a rock type formed by intense carbonate and silica alteration and replacement of serpentinized ultramafic rock. Gold occurs in faulted and sheared lenses in association with listvenite. The fault zone acts as a pathway for CO_2-rich fluids that react with ultramafic rocks and result in precipitation of metals. López-Kramer et al. (1998) pointed out an association of mercury with gold in Cuban listvenites.

The Descanso and Melonera deposits are located in the Villa Clara district (Fig. 2B). These are small deposits in which narrow alteration envelopes (3 to 4 meters across) host high-grade gold mineralization with associated arsenopyrite (López-Kramer, 1988). Another cluster of listvenite gold deposits (Nuevo Potosí, Agrupada, and Reina Victoria) occurs in a faulted ophiolite in the Holguín region (Fig. 2C) of eastern Cuba (Lavandero et al., 1988; López-Kramer et al., 1998). Nuevo Potosí is the largest of the deposits in the Aguas Claras district with over 100,000 ounces in past production. Listvenite gold deposits are assigned to the orogenic gold group based on their mineralogy and host rock.

Tungsten deposits

Tungsten was mined from the Lela Mine on the Isla de la Juventud (Fig. 1). Mineralization occurs in veins that are associated with porphyritic dikes that intrude the metamorphic host rocks (Page and McAllister, 1944; Lavandero et al., 1988; Pardo, 1990; Kesler et al., 1990). Ferberite and small amounts of scheelite occur in quartz-tourmaline veins, tourmaline-bearing silicified rocks, and tourmaline-bearing schists and quartzites (Page and McAllister, 1944; López-Kramer et al., 2008a). Sulfide minerals include arsenopyrite, pyrite, chalcopyrite, pyrrhotite, bismuthinite and sphalerite.

ORTHOMAGMATIC (PODIFORM CHROMITE) DEPOSITS

Most ophiolites of the Greater Antilles consist of supra-subduction zone lithosphere (Proenza et al., 1999; García-Casco et al., 2006; Marchesi et al., 2006; Lewis et al., 2006). The supra-subduction zone is defined as lithosphere that forms directly above a subducted oceanic plate (Pearce et al., 1984; Dilek and Furnes, 2009). Mantle sequences of supra-subduction zone ophiolites in the Greater Antilles host numerous podiform chromite

deposits and occurrences, especially in the Mayarí, Moa-Baracoa and Camagüey ophiolites of Cuba (Fig. 2C). Mercedita, an intermittently active chromite mine, contains over 5Mt of ore and is one of the largest chromite resources in the Americas. The Camagüey ophiolitic massif of central Cuba is host to over 340 known refractory chromite occurrences (Thayer, 1942; Flint et al., 1948; González-Pontón, 1998; Henares et al., 2010). Chromite deposits are plotted on Fig. 2C; production and resource figures are provided in Table 7.

Chromite deposit clusters of the Mayarí-Baracoa belt, eastern Cuba (Fig. 2C) define three districts (Proenza et al., 1998a, 1999). The Mayarí district contains Cr-rich chromite, the Sagua de Tánamo district contains both Al- and Cr-rich chromite, and the Moa-Baracoa district contains Al-rich chromite (Proenza et al., 1999; Gervilla et al., 2005). Chromite deposits of the Mayarí district, with chromium numbers [Cr#=Cr/(Cr+Al)] of 0.69 to 0.83, are medium to small in size and occur in the deeper portions of the ophiolitic sequence, hosted by harzburgites and dunites. Chromite deposits of the Sagua de Tánamo district are enclosed in serpentinized dunites and harzburgites that show mantle tectonite textures. Sagua de Tánamo chromites exhibit large and continuous chemical variation from typical Al-rich (Cr#~0.45) to Cr-rich (Cr#~0.78) compositions (González-Jiménez et al., 2011). The Al-rich Moa-Baracoa chromite deposits (Cr#=0.40-0.55) occur at the mantle-crust transition, immediately beneath the exhumed Mohorovičić discontinuity, where they are associated with harzburgites, dunites, plagioclase-bearing peridotites, gabbro sills and gabbro dikes. Proenza et al. (1998a) provided a detailed description, with maps and stratigraphic columns, of the Mayarí-Baracoa ophiolite.

According to Proenza et al. (1999), the melts in equilibrium with Al-rich chromites are close to the composition of back-arc basin basalts whereas melts in equilibrium with the Cr-rich chromites are of magnesian andesitic or boninitic affinity, characteristic of fore-arc regions (Fig. 5).

BAUXITE AND LATERITIC NICKEL-COBALT DEPOSITS

Bauxite and lateritic nickel deposits formed after the Late Cretaceous to Paleocene collision of the Greater Antilles with North America. Strike-slip motion that began in Eocene time resulted in the uplift and exposure of ophiolites across the northern margin of the Caribbean plate and of platform carbonates in Jamaica. Although the last to form chronologically, bauxite and lateritic nickel-cobalt deposits, are by far the most important deposits in the Greater Antilles from an economic perspective. The Greater Antilles host roughly 10% of the world's nickel laterite resources (Dalvi et al., 2004; Lewis et al., 2006). Cuban laterite deposits contain some of the largest reserves of cobalt in the world (http://minerals.usgs.gov/minerals/pubs/commodity/cobalt/). Jamaica currently produces about 8% of the world's aluminium, down from a high of 18% during the 1970's (Jamaica Bauxite Institute).

Bauxite deposits

Bauxite is a weathering product containing a high proportion of hydrated aluminium oxides (gibbsite and boehmite). In Jamaica, the protolith is volcanic ash (Comer, 1971) which weathers to form a ferruginous soil rich in alumina and typically containing less than 5% silica. Ores typically run between 40% and 50% alumina and are mined from open pits. Processing employs the Bayer process which involves dissolution of alumina with sodium hydroxide followed by precipitation of dissolved silica, separation of solid waste, precipitation of pure gibbsite, and heating (calcination) to drive off water. The processing plant at Kirkvine went into production in 1952 followed by Ewarton, Nain (1969), Maggotty (1971), and Halse Hall (1973). These plants produce alumina for export to Europe and North America where it undergoes the energy-intensive conversion to aluminium metal.

The largest bauxite deposits in the Greater Antilles are located in the central highlands of Jamaica. The deposits occur as clusters of irregularly shaped pockets, pipes, fissures, and blankets that fill solution cavities within the Middle Eocene to Middle Miocene White Limestone Group (Fenton, 1981), a well-developed (up to 3000 meters in thickness) sequence of platform carbonates that extended across the Nicaraguan Rise (Mitchell, 2006). There is no cover other than a thin layer of soil and the contact between bauxite ore and the surrounding limestone, although typically sharp, is quite irregular. Individual pockets can contain as much as 5 million tonnes of ore although most are much smaller. Bauxite ore is locally as much as 30 meters in thickness and can extend along fractures for five or ten meters into the underlying limestone. The best ore occurs at an elevation of over 300 meters where there is a greater separation between bauxite and the water table (Hill, 1955; Fenton, 1981).

Jamaica produced its first bauxite in 1952 followed by Haiti in 1957 and the Dominican Republic in 1959. The industry thrived and, by 1957, Jamaica was the world's leading producer of aluminum. Production from Jamaica has continued to increase over the years to current levels of around 15 million metric tonnes (Mt) per year of bauxite and 4Mt of alumina, accounting for roughly 10% of Jamaica's gross domestic product (GDP). The Jamaica Bauxite Institute estimated total bauxite resources for the island at 2.5 billion tonnes in 2010. Bauxite mines in Haiti and the Dominican Republic closed in 1982 and 1991

TABLE 7 | **Orthomagmatic (Podiform Chromite) Deposits**

Deposit	Past production	Current resource	Observations	References
Moa-Baracoa district		> 6 Mt	Al-rich	Proenza et al. (1998a, 1998b, 1999), Rabchevsky (1994), Torres (1999), Bermudez-Lugo (2004, 2008), Gervilla et al. (2005)
Mercedita	695,487 tons (1990 – 2008)	> 5 Mt at 36% Cr_2O_3, 24.6% Cr	Intermittently active mine	
Amores		>100,000 tons		
Loro		>100,000 tons		
Yarey		>100,000 tons		
Piloto		>100,000 tons		
Cayo Guam	300,000 tons			
Potosí	300,000 tons			
Sagua de Tánamo district	1930-1940	42% Cr_2O_3 ave., or 28.7% Cr	35 small deposits; 10 Cr-rich and 25 Al-rich	Proenza et al. (1998a, 2003), Gervilla et al. (2005)
Mayarí district	500,000 tons	> 500,000 tons at 54% Cr_2O_3 ave., 36.9% Cr	Cr-rich	Lavaut et al. (1994), Proenza et al. (1998a, 2004), Gervilla et al. (2005)
Caledonia		200,000 tons		
Casimba		200,000 tons		
Estrella de Mayarí		200,000 tons		
Juanita		<100,000 tons		
Victoria		<100,000 tons		
Camagüey district		> 1 Mt	Al-rich	González-Pontón (1998), Henares et al. (2010)
Camagüey II		705,375 tons		
Victoria I		149,770 tons		
Mamina		97,450 tons		
Lolita		86,675 tons		
Ofelia		55,100 tons		
Ferrolana		52,985 tons		

respectively. Deposits are shown on Figures 1 and 3B; production and resources appear in Table 8.

Lateritic Ni-Co deposits

Cuba has been an important producer of nickel and cobalt from lateritic ore since 1943 when the Nicaro processing plant went into production followed by Moa and Punta Gorda. Nickel production in the Dominican Republic dates back to 1968 and comes from the Falcondo plant near Bonao. Falcondo currently draws ore from seven nearby deposits and produces approximately 50,000 tons of nickel annually. Cuba currently produces around 80,000 tons of nickel annually from active plants at Punta Gorda, Moa and Nicaro. Production from both countries has shown overall steady growth for the past twenty years. Deposits are shown on Fig. 2C and Fig. 3A; production and resource information is provided in Table 9.

Lateritic nickel deposits form by the weathering of ultramafic rock. Nickel, derived from the dissolution of olivine, concentrates in limonitic soil and in underlying saprolite. Open pit ore bodies typically contain between 1.5% and 2.5% nickel, representing enrichment by a factor of ten over their concentration in the original ultramafic source rock.

At Falcondo, nickel is recovered in an energy-intensive pyro-metallurgical process that involves heating in a reduction furnace to melt the ore, allowing nickel and iron to separate by gravity from lighter-weight slag. The final product is ferro-nickel (38% Ni and low impurities) in the form of a cone designed for the stainless steel industry. The Moa plant in Cuba uses sulphuric acid to leach nickel and cobalt, under pressure, from lateritic ore. Neutralization of the excess acid is accomplished with carbonate leaving gypsum as a waste product. Acid leaching, which is less expensive than pyrometallurgy, is feasible for laterites with low magnesium content.

In eastern Cuba, nickel laterite deposits are classified as the oxide-type, and the typical section through the profile consists of four principal horizons, from bottom to top: serpentinized peridotite, saprolite, limonite and ferricrete (Lewis et al., 2006). The nickel and cobalt occurs mainly in the limonite zone composed of Fe hydroxides and oxides as the dominant mineralogy in the upper part of the profile.

TABLE 8 | **Bauxite Deposits**

Deposit	Past production	Current resource	Observations	References
Nain, Jamaica	49,465,619 tons Al (1969 – 2007)	66.6 Mt at 21.1 % Al		Past production for each of the bauxite deposits in Jamaica has been estimated from published yearly production figures for Jamaica (US Bureau of Mines, US Geological Survey) apportioned among individual deposits according to years of operation and plant capacity.
Mocho, Jamaica	43,646,134 tons Al (1963 to 2007)	58.8 Mt at 21.2 % Al	Active mine	
Lydford, Jamaica	27,351,577 tons Al (1952 to 2007)	36.8 Mt at 21.2 % Al		
Water Valley, Jamaica	27,351,577 tons Al (1952 to 2007	36.8 Mt at 21.2 % Al	Active mine	Resources for each of the bauxite deposits in Jamaica has been estimated from published total resources for Jamaica apportioned according to plant capacity.
Kirkvine, Jamaica	18,913,325 tons Al (1952 to 2007)	25.4 Mt at 21.2% Al	Active mine	
Schwallenburg, Jamaica	18,913,325 tons Al (1952 to 2007)	25.4 Mt at 21.2 % Al	Active mine	
Pedernales, Dominican Republic	4,557,000 tons Al (1959-1991)			
Miragoane, Haiti	3,595,000 tons Al (1957-1982)			

Goethite particles contain up to 4.5% nickel (Proenza et al., 2007). The main cobalt ore minerals are lithiophorite, asbolane and products intermediate between lithiphorite and asbolane (Labrador et al., 2007; Roqué-Rossell et al., 2010).

In contrast, Dominican Republic deposits are classified as the hydrous silicate-type. The main Ni-bearing minerals are hydrated Mg-Ni silicates (serpentine and "garnierites") occurring in the saprolite horizon below a relatively thin cover of limonite (Lithgow, 1993; Lewis et al., 2006). The garnierites occur as veins filling fractures in the harder serpentinised peridotites in the lower part of the laterite profile. Many garnierite ores at Falcondo mine are made up of Ni-sepiolite-falcondoite or talc-like minerals consisting of fine-grained mixtures of Ni-bearing serpentine and talc (Proenza et al., 2008; Tauler et al., 2009).

Nickel-cobalt deposits in eastern Cuba formed on serpentinized harzburgite. The peneplain surface of the deposits varies from 60 to 360 meters in elevation and the weathering mantle attained a thickness of 10 to 50 meters (Linchenat and Shirakova, 1964). Weathering and lateritization of exposed serpentinite may have commenced as early as Eocene time; ultramafic rocks in the Dominican Republic were exposed to weathering during the Miocene. Lewis et al. (2006) have suggested that oxide-type laterites of Cuba were exposed to weathering for a longer time and were uplifted at a slower rate than the hydrous silicate-type laterites of the Dominican Republic.

ALLUVIAL AND BEACH PLACER DEPOSITS

Forty-nine alluvial gold deposits are reported from Cuba (Morales-Quintana and Moreira, 1998). Fluvial placers with Au and/or platinum group elements have been described from the Habana-Matanzas region (Morales-Quintana and Arzuaga, 1994) and the Sagua de Tánamo-Moa-Baracoa region (Díaz-Martínez et al., 1998; Proenza et al., 2004). Source rocks for the fluvial placer gold deposits are assumed to be nearby ophiolites and Cretaceous volcanic rocks.

Beach placers (e.g. Mejías deposit) are found on the northern coast of eastern Cuba (Díaz-Martínez et al., 1998). Mineralization consists of magnetite, titanomagnetite, chromite, ilmenite, rutile, native gold particles, mercurial gold and platinum group minerals (laurite, erlichmanite, irarsite).

In the Dominican Republic, the most important areas for alluvial gold placer deposits are Mao river basin near Monción in the Cordillera Central, Miches in the eastern part of the country, the Rio Haina near Villa Altagracia, and San Francisco de Macoris.

TABLE 9 | **Lateritic Nickel-Cobalt Deposits**

Deposit	Past production	Current resource	Observations	References
San Felipe, Cuba	none	250 Mt at 1.43 % Ni, 0.05 % Co		Brouwer and Martin (2008)
Pinares West, Cuba	100,000 tons Ni	131.3 Mt at 1.22 % Ni, 0.0116 Co	Active mine	Brouwer and Martin (2008)
Punta Gorda, Cuba	375,124 tons Ni (1986 – 2007)	106 Mt at 1.26 % Ni, 0.1 % Co	Active mine	Brouwer and Martin (2008)
Falcondo, Dominican Republic	798,702 tons Ni (1975 – 2007)	35.3 Mt at 1.73 % Ni	Active mine	Falconbridge Dominicana (1998)
Moa, Cuba	774,784 tons Ni (1959 – 2007)	62 Mt at 1.32 % Ni, 0.12 % Co	Active mine	Brouwer and Martin, 2008
Pinares de Mayarí, Cuba	400,000 tons Ni	38 Mt at 1.29 % Ni	Active mine	Brouwer and Martin (2008)
La Fangosa, Cuba	none	54 Mt at 1.38 % Ni, 0.84 % Co		Brouwer and Martin (2008)
Marti, Cuba	100,000 tons Ni	40 Mt at 1.36 % Ni, 0.1 % Co	Active mine	Brouwer and Martin (2008)
Guanajibo, Puerto Rico	none	46.8 Mt at 0.88 % Ni, 0.08% Co		Heidenreich and Reynolds (1959)
Las Iberias, Cuba	none	30.8 Mt at 1.23 % Ni		Brouwer and Martin (2008)
Las Mesas, Puerto Rico	none	25 Mt at 0.81% Ni, 0.12 % Co		Heidenreich and Reynolds (1959)
Camarioca Sur, Cuba	unknown	17.3 Mt at 1.31 % Ni	Active mine	Brouwer and Martin (2008)
Santa Teresita, Cuba	none	18.3 Mt at 1.14 % Ni, 0.11 % Co		Brouwer and Martin (2008)
Maricao East, Puerto Rico	none	5.6 Mt at 1.08% Ni, 0.11% Co		Heidenreich and Reynolds (1959)
Maricao West, Puerto Rico	none	5 Mt at 0.98% Ni, 0.1% Co		Heidenreich and Reynolds (1959)
Rosario North, Puerto Rico	none	4.8 Mt at 0.85% Ni, 0.07% Co		Heidenreich and Reynolds (1959)
Punta Guanajibo, Puerto Rico	none	2.1 Mt at 1.03 % Ni, 0.07% Co		Heidenreich and Reynolds (1959)
Rosario South, Puerto Rico	none	1.1 Mt at 0.71% Ni, 0.06 % Co		Heidenreich and Reynolds (1959)

SUMMARY AND CONCLUSIONS

Metallic mineral deposits formed throughout the tectonic evolution of the Greater Antilles. The most valuable deposits, in terms of contained metal value, are the bauxite and lateritic nickel-cobalt deposits, followed by the epithermal Pueblo Viejo Au-Ag-Cu district, and Cuban-type volcanogenic manganese.

We give below a conceptual outline of the occurrence and formation of the different types of mineral deposits as a series of events in the tectonic evolution of the Greater Antilles, based on our present knowledge. These events are matched with a series of cross sections (Fig. 5) adapted from García-Casco et al. (2009) that show the tectonic setting of each of the main deposit types with time. This gives a snapshot in time of the

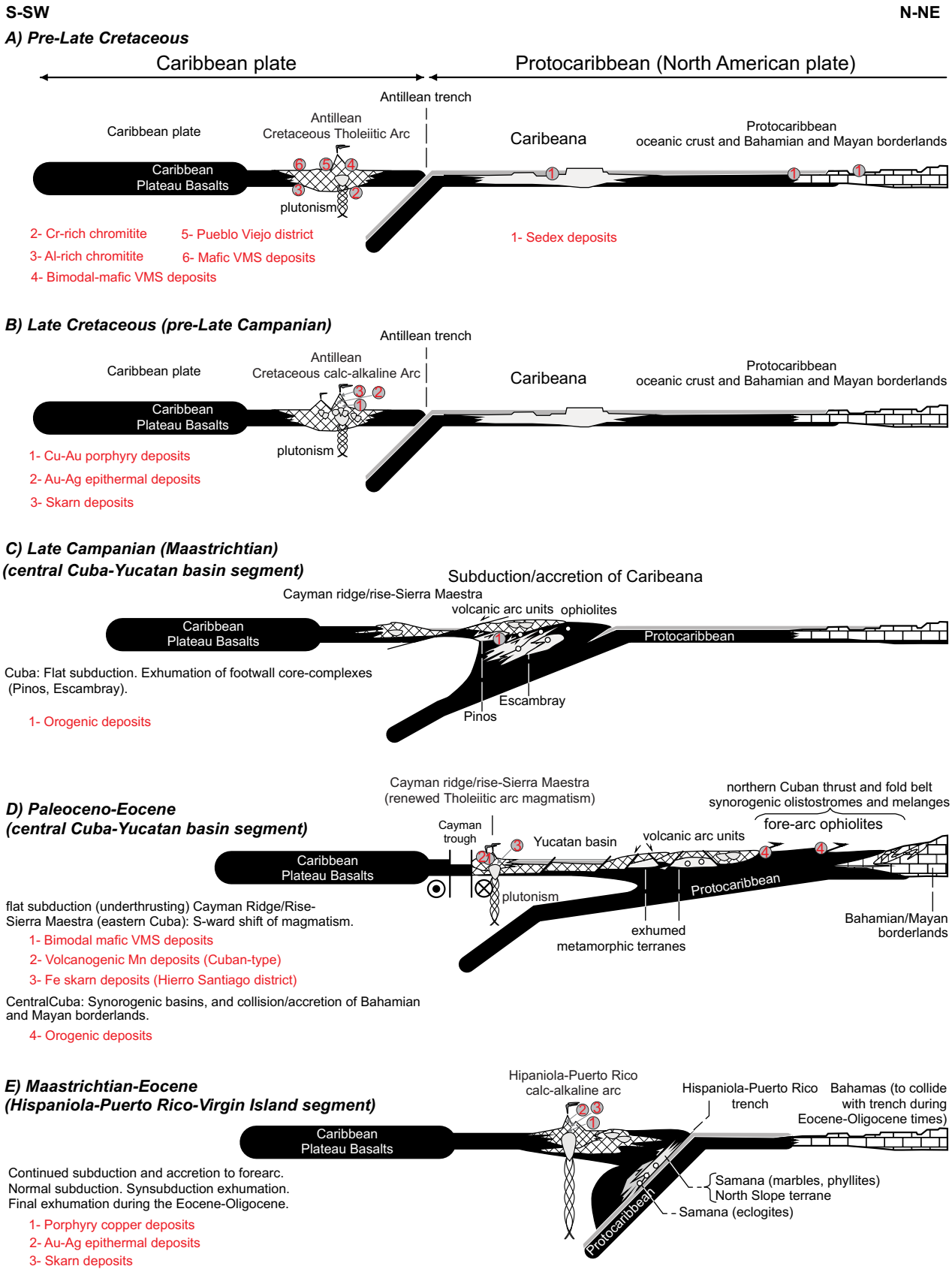

FIGURE 5 | **Tectonic setting of metallic mineral deposit types of the Greater Antilles shown on cross sections modified from Fig. 8 of García Casco et al. (2008). Deposit types discussed in this paper are shown in red.**

distribution of the deposits as the arc evolved. In fact this distribution varies across each sector along the arc.

A) The metallogenic evolution of the Greater Antilles began with the Jurassic breakup of Pangea and the formation of sedimentary exhalative deposits in rift-related terrestrial and marine sedimentary basins (Fig. 5A). The largest sedimentary exhalative deposits in the region are located in the Jurassic to Late Cretaceous San Cayetano basin of western Cuba. With the onset of subduction in Early Cretaceous time, a primitive intraoceanic island arc formed along the length of the Greater Antilles. Beneath this arc, chromite deposits formed in the mantle wedge above the subduction zone. Most Caribbean ophiolites are sections of supra-subduction zone lithosphere that were exposed much later after the collision of the Greater Antilles volcanic arc with North America. Cr-rich chromitites (Mayarí-type) formed, from boninitic magma, in the deep mantle section beneath a primitive island arc (Fig. 5A). Al-rich chromitites (Moa-Baracoa and Camagüey types) formed, from back-arc basin basalt, in the mantle-crust transition zone beneath a more evolved back-arc basin (Fig. 5A). Bimodal-mafic volcanogenic massive sulfide deposits formed in a fore-arc basin setting during the earliest stages of primitive island arc volcanism (Fig. 5A) in the Early Cretaceous. Mafic volcanogenic massive sulfide deposits formed later in mature back-arc basins (Fig. 5A). As the tholeiitic intraoceanic island arc emerged from the ocean, the Pueblo Viejo and Bayaguana high sulfidation epithermal districts formed in apical rifts or back-arc basins (Fig. 5A).

B) As Late Cretaceous island arc volcanism evolved from tholeiitic to calc-alkaline, porphyry copper, skarn and high-sulfidation and low-sulfidation epithermal Au-Ag deposits began to appear (Fig. 5B). Late Cretaceous calc-alkaline volcanic rocks in the Cordillera Central host epithermal and porphyry copper deposits in the Restauración district in the Dominican Republic, the Massif du Nord district in Haiti and the Camagüey district in Cuba.

C) Volcanic activity along the northwest margin of the Caribbean Plate was interrupted during the Late Cretaceous by the subduction of Caribeana (García-Casco et al., 2008). According to these authors, subduction-accretion of Caribeana may have blocked subduction and triggered the emplacement of metamorphic core complexes. Collision/accretion processes led to closure of the proto-Caribbean ocean basin and tectonic emplacement of ophiolites during latest Cretaceous and Paleocene times. Small orogenic gold and tungsten deposits, formed during collision and metamorphism (Fig. 5C), were exposed by later uplift and erosion.

D) During the Paleocene-Eocene in eastern Cuba new intraoceanic island arc-related volcanic activity occurred associated with the Cayman-Ridge Sierra Maestra arc. This island arc was possibly formed as a result of low-angle intra-arc detachment (Pindell et al., 2005). Bimodal-mafic volcanogenic massive sulphide, volcanogenic (Cuban-type) manganese and volcanic-hosted skarn deposits were formed during arc rifting (Fig. 5D).

E) Renewed volcanic arc activity also occurs in Hispaniola, Puerto Rico and Virgin Islands, during the Paleocene- Early Oligocene. In this case, the magmatism was the result of continued southwestward subduction of Proto-Caribbean crust. Small porphyry copper, skarn and epithermal gold deposits formed within and around calc-alkaline stocks (Fig. 5E). The largest of these porphyry copper deposits formed during Eocene to Early Oligocene rifting and intrusion of low-K plutons in Puerto Rico.

Finally, regional uplift exposed the peridotite massifs as a land surface to effective laterization in the beginning of the Miocene. Weathering and secondary enrichment produced economically important deposits of bauxite and lateritic nickel-cobalt in Cuba, Jamaica, Haiti, the Dominican Republic and Puerto Rico.

A connection between rifting and mineralization is the common thread that unites diverse metallic mineral deposit types throughout the tectonic evolution of the Greater Antilles. Jurassic rifting as North and South America drifted apart triggered the accumulation of sediment-hosted base metal deposits. As an intraoceanic tholeiitic island arc (IAT) began to develop in the Early Cretaceous, extension in the fore-arc basin led to the accumulation of bimodal-mafic volcanogenic massive sulfide deposits. Mafic VMS deposits formed in back-arc basins. At 108-112Ma (Pueblo Viejo district) and 116 Ma (Bayaguana district) epithermal Au-Ag-Cu deposits formed in an apical rift or back-arc setting. Eocene rifting at the eastern end of the arc (Puerto Rico) triggered emplacement of the region's largest porphyry copper deposits.

ACKNOWLEDGMENTS

This research is a contribution to IGCP-546, "Subduction Zones of the Caribbean", and the Spanish project CGL2009-10924. Thanks are due to many mining companies (Barrick, Everton, Globestar, Unigold, Xstrata, and others) and geologists (José Amarante, Max Baker, Giovanni Bloise, Salvador Brouwer, Xiomara Cazañas, Cevero Chavez, Edwin Devaux, Roberto Díaz, Hugo Dominguez, Julio Espaillat, Emiliano Gallardo, Sergio Gelcich, François Goulet, Marc L'Heureux, Jorge Jiménez, Angelica Llanes, Waldo Lavaut, Francisco Longo, Phil Pyle, David Rowe, Antonio Rodríguez, Ruben Ruiz, and others) with whom we have had the pleasure of working. The authors are also indebted to the editors, Antonio García-

Casco and Manuel Iturralde-Vinent, as well as to the referees, Antoni Camprubí and Javier Escuder-Viruete, for constructive criticism.

REFERENCES

Alfonso, P., Melgarejo, J.C., Proenza, J.A., Gubert, A., Gallardo, E., Cazañas, X., 2007. Mineralogy and sulphur isotopes of the San Fernando VMS deposit, central Cuba. In: Andrew, C.J. et al. (eds.). Diggin Deeper. Dublin (Ireland), Irish Association for Economic Geology, 2, 1089-1092.

Amarante, A., Jiménez, J., Lewis, J.F., 1989. Geology, hydrothermal alteration and geochemistry of epithermal Au-Ag mineralization in the Restauración area Dominican Republic. Barbados, 1986 Transactions 11th Caribbean Geological Conference, 1-15.

Amarante, J.A., Lewis, J.F., 1996. Geological setting and characteristics of base and precious metal mineralization in the Cordillera Central of the western Dominican Republic and Massif du Nord Haiti. Geological Society of America, Abstracts with Programs, A-240.

Andreu, E., Proenza, J.A., Tauler, E., Chavez, C., Espaillat, J., 2010. Gold and iodargyrite in the Gossan of Cerro de Maimón Deposit (Central Dominican Republic). Macla, 13, 41-42.

Anonymous, 1996. GeoMinera to back Joutel at Zona Barita. Northern Miner, 81, 48.

Anonymous, 1997. Balance Anual de las Reservas Minerales Estado. Cuba, Oficina Nacional de Recursos Minerales, unpublished report.

Astacio, V.A., 1997. Mineralogy, lithogeochemistry, and oxygen isotope study of the Cerro de Maimón massive sulfide deposit, Dominican Republic. Master Thesis. Socorro, New Mexico Institute of Mining and Technology, 100pp.

Barabas, A.H., 1982. Potassium-argon dating of magmatic events and hydrothermal activity associated with porphyry copper mineralization in west central Puerto Rico. Economic Geology, 77, 109-126.

Barroso, A., Lugo-Primelles, R., Torre-Domínguez, A., 1998. Nuevos resultados geólogo-geofísicos amplían las perspectividades de mineralización del yacimiento Golden Hill. III Congreso Cubano de Geología y Minería (GEOMIN´98). La Habana, Geología y Minería ´98, 49-50.

Batista-González, R., Montano, J.L., Martínez, J., Pérez-Nevot, N., 1998. Mapa de los Recursos Minerales, Cuba Central a escala 1:100 000. III Congreso Cubano de Geología y Minería (GEOMIN ´98). La Habana, Geología y Minería ´98, 53-55.

Bermudez-Lugo, O., 2004. The mineral industry of Cuba. United States Geological Survey Minerals, Cuba area report, Yearbook, 5pp.

Binns, R.A., Barriga, F.J.A.S., Miller, D.J., 2007. Leg 193 Synthesis: Anatomy of an active felsic-hosted hydrothermal system, eastern Manus Basin, Papua New Guinea. In: Barriga, F.J.A.S., Binns, R.A., Miller, D.J., Herzig, P.M. (eds.). Proceedings of the Ocean Drilling Program-Scientific Results. Texas, College Station, 193, 1-71.

Blein, O., Guillot, S., Lapierre, H., Mercier de Lépinay, B., Lardeaux, J.M., Millán-Trujillo, G., Campos, M., Garcia, A., 2003. Geochemistry of the Mabujina Complex, Central Cuba: Implications on the Cuban Cretaceous Arc Rocks. Journal of Geology, 111, 89-101.

Bloomer, S.H., Taylor, B., Macleod, C.J., Stern, R.J., Fryer, P., Hawkins, J.W., Johnson, L., 1995. Early arc volcanism and the ophiolite problem: a perspective from drilling in the western Pacific. In: Taylor, B., Natland, J.H. (eds.). Active Margins and Marginal Basins of the Western Pacific. American Geophysical Union Monograph, 88, 1-30.

Bortnikov, N.S., Kramer, Kh.L., Genkin, A.D., Kul'nev, A.S., 1989. The mineralogy and conditions of formation of the Delita gold deposit, Cuba. International Geology Review, 31, 1158-1172.

Bortnikov, N.S., Genkin, A.D., Chryssoulis, S., 1993. Deposition environment of gold-bearing arsenopyrite in mesothermal deposits. In: Fenoll Hach-Ali, P., Torres-Ruiz, J., Gervilla, F. (eds.). Current Research in Geology Applied to Ore Deposits. Granada (España), La Guioconda, 45-48.

Bottrill, T.J., Formell, C.F., Sethu, R.K., 2000. Los Mangos–San Fernando deposit, Santa Clara, Cuba: Geology and Mineralization in a Cretaceous Volcanic Arc. In: Sherlock, R.L., Logan, M.A.V., Browne, R. (eds.). Volcanogenic massive sulfide deposits of Latin America. Geological Association of Canada Mineral Deposits Division, 259-275.

Bowin, C.O., 1966. Geology of the Central Dominican Republic. Geological Society of America Memoir, 98, 11-84.

Brouwer, S., Martin, J.C., 2008. The Cuban ophiolite and resulting nickel laterite deposits. Santo Domingo, February 2008, 18th Conferencia Geológica del Caribe, unpublished.

Cabrera, R., 1986. Geología y regularidades de la distribución de los yacimientos de cobre y oro de la región mineral de Las Villas. La Habana, Instituto de Geología y Paleontología, Academia de Ciencias de Cuba, 130pp.

Cabrera, R., Tolkunov, A.E., 1979. Tipos y condiciones geológicas de formación de los yacimientos de oro de la zona mineral septentrional de la antigua provincia de Las Villas. Ciencias de la Tierra y del Espacio, 1, 51-68.

Camprubí, A., 2009. Major metallogenic provinces and epochs of México. Society for Geology Applied to Mineral Deposits (SGA) News, 25, 1-20.

Case, J.E., Holcombe, T.L., 1980. Geologic-Tectonic map of the Caribbean Region (1:2,500,000 scale). United States Geological Survey Miscellaneous Investigations Series Map I-1100.

Cazañas, X., Melgarejo, J.C., 1998. Introducción a la metalogenia de Mn en Cuba. Acta Geologica Hispanica, 33, 213-238.

Cazañas, X., Peldiakov, A., Escobar, E., Fernández, A., Ferro, P., La Rosa, A., Pérez, M., Santa-Cruz, M., 1989. Evaluación de las perspectivas de la mineralización ferrosa en el campo mineral Hierro Santiago y pronóstico de nuevas áreas para dicha materia prima. La Habana (Cuba), Oficina Nacional de Recursos Minerales, unpublished, 130pp.

Cazañas, X., Melgarejo, J.C., Luna, A., Barrabí, H., 1998a. El depósito volcanogénico de Cu–Zn–Pb–Au El Cobre, Cuba

Oriental: estructura y mineralogía. Acta Geologica Hispanica, 33, 277-333.

Cazañas, X., Proenza, J.A., Mattietti-Kysar, G., Lewis, J., Melgarejo, J.C., 1998b. Las rocas volcánicas de las series Inferior y Media del Grupo El Cobre en la Sierra Maestra (Cuba Oriental): volcanismo generado en un arco de islas tholeiítico. Acta Geologica Hispanica, 33, 57-74.

Cazañas, X., Melgarejo, J.C., Alfonso, P., Proenza, J.A., Cuba, S., 2003. Cuban-type volcanogenic manganese deposits. In: Eliopoulos et al. (eds.). Mineral Exploration and Sustainable Development. Rotterdam, Millpress, 1, 119-122.

Cazañas, X., Alfonso, P., Melgarejo, J.C., Proenza, J.A., Fallick, A.E., 2008. Geology, fluid inclusion and sulphur isotope characteristics of the El Cobre VHMS deposit, Southern Cuba. Mineralium Deposita, 43, 805-824.

Cheilletz, A., 1976. Etude géologique e métallogénique de indices à cuivdre et molybdène de type porphyre cuprifère de la zone de Vert de Gris–Jean Rabel, Presqui'île du Nord-Ouest, Haiti. Doctoral Thesis. Nancy, University of Nancy, 177pp.

Cheilletz, A., Kachrillo, J.J., Sonet, J., Zimmerman, J.L., 1978. Pétrographie et géochronologie de deux complexes intrusifs à porphyre cuprifères d'Haiti, Contribution à la connaissance de la province cuprifère laramienne de l'arc insulaire de Grande Antilles. Bulletin Societé Géologique de France, Serie 7, 20, 907-914.

Chenard, D., 2006. Evaluation of seven projects, Dominican Republic. Globestar Mining Inc. and Corporación Minera Dominicana S.A., unpublished, 52pp.

Childe, F., 2000. Volcanogenic massive sulfide mineralization in the Greater Antilles. In: Sherlock, R.L., Logan, M.A., Browne, R. (eds.). Volcanogenic massive sulfide deposits of Latin America. Geological Association of Canada, Mineral Deposits Division, 2 (Special Publications), 183-196.

Comer, J.B., 1971. Mineral composition of White Limestone insoluble residue and its implications on the origin of bauxite: a preliminary report. Journal Geological Society of Jamaica, Bauxite-Alumina symposium, 24-27.

Cox, D.P., 1985. Geology of the Tanamá and Helecho porphyry copper deposits and their vicinity, Puerto Rico. United States Geological Survey, 1327 (Professional Paper), 59pp.

Cox, D.P., Briggs, R.P., 1973. Metallogenic map of Puerto Rico. United States Geological Survey, Miscellaneous Geologic Investigations Map I-721.

Cruz, E.M., Simón, A., 1994. Desarrollo de las menas tipo Chipre del occidente de Cuba. Santiago de Cuba, Segundo Congreso Cubano de Geología y Minería, Libro de Programas y Resúmenes, 91.

Cumming, G.L., Kesler, S.E., Krstic, D., 1982. Source of lead in sulfide ore at the Pueblo Viejo gold-silver oxide deposit, Dominican Republic. Economic Geology, 77, 1939-1942.

Cumming, G.L., Kesler, S.E., 1987. Lead isotopic composition of the oldest volcanic rocks of the eastern Greater Antilles island arc. Chemical Geology, 65, 15-23.

Dalvi, A.D., Bacon, W.G., Osborne, R.C., 2004. Past and future of nickel laterite projects. In: Imrie, W.P., Lane, D.M. (eds.). International Nickel Laterite Symposium TMS 2004. Charlotte (N. Carolina), 133rd Annual Meeting and Exhibition, 23pp.

Díaz de Villalvilla, L., 1997. Caracterización geológica de las formaciones volcano-sedimentarias en Cuba Central, provincias Cienfuegos, Villa Clara, Sancti Spiritus. In: Furrazola, G.F., Nuñez-Cambra, K.E. (eds.). Estudios sobre Geología de Cuba. Ciudad de la Habana (Cuba), Instituto de Geología y Paleontología, 325-344.

Díaz de Villalvilla, L., Milia, I., Pacheco, M., Aguirre, G., 2003. Formación Los Pasos: Geología, geoquímica y su comparación con el Caribe. Estudios sobre los Arcos volcánicos de Cuba. La Habana, Centro Nacional de Información Geológica, Instituto de Geología y Paleontología, 54-61.

Díaz-Martínez, R., Proenza, J.A., Comas, J., Fernández-Bellon, O., Fabra, J.M., Guinart, O., Melgarejo, J.C., 1998. El placer lateral de playa Mejías (noreste de Cuba Oriental): un ejemplo de interacción de procesos aluviales y marinos en la concentración de minerales de elementos preciosos. Acta Geologica Hispanica, 33, 351-377.

Dilek, Y., Furnes, H., 2009. Structure and geochemistry of Tethyan ophiolites and their petrogenesis in subduction rollback systems. Lithos, 113, 1-20.

Donnelly, T.W., Rogers, J.J.W., 1981. Igneous series in island arcs: The northeastern Caribbean compared with worldwide island arc assemblages. Bulletin Volcanologique, 43, 347-382.

Draper, G., Lewis, J.F., 1982. Petrology, deformation, and tectonic significance of the Amina schist, northern Dominican Republic. In: Amigo del Hogar (ed.). Transactions of the 9th Caribbean Geological Conference. Santo Domingo (Dominican Republic), 53-64.

Draper, G., Lewis, J.F., 1991. Metamorphic belts in central Hispaniola. In: Mann, P., Draper, G., Lewis, J.F. (eds.). Geologic and tectonic development of the North American–Caribbean plate boundary in Hispaniola. Boulder (Colorado), Geological Society of America, 262 (Special Paper), 29-45.

Elswick, E.R., Maynard, J.B., 1998. Sulfur geochemistry of the Cu-Pb-Zn deposits of the Pinar del Rio district, western Cuba. Toronto (Ontario), Geological Society of America, Annual meeting, abstracts with programs, A-19.

Escuder-Viruete, J., Díaz de Neira, A., Hernáiz Huerta, P.P., Monthel, J., García Senz, J., Joubert, M., Lopera, E., Ullrich, T., Friedman, R., Mortensen, J., Pérez-Estaún, A., 2006. Magmatic relationships and ages of Caribbean island-arc tholeiites, boninites and related felsic rocks, Dominican Republic. Lithos, 90, 161-186.

Escuder-Viruete, J., Contreras, F., Joubert, M., Urien, P., Stein, G., Weis, D., Pérez-Estaún, A., 2007. Tectónica y geoquímica de la Formación Amina: registro del arco isla caribeño primitivo en la Cordillera Central, República Dominicana. Boletín Geológico y Minero, 118, 221-242.

Escuder-Viruete, J., Pérez-Estaún, A., Weis, D., Friedman, R., 2010. Geochemical characteristics of the Rio Verde Complex, Central Hispaniola: implications for the paleotectonic reconstruction of the Lower Cretaceous Caribbean island-arc. Lithos, 114, 168-185.

Espaillat, J., 1996. Caribbean Basin. Society of Economic Geologists Newsletter, 25, 39.

Espaillat, J., Bloise, G., Lewis, J.F., MacVeigh, G., 1989. Petrography and geochemistry of mafic rocks of the Peravillo Formation in the Sabana Potrero area, Central Dominican Republic. St. Croix, Transactions of the 12th Caribbean Geological Conference, 190-199.

Fenton, A., 1981. The mineral resources of Jamaica. Kingston (Jamaica), Geological Survey Division, 8, 143pp.

Feoktistov, V.P., Aniyatov, I.A., Norman, A., 1983. Metallogeny of western Cuba. International Geology Review, 25, 309-318.

Flint, D.E., de Albear, J.F., Guild, P.W., 1948. Geology and chromite deposits of the Camagüey distric, Camagüey Province, Cuba. United States Geological Survey Bulletin, 954-B, 39-63.

Franklin, J.M., Gibson, H.L., Jonasson, I.R., Galley, A.G., 2005. Volcanogenic massive sulfide deposits. In: Hedenquist, J.W., Thompson, J.F.H., Goldfarb, R.J., Richards, J.P. (eds.). Economic Geology, 100th Anniversary Volume, 523-560.

Frost, C.D., Schellekens, J.H., Smith, A.L., 1998. Nd, Sr, and Pb isotope characterization of Cretaceous and Paleogene volcanic and plutonic island arc rocks from Puerto Rico. Geological Society of America, 322 (Special Paper), 123-132.

García-Casco, A., Torres-Roldán, R.L., Iturralde-Vinent, M.A., Millan, G., Núñez Cambra, K., Lázaro, C., Rodríguez Vega, A., 2006. High pressure metamorphism of ophiolites in Cuba. Geologica Acta, 4(1-2), 63-88.

García-Casco, A., Iturralde-Vinent, M.A., Pindell, J., 2008. Latest Cretaceous collision/accretion between the Caribbean Plate and Caribeana: origin of metamorphic terranes in the Greater Antilles. International Geology Review, 50, 781-809.

Garrett, R.G., Lalor, G.C., Vutchokov, M., 2004. Geochemical exploration for gold in Jamaica: a comparison of stream sediment and soil surveys. Geochemistry, Exploration, Environment, Analysis, 4, 161-170.

Gervilla, F., Proenza, J.A., Frei, R., González-Jiménez, J.M., Garrido, C.J., Melgarejo, J.C., Meibom, A., Díaz-Martínez, R., Lavaut, W., 2005. Distribution of platinum-Group elements and Os isotopes in chromite ores from Mayarí-Baracoa Ophiolitic Belt (eastern Cuba). Contributions to Mineralogy and Petrology, 150, 589-607.

González-Jiménez, J.M., Proenza, J.A., Gervilla, F., Melgarejo, J.C., Blanco-Moreno, J.A., Ruiz-Sánchez, R., Griffin, W.L., 2011. High-Cr and high-Al chromitites from the Sagua de Tánamo district, Mayarí-Cristal Ophiolitic Massif (eastern Cuba): constraints on their origin from mineralogy and geochemistry of chromian spinel and platinum-group elements. Lithos, 125, 101-121.

González-Pontón, R., 1998. Mineralizaciones cromíticas de la asociación ofiolítica de Camagüey, Cuba. La Habana, III Congreso Cubano de Geología y Minería (GEOMIN '98), Geología y Minería '98, 281-283.

González-Sánchez, F., Camprubí, A., González-Partida, E., Puente-Solís, R., Canet, C., Centeno-García, E., Atudorei, V., 2009. Regional stratigraphy and distribution of epigenetic stratabound Celestine, fluorite, barite and Pb-Zn deposits in the MVT province of northeastern México. Mineralium Deposita, 44, 343-361.

Hall, C.M., Kesler, S.E., Russel, N., Piñero, E., Sánchez, R., Pérez, M., Moreira, J., Borges, M., 2004. Age and tectonic setting of the Camagüey volcanic-intrusive arc, Cuba: evidence for rapid uplift of the western Greater Antilles. Journal of Geology, 112, 521-542.

Hannington, M.D., 1993. Shallow submarine hydrothermal systems in modern island arc settings. The Gangue, 43, 6-8.

Hannington, M.D., Poulsen, K.H., Thompson, J.F.H., Sillitoe, R.H., 1999. Volcanogenic gold in the massive sulfide environment. In: Barrie, C.T., Hannington, M.D. (eds.). Volcanic-Associated Massive Sulfide Deposits: Processes and Examples in Modern and Ancient Settings. Reviews in Economic Geology, 8, 325-356.

Harnish, D.E., Brown, P.E., 1986. Petrogenesis of the Casseus Cu-Fe skarn, Terre Neuve District, Haiti. Economic Geology, 81, 1801-1807.

Henares, S., González-Jiménez, J.M., Gervilla, F., Proenza, J.A., Chang Rodríguez, A., González-Pontón, R.B., 2010. Las cromititas del Complejo Ofiolítico de Camagüey, Cuba: un ejemplo de cromitas ricas en Al. Boletín de la Sociedad Geológica Mexicana, 62, 173-185.

Herzig, P.M., Hannington, M.D., Arribas, A.Jr., 1998. Sulfur isotopic composition of hydrothermal precipitates from the Lau back-arc: implications for magmatic contributions to seafloor hydrothermal systems. Mineralium Deposita, 33, 226-237.

Heidenreich, W.L., Reynolds, B.M., 1959. Nickel–cobalt–iron bearing deposits in Puerto Rico. United States Bureau of Mines, Reports of Investigations, 5532, 68pp.

Hill, V.G., 1955. The mineralogy and genesis of White Limestone insoluble residue and its implications on the origin of bauxite: a preliminary report. American Mineralogist, 40, 676-688.

Hill, P.J., 1958. Banded pyrite deposits of Minas Carlota, Cuba. Economic Geology, 53, 966-1003.

Holbeck, P.M., Daubeny, P.H., 2000. Geology of the San Antonio concession, Dominican Republic. In: Sherlock, R.L., Logan, M.A.V., Browne, R. (eds.). Volcanogenic massive sulfide deposits of Latin America. Geological Association of Canada, Mineral Deposits Division, 197-212.

Hollister, V.F., 1978. Porphyry copper deposits of the Caribbean. In: Hollister, V.F. (ed.). Geology of the porphyry copper deposits of the Western Hemisphere. New York, Society of Mining Engineers, American Institute of Mining, Metallurgical and Petroleum Engineers, 149-157.

Horan, S.L., 1995. The geochemistry and tectonic significance of the Maimón-Amina schists, Cordillera Central, Dominican Republic. Master Thesis. Gainesville (Florida), University of Florida, 172pp.

Iturralde-Vinent, M., 1994. Cuban Geology: a new plate tectonic synthesis. Journal of Petroleum Geology, 17, 39-70.

Iturralde-Vinent, M., 1996. Ofiolitas y arcos volcanicos de Cuba. Miami, International Geological Correlation Program (IGCP), Project W. 364, 1 (Special Contribution), 265pp.

Iturralde-Vinent, M., 1998. Synopsis de la constitución geológica de Cuba. Acta Geologica Hispanica, 33, 9-56.

Iturralde-Vinent, M., 2006. Meso-Cenozoic Caribbean paleogeography: Implications for the historical biogeography of the region. International Geology Review, 48, 791-827.

Iturralde-Vinent, M., Díaz Otero, C., García-Casco, A., van Hinsbergen, D.J.J., 2008. Paleogene foredeep basin deposits of north-central Cuba: a record of arc-continent collision between the Caribbean and North American Plates. International Geology Review, 50, 868-884.

Jiménez, J., Lewis, J.F., 1989. Petrología del area de Restauración, República Dominicana. Cartagena, 1983, Transactions 10th Caribbean Geological Conference, 445-453.

Jolly, W.T., Lidiak, E.G., 2006. Role of crustal melting in petrogenesis of the Cretaceous Water Island Formation (Virgin Islands, northeast Antilles island arc). Geologica Acta, 4(1-2), 7-34.

Jolly, W.T., Lidiak, E.G., Dickin, A.P., Wu, T.W., 2001. Secular geochemistry of central Puerto Rican island arc lavas: constraints on Mesozoic tectonism in the eastern Greater Antilles. Journal of Petrology, 42, 2197-2214.

Jolly, W.T., Lidiak, E.G., Dickin, A.P., 2006. Cretaceous to Mid- Eocene pelagic sediment budget in Puerto Rico and the Virgin Islands (northeast Antilles Island arc). Geologica Acta, 4(1-2), 35-62.

Jolly, W.T., Lidiak, E.G., Dickin, A.P., 2008. Bimodal volcanism in northeast Puerto Rico and the Virgin Islands (Greater Antilles Island Arc): Genetic links with Cretaceous subduction of the mid-Atlantic ridge Caribbean spur. Lithos, 103, 393-414.

Kerr, A.C., Iturralde-Vinent, M., Saunders, A.D., Babbs, T.L., Tarney, J., 1999. A new plate tectonic model of the Caribbean: Implications from a geochemical reconnaissance of Cuban Mesozoic volcanic rocks. Geological Society of America Bulletin, 111, 1581-1599.

Kesler, S.E., 1968, Contact-localized ore formation at the Memé mine, Haiti. Economic Geology, 63, 541-552.

Kesler, S.E., 1978. Metallogenesis of the Caribbean region. Journal of the Geological Society of London, 135, 429-441.

Kesler, S.E., Fleck, R.J., 1967. Age and possible origin of a granitic intrusion in the Greater Antilles island arc. Geological Society of America, 115 (Special Paper), 115, 482.

Kesler, S.E., Jones, L.M., Walker, R.L., 1975. Intrusive rocks associated with porphyry copper mineralization in island arc areas. Economic Geology, 70, 515-526.

Kesler, S.E., Russell, N., Seaward, M., Rivera, J., McCurdy, K., Cumming, G.L., Sutter, J.F., 1981. Geology and geochemistry of sulfide mineralization underlying the Pueblo Viejo gold-silver oxide deposit, Dominican Republic. Economic Geology, 76, 1096-1117.

Kesler, S.E., Levy, E., Martin, F.C., 1990. Metallogenic evolution of the Caribbean Region. In: Dengo, G., Case, J.E. (eds.). The Caribbean Region, The Geology of North America. Boulder (Colorado), Geological Society of America, H, 459-482.

Kesler, S.E., Sutter, J.F., Speck, R.C., 1991. Age of intrusive rocks in northern Hispaniola. In: Mann, P., Draper, G., Lewis, J.F. (eds.). Geologic and tectonic development of the North America–Caribbean plate boundary in Hispaniola. Boulder (Colorado), Geological Society of America, 262 (Special Paper), 165-185.

Kesler, S.E., Russell, N., Bell, D., 1996. Gold-silver mineralization in Cuba and its geologic setting in the Greater Antilles. In: Conyer, A.R., Fahey, P.L. (eds.). Geology and Ore Deposits of the American Cordillera. Reno/Sparks (Nevada), April 1995, Geological Society of Nevada Symposium Proceedings, 1433-1441.

Kesler, S.E., Hall, C.M., Russell, N., Pinero, E., Sánchez, C.R., Pérez, R.M., Moreira, J., 2004. Age of the Camagüey gold-silver district, Cuba: tectonic evolution and preservation of epithermal mineralization in volcanic arcs. Economic Geology, 99, 869-886.

Kesler, S.E., Campbell, I.H., Smith, C.N., Hall, C.H., Allen, C.M., 2005a. Age of the Pueblo Viejo Gold-Silver Deposit and its significance to models for high sulfidation epithermal mineralization. Economic Geology, 100, 253-272.

Kesler, S.E., Campbell, I.H., Allen, C.M., 2005b. Age of the Los Ranchos Formation, Dominican Republic: Timing and tectonic setting of primitive island arc volcanism in the Caribbean region. Geological Society of America Bulletin, 117, 987-995.

Koschmann, A.H., Gordon, M., 1950. Geology and mineral resources of the Maimón-Hatillo district, Dominican Republic. United States Geological Survey Bulletin, 964-D, 307-360.

Krason, J., 1999. Cuba. Mining Journal, 3, 126-127.

Kysar-Mattietti, G., 2001. The role of Paleogene magmatism in the evolution of the northern Caribbean margin. The Sierra Maestra (southern Cuba). Doctoral Thesis. Washington D.C, George Washington University, 187pp.

Labrador, M., Proenza, J.A., Galí, S., Melgarejo, J.C., Tauler, E., Rojas-Purón, A.L., Muñoz-Gómez, N., Blanco-Moreno, J.A., 2007. Supergene Co-Ni-Mn mineralization in Ni-laterite deposits from northeast Cuba. In: Andrew, C.J. et al. (eds.). Diggin Deeper. Dublin (Ireland), Irish Association for Economic Geology, 2, 1397-1400.

Lamouille, B., Save, M., Gentilhomme, P., Trehin, J.L., Coste, B., Hocquard, C, Peguero, V., Rodríguez, J.J., 1998. Proyecto Depósitos Auríferos de Restauración. Bureau de Recherches Géologiques et Minières –Rosario Dominicana.

Lastra, J.F., Lara, J., 1998. Geoquímica y metalogenia de la estructura Francisco-Loma Hierro, distrito metalogenético Dora-Francisco, Cuba Occidental. La Habana, III Congreso Cubano de Geología y Minería (GEOMIN '98), Geología y Minería '98, 337-340.

Lavandero, R.M., Estrugo, M., Santa Cruz-Pacheco, M., Bravo, F., Melnikova, A.A., Cabrera, R., Trofimov, V.A., Romero, J., Altarriba, I., Álvarez, P., Aniatov, I.I., Badamgavin, B., Barishev, A.N., Carrillo, D.J., Cazañas, X., Cuellar, N., Dovbnia, A.V., Formell, F., García, M., González, D., Gue, G.G., Janchivin, A., Krapiva, L.J., López, J., Lozanov, I., Montenegro, J., Pantaleon, G., Stefanov, N., Vázques, O., Zaagoskin, A.M., Zhidkov, Ya., A., 1988. Mapa de yacimientos

minerales metálicos y aguas minerales de la República de Cuba. (1:500,000). Ciudad de la Habana (Cuba), Instituto de Geología y Paleontología, Ministerio de la Industria Básica, 4.

Lavandero, R.M., Bravo, F., 1994. Ambientes geodinámicos y su relación con los yacimientos minerales metálicos en la Isla de Cuba. Santiago de Cuba, Segundo Congreso Cubano de Geología y Minería, libro de programas y resúmenes, 97.

Lavaut, W., Medina, A., Acosta, J., Guerra, M., Figueredo, D., 1994. Investigaciones geologo-geofísicas actuales del macizo ofiolítico Sierra de Nipe: un sistema para el pronóstico y prospección de cromitas metalúrgicas. Santiago de Cuba, Segundo Congreso Cubano de Geología y Minería, libro de programas y resúmenes, 108.

Leach, D.L., Sangster, D.F., Kelley, K.D., Large, R.R., Garven, G., Allen, C.R., Gutzmer, J., Walters, S., 2005. Sediment-hosted lead-zinc deposits: a global perspective. Economic Geology, 100th Anniversary Volume, 561-607.

Lefebure, D., 1997. New mineral deposit models of the Cordillera. Geoscience Canada, 24(3), 143-149.

Lewis, J.F., Harper, C.T., Kemp, A.W., Stipp, J.J., 1973. Potasium-argon retention ages of some Cretaceous rocks from Jamaica. Geological Society of America Bulletin, 84, 335-340.

Lewis, J.F., Draper, G., 1990. Geological and tectonic evolution of the northern Caribbean margin. In: Dengo, G., Case, J.E. (eds.). The Caribbean Region. Boulder (Colorado), Geological Society of America, The Geology of North America, H, 77-140.

Lewis, J.F., Draper, G., Bowin, C., Bourdon, L., Maurrasse, F., Nagle, F., 1990. Hispaniola. In: Dengo, G., Case, J.E. (eds.). The Caribbean Region. Boulder (Colorado), Geological Society of America, The Geology of North America, H, 94-112.

Lewis, J.F., Amarante, A., Bloise, G., Jiménez, J.G., Dominguez, H.D., 1991. Lithology and stratigraphy of upper Cretaceous volcanic and volcaniclastic rocks of the Tireo Group, Dominican Republic, and correlations with the Massif du Nord in Haiti. In: Mann, P., Draper, G., Lewis, J.F. (eds.). Geologic and Tectonic development of the North America-Caribbean plate boundary in Hispaniola. Boulder (Colorado), Geological Society of America, 262 (Special Paper), 143-163.

Lewis, J.F., Perfit, M., Horan, S., Díaz de Villalvilla, L., 1995. Geochemistry and petrotectonic significance of early arc bimodal volcanism in the Greater Antilles arc. New Orleans, Annual Meeting Geological Society of America, abstracts with programs, A227.

Lewis, J.F., Astacio, V.A., Espaillat, J., Jiménez, J., 2000. The occurrence of volcanogenic massive sulfide deposits in the Maimón Formation, Dominican Republic: the Cerro de Maimón, Loma Pesada and Loma Barbuito deposits. In: Sherlock, R.L., Logan, M.A.V., Browne, R. (eds.). Volcanogenic massive sulfide deposits of Latin America. Geological Association of Canada, Mineral Deposits Division, 213-239.

Lewis, J.F., Escuder-Viruete, J., Hernaiz-Huerta, P.P., Gutiérrez, G., Draper, G., Pérez-Estaún, A., 2002. Subdivisión geoquímica del arco de Isla Circum-Caribeño, Cordillera Central Dominicana: Implicaciones para la formación, acreción y crecimiento cortical en un ambiente intraoceánico. Acta Geologica Hispanica, 37(2-3), 81-122.

Lewis, J.F., Draper, G., Proenza, J.A., Espaillat, J., Jiménez, J., 2006. Ophiolite-Related Ultramafic Rocks (Serpentinites) in the Caribbean Region: A Review of their Occurrence, Composition, Origin, Emplacement and Nickel Laterite Soils. Geologica Acta, 4(1-2), 237-263.

Lidiak, E.G., Jolly, W.T., 1996. Circum-Caribbean granitoids: Characteristics and origin. International Geology Review, 38, 1098-1133.

Linchenat, A., Shirakova, I., 1964. Individual characteristics of nickeliferous iron (laterite) deposits of the northeast part of Cuba (Pinares de Mayarí, Nicaro and Moa). Montreal, 1964, 24th International Geological Congress, Part 14, Section 14, 172-187.

Lithgow, E.W., 1993. Nickel laterites of central Dominican Republic Part I. Mineralogy and ore dressing. In: Reddy, R.G., Weizenbach, R.N. (eds.). The Paul E. Queneau International Symposium Extractive Metallurgy of Copper, Nickel and Cobalt, Volume I: Fundamental Aspects. Warrendale (Pennsylvania, USA), The Minerals, Metals & Materials Society, 403-425.

López-Kramer, J.M., 1988. Composición sustancial y asociaciones mineralógicas de los yacimientos auríferos hidrothermales de Cuba. Doctoral Thesis. La Habana, Instituto de Geología y Paleontología, summary, 15pp.

López-Kramer, J.M., Moreira, J., Pantaleon, G.J., Lavandero, R.M., Montano, J., Cruz-Martin, J., 1998. Tipos mineralógicos de algunos yacimientos auríferos de Cuba. La Habana, III Congreso Cubano de Geología y Minería (GEOMIN '98), 371-374.

López-Kramer, J.M., Moreira, J., Gandarillas, J., 2006. Geology of the Florencia gold-telluride deposit (Camagüey, Cuba) and some metallurgical considerations. Earth Sciences Research Journal, 10, 105-116.

López-Kramer, J. M., Pimentel, H., Moreira-Martínez, J., Gandarillas-Hevia, J., 2007. La mineralización Auro–Teluridica en el Arco Volcánico Cretácico. Cuba. Implicaciones regionales. Caracas, Octubre 21-25, IX Congreso Venezolano de Geología, 1-13.

López-Kramer, J.M., Pérez-Vázquez, RG., Redwood, S.D., Nelson, C.E., 2008a. La mineralización de oro y plata en terrenos de afinidad continental de Cuba SW (Guaniguanico, Pinos y Guamuhaya). GeoMinas, 36, 17-21.

López-Kramer, J.M., Pimentel, H., Redwood, S., Gandarillas-Hevia, J., Pérez-Vázquez, R.G., 2008b. Depósitos primarios de oro y plata del archipiélago Cubano. Revista Ciencias de la Tierra y el Espacio, 9. May 2011, website: http://www.iga.cu/Publicaciones/revista/cte_09/art_09-07/id79.htm

Louca, K., 1990. Geological setting and base and precious metal deposits of Northern Haiti. In: Larue, D.K., Draper, G. (eds.). Transactions of the 12th Caribbean Geological Conference. St. Croix (United States, Virgin Islands), Miami Geological Society, 200-216.

Lugo-Primelles, R., Barroso, A., Lugo, R., Escobar, E., 1998. Geología y metalogenia del campo mineral Guaimaro. Enfoque actual. La Habana, III Congreso Cubano de Geología y Minería (GEOMIN '98), Geología y Minería '98, 390-393.

Luna, J.A., 1994. Características del yacimiento El Cobre y su campo menífero. Santiago de Cuba, Segundo Congreso Cubano de Geología y Minería, libro de programas y resúmenes, 104.

Mann, P., 2007. Overview of the tectonic history of Northern Central America. Geological Society of America, 428 (Special Paper), 428, 1-20.

Marchesi, C., Garrido, C.J., Boch, D., Proenza, J.A., Gervilla, F., Monié, P., Rodríguez-Vega, A., 2007. Geochemistry of Cretaceous Magmatism in Eastern Cuba: Recycling of North American Continental Sediments and Implications for Subduction Polarity in the Greater Antilles Paleo-Arc. Journal of Petrology, 48, 1813-1840.

Marchesi, C., Garrido, C.J., Godard, M., Proenza, J.A., Gervilla, F., Blanco-Moreno, J., 2006. Petrogenesis of highly depleted peridotites and gabbroic rocks from the Mayarí-Baracoa Ophiolitic Belt (eastern Cuba). Contributions to Mineralogy and Petrology, 151, 717-736.

Maynard, J.B., Morton, J., 1995. Lead-zinc-barite deposits in Jurassic rock of Western Cuba: indicators of a cratonic rift tectonic setting. New Orleans, Geological Society of America, annual meeting, A-239.

McFarlane, N.A., 1977. Geologic map of Jamaica (1:250,000 scale). Kingston (Jamaica), Ministry of Mining and Natural Resources, Mines and Geology Division.

Meschede, M., Frisch, W., 1998. A plate tectonic model for the Mesozoic and Early Cenozoic history of the Caribbean plate. Tectonophysics, 296, 269-291.

Méndez, I., Rodríguez, R., Rodríguez, E., Fernández, A., Rodríguez, M., Ruiz, R., Hernández, R., 1994. Atlas de rocas de la Sierra Maestra. Santiago de Cuba, Editorial Oriente, 125pp.

Millán, G., 1996. Metamorfitas de la asociación ofiolítica de Cuba. In: Iturralde-Vinent, M. (ed.). Ofiolitas y arcos volcánicos de Cuba. Miami (USA), International Geological Correlation Program (IGCP) Project 364, 1 (Special Contribution), 131-153.

Mitchell, S.F., 2003, Sedimentology and tectonic evolution of the Cretaceous rocks of Central Jamaica: relationships to the plate tectonic evolution of the Caribbean. In: Bartolini, C., Buffler, R.T., Blickwede, J. (eds.). The Circum-Gulf of Mexico and the Caribbean: Hydrocarbon habitats, basin formation, and plate tectonics. American Association of Petroleum Geologists, 79 (Memoir), 605-623.

Mitchell, S.F., 2006. Timing and implications of Late Cretaceous tectonic and sedimentary events in Jamaica. Geologica Acta, 4(1-2), 171-178.

Montano-Pérez, J.L., Moreira, J., Cruz-Martín, J., Bravo, F., González, D., 1998. Mapa metalogénetico de Cuba Central a escala 1:250,000. La Habana, III Congreso Cubano de Geología y Minería (GEOMIN '98), Geología y Minería '98, 449-452.

Morales-Quintana, A.R., Arzuaga, H., 1994. Perspectivas metalíferas de la region Habana-Matanzas. Santiago de Cuba, Segundo Congreso Cubano de Geología y Minería, libro de programas y resúmenes, 106pp.

Morales-Quintana, A.R., Moreira, J., 1998. Mapa metalogénico-pronóstico de los placeres de oro en la región de Habana-Matanzas. La Habana, III Congreso Cubano de Geología y Minería (GEOMIN '98), Geología y Minería '98, 470-473.

Moreira, J., Torres, J.L., Montano, J., Lavandero, R., Sánchez, R., Cazañas, X., 2001. Depósitos de skarn de Cuba. La Habana, IV Congreso de Geología y Minería, Memorias GEOMIN 2001, 91-111.

Mosier, D.L., Page, N.J., 1998. Descriptive and tonnage models of volcanogenic manganese deposits in oceanic environments-a modification. United States Geological Survey Bulletin, 1811, 28pp.

Mueller, A.G., Hall, G.C., Nemchin, A.A., O'Brien, D., 2008. Chronology of the Pueblo Viejo epithermal gold-silver deposit, Dominican Republic: formation in an Early Cretaceous intra-oceanic island arc and burial under ophiolite. Mineralium Deposita, 43, 873-890.

Muntean, J.L, Kesler, S.E., Russell, N., Polanco, J., 2007. Evolution of the Monte Negro acid-sulfate Au-Ag deposit, Pueblo Viejo, Dominican Republic; important factors in grade development. Economic Geology, 85, 1738-1758.

Myczynski, R., Iturralde-Vinent, M., 2005. The Late Lower Albian invertebrate fauna of the Rio Hatillo Formation of Pueblo Viejo, Dominican Republic. Caribbean Journal of Science, 41, 782-796.

Nelson, C.E., 2000a. Volcanic domes and gold mineralization in the Pueblo Viejo District, Dominican Republic. Mineralium Deposita, 35, 511-525.

Nelson, C.E., 2000b. Volcanic dome emplacement and Au-Ag-Zn mineralization at the Moore Deposit, Pueblo Viejo District, Dominican Republic. In: Cluer, J.K., Price, J.G., Struhsacker, E.M., Hardyman, R.F., Morris, C.L. (eds.). Geology and Ore Deposits 2000: The Great Basin and Beyond. May 15-18, Geological Society of Nevada Symposium Proceedings, 67-77.

Niccolini, Ph., 1977. Les porphyres cuprifères et les complexes ultrabasiques du Nord Est d'Haiti. Essai de typologie prévisionelle. Doctoral Thesis. Paris, Université Pierre et Marie Curie, VI, 203pp.

Page, N.J., McAllister, 1944. Tungsten deposits, Isla de Pinos, Cuba. United States Geological Survey Bulletin, 935-D, 177-246.

Pardo, M., 1990. La constitución geológica del macizo Isla de la Juventud y la metalogenia endógena vinculada al magmátismo ácido. St. Croix (United States, Virgin Islands), Transactions of the 12th Caribbean Geological Conference, Miami Geological Society, 68-81.

Park, C.F., 1942. Manganese deposits of Cuba. United States Geological Survey Bulletin, 935-B, 75-97.

Park, C.F., Cox, M.W., 1944. Manganese deposits in part of the Sierra Maestra, Cuba. United States Geological Survey Bulletin, 935-F, 307-355.

Paulick, H., Vanko, D.A., Yeats, C.J., 2004. Drill core-based facies reconstruction of a deep-marine felsic volcano hosting an active hydrothermal system (Paul Ridge, Papua New Guinea, ODP Leg 193). Journal of Volcanology and Geothermeral Research, 130, 31-50.

Pearce, J.A., Lippard, S.J., Roberts, S., 1984. Characteristics and tectonic significance of suprasubduction zone ophiolites. In: Kokelaar, B.P., Howells, M.F. (eds.). Marginal Basin Geology. London, Geological Society, 16 (Special Publications), 77-94.

Pérez-Rodríguez, M., Santa Cruz, M., 1991. Estudio de la mineralización metálica y no metálica del Sector La Grande (campo mineral Hierro Santiago). Revista Tecnológica, 21(1), 3-10.

Pérez-Rodríguez, M., Sukar, K., 1997. Granitoides del arco volcánico Cretácico de la región central de Cuba (Antigua Provincia de Camagüey). In: Furrazola, G.F., Núñez, K.E. (eds.). Estudios sobre geología de Cuba. La Habana (Cuba), Instituto Nacional de Geología y Paleontología, Centro Nacional de Información Geológica, 387-398.

Pérez-Vázquez, R.G., Melgarejo, J.C., 1998. El yacimiento Matahambre (Pinar del Río, Cuba): estructura y mineralogía. Acta Geologica Hispanica, 33, 133-152Pindell, J., Barrett, S., 1990. Geological evolution of the Caribbean region; a plate-tectonic perspective. In: Dengo, G., Case, J. (eds.). The Caribbean Region, The Geology of North America, H. Boulder (Colorado), Geological Society of America, 405-432.

Pindell, J., Kennan, L., Maresch, W.V., Stanek, K.P., Draper, G., Higgs, R., 2005. Plate-kinematics and crustal dynamics of circum-Caribbean arc-continent interactions: tectonic controls on basin development in Proto-Caribbean margins. Geological Society of America, 394 (Special Paper), 7-52.

Pindell, J., Kennan, L., Stanek, K.P., Maresch, W.V., Draper, G., 2006. Foundations of Gulf of México and Caribbean evolution: eight controversies resolved. Geologica Acta, 4(1-2), 303-341.

Pindell, J., Kennan, L., 2009. Tectonic evolution of the Gulf of México, Caribbean and northern South America in the mantle reference frame: an update. In: James, K., Lorente, M.A., Pindell, J. (eds.). The geology and evolution of the region between North and South America. Geological Society of London, 328 (Special Publications), 1-55. doi: 10.1144/SP328.1

Piñero, E., Qiontana, M.E., Marí, T., 1997. Caracterización geológica de los depósitos vulcanógenos-sedimentarios de región Ciego-Camagüey-Las Tunas. In: Furrazola, G.F., Núñez, K.E. (eds.). Estudios sobre geologia de Cuba. La Habana (Cuba), Instituto Nacional de Geología y Paleontología, Centro Nacional de Información Geológica, 345-356.

Pollard, P.J., 2006. An intrusion-related origin for Cu-Au mineralization in iron oxide-copper-gold (IOCG) provinces. Mineralium Deposita, 41, 179-187.

Porter, A.R.D., 1970. Geology of the Ginger Ridge granodiorite stock, and associated rocks, St. Catherine, Jamaica. Masters Thesis. University of the West Indies, 94pp.

Proenza, J.A., Melgarejo, J.C., 1998. Una introdución a la metalogenia de Cuba bajo la perspectiva de la tectónica de placas. Acta Geologica Hispanica, 33, 89-132.

Proenza, J.A., Melgarejo, J.C., Gervilla, F., Lavaut, W., Revé, D., Rodríguez, G., 1998a. Cromititas podiformes en la faja ofiolítica Mayarí-Baracoa (Cuba). Acta Geologica Hispanica, 33, 153-178.

Proenza, J.A., Gervilla, F., Melgarejo, J.C., Revé, D., Rodríguez, G., 1998b. Las cromititas ofiolíticas del yacimiento Mercedita (Cuba). Acta Geologica Hispanica, 33, 179-212.

Proenza, J., Gervilla, F., Melgarejo, J.C., Bodinier, J.L., 1999. Al- and Cr-rich chromitites from the Mayarí-Baracoa Ophiolitic Belt (eastern Cuba): consequence of interaction between volatile-rich melts and peridotites in suprasubduction mantle. Economic Geology, 94, 547-566.

Proenza, J.A., Melgarejo, J.C., Gervilla, F., Rodríguez-Vega, A., Díaz Martínez, R., Ruiz-Sánchez, R., Lavaut, W., 2003. Coexistence of Cr- and Al-rich ophiolitic chromitites in a small area: The Sagua de Tánamo district, Eastern Cuba. In: Eliopoulos, D.G. et al. (eds.). Mineral Exploration and Sustainable development. Rotterdam, Millpress Science Publishers, 1, 631-634.

Proenza, J.A., Rodríguez-Vega, A., Díaz-Martínez, R., Gervilla, F., Melgarejo, J.C., Ramayo, L., Vila, A.R., 2004. Distribución de elementos del grupo del platino (EGP) y Au en la faja ofiolítica Mayarí-Baracoa (Cuba oriental). In: Pereira, E., Castroviejo, R., Ortiz, F. (eds.). Complejos ofiolíticos en Iberoamérica: guías de prospección para metales preciosos. Proyecto XIII.1 – CYTED, ISBN: 84-96023-24-9, 309-336.

Proenza, J.A., Díaz-Martínez, R., Iriondo, A., Marchesi, C., Melgarejo, J.C., Gervilla, F., Garrido, C.J., Rodríguez-Vega, A., Lozano-Santacruz, R., Blanco-Moreno, J.A., 2006. Primitive island-arc volcanic rocks in eastern Cuba: the Téneme Formation. Geologica Acta, 4(1-2), 103-121.

Proenza, J.A., Tauler, E., Melgarejo, J.C., Galí, S., Labrador, M., Marrero, N., Pérez-Melo, N., Rojas-Purón, A.L., Blanco-Moreno, J.A., 2007. Mineralogy of oxide and hydrous silicate Ni-laterite profiles in Moa Bay area, northeast Cuba. In: Andrew, C.J. et al. (eds.). Diggin' Deeper. Dublin (Ireland), Irish Association for Economic Geology, 2, 1389-1392.

Proenza, J.A., Lewis, J.F., Galí, S., Tauler, E., Labrador, M., Melgarejo, J.C., Longo, F., Bloise, G., 2008. Garnierite mineralization from Falcondo Ni-laterite deposit (Dominican Republic). Macla, 9, 197-198.

Pszczólkowski, A., 1999. The exposed passive margin of North America in western Cuba. In: Mann, P. (ed.). Caribbean Basins. Amsterdam, Elsevier, Sedimentary Basins of the World, 4, 93-121.

Rabchevsky, G.A., 1994. The mineral industry of Cuba. United States Geological Survey Minerals, Cuba area report, Yearbook, 235-241.

Rivero-Manzano, J.J., 1998. Características metalogenéticas del complejo ofiolítico de Cuba Central. La Habana, III Congreso Cubano de Geología y Minería (GEOMIN '98), Geología y Minería '98, 611-613.

Robertson, R., 1996. Northern Orion firms up property holdings in Cuba and Argentina. Northern Miner, 81, 48.

Rodríguez-Romero, M., 2003. Las Minas de Matahambre y la comunidad geologico-minero de Cuba. 5th Cuban Congress on Geology and Mining, 388-389.

Rojas-Agramonte, Y., Kröner, A., García-Casco, A., Iturralde-Vinent, M.A., Wingate, M.T.D., Liu, D.Y., 2006a. Review of zircon ages from Cuba and their geodynamic interpretations. Geophysical Research, abstracts, 8.

Rojas-Agramonte, Y., Neubauer, F., Bojar, A.V., Hejl, E., Handler, R., García-Delgado, D.E., 2006b. Geology, age and tectonic evolution of the Sierra Maestra Mountains, southeastern Cuba. Geologica Acta, 4(1-2), 123-150.

Rojas-Agramonte, Y., Kröner, A., Pindell, J., García-Casco, A., García-Delgado, D., 2008. Detrital zircon geochronology of Jurassic sandstones of western Cuba (San Cayetano formation): implications for the Jurassic paleogeography of the NW Proto-Caribbean. American Journal of Science, 308, 639-656.

Roqué-Rosell, J., Mosselmans, F., Proenza, J.A., Labrador, M., Galí, S., Atkinson, K.D., Quinn, P.D., 2010. Sorption of Ni by "lithiophorite-asbolane" intermediates in Moa Bay lateritic deposits, eastern Cuba. Chemical Geology, 275, 9-18.

Ruiz, J.A., 1997. Partial privitization of Rosario Dominicana: Mining, Environment and Nature-Possibilities and Compatibilities (in Spanish). Santo Domingo, March 7, A seminar sponsored by CEDEMPRESA and the law firm of Russin, Vecchi, and Heredia Bonetti.

Russell, N., Kesler, S.E., 1991. Geology of the maar-diatreme complex hosting precious metal mineralization at Pueblo Viejo, Dominican Republic. In: Mann, P., Draper, G., Lewis, J.F. (eds.). Geologic and tectonic development of the North America-Caribbean plate boundary in Hispaniola. Boulder (Colorado), Geological Society of America, 262 (Special Paper), 203-215.

Russell, N., Moreira, J., Sánchez, R., 2000. Volcanogenic massive sulfide deposits of Cuba. In: Sherlock, R.L., Logan, M.A., Browne, R. (eds.). Volcanogenic massive sulfide deposits of Latin America. Geological Association of Canada, Mineral Deposits Division, 2 (Special Publications), 241-258.

Sánchez-Cruz, R., Russell, N., Oviedo, A., Lavandero, R.M., Escobar, E., Ferro-Espinosa, P., Bárzan, J.A., 1998. Mapa de minerales útiles metálicos de la región de la Gran Piedra con las nuevas manifestaciones auríferas. La Habana, III Congreso Cubano de Geología y Minería (GEOMIN '98), Geología y Minería '98, 661-664.

Sherlock, R., Michaud, M., 2000. Volcanogenic massive sulfide deposits of Latin America–An overview. In: Sherlock, R.L., Logan, M.A., Browne, R. (eds.). Volcanogenic massive sulfide deposits of Latin America. Geological Association of Canada, Mineral Deposits Division, 2 (Special Publications), 19-46.

Sillitoe, R.H., 2003. Iron oxide-copper-gold deposits: an Andean view. Mineralium Deposita, 38, 787-812.

Sillitoe, R.H., Bonham, H.F., 1984. Volcanic landforms and ore deposits. Economic Geology, 79, 1286-1298.

Sillitoe, R.H., Hannington, M.D., Thompson, J.F.H., 1996. High sulfidation deposits in the volcanogenic massive sulfide environment. Economic Geology, 91, 204-212.

Sillitoe, R.H., Hall, D.J., Redwood, S.D., Waddell, A., 2006. Pueblo Viejo high sulfidation epithermal gold-silver deposit, Dominican Republic: a new model of formation beneath barren limestone cover. Economic Geology, 101, 1427-1435.

Simón, A., 1995. The Matahambre-Santa Lucia ore district, western Cuba. New Orleans, Geological Society of America, annual meeting, A-239.

Simon, G., Kesler, S.E., Russell, N., Hall, C.M., Bell, D., Pinero, E., 1999. Epithermal gold mineralization in an old volcanic arc: the Jacinto deposit, Camagüey District, Cuba. Economic Geology, 94, 487-506.

Simons, F.S., Straczek, J.A., 1958. Geology of manganese deposits of Cuba. United States Geological Survey Bulletin, 1057, 1-289.

Smith, H.A., Stephenson, P.R., Butcher, M.G., Carr, C.A., 2008. Pueblo Viejo Gold Project, Dominican Republic. Technical report prepared for Gold de Corp Inc., 189pp.

Sokolova, E.A., Brito, A., Coutin, D.P., 1974. La formación manganífera El Cobre (Provincia de oriente, Cuba). In: Geología de los yacimientos minerales útiles de Cuba. La Habana, Academia de Ciencias de Cuba, 92-124.

Stanek, K.P., Maresch, W.V., Pindell, J.L., 2009. The geotectonic story of the northwestern branch of the Caribbean Arc: implications from structural and geochronological data of Cuba. London, Geological Society, 328 (1, Special Publications), 361-398.

Tauler, E., Proenza, J.A., Galí, S., Lewis, J.F., Labrador, M., García-Romero, E., Suarez, M., Longo, F., Bloise, G., 2009. Ni-sepiolite-falcondoite in garnierite mineralization from Falcondo Ni-laterite deposit, Dominican Republic. Clay Minerals, 44, 435-454.

Thayer, T.P., 1942. Chrome resources of Cuba. United States Geological Survey Bulletin, 93-A, 1-74.

Tolkunov, A.E., Bolotin, Y.A., Cabrera, R., Maximov, A., Zarianov, D.P., 1974a. Regularidades de la distribución y condiciones de formación de los yacimientos tipo Lentes Piritosas en el anticlinorio de Trinidad. La Habana, Geología de los yacimientos minerales útiles de Cuba, Academia de Ciencias de Cuba, 62-81.

Tolkunov, A.E., Malinovski, E.P., Cabrera, R., Carassou, G., 1974b. Características comparativas de los yacimientos de cobre de Cuba. Geología de los yacimientos minerales útiles de Cuba, La Habana, Academia de Ciencias de Cuba, 7-61.

Toloczyki, M., Ramirez, I., 1991. Geologic map of the Dominican Republic 1:250,000. Ministry of Industry and Commerce, Department of Mining, Geographic Institute of the Univerisity of Santo Domingo.

Torres, I.E., 1995. The mineral industry of Cuba. United States Geological Survey Minerals Yearbook, Cuba Area Report. 5pp.

Torres, I.E., 1999. The mineral industry of Cuba. United States Geological Survey Minerals, Cuba Area Report, Yearbook, 5pp.

Torres, M., Sastroputro, S., Ulloa, M., Pérez, M., De la Nuez, D., Santa-Cruz, M., Alvarado, B., 2005. Petrología, Mineralogía y Alteración hidrotermal de la manifestación de Cu porfídico del sector Palo Seco. Camagüey (Cuba). I Convención Cubana de Ciencias de la Tierra, Geociencias, 141-150.

Ulloa-Santana, M.M., Abrahão Moura, M., Olivo, G.R., Botelho, N.F., Kyser, T.K., Bühn, B., 2011. The La Unión Au±Cu prospect, Camagüey District, Cuba: fluid inclusion and stable isotope evidence for ore-forming processes. Mineralium Deposita, 46, 91-104.

Valdés-Nodarse, E.L., Díaz-Carmona, A., Davies, J.F., Whitehead, R.E., Fonseca, L., 1993. Cogenetic sedex Zn-Pb and stockwork Cu ore, western Cuba. Exploration and Mining Geology, 2, 297-305.

Valdés-Nodarse, E.L., 1998. Pb-Zn Sedex deposits and their copper stockwork roots, western Cuba. Mineralium Deposita, 33, 560-567.

Vila, J.-M., Butterlin, J., Calmus, T., Mercier de Lépinay, B., van den Berghe, B., 1985. Carte Géologique d'Haïti au 1/1,000,000 Avec Notice Explicative Détaillée (Geologic Map of Haiti at 1:1,000,000 with Detailed Explicative Notes). Centre national de la recherche scientifique (CNRS), Bordeaux, France.

Watkins, J., 1990. Geologic setting of the Cerro de Maimón deposit, Dominican Republic. Santo Domingo, Falconbridge Dominicana, unpublished, 43pp.

Whitehead, R.E., Davies, J.F., Valdés-Nodarse, E.L., Díaz-Carmona, A., 1996. Mineralogical and chemical variations, Castellanos shale-hosted Zn-Pb-Ba deposits, Northwestern Cuba. Economic Geology, 91, 713-722.

Williams, P.J., Barton, M.D., Johnson, D.A., Fontbote, L., De Haller, A., Mark, G., Oliver, N.H.S., Marschik, R., 2005. Iron oxide copper-gold deposits: geology, space-time distribution, and possible modes of origin. Economic Geology 100th Anniversary Volume 1905-2005. Colorado, Society of Economic Geologists Inc., 371-405.

Zhidkov, A., Ovsiannikov, V., del Pino, J., 1975. Papel de la materia orgánica en la formación del yacimiento Santa Lucía. Revista Minería en Cuba, 2, 12-18.

Manuscript received February 2011;
revision accepted July 2011;
published Online July 2011.

Geologica Acta, Vol.9, Nos 3-4, September - December 2011, 265-272
DOI: 10.1344/105.000001698
Available online at www.geologica-acta.com

geologica acta

U-Pb Geochronology of detrital zircons from the Venezuelan passive margin: implications for an Early Cretaceous Proto-Orinoco river system and Proto-Caribbean ocean basin paleogeography

M.I. NOGUERA [1] [2] **J.E. WRIGHT** [1] [*] **F. URBANI** [3] **J. PINDELL** [4]

[1] **Department of Geology, University of Georgia**
Athens, GA 30602

[2] **Current address: Swift Energy Operating, LLC**
16825 Northchase Drive, Suite 400, Houston, TX 77060

[3] **FUNVISIS, El Llanito and Universidad Central de Venezuela, Escuela de Geología**
Final Calle Mara, Caracas, Venezuela

[4] **Department of Earth Science, Rice University Keith-Weiss Geological Laboratory**
6100 Main Street, Houston, TX 77005 and Tectonic Analysis Ltd., Chestnut House, Burton Park, Duncton, West Sussex, GU28 0LH, England

[*] Corresponding author: James E. Wright, Jwright@gly.uga.edu, phone: 706-542-4394, fax: 706-542-2425

ABSTRACT

The Guyana Shield has long been interpreted as the source of siliciclastic detritus within the Cretaceous passive margin strata of northern Venezuela. We have determined U-Pb ages of detrital zircons separated from Early Cretaceous strata of the passive margin. Although the Guyana shield is the probable source for much of the Archean, Paleoproterozoic and early Mesoproterozoic detrital zircon grains, there is a prominent age population (ca.0.95-1.2Ga) that is not easily explained as being derived from the shield. A western source in the Venezuelan and/or northern Colombian Andes is suggested for this detrital component. We propose that a Proto-Orinoco river system drained both the Guyana Shield and the Venezuelan and Colombian Andes and that branches of this river system were funneled through Triassic/Jurassic rift basins that formed during initial opening of the Proto-Caribbean Seaway. The detrital zircon age data have implications for paleogeographic reconstructions of the Caribbean region prior to the breakup of Pangea and the longevity of continental scale river systems.

KEYWORDS | **Detrital Zircon. Passive Margin. Venezuela.**

INTRODUCTION

The provenance of sandstones as determined by U-Pb detrital zircon geochronology has become a widely used tool in global plate tectonic reconstructions. For example, it has been used to help reconstruct Pangea in the Caribbean region prior to the opening of the Proto-Caribbean as a number of detrital zircon investigations have suggested a northern South American provenance for Paleozoic strata now found in Mexico (e.g. Weber et al., 2006, 2008; Ortega-Obregon et al., 2009). In addition, currently geographically dispersed Jurassic to Cenozoic sediments of the Caribbean region are interpreted to have been derived from northern Venezuela (e.g. Rojas-Agramonte et al., 2008; Pindell et al., 2009). However, there are no published U-Pb detrital zircon provenance studies for the northern South American margin to test these hypotheses yet. We report the first U-Pb detrital zircon ages from the passive margin of Venezuela in order to establish a provenance barcode that can be used to quantitatively assess Pangean paleogeography in this region.

In addition, a number of detrital zircon investigations have been used to provide evidence for the presence and/or location of continental scale paleofluvial drainage systems (Riggs et al., 1996; Dickinson and Gehrels, 2003; Prokopiev et al., 2008). Our data, in conjunction with previous investigations, clearly identifies such a system that operated in northern South America.

GEOLOGICAL SETTING

Separation of North and South America during the breakup of western Pangaea created the Proto-Caribbean seaway and resulted in the establishment of an Early Cretaceous passive margin in northern Venezuela. During the Triassic and Jurassic, continental breakup led to formation of numerous rift basins that were filled with continental red beds and associated volcanic rocks (Yoris et al., 1997; Ramos, 2009). Although rocks associated with the early rifting phase of passive margin development are exposed in western Venezuela (Perijá and Mérida Andes) where they attain a thickness of 300 to 3400m (Schubert, 1986), in central and eastern Venezuela these deposits are buried by younger strata and are known only from drill hole data (Feo-Codecido et al., 1984). For example, the Espino Graben (Fig. 1) is a buried rift basin that trends WSW-ENE across northern Venezuela and is known from wells to contain as much as 1.5km of Jurassic red beds and volcanic rocks dated at 162Ma (Feo-Codecido et al., 1984; Motiscka, 1985; Rodríguez and Rodríguez, 2003).

The Triassic-Jurassic rifting phase was followed by the development of an Early Cretaceous passive margin dominated by siliciclastic sedimentation above a regional transgressive peneplain. Regional transgression onto the subsiding passive margin led to onlap of continental to shallow marine facies, followed by deeper water facies which reached a maximum in the Late Cretaceous (Turonian-Coniacian) and is reflected in the Cretaceous stratigraphic record by a gradual change from siliciclastic dominated sedimentation in the Early Cretaceous to more pelagic shale and carbonate sedimentation in the Late Cretaceous (Pindell and Erikson, 1994).

We have obtained a total of 560 detrital zircon analyses from six samples of siliciclastic Early Cretaceous passive-margin units along northern Venezuela (Fig. 1). Sample locations and analytical data are contained in the supplementary files.

PASSIVE MARGIN SAMPLES

Four Early Cretaceous stratigraphic units (six samples) of the Venezuelan passive margin were sampled for detrital zircon dating (Fig. 1). The stratigraphic terminology of the passive margin strata of northern Venezuela varies from west to east. The samples for this study were collected from the Early Cretaceous Aguardiente (westernmost unit sampled), Bobare, Araure and Barranquín (easternmost unit sampled) formations.

A single sample of quartz arenite was collected from the Aguardiente Formation (Barremian-Aptian) which contains quartz-rich sandstones with local glauconitic sandstone and limestone beds and is interpreted to have been deposited in a shallow marine deltaic setting (Salvador, 1961).

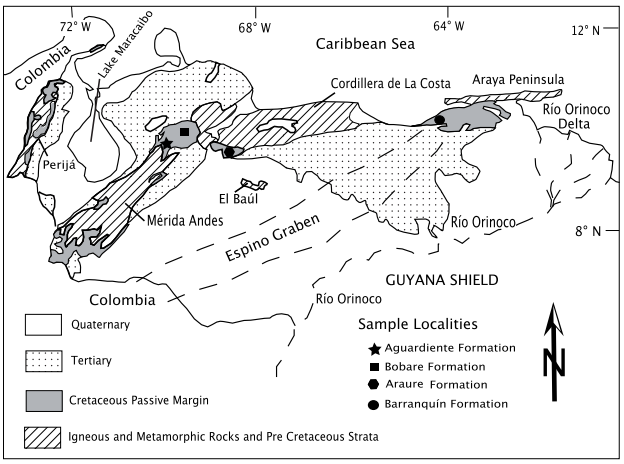

FIGURE 1 | **Simplified geologic map of northern Venezuela showing the location of Early Cretaceous passive margin samples collected for this study.**

Two samples of quartz arenite were analyzed from the Bobare Formation (Barremian-Albian) of northwestern Venezuela. Bellizzia and Rodríguez (1967) described the unit as being composed of massive, sometimes conglomeratic, quartz-rich-sandstone, shale and siltstone and interpreted the Bobare to have been deposited in an unstable shelf environment.

One sample of a schistose quartz-sandstone from the Araure Formation (Neocomian-Barremian?) was collected. Renz and Short (1960) and Bushman (1967) described the unit as containing thick conglomerate layers, alternating with arkosic sandstone, quartz sandstone and silty shales; it is interpreted to have been deposited in continental to shallow marine waters.

Two samples (quartz arenites and sublitharenites) were sampled for zircons and analyzed from the Barranquín Formation (Barremian-Aptian) of eastern Venezuela. The unit is composed of quartz sandstone, intercalated with shale and occasional limestone, and is considered to have been deposited in deltaic to internal inner shelf (bar) environments (Pindell and Erikson, 1994; Erikson and Pindell, 1998a, b).

ANALYTICAL METHODS

U-Pb geochronology of zircons was conducted by laser ablation multicollector inductively coupled plasma mass spectrometry (LA-MC-ICPMS) at the Arizona LaserChron Center. Analytical protocols followed Gehrels et al., 2006. The analyses involve ablation of zircon with a New Wave/Lambda Physik DUV193 Excimer laser (operating at a wavelength of 193nm) using a spot diameter of 30microns. The ablated material is carried in helium into the plasma source of a GVI Isoprobe, which is equipped with a flight tube of sufficient width that U, Th, and Pb isotopes are measured simultaneously. All measurements are made in static mode, using 10^{11} ohm Faraday detectors for ^{238}U, ^{232}Th, ^{208}Pb, and ^{206}Pb, a 10^{12} ohm faraday collector for ^{207}Pb, and an ion-counting channel for ^{204}Pb. Ion yields are ~1.0mv per ppm. Each analysis consists of one 12-second integration on peaks with the laser off (for backgrounds), 12 one-second integrations with the laser firing, and a 30 second delay to purge the previous sample and prepare for the next analysis. The ablation pit is ~12 microns in depth. For each analysis, the errors in determining $^{206}Pb/^{238}U$ and $^{206}Pb/^{204}Pb$ result in a measurement error of ~1-2% (at 2-sigma level) in the $^{206}Pb/^{238}U$ age. The errors in measurement of $^{206}Pb/^{207}Pb$ and $^{206}Pb/^{204}Pb$ also result in ~1-2% (at 2-sigma level) uncertainty in age for grains that are >1.0Ga, but are substantially larger for younger grains due to low intensity of the ^{207}Pb signal. For most analyses, the cross-over in precision of $^{206}Pb/^{238}U$ and $^{206}Pb/^{207}Pb$ ages occurs at 0.8-1.0Ga. Common Pb correction is accomplished by using the measured ^{204}Pb and assuming an initial Pb composition from Stacey and Kramers (1975) (with uncertainties of 1.0 for $^{206}Pb/^{204}Pb$ and 0.3 for $^{207}Pb/^{204}Pb$). Our measurement of ^{204}Pb is unaffected by the presence of ^{204}Hg because backgrounds are measured on peaks (thereby subtracting any background ^{204}Hg and ^{204}Pb), and because very little Hg is present in the argon gas. Inter-element fractionation of Pb/U is generally ~20%, whereas apparent fractionation of Pb isotopes is generally ~2%. In-run analysis of fragments of a large zircon crystal (generally every fifth measurement) with known age of 564±4Ma (2-sigma error) is used to correct for this fractionation. The uncertainty resulting from the calibration correction is generally 1-2% (2-sigma) for both $^{206}Pb/^{207}Pb$ and $^{206}Pb/^{238}U$ ages. The analytical data are reported in the supplementary document files. Uncertainties shown in these tables are at the 1-sigma level, and include only measurement errors. Interpreted ages are based on $^{206}Pb/^{238}U$ for <1000Ma grains and on $^{206}Pb/^{207}Pb$ for >1000Ma grains. This division at 1000Ma results from the increasing uncertainty of $^{206}Pb/^{238}U$ ages and the decreasing uncertainty of $^{206}Pb/^{207}Pb$ ages as a function of age. The resulting interpreted ages are shown on relative age-probability diagrams (from Ludwig, 2003). These diagrams show each age and its uncertainty (for measurement error only) as a normal distribution, and sum all ages from a sample into a single curve.

We obtained 560 U-Pb zircon ages (Supplementary Data), derived from six samples of four Early Cretaceous passive margin formations of northern Venezuela.

PROVENANCE OF THE EARLY CRETACEOUS PASSIVE MARGIN

Previous investigations interpreted the Early Cretaceous siliciclastic passive margin strata to have been derived entirely from the Guyana Shield to the south (van Andel, 1958; González de Juana et al., 1980), with few indications of any particular drainage systems. The ages of detrital zircons from the passive margin units range from late Archean (2731Ma) to Silurian (415Ma), and all samples display similar distribution patterns with the exception of the Araure Formation (Fig. 2). The data are similar to U-Pb detrital zircon ages obtained from the modern Orinoco River and its tributaries which drain the northern Andes of Colombia and Venezuela as well as the Guyana Shield (Goldstein et al., 1997). Prominent Precambrian age peaks in the passive margin samples occur at ca.2.0, 1.8, 1.4 to 1.6, and 1.2- 0.95Ga. There are also a few grains that gave

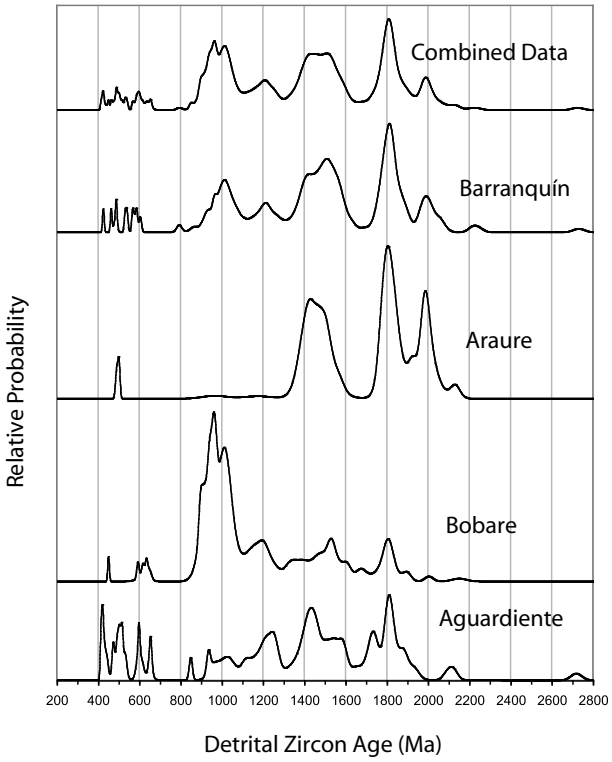

FIGURE 2 | **Probability density plot of U-Pb zircon detrital zircon ages from Early Cretaceous passive margin samples.**

late Archean ages. In addition, about 6 percent of the grains fall into the ca. 400-650Ma age range.

The Archean, Paleoproterozoic, and early Mesoproterozoic detrital zircon populations are a good match to known age provinces in the Guayana Shield (Fig. 3). Archaen rocks are present in the Imataca Complex of the Central Amazonian Province, and age peaks of ca.1.8 and 2.0Ga plus a few grains of ca.2.1 and 2.2Ga are a good match to the Maroni-Itacaiunal, Ventuari-Tapajos and Río Negro-Jurena Provinces (Fig. 3). The ca. 1.5Ga age peak is most likely derived from Rapakivi granites, including the 30,000km^2 Parguaza Batholith, which intrude older rocks of the Amazonia Craton (Gaudette et al., 1978; Mendoza, 1978, 2005), especially within the Ventuari-Tapajos Province.

The most remarkable feature of our dataset is the large proportion of detrital zircons giving prominent peaks at ca. 1.2 and 0.95-1.1Ga. The only known southern source area for this age population is the Sunsas province that lies far to the south in the Amazonian craton of Bolivia (Fig. 3). Rocks of this age, however, are also known from the basement inliers of the northern Andes of Colombia (Santa Marta, Santander, and Garzón massifs; e.g. Kroonemberg, 1982; Restrepo-Pace et al., 1997; Cordani et al., 2005; Fig. 3) and may also be present in the Mérida Andes (Figs. 1, 3; Burkley, 1976). Paleozoic strata from these areas are also a potential source for detrital zircons but there are no published data to evaluate that possibility. We speculate that the ca. 0.95-1.2Ga age population of detrital zircon was derived from the basement rocks of Colombia and possibly the Mérida Andes, and their Paleozoic cover, rather than the Sunsas Province senso stricto. The paleogeographic implications of this interpretation are discussed below.

There are several potential source areas for the Paleozoic and late Neoproterozoic detrital populations (ca. 415-650Ma) which only account for approximately 6 percent of the total number of analyses. The Neoproterozoic Brasiliano and Pampean Provinces contain ages ranging from ca. 0.7-0.5Ga, and the Famatinian arc terrane is a potential source terrane for zircons in the 0.5-0.4Ga age range (Fig. 3). These provinces are, however, located extremely far from the Early Cretaceous passive margin of Venezuela. Other potential source regions exist in the Mérida Andes and the Perijá Range (Fig. 2). These areas are uplifted blocks that contain Paleozoic and Precambrian rocks overlain by Cretaceous passive margin strata. In addition, the Cordillera de la Costa Belt of northern Venezuela and the northern Colombian Andes are possible source regions for this detrital population. The older rocks in all of these areas probably represent windows into the crust that underlies much of the Llanos Cenozoic foreland to the Colombian and Venezuelan thrustbelts (Feo-Codecido et al., 1984; Fig. 1). Unfortunately, little modern geochronology has been done in these regions. In the Cordillera de la Costa area (Fig. 1) Sisson et al. (2005) reported early Paleozoic (Cambrian and Ordovician) U-Pb zircon ages from several granitoid intrusions. Urbani et al. (2007) also reported a Cambrian (508Ma) U-Pb zircon age from the Todasana metadiorite located in the Cordillera de la Costa belt. Viscarret et al. (2007) reported early Paleozoic (Cambro/Ordovician) as well as late Paleozoic (Permian) U-Pb zircon ages determined on volcanic and plutonic rocks from the El Baúl area (Fig. 1). Burkley (1976) carried out an extensive U-Pb zircon geochronology project in the Mérida Andes. Although all his samples are complicated by Pb loss and/or the presence of inherited older zircon, he was able to determine early Paleozoic ages (Devonian, Silurian and Ordovician) on a number of granitoid bodies as well as some late Neoproterozoic ages of ca. 600Ma from three other granitoid intrusions. Thus, a local Venezuelan source region is a possibility for this detrital component. Paleozoic strata of Colombia and the Mérida Andes of Venezuela are also a potential source region for this detrital population, but no detrital zircon geochronology exists for these rock units.

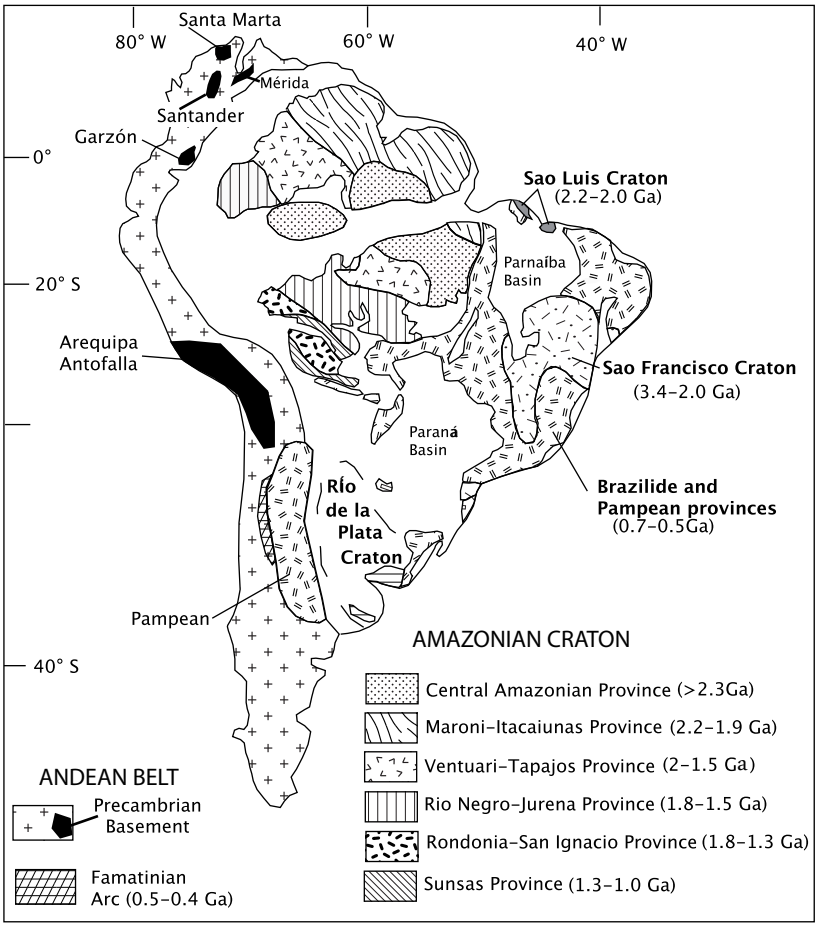

FIGURE 3 | **Generalized geologic map of the South American cratons depicting major tectonic provinces. Modified from Cordani et al. (2000) and Tassinari et al. (2000).**

PALEOGEOGRAPHIC IMPLICATIONS FOR THE PASSIVE MARGIN OF VENEZUELA

The modern Orinoco river system drains both the Guyana Shield and the Andes of Colombia and Venezuela and contains a population of detrital zircons that is similar to our Early Cretaceous passive margin samples, including the prominent ca. 0.95-1.2Ga population (Goldstein et al., 1997). Kasper and Larue (1986) attributed the great thickness of Paleocene and Eocene clastic detritus in the Lake Maracaibo Basin (Fig. 1) to a north-flowing paleofluvial system that drained the Colombian Andes and Guyana shield regions which they called the Proto-Orinoco River. In addition, Hoorn et al. (1995) likewise came to the conclusion that a northwest-flowing Proto-Orinoco River system drained the Andes and the Guyana shield prior to the Late Miocene forming a delta in the Lake Maracaibo region. By the Middle Miocene, uplift in Colombia and the Mérida Andes of Venezuela is postulated to have deflected the paleofluvial system into a more east-west orientation, marking the beginning of the current Orinoco drainage (Díaz de Gamero, 1996).We suggest that a similar Proto-Orinoco river system was responsible for the detrital zircon provenance of the Early Cretaceous passive margin of Venezuela. Our sample localities are shown in Figure (4A) in relation to the Jurassic Espino and Uribante rift structures. Note that the deltaic to shallow shelf deposits of the Barranquín formation occur on strike with the Espino Graben, and the Aguardiente and Bobare sample collection sites lie above the Uribante rift. We suggest that a paleo-river system drained eastern Colombia and western Venezuela and flowed down broad valleys above both the Espino Graben and Uribante rifts, following the principal that rifts are where subsidence is greatest, thus supplying the 0.95-1.2Ga detrital zircon component (Fig. 4A) before and during initial marine transgression in these areas.

REGIONAL PALEOGEOGRAPHIC IMPLICATIONS

Rojas-Agramonte et al. (2008) analysed 19 detrital zircon grains from the clastic sediments of the Early (?) to Late Jurassic (Oxfordian) San Cayetano Formation of western Cuba. The San Cayetano Formation is considered

to have been deposited in and above rift basins developed during breakup of Pangea during initial opening of the Proto-Caribbean (Pindell, 1985; Martön and Buffler, 1994, 1999; Iturralde-Vinent, 2003). Although a number of possible source areas have been suggested (including a Laurentian source), Rojas-Agramonte et al. (2008) concluded from their detrital zircon data that the San Cayetano Formation most likely had a Gondwanan (South American) provenance. They further speculated that the basin was geographically located off the current northeastern Venezuelan margin near the termination of the Espino Graben (Fig. 4B) and that it was fed in part by a river system running through the Espino and Uribante rifts. Although not explicitly discussed in their paper, the occurrence of a ca.1.5-1.6Ga detrital zircons in the San Cayetano Formation strongly supports a South American provenance as this age range lies within the Laurentian magmatic gap but is a prominent age found within the Amazonian craton as previously discussed and as shown by our detrital zircon data (Fig. 2). Also, their data (albeit very limited) exhibit very similar age populations to those of the Venezuelan passive margin strata in support of their general paleogeographic model. It thus appears that the Espino Graben and Uribante rifts hosted a Jurassic to Early Cretaceous Proto-Orinoco river system.

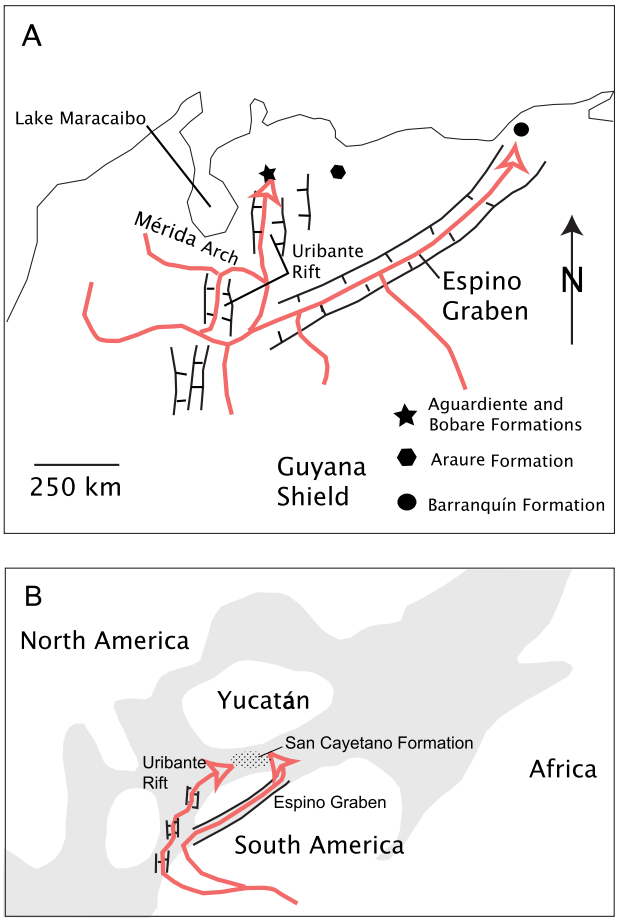

FIGURE 4 | **A) Proposed paleogeography of northern Venezuela depicting the Early Cretaceous Proto-Orinoco river drainage system. Arrows indicate possible sedimentary transport along a Proto-Orinoco river system. B) Paleogeography of the San Cayetano Formation as proposed by Rojas-Agramonte et al. (2008). Gray areas denote highly extended continental crust. The figure is adapted from Pindell and Kennan (2001) and Rojas-Agramonte et al. (2008).**

The paleofluvial system postulated here for the Jurassic and Early Cretaceous marked the beginning of a continental-scale drainage system that was resumed, after middle Cretaceous drowning of the paleo-river valleys (Villamil and Pindell, 1998), in the Paleogene, when the Caribbean collisional foredeep was first imposed on the western reaches of the northern South American passive margin (Pindell et al., 1998). It continues today as the Orinoco river, after a long history of persistent eastward deflection along the Venezuela-Trinidad margin due to the eastward-younging oblique collision of the Caribbean Plate and associated eastward lengthening of the zone of orogenic uplift (Díaz de Gamero, 1996). Thus, the continental scale Orinoco fluvial system seems to have persisted since the initial formation of the northern South American passive margin during the breakup of Pangea, suggesting that the longevity of such river systems may be the same order of magnitude as that of plate boundaries (eg. Prokopiev et al., 2008).

ACKNOWLEDGMENTS

This paper is a contribution to the BOLIVAR project supported by NSF grants EAR 0607533 and 0087361 to Wright, and support from NSF EAR-0003572 is acknowledged by Pindell. The GEODINOS project (Fundación Venezolana de Investigaciones Sismológicas and Universidad Central de Venezuela) provided logistical support in the field. Noguera received grant support from AAPG, the University of Georgia, Miriam Watts–Wheeler Scholarship Fund, and the Latin American and Caribbean Studies Institute at the University of Georgia. University of Georgia undergraduate students Ted Lord, Emily First, Auggie Parinello and Corin Steadman helped with mineral spearation and/or the LA-MC-ICPMS analyses. Student travel and LA-MC-ICPMS analyses were subsidized by the Arizona LaserChron center through NSF grants EAR 0443387 and 0732436.

REFERENCES

Bellizzia, A., Rodríguez, D., 1967. Excursión a la región de Duaca–Barquisimeto–Bobare. Caracas, Boletín de Geología, 16, 289-309.

Burkley, L.A., 1976. Geochronology of the Central Andes, Venezuela. Doctoral Thesis. Cheveland (Ohio), Case Western Reserve University, 159pp.

Bushman, J.R., 1967. Geología de la región de Agua Blanca y San Carlos, Venezuela. Caracas, Boletín de Geología, 16, 311-336.

Cordani, U.G., Sato, K., Teixeira, W., 2000. Crustal evolution of the South American platform. In: Cordani, U.G., Milani, E.J., Filho, A.T. (eds.). Tectonic evolution of South America. Rio de Janeiro, 31st International Geological Congress, 19-40.

Cordani, U., Cardona, A., Jiménez, D.M., 2005. Geochronology of Proterozoic basement inliers in the Colombian Andes: tectonic history of remnants of a fragmented Grenville belt. In: Vaughan, A.P.M., Leat, P.T., Pankhurst, R.J. (eds.). Terrane Processes of the Margins of Gondwana. London, Geological Society, 246 (Special Publications), 329-346.

Díaz de Gamero, M.L., 1996. The changing course of the Orinoco River during the Neogene: a review. Paleogeography, Paleoclimatology, Palaeoecology, 123, 385-402.

Dickinson, W.R., Gehrels, G.E., 2003. U-Pb ages of detrital zircons from Permian and Jurassic eolian sandstones of the Colorado Plateau, USA: Paleogeographic implications. Sedimentary Geology, 163, 29-66.

Erikson, J.P., Pindell, J.L., 1998a. Cretaceous through Eocene sedimentation and Paleogeography of a Passive Margin in northeastern Venezuela. In: Pindell, J.L., Drake, C.L. (eds.). Paleogeographic Evolution and Non-Glacial Eustasy, Northern South America. Society for Sedimentary Geology (SEPM), 58 (Special Publications), 218-259.

Erikson, J.P., Pindell, J.L., 1998b. Sequence stratigraphy and relative sea-level history of the Cretaceous to Eocene passive margin of North-East Venezuela and the possible tectonic and eustatic causes of stratigraphic development. In: Pindell, J.L., Drake, C.L. (eds.). Paleogeographic Evolution and Non-Glacial Eustasy, Northern South America. Society for Sedimentary Geology (SEPM), 58 (Special Publications), 261-281.

Feo-Codecido, G., Smith, F.Jr., Aboud, N., Di Giacomo, E., 1984. Basement and Paleozoic rocks of the Venezuelan Llanos Basin. Geological Society of America Memoir, 162, 175-187.

Gaudette, H.E., Mendoza, V., Hurley, F.M., 1978. Geology and age of the Parguaza Rapakivi Granite, Venezuela. Geological Society of America Bulletin, 89, 1135-1340.

Gehrels, G.E., Valencia, V., Pullen, A., 2006. Detrital zircon geochronology by laser-ablation multicollector ICPMS at the Arizona Laser-Chron Center. In: Olszewski, T., Huff, W. (eds.). Geochronology: Emerging opportunities. Philadelphia, Paleontological Society Short Course, 1-10.

Goldstein, S.L., Arndt, N.T., Stallard, R.F., 1997. The history of a continent from U-Pb ages of zircons from Orinoco River sand and Sm-Nd isotopes in Orinoco basin river sediments. Chemical Geology, 139, 271-286.

González de Juana, C., Iturralde, J.M., Piccard, X., 1980. Geología de Venezuela y de sus Cuencas Petrolíferas. Caracas, Foninves, 1031pp.

Hoorn, C., Guerrero, J., Sarmiento, G.A., Lorente, M.A., 1995. Andean tectonics as a cause for changing drainage patterns in Miocene northern South America. Geology, 23, 237-240.

Iturralde-Vinent, M.A., 2003. A brief account of the evolution of the Caribbean seaway: Jurassic to present. In: Prothero, D., Ivany, L., Nesbitt, E., (eds.). From greenhouse to icehouse: The marine Eocene–Oligocene transition. New York, Columbia University Press, 386-396.

Kasper, D.A., Larue, D.K., 1986. Paleogeographic and tectonic implications of quartzose sandstones of Barbados. Tectonics, 5, 837-854.

Kroonemberg, G.S., 1982. A Grenvillian granulite belt in the Colombian Andes and its relations to the Guyana Shield. Geologie en Mijnbouw, 61, 325-333.

Ludwig, K.R., 2003. Isoplot 3.00. Berkeley Geochronology Center, 4 (Special Publications), 70pp.

Marton, G., Buffler, R.T., 1994. Jurassic reconstruction of the Gulf of Mexico Basin. International Geology Review, 36, 545-586.

Marton, G., Buffler, R.T., 1999. Jurassic-Early Cretaceous tectono-paleogeographic evolution of the southeastern Gulf of Mexico Basin. In: Mann, P. (ed.). Caribbean Basins. Amsterdam, Elsevier Science, Series Sedimentary Basins of the World, 4, 63-91.

Mendoza, V., 1978. Petrogénesis del granito rapakivi del Parguaza, NO del Escudo de Guyana, Venezuela. Caracas, Boletín de Geología, 7(5) (Special Publications), 3549-3588.

Mendoza, V., 2005. Geología de Venezuela. Geos, 38, 119-123 and 783pp. in CD.

Moticska, P., 1985. Volcanismo Mesozoico en el subsuelo de la Faja Petrolífera de Orinoco. Caracas, Memoria VI Congreso Geológico Venezolano, 3, 1929-1943.

Ortega-Obregon, C., Keppie, J.D., Murphy, J.B., 2009. Geology and geochronology of Paleozoic rocks in western Acatlan Complex. Southern Mexico: Evidence for contiguity across an extruded high-pressure belt and constraints on Paleozoic reconstructions. Geological Society of America Bulletin, 121, 1678-1694.

Pindell, J.L., 1985. Alleghanian reconstruction and the subsequent evolution of the Gulf of Mexico, Bahamas, and Proto-Caribbean Sea. Tectonics, 4, 1-39.

Pindell, J.L., Erikson, J.P., 1994. Mesozoic passive margin of northern South America. In: Salfity, J.A. (ed.). Cretaceous tectonics in the Andes. Vieweg Publishing, Earth Evolution Sciences, International Monograph Series, 1-60.

Pindell, J.L., Higgs, R., Dewey, J.F., 1998. Cenozoic palinspastic reconstruction, paleogeographic evolution, and hydrocarbon setting of the northern margin of South America. In: Pindell, J.L., Drake, C.L. (eds.). Paleogeographic Evolution and Non-glacial Eustasy, northern South America. Tulsa, Society for Sedimentary Geology (SEPM), 58 (Special Publications), 45-86.

Pindell, J.L., Kennan, L.J.G., 2001, Kinematic evolution of the Gulf of Mexico and the Caribbean. In: Fillon, R. (ed.). Transactions, 21st Bob Perkins Gulf Coast Section of the Society of Economic and Paleontologists and Mineralogists (GCSSEPM) Research Conference, Gulf Coast Section of the Society of Economic and Paleontologists and Mineralogists, 193-220.

Pindell, J., Kennan, L., Wright, D., Erikson, J., 2009. Clastic domains of sandstones in central/eastern Venezuela, Trinidad and Barbados: heavy mineral and tectonic constraints on

provenance and palaeogeography. In: James, K.H., Lorente, M.A., Pindell, J.L. (eds.). The Origin and Evolution of the Caribbean Plate. London, Geological Society, 328 (Special Publications), 739-794.

Prokopiev, A.V., Toro, J., Miller, E.L., Gehrels, G.E, 2008. The paleo-Lena River-200 m.y. of transcontinental zircon transport in Siberia. Geology, 36(9), 699-702.

Ramos, V.A., 2009. Anatomy and global context of the Andes: Main geologic features and the Andean orogenic cycle. In: Kay, S.M., Ramos, V.A., Dickinson, W.R. (eds.). Backbone of the Americas: Shallow subduction, plateau uplift, and ridge and terrane collision. Geological Society of America Memoir, 204, 31-65.

Renz, O., Short, K.C., 1960. Estratigrafía de la región comprendida entre el Pao y Acarigua, estados Cojedes y Portuguesa. Caracas, Memoria III Congreso Geológico Venezolano, 1, 277-315.

Restrepo-Pace, P.A., Ruiz, J., Gehlers, G., 1997. Geochronology and Nd isotopic data of Grenville-age rocks in the Colombian Andes: new constraints for Late Proterozoic-Early Palezoic paleocontinental reconstructions of the Americas. Earth and Planetary Science Letters, 150, 427-441.

Riggs, N.R., Lehman, T.M., Gehrels, G.E., 1996. Detrital zircon link between headwaters and terminus of the Upper Triassic Chinle-Dockum paleoriver system. Science, 273, 97-100.

Rodríguez, I., Rodríguez, J., 2003. Gravity and magnetic modelling across the Guárico Sub-basin, Espino Graben, Venezuela. Institut de Recherche pour le développement (IRD) – Université Paul Sabatier, Andean Geodynamics, Extended Abstracts, 533-536.

Rojas-Agramonte, Y., Kroner, A., Pindell, J., 2008. Detrital zircon geochronology of Jurassic sandstones of western Cuba (San Cayetano Formation): Implications for the Jurassic paleogeography of the NW Proto-Caribbean. American Journal of Science, 308, 639-656.

Salvador, A., 1961. Guidebook to the geology of northeastern Trujillo. Maracaibo, Sociedad Venezolana de Geólogos, Region Occidental, 3, 33pp.

Schubert, C., 1986. Stratigraphy of the Jurassic La Quinta Formation, Mérida Andes, Venezuela: type sections. Zeitschrift der Deutsche Geologische Gesellschaft, 137, 391-411.

Sisson, V., Avé Lallemant, H.G., Ostos, M., Blythe, A.F., Snee, L.W., Copeland, P., Wright, J.E., Donelick, R.A., Guth, L.R., 2005. Overview of radiometric ages in three allochthonous belts of northern Venezuela: Old ones, new ones, and their impact on regional geology. In: Avé-Lallemant, H., Sisson, V., (eds.). Caribbean-South American Plate Interactions, Venezuela. Geological Society of America, 394 (Special Paper), 91-117.

Stacey, J.S., Kramers, J.D., 1975. Approximation of terrestrial lead isotope evolution by a twostage model. Earth and Planetary Science Letters, 26, 207-221.

Tassinari, C.C.G., Bettencourt, J.S., Geraldes, M.C., 2000. The Amazon craton. In: Cordani, U.G., Milani, E.J., Thomaz-Filho, A., Campos, D.A. (eds.). Tectonic evolution of South America. Rio de Janeiro, 31st International Geological Congress, 41-95.

Urbani, F., Wright, J., Grande, S., 2007. La Metadiorita de Todasana, Cordillera de la Costa, estado Vargas: Geología y geocronología. Caracas, Geos, 39, 93-94 and 33pp in CD.

Van Andel, T., 1958. Origin and classification of Cretaceous, Paleocene and Eocene sandstones of Western Venezuela. American Association of Petroleum Geologists Bulletin, 42, 734-763.

Viscarret, P., Wright, J.E., Urbani, F., 2007. Dataciones U/Pb SHRIMP en circón de rocas del macizo de El Baúl, estado Cojedes, Venezuela. Caracas, Geos, 39, 94-95 and 37pp in CD.

Villamil, T., Pindell, J.L., 1998. The Mesozoic of northern South America: foundations for sequence stratigraphic studies in passive margin strata deposited during non-glacial times. In: Pindell, J.L., Drake, C.L. (eds.). Paleogeographic Evolution and Non-glacial Eustasy, northern South America. Tulsa, Society for Sedimentary Geology (SEPM), 58 (Special Publications), 283-318.

Weber, B., Schaaf, P., Valencia, V.A., Iriondo, A., Ortega–Gutiérrez, F., 2006. Provenance ages of late Paleozoic sandstones (Santa Rosa Formation) from the Maya block, SE Mexico. Implications on the tectonic evolution of western Pangea. Revista Mexicana de Ciencias Geologicas, 23, 262-276.

Weber, B., Valencia, V.A., Schaaf, P., Pompa-Mera, V., Ruiz, J., 2008. Significance of provenance ages from the Chiapas Massif Complex (southeastern Mexico): Redefining the Paleozoic basement of the Maya block and its evolution in a Peri-Gondwanan realm. Journal of Geology, 116, 619-639.

Yoris, F., Ostos, M., Zamora, L., 1997. Petroleum Geology of Venezuela. In: Singer, J.M. (ed.). 1997 Venezuela Well Evaluation Conference. Schlumberger Surenco. Houston, Jolley Printing, 1-44.

Manuscript received November 2010;
revision accepted May 2011;
published Online June 2011.

ELECTRONIC APPENDIX

Sample Number	Unit	Longitude W	Latitude N
VMN-7	Aguardiente	70.109	10.1466
VMN-16	Bobare	69.448	10.4371
VMN-17	Bobare	69.4083	10.4024
VMN-18	Araure	69.097	9.6701
VMN-32	Barranquín	64.5351	10.2328
VMN-35	Barranquín	64.384	10.2919

Analysis	U (ppm)	^{206}Pb ^{204}Pb	U/Th	$^{206}Pb^*$ $^{207}Pb^*$	± (%)	Isotope ratios $^{207}Pb^*$ $^{235}U^*$	± (%)	$^{206}Pb^*$ ^{238}U	± (%)	error corr.	Apparent ages (Ma) $^{206}Pb^*$ $^{238}U^*$	± (Ma)	$^{207}Pb^*$ ^{235}U	± (Ma)	$^{206}Pb^*$ $^{207}Pb^*$	± (Ma)	Best age (Ma)	± (Ma)
VMN7-1	66	4764	2.9	14.0971	1.9	1.5638	3.2	0.1599	2.5	0.80	956.1	22.6	956.0	19.7	955.6	39.3	956.1	22.6
VMN7-2	150	15084	2.5	10.5063	1.1	3.4787	1.5	0.2651	1.0	0.68	1515.8	13.5	1522.4	11.7	1531.6	20.6	1531.6	20.6
VMN7-3	370	14824	2.7	17.3221	1.3	0.6340	2.0	0.0796	1.5	0.76	494.0	7.3	498.6	8.0	519.5	29.1	494.0	7.3
VMN7-4	272	11912	4.3	16.6961	1.6	0.7951	2.5	0.0963	1.9	0.77	592.5	10.8	594.0	11.2	599.7	34.6	592.5	10.8
VMN7-5	277	25030	3.7	12.1967	1.5	2.2986	1.8	0.2033	1.0	0.56	1193.2	10.9	1211.9	12.7	1245.2	29.2	1245.2	29.2
VMN7-6	189	20970	1.3	10.3510	1.9	3.3996	2.1	0.2552	1.0	0.48	1465.3	13.5	1504.3	16.8	1559.6	35.1	1559.6	35.1
VMN7-7	207	26340	1.2	9.0124	1.4	4.7460	1.9	0.3102	1.3	0.67	1741.8	19.1	1775.4	15.7	1815.2	25.4	1815.2	25.4
VMN7-8	118	18190	1.7	8.9888	1.2	4.9720	2.0	0.3241	1.6	0.80	1809.9	24.9	1814.6	16.7	1819.9	21.4	1819.9	21.4
VMN7-9	66	7260	2.9	11.1524	1.3	2.9133	1.7	0.2356	1.0	0.60	1364.0	12.3	1385.4	12.7	1418.4	25.8	1418.4	25.8
VMN7-10	131	24314	1.3	7.6959	1.3	6.7098	1.6	0.3745	1.0	0.61	2050.6	17.6	2073.9	14.5	2097.1	22.8	2097.1	22.8
VMN7-11	523	44220	5.7	10.8854	1.1	2.9765	2.4	0.2350	2.1	0.89	1360.6	26.2	1401.6	18.2	1464.6	20.5	1464.6	20.5
VMN7-12	110	14620	2.1	9.0325	1.3	4.9843	1.9	0.3265	1.4	0.73	1821.5	21.9	1816.7	15.9	1811.1	23.3	1811.1	23.3
VMN7-13	126	13312	1.2	11.7191	1.3	2.6461	2.4	0.2249	2.1	0.85	1307.7	24.4	1313.6	17.9	1323.0	25.1	1323.0	25.1
VMN7-14	350	12628	1.8	16.6953	3.9	0.6585	8.5	0.0797	7.5	0.89	494.5	35.8	513.7	34.2	599.8	85.2	494.5	35.8
VMN7-15	76	8036	1.5	11.4783	1.4	2.7528	2.4	0.2292	1.9	0.80	1330.1	22.8	1342.9	17.7	1363.1	27.5	1363.1	27.5
VMN7-16	576	60090	2.7	9.3984	1.1	4.2008	2.5	0.2863	2.2	0.90	1623.2	32.0	1674.2	20.4	1738.6	20.3	1738.6	20.3
VMN7-17	270	28766	1.7	10.6598	1.0	3.2629	3.2	0.2523	3.0	0.95	1450.1	38.8	1472.3	24.5	1504.3	18.9	1504.3	18.9
VMN7-18	89	3436	0.9	17.9046	4.3	0.6438	4.5	0.0836	1.0	0.22	517.6	5.0	504.7	17.7	446.5	96.5	517.6	5.0
VMN7-19	166	14992	2.0	10.4255	1.7	3.6076	1.9	0.2728	1.0	0.52	1554.9	13.8	1551.2	15.4	1546.2	31.2	1546.2	31.2
VMN7-20	181	15116	2.3	11.2770	1.4	2.8485	2.3	0.2330	1.9	0.80	1350.1	22.7	1368.4	17.5	1397.2	26.7	1397.2	26.7
VMN7-21	227	5660	1.5	18.0454	3.0	0.5181	3.2	0.0678	1.0	0.33	423.0	4.3	423.9	11.0	429.0	67.0	423.0	4.3
VMN7-22	442	11662	3.8	17.5705	1.0	0.6334	3.3	0.0807	3.2	0.95	500.4	15.2	498.2	13.1	488.2	22.2	500.4	15.2
VMN7-23	322	8688	1.8	18.0769	1.0	0.5405	2.3	0.0709	2.1	0.89	441.3	8.7	438.7	8.2	425.1	22.8	441.3	8.7
VMN7-24	212	19058	3.2	12.4806	1.5	2.2619	2.1	0.2047	1.5	0.69	1200.7	16.1	1200.5	14.9	1200.0	30.0	1200.0	30.0
VMN7-25	108	11116	1.5	8.7304	1.0	5.3717	1.4	0.3401	1.0	0.71	1887.3	16.4	1880.3	12.1	1872.7	18.0	1872.7	18.0
VMN7-26	99	7878	2.6	13.8714	2.1	1.5869	2.3	0.1596	1.0	0.43	954.8	8.9	965.1	14.5	988.5	42.7	988.5	42.7
VMN7-27	162	14648	0.9	11.0021	1.7	2.4036	2.3	0.1918	1.5	0.65	1131.1	15.4	1243.7	16.4	1444.3	33.1	1444.3	33.1
VMN7-28	187	8750	1.8	17.7328	5.6	0.5934	5.8	0.0763	1.5	0.25	474.1	6.6	473.0	21.9	467.8	124.0	474.1	6.6
VMN7-30	50	7716	1.7	9.0622	1.6	4.8809	1.9	0.3208	1.0	0.52	1793.6	15.7	1799.0	16.2	1805.1	29.9	1805.1	29.9
VMN7-31	273	36986	3.6	10.2378	1.5	3.4655	2.2	0.2573	1.6	0.73	1476.1	20.8	1519.4	17.0	1580.2	27.3	1580.2	27.3
VMN7-32	680	80546	5.0	10.4007	1.1	3.4394	1.5	0.2594	1.0	0.69	1487.0	13.3	1513.4	11.5	1550.6	19.9	1550.6	19.9
VMN7-33	228	16602	3.5	13.6182	1.6	1.6794	1.9	0.1659	1.0	0.52	989.3	9.2	1000.8	12.1	1025.9	32.8	1025.9	32.8
VMN7-34	553	19184	5.7	15.2595	1.0	0.9616	2.5	0.1064	2.2	0.91	651.9	13.8	684.1	12.2	791.5	21.7	651.9	13.8
VMN7-35	181	11012	2.9	12.3779	1.6	2.0255	2.8	0.1818	2.3	0.82	1077.0	22.6	1124.1	18.9	1216.3	31.1	1216.3	31.1
VMN7-36	285	32606	2.7	9.4420	1.6	4.2635	2.5	0.2920	1.9	0.76	1651.3	27.1	1686.3	20.2	1730.1	29.4	1730.1	29.4
VMN7-37	259	18022	2.7	13.4915	1.4	1.7730	1.7	0.1735	1.0	0.59	1031.3	9.5	1035.6	10.9	1044.7	27.3	1044.7	27.3
VMN7-38	150	4874	2.1	18.4810	4.1	0.5129	4.4	0.0687	1.6	0.35	428.6	6.4	420.4	15.2	375.6	92.9	428.6	6.4
VMN7-39	49	4636	1.5	11.1848	1.7	2.8587	2.4	0.2319	1.6	0.69	1344.4	19.9	1371.1	17.9	1412.9	33.1	1412.9	33.1
VMN7-40	107	10662	5.7	12.1272	1.4	2.4690	1.7	0.2172	1.0	0.59	1266.8	11.5	1263.0	12.3	1256.4	26.8	1256.4	26.8
VMN7-41	268	29192	3.1	9.0964	1.3	4.7650	2.2	0.3144	1.8	0.82	1762.1	27.8	1778.7	18.4	1798.3	22.9	1798.3	22.9
VMN7-42	217	24674	1.9	9.0510	1.1	4.8895	1.5	0.3210	1.0	0.69	1794.4	15.7	1800.4	12.3	1807.4	19.3	1807.4	19.3
VMN7-43	235	23662	2.3	9.5679	1.3	3.9897	1.7	0.2769	1.0	0.60	1575.5	14.0	1632.1	13.4	1705.8	24.3	1705.8	24.3
VMN7-44	75	3304	2.6	13.1479	3.8	1.8502	4.0	0.1764	1.0	0.26	1047.5	10.1	1063.5	26.1	1096.6	76.5	1096.6	76.5
VMN7-45	260	4476	1.4	5.3367	1.5	12.1056	1.8	0.4685	1.0	0.56	2477.2	20.6	2612.6	16.9	2719.3	24.6	2719.3	24.6
VMN7-46	252	10330	5.2	15.9285	2.4	0.8440	2.6	0.0975	1.0	0.39	599.7	5.7	621.3	12.1	700.8	51.0	599.7	5.7

DOI: 10.1344/105.000001698

Analysis	U (ppm)	^{206}Pb ^{204}Pb	U/Th	$^{206}Pb^*$ $^{207}Pb^*$	± (%)	Isotope ratios $^{207}Pb^*$ $^{235}U^*$	± (%)	$^{206}Pb^*$ ^{238}U	± (%)	error corr.	Apparent ages (Ma) $^{206}Pb^*$ $^{238}U^*$	± (Ma)	$^{207}Pb^*$ ^{235}U	± (Ma)	$^{206}Pb^*$ $^{207}Pb^*$	± (Ma)	Best age (Ma)	± (Ma)
VMN7-47	154	14614	2.6	10.9279	1.6	3.2214	1.9	0.2553	1.0	0.53	1465.9	13.1	1462.3	14.7	1457.2	30.5	1457.2	30.5
VMN7-48	465	30088	16.7	12.6979	1.6	2.0820	1.9	0.1917	1.0	0.53	1130.8	10.4	1142.9	12.9	1165.9	31.7	1165.9	31.7
VMN7-49	105	9874	1.9	11.2009	2.2	3.0753	2.6	0.2498	1.4	0.53	1437.6	17.7	1426.5	19.8	1410.1	41.9	1410.1	41.9
VMN7-50	195	23450	2.7	10.8089	1.4	3.3093	1.7	0.2594	1.0	0.59	1486.9	13.3	1483.2	13.1	1478.0	25.6	1478.0	25.6
VMN7-51	191	2322	0.4	9.1721	6.8	4.0125	7.3	0.2669	2.8	0.38	1525.2	38.0	1636.7	59.7	1783.2	123.7	1783.2	123.7
VMN7-52	60	4732	1.6	12.6407	1.9	2.2285	2.2	0.2043	1.0	0.46	1198.4	10.9	1190.0	15.2	1174.9	38.1	1174.9	38.1
VMN7-54	60	6504	1.6	10.9445	1.1	3.2314	1.5	0.2565	1.0	0.67	1471.9	13.2	1464.7	11.6	1454.3	21.3	1454.3	21.3
VMN7-55	138	6582	2.1	10.9826	3.1	3.1980	3.2	0.2547	1.0	0.31	1462.8	13.1	1456.7	25.0	1447.7	58.4	1447.7	58.4
VMN7-57	298	19026	3.2	8.8660	1.1	4.5403	4.8	0.2920	4.7	0.97	1651.3	68.2	1738.4	40.1	1844.8	20.3	1844.8	20.3
VMN7-58	158	15400	2.5	10.0679	2.3	3.7593	2.5	0.2745	1.0	0.39	1563.6	13.9	1584.1	20.4	1611.5	43.7	1611.5	43.7
VMN7-59	122	19108	1.4	8.6147	1.5	5.5143	1.8	0.3445	1.0	0.54	1908.4	16.5	1902.8	15.8	1896.7	27.7	1896.7	27.7
VMN7-60	175	25064	1.5	9.3360	1.0	4.4268	1.4	0.2997	1.0	0.71	1690.0	14.9	1717.4	11.7	1750.8	18.3	1750.8	18.3
VMN7-61	257	25656	4.1	12.2281	1.5	2.4207	2.0	0.2147	1.4	0.66	1253.7	15.4	1248.8	14.6	1240.2	29.8	1240.2	29.8
VMN7-62	187	32398	3.2	9.0226	1.8	5.0578	2.0	0.3310	1.0	0.50	1843.1	16.0	1829.1	17.1	1813.1	31.8	1813.1	31.8
VMN7-63	328	31360	4.0	12.4118	1.0	2.3180	1.9	0.2087	1.7	0.86	1221.7	18.6	1217.8	13.8	1210.9	19.8	1210.9	19.8
VMN7-64	291	14360	1.7	8.7138	2.9	3.7649	6.1	0.2379	5.4	0.88	1376.0	66.3	1585.3	48.8	1876.1	52.0	1876.1	52.0
VMN7-65	29	3146	2.3	11.1436	3.0	3.1483	3.2	0.2545	1.0	0.31	1461.4	13.1	1444.6	24.7	1419.9	58.3	1419.9	58.3
VMN7-66	180	19970	1.6	9.0436	1.0	4.9239	1.4	0.3230	1.0	0.71	1804.2	15.7	1806.4	11.9	1808.9	18.2	1808.9	18.2
VMN7-67	60	5000	2.1	13.6733	2.0	1.7237	2.2	0.1709	1.0	0.45	1017.3	9.4	1017.4	14.2	1017.7	39.7	1017.7	39.7
VMN7-68	27	3274	0.7	10.4124	2.1	3.6314	2.4	0.2742	1.2	0.49	1562.3	16.1	1556.4	18.8	1548.5	38.6	1548.5	38.6
VMN7-69	148	17956	2.0	9.5061	2.5	3.6897	4.7	0.2544	4.0	0.85	1461.0	52.6	1569.1	37.8	1717.7	45.8	1717.7	45.8
VMN7-70	305	9260	1.8	17.1814	1.3	0.6909	2.1	0.0861	1.7	0.79	532.4	8.5	533.3	8.8	537.4	28.8	532.4	8.5
VMN7-71	108	11984	4.0	10.6289	1.3	3.3963	1.6	0.2618	1.0	0.61	1499.1	13.4	1503.5	12.8	1509.8	24.4	1509.8	24.4
VMN7-72	502	13322	2.7	18.2059	1.4	0.5037	1.7	0.0665	1.0	0.59	415.1	4.1	414.2	5.8	409.2	30.7	415.1	4.1
VMN7-73	168	13830	3.4	12.9019	1.9	1.9891	2.6	0.1861	1.8	0.68	1100.4	17.9	1111.8	17.7	1134.3	38.4	1134.3	38.4
VMN7-74	360	41838	3.1	9.8368	1.3	4.1145	3.8	0.2935	3.6	0.94	1659.2	51.9	1657.2	30.8	1654.6	23.4	1654.6	23.4
VMN7-75	88	12158	2.3	11.3293	2.1	3.0177	2.5	0.2480	1.4	0.55	1427.9	17.7	1412.1	19.2	1388.3	40.6	1388.3	40.6
VMN7-76	57	8176	1.3	10.1719	1.0	3.7919	1.4	0.2797	1.0	0.71	1590.1	14.1	1591.0	11.4	1592.3	18.8	1592.3	18.8
VMN7-77	76	5434	1.2	14.9917	2.7	1.2972	2.9	0.1410	1.0	0.35	850.6	8.0	844.5	16.6	828.5	56.7	850.6	8.0
VMN7-78	352	57368	6.4	8.4232	1.3	5.7625	1.6	0.3520	1.0	0.62	1944.3	16.8	1940.8	14.1	1937.0	22.9	1937.0	22.9
VMN7-79	72	11060	1.4	9.4395	1.3	4.4842	1.6	0.3070	1.0	0.61	1725.9	15.1	1728.0	13.6	1730.6	23.9	1730.6	23.9
VMN7-80	218	20446	3.3	12.1205	1.0	2.4329	1.4	0.2139	1.0	0.71	1249.4	11.4	1252.4	10.2	1257.5	19.6	1257.5	19.6
VMN7-81	167	7852	2.2	16.5881	1.9	0.8300	2.6	0.0999	1.8	0.68	613.6	10.2	613.6	11.9	613.8	40.8	613.6	10.2
VMN7-82	211	28214	2.3	11.2215	1.5	2.9324	2.1	0.2387	1.5	0.72	1379.7	18.8	1390.3	15.9	1406.6	27.8	1406.6	27.8
VMN7-83	118	15510	1.2	9.4434	1.0	4.5451	1.8	0.3113	1.5	0.83	1747.1	22.6	1739.3	14.9	1729.9	18.4	1729.9	18.4
VMN7-84	279	10600	3.1	17.5872	1.0	0.6409	1.7	0.0818	1.3	0.80	506.6	6.5	502.9	6.7	486.1	22.3	506.6	6.5
VMN7-86	114	7818	1.8	8.6526	1.0	5.4525	2.2	0.3422	2.0	0.89	1897.1	32.2	1893.1	19.0	1888.8	18.4	1888.8	18.4
VMN7-87	174	9834	2.7	11.0736	1.0	3.0611	1.4	0.2458	1.0	0.69	1417.0	12.7	1423.0	11.1	1432.0	19.9	1432.0	19.9
VMN7-88	439	32810	3.6	12.1402	1.2	2.4680	1.5	0.2173	1.0	0.66	1267.6	11.5	1262.7	11.0	1254.3	22.5	1254.3	22.5
VMN7-89	391	13794	2.3	16.4681	1.9	0.8962	2.2	0.1070	1.0	0.46	655.5	6.2	649.7	10.4	629.4	41.4	655.5	6.2
VMN7-90	79	4328	1.8	13.8176	2.1	1.7006	2.3	0.1704	1.1	0.46	1014.5	9.9	1008.8	14.8	996.4	41.8	996.4	41.8
VMN7-91	173	21374	2.8	11.1451	1.0	2.9178	1.4	0.2358	1.0	0.70	1365.1	12.3	1386.5	10.8	1419.7	19.5	1419.7	19.5
VMN7-92	200	20584	2.2	9.0117	1.2	4.8262	2.4	0.3154	2.1	0.86	1767.4	31.7	1789.5	20.2	1815.3	22.5	1815.3	22.5
VMN7-93	50	4734	1.6	12.2103	2.1	2.4334	2.3	0.2155	1.0	0.44	1258.0	11.4	1252.5	16.5	1243.1	40.3	1243.1	40.3
VMN7-94	59	5898	3.7	12.7241	2.5	2.0662	2.8	0.1907	1.2	0.42	1125.0	12.1	1137.7	19.1	1161.8	50.3	1161.8	50.3

DOI: 10.1344/105.000001698

Analysis	U	^{206}Pb	U/Th	$^{206}Pb^*$	±	Isotope ratios $^{207}Pb^*$	±	$^{206}Pb^*$	±	error	Apparent ages (Ma) $^{206}Pb^*$	±	$^{207}Pb^*$	±	$^{206}Pb^*$	±	Best age	±
	(ppm)	^{204}Pb		$^{207}Pb^*$	(%)	$^{235}U^*$	(%)	^{238}U	(%)	corr.	$^{238}U^*$	(Ma)	^{235}U	(Ma)	$^{207}Pb^*$	(Ma)	(Ma)	(Ma)
VMN7-95	200	16444	4.7	13.8750	1.3	1.5545	1.6	0.1564	1.0	0.62	936.9	8.7	952.3	10.0	988.0	25.9	936.9	8.7
VMN7-96	249	19972	4.8	9.0103	1.0	4.4705	1.4	0.2921	1.0	0.71	1652.2	14.6	1725.5	11.7	1815.6	18.2	1815.6	18.2
VMN7-97	260	26020	1.9	7.5682	1.0	6.0310	1.4	0.3310	1.0	0.70	1843.4	16.0	1980.3	12.4	2126.5	17.9	2126.5	17.9
VMN7-98	142	14778	4.0	13.0275	1.0	1.9202	1.4	0.1814	1.0	0.70	1074.8	9.9	1088.2	9.5	1115.0	20.1	1115.0	20.1
VMN7-99	149	14188	2.6	10.9750	1.0	2.9202	1.9	0.2324	1.6	0.85	1347.3	19.9	1387.2	14.5	1449.0	19.1	1449.0	19.1
VMN7-100	420	46768	2.9	10.2054	1.1	3.4354	3.6	0.2543	3.4	0.95	1460.5	44.7	1512.5	28.2	1586.2	20.0	1586.2	20.0
VMN16-1	212	22328	3.1	13.0226	1.8	1.9354	2.0	0.1828	1.0	0.50	1082.2	10.0	1093.4	13.5	1115.7	34.9	1115.7	34.9
VMN16-2	120	11214	2.2	13.8972	1.7	1.5803	2.0	0.1593	1.1	0.52	952.8	9.3	962.5	12.7	984.7	35.5	952.8	9.3
VMN16-3	100	9836	3.1	14.1958	1.3	1.5741	1.8	0.1621	1.2	0.67	968.3	10.8	960.1	11.1	941.3	27.1	968.3	10.8
VMN16-4	256	22858	1.9	9.7466	1.0	3.3663	5.6	0.2380	5.5	0.98	1376.1	67.9	1496.6	43.6	1671.7	18.5	1671.7	18.5
VMN16-5	185	14056	1.2	14.3542	1.0	1.4351	1.4	0.1494	1.0	0.71	897.6	8.4	903.7	8.5	918.5	20.6	897.6	8.4
VMN16-6	54	4762	2.2	14.3276	1.5	1.5027	1.8	0.1561	1.0	0.55	935.3	8.7	931.5	11.1	922.3	31.1	935.3	8.7
VMN16-7	105	9022	2.3	14.1570	1.4	1.4769	1.7	0.1516	1.0	0.58	910.2	8.5	921.0	10.4	946.9	28.5	910.2	8.5
VMN16-8	176	21734	1.5	10.4973	1.1	3.3317	1.5	0.2537	1.0	0.69	1457.3	13.0	1488.5	11.3	1533.3	19.8	1533.3	19.8
VMN16-9	144	13404	1.8	13.9292	2.1	1.5510	2.3	0.1567	1.0	0.44	938.4	8.7	950.9	14.1	980.0	41.9	938.4	8.7
VMN16-10	668	33500	1.8	10.5920	1.9	2.4416	3.2	0.1876	2.6	0.80	1108.2	26.0	1254.9	23.0	1516.3	36.2	1516.3	36.2
VMN16-11	220	18502	2.5	13.7947	1.8	1.6176	2.1	0.1618	1.0	0.48	967.0	9.0	977.0	13.0	999.8	36.8	999.8	36.8
VMN16-12	171	14464	4.2	13.7377	1.6	1.6810	1.9	0.1675	1.0	0.53	998.2	9.2	1001.4	12.0	1008.2	32.6	1008.2	32.6
VMN16-13	106	10458	2.4	14.0828	1.7	1.5335	2.0	0.1566	1.0	0.50	938.0	8.7	943.9	12.3	957.6	35.4	938.0	8.7
VMN16-14	130	12136	2.7	13.8778	1.5	1.6007	1.8	0.1611	1.0	0.56	963.0	8.9	970.5	11.2	987.5	30.3	987.5	30.3
VMN16-16	116	13992	1.8	11.0896	1.6	3.0780	1.9	0.2476	1.0	0.53	1425.9	12.8	1427.2	14.4	1429.2	30.4	1429.2	30.4
VMN16-17	147	12812	3.9	14.0921	1.1	1.5738	1.5	0.1608	1.0	0.68	961.5	9.3	959.9	9.5	956.3	23.0	961.5	9.3
VMN16-18	148	25412	1.5	9.0216	1.1	4.8612	1.5	0.3181	1.0	0.66	1780.3	15.6	1795.6	12.7	1813.3	20.5	1813.3	20.5
VMN16-19	82	14772	1.6	9.2266	1.4	4.6623	1.7	0.3120	1.0	0.58	1750.5	15.3	1760.5	14.4	1772.4	25.6	1772.4	25.6
VMN16-20	354	27674	3.2	12.6796	2.2	1.8306	3.1	0.1683	2.2	0.70	1003.0	20.4	1056.5	20.5	1168.8	44.0	1168.8	44.0
VMN16-21	182	19212	2.5	12.6124	1.8	2.1831	2.0	0.1997	1.0	0.49	1173.7	10.7	1175.7	14.2	1179.3	35.2	1179.3	35.2
VMN16-22	130	11852	1.2	13.7905	1.9	1.6616	2.2	0.1662	1.2	0.53	991.1	10.7	994.0	14.0	1000.4	38.0	1000.4	38.0
VMN16-23	106	17714	1.8	9.0263	1.0	4.9341	1.4	0.3230	1.0	0.71	1804.4	15.7	1808.1	11.9	1812.4	18.2	1812.4	18.2
VMN16-24	114	21160	2.3	9.1060	2.1	4.8017	2.3	0.3171	1.0	0.44	1775.7	15.5	1785.2	19.2	1796.4	37.3	1796.4	37.3
VMN16-25	50	7778	1.9	10.0103	1.7	3.8515	2.1	0.2796	1.2	0.57	1589.5	17.2	1603.6	17.1	1622.2	32.4	1622.2	32.4
VMN16-26	146	10216	2.9	13.7906	2.8	1.5596	3.4	0.1560	2.0	0.58	934.5	17.3	954.3	21.2	1000.4	56.5	934.5	17.3
VMN16-28	241	4536	1.9	11.3894	4.0	2.2737	7.9	0.1878	6.8	0.86	1109.6	69.0	1204.2	55.6	1378.1	77.2	1378.1	77.2
VMN16-29	371	41946	1.8	10.7799	4.3	2.7221	6.1	0.2128	4.4	0.72	1243.8	49.5	1334.5	45.5	1483.1	81.0	1483.1	81.0
VMN16-30	166	19552	1.5	12.2305	1.5	2.2232	2.1	0.1972	1.4	0.68	1160.3	15.1	1188.4	14.5	1239.8	29.7	1239.8	29.7
VMN16-31	175	15658	3.1	13.6246	1.6	1.6749	1.9	0.1655	1.0	0.53	987.3	9.2	999.1	11.9	1024.9	32.0	1024.9	32.0
VMN16-32	191	17966	3.6	13.5344	1.6	1.6608	2.2	0.1630	1.5	0.69	973.6	13.7	993.7	13.9	1038.3	32.0	1038.3	32.0
VMN16-33	85	13366	1.3	9.0361	1.4	4.7638	1.7	0.3122	1.0	0.59	1751.5	15.3	1778.5	14.2	1810.4	24.7	1810.4	24.7
VMN16-34	154	11062	0.7	8.5901	1.0	5.1933	1.6	0.3236	1.3	0.79	1807.0	20.2	1851.5	13.9	1901.8	18.1	1901.8	18.1
VMN16-35	42	2046	1.6	17.2447	6.2	0.7730	6.3	0.0967	1.1	0.17	594.9	6.1	581.5	27.9	529.3	135.9	594.9	6.1
VMN16-36	190	25318	1.6	10.0772	1.0	3.8798	1.4	0.2836	1.0	0.71	1609.3	14.2	1609.5	11.4	1609.8	18.6	1609.8	18.6
VMN16-37	235	12042	3.9	13.0309	1.8	1.7821	2.0	0.1684	1.0	0.49	1003.4	9.3	1039.0	13.3	1114.4	35.7	1114.4	35.7
VMN16-38	78	6850	3.4	13.8067	3.0	1.7509	3.2	0.1753	1.0	0.31	1041.4	9.6	1027.5	20.6	998.0	61.4	998.0	61.4
VMN16-39	325	14404	3.6	13.6340	1.0	1.6141	1.4	0.1596	1.0	0.71	954.6	8.9	975.7	8.9	1023.5	20.3	1023.5	20.3
VMN16-40	195	18390	3.2	13.5666	2.2	1.7280	2.4	0.1700	1.0	0.42	1012.3	9.4	1019.0	15.4	1033.5	44.1	1033.5	44.1
VMN16-41	90	8440	1.4	12.9217	1.4	2.0100	2.3	0.1884	1.9	0.81	1112.5	19.3	1118.9	15.8	1131.2	27.3	1131.2	27.3

DOI: 10.1344/105.000001698

Analysis	U (ppm)	^{206}Pb / ^{204}Pb	U/Th	$^{206}Pb^*$ / $^{207}Pb^*$	± (%)	Isotope ratios $^{207}Pb^*$ / $^{235}U^*$	± (%)	$^{206}Pb^*$ / ^{238}U	± (%)	error corr.	Apparent ages (Ma) $^{206}Pb^*$ / $^{238}U^*$	± (Ma)	$^{207}Pb^*$ / ^{235}U	± (Ma)	$^{206}Pb^*$ / $^{207}Pb^*$	± (Ma)	Best age (Ma)	± (Ma)
VMN16-43	136	6512	1.5	13.6139	2.5	1.6645	3.9	0.1643	3.0	0.77	980.9	27.4	995.1	24.8	1026.5	50.5	1026.5	50.5
VMN16-44	200	10452	2.7	16.1816	1.3	0.9040	2.1	0.1061	1.6	0.78	650.0	10.1	653.9	10.1	667.1	28.4	650.0	10.1
VMN16-45	170	19896	1.1	10.4805	1.4	3.4286	3.1	0.2606	2.7	0.89	1493.0	36.5	1511.0	24.1	1536.3	25.8	1536.3	25.8
VMN16-46	166	13598	3.2	14.0613	3.8	1.5982	3.9	0.1630	1.0	0.25	973.4	9.0	969.5	24.6	960.8	78.0	973.4	9.0
VMN16-47	64	12402	1.3	9.2582	2.9	4.4409	3.1	0.2982	1.0	0.33	1682.3	14.8	1720.0	25.4	1766.1	53.0	1766.1	53.0
VMN16-48	359	33106	6.0	13.6003	1.3	1.6506	1.7	0.1628	1.0	0.60	972.4	9.0	989.8	10.5	1028.5	26.9	1028.5	26.9
VMN16-49	83	8136	3.0	14.2147	3.0	1.4759	3.1	0.1522	1.0	0.32	913.0	8.5	920.5	19.0	938.6	61.1	913.0	8.5
VMN16-50	71	6994	6.9	13.9116	2.9	1.4520	3.3	0.1465	1.5	0.45	881.3	12.3	910.7	19.9	982.6	60.1	881.3	12.3
VMN16-51	90	14824	2.8	10.7303	2.6	2.9477	2.8	0.2294	1.0	0.35	1331.3	12.0	1394.2	21.4	1491.8	50.0	1491.8	50.0
VMN16-52	100	10706	3.5	14.2681	1.9	1.5591	2.1	0.1613	1.0	0.47	964.2	9.0	954.1	13.3	930.9	39.0	964.2	9.0
VMN16-53	464	72538	5.8	10.4828	1.0	3.5232	1.4	0.2679	1.0	0.69	1529.9	13.6	1532.4	11.4	1535.9	19.6	1535.9	19.6
VMN16-54	84	11638	4.5	11.3254	2.3	2.8717	2.7	0.2359	1.6	0.57	1365.3	19.3	1374.5	20.7	1388.9	43.3	1388.9	43.3
VMN16-55	228	21696	2.2	14.3340	2.9	1.4344	3.1	0.1491	1.0	0.32	896.0	8.4	903.4	18.4	921.4	59.9	896.0	8.4
VMN16-56	110	11326	1.3	12.7392	1.3	2.1230	1.6	0.1961	1.0	0.62	1154.6	10.6	1156.3	11.1	1159.5	25.0	1159.5	25.0
VMN16-57	208	15828	3.0	14.0108	1.3	1.5853	1.7	0.1611	1.2	0.69	962.9	10.6	964.5	10.7	968.1	25.5	962.9	10.6
VMN16-58	93	9552	2.9	12.4737	1.3	2.2500	1.6	0.2036	1.0	0.61	1194.4	10.9	1196.8	11.4	1201.1	25.3	1201.1	25.3
VMN16-60	109	15716	1.8	8.6538	1.3	5.0338	1.9	0.3159	1.4	0.73	1769.9	22.1	1825.0	16.5	1888.6	23.8	1888.6	23.8
VMN16-61	113	9946	2.1	13.4479	2.5	1.7289	2.7	0.1686	1.0	0.37	1004.5	9.3	1019.3	17.6	1051.3	51.3	1051.3	51.3
VMN16-62	263	14096	0.5	16.5708	1.8	0.8626	2.1	0.1037	1.0	0.48	635.9	6.1	631.5	9.8	616.0	39.6	635.9	6.1
VMN16-63	33	3816	0.6	10.5936	2.2	3.4707	2.5	0.2667	1.0	0.41	1523.8	13.6	1520.6	19.4	1516.0	42.3	1516.0	42.3
VMN16-64	148	11832	3.1	13.5025	1.5	1.7455	1.8	0.1709	1.0	0.55	1017.3	9.4	1025.5	11.8	1043.1	30.9	1043.1	30.9
VMN16-65	200	18810	1.8	13.7987	2.5	1.6675	2.7	0.1669	1.0	0.38	994.9	9.2	996.2	16.9	999.2	50.2	999.2	50.2
VMN16-66	66	5554	2.2	14.3248	2.5	1.5431	2.7	0.1603	1.0	0.37	958.5	8.9	947.7	16.9	922.7	52.3	958.5	8.9
VMN16-67	324	10184	1.6	17.6593	2.1	0.5664	2.3	0.0725	1.0	0.44	451.4	4.4	455.7	8.4	477.0	45.8	451.4	4.4
VMN16-68	171	14620	2.7	13.7893	1.7	1.6004	2.1	0.1601	1.2	0.60	957.1	11.0	970.4	13.0	1000.6	33.8	1000.6	33.8
VMN16-69	193	14112	3.0	14.3549	1.8	1.4289	2.0	0.1488	1.0	0.50	894.0	8.3	901.1	12.1	918.4	36.0	894.0	8.3
VMN16-70	144	12202	2.6	12.8701	1.3	2.0077	2.1	0.1874	1.6	0.77	1107.3	16.2	1118.1	13.9	1139.2	25.9	1139.2	25.9
VMN16-71	174	21176	3.4	10.7619	1.0	3.3596	1.4	0.2622	1.0	0.71	1501.2	13.4	1495.0	11.1	1486.3	19.0	1486.3	19.0
VMN16-72	284	26438	2.6	13.0644	2.1	1.9449	2.3	0.1843	1.0	0.44	1090.3	10.0	1096.7	15.4	1109.3	41.2	1109.3	41.2
VMN16-73	94	10706	1.9	11.7139	1.3	2.7025	1.7	0.2296	1.0	0.60	1332.4	12.0	1329.1	12.4	1323.9	26.1	1323.9	26.1
VMN16-74	42	3832	2.2	14.0321	3.3	1.5881	3.8	0.1616	1.9	0.49	965.8	16.6	965.6	23.6	965.0	67.7	965.8	16.6
VMN16-75	229	29694	2.2	10.2545	1.0	3.6845	2.6	0.2740	2.4	0.92	1561.2	32.6	1568.0	20.4	1577.2	18.7	1577.2	18.7
VMN16-76	122	13544	4.5	13.7312	1.4	1.6768	2.0	0.1670	1.4	0.72	995.5	13.1	999.8	12.6	1009.1	28.0	1009.1	28.0
VMN16-77	117	11058	3.3	13.5871	1.4	1.7469	1.8	0.1721	1.2	0.65	1023.9	11.0	1026.0	11.6	1030.5	27.6	1030.5	27.6
VMN16-78	123	14506	2.3	10.3286	1.4	2.9501	9.1	0.2210	9.0	0.99	1287.1	104.4	1394.9	68.8	1563.7	25.5	1563.7	25.5
VMN16-79	270	11432	1.9	12.3908	1.3	2.2649	1.7	0.2035	1.2	0.67	1194.3	12.6	1201.4	12.2	1214.3	25.5	1214.3	25.5
VMN16-80	746	53290	2.1	14.2053	1.4	1.4956	1.7	0.1541	1.0	0.60	923.8	8.6	928.6	10.2	939.9	27.7	923.8	8.6
VMN16-81	295	19580	2.9	13.5058	1.7	1.7990	2.0	0.1762	1.0	0.50	1046.3	9.7	1045.1	13.1	1042.6	35.2	1042.6	35.2
VMN16-82	67	8592	1.4	8.1085	1.0	6.0310	2.2	0.3547	2.0	0.89	1956.9	33.4	1980.3	19.3	2004.9	17.8	2004.9	17.8
VMN16-83	117	15106	1.6	9.0038	1.3	4.5725	1.8	0.2986	1.2	0.67	1684.3	17.3	1744.3	14.6	1816.9	23.8	1816.9	23.8
VMN16-84	181	10292	2.6	13.2436	4.5	1.7151	4.6	0.1647	1.3	0.28	983.1	11.9	1014.2	29.8	1082.0	89.3	1082.0	89.3
VMN16-85	268	20774	3.5	12.2173	1.5	2.2560	5.2	0.1999	5.0	0.96	1174.8	53.3	1198.7	36.4	1241.9	28.4	1241.9	28.4
VMN17-1	130	20484	2.1	8.9249	1.3	4.4875	2.3	0.2905	1.8	0.82	1643.9	26.7	1728.7	18.7	1832.8	23.6	1832.8	23.6
VMN17-2	80	10618	2.5	11.3360	1.2	2.6819	3.0	0.2205	2.7	0.91	1284.5	31.9	1323.5	22.2	1387.1	23.7	1387.1	23.7
VMN17-3	38	3244	2.7	14.7601	3.2	1.3761	4.6	0.1473	3.4	0.73	885.9	27.7	878.8	27.2	860.9	65.9	885.9	27.7

DOI: 10.1344/105.000001698

Analysis	U (ppm)	^{206}Pb / ^{204}Pb	U/Th	$^{206}Pb^*$ / $^{207}Pb^*$	± (%)	Isotope ratios $^{207}Pb^*$ / $^{235}U^*$	± (%)	$^{206}Pb^*$ / ^{238}U	± (%)	error corr.	Apparent ages (Ma) $^{206}Pb^*$ / $^{238}U^*$	± (Ma)	$^{207}Pb^*$ / ^{235}U	± (Ma)	$^{206}Pb^*$ / $^{207}Pb^*$	± (Ma)	Best age (Ma)	± (Ma)
VMN17-4	274	24778	3.0	12.3387	1.6	2.1186	2.5	0.1896	1.9	0.77	1119.2	19.9	1154.9	17.4	1222.5	31.7	1222.5	31.7
VMN17-5	142	17762	2.4	10.8512	2.0	3.1165	2.3	0.2453	1.0	0.44	1414.0	12.7	1436.8	17.5	1470.6	38.7	1470.6	38.7
VMN17-6	77	5846	2.4	14.0587	3.6	1.5831	3.7	0.1614	1.0	0.27	964.7	9.0	963.6	23.2	961.1	73.5	964.7	9.0
VMN17-7	44	3608	2.2	14.2737	4.0	1.5156	4.1	0.1569	1.0	0.24	939.5	8.7	936.7	25.2	930.1	82.1	939.5	8.7
VMN17-8	97	14750	1.4	9.0818	1.1	4.6520	3.8	0.3064	3.6	0.96	1723.0	54.6	1758.7	31.5	1801.2	19.7	1801.2	19.7
VMN17-9	272	14818	10.0	14.8904	1.8	0.9252	5.1	0.0999	4.8	0.94	613.9	28.2	665.1	25.1	842.6	38.0	613.9	28.2
VMN17-10	166	12654	1.3	14.1391	1.7	1.5645	3.5	0.1604	3.0	0.87	959.2	27.1	956.3	21.7	949.5	35.5	959.2	27.1
VMN17-11	166	18426	3.1	11.5998	1.7	2.4368	2.0	0.2050	1.0	0.50	1202.2	11.0	1253.5	14.3	1342.8	33.3	1342.8	33.3
VMN17-12	184	16782	0.8	13.6160	1.4	1.5955	2.3	0.1576	1.8	0.78	943.2	15.5	968.4	14.2	1026.2	29.0	1026.2	29.0
VMN17-13	82	7650	1.4	14.2498	2.1	1.4866	2.3	0.1536	1.0	0.43	921.3	8.6	924.9	14.2	933.5	43.5	921.3	8.6
VMN17-14	96	9514	2.2	13.6516	1.7	1.6911	2.0	0.1674	1.0	0.51	998.0	9.2	1005.2	12.5	1020.9	33.9	1020.9	33.9
VMN17-15	193	18072	2.9	12.5151	1.3	1.9433	1.9	0.1764	1.4	0.73	1047.2	13.4	1096.1	12.7	1194.6	25.5	1194.6	25.5
VMN17-16	68	5276	1.1	14.1047	2.2	1.5647	3.7	0.1601	3.0	0.81	957.1	26.9	956.3	23.0	954.5	44.2	957.1	26.9
VMN17-17	141	13228	2.5	13.8334	1.2	1.6065	2.1	0.1612	1.7	0.81	963.3	15.1	972.7	13.0	994.1	24.5	994.1	24.5
VMN17-18	46	3518	3.9	14.1313	2.9	1.5025	3.1	0.1540	1.0	0.33	923.3	8.6	931.4	18.6	950.6	59.1	923.3	8.6
VMN17-19	519	63186	2.6	10.5330	1.0	3.4345	1.6	0.2624	1.2	0.77	1501.9	16.1	1512.3	12.3	1526.9	18.8	1526.9	18.8
VMN17-20	85	7374	3.0	12.6042	1.4	2.1399	2.8	0.1956	2.4	0.86	1151.7	25.3	1161.8	19.3	1180.6	27.9	1180.6	27.9
VMN17-21	48	8120	1.7	8.9747	1.9	4.8513	2.2	0.3158	1.2	0.52	1769.1	17.8	1793.8	18.7	1822.8	34.4	1822.8	34.4
VMN17-22	38	3282	1.9	14.2944	3.8	1.5713	3.9	0.1629	1.0	0.26	972.9	9.1	959.0	24.2	927.1	77.3	972.9	9.1
VMN17-23	83	7538	2.0	13.9847	1.9	1.6074	2.2	0.1630	1.2	0.53	973.6	10.6	973.1	13.9	971.9	38.3	971.9	38.3
VMN17-24	53	4938	2.6	13.7654	2.9	1.6729	3.1	0.1670	1.0	0.32	995.7	9.2	998.3	19.8	1004.1	59.8	1004.1	59.8
VMN17-25	64	8192	1.5	11.8474	1.9	2.5610	2.2	0.2201	1.0	0.48	1282.2	12.1	1289.6	16.0	1301.9	37.3	1301.9	37.3
VMN17-26	54	4550	2.8	14.6758	3.0	1.4323	4.4	0.1525	3.2	0.73	914.7	27.4	902.5	26.1	872.8	61.5	914.7	27.4
VMN17-27	179	15490	2.4	13.6640	1.1	1.6590	2.6	0.1644	2.3	0.90	981.2	21.0	993.0	16.3	1019.1	22.8	1019.1	22.8
VMN17-28	67	6900	1.6	13.7884	1.7	1.6832	3.7	0.1683	3.3	0.89	1002.9	30.5	1002.2	23.4	1000.7	33.6	1000.7	33.6
VMN17-29	239	20716	4.8	13.7242	1.4	1.6578	2.3	0.1650	1.8	0.80	984.6	16.6	992.5	14.5	1010.2	28.0	1010.2	28.0
VMN17-30	84	6834	3.4	13.7796	1.8	1.5065	3.1	0.1506	2.5	0.80	904.1	21.0	933.0	18.9	1002.0	37.4	904.1	21.0
VMN17-31	46	4450	3.1	13.5818	2.8	1.8148	3.0	0.1788	1.0	0.33	1060.2	9.8	1050.8	19.6	1031.3	57.1	1031.3	57.1
VMN17-32	46	4030	1.7	14.0503	3.7	1.5480	3.8	0.1577	1.0	0.26	944.2	8.9	949.7	23.6	962.4	75.2	944.2	8.9
VMN17-33	49	4964	2.8	13.7219	1.9	1.7139	3.3	0.1706	2.8	0.83	1015.2	26.1	1013.7	21.5	1010.5	37.8	1010.5	37.8
VMN17-34	48	4724	2.7	14.3618	3.9	1.5041	4.1	0.1567	1.2	0.29	938.2	10.3	932.0	25.1	917.4	81.0	938.2	10.3
VMN17-35	101	10276	3.0	12.8341	2.3	2.0986	2.5	0.1953	1.0	0.39	1150.2	10.5	1148.3	17.4	1144.8	46.2	1144.8	46.2
VMN17-36	253	15320	2.4	13.7389	1.0	1.5827	1.9	0.1577	1.6	0.83	944.0	13.8	963.4	11.7	1008.0	21.2	1008.0	21.2
VMN17-37	42	5010	0.8	10.8904	2.1	3.0184	5.8	0.2384	5.4	0.93	1378.4	66.5	1412.3	43.9	1463.7	39.8	1463.7	39.8
VMN17-38	98	14724	3.7	10.8966	1.0	3.0634	2.1	0.2421	1.9	0.88	1397.6	23.5	1423.6	16.2	1462.7	19.1	1462.7	19.1
VMN17-39	238	25380	4.8	13.2395	1.7	1.7813	2.7	0.1710	2.2	0.80	1017.9	20.6	1038.7	17.9	1082.7	33.4	1082.7	33.4
VMN17-40	112	7754	2.2	14.1789	2.1	1.5457	2.7	0.1590	1.7	0.61	951.0	14.8	948.8	16.7	943.7	43.9	951.0	14.8
VMN17-41	94	7672	4.6	13.7303	1.6	1.6271	1.9	0.1620	1.0	0.54	968.0	9.0	980.7	11.7	1009.2	32.0	1009.2	32.0
VMN17-42	312	48046	5.4	10.6199	1.6	3.1518	1.8	0.2428	1.0	0.54	1401.0	12.6	1445.4	14.2	1511.4	29.3	1511.4	29.3
VMN17-43	142	8780	3.2	16.4087	1.0	0.8462	1.7	0.1007	1.3	0.80	618.5	7.9	622.6	7.8	637.2	21.8	618.5	7.9
VMN17-44	173	17798	3.9	12.4280	1.1	2.2843	1.7	0.2059	1.3	0.76	1206.9	14.5	1207.4	12.3	1208.3	22.5	1208.3	22.5
VMN17-45	145	10646	2.4	14.2932	1.7	1.5277	2.0	0.1584	1.0	0.53	947.7	9.2	941.6	12.0	927.3	34.0	947.7	9.2
VMN17-46	297	23774	4.4	13.5888	1.0	1.6208	2.1	0.1597	1.8	0.87	955.3	16.1	978.3	13.0	1030.2	20.3	1030.2	20.3
VMN17-47	127	10246	2.8	13.8381	1.2	1.6522	1.8	0.1658	1.4	0.78	989.0	13.2	990.4	11.7	993.4	23.5	993.4	23.5
VMN17-48	85	7008	2.3	13.9921	1.8	1.6213	2.4	0.1645	1.6	0.64	981.9	14.1	978.5	15.1	970.8	37.6	970.8	37.6

DOI: 10.1344/105.000001698

Analysis	U (ppm)	$^{206}Pb/^{204}Pb$	U/Th	$^{206}Pb^*/^{207}Pb^*$	± (%)	Isotope ratios $^{207}Pb^*/^{235}U^*$	± (%)	$^{206}Pb^*/^{238}U$	± (%)	error corr.	Apparent ages (Ma) $^{206}Pb^*/^{238}U^*$	± (Ma)	$^{207}Pb^*/^{235}U$	± (Ma)	$^{206}Pb^*/^{207}Pb^*$	± (Ma)	Best age (Ma)	± (Ma)
VMN17-49	218	13742	2.1	12.1049	1.2	1.6943	1.6	0.1488	1.2	0.70	894.0	9.6	1006.4	10.5	1260.0	22.9	1260.0	22.9
VMN17-50	148	19700	2.1	10.1057	1.0	3.8511	1.8	0.2823	1.5	0.83	1602.7	21.3	1603.5	14.5	1604.5	18.7	1604.5	18.7
VMN17-51	101	14754	1.6	11.4667	1.7	2.7946	1.9	0.2324	1.0	0.52	1347.1	12.2	1354.1	14.5	1365.1	31.9	1365.1	31.9
VMN17-52	138	18880	1.7	9.3416	1.8	4.3783	2.2	0.2966	1.3	0.58	1674.6	18.6	1708.3	18.1	1749.7	32.8	1749.7	32.8
VMN17-53	341	33630	5.4	12.4151	1.2	2.0381	1.6	0.1835	1.1	0.69	1086.2	11.1	1128.3	11.0	1210.4	23.0	1210.4	23.0
VMN17-54	43	3744	1.6	13.8669	3.6	1.6505	4.0	0.1660	1.8	0.45	990.0	16.5	989.7	25.5	989.1	73.4	989.1	73.4
VMN17-55	336	28072	2.0	14.2449	1.0	1.4652	2.3	0.1514	2.1	0.90	908.7	17.5	916.1	13.8	934.2	20.5	908.7	17.5
VMN17-56	30	3530	1.9	11.3769	3.7	2.9479	3.8	0.2432	1.0	0.26	1403.5	12.6	1394.3	28.9	1380.2	70.6	1380.2	70.6
VMN17-57	76	6854	3.2	13.9815	2.0	1.6077	2.3	0.1630	1.2	0.50	973.6	10.4	973.2	14.3	972.4	40.3	972.4	40.3
VMN17-58	149	12952	3.0	13.6284	1.7	1.7099	2.1	0.1690	1.3	0.61	1006.6	12.3	1012.2	13.8	1024.3	34.3	1024.3	34.3
VMN17-59	68	5716	2.7	14.2849	2.5	1.5385	2.7	0.1594	1.0	0.37	953.4	8.9	945.9	16.8	928.5	52.2	953.4	8.9
VMN17-60	179	15866	2.4	13.4252	1.5	1.8075	2.0	0.1760	1.3	0.66	1045.0	12.9	1048.2	13.4	1054.7	31.1	1054.7	31.1
VMN17-61	205	19684	4.6	13.5906	1.2	1.7334	1.6	0.1709	1.1	0.68	1016.8	10.5	1021.0	10.5	1030.0	24.1	1030.0	24.1
VMN17-62	56	5058	1.2	10.7941	2.8	3.3116	3.1	0.2593	1.4	0.45	1486.0	18.6	1483.8	24.4	1480.6	53.1	1480.6	53.1
VMN17-63	81	8652	3.9	12.7108	1.9	2.0555	3.5	0.1895	2.9	0.83	1118.6	29.6	1134.1	23.7	1163.9	38.4	1163.9	38.4
VMN17-64	241	16236	1.7	14.2124	1.0	1.4575	2.5	0.1502	2.3	0.92	902.3	19.6	913.0	15.3	938.9	20.7	902.3	19.6
VMN17-65	131	18144	1.5	10.4462	1.1	3.5095	1.7	0.2659	1.3	0.76	1519.9	17.9	1529.4	13.6	1542.4	20.9	1542.4	20.9
VMN17-66	174	22494	2.0	9.4063	4.1	4.2724	4.4	0.2915	1.7	0.38	1648.8	24.3	1688.1	36.3	1737.1	74.9	1737.1	74.9
VMN17-67	40	3622	2.0	13.8044	2.9	1.7450	3.1	0.1747	1.0	0.33	1038.0	9.6	1025.3	19.8	998.3	58.9	998.3	58.9
VMN17-69	134	11128	3.3	13.9543	1.8	1.6131	2.0	0.1633	1.0	0.49	974.8	9.0	975.3	12.8	976.3	36.2	976.3	36.2
VMN17-70	155	13398	3.8	13.7149	1.6	1.7019	1.9	0.1693	1.0	0.53	1008.2	9.3	1009.2	12.2	1011.5	32.9	1011.5	32.9
VMN17-71	75	7828	3.2	13.5219	1.2	1.7970	2.6	0.1762	2.3	0.88	1046.4	21.9	1044.4	16.9	1040.2	25.0	1040.2	25.0
VMN17-72	60	9514	1.1	9.1289	1.0	4.7247	1.4	0.3128	1.0	0.71	1754.6	15.4	1771.6	11.9	1791.8	18.2	1791.8	18.2
VMN17-73	85	13940	2.0	9.9234	2.0	4.1270	2.2	0.2970	1.0	0.45	1676.5	14.8	1659.7	18.4	1638.4	37.3	1638.4	37.3
VMN17-74	96	9514	3.1	13.8695	1.4	1.6092	1.9	0.1619	1.3	0.68	967.2	11.4	973.8	11.8	988.8	28.2	988.8	28.2
VMN17-75	85	7862	3.0	13.8852	2.1	1.6368	4.2	0.1648	3.7	0.87	983.6	33.8	984.5	26.7	986.5	42.0	986.5	42.0
VMN17-76	106	11792	6.5	13.6475	1.9	1.6635	2.1	0.1647	1.0	0.47	982.6	9.1	994.7	13.4	1021.5	37.8	1021.5	37.8
VMN17-77	245	21802	3.2	11.1807	2.0	2.4865	4.4	0.2016	3.9	0.89	1184.1	41.9	1268.1	31.6	1413.6	38.7	1413.6	38.7
VMN17-78	186	16582	2.6	14.1875	1.6	1.4637	1.9	0.1506	1.0	0.53	904.4	8.4	915.5	11.5	942.5	33.1	904.4	8.4
VMN17-79	212	21646	2.5	13.7366	1.1	1.5853	1.5	0.1579	1.0	0.69	945.3	8.8	964.4	9.1	1008.3	21.4	1008.3	21.4
VMN17-80	72	8190	1.9	11.1185	2.1	2.9946	2.3	0.2415	1.0	0.44	1394.4	12.5	1406.2	17.4	1424.2	39.4	1424.2	39.4
VMN17-81	462	25322	6.6	12.6367	1.5	1.7318	4.8	0.1587	4.6	0.95	949.6	40.4	1020.4	31.0	1175.5	29.1	1175.5	29.1
VMN17-82	48	4068	2.8	14.0894	2.5	1.6411	3.4	0.1677	2.3	0.68	999.4	21.1	986.1	21.3	956.7	50.9	956.7	50.9
VMN17-83	109	11350	3.2	12.6893	1.4	2.1176	1.7	0.1949	1.0	0.59	1147.8	10.5	1154.5	11.8	1167.3	27.4	1167.3	27.4
VMN17-84	79	13610	1.3	10.5591	1.2	3.3282	2.3	0.2549	1.9	0.85	1463.6	25.4	1487.7	17.9	1522.2	23.1	1522.2	23.1
VMN17-85	161	14324	1.2	14.3576	1.0	1.3848	3.0	0.1442	2.8	0.94	868.4	22.7	882.5	17.5	918.0	20.7	868.4	22.7
VMN17-86	111	11526	2.5	13.9427	1.5	1.6070	2.3	0.1625	1.7	0.75	970.7	15.5	972.9	14.3	978.0	30.8	978.0	30.8
VMN17-87	66	8440	1.3	11.6559	2.5	2.7453	3.1	0.2321	1.7	0.56	1345.4	21.0	1340.8	22.9	1333.5	49.2	1333.5	49.2
VMN17-88	107	10116	3.1	13.8168	1.5	1.6563	2.0	0.1660	1.3	0.66	989.9	11.8	992.0	12.4	996.5	30.1	996.5	30.1
VMN17-89	170	20486	0.9	11.6206	1.2	2.6982	2.3	0.2274	2.0	0.85	1320.9	23.3	1328.0	17.0	1339.4	23.4	1339.4	23.4
VMN17-90	51	4402	1.4	14.5388	3.2	1.4330	3.4	0.1511	1.0	0.30	907.1	8.5	902.8	20.2	892.2	66.5	907.1	8.5
VMN17-91	192	9742	2.1	7.4621	2.0	5.6396	2.9	0.3052	2.0	0.71	1717.1	30.5	1922.2	24.6	2151.2	35.3	2151.2	35.3
VMN17-92	37	3956	2.6	13.8406	2.2	1.6976	3.6	0.1704	2.8	0.79	1014.4	26.6	1007.6	22.8	993.0	44.4	993.0	44.4
VMN17-93	105	11276	3.7	13.6829	1.8	1.6274	3.0	0.1615	2.4	0.79	965.1	21.2	980.9	18.8	1016.3	37.1	1016.3	37.1
VMN17-94	106	9750	4.0	13.8029	1.6	1.6878	2.5	0.1690	2.0	0.77	1006.4	18.4	1003.9	16.2	998.5	32.7	998.5	32.7

DOI: 10.1344/105.000001698

Analysis	U (ppm)	^{206}Pb / ^{204}Pb	U/Th	$^{206}Pb^*$ / $^{207}Pb^*$	± (%)	Isotope ratios $^{207}Pb^*$ / $^{235}U^*$	± (%)	$^{206}Pb^*$ / ^{238}U	± (%)	error corr.	Apparent ages (Ma) $^{206}Pb^*$ / $^{238}U^*$	± (Ma)	$^{207}Pb^*$ / ^{235}U	± (Ma)	$^{206}Pb^*$ / $^{207}Pb^*$	± (Ma)	Best age (Ma)	± (Ma)
VMN17-95	326	34370	3.0	9.6363	1.2	3.4520	2.4	0.2413	2.0	0.86	1393.2	25.3	1516.3	18.6	1692.7	22.5	1692.7	22.5
VMN17-98	76	13608	1.6	9.0189	1.4	5.0185	1.7	0.3283	1.0	0.58	1830.0	15.9	1822.4	14.7	1813.8	25.8	1813.8	25.8
VMN18-1	143	12284	1.6	11.2946	2.4	2.5753	2.7	0.2110	1.2	0.43	1233.9	12.9	1293.7	19.5	1394.2	46.3	1394.2	46.3
VMN18-2	46	4864	0.5	10.6685	3.1	3.0557	4.7	0.2364	3.5	0.74	1368.1	42.9	1421.7	35.8	1502.7	59.0	1502.7	59.0
VMN18-3	131	9236	2.7	10.9675	2.6	2.9215	3.3	0.2324	2.0	0.60	1347.0	24.2	1387.5	24.9	1450.3	50.0	1450.3	50.0
VMN18-4	130	18370	2.0	10.6415	1.0	3.2138	1.4	0.2480	1.0	0.70	1428.4	12.8	1460.5	11.0	1507.5	19.2	1507.5	19.2
VMN18-5	97	13174	1.9	10.7126	1.2	3.1504	1.8	0.2448	1.3	0.73	1411.4	16.6	1445.1	13.8	1494.9	23.0	1494.9	23.0
VMN18-6	183	33798	2.3	8.0179	2.4	5.8047	2.8	0.3376	1.4	0.50	1874.9	22.3	1947.1	23.9	2024.8	42.3	2024.8	42.3
VMN18-7	40	5220	1.8	10.5880	3.4	3.1943	3.8	0.2453	1.6	0.41	1414.2	19.7	1455.8	29.2	1517.0	65.1	1517.0	65.1
VMN18-8	54	6916	1.8	10.5246	2.5	3.3583	3.2	0.2563	2.0	0.62	1471.1	25.9	1494.7	24.7	1528.4	46.6	1528.4	46.6
VMN18-9	71	2554	0.9	18.1797	5.2	0.6147	5.3	0.0810	1.0	0.19	502.4	4.8	486.5	20.7	412.5	117.4	502.4	4.8
VMN18-10	54	8774	1.2	9.0839	1.6	4.7601	1.9	0.3136	1.0	0.53	1758.4	15.4	1777.9	15.9	1800.8	29.2	1800.8	29.2
VMN18-11	95	12820	1.9	8.8527	1.8	4.9267	2.2	0.3163	1.4	0.63	1771.8	21.8	1806.8	19.0	1847.6	31.7	1847.6	31.7
VMN18-12	87	13760	1.3	8.1317	1.3	6.1679	1.6	0.3638	1.0	0.61	2000.0	17.2	1999.9	14.3	1999.8	23.1	1999.8	23.1
VMN18-13	79	8754	1.2	11.0015	1.2	2.9320	2.0	0.2339	1.6	0.80	1355.1	19.8	1390.2	15.3	1444.4	23.1	1444.4	23.1
VMN18-14	132	23378	1.2	8.8381	2.4	5.2035	2.7	0.3335	1.4	0.50	1855.5	22.1	1853.2	23.2	1850.5	42.5	1850.5	42.5
VMN18-15	195	24780	1.1	9.0011	1.2	4.7019	4.2	0.3070	4.0	0.95	1725.7	60.4	1767.6	35.0	1817.4	22.5	1817.4	22.5
VMN18-16	240	38882	1.7	9.0135	2.1	4.8872	3.5	0.3195	2.8	0.81	1787.2	44.3	1800.0	29.7	1814.9	37.8	1814.9	37.8
VMN18-17	290	7342	3.6	16.9432	3.1	0.6442	3.4	0.0792	1.4	0.42	491.1	6.7	504.9	13.5	567.8	67.0	491.1	6.7
VMN18-18	117	19694	1.4	8.2110	1.2	5.9271	1.6	0.3530	1.0	0.63	1948.8	16.8	1965.2	13.8	1982.6	21.9	1982.6	21.9
VMN18-19	97	16044	1.4	8.8337	2.2	4.8234	2.4	0.3090	1.0	0.42	1735.9	15.2	1789.0	20.1	1851.4	39.3	1851.4	39.3
VMN18-20	174	27470	1.7	8.4723	1.0	5.5698	2.1	0.3422	1.8	0.87	1897.5	30.1	1911.4	18.1	1926.6	18.7	1926.6	18.7
VMN18-21	66	9474	2.0	10.5232	1.6	3.2732	3.2	0.2498	2.8	0.86	1437.5	35.8	1474.7	25.1	1528.6	30.7	1528.6	30.7
VMN18-22	366	32066	3.0	10.2751	1.2	2.9161	2.7	0.2173	2.5	0.90	1267.7	28.2	1386.1	20.7	1573.4	22.9	1573.4	22.9
VMN18-23	87	11334	1.5	8.0347	1.7	6.1840	2.0	0.3604	1.1	0.54	1983.9	18.8	2002.2	17.9	2021.1	30.5	2021.1	30.5
VMN18-24	174	25190	2.1	10.9094	2.1	3.2326	2.3	0.2558	1.0	0.43	1468.2	13.1	1465.0	17.8	1460.4	39.4	1460.4	39.4
VMN18-25	215	34040	1.8	8.1837	1.0	5.8549	1.4	0.3475	1.0	0.71	1922.7	16.6	1954.6	12.3	1988.5	17.8	1988.5	17.8
VMN18-26	164	29672	2.0	8.4721	1.0	5.4037	1.5	0.3320	1.2	0.76	1848.2	18.6	1885.4	13.1	1926.7	17.9	1926.7	17.9
VMN18-27	202	31216	1.6	8.8638	1.0	4.9943	1.4	0.3211	1.0	0.71	1794.9	15.7	1818.4	12.0	1845.3	18.1	1845.3	18.1
VMN18-28	66	9828	1.8	11.1849	1.0	2.7367	2.1	0.2220	1.8	0.87	1292.5	21.0	1338.5	15.4	1412.9	19.9	1412.9	19.9
VMN18-29	94	19620	1.4	8.9448	1.5	5.0319	1.8	0.3264	1.0	0.57	1821.1	15.9	1824.7	14.9	1828.8	26.3	1828.8	26.3
VMN18-30	145	15762	1.4	10.7234	4.8	2.9623	6.0	0.2304	3.5	0.59	1336.6	42.5	1398.0	45.3	1493.0	91.2	1493.0	91.2
VMN18-31	101	15622	1.8	9.0192	2.0	4.7081	2.2	0.3080	1.1	0.47	1730.7	15.9	1768.7	18.6	1813.8	35.4	1813.8	35.4
VMN18-32	90	17128	1.2	7.5795	1.8	6.8542	2.0	0.3768	1.0	0.49	2061.2	17.6	2092.7	18.0	2123.9	31.0	2123.9	31.0
VMN18-33	134	17706	1.3	8.9094	2.1	4.4076	4.0	0.2848	3.5	0.86	1615.5	49.6	1713.8	33.5	1836.0	37.7	1836.0	37.7
VMN18-34	135	25996	1.4	8.1763	2.0	5.9752	2.5	0.3543	1.4	0.58	1955.2	24.1	1972.2	21.5	1990.1	35.9	1990.1	35.9
VMN18-36	103	13576	1.0	10.8332	1.5	3.2388	2.5	0.2545	2.1	0.81	1461.5	26.8	1466.5	19.7	1473.7	28.3	1473.7	28.3
VMN18-37	81	10164	0.6	10.7219	1.4	3.2225	2.1	0.2506	1.6	0.75	1441.5	20.0	1462.6	15.9	1493.3	25.6	1493.3	25.6
VMN18-38	187	34736	1.7	9.2098	1.0	4.5596	1.4	0.3046	1.0	0.71	1713.9	15.0	1741.9	11.8	1775.7	18.3	1775.7	18.3
VMN18-39	126	12306	1.9	11.1599	2.8	2.6055	7.1	0.2109	6.5	0.92	1233.5	73.1	1302.2	51.9	1417.1	52.6	1417.1	52.6
VMN18-40	151	16912	2.0	11.3098	1.7	2.8127	2.0	0.2307	1.1	0.54	1338.2	12.9	1358.9	14.9	1391.6	32.3	1391.6	32.3
VMN18-41	97	10064	1.6	9.0099	1.3	4.4578	1.7	0.2913	1.1	0.63	1648.0	15.7	1723.1	14.2	1815.7	24.0	1815.7	24.0
VMN18-42	206	20194	1.1	9.0535	1.4	4.0708	2.3	0.2673	1.8	0.78	1527.1	24.1	1648.5	18.4	1806.9	25.5	1806.9	25.5
VMN18-43	94	8326	1.0	10.8974	4.8	2.9370	8.9	0.2321	7.5	0.84	1345.6	90.6	1391.5	67.2	1462.5	90.9	1462.5	90.9
VMN18-44	117	25950	2.3	8.1595	1.8	5.9537	2.3	0.3523	1.4	0.61	1945.7	23.5	1969.1	20.1	1993.8	32.7	1993.8	32.7

DOI: 10.1344/105.000001698

Analysis	U (ppm)	$^{206}Pb/^{204}Pb$	U/Th	$^{206}Pb^*/^{207}Pb^*$	± (%)	Isotope ratios $^{207}Pb^*/^{235}U^*$	± (%)	$^{206}Pb^*/^{238}U$	± (%)	error corr.	Apparent ages (Ma) $^{206}Pb^*/^{238}U^*$	± (Ma)	$^{207}Pb^*/^{235}U$	± (Ma)	$^{206}Pb^*/^{207}Pb^*$	± (Ma)	Best age (Ma)	± (Ma)
VMN18-45	113	14648	1.1	11.0982	2.4	3.0786	2.6	0.2478	1.0	0.38	1427.1	12.8	1427.4	20.0	1427.7	46.0	1427.7	46.0
VMN18-46	103	14530	2.5	11.0598	1.5	2.9869	2.9	0.2396	2.5	0.85	1384.6	31.1	1404.3	22.3	1434.4	29.3	1434.4	29.3
VMN18-47	196	17432	1.6	9.1023	1.5	4.4485	1.8	0.2937	1.0	0.55	1659.9	14.6	1721.4	15.0	1797.1	27.4	1797.1	27.4
VMN18-48	331	37606	1.5	8.9614	2.1	4.4729	2.8	0.2907	1.8	0.66	1645.1	26.3	1725.9	22.9	1825.4	37.7	1825.4	37.7
VMN18-49	214	31044	4.0	9.0714	1.5	4.6638	1.8	0.3068	1.1	0.59	1725.1	16.2	1760.8	15.1	1803.3	26.4	1803.3	26.4
VMN18-50	76	12400	1.0	9.1021	1.4	4.7706	1.9	0.3149	1.4	0.70	1764.9	21.2	1779.7	16.3	1797.1	25.2	1797.1	25.2
VMN18-51	93	10686	0.8	10.7904	2.0	3.3721	2.2	0.2639	1.0	0.45	1509.7	13.5	1497.9	17.3	1481.2	37.2	1481.2	37.2
VMN18-52	64	10382	2.5	10.6048	2.0	3.3584	2.3	0.2583	1.1	0.48	1481.2	14.6	1494.7	17.8	1514.1	37.5	1514.1	37.5
VMN18-53	86	18620	1.3	9.0737	1.8	4.6969	2.8	0.3091	2.1	0.76	1736.3	32.6	1766.7	23.5	1802.8	33.1	1802.8	33.1
VMN18-54	95	15428	2.0	9.0499	1.7	4.5993	4.9	0.3019	4.6	0.94	1700.6	69.4	1749.1	41.3	1807.6	31.3	1807.6	31.3
VMN18-55	180	27146	1.5	9.1933	2.1	4.4872	3.0	0.2992	2.2	0.71	1687.3	32.2	1728.6	25.3	1779.0	38.9	1779.0	38.9
VMN18-56	111	15588	2.1	10.8810	2.5	3.0806	2.8	0.2431	1.3	0.46	1402.9	16.1	1427.9	21.3	1465.4	46.9	1465.4	46.9
VMN18-57	110	18036	1.3	8.9097	2.4	4.5533	3.6	0.2942	2.7	0.76	1662.6	39.9	1740.8	29.9	1835.9	42.6	1835.9	42.6
VMN18-58	135	23186	1.6	9.0799	2.8	4.8282	3.3	0.3180	1.8	0.54	1779.7	27.5	1789.8	27.5	1801.6	50.0	1801.6	50.0
VMN18-59	224	25486	2.0	11.0744	1.4	2.9160	1.9	0.2342	1.3	0.67	1356.6	15.8	1386.1	14.6	1431.8	27.3	1431.8	27.3
VMN18-60	48	10040	1.1	8.1952	1.5	5.9291	1.8	0.3524	1.0	0.55	1946.1	16.8	1965.5	15.8	1986.0	27.1	1986.0	27.1
VMN18-61	258	33450	1.3	10.6096	1.6	3.2442	2.0	0.2496	1.2	0.62	1436.6	15.7	1467.8	15.4	1513.2	29.5	1513.2	29.5
VMN18-62	35	3862	0.8	12.6362	3.6	2.1851	3.7	0.2003	1.1	0.28	1176.7	11.3	1176.3	26.1	1175.6	71.2	1175.6	71.2
VMN18-63	204	24510	2.0	10.9314	1.9	3.0296	2.1	0.2402	1.0	0.47	1387.7	12.5	1415.1	16.3	1456.6	36.0	1456.6	36.0
VMN18-64	67	12158	1.5	7.5347	1.0	6.9989	1.4	0.3825	1.0	0.70	2087.8	17.8	2111.3	12.8	2134.2	18.0	2134.2	18.0
VMN18-65	245	31998	2.1	11.1044	1.0	2.8945	1.4	0.2331	1.0	0.71	1350.8	12.2	1380.5	10.7	1426.7	19.1	1426.7	19.1
VMN18-66	95	16638	1.5	10.8624	1.1	3.0140	2.9	0.2374	2.7	0.93	1373.4	33.5	1411.2	22.2	1468.6	20.0	1468.6	20.0
VMN18-67	97	20790	2.8	8.4921	1.7	5.3895	3.4	0.3319	2.9	0.86	1847.8	46.9	1883.2	28.9	1922.4	30.5	1922.4	30.5
VMN18-68	100	17992	2.5	11.1809	2.4	2.9198	2.7	0.2368	1.3	0.48	1369.9	15.9	1387.1	20.4	1413.5	45.4	1413.5	45.4
VMN18-69	286	16980	1.2	8.8675	2.8	3.7371	4.8	0.2403	3.9	0.82	1388.5	48.8	1579.4	38.4	1844.5	50.1	1844.5	50.1
VMN18-70	67	11448	1.3	8.0625	2.0	6.0014	2.2	0.3509	1.1	0.48	1939.0	18.1	1976.0	19.4	2015.0	34.6	2015.0	34.6
VMN18-71	51	10320	2.0	8.9704	2.2	5.0291	4.1	0.3272	3.5	0.85	1824.7	55.9	1824.2	35.0	1823.6	39.3	1823.6	39.3
VMN18-72	113	17842	1.5	9.0037	1.6	4.8074	1.8	0.3139	1.0	0.54	1760.0	15.4	1786.2	15.5	1816.9	28.2	1816.9	28.2
VMN18-73	110	16854	2.0	11.3504	1.1	2.7879	2.4	0.2295	2.2	0.89	1331.9	26.1	1352.3	18.1	1384.7	20.8	1384.7	20.8
VMN18-74	255	48104	2.8	8.1022	2.2	5.6858	2.4	0.3341	1.0	0.42	1858.3	16.1	1929.2	20.5	2006.3	38.2	2006.3	38.2
VMN18-75	84	11186	1.1	10.5210	3.0	3.2753	3.1	0.2499	1.0	0.32	1438.1	12.9	1475.2	24.5	1529.0	56.2	1529.0	56.2
VMN18-76	75	14134	1.3	8.2747	2.4	5.7466	3.6	0.3449	2.7	0.74	1910.1	44.0	1938.4	31.1	1968.8	43.2	1968.8	43.2
VMN18-77	134	16576	2.1	11.4151	1.6	2.7182	3.1	0.2250	2.7	0.86	1308.4	31.5	1333.4	23.0	1373.8	30.6	1373.8	30.6
VMN18-78	78	11698	2.6	11.2115	1.2	2.9043	3.8	0.2362	3.6	0.95	1366.7	44.8	1383.0	28.9	1408.3	22.7	1408.3	22.7
VMN18-79	91	16048	1.6	9.1128	1.0	4.6777	2.6	0.3092	2.4	0.92	1736.6	36.1	1763.3	21.5	1795.0	18.3	1795.0	18.3
VMN18-80	125	25090	1.8	9.1900	1.0	4.5814	3.9	0.3054	3.8	0.97	1717.8	57.6	1745.9	32.9	1779.6	18.3	1779.6	18.3
VMN18-81	259	15292	1.7	10.5800	1.6	2.7054	3.0	0.2076	2.6	0.86	1216.0	28.5	1329.9	22.3	1518.5	29.4	1518.5	29.4
VMN18-82	214	28832	2.8	11.1152	1.6	2.9145	1.9	0.2349	1.0	0.53	1360.4	12.8	1385.7	14.7	1424.8	31.5	1424.8	31.5
VMN18-83	143	21508	2.3	7.9633	1.9	5.9059	2.7	0.3411	1.8	0.68	1891.9	29.7	1962.1	23.1	2036.9	34.4	2036.9	34.4
VMN18-84	146	20450	1.7	8.2117	1.0	5.4879	2.3	0.3268	2.0	0.90	1823.1	32.4	1898.7	19.5	1982.4	17.8	1982.4	17.8
VMN18-85	48	6130	1.7	11.3255	1.6	2.8209	1.8	0.2317	1.0	0.54	1343.5	12.1	1361.1	13.8	1388.9	29.8	1388.9	29.8
VMN18-86	162	23928	1.5	9.1931	1.2	4.6396	1.9	0.3093	1.5	0.78	1737.5	22.5	1756.4	15.9	1779.0	21.9	1779.0	21.9
VMN18-87	50	8546	1.3	9.1122	1.3	4.7831	1.6	0.3161	1.0	0.62	1770.7	15.5	1781.9	13.6	1795.1	23.2	1795.1	23.2
VMN18-88	205	23092	1.0	9.0129	1.9	4.3908	3.5	0.2870	2.9	0.84	1626.6	42.1	1710.6	28.8	1815.0	34.0	1815.0	34.0
VMN18-89	147	23224	0.8	8.1394	1.0	6.0716	1.4	0.3584	1.0	0.71	1974.7	17.0	1986.2	12.3	1998.1	17.8	1998.1	17.8

DOI: 10.1344/105.000001698

Analysis	U (ppm)	^{206}Pb / ^{204}Pb	U/Th	$^{206}Pb^*$ / $^{207}Pb^*$	± (%)	Isotope ratios $^{207}Pb^*$ / $^{235}U^*$	± (%)	$^{206}Pb^*$ / ^{238}U	± (%)	error corr.	Apparent ages (Ma) $^{206}Pb^*$ / $^{238}U^*$	± (Ma)	$^{207}Pb^*$ / ^{235}U	± (Ma)	$^{206}Pb^*$ / $^{207}Pb^*$	± (Ma)	Best age (Ma)	± (Ma)
VMN18-90	141	23446	2.3	8.6722	2.0	4.5201	3.6	0.2843	3.0	0.83	1613.0	42.7	1734.7	29.9	1884.7	36.0	1884.7	36.0
VMN18-91	123	26542	2.0	8.2314	1.0	5.6817	1.4	0.3392	1.0	0.71	1882.8	16.3	1928.6	12.2	1978.1	17.8	1978.1	17.8
VMN18-92	127	15746	0.8	8.1872	1.0	5.0053	3.2	0.2972	3.1	0.95	1677.5	45.5	1820.2	27.4	1987.7	17.8	1987.7	17.8
VMN18-93	217	36166	2.0	9.0309	1.0	4.7603	1.6	0.3118	1.3	0.78	1749.5	19.2	1777.9	13.4	1811.4	18.2	1811.4	18.2
VMN18-94	65	5428	1.7	14.0318	3.0	1.6506	3.2	0.1680	1.0	0.32	1000.9	9.3	989.8	19.9	965.1	61.1	965.1	61.1
VMN18-95	82	15756	1.1	8.2249	1.1	6.0042	1.5	0.3582	1.0	0.67	1973.5	17.0	1976.5	13.1	1979.6	20.0	1979.6	20.0
VMN18-96	151	17188	2.0	10.9950	1.6	3.0397	1.9	0.2424	1.0	0.53	1399.1	12.6	1417.6	14.4	1445.6	30.5	1445.6	30.5
VMN18-97	119	19610	1.9	10.9373	2.0	3.2174	2.5	0.2552	1.5	0.59	1465.3	19.3	1461.4	19.4	1455.6	38.5	1455.6	38.5
VMN18-98	203	46448	2.6	8.0588	2.6	6.4344	2.8	0.3761	1.0	0.36	2057.9	17.6	2037.0	24.3	2015.8	45.8	2015.8	45.8
VMN18-99	117	17206	1.7	8.5278	2.0	5.2781	2.3	0.3264	1.0	0.45	1821.1	16.0	1865.3	19.4	1914.9	36.4	1914.9	36.4
VMN18-100	94	15970	1.3	8.9149	2.4	4.9359	2.6	0.3191	1.2	0.45	1785.5	18.7	1808.4	22.3	1834.9	42.6	1834.9	42.6
VMN32-1	113	13024	2.6	12.3770	1.1	2.3140	1.5	0.2077	1.0	0.68	1216.6	11.1	1216.6	10.4	1216.5	21.0	1216.5	21.0
VMN32-2	74	10328	2.3	11.0659	1.0	3.0921	2.3	0.2482	2.1	0.90	1429.0	27.0	1430.7	18.0	1433.3	19.4	1433.3	19.4
VMN32-3	345	22840	2.7	15.2761	1.1	1.1837	2.1	0.1311	1.8	0.86	794.4	13.8	793.0	11.7	789.2	22.7	794.4	13.8
VMN32-4	88	12898	2.3	10.9732	1.0	3.1213	1.5	0.2484	1.1	0.74	1430.3	14.0	1438.0	11.4	1449.3	19.1	1449.3	19.1
VMN32-5	127	22038	1.0	9.2231	1.0	4.7468	2.5	0.3175	2.2	0.91	1777.6	34.8	1775.5	20.6	1773.1	18.3	1773.1	18.3
VMN32-6	396	16026	3.1	10.3326	3.4	3.1140	3.5	0.2334	1.0	0.28	1352.1	12.2	1436.2	27.2	1563.0	63.6	1563.0	63.6
VMN32-7	32	5906	1.8	10.9443	1.6	3.1597	1.9	0.2508	1.0	0.53	1442.6	12.9	1447.4	14.6	1454.3	30.7	1454.3	30.7
VMN32-8	125	18284	1.1	10.7815	1.3	3.1467	1.6	0.2461	1.0	0.62	1418.1	12.7	1444.2	12.5	1482.8	24.1	1482.8	24.1
VMN32-9	68	14842	1.6	8.1747	1.6	5.8819	1.9	0.3487	1.0	0.53	1928.5	16.7	1958.6	16.2	1990.5	28.1	1990.5	28.1
VMN32-10	164	15290	2.7	13.7095	1.0	1.6974	1.4	0.1688	1.0	0.70	1005.3	9.3	1007.5	9.1	1012.3	20.7	1012.3	20.7
VMN32-10a	111	10706	2.5	13.9561	1.6	1.6699	1.9	0.1690	1.0	0.53	1006.8	9.3	997.2	12.0	976.1	32.7	976.1	32.7
VMN32-11	83	13240	0.9	10.5971	1.2	3.4293	1.5	0.2636	1.0	0.65	1508.1	13.4	1511.1	12.2	1515.4	22.3	1515.4	22.3
VMN32-12	73	9278	1.1	11.4039	1.5	2.8762	1.8	0.2379	1.0	0.56	1375.7	12.4	1375.7	13.5	1375.7	28.7	1375.7	28.7
VMN32-13	87	16410	2.3	9.4151	1.2	4.5846	2.0	0.3131	1.6	0.79	1755.7	24.4	1746.5	16.8	1735.4	22.6	1735.4	22.6
VMN32-15	46	7200	2.3	11.5627	2.4	2.8494	2.7	0.2390	1.2	0.44	1381.3	14.5	1368.7	20.0	1349.0	46.2	1349.0	46.2
VMN32-16	21	3304	0.6	10.9054	3.5	3.2639	3.7	0.2582	1.2	0.33	1480.4	16.3	1472.5	28.7	1461.1	66.2	1461.1	66.2
VMN32-17	75	10968	1.6	10.5663	1.6	3.2968	4.2	0.2526	3.9	0.92	1452.1	50.2	1480.3	32.7	1520.9	30.8	1520.9	30.8
VMN32-18	142	14562	3.2	13.7389	1.8	1.6675	2.0	0.1662	1.0	0.49	990.9	9.2	996.2	12.9	1008.0	36.0	1008.0	36.0
VMN32-20	29	4590	1.2	10.8795	1.1	3.2612	1.7	0.2573	1.2	0.73	1476.1	16.4	1471.8	13.1	1465.6	21.7	1465.6	21.7
VMN32-21	159	20314	2.6	12.6519	1.2	2.2098	1.6	0.2028	1.0	0.63	1190.2	10.9	1184.1	11.1	1173.1	24.4	1173.1	24.4
VMN32-22	57	8270	1.6	11.4692	2.9	2.8693	3.1	0.2387	1.0	0.33	1379.8	12.4	1373.9	23.1	1364.7	55.8	1364.7	55.8
VMN32-24	56	13870	1.5	9.0886	1.1	4.8525	2.1	0.3199	1.8	0.85	1789.1	28.1	1794.1	17.8	1799.8	20.1	1799.8	20.1
VMN32-25	113	10178	3.3	13.4775	1.3	1.7751	2.4	0.1735	2.0	0.85	1031.4	19.3	1036.4	15.5	1046.8	25.3	1046.8	25.3
VMN32-26	113	12146	1.9	11.1366	1.0	3.0596	1.8	0.2471	1.6	0.84	1423.6	19.8	1422.6	14.1	1421.1	19.1	1421.1	19.1
VMN32-27	104	19006	2.0	9.1005	1.0	4.8689	1.9	0.3214	1.6	0.84	1796.4	24.5	1796.9	15.6	1797.5	18.2	1797.5	18.2
VMN32-28	66	12828	1.4	9.1034	1.0	4.8181	1.4	0.3181	1.0	0.71	1780.5	15.6	1788.1	11.9	1796.9	18.2	1796.9	18.2
VMN32-29	68	7872	1.9	12.0883	1.7	2.4205	2.0	0.2122	1.0	0.50	1240.6	11.3	1248.7	14.5	1262.7	34.1	1262.7	34.1
VMN32-30	218	25208	1.5	9.0126	1.0	3.9639	7.8	0.2591	7.8	0.99	1485.3	103.2	1626.8	63.7	1815.1	18.7	1815.1	18.7
VMN32-31	183	18768	3.8	12.1301	2.2	2.3698	2.4	0.2085	1.0	0.42	1220.7	11.1	1233.5	17.1	1256.0	42.6	1256.0	42.6
VMN32-32	250	16450	1.2	8.1283	2.4	4.4323	3.7	0.2613	2.9	0.77	1496.5	38.6	1718.4	30.9	2000.6	41.9	2000.6	41.9
VMN32-33	77	11222	2.0	11.3270	1.1	2.8425	1.5	0.2335	1.0	0.66	1352.9	12.2	1366.8	11.4	1388.7	21.8	1388.7	21.8
VMN32-34	101	9216	1.5	13.9951	2.5	1.6283	2.6	0.1653	1.0	0.38	986.0	9.1	981.2	16.7	970.4	50.0	970.4	50.0
VMN32-36	90	23082	1.4	8.0171	1.9	6.2796	2.4	0.3651	1.6	0.64	2006.4	26.7	2015.6	21.1	2025.0	32.8	2025.0	32.8
VMN32-37	276	19852	1.5	10.3160	2.1	2.9497	5.4	0.2207	4.9	0.92	1285.5	57.5	1394.8	40.7	1566.0	39.5	1566.0	39.5

DOI: 10.1344/105.000001698

Analysis	U (ppm)	^{206}Pb / ^{204}Pb	U/Th	$^{206}Pb^*$ / $^{207}Pb^*$	± (%)	Isotope ratios $^{207}Pb^*$ / $^{235}U^*$	± (%)	$^{206}Pb^*$ / ^{238}U	± (%)	error corr.	Apparent ages (Ma) $^{206}Pb^*$ / $^{238}U^*$	± (Ma)	$^{207}Pb^*$ / ^{235}U	± (Ma)	$^{206}Pb^*$ / $^{207}Pb^*$	± (Ma)	Best age (Ma)	± (Ma)
VMN32-38	24	5812	2.6	8.3655	3.3	5.3935	4.5	0.3272	3.0	0.67	1825.0	47.4	1883.8	38.3	1949.3	59.6	1949.3	59.6
VMN32-39	172	35986	2.3	8.9442	1.0	4.6272	1.4	0.3002	1.0	0.70	1692.1	14.9	1754.2	12.0	1828.9	18.7	1828.9	18.7
VMN32-40	152	26992	1.1	8.0582	1.7	6.0441	2.0	0.3532	1.0	0.50	1950.0	16.8	1982.2	17.5	2015.9	30.9	2015.9	30.9
VMN32-14	559	31100	4.7	16.9882	1.2	0.7481	1.6	0.0922	1.0	0.63	568.4	5.4	567.1	6.9	562.1	26.8	568.4	5.4
VMN32-41	160	26612	1.1	8.1384	1.6	5.4647	2.7	0.3226	2.2	0.81	1802.2	34.6	1895.1	23.3	1998.4	28.1	1998.4	28.1
VMN32-42	127	5384	1.6	18.4203	4.2	0.5126	4.3	0.0685	1.0	0.23	427.0	4.1	420.2	14.9	383.0	94.7	427.0	4.1
VMN32-43	102	15298	1.2	10.5952	2.3	3.3581	2.5	0.2580	1.0	0.40	1479.8	13.2	1494.7	19.7	1515.8	43.6	1515.8	43.6
VMN32-44	136	23756	2.2	11.2281	1.3	3.0187	2.0	0.2458	1.6	0.78	1416.9	20.0	1412.4	15.4	1405.5	24.1	1405.5	24.1
VMN32-45	40	7032	1.1	10.6402	2.2	3.4217	3.2	0.2640	2.4	0.74	1510.5	32.5	1509.4	25.5	1507.8	40.9	1507.8	40.9
VMN32-46	479	39246	2.2	13.8805	1.7	1.6680	2.1	0.1679	1.3	0.60	1000.6	12.0	996.4	13.6	987.2	34.8	987.2	34.8
VMN32-47	25	4746	0.5	8.8749	1.8	5.1974	2.1	0.3345	1.0	0.48	1860.3	16.2	1852.2	17.7	1843.0	33.1	1843.0	33.1
VMN32-49	95	9778	0.7	10.9222	1.0	3.2271	1.4	0.2556	1.0	0.71	1467.5	13.1	1463.7	11.0	1458.2	19.1	1458.2	19.1
VMN32-51	156	30904	1.1	8.1394	1.4	6.2364	1.7	0.3681	1.0	0.58	2020.7	17.3	2009.6	15.1	1998.1	25.1	1998.1	25.1
VMN32-52	84	11722	1.0	9.0055	1.0	4.7113	1.4	0.3077	1.0	0.71	1729.4	15.2	1769.2	11.9	1816.5	18.2	1816.5	18.2
VMN32-53	211	39740	1.8	8.9886	1.0	4.9231	1.4	0.3209	1.0	0.71	1794.3	15.7	1806.2	11.9	1820.0	18.2	1820.0	18.2
VMN32-54	53	8404	1.2	10.6342	1.4	3.4797	1.7	0.2684	1.0	0.57	1532.6	13.6	1522.6	13.8	1508.8	27.1	1508.8	27.1
VMN32-55	115	17552	2.5	10.6956	1.2	3.3997	1.5	0.2637	1.0	0.66	1508.8	13.5	1504.3	12.0	1497.9	21.8	1497.9	21.8
VMN32-56	53	5700	1.6	12.9090	1.6	2.0426	2.4	0.1912	1.7	0.73	1128.1	17.9	1129.8	16.1	1133.2	32.0	1133.2	32.0
VMN32-57	51	6800	1.0	10.4631	1.9	3.4807	2.5	0.2641	1.5	0.62	1511.0	20.7	1522.8	19.5	1539.4	36.3	1539.4	36.3
VMN32-58	56	10004	1.3	8.9939	1.8	4.9915	2.0	0.3256	1.0	0.49	1817.0	15.8	1817.9	17.2	1818.9	32.2	1818.9	32.2
VMN32-59	121	17034	1.9	9.2001	1.0	4.2959	2.5	0.2866	2.3	0.92	1624.8	32.9	1692.6	20.6	1777.6	18.3	1777.6	18.3
VMN32-60	55	9150	1.4	10.6086	1.8	3.4824	2.4	0.2679	1.5	0.65	1530.3	20.7	1523.2	18.5	1513.4	33.8	1513.4	33.8
VMN32-61	129	25996	1.5	8.9669	1.6	4.8738	2.5	0.3170	1.9	0.77	1774.9	29.5	1797.7	20.8	1824.3	28.5	1824.3	28.5
VMN32-62	146	19502	2.2	10.2669	1.0	3.7360	1.5	0.2782	1.2	0.76	1582.3	16.4	1579.1	12.4	1574.9	18.8	1574.9	18.8
VMN32-63	73	9914	1.5	10.3069	2.1	3.4260	2.6	0.2561	1.6	0.62	1469.9	21.6	1510.4	20.7	1567.6	38.7	1567.6	38.7
VMN32-64	116	23458	2.1	9.1262	1.6	4.5645	2.4	0.3021	1.8	0.73	1701.8	26.3	1742.8	20.0	1792.3	29.7	1792.3	29.7
VMN32-65	73	14916	1.3	8.8302	1.3	5.2167	1.6	0.3341	1.0	0.62	1858.2	16.1	1855.3	13.9	1852.2	23.2	1852.2	23.2
VMN32-66	111	16876	2.0	11.1846	1.0	2.8491	3.0	0.2311	2.8	0.94	1340.3	33.6	1368.6	22.2	1412.9	19.2	1412.9	19.2
VMN32-67	221	57770	1.9	5.2963	1.6	13.7035	3.4	0.5264	3.0	0.88	2726.2	67.6	2729.4	32.6	2731.8	26.7	2731.8	26.7
VMN32-68	78	17510	1.7	9.0394	1.2	4.9407	1.6	0.3239	1.0	0.63	1808.8	15.8	1809.2	13.5	1809.7	22.6	1809.7	22.6
VMN32-69	84	11260	1.0	10.5311	1.1	3.4775	1.5	0.2656	1.0	0.69	1518.5	13.5	1522.1	11.5	1527.2	20.0	1527.2	20.0
VMN32-70	59	11734	1.7	8.8498	1.3	5.1569	1.6	0.3310	1.0	0.61	1843.2	16.0	1845.5	14.0	1848.1	23.6	1848.1	23.6
VMN32-71	74	15986	1.7	9.0280	1.1	4.9540	1.5	0.3244	1.0	0.68	1811.1	15.8	1811.5	12.4	1812.0	19.5	1812.0	19.5
VMN32-72	77	16418	1.8	9.2176	2.2	4.6670	2.4	0.3120	1.0	0.42	1750.5	15.3	1761.3	20.1	1774.2	40.0	1774.2	40.0
VMN32-73	243	29488	2.4	13.6854	1.8	1.7025	2.5	0.1690	1.7	0.69	1006.5	16.2	1009.5	16.0	1015.9	36.5	1015.9	36.5
VMN32-74	32	5562	1.3	10.6296	1.4	3.4764	1.7	0.2680	1.0	0.61	1530.7	14.2	1521.9	13.5	1509.6	25.6	1509.6	25.6
VMN32-75	150	28750	1.9	8.9593	1.0	4.9962	1.4	0.3246	1.0	0.71	1812.4	15.8	1818.7	12.0	1825.9	18.1	1825.9	18.1
VMN32-76	93	20332	115.4	7.9805	1.6	6.4241	1.9	0.3718	1.0	0.53	2038.0	17.5	2035.6	16.7	2033.1	28.5	2033.1	28.5
VMN32-77	56	8060	0.8	10.5410	1.2	3.4768	1.6	0.2658	1.0	0.63	1519.4	13.5	1522.0	12.5	1525.4	23.1	1525.4	23.1
VMN32-78	89	14666	2.1	10.2043	1.4	3.7646	1.7	0.2786	1.0	0.59	1584.4	14.0	1585.2	13.6	1586.4	25.5	1586.4	25.5
VMN32-79	63	4864	2.6	13.4003	1.8	1.7376	2.3	0.1689	1.4	0.62	1005.9	13.0	1022.6	14.6	1058.4	36.0	1058.4	36.0
VMN32-80	216	16324	1.9	11.2762	1.6	2.6805	2.4	0.2192	1.8	0.74	1277.7	20.5	1323.1	17.6	1397.3	30.7	1397.3	30.7
VMN32-81	101	11744	3.2	14.1633	2.2	1.5721	2.4	0.1615	1.0	0.42	965.1	9.0	959.3	14.8	946.0	44.5	965.1	9.0
VMN32-82	305	22362	2.1	14.2950	1.5	1.4608	2.3	0.1515	1.7	0.74	909.1	14.3	914.3	13.8	927.0	31.7	909.1	14.3
VMN32-83	50	10456	2.0	8.2680	1.1	6.0199	1.5	0.3610	1.0	0.68	1986.8	17.1	1978.7	12.8	1970.3	19.3	1970.3	19.3

DOI: 10.1344/105.000001698

Analysis	U (ppm)	$^{206}Pb/^{204}Pb$	U/Th	$^{206}Pb^*/^{207}Pb^*$	± (%)	Isotope ratios $^{207}Pb^*/^{235}U^*$	± (%)	$^{206}Pb^*/^{238}U$	± (%)	error corr.	Apparent ages (Ma) $^{206}Pb^*/^{238}U^*$	± (Ma)	$^{207}Pb^*/^{235}U$	± (Ma)	$^{206}Pb^*/^{207}Pb^*$	± (Ma)	Best age (Ma)	± (Ma)
VMN32-84	171	12938	0.9	13.8297	2.2	1.6493	2.4	0.1654	1.0	0.42	986.9	9.2	989.3	15.2	994.6	44.3	994.6	44.3
VMN32-85	340	26616	3.7	13.8909	1.4	1.5887	1.7	0.1601	1.0	0.59	957.1	8.9	965.8	10.6	985.6	27.9	985.6	27.9
VMN32-86	64	10520	2.1	11.3544	1.9	2.9331	2.2	0.2415	1.0	0.46	1394.7	12.5	1390.5	16.3	1384.0	36.7	1384.0	36.7
VMN32-87	69	7552	3.8	13.8848	1.5	1.6862	1.8	0.1698	1.0	0.54	1011.1	9.4	1003.3	11.7	986.5	31.4	986.5	31.4
VMN32-88	123	20132	1.3	10.3865	1.4	3.6391	1.7	0.2741	1.0	0.59	1561.7	13.9	1558.1	13.5	1553.2	25.7	1553.2	25.7
VMN32-89	94	14302	2.0	11.1958	1.1	2.9782	1.6	0.2418	1.1	0.68	1396.2	13.3	1402.1	11.9	1411.0	21.9	1411.0	21.9
VMN32-90	67	4672	1.1	16.8824	3.4	0.7668	3.6	0.0939	1.4	0.38	578.5	7.7	577.9	16.1	575.7	73.2	578.5	7.7
VMN32-91	99	19378	1.6	8.9642	1.0	5.0277	1.4	0.3269	1.0	0.71	1823.2	15.9	1824.0	12.0	1824.9	18.1	1824.9	18.1
VMN32-92	42	9416	1.6	9.1497	1.4	4.8412	2.0	0.3213	1.4	0.71	1795.9	22.1	1792.1	16.7	1787.6	25.4	1787.6	25.4
VMN32-93	82	8828	0.9	10.2979	2.1	3.6697	2.8	0.2741	1.9	0.67	1561.5	25.8	1564.8	22.2	1569.3	38.6	1569.3	38.6
VMN32-94	83	17234	1.3	8.2557	1.5	5.9507	2.0	0.3563	1.4	0.69	1964.6	23.7	1968.7	17.5	1972.9	25.8	1972.9	25.8
VMN32-95	79	13784	2.3	11.0779	1.4	3.0740	2.2	0.2470	1.7	0.78	1422.9	22.1	1426.2	17.1	1431.2	26.9	1431.2	26.9
VMN32-96	111	16540	2.2	10.6406	1.4	3.3436	1.9	0.2580	1.4	0.71	1479.8	17.8	1491.3	14.9	1507.7	25.5	1507.7	25.5
VMN32-97	155	7890	2.2	16.6829	1.5	0.8144	1.8	0.0985	1.0	0.55	605.9	5.8	604.9	8.3	601.4	33.1	605.9	5.8
VMN32-98	116	4908	1.1	17.6897	2.3	0.6152	2.5	0.0789	1.0	0.40	489.7	4.7	486.8	9.7	473.2	51.2	489.7	4.7
VMN32-99	163	31680	2.4	7.8002	1.3	6.2472	1.7	0.3534	1.0	0.60	1950.9	16.8	2011.1	14.5	2073.4	23.3	2073.4	23.3
VMN32-100	87	7866	2.4	13.7933	1.5	1.5831	1.8	0.1584	1.0	0.55	947.7	8.8	963.6	11.3	1000.0	30.7	1000.0	30.7
VMN35-1	39	3936	2.5	12.6549	2.5	2.2148	3.0	0.2033	1.5	0.52	1192.9	16.7	1185.7	20.7	1172.6	50.3	1172.6	50.3
VMN35-2	46	1642	1.5	16.6669	6.5	0.7245	6.6	0.0876	1.1	0.17	541.2	5.7	553.3	28.0	603.5	140.4	541.2	5.7
VMN35-3	115	13330	0.8	8.8906	1.6	4.8178	1.9	0.3107	1.0	0.54	1743.9	15.3	1788.0	15.6	1839.8	28.3	1839.8	28.3
VMN35-4	223	26040	2.5	9.1266	1.3	4.0207	1.6	0.2661	1.0	0.64	1521.2	14.1	1638.4	13.3	1792.3	23.0	1792.3	23.0
VMN35-5	81	9682	1.2	11.2410	2.1	3.0290	2.5	0.2469	1.4	0.54	1422.7	17.5	1415.0	19.3	1403.3	40.7	1403.3	40.7
VMN35-6	47	4014	1.7	14.3164	2.8	1.5166	3.3	0.1575	1.7	0.52	942.7	15.3	937.1	20.4	923.9	58.4	942.7	15.3
VMN35-7	156	18208	1.4	8.1537	1.0	4.9549	2.1	0.2930	1.8	0.87	1656.6	26.4	1811.7	17.5	1995.0	18.0	1995.0	18.0
VMN35-8	270	33926	3.4	11.6910	1.5	2.6293	1.9	0.2229	1.3	0.65	1297.4	14.9	1308.9	14.3	1327.7	28.5	1327.7	28.5
VMN35-9	102	11960	1.6	9.0280	2.8	3.8601	6.2	0.2527	5.5	0.89	1452.6	71.8	1605.4	49.9	1812.0	50.7	1812.0	50.7
VMN35-10	159	10702	2.9	13.4414	3.4	1.4761	4.2	0.1439	2.4	0.58	866.7	19.5	920.6	25.2	1052.2	68.4	866.7	19.5
VMN35-11	74	11656	2.0	9.6719	1.3	3.9821	2.2	0.2793	1.8	0.80	1588.0	24.8	1630.6	17.8	1685.9	24.1	1685.9	24.1
VMN35-12	68	9476	3.3	10.7183	1.2	3.1157	2.1	0.2422	1.8	0.84	1398.1	22.4	1436.6	16.4	1493.9	22.1	1493.9	22.1
VMN35-13	113	9868	2.0	12.4898	1.1	2.1891	1.5	0.1983	1.1	0.69	1166.2	11.3	1177.6	10.8	1198.6	22.2	1198.6	22.2
VMN35-14	117	20810	1.5	8.9152	1.8	4.7654	3.1	0.3081	2.5	0.82	1731.5	38.6	1778.8	25.9	1834.8	31.9	1834.8	31.9
VMN35-15	197	30504	1.4	8.8958	1.6	4.8796	5.1	0.3148	4.8	0.95	1764.4	74.4	1798.7	42.9	1838.8	29.5	1838.8	29.5
VMN35-16	167	26810	2.7	9.1372	1.0	4.4867	1.4	0.2973	1.0	0.71	1678.0	14.8	1728.5	11.7	1790.1	18.2	1790.1	18.2
VMN35-17	358	45606	3.8	11.2841	1.3	2.9591	3.3	0.2422	3.1	0.92	1398.0	38.6	1397.2	25.4	1395.9	25.7	1395.9	25.7
VMN35-18	80	10870	1.9	11.1894	2.4	2.8550	2.6	0.2317	1.0	0.38	1343.4	12.1	1370.1	19.9	1412.1	46.7	1412.1	46.7
VMN35-20	170	11872	2.2	13.5598	2.1	1.7297	2.3	0.1701	1.0	0.44	1012.7	9.4	1019.6	14.7	1034.5	41.5	1034.5	41.5
VMN35-21	34	1502	1.2	18.8217	7.6	0.5477	7.7	0.0748	1.1	0.14	464.8	4.7	443.5	27.7	334.3	173.4	464.8	4.7
VMN35-22	167	30424	1.3	8.9971	1.0	4.7701	2.4	0.3113	2.1	0.91	1746.9	32.6	1779.7	19.8	1818.2	18.2	1818.2	18.2
VMN35-23	98	10674	1.9	11.1910	2.3	2.7731	5.4	0.2251	4.9	0.91	1308.7	57.7	1348.3	40.1	1411.8	43.1	1411.8	43.1
VMN35-24	286	43822	2.3	10.5872	1.3	3.3014	1.6	0.2535	1.0	0.62	1456.5	13.0	1481.4	12.5	1517.2	23.6	1517.2	23.6
VMN35-25	282	20626	1.0	9.2839	1.2	3.5459	6.1	0.2388	5.9	0.98	1380.2	73.7	1537.5	48.0	1761.1	22.3	1761.1	22.3
VMN35-26	243	20028	3.3	13.6552	1.2	1.7662	1.8	0.1749	1.4	0.76	1039.2	13.4	1033.1	11.9	1020.4	23.9	1020.4	23.9
VMN35-27	126	5968	1.1	17.8758	4.2	0.6646	4.3	0.0862	1.1	0.25	532.8	5.5	517.4	17.5	450.0	93.1	532.8	5.5
VMN35-28	129	24002	1.0	8.5969	1.0	5.4992	1.5	0.3429	1.1	0.74	1900.5	18.3	1900.5	12.8	1900.4	18.0	1900.4	18.0
VMN35-29	155	19734	1.6	8.8645	1.1	5.1214	2.6	0.3293	2.4	0.90	1834.8	37.8	1839.7	22.3	1845.2	20.5	1845.2	20.5

DOI: 10.1344/105.000001698

Analysis	U (ppm)	^{206}Pb ^{204}Pb	U/Th	$^{206}Pb^*$ $^{207}Pb^*$	± (%)	Isotope ratios $^{207}Pb^*$ $^{235}U^*$	± (%)	$^{206}Pb^*$ ^{238}U	± (%)	error corr.	Apparent ages (Ma) $^{206}Pb^*$ $^{238}U^*$	± (Ma)	$^{207}Pb^*$ ^{235}U	± (Ma)	$^{206}Pb^*$ $^{207}Pb^*$	± (Ma)	Best age (Ma)	± (Ma)
VMN35-30	123	6048	1.8	17.2466	3.5	0.6246	3.9	0.0781	1.8	0.46	485.0	8.3	492.7	15.2	529.1	76.2	485.0	8.3
VMN35-32	289	24568	3.1	13.4925	2.2	1.8614	2.6	0.1822	1.5	0.57	1078.7	15.0	1067.5	17.4	1044.6	43.4	1044.6	43.4
VMN35-33	115	18484	1.2	8.9679	1.3	4.7469	2.2	0.3087	1.7	0.80	1734.5	26.5	1775.6	18.1	1824.1	23.3	1824.1	23.3
VMN35-34	48	6694	0.9	10.3684	1.5	3.6607	1.8	0.2753	1.0	0.56	1567.5	13.9	1562.8	14.1	1556.5	27.4	1556.5	27.4
VMN35-35	86	14290	1.5	8.6550	1.8	5.4298	2.3	0.3408	1.5	0.66	1890.7	25.2	1889.6	20.1	1888.3	31.7	1888.3	31.7
VMN35-36	149	25796	2.1	8.6373	1.1	5.4212	1.6	0.3396	1.2	0.73	1884.8	19.0	1888.2	13.6	1892.0	19.6	1892.0	19.6
VMN35-37	296	31526	2.1	8.0874	1.1	4.6566	2.8	0.2731	2.5	0.92	1556.7	35.1	1759.5	23.0	2009.5	19.0	2009.5	19.0
VMN35-39	145	24910	1.7	8.8354	1.4	5.1577	3.0	0.3305	2.7	0.88	1840.8	42.4	1845.7	25.5	1851.1	25.3	1851.1	25.3
VMN35-40	164	23970	1.2	8.9805	1.0	5.0184	2.0	0.3269	1.7	0.86	1823.2	27.3	1822.4	16.9	1821.6	18.2	1821.6	18.2
VMN35-41	125	10552	2.5	14.1137	1.5	1.5128	2.1	0.1548	1.5	0.69	928.1	12.5	935.6	12.8	953.2	30.7	928.1	12.5
VMN35-42	82	12136	4.1	12.9771	1.9	2.0310	2.2	0.1912	1.0	0.46	1127.6	10.3	1126.0	14.8	1122.7	38.5	1122.7	38.5
VMN35-43	594	56202	2.2	13.6907	1.7	1.6715	2.8	0.1660	2.2	0.79	989.9	20.3	997.8	17.7	1015.1	34.3	1015.1	34.3
VMN35-44	159	12660	3.2	13.6458	1.2	1.6777	2.0	0.1660	1.6	0.81	990.2	14.8	1000.1	12.7	1021.8	23.8	1021.8	23.8
VMN35-45	129	16600	1.9	11.4426	2.1	2.9038	2.6	0.2410	1.6	0.59	1391.8	19.4	1382.9	19.8	1369.1	40.8	1369.1	40.8
VMN35-46	148	14108	1.8	12.0148	1.5	2.5663	2.2	0.2236	1.6	0.73	1301.0	18.6	1291.1	15.8	1274.6	28.7	1274.6	28.7
VMN35-47	146	22942	1.4	9.0671	1.1	4.9099	1.5	0.3229	1.0	0.67	1803.8	15.7	1804.0	12.6	1804.2	20.2	1804.2	20.2
VMN35-48	84	18350	1.6	9.1032	1.4	4.7112	1.7	0.3110	1.0	0.58	1745.9	15.3	1769.2	14.4	1796.9	25.3	1796.9	25.3
VMN35-49	127	11800	4.7	13.7126	1.3	1.5933	1.7	0.1585	1.0	0.62	948.2	9.2	967.6	10.5	1011.9	26.7	1011.9	26.7
VMN35-50	73	10810	5.3	10.7909	1.5	3.2806	2.2	0.2567	1.7	0.74	1473.2	21.7	1476.5	17.2	1481.2	28.0	1481.2	28.0
VMN35-51	139	20828	1.3	10.4330	1.9	3.3967	2.5	0.2570	1.7	0.68	1474.6	22.8	1503.6	19.9	1544.8	35.0	1544.8	35.0
VMN35-52	93	13862	1.3	8.9111	2.1	4.9816	2.4	0.3220	1.1	0.46	1799.3	17.3	1816.2	20.3	1835.6	38.6	1835.6	38.6
VMN35-53	39	6240	1.6	10.9515	2.6	3.2591	3.4	0.2589	2.2	0.64	1484.0	29.2	1471.4	26.7	1453.1	50.1	1453.1	50.1
VMN35-54	94	12092	1.6	10.5291	2.1	3.5455	2.6	0.2707	1.5	0.56	1544.6	20.1	1537.4	20.5	1527.6	40.2	1527.6	40.2
VMN35-55	119	11494	2.8	13.3034	1.1	1.8727	1.5	0.1807	1.0	0.67	1070.7	9.9	1071.5	9.8	1073.0	22.0	1073.0	22.0
VMN35-56	194	25238	1.4	9.3108	1.0	4.3801	1.8	0.2958	1.5	0.83	1670.3	21.6	1708.6	14.7	1755.8	18.3	1755.8	18.3
VMN35-57	85	15096	0.9	8.7025	1.2	5.3302	1.8	0.3364	1.4	0.75	1869.4	22.4	1873.7	15.8	1878.4	22.0	1878.4	22.0
VMN35-58	48	5964	2.4	12.6933	2.7	2.1886	3.0	0.2015	1.3	0.42	1183.3	13.6	1177.4	20.7	1166.6	53.3	1166.6	53.3
VMN35-59	188	23462	2.2	12.2902	1.8	2.3092	2.4	0.2058	1.6	0.68	1206.6	18.0	1215.1	17.1	1230.3	34.8	1230.3	34.8
VMN35-60	142	19226	2.2	10.7099	1.3	3.3745	1.6	0.2621	1.0	0.61	1500.7	13.4	1498.5	12.9	1495.4	24.6	1495.4	24.6
VMN35-61	77	9592	1.3	10.7457	1.4	3.1803	3.2	0.2479	2.8	0.89	1427.4	36.1	1452.4	24.4	1489.1	27.1	1489.1	27.1
VMN35-62	196	26998	3.3	10.3521	1.1	3.5856	1.5	0.2692	1.0	0.67	1536.8	13.7	1546.3	11.9	1559.4	21.0	1559.4	21.0
VMN35-63	196	19894	1.6	12.3848	1.0	2.3257	1.5	0.2089	1.2	0.76	1222.9	13.1	1220.2	11.0	1215.2	19.7	1215.2	19.7
VMN35-64	147	15636	2.3	12.1129	1.3	2.4306	1.6	0.2135	1.0	0.62	1247.6	11.3	1251.7	11.6	1258.7	24.6	1258.7	24.6
VMN35-65	148	18164	1.0	9.1492	1.7	4.7188	2.3	0.3131	1.6	0.70	1756.1	24.9	1770.6	19.4	1787.8	30.1	1787.8	30.1
VMN35-66	79	11658	2.1	10.7872	1.5	3.2874	1.9	0.2572	1.0	0.55	1475.5	13.5	1478.1	14.4	1481.8	29.3	1481.8	29.3
VMN35-67	80	3374	1.2	16.9458	2.4	0.7771	2.7	0.0955	1.1	0.40	588.0	6.0	583.8	11.8	567.5	53.3	588.0	6.0
VMN35-68	169	17480	2.8	12.6762	1.3	2.1985	2.4	0.2021	2.0	0.84	1186.7	22.0	1180.6	16.8	1169.3	25.6	1169.3	25.6
VMN35-69	68	13292	1.4	8.2427	1.0	5.9467	1.5	0.3555	1.1	0.73	1960.8	18.9	1968.1	13.3	1975.7	18.4	1975.7	18.4
VMN35-70	52	7834	1.2	10.9408	1.5	3.1675	2.1	0.2513	1.5	0.72	1445.4	19.6	1449.3	16.2	1455.0	27.7	1455.0	27.7
VMN35-71	150	19758	0.9	8.7383	1.0	5.3219	1.4	0.3373	1.0	0.71	1873.6	16.3	1872.4	12.1	1871.1	18.1	1871.1	18.1
VMN35-72	157	18628	2.0	9.9407	1.0	3.9714	1.4	0.2863	1.0	0.71	1623.1	14.3	1628.4	11.5	1635.1	18.6	1635.1	18.6
VMN35-73	86	10312	1.2	11.2792	1.8	3.0074	2.1	0.2460	1.1	0.52	1417.9	13.7	1409.5	15.9	1396.8	34.1	1396.8	34.1
VMN35-74	97	12848	0.9	10.1012	1.3	3.8417	1.6	0.2814	1.0	0.62	1598.6	14.2	1601.5	12.9	1605.3	23.3	1605.3	23.3
VMN35-75	67	6474	1.6	12.3271	1.9	2.4110	2.2	0.2156	1.0	0.46	1258.3	11.4	1245.9	15.5	1224.4	37.6	1224.4	37.6
VMN35-77	217	25090	2.0	10.8724	1.3	3.2429	1.6	0.2557	1.0	0.62	1467.9	13.1	1467.5	12.5	1466.9	23.9	1466.9	23.9

DOI: 10.1344/105.000001698

Analysis	U (ppm)	^{206}Pb ^{204}Pb	U/Th	$^{206}Pb^*$ $^{207}Pb^*$	± (%)	Isotope ratios $^{207}Pb^*$ $^{235}U^*$	± (%)	$^{206}Pb^*$ ^{238}U	± (%)	error corr.	Apparent ages (Ma) $^{206}Pb^*$ $^{238}U^*$	± (Ma)	$^{207}Pb^*$ ^{235}U	± (Ma)	$^{206}Pb^*$ $^{207}Pb^*$	± (Ma)	Best age (Ma)	± (Ma)
VMN35-78	180	20142	0.8	10.3994	1.0	3.5695	1.8	0.2692	1.5	0.82	1536.9	19.8	1542.8	14.0	1550.9	18.8	1550.9	18.8
VMN35-80	110	2886	1.5	11.3766	4.6	2.6466	4.9	0.2184	1.7	0.35	1273.3	19.8	1313.7	35.9	1380.3	87.5	1380.3	87.5
VMN35-81	31	2972	2.1	13.9961	3.3	1.6628	3.6	0.1688	1.4	0.40	1005.4	13.3	994.4	22.7	970.3	67.1	970.3	67.1
VMN35-82	106	10362	1.9	13.8472	1.9	1.6541	2.8	0.1661	2.0	0.73	990.7	18.4	991.1	17.5	992.0	38.6	992.0	38.6
VMN35-83	509	45892	3.7	10.3142	1.6	3.7371	3.4	0.2796	3.0	0.89	1589.1	42.4	1579.4	27.2	1566.3	29.6	1566.3	29.6
VMN35-84	133	32152	3.3	7.0779	1.4	7.9676	2.2	0.4090	1.8	0.78	2210.4	32.7	2227.4	20.2	2243.0	24.2	2243.0	24.2
VMN35-85	112	19220	1.1	7.8639	1.0	6.6605	1.4	0.3799	1.0	0.71	2075.7	17.7	2067.4	12.5	2059.1	17.7	2059.1	17.7
VMN35-86	148	11418	1.7	13.3320	2.2	1.8969	2.4	0.1834	1.1	0.45	1085.6	10.9	1080.0	16.2	1068.7	43.9	1068.7	43.9
VMN35-87	103	11484	1.5	12.3783	1.2	2.3118	1.6	0.2075	1.0	0.65	1215.7	11.1	1215.9	11.0	1216.2	23.3	1216.2	23.3
VMN35-88	190	25886	2.3	10.1803	1.3	3.8143	1.7	0.2816	1.1	0.64	1599.5	15.6	1595.8	13.8	1590.8	24.7	1590.8	24.7
VMN35-89	182	35642	2.8	9.2022	1.2	4.4845	1.8	0.2993	1.4	0.74	1687.8	20.3	1728.1	15.3	1777.2	22.4	1777.2	22.4
VMN35-90	531	77414	6.1	10.4036	1.6	3.5754	2.7	0.2698	2.2	0.80	1539.7	29.7	1544.1	21.5	1550.1	30.4	1550.1	30.4
VMN35-91	13	1556	1.1	11.0833	1.6	3.1392	2.3	0.2523	1.8	0.75	1450.5	22.7	1442.4	18.0	1430.3	29.6	1430.3	29.6
VMN35-92	56	5028	1.8	13.5824	2.3	1.8269	2.5	0.1800	1.0	0.39	1066.8	9.8	1055.2	16.7	1031.2	47.3	1031.2	47.3
VMN35-93	55	7704	0.6	7.1906	1.2	6.5398	1.5	0.3411	1.0	0.65	1891.7	16.4	2051.3	13.5	2215.7	20.2	2215.7	20.2
VMN35-95	61	6058	1.7	13.1500	2.0	1.9852	2.4	0.1893	1.4	0.56	1117.8	14.1	1110.5	16.4	1096.3	40.3	1096.3	40.3
VMN35-96	169	39042	4.5	8.4099	2.2	5.6463	3.7	0.3444	3.0	0.80	1907.8	49.0	1923.2	31.9	1939.9	39.4	1939.9	39.4
VMN35-97	199	31920	2.3	9.0972	1.4	4.6383	1.8	0.3060	1.1	0.62	1721.1	16.6	1756.2	14.8	1798.1	25.3	1798.1	25.3
VMN35-99	146	17330	4.7	13.5798	1.5	1.6912	2.1	0.1666	1.4	0.67	993.1	12.9	1005.2	13.3	1031.6	31.2	1031.6	31.2
VMN35-100	45	6718	1.7	10.6844	2.9	3.3770	3.9	0.2617	2.6	0.66	1498.5	34.1	1499.1	30.5	1499.9	55.5	1499.9	55.5

DOI: 10.1344/105.000001698

Geologica Acta, Vol.9, Nos 3-4, September-December 2011, 273-287
DOI: 10.1344/105.000001715
Available online at www.geologica-acta.com

geologica acta

Pre-arc basement complex and overlying early island arc strata, Southwestern Puerto Rico: overview, geologic evolution, and revised data bases

E.G. LIDIAK [1] **W.T. JOLLY** [2 ‖ †] **A.P. DICKIN** [3]

[1] **Department of Geology and Planetary Science, University of Pittsburgh**
Pittsburgh, PA., USA 15260 E-mail: egl@pitt.edu

[2] **Department of Earth Sciences, Brock University**
St. Catharines, Ontario, Canada L2S 3A1

[3] **Department of Geography and Geology, McMaster University**
Hamilton, ON CANADA L8S 4M1 E-mail: dickin@mcmaster.ca

† Deceased

ABSTRACT

The pre-arc basement complex in southwestern Puerto Rico consists of rocks exposed in the Bermeja complex. The oldest rocks are highly serpentinized peridotites that occur in three belts (Monte del Estado, Río Guanajibo, and Sierra Bermeja). These serpentinites were emplaced into a sequence of Jurassic to mid-Cretaceous pelagic chert (Mariquita chert) that contains abundant rafts and blocks of N-MORB-type amphibolites (Las Palmas amphibolite) and tholeiite and associated trondhjemite fractionates (Lower Cajul MORB) also of N-MORB affinity. The rocks are apparently overlain by a younger sequence of pre-arc plateau basaltic and andesitic lava flows (Upper Cajul Formation) that occur in two distinct geographic sequences, one having E-MORB and the other OIB geochemical characteristics. Overlying these pre-arc rocks in western Puerto Rico are northwest-trending Late Cretaceous to Eocene (85 to 45Ma) island arc strata that chronologically overlap later volcanic phases in central Puerto Rico. These western Puerto Rico arc rocks have elevated incompatible element concentrations together with conspicuously shallow negative Nb-anomalies, slightly positive Zr-Hf anomalies, and exceedingly high OIB-like Nb/Zr, all indicative of enriched source compositions. Trace element patterns are reproduced by multiple component mixing models involving highly depleted spinel peridotite (RMM15 to 20) overprinted by small OIB-type (up to ~2%) and pelagic sediment components. Trace element abundances are too high to qualify Atlantic Cretaceous pelagic sediment as a potential contaminant, but mantle-melting models (f=0.25) are consistent with the incorporation of variable proportions of Caribbean Cretaceous pelagic sediment through north-dipping subduction of the Caribbean basin. Anomalous two-pyroxene-bearing andesites with extraordinarily high SiO_2/MgO compared with normal mantle basaltic compositions, also indicate the incorporation of Jurassic to Early Cretaceous pelagic chert from the Caribbean. The high degree of source enrichment in western Puerto Rico is inconsistent with regional within-plate plume tectonics. Instead, it is inferred that the younger north-dipping western Puerto Rico arc (dating from ~85Ma) sampled an upper mantle enrichment zone generated in the back-arc region of the older (125 to ~85Ma) south-dipping arc system in central Puerto Rico.

KEYWORDS | **Caribbean. Island Arc. Ophiolite Complex. Pelagic Sediment. Subduction.**

INTRODUCTION

The Greater Antilles Island Arc platform, which represents the only major Mesozoic destructive plate margin associated with the North Atlantic Ocean, forms the long-lived and fragmented northern boundary of the Caribbean Plate. Preserved within the platform in Puerto Rico are both 1) pre-arc thoeliitic basalt and associated amphibolite of oceanic crustal origin (Fig. 1, 2) a pair of independent, partly simultaneous but geochemically distinct island arc systems, one with depleted N-MORB affinities (central Puerto Rico, northeast Puerto Rico) (Jolly et al., 2008a) and another with highly enriched, OIB-like compositions (western Puerto Rico) (Jolly et al., 2007). Consequently, an understanding of the pre-arc geochemical characteristics prior to the development of the island arc sequences in the Antilles is important in helping to resolve the tectonic relations both within and among the islands of Cuba (Iturralde-Vinent, 1998; García-Casco et al., 2006; Proenza et al., 2006; Marchesi et al., 2007), Hispaniola (Lewis et al., 2002), Jamaica (Draper, 1986; Mitchell, 2006), and Puerto Rico (Jolly et al., 1998b, 2007; Schellekens, 1998), and in interpreting interactions between the adjacent North American and Caribbean Plates. The regional role of an incompatible element enriched OIB-type component in the Antilles mantle wedge, for example, remains an important question. Equally significant are the geochemical links between arc lavas and subducted Atlantic and Caribbean Mesozoic pelagic sediments. The data presented in this study addresses the geochemical characteristics of the older rocks of the western Puerto Rican segment of the Greater Antilles island arc.

The specific objectives of this investigation are to provide an updated overview of the older rocks that compose the pre-arc complex of southwestern Puerto Rico, to evaluate the geologic and geochemical evolution of the immediately overlying island arc sequence, to make minor revisions in the stratigraphic nomenclature for enhanced clarity, to correct errors in several published databases, and to present previously unpublished datasets for these older rocks.

GEOLOGICAL SETTING

The island of Puerto Rico is located south of the broad, structurally diffuse Puerto Rico Trench Megathrust (Fig. 1A), and north of the west-trending Los Muertos Trench Thrust, which respectively represent the north and south boundaries of the Puerto Rico-Virgin Islands block. The Greater Antillean islands of Hispaniola, Jamaica, and Cuba lie west of Puerto Rico. To the east are the Virgin Islands and the modern Lesser Antilles arc. The Puerto Rico block or microplate (Jansma et al., 2000) bridges the transition between these two segments.

Volcanic strata in eastern and central Puerto Rico are distributed within five west-trending volcanic belts, representing principal volcanic axes during discrete eruptive phases (volcanic phases I through V) (Jolly et al., 1998b; Schellekens, 1998) and ranging in age from Aptian to Late Eocene (120 to 45my). Predominant westerly trends in central Puerto Rico are truncated by the northwest-trending Greater Southern Puerto Rico Fault Zone (Glover, 1971) and sub-parallel volcanic belts in western Puerto Rico. The Sierra Bermeja Complex of western Puerto Rico incorporates rock types associated with ocean basins, including partly serpentinized spinel peridotite (Mattson, 1979; Jolly et al., 1998b) that occupies three main belts (Monte del Estado ((Electronic Appendix Table I, available in www.geologica-acta.com)), Río Guanajibo, and Sierra Bermeja; Fig. 1B). The Mesozoic oceanic basement complex is succeeded by western Puerto Rico arc strata dating from Santonian time (Jolly et al., 2007), the distribution of which is shown in Figure 1C. The serpentinites were periodically emplaced along with arc volcanism from Santonian to Late Eocene time (Krushensky and Monroe, 1978; Martinez-Colon, 2003).

FIGURE 1 | **Map of the Caribbean region showing principal structural elements of the tectonic boundary between the North American - Carribean Plates (lines represent fault zones, teeth represent polarity of subduction zones. The vector, indicating motion of the Atlantic Basin with respect to a stable Caribbean, is from Jansma et al. (2000). Locations of DSDP drilling sites within the Caribbean Cretaceous Basalt Plateau (CCBP) are indicated. Contours in the Caribbean Basin represent thickness (km) of oceanic crust (seismic velocity < 7.4km/sec; Mauffret and Leroy, 1997). "X" represents the Sierra de Bahoruco region, from which representative Caribbean Late Cretaceous pelagic sediment (CKPS, Río Arriba Fm. (Llinas, 1972) was collected. Additional features identified as follows; AF: Anegada Fault; AI: Aves Island; CLIP: Caribbean large igneous province of Hauff et al. (2000); CT: Cayman Trough spreading center; GP: Gonive Microplate; HS: Hispaniola microplate; LMTT: Los Muertos Trench Thrust; MP: Mona Passage; PR: Puerto Rico; PRTMT: Puerto Rico Trench Megathrust; PR-VI: Puerto Rico - Virgin Islands Microplate; SITF: Swan Island Transform Fault; WF: Walton Fault. B) Map of tectonic elements in western Puerto Rico (WPR), including serpentinized peridotite (purple hachure pattern), Jurassic pelagic chert (yellow stipple), MORB basalt (black), back-arc strata (parallel), volcanic arc strata (green shaded); other symbols include; A: amphibolite; BQN: Boquerón Fm.; C: chert; PL: Parguera Ls (includes lesser IAB volcanic strata and plutonic rocks); E: Eocene Jicara Fm. (shale); LJS: Lajas Fm.; QT and Q: Quaternary alluvium; RL: Río Loco Lava (green parallel dots); S: serpentinite; V: volcanic rocks. Tectonic block names adopted from synformal terminology of Mattson (1960). C) Sierra Bermeja region, southwest Puerto Rico illustrating exposures of serpentinized spinel peridotite mélange containing numerous blocks of amphibolite (SP), Mariquita Chert (MQT), Las Palmas amphibolite mélange (A), and altered Cajul basalts (LCAJ, UCAJN, UCAJS-see text). Adapted and modified from Volckmann (1984a, b, c).**

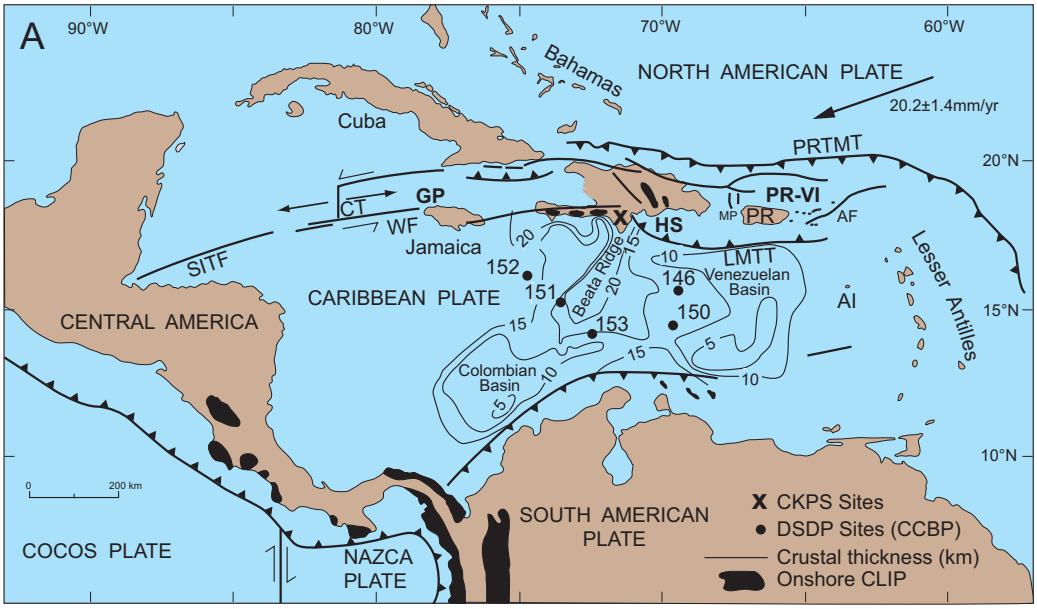
A
90°W
80°W
70°W
60°W
Bahamas
NORTH AMERICAN PLATE
20.2±1.4mm/yr
Cuba
PRTMT
20°N
GP
CT
WF
Jamaica
X
HS
PR-VI
MP
PR
AF
SITF
CARIBBEAN PLATE
CENTRAL AMERICA
152
151
153
150
146
Beata Ridge
LMTT
Venezuelan Basin
AI
Lesser Antilles
15°N
Colombian Basin
10°N
0
200 km
SOUTH AMERICAN PLATE
COCOS PLATE
NAZCA PLATE
X CKPS Sites
DSDP Sites (CCBP)
Crustal thickness (km)
Onshore CLIP

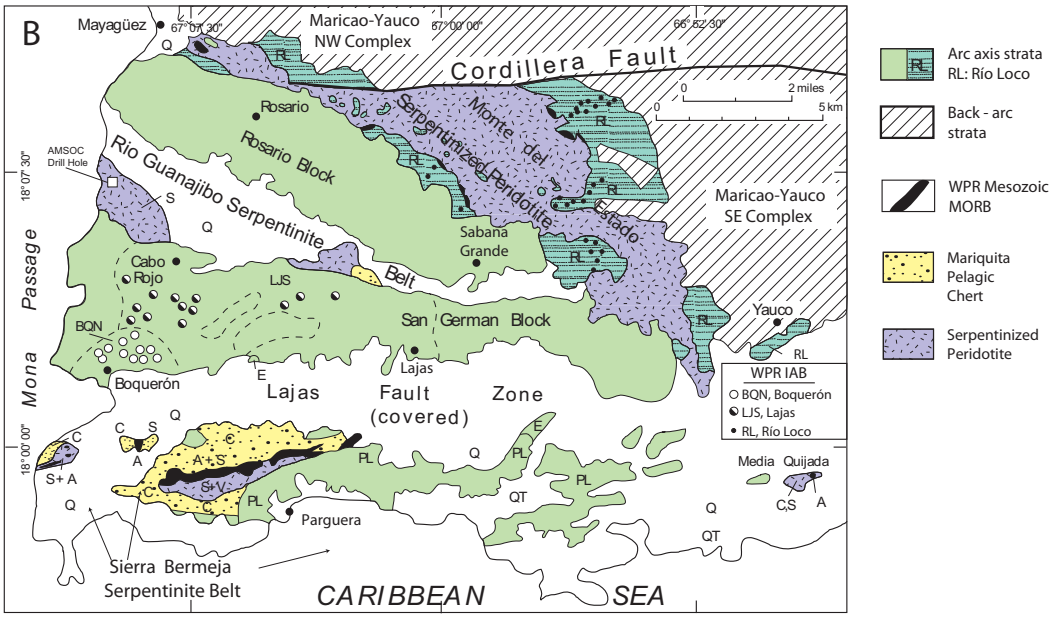
B
Mayagüez
Maricao-Yauco NW Complex
Cordillera Fault
Rosario
Rosario Block
Río Guanajibo Serpentinite
Serpentinized Peridotite
Monte del Estado
Maricao-Yauco SE Complex
AMSOC Drill Hole
Sabana Grande
Cabo Rojo
LJS
Belt
San German Block
Yauco
BQN
Boquerón
Lajas
Lajas Fault Zone (covered)
WPR IAB
BQN, Boquerón
LJS, Lajas
RL, Río Loco
Media Quijada
Parguera
Sierra Bermeja Serpentinite Belt
CARIBBEAN SEA
Mona Passage
Arc axis strata
RL: Río Loco
Back - arc strata
WPR Mesozoic MORB
Mariquita Pelagic Chert
Serpentinized Peridotite

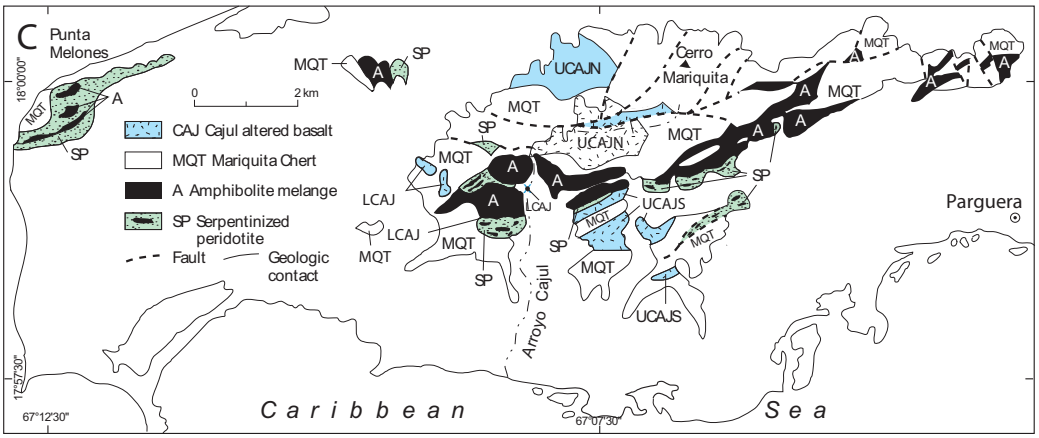
C
Punta Melones
CAJ Cajul altered basalt
MQT Mariquita Chert
A Amphibolite melange
SP Serpentinized peridotite
Fault
Geologic contact
UCAJN
Cerro Mariquita
LCAJ
UCAJS
Parguera
Arroyo Cajul
Caribbean Sea

PRE-ARC BASEMENT COMPLEX, SOUTHWEST PUERTO RICO

The pre-arc basement discussed in this report comprises the rocks exposed in the Sierra Bermeja Complex (Mattson, 1960). The oldest rocks consist of a mélange of serpentinized spinel peridotite (Schellekens et al., 1991; Jolly et al., 1998b, 2007; Schellekens, 1998). The serpentinite contains abundant blocks of N-MORB type amphibolite (Las Palmas amphibolite) (Fig. 1C, 2) and local xenolithic clasts of Jurassic tholeiitic pillow lava of N-MORB affinity (Lower Cajul MORB, LCAJ in Fig. 1C, 2). Overlying this mélange is a thick sequence of pelagic sedimentary rock (Mariquita chert) of Early Jurassic to Mid-Cretaceous age and of Pacific provenance (Montgomery et al., 1994a, b). The uppermost units in the pre-arc sequence are aphanitic basalts (Upper Cajul Formation), probably representing a local facies of the Late Cretaceous basalt plateau (Hauff et al., 2000; Kerr et al., 2002) of the Caribbean basin. The Upper Cajul basalts are the uppermost pre-arc sequence, consisting of a northern facies of plateau basalt of E-MORB affinity and a southern facies of OIB affinity (Fig. 1C, 3).

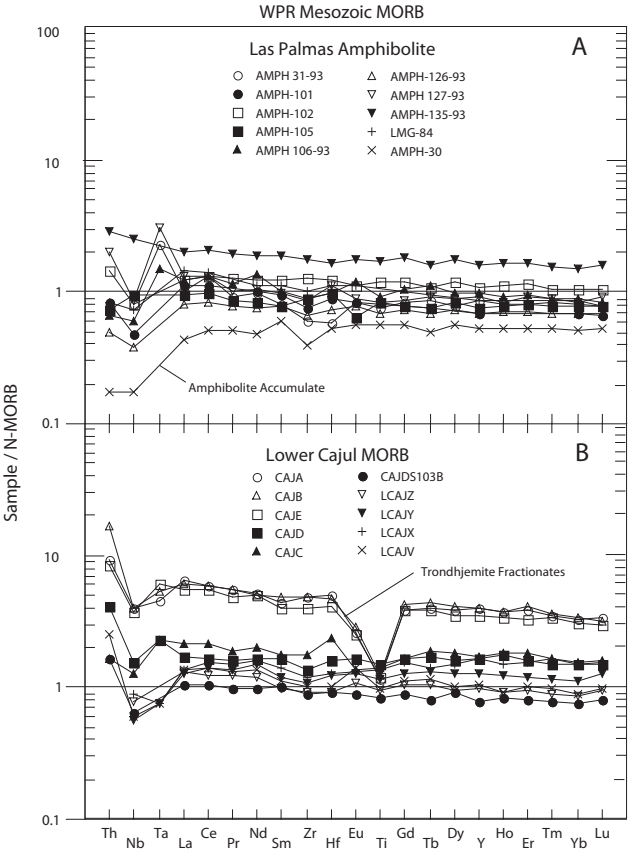

FIGURE 2 | **N-MORB-normalized incompatible element patterns. A) Las Palmas amphibolites and B) Lower Cajul MORB basalt and fractoniated trondhjemite.**

Western Puerto Rico Mesozoic MORB

Tholeiitic pillow basalt and associated trondhjemite fractionates (Lower Cajul MORB) along with massive to schistose and foliated plagioclase-hornblende amphibolite (Las Palmas Amphibolite) are prominent in the pre-arc basement in southwest Puerto Rico (Fig. 1C). The rocks occur as engulfed xenolithic blocks, reaching hundreds of meters in diameter, within marginal parts of the serpentinized peridotite (Mattson, 1960; Curet, 1986; Martínez-Colon, 2003). Amphibolite and tholeiitic pillow lavas are closely associated with the black to pale grey radiolarian Mariquita chert of Pacific provenance (Montgomery et al., 1994a) both 1) as xenolithic inclusions in serpentinite mélange, as in Sierra Bermeja and in central parts of the Monte del Estado peridotite (Llerandi-Roman, 2004), or 2) as clasts in pre-volcanic chert-amphibolite-pebble conglomerate overlying fragmental serpentinite along the north border zone of the Monte del Estado serpentinized peridotite (McIntyre, 1975). At Sierra Bermeja the basement complex is succeeded by up to 300m of pelagic chert (Mariquita Chert), ranging from mid-Jurassic (Pliensbachian, ~185Ma) to Early Cretaceous in age (Montgomery et al., 1994a). Hence, stratigraphic relations indicate the western Puerto Rico amphibolites, tholeiitic basalts and fractionates represent remnants of pre-arc Jurassic MORB (Schellekens et al., 1991; Jolly et al., 1998b) from the Mesozoic proto-Pacific (Farallon) Plate (Pindell et al., 1988; Donnelly, 1989; Pindell and Barrett, 1990; Montgomery et al., 1994a).

In conformity with the suggestion of a MORB origin, the pre-arc basalts and amphibolites have depleted normalized incompatible element patterns and compositions (Fig. 2; Electronic Appendix Tables II, IV) overlapping the N-MORB trend together with low La/Nb and La/Sm, averaging 1.7 and 1.1 respectively, similar to modern Atlantic MORB (Dosso et al., 1993), altered Cretaceous Atlantic MORB (Jahn et al., 1980) and N-MORB (0.95 and 1.1 (Sun and McDonough, 1989)). In addition, isotopic data (Appendix Table 4) reveal the rocks have uniformly MORB-like ε_{Nd}-values (average 8.3) and elevated initial $(i)^{87}Sr/^{86}Sr$ (average 0.7039), overlapping the field of altered Cretaceous Atlantic MORB (average 0.7040). The presence of normal-type Mesozoic MORB in the pre-arc basement is inferred to reflect original fertile MORB mantle type compositions in the upper mantle beneath Puerto Rico.

Upper Cajul Formation

The uppermost unit in the pre-arc basement sequence is the Upper Cajul Formation. The formation consists of two distinct geographic and geochemical facies (northern and southern) of plateau basaltic and andesitic (volatile-free basis) lava flows that are characterized by incompatible

element-enriched compositions. The contacts between the lava flows and the apparently underlying Mariquita chert are not exposed but the relative stratigraphic positions and evolved compositions suggest the Upper Cajul flows were erupted late in the pre-arc sequence. The northern facies occurs in fault blocks in the Mariquita chert, mainly along the northern flank of Sierra Bermeja (Fig. 1C), whereas the southern facies is interlayered with the Mariquita chert on the southern flank of the massif (Volckmann, 1984a). The two units probably represent local facies of the Late Cretaceous Caribbean basalt plateau that is dated at about 90Ma (Lapierre et al., 1999; Kerr and Tarney, 2005), although we do not exclude an earlier origin of these basalts.

Samples from the northern facies have normalized incompatible element patterns that approximate E-MORB patterns (Fig. 3A; Electronic Appendix Table V). Isotope data for the northern rocks are uniformly more enriched in Sr and Nd than western Puerto Rico Mesozoic MORB, containing average ε_{Nd}-values of 6.9 and elevated initial $(i)^{87}Sr/^{86}Sr$ 0.70465. In comparison, the southern facies have incompatible trace element patterns that closely coincide with OIB compositions (Fig. 3B; Electronic Appendix Table VI). Similarly, the average initial Sr and Nd ratios is slightly more evolved for the southern facies than for the northern facies, with $(i)^{87}Sr/^{86}Sr$=0.70472 and ε_{Nd}=4.7.

Caribbean Cretaceous Basalt Plateau

Presence of pelagic chert of Pacific provenance (Montgomery et al., 1994a) indicates the western Puerto Rico pre-arc crustal sequence originated within the ancient proto-Pacific (Farallon) Plate (Pindell et al., 1988; Donnelly, 1989; Pindell and Barrett, 1990; Montgomery et al., 1994a). The Caribbean Basin has subsequently undergone at least two within-plate basalt plateau-forming events (Hauff et al., 1997, 2000; Lewis et al., 2002). The oldest, Plateau I of Lewis et al. (2002), occurred concurrent with the initiation of the mid-Atlantic ridge (about 175Ma). E-MORB-type basalt produced by Plateau I were subsequently obducted onto central Hispaniola during early Albian time (Duarte Complex). A second event (Plateau II), dating between 91 to 88Ma, is correlated with the initiation of the East Pacific Rise and with widespread within-plate basalt activity comprising the Caribbean Large Igneous Province of Hauff et al. (2000) including 1) eruption and obduction of basalt along the southern Caribbean margin in Columbia and Central America, 2) mafic plutonism in Hispaniola (Siete Cabezas Complex, Lewis et al., 2002), and 3) development of the Caribbean Cretaceous Basalt Plateau in the Caribbean Basin (Donnelly, 1994). Crustal variations within the Caribbean (Fig. 1A) reveal that the Caribbean Cretaceous Basalt Plateau attains a maximum thickness of 20km along the Beata Ridge and thins laterally to less than 10km south of Puerto Rico (Mauffret and Leroy, 1997).

Seven Deep Sea Drilling Project core samples of the Caribbean Cretaceous Basalt Plateau were analyzed (Electronic Appendix Table VII). The basalts have variable trace element compositions (Fig. 4). Samples from sites 146, 150, 152, and 153 (Fig. 1A) have LREE, Th, and Nb compositions between N-MORB and E-MORB, and MREE and HREE compositions approximating E-MORB. In contrast, two basalts from site 151 have LREE, MREE, Th, and Nb essentially intermediate between E-MORB and OIB.

MESOZOIC PELAGIC SEDIMENTS, ANTILLES REGION

Atlantic Cretaceous Pelagic Sediment

Eight Atlantic Cretaceous pelagic sediment samples from the Deep Sea Drilling Project drill cores at sites 105 and 417 in the eastern North Atlantic (Electronic Appendix Fig. I) are presented in Figure 5A and Tables 8

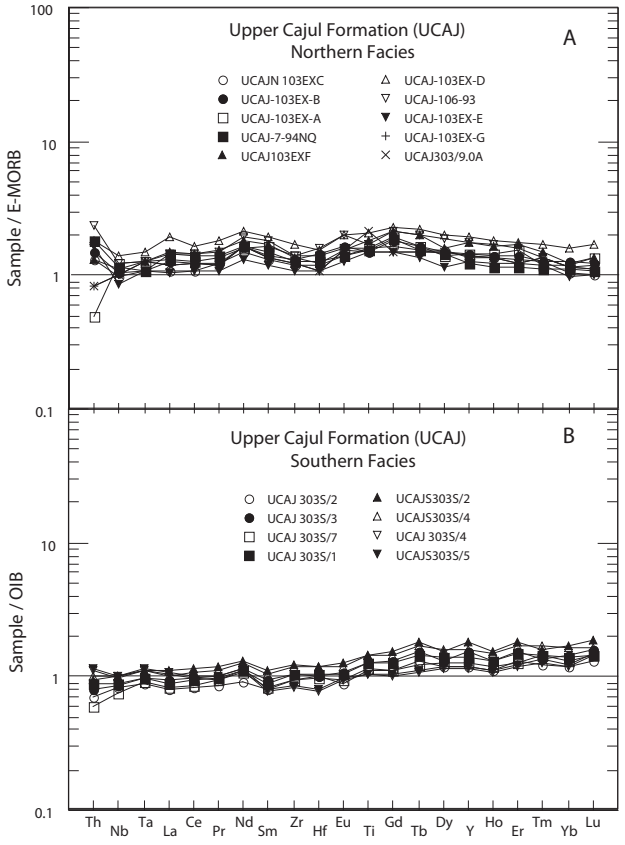

FIGURE 3 | **Normalized incompatible element patterns of Upper Cajul Formation. A) Northern facies, normalized to E-MORB and B) Southern facies, normalized to OIB.**

and 9; inferred paleontological ages are given in Jolly et al. (2008b). Total thicknesses of recovered cores averaged about 100m, of which Cretaceous sediment comprised about 65m. Proportions of analyzed samples approximate total relative abundances of Cretaceous rock types, averaging 60% claystone and 40% calcareous claystone and limestone. Earliest Atlantic strata (>150 to 110Ma) are dominated by carbonate and calcareous clay, which was supplanted by black and green claystone during Late Cretaceous time.

Pacific (Farallon) mid-Jurassic to Early Cretaceous pelagic chert

Caribbean pelagic sediment is represented in south-western Puerto Rico by radiolarian chert (Mari-quita chert) of Mid-Jurassic to Early Cretaceous age (Mattson, 1960; Llerandi-Roman, 2004), up to 300m of which occurs in the Sierra Bermeja ultramafic complex (Fig. 1B, C). Presumably correlative xenolithic chert is reported from the Monte del Estado serpentinized peridotite (Llerandi-Roman, 2004) suggesting widespread distribution within the pre-arc basement. The Mariquita chert contains from 95% to almost 100% SiO_2 (Table 8) and is extremely depleted in incompatible elements compared with Late Cretaceous pelagic sediment (Fig. 5), rendering it ineffective as a mantle contaminant, except as a dilutant. The chert has low La/Sm (3 to 4.5), and a broad range of Yb/Sm (from 0.35 to 0.8), and partly overlaps the field of highly scavenged south Pacific clay (Plank and Langmuir, 1998; Woodhead et al., 1998; Pearce et al., 1999).

Caribbean Late Cretaceous pelagic sediment

Mid- to Late Cretaceous Caribbean pelagic sediment contains higher proportions of calcareous clay and claystone, and correspondingly lower proportions of silica, compared with Jurassic chert, reflecting a global shift from radiolarian- to foraminifera-dominated pelagic assemblages during that interval (Montgomery et al., 1994a). On-shore exposures of Late Cretaceous pelagic strata in Puerto Rico are heavily contaminated with arc-related detritus, including lenses of sandstone and ash-fall tuff, due to proximity to the Antilles arc platform, and therefore do not represent compositions of subducted sediment from the Caribbean Plate. Instead, Caribbean Cretaceous pelagic sediment is represented (Tables 8 and 9) by pelagic sediment from the Sierra de Bahoruco region of southern Hispaniola, which was obducted northward from the central Caribbean Basin onto older arc-bearing terranes during Tertiary time (Lewis and Draper, 1990; Mann et al., 1991). In particular, full analytical data for six samples of calcareous claystone from the Río Arriba Formation, consisting of over 500m of Albian to Maastrichtian chert, pelagic limestone, and claystone (Llinas, 1972) are given in Electronic Appendix Tables VIII and IX. These six samples from Hispaniola are tentatively regarded as being representative of Late Cretaceous Caribbean pelagic sediments. However, it is evident that given the small number of samples and the limited geographic distribution, additional analyses are necessary to establish a statistically more representative Caribbean Cretaceous pelagic sediment average.

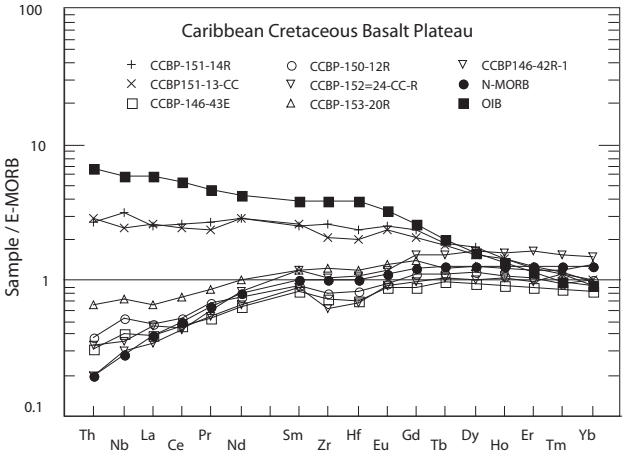

FIGURE 4 | **E-MORB-normalized incompatible element patterns of Caribbean Cretaceous Basalt Plateau. See Figure 1A for site locations.**

Distinguishing geochemical features of Atlantic and Caribbean Cretaceous pelagic sediments, and Jurassic to Early Cretaceous pelagic chert

Mesozoic pelagic sediments typically form broad positive fields sub-parallel to 1:1 MORB and OIB vectors in La-Yb element-element diagrams (Electronic Appendix Fig. II). Atlantic Cretaceous pelagic sediment distribution is subdivided into two sub-fields, one consisting predominantly of calcareous claystone and limestone and another of claystone. Slopes of both fields (La/Yb=15) are similar to Caribbean Cretaceous pelagic sediment (La/Yb=16), but this has much lower La abundances (ranging from 15 to 35 compared with 25 to 65).

Both Atlantic and Caribbean Cretaceous pelagic sediments have shallow curvilinear shapes with strongly enriched LREE segments in chondrite-normalized diagrams (Fig. 5), broadly similar to modern authigenic pelagic sediments (Taylor and McLennan, 1985). The Atlantic Cretaceous pelagic sediment pattern overlaps Pacific average authigenic sediment (Ben Othman et al., 1989) and is similar to Atlantic authigenic pelagic sediment (White et al., 1985; White and Dupré, 1986; Davidson, 1987), while Caribbean Cretaceous pelagic sediment more closely resembles south Pacific sediment.

ANALYTICAL DATA AND GEOCHEMICAL PARAMETERS

Major element Inductively-Coupled Plasma-Emission Spectrometry (ICP-ES) and trace element Inductively Coupled Plasma-Mass Spectrometry (ICP-MS) analyses reported here were performed at Acme Analytical Laboratories, Vancouver, Canada. Duplicate analyses reveal precision is within 1 to 5% of the amount present for most trace elements. Isotopic analyses were carried out by Alan P. Dickin (Jolly et al., 2007, 2008b). Samples analyzed for isotopes were leached overnight in warm diluted HCl to minimize effects of low-temperature alteration. Analytical techniques and precision limits are summarized elsewhere (Jolly et al., 1998a).

Mineralogical modes adopted for use in calculations discussed subsequently, representing a spinel lherzolite N-MORB source (fertile MORB mantle) of Pearce and Parkinson (1993), include 57.5% olivine (ol), 27.0% orthopyroxene (opx), 12.5% clinopyroxene (cpx), and 2.0% spinel. It is inferred that phases disappear from the source at constant rates during melting, and that orthopyroxene melts incongruently to olivine during early stages of fusion. Rates of phase disappearance adopted include clinopiroxene, 25% (McKenzie and O'Nions, 1991); ortopiroxene, 40% Al-spinel, 80% (Pearce and Parkinson, 1993). Mineral modes of residua from melting of spinel lherzolite are similar to ranges discussed by Pearce and Parkinson (1993). The trace element composition of fertile MORB mantle and mineral/melt trace element partition coefficients (D-values) for mantle melts are adopted from Bédard (1999). Mineral/melt partition coefficients for fractional crystallization of basalts are from Jenner et al. (1991).

PETROGENESIS OF ISLAND ARC MAGMAS, WESTERN PUERTO RICO

Major element distribution

Overlying the pre-arc basement complex of western Puerto Rico is a thick sequence of island arc rocks that decrease in age from Santonian in the southwest to mid-Eocene (~85 to 45Ma) in the northeast. The entire island arc sequence of western Puerto Rico displays a wide range of major element compositions broadly similar to global series from island arc settings, ranging from mafic basalts with low SiO_2 (<46%) to siliceous rhyolites with over 72% SiO_2, reflecting subvolcanic fractional crystallization of parental magmas (Fig. 6). The earliest of these units, and which are discussed in this report, include the prominent Boquerón (Santonian), Lajas (Santonian), and Río Loco (Early Campanian) formations (Electronic Appendix Table X). Individual units within this broad western Puerto Rico sequence have more limited compositional ranges, such that Río Loco lavas and associated rocks (Slodowski, 1956; Mattson, 1960; Krushensky and Monroe, 1978; Volckmann, 1984c) have between 6 and 13% MgO, compared to much lower values in the Boquerón-Lajas suite ranging from less than 1 to almost 5% (Fig. 6A). Silica content of Río Loco lavas, however, stands out distinctly from other members of the western Puerto Rico arc assemblage. Although MgO concentrations for most of the rocks have a normal range for basaltic mantle melts, Río Loco samples have anomalous, elevated andesitic SiO_2, ranging from 55 to over 60% (Fig. 6A), and have been recognized as being high-Mg andesites (Jolly et al., 2007). These compositions are sufficient to

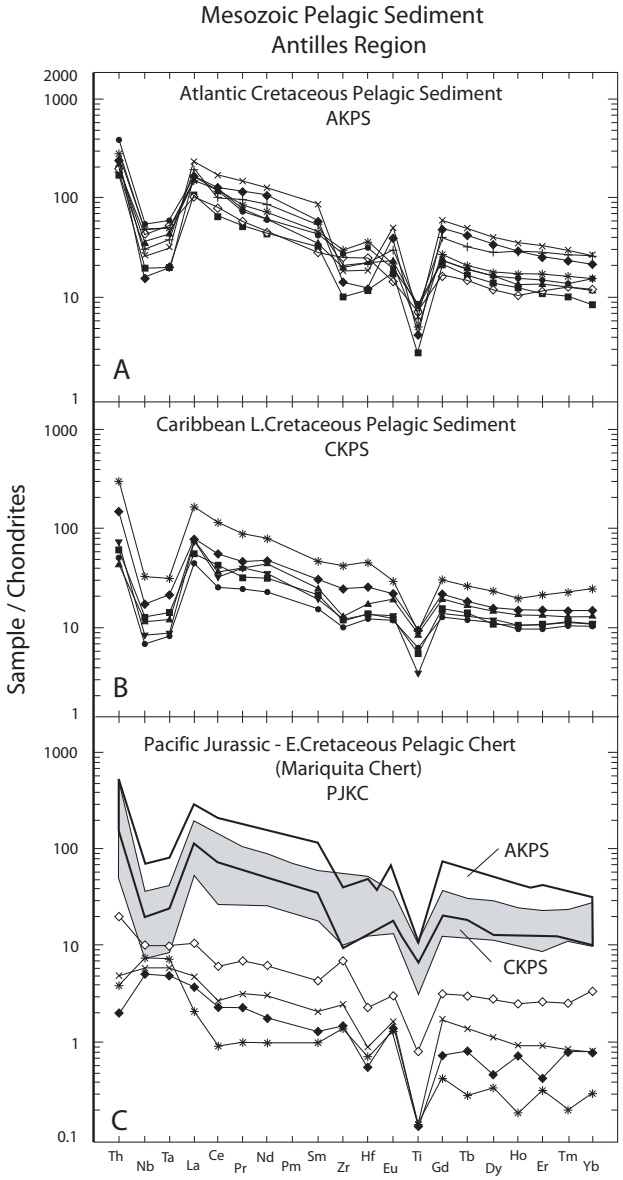

FIGURE 5 | **Chondrite-normalized incompatible element patterns of Mesozoic pelagic sediments, Antilles region. A) Atlantic Cretaceous pelagic sediment (AKPS); B) Caribbean Cretaceous pelagic sediment (CKPS); C) Pacific Jurassic-Cretaecous pelagic chert (PJKC).**

trigger a characteristic two-pyroxene-bearing, bronzite (opx) + ferroaugite (cpx) phenocryst assemblage for the Río Loco. Compositional differences reveal a consistent 19% SiO_2 surplus in average Río Loco lava (57.4% SiO_2) relative to typical mantle basalts of similar MgO content. Conversely, other major elements (including Al_2O_3, CaO, Fe_2O_3t, and TiO_2), are systematically depleted by approximately 30% (29, 30, 31, and 29%, respectively; Fig. 6B-E).

Consistent geochemical variations preclude silica enrichment through shallow crustal contamination. Instead, the observed distribution is consistent with north-dipping subduction of a ~300m thick section of Jurassic and Early Cretaceous pelagic chert (Mariquita Chert, SiO_2=86 to ~100%, Electronic Appendix Table VIII)) together with a significant complement of Late Cretaceous clay and calcareous limestones (Caribbean Cretaceous pelagic sediment) of mantle wedge source. Compositional contrasts are inferred to arise from phase transformations produced in the mantle by equilibration with an influx of siliceous melt (*i.e.*, forsterite + quartz = 2enstatite). This process enhances modal orthopyroxene in the source at the expense of olivine (ol), and dramatically alters melting patterns, leading to silica-enrichment of both melts and residua.

Except for the Río Loco Lava itself, a series of small, presumably correlative two-pyroxene basalt stocks reported by Mattson (1960) in Sierra Bermeja, and a few isolated outcrops, ranging in age from Campanian to Eocene, reported by Krushensky and Monroe (1978) from elsewhere in the volcanic sequence, silica enriched mafic compositions are rare in western Puerto Rico. Their scarcity implies special circumstances were required to incorporate subducted chert into mantle melts, as might be expected in view of extremely elevated melting points of relatively pure silica, even when wet (>1700°C, $P_{total}=P_{H2O}$). It is inferred that the high buoyancy of Mariquita chert, compared with more mafic compositions, promoted turbulent flow in the mantle wedge during initial stages of subduction, leading to isolation and fragmentation of quartz-rich mantle domains. This issue is discussed in more detail elsewhere (Jolly et al., 2007).

Multiple component mixing models

Dominance of N-MORB-type tholeiites in the western Puerto Rico pre-arc basement overlain by geochemically enriched island arc strata indicates the mantle wedge was originally comprised of fertile MORB mantle-type material, or more probably of residue from a fertile MORB mantle-type source during plate formation. Consistent with this idea, Jolly et al. (2007) proposed the development of a north-dipping island arc whose source magmas in

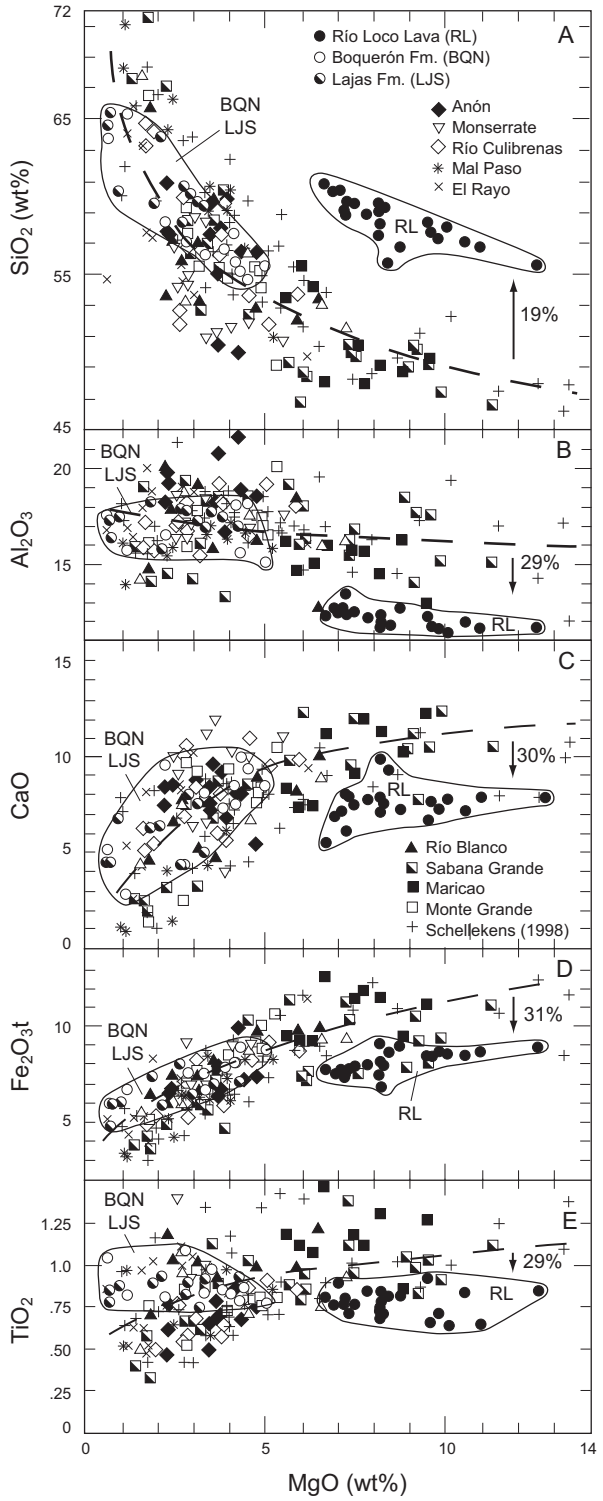

FIGURE 6 | **Major element distribution in Western Puerto Rico island arc basalt. Covariation of MgO (weight percent) and other major elements in Western Puerto Rico lavas: A) SiO_2, B) Al_2O_3, C) CaO, D) total Fe as Fe_2O_3t, and E) TiO_2. Main trends are indicated by dashed curves; fields of earliest units include Río Loco Lava (RL), and Boquerón-Lajas Fms (BQN-LJS) and are outlined. With respect to MgO, SiO_2 is enriched by 19%, while other major oxides are consistently depleted by approximately 30% in Río Loco lavas (high-Mg of Jolly et al., 2007). Deviations are consistent with incorporation of subducted Mariquita Chert (Appendix Table 8) rather than crustal assimilation. For stratigraphic succession of volcanic units see Jolly et al. (1998b, 2007).**

the mantle wedge incorporated an Atlantic Cretaceous pelagic sediment component. However, concentrations of distinctly incompatible elements (such as the LREE La, Fig. 7) in early IAB more closely correspond to Caribbean Cretaceous pelagic sediment than to Atlantic Cretaceous pelagic sediment, suggesting that the latter played only an insignificant role as a subduction component in western Puerto Rico. Moreover, incompatible element ratios of early island arc strata, including La/Nb vs Nb/Zr (Fig. 8) and Sm/Yb vs Zr/Sm (Fig. 9) are mainly intermediate between OIB and Caribbean pelagic sediments, indicating an enriched mantle source composition modified by a Caribbean Cretaceous pelagic sediment component. Geochemical trends thus favor incorporation of Caribbean Cretaceous pelagic sediment, which has lower, more appropriate trace element concentrations. Hence, geochemical relations support a tectonic model involving north-dipping subduction of the Caribbean basin involving a Caribbean Cretaceous pelagic sediment component, and establishment of a younger western Puerto Rico arc within the broad back-arc region of the older south-dipping central Puerto Rico arc.

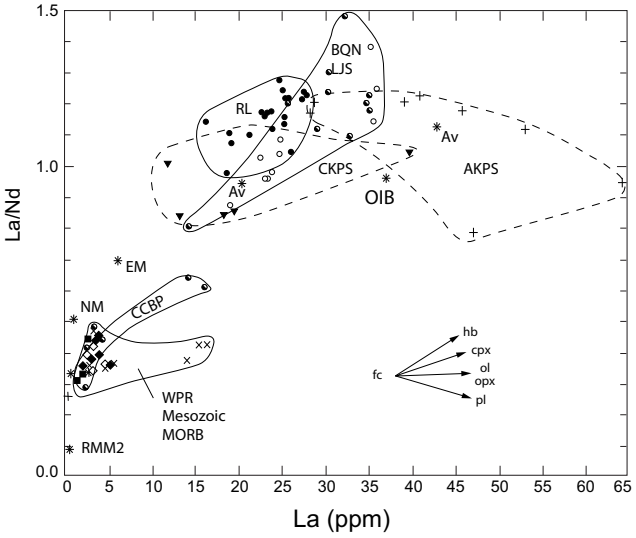

FIGURE 7 | **Trace element ratios in Western Puerto Rico (WPR). La and La/Nd. Distribution of LREE is controlled by fractional crystallization, which produces slight rightward deflection of fields, and by contaminating pelagic sediment.**

In support of this tectonic scenario is a detailed evaluation of several multiple component-mixing models that utilize OIB and Caribbean Cretaceous pelagic sediment as end members. Mineralogical modes (discussed previously) of lithospheric back-arc material are potentially highly variable due to a combination of depletion by high-degree decompression melting during plate formation and enrichment by introduction of low-degree silicate melts generated by pressure release melting as mantle material is drawn up into the melting zone (Arculus and Powell, 1986; McCulloch and Gamble, 1991). Simplified multiple component melting models are constructed from four basic modal compositions, representing variably depleted variants of a fertile MORB mantle-type spinel peridotite source, including RMM2, RMM10, RMM15, and RMM20 (Fig. 8, 9) where RMM2 represents, for example, residual MORB mantle depleted by 2% melt extraction. From each of these basic sources a further series of incompatible element-enriched starting compositions is calculated by combining various proportions (0.05, 0.02, 0.06, 0.10) of OIB (mixes denoted RMM2OIB10; RMM2OIB6 (Fig. 8, 9)). To simplify models further, calculations neglect changes in modal source composition due to addition of chert or of low-degree melt, the latter of which potentially reverses modal depletion from earlier melting events (Boudinier et al., 1988). Degree of melting in enriched sources is difficult to estimate, because Yb concentrations in depleted sources is elevated by minute proportions of OIB. To provide results comparable with central Puerto Rico and northeast Puerto Rico (Jolly et al., 2008a), melting factors are maintained at f=0.25 in figures 8 and 9; models involving other reasonable melting parameters produce similar results.

Compositions of sources derived from a given residual MORB mantle (RMM) source are distributed along the mantle line proportionally between fertile MORB mantle and OIB, such that systematic variations provide limits on mantle compositions and sediment proportions involved in production of western Puerto Rico IAB. Spacing between various source combinations depends not only on proportions of OIB added, but also on, at least, two further factors, including degree of incompatibility of a given element (Nb, for instance, is more depleted in residual sources than Zr and therefore is more sensitive to addition of small proportions of OIB), and to the degree of depletion of the starting composition (smaller proportions of sediment are required to change RMM15 or RMM20 compared with RMM2 or RMM10, for example). Lengths of melting vectors depend not only on proportion of appropriate sediment added to a mix, but also on proximity of the pelagic sediment field to the mantle trend. In La/Nb-Nb/Zr plots, lengths of vectors produced are inversely proportional to OIB, such that the addition of 10% Caribbean Cretaceous pelagic sediment to RMM2OIB2 produces a mixing line four times longer than an identical sediment proportion produces in RMM2OIB10 (Fig. 8). In Sm/Yb plots (Fig. 9) minimum vector lengths are produced by moderate proportions of OIB.

Due to the excessive number of variables involved in melting models, including degree of source depletion and proportions of both OIB and Caribbean Cretaceous pelagic sediment, estimates of sediment proportions in western Puerto Rico IAB are poorly constrained. However, analysis of melting trends for combinations of key elemental ratios provides considerable insight into the degree of source

depletion and proportions of OIB-type component. Results for highly incompatible trace elements (La/Nb-Nb/Zr, Fig. 8), for example, reveal melting vectors from RMM2 sources with appropriate Nb/Zr (~0.15) are not long enough to track across western Puerto Rico IAB fields (Fig. 8A), while all melts from sources >RMM10 have suitable OIB-like Nb/Zr (Fig. 8B-D). Other constraints are provided by moderately incompatible elements (Sm/Yb-Zr/Sm, Fig. 9),

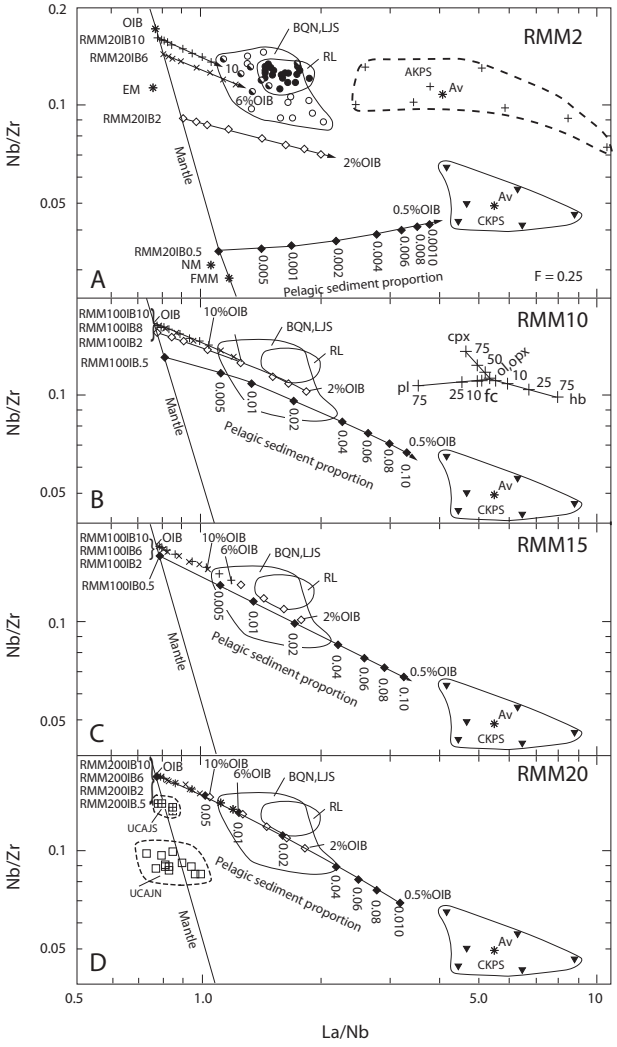

FIGURE 8 | **Multiple component melting models for La/Nb—Nb/Zr reveal extremely depleted mantle sources enriched by small proportions of both OIB-like and pelagic sediment components are required to produce WPR IAB. A) Calculated spinel peridotite sources (RMM20IB0.5, RMM20IB2, RMM20IB6, RMM20IB10), composed of RMM2 combined with various proportions of OIB (0.5, 2, 6, 10%), are aligned along the mantle trend. Fusion (f=0.25) of these sources mixed with various proportions (0.005, 0.01, 0.02, 0.04, 0.06, 0.08, 0.10) of CKPS produces melting vectors of variable lengths, depleted sources giving rise to longer vectors than enriched ones. Vectors from sources with 6 and 10% OIB have appropriate Nb/Zr to track across WPR lava fields, but these vectors indicate unlikely sediment proportions (>>10%). B) As in A, RMM10 starting source composition. C) RMM15-type starting composition. D) RMM20-type starting composition. B-D reveal sources more depleted than RMMN10 and with less than 2% OIB are required to produce melting vectors tracking across the Western Puerto Rico IAB field.**

which reveal only depleted sources (RMM15 to RMM20) with small OIB-type components (~2%) have sufficiently high Sm/Yb to produce melting vectors that intersect western Puerto Rico IAB fields.

Isotope geochemistry and isotope mixing model

Sr, Nd, and Pb isotope ratios of pre-arc and early island arc lavas of western Puerto Rico are summarized in Appendix Tables 4 and 6. Initial Sr-isotope ratios of the pre-arc basement units (Las Palmas amphibolite, Lower Cajul Formation, and Upper Cajul Formation), in particular, are displaced toward higher radiogenic compositions relative to the mantle array of Figure 10. Furthermore, ε_{Nd} values are more enriched in the Upper Cajul rocks than in the Las Palmas and Lower Cajul units. The two early island arc units (Boquerón and Río Loco) display behavior similar to the Upper Cajul in showing modest enrichment in both (i)$^{87}Sr/^{86}Sr$ and ε_{Nd}. The scatter displayed in these Sr and Nd isotope ratios are probably real and give a fairly realistic picture of the genesis of these western Puerto Rico lavas and their complex origin which, as previously discussed, are apparently dominated by a Caribbean Cretaceous pelagic sediment component, sediment component, (shown in Figure 10 and sediment isotope data summarized in Electronic Appendix Table IX). These Caribbean sediments are enriched in (i)$^{87}Sr/^{86}Sr$ and ε_{Nd}, as well as in $^{207}Pb/^{204}Pb$ and $^{208}Pb/^{204}Pb$ relative to the pre-arc and island-arc strata of western Puerto Rico, but to a much lesser extent than are Atlantic Cretaceous pelagic sediments (compare Electronic Appendix Table IX and Jolly et al., 2006, 2007). Sub-parallel fields between the Boquerón basalt and the Caribbean Cretaceous pelagic sediment suggest a possible mixing relationship. Accordingly, an isotope mixing line (Langmuir et al., 1978) has been calculated between the least radiogenic early arc Boquerón lava and the most radiogenic Caribbean Cretaceous pelagic sediment sample (Fig. 10). These results are consistent with the previously discussed trace element mixing data that Caribbean Cretaceous pelagic sediment is a likely sediment contaminant of the early arc lavas. Of course, these Sr and Nd isotope variations do not prove that the early arc lavas are solely the result of Caribbean Cretaceous pelagic sediment contamination, as some compositional input of an enriched mantle source (OIB component) may be involved, along with a possible Sr isotope spike from slab-derived fluids that displaced the Sr isotope ratios to higher values. Notably, however, these data stand in strong contrast to central Puerto Rico data correlations (Jolly et al., 2007) that show a strong trend toward Atlantic Cretaceous pelagic sediment.

TECTONIC IMPLICATIONS

Arc basalts in central Puerto Rico and northeast Puerto Rico (Jolly et al., 2006, 2008a) have prominent incompatible

trace element features resembling the signature of pelagic sediments, including 1) variably fractionated chondrite-normalized distribution patterns with elevated LREE and Th abundances, 2) flat HREE segments compared with low HREE compared with N-MORB, and 3) MORB-like HFSE (high field strength elements) abundances with deep negative Nb-Ta and Ti anomalies. Consequently, members of the central Puerto Rico and northeast Puerto Rico suites have trace element abundances intermediate between MORB and Atlantic Cretaceous pelagic sediment. Normalized patterns, for most elements, are reproduced by models involving fusion (f=0.25) of an RMM2-type spinel peridotite source contaminated with various proportions of Atlantic Cretaceous pelagic sediment. Lower trace element concentrations make Caribbean Cretaceous pelagic sediment less attractive as a potential contaminant for central Puerto Rico and northeast Puerto Rico, because excessive proportions (>>10%) are required. Hence, available data are consistent with the incorporation of a sediment component through south-dipping subduction of the North Atlantic basin.

Anomalously high Sm/Yb and Zr/Sm and low La/Sm in central Puerto Rico basalts reflect the presence of a distinct, low-Zr/Sm slab-derived basaltic component in addition to Atlantic Cretaceous pelagic sediment. Candidates include low-degree basalt melt generated from a wide variety of potential sources within the subducted oceanic crust, such as partly eclogized hornblende gabbro of accumulate (low-Zr/Sm) origin. The question of how amphibolite-bearing material is preserved to sufficient depths within the subducted slab to reach melting temperatures is the subject of considerable debate (Defant and Drummond, 1990; Defant et al., 1991; Elthon, 1991; Drummond et al., 1996; Bédard, 1999). Presumably in central Puerto Rico, coarse-grained, low-melting gabbroic accumulates within the descending oceanic slab retained adequate hornblende to promote fusion at some stage of subduction. Sediment: slab melt ratios tended to rise throughout volcanism, from 1:2 in early volcanic phases I and II, to between 1:1 and 1:0 in phases III and IV. Trends are consistent with progressively decreasing temperatures in the slab, as outlined in the models of Peacock (Peacock, 1993; Peacock et al., 1994), and with a concurrent decrease in slab melt proportion. The decline in basaltic slab melt was accompanied by increasing sediment proportions, from moderate levels between 0.5-2% during phases I and II to extremely elevated concentrations exceeding 5% during phases III and IV. Consequently, proportions of basaltic slab melt and Atlantic Cretaceous pelagic sediment are roughly inversely proportional. Unusually high sediment proportions in later volcanic phases compared with modern arc systems are inferred to arise from subduction of a progressively thickening sediment pile. Introduction of a significant OIB-type component into the central Puerto Rico mantle wedge source at any stage is precluded by the high magnitude of negative Nb-anomalies.

In marked contrast with central Puerto Rico, trace element abundances in western Puerto Rico IAB more closely resemble OIB than N-MORB. Significantly, Atlantic Cretaceous pelagic sediment is excluded as a possible component in western Puerto Rico by elevated abundances of many more incompatible elements, which exceed concentrations in OIB. Instead, the rocks have trace element ratios intermediate between Caribbean Cretaceous pelagic sediment and OIB, consistent with north-dipping subduction of the Caribbean Basin. Accordingly, although sediment proportions are poorly constrained due to an

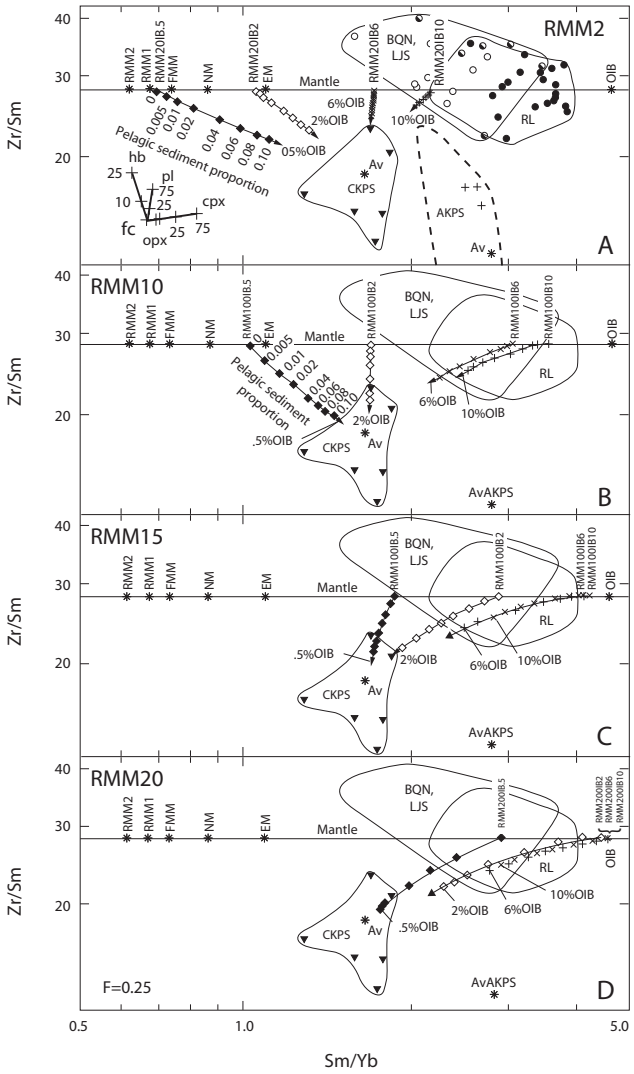

FIGURE 9 | **Multiple component melting models for Sm/Yb-Zr/Sm further constrain suitable source compositions in Western Puerto Rico. Suitable melting vectors tracking across WPR lava fields (<5% CKPS) are produced only by highly depleted sources (RMM15 TO RMM20) mixed with small proportions of IOB (0.5 to 2%) as in Figure 8; symbols and parameters as in Figure 8.**

excessive number of variables, multiple component melting models (f=0.25) generate suitable melting vectors that track across the western Puerto Rico IAB fields on variation diagrams (Fig. 8, 9). The most appropriate models involve fusion of highly depleted spinel peridotite (RMM15 to RMM20), lightly overprinted by addition of a small OIB-type component (up to 2%), and mixed with various proportions of Caribbean Cretaceous pelagic sediment. The occurrence of anomalous, SiO_2-enriched, two-pyroxene-bearing basalt in the western Puerto Rico assemblage, apparently generated by incorporation of subducted Jurassic Mariquita Chert of Pacific (Farallon) origin, is also consistent with tectonic models involving north-dipping subduction.

The geographic position of the second, north-dipping western Puerto Rico subduction zone within the broad back-arc region of the original south-dipping Antillean arc system leads naturally to the conclusion that enrichment of the western Puerto Rico mantle source occurred through variable veining of lithosphere by low-degree, decompression melts associated with back-arc counter-flow in the older arc. Accordingly, it is inferred that small proportions of OIB-like, low-degree basalt melt were added to back-arc lithospheric mantle peridotite that had already been strongly depleted during original plate formation. The overprinted lithosphere, representing a back-arc upper mantle enrichment zone, was subsequently sampled by the younger (~85Ma) western Puerto Rico arc.

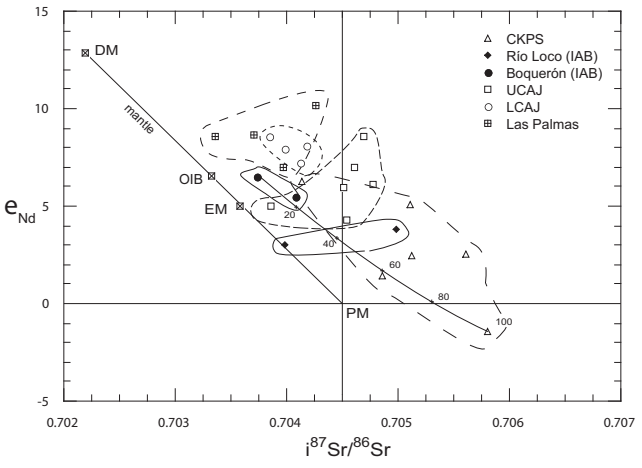

FIGURE 10 | **Sr- and Nd-isotope ratios of pre-arc basement and early island arc lavas of WPR. Representative mantle array from Hart (1988) and Rollinson (1993). Pre-arc basement complex includes MORB tholeiites from the Jurassic Lower Cajul Formation (LCAJ), related Las Palmas amphibolite, and plateau basalts from the Upper Cajul Formation (UCAJ); early island arc lavas are from the Boquerón and Río Loco formations; CKPS represents Caribbean Cretaceous pelagic sediments.**

CONCLUSIONS

In this paper we present an overview of the pre-arc basement complex of southwestern Puerto Rico, summarize the geological and geochemical characteristics of the basement complex, and discuss the geochemical and tectonic evolution of the early island arc basaltic rocks in western Puerto Rico that overlie the pre-arc complex, utilizing major element, trace element, and Sr, Nd, and Pb isotope ratio data. The incompatible element distribution and multiple component fractional mixing models presented here, based on fusion of modified fertile MORB mantle-type mantle sources, are consistent with the following conclusions:

Incompatible trace element abundances of island arc strata in western Puerto Rico (~85 to 45Ma) are intermediate between OIB and pelagic sediments, indicating the rocks were derived from a highly enriched mantle source with OIB-like compositions.

Enriched incompatible element abundances in western Puerto Rico IAB, equal to or higher than OIB, preclude Atlantic Cretaceous pelagic sediment as a possible component, but are consistent with the incorporation of Caribbean Cretaceous pelagic sediment, and with north-dipping subduction of the Caribbean Basin. Elevated SiO_2, which triggered a two-pyroxene phenocryst mineralogy in certain early western Puerto Rico arc lavas, is consistent with incorporation of subducted chert, represented in the western Puerto Rico basement by Mariquita Chert of Jurassic Pacific (Farallon) provenance.

Multiple component mixing models reveal that shallow negative Nb- and slighty positive Zr-Hf-normalized anomalies and elevated Nb/Zr in western Puerto Rico IAB reflect the presence, in addition to Caribbean Cretaceous pelagic sediment, of a small OIB-type source component (up to ~2%) superimposed on a highly depleted (RMM15 to RMM20) mantle residuum.

The western Puerto Rico arc system (dating from ~85Ma) developed within and sampled lithospheric material from the back-arc upper mantle enrichment zone associated with the older, south-dipping central Puerto Rico arc (from ~125Ma).

The data on which this paper is based is presented in an online appendix (Tables 1-10) that includes both the pre-arc basement complex and the overlying early island arc sequence.

ACKNOWLEDGMENTS

The authors acknowledge with gratitude the constructive reviews of John F. Lewis and J. A. Proenza whose comments and suggestions greatly improved the manuscript.

REFERENCES

Arculus, R.J., Powell, R., 1986. Source component mixing in the regions of arc magma generation. Journal of Geophysical Research, 91, 5913-5926.

Bédard, J.H., 1999. Petrogenesis of boninites from the Betts Cove Ophiolite, Newfoundland, Canada: Identification of subducted source components. Journal of Petrology, 40, 1853-1889.

Ben Othman, D., White, W.M., Patchett, J., 1989. The geochemistry of marine sediments, island arc magma genesis, and crust-mantle recycling. Earth and Planetary Science Letters, 94, 1-21.

Boudinier, J.L., Dupuy, C., Dostal, J., 1988. Geochemistry and petrogenesis of eastern Pyrenean peridotites. Geochimica et Cosmochimica Acta, 52, 2893-2907.

Curet, A.F., 1986. Geologic map of the Mayagüez and Rosario quadrangles. Puerto Rico. U.S. Geological Survey Miscellaneous Investigations Map, I-1657, scale 1:20,000.

Davidson, J.P., 1987. Crustal contamination *versus* subduction zone enrichment: Examples from the Lesser Antilles and implications for mantle source compositions of island arc volcanic rocks. Geochimica et Cosmochimica Acta, 51, 2185-2198.

Defant, M.J., Drummond, M.S., 1990. Derivation of some modern arc magmas by melting of young subducted lithosphere. Nature, 347, 662-665.

Defant, M.J., Richardson, P.M., De Boer, J.Z., Stewart, R.H., Maury, R.C., Bellon, H., Drummond, M.S., Feigenson, M.D., Jackson, T.E., 1991. Dacite genesis via both slab melting and differentiation: Petrogenesis of La Yeguada volcanic complex, Panama. Journal of Petrology, 32, 1101-1142.

Donnelly, T.W., 1989. Geologic history of the Caribbean and Central America. In: Bally, A.W., Palmer, A.R. (eds.). The Geology of North America-An overview. Boulder (Colorado), Geological Society of America, A, 299-321.

Donnelly, T.W., 1994. The Caribbean Cretaceous basalt association: A vast igneous province that includes the Nicoya complex of Costa Rica. In: Seyfried, H., Hellman, W. (eds.). Geology of an Evolving Island Arc: The Isthmus of Southern Nicaragua, Costa Rica, and Western Panama: Stuttgart, Germany, Profile (Band 7). Institut für Geologie und Palaontologie, 17-45.

Dosso, L., Bougault, H., Joron, J.-L., 1993. Geochemical morphology of the north mid-Atlantic Ridge, 10-24°: Trace element-isotope complementarity. Earth and Planetary Science Letters, 120, 443-462.

Draper, G., 1986. Blueschists and associated rocks in eastern Jamaica and their significance for Cretaceous plate-margin development in the northern Caribbean. Geological Society of America Bulletin, 97, 48-60.

Drummond, M.S., Defant, M.J., Kepezhinski, P.K., 1996. Petrogenesis of slab-derived trondhjemite-tonalite-dacite/adakite magmas. Transactions of the Royal Society of Edinburgh, 87, 205-215.

Elthon, D., 1991. Geochemical evidence for formation of the Bay of Islands ophiolite above a subduction zone. Nature, 354, 140-143.

García-Casco, A., Torres-Roldán, R., Millán, G., Iturralde-Vinent, M.A., Núñez Cambra, K., Lázaro Calisalvo, C., Rodríguez Vega, A., 2006. High-pressure metamorphism of ophiolites in Cuba. Geologica Acta, 4(1-2), 63-88.

Glover, L. III, 1971. Geology of the Coamo area, Puerto Rico, and its relation to the volcanic arc-trench association. U.S. Geological Survey Professional Paper, 636, Washington, D. C., 102pp.

Hart, S.R., 1988. Heterogeneous mantle domains: signatures, genesis and mixing chronologies. Earth and Planetary Science Letters, 90, 273-296.

Hauff, F., Hoernle, K., Schminke, H.-U., Werner, R., 1997. A Mid Cretaceous origin for the Galapagos hotspot: Volcanological, petrological and geochemical evidence from Costa Rican oceanic crustal segments. Geologische Rundschau, 86, 141-155.

Hauff, F., Hoernle, K., Tilton, G., Graham, D.W., Kerr, A.C., 2000. Large volume recycling of oceanic lithosphere over short time scales: geochemical constraints from the Caribbean Large Igneous Province. Earth and Planetary Science Letters, 174, 247-263.

Iturralde-Vinent, M.A., 1998. Synopsis of the geological constitution of Cuba. Acta Geologica Hispanica, 33, 9-56.

Jahn, B., Bernard-Griffiths, J., Charlot, R., Cornichet, J., Vidal, F., 1980. Nd and Sr isotopic composition and REE abundances of Cretaceous MORB (holes 417D and 418A, legs 51, 52, and 53). Earth and Planetary Science Letters, 48, 171-184.

Jansma, P., Mattioli, G., López, A., DeMets, C., Dixon, T., Mann, P., Calais, E., 2000. Neotectonics of Puerto Rico and the Virgin Islands, northeastern Caribbean, from GPS geodesy. Tectonics, 19, 1021-1037.

Jenner, G.A., Dunning, G.R., Malpas, J., Brown, M., Bruce, T., 1991. Bay of Islands and Little Port complex, revisited: age, geochemical and isotope evidence confirm suprasubduction zone origin. Canadian Journal of Earth Sciences, 28, 1635-1652.

Jolly, W.T., Lidiak, E.G., Dickin, A.P., 2006. Cretaceous to Mid-Eocene pelagic sediment budget in Puerto Rico and the Virgin Islands (northeast Antilles island arc). Geologica Acta, 4(1-2), 35-62.

Jolly, W.T., Lidiak, E.G., Dickin, A.P., 2008a. Bimodal volcanism in northeast Puerto Rico and the Virgin Islands (Greater Antilles Island Arc): Genetic links with Cretaceous subduction of the mid-Atlantic ridge Caribbean spur. Lithos, 103, 393-414.

Jolly, W.T., Lidiak, E.G., Dickin, A.P., 2008b. The case for persistent southwest-dipping Cretaceous convergence in the northeast Antilles: Geochemistry, melting models, and tectonic implications. Geological Society of America Bulletin, 120, 1036-1052.

Jolly, W.T., Lidiak, E.G., Dickin, A.P., Wu, T.-W., 1998a. Geochemical diversity of Mesozoic island arc tectonic blocks in eastern Puerto Rico. In: Lidiak, E.G., Larue, D.K. (eds.). Tectonics and Geochemistry of the Northeastern Caribbean. Boulder (Colorado), Geological Society of America, 322 (Special Paper), 67-98.

Jolly, W.T., Lidiak, E.G., Schellekens, J.H., Santos, H., 1998b. Volcanism, tectonics, and stratigraphic correlations in Puerto Rico. In: Lidiak, E.G., Larue, D.K. (eds.). Tectonics and Geochemistry of the Northeastern Caribbean. Boulder (Colorado), Geological Society of America, 322 (Special Paper), 1-34.

Jolly, W.T., Schellekens, J.H., Dickin, A.P., 2007. High-Mg andesites and related lavas from southwest Puerto Rico (Greater Antilles Island Arc): Petrogenetic links with emplacement of the Late Cretaceous Caribbean mantle plume. Lithos, 98, 1-26.

Kerr, A.C., Tarney, J., 2005. Tectonic evolution of the Caribbean and northwestern South America: The case for accretion of two Late Cretaceous oceanic plateaus. Geology, 33, 269-272.

Kerr, A.C., Tarney, J., Kempton, P., Spadea, P., Nivia, A., Marriner, G., Duncan, R., 2002. Pervasive mantle plume head heterogeneity: Evidence from the late Cretaceous Caribbean-Colombian oceanic plateau. Journal of Geophysical Research, 107, ECV 2-1.

Krushensky, R.D., Monroe, W.H., 1978. Geologic map of the Yauco and Punta Verraco quadrangles. Puerto Rico. U.S. Geological Survey Miscellaneous Investigations Map, I-1147, scale 1:20,000.

Langmuir, C.H., Vocke, R.D.Jr., Hanson, G.N., Hart, S.R., 1978. A general mixing equation with applications to Icelandic basalts. Earth and Planetary Science Letters, 37, 380-392.

Lapierre, H., Dupuis, V., Mercier de Lepinay, B., Bosch, D., Monie, P., Tardy, M., Maury, R.C., Hernandez, J., Polve, M., Yeghicheyan, D., Cotten, J., 1999. Late Jurassic oceanic crust and Upper Cretaceous Caribbean plateau picritic basalts exposed in the Duarte Igneous Complex, Hispaniola. Journal of Geology, 107, 193-207.

Lewis, J.F., Draper, G., 1990. Geology and tectonic evolution of the northern Caribbean margin. In: Dengo, G., Case, J.E. (eds.). The Caribbean region. Boulder (Colorado), Geological Society of America, H, 77-140.

Lewis, J.F., Escuder-Viruete, J.E., Hernaiz Huerta, P.P., Gutierrez, G., Draper, G., Pérez-Estaún, A., 2002. Subdivisión geoquímica del arco isla Circum-caribeno, Cordillera Central Dominicana: Implicaciones para la formación, acreción y crecimiento cortical en un ambiente interoceánico. Acta Geológica Hispanica, 37, 81-122.

Llerandi-Roman, P.A., 2004. Geologic and Tectonic History of the Western Section of the Sabana grande Quadrangle. M.S. Thesis. Mayagüez (Puerto Rico), University of Puerto Rico, 134pp.

Llinas, R., 1972. Geologia del area Polo Duverge, Cuenca de Enriquillo. Codia, Publicación del Colegio Dominicano de Ingenieros, Arquitectos y Agrimensores, part 1(31), 55-65.

Mann, P., Draper, G., Lewis, J.F., 1991. An overview of the geologic and tectonic development of Hispaniola. In: Mann, P., Draper, G., Lewis, J.F. (ed.). Geologic and tectonic development of the North American-Caribbean plate boundary in Hispaniola. Boulder (Colorado), Geological Society of America, 262 (Special Paper), 1-28.

Marchesi, C., Garrido, C., Bosch, D., Proenza, J., Gervilla, F., Monie, P., Rodríguez-Vega, R., 2007. Geochemistry of Cretaceous magmatism in eastern Cuba: Recycling of North American continental sediments and implications for subduction polarity in the Greater Antilles paleo-arc. Journal of Petrology, 48, 1813-1840.

Martínez-Colon, M., 2003. Geologic and Tectonic History of the Eastern Section of the Sabana Grande Quadrangle. M.S. Thesis. Mayagüez (Puerto Rico), University of Puerto Rico, 104pp.

Mattson, P.H., 1960. Geology of the Mayagüez area, Puerto Rico. Geological Society of America Bulletin, 71, 319-362.

Mattson, P.H., 1979. Subduction, buoyant braking, flipping and strike-slip faulting in the northern Caribbean. Journal of Geology, 87, 293-304.

Mauffret, A., Leroy, S., 1997. Seismic stratigraphy and structure of the Caribbean igneous province. Tectonophysics, 283, 61-104.

McCulloch, M.T., Gamble, J.A., 1991. Geochemical and geodynamical constraints on subduction zone magmatism. Earth and Planetary Science Letters, 102, 358-374.

McIntyre, D.H., 1975. Geologic map of the Maricao quadrangle, western Puerto Rico. U.S. Geological Survey Miscellaneous Investigations Map, I-918, scale 1:20,000.

McKenzie, D., O'Nions, R.K., 1991. Partial melt distributions from inversion of rare earth element concentrations. Journal of Petrology, 32, 1021-1091.

Mitchell, S.F., 2006. Timing and implications of Late Cretaceous tectonic and sedimentary events in Jamaica. Geologica Acta, 4(1-2), 171-178.

Montgomery, H., Pessagno, E.A.Jr., Lewis, J.F., Schellekens, J.H., 1994a. Paleogeography of Jurassic fragments in the Caribbean. Tectonics, 13, 725-732.

Montgomery, H., Pessagno, E.A.Jr., Pindell, J.L., 1994b. A 195Ma terrane in a 165Ma sea: Pacific origin of the Caribbean plate. GSA Today, 4, 1-6.

Peacock, S., 1993. Large-scale hydration of the lithosphere above subducting slabs. Chemical Geology, 108, 49-59.

Peacock, S.M., Rushmer, T., Thompson, A.B., 1994. Partial melting of subducting oceanic crust. Earth and Planetary Science Letters, 121, 227-244.

Pearce, J.A., Kempton, P.D., Nowell, G.M., Noble, S.R., 1999. Hf-Nd element and isotope perspective on the nature and provenance of mantle and subduction components in western Pacific arc-basin systems. Journal of Petrology, 40, 1579-1611.

Pearce, J.A., Parkinson, I.J., 1993, Trace element models for mantle melting: Application to volcanic arc petrogenesis. Geological Society of London, 76 (Special Paper), 76, 373-403.

Pindell, J.L., Barrett, S.F., 1990. Geological evolution of the Caribbean region: a plate tectonic perspective. In: Dengo, G., Case, J.E. (eds.). The Caribbean Region. Boulder (Colorado), Geological Society of America, The Geology of North America, H, 405-432.

Pindell, J.L., Cande, S.C., Pitman, W.C.III, Rowley, D.B., Dewey, J.F., La Brecque, J., Haxby, W., 1988. A plate-

kinematic framework for models of Caribbean evolution. Tectonophysics, 155, 121-138.

Plank, T., Langmuir, C.H., 1998. The chemical composition of subducting sediment and its consequences for the crust and mantle. Chemical Geology, 145, 325-394.

Proenza, J.A., Díaz-Martínez, R., Marchesi, C., Melgarejo, J.C., Gervilla, F., Garrido, C.J., Rodríguez-Vega, A., Lazano-Santacruz, R., Blanco-Moreno, J.A., 2006. Primitive island-arc Cretaceous volcanic rocks in eastern Cuba: the Teneme Formation. Geologica Acta, 4(1-2), 103-122.

Rollinson, H., 1993. Using Geochemical Data: Evaluation, Presentation, Interpretation. Essex (England), Longman Scientific & Technical, 352pp.

Schellekens, J.H., 1998. Geochemical evolution and tectonic history of Puerto Rico. In: Lidiak, E.G., Larue, D.K. (eds.). Tectonics and Geochemistry of the Northeastern Caribbean. Boulder (Colorado), Geological Society of America, 322 (Special Paper), 35-66.

Schellekens, J.H., Montgomery, H., Joyce, J., Smith, A.L., 1991. Late Jurassic to late Cretaceous development of island arc crust in southwestern Puerto Rico. In: Larue, D.K., Draper, G. (eds.). 12th Caribbean Geological Conference Transactions, St. Croix, U. S. Virgin Islands, Miami Geological Society, 268-281.

Slodowski, T.R., 1956. Geology of the Yauco area, Puerto Rico. Ph. D. Thesis. Princeton (New Jersey), Princeton University, 130pp.

Sun, S.-S., McDonough, W.F., 1989. Chemical and isotopic systematics of oceanic basalts: implications for mantle composition and processes. In: Saunders, A.D., Norry, M.J. (eds.). Magmatism in the Ocean Basins. Oxford (United Kingdom), Blackwell Scientific Publications, Geological Society, 42 (Special Publications), 313-345.

Taylor, S.R., McLennan, S.M., 1985. The Continental Crust: its Composition and Evolution. Oxford, Blackwell Scientific Publications, 312pp.

Volckmann, R.P., 1984a. Geologic map of the Cabo Rojo and Parguera quadrangles, southwest Puerto Rico. U.S. Geological Survey Miscellaneous Investigations Map, I-1557, scale 1:20,000.

Volckmann, R.P., 1984b. Geologic map of the Puerto Real quadrangle, southwest Puerto Rico. U.S. Geological Survey Miscellaneous Investigations Map, I-1559, scale 1:20,000.

Volckmann, R.P., 1984c. Geologic map of the San German quadrangle, southwest Puerto Rico. U.S. Geological Survey Miscellaneous Investigations Map, I-1558, scale 1:20,000.

White, W.M., Dupré, B., 1986. Sediment subduction and magma genesis in the Lesser Antilles: Isotopic and trace element constraints. Journal of Geophysical Research, 91, 5927-5941.

White, W.M., Dupré, B., Vidal, P., 1985. Isotope and trace element geochemistry of sediments from the Barbados ridge-Demerara plain region, Atlantic Ocean. Geochimica et Cosmochimica Acta, 49, 1875-1886.

Woodhead, J.D., Eggins, S.M., Johnson, R.W., 1998. Magma genesis in the New Britain island arc: Further insights into melting and mass transfer processes. Journal of Petrology, 39, 1641-1668.

Manuscript received November 2010;
revision accepted June 2011;
published Online June 2011.

ELECTRONIC APPENDIX

Supplementary data associated with this article can be found in the online version of this manuscript.

APPENDIX TABLES

Table	Status
1) Monte del Estado Peridotite	New Data
2) Las Palmas Amphibolite	New Data
3) Lower Cajul MORB (LCAJ)	Revised Data
4) Las Palmas and LCAJ Isotopes	New and Revised
5) Upper Cajul MORB (UCAJ)	Revised Data
6) Upper Cajul MORB (UCAJ) Isotopes	Revised Data
7) Caribbean Cretaceous Basalt Plateau (CCBP)	Revised Data
8) Pelagic Sediments	New and Revised
9) Pelagic Sediments Isotopes	New and Revised
10) Early Island Arc Volcanic Rocks (WPR)	Revised Data

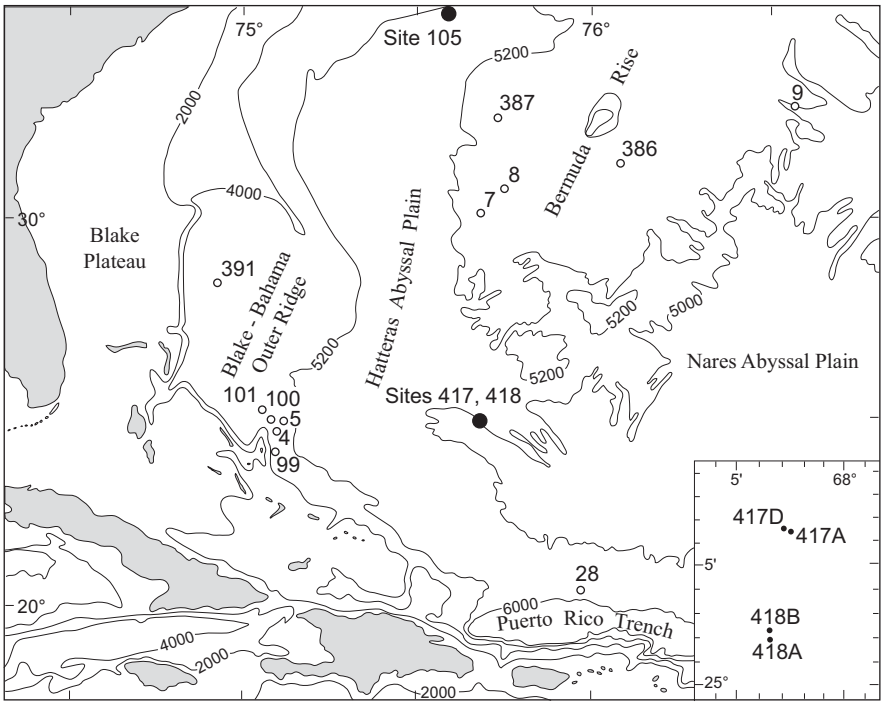

FIGURE I | **Map of southwestern North Atlantic area showing locations of DSDP drill sites, the source of analyzed samples (Table 8) of Atlantic Cretaceous pelagic sediments (AKPS).**

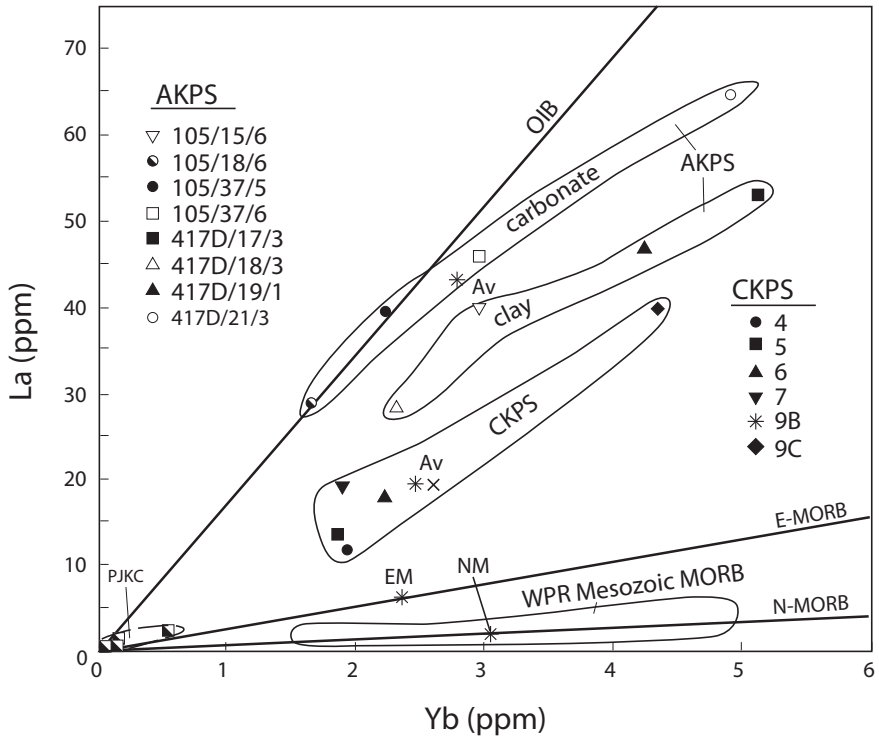

FIGURE II | **La and Yb compared to WPR Mesozoic MORB and trends of major oceanic basalt series (Sun and McDonough, 1989). AKPS forms two elongate fields sub-parallel to the OIB trend, one of carbonate with relatively high La and low Zr, and another of abyssal claystone with lower La and relatively high Zr. CKPS forms a subparallel field more depleted in La, reflecting a higher mafic volcanogenic component, as in South Pacific sediments.**

TABLE I | **Major and trace element data, Monte del Estado Serpentinized Peridotite, Puerto Rico**

Sample	001-96	002-96	012-94	014-94	017-94	021-94	30-94	32-94	37-94	50A-94	52-94	59-93	60-93	61-93	62-93	63-93	78-94	71-94	77H-94	90-93	92-94	92A-94	154-94	Avg Lherz	Avg Harz
Unit	H2	H2					H	L		L	L	L	L		L	L		H	H				H2		
SiO_2	40.18	39.45	39.82	39.30	40.33	39.73	41.28	39.64	39.82	40.83	39.52	35.02	38.19	38.38	41.23	38.42	39.24	39.86	39.50	38.89	38.72	38.64	39.88	45.43	43.73
TiO_2	0.04	0.05	0.01	0.05	0.06	0.07	0.02	0.04	0.07	0.05	0.04	0.07	0.05	0.05	0.07	0.04	0.02	0.01	0.02	0.04	0.04	0.03	0.05	0.45	0.28
Al_2O_3	1.49	1.65	1.10	1.86	2.59	2.50	0.98	2.12	2.54	1.77	2.25	2.39	2.19	1.98	2.36	1.87	1.66	1.14	1.37	1.83	1.95	1.58	1.77	4.39	2.57
Fe_2O_3	7.45	7.30	7.40	6.64	8.13	7.96	6.67	7.91	8.06	6.93	7.95	8.39	7.56	7.60	8.09	8.28	7.98	7.04	6.86	7.05	8.02	8.29	7.80	5.15	6
FeO	0.00	0.00	0.00	0.00	0.00	0.00	0.00	0.00	0.00	0.00	0.00	0.00	0.00	0.00	0.00	0.00	0.00	0.00	0.00	0.00	0.00	0.00	0.00	7.44	7.09
MnO	0.13	0.11	0.11	0.12	0.11	0.11	0.17	0.11	0.11	0.12	0.11	0.13	0.12	0.13	0.12	0.13	0.11	0.12	0.15	0.09	0.11	0.13	0.10	0.17	0.16
MgO	36.73	37.62	35.11	35.55	35.54	35.87	43.57	36.61	36.48	37.09	36.68	40.12	36.99	36.35	36.34	36.45	35.79	39.86	35.58	36.11	36.98	35.60	35.94	30.31	36.34
CaO	0.52	0.46	0.35	2.31	2.95	2.77	0.64	2.20	3.01	3.21	2.29	2.51	2.03	0.28	2.73	0.14	1.15	0.39	0.94	1.97	2.13	0.72	0.63	5.68	3.18
Na_2O	0.18	0.16	0.01	0.05	0.06	0.04	0.10	0.03	0.09	0.03	0.02	0.23	0.04	0.00	0.07	0.20	0.01	0.09	0.00	0.02	0.03	0.03	0.01	0.59	0.34
K_2O	0.01	0.00	0.00	0.00	0.00	0.00	0.00	0.00	0.00	0.00	0.00	0.01	0.00	0.00	0.00	0.01	0.00	0.00	0.00	0.00	0.00	0.00	0.00	0.27	0.15
P_2O_5	0.00	0.00	0.09	0.08	0.08	0.08	0.00	0.08	0.08	0.07	0.05	0.00	0.07	0.09	0.07	0.08	0.07	0.07	0.08	0.06	0.06	0.07	0.07	0.12	0.14
LOI	13.11	13.28	15.30	13.30	9.40	10.10	6.61	10.50	9.00	9.10	10.30	10.95	11.90	14.30	8.20	13.80	13.20	12.00	14.70	13.20	11.20	14.10	13.20	0	0
Subtotal	99.84	100.08	99.30	99.26	99.25	99.23	100.04	99.24	99.26	99.20	99.21	99.82	99.14	99.16	99.28	99.42	99.23	100.58	99.20	99.26	99.24	99.19	99.45	100.00	99.98
Cr	3282	3068			2892		3399	2700		3098	2879	2575	3069	2763	3056	2687		1809	3341				2175		
Ni	2030	1980			1912		2307	2177		1879	2046	2100	1975	1968	2022	2256		2350	2245				2021		
Ta	0	0					0.01	0		0	0	0	0	0.015	0	0.05		0.01	0.01				0.088		
Nb	0.238	0.291					0.01	0.4		0.01	0.27	0.29	0.326	0.2	0.21	0		0	0.06				0.2		
Hf	0	0.082					0	0.018		0	0.082	0.027	0.031	0	0.026	0.1		0.06	0				0		
Zr	0.281	0.17					0.27	0.19		0.2	0.888	1.258	0.888	0.537	0.962	0		1.52	0.39				1.232		
Ti	114	440					119.9	182		570	226.5	418	365	359.7	365	0		59.95	179.9				299.8		
Y	0.56	1.148					0.63	1.092		1.96	2.156	1.596	1.988	1.391	1.848	1		1	0.77				0.73		
Th	0.165	0.206					0.01	0.3		1.32	0.38	1.201	1.313	0.23	0.234	0.2		0.01	0.01				0.029		
U	2.29	0.46					0.007	0		0	0	0	0.98	0.039	0	0.1		0	0				0		
La	0.53	0.6					0.01	1.18		10.53	7.375	2.95	10	0.062	2.552	1.61		0.01	0.04				0.09		
Ce	0.6	0.7					0.02	1.112		11.25	4.275	2.925	6.66	0.1	2.52	1.78		0.04	0.07				0.297		
Pr	0.015	0.024					0	0.06		0.1	0.14	0.08	0.14	0.014	0.13	0		0.01	0.01				0.037		
Nd	0.1	0.128					0	0.15		0.21	0.205	0.19	0.41	0.1	0.35	1		0	0.07				0.188		
Sm	0.024	0.033					0	0.039		0.063	0.066	0.053	0.13	0.077	0.103	0.07		0	0.03				0.074		
Eu	0.01	0.02					0	0.018		0.046	0.049	0.033	0.044	0.022	0.037	0.02		0	0.01				0.024		
Gd	0.077	0.103					0.04	0.085		0.191	0.247	0.147	0.191	0.129	0.166	0		0	0.03				0.117		
Tb	0.011	0.021					0.01	0.019		0.04	0.046	0.03	0.04	0.027	0.033	0.04		0	0.01				0.024		
Dy	0.086	0.176					0.075	0.153		0.284	0.333	0.23	0.279	0.275	0.213	0		0.033	0.13				0.219		
Ho	0.024	0.048					0.03	0.042		0.077	0.081	0.061	0.08	0.057	0.071	0		0	0.03				0.048		
Er	0.092	0.151					0.1	0.134		0.241	0.244	0.202	0.252	0.171	0.226	0		0	0.08				0.107		
Tm	0.016	0.025					0.02	0.024		0.039	0.037	0.036	0.041	0.028	0.036	0		0	0.02				0.023		
Yb	0.119	0.189					0.13	0.186		0.278	0.284	0.265	0.302	0.212	0.275	0.21		0.16	0.16				0.202		
Lu	0.021	0.036					0.03	0.035		0.045	0.046	0.045	0.051	0.04	0.046	0.03		0	0.03				0.02		

DOI: 10.1344/105.000001715

TABLE II | **Major and trace element data, Bermeja Amphibolite, Puerto Rico**

Sample	AMPH-30	AMPH 31-93	AMPH 87-93	AMPH-101	AMPH-102	AMPH-105	AMPH 106-93	AMPH 108-93	AMPH 121-93	AMPH 125-93	AMPH-126-93	AMPH 127-93	AMPH-135-93	AMPH 136-93	LMG-84	LMG-89
SiO_2	48.79	45.95	45.28	-	50.91	53.36	43.77	40.95	44.35	50.72	51.76	50.74	47.42	50.70	-	-
TiO_2	0.71	0.96	1.18	-	1.53	1.05	1.16	0.88	1.17	1.83	0.88	1.05	2.14	0.99	-	-
Al_2O_3	12.09	12.53	13.24	-	13.17	15.13	13.86	14.47	12.86	13.33	15.54	15.46	14.65	14.54	-	-
Fe_2O_3	9.64	10.13	9.92	-	12.05	10.51	9.06	8.96	9.55	12.96	9.43	9.35	14.58	9.83	-	-
MnO	0.15	0.16	0.17	-	0.18	0.18	0.18	0.18	0.22	0.22	0.17	0.16	0.22	0.17	-	-
MgO	17.04	9.65	7.66	-	12.10	6.90	8.38	13.19	9.71	6.69	8.00	7.27	7.77	7.85	-	-
CaO	9.40	15.74	18.29	-	6.60	8.65	18.20	15.01	17.20	9.57	10.90	10.35	9.66	9.64	-	-
Na_2O	1.46	0.92	0.76	-	3.26	3.84	0.41	0.35	0.38	2.85	2.86	3.10	2.95	3.70	-	-
K_2O	0.05	0.06	0.07	-	0.41	0.27	0.07	0.03	0.09	0.13	0.47	0.65	0.51	0.26	-	-
P_2O_5	0.05	0.09	0.11	-	0.14	0.09	0.12	0.10	0.13	0.17	0.07	0.07	0.19	0.11	-	-
LOI	0.05	3.60	3.00	-	0.05	0.01	4.80	5.80	4.40	1.30	0.03	1.60	0.01	2.10	-	-
Subtotal	99.43	99.79	99.68	-	100.40	99.99	100.01	99.92	100.06	99.77	100.11	99.80	100.10	99.89	-	-
Cr	801	-	-	-	504	182	-	-	-	-	178	0	162	-	-	-
Ni	700.7304	178.1	297.2	-	457.573	64.7105	21	84.3	32.8	19.8	76.3691	25.8	83.6756	39.6	-	-
Co	0	56.7	57.3	-	-	-	42.3	47.7	59.6	60.6	-	52.9	0	57.7	-	-
Sc	39	35	42	40.1	31	30	34	35	35	42	31	37	59	39	34.1	42.2
V	216	266	288	-	324	271	253	270	266	396	254	295	4.07	263	-	-
Cu	61.0	28.3	50.7	-	45.8	5.2	58.3	85.3	19.5	58.0	34.6	75.5	22.4	25.2	-	-
Pb	2.0	0.8	0.3	-	-0.5	-0.4	1.2	1.1	1.4	0.4	1.7	0.4	3.8	0.4	-	-
Zn	41.9	18.0	20.0	-	66.5	82.4	14.0	31.0	21.0	26.0	46.0	13.0	105.0	31.0	-	-
W	0.0	107.1	139.7	-	-	-	73.7	48.8	165.7	153.6	-	119.4	-	110.8	-	-
Mo	0	0.1	0.1	-	-	-	0.1	0.1	0.2	0.1	-	0.1	-	0.1	-	-
Rb	0.18	0.70	2.00	-	1.94	3.22	0.90	1.20	1.30	2.10	7.02	10.70	6.64	4.80	-	-
Cs	-	0.1	0.2	0.2	-	-	-	0.3	-	0.1	-	0.4	-	0.1	0.25	0.25
Ba	115.8	77.0	14.0	-	107.8	55.6	167.0	177.0	68.0	27.0	128.9	711.0	53.0	60.0	-	-
Sr	296.2	246.7	347.9	-	141.0	176.3	40.7	43.0	36.7	182.6	511.5	445.6	143.0	148.9	-	-
Ga	11.9	13.9	14.1	-	15.7	14.1	16.2	14.3	16.0	19.5	11.8	16.8	18.7	18.6	-	-
Ta	-	0.3	0.3	-	-	-	0.2	0.2	0.5	0.6	-	0.4	-	0.4	-	-
Nb	0.4	1.9	2.4	1.1	1.9	2.2	1.4	1.1	1.8	3.2	0.9	2.0	5.9	2.2	1.7	1.4
Hf	1.1	1.2	0.9	1.8	2.5	2.0	2.0	0.9	2.2	3.1	1.5	2.3	3.4	1.9	2.3	2.5
Zr	29.4	45.0	22.9	55.0	95.0	66.3	65.1	22.1	68.0	99.0	49.5	63.9	129.7	53.9	74.0	75.0
Ti	4256.5	5755.0	7074.0	-	9172.0	6295.0	6954.0	0.0	7014.0	0.0	5276.0	6295.0	12829.0	5935.0	0.0	0.0
Y	14.6	23.7	23.2	19.0	30.2	20.9	27.0	19.8	29.2	45.2	18.8	25.4	44.2	27.0	23.9	25.8
Th	0.0	-	0.2	0.1	0.2	0.1	0.1	-	0.1	-	0.1	0.2	0.3	0.4	0.1	0.1
U	-0.6	-	-	0.1	1.9	0.0	-	-	-	-	-2.5	0.1	3.2	-	0.2	0.2
La	1.09	2.50	2.00	2.80	3.11	2.39	3.10	2.10	3.20	4.70	2.00	3.25	5.00	3.00	3.57	3.59
Ce	3.88	10.00	6.10	8.49	9.76	7.24	9.80	7.40	11.10	13.90	6.15	9.85	15.44	8.80	10.47	10.22
Pr	0.68	1.22	0.97	-	1.68	1.13	1.50	0.95	1.68	2.26	1.02	1.32	2.58	1.21	-	-
Nd	3.53	7.20	6.40	7.35	9.03	6.06	9.90	5.50	9.20	13.20	5.52	7.62	13.73	8.70	8.15	8.32
Sm	1.60	2.10	2.30	2.47	3.25	2.07	2.70	2.00	2.90	4.50	2.03	2.61	4.97	2.50	2.96	3.24
Eu	0.58	0.84	1.02	0.86	1.14	0.66	1.20	0.72	1.10	1.63	0.79	0.91	1.82	0.84	1.15	1.01
Gd	2.08	3.03	3.47	-	4.31	2.90	3.81	2.28	3.99	6.69	2.71	3.19	6.76	3.58	-	-
Tb	0.33	0.58	0.58	0.50	0.72	0.50	0.74	0.50	0.80	1.10	0.46	0.62	1.06	0.63	0.64	0.73
Dy	2.54	3.57	4.15	-	5.43	3.72	4.49	3.10	4.99	7.18	3.33	4.02	8.01	4.09	0.00	0.00
Ho	0.53	0.82	0.80	-	1.13	0.80	0.93	0.67	0.95	1.52	0.72	0.84	1.66	0.85	0.00	0.00
Er	1.57	2.42	2.48	-	3.37	2.40	2.81	2.02	2.89	4.48	2.11	2.68	4.86	2.70	0.00	0.00
Tm	0.24	0.38	0.37	-	0.48	0.35	0.41	0.29	0.43	0.73	0.31	0.41	0.70	0.44	0.00	0.00
Yb	1.55	2.43	2.27	2.06	3.14	2.38	2.69	2.01	2.77	4.95	2.07	2.50	4.50	2.90	2.59	2.73
Lu	0.24	0.35	0.36	0.30	0.48	0.36	0.38	0.31	0.39	0.70	0.31	0.42	0.72	0.47	0.35	0.35

DOI: 10.1344/105.000001715

TABLE III | **Major and trace element data, Lower Cajul Formation, Puerto Rico**

Sample Number	CAJ D	CAJ E	CAJ A	CAJ B	CAJ C	CAJDS 103B	LCAJ Z	LCAJ Y	LCAJ X	LCAJ V	LCAJ U
SiO_2	49.65	68.98	66.16	68.50	54.19	51.45	46.29	53.00	53.48	45.21	69.45
TiO_2	1.89	1.50	1.44	1.57	1.79	1.05	1.22	1.46	1.71	1.26	1.60
Al_2O_3	13.55	9.63	10.62	10.00	11.92	15.09	12.88	13.52	10.85	12.82	9.46
Fe_2O_3	12.38	6.71	9.18	8.22	13.57	9.96	9.11	11.02	12.78	9.26	7.35
MnO	0.21	0.07	0.10	0.08	0.15	0.19	0.18	0.17	0.15	0.18	0.08
MgO	6.99	1.80	2.13	1.58	4.81	7.70	10.24	6.63	4.91	11.82	1.61
CaO	8.78	4.98	4.88	4.81	6.44	10.03	15.48	8.22	9.75	14.21	5.26
Na_2O	2.99	3.56	3.48	3.77	4.06	3.09	0.45	3.64	2.26	0.37	3.06
K_2O	0.71	0.24	0.18	0.28	0.56	0.77	0.10	0.47	0.07	0.09	0.13
P_2O_5	0.15	0.35	0.32	0.38	0.17	0.08	0.12	0.15	0.17	0.13	0.36
LOI	2.60	2.10	1.40	0.70	2.20	0.03	3.90	1.60	3.80	4.60	1.60
SubTotal	99.90	99.92	99.89	99.89	99.86	99.44	99.97	99.88	99.93	99.95	99.96
Ni	34.6	10.9	11.2	16.3	24.8	50.3	28.5	33.3	22.9	42.7	11.3
Co	47.7	17.2	19.4	18.1	32.4	0	33.1	36.4	30.9	34.2	17.3
Sc	43	24	20	21	38	39	32	37	39	33	23
V	429	182	169	189	368	281	263	340	342	258	176
Cu	69.9	39.9	38.2	57.6	34.8	52.7	144.5	91.5	39.9	52.5	40
Pb	1.9	1.9	1	0.6	1.8	0.7	9.1	18.4	3.4	16.7	5.6
Zn	83	113	80	102	83	55	16	24	80	21	89
Rb	12.7	4.6	2	5.1	9.8	12.4	1	9	0	0.8	1.9
Cs	0.1	0.1	0	0.1	0	0	0	0.3	0	0	0
Ba	399	64	324	42	71	217	48	576.2	185.2	26	25.1
Sr	169.5	56.4	102.7	73.6	96	256.7	24.7	164.8	30.1	26.8	42.1
Ga	18.8	15.8	20	19.2	16.8	14.6	13.9	17.7	17.9	14.1	16.8
Ta	0.3	0.8	0.6	0.7	0.3	0	0	0.1	0.1	0.1	0.5
Nb	3.6	8.8	9.3	9.2	3	1.5	1.8	1.3	2.1	1.4	7.6
Hf	3.3	8.3	10.3	9.7	4.8	1.9	1.9	2.5	2.6	2.1	8.2
Zr	101	290	355.5	355	129.1	64.7	67.9	80.9	86.9	74.1	269.1
Y	46.2	97.9	110.1	111.7	48.1	22.1	27.5	36	46.8	29.3	91.1
Th	0.5	1	1.1	2	0.2	0.2	0	0	0	0.3	1.1
U	1	0.8	0.1	0.4	0	0	0	0	0	0	0.4
La	4.30	13.60	16.10	15.30	5.40	2.62	3.30	3.20	3.40	3.40	11.90
Ce	12.40	41.20	44.00	44.40	16.00	7.83	9.20	10.40	11.40	10.50	35.30
Pr	2.11	6.44	7.18	7.34	2.51	1.31	1.60	1.78	1.95	1.73	5.81
Nd	12.20	36.70	38.00	36.00	14.70	7.19	8.80	10.80	11.50	9.90	32.80
Sm	4.30	10.30	11.70	12.70	4.70	2.65	2.60	3.10	3.70	2.90	9.80
Eu	1.66	2.58	2.63	2.91	1.38	0.91	1.10	1.30	1.33	1.41	2.36
Gd	5.99	14.02	14.35	15.85	6.13	3.24	3.90	4.63	5.63	4.13	12.91
Tb	1.13	2.59	2.67	2.92	1.27	0.54	0.70	0.87	0.93	0.78	2.31
Dy	7.29	15.78	17.55	18.82	8.24	4.12	4.38	5.80	6.70	4.64	14.84
Ho	1.76	3.44	3.74	3.77	1.83	0.85	0.92	1.24	1.49	0.92	3.10
Er	4.68	9.55	11.58	12.01	5.46	2.38	2.77	3.51	4.53	3.01	9.02
Tm	0.68	1.52	1.58	1.62	0.76	0.36	0.40	0.52	0.74	0.44	1.38
Yb	4.52	9.42	10.00	10.27	4.66	2.33	2.66	3.41	4.50	2.75	9.22
Lu	0.68	1.35	1.56	1.46	0.73	0.37	0.43	0.58	0.70	0.45	1.37

Geologica Acta, 9(3-4), 273-287 (2011)
DOI: 10.1344/105.000001715

TABLE IV | **Sr-, Nd-, and Pb-isotope data, Pre-Arc Complex, southwestern Puerto Rico**

Sample	Unit	Rb	Sr	Sm	Nd	Pb	$m^{87}Sr/^{86}Sr$	$i^{87}Sr/^{86}Sr$	$m^{143}Nd/^{144}Nd$	$i^{143}Nd/^{144}Nd$	eNd	$^{206}Pb/^{204}PB$	$^{207}Pb/^{204}PB$	$^{208}Pb/^{204}PB$	Δ207/204	Δ208/204	Age (Ma)
AMPH-30	Las Palmas	0.2	296	1.6	3.5	2.0	0.703360	0.703355	0.513173	0.512838	8.56	18.35	15.72	38.35	23.99	53.79	185
AMPH-102	Las Palmas	1.9	141	3.2	9.0		0.704373	0.704270	0.513182	0.512916	10.18						185
AMPH-105	Las Palmas	3.2	176	2.1	6.1		0.703848	0.703714	0.513094	0.512842	8.63						185
AMPH-126-93	Las Palmas	7.0	511				0.703926	0.703825	ND								185
AMPH-127-93	Las Palmas	6.6	143	5.0	13.7		0.704319	0.703979	0.513027	0.512760	7.02						185
LCAJA	Lower Cajul	2.0	103	11.7	38.0	1.0	0.704330	0.704187	0.513040	0.512815	8.09	19.55	15.57	38.86	-4.02	-70.30	185
LCAJB	Lower Cajul	5.1	74	12.7	36.0	0.6	0.704500	0.703993	0.513066	0.512808	7.96	19.39	15.57	38.72	-2.29	-34.95	185
LCAJC	Lower Cajul	9.8	96	4.7	14.7	1.8	0.705160	0.704380	0.513070	0.512836	8.51	18.95	15.55	38.48	0.48	-5.76	185
LCAJDS/103B	Lower Cajul	12.4	257	2.7	7.2	0.7	0.704486	0.704131	0.513043	0.512768	7.19	18.70	15.55	38.16	3.19	-7.53	185
LCAJE	Lower Cajul	4.6	56	10.3	36.7	1.9	0.704450	0.703845	0.513046	0.512841	8.60	19.97	15.56	39.01	-9.58	-76.07	185

TABLE V | **Major and trace element data, Upper Cajul Formation, Puerto Rico**

Sample	UCAJN 103EXC	UCAJ-103EX-B	UCAJ-103EX-A	UCAJ-7-94NQ	UCAJ103EXF	UCAJ-103EX-D	UCAJ-106-93	UCAJ-103EX-E	UCAJ-103EX-G	UCAJ303/9.0A	UCAJ301/303A	UCAJNCOD	UCAJ99-93	UCAJ 303S/2	UCAJ 303S/3	UCAJ 303S/7	UCAJ 303S/1	UCAJS303S/2	UCAJS303S/4	UCAJ 303S/4	UCAJS303S/5
Facies	North	North	North	North	North	North	North	North	North	North	North	North	North	South	South	South	South	South	South	South	South
SiO_2	45.16	46.39	46.99	47.48	48.70	48.75	49.16	49.30	49.79	49.95	50.82	51.24	53.71	41.51	42.59	44.71	48.07	48.52	53.40	56.21	56.86
TiO_2	1.58	1.51	1.58	1.56	1.81	2.10	1.69	1.52	1.51	2.14	1.84	1.87	2.02	3.24	3.70	3.35	3.60	4.14	4.10	2.99	3.03
Al_2O_3	15.81	13.57	14.71	14.65	15.99	15.77	15.95	15.90	15.74	17.62	16.60	17.05	13.96	11.47	13.00	11.40	12.47	14.55	13.85	15.26	14.44
Fe_2O_3	9.44	11.97	8.89	11.09	10.47	12.28	8.56	8.80	10.21	11.59	10.74	10.34	11.31	9.63	10.48	10.12	9.93	9.63	9.70	9.70	9.81
MnO	0.03	0.16	0.12	0.16	0.10	0.16	0.10	0.19	0.20	0.15	0.16	0.15	0.09	0.13	0.08	0.10	0.08	0.09	0.09	0.10	0.10
MgO	4.67	5.45	5.36	4.91	3.68	3.75	3.82	4.84	4.65	2.85	3.91	3.61	4.51	2.44	2.18	3.43	2.56	2.44	2.83	1.45	1.47
CaO	9.50	9.27	9.96	8.80	6.63	7.37	7.33	9.00	7.14	5.99	5.13	4.63	5.24	15.48	13.19	13.45	9.93	8.45	6.23	3.34	3.38
Na_2O	3.72	3.45	3.52	4.29	2.94	3.95	3.16	3.79	4.56	3.63	5.27	5.31	4.05	3.32	4.11	3.49	3.95	4.60	4.39	7.06	7.14
K_2O	1.24	1.02	1.26	0.86	1.83	1.20	1.43	1.00	0.90	1.51	1.29	1.28	0.78	0.70	1.02	0.81	0.91	1.14	1.01	0.75	0.76
P_2O_5	0.19	0.19	0.19	0.19	0.24	0.25	0.21	0.17	0.18	0.38	0.24	0.25	0.20	0.55	0.70	0.63	0.70	0.78	0.78	0.70	0.70
LOI	7.50	6.50	6.50	5.40	6.80	4.40	7.70	5.00	4.30	4.10	3.80	4.00	3.10	11.20	8.60	8.40	7.50	4.60	3.50	2.30	2.30
SubTotal	98.84	99.48	99.08	99.39	99.19	99.98	99.11	99.51	99.18	99.91	99.80	99.73	98.97	99.67	99.65	99.89	99.70	98.94	99.88	99.86	99.99
Cr	165	0	0	0	172	0	0	0	0	129	41	48	82	0	0	0	0	7	41	0	7
Ni	45	43.2	63.5	26	49	26.9	57	71.7	42.8	43	49	59	37	86.8	100.4	23.3	79.2	118	91	74	77
Co	42	53.6	41.3	35.9	31	41.5	37.4	46	36.5	37	36	40	44	47.7	57.6	35.2	52.2	68	60	42.9	44
Sc	52	44	48	38	54	47	52	52	52	52	52	52	45	24	27	23	26	32	30	20	21
V	255	374	316	294	195	276	259	223	245	245	225	200	326	270	330	294	317	387	365	214	222
Cu	58	51.6	46.6	56.5	45	43.6	37.4	69	52.1	52	65	45	86	66.8	74	33.1	74.1	87	85	25.5	26
Pb	2	3.4	2.3	2.2	3	2.1	3.3	1.7	9.9	10	7	7	2	11.4	7.4	6.9	4.8	9	6	4.5	5
Zn	85	97	75	73	92	105	88	76	81	81	79	80	119	101	105	91	110	123	127	114	118
K	10294	8467	10460	7139	15191	9962	11871	8301	7471	12535	10709	9999	6475	5811	8467	6724	7554	9937	8695	6226	6446
Rb	32	25.3	28.9	16.7	40	32.6	32.7	22.4	27.7	28	27	30	14	5.6	7.9	14.2	7.7	9	9	18.1	17
Cs	0.9	1.3	0.9	1.2	1.9	1	1	0.7	1	1	0.5	0.7	0.4	0	0	0	0	0	0	0	0
Ba	163	175	170	442	160	163	176	146	187	187	120	139	225	596.2	264.3	218.1	345	310	397	153	158
Sr	246	221.8	246	507.2	193	286.3	219.3	249.2	377.3	377	281	309	267	276.8	263.1	257	249.4	309	287	471.7	488
Ga	18	16.4	18.3	18.5	16	19.2	18.2	14.2	16.8	17	16	19	16	17.7	18.1	20.5	19.3	21	22	15.3	16
Ta	0.5	0.5	0.6	0.5	0.6	0.7	0.6	0.5	0.6	0.6	0.7	0.7	0.8	2.4	2.6	2.5	2.6	3.05	2.99	3	3.11
Nb	8	8.7	10.2	9.5	9.3	11.5	10.2	7.1	8.3	8.3	8.8	9.3	10.9	39.5	41.6	36.5	42.5	48.8	48.9	46.4	48
Hf	2.4	2.9	2.8	2.6	2.5	3.1	3.2	2.2	2.2	2.2	3	3.3	3.5	7.8	8	7.6	8.1	9.39	9.32	6.1	6.32
Zr	88	94.9	100.9	93.3	99	125.9	102.5	79.6	88.7	89	101	106	118	268.7	293.2	264.5	290.3	344	334	233.3	242
Ti	9472	9052	9472	9352	10851	12589	10132	9112	9052	9052	11031	11211	12110	19424	22182	20083	21582	26032	24843	17925	18558
Y	30	31.6	31.7	27.2	39	42.8	38.3	27.7	30.6	31	39	42	36	34.1	44.1	37.4	40.5	52	47	33.8	35
Th	0.8	0.9	0.3	1.1	0.8	1.1	1.4	1	0.5	0.5	0.8	0.9	0.8	2.8	3.2	2.4	3.5	3.76	4.03	4.4	4.56
U	0.3	0.4	0.7	0.3	0.3	0.4	0.3	0.5	0.3	0.3	0.4	0.4	0.7	4.6	3.6	1.9	4.6	4.22	5.29	0.8	0.83
La	6.9	8.1	8.3	9	9.3	12.2	9.1	6.6	7.5	7.5	9.5	10.4	9.9	30	34.9	30.6	32.9	40.96	37.87	38.3	39.65
Ce	16.4	18.3	19.3	20.8	21.9	25.1	21.7	16	18.2	18.2	22.4	25	22.3	67.5	78	67.8	74.7	91.54	85.99	78	80.76
Pr	2.48	2.52	2.8	2.88	3.12	3.73	3.11	2.24	2.47	2.47	3.08	3.52	3.44	8.28	9.75	9.06	9.51	11.44	10.95	9.33	9.66
Nd	13.6	14.7	14.4	14.7	16.3	19.4	17.3	12	14.8	14.8	15.8	16.6	19.1	35.3	43.7	42.2	42.7	51.29	49.15	42.8	44.31
Sm	3.4	3.7	4.3	3.9	4.4	5.1	4.7	3.1	3.5	3.5	4.3	4.7	4.2	8.1	9.5	8.4	9	11.15	10.36	7.8	8.08
Eu	1.28	1.48	1.44	1.27	1.39	1.83	1.81	1.17	1.39	1.39	1.65	1.78	1.7	2.67	3.27	2.82	3.13	3.84	3.6	2.83	2.93
Gd	4.95	5.43	5.7	5.55	6.36	6.7	6.31	4.47	4.44	4.44	5.72	6.5	6.57	8.55	9.91	8.52	9.61	11.63	11.06	7.6	7.87
Tb	0.81	0.86	0.87	0.81	1.07	1.17	1.06	0.73	0.8	0.8	1	1.12	1.07	1.37	1.63	1.31	1.54	1.91	1.77	1.14	1.18
Dy	5.52	5.28	5.03	5.13	5.69	7	6.66	4.07	5.27	5.27	6.15	6.85	5.8	6.56	7.31	7.2	7.74	8.58	8.91	6.54	6.77
Ho	1.07	1.12	1.14	0.92	1.3	1.43	1.35	0.96	1.08	1.08	1.28	1.43	1.27	1.18	1.4	1.27	1.4	1.64	1.61	1.13	1.17
Er	3.06	3.22	3.52	2.66	3.88	4.01	3.65	2.86	2.87	2.87	3.69	4.05	3.77	3.43	4.08	3.31	3.93	4.79	4.52	3.15	3.26
Tm	0.45	0.45	0.43	0.4	0.53	0.61	0.49	0.42	0.48	0.48	0.57	0.63	0.51	0.43	0.48	0.51	0.51	0.56	0.59	0.45	0.47
Yb	2.5	3.02	2.81	2.65	2.94	3.76	2.71	2.29	2.76	2.76	3.4	3.75	3.37	2.56	3.14	2.83	3.07	3.69	3.53	2.59	2.68
Lu	0.36	0.44	0.48	0.38	0.48	0.61	0.42	0.36	0.39	0.39	0.5	0.57	0.5	0.4	0.48	0.44	0.43	0.56	0.49	0.43	0.45

TABLE VI | **Sr-, Nd- and Pb-isotope data, Upper Cajul Formation, southwestern Puerto Rico**

Sample	Unit	Rb	Sr	Sm	Nd	Pb	$m^{87}Sr/^{86}Sr$	$i^{87}Sr/^{86}Sr$	$m^{143}Nd/^{144}Nd$	$i^{143}Nd/^{144}Nd$	eNd	$^{206}Pb/^{204}PB$	$^{207}Pb/^{204}PB$	$^{208}Pb/^{204}PB$	Δ207/204	Δ208/204	Age (Ma)
UCAJN103C	Upper Cajul	32.0	246	3.4	13.6	2.0	0.705220	0.704780	0.512925	0.512841	6.09	18.85	15.65	38.50	11.57	8.34	85
UCAJN103D	Upper Cajul	33.0	286	5.1	19.4	2.1	0.704910	0.704520	0.512921	0.512833	5.93	19.24	15.57	39.05	-0.66	16.18	85
UCAJN103G	Upper Cajul	27.7	377	3.5	14.8	9.9	0.704950	0.704702	0.513047	0.512967	8.56	19.25	15.59	38.90	1.23	-0.03	85
UCAJN103A	Upper Cajul	28.9	246	4.3	14.4	2.3	0.705010	0.704613	0.512985	0.512885	6.95	19.29	15.60	39.18	1.80	23.14	85
UCAJS303/S3	Upper Cajul	7.9	263	9.5	43.7	7.4	0.704640	0.704539	0.512823	0.512750	4.32	21.15	15.65	40.43	-13.37	-76.74	85
UCAJS303/S5	Upper Cajul	17.0	488	8.1	44.3	5.0	0.703980	0.703862	0.512848	0.512787	5.03	21.01	15.67	40.51	-9.85	-51.81	85

TABLE VII | **Major and trace element data, Caribbean Cretaceous Basalt Plateau**

Sample	CCBP-146-43E	CCBP-150-12R	CCBP-151-14R	CBP-152=24-CC-R	CCBP-153-20R	CCBP151-13-CC	CCBP146-42R-1	OIB	NMORB	E-MORB
SiO_2	48.42	46.60	48.69	48.65	49.29	46.78	46.88	-	-	-
TiO_2	1.08	1.23	3.33	1.69	1.79	2.74	0.97	-	-	-
Al_2O_3	14.77	14.07	12.60	11.69	13.71	14.28	13.72	-	-	-
Fe_2O_3	11.36	11.43	13.19	15.26	13.48	12.72	10.92	-	-	-
MnO	0.16	0.21	0.12	0.12	0.28	0.09	0.20	-	-	-
MgO	10.37	9.00	9.10	9.36	10.32	5.69	7.80	-	-	-
CaO	11.88	12.95	8.01	8.70	9.50	8.84	13.33	-	-	-
Na_2O	2.10	2.13	2.56	2.28	2.52	2.36	1.77	-	-	-
K_2O	0.08	0.09	0.92	1.05	0.10	1.15	0.30	-	-	-
P_2O_5	0.10	0.10	0.26	0.17	0.12	0.31	0.11	-	-	-
LOI	-	-	-	-	-	4.60	3.50	-	-	-
Subtotal	100.32	97.81	98.78	98.97	101.11	99.56	99.50	-	-	-
Cr	363	329	410	251	149	0.043	0.045	-	-	-
Ni	121	115	132	56	90	133	156	-	-	-
Co	-	-	-	-	-	49.7	75.5	-	-	-
Sc	44	45	43	53	60	39	45	-	-	-
V	296	315	491	459	506	406	296	-	-	-
Cu	125	143	222	44	192	-	-	-	-	-
Pb	0.4	0.3	2.78	0.78	18.31	0.8	0.1	-	-	-
Zn	54	58	132	115	106	-	-	-	-	-
Rb	1.3	0.69	14.7	24.2	1.9	38.1	5.3	-	-	-
Cs	0.03	0	0.13	0.37	0.01	0.7	-	-	-	-
Ba	12.16	10.85	80	7.18	20.35	51	13	-	-	-
Sr	125.6	113.6	332.5	96.3	161.5	301.3	125	-	64	6.4
Ga	14	16	25	17	19	22.1	16.1	-	-	-
Ta	0.58	0.49	1.64	0.41	0.56	1.5	0.6	2.7	0.132	0.47
Nb	3.4	4.4	26.4	2.5	6.1	20.2	3	48	2.33	8.3
Hf	1.43	1.67	4.82	2.19	2.445	4.1	1.4	7.8	2.05	2.03
Zr	53.7	59.5	188.6	77.4	89.4	150	45.8	280	74	73
Ti	6474.6	7373.85	19963.35	10131.55	10731.05	-	-	17200	7600	6000
Y	18.6	22.6	28.8	33.22	24.01	30.9	21.8	29	28	22
Th	0.19	0.231	1.616	0.12	0.4	1.7	0.2	4	0.12	0.6
U	0.045	0.32	1.21	0.315	0.18	1.9	0.2	1.02	0.047	0.18
La	2.45	2.99	15.83	2.17	4.12	16.4	2.9	37	2.5	6.3
Ce	6.85	7.97	38.83	6.52	11.21	36.7	6.7	80	7.5	15
Pr	1.09	1.38	5.58	1.24	1.76	4.91	1.11	9.7	1.32	2.05
Nd	5.82	6.8	25.89	7.5	9.24	25.5	5.9	38.5	7.3	9
Sm	2.15	2.41	6.52	3.07	3.12	6.7	2.3	10	2.63	2.6
Eu	0.8	0.86	2.29	1.1	1.2	2.17	0.83	3	1.02	0.91
Gd	2.67	3.33	7	4.54	4.1	6.23	2.95	7.62	3.68	2.97
Tb	0.52	0.6	1	0.83	0.65	0.96	0.55	1.05	0.67	0.53
Dy	3.328	4.06	6.145	5.87	4.54	5.54	3.63	5.6	4.55	3.55
Ho	0.72	0.86	1.15	1.27	0.97	1.16	0.82	1.06	1.01	0.79
Er	2.04	2.43	2.98	3.81	2.74	2.8	2.29	2.62	2.97	2.31
Tm	0.31	0.34	0.41	0.55	0.42	0.4	0.4	0.35	0.456	0.356
Yb	1.94	2.41	2.29	3.6	3.08	2.37	2.14	2.16	3.05	2.37
Lu	0.31	0.37	0.33	0.53	0.49	0.34	0.39	0.3	0.455	0.345

TABLE VIII | **Major and trace element data, Atlantic and Caribbean Pelagic Sediments**

Sample	Unit	SiO_2	TiO_2	Al_2O_3	Fe_2O_3	MnO	MgO	CaO	Na_2O	K_2O	P_2O_5	LOI	SubTotal	Cr	Ni
105/15/6	AKPS	54.78	0.64	14.60	5.92	0.02	2.30	0.48	1.88	3.00	0.05	16.00	99.67	0.007	154
105/18/6	AKPS	14.63	0.14	3.20	1.89	0.05	0.83	40.28	0.74	0.88	0.03	36.80	99.47	0.002	47
105/37/5	AKPS	47.04	0.42	9.59	5.13	0.19	1.90	14.40	0.93	2.17	0.07	18.00	99.84	0.004	94
105/37/6	AKPS	44.43	0.53	10.63	6.18	0.58	2.35	13.62	0.94	2.80	0.05	17.50	99.61	0.007	113
417D/17/3	AKPS	55.53	0.41	9.11	3.93	0.03	3.37	2.85	1.11	2.17	1.58	19.60	99.69	0.017	122
417D/18/2	AKPS	56.78	0.51	11.85	5.46	0.05	4.89	0.50	1.45	2.67	0.09	15.50	99.75	0.014	75
417D/19/1	AKPS	74.60	0.31	7.06	4.00	0.02	1.76	0.62	0.81	1.91	0.26	8.30	99.65	0.008	61
417D/21/3	AKPS	25.62	0.24	4.78	15.18	0.06	1.53	7.85	0.74	1.90	0.46	32.50	90.86	0.006	192
CKPS 4	CKPS	35.76	0.39	8.40	5.71	0.20	2.76	24.39	1.43	1.82	0.17	18.60	99.63	-	101.6
CKPS 5	CKPS	55.04	0.38	9.68	4.82	0.15	1.97	12.30	2.63	1.81	0.15	10.60	99.53	-	39.5
CKPS 6	CKPS	58.71	0.59	13.94	8.42	0.22	2.18	3.42	2.43	2.54	0.20	7.30	99.95	-	35
CKPS 7	CKPS	45.25	0.21	5.16	2.47	0.17	1.03	24.41	0.88	0.92	0.12	19.20	99.82	-	23.1
CKPS 9ABLU	CKPS	63.05	0.64	15.33	3.58	0.11	1.21	1.22	5.15	3.88	0.15	5.20	99.52	-	2.4
CKPS 9AGRN	CKPS	64.51	0.67	14.35	3.58	0.12	1.26	1.51	4.99	3.20	0.17	5.00	99.36	-	3.1
CKPS 9B	CKPS	58.06	0.59	14.29	3.04	0.07	1.63	5.33	1.17	2.28	0.16	12.70	99.32	-	2.7
CKPS 9C	CKPS	59.65	0.68	14.74	6.24	0.19	2.48	5.01	4.59	2.26	0.28	3.70	99.82	-	22
MQT-1	PJKC	95.19	0.01	0.25	0.01	-	0.03	0.02	-	0.03	-	-	95.54	26	-
MQT-64	PJKC	97.24	0.01	0.48	0.12	-	0.15	0.04	-	0.08	0.01	-	98.13	90	-
MQT-65-94PG	PJKC	96.60	0.02	0.61	0.39	0.01	0.07	0.15	0.05	0.07	0.02	0.50	98.49	-	1.8
MQT-66-94G	PJKC	96.09	0.04	0.92	0.79	0.01	0.10	0.12	0.12	0.07	0.03	0.90	99.19	-	6.1
MQT-88	PJKC	98.83	0.06	1.14	0.30	0.01	0.23	0.13	0.32	0.16	0.02	0.00	101.20	96	21
MQT-94-94DG	PJKC	96.57	0.04	0.71	0.49	0.01	0.09	0.12	0.11	0.07	0.03	0.70	98.94	-	4.2
MQT-96A-94RR	PJKC	86.40	0.02	0.24	11.63	0.02	0.07	0.11	0.02	0.02	0.04	1.00	99.57	-	19
MQT-JUR	PJKC	100.24	0.01	0.33	0.07	-	0.16	0.05	0.02	0.04	-	-	100.92	33	-
oib	WIP	-	-	-	-	-	-	-	-	-	-	-	-	-	-
e-morb	WIP	-	-	-	-	-	-	-	-	-	-	-	-	-	-
n-morb	WIP	-	-	-	-	-	-	-	-	-	-	-	-	-	-

Sample	Co	Sc	V	Cu	Pb	K	Rb	Cs	Ba	Sr	Ga	Ta	Nb	Hf	Zr	Ti	Th	U
105/15/6	29	15	125	-	17.3	24904	125	7.1	524	184.7	18.3	0.8	12.7	3.2	101.4	3837	11.3	2.6
105/18/6	12.9	4	54	-	7.6	7305	38.4	1.9	1000	493.6	4.3	0.2	3.5	0.9	28	839	3.6	2.2
105/37/5	26.8	10	65	-	15.9	18014	91.3	4.4	176	141.5	13	0.6	8.3	2.2	74.5	2518	6	0.7
105/37/6	47.2	12	89	-	17.8	23244	108.4	6	243	146.6	15	0.7	10.6	3.5	105.6	3177	7.7	0.9
417D/17/3	16.4	11	283	-	13	18014	90.8	5.1	1000	139.8	12.7	0.5	7.2	1.9	74.4	2458	6.4	9.6
417D/18/2	15.6	14	92	-	12.6	22164	124.3	6	635	67.5	19.8	0.7	9.4	2.6	95.9	3057	7	2.2
417D/19/1	12	10	81	-	15.6	15855	83.6	4.7	1948	95.5	7.8	0.3	4	1.4	54.3	1858	7.4	0.6
417D/21/3	10.5	5	480	-	13.4	15772	72.4	3	1015	134.6	7.6	0.3	4.4	1.3	48.7	1439	3.8	7.1
CKPS 4	23	15	149	77.3	26.1	15108	71.9	0.7	954	401.4	13.1	0.097	1.4	1.1	32.9	2338	1.2	0.9
CKPS 5	16.7	12	116	65.1	12.2	15025	49.9	0.3	1962	583.9	11.8	0.18	2.8	1.3	43.6	2278	1.6	0.8
CKPS 6	23.1	16	189	127.6	10.1	21085	99.8	1.2	1383	369	20.6	0.16	2.6	1.7	46.5	3537	1.2	0.5
CKPS 7	9.7	4	52	42.3	21.6	7637	26.3	1.5	1933	535.9	6.5	0.1	1.7	1.2	36.3	1259	1.8	0.6
CKPS 9ABLU	1.5	6	37	11.2	11.7	-	88.3	4.8	887	153.6	17.9	0.4	7.6	3.8	153.6	-	7.1	1.7
CKPS 9AGRN	4.3	7	36	12.9	11.4	-	61.3	4.2	839	169.8	13.3	0.4	7	3.8	148.2	-	6	2.2
CKPS 9B	2.1	6	32	11.8	15.1	18927	94.1	1.2	3235	3234	16.9	0.4	7.2	4.3	145.3	3537	7.9	2.6
CKPS 9C	16	18	122	43.6	47.7	18761	34.1	-	923	190	16.4	0.3	4.1	2.7	93.8	4077	4.3	1.4
MQT-1	-	-	-	-	0.82	249	0.94	0.14	1726	141.1	-	0.1	1.7	0.07	4.95	60	0.11	0.24
MQT-64	-	-	6	-	0.87	664	2.08	0.09	390	12.99	3	0.08	1.4	0.09	9.1	60	0.14	0.1
MQT-65-94PG	-	2	42	6.7	0.9	-	1.7	-	6951	65.8	1.1	0.2	1	-	10	-	0.2	0.2
MQT-66-94G	1.4	1	12	31.1	3.4	-	2.6	-	1400	36.2	1.5	-	0.7	-	14.4	-	0.2	0.4
MQT-88	-	-	23	110	3.37	1328	4.55	0.13	768	24.19	-	0.14	2.5	0.24	26.6	360	0.58	0.37
MQT-94-94DG	2.9	2	25	27.5	2.6	-	2	-	1178	28.7	2.3	-	1.6	-	16.6	-	0.3	1
MQT-96A-94RR	2.7	-	23	16.9	1.6	-	-	-	2671	16.4	0.9	-	0.6	-	3.6	-	0.3	0.1
MQT-JUR	-	-	24	-	3.34	332	1	0.09	717	15.7	-	0.07	1.3	0.06	5.6	60	0.06	0.11
oib	-	-	-	-	3.2	12000	21	0.387	350	660	-	2.7	48	7.8	280	17200	4	1.02
e-morb	-	-	-	-	0.6	2100	5.04	0.063	57	155	-	0.47	8.3	2.03	73	6000	0.6	0.18
n-morb	-	-	-	-	0.33	600	0.56	0.007	6.3	510	-	0.132	2.33	2.05	74	7600	0.12	0.047

TABLE VIII | **Continued**

Sample	La	Ce	Pr	Nd	Sm	Eu	Gd	Tb	Dy	Ho	Er	Tm	Yb	Lu
105/15/6	34	69.3	6.81	27.7	6.2	1.04	4.51	0.69	4.04	0.81	2.26	0.32	2.47	0.37
105/18/6	18	28.6	3.61	14.9	3.6	0.68	3.13	0.42	2.47	0.5	1.29	0.18	1.03	0.18
105/37/5	32.1	62.6	6.66	26.6	5	1.19	4.38	0.65	3.88	0.72	2.04	0.31	1.82	0.28
105/37/6	37.6	69.9	7.51	31.8	6.4	1.14	5.13	0.7	4.04	0.88	2.53	0.38	2.43	0.37
417D/17/3	42.6	58.8	8.49	38	7.7	1.64	7.57	1.1	6.54	1.53	4.19	0.63	4.11	0.61
417D/18/2	23.8	46.3	5.26	20.3	4.2	0.79	3.25	0.53	2.81	0.57	1.79	0.31	1.94	0.31
417D/19/1	42.9	83.1	11.86	54.3	9.1	2.46	9.95	1.65	8.77	1.71	4.34	0.61	3.88	0.54
417D/21/3	37.7	71.5	9.34	39.5	9	1.93	8.22	1.23	6.71	1.3	3.55	0.49	2.88	0.47
CKPS 4	9.3	13.1	2.03	9.2	2	0.62	2.24	0.39	2.31	0.47	1.4	0.23	1.55	0.21
CKPS 5	11.9	23.5	2.74	14.2	2.9	0.64	2.83	0.46	2.52	0.53	1.63	0.26	1.63	0.25
CKPS 6	16.8	21.8	3.65	19.8	3.6	1.08	3.81	0.6	3.9	0.74	2.06	0.31	2.07	0.31
CKPS 7	15.5	16.9	3.04	14	2.4	0.64	2.69	0.39	2.47	0.49	1.59	0.25	1.5	0.21
CKPS 9ABLU	32	58.8	6.96	31.7	6.2	1.64	5.33	0.72	4.32	0.89	2.35	0.35	2.43	0.36
CKPS 9AGRN	36.5	65.5	7.68	36.2	6	1.58	5.45	0.8	4.92	1	2.73	0.44	2.65	0.49
CKPS 9B	34.3	64.3	7.68	33.2	6.4	1.53	5.61	0.89	5.46	1.01	3.2	0.51	3.76	0.48
CKPS 9C	18.6	33.8	4.35	21.6	4.6	1.27	4.35	0.66	3.78	0.82	2.44	0.36	2.48	0.37
MQT-1	0.47	0.54	0.09	0.44	0.14	0.078	0.08	0.01	0.08	0.01	0.05	0.005	0.05	0.009
MQT-64	1.09	1.62	0.29	1.41	0.3	0.09	0.34	0.05	0.27	0.05	0.15	0.02	0.13	0.03
MQT-65-94PG	1.3	2.2	0.36	1.6	0.5	-	0.46	0.1	0.35	0.06	0.13	-	0.17	0.01
MQT-66-94G	2.7	4.1	0.61	2.7	0.3	-	0.58	0.09	0.58	0.13	0.39	0.08	0.55	0.1
MQT-88	2.48	3.81	0.66	2.89	0.66	0.17	0.63	0.11	0.69	0.14	0.42	0.062	0.55	0.08
MQT-94-94DG	2.4	3.1	0.59	2.8	0.5	0.11	0.59	0.09	0.54	0.09	0.24	0.06	0.35	0.04
MQT-96A-94RR	2.8	2.6	0.51	2.5	0.2	0.08	0.68	0.09	0.62	0.12	0.25	-	0.25	0.03
MQT-JUR	0.88	1.44	0.22	0.79	0.2	0.08	0.15	0.03	0.12	0.04	0.07	0.02	0.13	0.02
oib	37	80	9.7	38.5	10	3	7.62	1.05	5.6	1.06	2.62	0.35	2.16	0.3
e-morb	6.3	15	2.05	9	2.6	0.91	2.97	0.53	3.55	0.79	2.31	0.356	2.37	0.354
n-morb	2.5	7.5	1.32	7.3	2.63	1.02	3.68	0.67	4.55	1.01	2.97	0.456	3.05	0.455

TABLE IX | **Sr-,Nd- and Pb-isotope data, Atlantic and Caribbean Pelagic Sediments**

Sample	Rb	Sr	Sm	Nd	Pb	$m^{87}Sr/^{86}Sr$	$i^{87}Sr/^{86}Sr$	$m^{143}Nd/^{144}Nd$	$i^{143}Nd/^{144}Nd$	eNd	$^{206}Pb/^{204}PB$	$^{207}Pb/^{204}PB$	$^{208}Pb/^{204}PB$	Δ207/204	Δ208/204	Age (my)
CKPS4	71.9	401.4	2.0	9.2	26.1	0.70577	0.70513	0.512726	0.512649	2.467	18.90	15.65	38.60	11.02	12.29	90
CKPS5	49.9	583.9	2.9	14.2	12.2	0.70592	0.70561	0.512727	0.512654	2.578	18.92	15.61	38.68	6.81	17.87	90
CKPS6	99.8	369.0	3.6	19.8	10.1	0.70583	0.70486	0.512659	0.512594	1.407	18.94	15.61	38.75	6.59	22.45	90
CKPS7	26.3	535.9	2.4	14.0	21.6	0.70598	0.70580	0.512512	0.512451	-1.389	18.87	15.65	38.63	11.35	18.92	90
CKPS9b	94.1	3234.4	6.4	33.2	15.1	0.70522	0.70512	0.512851	0.512782	5.077	19.11	15.62	38.89	5.75	15.90	90
CKPS9c	34.1	190.0	4.6	21.6	47.7	0.70478	0.70414	0.512921	0.512845	6.302	18.89	15.65	38.60	11.13	13.50	90
417D/12/3	90.8	139.8	7.7	38.0	16	0.71489	0.71243	0.512083	0.512007	-9.929						95
105/15/6	125.0	184.7	6.2	27.7	17	0.71436	0.71140	0.512119	0.512022	-9.266	18.88	15.69	38.93	15.24	47.71	110
417D/18/2	124.3	67.5	4.2	20.3	15	0.72837	0.72103	0.511963	0.511881	-12.256	18.99	15.68	39.06	13.05	47.41	100
105/18/6	38.4	493.6	3.6	14.9	12	0.70821	0.70785	0.512196	0.512086	-7.882	18.93	15.68	38.86	13.70	34.66	115
417D/19/1	83.6	95.5	11.1	54.3	17	0.71488	0.71122	0.512187	0.512102	-7.821	18.90	15.72	39.08	18.02	60.29	105
417D/21/3	72.4	134.6	9.0	39.5	24	0.71302	0.71067	0.512202	0.512103	-7.681	19.33	15.71	38.86	12.36	-13.70	110
105/37/5	91.3	141.5	5.0	26.6	20	0.71425	0.71065	0.512151	0.512047	-8.020	18.75	15.70	38.97	17.65	67.43	140
105/37/6	108.4	146.6	6.4	31.8	22	0.71661	0.71234	0.512135	0.512020	-8.428	18.73	15.69	38.92	16.87	64.84	145

DOI: 10.1344/105.000001715

TABLE X | **Major and trace element data, Early Island Arc, Western Puerto Rico**

Sample*	BQN 300-3.6D	BQN 103-9.8A	BQN 300-1.7A	BQN 300-8	BQN 103-9.8D	BQN 300-1.2D	BQN 118-93	BQN 300-1.7C	BQN 103-9.8B	BQN 103-9.8C	BQN 300-1.7B
SiO_2	50.33	52.05	52.63	52.72	53.69	53.99	54.06	54.28	54.53	62.40	63.63
TiO_2	0.72	0.75	0.84	1.01	0.80	0.75	0.75	0.81	0.82	1.02	0.80
Al_2O_3	14.21	16.27	17.48	15.80	17.33	14.67	15.34	17.39	16.86	17.11	15.35
Fe_2O_3	9.15	8.14	8.88	7.87	8.72	9.46	6.29	8.06	8.46	6.64	7.32
MnO	0.20	0.10	0.20	0.17	0.14	0.14	0.37	0.17	0.16	0.09	0.09
MgO	3.95	3.72	4.36	2.61	4.00	4.87	2.07	3.20	3.70	0.60	1.12
CaO	9.14	7.64	9.05	6.80	7.25	8.24	8.89	7.96	7.10	5.05	2.74
Na_2O	3.44	1.77	2.47	5.55	2.99	3.51	4.81	3.29	3.05	3.24	6.30
K_2O	0.61	0.29	0.79	0.61	1.86	2.21	0.42	1.67	2.11	2.09	0.50
P_2O_5	0.32	0.33	0.34	0.36	0.36	0.33	0.28	0.36	0.37	0.32	0.31
LOI	7.4	8.8	2.7	6.3	2.7	2.0	6.4	3.0	2.5	1.4	2.1
Total	99.47	99.86	99.74	99.80	99.84	100.17	99.68	100.19	99.66	99.96	100.26
Cr	369	21	22	7	22	335	103	28	27	28	21
Ni	112	8.4	8.9	6.2	14.9	32.9	42.7	13.9	12.6	6	6.5
Co	35.3	22.7	27.2	20.2	27.2	35.3	25.5	25.3	22.2	10.7	15.2
Sc	29	18	23	17	23	35	25	25	20	17	17
V	143	188	228	180	197	244	190	225	202	165	176
Cu	55.5	16.9	97.1	44.7	73.3	7.3	101.6	16.4	57.4	22.9	32.8
Pb	6.2	3.1	26.8	7.5	31.4	3	2.4	4.2	2.2	3.6	4.4
Zn	54	47	50	68	67	50	62	76	70	46	33
Rb	14.7	2.2	6.2	11.1	41.5	39.9	5.4	26.5	42.6	48.4	8.4
Cs	0.5	0.7	0	0.9	0.3	0.9	0.3	0.8	0.2	0.8	0.9
Ba	398	289	1046	444	865	1394	1427	1399	895	943	437
Sr	561.6	360.4	1384.6	474.1	581	651.7	572.9	752.6	566.4	525.4	505.3
Ga	17.3	19.9	19.2	16.1	19.9	16.2	15.7	20.4	20.3	18	12.9
Ta	0.8	0.9	0.8	1.7	1	0.8	0.9	1	0.8	1.8	1.6
Nb	10.9	11.8	11.6	24.9	13.4	10.6	11.8	13.3	13.4	26	23.5
Hf	3.8	3.5	3.6	4.5	3.4	3.3	3.7	3.9	3.6	4.9	4.8
Zr	121.8	136.1	111.6	184.3	125.4	114.7	124	129.5	147	181.2	160.2
Y	21.4	20.2	20.5	24	23.4	19.7	21.1	22.5	21.7	35.8	18.6
Th	3.2	3.5	3.9	3.8	4.4	4.4	3.3	4.7	3.7	5.9	5.3
U	0.4	1.1	1.7	1.3	1.6	0.8	1.1	1.4	1.5	1.8	1.5
La	22.7	20.7	22.2	33.5	23	18.5	23.1	22.6	21.9	35	34.6
Ce	43.5	40.2	40.8	60.1	43.9	36.7	40.6	41.8	43.1	60.8	56.4
Pr	5.34	4.83	5.23	7.24	5.76	4.79	5.3	5.59	5.29	7.68	6.57
Nd	21.8	19.6	23.1	26.9	23.6	21.2	21.3	23.5	21.3	30.4	25
Sm	4.3	3.7	4.3	6	4.7	4.1	4.2	4.7	4.2	5	4.9
Eu	1.19	1.46	1.19	1.67	1.36	1.09	1.26	1.33	1.38	1.78	1.33
Gd	3.71	3.63	4.16	4.4	4.22	4.38	4.46	4.47	4.08	4.76	3.86
Tb	0.61	0.62	0.61	0.68	0.65	0.6	0.63	0.66	0.59	0.82	0.55
Dy	3.35	4	3.54	3.96	3.99	3.49	3.63	3.59	3.99	5.04	3.44
Ho	0.66	0.72	0.67	0.69	0.72	0.74	0.69	0.85	0.73	1.14	0.66
Er	2	2.13	1.9	2.15	2	1.94	1.98	2.2	2.11	3.17	1.86
Tm	0.3	0.32	0.3	0.34	0.35	0.32	0.29	0.32	0.25	0.47	0.29
Yb	2.1	2.31	1.83	2.29	2.21	1.99	1.94	1.96	1.93	3.14	1.77
Lu	0.36	0.31	0.34	0.34	0.31	0.32	0.35	0.38	0.31	0.45	0.32

* Boquerón (BQN) & Río Loco (RL) data adapted from Jolly et al. (2007).

DOI: 10.1344/105.000001715

TABLE X | **Continued**

Sample*	LJS 07-02	LJS 100-9.3	LJS 300-5.1	LJS 103-5.7	LJS 103-12.3B	LJS 110-93	LJS 300-4.8	LJS 300-4.1	LJS 301-4.2	LJS 312-2.1A	RL371/4.1
SiO_2	55.42	55.75	55.97	56.79	56.98	57.17	58.30	62.11	62.22	63.88	51.74
TiO_2	0.83	1.17	0.71	0.82	0.85	0.88	0.81	0.75	0.91	0.83	0.75
Al_2O_3	16.32	17.13	16.19	16.46	17.53	16.09	17.60	16.64	15.30	16.03	10.84
Fe_2O_3	6.68	8.45	6.65	6.35	7.90	7.56	7.09	5.13	6.45	6.53	8.97
MnO	0.11	0.14	0.17	0.20	0.19	0.12	0.10	0.07	0.09	0.05	0.19
MgO	2.65	2.53	2.93	0.86	1.74	4.07	2.68	0.63	2.03	0.70	7.78
CaO	7.32	4.12	7.09	6.34	6.04	3.06	4.16	4.26	6.21	4.38	8.61
Na_2O	2.86	5.91	2.99	5.14	3.79	3.94	3.26	5.71	3.10	3.43	2.93
K_2O	0.34	0.78	1.61	1.67	1.22	2.39	2.70	1.09	1.50	2.34	1.65
P_2O_5	0.29	0.33	0.32	0.28	0.26	0.32	0.29	0.30	0.29	0.24	0.24
LOI	7.0	3.5	5.4	5.4	3.3	4.1	3.2	3.0	1.8	1.4	6.4
Total	99.82	99.81	100.03	100.31	99.80	99.70	100.19	99.69	99.90	99.81	100.10
Cr	-	-	-	-	-	-	-	-	-	-	422
Ni	2.8	9.4	4.2	11.3	6.5	6.7	6.1	3.9	52.7	14.4	60
Co	17.7	19.7	15.5	13	22.8	19.3	18.6	6.7	14.6	12.3	36
Sc	15	17	12	17	16	17	17	13	17	17	26
V	146	182	130	149	173	143	112	149	175	114	221
Cu	25.5	38.2	16.4	36.4	19.1	18.4	12	92.2	29.6	26.6	33
Pb	2.4	4	3.6	2.3	2.5	18.5	3.3	14	35.9	31.5	1
Zn	48	76	53	34	73	59	56	18	28	18	70
Rb	3.5	11.4	36	35.4	21.8	40.3	56.4	24.5	34.1	47.8	33
Cs	0.7	0.6	1	0.8	0.5	0.5	0.4	0.9	0.4	0.4	0.3
Ba	654	616	988	899	961	974	1191	678	1059	1515	1486
Sr	369.4	563.5	546.6	581.3	511.3	400.3	489.8	676.8	546.4	549.9	212
Ga	18.2	20	17.8	19.3	18.7	20.4	20.3	14.6	19.9	17.7	19
Ta	1.7	1.6	1.6	1.4	1.6	1.4	1.5	1.6	1.4	1.3	0.8
Nb	21	29.1	22.8	19	22.7	19	18.9	21.1	20.7	18.3	11.9
Hf	4	5.6	4.8	4.4	4.7	4.7	4.1	4.6	4.1	5.1	2.5
Zr	159.1	208.6	189.5	164	179.9	170.3	139.5	170.6	156.8	186.1	94
Y	19	23	20.3	17.3	18.1	18.9	26.1	15.8	19.1	14.7	14
Th	6.2	5.9	5.2	3.4	4.9	5.5	5	4.9	4.5	4.3	2.5
U	1.3	1.4	1.3	1.2	1.6	1	1.1	1.1	1.6	1.1	1.2
La	25.9	33.9	33.2	28.8	29.3	26.3	33.7	31.3	28.3	25.2	17.6
Ce	47.6	64.5	56.4	48.4	49.7	48.4	48.6	52.1	49.5	44.3	33.6
Pr	5.59	7.73	6.72	5.88	5.77	5.73	6.92	5.85	6.2	5.33	4.28
Nd	21.7	28.8	27	23.2	22.5	21.3	28.1	21.1	25.3	21	18
Sm	3.8	6.7	5.5	4.7	3.6	4.3	6.4	3.6	4.7	3.7	3.9
Eu	1.22	1.6	1.41	1.34	1.47	1.14	1.74	1.01	1.52	1.31	1.03
Gd	3.54	4.6	3.91	3.68	3.87	3.43	5.4	2.98	4.15	3.51	3.23
Tb	0.59	0.78	0.61	0.5	0.55	0.58	0.75	0.51	0.59	0.51	0.45
Dy	3.65	3.86	3.47	3.33	2.96	3.32	4.26	2.71	3.5	2.54	2.55
Ho	0.77	0.76	0.66	0.58	0.62	0.64	0.91	0.56	0.7	0.5	0.48
Er	1.94	2.13	2.12	1.63	1.84	2.11	2.57	1.63	1.8	1.42	1.35
Tm	0.28	0.29	0.29	0.2	0.27	0.28	0.34	0.22	0.24	0.21	0.22
Yb	1.91	1.92	2.02	1.54	1.81	2.07	2.34	1.31	1.89	1.55	1.35
Lu	0.31	0.28	0.33	0.28	0.29	0.23	0.37	0.22	0.26	0.23	0.19

* Boquerón (BQN) & Río Loco (RL) data adapted from Jolly et al. (2007).

TABLE X | **Continued**

Sample*	RL01-02	RL5A	RL06-02	RL366/1.3	RL365/7.1	RL03-02	RL43-94	Rl365/3.6	RL366/1.4	RL365/3.8	RL366/1.3
SiO_2	53.68	53.71	54.32	55.03	55.08	55.61	56.47	56.67	57.01	57.04	57.41
TiO_2	0.61	0.61	0.78	0.62	0.80	0.61	0.81	0.75	0.77	0.72	0.69
Al_2O_3	10.93	10.75	12.08	11.17	11.76	10.86	11.62	11.85	12.93	11.72	11.78
Fe_2O_3	9.11	7.10	9.62	8.89	9.74	9.16	8.61	8.61	8.03	8.60	8.34
MnO	0.14	0.12	0.15	0.14	0.14	0.14	0.13	0.13	0.12	0.12	0.14
MgO	10.33	7.52	8.34	9.12	7.79	9.59	7.47	7.85	6.97	7.84	6.97
CaO	7.50	9.11	6.93	7.31	7.53	7.46	7.46	6.83	5.93	6.79	7.64
Na_2O	2.35	3.00	2.19	2.45	2.19	2.35	1.90	1.86	2.41	1.67	3.04
K_2O	0.52	0.67	1.97	1.24	1.48	0.65	2.02	2.00	3.12	2.00	0.72
P_2O_5	0.29	0.28	0.29	0.26	0.26	0.29	0.24	0.28	0.31	0.28	0.27
LOI	4.1	6.9	2.8	3.5	3.0	2.8	3.2	2.9	2.1	2.9	2.6
Total	99.56	99.77	99.47	99.73	99.77	99.52	99.93	99.73	99.70	99.68	99.60
Cr	246	246	280	510	420	270	287	363	253	368	335
Ni	158	38	120	63	46	174	100	45	51	49	40
Co	40	27	39	37	41	41	33	32	30	33	30
Sc	30	20	27	27	30	31	26	27	21	26	24
V	195	184	223	189	234	185	174	212	208	201	205
Cu	0	72	0	57	77	0	85	67	88	70	58
Pb	3	22	2	94	4	4	2	5	15	9	157
Zn	0	41	0	48	54	0	70	52	54	55	43
Rb	12	13	43	24	24	12	40	53	54	48	13
Cs	0	0	0.9	0.2	0.2	0	0.2	0.8	0.5	0.7	0.1
Ba	662	904	1434	825	762	747	1222	1886	1452	1803	876
Sr	521	540	455	450	472	549	421	682	615	707	591
Ga	15	13	16	16	17	13	14	16	17	17	14
Ta	0.7	1.1	0.7	0.8	0.7	0.7	0.9	1.2	1	1	0.8
Nb	12.5	14	11.9	11.6	10.8	12.2	13.6	17.2	16.1	15.7	13.1
Hf	2.7	3.3	2.4	2.3	2.5	2.2	2.7	3.5	2.9	3.4	2.8
Zr	95	111	92	95	91	95	100	131	122	124	111
Y	12	14	13	12	15	12	12	15	17	15	13
Th	4	4.6	3.6	3.6	3.4	3.1	3.3	5.1	4.4	4.5	4.7
U	1.6	1.7	0.9	0.8	0.8	1.2	1.4	1	1.3	1.3	1.7
La	22.4	23.4	18.5	22.2	18.3	22	20.6	26.4	24.4	26.6	23.1
Ce	38.5	41.8	32.7	39.4	32.3	38	35.7	48.2	42.6	45.2	41.4
Pr	4.59	5.16	4.12	4.77	4.17	4.57	4.5	5.73	4.94	5.5	5.2
Nd	19.1	20.3	17.2	19.1	16.5	18.8	18.7	21.8	29.6	21.5	19.7
Sm	3.6	4.3	3.6	3.5	3.4	3.8	3.3	4.5	3.5	4.1	4.1
Eu	0.99	1.04	0.98	0.97	1.02	0.93	0.93	0.81	0.88	0.84	1.12
Gd	2.94	3	3.26	3.15	3.19	2.66	2.67	3.85	3.51	3.54	3.12
Tb	0.39	0.39	0.44	0.4	0.44	0.38	0.36	0.46	0.47	0.43	0.38
Dy	1.78	2.52	2.25	2.1	2.41	2	1.97	2.37	2.53	2.52	2.46
Ho	0.4	0.39	0.43	0.36	0.53	0.4	0.37	0.49	0.51	0.48	0.44
Er	0.98	1.2	1.19	1.15	1.45	1.09	1.07	1.39	1.32	1.22	1.29
Tm	0.14	0.2	0.15	0.19	0.19	0.17	0.14	0.21	0.2	0.19	0.17
Yb	0.98	1.21	1.06	1.24	1.56	0.98	1.04	1.29	1.36	1.19	1.11
Lu	0.17	0.15	0.18	0.15	0.21	0.17	0.16	0.21	0.19	0.17	0.18

* Boquerón (BQN) & Río Loco (RL) data adapted from Jolly et al. (2007).

DOI: 10.1344/105.000001715

TABLE X | **Continued**

Sample*	RL366/2.5	RL366/2.0	RL365/3.2	RL365/3.2	RL79-94	RL366/5.4
SiO_2	57.43	57.52	58.05	58.05	58.37	58.50
TiO_2	0.69	0.74	0.73	0.73	0.87	0.77
Al_2O_3	11.69	12.05	12.15	12.15	11.97	11.79
Fe_2O_3	8.02	8.54	8.02	8.02	8.31	8.34
MnO	0.12	0.12	0.12	0.12	0.13	0.12
MgO	7.85	7.18	6.63	6.63	6.82	6.38
CaO	7.66	7.26	6.62	6.62	6.90	5.30
Na_2O	1.72	2.43	3.27	3.27	1.75	2.80
K_2O	1.81	1.25	1.11	1.11	2.15	2.72
P_2O_5	0.27	0.28	0.28	0.28	0.28	0.29
LOI	2.4	2.4	2.8	2.8	2.0	2.2
Total	99.66	99.77	99.78	99.78	99.55	99.21
Cr	335	335	253	288	275	300
Ni	48	41	40	40	112	51
Co	30	31	29	29	30	32
Sc	25	25	24	24	26	24
V	196	202	189	189	204	225
Cu	75	52	68	68	0	82
Pb	3	3	11	11	4	4
Zn	47	49	51	51	0	51
Rb	39	28	21	21	53	69
Cs	0.1	0.2	0.3	0.3	1	0.7
Ba	1791	981	771	771	1191	1440
Sr	662	621	465	465	589	389
Ga	16	18	16	16	15	18
Ta	0.9	1.1	1	1	1.2	1.1
Nb	15	16	15.9	15.9	17.1	16.5
Hf	3.3	3.5	2.9	2.9	3.2	3.3
Zr	122	125	122	122	129	132
Y	15	15	15	15	14	14
Th	5.5	4.4	4.1	4.1	4.3	3.5
U	1	1.1	1.7	1.7	2.4	1.7
La	24.6	25.1	24.6	24.6	25.5	27
Ce	42.8	44.8	45.8	45.8	46.9	49
Pr	5.17	5.16	5.18	5.18	5.62	5.77
Nd	21.7	20.6	20.2	20.2	24.3	22
Sm	4.3	4.9	3.7	3.7	4.1	4.3
Eu	0.86	1.05	1.16	1.16	1.13	1.05
Gd	3.35	3.15	3.27	3.27	3.05	3.18
Tb	0.38	0.44	0.48	0.48	0.48	0.47
Dy	2.11	2.34	2.86	2.86	2.53	2.63
Ho	0.42	0.47	0.47	0.47	0.46	0.47
Er	1.2	1.16	1.52	1.52	1.29	1.38
Tm	0.19	0.2	0.23	0.23	0.18	0.18
Yb	1.17	1.28	1.15	1.15	1.08	1.19
Lu	0.17	0.16	0.15	0.15	0.2	0.19

* Boquerón (BQN) & Río Loco (RL) data adapted from Jolly et al. (2007).

Geologica Acta, Vol.9, Nos 3-4, September-December 2011, 289-306
DOI: 10.1344/105.000001713
Available online at www.geologica-acta.com

geologica acta

Petrogenesis of fertile mantle peridotites from the Monte del Estado massif (Southwest Puerto Rico): a preserved section of Proto-Caribbean lithospheric mantle?

C. MARCHESI [1] [2] [*] **W.T. JOLLY** [3] [†] **J.F. LEWIS** [4] **C.J. GARRIDO** [2] **J.A. PROENZA** [5] **E.G. LIDIAK** [6]

[1] **Géosciences Montpellier**
UMR 5243, CNRS-Université Montpellier II, Place E. Bataillon, 34095 Montpellier, France. E-mail: claudio.marchesi@gm.univ-montp2.fr

[2] **Instituto Andaluz de Ciencias de la Tierra, CSIC-Universidad de Granada**
Avenida de las Palmeras 4, 18100 Armilla (Granada), Spain. Marchesi E-mail: claudio@iact.ugr-csic.es Garrido E-mail: garrido@iact.ugr-csic.es

[3] **Department of Earth Sciences, Brock University, St Catharines**
Ontario L2S 3A1, Canada

[4] **Department of Earth and Environmental Sciences, The George Washington University**
Washington DC 20052, U.S.A. E-mail: jlewis@gwu.edu

[5] **Departament de Cristal·lografia, Mineralogia i Dipòsits Minerals, Facultat de Geologia, Universitat de Barcelona (UB)**
Martí i Franquès s/n, 08028 Barcelona, Spain. E-mail: japroenza@ub.edu

[6] **Department of Geology and Planetary Science, University of Pittsburgh**
Pittsburgh PA 15269, U.S.A. E-mail: egl+@pitt.edu

* Corresponding author
† Deceased

ABSTRACT

The Monte del Estado massif is the largest and northernmost serpentinized peridotite belt in southwest Puerto Rico. It is mainly composed of spinel lherzolite and minor harzburgite with variable clinopyroxene modal abundances. Mineral and whole rock major and trace element compositions of peridotites coincide with those of fertile abyssal mantle rocks from mid ocean ridges. Peridotites lost 2-14 wt% of relative MgO and variable amounts of CaO by serpentinization and seafloor weathering. HREE contents in whole rock indicate that the Monte del Estado peridotites are residues after low to moderate degrees (2-15%) of fractional partial melting in the spinel stability field. However, very low LREE/HREE and MREE/HREE in clinopyroxene cannot be explained by melting models of a spinel lherzolite source and support that the Monte del Estado peridotites experienced initial low fractional melting degrees (~ 4%) in the garnet stability field. The relative enrichment of LREE in whole rock is not due to alteration processes but probably reflects the capture of percolating fluid/melt fractions or the crystallization of sub-percent amounts of hydrous minerals (e.g., amphibole, phlogopite) along grain boundaries or as microinclusions in minerals.

We propose that the Monte del Estado peridotite belt represents a section of ancient Proto-Caribbean (Atlantic) lithospheric mantle originated by seafloor spreading between North and South America in the Late Jurassic-Early Cretaceous. This portion of oceanic lithospheric mantle was subsequently trapped in the forearc region of the Greater Antilles paleo-island arc generated by the northward subduction of the Caribbean plate beneath the Proto-Caribbean ocean. Finally, the Monte del Estado peridotites belt was emplaced in the Early Cretaceous probably as result of the change in subduction polarity of the Greater Antilles paleo-island arc without having been significantly modified by subduction processes.

KEYWORDS | **Abyssal peridotite. Fractional melting. Ophiolite. Proto-Caribbean plate. Puerto Rico.**

INTRODUCTION

Ophiolitic peridotites are an important source of information on the composition of the oceanic lithospheric upper mantle (e.g., Bodinier and Godard, 2003) and their petrological study offers complementary knowledge on ophiolite origin to that obtained from crustal rocks. In the Caribbean region, mantle peridotites mainly crop out as isolated dismembered bodies in tectonic belts along the northern margin of the Caribbean plate (Lewis et al., 2006a). The most extensive exposures are in eastern Cuba but good outcrops are also found in Guatemala, Jamaica, Hispaniola and Puerto Rico (Fig. 1). Detailed geochemical studies in Cuba (Proenza et al., 1999a, b; Marchesi et al., 2006) and preliminary studies in central Hispaniola (Lewis et al., 2006b) demonstrated that most Caribbean ophiolites are sections of supra-subduction lithosphere tectonically associated with arc-related rocks. However, preliminary mineralogical studies of peridotites from Loma Caribe in the central Dominican Republic (Lewis et al., 2006b; Proenza et al., 2007) and the Río Guanajibo belt in southwest Puerto Rico (Jolly et al., 2008a) showed that the Caribbean ophiolites are compositionally highly heterogeneous at the massif scale and that different types of Jurassic-Cretaceous oceanic lithospheric mantle crop out in the northern Caribbean plate margin.

In southwest Puerto Rico, three main ultramafic massifs crop out: the Monte del Estado, the Río Guanajibo, and the Sierra Bermeja peridotite belts (Fig. 2A). They were probably emplaced in the Early Cretaceous (Mattson, 1979; Curet, 1986; Jolly et al., 1998; Schellekens, 1998) and are possibly dismembered portions of an originally unique peridotite body. In this paper we present mineral and whole rock major and trace element compositions of mantle peridotites from the Monte del Estado massif, the largest and northernmost ultramafic belt in southwest Puerto Rico. In particular, we present the first in situ trace element Laser Ablation-Multi Collector Inductively Coupled Plasma-Mass Spectrometry (LA-ICP-MS) analyses of clinopyroxene and orthopyroxene in these rocks. We mainly exploit the data to: 1) assess the role of alteration on the whole rock composition of peridotites; 2) characterize the primary magmatic processes (i.e., partial melting and melt-rock interaction) recorded in their mineral and whole rock compositions; and 3) discuss the origin and tectonic setting of the Monte del Estado mantle section in the frame of the Mesozoic tectonic evolution of the Caribbean.

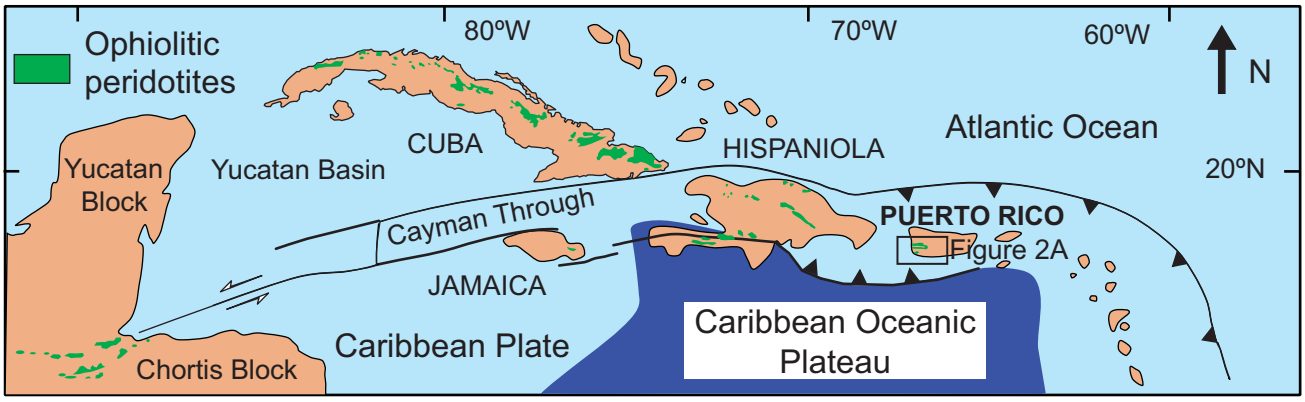

FIGURE 1 | **Geographic location of ophiolitic peridotites in the northern Caribbean (coloured areas).**

GEOLOGICAL SETTING

In southwest Puerto Rico serpentinized peridotites are exposed in three east-west to northwest-southeast trending belts. Originally all three belts were geologically grouped together as the Bermeja Complex (Mattson, 1960) but were subsequently distinguished as the Monte del Estado, the Río Guanajibo and the Sierra Bermeja serpentinized peridotite belts (after Jolly et al., 1998) (Fig. 2A).

The Monte del Estado massif is the largest and northernmost peridotite body in SW Puerto Rico and forms a continuous outcrop that extends for ~ 30km from the city of Mayagüez at the west coast southeastward to the municipality of Yauco (Fig. 2A). The belt is 6km wide near its centre but narrows to about 1 to 3km wide along the northwest region. The dominant lithology is lherzolite that is variably sheared in the different areas of the massif. Orthopyroxene-bearing microgabbros (the Río Loco Formation) of probable Campanian age (Llerandi Román, 2004; Jolly et al., 2007) and minor pillow lavas are in direct contact with the mantle rocks and are mainly concentrated along the margins of the massif. Deformed and fragmented basaltic dykes and pod-like segregations also frequently intrude the peridotites.

The Cordillera Fault, associated with a left-lateral displacement of ~ 10km, bounds the Monte del Estado massif on the north (Fig. 2A). In this area the Monte del Estado peridotite is overlain by the Yauco Formation of Campanian-Maastrichtian age which consists of volcanoclastic and calcareous sedimentary rocks, sandstone, bedded chert and conglomerate with minor blocks of limestone occasionally enclosed in the peridotite (Mattson, 1960; McIntyre et al., 1970; Volckmann, 1984). To the southwest of the peridotite body, the Rosario domain separates the Monte del Estado massif from the Río Guanajibo peridotite belt (Fig. 2A). The Rosario domain exposes the Sabana Grande Formation which consists of andesitic volcanic rocks, breccia and lava flows, conglomerate, sandstone, calcareous mudstone, rare tuff, amphibolite and serpentinite blocks (Mattson, 1960; Llerandi Román, 2004).

An extensive unit of fragmental serpentinite forms a thick (0.5km) regolith inter-fingered with the Lower Yauco Formation along the northeastern contacts of the Monte del Estado peridotite belt. Similar regolithic material is present along the southwest margin of the ultramafic body where it forms ~ 10m thick, discontinuous units (Curet, 1986).

The emplacement of Monte del Estado peridotite has been ascribed to a collisional or diapiric event in the Early Cretaceous (Mattson, 1979; Curet, 1986; Jolly et al., 1998; Schellekens, 1998). In addition, recent structural data indicate that after the emplacement the serpentinite body was thrust southward in the Paleocene-Early Oligocene (Laó-Dávila, 2008).

SAMPLING AND PETROGRAPHY

For this study we selected 19 mantle peridotites that crop out in the different areas of the Monte del Estado massif (Fig. 2B) and are representative of all the lithological types recognized during the comprehensive sampling carried out by W.T. Jolly and E.G Lidiak. Careful petrographic observations show that 11 samples are spinel lherzolites, 3 are clinopyroxene-rich spinel lherzolites, 3 are clinopyroxene-poor spinel lherzolites and 2 are spinel harzburgites.

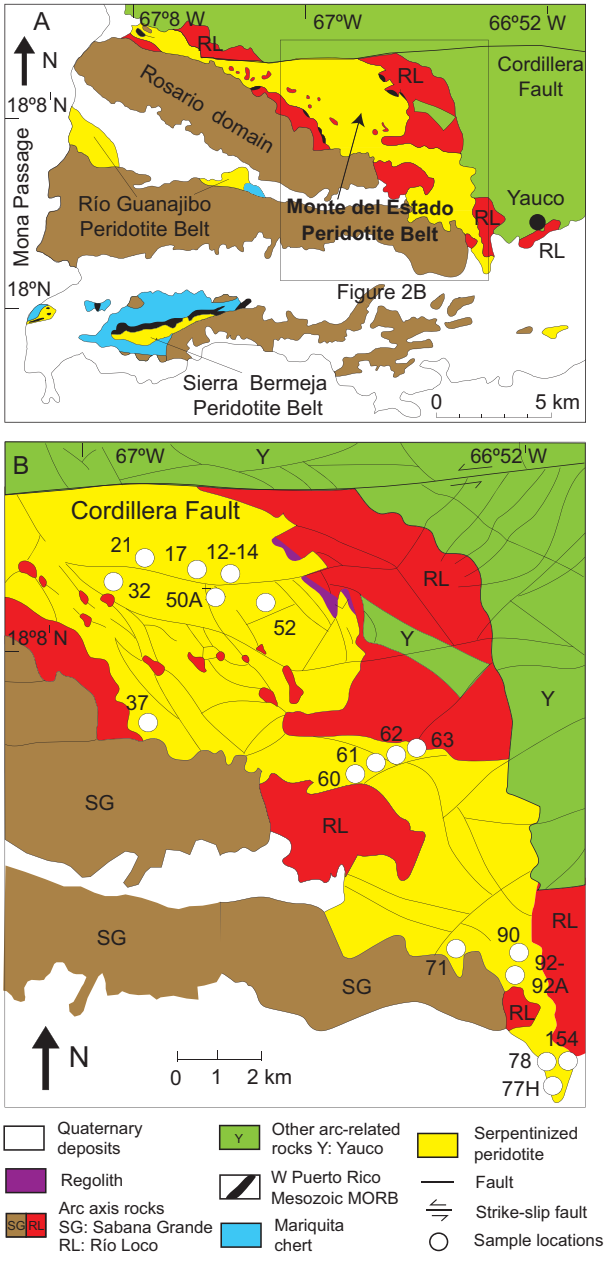

FIGURE 2 | **A) Geological sketch map of SW Puerto Rico with the location of the Monte del Estado, Río Guanajibo and Sierra Bermeja peridotite belts. B) Geological sketch map of the Monte del Estado massif with the location of the samples (circles).**

In hand specimen, least altered rocks are black to dark greenish brown, while altered types are typically pale green. Widespread secondary veining and serpentinization are common in all the samples but petrographic analysis was possible because secondary processes preserved the original grain textures, and because alteration of olivine, orthopyroxene, clinopyroxene and spinel produced distinctive pseudomorphic textural features that are substantially different from each other.

Relict olivine occurs as colorless clear grains measuring from 0.5 to 2.5mm in diameter, averaging about 1mm. Serpentinized olivine grains are readily identifiable and they are normally encircled by fibrous serpentine and magnetite-rich rims. Usually olivine pseudomorphs are anhedral and have hourglass or radial extinction. Orthopyroxene is pale brownish or colorless, euhedral to subhedral in shape, and commonly occurs as large porphyroclasts up to 5cm in diameter or as a minor 1-4mm component of the matrix. Round orthopyroxene porphyroclasts are occasionally arranged in clusters that show a weak alignment. Orthopyroxene also forms strongly elongated 1-3mm grains with lobate boundaries that suggest resorption by olivine. Many porphyroclasts have undulose extinction and kink banding of clinopyroxene exsolution lamellae that normally are unaltered even in completely serpentinized enclosing grains. Alteration mainly occurs along cleavage planes. Relict clinopyroxene is colorless to slightly pale green, and occurs with anhedral to subhedral prismatic habit. Grains range in diameter from 0.2 to about 2mm. Average 2V optic angles are about 60°, indicating Ca-rich diopside compositions. Altered clinopyroxene appears as a mass of inter-fingering fibers of slightly greenish serpentine commonly associated with brownish brucite. Original prismatic shapes and cleavages are preserved in altered grains, and, in contrast to serpentinized orthopyroxene, clinopyroxene bastite has as a mesh-like texture. Spinel usually occurs as fresh, small and relatively abundant grains that have uniform brown to reddish brown color. The grains range from 0.5 to 3 mm in diameter and are ubiquitously altered along margins to Fe-rich spinel, globular masses of magnetite and lesser hematite. The common shape of spinel grains is highly vermicular suggesting a residual nature.

Serpentine appears frequently in localized veins, up to 5mm thick, that show an internal layering. Individual grains of main minerals split by these veins are rarely displaced, thus indicating that little deformation occurred following serpentinization. Magnetite normally forms granular octahedral crystals along margins of olivine relicts and irregular rims or masses close to spinel. Magnetite is commonly altered, at a late stage, to hematite, which usually stains entire specimens producing pink colors in hand specimens. Tiny grains of clear, pale brown, granular brucite are restricted to relicts of clinopyroxene, where it appears in association with fibrous serpentine or isolated in embayments or pods.

ANALITYCAL TECHNIQUES

Mineral chemistry

Major element compositions of minerals were obtained in rock thin sections by electron microprobe analysis using a CAMECA SX 50 instrument at the Serveis Cientificotècnics of the Universitat de Barcelona (Spain). Excitation voltage was 20kV and beam current 15nA, except for analyses of Cr spinel for which a current of 20nA was preferred. Most elements were measured with a counting time of 10s, except for Ni, V and Zn (30s). Representative electron microprobe analysis data of minerals are given in Tables 1-4.

In situ trace element analyses of clinopyroxene and orthopyroxene were carried out by LA-ICP-MS in ~150μm thick sections of 6 samples (three lherzolites, one clinopyroxene-rich lherzolite, one clinopyroxene-poor lherzolite

TABLE 1 | **Representative EMP analyses of olivine in Monte del Estado peridotites**

Lithology	Lherzolite												Cpx-rich lherzolite					
Sample	60-93					62-93					50A-94		17-94					
SiO_2 (wt%)	42.09	41.76	41.65	40.83	41.95	41.81	41.33	41.48	41.76	41.11	42.31	43.13	41.07	41.54	43.02	41.69	41.52	41.16
TiO_2	0.02	0.02	0.00	0.02	0.01	0.00	0.00	0.01	0.00	0.01	0.01	0.01	0.00	0.00	0.00	0.02	0.01	0.02
Al_2O_3	0.00	0.00	0.00	0.00	0.00	0.00	0.00	0.01	0.01	0.01	0.00	0.00	0.00	0.00	0.00	0.00	0.00	0.00
Cr_2O_3	0.03	0.03	0.02	0.02	0.02	0.04	0.01	0.00	0.01	0.01	0.05	0.01	0.01	0.00	0.01	0.00	0.03	0.04
FeO	9.73	9.80	9.90	9.45	9.64	9.41	9.80	9.80	9.77	9.87	9.34	9.30	10.15	10.03	10.08	10.22	10.20	10.14
MnO	0.17	0.05	0.16	0.17	0.16	0.16	0.13	0.12	0.17	0.16	0.12	0.16	0.15	0.12	0.13	0.10	0.16	0.15
MgO	48.05	48.71	47.81	48.64	48.18	48.49	48.36	48.26	47.93	48.53	47.61	47.86	48.42	47.95	46.31	47.57	48.68	49.22
NiO	0.40	0.40	0.39	0.45	0.41	0.39	0.39	0.37	0.35	0.43	0.40	0.36	0.45	0.36	0.43	0.46	0.49	0.42
CaO	0.02	0.03	0.00	0.03	0.00	0.01	0.02	0.03	0.00	0.03	0.08	0.03	0.01	0.01	0.00	0.01	0.00	0.01
Total	100.51	100.80	99.93	99.61	100.37	100.31	100.04	100.08	100.00	100.16	99.92	100.86	100.26	100.01	99.98	100.07	101.09	101.16
Mg #	89.7	89.8	89.7	90.4	89.7	90.3	89.8	89.8	89.7	89.8	90.1	90.1	89.4	89.7	88.9	89.2	89.3	89.4

Cpx = clinopyroxene; Mg # = 100*Mg/(Mg+Fe^{2+}) cationic ratio

TABLE 2 | **Representative EMP analyses of orthopyroxene in Monte del Estado peridotites**

Lithology	Lherzolite														Cpx-rich	
Sample	60-93						62-93						50A-94	52-94	37-94	
SiO_2 (wt%)	56.57	56.60	56.68	56.82	55.84	53.91	56.92	57.21	56.18	57.88	56.71	57.14	53.89	53.25	54.16	54.65
TiO_2	0.09	0.08	0.09	0.09	0.09	0.07	0.12	0.12	0.12	0.11	0.09	0.10	0.06	0.05	0.08	0.06
Al_2O_3	3.92	4.22	4.26	4.31	5.28	4.68	3.52	3.82	3.98	3.49	3.69	3.90	5.38	5.43	4.65	5.19
Cr_2O_3	0.41	0.46	0.47	0.51	0.66	0.56	0.38	0.38	0.43	0.34	0.39	0.40	0.66	0.77	0.47	0.63
FeO	6.49	6.41	6.39	6.28	6.38	6.59	6.70	6.50	6.57	6.57	6.30	6.37	6.43	6.73	6.48	6.17
MnO	0.16	0.15	0.12	0.17	0.10	0.11	0.21	0.16	0.23	0.11	0.20	0.18	0.19	0.12	0.16	0.12
MgO	32.13	32.43	32.38	32.00	31.31	33.43	32.67	32.32	32.51	32.16	32.22	32.22	32.72	32.84	32.85	32.18
CaO	0.50	0.62	0.69	0.72	0.82	0.52	0.55	0.67	0.65	0.50	0.67	0.62	0.59	0.42	0.56	1.93
Na_2O	0.03	0.06	0.01	0.04	0.04	0.00	0.00	0.06	0.04	0.04	0.05	0.03	0.00	0.01	0.02	0.07
Total	100.30	101.03	101.09	100.94	100.52	99.87	101.07	101.24	100.71	101.20	100.32	100.96	99.92	99.62	99.43	101.00
Mg #	89.6	90.2	90.1	90.1	89.9	90.0	89.7	89.6	89.7	89.6	90.2	90.1	90.3	90.0	90.2	90.4

Cpx = clinopyroxene; Mg # = 100*Mg/(Mg+Fe^{2+}) cationic ratio

TABLE 3 | **Representative EMP analyses of clinopyroxene in Monte del Estado peridotites**

Lithology	Lherzolite																			
Sample	60-93						62-93									91-94				
SiO_2 (wt%)	52.02	51.90	52.84	52.46	52.71	51.65	53.02	51.86	51.94	52.39	52.13	53.61	53.72	53.20	52.76	53.42	54.09	53.21	53.43	52.83
TiO_2	0.28	0.27	0.28	0.31	0.27	0.35	0.47	0.41	0.46	0.43	0.45	0.47	0.47	0.52	0.45	0.15	0.19	0.26	0.22	0.23
Al_2O_3	6.39	6.19	6.28	6.44	6.33	5.07	5.32	5.82	5.95	5.87	5.75	4.60	4.96	5.15	4.93	3.55	3.10	4.08	4.00	4.02
Cr_2O_3	1.07	1.01	1.04	1.10	1.06	0.85	0.72	0.81	0.97	0.99	0.89	0.60	0.64	0.68	0.58	0.71	0.53	0.76	0.72	0.74
FeO	2.50	2.42	2.69	2.53	2.53	2.13	2.25	2.48	2.35	2.40	2.31	2.27	2.46	2.53	1.95	2.24	2.31	2.29	2.28	2.34
MnO	0.07	0.08	0.05	0.11	0.05	0.13	0.11	0.07	0.06	0.06	0.11	0.01	0.06	0.09	0.12	0.06	0.08	0.10	0.11	0.08
MgO	14.94	15.18	15.13	14.73	14.66	16.02	16.08	15.27	14.94	14.76	15.14	15.82	15.66	15.64	16.92	16.40	17.14	16.80	16.43	16.77
CaO	22.55	22.16	22.27	22.57	22.52	21.90	22.59	23.13	22.93	22.95	23.14	23.03	22.85	22.39	22.48	23.59	23.10	23.05	23.44	23.17
Na_2O	0.73	0.68	0.78	0.82	0.84	0.69	0.56	0.64	0.64	0.64	0.62	0.55	0.57	0.57	0.53	0.28	0.32	0.25	0.24	0.21
Total	100.55	99.89	101.36	101.07	100.97	98.79	101.12	100.49	100.24	100.49	100.54	100.96	101.39	100.77	100.72	100.40	100.86	100.80	100.87	100.39
Mg #	90.9	92.1	91.0	90.8	90.7	93.1	92.5	91.1	92.0	91.9	92.0	92.4	92.2	91.3	93.8	92.6	92.9	92.8	92.6	92.8

Mg # = 100*Mg/(Mg+Fe^{2+}) cationic ratio

TABLE 4 | **Representative EMP analyses of spinel in Monte del Estado peridotites**

Lithology	Lherzolite														Cpx-rich lherzolite							
Sample	60-93			62-93			50A-94			52-94					17-94				37-94			
SiO_2 (wt%)	0.00	0.00	0.00	0.00	0.00	0.00	0.00	0.00	0.00	0.00	0.00	0.06	0.04		0.00	0.00	0.00	0.00	0.02	0.00	0.07	0.03
TiO_2	0.11	0.06	0.09	0.07	0.08	0.08	0.05	0.02	0.03	0.07	0.06	0.11	0.11		0.05	0.05	0.05	0.06	0.09	0.06	0.09	0.04
Al_2O_3	53.03	52.93	53.25	55.74	56.05	54.91	54.88	55.04	54.76	53.06	53.57	51.47	51.03		55.01	55.66	54.91	54.12	55.13	55.55	55.83	55.06
Cr_2O_3	14.58	14.70	14.70	12.22	11.88	12.46	12.58	12.62	12.80	14.62	14.36	16.22	16.20		11.80	11.75	11.51	12.78	12.52	12.43	12.43	12.36
FeO	10.54	10.68	10.93	11.33	10.92	11.11	10.85	10.69	10.88	11.55	11.85	11.22	10.79		11.39	11.29	11.07	11.26	10.15	9.90	10.50	10.16
Fe_2O_3	1.63	1.52	1.21	0.67	0.85	1.35	1.49	1.60	1.66	1.32	1.33	1.72	1.94		2.03	1.81	2.20	2.16	1.19	1.72	1.18	1.68
MnO	0.13	0.11	0.11	0.12	0.13	0.08	0.12	0.13	0.06	0.16	0.10	0.14	0.07		0.08	0.14	0.09	0.14	0.09	0.09	0.16	0.11
MgO	19.37	19.22	19.15	19.10	19.41	19.15	19.31	19.46	19.35	18.68	18.69	18.71	18.70		19.00	19.22	19.10	19.00	19.59	19.95	19.66	19.57
V_2O_3	0.06	0.06	0.09	0.08	0.05	0.07	0.05	0.10	0.09	0.08	0.10	0.14	0.09		0.05	0.07	0.08	0.17	0.07	0.04	0.06	0.07
NiO	0.39	0.44	0.39	0.39	0.41	0.32	0.40	0.34	0.37	0.34	0.37	0.34	0.38		0.41	0.40	0.40	0.35	0.34	0.33	0.33	0.31
ZnO	0.07	0.21	0.19	0.19	0.21	0.25	0.17	0.20	0.18	0.18	0.13	0.07	0.30		0.16	0.10	0.20	0.13	0.08	0.09	0.09	0.14
Total	99.91	99.93	100.11	99.91	99.99	99.78	99.90	100.20	100.18	100.06	100.56	100.20	99.65		99.98	100.49	99.61	100.17	99.27	100.16	100.40	99.53
Cr #	0.16	0.16	0.16	0.13	0.12	0.13	0.13	0.13	0.14	0.16	0.15	0.17	0.18		0.13	0.12	0.12	0.14	0.13	0.13	0.13	0.13
Mg #	76.6	76.3	75.8	75.0	76.0	75.4	76.0	76.5	76.0	74.2	73.8	74.8	75.5		74.8	75.3	75.5	75.0	77.5	78.2	76.9	77.5

Cpx = clinopyroxene; Cr # = Cr/(Cr+Al) cationic ratio; Mg # = 100*Mg/(Mg+Fe^{2+}) cationic ratio

and one harzburgite). Analyses were performed at the Géosciences Montpellier laboratory (Montpellier, France) using a ThermoFinnigan ELEMENT XR high resolution (HR) Inductively Coupled Plasma-Mass Spectrometry (ICP-MS), coupled with a Geolas (Microlas) automated platform housing a 193nm Compex 102 laser from LambdaPhysik. Signals were acquired in Time Resolved Acquisition, devoting 2 minutes for the blank and 1 minute for measurement of the analytes. The laser was fired employing an energy density of 15J/cm^2 at a frequency of 5Hz and using a spot size of 77μm. Oxide level, measured by the ThO/Th ratio, was below 0.8%. Reference sample BIR-1G was analyzed as unknown during the analytical runs and shows good agreement with working values for this international standard (Gao et al., 2002) (Table 5). Ca and Si were used as internal standards for the analyses of clinopyroxene and

orthopyroxene, respectively. Analyte concentrations were calibrated against the NIST 612 rhyolitic glass, according to the values of Pearce et al. (1997). Data were subsequently reduced using the GLITTER software (van Achterbergh et al., 2001) by inspecting the time-resolved analysis to check for lack of heterogeneities in the analyzed volume. 3 to 8 mineral analyses were performed in each thin section. Representative LA-ICP-MS data are shown in Tables 5 and 6.

Whole rock composition

For whole rock analyses, secondary veins and Fe oxy-hydroxide/clay crust were carefully removed before sample crushing. Sample powders were made by crushing and powdering large amounts of each sample (usually > 3kg) in an agate ring mill. Whole rock major elements and Ni were analysed by X-ray diffraction (XRF) at the Department

TABLE 5 | **Representative LA-ICP-MS analyses of orthopyroxene in Monte del Estado peridotites. LA-ICP-MS results for international reference material (BIR-IG) run as unknown at the Géoosciences Montpellier laboratory are also shown**

Lithology	Harzburgite				Cpx-poor		Lherzolite						Cpx-rich		LA-ICP-MS standard		
Sample	12-94				78-94		60-93		62-93		92-94		17-94		BIR-1G (n = 8)	RSD (%)	Gao et al. (2002)
Ti (ppm)	154	200	650	507	308	337	657	622	264	332	384	508	553	732	6449	3	5532
Rb	0.050	0.094	0.067	0.056	0.190	0.082	0.850	bdl	0.023	bdl	0.200	0.130	0.022	0.055	0.20	9	0.26
Sr	3.28	4.23	4.86	4.84	0.19	1.23	2.25	1.48	5.21	10.51	45.79	0.51	5.70	5.05	102	4	104
Y	1.23	1.18	1.98	1.63	0.70	0.94	1.69	1.13	1.08	2.21	1.30	1.55	0.84	1.80	13	3	13.3
Zr	0.041	0.038	0.089	0.066	0.008	0.011	bdl	bdl	0.074	0.096	bdl	1575.0	0.076	0.252	13	8	12.9
Nb	0.0051	0.0033	0.0053	0.0058	0.0077	0.0024	0.0295	bdl	bdl	0.0038	0.0029	0.0154	0.0016	0.0023	0.48	5	0.48
Ba	0.312	0.358	3.0	0.800	0.041	0.897	bdl	0.107	0.467	0.543	3.5	0.138	0.837	0.726	5.9	4	6.3
La	0.0004	0.0003	bdl	bdl	0.0709	0.0038	bdl	bdl	0.0006	bdl	0.0005	0.0075	bdl	bdl	0.58	4	0.6
Ce	0.0025	0.0022	0.0014	0.0004	0.0236	0.0028	0.0212	bdl	0.0017	0.0023	bdl	bdl	0.0029	0.0016	1.9	5	1.9
Pr	0.0013	0.0005	0.0015	0.0010	0.0064	bdl	0.0028	bdl	0.0005	0.0011	bdl	0.0010	bdl	0.0014	0.36	5	0.36
Nd	0.015	0.021	0.018	0.019	0.008	bdl	0.015	bdl	0.006	0.025	0.013	0.006	0.002	0.031	2.2	4	2.3
Sm	0.024	0.021	0.047	0.026	0.008	0.005	0.033	bdl	0.013	0.041	0.008	0.028	bdl	0.040	1.0	4	1.1
Eu	0.011	0.0083	0.023	0.019	0.0038	0.0024	0.013	0.0024	0.0064	0.020	0.0062	0.014	0.0014	0.016	0.49	5	0.51
Gd	0.073	0.084	0.14	0.11	0.013	0.019	0.072	0.028	0.054	0.13	0.044	0.062	0.011	0.11	1.7	5	1.6
Tb	0.019	0.020	0.036	0.027	0.0095	0.0084	0.019	0.0088	0.016	0.032	0.013	0.020	0.0066	0.027	0.33	4	0.32
Dy	0.17	0.19	0.33	0.25	0.071	0.10	0.23	0.13	0.14	0.31	0.17	0.20	0.082	0.26	2.5	4	2.3
Ho	0.046	0.049	0.082	0.068	0.029	0.035	0.059	0.046	0.043	0.083	0.056	0.058	0.030	0.069	0.55	4	0.51
Er	0.16	0.15	0.27	0.22	0.11	0.15	0.23	0.18	0.14	0.28	0.22	0.23	0.14	0.24	1.6	4	1.5
Tm	0.027	0.024	0.040	0.036	0.028	0.034	0.047	0.034	0.023	0.049	0.042	0.042	0.031	0.047	0.24	5	0.22
Yb	0.21	0.21	0.30	0.27	0.22	0.31	0.39	0.32	0.20	0.39	0.39	0.38	0.32	0.44	1.7	4	1.5
Lu	0.040	0.034	0.049	0.048	0.048	0.058	0.072	0.061	0.034	0.067	0.074	0.072	0.057	0.074	0.25	4	0.23
Hf	0.012	0.011	0.027	0.015	0.0063	0.0057	0.033	0.026	0.018	0.020	0.0086	0.018	0.016	0.050	0.54	6	0.53
Ta	bdl	bdl	bdl	bdl	0.013	bdl	bdl	bdl	bdl	0.0012	0.0018	bdl	0.00068	bdl	0.037	5	0.032
Pb	0.045	0.015	0.0084	0.0094	1.3	0.020	0.27	0.035	0.014	0.016	bdl	0.12	0.018	0.049	3.9	5	3.6
Th	0.0032	0.00024	0.00029	0.00086	0.0011	bdl	0.010	bdl	bdl	bdl	bdl	0.0051	bdl	bdl	0.031	6	0.028
U	0.0019	0.00031	0.000060	0.00022	0.020	0.020	0.0058	bdl	0.0024	bdl	bdl	0.054	bdl	bdl	0.020	7	0.032

Cpx = clinopyroxene; RSD (%) = Relative standard deviation (percentage) of "n" analyses; bdl = below detection limit

TABLE 6 | **LA-ICP-MS analyses of clinopyroxene in Monte del Estado peridotites**

Lithology	Lherzolite												Cpx-rich lherzolite		
Sample	60-93				62-93			92-94					17-94		
Ti (ppm)	2145	1827	2016	2121	1685	1462	1587	1633	1548	1276	1430	1512	2258	2369	2043
Rb	bdl	0.011	bdl	bdl	bdl	bdl	bdl	0.026	bdl	0.0057	bdl	bdl	bdl	0.0092	bdl
Sr	7.9	12	9.5	12	1.4	1.1	0.88	4.6	13	2.1	1.9	0.77	12.1	12.9	3.1
Y	15	15	15	15	13	12	13	11	9.7	10	12	12	18	18	16
Zr	0.92	1.5	1.6	1.7	0.92	0.85	0.91	0.50	bdl	0.14	0.35	0.38	1.8	1.8	1.5
Nb	0.10	0.029	0.0049	0.0024	0.0018	0.0053	0.0025	0.0057	0.010	0.0019	0.0045	0.0036	0.0047	0.0036	0.0033
Ba	0.85	0.48	0.62	0.84	0.11	0.047	0.069	6.0	1.1	0.11	0.073	0.067	1.3	1.3	0.40
La	bdl	0.010	0.0021	0.0012	bdl	bdl	bdl	0.0026	bdl	bdl	0.0011	bdl	0.0016	0.015	0.00075
Ce	0.094	0.18	0.037	0.036	0.012	0.012	0.012	0.016	0.028	bdl	0.0047	0.0052	0.044	0.13	0.044
Pr	0.080	0.049	0.040	0.040	0.016	0.019	0.018	0.010	0.010	0.0063	0.0086	0.0080	0.049	0.051	0.047
Nd	0.72	0.68	0.64	0.62	0.34	0.32	0.33	0.22	bdl	0.19	0.22	0.22	0.79	0.78	0.75
Sm	0.71	0.76	0.68	0.72	0.44	0.46	0.48	0.37	0.28	0.33	0.41	0.38	0.85	0.86	0.81
Eu	0.35	0.32	0.32	0.32	0.21	0.21	0.22	0.18	0.15	0.17	0.19	0.18	0.40	0.41	0.38
Gd	1.6	1.6	1.5	1.7	1.2	1.2	1.2	0.97	0.85	0.94	1.1	1.1	1.9	1.9	1.7
Tb	0.35	0.33	0.33	0.34	0.27	0.25	0.27	0.23	0.20	0.21	0.24	0.24	0.41	0.41	0.38
Dy	2.6	2.6	2.7	2.7	2.2	2.1	2.2	1.9	1.7	1.8	2.0	2.0	3.3	3.3	2.9
Ho	0.66	0.63	0.62	0.63	0.50	0.48	0.51	0.44	0.39	0.41	0.48	0.48	0.72	0.74	0.66
Er	1.8	1.8	1.8	1.9	1.6	1.5	1.5	1.3	1.2	1.2	1.4	1.4	2.2	2.2	2.0
Tm	0.29	0.27	0.27	0.28	0.23	0.22	0.23	0.19	0.17	0.19	0.21	0.21	0.32	0.31	0.29
Yb	1.9	1.8	1.8	1.8	1.5	1.4	1.5	1.2	1.1	1.2	1.4	1.4	2.2	2.1	2.0
Lu	0.27	0.26	0.26	0.26	0.21	0.21	0.22	0.18	0.17	0.17	0.21	0.19	0.30	0.29	0.30
Hf	0.20	0.23	0.23	0.24	0.17	0.16	0.16	0.12	0.11	0.095	0.10	0.11	0.26	0.26	0.26
Ta	bdl	0.0020	bdl	bdl	bdl	bdl	bdl	0.00068	bdl	bdl	0.00080	bdl	bdl	bdl	bdl
Pb	bdl	0.31	0.0087	0.0049	0.024	0.036	0.013	0.076	bdl	bdl	0.012	0.0092	0.035	0.030	0.0088
Th	bdl	0.012	bdl	0.00014	bdl	bdl	bdl	0.015	0.065	bdl	0.00014	bdl	bdl	0.00092	0.00084
U	0.20	bdl	bdl	0.00012	bdl	0.00018	bdl	0.091	0.030	bdl	0.00076	bdl	0.030	0.00018	bdl

of Earth Sciences of the Memorial University in Newfoundland (Canada) by a Fisons/ARL 8420+ instrument using standard sample preparation and analytical procedures. Whole rock contents of major elements are given in Table 7.

Whole rock trace elements (Rb, Sr, Y, Zr, Nb, Cs, Ba, REE, Hf, Ta, Pb, Th and U) were analysed by a ThermoFinnigan ELEMENT XR HR ICP-MS at the Géosciences Montpellier laboratory. Sample dissolution was performed following the HF-$HClO_4$ digestion procedure described by Ionov et al. (1992). Element concentrations were determined by external calibration except for Nb and Ta that were calibrated by using Zr and Hf as internal standards, respectively. This technique was applied to avoid memory effects due to the intake of concentrated Nb-Ta solutions in the instrument and is an implementation to ICP-MS analysis of the method described by Jochum et al. (1990) for Nb measurement by spark-source mass spectrometry.

The assessment of the analysis precision of a given element was made using 3-run measurements in the same solution and estimating the standard deviation (σ_s) from the standard deviations of the sample (σ_s), instrumental (σ_i) and procedural blank (σ_p) measurements as: $\sigma_S = \sqrt{\sigma_i^2 + \sigma_p^2 + \sigma_s^2}$ (see Godard et al., 2000). The compositions of the reference samples PCC-1 and UBN, analyzed as unknowns during the analytical runs, show good agreement with working values for these international standards (Govindaraju, 1994; Garrido, 1995) (Table 7). Whole rock trace element data are reported in Table 7.

MINERAL CHEMISTRY

Major elements

Mg# [100 x Mg/(Mg+Fe^{2+})] and NiO of olivine range from 88.9 to 90.5 and from 0.32 to 0.52wt%, respectively. Orthopyroxene has Mg# = 89.4-90.4, Al_2O_3 = 3.49-5.54wt% and Cr_2O_3 = 0.34-0.77wt%. Mg# in clinopyroxene spans from 90.7 to 93.8, Al_2O_3 from 2.68 to 6.44wt%, TiO_2 from 0.15 to 0.52wt% and Cr_2O_3 from 0.37 to 1.10wt%. Spinel has Cr# [Cr/(Cr+Al)] = 0.12-0.18, Mg# = 72.7-78.2 and TiO_2 = 0.02-0.13wt%. In the olivine Mg# versus spinel Cr# diagram the mineral composition of the Monte del Estado peridotites plots at the bottom of the abyssal peridotite field and notably differs from the compositions of minerals in the eastern Cuban and Dominican ophiolites (Fig. 3).

Trace elements in clinopyroxene and orthopyroxene

Figure 4A displays the chondrite-normalized rare earth element (REE) patterns of clinopyroxene in lherzolite and in clinopyroxene-rich lherzolite. HREE contents are rather

TABLE 7 | **Whole-rock major and trace element compositions of studied sample from the Monte del Estado massif. ICP-MS results for international reference materials (PCC-1, UBN) run as unknowns at the Géosciences Montpellier laboratory are also shown**

Lithology	Harzburgite		Cpx-poor lherzolite			Lherzolite											Cpx-rich lherzolite			ICP-MS standards				
Sample	12-94	71-94	77H-94	78-94	92A-94	60-93	61-93	62-93	63-93	154B-93	14-94	32-94	50A-94	52-94	90-94	92-94	17-94	21-94	37-94	PCC-1	Garrido (1995)	UBN	RSD (%) n =	Govin. (1994)
SiO_2 (wt%)	39.82	39.86	39.50	39.24	38.64	38.19	38.38	41.23	38.42	39.88	39.30	39.64	40.83	39.52	38.89	38.72	40.33	39.73	39.82					
TiO_2	0.01	0.01	0.02	0.02	0.03	0.05	0.05	0.07	0.04	0.05	0.05	0.04	0.05	0.04	0.04	0.04	0.06	0.07	0.07					
Al_2O_3	1.10	1.14	1.37	1.66	1.58	2.19	1.98	2.36	1.87	1.77	1.86	2.12	1.77	2.25	1.83	1.95	2.59	2.50	2.54					
Cr_2O_3	0.23	0.26	0.33	0.33	0.35	0.38	0.34	0.29	0.33	0.24	0.29	0.31	0.34	0.35	0.31	0.33	0.30	0.31	0.32					
Fe_2O_{3t}	7.40	7.04	6.86	7.98	8.29	7.56	7.60	8.09	8.28	7.80	6.64	7.91	6.93	7.95	7.05	8.02	8.13	7.96	8.06					
MnO	0.11	0.12	0.15	0.11	0.13	0.12	0.13	0.12	0.13	0.10	0.12	0.11	0.12	0.11	0.09	0.11	0.11	0.11	0.11					
MgO	35.11	35.61	35.58	35.79	35.60	36.99	36.35	36.34	36.45	35.94	35.55	36.61	37.09	36.68	36.11	36.98	35.54	35.87	36.48					
CaO	0.35	0.39	0.94	1.15	0.72	2.03	0.28	2.73	0.14	0.63	2.31	2.20	3.21	2.29	1.97	2.13	2.95	2.77	3.01					
Na_2O	0.01	bdl	0.01	0.01	0.03	0.04	bdl	0.07	bdl	bdl	0.05	0.03	0.03	0.02	0.02	0.03	0.06	0.04	0.09					
P_2O_5	0.09	0.07	0.08	0.07	0.07	0.07	0.09	0.07	0.08	0.08	0.08	0.08	0.07	0.05	0.06	0.06	0.08	0.08	0.08					
LOI	15.30	15.00	14.70	13.20	14.10	11.90	14.30	8.20	13.80	13.20	13.30	10.50	9.10	10.30	13.20	11.20	9.40	10.10	9.00					
Total	99.53	99.50	99.54	99.56	99.54	99.52	99.50	99.57	99.54	99.69	99.55	99.55	99.54	99.56	99.57	99.57	99.55	99.54	99.58					
Ni (ppm)	2796	2803	2480	2355	2438	2396	2452	2331	2344	2026	2349	2284	2456	2187	2240	2266	2250	2264	2245					
Rb	0.44	0.15	0.16	0.28	0.16	0.12	0.17	0.095	0.20	0.12	n.a.	0.095	0.25	0.14	0.37	0.19	0.30	0.31	0.41	0.059	0.068	3.2	2	4.0
Sr	8.8	5.1	3.3	5.6	4.5	42	4.8	7.6	4.0	3.3	n.a.	2.7	15	9.7	15	16	34	33	22	0.34	0.38	7.0	2	9.0
Y	0.65	0.39	0.84	0.83	0.97	1.7	1.4	1.4	1.4	0.78	n.a.	0.81	1.2	1.5	1.3	1.2	1.9	2.1	2.0	0.080	0.087	2.5	3	2.5
Zr	1.3	3.2	0.45	0.71	0.60	0.68	1.6	0.60	0.71	0.72	n.a.	0.45	0.69	0.57	1.1	1.0	0.87	11	1.5	0.13	0.13	3.7	3	4.0
Nb	0.15	0.030	0.030	0.030	0.045	0.039	0.042	0.028	0.033	0.046	n.a.	0.014	0.033	0.024	0.030	0.028	0.049	0.050	0.064	0.018	0.042	0.063	3	0.050
Cs	0.0050	0.0074	0.0092	0.016	0.0056	0.021	0.015	0.014	0.010	0.011	n.a.	0.0049	0.047	0.015	0.028	0.044	0.014	0.048	0.024	0.011	0.0055	11	3	10
Ba	11	3.7	2.3	7.9	2.7	4.4	2.6	1.5	2.6	7.6	n.a.	2.3	3.0	3.3	5.5	3.2	6.2	3.9	4.1	1.0	0.68	25	1	27
La	0.34	0.32	0.10	0.12	0.24	0.078	0.17	0.16	0.12	0.16	n.a.	0.069	0.11	0.090	0.37	0.21	0.16	0.63	0.19	0.031	0.039	0.38	9	0.35
Ce	0.65	0.30	0.16	0.22	0.49	0.12	0.18	0.35	0.24	0.35	n.a.	0.12	0.24	0.19	0.53	0.19	0.31	0.49	0.40	0.058	0.057	0.80	6	0.80
Pr	0.079	0.032	0.019	0.024	0.050	0.016	0.028	0.026	0.028	0.028	n.a.	0.013	0.029	0.021	0.053	0.020	0.039	0.083	0.053	0.0073	0.0085	0.11	5	0.12
Nd	0.30	0.12	0.090	0.10	0.20	0.10	0.15	0.11	0.15	0.12	n.a.	0.055	0.14	0.12	0.18	0.091	0.23	0.40	0.30	0.028	0.030	0.62	6	0.60
Sm	0.052	0.024	0.031	0.028	0.042	0.065	0.073	0.048	0.068	0.027	n.a.	0.022	0.052	0.060	0.043	0.042	0.10	0.14	0.13	0.0062	0.0080	0.21	3	0.20
Eu	0.019	0.0089	0.012	0.011	0.017	0.032	0.025	0.022	0.020	0.011	n.a.	0.010	0.022	0.028	0.019	0.019	0.045	0.061	0.051	0.0013	0.0018	0.080	4	0.080
Gd	0.069	0.037	0.064	0.065	0.089	0.16	0.14	0.12	0.14	0.063	n.a.	0.058	0.11	0.14	0.11	0.11	0.20	0.26	0.23	0.0061	0.0080	0.32	4	0.30
Tb	0.012	0.0078	0.015	0.015	0.020	0.035	0.029	0.027	0.031	0.015	n.a.	0.014	0.025	0.031	0.024	0.024	0.043	0.052	0.046	0.0012	0.0015	0.062	3	0.060
Dy	0.085	0.060	0.13	0.13	0.17	0.27	0.24	0.22	0.24	0.12	n.a.	0.12	0.21	0.26	0.21	0.20	0.33	0.39	0.35	0.010	0.013	0.45	3	0.38
Ho	0.020	0.014	0.033	0.033	0.040	0.065	0.056	0.054	0.057	0.031	n.a.	0.031	0.049	0.060	0.051	0.048	0.076	0.087	0.078	0.0027	0.0038	0.10	3	0.090
Er	0.059	0.046	0.11	0.10	0.12	0.20	0.17	0.17	0.17	0.095	n.a.	0.10	0.15	0.18	0.16	0.15	0.23	0.26	0.23	0.011	0.012	0.29	5	0.28
Tm	0.010	0.0088	0.018	0.017	0.019	0.031	0.026	0.027	0.028	0.017	n.a.	0.017	0.025	0.029	0.025	0.024	0.036	0.040	0.035	0.0027	0.0025	0.045	4	0.045
Yb	0.071	0.062	0.13	0.13	0.14	0.21	0.18	0.18	0.19	0.11	n.a.	0.13	0.17	0.19	0.18	0.16	0.24	0.26	0.24	0.022	0.022	0.29	1	0.28
Lu	0.013	0.013	0.024	0.023	0.025	0.037	0.032	0.032	0.033	0.021	n.a.	0.023	0.030	0.035	0.030	0.030	0.040	0.046	0.039	0.0050	0.0049	0.050	4	0.045
Hf	0.029	0.012	0.017	0.022	0.021	0.036	0.030	0.026	0.033	0.020	n.a.	0.010	0.026	0.030	0.033	0.019	0.046	0.080	0.061	0.0036	0.0055	0.12	2	0.10
Ta	0.010	0.0020	0.0020	0.0021	0.0027	0.0015	0.0020	0.0022	0.0020	0.0032	n.a.	0.0012	0.0024	0.0015	0.0022	0.0019	0.0038	0.0033	0.0043	0.00072	0.0030	0.022	10	0.020
Pb	0.51	5.3	17	4.8	6.1	2.9	13	3.8	34	16	n.a.	4.4	25	11	12	9.2	2.7	39	19	8.9	8.5	13	14	13
Th	0.029	0.012	0.012	0.015	0.013	0.0075	0.013	0.0083	0.013	0.0094	n.a.	0.0089	0.013	0.0094	0.013	0.010	0.062	0.026	0.024	0.012	0.010	0.060	16	0.070
U	0.010	0.0078	0.0034	0.015	0.0078	0.0049	0.0034	0.0047	0.0039	0.0033	n.a.	0.010	0.0046	0.0031	0.011	0.0041	0.025	0.008	0.010	0.0045	0.0042	0.047	6	0.070

Cpx = clinopyroxene; LOI = loss on ignition; bdl = below detection limit; n.a. = not analysed; RSD (%) = Relative standard deviation (percentage)

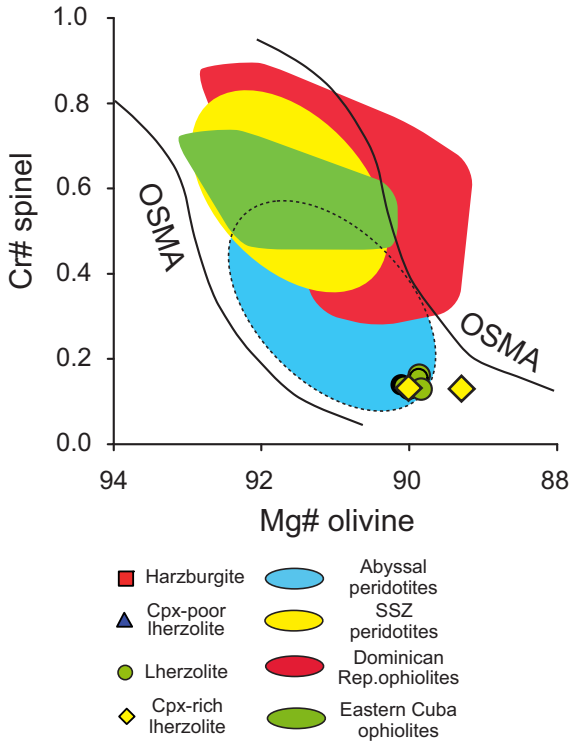

FIGURE 3 | **Average Mg# of olivine versus Cr# of spinel in the Monte del Estado peridotites. Red squares: harzburgite; blue triangles: clinopyroxene (Cpx)-poor lherzolite; green circles: lherzolite; yellow diamonds: Cpx-rich lherzolite. Fields of olivine-spinel mantle array (OSMA), abyssal (light blue area) and supra-subduction zone (SSZ) (yellow area) peridotites from Arai (1994). Fields of the Dominican Republic (red area) and Eastern Cuba (green area) ophiolites from Proenza et al. (2007) and Marchesi et al. (2006), respectively.**

homogeneous and vary between 6.4 and 13.5 the values of chondrite; on the other hand, the MREE and especially the LREE normalized abundances are more variable and the last span from 0.003 to 5.6. Clinopyroxene has convex-upward MORB-type patterns characterized by regular increasing concentrations from LREE to HREE and its composition is similar to that of clinopyroxene in residual abyssal peridotites from ocean ridges (Fig. 4A). Abundances of the most incompatible trace elements (from Rb to Ta) are highly variable (Fig. 4B). Ba, U and Pb generally show positive spikes in the multi-elemental variation (spider) diagram whereas Zr and Ti are depleted compared to the adjacent elements (Fig. 4B). No appreciable differences exist between the compositions of grain cores and rims. The trace element contents of clinopyroxene (especially the HREE) are generally related to the modal composition of the samples, i.e. the concentrations of grains in clinopyroxene-rich lherzolite are slightly higher than those in lherzolite.

REE contents of orthopyroxene are lower than those of clinopyroxene but have a similar variability, i.e. the concentrations of HREE are more homogeneous than those of MREE and LREE (Fig. 5A). In particular, HREE vary between 0.51 and 2.9 the values of chondrite and LREE between 0.001 and 0.31. REE patterns generally show linear increasing concentrations from LREE to HREE except for few grains that exhibit a relative enrichment in LREE. U, Ta, Pb, Sr and Ti usually show prominent positive spikes in the spider diagram whereas Zr is normally depleted (Fig. 5B). Contrary to clinopyroxene, no clear correlation exists between the trace element abundances in orthopyroxene and the modal composition of the samples.

WHOLE ROCK GEOCHEMISTRY

The LOI values of Monte del Estado peridotites range from 8.2 to 15.3wt% (Table 7) indicating important addi-

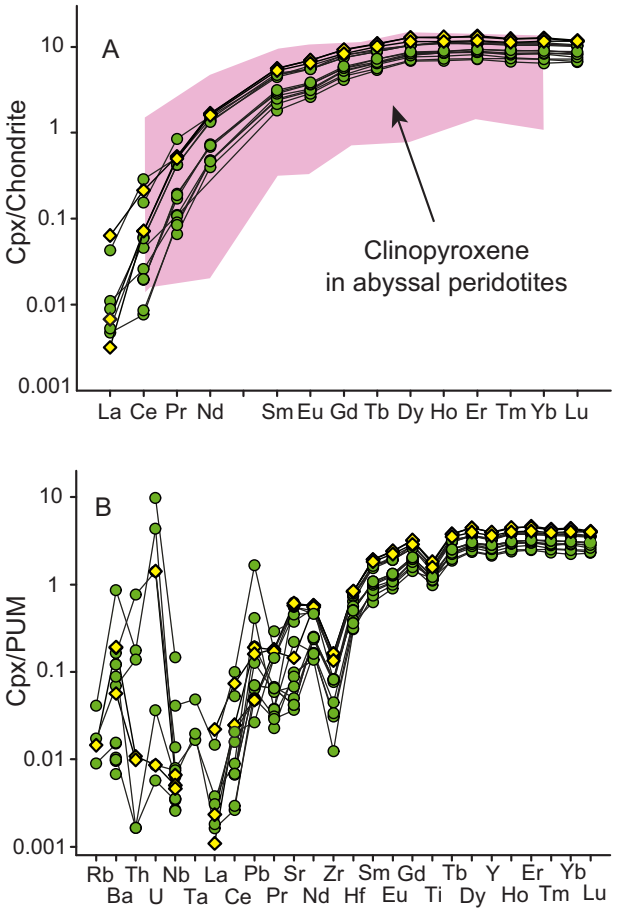

FIGURE 4 | **Representative A) chondrite-normalized rare earth element patterns and B) primitive upper mantle (PUM)-normalized trace element patterns of clinopyroxene in the Monte del Estado peridotites. Symbols as in Figure 3. Normalizing values from Sun and McDonough (1989). Field of clinopyroxene composition in abyssal peridotites in (A) from Bodinier and Godard (2003).**

tion of volatile components during alteration. The Al_2O_3 contents of these rocks (1.3-2.9 anhydrous wt%) is related to the clinopyroxene abundances of the samples and coincide with those of mildly fertile mantle rocks (Fig.6). SiO_2 varies between 43.6 and 47.3wt% on an anhydrous basis and is rather higher in harzburgite and in one clinopyroxene-poor lherzolite than values usually reported for oceanic peridotites (Fig. 6A). As customarily observed in mantle rocks, FeOt and TiO_2 exhibit different variations relative to Al_2O_3: FeOt does not show any particular trend in Figure 6B whereas TiO_2 and Al_2O_3 have a good positive correlation (Fig. 6C).

The chondrite-normalized REE patterns of the Monte del Estado peridotites are displayed in Figure 7. The sample/chondrite REE concentrations of these rocks are quite variable ($0.12 < LREE_N < 2.68$ and $0.25 < HREE_N < 1.79$) and their HREE contents generally reflect the clinopyroxene proportions in the samples, i.e. harzburgite has the lowest HREE abundances and clinopyroxene-rich lherzolite the highest ones. The REE patterns of harzburgite are "U-shaped", i.e. they are characterized by relatively high LREE/MREE and low MREE/HREE ratios (Fig. 7A); their normalized concentrations of HREE are more homogeneous than those of MREE and LREE (except for La) and show a linear increase thus resembling the orthopyroxene patterns (Fig. 5A). REE patterns of clinopyroxene-poor lherzolite have LREE-enriched segments and relatively constant

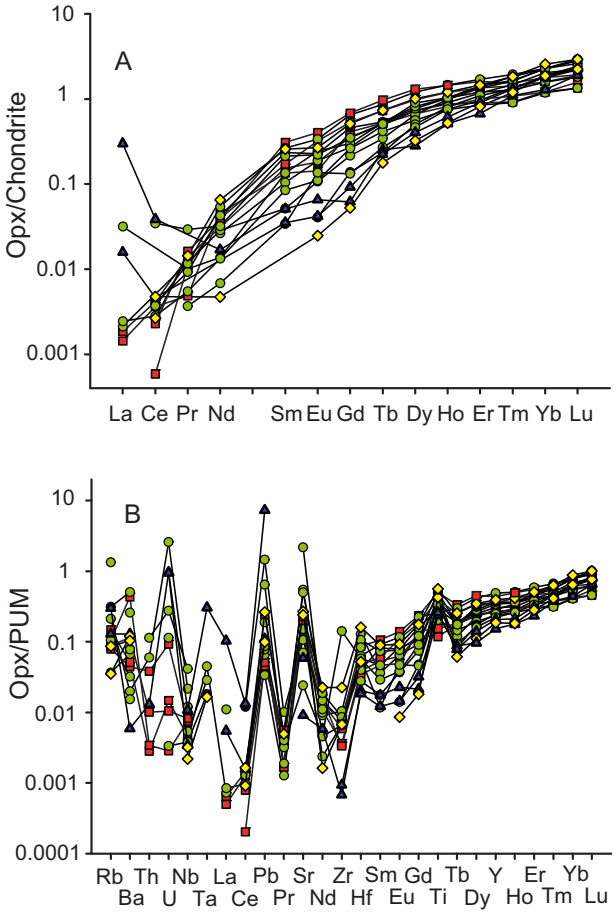

FIGURE 5 | **Representative A) chondrite-normalized rare earth element patterns and B) primitive upper mantle-normalized trace element patterns of orthopyroxene in the Monte del Estado peridotites. Symbols as in Figure 3. Normalizing values from Sun and McDonough (1989).**

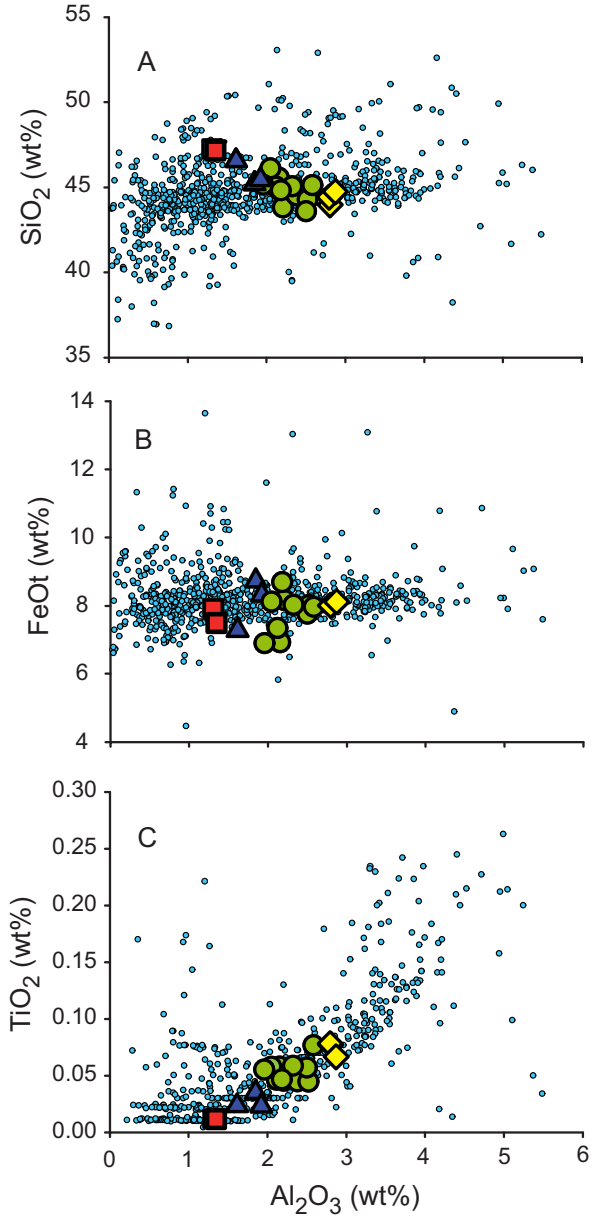

FIGURE 6 | **Whole rock abundances of Al2O3 versus A) SiO2, B) FeOt, and C) TiO2 in the Monte del Estado peridotites and published data for peridotites from different tectonic settings (small light blue circles) (Bodinier and Godard, 2003 and references therein). Symbols as in Figure 3. All data on anhydrous basis in wt%.**

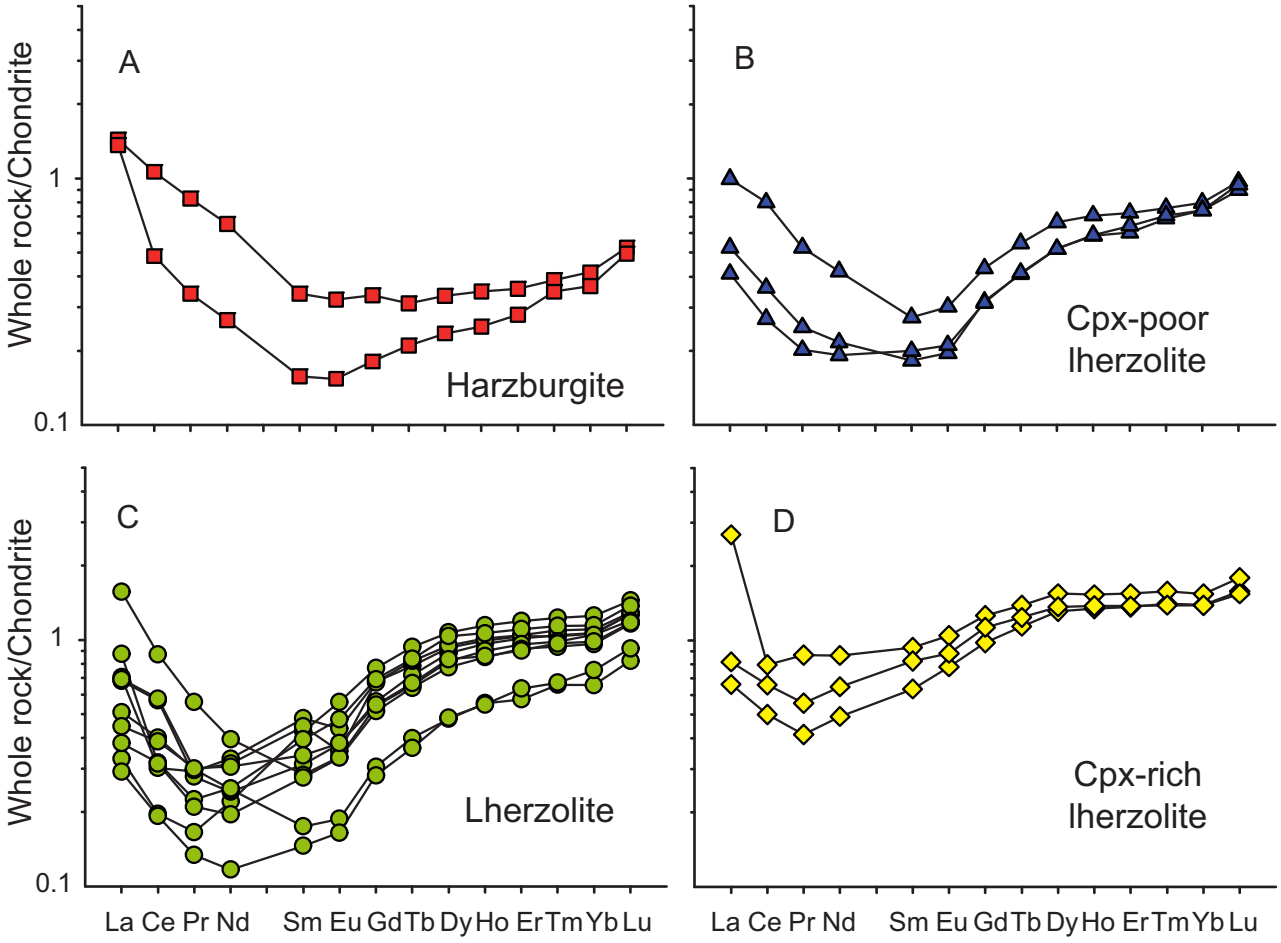

FIGURE 7 | **Chondrite-normalized abundances of REE in the Monte del Estado peridotites (whole rock analyses): A) Harzburgite, B) Clinopyroxene-poor lherzolite; C) Lherzolite; D) Clinopyroxene-rich lherzolite. Symbols as in Figure 3. Normalizing values from Sun and McDonough (1989).**

HREE concentrations similarly to the harzburgite patterns but differ from those of slightly hump-shaped MREE segments (Fig. 7B); very similar patterns are displayed by lherzolites but they have more variable REE and generally higher HREE concentrations than clinopyroxene-poor lherzolite (Fig. 7C). Finally, clinopyroxene-rich lherzolites exhibit REE patterns flatter than the other samples which are characterized by relatively higher LREE contents and less humped MREE segments (Fig. 7D).

The concentrations of lithophile trace elements in the Monte del Estado peridotites are usually above 0.1 the values of the primitive mantle and coincide with those of abyssal peridotites from ocean ridges (Fig. 8). Ba, U, Pb and Sr display prominent positive spikes in most of the samples whereas Nb and Ta are firmly depleted relative to Th and La as also observed in oceanic abyssal peridotites (Niu, 2004). In particular, the Nb/Ta normalized ratio is usually < 1 (Fig. 8) thus confirming the slightly more incompatible character of Nb compared to Ta ($D_{Nb}/D_{Ta} < 1$) during mantle melting, in agreement with experimental data on the partitioning properties of these elements into clinopyroxene (e.g., Münker et al., 2004). Zr and Hf commonly have normalized values comparable to adjacent LREE except in one harzburgite and one clinopyroxene-rich lherzolite that show evident positive Zr anomalies (Fig. 8).

DISCUSSION

Effects of alteration on whole rock composition

Major elements

As the Monte del Estado peridotites are in general highly serpentinised, interpretations of their whole rock compositions in terms of primary magmatic processes require first an assessment of the potential effects of alteration on elemental mobility. Figure 9A shows that most Monte del Estado peridotites plot below the terrestrial mantle array (Jagoutz et al., 1979; Hart and Zindler, 1986) in the Al_2O_3/SiO_2 versus MgO/SiO_2 diagram. This departure from the com-

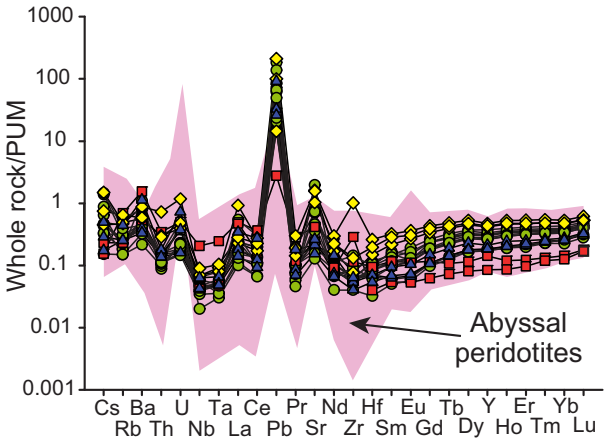

FIGURE 8 | **Primitive mantle-normalized trace element patterns of the Monte del Estado peridotites (whole rock analyses). Symbols as in Figure 3. Normalizing values from Sun and McDonough (1989). Pink area encloses the compositional range of abyssal peridotites (Niu, 2004).**

positions of common residual mantle rocks is especially marked for harzburgite and one clinopyroxene-poor lherzolite that display the lowest MgO/SiO_2 ratios. As Al_2O_3/SiO_2 is considered to be unaffected by alteration (Snow and Dick, 1995; Niu, 2004), low MgO/SiO_2 ratios in such altered peridotites are normally ascribed to MgO loss during seafloor weathering rather than to post-melting SiO_2 (orthopyroxene) addition (Snow and Dick, 1995; Niu, 2004). In particular, adding relative MgO of 2-14wt% to the compositions of the Monte del Estado peridotites makes them overlap with the mantle array; this relative MgO loss is consistent with previous Mg-loss estimates for variably altered abyssal peridotites (Niu, 2004). Hence we infer that the rather high anhydrous SiO_2 content of harzburgite and one clinopyroxene-poor lherzolite (Fig. 6A) are probably artefacts due to normalization of their compositions after partial MgO loss, as also confirmed by petrographic observation that there is no evidence of unusual orthopyroxene enrichment in these samples.

Another common effect of interaction between seawater and oceanic peridotites is alteration of pyroxene to serpentine, chlorite, talc and amphibole that leads to release of Ca, Si and H_2 in fluids and possible rodingitization of adjacent gabbros (e.g., Bach et al., 2004; Austrheim and Prestvik, 2008). The Monte del Estado peridotites generally show a good positive correlation between CaO and Al_2O_3/SiO_2 (Fig. 9B) which suggests that Ca was relatively immobile during alteration. However, four lherzolites depart from this trend and in particular three of them have anomalously low CaO contents and one is relatively CaO-enriched (Fig. 9B). This probably indicates that three of our samples partly lost their original CaO abundances owing to replacement of (clino)pyroxene by secondary phases, whereas carbonate veinlets were possibly not fully removed from one lherzolite despite our efforts during sample sawing.

Trace elements

The chondrite-normalized REE patterns of the Monte del Estado peridotites are variably enriched in LREE (especially in La, Ce, Pr and Nd) (Fig. 7). This is a common feature of mantle peridotites from different tectonic

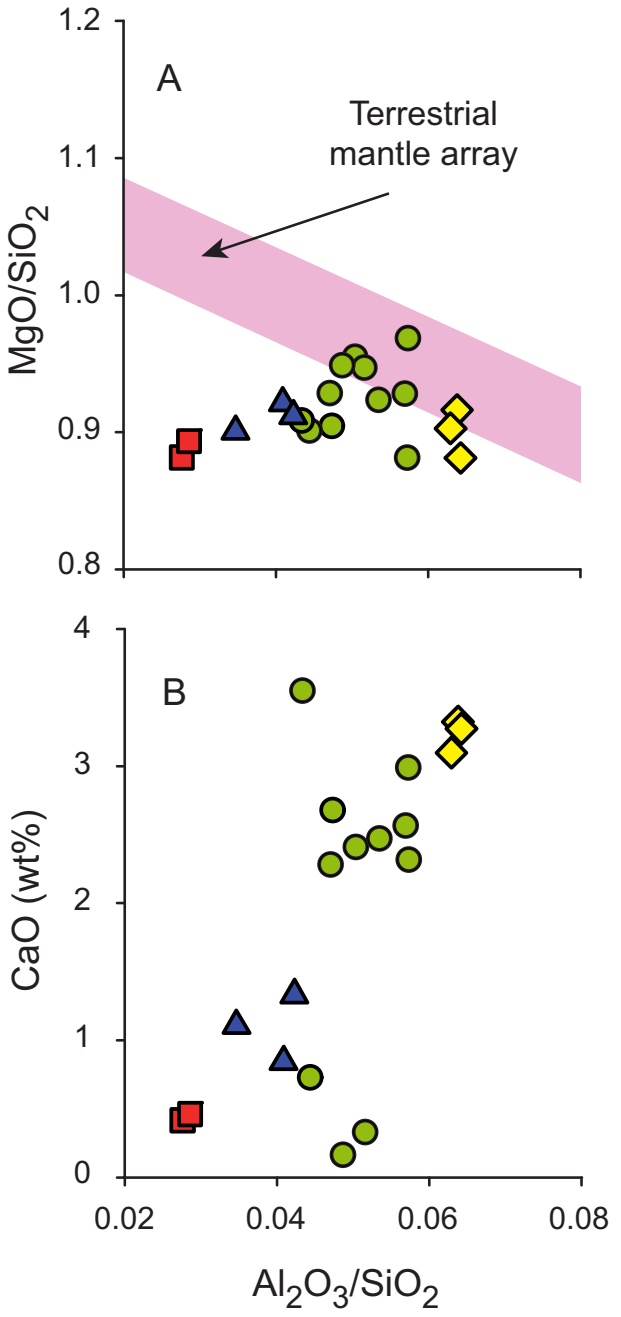

FIGURE 9 | **Al_2O_3/SiO_2 versus A) MgO/SiO_2 and B) CaO in the Monte del Estado peridotites. Symbols as in Figure 3. All data on anhydrous basis in wt%. Terrestrial mantle array in (A) from Jagoutz et al. (1979) and Hart and Zindler (1986).**

settings and is either interpreted as evidence of primary mantle processes (e.g., Bodinier et al., 1990; Godard et al., 2000; Niu, 2004) or as consequence of low T serpentinization, seafloor alteration and/or contamination by crustal fluids (Sharma and Wasserburg, 1996; Gruau et al., 1998; Paulick et al., 2006). High field strength elements (HFSE: e.g., Nb, Ta, Zr and Hf) are immobile during the circulation of low T (< 400ºC) hydrothermal fluids (You et al., 1996; Kogiso et al., 1997) and positive correlation between similarly incompatible LREE and high field strengh elements (HFSE) in altered peridotites indicates that LREE were principall controlled by magmatic processes (Niu, 2004; Paulick et al., 2006). Nb and Hf in the Monte del Estado peridotites generally show good positive correlations with La-Ce-Pr (Fig. 10A-C) and Nd (Fig. 10D) respectively, thus strongly suggesting that LREE were mostly immobile during alteration. Possible minor exceptions to this general conclusion are La in one harzburgite (Fig. 10A), La, Ce, Pr in one lherzolite and in one clinopyroxene-rich lherzolite (Fig. 10A-C), Ce in one clinopyroxene-poor lherzolite (Fig. 10B), and Nd in one harzburgite and in one clinopyroxene-poor lherzolite (Fig. 10D), which significantly deviate from the general correlation.

Finally, Cs, Rb, Ba, U, Pb and Sr are commonly reputed variably mobile during alteration of mantle rocks (e.g., Niu, 2004). This is confirmed in the Monte del Estado peridotites as these elements exhibit poor correlations with HFSE of similar incompatible degree (e.g., Ba with Nb and Sr with Hf, Fig. 11). For this reason they will not be treated in the following discussion on the primary magmatic processes that determined the composition of peridotites.

Partial melting processes constrained by whole rock and clinopyroxene compositions

The Monte del Estado peridotites exhibit a relatively fertile signature in terms of mineral chemistry and whole rock content in major and incompatible trace elements, suggesting that they are residues after low to moderate extents of partial melting. This fertile character is in particular attested by: 1) low Mg# of olivine and Cr# of spinel that coincide with the values of the most fertile abyssal peridotites in ocean ridge settings (Fig. 3); 2) relative high contents of Al_2O_3 in pyroxene (Tables 2, 3) and HREE in clinopyroxene (Fig. 4); and 3) variable but relatively high whole rock Al_2O_3 ($1.3 < Al_2O_3$ anhydrous wt% < 2.9) (Fig. 6), HREE ($0.4 < Yb_N < 1.5$) (Fig. 7) and lithophile trace element abundances that are generally comparable to those of abyssal peridotites (Fig. 8). Figure 12A displays the chondrite-normalized whole rock REE patterns of the Monte del Estado peridotites and the curves calculated for non-modal fractional melting of the depleted MORB mantle in the spinel lherzolite facies. HREE and MREE variations coincide with the patterns calculated for 2-5% melt extrac-

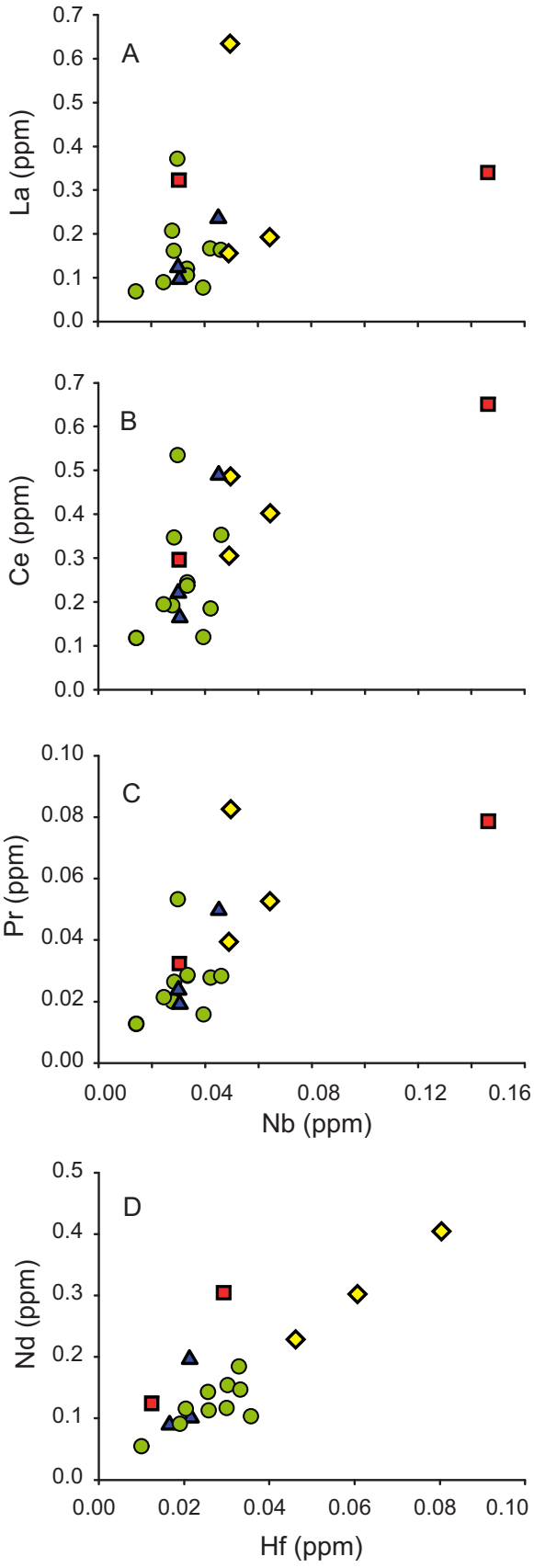

FIGURE 10 | **Nb versus A) La B) Ce C) Pr and D) Hf versus Nd in the Monte del Estado peridotites. Symbols as in Figure 3.**

tion for clinopyroxene-rich lherzolite, 5-10% for lherzolite and clinopyroxene-poor lherzolite, and 10-15% for harzburgite. On the other hand, LREE abundances in whole rock clearly depart from the predictions of the melting model and are governed by different magmatic processes (see below). However, a similar fractional melting model in the spinel stability field does not successfully reproduce the REE patterns of clinopyroxene in lherzolite and clinopyroxene-rich lherzolite and in particular their depletion in LREE and MREE compared to HREE (Fig.12B). Similar results have been obtained for clinopyroxene in abyssal peridotites from the Central Indian Ridge (Hellebrand et al., 2002) and have been interpreted as evidence of melting in the presence of residual garnet that preferentially retains HREE over LREE and MREE (e.g., Johnson, 1998). A combination of initial fractional melting in the garnet stability field and additional melting in the spinel stability field does not properly predict the slightly humped MREE segments of the whole rock patterns (Fig.12C) but well reproduces the REE variations of clinopyroxene and in particular its relative high LREE/HREE and MREE/HREE

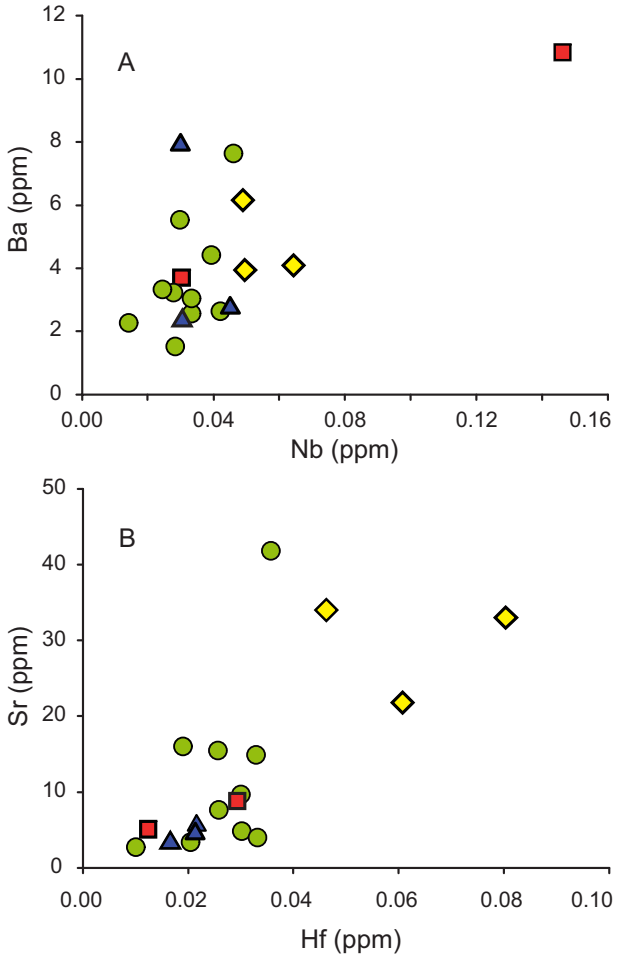

FIGURE 11 | **A) Nb versus Ba and B) Hf versus Sr in the Monte del Estado peridotites. Symbols as in Figure 3.**

fractionations (Fig. 12D). In particular, the low LREE and MREE concentrations of clinopyroxene in lherzolite and clinopyroxene-rich lherzolite are matched by ~ 4% fractional melt extraction in the garnet stability field followed by 0-5% in the spinel stability field. These initial low fractional melting degrees of a garnet lherzolite source are similar to previous estimates obtained for abyssal (Hellebrand et al., 2002) and ophiolite peridotites (Jean et al., 2010). The discrepancy between the shapes of the REE patterns of clinopyroxene and whole rocks (Figs. 4A, 7) indicates that the trace element budgets of the Monte del Estado peridotites are influenced by repositories other than clinopyroxene and that the whole rock composition records additional magmatic processes besides partial melting (see below).

Post-melting interaction with migrating melts

Partial melting alone cannot account for several geochemical characteristics of the Monte del Estado peridotites. In the MgO versus SiO_2 diagram neither the actual nor the recalculated compositions after the inferred MgO loss follow the predictions of different melting models at variable pressures (Fig. 13); in particular, the recalculated compositions have unusually low SiO_2 contents to be simple residues of partial melting as also observed for ocean ridge peridotites (Niu, 1997, 2004). These variations are commonly interpreted as due to post-melting addition of olivine by fractional crystallization of basaltic melts migrating through the uppermost mantle (Niu, 1997). Moreover, the chondrite normalized REE patterns of the Monte del Estado peridotites display relatively high LREE/HREE whole rock ratios (Fig. 7) that cannot be explained by alteration processes (Fig. 10) or partial melting (Fig. 12A, C). Enrichment in the most incompatible trace elements is usually observed in oceanic and subcontinental peridotites (e.g., Bodinier and Godard, 2003 and references therein) and may be ascribed to chromatographic re-equilibration of the lithospheric mantle with percolating melts during melt transport by reactive porous flow (e.g., Navon and Stolper, 1987; Bodinier et al., 1990; Vernières et al., 1997). Additionally, these processes may also explain the slightly hump-shaped MREE segments (Hellebrand et al., 2002) in the whole rock patterns of the Monte del Estado peridotites (Fig. 7). However, as post-melting re-equilibration is only recorded by whole rock and not by clinopyroxene compositions at cores and rims (Fig. 12), the melt ascending through the Monte del Estado mantle section was likely unable to react with clinopyroxene and enrich its composition in incompatible trace elements. This suggests that melt/rock interaction occurred in the relatively cold uppermost mantle region beneath the crust (i.e., the thermal boundary layer, Niu, 2004). So, the storage of excess incompatible trace elements (in particular the LREE) was possibly accommodated by trapping of fluid/melt fractions or crystallization of sub-percent amounts of micro-phases

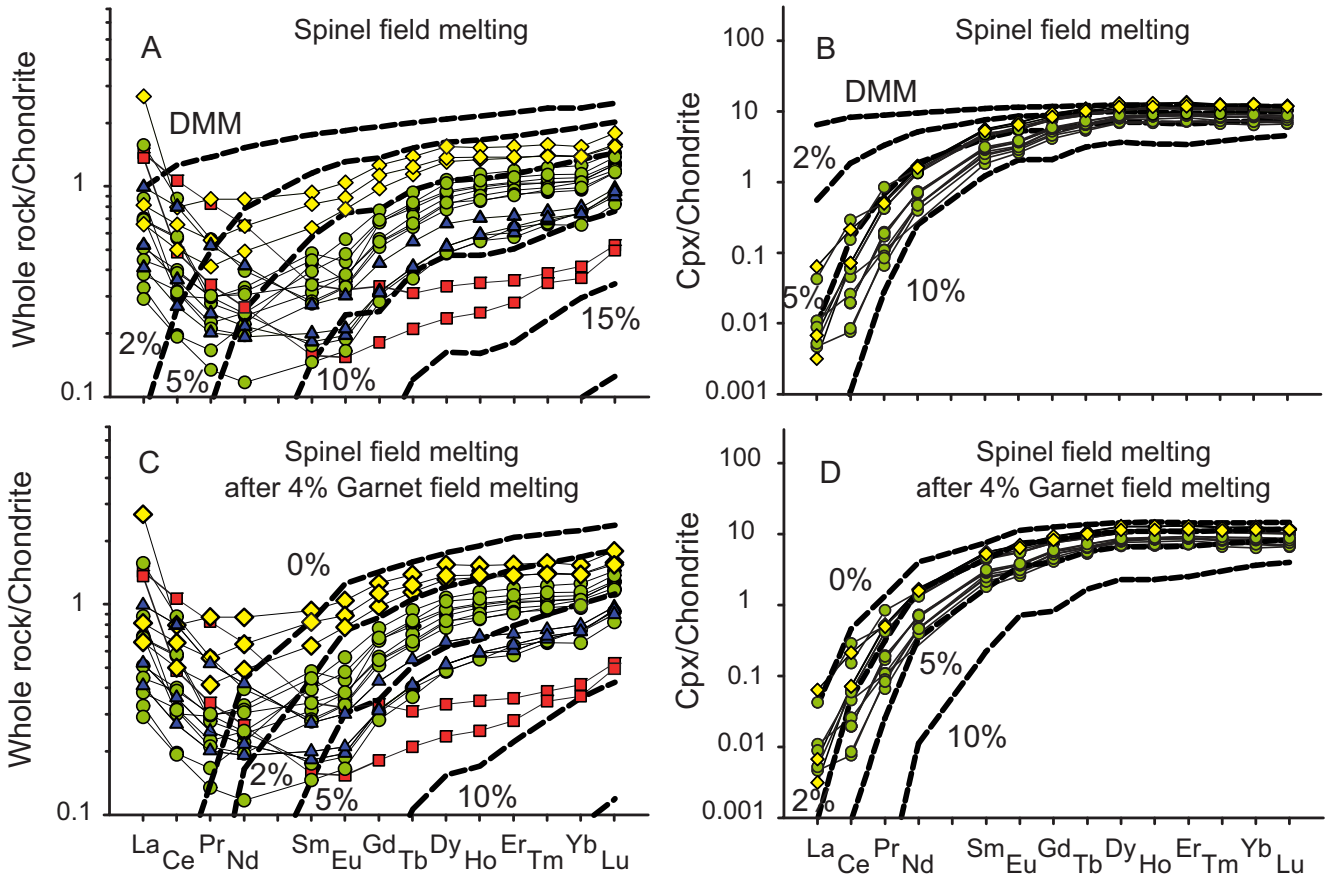

FIGURE 12 | **Chondrite-normalized REE patterns of the Monte del Estado A) peridotites and B) clinopyroxene compared with non-modal fractional melting curves (dashed lines) of spinel lherzolite [source and melting ol:opx:cpx modal proportions 0.57:0.28:0.15 and -0.03:0.50:0.53, respectively (Niu, 1997 at 2 GPa)]. 4% non-modal fractional melting in the garnet stability field [source and melting ol:opx:cpx:grt modal proportions 0.57:0.21:0.13:0.09 and 0.12:-0.94:1.37:0.45, respectively (Walter et al., 1995 at 3.5 GPa)] followed by the same melting model in the spinel stability field of (a) and (b) compared to chondrite-normalized REE patterns of the Monte del Estado C) peridotites and D) clinopyroxene. Mode of the spinel peridotite source after partial melting in the garnet stability field calculated by the equation of Johnson (1990). Symbols as in Figure 3. Labels indicate partial melting degrees. The source composition is equal to the depleted MORB mantle (DMM) (Salters and Stracke, 2004). Partition coefficients from Bedini and Bodinier (1999), Su and Langmuir (2003) and Donnelly et al. (2004). Normalizing values from Sun and McDonough (1989).**

(e.g., amphibole, phlogopite) along grain boundaries or as microinclusions in minerals during melt percolation (Niu and Hékinian, 1997; Niu et al., 1997; Garrido et al., 2000; Niu, 2004). Alternatively, the enrichment in incompatible trace elements along grain boundaries in peridotite may result from near-equilibrium partitioning between grain boundaries and grain interiors (Hiraga et al., 2007).

Tectonic setting of the Monte del Estado peridotite belt

Abyssal peridotites represent mantle residues produced by partial melting beneath mid ocean ridges where common MORB are generated (e.g., Dick and Bullen, 1984). They normally differ from supra-subduction peridotites that experience intense melting above a subduction zone and are usually highly depleted in terms of modal (low clinopyroxene proportions, Parkinson and Pearce, 1998), mineral (high Cr# in spinel, Arai, 1994; low HREE in clinopyroxene, e.g., Jean et al., 2010) and whole rock (low Al_2O_3, CaO and HREE, Parkinson et al., 1992) compositions. However, distinguishing between these two tectonic settings purely on geochemical evidence for residual mantle rocks is not straightforward, as the compositions of abyssal and supra-subduction peridotites significantly overlap.

The mineral and whole rock compositions of the Monte del Estado peridotites coincide with those of the abyssal peridotites dredged on the ocean floor (Fig. 3, 4A, 8). Considering the paleo-tectonic reconstructions of the Caribbean realm in the Cretaceous (e.g., Pindell and Barrett, 1990; Meschede and Frisch, 1998; Pindell et al., 2006; Pindell and Kennan, 2009), the Monte del Estado peridotite belt may either constitute a portion of the Caribbean (Pacific-Farallon) or of the Proto-Caribbean (North American-Proto Atlantic) lithospheric mantle. In the Mesozoic

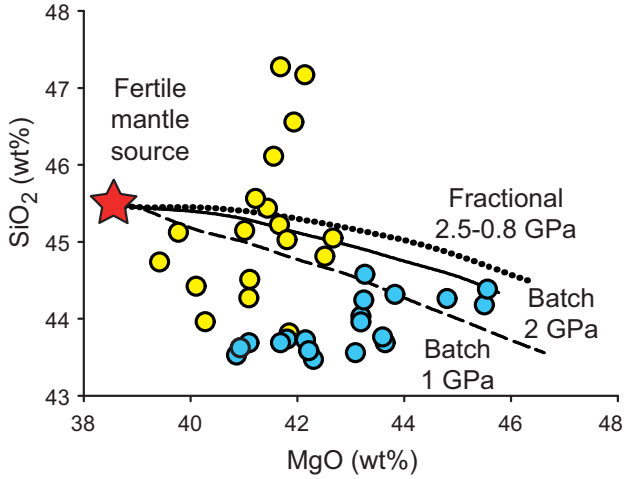

FIGURE 13 | **MgO versus SiO_2 of actual whole rock analyses (yellow circles) and recalculated whole rock compositions after MgO addition (blue circles) for the Monte del Estado peridotites. All data on anhydrous basis in wt%. Curves of polybaric near-fractional and isobaric batch melting of fertile mantle source (star) from Niu (1997).**

and Cenozoic, the convergence between these two plates was accommodated by an extinct intra-oceanic margin, namely the Greater Antilles paleo-island arc, associated to the relatively short-lived NE-dipping subduction of the Caribbean plate beneath the Proto-Caribbean ocean in the Early Cretaceous and by the opposite SW-dipping subduction geometry from the Aptian to the Eocene (Pindell and Barrett, 1990; Pindell et al., 2006; Marchesi et al., 2007; Jolly et al., 2008b; Lázaro et al., 2009; Pindell and Kennan, 2009). Most well-preserved ophiolites in the world probably represent ancient forearc lithospheric sections and not mid oceanic lithosphere generated at ridges as the last is normally subducted beneath the arc system and its obduction onto the convergent margin is highly unlikely (Stern, 2004). Actually, many ophiolitic complexes, e.g. Oman (Tamura and Arai, 2006), Cyprus (Batanova and Sobolev, 2000) and California (Jean et al., 2010), have mantle and crustal compositions of both supra-subduction and mid-oceanic affinities, as occurs in the forearc regions of actual arc systems (e.g., Parkinson and Pearce, 1998; Pearce et al., 2000). In these subduction-related settings, the preservation of abyssal-type peridotites is ascribed to the accretion of oceanic lithosphere that was least modified by the petrological processes active in the subduction zone.

The Monte del Estado peridotite belt was probably emplaced in the Early Cretaceous (Mattson, 1979; Curet, 1986; Jolly et al., 1998; Schellekens, 1998; Laó-Dávila, 2008) when the Caribbean plate was subducting beneath the Proto-Caribbean ocean in a SW-facing arc system. We thus propose that the Monte del Estado peridotites represent a portion of ancient Proto-Caribbean lithospheric mantle originally involved in seafloor spreading between North and South America in Late Jurassic-Early Cretaceous. This mantle section was subsequently trapped in the forearc region of the Greater Antilles paleo-island arc in the Early Cretaceous without having been significantly modified by subduction processes before its emplacement, which was probably related to a polarity reversal of the subduction zone in the Aptian-Albian (Mattson, 1979).

CONCLUSIONS

Spinel lherzolite and minor harzburgite from the Monte del Estado serpentinized belt in southwest Puerto Rico have mineral and whole rock compositions that generally coincide with those of fertile abyssal peridotites from mid ocean ridges. Serpentinization and seafloor weathering induced variable MgO and CaO loss in the peridotites but did not affect their LREE budgets that positively correlate with abundances of HFSE (e.g., Nb and Hf) not mobilized by low T hydrothermal fluids. HREE contents in whole rock indicate that the Monte del Estado peridotites are residues after low to moderate (2-15%) fractional melting degrees in the spinel stability field. However, clinopyroxene in lherzolite and in clinopyroxene-rich lherzolite has very low LREE and MREE concentrations supporting that they result from initial low (~ 4%) fractional melt extraction from a garnet lherzolite source followed by variable melting degrees (0-5%) in the spinel stability field. Relatively low reconstructed SiO_2 and high LREE abundances in whole rock were produced by interaction of melting residues with liquids ascending through the oceanic upper mantle. This interaction is not recorded by clinopyroxene composition but only in whole rock, suggesting that it likely occurred in the uppermost relatively cold mantle region where fluid/melt fractions were trapped or submicroscopic hydrous phases were crystallized along grain boundaries or as microinclusions in minerals.

The Monte del Estado peridotite belt probably constitutes a section of ancient Proto-Caribbean (Atlantic) lithospheric mantle generated in the Late Jurassic-Early Cretaceous by oceanic spreading between North and South America. In the Early Cretaceous this portion of the mantle lithosphere was accreted to the forearc region of the extinct SW-facing Greater Antilles paleo-island arc but was not significantly affected by subduction-related melting before its emplacement into the crust.

ACKNOWLEDGMENTS

We are grateful to Michel Grégoire and Johannes H. Schellekens for their constructive comments on the submitted version of the manuscript. Mike Lozon (Brock University) is kindly thanked for providing the electronic geological sketch map of SW Puerto

Rico. This research has been financially assisted by the Spanish "Ministerio de Ciencia e Innovación (MICINN)" through research grants CGL2006-07384, CGL2007-61205-BTE, HF2008-0073, CGL2009-12518, by the CSIC grant 200830I014, and by the Junta de Andalucía grant 2009-RNM-4495 and research group RNM 131. C.M.'s research has been supported by a Marie Curie Intra European Fellowship within the 7th European Community Framework Programme.

REFERENCES

Arai, S., 1994. Characterization of spinel peridotites by olivine-spinel compositional relationships: Review and interpretation. Chemical Geology, 113, 191-204.

Austrheim, H., Prestvik, T., 2008. Rodingitization and hydration of the oceanic lithosphere as developed in the Leka ophiolite, north–central Norway. Lithos, 104, 177-198.

Bach, W., Garrido, C.J., Paulick, H., Harvey, J., Rosner, M., 2004. Seawater-peridotite interactions: First insights from ODP Leg 209, MAR 15º N. Geochemistry Geophysics Geosystems, 5, Q09F26. doi:10.1029/2004GC000744.

Batanova, V.G., Sobolev, A.V., 2000. Compositional heterogeneity in subduction-related mantle peridotites, Troodos massif, Cyprus. Geology, 28, 55-58.

Bedini, R.M., Bodinier, J.-L., 1999. Distribution of incompatible trace elements between the constituents of spinel peridotite xenoliths: ICP-MS data from the East African Rift. Geochimica et Cosmochimica Acta, 63(22), 3883-3900.

Bodinier, J.-L., Godard, M., 2003. Orogenic, Ophiolitic, and Abyssal Peridotites. In: Carlson, R.W. (ed.). The Mantle and Core. Treatise on Geochemistry. Elsevier, 2, 103-170.

Bodinier, J.-L., Vasseur, G., Vernieres, J., Dupuy, C., Fabriès, J., 1990. Mechanisms of mantle metasomatism: geochemical evidence from the Lherz orogenic peridotite. Journal of Petrology, 31, 597-628.

Curet, A.F., 1986. Geologic map of the Mayagüez and Rosario quadrangles, Puerto Rico. Miscellaneous Investigations Series Map, U.S. Geological Survey, I-1657.

Dick, H.J.B., Bullen, T., 1984. Chromian spinel as a petrogenetic indicator in abyssal and alpine-type peridotites and spatially associated lavas. Contributions to Mineralogy and Petrology, 86(1), 54-76.

Donnelly, K.E., Goldstein, S.L., Langmuir, C.H., Spiegelman, M., 2004. Origin of enriched ocean ridge basalts and implications for mantle dynamics. Earth and Planetary Science Letters, 226, 347-366.

Gao, S., Liu, X., Yuan, H., Hattendorf, B., Günther, D., Chen, L., Hu, S., 2002. Determination of forty two major and trace elements in USGS and NIST SRM glasses by laser ablation-inductively coupled plasma-mass spectrometry. Geostandards Newsletter, 26(2), 181-196.

Garrido, C.J., 1995. Estudio Geoquímico de las Capas Máficas del Mazico Ultramáfico de Ronda (Cordillera Bética, Sur de España). Ph.D. Thesis. Granada, Universidad de Granada, 273pp.

Garrido, C.J., Bodinier, J.-L., Alard, O., 2000. Incompatible trace element partitioning and residence in anhydrous spinel peridotites and websterites from the Ronda orogenic peridotite. Earth and Planetary Science Letters, 181(3), 341-358.

Godard, M., Jousselin, D., Bodinier, J.-L., 2000. Relationships between geochemistry and structure beneath a palaeo-spreading centre: a study of the mantle section in the Oman ophiolite. Earth and Planetary Science Letters, 180(1-2), 133-148.

Govindaraju, K., 1994. Compilation of working values and sample description for 383 geostandards. Geostandards Newsletter, XVIII (Special Issue), 1-158.

Gruau, G., Griffiths, J.B., Lécuyer, C., 1998. The origin of U-shaped rare earth patterns in ophiolite peridotites: Assessing the role of secondary alteration and melt/rock reaction. Geochimica et Cosmochimica Acta, 62, 3545-3560.

Hart, S.R., Zindler, A., 1986. In search of a bulk-Earth composition. Chemical Geology, 57, 247-267.

Hellebrand, E., Snow, J.E., Hoppe, P., Hofmann, A.W., 2002. Garnet-field melting and late-stage refertilization in 'residual' abyssal peridotites from the Central Indian Ridge. Journal of Petrology, 43(12), 2305-2338.

Hiraga, T., Hirschmann, M.M., Kohlstedt, D.L., 2007. Equilibrium interface segregation in the diopside–forsterite system II: applications of interface enrichment to mantle geochemistry. Geochimica et Cosmochimica Acta, 71, 1281-1289.

Ionov, D.A., Savoyant, L., Dupuy, C., 1992. Application of the ICP-MS technique to trace-element analysis of peridotites and their minerals. Geostandards Newsletter, 16(2), 311-315.

Jagoutz, E., Palme, H., Baddenhausen, H., Blum, H., Cendales, M., Dreibus, G., Spettel, B., Lorenz, V., Wanke, H., 1979. The abundances of major, minor and trace elements in the Earth's mantle as derived from primitive ultramafic nodules. Geochimica et Cosmochimica Acta, 11, 2031-2050.

Jean, M.M., Shervais, J.W., Choi, S.H., Mukasa, S.B., 2010. Melt extraction and melt refertilization in mantle peridotite of the Coast Range ophiolite: an LA–ICP–MS study. Contributions to Mineralogy and Petrology, 159, 113-136.

Jochum, K.P., Seufert, H.M., Thirwall, M.F., 1990. Multi-element analysis of 15 international standard rocks by isotope-dilution spark source mass spectrometry (ID-SSMS). Analytical Chemistry, 331, 104-110.

Johnson, K.T.M., 1990. Melting in the Oceanic Upper Mantle: An Ion Microprobe Study o f Diopsides in Abyssal Peridotites. Journal of Geophysical Research, 95(B3), 2661-2678.

Johnson, K.T.M., 1998. Experimental determination of partition coefficients for rare earth and high-field-strength elements between clinopyroxene, garnet and basaltic melt at high pressures. Contributions to Mineralogy and Petrology, 133, 60-68.

Jolly, W.T., Lidiak, E.G., Schellekens, J.H., Santos, H., 1998. Volcanism, tectonics, and stratigraphic correlations in Puerto Rico. In: Lidiak, E.G., Larue, D.K. (eds.). Tectonics and geochemistry of the northeastern Caribbean. Geological Society of America, 322 (Special Paper), 1-34.

Jolly, W.T., Schellekens, J.H., Dickin, A.P., 2007. High-Mg andesites and related lavas from southwest Puerto Rico (Greater Antilles Island Arc): Petrogenetic links with emplacement of the Late Cretaceous Caribbean mantle plume. Lithos, 98, 1-26.

Jolly, W.T., Lewis, J.F., Proenza, J.A., 2008a. Mineralogy and mineral chemistry of the Rio Guanajibo peridotites, southwest Puerto Rico, with comparisons. In: Gil Argelés, J. (ed.). 18th Caribbean Geological Conference. Santo Domingo (Dominican Republic), Programa y Resúmenes, 34.

Jolly, W.T., Lidiak, E.G., Dickin, A.P., 2008b. The case for persistent southwest-dipping Cretaceous convergence in the northeast Antilles: Geochemistry, melting models, and tectonic implications. Geological Society of America Bulletin, 120, 1036-1052.

Kogiso, T., Tatsumi, Y., Nakano, S., 1997. Trace element transport during dehydration processes in the subducted oceanic crust: 1. Experiments and implications for the origin of ocean island basalts. Earth and Planetary Science Letters, 148, 193-205.

Laó-Dávila, D., 2008. Serpentinite emplacement and deformation in western Puerto Rico and their implications for the Caribbean-North America plate boundary tectonic history. Ph.D. Thesis. Pittsburgh, University of Pittsburgh, 293pp.

Lázaro, C., García-Casco, A., Rojas Agramonte, Y., Kröner, A., Neubauer, F., Iturralde-Vinent, M.A., 2009. Fifty-five-million-year history of oceanic subduction and exhumation at the northern edge of the Caribbean plate (Sierra del Convento mélange, Cuba). Journal of metamorphic Geology, 27, 19-40.

Lewis, J.F., Draper, G., Proenza, J.A., Espaillat, J., Jiménez, J., 2006a. Ophiolite-Related Ultramafic Rocks (Serpentinites) in the Caribbean Region: A Review of their Occurrence, Composition, Origin, Emplacement and Ni-Laterite Soil Formation. Geologica Acta, 4(1-2), 237-263.

Lewis, J.F., Proenza, J.A., Jolly, W.T., Lidiak, E.G., 2006b. Monte del Estado (Puerto Rico) and Loma Caribe (Dominican Republic) peridotites: A look at two different Mesozoic mantle sections within northern Caribbean region. Geophysical Research Abstracts, 8, A-08798.

Llerandi Román, P.A., 2004. The Geology of the western section of the Sabana Grande quadrangle: implications for the geological evolution of southwestern Puerto Rico. M.S. Thesis. Mayagüez, University of Puerto Rico, 134pp.

Marchesi, C., Garrido, C.J., Godard, M., Proenza, J.A., Gervilla, F., Blanco-Moreno, J., 2006. Petrogenesis of highly depleted peridotites and gabbroic rocks from the Mayarí-Baracoa Ophiolitic Belt (eastern Cuba). Contributions to Mineralogy and Petrology, 151, 717-736.

Marchesi, C., Garrido, C.J., Bosch, D., Proenza, J.A., Gervilla, F., Monié, P., Rodríguez-Vega, A., 2007. Geochemistry of Cretaceous Magmatism in Eastern Cuba: Recycling of North American Continental Sediments and Implications for Subduction Polarity in the Greater Antilles Paleo-arc. Journal of Petrology, 48, 1813-1840.

Mattson, P.H., 1960. Geology of the Mayagüez area, Puerto Rico. Geological Society of America Bulletin, 71, 319-362.

Mattson, P.H., 1979. Subduction, buoyant breaking, flipping and strike-slip faulting in the northern Caribbean. Journal of Geology, 87, 293-304.

McIntyre, D.H., Aaron, J.M., Tobisch, O.T., 1970. Cretaceous and lower Tertiary stratigraphy in northwestern Puerto Rico. U.S. Geological Survey Bulletin, 1294-D, 16.

Meschede, M., Frisch, W., 1998. A plate tectonic model for the Mesozoic and Early Cenozoic history of the Caribbean plate. Tectonophysics, 296, 269-291.

Münker, C., Wörner, G., Yogodzinski, G., Churikova, T., 2004. Behaviour of high field strength elements in subduction zones: constraints from Kamchatka–Aleutian arc lavas. Earth and Planetary Science Letters, 224, 275-293.

Navon, O., Stolper, E., 1987. Geochemical consequence of melt percolation: the upper mantle as a chromatographic column. Journal of Geology, 95, 285-307.

Niu, Y., 1997. Mantle melting and melt extraction processes beneath ocean ridges: evidence from abyssal peridotites. Journal of Petrology, 38, 1047-1074.

Niu, Y., Hékinian, R., 1997. Basaltic liquids and harzburgitic residues in the Garrett transform: a case study at fast-spreading ridges. Earth and Planetary Science Letters, 146, 243-258.

Niu, Y., Langmuir, C.H., Kinzler, R.J., 1997. The origin of abyssal peridotites: a new perspective. Earth and Planetary Science Letters, 152, 251-265.

Niu, Y., 2004. Bulk-rock major and trace element compositions of abyssal peridotites: Implications for mantle melting, melt extraction and post-melting processes beneath mid-ocean ridges. Journal of Petrology, 45(12), 2423-2458.

Parkinson, I.J., Pearce, J.A., 1998. Peridotites from the Izu-Bonin-Mariana Forearc (ODP Leg 125): Evidence for mantle melting and melt-mantle interaction in a supra-subduction zone setting. Journal of Petrology, 39, 1577-1618.

Parkinson, I.J., Pearce, J.A., Thirlwall, M.F., Johnson, K.T.M., Ingram, G., 1992. Trace elements geochemistry of peridotites from the Izu–Bonin–Mariana forearc, Leg 125. In: Fryer, P., Pearce, J.A., Stokking, L.B. (eds.). Proceedings of the Ocean Drilling Program. Scientific Results, 125, 487-506.

Paulick, H., Bach, W., Godard, M., De Hoog, J.C.M., Suhr, G., Harvey, J., 2006. Geochemistry of abyssal peridotites (Mid-Atlantic Ridge, 15°20'N, ODP Leg 209): Implications for fluid/rock interaction in slow spreading environments. Chemical Geology, 234, 179-210.

Pearce, N.J., Perkins, W.T., Westgate, J.A., Gorton, M.P., Jackson, S.E., Neal, C.R., Chenery, S.P., 1997. A compilation of new and published major and trace element data for NIST SRM 610 and NIST SRM 612 glass reference materials. Geostandards Newsletter, 21, 115-144.

Pearce, J.A., Barker, P.F., Edwards, S.J., Parkinson, I.J., Leat, P.T., 2000. Geochemistry and tectonic significance of peridotites from the South Sandwich arc-basin system, South Atlantic. Contributions to Mineralogy and Petrology, 139, 36-53.

Pindell, J.L., Barrett, S.F., 1990. Geological evolution of the Caribbean Region; A plate-tectonic perspective. In: Dengo, G., Case, J. (eds.). The Geology of North America, The Caribbean Region. The Geological Society of America, H, 405-432.

Pindell, J.L., Kennan, L., 2009. Tectonic evolution of the Gulf of Mexico, Caribbean and northern South America in the mantle reference frame: an update. In: James, K., Lorente, M.A., Pindell, J.L., (eds.). The Origin and Evolution of the Caribbean Plate. Geological Society of London, 328 (Special Publications), 1-55.

Pindell, J.L., Kennan, L., Stanek, K.P., Maresch, W.V., Draper, G., 2006. Foundations of Gulf of Mexico and Caribbean evolution: eight controversies resolved. Geologica Acta, 4(1-2), 303-341.

Proenza, J.A., Gervilla, F., Melgarejo, J.C., 1999a. La Moho Transition Zone en el Macizo Ofiolítico Moa-Baracoa: un ejemplo de interacción magma/peridotita. Revista de la Sociedad Geológica de España, 12, 309-327.

Proenza, J.A., Gervilla, F., Melgarejo, J.C., Bodinier, J.-L., 1999b. Al- and Cr-rich chromitites from the Mayarí-Baracoa Ophiolitic Belt (Eastern Cuba): consequence of interaction between volatile-rich melts and peridotite in suprasubduction mantle. Economic Geology, 94, 547-566.

Proenza, J.A., Zaccarini, F., Lewis, J.F., Longo, F., Garuti, G., 2007. Chromite composition and platinum-group mineral assemblage of PGE-rich Loma Peguera chromitites, Loma Caribe peridotite, Dominican Republic. Canadian Mineralogist, 45, 211-228.

Salters, V.J.M., Stracke, A., 2004. Composition of the depleted mantle. Geochemistry Geophysics Geosystems, 5(5), Q05004. doi:10.1029/2003GC000597.

Schellekens, J.H., 1998. Geochemical evolution and tectonic history of Puerto Rico. In: Lidiak, E.G., Larue, D.K. (eds.). Tectonics and geochemistry of the northeastern Caribbean. Geological Society of America, 322 (Special Paper), 35-66.

Sharma, M., Wasserburg, G.J., 1996. The neodymium isotopic compositions and rare earth patterns in highly depleted ultramafic rocks. Geochimica et Cosmochimica Acta, 60, 4537-4550.

Snow, J.E., Dick, H.J.B., 1995. Pervasive magnesium loss by marine weathering of peridotite. Geochimica et Cosmochimica Acta, 59(20), 4219-4235.

Stern, R.J., 2004. Subduction initiation: spontaneous and induced. Earth and Planetary. Science Letters, 226, 275-292.

Su, Y., Langmuir, C.H., 2003. Global MORB chemistry compilation at the segment scale. Ph.D. Thesis. New York, Columbia University.

Sun, S.-S., McDonough, W.F., 1989. Chemical and isotopic systematics of oceanic basalts: implications for mantle composition and processes. In: Saunders, A.D., Norry, M.J. (eds.). Magmatism in the Ocean Basins. Geological Society of London, 42 (Special Publications), 313-345.

Tamura, A., Arai, S., 2006. Harzburgite–dunite–orthopyroxenite suite as a record of supra-subduction zone setting for the Oman ophiolite mantle. Lithos, 90, 43-56.

van Achterberg, E., Ryan, C.G., Jackson, S.E., Griffin, W., 2001. Data reduction software for LA-ICP-MS. In: Sylvester, P. (ed.). Laser ablation ICP-MS in the Earth Science. Mineralogical Association of Canada, 29, 239-243.

Vernières, J., Godard, M., Bodinier, J.-L., 1997. A plate model for the simulation of trace element fractionation during partial melting and magma transport in the Earth's upper mantle. Journal of Geophysical Research, 102, 24771-24784.

Volckmann, R.P., 1984. Upper Cretaceous stratigraphy of southwest Puerto Rico: A revision. U.S. Geological Survey Bulletin, 1537-A, A73-A83.

Walter, M.J., Sisson, T.W., Presnall, D.C., 1995. A mass proportion method for calculating melting reactions application to melting of model upper mantle lherzolite. Earth and Planetary Science Letters, 135, 77-90.

You, C.-F., Castillo, P.R., Gieskes, J.M., Chan, L.H., Spivack, A.J., 1996. Trace element behavior in hydrothermal experiments: implications for fluid processes at shallow depths in subduction zones. Earth and Planetary Science Letters, 140, 41-52.

Manuscript received November 2010;
revision accepted January 2011;
published Online February 2011.

Geologica Acta, Vol.9, Nos 3-4, September-December 2011, 307-328
DOI: 10.1344/105.000001716
Available online at www.geologica-acta.com

geologica acta

The Pelona-Pico Duarte basalts Formation, Central Hispaniola: an on-land section of Late Cretaceous volcanism related to the Caribbean large igneous province

J. ESCUDER-VIRUETE [1] [*] A. PÉREZ-ESTAÚN [2] M. JOUBERT [3] D. WEIS [4]

[1] **Instituto Geológico y Minero de España**
C. La Calera 1, 28760 Tres Cantos, Madrid. Spain. E-mail: j.escuder@igme.es

[2] **Instituto Ciencias Tierra Jaume Almera-CSIC**
Lluís Solé Sabarís s/n. 08028 Barcelona, Spain. E-mail: andres@ija.csic.es

[3] **Bureau de Recherches Géologiques et Minières**
Av. C. Guillemin. 45060 Orléans. France. E-mail: m.joubert@brgm.fr

[4] **Pacific Centre for Isotopic and Geochemical Research. University of British Columbia**
6339 Stores Road Vancouver, BC V6T-1Z4. Canada. E-mail: dweis@eos.ubc.ca

* Corresponding author

ABSTRACT

Located in Central Hispaniola, the Pelona-Pico Duarte basalts Formation (Fm.) offers an opportunity to study the Late Cretaceous Caribbean large igneous province magmatism on land. It is composed by a ~2.5km-thick pile of massive and monotonous submarine flows of basalts, locally intruded by synvolcanic dikes and sills of dolerite. The Pelona-Pico Duarte basalts Fm. was emplaced onto Turonian-Lower Campanian island-arc volcanic and sedimentary sequences, and is overlain by Maastrichtian platformal carbonates. Two $^{40}Ar/^{39}Ar$ plateau ages indicate both extrusive and intrusive magmatic activity at least during the 79-68Ma interval (Middle Campanian to Maastrichtian), so the magmas were in part coeval with the late phases of the Caribbean large igneous province. The basalts have a restricted major-and trace-element, and isotopic, compositional variation. For a range of 47.6-50.2wt.% SiO_2, the Pelona-Pico Duarte basalts Fm. has relatively high contents in TiO_2 (1.5-3.6wt.%) and Fe_2O_{3T} (10.7-13.1wt.%). On the basis of MgO contents, samples can be classified into tholeiitic basalts (<8wt.%) and high-Mg basalts (8-12wt.%). Mineral assemblages and major element compositional trends indicate that basalts derived from tholeiitic parental magmas by fractionation of olivine plus spinel, clinopyroxene and orthopyroxene, observed as microphenocrysts, as well as plagioclase and Fe-Ti oxides. In a MORB-normalized multi-element plot, the basalts have light rare earth elements (LREE) enriched ($[La/Nd]_N$=1.5-2.2) and heavy rare earth elements (HREE) depleted ($[Sm/Yb]_N$=2.1-3.7) patterns, with very high Nb contents (11-30ppm). These patterns and the values of trace element ratios (K/Ba<20, Ti/V>20 and Zr/Nb<10) are characteristic of transitional and alkalic oceanic-island basalts. In terms of Sr-Nd isotopic composition, the samples are homogeneous and enriched relative to older Caribbean large igneous province units in Hispaniola, with $(^{87}Sr/^{86}Sr)_i$ ratios between 0.70330

and 0.70348 for a very restricted range of $(\varepsilon_{Nd})_i$ values between +5.0 and +5.9 (where *i*=70Ma). The Pelona-Pico Duarte basalts Fm. are interpreted as partial melts of a plume-related, deep enriched source, which have not been contaminated by active subduction. Mantle melt modelling indicates that both high-Mg basalts and basalts formed by mixed melts of both garnet and spinel lherzolite in variable amounts. Melts incorporated at different mantle depths, most probably in relation to the melt column processes in an upwelling plume.
The Pelona-Pico Duarte basalts Fm. has significantly different values of petrogenetic tracers compared to underlying arc-related lavas, indicating a fundamental change in the mantle sources. It has geochemical affinities with the mantle domain influenced by the Late Cretaceous Caribbean plume, suggesting that enriched mantle was flowing toward the NE, to the mantle wedge region of the Caribbean island-arc, in response to rollback of the SW-directed subduction of the proto-Caribbean slab.

KEYWORDS | **Caribbean large igneous province. Mantle source. Hispaniola. Caribbean plate.**

INTRODUCTION

Most Late Cretaceous lavas in Hispaniola have a typical subduction-related geochemical signature and therefore record the magmatic activity of the Caribbean paleoisland-arc (Lewis et al., 1991; Lebron and Perfit, 1994). Nevertheless, thick sequences of volcanic rocks cropping out in the axial sector of the Cordillera Central have trace element and isotopic compositions with an enriched mid-ocean ridge basalt (E-MORB) to ocean island basalt (OIB) affinities (e.g. Ba/La<40, La/Yb>10, ε_{Nd}=+6 to +8; Escuder-Viruete et al., 2008). These magmas intruded into and extruded onto arc volcanic rocks of the Cenomanian-Lower Campanian Tireo Group and related intrusions of gabbros and tonalites. Therefore, mantle wedge-derived Caribbean island-arc magmatism was replaced by non-arc-like magmatism during the uppermost Late Cretaceous in Central Hispaniola. These relations raise questions about the timing of formation of these non arc-like magmas, the relatively fast change of magma sources, their relationship with the Caribbean large igneous province (in the sense of Sinton et al., 1998; Hauff et al., 2000; Hoernle et al., 2004), and the Late Cretaceous geodynamical evolution of the northeast edge of the Caribbean plate.

A hypothesis is that change in the magmatism was induced by Caribbean arc-rifting, extension and, eventually, back-arc basin development and, as a result, it had an origin from processes not directly related to a Caribbean mantle plume. During arc rifting and back-arc development a changing style in the petrogenesis of the magmas and nature of the mantle sources occurs. And these characteristics evolve from those typical of volcanic arcs to those of sea-floor spreading (Gribble et al., 1998; Ewart et al., 1998; Taylor and Martínez, 2003). Physical models proposed for this evolution imply a reorganization of mantle convective regimes beneath evolving back-arc basins, where an advective system similar to that of mid-ocean ridges is superimposed on a suprasubduction zone corner flow field (Martínez and Taylor, 2002). Owing to continued spreading, the extension axis separates from the volcanic front and the flux of fluids/melts from the subducting slab to the mantle wedge decreases (Walker et al., 2003). Mantle source changes when, eventually, the back-arc spreading system separates sufficiently from the volcanic front and it is not significantly affected by hydration and slab-derived geochemical components (Martínez and Taylor, 2002). In this tectonic context, fertile MORB-source mantle must be advecting into the mantle wedge to balance the overall roll-back of the subducting slab. Such a mantle flow has been inferred under back-arcs on the basis of temporal changes in geochemical and isotopic signature of basin lavas (Taylor and Martínez, 2003), mapping upper mantle seismic anisotropy (Smith et al., 2001), laboratory analogical modelling (Kincaid and Griffiths, 2003), and thermomechanical numerical modelling (Nikolaeva et al., 2008).

In this tectonic context, the change of magma sources recorded in Central Hispaniola during the Late Cretaceous might be the consequence of mantle flow that drags the plume source of the Caribbean large igneous province under the extended island-arc. In this paper, we examine the field relationships, petrography, Ar-Ar geochronology, major trace elements and Sr-Nd isotopic compositions of the Pelona-Pico Duarte basalts Fm. from Central Hispaniola to assess the nature of the mantle source, the conditions of melting and the magmatic history of the region in the context of the construction of the Late Cretaceous Caribbean large igneous province. These data, in conjunction with published data of coeval island-arc and Caribbean plateau-related units in Hispaniola, allow us to address two main issues: 1) the change of mantle sources in the late Cretaceous; and 2) the original tectonic setting of the basalts. Finally, we propose a tectonomagmatic evolutive model for Central Hispaniola during the Campanian-Maastrichtian.

GEOLOGICAL SETTING

The Caribbean large igneous province

The Caribbean large igneous province formed in a period of extreme magmatic activity in the Late Cretaceous which originated an oceanic plateau that was subsequently incorporated in the Caribbean plate (Kerr et al., 1997; Sinton et al., 1998; Hauff et al., 2000; Hoernle et al., 2002). The submerged portion of the plateau in the Caribbean Sea was sampled by drilling during Deep Sea Drilling Project Leg 15 and Ocean Drilling Programme Leg 163 (Donnelly et al., 1990). The on-land portion was sampled in exposed sequences of the Caribbean large igneous province outcrop in Jamaica, Hispaniola, Puerto Rico, coastal borderlands of Venezuela, Curaçao and Aruba islands, the Pacific coast of Central America and western Colombia and Ecuador (Lapierre et al., 2000; Kerr et al., 2002). The Caribbean large igneous province includes volcanic rocks erupted during three phases of broadly different age: 124-112Ma (Lapierre et al., 2000; Escuder-Viruete et al., 2007b), 94-83Ma (the main magma production phase; Kerr et al., 1997; Sinton et al., 1998; Hastie et al., 2008) and 80-72Ma (Révillon et al., 2000). These phases have also been recognized by Hauff et al. (2000) and Hoernle et al. (2004) in Costa Rica and in other Cretaceous oceanic plateaus from the Western Pacific (Kerr, 2003), where plume magmatism occurred for 50Ma or more at variable eruptive rates. The youngest Caribbean large igneous province rocks are found in the Dominican Republic (69Ma) and the Quepos Peninsula of Costa Rica (63Ma; Sinton et al., 1998). Thus, magmatism of the Caribbean large igneous province magmatism occurred from the Aptian to the Maastrichtian, with a peak at around the Turonian-Coniacian (92-88Ma), and not in one voluminous burst at ~90Ma, as was originally postulated.

A Pacific origin for the Caribbean plateau is generally accepted (e.g., Duncan and Hargraves, 1984; Pindell et al., 2005), especially in light of evidence that fragments of oceanic crust were accreted to the margins of the Caribbean region, as in Hispaniola and Puerto Rico, which are closely associated with radiolarian cherts containing fauna of Pacific provenance (Montgomery et al., 1994; Baumgartner et al., 2008; Jolly et al., 2008; Escuder-Viruete et al., 2009). Modelling of the plate tectonic evolution suggests that the eastward movement of the Farallon plate in the Late Cretaceous-Early Tertiary forced the motion of the northern half of the Caribbean large igneous province into the ocean basin that had been opening between North and South America since the Jurassic (Mann, 1999; Pindell et al., 2005). However, the mechanism of motion toward the NE of the plateau remains unclear, especially its relation with the Campanian initiation of subduction in the Costa Rica-Panama arc (see revision of Pindell and Kennan, 2009). Using a fixed hotspot reference frame, Duncan and Hargraves (1984) suggested that the magmas of the Caribbean large igneous province were produced by partial melting within the initial "plume head" of the Galápagos hotspot. However, Meschede (1998) argued against a Galápagos origin for the Caribbean large igneous province and Kerr and Tarney (2005) proposed that the Caribbean large igneous province results from the accretion of two separated Late Cretaceous oceanic plateaus, related to two independent hotspots.

The sequence of melting events associated with a mantle plume (or plumes) that occurred beneath the Caribbean plate is not well established because the internal volcanic stratigraphy of the igneous province is not well known. The uppermost surface of the Caribbean large igneous province has been identified seismically as the B discontinuity, which is interpreted to be the upper surface of the plateau lavas (Mauffret and Leroy, 1997). The discontinuity has been drilled in five localities of the Caribbean basin: Deep Sea Drilling Project sites 146, 150, 151 and 152, and Ocean Drilling Programme Site 1001. At Deep Sea Drilling Project Site 152 and Ocean Drilling Programme Site 1001 (only ~40km far away), a thin basalt sill overlying the basement was drilled, but the basement was not reached. The compositional similarity of basalts from sites 152 and 1001 has led to the suggestion that they are part of the same horizon (Sinton et al., 1998). The basalt sill penetrated at site 152 intrudes Campanian (83-70Ma) sediment, and ^{40}Ar-^{39}Ar dating of basalts from site 1001 yields ages of around 81Ma (Sinton et al., 2000). Basalts are therefore younger than the main phase of plateau construction (i.e. ~90Ma), and also appear to be part of a different seismic horizon (Mauffret et al., 2000). Thus, the basalts sampled at sites 152 and 1001 may not be part of the bulk plateau, but rather the product of late-stage rifting of the Caribbean crust after plateau formation (Sinton et al., 1998). Samples recovered by submersible from the Beata Ridge, a topographic high in the central Caribbean basin, show this structure to be composed mainly of gabbros, dolerites and rare pillow basalts (Révillon et al., 2000), with a geochemical signature very similar to that of basalts from other parts of the Caribbean large igneous province. Most samples have ages between 80 and 75Ma, which are consistent with previous ages within the province, but others are very young, around 55Ma. Following Révillon et al. (2000), the "Galápagos" hotspot was probably responsible for the main plume-related magmatic event at 90Ma, and the 76Ma and 55Ma episodes are related to lithospheric thinning of the Central Caribbean (Mauffret and Leroy, 1997).

Though the Caribbean large igneous province comprises a wide diversity of basaltic magma compositions, the vast majority of the lavas show signatures with ε_{Nd} ranging from

+8.5 to +6 and flat to slightly LREE-enriched chondrite normalized patterns (Kerr et al., 1997, 2002; Sinton et al., 1998; Hauff et al., 2000; Lapierre et al., 2000; Révillon et al., 2000; Thompson et al., 2004; Jolly et al., 2007; Escuder-Viruete et al., 2008). The existence of a very similar geochemical and isotopic signature for basalts of ages from 124 to 63Ma, and from very distant parts of the Caribbean, raises questions about the validity of generally accepted rising mantle-plume models for the formation of the whole Caribbean large igneous province. Therefore, alternative models that reconcile geologic data, petrology and plate tectonic history should be considered.

Occurrences of the Caribbean large igneous province in Hispaniola

In Hispaniola, fragments of obducted/accreted oceanic plateau-like basalts include the Dumisseau Fm. in southwestern Haiti (Sen et al., 1988), equivalent lithostratigraphic units in the Sierra de Bahoruco in southwestern Hispaniola (Escuder-Viruete et al., 2008), the Siete Cabezas Fm. (Donnelly et al., 1990; Sinton et al., 1998), and the Duarte Complex in Central Cordillera (Lewis et al., 1991; Lapierre et al., 1997, 2000; Lewis et al., 2002; Escuder-Viruete et al., 2007b). The Dumisseau Fm. consists of pillow and massive basalt flows and minor picrites interlayered with pelagic limestones, volcanogenic and biogenic turbidites, cherts, and siltstones. Fossil ages of the sediments are Early Cretaceous to Santonian for the lower basalts, and Late Campanian for the upper basalts. Sinton et al. (1998) obtained ^{40}Ar-^{39}Ar ages between 88.7±1.5 and 92.0±4.8Ma for the lower basalts. However, the upper basalts of the Dumisseau Fm. should be younger, given the Late Campanian fossil age of the sediments and the 75.0±1.5Ma K-Ar age provided by a late-stage sill intruding the upper sequence (Sen et al., 1988). This formation is overlain by late Campanian to Maastrichtian limestones. In Central Hispaniola, the Siete Cabezas Fm. unconformably overlies the Duarte Complex directly (Escuder-Viruete et al., 2008). It is composed of massive and pillowed aphyric basalts, with minor pyroclastic breccias, vitric tuffs and cherts, intruded by dolerite dikes. Radiolarian content in the sediments yields a Middle Campanian to Maastrichtian age (Montgomery and Pessagno, 1999). Sinton et al. (1998) obtained consistent ^{40}Ar-^{39}Ar ages by whole-rock (69.0±0.7Ma) and plagioclase (68.5±0.5Ma) analyses. These ages and the geochemical characteristics of the lavas (tholeiitic basalts with flat REE patterns) led Lewis et al. (2002) to attribute this unit to the Caribbean large igneous province. The Duarte Complex comprises a ~3km thick sequence of heterogeneously deformed and metamorphosed mafic to ultramafic volcanic rocks, intruded by Late Cretaceous arc-related batholiths (91-83Ma; Escuder-Viruete et al., 2007a, 2008). The complex includes olivine-clinopyroxene phyric meta-picrites and high-Mg meta-basalts, chemically related to plume-generated magmas (Lewis et al., 2002) and similar to the most enriched Caribbean large igneous province lavas (Lapierre et al., 1997, 2000; Escuder-Viruete et al., 2007b). Foliated amphibolites of the Duarte Complex yield ^{40}Ar-^{39}Ar hornblende plateau ages of 93.9±1.4 and 95.8±1.9Ma (Cenomanian) that demonstrate an older age of the protholiths, probably Albian (>96Ma). Therefore, this complex records an Early Cretaceous phase of the Caribbean large igneous province construction in Hispaniola.

Structural blocks in Central Hispaniola

Central Hispaniola is a composite of oceanic derived units bound by the left-lateral strike-slip Hispaniola fault zone and the San Juan-Restauración fault zone (Fig. 1). Accreted units mainly include the serpentinized Loma Caribe peridotites, MORB-type gabbros and basalts, Late Jurassic deep-marine sediments, Cretaceous volcanic units related to the Caribbean large igneous province, and Late Cretaceous arc-related igneous and sedimentary rocks (Draper and Lewis, 1991; Lewis et al., 1991, 2002; Escuder-Viruete et al., 2007a, 2009; Lapierre et al., 1997, 1999). These units were variably deformed and metamorphosed in prehnite-pumpellyte, greenschist and amphibolite facies conditions, but the textures of the protoliths are often preserved. The internal structure of Central Hispaniola is characterized by several km-scale NNW-SSE to WNW-ESE trending fault zones (Fig. 2), which bound three crustal domains or tectonic blocks, namely: Jicomé, Jarabacoa, and Bonao. These tectonic blocks are characterized by different Turonian-Campanian volcanic stratigraphies, geochemical compositions and physical characteristics of their constituent igneous rocks (Escuder-Viruete et al., 2008). The Loma de Cabrera, Loma del Tambor, Macutico and Arroyo Caña gabbro-tonalitic batholiths were intruded syn- to late-kinematically along these shear and fault zones mainly during the Coniacian-Santonian interval (90-84Ma; Escuder-Viruete et al., 2006). Turbiditic sedimentary basins filled with the Tavera Group, which was unconformably deposited over these juxtaposed tectonic blocks, indicate that the main ductile structure of Central Hispaniola was pre-Middle Eocene. Late Cretaceous fault zones were variably reactivated during the Upper Eocene-Oligocene brittle thrusting and the Miocene to Recent uplift of the Cordillera Central.

The Jicomé block is composed of a >3km thick sequence of arc- and Caribbean large igneous province-related volcanic, subvolcanic and volcano-sedimentary rocks of the Tireo Group and the overlying Peña Blanca and Pelona-Pico Duarte Fms. (Fig. 2). The Tireo Group includes two main volcanic sequences with different geochemical characteristics (Escuder-Viruete et al., 2007a).

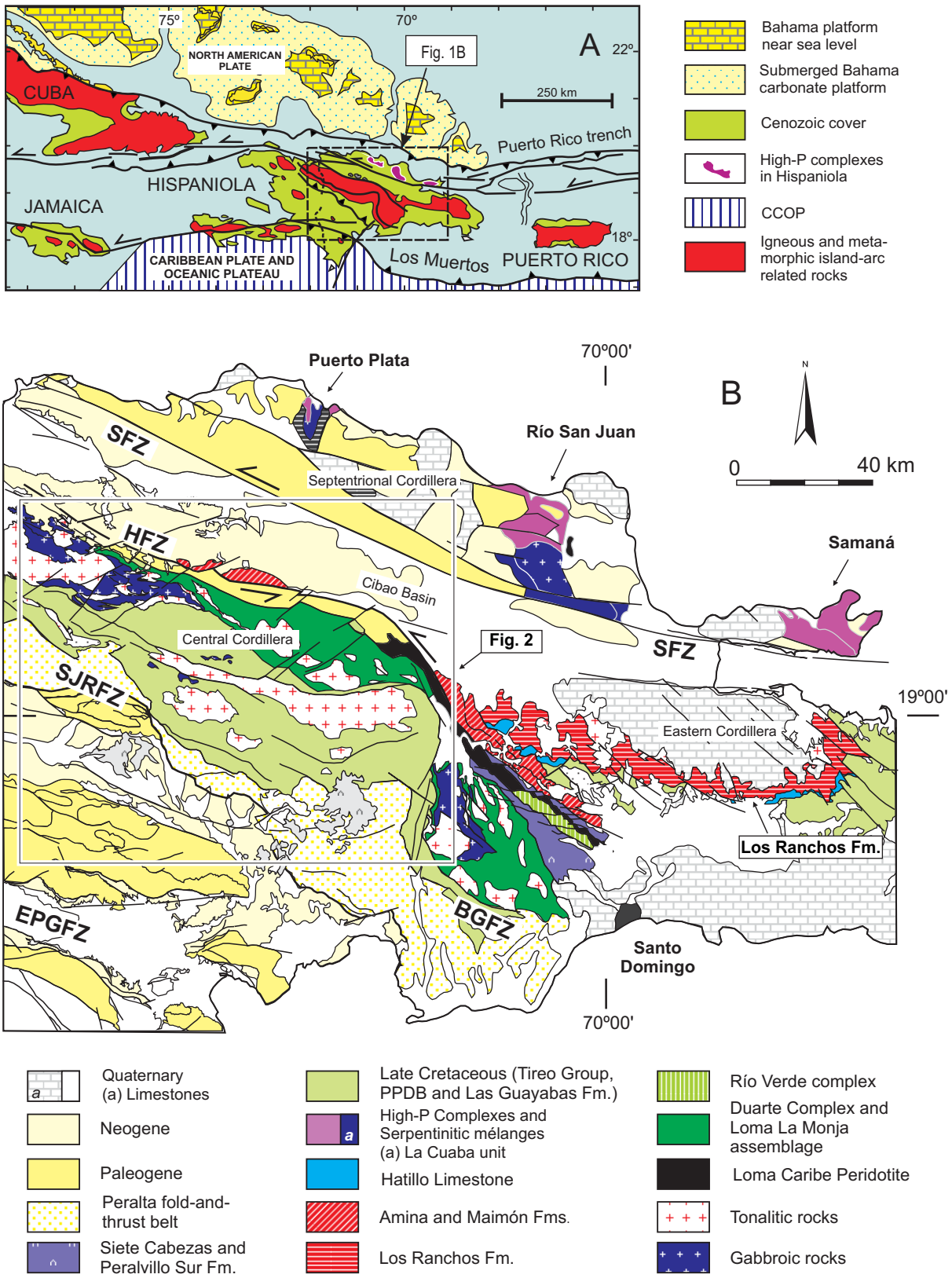

FIGURE 1 | **A) Map of the northeastern Caribbean plate margin. Box shows location of the study area. B) Schematic geological map of Central, Septentrional and Eastern Cordilleras in Hispaniola. SFZ: Septentrional fault zone; HFZ: Hispaniola fault zone; BGFZ: Bonao-La Guácara fault zone; SJRFZ: San José-Restauración fault zone; EPGFZ: Enriquillo-Plantain Garden fault zone. Box shows location of Fig. 2.**

The lower Constanza Fm. constitutes an Albian to Turonian tholeiitic suite, dominated by submarine vitric-lithic tuffs and breccias of basaltic to andesitic composition, with minor interbedded basaltic flows. The upper Restauración Fm. is characterized by a spatial and temporal association of subduction-related adakites, high-Mg andesites and basalts, and Nb-enriched basalts. This stratigraphic interval is mainly represented by

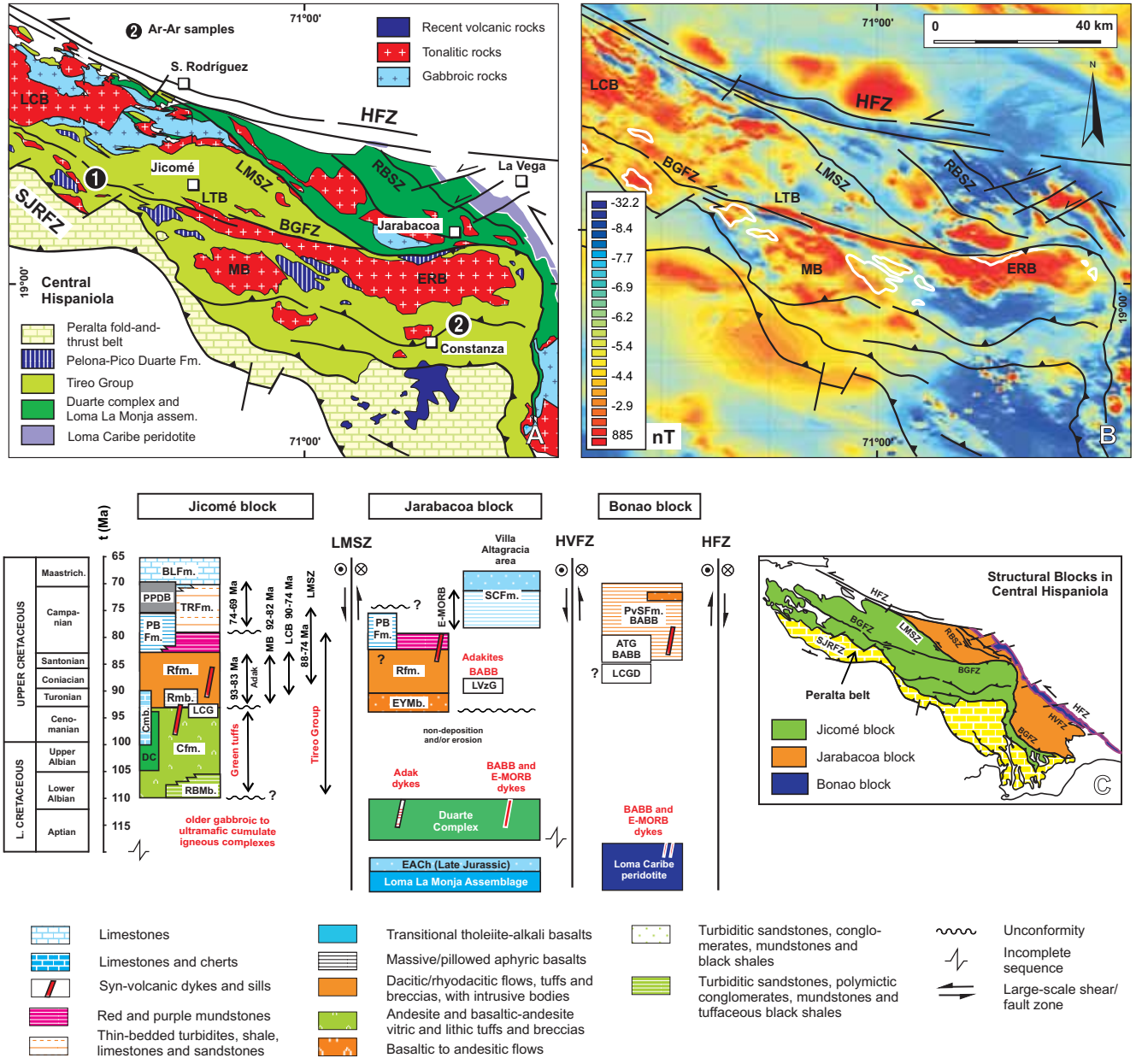

FIGURE 2 | **A) Schematic geological map of the studied area in Central Hispaniola. Encircled numbers show locations of samples for Ar-Ar geochronology. B) Total magnetic field shown. WNW-ESE-trending bands and elongated anomalies correlated respectively with main fault zones and outcrops of gabbro-tonalitic batholiths and basalts of the Pelona-Pico Duarte Fm. (white outlines). C) Schematic lithostratigraphic columns of the three crustal domains or tectonic blocks in Central Hispaniola, namely Jicomé, Jarabacoa and Bonao, as well as of the Eastern Cordillera. LMSZ: La Meseta; RBSZ: Río Baiguaque; HVFZ: Hato Viejo; BGFZ: Bonao-La Guácara shear or fault zones. TG: Tireo Group; RBMb: Río Blanco Member; CFm: Constanza Fm.; DC: Dajabón Chert; CMb: Constanza Member; RFm: Restauración Fm.; LCG: La Cana gabbro; PBFM: Peña Blanca Fm.; BPPD: basalts of Pelona-Pico Duarte Fm.; TRFm: Trois Rivières Fm.; BLFm: Bois de Lawrence Fm.; EYMb: El Yujo Member; LVzG: Los Velazquitos gabbros; SCFm: Siete Cabezas Fm.; ATG: Arroyo Toro gabbros; LCGD: Loma Caribe related-gabbros/diorites; PvSFm: Peralvillo Sur Fm. Ranges of age data in the Jicomé block from Escuder-Viruete et al., (2006a, 2007b, 2008). Adak: adakites; MB: Macutico batholith; LTB: Loma del Tambor batholith; LCB: Loma de Cabrera batholith; LMSZ: La Meseta shear zone; TBA: tholeitic basalt/andesite suite; HMA: high-Mg andesites; NEBA: Nb-enriched basalts and andesites; BABB: back-arc basin basalts. Other abbreviations as in Fig. 1.**

dacitic/rhyolitic explosive volcanism of calc-alkaline affinity, with subaerial to episodic aerial eruptions and emplacement of sub-volcanic domes (Lewis et al., 1991, 2002). Fossil and U-Pb/Ar-Ar geochronological data show that the upper sequence began to extrude at the Turonian-Coniacian boundary (~89Ma) and continued in the Santonian to Lower Campanian. The Peña Blanca Fm. is composed of a 150-250m-thick succession of aphyric, non-vesicular basaltic flows. The basalts have relatively high-Ti contents and high Nb/Th ratios (4-22), as well as slightly LREE-enriched and flat HREE patterns, with a positive Nb anomaly. These characteristics indicate that magmas were derived from a relatively enriched spinel mantle source, which had not been contaminated by a subducting slab (Escuder-Viruete et al., 2008). In the Late Campanian-Maastrichtian, the platform limestones of the Bois de Lawrence Fm. were deposited on top of the extinct arc.

Stratigraphy of the Pelona-Pico Duarte basalts

The Pelona-Pico Duarte basalts Fm. has been defined recently during regional mapping studies (1:50000 scale) of the SYSMIN Project in the Dominican Republic. Exposures of this unit are localized in the axial sector of the Cordillera Central, mainly between 1500 and 3000m of altitude, and are only accessible by walking. However, the strong magnetism of basalts has helped in its cartography. As shown in Fig. 2B, the total magnetic field map of Central Hispaniola is characterized by WNW-ESE trending bands and subparallel elongated anomalies, which are correlated with the main fault zones, and outcrops of the gabbro-tonalitic batholiths and the Pelona-Pico Duarte basalts Fm. (white outlines).

The Pelona-Pico Duarte basalts Fm. is composed of a massive and homogeneous ~2.5km thick pile of basaltic submarine flows, mostly aphyric and amygdalar, frequently banded and rarely porphyritic (Fig. 3). Lava flows are locally interlayered with mafic tuffs, hyaloclastite, and intruded by synvolcanic dikes and sills of basalt and dolerite. Basaltic flows and lobes (<5m thick) are marked mainly by amygdaloidal horizons, often filled by quartz-carbonate in cooling-contraction cracks. Toward the top of the unit, lava flows locally grade to tuff breccias with rare chert clasts. The presence of these breccias on the top of the lava pile suggests that eruptions may have occurred in shallower water; nevertheless, no evidence of subaerial eruptions has been found. Felsic volcanic rocks are absent. In the Loma Guandules area (southeast Restauración), the uppermost flows are overlain by shallow-water limestones of the Bois de Lawrence Fm. (Late Campanian-Maastrichtian). Under the microscope, samples of the Pelona-Pico Duarte basalts Fm. were divided into two main groups: tholeiitic basalts and picritic high-Mg basalts. Tholeiitic basalts typically have a microporphyritic/glomeroporphyritic texture with olivine, Ti-augite, orthopyroxene microphenocrysts in a devitrified glassy to intersertal/subophitic groundmass (Fig. 3). Plagioclase occurs as microprisms in the groundmass and in rarely plagioclase-phyric lavas. High-Mg basalts form massive flow units characterized by a high frequency of euhedral olivine and pyroxene phenocrysts. Accessory phases are small grains of Fe-Ti oxides and apatite. Amygdales and veins are filled by chlorite and quartz, with or without pumpellyte, calcite, zeolite, yellow epidote, albite, clays and opaque minerals.

^{40}AR/^{39}AR-GEOCHRONOLOGY

Analytical results

Two samples were selected for $^{40}Ar/^{39}Ar$ analysis (Fig. 4) with the aim of dating the cooling ages after extrusion of the lavas or emplacement of Pelona-Pico Duarte basalts Fm.-related intrusions. The methodology and the complete data set of the incremental heating ^{40}Ar-^{39}Ar experiments are included in Appendixes I and II. All ages are quoted at the 2σ level of uncertainty. Sample 5873I-SG9015 is a very high-Ti (TiO_2=3.6wt.%) and Nb (25ppm) aphyric basalt from the Loma Guandules in the Restauración area. For seven steps (4-10), the obtained plateau age from whole rock is 68.4±0.75Ma representing 71.0% of the ^{39}Ar released. Sample 6JE13A is a high-Ti (1.6wt.%) and Nb (14.5ppm) basaltic dike, intrusive in the volcanic sequence of the Tireo Group at Constanza. This mafic intrusive has a similar normalized trace element pattern to the one in rocks of the Pelona-Pico Duarte basalts Fm. (see below), indicating that it is probably a feeder dike of the basalts. For seven steps (3-9), the obtained plateau age of hornblende is 79.4±1.0Ma for 86.1% of the ^{39}Ar released.

Interpretation

Fig. 5 includes the Ar-Ar ages obtained for this study and other relevant regional data, which allow us to constrain the duration of the Pelona-Pico Duarte basalts Fm. magmatism and to establish correlations with coeval units of the Caribbean large igneous province. The two $^{40}Ar/^{39}Ar$ whole-rock and hornblende plateau ages obtained from geochemically similar rocks indicate both extrusive and intrusive magmatic activity at least during the 79-68Ma interval (middle Campanian to Maastrichtian; scale of Gradstein et al., 2004). This range of ages for Pelona-Pico Duarte basalts Fm. magmatism is similar to the $^{40}Ar/^{39}Ar$ ages of 69-68Ma obtained for the basalts of the Siete Cabezas Fm. (Sinton et al., 1998) of

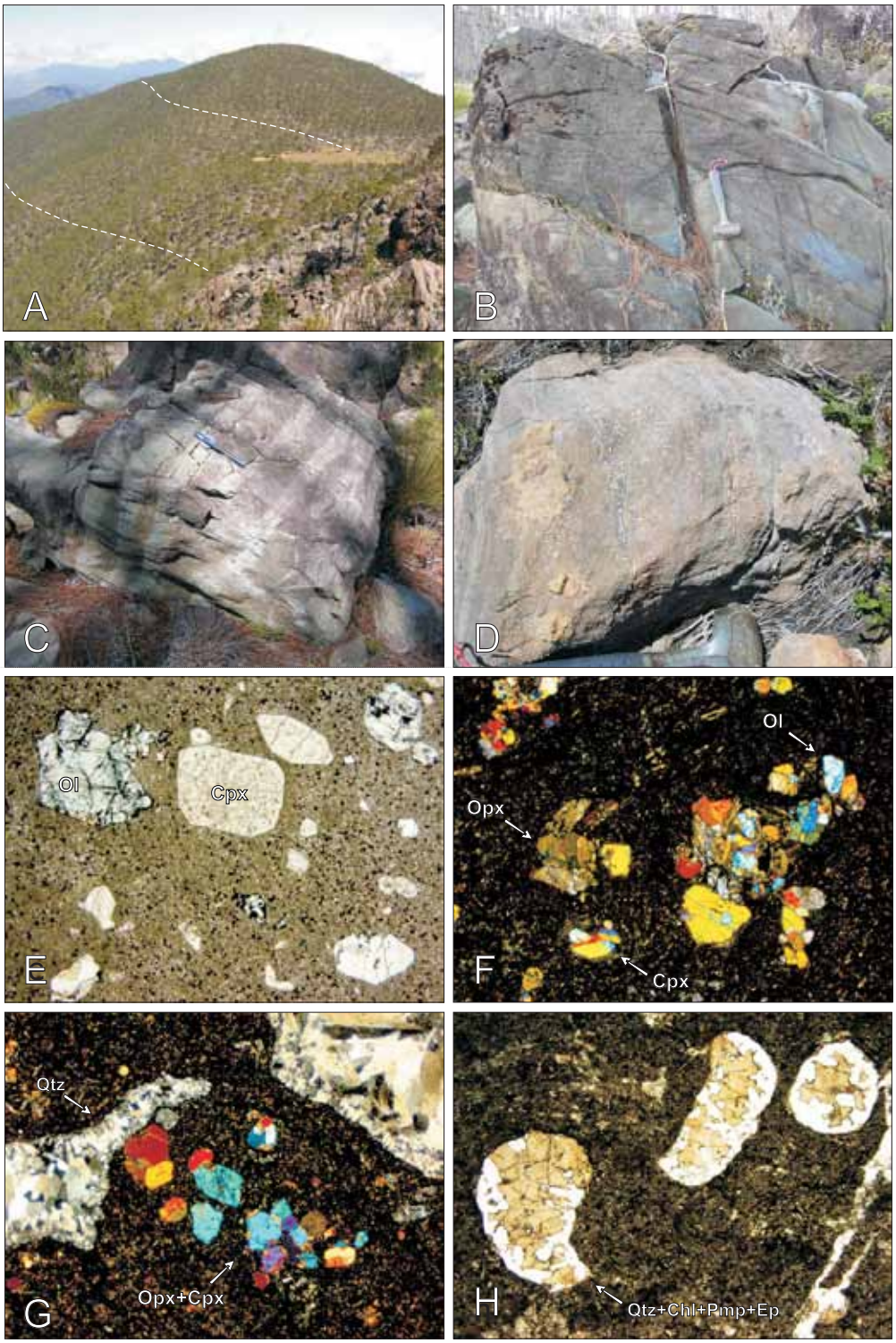

FIGURE 3 | **Field structures: A) Photograph from the Duarte peak (3087m) of ~400m-thick sequence of continuous massive and amygdaloidal flood basalts at the upper stratigraphical levels of the PPDB in the Pelona peak, Central Cordillera, Dominican Republic. The yellow line marks the bedding. B) Massive submarine flows of basalts with margins defined by vesicular and laminated horizons at Lilys valley. C) Massive flows and lobes with amygdaloidal horizons and subparallel infilling of quartz-carbonate in cooling-contraction cracks, south face of El Yaque peak. D) Close-up photograph of stretched vesicules in basaltic flows. Microphotographs: E) Porphyritic basalt with euhedral olivine (Ol; pseudomorphs) and Ti-augite (Cpx) phenocrysts (PPL). F) Basalt with microporphyritic to glomeroporphyritic textures defined by olivine (Ol), clinopyroxene (Cpx) and orthopyroxene (Opx) micro-phenocrysts (XPL). G) Amygdaloidal basalt with micro-phenocrysts of clino and orthopyroxene in a recrystallized glassy to intersertal groundmass rich in Fe-Ti oxides. Note zoned quartz infilling in vesycles (XPL). H) Amygdaloidal and aphyric basalt composed by a recrystallized glassy to intersertal groundmass rich in Fe-Ti oxides and vesycles filled by epidote, quartz and calcite (PPL). Width field in (e) to (h) ~3.5mm.**

the Jarabacoa block, which also have intercalated cherts with radiolarians of middle Campanian to Maastrichtian age (Montgomery and Pessagno, 1999). Also, these ages are similar to those of the Nb-enriched mafic lavas of the Sabana Grande Fm. in southwest Puerto Rico (Campanian; Jolly et al., 2007), the K-Ar age of 75.0±1.5Ma of a sill intruding the upper sequence of the Dumisseau Fm. in Haiti (Sen et al., 1988), and the predominant Campanian magmatic activity recorded in the Beata Ridge (80-75Ma; Révillon et al., 2000); all attributed to the Caribbean large igneous province. Temporarily, this magmatism can be related to the third phase of the Caribbean large igneous province construction (Kerr et al., 2002) and the related volcanic rocks of Costa Rica (Hoernle et al., 2004; Denyer and Baumgartner, 2006; Denyer et al., 2006). In summary, the Ar-Ar ages indicate that the Pelona-Pico Duarte basalts Fm. magmas were in part coeval with the extensive mafic volcanism of the Late Cretaceous Caribbean plateau.

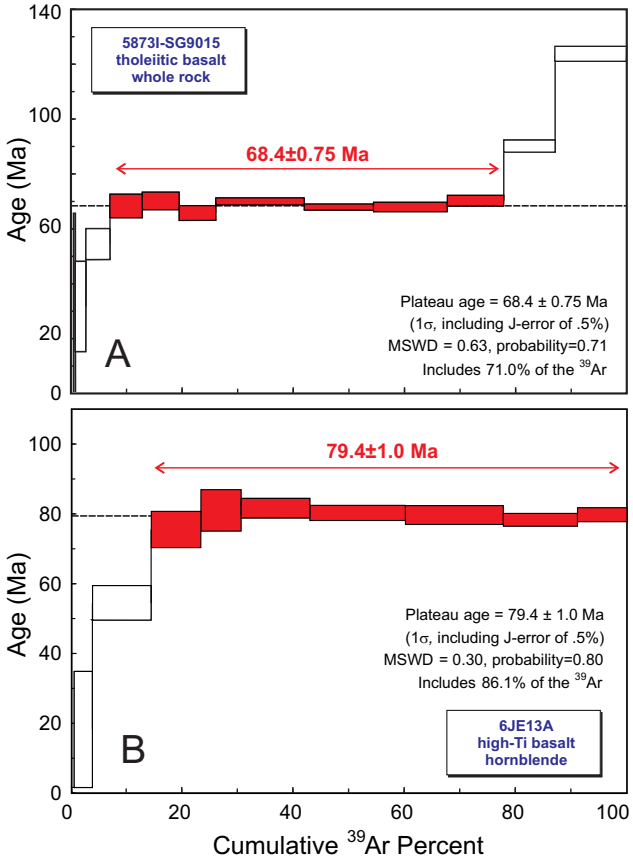

FIGURE 4 | **$^{40}Ar/^{39}Ar$ spectrum of whole rock and hornblende in samples from Pelona-Pico Duarte basalts Fm. and related dikes. The plateau ages were calculated following techniques described in Appendix I. A summary of ^{40}Ar–^{39}Ar incremental heating experiments is in Appendix II. Plateau steps are filled and rejected open. See text for discussion.**

GEOCHEMISTRY

Analytical methods

Samples were powdered in an agate mill, and analysed for major oxides by Inductively-Coupled Plasma-Emission Spectrometry (ICP-ES) and trace elements by Inductively-Coupled Plasma-Mass Spectrometry (ICP-MS). This analytical work was done at the ACME Analytical Laboratories Ltd in Vancouver and the results are reported in Table 1. Details of analytical accuracy and reproducibility are included in Appendix I. A representative subset of samples (Table 2) was also analysed for Sr and Nd isotopic compositions at the Pacific Centre for Isotopic and Geochemical Research of the University of British Columbia. Rb, Sr, Sm and Nd concentrations were measured by a Thermo Finnigan Element2, a double focussing (i.e., high resolution) Inductively Coupled Plasma-Mass Spectrometer (Pretorius et al., 2006). For isotopic analysis, samples were repeatedly leached with HCl6N to remove secondary alteration. Sr and Nd were separated using the method described in Weis et al. (2006). Isotope ratios were measured by a Thermo Finnigan Triton-TI Thermal Ionization Mass Spectrometry (TIMS) in static mode with relay matrix rotation on single Ta filament and double Re-Ta filament for Sr and Nd isotopic analyses respectively. Sr and Nd isotopic compositions were corrected for fractionation using $^{86}Sr/^{88}Sr=0.1194$ and $^{146}Nd/^{144}Nd=0.7219$. During the analyses, the NBS987

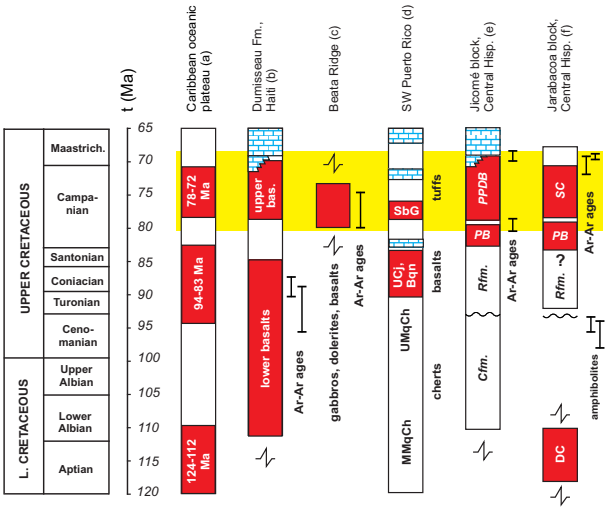

FIGURE 5 | **A) Summary of paleontological and geochronological ages for Caribbean large igneous province units (in black) in the northern Caribbean. Sources; a) Kerr et al. (2002); b) Sen et al. (1988); c) Révillon et al. (2000); d) Jolly et al. (2007); e) this work; and f) Sinton et al. (1998). MMqCh: Middle Mariquita Chert; UMqCh: Upper Mariquita Chert; UCj: Upper Cajul Fm.; Bqn: Boquerón Fm.; SbG: Sabana Grande Fm.; CFm: Constanza Fm.; RFm: Restauración Fm.; PB: Peña Blanca Fm.; PPDB: Pelona-Pico Duarte basalts Fm.; SC: Siete Cabezas Fm. Ar-Ar ages are the error bars (in 2). Time scale from Gradstein et al. (2004).**

TABLE 1 | **Major and trace element data of representative rocks from the Pelona-Pico Duarte Formation and related mafic intrusives**

Map	Manabao							Constanza
X(UTM)	-70.9112	-70.9134	-70.9363	-70.9942	-70.9958	-70.998	-70.951	324221
Y(UTM)	19.0287	19.02553	19.03277	19.03024	19.0273	19.02302	19.03547	2089101
Rock[a]	MBAS	MBAS	MBAS	MBAS	MBAS	MBAS	MBAS	BAS/DOL
Sample	41MJ9020	41MJ9022	41MJ9026	41MJ9033	41MJ9034	41MJ9036	41MJ9044	6JE13A
SiO_2	49.19	48.29	50	43.64	47.6	46.23	49.57	53.31
TiO_2	2.04	2.39	1.35	1.22	1.21	1.35	1.68	1.62
Al_2O_3	14.62	14.29	13.39	13.25	12.74	15.8	13.41	14.19
Fe_2O_3	12.11	13.04	11.6	12.44	11.36	11.84	11.66	11.66
MgO	6.59	6.46	7.19	9.45	9.7	5.45	7.56	5.51
CaO	10.25	9.8	11.78	15.85	12.72	11.95	11.22	4
Na_2O	1.95	1.75	2.16	0.41	1.38	2.31	1.94	4
K_2O	0.25	0.27	0.39	0.11	0.24	1.22	0.28	0.38
P_2O_5	0.174	0.221	0.152	0.131	0.104	0.45	0.139	0.24
MnO	0.18	0.2	0.22	0.22	0.19	0.19	0.21	0.14
Cr_2O_3	0.042	0.034	0.046	0.062	0.08	0.009	0.06	0.006
LOI	2.4	2.9	1.5	2.9	2.4	2.8	2	4.8
C/TOT	0.05	0.03	0.05	0.03	0.08	0.06	0.06	0.07
S/TOT	<0.02	<0.02	<0.02	<0.02	<0.02	<0.02	<0.02	0.08
SUM	99.84	99.67	99.82	99.71	99.80	99.65	99.78	99.86
Mg#[b]	52	50	55	60	63	48	56	48
Cr	-	-	-	-	-	-	-	41.0
Co	41.4	45.5	48.7	63.5	57.2	42	45.9	34.6
Ni	14.7	19.1	47	70.8	81.3	54	42.5	17.0
V	366	414	318	333	320	334	349	253
Rb	4.9	4.2	12	1.3	4	13.4	5.1	3.1
Ba	71	85	119	46	77	387	64	106.5
Th	1.2	1.3	1.3	0.8	1.1	1	1.4	1.3
U	0.4	0.4	0.3	0.3	0.2	0.4	0.4	0.5
Nb	12	15.9	10	8.6	7.9	21.1	9.7	14.5
Ta	0.8	1.1	0.7	0.5	0.6	1.1	0.8	0.9
La	11.6	14.6	10.1	7.1	7.1	16.3	10.1	12.1
Ce	27.9	35.4	22.2	16.1	16.5	31.7	23.7	28.5
Pb	0.6	0.7	0.5	0.3	0.4	0.4	0.3	1.5
Pr	4.05	5.04	3.11	2.35	0.4	4.09	3.33	3.94
Mo	0.2	0.3	1.5	0.7	0.6	0.8	0.7	0.6
Sr	234.7	224.6	222.5	329.3	207.3	313.4	218.6	125.6
Nd	19.4	23.5	14.1	10.8	11.8	16.2	14.6	18.1
Sm	4.72	6.07	3.24	2.99	2.78	3.87	3.88	4.2
Zr	118.2	148.9	88	60.6	59.6	92.9	97.7	113.2
Hf	3.3	4.6	2.5	1.9	2	2.7	2.6	3.2
Eu	1.59	1.83	1.09	1.09	0.94	1.17	1.3	1.42
Gd	5.08	6.31	3.65	3.36	2.99	3.68	4.27	4.2
Tb	0.87	1.07	0.64	0.61	0.51	0.65	0.74	0.8
Dy	4.55	5.92	3.71	3.49	2.91	3.61	3.85	4.05
Y	26.2	32.7	20.9	19.9	16.5	19.6	22.6	21.5
Ho	0.94	1.27	0.78	0.73	0.61	0.73	0.82	0.79
Er	2.49	3.11	2.1	1.84	1.55	1.85	2.12	2.23
Tm	0.37	0.45	0.32	0.31	0.28	0.33	0.34	0.31
Yb	2.2	2.67	1.85	1.69	1.36	1.62	1.85	1.79
Lu	0.33	0.44	0.3	0.28	0.22	0.28	0.31	0.27

Data of samples SG9015, SG9016, SG9017, MJ9377 and MJ9365 are included in Escuder-Viruete et al. (2008).

[a] Rock type abbreviations: DOL, dolerite; MBAS, massive basalt; VBAS, vesicular/amygdalar basalt

Major elements in wt.%; trace elements in ppm.

[b] Mg# = 100 * mol MgO/ mol (FeO + MgO); for $Fe_2O_3/FeO = 0.2$. Total Fe as Fe_2O_3.

TABLE 2 | **Sr-Nd isotope ratios for representative basat samples of Pelona-Pico Duarte Formation**

Sample	Type	Rb	Sr	$^{87}Sr/^{86}Sr$	$(^{87}Sr/^{86}Sr)_i$	Sm	Nd	$^{143}Nd/^{144}Nd$	$(^{143}Nd/^{144}Nd)_i$	$(\varepsilon_{Nd})_i$
6JE68	BAS	4.3	315.4	0.703354 (7)	0.703304	4.08	15.8	0.512923 (7)	0.512831	6.02
MJ9020	BAS	4.9	234.7	0.703540 (8)	0.703480	4.72	19.4	0.512922 (8)	0.512855	5.99
MJ9026	BAS	12	222.5	0.703457 (8)	0.703301	3.24	14.1	0.512896 (7)	0.512833	5.55
MJ9034	HMB	4	207.3	0.703408 (9)	0.703352	2.78	11.8	0.512896 (7)	0.512830	5.51
MJ9036	BAS	13.4	313.4	0.703496 (9)	0.703373	3.87	16.2	0.512890 (8)	0.512824	5.39
MJ9036B	BAS	13.4	313.4	0.703495 (7)	0.703372	3.87	16.2	0.512898 (9)	0.512832	5.54
SG9015	BAS	7.4	346.7	0.703409 (9)	0.703349	7.2	29.9	0.512904 (8)	0.512840	5.64
SG9016	BAS	12	406.7	0.703486 (9)	0.703404	7.5	33.3	0.512869 (7)	0.512809	5.04

All samples were leached and digested on hotplate. BAS; basalts; HMB; high-Mg basalts. Rb, Sr, Sm and Nd values in ppm.
Calculated initial ratios (*i*) and e_{Nd}-values calculated at *t*=70 Ma. Number in brackets is the absolute 2s error in the last decimal places.
e_{Nd} values are relative to $^{143}Nd/^{144}Nd$=0.512638 and $^{147}Sm/^{144}Nd$=0.1966 for present day CHUR (Jacobsen and Wasserburg. 1980) and lambda ^{147}Sm= 6.54×10^{-12}/year

Sr standard gave an average of 0.710253±0.000009 (n=6) and the La Jolla Nd standard gave an average value of 0.511851±0.000013 (n=5). $^{147}Sm/^{144}Nd$ ratio errors are approximately ~1.5%, or ~0.006.

Chemical changes due to alteration and metamorphism

The analyzed basalts have been variably altered and metamorphosed to zeolitic- and prehnite-pumpellyite metamorphic facies conditions. Consequently, changes of the bulk-rock chemistry are expected as a consequence of selected mobility of relevant elements during these processes. Many major (e.g., Si, Na, K, Ca) and trace (e.g., Cs, Rb, Ba, Sr) elements are easily mobilised by late and/or post-magmatic fluids and metamorphism; however, the high field strength elements (HFSE) (Y, Zr, Hf, Ti, Nb and Ta), REE, transition elements (V, Cr, Ni and Sc) and Th, are generally unchanged under a wide range of metamorphic conditions, including seafloor alteration at low to moderate water/rock ratios (Bédard, 1999). Therefore, the geochemical characterization of the Pelona-Pico Duarte basalts Fm. and the petrogenetic discussion will be based mostly on the HFSE and REE, as well as Nd-isotopes, as it can be assumed that they were not significantly affected by alteration or metamorphism.

Major and trace-element compositions

As a suite, the basalts of the Pelona-Pico Duarte basalts Fm. have a very restricted range in SiO_2 content, ranging from 47.6 to 50.2wt.% (Table 1), and high TiO_2 contents between 1.2 and 3.6wt.% (Fig. 6A). On the basis of MgO contents (Fig. 6d), samples can be divided into tholeiitic basalts (<8wt.%) and high-Mg basalts (8-12wt.%). The Mg# values of 63-48 indicate that these lavas have undergone low to moderate amounts of fractionation. They have relatively low contents in CaO (9.8-15.8wt.%) and Al_2O_3 (10.8-14.6wt.%), and relatively high contents in alkalis (2.0-2.6wt.%), P_2O_5 (0.1-0.4wt.%) and Fe_2O_{3T} (11.6-13.0wt.%). These rocks show an increase of SiO_2, Fe_2O_{3T}, TiO_2, CaO, Al_2O_3, alkalis, Zr and Nb, and a decrease in Cr and Ni for decreasing MgO (not all shown in Fig. 6). These trends are tholeiitic and can be attributed to the fractionation of olivine plus Cr-spinel, clinopyroxene and orthopyroxene, observed as microphenocrysts in the lavas, as well as plagioclase and Fe-Ti oxides. These rocks are quartz or olivine normative, with diopside, hyperstene and Cr-spinel. Based on immobile trace element classification schemes (Fig. 7A), the samples are transitional and alkalic basalt (Nb/Y>0.4), which is compatible with their major element compositions, norm and mineralogy. In the tectonic discrimination diagrams of Wood (1980) and Meschede (1986), basalts of the Pelona-Pico Duarte basalts Fm. and related intrusive dikes both plot consistently in within-plate tholeiitic and alkalic basalt fields (Fig. 7B, C).

In a MORB-normalized multi-element plot (Fig. 8), the basalts of the Pelona-Pico Duarte basalts Fm. have LREE enriched ($[La/Nd]_N$=1.5-2.2) and depleted HREE ($[Sm/Yb]_N$=2.1-3.7) patterns, with very high Nb contents (8-30ppm). They do not have positive Pb, K and Sr spikes, and negative Nb-Ta anomalies, typical of subduction-related rocks. However, some samples have a small selective enrichment in some fluid-mobile LILE (Rb, Ba and U), which probably results from seafloor alteration. The slight negative Eu and positive Ti anomalies present in some evolved basalts are related to plagioclase and Fe-Ti oxide fractionation/accumulation, respectively. These patterns and the values of the trace element ratios Ti/V>20 and Zr/Nb<10 (6.2-8.4) are characteristic of modern day transitional and alkalic oceanic-island basalts (Pearce, 2008). The high TiO_2 content and $(Sm/Yb)_N$ ratios suggest that the mantle source of these basalts was relatively enriched and contained garnet (Greene et al., 2009). These rocks are interpreted as partial melts of a plume-related, deep enriched source, which have not been contaminated by active subduction (Nb/Th>8; Fig. 6).

In Fig. 8, the basalts of the Peña Blanca and Siete Cabezas Fm. of the Jicomé and Jarabacoa blocks are plotted for comparison. These sub-alkaline basalts have

distinctive slightly LREE-enriched ($[La/Nd]_N$=1.0-1.8) and flat HREE ($[Sm/Yb]_N$=0.9-1.5) patterns, with a positive Nb anomaly (Nb/Nb*=1.2-2.3). All these features, as well as their incompatible element ratios (Zr/Nb<15 and La/Sm>1.5), are characteristic of enriched MORB (Donnelly et al., 2004). Relatively high-Ti contents, Nb/Th ratios (4-22) and flat-HREE indicate that these magmas were derived from a relatively enriched spinel mantle source, which had not been contaminated by a subducting slab. Probably, these basalts represent a tholeiitic volcanism in distal areas from the arc, such as back-arc areas or dorsal segments affected by mantle plume activity (Escuder-Viruete et al., 2008). On the other hand, the patterns are similar to those of the gabbros and dolerites dredged from the Beata Ridge (Révillon et al.,

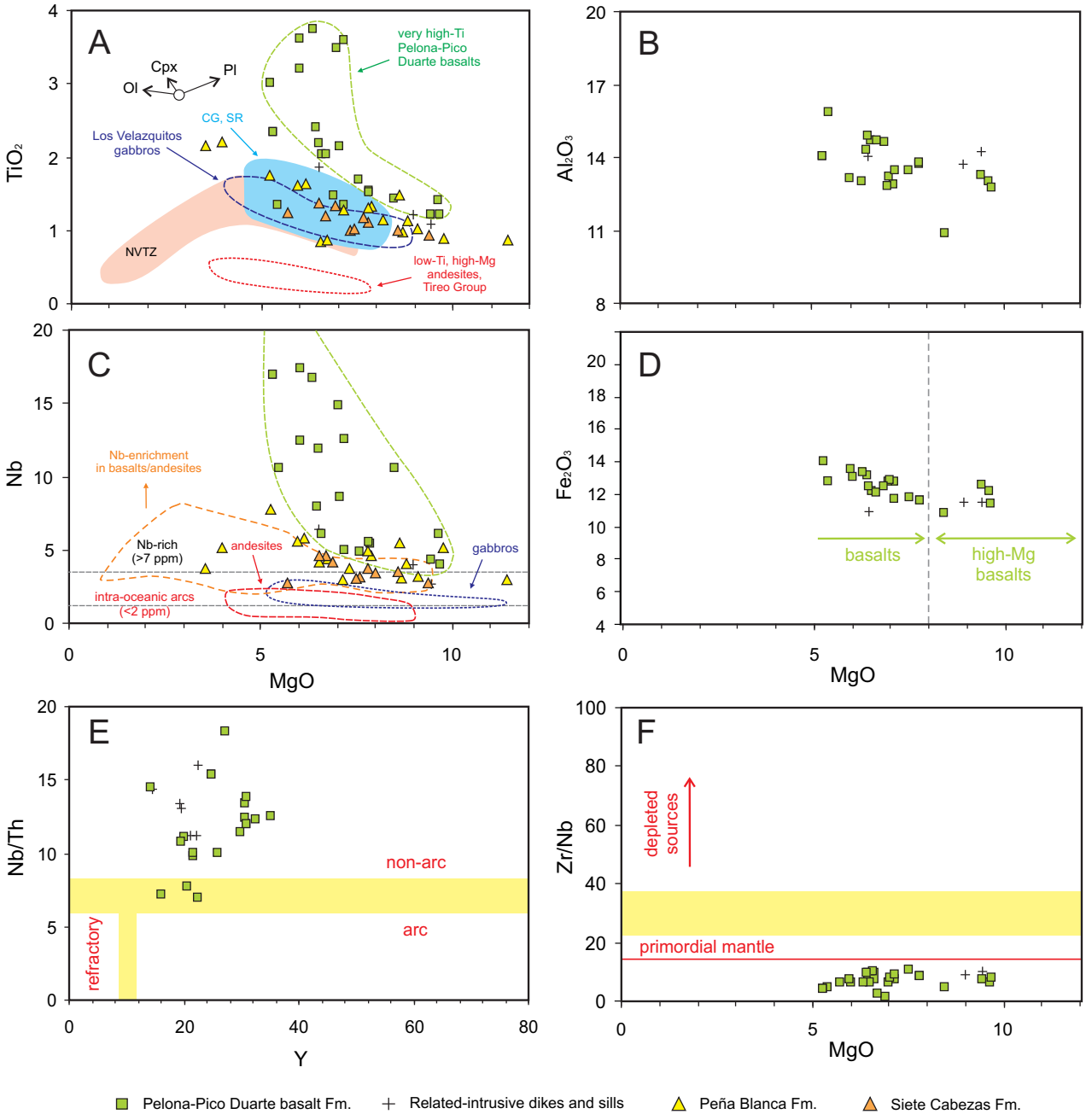

FIGURE 6 | **TiO_2, Al_2O_3, Fe_2O_3, Nb, Zr/Nb *versus* MgO, and Nb/Th *versus* Y, for the basalts, high-Mg basalts and related-intrusive dikes of the PPDB in Central Hispaniola. Basalts from the Peña Blanca and Siete Cabezas Fms. are shown for comparisons. NVTZ, CG and SR fields are Northern Volcano-Tectonic Zone, Central Graben and Spreading ridge fields of the Mariana Arc-Trough system from Gribble et al. (1998), which are shown for comparisons with a modern analogue. Also indicated in (a) are 5% fractional crystallization vectors for olivine (Ol), clinopyroxene (Cpx), and plagioclase (Pl), determined from the average PPDB composition.**

2000), Deep Sea Drilling Project sites 146-153 (except 151; re-analyzed by Jolly et al., 2007) and basalts of the Dumisseau Fm. (Sen et al., 1988). These E-MORB-like characteristics are common in most of the Caribbean large igneous province mafic lavas (Kerr et al., 2002) and suggest a similar Caribbean plume-related source.

Sr-Nd isotopic compositions

The Sr and Nd isotope ratios for basalts and high-Mg basalts of the Pelona-Pico Duarte basalts Fm. are listed in Table 2 and plotted in Fig. 9. The $(\varepsilon_{Nd})_i$ range in all rocks is restricted to values between +5.03 and +6.01 (i=70Ma). $(^{87}Sr/^{86}Sr)_i$ ratio values range between 0.70330 and 0.70348 clustering in the MORB array, which probably reflects that the primary composition has been little modified by subsolidus, hydrothermal alteration. The relatively low $(\varepsilon_{Nd})_i$ values of the Pelona-Pico Duarte basalts Fm. samples are compatible with a relatively homogeneous source dominated by enriched mantle, similar to the enriched MORB mantle composition of Klein (2003), with minimal incorporation of a subducted sedimentary component. This composition is similar to those of other Caribbean large igneous province units (Fig. 9), particularly the most enriched Duarte Complex, Deep Sea Drilling Project Leg 151 and Dumisseau Fm. Therefore, Sr-Nd isotopic compositions of the Pelona-Pico Duarte basalts Fm. suggest that they formed from plume-type mantle containing an enriched component also present in other Caribbean large igneous province units. This similar source also corroborates that the Pelona-Pico Duarte basalts Fm. constitutes an on-land occurrence of the Late Cretaceous Caribbean large igneous province in Central Hispaniola. On the other hand, initial Sr-Nd isotopic ratios values in the basalt of Peña Blanca and Siete Cabezas Fms. basalts define a horizontal trend in Fig. 9 and are restricted to slightly higher $(\varepsilon_{Nd})_i$ values between +6.7 to +7.6, as the relatively depleted Caribbean large igneous province units drilled at the Deep Sea Drilling Project Leg 15. In these basalts, the $(^{87}Sr/^{86}Sr)_i$ ratios are highly variable (0.70302-0.70575), similar to altered rocks in an oceanic environment, and consistent with seawater alteration that shifts the samples from the MORB array to the right (e.g. Hauff et al., 2000a). In summary, during the Late Cretaceous two slightly different Caribbean plume-related sources seem to coexist in Central Hispaniola: the relatively enriched Pelona-Pico Duarte basalts Fm. source and the relatively depleted Peña Blanca and Siete Cabezas Fms. source.

PETROGENESIS AND COMPARISONS

Modelling of mantle melting and magma sources

Introduction to modelling

REE composition of a melt can be particularly diagnostic of source mineralogy and degree of melting; REE are lithophile elements whose behavior has been well characterized and their partition coefficients between major mantle minerals and basaltic melts are well known (Salters and Stracke, 2004). Mantle assemblages containing garnet strongly affect the relationship between light REE (LREE)

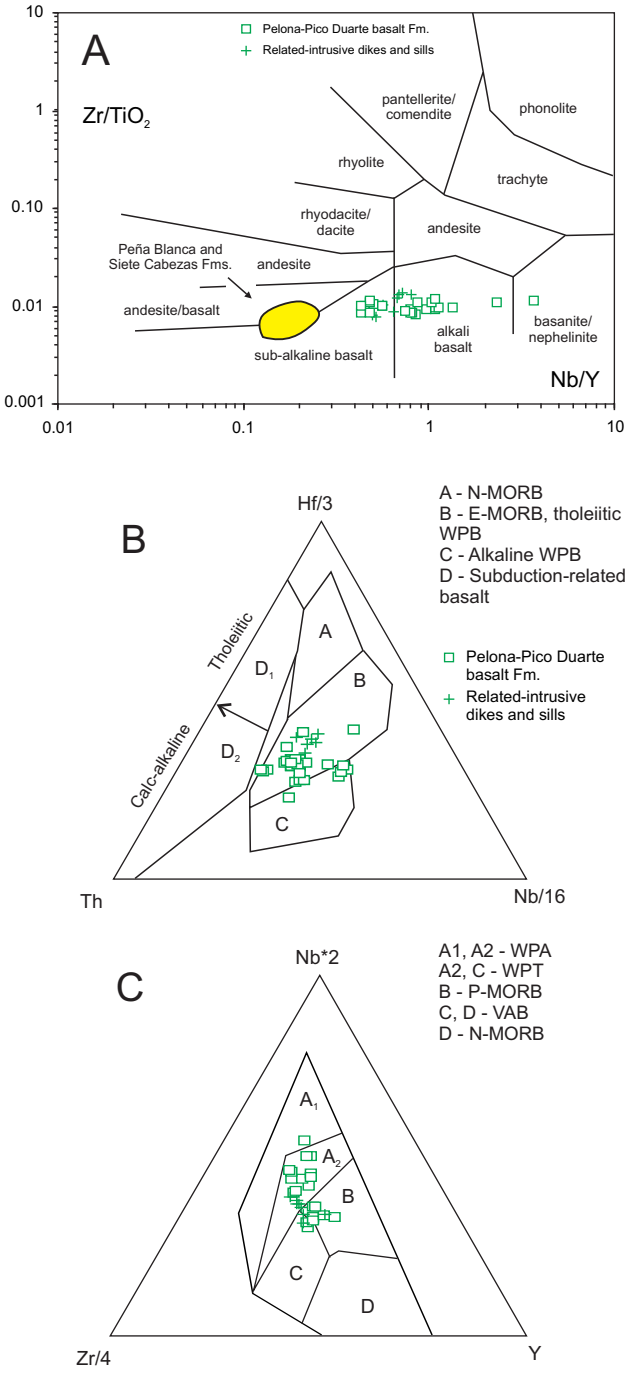

FIGURE 7 | **A) Nb/Y *versus* Zr/TiO_2 diagram of Winchester and Floyd (1977), for basalts, high-Mg basalts and related-intrusive dikes of the PPDB in Central Hispaniola, B) Hf-Nb-Th plot with fields defined by Wood (1980), and C) Nb-Zr-Y plot with fields defined by Meschede (1986).**

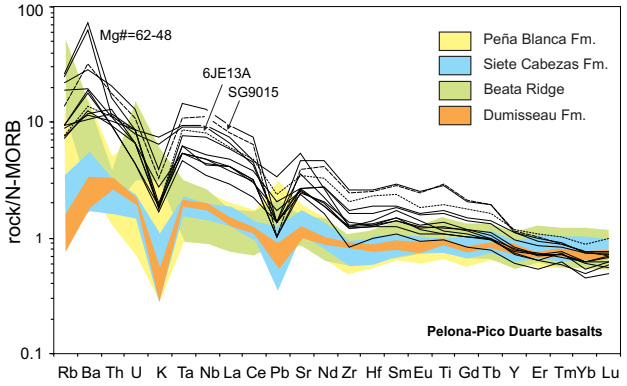

FIGURE 8 | **MORB-normalized multi-element plots for the basalts of the Pelona-Pico Duarte Fm. The fields for geographycally nearest CLIP units are shown for comparison (data taken from Révillon et al., 2000; Sen et al., 1988; Sinton et al., 1998; Escuder-Viruete et al., 2008). Normalization values are taken from Sun and McDonough (1989).**

and heavy REE (HREE) elements, due to the high partition coefficients of the HREE in garnet. For this reason, models of spinel lherzolite and garnet lherzolite melting are used to test the influence of varying source mineralogy on REE concentrations, and on LREE/HREE and MREE/HREE ratios. The approach followed in this study consists of making comparisons between the primitive compositions of the Pelona-Pico Duarte basalts Fm. and the melt calculations for various possible mantle sources.

The details of the model starting assemblages, bulk partition coefficients, and source compositions are summarized in Appendix III. Because the main objective of these calculations is to determine the influence of source mineralogy on the melt composition, the initial chemical compositions have been held constant for both source lithologies and assumed to be the mantle composition of Salters and Stracke (2004). The equation used to derive the melting curves in Figure 10 is the aggregated non-modal fractional melting equation of Shaw (1970):

$$[x_i] = [x_o]\ (1/D_o)\ (1- ((P\ F)/D_o))^{(1/P-1)}$$

where x_i is the concentration in the liquid, x_o is the concentration in the source, D_o is the bulk partition coefficient, F is the degree of melting and P is the proportion in which each phase contributes to the melt.

Source characterization

The results of these calculations suggest that the Pelona-Pico Duarte basalts Fm. melts may have been produced by variable amounts of melting in the garnet and spinel lherzolite fields (Fig. 10). The degree of melting in each field varies slightly depending on the choice of REE ratios used (in this study chrondrite-normalized $[La/Yb]_C$ and $[Tb/Yb]_C$), but garnet lherzolite is always implicated due to the depleted composition in HREE of the lavas of the Pelona-Pico Duarte basalts Fm. Both high-Mg basalts and tholeiitic basalts represent aggregate melts produced from continuous melting throughout the depth of the melting column. In general, all basalts can be produced by mixing of melts in the garnet lherzolite field (generated by 1.6% to 4.0% melting at depth) with melts from the spinel field (produced by melting degrees between 1.8% and 6.0% at low pressure). In Figure 10, the basalts mainly define two groups relative to the melt proportions produced in each field: a) 10-30% garnet lherzolite with 70-90% spinel lherzolite mixing melts, and b) 30-60% garnet lherzolite with 40-70% spinel lherzolite mixing melts. The modelling indicates that the aggregate melts that formed the high-Mg basalts and the less evolved basalts have involved lesser proportions of enriched melts generated at depth, and greater amounts of depleted melts generated at lower pressure (25 garnet lherzolite/75 spinel lherzolite on average). Fraccionated basalts have been produced by higher proportions of melts generated at depth in the garnet stability field (40 garnet lherzolite/60 spinel lherzolite on average). The variable proportion of melts generated and incorporated at different mantle depths are most probably the consequence of melt column processes related to an upwelling plume.

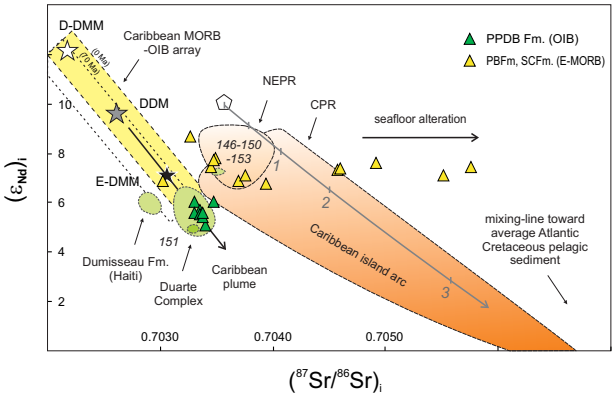

FIGURE 9 | **Initial Sr-Nd isotopes ratios (*i*=70Ma) for the different Late Cretaceous basalts in Central Hispaniola. The fields for the Duarte Complex, DSDP site 15 (CLIP) and Caribbean island-arc lavas from Northeastern and Central Puerto Rico, are taken from Escuder-Viruete et al. (2007a), Hastie et al. (2008; and references therein), Hauff et al. (2000), Jolly et al. (2006, 2007) and Thompson et al. (2004). The MORB-OIB array is defined by the subduction-unmodified lavas from the East Pacific Ridge (data from PETDB, 2007; and references herein). Depleted MORB mantle (DMM) Sr–Nd isotopic compositions are taken from Su and Langmuir (2003): DMM average for MORBs far from plumes; D-DMM is 2σ depleted and E-DMM is 2σ enriched over the average. Field and mantle components are age corrected. Caribbean island-arc field is subparallel to a calculated mixing line between pelagic sediments and representative arc basalt (Jolly et al., 2006; Escuder-Viruete et al., 2008). NEPR: Northeastern Puerto Rico I-III (Albian-Maastrichtian); CPR: Central Puerto Rico I-IV (Albian-Maastrichtian).**

In contrast, the flat HREE compositions of the Peña Blanca and Siete Cabezas Fms. require melting exclusively of a relatively depleted spinel lherzolite source. The results indicate a high degree of melting (8-25%) of this source. Therefore, the mantle source of the Peña Blanca and Siete Cabezas Fms. is shallower and underwent higher degrees of melting than the source of the Pelona-Pico Duarte basalts Fm. However, a small contribution of melts generated in the garnet stability field as small (<1%) non-modal instantaneous fractional melts cannot be ruled out. The basalts from the Deep Sea Drilling Project Leg 15, as well as gabbros and dolerites from the Beata Ridge, are also melts produced by high degrees of partial melting at low pressure of a similar source. However, the basalts from the 151-site proceed from enriched garnet lherzolite sources, as the evolved basalts of the Pelona-Pico Duarte basalts Fm. (Fig. 10).

In summary, melting models suggest the existence of different sources in middle Campanian-Maastrichtian plume-related units of Central Hispaniola: high-Mg basalts and tholeiitic basalts of the Pelona-Pico Duarte basalts Fm. involved deep melting of garnet and spinel lherzolite and were extruded in the Jicomé block; whereas basalts of the Peña Blanca and Siete Cabezas Fms. require high-degree of melting of a more shallower and depleted spinel lherzolite and were extruded in the Jarabacoa block. These sources were unaffected by subduction influence, but basalts were emplaced in Central Hispaniola onto older Cretaceous arc volcanic sequences. Therefore, a change in the source happened through time, which is recorded by changes in the composition of the pre-Middle Campanian mafic igneous rocks.

Changing trace elements and Sr-Nd isotopic compositions through time

A change in the physical characteristics and geochemical compositions of the Late Cretaceous magmatism of Central Hispaniola has been recently proposed by Escuder-Viruete et al. (2008). This change is recorded by distinctive compositional groups of mafic rocks, which correlate with four successive stages in the magmatic evolution (Fig. 11A, B). The >90Ma tholeiitic to calc-alkaline basalts and andesites and associated ultramafic cumulate complexes of stage I represent the older Cenomanian-Turonian Caribbean island-arc magmatism, which is equivalent to coeval magmatism in Cordillera Oriental and Puerto Rico (Jolly et al., 2007, 2008). At 90-88Ma, the onset of extrusion of low-Ti, high-Mg andesites and basalts, Nb-enriched basalts and adakitic dacites to rhyolites characterizes the stage II of arc rift magmatism (Turonian-Coniacian). Immediately following or temporally overlapping the extrusion of felsic volcanics, gabbroic/doleritic and back-arc basin basalt (BABB) -like magmatism intruded and extruded the NE sector of Jarabacoa and Bonao blocks. This BABB-like

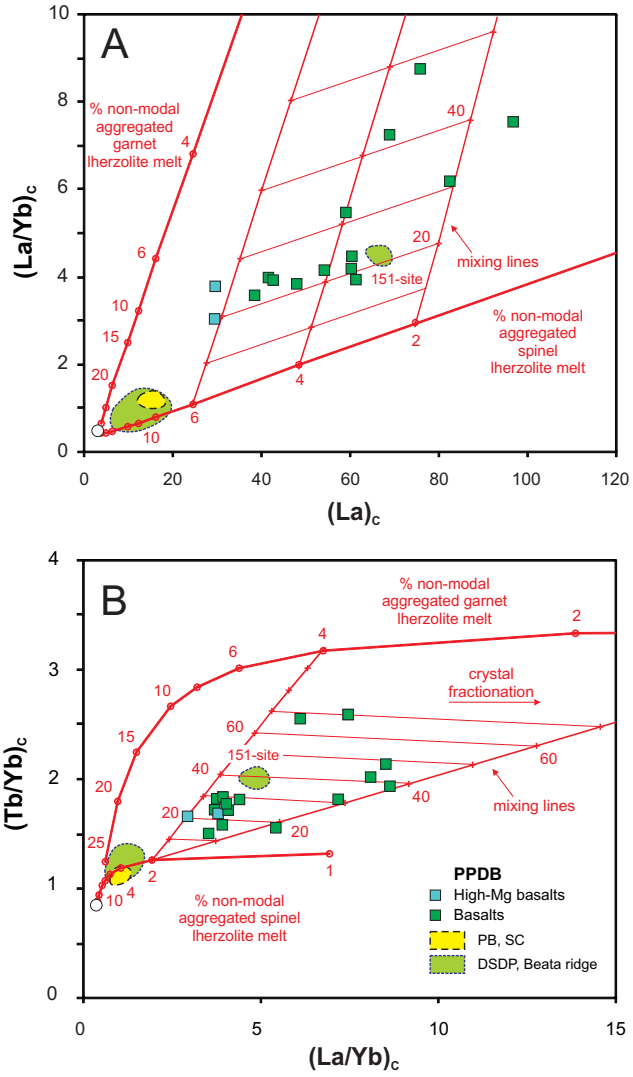

FIGURE 10 | **Results of the non-modal aggregated melt calculations for spinel lherzolite and garnet lherzolite assemblages (solid lines): A) $(La/Yb)_c$ *versus* $(La)_c$ and $(Tb/Yb)_c$ *versus* $(La/Yb)_c$. Gray grid shows mixing between melts produced by variable degrees of spinel lherzolite melt mixed with a 2.5% aggregated non-modal fractional melt of garnet lherzolite. Open square in the lower left hand corner is the depleted mantle composition of Salters and Stracke (2004), used as the source in these calculations. All values on both diagrams are normalized to the chondrite values from Sun and McDonough (1989). Partition coefficients used in the model calculations are from Salters and Stracke (2004), 2.0GPa coefficients were used in the spinel lherzolite melting calculations and the 3.0GPa coefficients were used in the garnet lherzolite melting calculations. The arrow on the right demonstrates the general direction at which crystal fractionation proceeds. Both high-Mg basalts and basalts of the PPDB plot well above the curve generated for spinel lherzolite melting in both diagrams, suggesting that part of the melt generation occurred in the garnet lherzolite field. Basalts from the Peña Blanca and Siete Cabezas Fm., as well as from the DSDP sites 146-150-152-153-site (re-analyzed by Jolly et al., 2008) and the Beata Ridge (Révillon et al., 2000), plot on the lower left side of the diagrams, indicating that melts produced by high degrees of melting in the spinel lherzolite field (i.e. at lower pressure).**

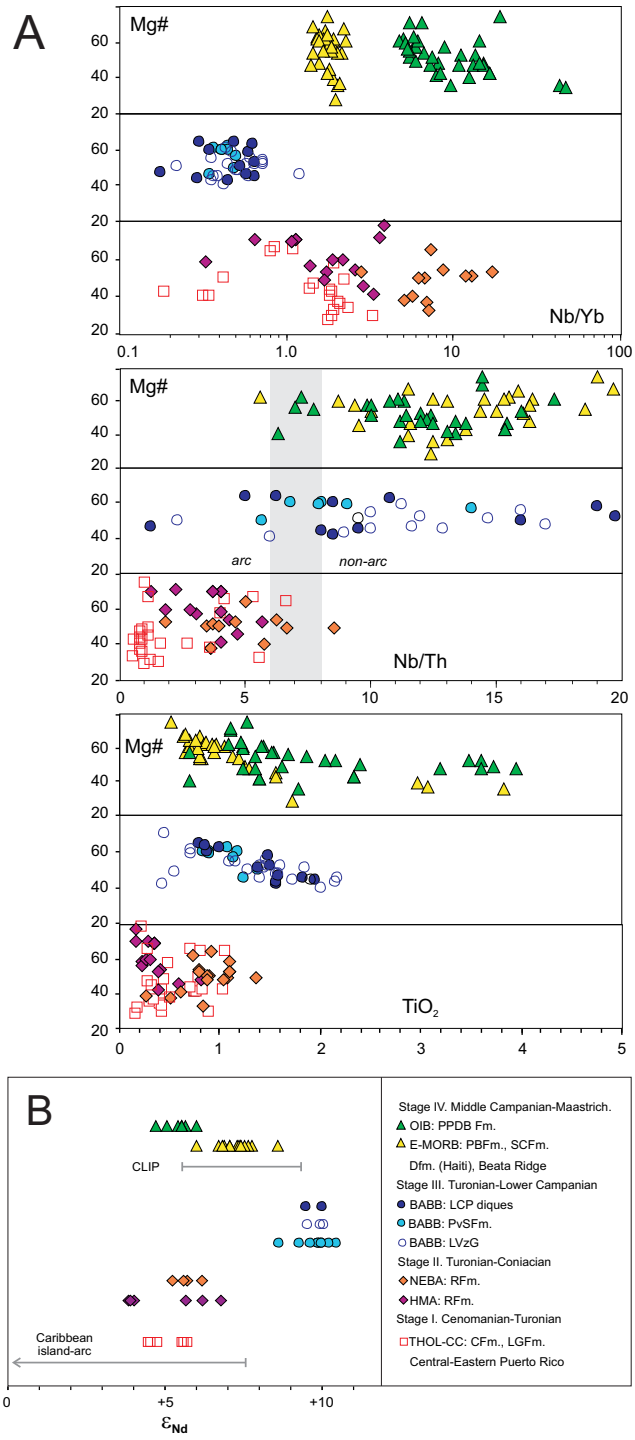

FIGURE 11 | **A) Values of selected geochemical parameters and B) initial ε_{Nd} values for the succesive stages of the Late Cretaceous magmatic evolution of Central Hispaniola (Escuder-Viruete et al., 2007, 2008, this work and unpublished). The Caribbean island-arc volcanic rocks of Puerto Rico are from Jolly et al. (2006, 2007, 2008). Beata Ridge data are from Révillon et al. (2000). THOL: tholeiitic; CC: calc-alkaline; RFm: Restauración Fm.; HMA: high-Mg andesites/basalts; NEBA: Nb-enriched basalts; BABB: back-arc basin basalts; CFm: Constanza Fm.; LGFm: Las Guayabas Fm. (Eastern Cordillera); LCP: Loma Caribe peridotite (Bonao block); LVzG: Los Velazquitos gabbros (Jarabacoa block); PVSFm: Peralvillo Sur Fm. (Bonao block); PBFm: Peña Blanca Fm.; SCFm: Siete Cabezas Fm. (NE sector Jarabacoa block); DFm: Dumisseau Fm. (SW Haiti).**

magmatism, and the related hydrothermal activity and deep-marine sedimentation, represent the Coniacian to Lower Campanian stage III of arc extension. The tholeiitic, transitional and alkalic basalts of the Peña Blanca, Siete Cabezas and Pelona-Pico Duarte Fms. erupted during the Middle Campanian to Maastrichtian and represent the subsequent stage IV of back-arc magmatism. The deposition on top of the platform limestones of the Bois de Lawrence Fm. indicates the ending of magmatic activity in the latest Campanian- Maastrichtian.

This magmatic evolution is shown in Fig. 11 in terms of selected trace elements parameters and isotopic compositions for Late Cretaceous igneous rocks of Central Hispaniola, and suggests changes of the magma sources as a response to geodynamic evolution. Drawn versus Mg# (vol.% MgO/(FeO+MgO) for $Fe_2O_3/FeO=0.2$), or degree of magmatic fractionation, the Ti-content and the Nb/Yb ratio are good parameters to monitorize enrichment and depletion of magma source in low fractionation rocks (Mg#>50), because they should be insensitive to partial melting and largely unaffected by the addition of mobile components from the subducting slab (Pearce and Peate, 1995). By contrast, Nb/Th ratios in arc magma sources are highly susceptible to slab contributions, which enable characterization of arc-like and non-arc-like igneous rocks. In this sense, the low TiO_2 contents (<1wt.%) and low Nb/Th ratio values (<6) of the stage I rocks older than 90Ma in Central Hispaniola (Fig. 11A) suggest derivation from a depleted to very depleted mantle wedge modified by slab-derived components, as is typical for "normal" arc magmatism. However, the magmas related to arc rifting and onset of back-arc spreading, as Mg-rich and BABB-like mafic volcanics of the stages II and III, are mainly characterized by intermediate TiO_2 contents (0.7-2.1wt.%), higher Nb/Th (5-19) and lower Nb/Yb (<7) ratios. These values are typical of a transitional IAT to N-MORB geochemistry and indicate a mantle depleted source progressively less affected by subduction components. The general high TiO_2 contents (0.6-3.9%) and higher Nb/Th (5.5-20) and Nb/Yb (1-14) ratio values of the Peña Blanca, Siete Cabezas and Pelona-Pico Duarte Fm. basalts of stage IV, imply relatively enriched mantle sources and a magmatic activity unaffected by the influence of the subducting slab in the Middle Campanian-Maastrichtian. Therefore, from stages I to IV, the mantle source is progressively more enriched and the subduction component decreased.

Sr-Nd isotope variations permit similar petrogenetic interpretations (Fig. 11b). The Middle-Campanian to Maastrichtian non-arc-like basalts of stage IV have a more restricted range of $(\varepsilon_{Nd})_i$ values (+4.7 to +6.0 for Pelona-Pico Duarte basalts Fm.; +6.8 to +8.6 for Peña Blanca and Siete Cabezas Fm.) than older rocks of the Caribbean island arc stages I and II (generally <+6.8; Escuder-Viruete et al.,

2008), which are extended to lower $(\varepsilon_{Nd})_i$ values as in arc lavas of Eastern Puerto Rico (Jolly et al., 2007, 2008). Also, these restricted $(\varepsilon_{Nd})_i$ values of stage IV are lower than the slightly older mafic rocks of stage III (between +8.6 and +10.5), related to arc rifting. Therefore, the change in the ratio values of Nd-isotopes also records a change in the mantle sources from the slab-influenced island arc-related magmatism of stage I and the arc rifting-related magmas of stage II, to the non-arc-like basalts of stages III and IV. On the other hand, the range of $(\varepsilon_{Nd})_i$ values of the stage IV basalts is similar to those of the mafic rocks sampled in the Beata Ridge, the Deep Sea Drilling Project Leg 15 sites and the Dumisseau Fm of Haití (i.e., the Caribbean large igneous province; Sen et al., 1988; Révillon et al., 2000; Kerr et al., 2002; Jolly et al., 2007; Escuder-Viruete et al., 2008). This suggests that basalts of the coeval Peña Blanca, Siete Cabezas and Pelona-Pico Duarte Fms. are melts that sampled a Caribbean plume component that migrated into the back-arc area of the extended Caribbean island-arc, and this component was relatively more depleted in the basalts extruded in the NE sector of Central Hispaniola.

Tectonomagmatic model

Any model proposed for the tectonic and magmatic evolution of Central Hispaniola during the Late Cretaceous has to explain the following observations: 1) Caribbean island-arc normal magmatism at about ~92-90Ma; 2) in the 90-80Ma interval, a change from mantle-wedge melting affected by slab-derived geochemical components (Restauración Fm.) to mantle melting unaffected by slab-derived components in both Jicomé and Jarabacoa blocks (Peña Blanca Fm.); 3) in the 80-68Ma interval, an extrusion of the non-arc-like basalts of the Siete Cabezas Fm. in the Jarabacoa block (NE sector of Central Hispaniola) and the Pelona-Pico Duarte basalts Fm. in the Jicomé block (SW sector). These basalts are compositionally similar to the depleted and enriched heterogeneous sources of the Caribbean large igneous province.

In orden to explain these observations, we built a model of the Late Cretaceous Caribbean plume magmatism dragged by roll-back of the subducting proto-Caribbean oceanic lithosphere (Fig. 12). The consequences of this slab roll-back for magmatic evolution were: Stage I: the motion towards the SW of the proto-Caribbean subducting slab drives corner flow advection in the mantle wedge. Fluids released by the slab promote partial melting in the mantle, which is progressively depleted of a melt component toward the volcanic front. These melts produced the older than 90Ma tholeiitic to calc-alkaline magmas in the Caribbean island-arc; Stage II: When Caribbean island-arc extension starts, at 90-88Ma, the lithosphere rifts near the rheologically weak volcanic front, and hydrated mantle is advected upward into the stretching and thinning lithosphere, leading to high degrees of melting in the rift phase. As the mantle had been previously depleted, the melts are low-Ti, high-Mg andesites and basalts, extruded in the Jarabacoa block; Stage III: With increasing extension and rifting, an incipient seafloor spreading centre is established near the volcanic front advecting highly hydrated mantle and, as a consequence, BABB-like magmas intruded in the Jarabacoa and incipient Bonao blocks; Stage IV: With continued spreading the extension axis separates from the volcanic front and mantle hydration from the slab decreases. Eventually, at 85-80Ma (Santonian-Lower Campanian) the back-arc spreading system (Bonao block) separates sufficiently from the volcanic front and is not significantly affected by slab-derived geochemical components at this stage. The spreading centre produces MORB-like melts, whose source is modified by a Caribbean-plume enriched component incorporated by lateral flow below the arc from the SW. This plume-related magmatism causes the extrusion of the basalts of Peña Blanca Fm. in the Jarabacoa and Jicomé blocks, and those of the Siete Cabezas Fm. in the Jarabacoa block during the Campanian. At 80-68Ma (Campanian-Maastrichtian), melts derived from a similar but deeper and more enriched Caribbean-plume source gave rise to the off-ridge magmatism of the Pelona-Pico Duarte basalts Fm. in the back-arc area of the Jicomé block.

We speculate if collision of a ridge or other buoyant feature with the subduction-zone forearc at ~90Ma and/or collision of the Cuban forearc with the SE edge of the Maya Block/Caribeana in the Campanian (Pindell et al., 2005; Escuder-Viruete et al., 2007a; García-Casco et al., 2008; Lázaro et al., 2008) might have induced the Caribbean island-arc rifting and subsequent opening of a back-arc basin. Probably, the collision was oblique and diachronic (i.e. older toward the NW) and caused the blockage of the subduction zone in the western segment, where intraoceanic arc accretion and ophiolite emplacement are recorded (García Casco et al., 2008; Talavera-Mendoza et al., 2008; Brueckner et al., 2009). Moreover, collision may also have caused a quick rotation of the Caribbean plate and triggered the migration of the eastern segment of the subduction zone toward the NE, because the Caribbean island-arc remains active in Cordillera Oriental of Hispaniola and Central-Eastern Puerto Rico (Jolly et al., 2007, 2008). In this tectonic scenario, arc roll-back forces induced back-arc opening in Central Hispaniola and dragged the Late Cretaceous Caribbean plume magmatism, similarly to the plate-scale mechanism of collision and induced rotation proposed by Wallace et al. (2005). The structural juxtaposition of the different tectonic blocks that made up Central Hispaniola took place during the closure of the back-arc basin, probably in the Middle Eocene arc-continent hard collision. This is consistent with the Caribbean island-arc burial beneath the unconformable Eocene–Oligocene overlapping sequence of the Tavera Group and with the evolution of the Late

Eocene–Early Miocene syn-collisional turbiditic El Mamey Group farther to the northeast.

Hoerne et al. (2004) establish that the Caribbean large igneous province does not represent a single oceanic plateau, but instead consists of remnants of multiple smaller igneous structures (e.g., oceanic plateaus, paleo-hotspot tracks and flood basalt units) formed over at least 42Ma (125-83Ma). In this sense, the young non-arc-like volcanic rocks at Central Hispaniola and possibly at other locations

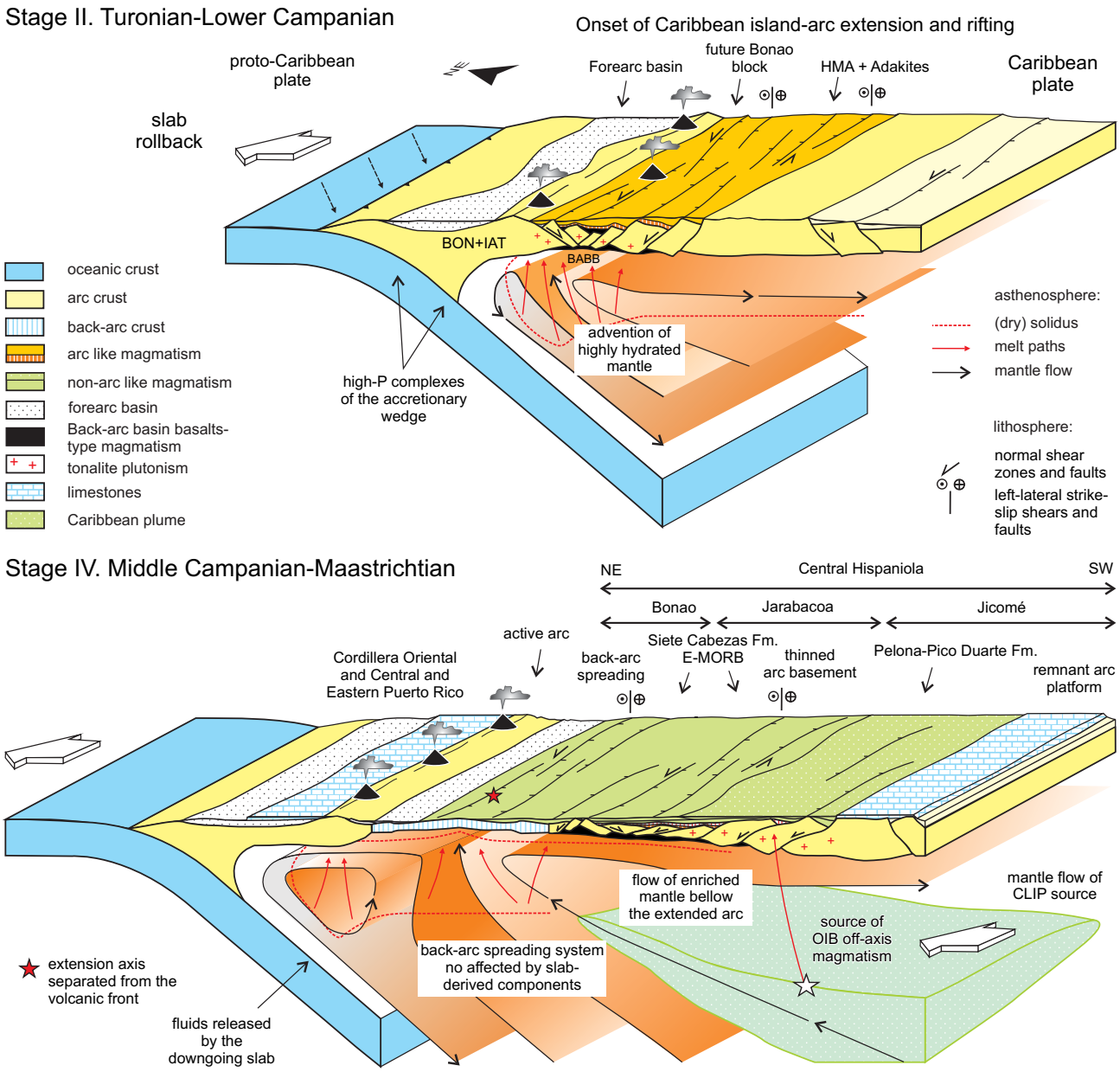

FIGURE 12 | **Schematic tectonomagmatic model for Late Cretaceous magmatic evolution in Central Hispaniola. HMA: high-Mg andesites; NEBA: Nb-enriched basalts; CLIP: Caribbean large igneous province. A) In the Turonian-Coniacian, the SW-directed motion of the subducting proto-Caribbean slab drives corner flow advection in the mantle wedge. Water released by the downgoing slab promotes partial melting in the mantle above the solidus (heavy dashed lines), and generated arc magmatism. When arc extension started, lithosphere rifts near the rheologically weak volcanic front. B) Hydrated mantle is advected upward into the stretching and thinning lithosphere, leading to high degrees of melting in the rift phase and extrusion of high-Mg andesites, and promotes the lower arc crust melting and development of felsic volcanism and tonalitic plutonism. With increasing extension a seafloor spreading centre is established near the volcanic front advecting highly hydrated mantle. As consequence, BABB-like magmas result in a SW position with respect to the volcanic front. In the middle Campanian-Maastrichtian, melts derived from a deeper Caribbean-plume enriched source are incorporated by lateral flow from the SW and produced the OIB-like off-ridge magmatism of the PPDB, which is not affected by slab-derived geochemical components.**

along the northern margin of the Caribbean plate may have been generated through a late-stage pulsing of the plume (78-69Ma), separated from the Pacific mantle by the Costa Rica-Panama subduction zone. Alternatively, they were generated through unrelated and spatially distinct mantle-melting events that sampled similar source material, but they were controlled by plate-scale mechanisms as the previously described.

CONCLUSIONS

The Pelona-Pico Duarte basalts Fm. is composed by a ~2.5km-thick pile of massive and homogeneous flows of basalts, locally intruded by synvolcanic dikes and sills. This volcanic sequence was extruded in a submarine environment at high effusive rate indicated by the absence of intercalated pelagic sediments. Evidences of a subaerial eruptive environment are lacking. The basalts have restricted major- and trace-element and isotopic compositional variations. Mineral assemblages and major element compositions indicate that basalts were derived by fractional crystallization from tholeiitic parental magmas. The samples generally have increasing REE contents at decreasing Mg#, which is a likely effect of fractional crystallization. The relative depletion of HREE in the basalts can be interpreted in terms of partial melting in the stability field of garnet. Sr-Nd isotopic compositions of the Pelona-Pico Duarte basalts Fm. samples plot in the enriched part of the Caribbean MORB-OIB mantle array, as other relatively enriched Caribbean large igneous province units. The relatively low $(\varepsilon_{Nd})_i$ values in the basalts are consistent with the role of an enriched Caribbean plume component in their genesis. Mantle melt modelling suggests that high-Mg basalts and basalts formed by aggregate melts of both garnet and spinel lherzolite sources.The obtained $^{40}Ar/^{39}Ar$ plateau ages of 79-68Ma give evidence that the Pelona-Pico Duarte basalts Fm. volcanism was in part coeval with the Late Cretaceous magmatism of the Caribbean large igneous province, particularly with the 80-75Ma younger event.

The trace element and Sr-Nd isotopic compositions of the Late Cretaceous mafic igneous rocks in Central Hispaniola record an evolution from arc-like to non-arc like magmatism, and suggest a change of the mantle sources through time. These changes are interpreted as the record of proto-Caribbean slab roll-back and migration of the Caribbean island arc volcanic front toward the NE. To balance the roll-back, mantle influenced by the Caribbean plume was advected into the mantle wedge of the extended island-arc. The upwelling of this enriched mantle toward the back-arc spreading centre produced relatively enriched-MORB-type magmas in the Jarabacoa block (NE sector of Central Hispaniola), and off-axis OIB-type magmas in the Jicomé block (SW sector).

ACKNOWLEDGMENTS

The authors thank John Lewis, Gren Draper, Peter Baumgartner and many colleagues of the IGME-BRGM team for help and discussions on the igneous rocks in the Dominican Republic. The Dirección General de Minería of the Dominican Government is also thanked for its support. Elisa Dietrich-Sainsaulieu and Thomas Ulrich are thanked for their help with the Sr-Nd and Ar-Ar isotopic analyses at PCIGR, respectively. This work is part of the MCYT/MCI projects CGL2005-02162/BTE and CGL2009-08674/BTE and also received aid from the cartographic project of the Dominican Republic funded by the SYSMIN Program of the European Union. Careful reviews from Drs. Claudio Marchesi and Domingo Gimeno are much appreciated.

REFERENCES

Baumgartner, P.O., Flores, K., Bandini, A.N., Girault, F., Cruz, D., 2008. Late Triassic to Cretaceous Radiolaria from Nicaragua and Northern Costa Rica–The Mesquito Oceanic terrane. Ofioliti, 33, 1-19.

Bédard, J.H., 1999. Petrogenesis of Boninites from the Betts Cove Ophiolite, Newfoundland, Canada: Identification of Subducted Source Components. Journal of Petrology, 40, 1853-1889.

Brueckner, H.K., Avé Lallemant, H.G., Sisson, V.B., Harlow, G., Hemming, S.R., Martens, U., Tsujimori, T., Sorensen, S.S., 2009. Metamorphic reworking of a high pressure–low temperature mélange along the Motagua fault, Guatemala: A record of Neocomian and Maastrichtian transpressional tectonics. Earth and Planetary Science Letters, 284, 228-235.

Denyer, P., Baumgartner, P.O., 2006. Emplacement of Jurassic-Lower Cretaceous radiolarites of the Nicoya Complex (Costa Rica). Geologica Acta, 4(1-2), 203-218.

Denyer, P., Baumgartner, P.O., Gazel, E., 2006. Characterization and tectonic implications of Mesozoic-Cenozoic oceanic assemblages of Costa Rica and Western Panama. Geologica Acta, 4(1-2), 219-235.

Donnelly, T.W., Beets, D., Carr, M.J., Jackson, T., Klaver, G., Lewis, J., Maury, R., Schellenkens, H., Smith, A.L., Wadge, G., Westercamp, D., 1990. History and tectonic setting of Caribbean magmatism. In: Dengo, G., Case, J. (eds.). The Caribbean Region. The Geology of North America. Geological Society of America, H, 339-374.

Donnelly, K., Goldstein, S., Langmuir, C., Spiegelman, M., 2004. Origin of enriched ocean ridge basalts and implications for mantle dynamics. Earth Planetary Science Letters, 226, 347-366.

Draper, G., Lewis, J.F, 1991. Metamorphic belts in Central Hispaniola. In: Mann, P., Draper, G., Lewis, J.F. (eds.). Geologic and Tectonic Development of the North America-Caribbean Plate Boundary in Española. Geological Society of America Special Paper, 262, 29-46.

Duncan, R.A., Hargraves, R.B., 1984. Plate tectonic evolution of the Caribbean region in the mantle reference frame. In: Bonini, W.E., Hargraves, R.B., Shagam, R. (eds.). The Caribbean-South American plate boundary and regional tectonics. Geological Society of America, 162 (Memoir), 81-93.

Escuder-Viruete, J., 2008. Petrología y Geoquímica de Rocas Ígneas y Metamórficas: Hojas de Polo, La Ciénaga, Enriquillo, Sabana Buey y Nizao. Informe Complementario al Mapa Geológico de la República Dominicana a escala 1:50.000. Santo Domingo, Instituto Geológico y Minero de España-Bureau de Recherches Géologiques et Minières, 57pp.

Escuder-Viruete, J., Contreras, F., Stein, G., Urien, P., Joubert, M., Ullrich, T.D., Mortensen, J., Pérez-Estaún, A., 2006. Transpression and strike-slip partitioning in the Caribbean island arc: fabric development, kinematics and Ar-Ar ages of syntectonic emplacement of the Loma de Cabrera batholith, Dominican Republic. Journal of Structural Geology, 28, 1496-1519.

Escuder-Viruete, J., Contreras, F., Stein, G., Urien, P., Joubert, M., Pérez-Estaún, A., Friedman, R., Ullrich, T.D., 2007a. Magmatic relationships and ages between adakites, magnesian andesites and Nb-enriched basalt-andesites from Hispaniola: record of a major change in the Caribbean island arc magma sources. Lithos, 99, 151-177. doi: 10.1016/j.lithos.2007.01.008.

Escuder-Viruete, J., Pérez-Estaún, A., Contreras, F., Joubert, M., Weis, D., Ullrich, T.D., Spadea, P., 2007b. Plume mantle source heterogeneity through time: insights from the Duarte Complex, Central Hispaniola. Journal of Geophysical Research, 112, B04203. doi: 10.1029/2006JB004323.

Escuder-Viruete, J., Joubert, M., Urien, P., Friedman, R., Weis, D., Ullrich, T., Pérez-Estaún, A., 2008. Caribbean island-arc rifting and back-arc basin development in the Late Cretaceous: geochemical, isotopic and geochronological evidence from Central Hispaniola. Lithos, 104, 378-404. doi:10.1016/j.lithos.2008.01.003.

Escuder-Viruete, J., Pérez-Estaún, A., Weis, D., 2009. Geochemical constraints on the origin of the late Jurassic proto-Caribbean oceanic crust in Hispaniola. International Journal of Earth Sciences, 98, 407-425. doi: 10.1007/s00531-007-0253-4.

Ewart, A., Collerson K.D., Regelous M., Wendt, J.I., Niu, Y., 1998. Geochemical evolution within the Tonga-Kermadec-Lau Arc-Back-arc system: the role of varying mantle wedge composition in space and time. Journal of Petrology, 39, 331-368.

García-Casco, A., Iturralde-Vinent, M.A., Pindell, J., 2008. Latest Cretaceous collision/accretion between the Caribbean Plate and Caribeana: origin of metamorphic terranes in the Greater Antilles. International Geology Review, 50, 781-809.

Gradstein, F.M., Ogg, J.G., Smith, A.G., 2004. A geologic time scale 2004. Cambridge (United Kingdom). Cambridge University Press, 610pp.

Greene, A.R., Scoates, J.S., Weis, D., Nixon, G.T., Kieffer, B., 2009. Melting history and magmatic evolution of basalts and picrites from the accreted Wrangellia oceanic plateau on Vancouver Island, Canada. Journal of Petrology, 50, 467-505.

Gribble, R.F., Stern, R.J., Newman, S., Bloomer, S.H., O'Hearn, T., 1998. Chemical and isotopic composition of lavas from the northern Mariana Trough: implications for magma genesis in back-arc basins. Journal of Petrology, 39, 125-154.

Hastie, A.R., Kerr, A.C., Mitchell, S.F., Millar, I.L., 2008. Geochemistry and petrogenesis of Cretaceous oceanic plateau lavas in eastern Jamaica. Lithos, 101, 323-343.

Hauff, F., Hoernle, K., Tilton, G., Graham, DW., Kerr, A.C., 2000a. Large volume recycling of oceanic lithosphere over short time scales: geochemical constraints from the Caribbean large igneous province. Earth Planetary Science Letters, 174, 247-263.

Hauff, F., Hoernle, K., van den Bogaard, P., Alvarado, G.E., Garbe-Schönberg, D. 2000b. Age and geochemistry of basaltic complexes in western Costa Rica: Contributions to the geotectonic evolution of Central America. Geochemistry, Geophysics, Geosystems, 1(5), 1009, 41pp. doi:10.1029/1999GC000020.

Hoernle, K., Bogaard, P. van den, Werner, R., Lissinna, B., Hauff, F., Alvarado, G.E., Garbe-Schönberg, D., 2002. Missing history (16-71 Ma) of the Galapagos hotspot: Implications for the tectonic and biological evolution of the Americas. Geological Society American Bulletin, 30(9), 795-798.

Hoernle, K., Hauff, F., Bogaard, P. van den, 2004. A 70 Myr history (139-69 Ma) for the Caribbean large igneous province. Geology, 32, 697-700. doi:10.1130/G20574.1.

Jolly, W.T., Lidiak, E.G., Dickin, A.P., 2006, Cretaceous to mid-Eocene pelagic sediment budget in Puerto Rico and the Virgin Islands (northeast Antilles Island Arc). Geologica Acta, 4 (1-2), 35-62.

Jolly, W.T., Schellekens, J.H., Dickin, A.P., 2007. High-Mg andesites and related lavas from southwestern Puerto Rico (Greater Antilles Island Arc): petrogenetic links with emplacement of the Caribbean mantle plume. Lithos, 98, 1-26.

Jolly, W.T., Lidiak, E.G., Dickin, A.P., 2008. Bimodal volcanism in northeast Puerto Rico and the Virgin Islands (Greater Antilles Island Arc): Genetic links with Cretaceous subduction of the mid-Atlantic ridge Caribbean spur. Lithos, 103, 393-414.

Kerr, A.C., 2003. Oceanic Plateaus. In: Rudnick, R. (ed.). The Crust. Oxford, Elsevier Science, Treatise on Geochemistry, 3, 537-565. Avaiable online: www.TreatiseOnGeochemistry.com

Kerr, A.C., Tarney, J., Marriner, G.F., Nivia, A., Saunders, A.D., 1997. The Caribbean–Colombian Cretaceous igneous province: The internal anatomy of an oceanic plateau. In: Mahoney, J., Coffin, M.F. (eds.). Large igneous Provinces. Washington DC., American Geophysical Union (AGU), 123-144.

Kerr, A.C., Tarney, J., Kempton, P.D., Spadea, P., Nivia, A., Marriner, G.F., Duncan, R.A., 2002. Pervasive mantle plume head heterogeneity: evidence from the late Cretaceous Caribbean–Colombian oceanic plateau. Journal

of Geophysical Research, 107, 2140, 13 pp. doi: 10.1029/2001JB0007Kerr, A.C., Tarney, J., 2005. Tectonic evolution of the Caribbean and northwestern South America: The case for accretion of two Late Cretaceous oceanic plateaus. Geology, 33, 269-272. doi: 10.1130/G21109.1.

Kincaid, C., Griffiths, R.W., 2003. Laboratory models of the thermal evolution of the mantle during rollback subduction. Nature, 425, 58-62.

Klein, E.M., 2003. Geochemistry of the Igneous Oceanic Crust. In: Holland, H.D., Turekian, K.K. (eds.). Treatise on Geochemistry. Oxford, Pergamon, 433-463pp. doi: 10.1016/B0-08-043751-6/03030-9.

Lapierre, H., Dupui, V., Lepinay, B.M., Tardy, M., Ruiz, J., Maury, R.C., Hernandez, J., Loubert, M., 1997. Is the Lower Duarte Complex (Hispaniola) a remnant of the Caribbean plume generated oceanic plateau? Journal of Geology, 105, 111-120.

Lapierre, H., Dupuis, V., de Lepinay, B.M., Bosch, D., Monié, P., Tardy, M., Maury, R.C., Hernández, J., Polvé, M., Yeghicheyan, D., Cotton, J., 1999. Late Jurassic oceanic crust and upper Cretaceous Caribbean plateau picritic basalts exposed in the Duarte igneous complex, Hispaniola. Journal of Geology, 107, 193-207.

Lapierre, H., Bosch, D., Dupuis, V., Polvé, M., Maury, R., Hernandez, J., Monié, P., Yeghicheyan, D., Jaillard, E., Tardy, M., de Lepinay, B., Mamberti, M., Desmet, A., Keller F., Senebier, F., 2000. Multiple plume events in the genesis of the peri-Caribbean Cretaceous oceanic plateau province. Journal of Geophysical Research, 105, 8403-8421.

Lázaro, C., García-Casco, A., Rojas Agramonte, Y., Kröner, A., Neubauer, F., Iturralde-Vinent, M., 2008. Fifty-five-million-year history of oceanic subduction and exhumation at the northern edge of the Caribbean plate (Sierra del Convento mélange, Cuba). Journal of Metamorphic Geology, 19-40. doi:10.1111/j.1525-1314.2008.00800.

Lebrón, M.C., Perfit, M.R., 1994. Petrochemistry and tectonic significance of Cretaceous island-arc-rocks, Cordillera Oriental, Dominican Republic. Tectonophysics, 229, 69-100.

Lewis, J.F., Amarante, A., Bloise, G., Jimenez, J.G., Dominguez, J., 1991. Lithology and stratigraphy of Upper Cretaceous rocks volcanic and volcaniclastic rocks of the Tireo Group, Dominican Republic and correlations with the Massif du Nord with Haiti. In: Mann, P., Draper, G., Lewis, J.F. (eds.). Geologic and tectonic development of the North America-Caribbean plate boundary in Hispaniola. Geological Society of America, 262 (Special Paper), 143-163.

Lewis, J.F., Escuder-Viruete, J., Hernaiz Huerta, P.P., Gutiérrez, G., Draper, G., 2002. Subdivisión Geoquímica del Arco Isla Circum-Caribeño, Cordillera Central Dominicana: Implicaciones para la formación, acreción y crecimiento cortical en un ambiente intraoceánico. Acta Geologica Hispanica, 37, 81-122.

Mann, P., 1999. Caribbean Sedimentary Basins: Classification and Tectonic Setting from Jurassic to Present. In: Mann, P. (ed.). Caribbean Basins. Sedimentary Basins of the World, 4, 3-31.

Martínez, F., Taylor, B., 2002. Mantle wedge control on backarc crustal accretion. Nature, 416, 417-420.

Mauffret, A., Leroy, S. 1997. Seismic stratigraphy and structure of the Caribbean igneous province. Tectonophysics, 283, l61-104.

Meschede, M., 1986. A method of discrimination between different types of mid-ocean basalts and continental tholeiites with the Nb-Zr-Y diagram. Chemical Geology, 56, 207-218.

Montgomery, H., Pessagno, E.A., Lewis, J.F., Schellekens, J., 1994. Paleogeography of Jurassic fragments in the Caribbean. Tectonics, 13, 725-732.

Montgomery, H., Pessagno, E.A., 1999. Cretaceous microfaunas of the Blue mountains, Jamaica, and of the Northern and Central Basement Complexes of Hispaniola. In: Mann, P. (ed.). Caribbean Basins. Sedimentary Basins of the World, 4, 237-246.

Nikolaeva, K., Gerya, T.V., Connolly, A.D., 2008. Numerical modelling of crustal growth in intraoceanic volcanic arcs. Physics of the Earth and Planetary Interiors, 171, 336-356.

Pearce, J.A., Peate, D.W., 1995. Tectonic implications of the composition of volcanic arc magmas. Earth and Planetary Science Annual Review, 23, 251-285.

Pearce, J.A., 2008. Geochemical fingerprinting of oceanic basalts with applications to ophiolite classification and the search for Archean oceanic crust. Lithos, 100, 14-48.

Pindell, J., Kennan, L., Maresch, W.V., Stanek, K.P., Draper, G., Higgs, R., 2005. Plate-kinematics and crustal dynamics of circum-Caribbean arc-continent interactions: Tectonic controls on basin development in Proto-Caribbean margins. In: Lallemant, A., Sisson, V.B. (eds.). Caribbean-South American plate interactions. Geological Society of America, 394 (Special Paper), 7-52.

Pindell, J., Kennan, L., 2009. Tectonic evolution of the Gulf of Mexico, Caribbean and northern South America in the mantle reference frame: an update. In. James, K., Lorente, M.A., Pindell, J. (eds.). The geology and evolution of the region between North and South America. Geological Society of London, 328 (Special Publications), 328, 1-55.

Pretorius, W., Weis, D., Williams, G., Hanano, D., Kieffer, B., Scoates, J.S., 2006. Complete trace elemental characterization of granitoid (USGSG-2,GSP-2) reference materials by high resolution inductively coupled plasma-mass spectrometry. Geostandards and Geoanalytical Research, 30(1), 39-54.

Révillon, S., Hallot, E., Arndt, N., Chauvel, C., Duncan, R.A., 2000. A Complex History for the Caribbean Plateau: Petrology, Geochemistry, and Geochronology of the Beata Ridge, South Hispaniola. Journal of Geology, 108, 641-661.

Salters, V.J.M., Stracke, A., 2004. Composition of the depleted mantle, Geochemistry, Geophysics, Geosystems, 5, Q05B07. doi: 10.1029/2003GC000597.

Sen, G., Hickey-Vargas, D.G., Waggoner, F., Maurasse, F., 1988, Geochemistry of basalts from the Dumisseau Formation. Southern Haiti: Implications for the origin of the Caribbean Sea crust. Earth Planetary Science Letters, 87, 423-437.

Shaw, D.M., 1970. Trace element fractionation during anatexis. Geochimica et Cosmochimica Acta, 34, 237-243.

Smith, G.P., Douglas, A., Karen, M.F., Leroy, M., Spahr, C.W., Hildebrand, J.A., 2001, A Complex Pattern of Mantle Flow in the Lau Backarc. Science, 292, 713-716.

Sinton, C.W., Duncan, R.A., Storey, M., Lewis, J., Estrada, J.J., 1998. An oceanic flood basalt province within the Caribbean plate. Earth Planetary Science Letters, 155, 221-235.

Sinton, C.W., Sigurdsson, H., Duncan, R.A., Leckie, R.M., Acton, G.D., Abrams, L.J., Bralower, T.J., Carey, S.N., Chaisson, W.P., Cotillon, P., Cunningham, A.D., Hondt, S.L., Droxler, A.W., Galbrun, B., Gonzalez, J., Haug, G.H., Kameo, K., King, J.W., Lind, I.L., Louvel, V., Lyons, T.W., Murray, R.W., Mutti, M., Myers, G., Pearce, R.B., Pearson, D.G., Peterson, L.C., Roehl, U., 2000. Geochronology and petrology of the igneous basement at the lower Nicaraguan Rise, Site 1001. Proceedings of the Ocean Drilling Program, Scientific Results, 165, 233-236.

Sun, S.S., McDonough, W.F., 1989. Chemical and isotopic systematics of oceanic basalts: Implications for mantle compositions and processes. In: Saunders, A.D., Norry, M.J. (eds.). Magmatism in the Ocean Basins. Geological Society of London, 42 (Special Publications), 313-345.

Talavera-Mendoza, O., Ruiz, J., Gehrels, G.E., Valencia, V.A., Centeno-García, E., 2007. Detrital zircon U/Pb geochronology of southern Guerrero and western Mixteca arc successions (southern Mexico): New insights for the tectonic evolution of southwestern North America during the late Mesozoic. Geological Society of America Bulletin, 119, 1052-1065. doi: 10.1130/B26016.1.

Taylor, B., Martínez, F., 2003. Back-arc basin systematics. Earth and Planetary Science Letters, 210, 481-497.

Thompson, P.M.E., Kempton, P.D., White, R.V., Saunders, A.D., Kerr, A.C., Tarney, J., Pringle, M.S., 2004. Elemental, Hf-Nd isotopic and geochronological constraints on an island arc sequence associated with the Cretaceous Caribbean Plateau: Bonaire, Dutch Antilles. Lithos, 74, 91-116.

Walker, J.A., Roggensack, K., Patino, L.C., Cameron, B.I., Otoniel, M., 2003. The water and trace element contents of melt inclusions across an active subduction zone. Contributions to Mineralogy and Petrology, 146, 62-77. doi:10.1007/s00410-003-0482-x.

Wallace, L.M., McCaffrey, R., Beavan, J., Ellis, S., 2005. Rapid microplate rotations and backarc rifting at the transition between collision and subduction. Geology, 33, 857-860.

Weis, D., Kieffer, B., Maerschalk, C., Barling, J., de Jong, J., Willians, G.A., Hanano, D., Pretorius, W., Scoates, J.S., Goolaerts, A., Friedman, R.M., Mahoney, J.B., 2006. High-precision isotopic characterization of USGS reference materials by TIMS and MC-ICP-MS. Geochemistry, Geophysics, Geosystems, 7, Q08006. doi: 10.1029/2006GC001283.

Winchester, J.A., Floyd, P.A., 1977. Geochemical discrimination of different magma series and their differentiation products using immobile elements. Chemical Geology, 20, 325-343.

Wood, D.A., 1980. The application of a Th-Hf-Ta diagram to problems of tectonomagmatic classification and to establishing the nature of crustal contamination of basaltic lavas of the British Tertiary volcanic province. Earth and Planetary Science Letters, 50, 11-30.

Manuscript received November 2010;
revision accepted June 2011;
published Online July 2011.

ELECTRONIC APPENDIX
Summary of analytical techniques

$^{40}Ar/^{39}Ar$ geochronology. Selected samples were crushed and sieved to obtain fragments ranging in the size range from 0.1 to 0.5mm. A hand magnet was passed over the samples to remove magnetic minerals and metallic crusher fragments/spall. The samples were rinsed in dilute nitric acid, washed in deionized water, rinsed and then air-dried at room temperature. Mineral separates were hand-picked, wrapped in aluminum foil and stacked in an irradiation capsule with similar-aged samples and neutron flux monitors (Fish Canyon Tuff sanidine, 28.02Ma; Renne et al., 1998). The samples were irradiated at the McMaster Nuclear Reactor in Hamilton, Ontario, for 56 MWH, with a neutron flux of $3x10^{16}$neutrons/cm^2. Analyses (n=54) of 18 neutron flux monitor positions produced errors of <0.5% in the J value. The mineral separates were step-heated at incrementally higher powers in the defocused beam of a 10W CO_2 laser (New Wave Research MIR10) until fused, at the Noble Gas Laboratory of the Pacific Centre for Isotopic and Geochemical Research, University of British Columbia. The gas evolved from each step was analyzed by a VG5400 mass spectrometer equipped with an ion-counting electron multiplier. All measurements were corrected for total system blank, mass spectrometer sensitivity, mass discrimination, radioactive decay during and subsequent to irradiation, as well as interfering Ar from atmospheric contamination and the irradiation of Ca, Cl and K. Isotope production ratios were ($^{40}Ar/^{39}Ar$)K=0.0302, ($^{37}Ar/^{39}Ar$)Ca =1416.4306, ($^{36}Ar/^{39}Ar$)Ca=0.3952, Ca/K=1.83($^{37}ArCa/^{39}ArK$). The plateau and correlation ages were calculated using Isoplot 3.09 software (Ludwig, 2003). Errors are quoted at the 2-σ (95% confidence) level and are propagated from all sources except mass spectrometer sensitivity and age of the flux monitor.

Whole rock geochemistry. Samples for geochemical analyses were obtained from the least weathered outcrops of the each unit. Sample locations are given as Universal Transverse Mercator in Table II. From a larger population, a subset of samples was screened in this study for the least alteration on the criteria of preservation of igneous textures, petrographic freshness, low values of loss on ignition (LOI), and coherent extended REE primitive mantle-normalized diagram for each given igneous suite. Selected samples were powdered in an agate mill, and analysed for major oxides and trace elements by inductively-coupled plasma-emission spectrometry (ICP-ES) and inductively-coupled plasma-mass spectrometry (ICP-MS) analysis with a $LiBO_2$ fusion, respectively. This analytical work was done at ACME Analytical Laboratories Ltd in Vancouver and results for selected samples of each geochemical group reported in Table II. For major elements oxides, the detection limits are less than 0.01% except for Fe_2O_3 (0.04%), P_2O_5 (0.001%) and Cr_2O_3 (0.002%). The detection limits for trace elements are typically less than 0.1ppm, except for Ba and Be (1ppm), Th (0.2ppm), Ga and Zr (0.5ppm); for some trace elements, they are as low as 0.05ppm. Analytical accuracy and reproducibility are estimated from measurements of duplicate analyses of samples, international rock standards CSC and STD O18 and blanks. The accuracy of the standards is within ± 10% of the suggested working values (Jenner et al., 1990), but generally better than ± 1% for refractory and rare earth elements. Duplicate analyses show reproducibility to be better than 1.0% except for the transition metals (e.g. Cr, Ni, Cu and Zn; <5.0%) and elements with very low concentrations (e.g. Tl), which show deviations of up to 10% (see below).

REFERENCES

Gerstenberger, H., Haase, G., 1997. A highly effective emitter substance for mass spectrometric Pb isotope ratio determinations. Chemical Geology, 136, 309-312.

Jenner, G.A., Longerich, H.P., Jackson, S.E., Fryer, B.J., 1990. A powerful tool for high-precision trace element analysis in earth sciences: evidence from analysis of selected U.S.G.S. reference samples. Chemical Geology, 83, 133-148.

Ludwig, K.R., 2003. User's manual for Isoplot 3.00 A Geochronological Toolkit for Microsoft Excel. Berkeley Geochronology Center, 4 (Special Publications), 71pp.

Renne, P.R., Swisher, C.C.III, Deino, A.L., Karner, D.B., Owens, T., DePaolo, D.J., 1998. Intercalibration of standards, absolute ages and uncertainties in $^{40}Ar/^{39}Ar$ dating. Chemical Geology, 145, 117-152.

Roddick, J.C., 1987, Generalized numerical error analysis with application to geochronology and thermodynamics. Geochimica et Cosmochimica Acta, 51, 2129-2135.

Weis, D., Kieffer, B., Maerschalk, C., Barling, J., de Jong, J., Willians, G.A., Hanano, D., Pretorius, W., Scoates, J.S., Goolaerts, A., Friedman, R.M., Mahoney, J.B., 2006. High-precision isotopic characterization of USGS reference materials by TIMS and MC-ICP-MS. Geochemistry, Geophysics, Geosystems, 7, 1-30. doi:10.1029/2006GC001283.

TABLE I | **Isotopic analyses of standards**

Sample #	$^{87}Sr/^{86}Sr$	Error (±2σ)	Cycles	$^{86}Sr/^{88}Sr$	$^{143}Nd/^{144}Nd$	Error (±2 σ)	Cycles	$^{145}Nd/^{144}Nd$	Error (±2 σ)	$^{146}Nd/^{144}Nd$
SRM987 600ng	0.710249	0.000008	123	0.1193						
SRM987 600ng	0.710249	0.000009	119	0.119						
SRM987 600ng	0.710250	0.000008	124	0.1194						
SRM987 600ng	0.710257	0.000009	125	0.1197						
SRM987 300ng	0.710256	0.000010	90	0.1190						
SRM987 600ng	0.710259	0.000007	124	0.1193						
La Jolla 150ng					0.511856	0.000006	114	0.348401	0.000004	0.7196
La Jolla 150ng					0.511854	0.000006	83	0.348402	0.000004	0.7204
La Jolla 150ng					0.511849	0.000006	116	0.348409	0.000004	0.7217
La Jolla 150ng					0.511857	0.000006	114	0.348399	0.000004	0.7203
La Jolla 150ng					0.511841	0.000007	116	0.348407	0.000004	0.7207
Average	0.710253	n=6			0.511851	n=5		0.348403		
Error	0.000009				0.000013			0.000008		

TABLE II | **Summary of ^{40}Ar-^{39}Ar incremental heating experiments of mineral separates**

5873I-SG9015	Whole-Rock Isotope		(sample/mineral)							
Laser Power(%)	Ratios 40Ar/39Ar	38Ar/39Ar	37Ar/39Ar	36Ar/39Ar	Ca/K	Cl/K	%40Ar atm	f 39Ar	40Ar*/39ArK	Age
2	59.563±0.018	0.319±0.047	0.841±0.026	0.291±0.054	8.124	0.057	101.97	0.3	- 1.155±4.619	- 21.63±87.07
2,2	22.037 0.007	0.076 0.057	0.816 0.015	0.084 0.036	8.59	0.01	91.99	1.89	1.685 0.902	31.11 16.52
2,4	10.992 0.006	0.034 0.033	0.692 0.016	0.034 0.031	7.332	0.003	72.12	4.34	2.948 0.314	54.08 5.67
2,6	8.533 0.007	0.025 0.040	0.488 0.017	0.022 0.038	5.158	0.001	54.81	5.81	3.716 0.243	67.91 4.36
2,8	8.084 0.007	0.022 0.057	0.460 0.016	0.019 0.032	4.866	0.001	51.09	6.66	3.819 0.180	69.75 3.23
3	7.224 0.007	0.020 0.059	0.443 0.015	0.017 0.029	4.721	0	48.51	6.63	3.577 0.150	65.42 2.69
3,3	6.404 0.005	0.017 0.053	0.467 0.013	0.011 0.021	5.009	0	39.14	15.99	3.814 0.071	69.66 1.27
3,5	5.770 0.005	0.019 0.046	0.427 0.015	0.010 0.022	4.577	0.001	34.08	12.44	3.696 0.066	67.56 1.18
3,7	5.515 0.005	0.021 0.045	0.573 0.013	0.009 0.034	6.158	0.001	31.06	13.29	3.699 0.094	67.60 1.69
4	5.876 0.005	0.027 0.039	0.754 0.016	0.011 0.034	8.115	0.002	32.74	10.2	3.831 0.109	69.97 1.96
4,5	8.189 0.005	0.047 0.028	1.636 0.013	0.017 0.025	17.713	0.007	38.3	9.23	4.952 0.125	89.95 2.22
6	11.990 0.005	0.087 0.020	3.407 0.013	0.025 0.021	37.208	0.016	42.66	13.22	6.873 0.159	123.66 2.76
Total/Average	7.825±0.001	0.033±0.006	5.968±0.001	0.014±0.006	10.967	0.008		100	4.177±0.024	
J=0.010323±0.000014			Volume 39ArK = 358.99							
Plateau Age = 68.40±0.75 Ma			(1s, including J-error of .5%)		MSWD = 0.63, probability = 0.71			71% of the 39Ar, steps 4 through 10		
Inverse isochron results: Model (±95%-conf.) on 7 points				Age = 67.8±4.8 Ma			40/36 intercept: 300±33, MSWD = 0.72, Probability = 0.61 (at J=.010323±.5% 1s)			

6JE13A	Hornblende		(sample/mineral)							
Power(%)	40Ar/39Ar	38Ar/39Ar	37Ar/39Ar	36Ar/39Ar	Ca/K	Cl/K	%40Ar atm	f 39Ar	40Ar*/39ArK	Age
2	40.880±0.015	0.088±0.026	0.718±0.020	0.143±0.021	7.898	0.011	97.57	3.27	0.959±0.906	17.78±16.71
2,3	12.379 0.019	0.035 0.036	0.674 0.023	0.035 0.026	7.673	0.003	75.75	10.63	2.954 0.275	54.19 4.97
2,6	13.673 0.015	0.041 0.028	0.544 0.020	0.036 0.026	6.139	0.005	69.35	8.96	4.130 0.291	75.33 5.20
2,9	11.852 0.016	0.028 0.054	0.447 0.020	0.029 0.037	4.979	0.002	61.86	7.3	4.440 0.334	80.85 5.95
3,2	7.296 0.018	0.025 0.044	0.194 0.024	0.012 0.036	2.126	0.002	37.47	12.35	4.476 0.156	81.50 2.78
3,5	6.299 0.018	0.017 0.037	0.191 0.023	0.008 0.038	2.128	0	28.96	17.28	4.398 0.123	80.11 2.19
3,8	6.154 0.012	0.022 0.050	0.307 0.021	0.008 0.060	3.462	0.001	27.88	17.61	4.364 0.149	79.50 2.66
4,1	5.648 0.009	0.021 0.045	0.198 0.018	0.006 0.050	2.184	0.001	22.4	13.37	4.288 0.104	78.14 1.86
5	5.913 0.012	0.023 0.046	0.184 0.027	0.008 0.043	1.972	0.002	24.02	9.22	4.371 0.115	79.62 2.05
Total/Average	9.016±0.003	0.026±0.007	2.019±0.002	0.017±0.006	3.7	0.003		100	4.098±0.036	
J = 0.010324±0.000014			Volume 39ArK = 314.28							
Plateau Age = 79.4±1.0 Ma			(1s, including J-error of .5%)		MSWD = 0.30, probability = 0.94			86.1% of the 39Ar, steps 3 through 9		
Inverse isochron results: Model (±95%-conf.) on 7 points				Age = 79.7±3.0 Ma			40/36 intercept: 293±18, MSWD = 0.35, Probability = 0.88, (at J=.010324±.5% 1s)			
Volumes are 1E-13 cm3 NPT			Neutron flux monitors: 28.02 Ma FCs (Renne et al., 1998)							
Isotope production ratios: (40Ar/39Ar)K=0.0302±0.00006, (37Ar/39Ar)Ca=1416.4±0.5, (36Ar/39Ar)Ca=0.3952±0.0004,								Ca/K=1.83±0.01(37ArCa/39ArK).		

Sample description

Sample 5873I-SG9015 is a basaltic flow from the Loma Los Guandules in the Restauración area. The basalt is composed of euhedral olivine phenocrysts (totally replaced by iddingsite and/or clay minerals), phenocrysts, and microcrysts of augite, plagioclase microlites, and opaque minerals. The mesostasia is devitrified glassy and vesicular.

Sample 6JE13A is a basaltic dike intruding the Constanza Formation of the Tireo group in the Constanza area. The textures are fine-grained intersectal to cryptocrystalline. It is composed of plagioclase, augitic clinopyroxene and hornblende micro-phenocrysts, and very-fine grained Fe-Ti oxides as accesory phases.

TABLE III | **Parameters used in forward melt models**

Modal abundances

	olivine	orthopyroxene	clinopyroxene	spinel	garnet
spinel lherzolite	0.5	0.3	0.15	0.05	0
garnet lherzolite	0.5	0.3	0.12	0	0.08

Partition coefficients -spinel lherzolite

Element	ol/liq	opx/liq	cpx/liq	sp/liq	Bulk D (sp)	P (sp)	Source	F=9%
La	0.0005	0.0031	0.03	0	0.0056	0.0188	0.234	2.6
Ce	0.0005	0.004	0.08	0.0005	0.0133	0.049	0.772	8.58
Sr	0.00004	0.0007	0.091	0	0.0137	0.0545	9.8	109
Nd	0.00042	0.012	0.088	0.0008	0.0168	0.0561	0.713	7.91
Zr	0.00131	0.021	0.18575	0.05	0.0371	0.1198	7.94	83.2
Sm	0.0011	0.02	0.299	0.0009	0.0508	0.1844	0.27	2.65
Eu	0.00805	0.053	0.3245	0.0009	0.0678	0.2098	0.107	0.94
Ti	0.015	0.086	0.35	0.1	0.0903	0.2406	798	6030
Gd	0.0011	0.065	0.35	0	0.0716	0.2282	0.395	3.39
Tb	0.0019	0.038	0.375	0.00075	0.0678	0.2351	0.075	0.66
Dy	0.0027	0.011	0.4	0.0015	0.0639	0.242	0.531	4.85
Ho	0.00785	0.028	0.41	0.00225	0.0731	0.2534	0.122	1.05
Er	0.013	0.045	0.42	0.003	0.0822	0.2647	0.371	2.99
Yb	0.02	0.08	0.45	0.0045	0.1006	0.2935	0.401	2.88

Partition coefficients -garnet lherzolite

Element	ol/liq	opx/liq	cpx/liq	gar/liq	Bulk D (gar)	P (gar)	Source	F=1.7%
La	0.0005	0.004	0.015	0.0007	0.0033	0.006	0.234	13.7
Ce	0.0005	0.004	0.038	0.017	0.0074	0.02	0.772	41.1
Sr	0.00004	0.0007	0.091	0.0007	0.011	0.0315	9.8	458
Nd	0.00042	0.012	0.0884	0.064	0.0198	0.0559	0.713	24.6
Zr	0.00076	0.018	0.1142	0.232	0.0394	0.1283	7.94	167
Sm	0.0011	0.02	0.1509	0.23	0.0443	0.1404	0.27	5.17
Eu	0.00805	0.053	0.14545	0.415	0.073	0.2133	0.107	1.34
Ti	0.015	0.086	0.14	0.6	0.1017	0.2863	798	7390
Gd	0.0011	0.065	0.16	1.2	0.1433	0.5117	0.395	2.68
Tb	0.0019	0.065	0.165	1.2	0.1443	0.5135	0.075	0.51
Dy	0.0027	0.065	0.17	2	0.215	0.8136	0.531	2.45
Ho	0.00785	0.065	0.175	2.5	0.2618	1.0024	0.122	0.47
Er	0.013	0.065	0.18	3	0.3085	1.1913	0.371	1.21
Yb	0.02	0.08	0.25	5.5	0.5427	2.1504	0.401	0.75

Partition coefficients are from Salters and Stracke (2004), 2.0 GPa for spinel lherzolite assemblage and 3.0 GPa for garnet lherzolite assemblage.
Values in italics are from Johnson et al. (1990). F=9% and F=1.7% are calculated melt compositions
for at the listed % of melting for spinel lherzolite and garnet lherzolite, respectively. P is the non-modal melt factor.

Geologica Acta, Vol.9, Nos 3-4, September-December 2011, 329-350
DOI: 10.1344/105.000001695
Available online at www.geologica-acta.com

geologica acta

The Chuacús Metamorphic Complex, central Guatemala: geochronological and geochemical constraints on its Paleozoic - Mesozoic evolution

L.A. SOLARI [1] [*] **A GÓMEZ-TUENA** [1] **F. ORTEGA-GUTIÉRREZ** [2] **C. ORTEGA-OBREGÓN** [2]

[1] **Centro de Geociencias, Universidad Nacional Autónoma de México**
Campus Juriquilla, 76230 Querétaro, México. E-mail: solari@servidor.unam.mx

[2] **Instituto de Geología, Universidad Nacional Autónoma de México**
Ciudad Universitaria, 04510, México D.F., México

* Corresponding author

ABSTRACT

The Chuacús Metamorphic Complex is located in Central Guatemala, between the Polochic and Motagua fault zones. It is made up of complexly intercalated, mafic and felsic high-grade gneisses, amphibolites, pelitic and quartzofeldsphatic metasediments and subordinate marbles. Mafic dikes and lenses metamorphosed to amphibolite and eclogite facies are tholeiitic and similar to mid-ocean ridge basalts. In contrast, metamorphosed intrusives (gabbro, diorite and granite) are calc-alkaline and have the geochemical signature of arc magmas. Laser Ablation Inductively Coupled Plasma Mass Spectrometry U-Pb zircon geochronology allows the recognition of three episodes of metamorphism. The first eclogite facies metamorphism (M1) is bracketed between Ordovician magmatism in the northern Chuacús Metamorphic Complex and the neighboring Rabinal granitic suite; the second corresponds to an Upper Triassic period of arc magmatism and migmatization (M2); the third high-grade metamorphic event (M3) occurred during the Late Cretaceous.

The tectonic evolution of the Chuacús Metamorphic Complex began during the Early Paleozoic as a basin in the Rheic Ocean that received detrital material from the Maya Block, Acatlán and southeastern México. The Chuacús Metamorphic Complex evolved to an active margin that subducted to HP conditions during the Mid-Late Paleozoic, and then was exhumed and involved in two tectonothermal events during the Upper Triassic and Late Cretaceous. The Chuacús Metamorphic Complex was accreted to the southern Maya Block during the Late Cretaceous, as a result of the convergent tectonics between the latter and either the Greater Antillean arc or the Chortís Block.

KEYWORDS | **Chuacús Complex. Guatemala. U-Pb geochronology. Maya Block. Caribbean. Basement Tectonics.**

INTRODUCTION

The tectonic limit between the North America and Caribbean plates is composed of a complex mosaic of crustal blocks, which are juxtaposed and limited by faults (e.g., Ortega-Gutiérrez et al., 2007; Rogers et al., 2007; Brueckner et al., 2009; Ratschbacher et al., 2009) (Fig. 1). Those crustal blocks range in age from the Proterozoic (e.g. Yoro area, central Honduras, Manton, 1996) to Early-Late Paleozoic and Mesozoic (Altos Cuchumatanes, Guatemala, Solari et al., 2009, 2010a; Maya Mountains, Belize, Martens et al., 2010; Rabinal suite, Guatemala, Ortega-Obregón et al., 2008; Chuacús Complex, Ortega-Gutiérrez et al., 2004; Ratschbacher et al., 2009; Las Ovejas Complex, Ratschbacher et al., 2009), and were finally amalgamated during the Late Mesozoic-Cenozoic (Harlow et al., 2004; Ortega-Gutiérrez et al., 2004; Martens et al., 2007; Brueckner et al., 2009; Ratschbacher et al., 2009). Recent works shed light on the tectonic evolution of the Motagua fault zone as the complex tectonic limit between the North America and Caribbean plates (Harlow et al., 2004; Brueckner et al., 2009; Pindell et al., 2006; Pindell and Kennan, 2009). The tectonic significance of the continental blocks involved in the suturing, however, is still a matter of debate, especially on the southernmost edge of the North America plate (i.e., the Maya Block). The classical view on the tectonic limit is represented by a suture along the Motagua fault, involving the Maya Block (North America plate) to the north, and the Chortís Block (Caribbean plate) to the south (e.g., Dengo, 1969). More recently, several works have added complexity to such a simple model, involving the collision of the Greater Antilles to the south of the Maya Block during the Late Cretaceous, prior to docking of the Chortís Block (e.g., Pindell and Barret, 1990; Harlow et al., 2004; Giunta et al., 2006; Brueckner et al., 2009; Pindell and Kennan, 2009; Ratschbacher et al., 2009). Further complications have arisen from the works of Ortega-Gutiérrez et al. (2007) and Ortega-Obregón et al. (2008), who suggested and argued for the existence of discrete crustal blocks or suspect terranes in the southern Maya Block, extending from central Guatemala across the Motagua suture zone to well inside the Chortís Block of southern Guatemala and Honduras (e.g. Rogers et al., 2007). One of the key localities to test the possible existence of those crustal entities, and one of the least studied, is the Sierra de Chuacús in central Guatemala. This paper presents new geochronological and geochemical data of crustal rocks in the Sierra de Chuacús in order to provide further constraints to its tectonic evolution and the ongoing discussions on its allochthonous vs. autochthonous nature and tectonic evolution.

PREVIOUS WORKS

The Sierra de Chuacús is located in central Guatemala, between the Polochic and Motagua faults (Fig.1 and 2). The Chuacús Metamorphic Complex is made up of an intricate sequence of polydeformed, locally retrograded high-grade metamorphic rocks, both igneous and sedimentary in origin. Previous works report Silurian ages with Grenvillian protoliths in the northern sector of the Sierra de Chuacús (Gomberg et al., 1968). The presence of a Carboniferous high-grade metamorphic event affecting a Grenvillian protolith was identified by Ortega-Gutiérrez et al. (2004) in El Chol, in the middle of the Sierra de Chuacús. Martens et al. (2005, 2007) questioned the precision of that age and reported a Triassic age for similar rocks. A recent work by Ratschbacher et al. (2009) reported Proterozoic ages in the northern Sierra de Chuacús, with some discordant analyses yielding imprecise lower intercepts in the 638-477Ma range. Another sample they dated in the southern Sierra de Chuacús yielded Proterozoic and Devonian inheritance, as well as Triassic magmatic ages that postdate eclogite metamorphism and were later affected by high-temperature (HT) metamorphism during the Late Cretaceous. Petrological data suggest the existence of a HT eclogite facies event (~680-750°C, ~22-24kbar, Ortega-Gutiérrez et al., 2004; Martens et al., 2007; Ratschbacher et al., 2009), which cooled to about 580-600°C and 10-14kbar during decompression (Ortega-Gutiérrez et al., 2004; Ratschbacher et al., 2009). While there is still debate about the existence of one or two eclogite facies from metamorphic pulses affecting the Chuacús Metamorphic Complex; pre-Carboniferous according to Ortega-Gutiérrez et al. (2004), pre-Triassic according to Ratschbacher et al. (2009), or after the Triassic but before the Late Cretaceous according to Martens et al. (2007); these authors agree on Late Cretaceous cooling and exhumation (broad K-Ar, Ar and Rb-Sr age range of ~75 to ~66Ma, see also Ortega-Obregón et al., 2008).

Metamorphic and igneous rocks of comparable age and metamorphic grade are present elsewhere in southern México and central-north Guatemala. In the Acatlán Complex of southern México, basement of the Mixteco terrane, megacrystic granites have yielded ~480-440Ma magmatic ages, similar to the ages calculated for rift-related tholeiites in the same unit (Miller et al. 2007; Keppie et al. 2008a, b). They are intimately associated with high pressure metamorphism that occurred either during the Cambro-Ordovician (Vega-Granillo et al., 2007) or the Devonian-Mississippian and was associated with the closure of the Rheic Ocean (e.g. Nance et al., 2006, and references therein). In southeastern México, the Guichicovi complex is characterized by Grenvillian granulites (Weber and Köhler, 1999) intruded by Permian granites (La Mixtequita Massif, Torres et al., 1999). The Chiapas Massif crops out farther to the southeast, toward the Guatemala border. The massif is characterized by Ordovician S-type granites and amphibolites (Pompa-Mera et al., 2008), as well as widespread Late Permian granites that intrude medium to high-grade metasediments and orthogneisses, with Nd model

ages between 1.0 and 1.4Ga (Schaaf et al., 2002; Weber et al., 2006a, 2007, 2008). The metasediments of the Lower Santa Rosa Formation, which crop out in the Chiapas Massif, were recently dated by Weber et al. (2009), establishing the maximum depositional ages as defined by youngest zircons clustering around 315-325 and 331-341Ma. In Central Guatemala, just north of the Baja Verapaz Fault Zone, Ortega-Obregón et al. (2008) dated several peraluminous granites between 453 and 462Ma (lower intercepts of discordant data, U-Pb by Isotope-Dilution Thermal Ionization Mass Spectrometry (ID-TIMS)) and placed them at the very edge of what they considered to be the tectonic southern limit of the Maya Block. In the Maya Mountains of Belize, Martens et al. (2010) reported an Early Devonian Laser Ablation Inductively Coupled Plasma Mass Spectrometry (LA-ICPMS) age of 406Ma for rhyolites interbedded with conglomerates, which confirms the ~405-420Ma ages previously published by Steiner and Walker (1996).

GEOLOGY OF THE CHUACÚS METAMORPHIC COMPLEX

The Chuacús Metamorphic Complex is a polymetamorphic, originally high-grade and essentially metasedimentary formation, which bears textural and mineralogical evidence of at least one eclogite-facies event following a P-T decompressional path that could have departed near the field of ultrahigh pressure metamorphism (UHPM) and, in any case, representing continental subduction (e.g. Ortega-Gutiérrez et al., 2004; Martens, 2009). The Chuacús Metamorphic Complex is mainly composed of quartzofeldspathic, garnet and mica bearing gneisses; two micas, garnet, kyanite, rutile schists; minor marbles and calcsilicates and abundant orthogneisses, which range from mafic (garnet, hornblende, rutile and plagioclase) to granitic in composition. A large, Late Cretaceous shear zone, named Baja Verapaz Shear Zone by Ortega-Obregón et al. (2008) limits the Chuacús Metamorphic Complex in the north. The kinematics of the

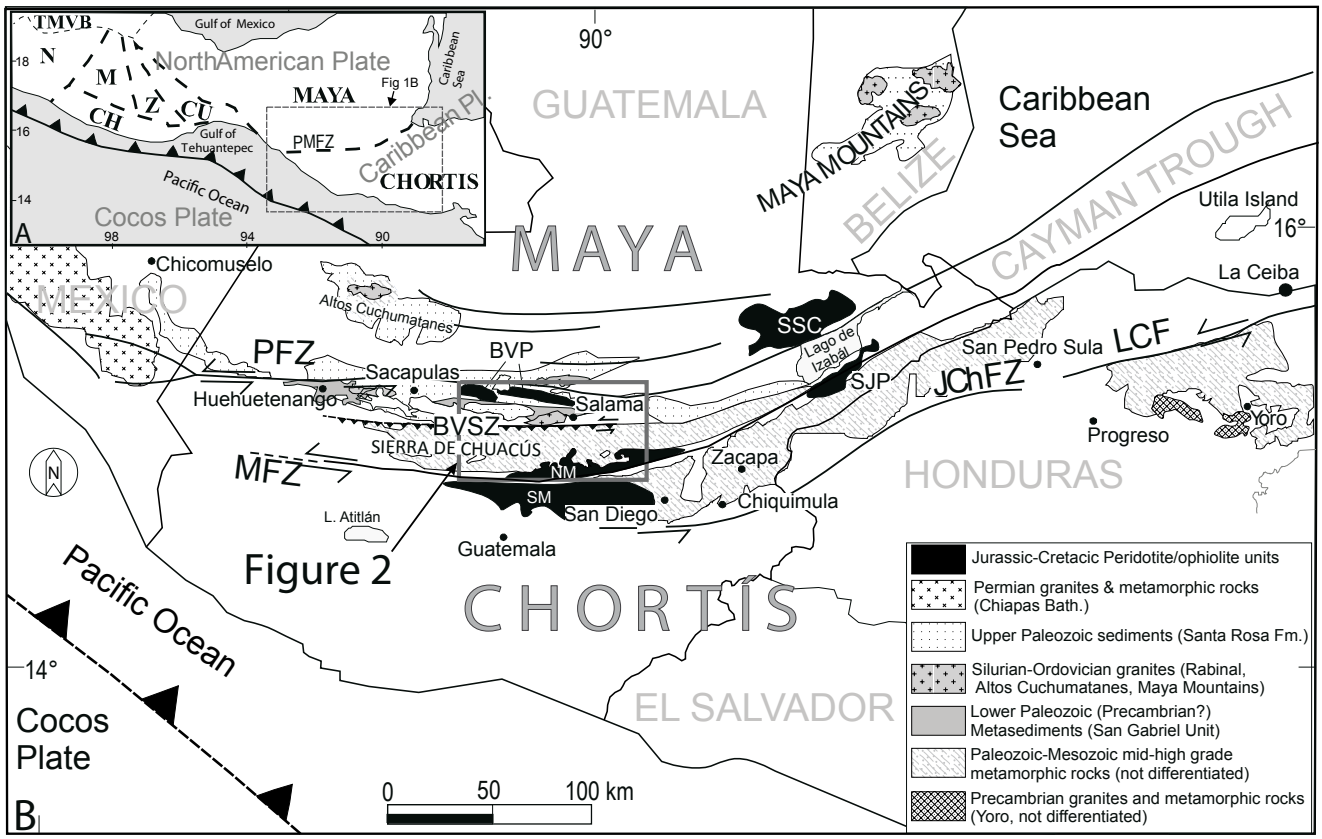

FIGURE 1 | **A) Main tectonic subdivision of crustal blocks in southern Mexico and Central America. N: Náhuatl-Guerrero terrane; TMVB: Trans-Mexican Volcanic Belt; M: Mixteco terrane; CH: Chatino terrane; Z: Zapoteco terrane; CU: Cuicateco terrane; MAYA: Maya Block; CHORTIS: Chortís block. Nomenclature after Sedlock et al. (1993). PMFZ: main (simplified) trace of the Polochic-Motagua fault zone. B) Schematic geological map showing basement rocks of central Guatemala, southeasternmost Mexico, and northwestern Honduras. Geology is recompiled from Kesler et al. (1970); Anderson et al. (1973); Steiner and Walker (1996); Weber et al. (2005, 2006); and unpublished data by the authors. PFZ: Polochic Fault Zone; MFZ: Motagua Fault Zone; BVFZ: Baja Verapaz Fault Zone; JChFZ: Jocotán-Chamelecón Fault Zone; LCF: La Ceiba Fault. Main ophiolitic bodies are shown in black: SSC: Sierra de Santa Cruz; BVP: Baja Verapaz; SJP: S. Juán de Paz; NM: north Motagua unit, ophiolite and mélange; SM: south Motagua unit, ophiolite and mélange. Modified from Ortega-Obregón et al. (2008).**

Baja Verapaz Shear Zone indicates thrusting to the NNE with a minor left-lateral component. It mainly affected a sequence of low-grade pre-Ordovician slates and phyllites, informally named the San Gabriel sequence, as well as some igneous units belonging to the Ordovician Rabinal Granite Suite (Ortega-Obregón et al., 2008). At the southern edge of the Baja Verapaz Shear Zone the low metamorphic grade increases to amphibolite facies, where the Chuacús Metamorphic Complex actually begins. Chuacús Metamorphic Complex orthogneisses present a large age range and variable degrees of deformation. However, intrusive contacts are often visible in fresh outcrops. One of the Chuacús Metamorphic Complex exposures which deserves a more detailed description is the El Chol. At this location, banded mafic gneisses are intimately associated with metamorphosed granitic-trondhjemitic dikes. Local pods of granitic melt, slightly discordant to concordant with the main foliation, strongly suggest that the mafic bands are migmatitic restites, whereas the granitic veins are neosomatic leucosomes. It is important to underline that El Chol is the only locality in the Chuacús Metamorphic Complex where at least three deformation events are superposed and clearly distinguishable. Pegmatites are also widespread throughout the entire Chuacús Metamorphic Complex, ranging from decimetric bands to more than several hundreds of meters wide. Eclogite is the most important lithology recognized in several outcrops. These high-pressure rocks are mainly present as deformed lenses in leucocratic and deformed gneisses, indicating a remnant of an important metamorphic event (cf. Ortega-Gutiérrez et al., 2004, for representative microprobe analyses).

The high-pressure metamorphism is widespread in the southern Sierra de Chuacús between El Chol and the northern Motagua allochthonous units, which constitute the tectonic southernmost limit of the Chuacús Metamorphic Complex. Eclogite-facies metamorphism is not recognized, however, in the western Chuacús (e.g. Kesler et al., 1970; Ratschbacher et al., 2009) or in the easternmost known outcrops, which are located in the southern Sierra de Las Minas (easternmost outcrops of Fig. 2).

MAIN PETROGRAPHIC FEATURES

The following petrological data summarize and complement previous work (Ortega-Gutiérrez et al., 2004) on some fundamental petrographic and textural

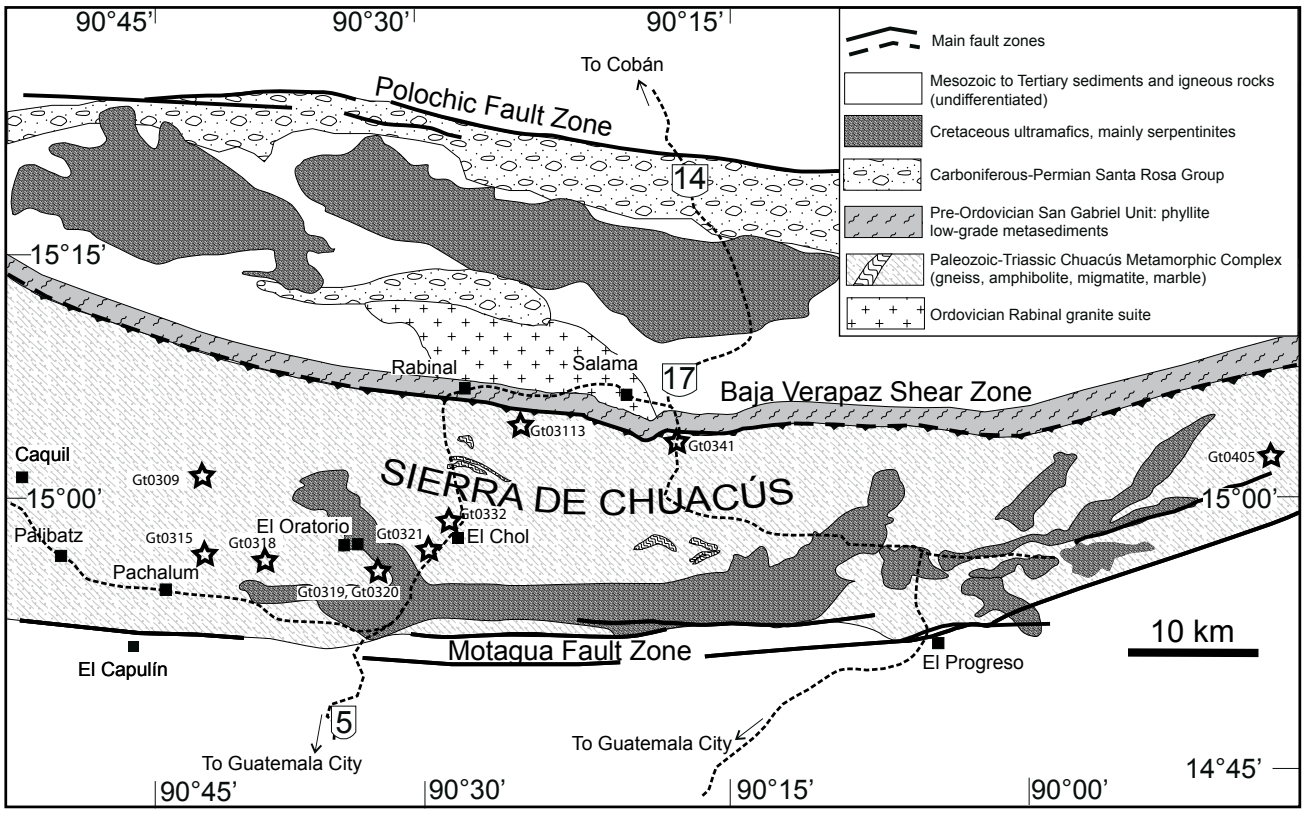

FIGURE 2 | **Simplified geologic map of the Sierra de Chuacús area, Central Guatemala. Modified from Ortega-Gutiérrez et al. (2004). Sampled localities are indicated.**

characteristics of the Chuacús Metamorphic Complex as studied at its type-area, the Sierra Chuacús between Granados and Salamá in central Guatemala. Based on detailed petrographic studies of representative samples, actual and relict evidence for high-pressure metamorphism may be found in most metapelitic, quartzofeldspathic, calcareous, and mafic lithologies of the Chuacús Complex in its type-area. The metapelites (see Table 1 for representative Wavelength Dispersive X-Ray Spectrometry (WDS) chemical analyses of the main aluminous phases) include the characteristic high-pressure assemblage kyanite - garnet - rutile - phengite - quartz, with minor phases in the matrix or as inclusions inside high-pyrope garnet ($Alm_{54}Pyr_{40.5}Gr_{4.2}Spes_{1.3}$) and kinked kyanite (Fig. 3A) such as quartz, phengite, ilmenite, titanomagnetite, zoisite, tourmaline, staurolite, phlogopite/biotite, chloritoid and monazite. Rutile inclusions in kyanite and garnet are particularly abundant and commonly show non-prismatic shapes (Fig. 3D). The high-pressure assemblages in the calcareous rocks include: a) high-Mg carbonate - rutile/titanite - quartz - white mica, with zircon, pyrrhotite and apatite as minor phases (marbles), and b) amphibole (pargasite/tremolite) - zoisite - quartz - clinopyroxene - white mica - clinochlore - serpentine - titanite (calcsilicates). Energy Dispersive X-R ay Spectrometry (EDS) analyses of high relief grains detected inclusions of corundum in some reddish pleochroic titanites, and lamellar rutile needles up to 32x0.25μm (Fig. 3B) that may be oriented in three different crystallographic planes in the cores of some zoisites. The composite association tremolite - zoisite - titanite/rutile (S1) overprinted by jadeite - lawsonite - albite - quartz - carbonate (S2) (see Fig. 3F) locally refl ects two high-pressure events verified at contrasting higher and lower temperatures. Lawsonite and jadeite were not verified by chemical analyses, but both phases display their distinctive optical properties (Ortega-Gutiérrez et al., 2004).

Quartzo-feldspathic rocks are characterized by assemblages with quartz - garnet - albite - phengite - biotite - zoisite - rutile - subcalcic amphibole, with accessory potassium feldspar, carbonates and rare green clinopyroxene (probably omphacite) included in albite porphyroblasts, indicating relict high-pressure conditions. Common rounded zircons suggest an original sedimentary protolith. Mafic rocks contain hydrous and anhydrous eclogitic remnants with the typical assemblage omphacite - garnet - rutile - quartz accompanied by variable and comm only la rge amounts of amphibole (barroisite and taramite), phengite and zoisite/epidote. The eclogitic lithologies sometimes preserved radial cracking of garnet around quartz inclusions, as well as lamellar inclusions of rutile along 3-4 crystallographic directions and polycrystalline quartz - potassium feldspar inclusions.

TABLE 1 | **Chuacús Metamorphic Complex metapelite Wavelength Dispersive X-Ray Spectrometry (WDS) mineral chemistry. Methodology described in Ortega-Gutiérrez et al., 2004**

Oxide	St	St	St	St	Ky	Ky	Grt	Phe
SiO_2	28.02	28.03	28.10	27.95	36.13	36.83	41.17	50.49
TiO_2	0.46	0.43	0.42	0.37	0.00	0.00	0.00	0.12
Al_2O_3	52.31	52.44	52.82	52.83	61.96	62.97	24.15	26.61
Cr_2O_3	0.03	0.05	0.00	0.00	0.05	0.02	0.00	0.00
FeO	14.21	14.13	13.62	13.46	0.84	0.80	22.78	4.48
MnO	0.08	0.00	0.04	0.01	0.02	0.02	0.53	0.02
MgO	1.57	1.57	1.49	1.51	0.00	0.00	9.59	2.96
CaO	0.00	0.01	0.00	0.00	0.00	0.02	1.39	0.01
Na_2O	0.15	0.00	0.00	0.13	0.00	0.00	0.00	0.21
K_2O	0.00	0.00	0.00	0.00	0.00	0.00	0.00	11.63
Total	96.83	96.66	96.49	96.26	99.00	100.66	99.61	96.53
Oxygens	46	46	46	46	5	5	12	11
Cations								
Si	7.88	7.88	7.89	7.86	0.99	0.92	3.08	3.39
Ti	0.10	0.09	0.09	0.08	-	-	-	0.01
Al	17.33	17.37	17.48	17.52	2.00	2.00	2.13	2.10
Cr	0.02	0.03	-	-	0.01	-	-	
Fe	3.34	3.32	3.20	3.17	0.02	0.02	1.43	0.25
Mn	0.02	-	0.01	0.00	-	-	0.03	-
Mg	0.66	0.66	0.62	0.63	-	-	1.07	0.30
Ca	-	0.00	-	-	-	0.00	0.11	-
Na	0.08	-	-	-	-	-	-	0.03
K	-	-	-	-	-	-	-	0.99
Sum	29.42	29.35	29.29	29.26	3.02	2.94	7.85	7.07

St: staurolite; Ky: kyanite; Grt: garnet; Phe: phengite

The polymetamorphic evolution of the Chuacús Metamorphic Complex is evident in the wide variety of reaction (prograde and retrograde) textures that characterize most rocks, particularly the eclogitic units. Prograde coronas include garnet on omphacite (Fig. 3E), or on biotite, plagioclase, chlorite and apatite, as well as occasional rims of clinopyroxene on garnet followed by amphibole - plagioclase symplectites (Fig. 3C) that suggest alternating metamorphic episodes of hydration and dehydration. Retrograde or decompression coronitic textures are characterized by symplectites of amphibole-plagioclase and clinopyroxene - albite on omphacite, subcalcic amphibole and garnet, epidote on garnet, apatite on allanite, biotite on phengite, albite on white mica and garnet, titanite on ilmenite and rutile, epidote on zoisite, green on brown biotite, and chlorite on garnet.

ANALYTICAL METHODS

Geochemistry

Major and trace element analyses were performed at Actlabs (Ancaster, Canada). Major elements were determined by X-ray fluorescence, whereas trace elements were measured by ICP-MS employing lithium metaborate/tetraborate fusions. Sm-Nd isotopic ratios were measured by Thermal Ionization Mass Spectrometry (TIMS) at the Laboratorio Universitario de Geoquímica Isotópica of the Universidad Nacional Autónoma de México (UNAM), using a Finnigan MAT 262 system equipped with eight

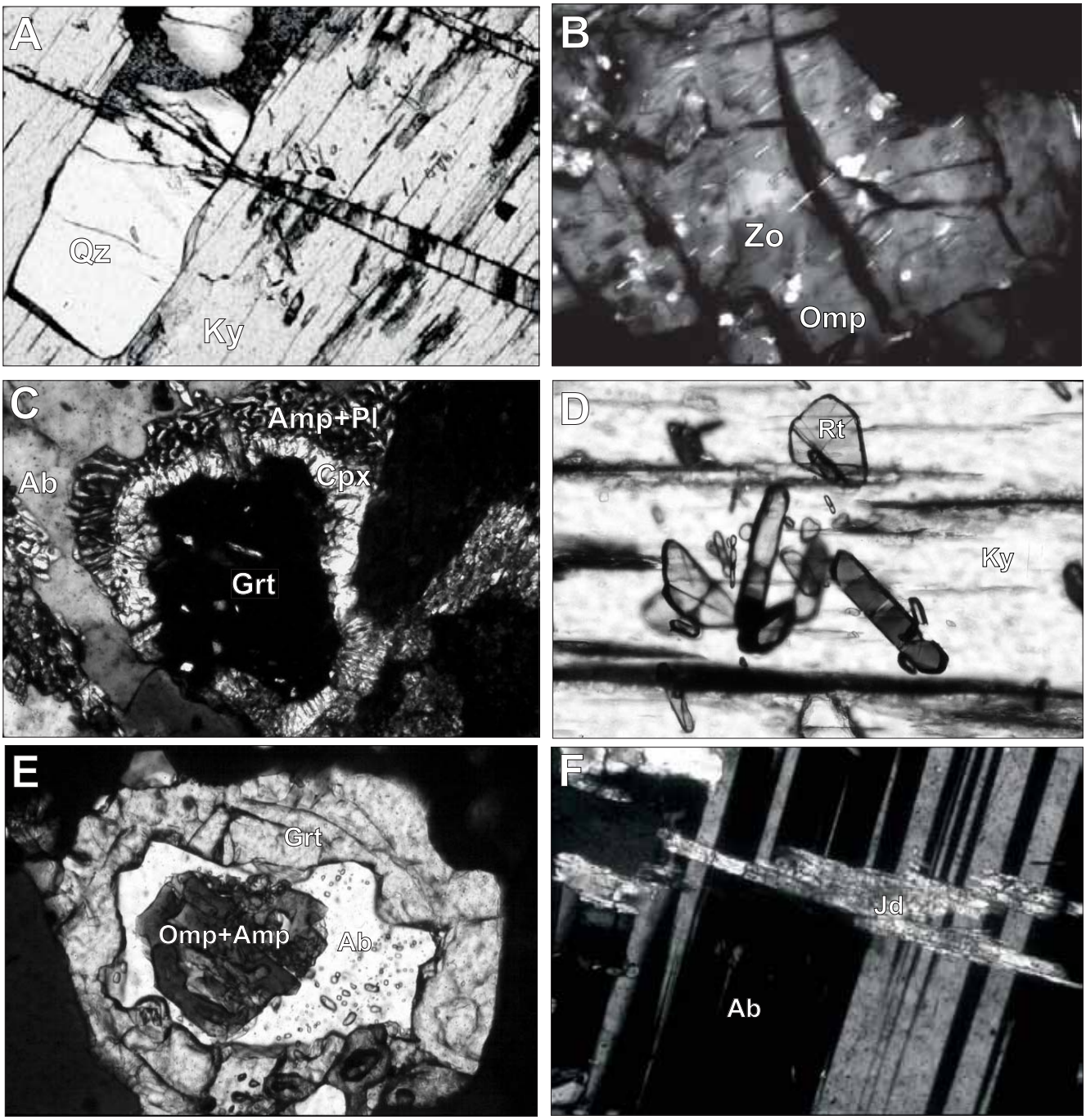

FIGURE 3 | **Some representative photomicrographs of petrographic features described in the text. A) Kink bands nucleated on an elongate quartz inclusion in kyanite. Plane polarized light, field of view is 560µm. B) Lamellar inclusions of rutile (bright needles) in zoisite in a high-pressure calc-silicate. Crossed polarized light, field of view is 220µm. C) Multiple coronas formed by retrogression of mafic eclogites; garnet appears rimmed by clinopyroxene, then by a symplectite of amphibole-plagioclase, and finally by an albite-rich matrix. Crossed polarized light, field of view is 2,240µm. D) Rutile inclusions in kyanite, many crystals show a peculiar "butterfly" shape and may be reddened by exsolution of hematite. Crossed polarized light, field of view is 220µm. E) Composite coronitic texture formed by a central zone of clinopyroxene-amphibole symplectite, rimmed by a wide band of albite followed by a band of garnet with rutile/titanite inclusions; this garnet forms a large inclusion in subcalcic amphibole. Plane polarized light, field of view is 2,240µm. F) Euhedral jadeite (optically determined by extinction angle, birefringence and relief) grown across an albite porphyroblast. Crossed polarized light, field of view is 220µm.**

Faraday cups. Sample preparation and measurement procedures for isotopic analyses have been described by Schaaf et al. (2005). $^{143}Nd/^{144}Nd$ ratios were normalized to $^{146}Nd/^{144}Nd=0.72190$ and corrected to a La Jolla standard value of $^{143}Nd/^{144}Nd=0.511860$. The long term reproducibility of La Jolla standard at Laboratorio Universitario de Geoquímica Isotópica ($^{143}Nd/^{144}Nd$) is 0.511875±22 (2σ, n=152). Geochemical results are reported in Table 2.

Geochronology

The samples selected for geochronology, (3 to 5kg) were crushed and the minerals separated following common techniques such as jaw crushing, milling, Wifley separation, Frantz magnetic separation, and heavy liquids (see also Solari et al., 2007). The zircon concentrates were carefully observed under a binocular microscope. Between 500 and 150 crystals were carefully selected from each sample, in order to obtain all the variations in morphology, shape and color. They were mounted in epoxy resin, ground to expose roughly half of the crystal, and then imaged by cathodolominescence using an ELM 3R luminoscope (Marshall, 1988).

LA-ICPMS U-Pb analyses were performed at Laboratorio de Estudios Isotópicos (LEI), Centro de Geociencias, UNAM, using a Resonetics "Resolution M50" 193nm excimer laser workstation coupled with Thermo Xii Series quadrupole mass spectrometry. Details of the analytical setup employed during this study are described in Solari et al. (2010b). 25s of gas background acquisition was followed by 30s of ablation, carried out in He atmosphere, employing 160mj laser energy, corresponding to an on-target fluence of 8J/cm^2, 34μm diameter spot and a repetition rate of 5Hz, generating a drill rate of ~0.7μm/s. The background average was subtracted from net intensities measured for each isotope. Acquisition involved an alternance of 2 analyses of Plešovice reference zircon (~337Ma, Sláma et al., 2008), NIST 610 standard glasses and 5 unknown zircons, using standard-unknown bracketing method (e.g. Solari et al., 2010b) to allow down-hole fractionation corrections to be performed using an in-house developed software (Tanner and Solari, 2009). NIST 610 glass standard is used to recalculate the concentrations of interest, for instance U and Th, by normalizing such elements with ^{29}Si. Other isotopes are observed during analysis; such as P, Ti, REE; to monitor the presence of inclusions (and in due case discard it) and to produce zircon REE patterns, which can be helpful to interpret the calculated ages. REE zircon patterns were normalized to chondrite values of McDonough and Sun (1995). Recalculated values are available in Table I (Electronic Appendix in www.geologica-acta.com). An estimation of the zircon crystallization temperature is calculated by the Ti content, according to the Ti-in thermometer of Watson et al. (2006). Precision on measured $^{207}Pb/^{206}Pb$, $^{206}Pb/^{238}U$ and $^{208}Pb/^{232}Th$ ratios typically was ~0.7% 1σ relative standard deviation. Replicate analyses of the Plešovice zircon indicate an external reproducibility of 0.8%, 0.7% and 1.6% on the measured $^{207}Pb/^{206}Pb$, $^{206}Pb/^{238}U$ and $^{208}Pb/^{232}Th$ ratios, respectively. These errors are quadratically included in the quoted uncertainties for individual analyses of the analyzed zircons. ^{204}Pb is not monitored during these analyses, because its signal is swamped by the ^{204}Hg contained in the carrier gases. Common Pb correction was thus performed employing the algebraic method of Andersen (2002). A filter was then applied to ensure the quality of selected analyses, consisting in evaluation of the concordance. For grains with ages of <1000Ma, the analysis was considered concordant if the $^{206}Pb/^{238}U$ and $^{207}Pb/^{235}U$ ages differed by less than 10%. For the grains with ages >1000Ma, the same test was carried out considering $^{206}Pb/^{238}U$ and $^{207}Pb/^{206}Pb$ ages. The concordia, probability density distribution and histogram plots, as well as age-error calculations are performed using Isoplot v. 3.70 (Ludwig, 2008). The Tuff-Zirc algorithm (Ludwig and Mundil, 2002) contained in the same software was used to calculate the mean $^{206}Pb/^{238}U$ ages and their errors, as well as to filter for outliers, which are preferred for grains younger than 1000Ma. Details of analyzed zircons, for each samples, are reported in Table II of the Electronic Appendix (www.geologica-acta.com).

RESULTS

Geochemistry

Most of the samples studied here underwent high-grade metamorphism, and therefore geochemical classifications and interpretations must be taken with caution. Nevertheless, comparisons of relatively immobile element concentrations and ratios of the studied rocks with those found in unaltered volcanic rocks can provide insights into the sources and processes that lead to their formation.

In terms of geochemistry and petrography, rocks from the Chuacús Metamorphic Complex can be divided in three different groups: tholeiitic metabasalts (amphibolites), calc-alkaline orthogneisses and pelitic gneisses. Migmatitic gneisses are also present, but they will be described separately for simplicity.

Amphibolites are found as metamorphosed lenses, or deformed dikes in orthogneisses and migmatites (e.g. samples Gt0322, Gt0327, Gt0329, Gt0334 in Table 2). They are fairly homogeneous in terms of their major elements, and show enrichment in Fe_2O_3 and TiO_2 when compared to the rest of the sequences (AFM diagram of Fig. 4A). Even though the MgO contents are not what would be expected

TABLE 2 | **Representative analyses of serpentine from antigorite serpentinites (normslized to 10 O and 8 OH)**

	Chuacús Metamorphic Complex																	
SAMPLE	Gt0303	Gt0309	Gt0314	Gt0319	Gt0320	Gt0321	Gt0322	Gt0327	Gt0329	Gt0333	Gt0334	Gt0341	GT0340	Gt03113	EC01	Gt0360	Gt0394	Gt03117
	Arc orthogneiss	Metasediment	Metasediment	Arc orthogneiss	Arc orthogneiss	Arc orthogneiss	MORB	MORB	MORB	Migmatite Leucosome	Migmatite Melanosome	Rabinal	Rabinal	Rabinal	MORB	Metasediment	MORB	MORB
SiO_2	50,72	74,81	71,91	52,90	46,78	69,43	48,15	47,65	49,60	73,02	46,55	64,35	73,45	75,84	48,44	52,25	48,13	47,56
Al_2O_3	16,05	13,45	13,81	16,24	12,04	14,90	13,78	13,76	13,19	15,34	15,47	15,45	13,05	13,17	13,55	22,65	13,91	14,29
Fe_2O_3	9,84	2,46	2,88	9,50	9,47	2,82	12,82	14,54	10,89	1,13	13,81	4,05	1,87	1,00	13,24	9,30	14,12	12,68
MnO	0,159	0,019	0,023	0,155	0,175	0,060	0,284	0,354	0,237	0,012	0,199	0,067	0,062	0,005	0,263	0,122	0,178	0,129
MgO	6,71	0,29	0,69	4,54	14,10	0,76	6,76	6,84	6,82	0,32	6,33	1,27	0,34	0,03	7,03	2,32	7,09	8,15
CaO	5,80	0,76	1,74	7,60	10,76	1,88	9,61	9,23	10,09	2,08	9,19	3,86	0,83	0,25	10,35	0,34	10,49	10,90
Na_2O	5,34	5,12	5,00	4,24	2,86	4,67	4,05	3,69	3,26	5,38	3,76	5,20	3,45	3,88	3,29	0,77	2,57	2,50
K_2O	1,42	2,19	1,98	1,58	0,62	3,66	1,14	0,66	2,80	1,50	1,24	2,04	4,97	5,51	0,15	5,48	0,29	0,23
TiO_2	1,828	0,280	0,582	1,622	1,231	0,483	2,300	2,594	1,560	0,132	2,507	0,723	0,271	0,026	1,931	1,022	1,470	1,322
P_2O_5	0,63	0,08	0,19	0,43	0,25	0,19	0,26	0,30	0,14	0,04	0,32	0,26	0,07	0,02	0,17	0,18	0,10	0,11
LOI	1,86	0,80	1,51	1,42	1,96	1,01	0,82	0,69	1,71	0,82	0,62	2,74	0,58	0,35	0,65	4,36	1,27	2,23
TOTAL	100,36	100,26	100,32	100,23	100,25	99,87	99,97	100,31	100,30	99,78	100,00	100,01	98,95	100,08	99,07	98,79	99,60	100,11
Sc	20	2	9	21	40	5	41	42	36	2	25	11	3	1	47	26	42	42
Be	2	2	1	2	1	2	2	2	2	1	1	2	5	2	1	5	BDL	BDL
V	134	13	27	200	172	28	381	370	270	13	245	65	18	5	423	104	337	325
Cr	111	BDL	BDL	28	1.020	BDL	213	122	189	BDL	67	BDL	BDL	50	209	79	173	251
Co	33	3	6	30	54	4	40	39	38	2	46	9	2	BDL	44	20	47	48
Ni	91	BDL	BDL	36	326	BDL	85	100	124	BDL	112	BDL	BDL	BDL	103	42	102	113
Cu	15	BDL	BDL	BDL	117	BDL	70	85	64	10	30	53	BDL	BDL	38	BDL	73	183
Zn	107	34	BDL	80	97	42	174	559	134	BDL	133	43	BDL	BDL	95	173	118	118
Ga	18	21	19	18	13	16	19	18	17	16	19	16	16	19	19	33	18	18
Ge	1,8	1,0	0,7	1,3	1,3	1,2	1,4	1,7	1,2	0,5	0,9	1,0	1,5	1,0	1,5	2,6	2,1	2,2
Rb	24	103	39	34	3	66	24	4	61	22	15	66	176	123	2	212	2	5
Sr	628	98	243	508	214	224	76	112	65	774	139	641	124	59	105	128	380	225
Y	36,3	17,1	31,4	28,7	21,8	25,2	49,6	59,9	40,6	1,1	29,5	15,5	27,9	11,7	50,9	76,5	23,5	22,2
Zr	237	210	436	206	126	230	156	160	83	75	158	321	180	85	141	157	80	75
Nb	8,6	6,3	13,7	13,6	12,0	17,8	10,8	8,2	8,8	4,6	14,3	14,5	28,1	6,4	3,2	26,9	7,3	5,6
Cs	0,3	0,2	0,2	0,7	-0,1	0,5	0,2	-0,1	0,6	-0,1	0,2	0,7	1,2	BDL	BDL	2,4	BDL	BDL
Ba	548	379	745	363	29	750	189	25	696	1.030	270	623	600	457	57	795	10	38
La	31,3	40,3	95,2	31,5	14,5	44,6	6,51	7,15	2,97	4,63	18,0	119	48,2	8,69	8,71	125	5,80	5,64
Ce	64,3	65,3	175	58,3	30,4	77,9	17,7	20,3	8,60	9,07	36,6	198	86,3	14,8	17,6	234	15,1	14,2
Pr	8,51	7,40	21,2	7,00	3,93	8,69	2,96	3,47	1,47	1,10	4,71	21,6	8,85	2,15	3,38	29,0	2,27	2,12
Nd	35,1	26,6	77,9	26,4	16,3	30,4	15,2	18,9	7,88	4,17	19,9	72,2	29,4	8,18	18,4	108	11,4	10,7
Sm	8,02	5,59	15,0	5,55	3,91	5,45	5,34	6,75	3,10	0,71	4,81	10,6	5,16	1,70	5,62	20,6	3,67	3,38
Eu	2,60	1,40	3,39	1,75	1,33	1,35	1,92	2,39	1,03	0,239	1,50	2,11	0,819	0,277	1,83	3,34	1,36	1,28
Gd	7,38	4,74	11,2	5,25	3,78	4,62	7,12	8,80	4,48	0,43	4,87	7,09	3,79	1,61	7,43	17,2	4,32	3,99
Tb	1,09	0,68	1,44	0,81	0,62	0,69	1,25	1,58	0,90	0,04	0,78	0,74	0,76	0,29	1,40	2,77	0,82	0,78
Dy	6,48	3,85	7,57	4,88	3,74	4,31	8,53	10,8	6,52	0,21	5,22	3,60	4,56	1,72	8,99	14,9	4,68	4,34
Ho	1,33	0,73	1,33	1,03	0,78	0,87	1,79	2,24	1,46	0,04	1,03	0,57	0,92	0,37	1,93	2,90	0,92	0,87
Er	3,52	1,81	3,11	2,80	2,08	2,51	5,20	6,43	4,26	0,10	2,92	1,37	2,94	1,22	5,94	9,07	2,76	2,58
Tm	0,532	0,245	0,404	0,428	0,305	0,414	0,847	1,02	0,708	0,014	0,448	0,159	0,549	0,196	0,884	1,35	0,388	0,372
Yb	3,46	1,48	2,32	2,72	1,96	2,72	5,28	6,38	4,38	0,11	2,67	1,10	3,40	1,34	5,53	8,02	2,38	2,27
Lu	0,513	0,210	0,310	0,410	0,288	0,432	0,785	0,951	0,676	0,022	0,389	0,173	0,533	0,223	0,811	1,21	0,358	0,329
Hf	5,5	6,6	11,8	4,7	2,8	5,9	4,6	5,0	2,8	2,5	4,3	8,3	5,5	3,4	4,1	4,6	2,4	2,5
Ta	0,56	0,10	0,48	0,83	0,48	0,96	0,26	0,25	0,28	BDL	0,90	0,40	2,99	0,63	0,12	1,25	0,25	0,21
W	0,8	BDL	BDL	BDL	BDL	BDL	0,6	0,6	BDL	BDL	0,9	BDL	0,6	0,8	BDL	BDL	BDL	BDL
Tl	0,14	0,47	0,18	0,21	BDL	0,29	0,13	0,08	0,26	0,09	0,06	0,28	0,87	1,04	0,07	2,12	BDL	0,10
Pb	9	BDL	BDL	BDL	BDL	8	BDL	BDL	BDL	10	BDL	12	13	7	BDL	8	BDL	BDL
Bi	BDL	BDL	BDL	BDL	BDL	BDL	BDL	BDL	BDL	-0,1	BDL	BDL	BDL	3,0	0,5	BDL	BDL	BDL
Th	3,08	2,81	2,56	3,05	1,31	6,15	0,38	0,39	0,20	0,34	1,08	23,1	20,8	4,91	0,26	29,0	0,43	0,42
U	0,73	1,35	0,67	0,69	0,38	1,35	0,31	0,44	0,21	0,15	0,25	2,56	4,68	2,64	0,10	3,52	0,12	0,12
$^{147}Sm/^{144}Nd$	0,125	0,115	0,103	0,115	0,132	0,107	0,196	0,202	0,221	0,092	0,139	0,062	0,104	-	-	-	-	-
$^{143}Nd/^{144}Nd$	0.512519 (19)	0.512033 (19)	0.511985 (18)	0.512603 (16)	0.512708 (20)	0.512406 (20)	0.513093 (16)	0.513055 (19)	0.512779 (19)	0.512206 (18)	0.512626 (19)	0.512166 (12)	0.512245 (18)	-	-	-	-	-
eNd	-2,32	-11,80	-12,74	-0,68	1,37	-4,53	8,88	8,13	2,75	-8,43	-0,23	-9,21	-7,67	-	-	-	-	-

Major elements expressed as wt%. Trace elements expressed as ppm

-: not determined

BLD: below than detection limits

*: last two digits in parentheses in the 143Nd/144Nd ratios refer to the 2 sigma absolute error

DOI: 10.1344/105.000001695

for pristine mantle-derived melts (Langmuir and Hanson, 1980), they have compositions that are typical of slightly differentiated tholeiitic basalts. Despite major element homogeneity, the REE patterns of these rocks are variable. Three samples have the typically depleted LREE and flat HREE pattern of normal mid-ocean ridge basalts (N-MORB) and display small negative Eu anomalies, whereas two samples have relatively flat LREE and depleted HREE without Eu anomalies (Fig. 5A). Extended incompatible trace element patterns are also similar to MORB, although fluid mobile elements (Cs, Rb, Ba, U) have been likely perturbed by weathering since they resemble the enrichments that are often observed in altered-oceanic crust (Staudigel et al., 1996; Fig 5A). In

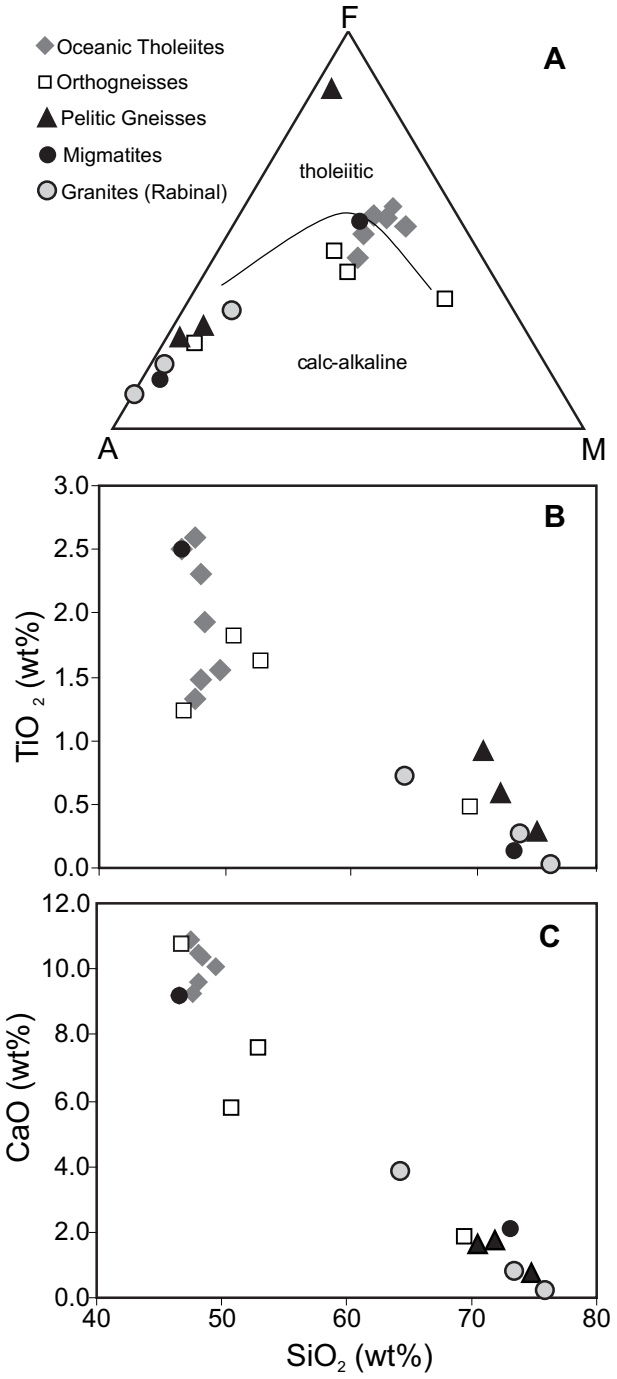

FIGURE 4 | **Major element compositions of rock suites from Chuacús Complex. A) AFM diagram after Irvine and Baragar (1971). B) TiO_2 vs SiO_2. C) CaO vs SiO_2.**

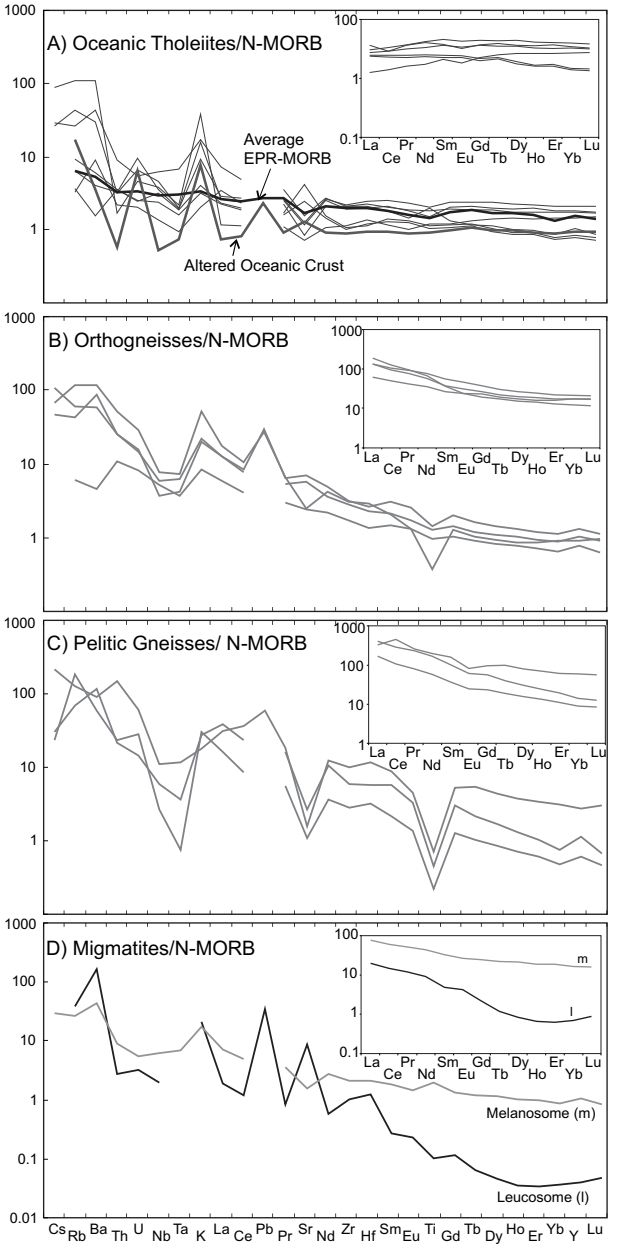

FIGURE 5 | **Trace element geochemical composition of rock suites from Chuacús Complex, normalized to the N-MORB values of Sun and McDonough (1989). REE elements normalized to the chondrite values of McDonough and Sun (1995). Also shown for comparison is the composition of an average EPR-MORB (Lehnert et al., 2000), and of a typically altered oceanic crust (Staudigel et al., 1996).**

fluid immobile elemental ratios (Th/Nd, La/Nd, Sr/Nd, Nd/Yb), these rocks display end-member compositions with values that overlap a typical Pacific MORB. Nonetheless, Nb/Ta ratios (up to 40) are much higher than in MORB, probably suggesting that an element like Ta did not remain completely immobile during high-grade metamorphism.

Orthogneisses (e.g., samples Gt0303, Gt0319, Gt0320, Gt0321 in Table 2) have variable compositions that range from gabbroic to granitic and display a systematic decrease in MgO, F_2O_3, and TiO_2 with increasing SiO_2, Na_2O and K_2O, characteristics that are typical of calc-alkaline magmas worldwide (Fig. 4A). Chondrite-normalized REE patterns show enrichment in LREE and slightly depleted HREE that are in contrast to what is observed in the tholeiitic amphibolites (Fig. 5B). A small negative Eu anomaly is only observed in a relatively evolved granite. Extended N-MORB normalized trace element patterns also display features that are typical of arc magmas, such as Large Ion Lithophile Elements (LILE) enrichment relative to the High Field Strength Elements (HFSE). It is possible that fluid mobile elements like Cs, Rb, and Ba were perturbed by weathering and/or metamorphism; but high LILE/High Field Strength Elements ratios are also coupled with relative enrichment in Th (i.e. high Th/Nb ratios), which are considered as fluid immobile. This suggests that the "arc-like" geochemical signatures of these magmas were likely acquired by crustal inputs, either in the form of subducted sediments or by crustal contamination during ascent. Yet the Th/Nb ratios of the least evolved calc-alkaline orthogneisses are higher than those of similarly evolved tholeiitic metabasalts, strongly suggesting a primary origin in a magmatic arc environment.

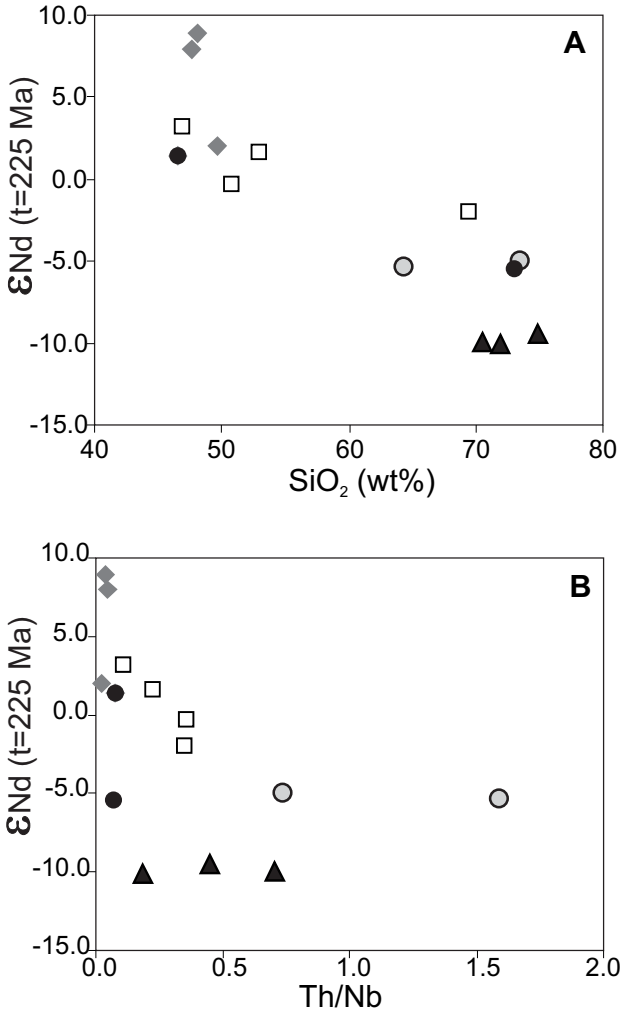

FIGURE 6 | **Initial Nd isotopic compositions calculated to 225Ma for the Chuacús Metamorphic Complex correlate inversely with A) SiO_2 contents and B) Th/Nb ratios.**

Pelitic gneisses are silica and potassium-rich and have overall chemical characteristics that are typical of hemipelagic sedimentation (e.g. samples Gt0309, Gt0314, Gt0360 in Table 2). They are LREE enriched, with either flat or depleted HREE, and usually display negative Eu anomalies. Incompatible trace element patterns also display mature upper crustal features, with highly enriched LILE/High Field Strength Elements ratios that are coupled with negative Sr and TiO_2 anomalies (Fig. 5C). Interestingly, Nb/Ta ratios are also unusually high for upper crustal lithologies (up to ~60), probably indicating a preferential mobilization of Ta during metamorphism.

Distinct magmatic phases from El Chol migmatites have different compositions. A sample taken from the melanosome (Gt0334, Table 2) has the chemical character of an enriched oceanic basalt, with relatively high Nb-Ta contents and fractionated REE patterns. In contrast, the leucosome (Gt0333) is silica-rich and trondhjemitic (K_2O/Na_2O=0.3). The incompatible trace element pattern of the leucosome displays strong positive anomalies in LILE, K_2O, Pb and Sr that are not accompanied by equivalent enrichments in elements like Th and U. Y and the HREE are strongly depleted when compared to the LREE, but the trondhjemitic leucosome also displays a distinctive concave upward pattern in which elements like Ho and Er have the lowest relative concentrations (Fig. 5D). Also noteworthy is that Zr and Hf are enriched when compared to their nearest neighbors, and form a distinctive positive anomaly. These chemical characteristic are indicative of melting under garnet amphibolite facies conditions (Foley et al., 2002).

Nd isotopic compositions were recalculated to 225Ma in accordance to the most important magmatic and recrystallization event recorded by U-Th/Pb geochronology (see below). All amphibolites have positive εNd (up to ~10) values that are close to those of the calculated depleted upper mantle for that age. In contrast, orthogneisses are less radiogenic (εNd=3.23 to -1.95), with isotopic values that correlate negatively

with SiO_2 and Th/Nb ratios (Fig. 6A, B). As it is commonly observed in ancient upper crustal lithologies, pelitic gneisses have very negative εNd (εNd=-10), with values that are even less radiogenic than the Ordovician Rabinal Granite. Interestingly, the melanosome at El Chol has a positive εNd whereas the trondhjemitic leucosome displays a very negative value, indicating that both components are genetically unrelated and that additional crustal lithologies underwent partial melting.

Geochronology

Gt 0315

Sample Gt0315 is a pegmatite which intrudes a gabbroic boudin neck in the locality of Quebrada Honda. Zircons separated from this pegmatite are colorless to pale pink, quite large (up to 280μm in length) and range in shape from large prismatic to stubby. Under cathodoluminescence they are mostly unzoned and characterized by low luminescence, although some show a faint sector-zoned to patchy-zoned cores, sometimes surrounded by moderately luminescent, faintly oscillatory-zoned rims (examples in Fig. 7). A total of 30 analyses were performed on 30 zircons belonging to this sample. The cores have an average age of 982±12Ma (Fig. 8A), as well as high Th/U ratios and typical REE anomalies indicative of igneous origin (e.g., Rubatto, 2002 and Fig. 9A). The overgrowths, as well as those zircons which show a uniform cathodoluminescence, have very low Th/U ratios of less than 0.01, and show LREE depletion compared to HREE (Fig. 9B). The mean $^{206}Pb/^{238}U$ age of 74+3/-1Ma obtained on such overgrowths

FIGURE 7 | **Cathodoluminescence image of some representative zircons analyzed in this work. The circles represent the 34µm LA-ICPMS analyzed spot.**

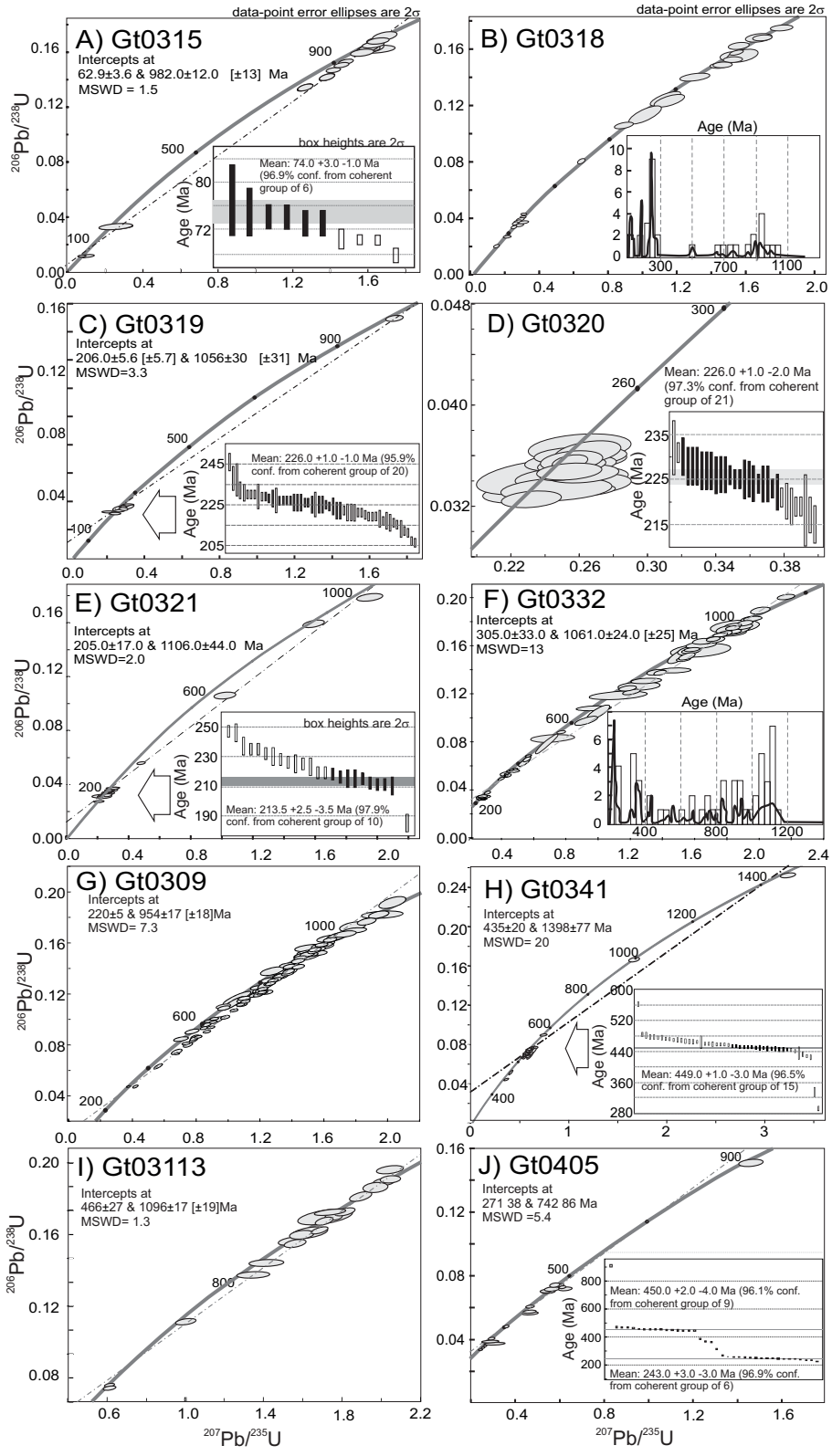

FIGURE 8 | **U-Pb concordia diagrams of the samples dated by LA-ICPMS. Concordia, ages and errors are calculated using Isoplot 3.7 (Ludwig, 2008). The mean $^{206}Pb/^{238}U$ ages in the insets, 2-sigma errors and outlier filtering are calculated with the *TuffZirc* algorithm of Ludwig and Mundil (2002). For those samples containing abundant detrital zircons, i.e. A, C, G, and I, the inset diagrams are combined histograms and probability density plots. Preferred ages are common-Pb corrected using the algebraic method of Andersen (2002). $^{206}Pb/^{238}U$ ages are used if <1000Ma, whereas $^{207}Pb/^{206}Pb$ are used if >1000Ma. See text for further explanations.**

is interpreted as indicating the recrystallization under high-grade metamorphic conditions (concordia of Fig. 8A).

Gt 0318

This sample is a high-grade metasedimentary rock cropping out in Los Altos, northeast of Pachalum (Fig. 2). It is made up of garnet, relic omphacite, white mica, hornblende and interstitial plagioclase. Rutile is present as an accessory mineral, often surrounded by titanite rims. We performed 45 U-Pb analyses on 45 zircons separated from this sample, 9 of which were discarded due to their large discordance. Zircons are in general elongated to ovoidal in shape, with polished terminations typical of sedimentary transport. Under cathodoluminescence they show complex zoning, with presence of inherited cores surrounded by variably luminescent overgrowths (examples in Fig. 7). The dated zircons yield a main cluster at 245Ma followed by other minor ones at 182, 895, 930, and concordant zircons at 125, 505, and several others between 606 and 1007Ma (concordia of Fig. 8B). Although the main provenance is thus Triassic, the few Jurassic to Cretaceous zircons indicate a young episode of sedimentation in the southern Sierra de Chuacús, postdated by high-grade metamorphism.

Gt 0319

This is a foliated gabbro cropping out in Los Limones locality, principally composed of clinopyroxene, garnet, plagioclase, minor biotite, titanite and opaque minerals. We dated 60 crystals by LA-ICPMS, 6 of which were discarded because their discordance was more than 10%. Under cathodoluminescence, the imaged zircons show a predominance of oscillatory (i.e., igneous) growth, with only minor bright overgrowths developed on some of the crystals (Fig. 7). Both oscillatory-zoned cores, as well as overgrowths, show an almost indistinguishable age pattern with a mean $^{206}Pb/^{238}U$ age of 226±1Ma. This age is interpreted as indicating the crystallization of the gabbroic protolith (concordia of Fig. 8C).

Gt 0320

Gt 0320 is an intermediate igneous rock composed of plagioclase, clinopyroxene, hornblende, opaque minerals, biotite, titanite, cropping out nearby sample Gt 0319. Cathodoluminscence shows the ubiquitous presence of oscillatory zoning, with eventual thin, high-luminescent rims developed around cores (Fig. 7). We dated 41 crystals belonging to this sample. Five analyses were omitted because of having >10% discordance. There is no inheritance in any of the dated crystals and therefore the mean $^{206}Pb/^{238}U$ age of 226+1/-2Ma is interpreted as an indication the crystallization of this sample (Fig. 8D).

Gt 0321

This is a granodioritic orthogneiss, intensely foliated, cropping out in the Barranca Agua Caliente. Leucocratic bands, such as the one dated, contain mafic pods up to 30cm in size, which were recognized as retrogressed eclogites (cf. Ortega-Gutiérrez et al., 2004). Zircons separated from this sample are up to 350μm in size and pale yellow to dark red in color. Under cathodoluminescence, they show a frequent presence of oscillatory-zoned cores, surrounded by variably developed zones of oscillatory overgrowths. Of the 50 analyses which were performed on 50 zircons belonging to this sample, 17 were discarded because they were highly (17-42%) discordant, probably as a consequence of partial Pb loss. The other analyses yield a poorly defined Grenvillian upper intercept (1106±44Ma) and a cluster of concordant to slightly discordant analyses corresponding to the lower intercept (Fig. 8E). Such analyses, showing an igneous Th/U ratio well above 0.05, yield a $^{206}Pb/^{238}U$ weighed mean age of 213.5+2.5/-3.5Ma, which is regarded as the best approximation of the crystallization age of this granodiorite.

Gt 0332

This sample belongs to a leucosome migmatitic orthogneiss of El Chol (Fig. 2). The poly-deformed leucocratic bands are interlayered, and some still preserve relict eclogitic assemblages. Previous U-Pb TIMS dating of zircons belonging to this sample yielded discordant results, with a lower intercept of 302±52Ma and an upper intercept of 1024±78Ma (Ortega-Gutiérrez et al., 2004). The lower intercept was interpreted as the age of migmatization.

The zircons selected for LA-ICPMS are of variable size, between 80 and 350μm. They are stubby to multifaceted and prismatic, and show a light pink to red color. Under cathodoluminescence they generally present one or two episodes of variably luminescent overgrowths, developed around more or less preserved relict cores. The cores often show oscillatory zoning (Fig. 7). U-Pb dating stresses the extreme complexity of such samples, and the record of several distinct events. The inherited cores are generally concordant, and broadly Grenvillian in age, ranging between ~900 to ~1100Ma (Fig. 8F). Their Th/U ratios (>>0.01) as well as the REE pattern, with marked positive Ce and negative Eu anomalies, strongly confirm the igneous nature of the protolith (Fig. 9C and Table I (electronic appendix in www.geologica-acta.com), (e.g. Hoskin and Schaltegger, 2003). The data obtained on the overgrowth analyses indicate the presence of at least two different events. A first recrystallization event occurred during the Mississippian (324-348Ma). The second overgrowth developed during the Triassic - Latest Permian

(218-253Ma), generating thin oscillatory bands under CL (Fig. 7). In all the overgrowth episodes the corresponding Th/U ratios are lower than igneous cores, and their REE patterns indicate an overall depletion in LREE (La to Eu) with respect to HREE (Gd to Lu), indicating the possible interaction with high-grade metamorphic fluids (Fig. 9D).

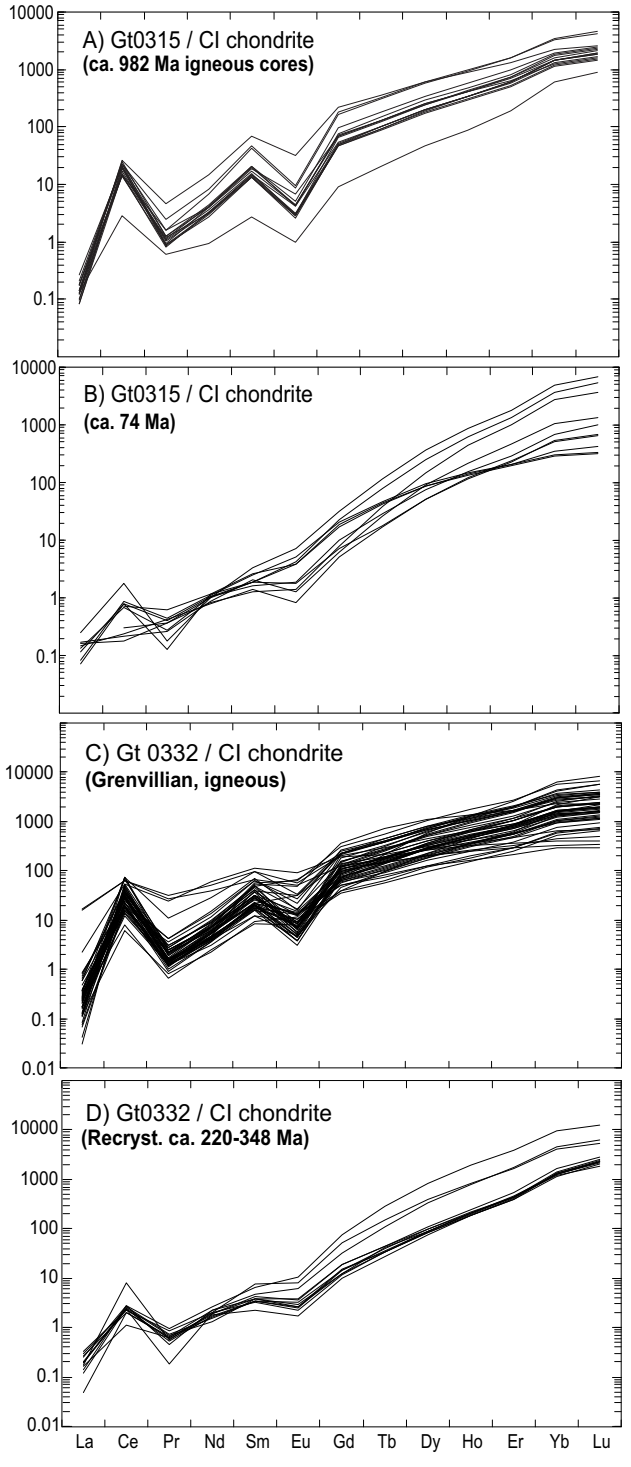

FIGURE 9 | **ircon REE elements patterns normalized to the chondrite values of McDonough and Sun (1995), obtained by LA-ICPMS on the same spot analyzed for U-Pb geochronology. A) ~982Ma igneous cores, pegmatite sample Gt0315; B) ~74Ma metamorphic zircons, pegmatite sample Gt0315; C) Grenvillian igneous zircons, sample Gt0332; D) 220-348Ma recrystallized metamorphic rims, sample Gt0332.**

Gt 0309

This sample is a pelitic metasedimentary rock made up of garnet, kyanite, phengite, quartz, biotite, plagioclase and abundant rutile. It crops out in the southern Sierra de Chuacús (Fig. 2), north of the unpaved road which connects Pachalúm with Caquíl. Separated zircons range between 40 and 320μm in size. They show different colors, varying between dark to pale red, and colorless to amber. They also show a different degree of roundness. One hundred crystals were analyzed, one analysis each, and 6 of them were discarded due to >10% discordance. Of the remaining grains, several yield Proterozoic frequency maximums at 915, 941, 961, and 1106Ma (Fig. 8G). Some younger grains are also concordant (e.g. between ~690 to ~702Ma), however the vast majority are slightly discordant. The lower intercept of such discordant grains is 220±5Ma. We interpret this lower intercept as indicative of the thermal event responsible for metamorphism and deformation of the sedimentary protholith, as well as for Pb loss in the variably discordant zircons.

Gt 0341

This orthogneiss crops out along the paved road which connects El Rancho with Cobán, near the turn off to Salamá (Fig. 2). It is made up of quartz, plagioclase, k-feldspar augens mantled by biotite and minor white mica. Pyrite is quite abundant as an opaque mineral. The concentrated zircons are colorless to pale colored, with yellow to orange tonalities. A total of 50 analyses were performed on 50 crystals and only one was discarded because of having >10% discordance. The remaining crystals define a principal cluster around 440Ma (concordia of Fig. 8H), with a weighted $^{206}Pb/^{238}U$ mean of 449+1/-3Ma, which is interpreted as the crystallization age of this sample (Fig. 8H inset). Few zircons are inherited from the source, and only two yield younger discordant ages, probably as a result of Pb loss.

Gt 03113

Sample Gt03113 is a granitic dike that cuts across high-grade metamorphic rocks (garnet+amphibole) in the northern Chuacús Complex (Fig. 2). Few zircons were concentrated from this sample. They are dark red, short prismatic, and in general show abundant cracks and inclusions. Only 30 analyses were performed on 30 selected crystals, 3 of which were discarded because of >10% discordance. The remaining analyses define a

well constrained upper intercept at 1096±17Ma, several variably discordant grains younger than 1100Ma and also a well constrained lower intercept at 466±27Ma, underlined by two analyses of crystal rims (Fig. 8I). Two interpretations are possible: either the upper intercept defines the crystallization age of the pegmatite, and the lower is coincident with a tectonothermal disturbance, or the upper intercept represents the inheritance from the protolith, and the lower intercept is the true crystallization age. Several features suggest that the last interpretation is correct: 1) all the analyzed grains have a high Th/U ratio, indicative of igneous crystallization; 2) the pegmatite is undeformed and does not show any metamorphism; and 3) its outcrop is in close vicinity with sample Gt0341, which has a similar age, and with the Rabinal granite suite, which also yielded Ordovician crystallization ages (e.g. Ortega-Obregón et al., 2008).

Gt 0405

This is a migmatitic gneiss which crops out in the southern Sierra de Las Minas, which has been considered as the eastern continuation of the Chuacús Metamorphic Complex. It is exposed along the Pasabien River, 5km northwest of Río Hondo. The gneiss is made up of up to 20cm thick leucocratic bands (quartz - plagioclase feldspar - biotite ± muscovite) alternated with garnet - amphibole - biotite pla gioclase horizons. Abundant zircons were separated from this sample. They range from 40 to 350μm in size, and are colorless to intensely red-amber colored. A total of 55 LA-ICPMS analyses were performed on 55 selected grains, 14 of which were rejected because of more than 10% discordance (Table I, electronic appendix in www.geologica-acta.com). The remaining analyses define a bimodal distribution in the concordia diagram of Fig. 8L, with two principal peaks at 450+2/-4Ma and 243±3Ma. Whereas the older age group corresponding to igneous cores (see cathodoluminescence images of Fig. 7) is readily interpreted as indicating an Ordovician magmatic event, the younger age group is more complex, being characterized by a series of 17 analyses straddling concordia between 255 and 220Ma. Moreover, those analyses are probably a mix of different zircons: igneous zircons characterized by Th/U ratios >0.1 and a mean $^{206}Pb/^{238}U$ age of 249.5±2Ma and dark red, high-U, metamict zircons with a Th/U ratio <0.02 and $^{206}Pb/^{238}U$ ages comprised between 243 and 220Ma. These last ages reflect a high-grade event maybe coincident with migmatization, which is responsible for the variable Pb loss in some of the analyzed zircons.

DISCUSSION

The new data presented in this paper on the Chuacús Metamorphic Complex allow a better definition of the tectonothermal events that affected it, as well as its possible paleogeographic settings. Three main events are discussed: 1) Ordovician magmatism, 2) Triassic magmatism and metamorphism and its tectonic implications, and 3) Late Cretaceous magmatism and metamorphism. The autochthonous vs. allochthonous nature of the Chuacús Metamorphic Complex with respect to the Maya Block will be discussed at the end of this chapter.

Ordovician magmatism

Although Grenvillian and other Mesoproterozoic inherited ages are present in most rocks, they are in general overprinted, or reworked by Ordovician magmatism at the southern edge of the Maya Block, as previously reported for the Rabinal-Salamá area of central Guatemala by Ortega-Obregón et al. (2008) who dated S-type granites between 455-462Ma. Ordovician bodies are also present nearby the Chiapas Massif of SE México, where Pompa-Mera et al. (2008) dated an S-type granite at 482±3Ma and an amphibolite at 456±14Ma (U-Pb, single-grain zircons), as well as in the Altos Cuchumatanes, where Solari et al. (2010a) reported an undeformed granite whose crystallization age was dated at 461+6/-3Ma. In Belize the magmatism is mainly Silurian, dated at ~410Ma (Martens et al., 2010). In the northern Sierra de Chuacús Ordovician magmatism is represented by orthogneisses and pegmatitic dikes (samples Gt0341 and Gt03113, respectively), which intrude greenschist facies metasediments belonging either to the San Gabriel unit or the Chuacús Metamorphic Complex (cf. Solari et al., 2009). Bimodal magmatism is widespread in the Acatlán Complex of southern México and associated to rifting of the Rheic Ocean (e.g. Miller et al., 2007; Ortega-Obregón et al., 2009). In northwestern México the Río Fuerte Formation (Late Ordovician) contains magmatic zircons of both Ordovician and Cambrian age (Vega-Granillo et al., 2008). Ordovician magmatism has been documented as well all around the Rheic Ocean realm, generally represented by continental, within-plate tholeiites and as felsic magmas originated by crustal melting of Neoproterozoic and Mesoproterozoic basement (Murphy et al., 2009, 2010, and references therein). Thus, the presence of some Ordovician rocks in the northernmost Chuacús Metamorphic Complex (sample Gt0341), as well as in the nearby Sierra de Las Minas (sample Gt0405) cannot be used as conclusive evidence to establish its autochthony relative to the Maya Block *sensu strictu* (cf. Ortega-Gutiérrez et al., 2007; Ortega-Obregón et al., 2008).

Upper Triassic magmatism and metamorphism

Ordovician magmatism was not recognized in the higher grade central and southern Sierra de Chuacús, where the main magmatic event is Upper Triassic (218-

226Ma, samples Gt0319, Gt0320, Gt0321) and has an arc-like geochemical signature. This magmatic event is also coincident with the tectonothermal event responsible for migmatization in El Chol (sample Gt0332) and Sierra de Las Minas (sample Gt0405). Because remnants of eclogite-facies mafic rocks are present within these deformed migmatites, and are also recognized as deformed lenses nearby the felsic orthogneisses (sample Gt0321, 218Ma) of Agua Caliente River (cf. Ortega-Gutiérrez et al., 2004), we interpret such Upper Triassic ages to be younger than the eclogite-facies metamorphism of the Chuacús Metamorphic Complex. It is interesting to note that none of the S-type Ordovician granites cropping out north of the Sierra de Chuacús (Rabinal-Salamá area), along the Baja Verapaz shear zone of Ortega-Obregón et al. (2008) contain xenoliths of eclogite-facies mafic rocks. This suggests that the eclogite facies metamorphism is constrained between the age of emplacement of the Ordovician granites and the Triassic arc magmas.

Late Cretaceous magmatism and metamorphism

Late Cretaceous metamorphic overprint is present in many of the Chuacús Metamorphic Complex rocks (e.g., Ortega-Gutiérrez et al., 2004, and references therein; Martens et al., 2007; Raschbacher et al., 2009). Some pegmatites were also generated by high-grade metamorphism during the Late Cretaceous, and sample Gt0315 is a clear example of this. Late Cretaceous metamorphism was also reported in the San Gabriel unit (Ortega-Obregón et al., 2008), along the Baja Verapaz Shear Zone, during overthrusting of the Chuacús Metamorphic Complex on top of the southern Maya Block edge. High-pressure metamorphism is also evidenced in several Ar-Ar ages calculated in phengites belonging to the Motagua mélange, which yielded 77-65Ma (Harlow et al., 2004) and were interpreted as the result of the Late Cretaceous collision of the Nicaragua Rise with the southern edge of the Maya Block. Tectonic convergence between the northern Caribbean and the southern North American plates caused subduction of the Chuacús Metamorphic Complex and HP-HT conditions followed by its exhumation, as well as by the northward obduction of El Tambor ophiolites and closure of the Proto-Caribbean Ocean along the paleo Motagua Suture Zone (e.g. Brueckner et al., 2009; see also García-Casco et al., 2008 for correlation with the Antilles).

Allochthony vs. autochthony of the Chuacús Metamorphic Complex with respect to the Maya Block

The Chuacús Metamorphic Complex constitutes the highest-grade metamorphic complex of all Central America. Major faults bound the complex to the north (Baja Verapaz) and south (Motagua fault system), and no similar rocks occur beyond those faults. Although the Chuacús Metamorphic Complex occurs next to typical Maya cover and basement units of pre-Jurassic age, its youngest cover is of Neogene age, and thus, in principle, it should be considered a suspect tectonostratigraphic unit presently located between the Maya and Chortís blocks. At least three points must be considered to further evaluate the allochthonous versus autochthonous nature of the Chuacús Metamorphic Complex with respect to the Maya Block.

The Maya Block north of the Baja Verapaz Shear Zone and, furthermore, north of the Polochic fault, does not record many of the tectonothermal events that have been recognized in the Chuacús Metamorphic Complex. These include HP metamorphism (e.g. Ortega-Gutiérrez et al., 2004; Ratschbacher et al., 2009, and this paper), Triassic magmatism and deformation/migmatization (Ratschbacher et al., 2009, and this paper), and widespread presence of Late Cretaceous, amphibolite facies reworking and magmatism (McBirney, 1963; Ortega-Gutiérrez et al., 2004; Martens et al., 2007; Martens, 2009; Ratschbacher et al., 2009, and this paper).

No other basement outcrop within the Maya Block (Guichicovi, Chiapas Massif, Maya Mountains) shares geological similarities with the Chuacús Metamorphic Complex. For instance the Guichicovi Complex is composed of Grenvillian (1000-1300Ma, Weber and Kohler, 1999) granulites, only affected by Permian intrusions; whereas the Chiapas Massif is made up of high temperature gneisses, intruded by Late Permian granites metamorphosed at 250-254Ma (Weber et al., 2005), and later covered by Jurassic red beds (Blair, 1988). The Maya Mountains are constituted by Silurian plutons, Devonian (and older) strata, covered by Early Devonian volcanics and sedimentary rocks of late Paleozoic age (Martens et al., 2010). None of the aforementioned units contain high pressure rocks. Furthermore the Chuacús Metamorphic Complex is characterized by the absence of Devonian and Permian ages, as well as by the absence of any sedimentary cover older than the Cenozoic.

The voluminous Late Permian granitic magmatism, recently dated by Schaaf et al. (2002) and Weber et al. (2005) in the Chiapas Massif, as well as by Solari et al. (2010a) in the Altos Cuchumatanes, is not represented by detrital zircon ages in any of the more than 500 zircons dated in this work. Furthermore, volcanic units in the Jurassic Todos Santos Formation, cropping out in Chiapas state, and farther to west, in the Cuicateco terrane of southern México, were recently dated by Godínez-Urban et al. (2011) and Pérez-Gutiérrez et al. (2009), respectively, and yet none of the dated samples show the presence of Middle-Upper Triassic zircons,

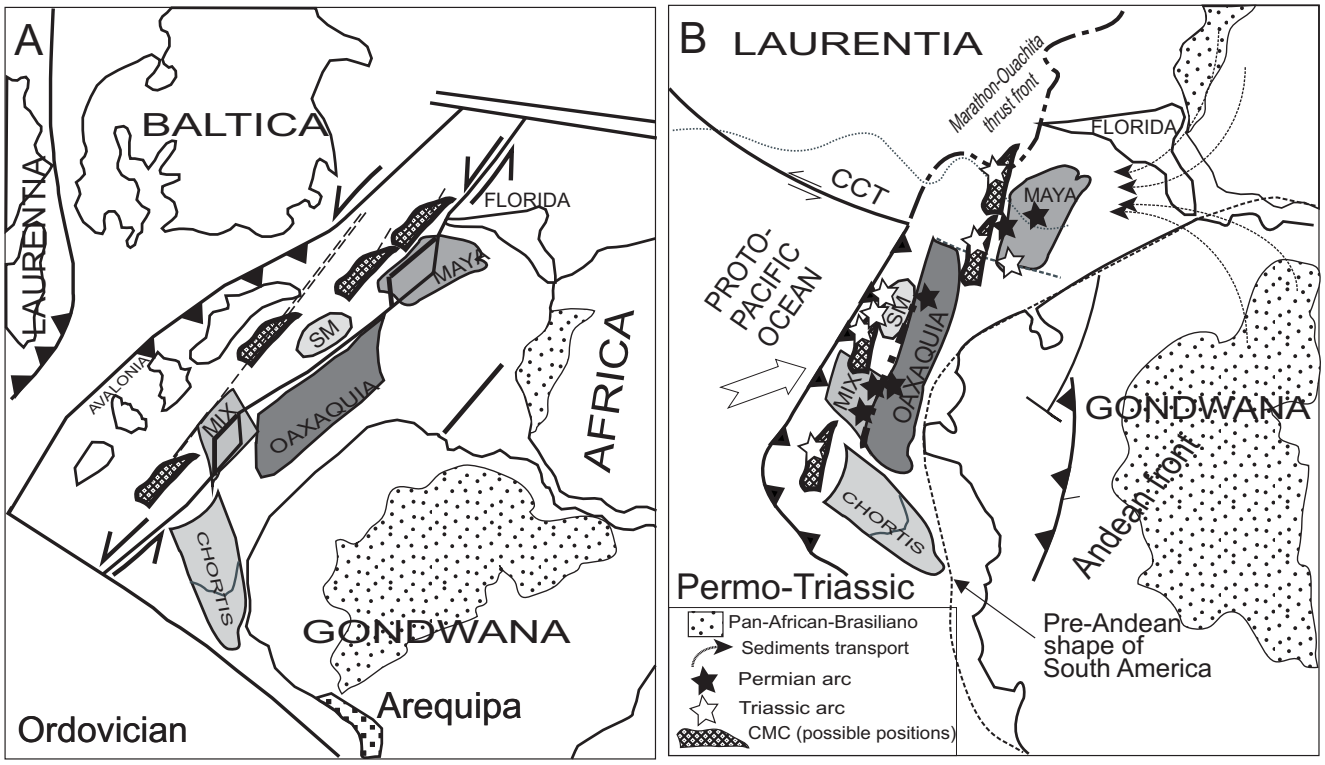

FIGURE 10 | **Paleogeographic models for the Ordovician A) and the Permo-Triassic B) Modified from Dickinson and Lawton (2001), Ortega-Obregón et al. (2008), Nance and Linnemann (2008), Weber et al. (2008), and Solari et al. (in press). MIX: Mixteco terrane; SM: Sierra Madre terrane; CCT: California-Coahuila Transform.**

such as those dated (213-226Ma) in this work. Although these features may not be considered as conclusive and further studies will be needed, they strongly support the allochthony of the Chuacús Metamorphic Complex with respect to the Maya Block.

On the other hand, correlation of the Chuacús Metamorphic Complex with the Chortís Block to the south of the major Guatemalan faults may be also discarded because the Chortís Black lies in on a different plate (the Caribbean plate, which is considered a far traveled unit originated in the Pacific). Moreover basement units in this block that are most proximal to the Chuacús Metamorphic Complex radically differ in fundamental geologic aspects, such as protoliths and contrasting metamorphic conditions (HP/HT in the Chuacús Metamorphic Complex, versus HT/LP in Las Ovejas Complex, or very low grade metamorphism of the pre-Mesozoic San Diego phyllite, Solari et al., 2009; Ratschbacher et al., 2009, and references therein).

Paleozoic-Triassic paleogeographic reconstructions

Paleogeographic reconstructions for the Late Ordovician–Early Silurian and Permo-Carboniferous suggest that the present southern edge of the Maya Block was located adjacent to northeastern México (e.g., Dickinson and Lawton, 2001; Keppie et al., 2006, 2008a; Weber et al., 2008) (Fig. 10A). These interpretations also agree with the Permian paleomagnetic data of Steiner (2005).

In these models, Paleozoic rocks of the Rabinal-Salamá area, just north of our studied area, would have lain close to NE México, north of Oaxaquia and near the Mixteco terrane, where megacrystic granites intruded a passive-margin sedimentary sequence older than ~460Ma (e.g., Nance et al., 2006). Those terranes would have been located close to northwestern Gondwana until the closure of the Rheic Ocean accompanying the amalgamation of Pangea in the late Carboniferous-Permian (e.g., Nance and Linnemann, 2008). The S-type granites cropping out to the north of the studied area could have been produced by partial crustal melting during the Cambro-Ordovician rifting episode coincident with the initial stages of the opening of the Rheic Ocean and the separation of Avalonia from Gondwana (e.g., Murphy et al., 2004).

This suggestion is in agreement with the zipper tectonics model invoked by Martens et al. (2010), which would explain the Silurian-Devonian shifting of magmatism to the Maya Mountains of Belize during subsequent extension related to the opening of the Rheic Ocean. From the Early Pennsylvanian to Permian, the oblique

convergence between Laurentia and Gondwana apparently caused the development of an E-dipping subduction zone with the onset of a new phase of magmatism in the Altos Cuchumatanes (312-317Ma, Solari et al., 2009), and thereafter in northwestern and eastern México (e.g. Torres et al., 1999), the Mixteco terrane (~288Ma, Yañez et al., 1991), the Oaxacan Complex (~275Ma, Solari et al., 2001), and in the Chiapas Massif (~272Ma, Weber et al., 2007).

In this scenario, the Chuacús Metamorphic Complex protoliths could have been deposited in a marginal basin receiving minor input of Ordovician zircons during the Silurian, as demonstrated by their presence in one metasedimentary sample dated by Solari et al. (2009) in the northernmost Sierra de Chuacús (Fig. 10A).

The proposed time constraint on HP metamorphism in the Chuacús Metamorphic Complex (Mid Ordovician to Upper Triassic) is roughly coincident with HP metamorphism reported in the Acatlán Complex of southern México, which was dated as Devonian and was exhumed during the Mississippian (e.g., Keppie et al., 2008). In this view, the Chuacús Metamorphic Complex would have been subducted during the Devonian and metamorphosed at high-grade conditions during the closure of the Rheic Ocean in the late Paleozoic. Exhumation would have taken place causing decompression melting, magmatism and migmatization in the Late Triassic (218-226Ma, Fig. 10B). The Triassic ages in the Chuacús Metamorphic Complex are only slightly younger than those of the Permo-Triassic arc of Chiapas (e.g. Weber et al., 2007), and this can be explained by an easternmost position for the Chuacús Metamorphic Complex in the evolving E-directed, proto-Pacific magmatic arc active since the Permo-Triassic (Fig. 10B).

CONCLUDING REMARKS

The discovery of high-grade metamorphic conditions in the Chuacús Metamorphic Complex of central Guatemala (Ortega-Gutiérrez et al., 2004) has awoken interest and appreciation as a key element for the geologic evolution of the Caribbean region. This contribution presents new geochronologic and geochemical data of some of the most distinctive lithologies of the complex, and provide important constraints to understand this formerly neglected piece of the Caribbean-North America tectonic realm. Indeed, the new results appear to be inconsistent with previous tectonic interpretations that considered the Chuacús Metamorphic Complex to be related to the Chortís-Maya collision, and instead support an independent evolution and an allochthonous provenance. Nevertheless we recognize that further research must be dedicated to address some other important questions that are still poorly understood, or that remained largely unexplored: Among those we can suggest the following:

The existence of ultrahigh pressure metamorphism (UHP) once suggested by (Ortega-Guitérrez et al., 2004) for the Chuacús Metamorphic Complex has yet to be confirmed. Nevertheless, intriguing minerals and peculiar textural features, coupled with thermobarometric calculations that approach such conditions, keep this possibility open for future petrologic work in the eclogitic domains that resisted retrogression inside the high-pressure gneisses.

It is still uncertain if the Chuacús Metamorphic Complex experienced only one eclogite-facies metamorphic event. Although there is clear evidence for a mid-late Paleozoic tectonothermal event, a pervasive Late Triassic magmatism and metamorphism as well as an intense Cretaceous tectonothermal overprint throughout most of the sequence; further and more detailed studies are needed to elucidate the kinematic history of its protracted tectonic evolution. In particular, the structural and kinematic history of the Chuacús Metamorphic Complex has remained almost unattended, despite its basic importance.

Finally, the lithotectonic nature of Chuacús Metamorphic Complex protoliths, as preliminary described in this work, should in the near future be an attractive target to unravel what is, perhaps, the most important question that has not been satisfactorily answered: Where does the Chuacús Metamorphic Complex come from, and which were its connections to the now adjacent Maya and Chortís blocks?

ACKNOWLEDGMENTS

We want to acknowledge several people who contributed to this work: U. Martens and S. Morán-Ical who introduced us to the Sierra de Chuacús and its fascinating rocks; O. Pérez-Arvizu, G. Solís-Pichardo, J.J. Morales, M.S. Hernández-Bernal, P. Schaaf who helped with some of the lab work; B. Martiny who kindly revised the English; and in general, the organizers and participants of the 2007 IGCP 546 excursion in central Guatemala, whose field discussions and suggestions helped to refine some of the models. CONACyT grant 54559 and PAPIIT-DGAPA grant 101407 to LAS covered some of the analytical costs. We also want to acknowledge the thoughtful reviews by U. Martens, V. Valencia and an anonymous reviewer, which greatly helped to improve the manuscript, as well as the editorial handling and suggestions of A. García-Casco.

REFERENCES

Andersen, T., 2002, Correction of common lead in U–Pb analyses that do not report 204Pb. Chemical Geology, 192, 59-79.

Brueckner, H.K., Avé Lallemant, H.G., Sisson, V.B., Harlow, G.E., Hemming, S.R., Martens, U., Tsujimori, T., Sorensen, S.S., 2009. Metamorphic reworking of a high pressure–low temperature mélange along the Motagua fault, Guatemala: A record of Neocomian and Maastrichtian transpressional tectonics. Earth and Planetary Sciences Letters, 284(1-2), 228-235. doi:10.1016/j.epsl.2009.04.032

Carswell, D.A., Wilson, R.N., Zhai, M., 1996. Ultra-high pressure aluminous titanites in carbonate-bearing eclogites at Shuanghe in Dabieshan, central China. Mineralogical Magazine, 60, 461-471.

Dengo, G., 1969. Problems of tectonic relations between Central America and the Caribbean. Transactions Gulf Coast Association Geological Society, 19, 311-320.

Dickinson, W.R., Lawton, T.F., 2001. Carboniferous to Cretaceous assembly and fragmentation of México. Geological Society of America Bulletin, 113(9), 1142-1160.

Foley, S., Tiepolo, M., Vannucci, R., 2002. Growth of early continental crust controlled by melting of amphibolite in subduction zones. Nature, 417, 837-840.

García-Casco, A., Iturralde-Vinent, M.A., Pindell, J., 2008. Latest Cretaceous collision/accretion between the Caribbean Plate and Caribeana: Origin of metamorphic terranes in the Greater Antilles. International Geology Review, 50, 781-809.

Giunta, G., Beccaluva, L., Siena, F., 2006. Caribbean plate margin evolution: constraints and current problems. Geologica Acta, 4(1-2), 265-277.

Godinez-Urbán, A., Lawton, T.F., Molina-Garza, R.S., Iriondo, A., Weber, B., López-Martínez, M., 2011. Jurassic volcanic and sedimentary rocks of the La Silla and Todos Santos Formations, Chiapas: Record of Nazas arc magmatism and rift-basin formation prior to opening of the Gulf of México. Geosphere, 7(1), 1-24.

Gomberg, D.M., Banks, P.O., McBirney, A.R., 1968. Guatemala: preliminary zircon ages from Central cordillera. Science, 162, 121-122.

Harlow, G.E., Hemming, S.R., Avé-Lallemant, H.G., Sisson, V.B., Sorensen, S.S., 2004. Two high-pressure-low temperature serpentinite-matrix mélange belts, Motagua fault zone, Guatemala: A record of Aptian and Maastrichtian collisions. Geology, 32, 17-20.

Hoskin, P.W.O, Schaltegger, U, 2003. The composition of zircon and igneous and metamorphic petrogenesis. Reviews in Mineralogy and Geochemistry, 53(1), 27-62.

Hwang, S.L., Shen, P., Chu, H.T., Yui, T.F., 2000. Nanometer-Size-PbO_2-Type TiO_2 in Garnet: A Thermobarometer for Ultrahigh-Pressure Metamorphism. Science, 288(5464), 321-324.

Irvine, T.N., Baragar, W.R.A., 1971. A guide to the chemical classification of the common volcanic rocks. Canadian Journal of Earth Sciences, 8, 523-548.

Keppie, J.D., Nance, R.D., Fernández-Suárez, J., Storey, C.D., Jeffries, T.E., Murphy, J.B., 2006. Detrital zircon data from the eastern Mixteca Terrane, southern México: evidence for an Ordovician-Mississippian continental rise and a Permo-Triassic clastic wedge adjacent to Oaxaquia. International Geology Review, 48, 97-111.

Keppie, J.D., Dostal, J., Murphy, J.B., Nance, R.D., 2008a. Synthesis and tectonic interpretation of the westernmost Paleozoic Variscan orogen in southern México: From rifted Rheic margin to active Pacific margin. Tectonophysics, 461(1-4), 277-290.

Keppie, J.D., Dostal, J., Miller, B.V., Ramos-Arias, M., Morales-Gámez, M., Nance, R.D., Murphy, J.B., Ortega-Rivera, A., Lee, J.K.W., Housh, T., 2008b. Ordovician–earliest Silurian rift tholeiites in the Acatlán Complex, southern México: Evidence of rifting on the southern margin of the Rheic Ocean. Tectonophysics, 461(1-4), 130-156.

Kesler, S.E., Josey, W.L., Collins, E.M., 1970. Basement rocks of western nuclear Central America: the western Chuacús Group, Guatemala. Geological Society of America Bulletin, 81, 3307-3322.

Langmuir, C., Hanson, G., 1980. An evaluation of major element heterogeneity in the mantle sources of basalts. Philosophical Transactions of the Royal Society London, A297, 383-407.

Lehnert, K., Su, Y., Langmuir, C., Sarbas, B., Nohl, U., 2000. A global geochemical database structure for rocks. Geochemistry Geophysics Geosystems, 1, 1012. doi:10.1029/1999GC000026, www.petdb.org.

Lenze, A., Stöckhert, B., Wirth, R., 2005. Grain scale deformation in ultra-high-pressure metamorphic rocks—an indicator of rapid phase transformation. Earth and Planetary Science Letters, 229, 217-230.

Ludwig, K.L., 2008. Isoplot 3.70. A geochronological toolkit for Microsoft Excel. Berkeley Geochronology Center, 4 (Special Publications), August 26, 1-77.

Ludwig, K.L., Mundil, R., 2002. Extracting reliable U-Pb ages and errors from complex populations of zircons from Phanerozoic tuffs. Davos (Switzerland), 12th Goldschmidt Conference, Journal of Conference Abstracts, A-463.

Manton, W.I., 1996. The Grenville of Honduras. Geological Society of America, Denver, Abstracts with Programs, A-493.

Marshall, D.J., 1988. Cathodoluminescence of geological materials. Boston, Sydney, Wellington, Unwin Hyman, 146pp.

Martens, U., 2009. Geologic evolution of the Maya Block (southern edge of the North American plate): an example of terrane transferral and crustal recycling. Doctoral Thesis. United States of America, Stanford University, 166pp.

Martens, U., Ratschbacher, L., McWilliams, M., 2005. U-Pb geochronology of the Maya Block, Guatemala. American Geophysical Union (AGU), Eos Transactions, Fall Meeting Supplement, 86(52), T51D-1387.

Martens, U., Mattinson, C.G., Wooden, J., Liou, J.G., 2007. Protolith and metamorphic ages of gneiss hosting eclogite in the Chuacús complex, Central Guatemala. American Geophysical Union (AGU), EOS Transactions, 88(23), Joint Assembly Supplement, Abstract, U53A-08.

Martens, U., Weber, B., Valencia, V.A., 2010. U/Pb geochronology of Devonian and older Paleozoic beds in the

southwestern Maya Block, Central America: its affinity with Peri-Gondwanan terranes. Geological Society of America Bulletin, 122, 815-829.

Massonne, H-J., Nasdala, L., 2003. Characterization of an early metamorphic stage through inclusions in zircon of a diamondiferous quartzofeldspathic rock from the Erzgebirge, Germany. American Mineralogist, 88, 883-889.

McBirney, A.R., 1963. Geology of a part of the central Guatemalan cordillera. California University Publications in Geological Sciences, 38, 177-242.

McDonough, W.F., Sun, S.S., 1995. Composition of the Earth. Chemical Geology, 120, 223-253. doi: 10.1016/0009-2541(94)00140-4.

Miller, B.V., Dostal, J., Keppie, J.D., Nance, R.D., Ortega-Rivera, A., Lee, J.W.K., 2007. Ordovician calc-alkaline granitoids in the Acatlán Complex, southern México: geochemical and geochronologic data and implications for tectonics of the Gondwanan margin of the Rheic Ocean. In: Linnemann, U., Nance, R.D., Zulaf, G., Kraft, P. (eds.). The Geology of Peri-Gondwana: The Avalonian-Cadomian Belt, Adjoining Cratons and the Rheic Ocean. Geological Society of America, 423 (Special Paper), 465-475. doi: 10.1130/2007.2423(23).

Murphy, J.B., Fernández-Suárez, J., Keppie, J.D., Jeffries, T.E., 2004. Contiguous rather than discrete Paleozoic histories for the Avalon and Meguma terranes based on detrital zircon data. Geology, 32, 585-588.

Murphy, J.B., Gutiérrez-Alonso, G., Nance, R.D., Fernández-Suárez, J., Keppie, J.D., Quesada, C., Dostal, J., Braid, J.A., 2009. Rheic ocean mafic complexes: overview and synthesis. In: Murphy, J.B., Keppie, J.D., Hynes, A.J. (eds.). Ancient orogens and modern analogues. Geological Society, London, 327 (Special Publications), 343-369.

Murphy, J.B., Keppie, J.D., Nance, R.D., Dostal, J., 2010, Comparative evolution of the Iapetus and Rheic Oceans: A North America perspective. Gondwana Research, 17, 482-499. doi:10.1016/j.gr.2009.08.009

Nance, R.D., Miller, B.V., Keppie, J.D., Murphy, J.B., Dostal, J., 2006. Acatlán Complex, southern México: Record spanning the assembly and breakup of Pangea. Geology, 34(10), 857-860.

Nance, R.D., Linnemann, U., 2008. The Rheic Ocean: Origin, evolution, and significance. GSA Today, 18(12), 4-12.

Ortega-Gutiérrez, F., Solari, L.A., Solé, J., Martens, U., Gómez-Tuena, A., Morán-Ical, S., Reyes-Salas, M., Ortega-Obregón, C., 2004. High Pressure eclogite facies Metamorphism in the Chuacús Complex, Sierra de Chuacús, Central Guatemala: Petrology, Geochronology, and Tectonic implications. International Geology Review, 46, 445-470.

Ortega-Gutiérrez, F., Solari, L.A., Ortega-Obregón, C., Elías-Herrera, M., Morán-Ical, S., Chiquín, M., Keppie, J.D., Torres de León, R., Schaaf, P., 2007. The Maya-Chortís boundary: a tectonostratigraphic approach. International Geology Review, 449, 996-1024.

Ortega-Obregón, C., Solari L.A., Keppie, J.D., Ortega-Gutiérrez, F., Solé, J., Morán-Ical, S., 2008. Middle – Late Ordovician magmatism and Late Cretaceous collision in the southern Maya block, Rabinal - Salamá area, central Guatemala: implications for North America-Caribbean plate tectonics. Geological Society of America Bulletin, 120, 556-570.

Ortega-Obregón, C., Keppie, J.D., Murphy, J.B., Lee, J.K.W., Ortega-Rivera, A., 2009. Geology and geochronology of Paleozoic rocks in western Acatlán Complex, southern México: Evidence for contiguity across an extruded high-pressure belt and constraints on Paleozoic reconstructions. Geological Society of America Bulletin, 121, 1678-1694.

Pérez-Gutiérrez, R., Solari, L.A., Gómez-Tuena, A., Valencia, V.A., 2009. El terreno Cuicateco: ¿una cuenca oceánica con influencia de subducción del Cretácico Superior en el sur de México? Nuevos datos estructurales, geoquímicos y geocronológicos. Revista Mexicana de Ciencias Geológicas, 26, 222-242.

Pindell, J., Kennan, L., Stanek, K.P., Maresch, W.V., Draper, G., 2006. Foundations of Gulf of México and Caribbean evolution: eight controversies resolved. Geologica Acta, 4(1-2), 303-341.

Pindell, J.L., Barret, S.F., 1990. Geological evolution of the Caribbean region; a plate-tectonic perspective. In: Dengo, G., Case, J.E. (eds.). The Geology of North America, The Caribbean Region. Boulder (Colorado), Geological Society of America, II, 405-432.

Pindell, J., Kennan, L., 2009. Tectonic evolution of the Gulf of México, Caribbean and northern South America in the mantle reference frame: an update. In: James, K., Lorente, M.A., Pindell, J. (eds.). The geology and evolution of the Caribbean Plate. Geological Society of London, 328 (Special Publications), 1-55.

Pompa-Mera, V., Schaaf, P., Weber, B., Solís-Pichardo, G., Hernández-Treviño, T., Ortega-Gutiérrez, F., 2008. Devonian-Ordovician Magmatism in Chiapas Massif, Southern Maya Block, México. American Geophysical Union (AGU), Eos Transactions, 89(53), Fall Meeting Supplement, Abstract, V31B-2138.

Ratschbacher, L., Franz, L., Min, M., Bachmenn, R., Martens, U., Stanek, K., Stubner, K., Nelson, B.K., Herrmann, U., Weber, B., López-Martínez, M., Jonckheere, R., Sperner, B., Tichomirowa, M., McWilliams, M.O., Gordon, M., Meschede, M., Bock, P., 2009. The North American–Caribbean plate boundary in México–Guatemala–Honduras. In: James, K.H., Lorente, M.A., Pindell, J.L. (eds.). The origin and Evolution of the Caribbean Plate. Geological Society of London, 328 (Special Publications), 219-293.

Rogers, R.D., Mann, P., Emmet, P.A., 2007. Tectonic terranes of the Chortis block based on integration of regional aeromagnetic and geologic data. In: Mann, P. (ed.). Geologic and tectonic development of the Caribbean plate in northern Central America. Geological Society of America, 428 (Special Paper), 65-88.

Rubatto, D., 2002. Zircon trace element geochemistry: partitioning with garnet and the link between U - Pb ages and metamorphism. Chemical Geology, 184, 123-138.

Schaaf, P., Weber, B., Weis, P., Gross, A., Ortega-Gutiérrez, F., Kohler, H, 2002. The Chiapas Massif (México) revised: new

geologic and isotopic data and basement characteristics. Neues Jahrbuch fur Geologie und Palaontologie Abhandlungen, 225, 1-23.

Schaaf, P., Stimac, J., Siebe, C., Macías, J.L., 2005. Geochemical Evidence for Mantle Origin and Crustal Processes in Volcanic Rocks from Popocatépetl and Surrounding Monogenetic Volcanoes, Central México. Journal of Petrology, 46(6), 1243-1282.

Sedlock, R., Ortega-Gutiérrez, F., Speed, R., 1993. Tectonostratigraphic terranes and tectonic evolution of México. Geological Society of America, 278 (Special Paper), 153.

Sláma, J., Košler, J., Condon, D.J., Crowley, J.L., Gerdes, A., Hanchar, J.M., Horstwood, M.S.A., Morris, G.A., Nasdala, L., Norberg, N., Schaltegger, U., Schoene, B., Tubrett, M.N., Whitehouse, M.J., 2008. Plešovice zircon - A new natural reference material for U-Pb and Hf isotopic microanalysis. Chemical Geology, 249, 1-35.

Solari, L.A., Dostal, J., Ortega-Gutiérrez, F., Keppie, J.D., 2001. The 275 Ma arc-related La Carbonera stock in the northern Oaxacan Complex of southern México: U-Pb geochronology and geochemistry. Revista Mexicana de Ciencias Geológicas, 18(2), 149-161.

Solari, L.A., Torres de León, R., Hernández-Pineda, G., Solé, J., Henández-Treviño, T., Solis, G., 2007. Tectonic significance of Cretaceous Tertiary magmatic and structural evolution of the northern margin of the Xolapa Complex, Tierra Colorada area, southern México. Geological Society of America Bulletin, 119, 1265-1279.

Solari, L.A., Ortega-Gutiérrez, F., Elías-Herrera, M., Schaaf, P., Norman, M., Torres De León, R., Ortega-Obregon, C., Chiquin, M., Morán-Ical, S., 2009. U-Pb zircon geochronology of Paleozoic units in Western and Central Guatemala: insights into the tectonic evolution of Middle America. In: James, K., Lorente, M.A., Pindell, J. (eds.). Origin and evolution of the Caribbean Plate. Geological Society of London, 328 (Special Publications), 293-311.

Solari, L.A., Ortega-Gutiérrez, F., Elías-Herrera, M., Gómez-Tuena, A., Schaaf, P., 2010a. Refining the age of magmatism in the Altos Cuchumatanes, western Guatemala, by LA-ICPMS, and tectonic implications. International Geology Review.

Solari, L.A., Gómez-Tuena, A., Bernal, J.P., Pérez-Arvizu, O., Tanner, M., 2010b. U-Pb zircon geochronology by an integrated LA-ICPMS microanalytical workstation: achievements in precision and accuracy. Geostandards and Geoanalytical Research, 34(1), 5-18.

Staudigel, H., Plank, T., White, B., Schmincke, H.-U., 1996. Geochemical fluxes during seafloor alteration of the basaltic upper oceanic crust: DSDP Sites 417-417. In: Bebout, G., Scholl, D., Kirby, S., Platt, J. (eds.). Subduction Top to Bottom. American Geophysical Union, Washington DC, Geophysical Monograph Series, 19-38.

Steiner, M.B., Walker, J.D., 1996. Late Silurian plutons in Yucatan. Journal of Geophysical Research, 101, 17,727-17,735.

Steiner, M.B., 2005. Pangean reconstruction of the Yucatan Block: Its Permian, Triassic, and Jurassic geologic and tectonic history. In: Anderson, T.H., Nourse, J.A., McKee, J.W., Steiner, M.B. (eds.). The Mojave-Sonora megashear hypothesis: Development, assessment, and alternatives. Geological Society of America, 393 (Special Paper), 457-480. doi: 10.1130/2005.2393(17).

Sun, S.S., McDonough, W.F., 1989. Chemical and isotopic systematics of oceanic basalts: implications for mantle composition and processes. In: Saunders, A.D., Norry, M.J. (eds.). Magmatism in the ocean basins. Geological Society of London, 42 (Special Publications), 313-345.

Tanner, M., Solari, L.A., 2009. Fast reduction of U-Pb data using R. Geochimica et Cosmochimica Acta, 1 (Supplement), 73-13, A1313.

Torres, R., Ruíz, J., Patchett, P.J., Grajales-Nishimura, J.M., 1999. Permo-Triassic continental arc in eastern México; tectonic implications for reconstructions of southern North America. In: Bartolini, C., Wilson, J.L., Lawton, T.F. (eds.). Mesozoic sedimentary and tectonic history of north-central México. Geological Society of America, 340 (Special Paper), 191-196.

Vega-Granillo, R., Talavera-Mendoza, O., Meza-Figueroa, D., Ruiz, J., Gehrels, G.E., López-Martínez, M., De La Cruz-Vargas, J.C., 2007. Pressure-temperature-time evolution of Paleozoic high-pressure rocks of the Acatlán Complex (southern México): Implications for the evolution of the Iapetus and Rheic Oceans. Geological Society of America Bulletin, 119(9), 1249-1264.

Vega-Granillo, R., Salgado-Souto, S., Herrera-Urbina, S., Valencia, V., Ruiz, J., Meza-Figueroa, D., Talavera-Mendoza, O., 2008. U-Pb detrital zircon data of the Rio Fuerte Formation (NW México): Its peri-Gondwanan provenance and exotic nature in relation to southwestern North America. Journal of South American Earth Sciences, 26, 343-354.

Watson, E.B., Wark, D.A., Thomas, J.B., 2006. Crystallization thermometers for zircon and rutile. Contributions to Mineralogy and Petrology, 151, 413-433.

Weber, B., Köhler, H., 1999. Sm-Nd, Rb-Sr and U-Pb geochronology of a Grenville terrane in southern México: origin and geologic history of the Guichicovi Complex. Precambrian Research, 96, 245-262.

Weber, B., Cameron, K., Osorio, M., Schaaf, P., 2005. A Late Permian Tectonothermal Event in Grenville Crust of the Southern Maya Terrane: U-Pb Zircon Ages from the Chiapas Massif, Southeastern México. International Geology Review, 47, 509-529.

Weber, B., Valencia, V.A., Iriondo, A., Ortega-Gutiérrez, F., 2006. Provenance ages of Late Peleozoic sandstones (Santa Rosa Formation) from the Maya block, SE México - implications on the tectonic evolution of western Pangea. Revista Mexicana de Ciencias Geológicas, 23, 262-276.

Weber, B., Iriondo, A., Premo, W.R., Hecht, L., Schaaf, P., 2007. New insights into the history and origin of the southern Maya

block, SE México: U-Pb-SHRIMP zircon geochronology from metamorphic rocks of the Chiapas massif. International Journal of Earth Sciences, 96(2), 253-269.

Weber, B., Valencia, V.A., Schaaf, P., Pompa-Mera, V., Ruiz, J., 2008. Significance of provenance ages from the Chiapas massif Complex (Southeastern México): redefining the Paleozoic basement of the Maya Block and its evolution in a Peri-Gondwanan Realm. The Journal of Geology, 116, 619-639.

Weber, B., Valencia, V.A., Schaaf, P., Ortega-Gutiérrez, F., 2009. Detrital zircon ages from the Lower Santa Rosa Formation, Chiapas: implications on regional Paleozoic stratigraphy. Revista Mexicana de Ciencias Geológicas, 26(1), 260-276.

Yañez, P., Ruíz, J., Patchett, P.J., Ortega-Gutiérrez, F., Gehrels, G., 1991. Isotopic studies of the Acatlan Complex, southern México: Implications for Paleozoic North American tectonics. Geological Society of America Bulletin, 103, 817-828.

Zhang, L.S., Ellis, D.J., Williams, S., Jiang, W., 2003. Ultrahigh-pressure metamorphism in eclogites from the western Tianshan, China-Reply. American Mineralogist, 88(7), 1157-1160.

Manuscript received November 2010;
revision accepted May 2011;
published Online June 2011.

ELECTRONIC APPENDIX

TABLE I | **Trace and REE concentrations of the selected zircons of Figure 9**

Sample number	P	Ti	Y	Nb	La	Ce	Pr	Nd	Sm	Eu	Gd	Tb	Dy	Ho	Er	Yb	Lu	Hf	Th	U	Log(Ti)	T°C
Gt0315, pegmatite																						
14°58'15.49"																						
90°43'29.88"																						
Gt0315 002	6	bdl	250	1.44	0.03	0.49	0.01	0.52	0.38	0.22	3.78	1.6	21	7	31	47	8	15449	0.07	54	bdl	
Gt0315 003	4	13	268	1.56	0.02	0.54	0.04	0.51	0.37	0.28	4.10	1.7	23	8	33	49	8	15998	0.06	57	1.103199066	762
Gt0315 004	70	bdl	1462	13.6	0.06	1.08	0.02	0.45	0.48	0.41	6.43	4.2	88	46	290	778	171	18943	0.14	945	bdl	
Gt0315 005	6	2	245	1.57	bdl	0.44	0.06	0.52	0.27	0.21	3.42	1.5	21	7	32	57	10	16040	0.05	52	0.396018219	632
Gt0315 007	bdl	6	423	2.93	0.04	0.13	0.02	0.40	0.30	0.07	1.21	0.9	23	12	74	167	33	18434	0.02	168	0.763894393	695
Gt0315 008	93	2	1078	4.53	0.02	0.49	0.04	0.49	0.27	0.24	4.43	2.8	61	33	213	594	131	18351	0.11	688	0.211118804	603
Gt0315 009	4	bdl	235	1.32	0.03	0.14	0.04	0.36	0.21	0.05	1.00	0.6	13	7	38	82	16	17691	0.01	33	bdl	
Gt0315 010	73	18	562	4.12	0.02	10.6	0.10	1.48	2.20	0.23	10.8	3.7	49	19	94	211	42	13183	71	189	1.243679001	793
Gt0315 011	47	25	502	4.52	0.03	8.95	0.07	1.48	2.11	0.16	10.0	3.4	45	17	83	189	37	13579	13	121	1.389978264	827
Gt0315 013	bdl	3	829	7.94	0.04	0.11	0.03	0.39	0.19	0.08	1.57	1.4	36	24	163	431	89	20941	0.01	82	0.521366919	653
Gt0315 014	80	19	690	4.16	0.02	9.18	0.15	1.81	2.48	0.25	13.9	4.6	61	23	116	259	51	13735	29	88	1.271995867	799
Gt0315 015	119	10	1600	6.39	0.04	13.9	0.23	3.71	6.98	0.53	36	11.9	151	54	259	538	103	13842	60	100	0.984846748	738
Gt0315 016	114	10	798	8.00	0.04	12.8	0.12	2.00	3.01	0.24	15.3	5.4	72	27	133	295	58	13892	36	76	1.010989262	743
Gt0315 017	13	3	275	1.74	0.03	0.41	0.03	0.47	0.24	0.11	1.98	1.1	19	8	46	111	24	16572	0.02	59	0.454141414	641
Gt0315 018	62	23	565	5.80	0.06	12.5	0.08	1.24	2.00	0.16	9.50	3.3	48	18	98	232	47	15266	257	1009	1.360248977	820
Gt0315 019	107	14	732	2.56	7.98	30	1.87	7.77	3.65	0.61	16.8	5.4	69	25	119	229	43	11723	86	191	1.151753091	773
Gt0315 020	67	7	657	3.78	0.03	8.78	0.10	1.91	2.86	0.25	14.2	4.6	62	23	112	235	44	13904	3.05	30	0.843004284	710
Gt0315 021	18	2	215	1.08	bdl	0.18	0.03	0.46	0.28	0.10	1.42	0.7	12	6	37	85	17	17363	0.02	45	0.339636339	623
Gt0315 022	93	20	462	4.14	0.04	8.61	0.08	1.40	1.95	0.16	9.18	3.2	43	16	79	182	35	14119	21	90	1.291892951	804
Gt0315 023	72	19	575	5.46	0.03	9.68	0.11	1.44	2.19	0.17	10.2	3.7	49	19	96	233	47	14421	151	397	1.286472869	802
Gt0315 024	123	25	1618	6.39	0.03	13.9	0.15	3.03	6.40	0.48	33	11.0	144	52	259	566	111	14055	392	706	1.405922792	830
Gt0315 025	48	24	562	5.65	0.02	12.0	0.08	1.37	1.97	0.15	9.58	3.6	48	18	95	228	46	13917	285	901	1.381290362	824
Gt0315 026	73	bdl	162	3.43	0.03	1.74	0.06	0.44	0.41	0.05	1.77	0.7	11	5	31	96	21	15183	34	390	bdl	
Gt0315 027	72	24	706	5.75	0.02	11.4	0.10	1.63	2.33	0.16	12.8	4.5	60	23	118	277	55	14155	302	901	1.379728486	824
Gt0315 028	100	13	966	5.16	0.03	15.3	0.12	1.80	3.04	0.28	19.4	6.5	85	32	157	310	59	13086	199	469	1.114091374	765
Gt0315 029	127	28	1390	2.22	0.03	15.9	0.43	6.82	10.3	1.79	45	12.9	149	48	213	355	65	10947	115	186	1.440732925	839
Gt0315 030	99	16	639	2.54	0.05	13.8	0.09	1.80	2.82	0.39	13.9	4.6	61	22	103	202	39	11737	71	169	1.199154779	783
Gt0319, deformed diorite																						
14°57'56.9"																						
90°32'49"																						
Gt0319 001	88	20	1651	2.06	0.05	30	0.32	4.05	6.05	2.45	30	10	139	52	271	568	112	9578	221	204	1.295550897	805
Gt0319 003	58	bdl	724	1.29	0.01	12	0.17	2.02	2.69	1.18	12	4	58	23	124	304	68	10035	184	203	bdl	
Gt0319 004	32	8.95	649	1.19	0.01	14	0.06	1.02	1.55	0.77	9	3	47	19	108	284	67	12442	165	238	0.951763132	731
Gt0319 005	64	bdl	896	2.00	0.06	18	0.33	3.47	4.32	2.13	16	5	68	27	147	371	83	8458	282	234	bdl	
Gt0319 006	173	bdl	2516	5.77	0.19	50	0.72	8.84	11.16	6.19	49	16	206	76	397	924	192	7752	991	549	bdl	
Gt0319 007	185	10	2039	3.63	0.19	31	0.74	10.39	12.52	6.06	47	14	176	64	322	709	146	6812	316	184	0.982921036	738
Gt0319 008	64	1.19	456	1.02	0.02	9.38	0.09	1.34	1.31	0.62	5.87	2.16	30	13	78	226	55	8655	79	99	0.077303038	583
Gt0319 009	48	bdl	190	0.62	0.01	4.06	0.05	0.82	0.63	0.26	2.49	0.85	13	6	35	113	29	8004	15	39	bdl	
Gt0319 010	148	4.53	1996	4.27	0.13	40	0.64	8.63	11.09	4.89	42	13	171	62	318	710	149	7812	470	280	0.656560103	676
Gt0319 011	62	3.28	542	1.00	0.03	9.71	0.24	2.65	2.63	1.13	10	3	42	16	88	229	51	7199	72	69	0.515478469	652
Gt0319 012	69	bdl	491	1.13	0.00	10.4	0.06	1.15	1.50	0.69	8	3	37	15	83	205	45	10755	95	113	bdl	
Gt0319 014	16	5.65	239	1.08	bld	6.56	0.03	0.64	0.54	0.22	2	0.98	15	7	43	134	32	11627	31	87	0.752050631	693
Gt0319 015	19	bdl	663	1.08	0.03	11.7	0.09	1.57	2.35	1.08	12	4	54	21	111	252	54	10338	193	204	bdl	
Gt0319 016	42	17	817	2.09	0.03	14.8	0.14	1.85	2.24	0.97	12	4	64	25	140	338	73	9560	247	294	1.240889137	792
Gt0319 017	104	8.82	1053	2.67	0.10	25	0.35	4.36	4.67	2.32	19	6	82	32	171	429	93	8463	344	259	0.945369276	730
Gt0319 018	34	6.60	526	1.14	0.02	8.97	0.06	1.23	1.38	0.70	7	3	37	16	90	243	61	10957	128	232	0.819354015	706
Gt0319 019	24	bdl	470	1.07	0.04	9.01	0.05	1.13	1.47	0.76	7	3	35	15	80	206	47	10977	131	169	bdl	
Gt0319 021	93	bdl	831	2.18	0.08	19.6	0.23	2.33	2.83	1.42	11	4	58	24	141	389	89	8269	250	247	bdl	
Gt0319 022	30	bdl	41	0.46	0.01	1.54	0.04	0.49	0.24	0.03	0.34	0.12	2.03	1.14	8	36	11	11556	3	43	bdl	
Gt0319 023	124	7.05	2233	3.61	0.07	59	0.38	5.26	8.38	3.52	44	15	196	72	362	690	133	10077	506	293	0.84829666	711
Gt0319 024	161	32	2044	3.03	0.04	20	0.40	5.39	7.70	3.13	40	14	182	68	334	651	128	8495	119	103	1.498371018	853

DOI: 10.1344/105.000001695

TABLE I | **Continued**

Sample number	P	Ti	Y	Nb	La	Ce	Pr	Nd	Sm	Eu	Gd	Tb	Dy	Ho	Er	Yb	Lu	Hf	Th	U	Log(Ti)	T°C
Gt0319 025	192	7.65	839	2.13	0.00	11.3	0.08	1.30	2.07	0.90	12	4	65	26	144	322	66	8386	28	44	0.883559191	718
Gt0319 026	150	8.93	1784	3.77	0.15	23	0.49	5.12	7.14	3.91	35	11	144	54	284	686	147	7112	463	292	0.950930639	731
Gt0319 027	115	bdl	572	1.53	0.00	11.4	0.05	0.90	1.27	0.48	7	3	41	18	103	267	61	10293	145	228	bdl	
Gt0319 028	16	5.80	125	1.03	0.03	6	0.05	0.58	0.24	0.10	1.27	0.49	8	4	23	71	18	11740	80	207	0.763214558	695
Gt0319 029	103	5.66	1616	3.09	0.08	16	0.25	3.78	5.26	2.42	30	10	140	53	265	535	106	8024	86	81	0.752565659	693
Gt0319 030	187	8.87	2536	9.27	0.02	38	0.28	3.94	6.79	2.55	37	14	200	82	435	907	182	8523	164	170	0.947703735	730
Gt0319 031	63	bdl	1014	2.01	0.05	16	0.19	2.72	3.30	1.07	19	7	88	33	172	362	74	9949	188	185	bdl	
Gt0319 033	146	1.42	1077	2.32	0.03	26	0.12	1.72	2.55	1.17	14	6	82	33	186	428	90	9270	166	180	0.153732124	594
Gt0319 034	87	6.10	899	2.27	0.08	16	0.21	2.43	3.42	1.84	16	5	69	27	145	384	83	7580	225	174	0.785504443	699
Gt0319 037	99	bdl	1379	1.87	0.04	15	0.23	3.72	5.82	2.40	28	9	123	45	228	448	87	8719	66	63	bdl	
Gt0319 038	72	bdl	873	1.45	0.07	16	0.29	3.67	3.44	1.70	16	5.29	69	26	140	350	75	8042	188	175	bdl	
Gt0319 039	37	3.59	951	1.65	0.02	18	0.20	2.45	3.34	1.85	16	5.33	75	29	162	401	90	10617	323	322	0.55558113	658
Gt0319 040	42	3.87	351	0.87	0.06	7.1	0.09	1.31	1.07	0.55	5	1.74	25	10	60	172	41	8855	51	72	0.588209591	664
Gt0319 041	49	11	675	1.24	0.07	13	0.29	3.30	3.43	1.43	13	4.08	54	20	110	274	59	7633	119	110	1.02155217	745
Gt0319 042	10	bdl	180	0.70	0.02	4.52	0.05	0.67	0.40	0.18	1.74	0.70	11	5	32	93	24	12253	56	97	bdl	
Gt0319 043	88	340	956	1.43	0.07	8.23	0.26	2.91	3.82	2.01	19	6	80	30	154	344	74	6633	151	135	2.530947298	1187
Gt0319 044	68	9.48	1212	2.43	0.10	21.17	0.37	4.23	5.24	2.70	22	7	98	37	196	468	100	7581	273	214	0.976713284	736
Gt0319 045	100	bdl	1766	2.24	0.05	16.44	0.33	5.41	7.75	2.83	36	12	159	58	289	560	109	7963	91	82	bdl	
Gt0319 046	120	5.43	1861	3.47	0.13	34	0.55	6.65	8.35	3.83	37	12	155	57	298	682	139	7454	407	294	0.734849388	690
Gt0319 047	48	bdl	805	1.73	0.07	12.89	0.21	2.73	2.92	1.51	14	5	63	25	131	328	71	9237	217	170	bdl	
Gt0319 048	68	12	462	1.27	0.03	8.93	0.14	1.64	1.58	0.63	6	2.31	33	14	78	207	47	7612	63	68	1.069009689	755
Gt0319 049	47	bdl	437	0.94	0.05	8.64	0.07	1.14	1.25	0.63	6	2.13	32	13	78	215	50	9933	86	126	bdl	
Gt0319 050	172	1.40	2148	2.90	0.07	17.49	0.43	6.03	9.02	3.56	44	15	198	72	358	669	132	7801	124	93	0.147002165	593
Gt0319 051	203	bdl	1407	3.88	0.03	30	0.17	2.47	3.28	1.68	18	7	103	43	241	591	126	7712	322	292	bdl	
Gt0319 053	20	bdl	180	0.75	0.05	4.27	0.06	0.76	0.71	0.28	3	0.95	13	5	32	93	23	9607	53	70	bdl	
Gt0319 054	123	6.16	1707	3.91	0.15	31	0.49	6.35	8.40	4.12	35	11	141	52	271	645	135	7897	497	305	0.789745011	700
Gt0319 055	36	5.10	1010	1.76	0.08	17	0.30	3.31	3.59	1.69	17	6	78	31	166	395	91	8902	279	248	0.707723998	685
Gt0319 056	81	bdl	1366	1.68	0.10	13	0.35	3.89	5.38	2.66	26	9	115	43	221	509	108	7901	263	228	bdl	
Gt0319 057	68	bdl	1276	1.30	0.01	22	0.20	3.12	4.49	2.10	23	8	108	42	209	436	89	10451	201	198	bdl	
Gt0319 058	23	bdl	525	1.09	0.06	11.28	0.06	0.86	1.43	0.79	9	2.96	41	17	90	217	48	11704	110	144	bdl	
Gt0319 059	134	7.97	2173	4.47	0.10	39	0.56	6.19	8.28	4.46	43	14	184	68	350	762	153	9058	560	410	0.901251809	721
Gt0319 060	80	10	766	1.42	0.10	12.2	0.37	3.79	3.81	1.95	15	5	62	23	127	311	67	7068	103	86	1.000299154	741
Gt0320, deformed gabbro																						
14°57'56.9"																						
90°32'49"																						
Gt0320 001	524	7.70	1756	2.98	0.06	19.27	0.36	4.92	7.50	3.38	39.02	12.09	158	58	271	595	107	7433	349	268	0.886218314	718
Gt0320 002	578	9.91	1391	2.28	0.14	16.54	0.37	4.41	5.79	2.84	30.80	9.47	121	45	212	468	88	7353	249	204	0.995998407	740
Gt0320 003	412	10.50	1117	6.45	0.05	23.12	0.14	1.81	1.92	1.12	12.64	4.88	75	34	192	517	103	11243	270	404	1.021189916	745
Gt0320 006	41	bdl	130	0.58	0.03	4.02	0.07	1.29	0.62	0.12	1.62	0.53	8	4	23	78	19	10373	31	58	bdl	
Gt0320 008	315	7.87	431	1.46	0.08	10.72	0.13	1.21	1.19	0.63	6.33	2.29	33	13	71	186	37	10434	44	60	0.896249179	720
Gt0320 009	564	0.64	1639	2.63	0.13	24.07	0.43	6.08	8.41	3.68	36.95	11.59	143	53	248	502	90	7519	256	199	-0.19603029	546
Gt0320 010	849	7.80	2218	4.46	0.11	35.60	0.57	7.05	10.23	4.47	49.97	15.72	197	71	336	680	124	6935	398	295	0.892123547	720
Gt0320 011	554	0.86	1924	2.97	bdl	24.32	0.39	6.18	8.62	3.40	43.31	13.33	173	62	295	562	100	9388	167	140	-0.0659347	563
Gt0320 012	664	1.28	2326	3.96	0.08	28.89	0.46	7.74	9.35	3.81	50.07	16.17	205	76	358	697	121	9447	224	181	0.105606177	587
Gt0320 013	247	7.39	664	2.66	0.07	11.49	0.10	1.57	1.69	0.73	8.43	3.16	45	20	114	308	66	8907	100	155	0.868745364	715
Gt0320 014	460	bdl	689	2.58	0.02	11.42	0.12	1.48	1.86	0.73	8.11	3.07	47	21	116	314	66	8476	95	140	bdl	
Gt0320 016	770	11.66	2478	4.17	0.06	29.20	0.44	6.10	8.63	3.82	47.82	16.43	214	82	382	774	133	8700	378	289	1.066725496	755
Gt0320 018	158	2.22	402	1.85	0.02	9.51	0.10	1.63	1.30	0.55	6.66	2.21	31	13	68	186	37	9413	41	88	0.346833695	624
Gt0320 020	967	3.30	1477	7.11	0.00	27.02	0.08	1.67	2.90	1.13	19.37	7.13	108	47	246	622	117	12343	193	281	0.517857267	652
Gt0320 021	244	5.77	1061	2.04	0.05	13.79	0.22	3.47	4.52	2.13	22.08	6.91	90	35	171	399	74	9554	209	194	0.761329923	695
Gt0320 022	196	bdl	414	0.88	bdl	5.69	0.15	1.79	1.55	0.51	6.28	1.99	31	13	75	235	49	10468	85	178	bdl	
Gt0320 023	356	6.06	637	2.92	0.03	10.94	0.13	1.70	1.75	0.81	8.79	3.15	46	20	108	295	59	9583	119	191	0.782565847	699
Gt0320 025	250	0.51	610	1.14	0.05	9.70	0.13	2.10	2.27	1.10	11.99	3.73	49	20	96	233	45	9216	123	135	-0.293224655	533
Gt0320 026	480	14.25	654	2.45	0.07	13.08	0.15	1.90	2.17	0.86	10.33	3.55	50	21	111	282	55	9652	130	185	1.153810115	773
Gt0320 027	378	bdl	852	2.11	0.11	16.75	0.38	4.55	4.89	2.26	20.44	6.40	78	28	131	287	50	7860	192	150	bdl	
Gt0320 028	818	4.08	1164	2.71	0.07	17.81	0.19	2.58	3.85	1.57	19.84	6.85	93	37	187	432	79	7164	121	131	0.610500573	668
Gt0320 029	149	10.04	216	0.84	0.07	4.98	0.08	1.32	1.05	0.44	4.54	1.45	19	7	35	82	15	7640	53	66	1.001905299	741

DOI: 10.1344/105.000001695

TABLE I | **Continued**

Sample number	P	Ti	Y	Nb	La	Ce	Pr	Nd	Sm	Eu	Gd	Tb	Dy	Ho	Er	Yb	Lu	Hf	Th	U	Log(Ti)	T°C
Gt0320 030	130	bdl	296	0.76	0.03	5.94	0.10	1.10	1.11	0.63	5.54	1.83	25	10	48	113	21	7954	88	99	bdl	
Gt0320 032	369	6.90	962	2.18	0.09	15.65	0.31	3.83	4.89	2.23	20.47	6.42	84	30	149	350	64	7961	162	139	0.839158302	709
Gt0320 033	327	2.09	676	1.16	0.06	9.26	0.21	2.50	2.85	1.39	12.38	4.22	54	21	110	282	55	8407	103	117	0.320630029	620
Gt0320 034	441	4.23	517	2.13	0.07	11.16	0.10	1.31	1.44	0.56	7.15	2.44	38	16	88	246	49	8373	74	160	0.62597851	671
Gt0320 035	187	7.00	378	1.32	0.02	6.34	0.11	1.59	1.64	0.65	6.50	2.15	31	12	64	177	35	8130	51	79	0.844869035	711
Gt0320 036	388	6.88	947	2.37	0.02	14.36	0.21	3.02	2.89	1.58	14.34	5.33	73	30	160	413	86	10503	330	382	0.837443497	709
Gt0320 037	547	1.79	472	1.22	0.01	8.24	0.10	1.26	1.31	0.74	6.46	2.42	36	15	80	227	47	9303	103	148	0.25242783	609
Gt0320 038	1052	6.33	3483	7.64	0.22	57.42	0.82	11.28	15.94	6.87	83.92	25.90	326	116	531	1047	178	8457	534	323	0.801597915	702
Gt0320 039	543	7.70	1409	2.73	bdl	24.79	0.18	2.36	3.92	1.86	25.42	8.70	118	47	233	526	97	13112	464	450	0.886220897	718
Gt0320 040	443	bdl	1673	3.36	0.04	24.84	0.21	3.26	5.84	2.67	31.32	10.66	145	55	271	604	111	12329	539	464	bdl	
Gt0320 041	383	3.29	639	3.20	0.00	16.22	0.09	1.23	1.52	0.72	8.09	2.96	44	20	112	311	63	12069	234	359	0.517786085	652
Gt0320 042	430	2.58	1199	3.03	0.09	16.41	0.31	4.11	5.22	2.61	27.54	8.27	107	39	186	421	73	7530	293	216	0.411205829	634
Gt0320 043	748	2.08	1260	3.66	0.00	20.40	0.15	2.18	3.44	1.49	17.83	6.89	98	41	213	552	106	10944	328	371	0.318707321	620
Gt0320 044	471	5.72	811	1.50	0.04	9.71	0.23	2.84	3.51	1.58	16.81	5.55	72	27	129	295	53	7938	119	122	0.757695036	694
Gt0321, Agua Caliente River felsic orthogneiss																						
14°56'07.8"																						
90°30'10.9"																						
Gt0321 006	-	5.5	2375	-	0.07	58	-	-	5.5	1.33	-	-	183	-	-	-	175	12389	226	440	0.743273313	692
Gt0321 007	-	7.6	1082	-	0.44	37	-	-	3.0	0.91	-	-	82	-	-	-	87	12656	98	182	0.882269836	718
Gt0321 009	-	bdl	881	-	0.01	32	-	-	2.4	0.57	-	-	71	-	-	-	67	12170	47	75	bdl	
Gt0321 010	-	0.85	1609	-	0.05	49	-	-	2.5	0.56	-	-	95	-	-	-	187	15203	753	955	-0.072605499	562
Gt0321 013	-	5.6	2491	-	0.06	61	-	-	7.1	1.79	-	-	202	-	-	-	146	12472	159	197	0.74612956	692
Gt0321 016	-	10	2500	-	0.10	59	-	-	7.4	1.84	-	-	203	-	-	-	159	10133	176	168	1.00441451	742
Gt0321 019	-	5.4	1800	-	0.11	51	-	-	3.9	1.02	-	-	135	-	-	-	139	12884	189	266	0.729411984	689
Gt0321 020	-	1.1	1967	-	0.06	62	-	-	3.8	0.89	-	-	152	-	-	-	155	14318	594	649	0.033785807	577
Gt0321 021	-	7.4	4358	-	1.3	113	-	-	12	2.86	-	-	356	-	-	-	269	12918	694	774	0.867115224	715
Gt0321 022	-	9.9	1416	-	0.05	57	-	-	3.1	1.0	-	-	112	-	-	-	105	12360	183	221	0.994758068	740
Gt0321 027	-	13	2666	-	39	153	-	-	26	8.12	-	-	217	-	-	-	185	10969	172	220	1.116793241	765
Gt0321 030	-	7.2	580	-	0.11	21	-	-	1.2	0.36	-	-	45	-	-	-	52	13687	53	92	0.857475871	713
Gt0321 033	-	8.0	1392	-	0.54	38	-	-	3.2	0.42	-	-	108	-	-	-	118	15678	307	474	0.900545554	721
Gt0321 034	-	4.1	1464	-	0.24	32	-	-	4.3	0.77	-	-	120	-	-	-	96	14191	156	386	0.617962445	669
Gt0321 037	-	3.6	1478	-	1.7	61	-	-	5.5	1.65	-	-	119	-	-	-	101	12309	204	206	0.5559389	658
Gt0321 044	-	7.1	1816	-	0.05	60	-	-	2.6	0.71	-	-	106	-	-	-	215	15017	986	1181	0.849242039	711
Gt0321 045	-	2.7	1734	-	3.7	84	-	-	4.2	1.07	-	-	126	-	-	-	148	11944	522	505	0.429099049	637
Gt0321 048	-	8.1	3083	-	0.30	59	-	-	11	3.48	-	-	260	-	-	-	197	11192	206	208	0.910885653	723
Gt0321 049	-	4.1	928	-	0.04	38	-	-	2.5	0.70	-	-	74	-	-	-	76	14300	120	189	0.611383906	668
Gt0321 051	-	5.8	1334	-	0.03	46	-	-	2.4	0.65	-	-	93	-	-	-	124	13930	378	460	0.761619418	695
Gt0321 052	-	11	2001	-	3.0	81	-	-	6.9	2.47	-	-	151	-	-	-	168	9694	221	298	1.038444237	749
Gt0321 055	-	6.6	2022	-	0.08	81	-	-	3.9	0.92	-	-	138	-	-	-	189	13765	764	777	0.817890144	705
Gt0321 056	-	bdl	2346	-	0.10	69	-	-	3.9	0.69	-	-	176	-	-	-	187	13721	330	499	bdl	
Gt0321 057	-	bdl	1594	-	19	95	-	-	5.2	1.05	-	-	110	-	-	-	146	13885	799	725	bdl	
Gt0321 058	-	bdl	1720	-	16	92	-	-	11	2.96	-	-	120	-	-	-	165	14579	517	660	bdl	
Gt0321 060	-	8.9	1279	-	8.3	63	-	-	4.6	0.97	-	-	102	-	-	-	99	13504	159	229	0.951678187	731
Gt0321 061	-	5.5	1180	-	0.14	34	-	-	3.7	0.43	-	-	101	-	-	-	81	14964	105	238	0.741255368	691
Gt0321 062	-	13.9	2190	-	7.2	93	-	-	5.8	1.46	-	-	134	-	-	-	210	14194	1619	1339	1.143553907	771
Gt0321 064	-	4.7	657	-	12.9	58	-	-	16	6.65	-	-	60	-	-	-	54	15921	55	187	0.670117775	678
Gt0332, El Chol migmatite leucosome																						
14°57'53.6"																						
90°29'12.5"																						
Gt0332 001	83	bdl	1914	3	0.05	11	0.09	1.6	3.2	1.8	29	11	158	64	318	697	140	13353	20	204	bdl	
Gt0332 002	4	22	2081	2	0.11	10	0.21	3.6	7.2	3.6	44	15	182	69	323	657	141	11779	20	195	1.337857028	814
Gt0332 004	49	6	573	3	0.05	11	0.14	2.4	3.1	0.29	13	4.1	50	19	93	210	42	15460	77	382	0.775688502	698
Gt0332 005	86	9	807	5	0.02	11	0.15	2.1	2.7	0.48	15	5.4	73	28	133	277	50	13974	7.3	133	0.941255496	729
Gt0332 006	20	bdl	2297	13	0.03	3.7	0.08	1.0	1.4	0.63	14	7.8	147	72	403	1005	199	17048	5.2	392	bdl	
Gt0332 007	bdl	bdl	412	1.4	0.06	1.3	0.06	0.89	0.64	0.21	4	1.6	24	12	72	225	63	16311	1.6	132	bdl	
Gt0332 008	116	bld	1620	4.6	0.20	13	0.24	3.0	4.2	0.32	27	10	136	54	258	499	90	13121	135	460	bdl	

DOI: 10.1344/105.000001695

TABLE I | **Continued**

Sample number	P	Ti	Y	Nb	La	Ce	Pr	Nd	Sm	Eu	Gd	Tb	Dy	Ho	Er	Yb	Lu	Hf	Th	U	Log(Ti)	T°C
Gt0332 009	144	13	3548	55	0.06	1.8	0.09	1.2	1.0	0.60	15	10	210	109	624	1536	314	23711	5.1	1465	1.111469047	764
Gt0332 011	176	6	1204	3.8	0.14	12	0.29	4.0	6.6	0.50	30	10	119	43	184	326	58	13412	21	107	0.776792954	698
Gt0332 012	83	8	2772	8.6	0.04	17	0.16	3.3	8.2	3.5	60	20	255	95	438	896	166	16607	106	562	0.882341149	718
Gt0332 013	88	bld	761	4.2	0.08	8.8	0.13	1.9	2.9	0.25	15	5.4	69	26	123	247	45	13655	50	176	bdl	
Gt0332 014	77	bld	1918	20	0.04	4.6	0.07	1.4	1.5	0.41	13	7.1	126	62	342	822	171	18907	17	462	bdl	
Gt0332 015	62	15	537	3.7	0.07	24	0.14	2.6	3.1	0.52	13	4.2	53	19	87	167	32	13272	37	67	1.184900596	780
Gt0332 016	20	2	461	4.6	0.06	22	0.25	4.5	7.0	1.0	28	6.8	65	17	58	65	10	14261	16	77	0.298330495	616
Gt0332 017	80	bdl	1390	3.1	0.04	5.0	0.05	0.93	1.1	0.46	10	5.4	95	46	262	667	131	16816	11	369	bdl	
Gt0332 018	50	bdl	358	1.9	0.08	1.4	0.08	0.91	0.5	0.13	2	1.2	22	12	70	199	45	16861	1.6	108	bdl	
Gt0332 020	21	17	760	3.6	0.06	4.9	0.06	1.2	1.3	0.44	8	3.4	54	24	132	347	77	15350	25	440	1.223226465	788
Gt0332 021	65	3.1	756	3.2	0.02	10	0.11	1.8	2.5	0.21	14	5.1	67	27	125	264	50	13618	54	237	0.496733833	648
Gt0332 022	9.1	6.5	323	1.9	0.04	0.7	0.06	0.85	0.33	0.10	2	1.0	19	10	64	218	56	18353	1.3	125	0.81329298	705
Gt0332 023	42	bdl	1488	5.5	bdl	6.0	0.07	1.0	1.2	0.5	12	5.9	103	48	261	652	131	16780	24	307	bdl	
Gt0332 024	bdl	bdl	413	1.5	0.04	1.3	0.08	0.79	0.54	0.20	3	1.4	25	13	73	222	63	17270	1.7	136	bdl	
Gt0332 025	125	1.0	1802	3.1	bdl	18	0.10	2.2	5.7	1.8	44	16	193	64	270	524	93	18142	44	453	0.016169753	575
Gt0332 026	125	8.0	891	4.5	0.02	31	0.15	2.8	4.6	0.4	24	8.0	97	34	146	238	40	14652	25	96	0.903888331	722
Gt0332 027	123	1.8	814	3.9	0.03	33	0.23	3.2	4.6	0.4	21	6.6	81	29	132	251	47	14014	77	68	0.265789719	611
Gt0332 028	153	11	1609	7.1	0.07	13	0.39	6.7	10	0.9	46	14	168	59	254	451	79	13858	117	361	1.04310827	750
Gt0332 029	156	9.1	2157	8.5	0.03	28	0.13	2.6	7.9	2.7	71	25	271	76	266	372	54	19179	244	696	0.959636191	733
Gt0332 030	73	18	256	1.5	0.04	8	0.13	2.1	2.6	0.7	10	2.9	31	9.1	33	47	7.3	12003	0.50	7.1	1.253629001	795
Gt0332 031	106	6.2	686	2.0	0.06	45	0.23	3.2	4.6	0.8	20	5.5	67	24	106	199	37	13144	115	111	0.789716169	700
Gt0332 033	91	5.3	819	3.0	0.07	11	0.12	2.4	4.0	0.7	21	6.8	84	30	129	230	40	13460	24	96	0.728288268	689
Gt0332 034	967	39	7108	24	4.6	34	2.2	15	11	4.2	63	30	493	223	1266	3611	696	33329	44	4137	1.59212312	877
Gt0332 035	118	14	778	8.8	0.01	30	0.18	3.1	4.7	0.5	22	6.8	79	28	124	219	40	15717	108	290	1.157080809	774
Gt0332 036	2929	17	1878	11	3.8	39	2.9	23	14	1.9	50	14	177	67	306	533	95	13870	195	438	1.232525512	790
Gt0332 037	56	bdl	302	1.2	0.09	21	0.20	2.8	3.2	0.7	10	2.7	31	11	48	96	18	11363	17	18	bdl	
Gt0332 038	4754	5.0	635	1.2	0.53	33	2.3	28	17	5.0	38	7.8	74	23	93	154	27	10533	47	38	0.694706402	683
Gt0332 039	95	2.5	537	6.8	0.03	22	0.23	3.3	5.5	0.3	23	6.6	68	20	75	103	17	14927	19	135	0.39315191	631
Gt0332 040	145	11	1658	13	0.08	22	0.20	3.9	6.1	0.4	36	12	154	59	273	494	88	14381	193	406	1.052586702	752
Gt0332 041	50	151	374	5.8	0.15	24	0.20	3.4	5.5	0.7	22	5.4	49	14	52	72	12	14819	13	132	2.178634801	1053
Gt0332 042	33	18	366	5.4	0.05	18	0.19	3.3	4.7	0.4	20	5.3	51	14	46	52	8	15096	16	168	1.261846578	797
Gt0332 043	194	11	2081	5.2	0.20	15	0.39	6.2	9.4	1.2	51	16	202	74	327	563	99	12659	114	218	1.058710446	753
Gt0332 044	117	5.3	972	9.5	0.07	16	0.11	1.7	2.7	0.2	17	6.4	85	34	165	332	61	15647	106	370	0.726617297	689
Gt0332 045	92	22	976	5.8	0.09	12	0.12	1.9	3.0	0.4	19	6.6	88	35	164	324	59	14811	69	247	1.338619267	814
Gt0332 046	153	12	1592	3.5	0.06	9	0.33	5.4	9.4	1.5	46	14	165	58	251	428	77	12165	38	72	1.095834104	761
Gt0332 047	192	64	1089	11	0.09	18	0.14	2.0	3.1	0.2	17	6.3	89	37	187	414	81	15475	247	698	1.804898427	935
Gt0332 048	130	3.2	1474	8.8	0.03	19	0.14	2.4	4.4	0.3	26	9.2	128	51	245	487	89	15351	195	464	0.506379204	650
Gt0332 049	87	22	239	1.3	0.04	20	0.15	1.8	1.8	0.5	7	2.1	23	8.3	39	83	16	12113	5.2	13	1.334855881	814
Gt0332 051	74	6	454	2.7	0.05	27	0.14	2.1	2.9	0.6	13	3.7	45	17	75	152	28	12896	37	63	0.749366097	693
Gt0332 052	129	bdl	956	2.1	0.08	44	1.0	13	14	3.2	41	11	109	35	145	259	45	11846	95	80	bdl	
Gt0332 053	73	19	379	1.3	0.06	21	0.20	2.8	3.2	0.82	12	3.4	40	14	62	124	23	10248	10	10	1.269906469	799
Gt0332 055	109	7.0	779	8.4	0.04	14	0.09	1.7	2.4	0.17	13	5.1	68	27	132	271	49	15701	80	282	0.845070784	711
Gt0332 056	147	7.0	708	5.3	0.06	12	0.12	1.8	2.9	0.26	16	5.5	72	26	119	209	38	14217	17	65	0.845419222	711
Gt0332 057	196	23	1996	30	0.14	40	0.26	4.3	7.5	0.37	42	14	188	71	324	603	106	14402	315	655	1.36165927	820
Gt0332 058	101	7	1303	11	0.17	25	0.29	4.1	6.2	0.36	30	10	127	47	211	386	69	14869	182	467	0.86014947	713
Gt0332 059	88	19	715	8.6	0.06	19	0.13	2.4	3.5	0.25	18	5.8	72	26	116	218	39	15180	62	250	1.284174333	802
Gt0332 060	93	7.7	1041	6.2	0.04	12	0.15	2.7	4.2	0.47	24	7.9	101	37	171	316	56	14114	54	101	0.885497713	718
Gt0332 061	bdl	bdl	1381	16	0.01	1.2	0.06	1.1	0.69	0.34	6.5	4.1	85	44	280	741	156	19846	2.9	305	bdl	
Gt0332 062	41	19	365	1.3	0.07	1.5	0.05	0.79	0.52	0.18	2.9	1.3	22	11	69	202	54	17636	2.0	174	1.280145715	801
Gt0332 063	64	bdl	375	1.6	0.05	1.4	0.06	0.74	0.52	0.14	2.9	1.5	24	11	74	210	56	18693	2.3	171	bdl	
Gt0332 064	31	bdl	326	1.2	0.05	1.6	0.07	0.71	0.53	0.15	3.1	1.3	21	10	63	187	51	18171	2.6	264	bdl	
Gt0332 065	54	171	336	1.4	0.03	1.7	0.04	1.0	0.56	0.15	2.5	1.2	21	10	68	211	58	19682	1.9	279	2.232300797	1072
Gt0332 066	bdl	bdl	437	1.3	0.05	1.5	0.02	0.88	0.58	0.22	3.7	1.6	27	14	86	263	71	19842	1.6	181	bdl	
Gt0332 067	bdl	bdl	362	1.1	0.03	1.5	0.06	0.63	0.57	0.17	2.5	1.5	22	11	72	208	57	17884	1.8	141	bdl	

Gt0405 migmatite Rio Pasabien
15°02'21.4"
89°41'02.4"

DOI: 10.1344/105.000001695

TABLE I | **Continued**

Sample number	P	Ti	Y	Nb	La	Ce	Pr	Nd	Sm	Eu	Gd	Tb	Dy	Ho	Er	Yb	Lu	Hf	Th	U	Log(Ti)	T°C
Gt0405 002	-	5.99	1026	6.4	0.02	16	0.07	1.5	3.4	0.78	19	6.8	87	34	157	315	61	12295	160	460	0.777501147	698
Gt0405 003	-	10	1032	1.5	0.00	3.2	0.09	1.6	3.4	0.16	21	7.1	93	35	156	280	54	12666	38	112	1.006260193	742
Gt0405 004	-	13	870	1.5	0.02	9.4	0.12	1.7	3.3	0.50	17	5.7	74	29	135	275	56	11596	98	171	1.116968356	765
Gt0405 005	-	16	781	1.8	0.03	5.9	0.08	1.4	2.3	0.18	13	4.9	69	26	126	245	49	11986	78	201	1.207314235	785
Gt0405 006	-	21	1236	1.6	0.05	3.9	0.18	2.7	5.3	0.31	26	8.9	115	43	190	354	68	10483	78	193	1.325347534	811
Gt0405 007	-	14	1095	4.3	0.26	14	0.18	1.9	3.1	0.15	19	7.0	94	37	177	348	67	13022	204	531	1.139556347	770
Gt0405 008	-	bdl	625	1.7	0.01	9.4	0.04	1.0	1.6	0.15	11	3.9	54	21	102	210	41	11412	56	150	bdl	
Gt0405 011	-	bdl	812	2.4	0.03	9.3	0.08	1.3	2.2	0.24	14	5.1	70	28	129	258	50	11798	80	222	bdl	
Gt0405 012	-	5.86	1260	5.7	0.34	15	0.34	4.0	5.0	0.27	24	8.6	113	43	203	395	76	13094	224	637	0.767977955	696
Gt0405 014	-	12.6	1507	3.1	0.34	18	0.41	4.7	7.6	1.2	38	12	141	50	225	417	79	11634	327	674	1.100910944	762
Gt0405 015	-	bdl	1890	9.3	0.70	14	0.38	3.4	5.0	0.57	29	12	165	64	310	676	132	13640	386	2792	bdl	
Gt0405 017	-	7.98	1277	4.7	0.04	24	0.18	3.3	6.1	0.98	32	9.6	120	44	193	369	71	11760	334	650	0.901998803	722
Gt0405 018	-	63	1091	3.9	0.05	13	0.12	1.9	3.8	0.25	21	7.5	100	38	172	333	63	12019	115	250	1.802549922	934
Gt0405 019	-	12	2435	4.0	61	194	24	120	38	3.3	89	22	248	84	350	611	114	12264	585	870	1.092074453	760
Gt0405 020	-	1.11	1090	5.1	0.03	16	0.10	1.7	3.6	0.60	21	7.2	93	36	174	375	76	12309	221	794	0.043410358	578
Gt0405 021	-	bdl	996	3.7	0.01	15	0.11	1.5	3.1	0.15	19	6.5	88	34	158	312	60	11693	147	359	bdl	
Gt0405 023	-	12	1067	2.1	5.7	24	1.8	10.0	5.6	0.51	24	7.6	98	37	166	319	61	10494	86	174	1.066278244	755
Gt0405 024	-	3.66	727	11	0.14	2.8	0.08	0.82	0.95	0.12	7.1	3.0	51	23	133	386	83	14260	41	1681	0.563937352	660
Gt0405 025	-	bdl	673	2.2	0.03	12	0.06	0.93	1.3	0.26	10	3.6	53	22	112	278	59	13447	165	492	bdl	
Gt0405 026	-	bdl	618	3.3	0.02	4.4	0.07	1.05	1.2	0.22	9.4	3.2	49	21	108	277	61	12576	56	608	bdl	
Gt0405 028	-	5.34	1858	2.5	0.02	12	0.30	5.00	9.5	1.4	49	16	190	69	298	524	99	10135	207	437	0.727853861	689
Gt0405 029	-	2.29	1198	5.1	2.87	11	1.01	5.41	2.7	0.15	14	5.9	91	39	198	476	96	15684	130	1802	0.359597789	626
Gt0405 030	-	10	1610	2.7	1.91	25	0.89	7.95	10	1.6	44	14	153	54	235	412	79	11647	344	481	1.017094093	744
Gt0405 031	-	8.22	1108	2.0	6.87	27	2.75	15.41	7.3	0.63	26	8.3	103	39	174	326	63	9735	112	215	0.914636804	724
Gt0405 034	-	1.08	833	5.8	0.03	42	0.09	1.09	1.8	0.45	11	3.8	56	25	135	382	89	12054	464	670	0.03361381	577
Gt0405 035	-	2.48	2237	2.9	0.07	25	0.28	4.61	8.7	1.8	51	17	218	81	361	650	124	10592	157	211	0.3939897	632
Gt0405 036	-	3.31	2141	8.8	0.36	2.2	0.17	1.49	2.0	0.48	16	8.6	151	69	381	954	200	19038	88	5406	0.520450964	652
Gt0405 038	-	7.11	2866	12.6	0.32	1.7	0.19	1.67	2.4	0.53	23	13	214	90	487	1407	294	18771	87	8019	0.851755007	712
Gt0405 039	-	bdl	2775	10.8	0.54	3.6	0.23	1.96	2.7	0.65	22	12	199	90	475	1114	226	17361	127	6488	bdl	
Gt0405 042	-	6.39	2648	10.9	0.95	3.2	0.42	3.14	3.5	0.90	27	13	200	82	427	1257	294	17651	62	5585	0.805750805	703
Gt0405 044	-	bdl	2250	7.2	0.03	1.7	0.05	0.60	1.4	0.12	17	9.5	165	76	373	692	132	16700	84	4382	bdl	
Gt0405 045	-	14.8	3148	27	225	470	56	239	79	2	126	31	318	102	463	1321	306	30804	133	3509	1.17033651	777
Gt0405 046	-	1.45	464	1.87	0.02	0.21	0.04	0.48	0.34	0.05	3	1.66	32	15	87	282	65	23831	9	1632	0.162698655	596
Gt0405 048	-	4.35	2526	10.13	0.05	2.01	0.05	0.65	1.72	0.12	17	10	178	82	442	1090	225	18507	117	6442	0.638377542	673
Gt0405 050	-	4.67	1458	4.56	0.02	1.67	0.05	0.56	0.84	0.08	9	5.7	104	48	247	528	104	17076	41	2762	0.669399534	678
Gt0405 051	-	3.62	1907	6.3	0.59	2.3	0.34	2.7	2.2	0.42	15	8.1	136	61	325	801	170	19009	60	3765	0.558921999	659
Gt0405 052	-	4.34	6890	20	18	71	5.4	30	24	12	125	47	636	227	972	1906	366	18246	243	8981	0.637967392	673
Gt0405 053	-	bdl	1255	6.5	0.21	1.22	0.10	1.10	1.12	0.24	9.1	4.8	85	40	227	642	139	19232	33	2862	bdl	

Trace and REE elemental concentrations in ppm

Elemental concetrations are calibrated relative to the analysis of NIST 610 trace element standard glass

Zircon crystallization temperature calculated according to the method and formulas of Watson et al. (2006)

bdl: below detection limits

-: not determined

DOI: 10.1344/105.000001695

TABLE II | **U-Pb data, Chuacús Complex, Central Guatemala**

				CORRECTED RATIOS[2]									CORRECTED AGES (Ma)								
Sample number	U[1] (ppm)	Th[1] (ppm)	Th/U	$^{207}Pb/^{206}Pb$	±1σ[3]	$^{207}Pb/^{235}U$	±1σ[3]	$^{206}Pb/^{238}U$	±1σ[3]	$^{208}Pb/^{232}Th$	±1σ[3]	Rho	$^{206}Pb/^{238}U$	±1σ	$^{207}Pb/^{235}U$	±1σ	$^{207}Pb/^{206}Pb$	±1σ	Best age (Ma)	±1σ	% disc
Gt0309 Metapelite. 15°01'18.3" 90°42'53.9"																					
Gt0309 001	513	169	0.33	0.07275	0.0007	1.6085	0.0169	0.16054	0.0007	0.0485	0.0006	0.4	960	4	974	7	1007	19	960	4	1.4
Gt0309 002	608	114	0.19	0.07076	0.0007	1.39806	0.0176	0.14329	0.0009	0.04344	0.0003	0.6	863	5	888	7	951	19	863	5	2.8
Gt0309 003	711	84	0.12	0.07209	0.0007	1.3886	0.0156	0.13987	0.0009	0.04342	0.0006	0.6	844	5	884	7	988	17	844	5	4.5
~~Gt0309 004~~	~~149~~	~~63~~	0.42	~~0.07434~~	~~0.0013~~	~~1.193~~	~~0.0215~~	~~0.11649~~	~~0.0007~~	~~0.05555~~	~~0.0008~~	~~0.3~~	~~710~~	~~4~~	~~797~~	~~10~~	~~1051~~	~~34~~	~~710~~	~~4~~	~~10.9~~
Gt0309 005	206	68	0.33	0.07429	0.001	1.73	0.0279	0.16889	0.001	0.05092	0.0003	0.5	1006	6	1020	10	1049	27	1049	27	4.1
Gt0309 006	1050	132	0.13	0.06966	0.0007	1.18858	0.0211	0.12374	0.0015	0.03759	0.0005	0.8	752	9	795	10	918	21	752	9	5.4
Gt0309 007	612	220	0.36	0.07094	0.0009	1.39745	0.0228	0.14286	0.0009	0.0433	0.0003	0.5	861	5	888	10	956	26	861	5	3.0
Gt0309 008	836	131	0.16	0.07062	0.0008	1.34313	0.0255	0.13793	0.0017	0.04183	0.0005	0.7	833	10	865	11	947	24	833	10	3.7
~~Gt0309 010~~	~~2026~~	~~149~~	0.07	~~0.06442~~	~~0.0006~~	~~0.65529~~	~~0.0073~~	~~0.07377~~	~~0.0004~~	~~0.02264~~	~~0.0002~~	~~0.5~~	~~459~~	~~2~~	~~512~~	~~4~~	~~756~~	~~19~~	~~459~~	~~2~~	~~10.4~~
Gt0309 011	116	46	0.40	0.07292	0.0012	1.54793	0.0288	0.15397	0.0008	0.04652	0.0003	0.3	923	5	950	11	1012	32	923	5	2.8
Gt0309 012	374	87	0.23	0.07208	0.0008	1.55972	0.0191	0.15693	0.0008	0.04747	0.0002	0.5	940	4	954	8	988	20	940	4	1.5
Gt0309 013	528	152	0.29	0.07177	0.0008	1.5127	0.0187	0.15287	0.0007	0.04627	0.0002	0.4	917	4	936	8	979	21	917	4	2.0
Gt0309 014	1052	131	0.12	0.07115	0.0007	1.20944	0.0146	0.12329	0.0008	0.03738	0.0002	0.5	749	4	805	7	962	19	749	4	7.0
Gt0309 015	1935	240	0.12	0.06482	0.0007	0.7824	0.0109	0.08754	0.0007	0.02683	0.0002	0.7	541	4	587	6	769	20	541	4	7.8
~~Gt0309 016~~	~~2333~~	~~294~~	0.13	~~0.06877~~	~~0.0006~~	~~0.91113~~	~~0.0092~~	~~0.09609~~	~~0.0004~~	~~0.02926~~	~~0.0001~~	~~0.5~~	~~591~~	~~2~~	~~658~~	~~5~~	~~892~~	~~17~~	~~591~~	~~2~~	~~10.2~~
Gt0309 017	2338	267	0.11	0.06523	0.0006	0.90328	0.0096	0.10044	0.0004	0.03074	0.0002	0.5	617	2	653	5	782	19	617	2	5.5
Gt0309 018	500	95	0.19	0.07003	0.0007	1.45129	0.0169	0.1503	0.0007	0.04561	0.0002	0.4	903	4	910	7	929	20	903	4	0.8
Gt0309 019	1989	232	0.12	0.06731	0.0006	0.86275	0.0093	0.09296	0.0004	0.02837	0.0001	0.5	573	3	632	5	847	18	573	3	9.3
Gt0309 020	~~1373~~	~~118~~	0.09	~~0.06569~~	~~0.0007~~	~~0.70301~~	~~0.0085~~	~~0.07762~~	~~0.0005~~	~~0.02377~~	~~0.0002~~	~~0.6~~	~~482~~	~~3~~	~~541~~	~~5~~	~~797~~	~~19~~	~~482~~	~~3~~	~~10.9~~
Gt0309 021	1911	441	0.23	0.06266	0.0008	0.87439	0.0125	0.1012	0.0005	0.03111	0.0002	0.4	621	3	638	7	697	25	621	3	2.7
Gt0309 022	2845	526	0.18	0.06539	0.0007	0.77848	0.0115	0.08635	0.0008	0.02644	0.0002	0.7	534	4	585	7	787	20	534	4	8.7
Gt0309 023	344	110	0.32	0.06807	0.0009	1.24584	0.0197	0.13273	0.0008	0.04041	0.0003	0.5	803	5	822	9	871	25	803	5	2.3
Gt0309 024	211	86	0.41	0.07151	0.0012	1.50035	0.0332	0.15217	0.0015	0.04607	0.0005	0.6	913	9	931	13	972	32	913	9	1.9
Gt0309 025	2263	230	0.10	0.06597	0.0007	0.80816	0.0095	0.08885	0.0005	0.02718	0.0002	0.5	549	3	601	5	805	20	549	3	8.7
Gt0309 026	324	53	0.16	0.07077	0.0008	1.4934	0.0189	0.15304	0.0008	0.04639	0.0002	0.4	918	4	928	8	951	22	918	4	1.1
Gt0309 027	223	85	0.38	0.07276	0.0009	1.237	0.0163	0.12352	0.0007	0.05038	0.0007	0.4	751	4	818	7	1007	23	751	4	8.2
Gt0309 028	1059	244	0.23	0.06491	0.0009	1.02931	0.0283	0.11502	0.0021	0.03521	0.0006	0.9	702	12	719	14	771	26	702	12	2.4
Gt0309 029	377	174	0.46	0.07313	0.0009	1.68506	0.0289	0.16713	0.0014	0.05047	0.0004	0.6	996	7	1003	11	1017	24	1017	24	2.1
Gt0309 030	2175	174	0.08	0.0709	0.0006	1.20841	0.0117	0.12362	0.0005	0.03749	0.0002	0.4	751	3	804	5	954	17	751	3	6.6
Gt0309 031	2165	611	0.28	0.06682	0.0007	1.17028	0.0144	0.12703	0.0006	0.03876	0.0002	0.5	771	4	787	7	832	20	771	4	2.0
Gt0309 032	1163	194	0.17	0.06862	0.0007	1.18335	0.0143	0.12507	0.0008	0.03806	0.0002	0.6	760	4	793	7	887	19	760	4	4.2
~~Gt0309 033~~	~~1449~~	~~81~~	0.06	~~0.06498~~	~~0.0007~~	~~0.63163~~	~~0.0106~~	~~0.0705~~	~~0.0008~~	~~0.02163~~	~~0.0003~~	~~0.8~~	~~439~~	~~5~~	~~497~~	~~7~~	~~774~~	~~21~~	~~439~~	~~5~~	~~11.7~~
Gt0309 034	1192	262	0.22	0.05999	0.0012	0.77025	0.0183	0.09312	0.0008	0.02876	0.0003	0.6	574	5	580	10	603	40	574	5	1.0
Gt0309 035	1298	73	0.06	0.05975	0.0008	0.41601	0.0071	0.0505	0.0005	0.01565	0.0002	0.6	318	3	353	5	595	27	318	3	9.9
Gt0309 036	168	102	0.61	0.07596	0.0008	1.8654	0.0237	0.1784	0.0011	0.05643	0.0008	0.5	1058	6	1069	8	1094	21	1094	21	3.3
Gt0309 037	770	173	0.22	0.07233	0.0007	1.6352	0.0167	0.16423	0.0007	0.04907	0.0006	0.4	980	4	984	6	995	18	980	4	0.4
Gt0309 038	665	127	0.19	0.07154	0.0007	1.5825	0.016	0.16056	0.0006	0.04891	0.0006	0.4	960	4	963	6	973	18	960	4	0.3
Gt0309 039	1000	160	0.16	0.06974	0.0007	1.21279	0.0129	0.12612	0.0005	0.03831	0.0002	0.4	766	3	806	6	921	18	766	3	5.0
Gt0309 040	1099	256	0.23	0.07194	0.0007	1.36868	0.0152	0.13799	0.0007	0.04177	0.0002	0.5	833	4	876	7	984	18	833	4	4.9
Gt0309 041	1284	266	0.21	0.06968	0.0007	1.19079	0.0147	0.12395	0.0008	0.03765	0.0002	0.6	753	4	796	7	919	19	753	4	5.4
Gt0309 042	3076	447	0.15	0.06126	0.0007	0.55771	0.0109	0.06603	0.0009	0.02037	0.0003	0.8	412	5	450	7	648	22	412	5	8.4
Gt0309 043	2338	249	0.11	0.06917	0.0006	1.15717	0.0124	0.12133	0.0007	0.03689	0.0002	0.5	738	4	781	6	904	17	738	4	5.5
Gt0309 044	2621	442	0.17	0.06386	0.0007	0.84272	0.0103	0.0957	0.0005	0.02936	0.0002	0.5	589	3	621	6	737	21	589	3	5.2
Gt0309 045	1821	166	0.09	0.06447	0.0006	0.67321	0.0076	0.07574	0.0003	0.02324	0.0001	0.4	471	2	523	5	757	21	471	2	9.9
Gt0309 046	239	132	0.56	0.06915	0.0011	1.37892	0.025	0.14462	0.0008	0.04395	0.0002	0.4	871	5	880	11	903	30	871	5	1.0
Gt0309 047	1195	344	0.29	0.0632	0.0008	0.85747	0.0134	0.09839	0.0006	0.03022	0.0002	0.6	605	4	629	7	715	25	605	4	3.8
Gt0309 048	1619	164	0.10	0.07074	0.0006	1.183	0.012	0.12146	0.0006	0.03703	0.0005	0.5	739	3	793	6	950	17	739	3	6.8
Gt0309 049	901	137	0.15	0.07107	0.0007	1.33183	0.0162	0.13591	0.0009	0.04119	0.0003	0.5	821	5	860	7	959	20	821	5	4.5
Gt0309 050	1721	340	0.20	0.07043	0.0007	1.29521	0.0147	0.13338	0.0007	0.04046	0.0002	0.5	807	4	844	6	941	19	807	4	4.4
Gt0309 051	128	44	0.34	0.07231	0.0011	1.58898	0.0289	0.15937	0.001	0.04819	0.0003	0.4	953	6	966	11	995	32	953	6	1.3
Gt0309 052	1976	165	0.08	0.05361	0.0007	0.37253	0.0057	0.0504	0.0003	0.01578	0.0002	0.5	317	2	322	4	355	29	317	2	1.6
Gt0309 053	219	43	0.20	0.05838	0.0013	0.70152	0.0184	0.08715	0.0008	0.027	0.0004	0.5	539	4	540	11	544	49	539	4	0.2
~~Gt0309 054~~	~~195~~	~~98~~	0.50	~~0.07673~~	~~0.0008~~	~~1.7662~~	~~0.0231~~	~~0.16728~~	~~0.0012~~	~~0.05818~~	~~0.0008~~	~~0.6~~	~~997~~	~~7~~	~~1033~~	~~8~~	~~1114~~	~~22~~	~~1114~~	~~22~~	~~10.5~~
Gt0309 055	1391	228	0.16	0.06399	0.0007	0.90895	0.0115	0.10302	0.0005	0.03159	0.0002	0.4	632	3	656	6	741	23	632	3	3.7
Gt0309 056	120	67	0.56	0.0697	0.0017	1.51657	0.0415	0.15781	0.0012	0.04791	0.0004	0.4	945	7	937	17	919	48	945	7	-0.9
Gt0309 057	421	118	0.28	0.0699	0.0009	1.46318	0.0219	0.15182	0.0008	0.04608	0.0003	0.5	911	5	915	9	925	26	911	5	0.4
Gt0309 058	781	244	0.31	0.06398	0.0012	1.05048	0.0355	0.11908	0.0022	0.03651	0.0006	0.9	725	13	729	18	741	41	725	13	0.5
Gt0309 059	1140	363	0.32	0.06707	0.0008	1.09909	0.0164	0.11884	0.0006	0.03625	0.0002	0.5	724	4	753	8	840	26	724	4	3.9

DOI: 10.1344/105.000001695

TABLE II | **Continued**

				CORRECTED RATIOS[2]									CORRECTED AGES (Ma)								
Sample number	U[1] (ppm)	Th[1] (ppm)	Th/U	$^{207}Pb/^{206}Pb$	$\pm1\sigma^3$	$^{207}Pb/^{235}U$	$\pm1\sigma^3$	$^{206}Pb/^{238}U$	$\pm1\sigma^3$	$^{208}Pb/^{232}Th$	$\pm1\sigma^3$	Rho	$^{206}Pb/^{238}U$	$\pm1\sigma$	$^{207}Pb/^{235}U$	$\pm1\sigma$	$^{207}Pb/^{206}Pb$	$\pm1\sigma$	Best age (Ma)	$\pm1\sigma$	% disc
Gt0309 062	2150	301	0.14	0.06962	0.0007	1.20089	0.0142	0.12511	0.0008	0.03801	0.0003	0.6	760	5	801	7	917	19	760	5	5.1
Gt0309 063	2891	610	0.21	0.06872	0.0007	1.10261	0.0123	0.11636	0.0006	0.03541	0.0002	0.5	710	3	755	6	890	19	710	3	6.0
Gt0309 064	69	27	0.39	0.07397	0.0013	1.7762	0.0339	0.17459	0.0015	0.0535	0.0009	0.5	1037	8	1037	12	1041	34	1041	34	0.4
Gt0309 065	834	184	0.22	0.07246	0.0007	1.6023	0.0247	0.16024	0.0019	0.05002	0.0008	0.8	958	11	971	10	999	19	958	11	1.3
Gt0309 066	418	103	0.25	0.0728	0.0007	1.6214	0.0179	0.16179	0.0008	0.0491	0.0006	0.4	967	4	979	7	1008	20	967	4	1.2
Gt0309 067	1303	99	0.08	0.06959	0.0006	1.25083	0.0134	0.13035	0.0007	0.0396	0.0002	0.5	790	4	824	6	916	19	790	4	4.1
Gt0309 068	70	38	0.54	0.07745	0.0019	1.96302	0.0532	0.18382	0.0012	0.05516	0.0003	0.3	1088	6	1103	18	1133	48	1133	48	4.0
Gt0309 069	1704	305	0.18	0.06991	0.0006	1.27777	0.0137	0.13256	0.0006	0.04025	0.0002	0.5	802	4	836	6	926	19	802	4	4.1
Gt0309 070	1061	199	0.19	0.06964	0.0007	1.37946	0.0157	0.14366	0.0008	0.04362	0.0002	0.5	865	4	880	7	918	19	865	4	1.7
~~Gt0309 072~~	~~145~~	~~57~~	0.39	~~0.07335~~	~~0.0011~~	~~1.0519~~	~~0.0176~~	~~0.10411~~	~~0.0008~~	~~0.05376~~	~~0.0008~~	~~0.4~~	~~638~~	~~4~~	~~730~~	~~9~~	~~1024~~	~~30~~	~~638~~	~~4~~	~~12.6~~
Gt0309 073	557	177	0.32	0.07272	0.0007	1.4359	0.0156	0.14339	0.0007	0.05463	0.0007	0.4	864	4	904	7	1006	20	864	4	4.4
Gt0309 074	460	117	0.25	0.0698	0.0008	1.4622	0.0206	0.15192	0.0009	0.04612	0.0003	0.5	912	5	915	8	923	24	912	5	0.3
~~Gt0309 075~~	~~206~~	~~93~~	0.45	~~0.07702~~	~~0.0008~~	~~2.2426~~	~~0.0269~~	~~0.2115~~	~~0.0014~~	~~0.06238~~	~~0.0008~~	~~0.6~~	~~1237~~	~~7~~	~~1194~~	~~8~~	~~1122~~	~~20~~	~~1122~~	~~20~~	~~-10.2~~
Gt0309 076	438	70	0.16	0.06329	0.0009	0.96965	0.0161	0.11112	0.0008	0.03411	0.0003	0.5	679	4	688	8	718	29	679	4	1.3
Gt0309 077	1024	207	0.20	0.07032	0.0007	1.43331	0.0165	0.14782	0.0007	0.04484	0.0002	0.5	889	4	903	7	938	20	889	4	1.6
Gt0309 078	305	181	0.59	0.0757	0.0011	1.79123	0.03	0.17161	0.0009	0.05163	0.0002	0.4	1021	5	1042	11	1087	28	1087	28	6.1
Gt0309 079	2298	272	0.12	0.0668	0.0006	0.88747	0.0097	0.09636	0.0005	0.02943	0.0002	0.5	593	3	645	5	831	19	593	3	8.1
Gt0309 080	1642	172	0.10	0.06342	0.0008	0.73323	0.0103	0.08385	0.0004	0.02576	0.0002	0.5	519	2	558	6	722	26	519	2	7.0
Gt0309 081	2406	585	0.24	0.07026	0.0006	1.2602	0.0124	0.13027	0.0006	0.04004	0.0005	0.5	789	3	828	6	936	18	789	3	4.7
Gt0309 082	1966	132	0.07	0.0684	0.0006	1.03396	0.0101	0.10963	0.0005	0.03338	0.0002	0.4	671	3	721	5	881	18	671	3	6.9
Gt0309 083	1469	125	0.08	0.06836	0.0006	1.07376	0.0109	0.11393	0.0005	0.03469	0.0002	0.4	696	3	741	5	879	19	696	3	6.1
Gt0309 084	138	48	0.35	0.06605	0.0012	1.27482	0.0307	0.13998	0.0014	0.04275	0.0004	0.6	845	8	835	14	808	38	845	8	-1.2
Gt0309 085	620	72	0.12	0.0657	0.0008	0.92525	0.0165	0.10214	0.001	0.03124	0.0004	0.7	627	6	665	9	797	26	627	6	5.7
Gt0309 086	1435	208	0.15	0.06441	0.0007	0.78902	0.011	0.08884	0.0006	0.02724	0.0002	0.6	549	4	591	6	755	23	549	4	7.1
Gt0309 087	539	66	0.12	0.06927	0.0009	1.24087	0.0241	0.12992	0.0017	0.03949	0.0005	0.7	787	10	819	11	907	25	787	10	3.9
Gt0309 088	929	204	0.22	0.07171	0.0007	1.5355	0.0164	0.15557	0.0008	0.04779	0.0007	0.5	932	5	945	7	978	19	932	5	1.4
Gt0309 089	1791	366	0.20	0.0681	0.0007	0.97778	0.0116	0.10413	0.0006	0.03173	0.0002	0.5	639	3	692	6	872	20	639	3	7.7
Gt0309 090	1353	143	0.11	0.06894	0.0007	1.08311	0.0129	0.11395	0.0006	0.03467	0.0002	0.5	696	3	745	6	897	21	696	3	6.6
Gt0309 091	296	89	0.30	0.06221	0.001	0.96661	0.0186	0.11269	0.0008	0.03465	0.0003	0.5	688	4	687	10	681	33	688	4	-0.1
Gt0309 092	121	78	0.65	0.07674	0.0009	1.9414	0.0263	0.18392	0.0012	0.05619	0.0008	0.5	1088	6	1095	9	1114	24	1114	24	2.3
Gt0309 093	658	115	0.17	0.07008	0.0008	1.31643	0.0172	0.13624	0.0008	0.04135	0.0003	0.5	823	5	853	8	931	22	823	5	3.5
Gt0309 094	861	170	0.20	0.07153	0.0007	1.5424	0.0158	0.15665	0.0007	0.04723	0.0006	0.4	938	4	947	6	973	19	938	4	1.0
Gt0309 095	268	19	0.07	0.06324	0.001	0.67264	0.0135	0.07715	0.0009	0.02371	0.0004	0.6	479	5	522	8	716	32	479	5	8.2
Gt0309 096	122	69	0.57	0.07116	0.0015	1.51462	0.0361	0.15438	0.001	0.04676	0.0003	0.4	925	6	936	15	962	41	925	6	1.2
Gt0309 097	1067	316	0.30	0.06754	0.0009	1.09296	0.0175	0.11737	0.0008	0.03578	0.0003	0.5	715	5	750	8	854	26	715	5	4.7
Gt0309 098	144	73	0.51	0.07628	0.0011	2.0268	0.0349	0.1933	0.0019	0.05936	0.001	0.6	1139	10	1125	12	1102	28	1102	28	-3.4
Gt0309 099	1683	163	0.10	0.06514	0.0008	0.74321	0.0114	0.08275	0.0007	0.02535	0.0003	0.6	513	4	564	7	779	24	513	4	9.0
Gt0309 100	2512	510	0.20	0.07061	0.0007	1.3206	0.0155	0.13598	0.0008	0.04188	0.0005	0.5	822	5	855	7	946	19	822	5	3.9
Gt0315, pegmatite. 14°58'15.49" 90°43'29.88"																					
~~Gt0315 001~~	~~40.4~~	~~0.67~~	~~0.0167~~	~~0.0586~~	~~0.0075~~	~~0.265~~	~~0.0366~~	~~0.0328~~	~~0.0008~~	~~0.01016~~	~~0.0032~~	~~0.4~~	~~208~~	~~5~~	~~239~~	~~29~~	~~552~~	~~266~~	~~208~~	~~5~~	~~13.0~~
Gt0315 002	45.3	0.06	0.0014	0.05629	0.0051	0.08862	0.0083	0.01142	0.0002	0.00355	0.0068	0.3	73	1	86	8	464	188	73	1	5.1
Gt0315 003	45.9	0.05	0.0012	0.05546	0.0043	0.08815	0.007	0.01153	0.0002	0.00359	0.0057	0.2	74	1	86	7	431	173	74	1	5.1
Gt0315 004	787.4	0.12	0.0002	0.04882	0.001	0.07367	0.0015	0.01097	7E-05	0.03316	0.0163	0.3	70.3	0.4	72	1	139	44	70.3	0.4	2.4
Gt0315 005	43.0	0.04	0.0010	0.06416	0.0058	0.1015	0.0095	0.01147	0.0002	0.00352	0.0033	0.3	74	1	98	9	747	179	74	1	15.7
~~Gt0315 006~~	~~37.2~~	~~0.04~~	~~0.0009~~	~~0.06058~~	~~0.0055~~	~~0.09603~~	~~0.009~~	~~0.01166~~	~~0.0003~~	~~0.34938~~	~~0.2166~~	~~0.2~~	~~75~~	~~2~~	~~93~~	~~8~~	~~624~~	~~185~~	~~75~~	~~2~~	~~19.4~~
Gt0315 007	139.0	0.01	0.0001	0.05178	0.002	0.07489	0.003	0.01054	0.0001	0.65195	0.2608	0.2	67.6	0.6	73	3	276	83	67.6	0.6	7.4
Gt0315 008	577.3	0.09	0.0002	0.04882	0.0011	0.07382	0.0018	0.01095	6E-05	0.06517	0.0287	0.3	70.2	0.4	72	2	139	50	70.2	0.4	2.5
Gt0315 009	20.9	0.01	0.0003	0.07087	0.0092	0.11384	0.0154	0.01198	0.0004	4.2841	2.0564	0.3	77	3	109	14	954	255	77	3	15.8
Gt0315 010	157.8	60.15	0.3811	0.07311	0.0009	1.622	0.0213	0.16095	0.0009	0.04788	0.0008	0.4	962	5	979	8	1017	24	962	5	1.7
Gt0315 011	100.6	11.39	0.1132	0.07225	0.0009	1.6325	0.0232	0.16385	0.0009	0.04699	0.0011	0.4	978	5	983	9	993	26	978	5	0.5
~~Gt0315 012~~	~~36.4~~	~~0.04~~	~~0.0010~~	~~0.05784~~	~~0.0035~~	~~0.09493~~	~~0.006~~	~~0.01201~~	~~0.0002~~	~~0.17545~~	~~0.1456~~	~~0.3~~	~~77~~	~~1~~	~~92~~	~~6~~	~~524~~	~~133~~	~~77~~	~~1~~	~~16.3~~
Gt0315 013	68.5	0.01	0.0001	0.05505	0.0029	0.08345	0.0045	0.01098	0.0001	0.9008	0.4684	0.2	70.4	0.8	81	4	414	116	70.4	0.8	7.5
Gt0315 014	73.1	24.81	0.3392	0.07299	0.0012	1.6273	0.0286	0.16157	0.0012	0.04731	0.001	0.4	965	6	981	11	1014	32	965	6	1.6
Gt0315 015	82.9	50.34	0.6071	0.07247	0.0009	1.6642	0.0234	0.16667	0.0009	0.04811	0.0009	0.4	994	5	995	9	999	26	994	5	0.1
Gt0315 016	64.0	30.13	0.4708	0.07235	0.0011	1.5771	0.0255	0.15818	0.001	0.04595	0.0009	0.4	947	5	961	10	996	30	947	5	1.5
Gt0315 017	49.3	0.02	0.0004	0.05231	0.0059	0.08262	0.0095	0.01146	0.0002	0.0036	0.1502	0.2	73	1	81	9	299	233	73	1	9.9
Gt0315 018	840.8	215.91	0.2568	0.07165	0.0007	1.39	0.0173	0.14059	0.0011	0.04331	0.0008	0.6	848	6	885	7	976	20	848	6	4.2
Gt0315 019	158.8	72.51	0.4565	0.07237	0.0009	1.6101	0.0215	0.16143	0.0009	0.0474	0.0008	0.4	965	5	974	8	996	24	965	5	0.9
Gt0315 020	24.6	2.57	0.1044	0.07468	0.0017	1.6513	0.0401	0.16075	0.0013	0.04808	0.0018	0.3	961	7	990	15	1060	46	1060	46	9.3
Gt0315 021	37.8	0.02	0.0004	0.05942	0.0065	0.0925	0.0105	0.01167	0.0003	1.0194	0.3364	0.2	75	2	90	10	583	226	75	2	3.8
Gt0315 022	73.8	17.69	0.2397	0.0724	0.001	1.6983	0.0272	0.17012	0.0013	0.0518	0.001	0.5	1013	7	1008	10	997	28	997	28	-0.5
Gt0315 023	329.9	127.26	0.3857	0.07219	0.0008	1.6278	0.0202	0.16345	0.0009	0.04831	0.0008	0.5	976	5	981	8	991	22	976	5	0.5
Gt0315 024	585.9	329.42	0.5622	0.07171	0.0007	1.6004	0.0181	0.16177	0.0009	0.04673	0.0008	0.5	967	5	970	7	978	20	967	5	0.3
~~Gt0315 025~~	~~746~~	~~239~~	0.32	~~0.07135~~	~~0.0007~~	~~1.4909~~	~~0.0166~~	~~0.1515~~	~~0.0008~~	~~0.04452~~	~~0.0008~~	~~0.5~~	~~909~~	~~5~~	~~927~~	~~7~~	~~967~~	~~20~~	~~909~~	~~5~~	~~1.9~~

DOI: 10.1344/105.000001695

TABLE II | **Continued**

				CORRECTED RATIOS[2]									CORRECTED AGES (Ma)								
Sample number	U[1] (ppm)	Th[1] (ppm)	Th/U	$^{207}Pb/^{206}Pb$	±1σ[3]	$^{207}Pb/^{235}U$	±1σ[3]	$^{206}Pb/^{238}U$	±1σ[3]	$^{208}Pb/^{232}Th$	±1σ[3]	Rho	$^{206}Pb/^{238}U$	±1σ	$^{207}Pb/^{235}U$	±1σ	$^{207}Pb/^{206}Pb$	±1σ	Best age (Ma)	±1σ	% disc
Gt0315 026	325.9	28.94	0.0888	0.0693	0.0007	1.27239	0.0172	0.13316	0.0011	0.04045	0.0003	0.6	806	6	833	8	908	21	806	6	3.2
Gt0315 027	752.0	255.40	0.3396	0.07097	0.0007	1.4249	0.0156	0.14563	0.0008	0.04186	0.0007	0.5	876	4	899	7	957	19	876	4	2.6
Gt0315 028	393.4	169.07	0.4297	0.07131	0.0007	1.4685	0.0164	0.14923	0.0008	0.04353	0.0007	0.5	897	4	918	7	966	20	897	4	2.3
Gt0315 029	154.2	95.55	0.6196	0.07219	0.0009	1.6024	0.0212	0.161	0.0009	0.04586	0.0008	0.4	962	5	971	8	991	24	962	5	0.9
Gt0315 030	139.9	59.93	0.4283	0.07179	0.0008	1.6533	0.0202	0.16699	0.0009	0.04836	0.0009	0.4	996	5	991	8	980	21	996	5	-0.5
Gt0318, High pressure arkose. 14°54'56.01" 90°37'54.62"																					
Gt0318 002	44	17	0.38	0.07184	0.0012	1.5254	0.0278	0.1544	0.001	0.04742	0.0008	0.4	926	6	941	11	981	33	926	6	1.6
~~Gt0318 003~~	~~118~~	~~3~~	0.03	~~0.06103~~	~~0.0018~~	~~0.16126~~	~~0.005~~	~~0.01912~~	~~0.0002~~	~~0.03933~~	~~0.0016~~	~~0.3~~	~~122~~	~~1~~	~~152~~	~~4~~	~~640~~	~~59~~	~~122~~	~~1~~	~~19.7~~
Gt0318 004	38	13	0.34	0.07337	0.0016	1.576	0.0395	0.15558	0.0019	0.04884	0.0009	0.5	932	10	961	16	1024	45	932	10	3.0
Gt0318 005	67	19	0.28	0.07043	0.0011	1.5083	0.0247	0.15541	0.001	0.04687	0.0007	0.4	931	6	934	10	941	31	931	6	0.3
Gt0318 006	153	3	0.02	0.0481	0.0015	0.13049	0.0041	0.01968	0.0002	0.00624	0.0012	0.3	126	1	125	4	104	70	126	1	-0.8
Gt0318 007	84	29	0.34	0.07242	0.001	1.52632	0.0238	0.15286	0.0008	0.04621	0.0002	0.4	917	4	941	10	998	29	917	4	2.6
Gt0318 008	91	30	0.33	0.06521	0.0012	1.13073	0.0365	0.12575	0.0022	0.03847	0.0006	0.8	764	13	768	17	781	41	764	13	0.5
Gt0318 009	258	45	0.17	0.05717	0.0007	0.63994	0.0098	0.08127	0.0007	0.02457	0.0005	0.5	504	4	502	6	498	29	504	4	-0.4
Gt0318 010	228	73	0.32	0.05035	0.0009	0.19844	0.0042	0.02862	0.0003	0.01172	0.0002	0.5	182	2	184	4	211	39	182	2	1.1
Gt0318 011	67	31	0.47	0.072	0.001	1.6672	0.0269	0.16831	0.0014	0.05035	0.0008	0.5	1003	7	996	10	986	26	1003	7	-1.7
~~Gt0318 012~~	~~45~~	~~9~~	0.19	~~0.07127~~	~~0.0024~~	~~0.82519~~	~~0.0441~~	~~0.08463~~	~~0.0036~~	~~0.05066~~	~~0.0039~~	~~0.8~~	~~524~~	~~21~~	~~611~~	~~25~~	~~965~~	~~62~~	~~524~~	~~21~~	~~14.2~~
Gt0318 013	127	86	0.67	0.05165	0.001	0.27432	0.0055	0.03865	0.0002	0.01244	0.0002	0.3	244	1	246	4	270	40	244	1	0.8
Gt0318 014	61	67	1.11	0.05187	0.0016	0.28999	0.0094	0.04074	0.0004	0.01267	0.0002	0.3	257	2	259	7	280	66	257	2	0.8
Gt0318 015	183	79	0.43	0.07012	0.0008	1.4349	0.0172	0.14864	0.0007	0.04746	0.0006	0.4	893	4	904	7	932	21	893	4	1.2
~~Gt0318 016~~	~~108~~	~~2~~	0.02	~~0.06483~~	~~0.0026~~	~~0.17144~~	~~0.0073~~	~~0.0196~~	~~0.0003~~	~~0.27703~~	~~0.0693~~	~~0.4~~	~~125~~	~~2~~	~~161~~	~~6~~	~~769~~	~~78~~	~~125~~	~~2~~	~~22.4~~
Gt0318 017	113	19	0.17	0.05155	0.0012	0.24863	0.0065	0.03498	0.0004	0.011	0.0001	0.4	222	2	225	5	266	49	222	2	1.3
Gt0318 018	43	42	0.97	0.05298	0.0018	0.28298	0.0099	0.0389	0.0003	0.01186	0.0002	0.2	246	2	253	8	328	73	246	2	2.8
Gt0318 019	59	8	0.14	0.065	0.0016	1.01867	0.0379	0.11367	0.0026	0.03478	0.0008	0.7	694	15	713	19	774	52	694	15	2.7
Gt0318 020	64	13	0.21	0.06064	0.0013	0.89087	0.0224	0.10654	0.0011	0.03286	0.0004	0.5	653	7	647	12	627	42	653	7	-0.9
Gt0318 021	474	102	0.21	0.07107	0.0007	1.5468	0.0165	0.15803	0.0008	0.04752	0.0006	0.5	946	5	949	7	959	18	946	5	0.3
~~Gt0318 022~~	~~3~~	~~0~~	0.01	~~0.41014~~	~~0.0357~~	~~1.8124~~	~~0.1846~~	~~0.03441~~	~~0.0018~~	~~2.4419~~	~~0.2686~~	~~0.5~~	~~218~~	~~11~~	~~1050~~	~~67~~	~~3947~~	~~134~~	~~3947~~	~~134~~	~~94.5~~
Gt0318 023	69	22	0.32	0.06952	0.001	1.5598	0.0235	0.16289	0.0009	0.0475	0.0007	0.4	973	5	954	9	914	27	973	5	-2.0
~~Gt0318 024~~	~~20~~	~~0~~	0.02	~~0.25912~~	~~0.0382~~	~~0.9964~~	~~0.1524~~	~~0.02789~~	~~0.0014~~	~~0.00742~~	~~0.0004~~	~~0.3~~	~~177~~	~~9~~	~~702~~	~~78~~	~~3241~~	~~227~~	~~3241~~	~~227~~	~~94.5~~
Gt0318 025	34	36	1.07	0.05304	0.0018	0.28224	0.0101	0.03892	0.0004	0.01167	0.0002	0.3	246	3	252	8	331	73	246	3	2.4
Gt0318 026	50	38	0.77	0.05269	0.002	0.27174	0.0119	0.0374	0.0004	0.01173	0.0001	0.4	237	3	244	10	316	82	237	3	2.9
Gt0318 027	54	45	0.83	0.05384	0.0019	0.21146	0.0076	0.02858	0.0002	0.00908	0.0002	0.2	182	1	195	6	364	75	182	1	6.7
Gt0318 028	196	74	0.38	0.05225	0.0012	0.13492	0.0032	0.01883	0.0002	0.00856	0.0001	0.4	120	1	129	3	296	48	120	1	7.0
Gt0318 029	31	25	0.81	0.05586	0.0021	0.28161	0.011	0.03699	0.0004	0.01233	0.0002	0.3	234	3	252	9	447	78	234	3	7.1
Gt0318 030	59	7	0.11	0.04914	0.0025	0.14797	0.0079	0.02165	0.0004	0.02083	0.0052	0.3	138	2	140	7	155	107	138	2	1.4
Gt0318 031	79	24	0.30	0.07475	0.0011	1.8076	0.027	0.17543	0.0009	0.049	0.0007	0.3	1042	5	1048	10	1062	27	1062	27	1.9
~~Gt0318 032~~	~~89~~	~~20~~	0.22	~~0.05641~~	~~0.0049~~	~~0.20335~~	~~0.0186~~	~~0.02614~~	~~0.0004~~	~~0.00813~~	~~0.0002~~	~~0.4~~	~~166~~	~~3~~	~~188~~	~~16~~	~~469~~	~~182~~	~~166~~	~~3~~	~~11.7~~
Gt0318 033	75	16	0.21	0.07333	0.001	1.7008	0.0241	0.1684	0.001	0.04997	0.0008	0.4	1003	5	1009	9	1023	25	1023	25	2.0
~~Gt0318 034~~	~~178~~	~~6~~	0.04	~~0.06709~~	~~0.001~~	~~0.67012~~	~~0.0142~~	~~0.07244~~	~~0.0011~~	~~0.02209~~	~~0.0004~~	~~0.8~~	~~451~~	~~7~~	~~521~~	~~9~~	~~841~~	~~28~~	~~451~~	~~7~~	~~13.4~~
Gt0318 035	82	66	0.80	0.05088	0.0011	0.30734	0.0068	0.04399	0.0003	0.01325	0.0002	0.3	278	2	272	5	235	46	278	2	-2.2
Gt0318 037	48	40	0.82	0.05452	0.0032	0.29172	0.0183	0.03881	0.0004	0.01212	0.0001	0.2	245	2	260	14	393	126	245	2	5.8
Gt0318 038	71	69	0.96	0.05143	0.0012	0.28315	0.0072	0.04001	0.0003	0.01249	0.0002	0.3	253	2	253	6	260	52	253	2	0.0
Gt0318 039	131	81	0.62	0.05194	0.001	0.30048	0.0063	0.04198	0.0002	0.01342	0.0002	0.3	265	1	267	5	283	43	265	1	0.7
~~Gt0318 040~~	~~135~~	~~41~~	0.31	~~0.06567~~	~~0.0017~~	~~0.20833~~	~~0.0057~~	~~0.02308~~	~~0.0002~~	~~0.01522~~	~~0.0003~~	~~0.3~~	~~147~~	~~1~~	~~192~~	~~5~~	~~796~~	~~52~~	~~147~~	~~1~~	~~23.4~~
Gt0318 041	47	32	0.69	0.07168	0.001	1.4735	0.0222	0.14927	0.0008	0.04616	0.0007	0.4	897	5	920	9	977	27	897	5	2.5
Gt0318 042	35	13	0.37	0.06799	0.0016	1.16322	0.036	0.12408	0.0018	0.03778	0.0005	0.6	754	10	783	17	868	45	754	10	3.7
~~Gt0318 043~~	~~29~~	~~11~~	0.36	~~0.06969~~	~~0.0018~~	~~0.83151~~	~~0.0232~~	~~0.08693~~	~~0.0009~~	~~0.03859~~	~~0.0008~~	~~0.4~~	~~537~~	~~5~~	~~614~~	~~13~~	~~919~~	~~51~~	~~537~~	~~5~~	~~12.5~~
Gt0318 044	25	10	0.40	0.06737	0.0016	1.30853	0.0361	0.14087	0.0013	0.04293	0.0004	0.4	850	7	849	16	849	47	850	7	-0.1
Gt0318 045	112	127	1.13	0.05096	0.001	0.26984	0.0056	0.03845	0.0002	0.01186	0.0002	0.3	243	1	243	5	239	47	243	1	0.0
Gt0318 046	214	139	0.65	0.05306	0.0008	0.28424	0.0045	0.03892	0.0002	0.01214	0.0002	0.3	246	1	254	4	331	35	246	1	3.1
Gt0318 047	130	96	0.74	0.05107	0.0016	0.2644	0.009	0.03755	0.0002	0.01182	7E-05	0.3	238	1	238	7	244	73	238	1	0.0
Gt0319, deformed diorite. 14°57'56.9" 90°32'49"																					
Gt0319 001	174	190	1.10	0.05289	0.0013	0.24357	0.0061	0.03347	0.0002	0.01064	0.0002	0.3	212	1	221	5	324	52	212	1	4.1
~~Gt0319 002~~	~~115~~	~~80~~	0.70	~~0.05611~~	~~0.0033~~	~~0.21867~~	~~0.0128~~	~~0.02816~~	~~0.0003~~	~~0.00956~~	~~0.0002~~	~~0.2~~	~~179~~	~~2~~	~~201~~	~~11~~	~~457~~	~~124~~	~~179~~	~~2~~	~~10.9~~
Gt0319 003	152	130	0.85	0.05278	0.0029	0.26072	0.0158	0.03583	0.0004	0.01123	0.0001	0.3	227	3	235	13	319	121	227	3	3.4
Gt0319 004	193	137	0.71	0.05156	0.0014	0.23067	0.0071	0.03245	0.0002	0.0102	6E-05	0.3	206	1	211	6	266	62	206	1	2.4
Gt0319 005	193	236	1.22	0.05357	0.001	0.26817	0.0053	0.03628	0.0002	0.01145	0.0002	0.3	230	1	241	4	353	41	230	1	4.6
Gt0319 006	454	836	1.84	0.05139	0.0008	0.24465	0.0039	0.03455	0.0002	0.01056	0.0001	0.3	219	1	222	3	258	33	219	1	1.4
Gt0319 007	155	266	1.72	0.05448	0.0012	0.25889	0.0059	0.03454	0.0002	0.01079	0.0001	0.3	219	1	234	5	391	47	219	1	6.4
Gt0319 008	88	74	0.84	0.05705	0.0014	0.26964	0.0071	0.03432	0.0003	0.01086	0.0002	0.3	218	2	242	6	494	53	218	2	9.9
Gt0319 009	33	12	0.37	0.05327	0.0022	0.26483	0.0116	0.03623	0.0004	0.01115	0.0004	0.3	229	3	239	9	340	92	229	3	4.2
~~Gt0319 010~~	~~235~~	~~396~~	1.68	~~0.05158~~	~~0.0011~~	~~0.24375~~	~~0.0056~~	~~0.0343~~	~~0.0002~~	~~0.01052~~	~~0.0001~~	~~0.3~~	~~217~~	~~1~~	~~221~~	~~5~~	~~267~~	~~48~~	~~217~~	~~1~~	~~1.8~~

DOI: 10.1344/105.000001695

TABLE II | **Continued**

				CORRECTED RATIOS[2]									CORRECTED AGES (Ma)								
Sample number	U[1] (ppm)	Th[1] (ppm)	Th/U	$^{207}Pb/^{206}Pb$	±1σ[3]	$^{207}Pb/^{235}U$	±1σ[3]	$^{206}Pb/^{238}U$	±1σ[3]	$^{208}Pb/^{232}Th$	±1σ[3]	Rho	$^{206}Pb/^{238}U$	±1σ	$^{207}Pb/^{235}U$	±1σ	$^{207}Pb/^{206}Pb$	±1σ	Best age (Ma)	±1σ	% disc
Gt0319 011	52	56	1.07	0.05677	0.0031	0.29136	0.0165	0.0374	0.0006	0.0116	0.0003	0.3	237	4	260	13	483	115	237	4	8.8
Gt0319 012	94	81	0.86	0.05524	0.0021	0.26562	0.0109	0.03488	0.0003	0.01088	9E-05	0.3	221	2	239	9	422	80	221	2	7.5
~~Gt0319 013~~	~~56~~	~~32~~	0.58	~~0.06762~~	~~0.0078~~	~~0.30529~~	~~0.0359~~	~~0.03274~~	~~0.0004~~	~~0.00997~~	~~0.0002~~	~~0.1~~	~~208~~	~~2~~	~~271~~	~~28~~	~~857~~	~~237~~	~~208~~	~~2~~	~~23.2~~
Gt0319 014	70	25	0.36	0.05173	0.0019	0.25589	0.0094	0.03597	0.0003	0.0124	0.0003	0.2	228	2	231	8	273	79	228	2	1.3
Gt0319 015	172	165	0.96	0.05349	0.0009	0.25762	0.0047	0.03497	0.0002	0.01103	0.0001	0.3	222	1	233	4	350	37	222	1	4.7
Gt0319 016	236	197	0.84	0.05147	0.001	0.24512	0.0051	0.03452	0.0002	0.01096	0.0002	0.3	219	1	223	4	262	44	219	1	1.8
Gt0319 017	205	265	1.29	0.0506	0.0009	0.25273	0.0045	0.03628	0.0002	0.0114	0.0002	0.3	230	1	229	4	223	38	230	1	-0.4
Gt0319 018	189	108	0.57	0.05215	0.0013	0.23961	0.0067	0.03332	0.0002	0.01046	7E-05	0.3	211	1	218	5	292	55	211	1	3.2
Gt0319 019	142	119	0.83	0.0527	0.0012	0.2614	0.006	0.0361	0.0002	0.01165	0.0002	0.3	229	1	236	5	316	48	229	1	3.0
~~Gt0319 020~~	~~103~~	~~144~~	1.41	~~0.05883~~	~~0.0015~~	~~0.28057~~	~~0.0073~~	~~0.0348~~	~~0.0003~~	~~0.01096~~	~~0.0001~~	~~0.3~~	~~221~~	~~2~~	~~251~~	~~6~~	~~561~~	~~52~~	~~221~~	~~2~~	~~12.0~~
Gt0319 021	199	203	1.02	0.05139	0.0008	0.2563	0.0044	0.03617	0.0002	0.01122	0.0002	0.4	229	1	232	4	258	35	229	1	1.3
Gt0319 022	35	12	0.34	0.05252	0.0023	0.26265	0.0119	0.03662	0.0004	0.01251	0.0009	0.2	232	2	237	10	308	96	232	2	2.1
Gt0319 023	287	538	1.88	0.05323	0.0008	0.26353	0.0043	0.03594	0.0002	0.01128	0.0002	0.4	228	1	238	3	339	33	228	1	4.2
Gt0319 024	83	96	1.16	0.04737	0.0048	0.2222	0.024	0.03402	0.0004	0.01081	0.0005	0.2	216	2	204	20	68	205	216	2	-5.9
Gt0319 025	36	23	0.64	0.05263	0.0027	0.25519	0.0134	0.03556	0.0004	0.01111	0.0003	0.2	225	3	231	11	313	111	225	3	2.6
Gt0319 026	232	365	1.57	0.05194	0.001	0.25638	0.0053	0.03581	0.0002	0.01116	0.0002	0.3	227	1	232	4	283	44	227	1	2.2
Gt0319 027	191	124	0.65	0.05074	0.001	0.25107	0.005	0.0359	0.0002	0.01077	0.0002	0.3	227	1	227	4	229	42	227	1	0.0
Gt0319 028	172	67	0.39	0.05307	0.0012	0.24866	0.0059	0.03406	0.0002	0.0112	0.0002	0.3	216	1	225	5	332	50	216	1	4.0
Gt0319 029	68	65	0.97	0.05209	0.0016	0.25531	0.008	0.03553	0.0003	0.01128	0.0002	0.3	225	2	231	6	289	66	225	2	2.6
Gt0319 030	137	133	0.97	0.05098	0.0013	0.2512	0.0065	0.03574	0.0003	0.01127	0.0002	0.3	226	2	228	5	240	55	226	2	0.9
Gt0319 031	152	155	1.02	0.05144	0.0011	0.24822	0.0057	0.03491	0.0002	0.01085	0.0002	0.3	221	1	225	5	261	48	221	1	1.8
~~Gt0319 032~~	~~28~~	~~10~~	0.36	~~0.05679~~	~~0.0029~~	~~0.24238~~	~~0.0139~~	~~0.03095~~	~~0.0005~~	~~0.00962~~	~~0.0002~~	~~0.4~~	~~197~~	~~3~~	~~220~~	~~11~~	~~484~~	~~110~~	~~197~~	~~3~~	~~10.5~~
Gt0319 033	168	171	1.02	0.0514	0.0009	0.25164	0.0048	0.03549	0.0002	0.01125	0.0002	0.3	225	1	228	4	259	40	225	1	1.3
Gt0319 034	137	161	1.17	0.05066	0.0014	0.25581	0.0077	0.03656	0.0004	0.01433	0.0003	0.4	231	2	231	6	225	62	231	2	0.0
~~Gt0319 036~~	~~466~~	~~59~~	0.13	~~0.0742~~	~~0.0007~~	~~1.7391~~	~~0.0186~~	~~0.16985~~	~~0.0008~~	~~0.05144~~	~~0.0007~~	~~0.5~~	~~1011~~	~~4~~	~~1023~~	~~7~~	~~1047~~	~~18~~	~~1047~~	~~18~~	~~3.4~~
Gt0319 037	52	55	1.06	0.05236	0.002	0.25793	0.0101	0.03573	0.0003	0.01116	0.0002	0.2	226	2	233	8	301	83	226	2	3.0
Gt0319 038	143	155	1.08	0.05019	0.0011	0.24805	0.0054	0.03592	0.0002	0.01107	0.0002	0.3	227	1	225	4	204	47	227	1	-0.9
Gt0319 039	273	289	1.06	0.05157	0.0008	0.25105	0.0043	0.03531	0.0002	0.01099	0.0002	0.4	224	1	227	4	266	35	224	1	1.3
Gt0319 040	56	39	0.70	0.05428	0.0019	0.28059	0.0101	0.03755	0.0005	0.01275	0.0003	0.3	238	3	251	8	383	74	238	3	5.2
Gt0319 041	92	100	1.09	0.05594	0.0011	0.26826	0.0056	0.0347	0.0002	0.01091	0.0002	0.3	220	1	241	5	450	43	220	1	8.7
Gt0319 042	77	42	0.55	0.0535	0.0017	0.2575	0.0083	0.03501	0.0003	0.01079	0.0003	0.3	222	2	233	7	350	67	222	2	4.7
Gt0319 043	108	121	1.12	0.05685	0.0013	0.2743	0.0066	0.03498	0.0003	0.01108	0.0002	0.3	222	2	246	5	486	49	222	2	9.8
Gt0319 044	188	248	1.32	0.05517	0.0012	0.24863	0.0057	0.03263	0.0002	0.01032	0.0001	0.3	207	1	225	5	419	47	207	1	8.0
Gt0319 045	67	76	1.12	0.05234	0.0024	0.24291	0.0131	0.03366	0.0004	0.01057	0.0001	0.3	213	2	221	11	300	101	213	2	3.6
Gt0319 046	230	315	1.37	0.05512	0.0011	0.25823	0.0052	0.03387	0.0002	0.01082	0.0002	0.3	215	1	233	4	417	41	215	1	7.7
Gt0319 047	129	163	1.27	0.05076	0.0016	0.24913	0.0079	0.0356	0.0003	0.01124	0.0002	0.2	226	2	226	6	230	69	226	2	0.0
Gt0319 048	55	51	0.92	0.05411	0.0033	0.26475	0.0174	0.03549	0.0004	0.01109	0.0001	0.3	225	2	238	14	376	131	225	2	5.5
Gt0319 049	105	73	0.70	0.05038	0.0012	0.25276	0.0063	0.03638	0.0002	0.01162	0.0002	0.3	230	1	229	5	213	53	230	1	-0.4
Gt0319 050	87	125	1.43	0.05655	0.0018	0.27414	0.0088	0.03533	0.0003	0.01121	0.0002	0.3	224	2	246	7	474	66	224	2	8.9
Gt0319 051	243	271	1.12	0.05041	0.0008	0.24875	0.0043	0.03579	0.0002	0.01118	0.0002	0.4	227	1	226	3	214	36	227	1	-0.4
~~Gt0319 052~~	~~302~~	~~440~~	1.46	~~0.01213~~	~~0.0009~~	~~0.05978~~	~~0.0046~~	~~0.03502~~	~~0.0002~~	~~0.01103~~	~~0.0001~~	~~0.1~~	~~222~~	~~1~~	~~59~~	4	~~-1199~~	~~53~~	~~222~~	~~1~~	~~-276.3~~
Gt0319 053	77	83	1.08	0.05724	0.0021	0.30673	0.0116	0.03885	0.0003	0.01591	0.0004	0.2	246	2	272	9	501	78	246	2	9.6
Gt0319 054	257	424	1.65	0.0508	0.0009	0.23996	0.0047	0.03426	0.0003	0.0106	0.0001	0.4	217	2	218	4	232	40	217	2	0.5
Gt0319 055	203	228	1.12	0.05244	0.0012	0.25258	0.0058	0.03492	0.0002	0.01068	0.0002	0.3	221	1	229	5	305	48	221	1	3.5
Gt0319 056	188	219	1.17	0.05084	0.001	0.25009	0.005	0.03564	0.0002	0.01112	0.0002	0.3	226	1	227	4	234	42	226	1	0.4
Gt0319 057	163	168	1.03	0.05094	0.001	0.24975	0.0051	0.03557	0.0003	0.01088	0.0001	0.4	225	2	226	4	238	42	225	2	0.4
Gt0319 058	118	91	0.78	0.05032	0.0012	0.24181	0.0058	0.03495	0.0003	0.01083	0.0002	0.3	221	2	220	5	210	51	221	2	-0.5
Gt0319 059	337	461	1.37	0.05028	0.0007	0.24739	0.0037	0.03568	0.0002	0.01109	0.0001	0.4	226	1	224	3	208	31	226	1	-0.9
Gt0319 060	71	86	1.20	0.05629	0.0015	0.27013	0.0077	0.0349	0.0003	0.01088	0.0002	0.3	221	2	243	6	464	57	221	2	9.1
Gt0320, deformed gabbro. 14°57'56.9" 90°32'49"																					
Gt0320 001	159	219	1.38	0.05193	0.0013	0.2425	0.0063	0.03389	0.0003	0.01083	0.0002	0.3	215	2	220	5	282	57	215	2	2.3
Gt0320 002	127	165	1.30	0.05008	0.002	0.22839	0.0102	0.03308	0.0003	0.01044	8E-05	0.3	210	2	209	8	198	84	210	2	-0.5
Gt0320 003	218	147	0.67	0.05047	0.0009	0.24749	0.0047	0.03559	0.0002	0.01153	0.0002	0.3	225	1	225	4	217	41	225	1	0.0
Gt0320 006	32	17	0.54	0.05578	0.0026	0.26003	0.0123	0.03382	0.0004	0.01043	0.0003	0.2	214	2	235	10	444	101	214	2	8.9
Gt0320 008	34	26	0.76	0.05062	0.003	0.23971	0.0164	0.03434	0.0006	0.01082	0.0002	0.4	218	4	218	13	224	131	218	4	0.0
Gt0320 009	113	147	1.30	0.05359	0.0013	0.25896	0.0065	0.03509	0.0003	0.01086	0.0002	0.3	222	2	234	5	354	54	222	2	5.1
Gt0320 010	176	245	1.39	0.05617	0.001	0.26754	0.0051	0.0346	0.0002	0.01085	0.0001	0.3	219	1	241	4	459	37	219	1	9.1
Gt0320 011	80	97	1.22	0.05419	0.0015	0.26309	0.0074	0.03528	0.0003	0.01077	0.0002	0.3	224	2	237	6	379	56	224	2	5.5
Gt0320 012	99	125	1.26	0.05035	0.0013	0.24619	0.0066	0.03548	0.0003	0.01126	0.0002	0.3	225	2	223	5	211	56	225	2	-0.9
Gt0320 013	84	55	0.66	0.0523	0.0015	0.25756	0.0077	0.03574	0.0003	0.011	0.0002	0.2	226	2	233	6	299	62	226	2	3.0
Gt0320 014	75	53	0.70	0.05437	0.0016	0.26781	0.008	0.03571	0.0003	0.01137	0.0002	0.3	226	2	241	6	386	61	226	2	6.2
~~Gt0320 015~~	~~114~~	~~140~~	1.23	~~0.05915~~	~~0.0012~~	~~0.26566~~	~~0.0059~~	~~0.0326~~	~~0.0002~~	~~0.01097~~	~~0.0002~~	~~0.3~~	~~207~~	~~1~~	~~239~~	~~5~~	~~573~~	~~42~~	~~207~~	~~1~~	~~13.4~~
Gt0320 016	158	215	1.36	0.05474	0.0024	0.25174	0.0119	0.03336	0.0002	0.01041	7E-05	0.2	212	1	228	10	401	91	212	1	7.0
~~Gt0320 017~~	~~85~~	~~103~~	1.21	~~0.06418~~	~~0.002~~	~~0.28442~~	~~0.0092~~	~~0.03209~~	~~0.0003~~	~~0.01138~~	~~0.0002~~	~~0.3~~	~~204~~	~~2~~	~~254~~	~~7~~	~~748~~	~~65~~	~~204~~	~~2~~	~~19.7~~

DOI: 10.1344/105.000001695

TABLE II | **Continued**

				CORRECTED RATIOS[2]									CORRECTED AGES (Ma)								
Sample number	U[1] (ppm)	Th[1] (ppm)	Th/U	$^{207}Pb/^{206}Pb$	±1σ[3]	$^{207}Pb/^{235}U$	±1σ[3]	$^{206}Pb/^{238}U$	±1σ[3]	$^{208}Pb/^{232}Th$	±1σ[3]	Rho	$^{206}Pb/^{238}U$	±1σ	$^{207}Pb/^{235}U$	±1σ	$^{207}Pb/^{206}Pb$	±1σ	Best age (Ma)	±1σ	% disc
Gt0320 018	49	24	0.49	0.05201	0.0017	0.25288	0.0086	0.03528	0.0003	0.01138	0.0003	0.2	224	2	229	7	286	70	224	2	2.2
~~Gt0320 019~~	~~74~~	~~50~~	0.67	~~0.06414~~	~~0.0019~~	~~0.27876~~	~~0.0086~~	~~0.03149~~	~~0.0003~~	~~0.01253~~	~~0.0003~~	~~0.3~~	~~200~~	~~2~~	~~250~~	~~7~~	~~746~~	~~60~~	~~200~~	~~2~~	~~20.0~~
Gt0320 020	147	101	0.69	0.05243	0.0011	0.26328	0.0055	0.03647	0.0002	0.01154	0.0002	0.3	231	1	237	4	304	42	231	1	2.5
Gt0320 021	105	115	1.10	0.05131	0.0013	0.25308	0.0068	0.03583	0.0003	0.01126	0.0002	0.3	227	2	229	6	255	55	227	2	0.9
Gt0320 022	89	33	0.38	0.05156	0.0013	0.25543	0.0066	0.03599	0.0003	0.01245	0.0003	0.3	228	2	231	5	266	53	228	2	1.3
Gt0320 023	96	62	0.65	0.05087	0.0016	0.24895	0.0087	0.03549	0.0003	0.01118	9E-05	0.3	225	2	226	7	235	67	225	2	0.4
~~Gt0320 024~~	~~65~~	~~65~~	1.00	~~0.06372~~	~~0.0028~~	~~0.283~~	~~0.014~~	~~0.03221~~	~~0.0004~~	~~0.00988~~	~~0.0001~~	~~0.3~~	~~204~~	~~2~~	~~253~~	~~11~~	~~732~~	~~91~~	~~204~~	~~2~~	~~19.4~~
Gt0320 025	74	68	0.92	0.05165	0.0024	0.26023	0.0124	0.0366	0.0004	0.01163	0.0002	0.3	232	3	235	10	270	104	232	3	1.3
Gt0320 026	101	74	0.74	0.05144	0.0011	0.2544	0.006	0.03591	0.0003	0.01167	0.0002	0.4	227	2	230	5	261	47	227	2	1.3
Gt0320 027	67	79	1.17	0.0527	0.0016	0.26	0.0083	0.03585	0.0003	0.0113	0.0002	0.3	227	2	235	7	316	65	227	2	3.4
Gt0320 028	74	70	0.95	0.05382	0.0017	0.26713	0.0085	0.03596	0.0003	0.01153	0.0002	0.2	228	2	240	7	364	69	228	2	5.0
Gt0320 029	37	31	0.84	0.05355	0.0026	0.24643	0.0133	0.03338	0.0004	0.01045	0.0001	0.3	212	2	224	11	352	107	212	2	5.4
Gt0320 030	52	48	0.91	0.05399	0.0026	0.25513	0.0135	0.03427	0.0004	0.01072	0.0001	0.3	217	2	231	11	371	106	217	2	6.1
~~Gt0320 031~~	~~141~~	~~182~~	1.30	~~0.05767~~	~~0.0016~~	~~0.25175~~	~~0.0073~~	~~0.03159~~	~~0.0002~~	~~0.01064~~	~~0.0002~~	~~0.3~~	~~200~~	~~1~~	~~228~~	~~6~~	~~517~~	~~60~~	~~200~~	~~1~~	~~12.3~~
Gt0320 032	74	86	1.16	0.0553	0.0018	0.26207	0.0087	0.03457	0.0003	0.01093	0.0002	0.3	219	2	236	7	424	70	219	2	7.2
Gt0320 033	63	55	0.86	0.05121	0.0015	0.25297	0.0078	0.03599	0.0003	0.01101	0.0002	0.2	228	2	229	6	250	68	228	2	0.4
Gt0320 034	85	40	0.47	0.05283	0.0016	0.25602	0.0079	0.03528	0.0003	0.0117	0.0002	0.3	224	2	231	6	322	67	224	2	3.0
Gt0320 035	60	57	0.95	0.05174	0.0016	0.23192	0.0072	0.03259	0.0003	0.01055	0.0002	0.3	207	2	212	6	274	68	207	2	2.4
Gt0320 036	195	175	0.90	0.05192	0.0009	0.24781	0.0047	0.03461	0.0002	0.01048	0.0002	0.4	219	1	225	4	282	40	219	1	2.7
Gt0320 037	88	60	0.68	0.05301	0.0015	0.26491	0.0079	0.03625	0.0004	0.01132	0.0002	0.4	230	2	239	6	329	62	230	2	3.8
Gt0320 038	180	299	1.66	0.05174	0.0009	0.24858	0.0047	0.03491	0.0002	0.0106	0.0002	0.3	221	1	225	4	274	41	221	1	1.8
Gt0320 039	240	260	1.09	0.05072	0.0008	0.24573	0.0042	0.03517	0.0002	0.01101	0.0002	0.3	223	1	223	3	228	36	223	1	0.0
Gt0320 040	247	303	1.23	0.052	0.0008	0.25266	0.0043	0.03528	0.0002	0.01106	0.0001	0.3	224	1	229	3	285	36	224	1	2.2
Gt0320 041	185	120	0.65	0.05303	0.001	0.26095	0.0052	0.03571	0.0002	0.01141	0.0002	0.3	226	1	235	4	330	43	226	1	3.8
Gt0320 042	104	140	1.34	0.05217	0.0015	0.25558	0.0075	0.03561	0.0003	0.01131	0.0002	0.3	226	2	231	6	293	63	226	2	2.2
Gt0320 043	203	176	0.87	0.0521	0.0008	0.25456	0.0044	0.03549	0.0002	0.01096	0.0002	0.4	225	1	230	4	290	36	225	1	2.2
Gt0320 044	66	66	1.00	0.05325	0.0016	0.25415	0.0079	0.03475	0.0003	0.01079	0.0002	0.2	220	2	230	6	339	67	220	2	4.3
Gt0321, Agua Caliente River felsic orthogneiss. 14°56'07.8" 90°30'10.9"																					
Gt0321 006	431	218	0.51	0.05126	0.0017	0.24029	0.0088	0.03395	0.0004	0.01079	0.0003	0.4	215	3	219	7	253	72	215	3	1.8
Gt0321 007	179	95	0.53	0.05188	0.0032	0.20801	0.0136	0.02908	0.0004	0.00914	0.0001	0.3	185	3	192	11	280	127	185	3	3.6
~~Gt0321 008~~	~~188~~	~~160~~	0.85	~~0.06164~~	~~0.0036~~	~~0.21883~~	~~0.0133~~	~~0.02578~~	~~0.0005~~	~~0.00981~~	~~0.0003~~	~~0.3~~	~~164~~	~~3~~	~~201~~	~~11~~	~~662~~	~~115~~	~~164~~	~~3~~	~~18.4~~
Gt0321 009	74	46	0.62	0.05423	0.004	0.24508	0.0196	0.03277	0.0006	0.01024	0.0002	0.2	208	3	223	16	381	153	208	3	6.7
Gt0321 010	937	726	0.78	0.05064	0.0013	0.23386	0.0064	0.03344	0.0004	0.00932	0.0002	0.4	212	2	213	5	224	53	212	2	0.5
~~Gt0321 012~~	~~179~~	~~162~~	0.90	~~0.05747~~	~~0.0034~~	~~0.27443~~	~~0.0175~~	~~0.03463~~	~~0.0004~~	~~0.01075~~	~~0.0001~~	~~0.2~~	~~219~~	~~2~~	~~246~~	~~14~~	~~510~~	~~119~~	~~219~~	~~2~~	~~11.0~~
Gt0321 013	193	155	0.81	0.05688	0.0022	0.27085	0.0106	0.03462	0.0004	0.01024	0.0003	0.3	219	2	243	9	487	77	219	2	9.9
~~Gt0321 014~~	~~261~~	~~191~~	0.73	~~0.05866~~	~~0.0025~~	~~0.29499~~	~~0.0141~~	~~0.03647~~	~~0.0003~~	~~0.01129~~	~~9E-05~~	~~0.3~~	~~231~~	~~2~~	~~262~~	~~11~~	~~554~~	~~87~~	~~231~~	~~2~~	~~11.8~~
~~Gt0321 015~~	~~116~~	~~86~~	0.75	~~0.06322~~	~~0.0037~~	~~0.32086~~	~~0.0189~~	~~0.03664~~	~~0.0004~~	~~0.01119~~	~~0.0003~~	~~0.2~~	~~232~~	~~2~~	~~283~~	~~15~~	~~716~~	~~114~~	~~232~~	~~2~~	~~18.0~~
Gt0321 016	170	176	1.04	0.05536	0.0032	0.28553	0.0166	0.03745	0.0004	0.01045	0.0003	0.2	237	3	255	13	427	118	237	3	7.1
~~Gt0321 018~~	~~177~~	~~52~~	0.29	~~0.06761~~	~~0.0051~~	~~0.317~~	~~0.025~~	~~0.034~~	~~0.0004~~	~~0.01036~~	~~0.0003~~	~~0.3~~	~~216~~	~~2~~	~~280~~	~~19~~	~~857~~	~~144~~	~~216~~	~~2~~	~~22.9~~
Gt0321 019	162	128	0.79	0.05307	0.0022	0.26791	0.0119	0.03634	0.0005	0.01046	0.0003	0.3	230	3	241	9	332	88	230	3	4.6
Gt0321 020	263	185	0.70	0.0561	0.0031	0.30224	0.0178	0.03908	0.0003	0.01216	0.0001	0.2	247	2	268	14	456	113	247	2	7.8
Gt0321 021	635	574	0.90	0.05042	0.0014	0.23915	0.0071	0.03437	0.0003	0.00984	0.0002	0.3	218	2	218	6	214	60	218	2	0.0
Gt0321 022	747	666	0.89	0.05077	0.001	0.23847	0.0053	0.03399	0.0003	0.01053	0.0002	0.4	215	2	217	4	230	43	215	2	0.9
~~Gt0321 024~~	~~217~~	~~177~~	0.82	~~0.05957~~	~~0.0017~~	~~0.2938~~	~~0.0087~~	~~0.03582~~	~~0.0003~~	~~0.01142~~	~~0.0003~~	~~0.3~~	~~227~~	~~2~~	~~262~~	~~7~~	~~588~~	~~56~~	~~227~~	~~2~~	~~13.4~~
~~Gt0321 025~~	~~217~~	~~195~~	0.90	~~0.05706~~	~~0.0019~~	~~0.29318~~	~~0.0104~~	~~0.03711~~	~~0.0004~~	~~0.01073~~	~~0.0003~~	~~0.3~~	~~235~~	~~2~~	~~261~~	~~8~~	~~494~~	~~69~~	~~235~~	~~2~~	~~10.0~~
~~Gt0321 026~~	~~143~~	~~92~~	0.64	~~0.05845~~	~~0.0027~~	~~0.27575~~	~~0.013~~	~~0.03424~~	~~0.0004~~	~~0.01105~~	~~0.0003~~	~~0.2~~	~~217~~	~~2~~	~~247~~	~~10~~	~~547~~	~~93~~	~~217~~	~~2~~	~~12.1~~
Gt0321 027	121	91	0.76	0.05678	0.0023	0.30485	0.0129	0.03885	0.0004	0.01191	0.0003	0.3	246	3	270	10	483	83	246	3	8.9
~~Gt0321 028~~	~~213~~	~~163~~	0.76	~~0.06631~~	~~0.0057~~	~~0.33287~~	~~0.0306~~	~~0.03641~~	~~0.0005~~	~~0.01112~~	~~0.0001~~	~~0.2~~	~~231~~	~~3~~	~~292~~	~~23~~	~~816~~	~~167~~	~~231~~	~~3~~	~~20.9~~
Gt0321 030	167	66	0.39	0.04961	0.0053	0.22667	0.0254	0.03314	0.0005	0.01047	0.0007	0.2	210	3	207	21	177	215	210	3	-1.4
~~Gt0321 031~~	~~86~~	~~48~~	0.56	~~0.0671~~	~~0.0042~~	~~0.32966~~	~~0.021~~	~~0.03567~~	~~0.0005~~	~~0.01069~~	~~0.0004~~	~~0.2~~	~~226~~	~~3~~	~~289~~	~~16~~	~~841~~	~~124~~	~~226~~	~~3~~	~~21.8~~
~~Gt0321 032~~	~~147~~	~~100~~	0.68	~~0.05806~~	~~0.003~~	~~0.28733~~	~~0.0155~~	~~0.03586~~	~~0.0007~~	~~0.01169~~	~~0.0003~~	~~0.3~~	~~227~~	~~4~~	~~256~~	~~12~~	~~532~~	~~107~~	~~227~~	~~4~~	~~11.3~~
Gt0321 033	1942	147	0.08	0.07937	0.0013	1.96167	0.0343	0.17926	0.0012	0.05365	0.0004	0.4	1063	7	1102	12	1181	30	~~1181~~	~~30~~	10.0
Gt0321 034	464	297	0.64	0.06082	0.0013	0.48084	0.0114	0.05725	0.0005	0.01158	0.0005	0.4	359	3	399	8	633	45	~~359~~	~~3~~	10.0
~~Gt0321 036~~	~~379~~	~~151~~	0.40	~~0.07518~~	~~0.0014~~	~~1.6405~~	~~0.0329~~	~~0.1583~~	~~0.001~~	~~0.03983~~	~~0.0009~~	~~0.3~~	~~947~~	~~6~~	~~986~~	~~13~~	~~1073~~	~~36~~	~~1073~~	~~36~~	~~11.7~~
Gt0321 037	1453	291	0.20	0.07227	0.0012	1.5936	0.0283	0.15958	0.0012	0.05373	0.0011	0.4	954	7	968	11	994	31	~~954~~	~~7~~	1.4
~~Gt0321 038~~	~~201~~	~~197~~	0.98	~~0.06541~~	~~0.0018~~	~~0.31677~~	~~0.0094~~	~~0.0353~~	~~0.0004~~	~~0.01139~~	~~0.0003~~	~~0.3~~	~~224~~	~~2~~	~~279~~	~~7~~	~~788~~	~~55~~	~~224~~	~~2~~	~~19.7~~
~~Gt0321 039~~	~~186~~	~~218~~	1.17	~~0.08744~~	~~0.0061~~	~~0.40081~~	~~0.0324~~	~~0.03324~~	~~0.0007~~	~~0.00985~~	~~0.0002~~	~~0.4~~	~~211~~	~~4~~	~~342~~	~~23~~	~~1370~~	~~130~~	~~211~~	~~4~~	~~38.3~~
~~Gt0321 040~~	~~213~~	~~11~~	0.05	~~0.06939~~	~~0.0033~~	~~0.15727~~	~~0.0077~~	~~0.01641~~	~~0.0002~~	~~0.03163~~	~~0.0013~~	~~0.2~~	~~104.9~~	~~1~~	~~148~~	~~7~~	~~910~~	~~94~~	~~105~~	~~1~~	~~29.1~~
~~Gt0321 042~~	~~191~~	~~170~~	0.89	~~0.05955~~	~~0.0024~~	~~0.29392~~	~~0.0122~~	~~0.03582~~	~~0.0004~~	~~0.0114~~	~~0.0003~~	~~0.3~~	~~227~~	~~2~~	~~262~~	~~10~~	~~587~~	~~82~~	~~227~~	~~2~~	~~13.4~~
~~Gt0321 043~~	~~114~~	~~100~~	0.88	~~0.05677~~	~~0.0025~~	~~0.27619~~	~~0.0125~~	~~0.03523~~	~~0.0004~~	~~0.01114~~	~~0.0003~~	~~0.2~~	~~223~~	~~2~~	~~248~~	~~10~~	~~483~~	~~93~~	~~223~~	~~2~~	~~10.1~~
Gt0321 044	581	619	1.07	0.05299	0.0019	0.24317	0.0089	0.03328	0.0003	0.00966	0.0002	0.3	211	2	221	7	328	75	211	2	4.5
Gt0321 045	1163	959	0.82	0.04827	0.0012	0.22207	0.0058	0.03327	0.0003	0.0099	0.0003	0.4	211	2	204	5	113	53	211	2	-3.4
~~Gt0321 046~~	~~493~~	~~506~~	1.03	~~0.06325~~	~~0.0036~~	~~0.29986~~	~~0.0186~~	~~0.03438~~	~~0.0003~~	~~0.01055~~	~~0.0001~~	~~0.2~~	~~218~~	~~2~~	~~266~~	~~14~~	~~717~~	~~116~~	~~218~~	~~2~~	~~18.0~~
~~Gt0321 048~~	~~159~~	~~142~~	0.89	~~0.05622~~	~~0.0024~~	~~0.2632~~	~~0.0115~~	~~0.03386~~	~~0.0004~~	~~0.01024~~	~~0.0003~~	~~0.3~~	~~215~~	~~3~~	~~237~~	~~9~~	~~461~~	~~89~~	~~215~~	~~3~~	~~9.3~~

TABLE II | **Continued**

				CORRECTED RATIOS[2]									CORRECTED AGES (Ma)								
Sample number	U^1 (ppm)	Th^1 (ppm)	Th/U	$^{207}Pb/^{206}Pb$	$\pm1\sigma^3$	$^{207}Pb/^{235}U$	$\pm1\sigma^3$	$^{206}Pb/^{238}U$	$\pm1\sigma^3$	$^{208}Pb/^{232}Th$	$\pm1\sigma^3$	Rho	$^{206}Pb/^{238}U$	$\pm1\sigma$	$^{207}Pb/^{235}U$	$\pm1\sigma$	$^{207}Pb/^{206}Pb$	$\pm1\sigma$	Best age (Ma)	$\pm1\sigma$	% disc
Gt0321 049	206	202	0.98	0.05473	0.0022	0.28063	0.0118	0.03714	0.0004	0.01061	0.0003	0.2	235	2	251	9	401	87	235	2	6.4
~~Gt0321 050~~	~~185~~	~~116~~	0.63	~~0.06559~~	~~0.0046~~	~~0.32865~~	~~0.0233~~	~~0.03666~~	~~0.0004~~	~~0.01289~~	~~0.0009~~	~~0.2~~	~~232~~	~~3~~	~~289~~	~~18~~	~~793~~	~~142~~	~~232~~	~~3~~	~~19.7~~
Gt0321 051	268	217	0.81	0.0552	0.0032	0.26841	0.0175	0.03527	0.0005	0.011	0.0001	0.3	223	3	241	14	420	124	223	3	7.5
Gt0321 052	450	364	0.81	0.04911	0.0011	0.2339	0.0057	0.03455	0.0003	0.01084	0.0003	0.4	219	2	213	5	153	51	219	2	-2.8
~~Gt0321 054~~	~~294~~	~~209~~	0.71	~~0.12527~~	~~0.0058~~	~~0.4311~~	~~0.0206~~	~~0.02427~~	~~0.0003~~	~~0.01601~~	~~0.0009~~	~~0.3~~	~~155~~	~~2~~	~~364~~	~~15~~	~~2033~~	~~77~~	~~2033~~	~~77~~	~~57.4~~
Gt0321 055	533	459	0.86	0.05149	0.0014	0.25623	0.0072	0.03599	0.0003	0.01169	0.0003	0.3	228	2	232	6	263	59	228	2	1.7
Gt0321 056	761	739	0.97	0.05314	0.0012	0.25035	0.0061	0.03414	0.0003	0.01022	0.0003	0.3	216	2	227	5	335	49	216	2	4.8
Gt0321 057	488	318	0.65	0.05476	0.0015	0.26903	0.0075	0.03566	0.0003	0.01101	0.0003	0.3	226	2	242	6	402	57	226	2	6.6
Gt0321 058	709	773	1.09	0.04941	0.0013	0.24287	0.0068	0.03559	0.0003	0.01049	0.0003	0.3	225	2	221	6	167	59	225	2	-1.8
Gt0321 060	647	498	0.77	0.05343	0.0025	0.26112	0.0143	0.03544	0.0005	0.0111	0.0001	0.5	225	3	236	11	347	100	225	3	4.7
Gt0321 061	223	153	0.69	0.05441	0.0017	0.27448	0.0089	0.0366	0.0004	0.01156	0.0003	0.3	232	2	246	7	388	66	232	2	5.7
Gt0321 062	229	99	0.43	0.06956	0.0019	1.0235	0.0291	0.10704	0.0009	0.02579	0.0006	0.3	656	5	716	15	915	49	~~656~~	~~5~~	8.4
~~Gt0321 063~~	~~1319~~	~~1568~~	1.19	~~0.06004~~	~~0.0011~~	~~0.25948~~	~~0.0061~~	~~0.03141~~	~~0.0005~~	~~0.00918~~	~~0.0002~~	~~0.6~~	~~199~~	~~3~~	~~234~~	~~5~~	~~605~~	~~37~~	~~199~~	~~3~~	~~15.0~~
Gt0321 064	182	158	0.87	0.05367	0.0018	0.27447	0.0096	0.03715	0.0003	0.01174	0.0003	0.2	235	2	246	8	357	73	235	2	4.5
Gt0332, El Chol migmatite leucosome. 14°57'53.6" 90°29'12.5"																					
Gt0332 001	156	15	0.10	0.05633	0.0008	0.46378	0.0074	0.05955	0.0003	0.01948	0.0005	0.4	373	2	387	5	465	33	373	2	3.6
Gt0332 002	148	15	0.10	0.05635	0.0021	0.44983	0.0173	0.0579	0.0005	0.01801	0.0003	0.3	363	3	377	12	466	76	363	3	3.7
~~Gt0332 003~~	~~284~~	~~39~~	0.14	~~0.07629~~	~~0.0009~~	~~1.62574~~	~~0.0274~~	~~0.15456~~	~~0.0015~~	~~0.04646~~	~~0.0005~~	~~0.6~~	~~926~~	~~8~~	~~980~~	~~11~~	~~1103~~	~~23~~	~~1103~~	~~23~~	~~16.0~~
Gt0332 004	263	53	0.20	0.07297	0.0008	1.5346	0.021	0.15235	0.0012	0.04762	0.0008	0.6	914	7	944	8	1013	21	914	7	3.2
Gt0332 005	105	5	0.05	0.06633	0.0012	0.98129	0.0294	0.10606	0.0026	0.04536	0.0064	0.8	650	15	694	15	817	38	650	15	6.3
Gt0332 006	299	4	0.01	0.05772	0.0008	0.53746	0.01	0.06753	0.0009	0.02095	0.0003	0.7	421	5	437	7	519	29	421	5	3.7
Gt0332 007	100	1	0.01	0.05546	0.0015	0.26155	0.0073	0.03432	0.0002	0.01188	0.0025	0.3	218	1	236	6	431	60	218	1	7.6
Gt0332 008	350	103	0.29	0.07138	0.0007	1.367	0.0157	0.13875	0.0008	0.04191	0.0006	0.5	838	4	875	7	968	20	838	4	4.2
Gt0332 009	1100	4	0.004	0.05453	0.0006	0.40614	0.0049	0.05405	0.0003	0.04423	0.0021	0.4	339	2	346	4	393	25	339	2	2.0
~~Gt0332 010~~	~~60~~	~~20~~	0.34	~~0.07494~~	~~0.0013~~	~~1.6493~~	~~0.0298~~	~~0.15927~~	~~0.001~~	~~0.04813~~	~~0.0008~~	~~0.4~~	~~953~~	~~6~~	~~989~~	~~11~~	~~1067~~	~~32~~	~~1067~~	~~32~~	~~10.7~~
Gt0332 011	80	16	0.20	0.07027	0.002	1.27995	0.0387	0.1321	0.0009	0.04007	0.0004	0.3	800	5	837	17	936	54	800	5	4.4
Gt0332 012	414	77	0.19	0.05658	0.0007	0.42168	0.0072	0.05401	0.0006	0.01729	0.0004	0.6	339	4	357	5	475	28	339	4	5.0
Gt0332 013	133	38	0.28	0.07302	0.0008	1.5136	0.0185	0.15011	0.0008	0.04653	0.0007	0.4	902	4	936	7	1015	21	902	4	3.6
Gt0332 014	349	12	0.03	0.05626	0.0007	0.54576	0.0074	0.07036	0.0004	0.02189	0.0003	0.4	438	2	442	5	463	25	438	2	0.9
Gt0332 015	51	29	0.57	0.07281	0.0015	1.62334	0.0392	0.1617	0.0012	0.04885	0.0003	0.4	966	7	979	15	1009	39	966	7	1.3
Gt0332 016	58	12	0.20	0.07515	0.0021	1.45896	0.0413	0.1408	0.0008	0.04239	0.0003	0.2	849	5	914	17	1073	52	849	5	7.1
Gt0332 017	269	8	0.03	0.05359	0.0007	0.40993	0.0062	0.05547	0.0003	0.01736	0.0001	0.4	348	2	349	4	354	29	348	2	0.3
Gt0332 018	84	1	0.01	0.05178	0.0014	0.39775	0.0114	0.05558	0.0007	0.02382	0.0026	0.4	349	4	340	8	276	56	349	4	-2.6
~~Gt0332 019~~	~~94~~	~~1~~	0.01	~~0.06401~~	~~0.0028~~	~~0.30196~~	~~0.0137~~	~~0.03421~~	~~0.0004~~	~~0.01049~~	~~0.0014~~	~~0.3~~	~~217~~	~~2~~	~~268~~	~~11~~	~~742~~	~~92~~	~~217~~	~~2~~	~~19.0~~
Gt0332 020	329	18	0.06	0.05804	0.001	0.51963	0.0151	0.06494	0.0013	0.02013	0.0004	0.8	406	8	425	10	531	35	406	8	4.5
Gt0332 021	181	41	0.23	0.07645	0.0008	1.9312	0.0238	0.18303	0.001	0.05405	0.0008	0.5	1084	6	1092	8	1107	21	1107	21	2.1
Gt0332 022	93	1	0.01	0.05264	0.0013	0.29048	0.0084	0.04002	0.0005	0.01255	0.0003	0.5	253	3	259	7	313	57	253	3	2.3
Gt0332 023	236	18	0.07	0.06059	0.0008	0.75052	0.0112	0.08984	0.0006	0.02771	0.0002	0.4	555	3	569	6	625	26	555	3	2.5
Gt0332 024	103	1	0.01	0.05421	0.0015	0.26188	0.0077	0.03504	0.0002	0.01095	0.0004	0.2	222	1	236	6	380	60	222	1	5.9
Gt0332 025	363	32	0.09	0.058	0.0009	0.66101	0.0289	0.0802	0.0033	0.0255	0.0011	0.9	497	20	515	18	530	31	497	20	3.5
Gt0332 026	75	20	0.27	0.07045	0.001	1.4959	0.0341	0.15327	0.0028	0.04859	0.001	0.8	919	15	929	14	942	27	919	15	1.1
Gt0332 027	51	57	1.13	0.07212	0.0011	1.6353	0.0264	0.16461	0.001	0.05075	0.0007	0.4	982	5	984	10	989	29	982	5	0.2
Gt0332 028	274	89	0.32	0.07746	0.0007	2.1525	0.0228	0.20122	0.0009	0.05931	0.0008	0.4	1182	5	1166	7	1133	18	1133	18	-4.3
Gt0332 029	530	187	0.35	0.05469	0.0007	0.44225	0.0059	0.05859	0.0003	0.01763	0.0003	0.4	367	2	372	4	400	26	367	2	1.3
Gt0332 030	5	0	0.07	0.07465	0.0033	1.61938	0.0768	0.15733	0.0023	0.0474	0.0008	0.4	942	13	978	30	1059	83	1059	83	3.7
Gt0332 031	84	88	1.05	0.07159	0.0012	1.551	0.0302	0.15707	0.0015	0.04713	0.0007	0.5	940	8	951	12	974	33	940	8	1.2
~~Gt0332 032~~	~~92~~	~~75~~	0.81	~~0.07044~~	~~0.0009~~	~~1.6456~~	~~0.0239~~	~~0.16929~~	~~0.0011~~	~~0.04881~~	~~0.0007~~	~~0.4~~	~~1008~~	~~6~~	~~988~~	~~9~~	~~941~~	~~25~~	~~1008~~	~~6~~	~~-7.1~~
Gt0332 033	73	18	0.25	0.06704	0.0011	1.16447	0.022	0.12598	0.0009	0.03841	0.0003	0.4	765	5	784	10	839	32	765	5	2.4
Gt0332 034	3129	35	0.01	0.05292	0.0009	0.37554	0.0077	0.05147	0.0006	0.01613	0.001	0.7	324	3	324	6	325	35	324	3	0.0
Gt0332 035	214	79	0.37	0.06621	0.0015	0.90604	0.0296	0.09925	0.0015	0.03031	0.0004	0.7	610	9	655	16	813	45	610	9	6.9
Gt0332 036	327	145	0.44	0.07	0.001	1.18686	0.0225	0.12298	0.0009	0.03732	0.0003	0.6	748	5	795	10	928	28	748	5	5.9
Gt0332 037	13	12	0.92	0.07048	0.003	1.2357	0.0537	0.12777	0.0014	0.03853	0.0009	0.3	775	8	817	24	942	81	775	8	5.1
Gt0332 038	28	36	1.26	0.06676	0.004	1.10625	0.0737	0.12018	0.0014	0.03666	0.0004	0.4	732	8	756	36	830	117	732	8	3.2
Gt0332 039	101	15	0.14	0.07222	0.001	1.561	0.0235	0.15669	0.0009	0.04896	0.001	0.4	938	5	955	9	992	27	938	5	1.8
Gt0332 040	301	142	0.47	0.07419	0.0007	1.7429	0.0182	0.17007	0.0007	0.05168	0.0007	0.4	1012	4	1025	7	1047	18	1047	18	3.3
Gt0332 041	99	10	0.10	0.07702	0.0013	1.82071	0.0353	0.17145	0.001	0.05148	0.001	0.4	1020	6	1053	13	1122	34	1122	34	9.1
Gt0332 042	126	12	0.10	0.07199	0.0008	1.56688	0.0196	0.15786	0.0007	0.04775	0.0002	0.4	945	4	957	8	986	22	945	4	1.3
Gt0332 043	168	89	0.53	0.07603	0.0008	1.9919	0.0252	0.19007	0.0012	0.05634	0.0008	0.5	1122	6	1113	9	1096	21	1096	21	-2.4
Gt0332 044	275	80	0.29	0.0764	0.0008	1.821	0.0218	0.17278	0.0008	0.05321	0.0007	0.4	1027	4	1053	8	1106	22	1106	22	7.1
Gt0332 045	185	52	0.28	0.07685	0.0009	1.944	0.0233	0.18323	0.0009	0.05497	0.0007	0.4	1085	5	1096	8	1117	22	1117	22	2.9
Gt0332 046	54	29	0.53	0.07689	0.0012	1.8505	0.0329	0.17446	0.0017	0.05039	0.0009	0.5	1037	9	1064	12	1118	30	1118	30	7.2
Gt0332 047	533	190	0.36	0.07324	0.0007	1.7632	0.0198	0.17447	0.0012	0.05385	0.0008	0.6	1037	6	1032	7	1021	18	1021	18	-1.6
Gt0332 048	345	146	0.42	0.07387	0.0007	1.6993	0.0176	0.16665	0.0008	0.05005	0.0007	0.4	994	4	1008	7	1038	19	1038	19	4.2
~~Gt0332 049~~	~~10~~	4	0.40	~~0.0596~~	~~0.0045~~	~~0.69668~~	~~0.0563~~	~~0.08478~~	~~0.0012~~	~~0.0262~~	~~0.0004~~	~~0.3~~	~~525~~	~~7~~	~~537~~	~~34~~	~~589~~	~~166~~	~~525~~	~~7~~	~~2.2~~

TABLE II | **Continued**

				CORRECTED RATIOS[2]										CORRECTED AGES (Ma)								
Sample number	U[1] (ppm)	Th[1] (ppm)	Th/U	$^{207}Pb/^{206}Pb$	±1σ[3]	$^{207}Pb/^{235}U$	±1σ[3]	$^{206}Pb/^{238}U$	±1σ[3]	$^{208}Pb/^{232}Th$	±1σ[3]	Rho	$^{206}Pb/^{238}U$	±1σ	$^{207}Pb/^{235}U$	±1σ	$^{207}Pb/^{206}Pb$	±1σ	Best age (Ma)	±1σ	% disc
~~3t0332 050~~	~~46~~	~~32~~	0.69	~~0.13981~~	~~0.0042~~	~~1.2565~~	~~0.0392~~	~~0.06512~~	~~0.0006~~	~~0.05394~~	~~0.0048~~	~~0.3~~	~~407~~	~~3~~	~~826~~	~~18~~	~~2225~~	~~52~~	~~2225~~	~~52~~	~~81.7~~
3t0332 051	47	28	0.59	0.06315	0.0027	0.95347	0.0448	0.10951	0.0009	0.03362	0.0003	0.3	670	5	680	23	713	92	670	5	1.5
3t0332 052	60	70	1.18	0.07002	0.0012	1.3441	0.0247	0.13917	0.001	0.04448	0.0006	0.4	840	5	865	11	929	35	840	5	2.9
3t0332 053	7	7	0.98	0.07508	0.0024	1.8334	0.0627	0.17686	0.0021	0.05342	0.0011	0.4	1050	12	1057	22	1071	65	1071	65	2.0
~~3t0332 054~~	~~25~~	~~18~~	0.72	~~0.08468~~	~~0.0102~~	~~1.7152~~	~~0.2063~~	~~0.14367~~	~~0.0012~~	~~0.04416~~	~~0.0007~~	~~0.1~~	~~865~~	~~7~~	~~1014~~	~~77~~	~~1308~~	~~244~~	~~1308~~	~~244~~	~~33.9~~
3t0332 055	211	61	0.29	0.07639	0.0008	1.895	0.0214	0.17968	0.0009	0.05463	0.0008	0.5	1065	5	1079	7	1105	20	1105	20	3.6
3t0332 056	48	13	0.27	0.07443	0.0011	1.70055	0.0292	0.1657	0.0011	0.04994	0.0003	0.5	988	6	1009	11	1053	29	1053	29	6.2
3t0332 057	492	237	0.48	0.07508	0.0007	1.8209	0.0188	0.17568	0.0008	0.05174	0.0006	0.4	1043	4	1053	7	1071	19	1071	19	2.6
3t0332 058	347	134	0.39	0.07494	0.0007	1.7691	0.02	0.17103	0.001	0.05259	0.0007	0.5	1018	6	1034	7	1067	19	1067	19	4.6
3t0332 059	189	47	0.25	0.07436	0.0008	1.8223	0.0219	0.17749	0.0009	0.05417	0.0008	0.4	1053	5	1054	8	1051	22	1051	22	-0.2
3t0332 060	77	42	0.54	0.07708	0.001	1.8798	0.0265	0.17684	0.001	0.05481	0.0009	0.4	1050	5	1074	9	1123	26	1123	26	6.5
3t0332 061	578	53	0.09	0.05113	0.0024	0.26071	0.0124	0.03711	0.0005	0.02728	0.003	0.3	235	3	235	10	247	95	235	3	0.0
3t0332 062	479	42	0.09	0.05066	0.0022	0.24796	0.0114	0.03546	0.0005	0.0232	0.0028	0.3	225	3	225	9	225	91	225	3	0.0
3t0332 063	605	57	0.09	0.04994	0.0026	0.25055	0.0131	0.03651	0.0004	0.01321	0.0028	0.2	231	3	227	11	192	106	231	3	-1.8
3t0332 064	1494	110	0.07	0.05484	0.002	0.26402	0.0098	0.03496	0.0003	0.02604	0.0034	0.3	222	2	238	8	406	73	222	2	6.7
3t0332 065	1888	374	0.20	0.05049	8E-05	0.24094	0.0025	0.03461	0.0003	0.08597	0.0059	0.3	219	2	219	2	218	3	219	2	0.0
3t0332 066	87	34	0.39	0.05049	7E-05	0.24103	0.0027	0.03462	0.0004	0.04323	0.0049	0.3	219	2	219	2	218	3	219	2	0.0
3t0332 067	275	63	0.23	0.05627	0.0024	0.27975	0.0124	0.03659	0.0005	0.02926	0.0044	0.3	232	3	250	10	463	84	232	3	7.2
3t0341, orthogneiss. 15°00'22.5" 90°14'24.4"																					
3t0341 001	171	146	0.85	0.05696	0.0009	0.57685	0.0093	0.07356	0.0004	0.02256	0.0003	0.4	458	3	462	6	490	32	458	3	0.9
3t0341 002	121	90	0.75	0.05805	0.0009	0.62159	0.0106	0.07786	0.0004	0.02405	0.0003	0.3	483	3	491	7	532	35	483	3	1.6
3t0341 003	86	43	0.50	0.0726	0.0009	1.6717	0.0235	0.16698	0.0009	0.04928	0.0007	0.4	995	5	998	9	1003	26	~~995~~	~~5~~	0.3
3t0341 004	509	398	0.78	0.05594	0.0006	0.52663	0.0059	0.0684	0.0004	0.02015	0.0002	0.5	427	2	430	4	450	22	427	2	0.7
3t0341 005	825	1760	2.13	0.06273	0.0008	0.60464	0.0141	0.0698	0.0014	0.02303	0.0012	0.9	435	8	480	9	699	25	435	8	9.4
3t0341 006	608	137	0.22	0.05622	0.0006	0.56093	0.0061	0.07241	0.0003	0.0233	0.0003	0.4	451	2	452	4	461	21	451	2	0.2
3t0341 007	165	130	0.79	0.05993	0.0015	0.63942	0.0192	0.07739	0.0007	0.0239	0.0002	0.4	481	4	502	12	601	53	481	4	4.2
3t0341 008	660	606	0.92	0.05813	0.0006	0.54479	0.0075	0.06804	0.0006	0.02017	0.0004	0.6	424	3	442	5	535	23	424	3	4.1
3t0341 009	326	279	0.86	0.05944	0.0008	0.61262	0.0088	0.07485	0.0004	0.02414	0.0003	0.4	465	3	485	6	583	27	465	3	4.1
3t0341 010	170	210	1.23	0.05707	0.001	0.59089	0.0114	0.07524	0.0005	0.02335	0.0003	0.3	468	3	471	7	494	39	468	3	0.6
3t0341 011	333	224	0.67	0.05674	0.0006	0.58979	0.0073	0.07552	0.0004	0.02228	0.0003	0.5	469	3	471	5	481	24	469	3	0.4
3t0341 012	429	241	0.56	0.05584	0.0006	0.57358	0.0064	0.07459	0.0004	0.02316	0.0003	0.5	464	2	460	4	446	22	464	2	-0.9
3t0341 013	84	103	1.22	0.05721	0.0009	0.6047	0.0104	0.07679	0.0005	0.02416	0.0003	0.4	477	3	480	7	500	35	477	3	0.6
~~3t0341 014~~	~~96~~	~~91~~	0.94	~~0.07632~~	~~0.0017~~	~~0.7605~~	~~0.0175~~	~~0.07284~~	~~0.0005~~	~~0.02695~~	~~0.0004~~	~~0.3~~	~~453~~	~~3~~	~~574~~	~~10~~	~~1103~~	~~44~~	~~453~~	~~3~~	~~21.1~~
3t0341 015	514	339	0.66	0.05649	0.0006	0.56201	0.0062	0.07225	0.0004	0.02185	0.0002	0.5	450	2	453	4	472	22	450	2	0.7
3t0341 016	653	941	1.44	0.05719	0.0006	0.56314	0.0065	0.07162	0.0004	0.02191	0.0003	0.5	446	3	454	4	499	21	446	3	1.8
3t0341 017	160	209	1.31	0.05624	0.0008	0.59385	0.0092	0.07674	0.0005	0.02436	0.0003	0.4	477	3	473	6	462	31	477	3	-0.8
3t0341 018	396	740	1.87	0.05658	0.0007	0.55058	0.0071	0.07072	0.0003	0.02142	0.0002	0.4	440	2	445	5	475	26	440	2	1.1
3t0341 019	463	585	1.26	0.05709	0.0006	0.56762	0.0064	0.07227	0.0004	0.02268	0.0003	0.5	450	2	456	4	495	22	450	2	1.3
3t0341 020	1187	1065	0.90	0.0559	0.0005	0.40887	0.0079	0.05314	0.0009	0.01643	0.0002	0.9	334	6	348	6	448	20	334	6	4.0
3t0341 021	215	89	0.41	0.05773	0.0008	0.58327	0.0081	0.07341	0.0004	0.02287	0.0003	0.4	457	2	467	5	520	28	457	2	2.1
3t0341 022	780	461	0.59	0.057	0.0005	0.56357	0.0062	0.07181	0.0004	0.02246	0.0003	0.5	447	2	454	4	492	21	447	2	1.5
3t0341 023	227	163	0.72	0.05571	0.0008	0.5853	0.0087	0.07639	0.0004	0.02386	0.0003	0.4	475	2	468	6	441	31	475	2	-1.5
3t0341 024	429	137	0.32	0.09328	0.0008	3.2453	0.0315	0.25199	0.0011	0.07075	0.0008	0.5	1449	6	1468	8	1494	16	~~1494~~	~~16~~	3.0
3t0341 025	429	160	0.37	0.05931	0.001	0.74541	0.015	0.09115	0.0005	0.02819	0.0001	0.4	562	3	566	9	579	38	562	3	0.7
3t0341 026	226	267	1.18	0.05684	0.0008	0.59058	0.0089	0.07545	0.0004	0.02336	0.0003	0.4	469	2	471	6	485	31	469	2	0.4
3t0341 027	120	150	1.26	0.05832	0.0011	0.60226	0.0116	0.07504	0.0005	0.02407	0.0003	0.4	466	3	479	7	542	39	466	3	2.7
3t0341 028	388	476	1.23	0.0578	0.0006	0.57568	0.0071	0.07234	0.0004	0.02303	0.0003	0.4	450	2	462	5	522	24	450	2	2.6
3t0341 029	364	216	0.59	0.05687	0.0007	0.57738	0.0076	0.0738	0.0004	0.02344	0.0003	0.4	459	2	463	5	487	26	459	2	0.9
3t0341 030	214	94	0.44	0.05744	0.0008	0.56823	0.0088	0.07187	0.0005	0.02234	0.0003	0.4	447	3	457	6	509	30	447	3	2.2
3t0341 031	305	258	0.85	0.06192	0.0009	0.63361	0.014	0.07444	0.0013	0.02034	0.0012	0.8	463	8	498	9	671	30	463	8	7.0
3t0341 032	331	130	0.39	0.05708	0.0006	0.59749	0.0073	0.07595	0.0004	0.02361	0.0003	0.4	472	2	476	5	495	24	472	2	0.8
3t0341 033	117	90	0.77	0.058	0.0013	0.36057	0.0092	0.04619	0.0005	0.02554	0.0005	0.4	291	3	313	7	530	50	291	3	7.0
3t0341 034	144	86	0.59	0.0571	0.0007	0.57709	0.0082	0.07341	0.0004	0.02258	0.0003	0.4	457	2	463	5	495	28	457	2	1.3
3t0341 035	94	257	2.74	0.05771	0.001	0.57238	0.0104	0.07208	0.0005	0.02227	0.0003	0.4	449	3	460	7	519	37	449	3	2.4
3t0341 036	105	224	2.13	0.05773	0.0009	0.59391	0.0096	0.0747	0.0004	0.02229	0.0003	0.4	464	3	473	6	520	33	464	3	1.9
3t0341 037	379	412	1.09	0.05791	0.0006	0.58736	0.007	0.07353	0.0004	0.02252	0.0003	0.4	457	2	469	4	526	24	457	2	2.6
3t0341 038	430	619	1.44	0.06178	0.0007	0.62011	0.0081	0.07274	0.0004	0.02355	0.0003	0.4	453	2	490	5	667	25	453	2	7.6
3t0341 039	630	500	0.79	0.05766	0.0006	0.57184	0.0064	0.07198	0.0004	0.02112	0.0005	0.4	448	2	459	4	517	22	448	2	2.4
3t0341 040	320	234	0.73	0.05752	0.0012	0.60057	0.0142	0.07572	0.0004	0.0235	0.0001	0.4	471	2	478	9	512	45	471	2	1.5
3t0341 041	674	478	0.71	0.05624	0.0006	0.55142	0.0061	0.07124	0.0003	0.02154	0.0002	0.4	444	2	446	4	462	22	444	2	0.4
3t0341 042	479	176	0.37	0.05789	0.0006	0.56778	0.0069	0.07121	0.0004	0.02575	0.0004	0.4	443	2	457	4	526	24	443	2	3.1
3t0341 043	1090	607	0.56	0.05645	0.001	0.56649	0.0119	0.07278	0.0004	0.02264	0.0001	0.5	453	2	456	8	470	40	453	2	0.7
3t0341 044	472	206	0.44	0.05706	0.0006	0.56638	0.0069	0.07217	0.0004	0.02267	0.0003	0.4	449	2	456	4	494	24	449	2	1.5
~~3t0341 045~~	~~205~~	~~132~~	0.64	~~0.05683~~	~~0.0007~~	~~0.59865~~	~~0.0082~~	~~0.07648~~	~~0.0005~~	~~0.02345~~	~~0.0003~~	~~0.5~~	~~475~~	~~3~~	~~476~~	~~5~~	~~485~~	~~26~~	~~475~~	~~3~~	~~0.2~~

TABLE II | **Continued**

				CORRECTED RATIOS[2]										CORRECTED AGES (Ma)								
Sample number	U[1] (ppm)	Th[1] (ppm)	Th/U	$^{207}Pb/^{206}Pb$	±1σ[3]	$^{207}Pb/^{235}U$	±1σ[3]	$^{206}Pb/^{238}U$	±1σ[3]	$^{208}Pb/^{232}Th$	±1σ[3]	Rho	$^{206}Pb/^{238}U$	±1σ	$^{207}Pb/^{235}U$	±1σ	$^{207}Pb/^{206}Pb$	±1σ	Best age (Ma)	±1σ	% disc
Gt0341 046	620	355	0.57	0.05663	0.0006	0.57147	0.0063	0.07329	0.0004	0.02283	0.0003	0.4	456	2	459	4	477	22	456	2	0.7
Gt0341 047	223	378	1.70	0.06149	0.0008	0.58726	0.0089	0.06937	0.0005	0.02113	0.0004	0.5	432	3	469	6	656	27	432	3	7.9
Gt0341 048	550	345	0.63	0.05665	0.0006	0.57569	0.0069	0.07386	0.0003	0.02323	0.0003	0.4	459	2	462	4	478	24	459	2	0.6
Gt0341 049	222	293	1.32	0.05911	0.0009	0.58091	0.0096	0.07134	0.0005	0.02469	0.0003	0.4	444	3	465	6	571	32	444	3	4.5
Gt0341 050	195	47	0.24	0.05777	0.0009	0.56646	0.0092	0.07126	0.0004	0.02264	0.0004	0.4	444	3	456	6	521	32	444	3	2.6
Gt03113 pegmatite dike. 15°03'24" 90°23'36.8"																					
Gt03113 001	256	80	0.31	0.07737	0.0009	2.0375	0.0243	0.19089	0.0009	0.05905	0.0009	0.4	1126	5	1128	8	1131	20	1131	20	0.4
Gt03113 002	300	92	0.31	0.07233	0.001	1.59942	0.0261	0.16037	0.0008	0.04848	0.0002	0.4	959	4	970	10	995	28	959	4	1.1
Gt03113 003	1051	122	0.12	0.06444	0.0013	1.00002	0.0223	0.11255	0.0006	0.03447	0.0005	0.5	688	4	704	11	756	41	688	4	2.3
~~Gt03113 004~~	~~106~~	~~19~~	0.18	~~0.05129~~	~~0.0157~~	~~0.82331~~	~~0.2728~~	~~0.11641~~	~~0.0032~~	~~0.03663~~	~~0.0238~~	~~0.2~~	~~710~~	~~18~~	~~610~~	~~152~~	~~254~~	~~498~~	~~710~~	~~18~~	~~-16.4~~
Gt03113 005	277	102	0.37	0.07603	0.0008	1.8186	0.0202	0.17351	0.0009	0.05358	0.0008	0.5	1031	5	1052	7	1096	19	1096	19	5.9
Gt03113 006	486	79	0.16	0.07096	0.0016	1.41842	0.0354	0.14498	0.0009	0.04393	0.0004	0.3	873	5	897	15	956	45	873	5	2.7
Gt03113 007	245	86	0.35	0.07668	0.0008	1.9842	0.0214	0.18765	0.0008	0.05568	0.0008	0.4	1109	5	1110	7	1113	19	1113	19	0.4
~~Gt03113 008~~	~~856~~	~~145~~	0.17	~~0.07219~~	~~0.0007~~	~~0.96358~~	~~0.0111~~	~~0.09689~~	~~0.0006~~	~~0.05909~~	~~0.0009~~	~~0.5~~	~~596~~	~~3~~	~~685~~	~~6~~	~~991~~	~~19~~	~~596~~	~~3~~	~~13.0~~
~~Gt03113 009~~	~~126~~	~~54~~	0.43	~~0.08395~~	~~0.0009~~	~~1.8372~~	~~0.0222~~	~~0.15822~~	~~0.0008~~	~~0.04441~~	~~0.0008~~	~~0.4~~	~~947~~	~~4~~	~~1059~~	~~8~~	~~1291~~	~~20~~	~~1291~~	~~20~~	26.6
Gt03113 010	386	102	0.27	0.07497	0.0007	1.6892	0.0183	0.16336	0.0008	0.0484	0.0007	0.4	975	4	1004	7	1068	19	1068	19	8.7
~~Gt03113 011~~	~~179~~	~~35~~	0.20	~~0.07672~~	~~0.005~~	~~1.77126~~	~~0.1238~~	~~0.16746~~	~~0.0018~~	~~0.0503~~	~~0.0007~~	~~0.2~~	~~998~~	~~10~~	~~1035~~	~~45~~	~~1114~~	~~128~~	~~1114~~	~~128~~	~~10.4~~
Gt03113 012	1113	88	0.08	0.05837	0.0011	0.60878	0.0123	0.07564	0.0004	0.02343	0.0003	0.4	470	2	483	8	544	39	470	2	2.7
Gt03113 013	109	32	0.29	0.07575	0.0009	2.0461	0.0264	0.19606	0.0009	0.05932	0.0009	0.4	1154	5	1131	9	1088	23	1088	23	-2.0
~~Gt03113 014~~	~~135~~	~~48~~	0.35	~~0.08283~~	~~0.0197~~	~~2.12074~~	~~0.5456~~	~~0.1857~~	~~0.0065~~	~~0.05532~~	~~0.0042~~	~~0.3~~	~~1098~~	~~36~~	~~1156~~	~~178~~	~~1265~~	~~511~~	~~1265~~	~~511~~	~~13.2~~
Gt03113 015	247	72	0.29	0.07676	0.0009	1.97327	0.0262	0.18645	0.0009	0.056	0.0003	0.4	1102	5	1106	9	1115	22	1115	22	1.2
Gt03113 016	98	32	0.33	~~0.07216~~	~~0.0146~~	~~1.61372~~	~~0.35~~	~~0.16218~~	~~0.0033~~	~~0.04905~~	~~0.0034~~	~~0.2~~	969	18	976	136	991	436	969	18	0.7
Gt03113 017	348	62	0.18	0.07423	0.0012	1.65157	0.0301	0.16137	0.0009	0.04865	0.0004	0.4	964	5	990	12	1048	32	1048	32	8.0
Gt03113 018	383	125	0.33	0.0774	0.0007	2.0198	0.0212	0.18931	0.0009	0.05888	0.0008	0.4	1118	5	1122	7	1132	18	1132	18	1.2
Gt03113 019	117	52	0.45	0.07405	0.0016	1.76258	0.0414	0.17264	0.0009	0.05206	0.0003	0.3	1027	5	1032	15	1043	41	1043	41	1.5
Gt03113 020	115	38	0.33	0.07731	0.0009	2.018	0.0244	0.1894	0.001	0.0553	0.0008	0.4	1118	5	1122	8	1129	21	1129	21	1.0
Gt03113 021	966	149	0.15	0.05726	0.0008	0.61043	0.0101	0.07731	0.0004	0.02401	0.0002	0.4	480	2	484	6	502	31	480	2	0.8
Gt03113 022	240	71	0.30	0.07466	0.0008	1.7564	0.0193	0.17075	0.0008	0.05223	0.0007	0.4	1016	4	1030	7	1059	19	1059	19	4.1
Gt03113 023	113	28	0.25	0.07301	0.002	1.71135	0.0556	0.17	0.0018	0.05134	0.0005	0.5	1012	10	1013	21	1014	55	1014	55	0.2
Gt03113 024	509	67	0.13	0.07067	0.0017	1.34641	0.0351	0.13817	0.0008	0.04188	0.0007	0.4	834	4	866	15	948	47	834	4	3.7
Gt03113 025	368	95	0.26	0.07109	0.0011	1.53755	0.0271	0.15686	0.0008	0.04752	0.0003	0.4	939	5	946	11	960	30	939	5	0.7
Gt03113 026	558	157	0.28	0.07294	0.0008	1.56093	0.0222	0.15522	0.0009	0.04688	0.0003	0.5	930	5	955	9	1012	22	930	5	2.6
Gt03113 027	522	137	0.26	0.07276	0.0013	1.62392	0.0329	0.16187	0.0011	0.04891	0.0004	0.5	967	6	980	13	1007	34	967	6	1.3
Gt03113 028	212	49	0.23	0.07609	0.0008	1.9658	0.0219	0.18741	0.0009	0.05855	0.0008	0.4	1107	5	1104	7	1097	19	1097	19	-0.9
Gt03113 029	208	50	0.24	0.07413	0.0007	1.7159	0.0193	0.16797	0.0009	0.05563	0.0008	0.5	1001	5	1014	7	1045	19	1045	19	4.2
Gt03113 030	120	50	0.42	0.07579	0.0008	1.9	0.0234	0.18189	0.001	0.05603	0.0008	0.5	1077	5	1081	8	1090	21	1090	21	1.2
Gt0405 migmatite Rio Pasabien. 15°02'21.4" 89°41'02.4"																					
~~Gt0405 001~~	~~91~~	~~70~~	0.77	~~0.05895~~	~~0.0054~~	~~0.31666~~	~~0.0303~~	~~0.03896~~	~~0.0004~~	~~0.01206~~	~~0.0002~~	~~0.2~~	~~246~~	~~3~~	~~279~~	~~23~~	~~565~~	~~211~~	~~246~~	~~3~~	~~11.8~~
Gt0405 002	411	143	0.35	0.05009	0.001	0.28745	0.0062	0.04166	0.0003	0.01242	0.0002	0.4	263	2	257	5	199	43	263	2	-2.3
Gt0405 003	99	34	0.34	0.07037	0.001	1.4623	0.0222	0.15106	0.0009	0.04561	0.0007	0.4	907	5	915	9	939	30	~~907~~	~~5~~	0.9
Gt0405 004	150	88	0.59	0.05505	0.0011	0.53816	0.0107	0.07111	0.0004	0.02147	0.0003	0.3	443	3	437	7	414	44	443	3	-1.4
Gt0405 005	178	70	0.39	0.05912	0.0026	0.59211	0.0272	0.07263	0.0004	0.02247	0.0002	0.3	452	3	472	17	572	99	452	3	4.2
Gt0405 006	169	69	0.41	0.05746	0.001	0.59155	0.0107	0.07492	0.0005	0.024	0.0004	0.3	466	3	472	7	509	38	466	3	1.3
Gt0405 007	466	181	0.39	0.0553	0.0007	0.56879	0.0074	0.0748	0.0004	0.02359	0.0003	0.4	465	2	457	5	424	27	465	2	-1.8
Gt0405 008	132	50	0.38	0.05595	0.0011	0.5506	0.0115	0.07158	0.0004	0.02195	0.0004	0.3	446	3	445	8	450	46	446	3	-0.2
~~Gt0405 009~~	~~403~~	~~262~~	0.65	~~0.16292~~	~~0.0033~~	~~1.8602~~	~~0.0402~~	~~0.08162~~	~~0.0007~~	~~0.06371~~	~~0.0019~~	~~0.4~~	~~506~~	~~4~~	~~1067~~	~~14~~	~~2486~~	~~35~~	~~2486~~	~~35~~	~~52.6~~
~~Gt0405 010~~	~~264~~	~~137~~	0.52	~~0.06109~~	~~0.0079~~	~~0.33609~~	~~0.0454~~	~~0.0399~~	~~0.0005~~	~~0.0123~~	~~0.0003~~	~~0.3~~	~~252~~	~~3~~	~~294~~	~~34~~	~~642~~	~~257~~	~~252~~	~~3~~	~~14.3~~
Gt0405 011	195	71	0.36	0.05627	0.001	0.55607	0.01	0.07184	0.0004	0.02203	0.0003	0.3	447	3	449	7	463	35	447	3	0.4
Gt0405 012	561	200	0.36	0.05594	0.0006	0.55692	0.0062	0.07232	0.0004	0.02237	0.0003	0.5	450	2	450	4	450	20	450	2	0.0
~~Gt0405 013~~	~~5108~~	~~2791~~	0.55	~~0.07245~~	~~0.0032~~	~~0.2156~~	~~0.0104~~	~~0.02158~~	~~0.0002~~	~~0.00652~~	~~8E-05~~	~~0.5~~	~~138~~	~~1~~	~~198~~	~~9~~	~~999~~	~~81~~	~~138~~	~~1~~	~~30.3~~
Gt0405 014	595	292	0.49	0.05195	0.0007	0.2837	0.0043	0.03964	0.0002	0.01237	0.0002	0.4	251	1	254	3	283	30	251	1	1.2
Gt0405 015	2490	342	0.14	0.05852	0.0018	0.46303	0.0151	0.05739	0.0004	0.01777	0.0003	0.4	360	2	386	11	549	61	360	2	6.7
~~Gt0405 016~~	~~4015~~	~~101~~	0.03	~~0.06211~~	~~0.0009~~	~~0.37609~~	~~0.006~~	~~0.04446~~	~~0.0002~~	~~0.06733~~	~~0.0024~~	~~0.3~~	~~280~~	~~1~~	~~324~~	~~4~~	~~678~~	~~30~~	~~280~~	~~1~~	~~13.6~~
Gt0405 017	570	295	0.52	0.05145	0.0007	0.27898	0.0042	0.03939	0.0002	0.01262	0.0002	0.4	249	1	250	3	261	30	249	1	0.4
Gt0405 018	220	102	0.46	0.05642	0.0012	0.55387	0.0132	0.0712	0.0004	0.02215	0.0001	0.3	443	2	448	9	469	44	443	2	1.1
Gt0405 019	764	519	0.68	0.05312	0.0007	0.27705	0.0039	0.03792	0.0002	0.01195	0.0002	0.4	240	1	248	3	334	27	240	1	3.2
Gt0405 020	705	195	0.28	0.05233	0.0006	0.29051	0.0038	0.04029	0.0002	0.0122	0.0002	0.4	255	1	259	3	300	25	255	1	1.5
Gt0405 021	315	130	0.41	0.056	0.0007	0.54684	0.0076	0.07097	0.0004	0.02172	0.0003	0.4	442	2	443	5	452	30	442	2	0.2
Gt0405 023	154	77	0.50	0.05595	0.0009	0.56322	0.0095	0.07301	0.0004	0.02281	0.0003	0.3	454	2	454	6	450	37	454	2	0.0
Gt0405 024	1488	37	0.02	0.05153	0.0018	0.28573	0.0103	0.04021	0.0002	0.01265	0.0011	0.3	254	1	255	8	265	82	254	1	0.4
~~Gt0405 025~~	~~432~~	~~147~~	0.34	~~0.05632~~	~~0.0007~~	~~0.55761~~	~~0.0072~~	~~0.07201~~	~~0.0004~~	~~0.02242~~	~~0.0003~~	~~0.4~~	~~448~~	~~2~~	~~450~~	~~5~~	~~465~~	~~27~~	~~448~~	~~2~~	~~0.4~~

DOI: 10.1344/105.000001695

TABLE II | **Continued**

				CORRECTED RATIOS[2]										CORRECTED AGES (Ma)								
Sample number	U[1] (ppm)	Th[1] (ppm)	Th/U	$^{207}Pb/^{206}Pb$	±1σ[3]	$^{207}Pb/^{235}U$	±1σ[3]	$^{206}Pb/^{238}U$	±1σ[3]	$^{208}Pb/^{232}Th$	±1σ[3]	Rho	$^{206}Pb/^{238}U$	±1σ	$^{207}Pb/^{235}U$	±1σ	$^{207}Pb/^{206}Pb$	±1σ	Best age (Ma)	±1σ	% disc
Gt0405 026	543	50	0.09	0.05476	0.0007	0.46443	0.0065	0.06143	0.0003	0.0236	0.0004	0.4	384	2	387	5	402	30	384	2	0.8
~~Gt0405 027~~	~~4341~~	~~861~~	~~0.20~~	~~0.05924~~	~~0.0069~~	~~0.40377~~	~~0.0494~~	~~0.04943~~	~~0.0007~~	~~0.01529~~	~~0.0006~~	~~0.4~~	~~311~~	~~4~~	~~344~~	~~36~~	~~576~~	~~268~~	~~311~~	~~4~~	~~9.6~~
Gt0405 028	388	185	0.48	0.05604	0.0007	0.58126	0.0079	0.07531	0.0005	0.02363	0.0003	0.5	468	3	465	5	454	27	468	3	-0.6
Gt0405 029	1608	114	0.07	0.05291	0.0005	0.35923	0.0042	0.04921	0.0003	0.02119	0.0003	0.5	310	2	312	3	325	23	310	2	0.6
Gt0405 030	425	307	0.72	0.05068	0.0008	0.26803	0.0043	0.03844	0.0002	0.01194	0.0002	0.4	243	1	241	3	226	36	243	1	-0.8
Gt0405 031	188	100	0.53	0.06236	0.001	0.6206	0.0104	0.07239	0.0004	0.02528	0.0004	0.3	451	2	490	6	686	35	451	2	8.0
~~Gt0405 032~~	~~807~~	~~175~~	0.22	~~0.06298~~	~~0.0082~~	~~0.56481~~	~~0.0779~~	~~0.06504~~	~~0.0008~~	~~0.01997~~	~~0.0013~~	~~0.4~~	406	~~5~~	455	~~51~~	~~708~~	~~302~~	406	~~5~~	~~10.8~~
~~Gt0405 033~~	~~2971~~	~~67~~	0.02	~~0.06245~~	~~0.0051~~	~~0.33815~~	~~0.0289~~	~~0.03927~~	~~0.0003~~	~~0.01207~~	~~0.0047~~	~~0.3~~	~~248~~	~~2~~	~~296~~	~~22~~	~~690~~	~~185~~	~~248~~	~~2~~	~~16.2~~
Gt0405 034	590	414	0.70	0.05989	0.0006	0.60858	0.0068	0.07379	0.0004	0.02311	0.0003	0.4	459	2	483	4	600	22	459	2	5.0
Gt0405 035	186	142	0.77	0.05703	0.001	0.56871	0.0106	0.07249	0.0006	0.02337	0.0004	0.4	451	3	457	7	493	38	451	3	1.3
Gt0405 036	4761	79	0.02	0.05076	0.0005	0.26191	0.003	0.03742	0.0002	0.01179	0.0002	0.4	237	1	236	2	230	25	237	1	-0.4
~~Gt0405 037~~	~~3872~~	~~414~~	0.11	~~0.08749~~	~~0.0234~~	~~0.60095~~	~~0.1609~~	~~0.04982~~	~~0.0016~~	~~0.01475~~	~~0.0049~~	~~0.3~~	~~313~~	~~10~~	~~478~~	~~108~~	~~1371~~	~~597~~	~~313~~	~~10~~	~~34.5~~
Gt0405 038	7036	78	0.01	0.05097	0.0005	0.27027	0.0029	0.03846	0.0002	0.01211	0.0002	0.5	243	1	243	2	239	22	243	1	0.0
Gt0405 039	5709	113	0.02	0.05571	0.0041	0.29857	0.0225	0.03887	0.0003	0.01211	0.0028	0.2	246	2	265	18	441	170	246	2	7.2
~~Gt0405 040~~	~~3298~~	~~47~~	0.01	~~0.05967~~	~~0.0463~~	~~0.29217~~	~~0.2744~~	~~0.03551~~	~~0.0028~~	~~0.01097~~	~~0.3102~~	~~0.7~~	225	~~18~~	260	~~216~~	~~592~~	###	225	~~18~~	~~13.5~~
~~Gt0405 041~~	~~6747~~	~~112~~	0.02	~~0.06819~~	~~0.0224~~	~~0.33609~~	~~0.1225~~	~~0.03575~~	~~0.0015~~	~~0.01088~~	~~0.0642~~	~~0.5~~	226	~~9~~	294	~~93~~	~~874~~	~~695~~	226	~~9~~	~~23.1~~
Gt0405 042	4903	55	0.01	0.05251	0.0011	0.27846	0.0065	0.03846	0.0002	0.01207	0.0011	0.3	243	1	249	5	308	50	243	1	2.4
~~Gt0405 043~~	~~6407~~	~~90~~	0.01	~~0.08375~~	~~0.0255~~	~~0.41899~~	~~0.1408~~	~~0.03628~~	~~0.0014~~	~~0.0108~~	~~0.0477~~	~~0.5~~	~~230~~	~~9~~	~~355~~	~~101~~	~~1287~~	~~681~~	~~230~~	~~9~~	~~35.2~~
Gt0405 044	3838	74	0.02	0.05101	0.0005	0.25501	0.0027	0.03628	0.0002	0.01243	0.0002	0.5	230	1	231	2	241	21	230	1	0.4
Gt0405 045	3095	117	0.04	0.05716	0.0013	0.46073	0.0119	0.05846	0.0004	0.01816	0.001	0.5	366	2	385	8	498	51	366	2	4.9
Gt0405 046	1431	8	0.01	0.05068	0.0006	0.2418	0.0032	0.03466	0.0002	0.01143	0.0005	0.4	220	1	220	3	226	28	220	1	0.0
~~Gt0405 047~~	~~7850~~	~~101~~	0.01	~~0.06913~~	~~0.0144~~	~~0.35174~~	~~0.0782~~	~~0.0369~~	~~0.0009~~	~~0.01121~~	~~0.025~~	~~0.3~~	~~234~~	~~5~~	~~306~~	~~59~~	~~903~~	~~461~~	~~234~~	~~5~~	~~23.5~~
Gt0405 048	5658	105	0.02	0.05148	0.0005	0.27134	0.0037	0.03826	0.0004	0.01608	0.0006	0.8	242	2	244	3	262	21	242	2	0.8
~~Gt0405 049~~	~~2008~~	~~22~~	0.01	~~0.07552~~	~~0.0013~~	~~0.3937~~	~~0.0069~~	~~0.03809~~	~~0.0002~~	~~0.34427~~	~~0.0169~~	~~0.3~~	~~241~~	~~1~~	~~337~~	~~5~~	~~1082~~	~~34~~	~~241~~	~~1~~	~~28.5~~
Gt0405 050	2428	36	0.01	0.05111	0.0005	0.26734	0.0029	0.03797	0.0002	0.01583	0.0005	0.5	240	1	241	2	246	22	240	1	0.4
Gt0405 051	3299	53	0.02	0.05166	0.0008	0.25688	0.0044	0.03606	0.0002	0.01134	0.0009	0.4	228	1	232	4	271	36	228	1	1.7
Gt0405 052	7887	216	0.03	0.05272	0.0025	0.28703	0.0147	0.03949	0.0003	0.01238	0.0015	0.4	250	2	256	12	317	109	250	2	2.3
Gt0405 053	2522	29	0.01	0.05129	0.0005	0.26119	0.003	0.03693	0.0002	0.01162	0.0002	0.4	234	1	236	2	254	23	234	1	0.8
~~Gt0405 054~~	~~2118~~	~~64~~	0.03	~~0.06224~~	~~0.0056~~	~~0.45052~~	~~0.0422~~	~~0.0525~~	~~0.0005~~	~~0.01614~~	~~0.0023~~	~~0.2~~	~~330~~	~~3~~	~~378~~	~~30~~	~~682~~	~~198~~	~~330~~	~~3~~	~~12.7~~
~~Gt0405 055~~	~~1522~~	~~19~~	0.01	~~0.05607~~	~~0.0107~~	~~0.26928~~	~~0.0549~~	~~0.03483~~	~~0.0006~~	~~0.01084~~	~~0.038~~	~~0.3~~	~~221~~	~~4~~	~~242~~	~~44~~	~~455~~	~~399~~	~~221~~	~~4~~	~~8.7~~

[1]: U and Th concetrations are calibrated relative to the analysis of NIST 612 trace element standard glass

[2]: Isotopic ratios are corrected relative to analysis of a standard zircon for mass bias and down-hole fractionation (see text for further explanations and the used zircon standards). The Andersen (2002) common Pb correction m

[3]: Isotopic ratio errors are absolute and expressed at 1-sigma level. See text for further explanations

Apparent age errors are expressed at ± 1 sigma

Strikethrough analyses were discarded from calculations because >10% <-5% discordant. This criteria was released to >15% for the sample Gt0315 because of the difficulty to measure 207Pb in such young zircons

DOI: 10.1344/105.000001695

Geologica Acta, Vol.9, Nos 3-4, September-December 2011, 351-362
DOI: 10.1344/105.000001697
Available online at www.geologica-acta.com

geologica acta

$^{40}Ar/^{39}Ar$ ages from blueschists of the Jambaló region, Central Cordillera of Colombia: implications on the styles of accretion in the Northern Andes

A. BUSTAMANTE [1] C. JULIANI [1] C.M. HALL [2] E.J. ESSENE [2] [†]

[1] Universidade de São Paulo, Instituto de Geociências
Rua do Lago 562, CEP 05508-080, São Paulo, SP, Brasil

[2] University of Michigan, Department of Geological Sciences
2534 CC Little Building, 1100 North University Ave, Ann Arbor, MI 48109-1005, USA

[†] Deceased May 20, 2010

ABSTRACT

This paper presents the first argon dating of blueschists from the Jambaló area (Cauca Department) in the Central Cordillera of the Colombian Andes. Step-heating $^{40}Ar/^{39}Ar$ spectra were obtained for mica from several lenses of blueschists including greenschist facies rocks. The blueschists are mainly constituted of preserved lenticular cores in strongly mylonitic rocks, which resulted from retrometamorphic processes that affected the high pressure rocks during their exhumation. The majority of $^{40}Ar/^{39}Ar$ data points to metamorphic ages close to 63±3Ma, but some ages are older than 71Ma. These Maastritchtian–Danian ages correspond to the timing of exhumation of the blueschists near metamorphic peak conditions, because the dated paragonite and phengite crystallized during development of the mylonitic foliation. The continuous exhumation of this blueschist belt between 71–63Ma reflects the flow on an accretionary system/subduction channel environment that was interrupted by the collision of an intra-oceanic arc with the continental margin. Regional geological correlations suggest that this arc–continent collision also took place in Ecuador. This collisional event, although synchronous with other arc–continent collisions in the Northern Andes, was apparently not related to the formation of the great Caribbean arc, but to an arc built in the southeastern margin of the Caribbean plate.

KEYWORDS | Blueschists. Colombian Andes. Jambaló area. $^{40}Ar/^{39}Ar$ geochronology.

INTRODUCTION

Because blueschist facies rocks are associated with convergent limits of tectonic plates (Bowes, 1989), metamorphic and deformational events registered in the blueschists may reveal the type of subduction and the characteristics of the collisional and exhumation regimes (Ernst, 1988; Smith et al., 1999). Usually these high-pressure and low-temperature rocks record the P–T variations with time, which can reflect the complex exhumation

processes associated with either subduction or collisional events or with later transpressive regimes (Cloos, 1982). Consequently, the identification and characterization of blueschists in the geological record can provide insights on the nature and timing of the convergence zones that characterize the terranes in which they occur (Draper and Lewis, 1991; Avé-Lallemant, 1996).

The Meso-Cenozoic orogeny in the Northern Andes, especially in Ecuador, Colombia and Caribbean, is characterized by a series of island arc and plateau collisions against the South American continental margin, accompanied by subduction and tectonic imbrication of slices of oceanic crust, either in the continental margin or intra-oceanic domains (Kerr et al., 1997, 2002; Luzieux et al., 2006). These processes resulted in obduction of ophiolitic complexes, Barrovian metamorphic belts, high-pressure metamorphic rock units, and in the amalgamation and strong interaction of several tectonic terranes (Ramos, 1999; Ramos and Aleman, 2000; Kerr et al., 1997, 2002; Giunta et al., 2002). Some suture zones, such as those recognized in Colombia (González, 1977; Chicangana, 2005), are marked by the occurrence of tectonic slices of blueschist-facies metamorphic rocks, which have been considered as late Cretaceous in age (Orrego et al., 1980a; De Souza et al., 1984). The origin of these blueschists has been related to oceanic subduction, accretion or collision of an oceanic plate coming from northwest and reaching the South American plate (Feininger, 1980; Aspden and McCourt, 1986; Mégard, 1987; Bourgois et al., 1987; Aspden et al., 1995). In order to test such possibilities, the detailed petrotectonic evolution and the ages of the different Mesozoic Barrovian and high-pressure metamorphic belts in western Colombia should be established by means of detailed geochronologic dating. In this contribution new Ar–Ar data are presented for white mica of the blueschists of the Jambaló region, in the western flank of the Central Cordillera of the Colombian Andes.

GEOLOGICAL SETTING

In Colombia, the Andean Cordillera is divided into three mountain ranges, the Eastern, Central and Western Cordilleras (Fig. 1), which underwent different tectonic and geologic histories. The Eastern Cordillera is composed mainly of a Paleozoic to Tertiary thick sedimentary sequence (Restrepo and Toussaint, 1982; Forero-Suárez, 1991). The Western Cordillera is made up of oceanic volcanic sequences accreted since Cretaceous times, whereas the Central Cordillera comprises a polymetamorphic complex associated with syn-tectonic granitoids, with K-Ar ages varying between Paleozoic to Cretaceous (Restrepo and Toussaint, 1982, 1988; Restrepo, 1986). Well defined blueschist occurrences have been recognized in the

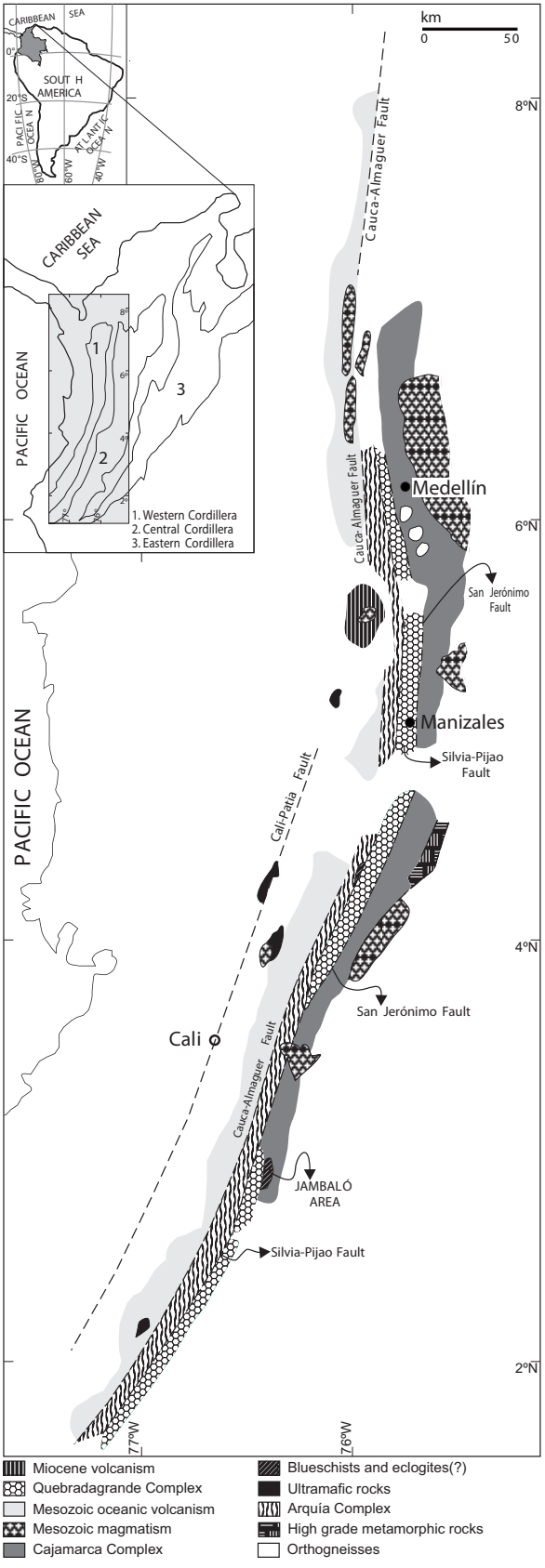

FIGURE 1 | **Lithodemic units of the Central Cordillera of Colombia, after Maya and González, (1995).**

western flank of the Central Cordillera in Jambaló and Barragán. Another occurrence of blueschist rocks has been described in the Pijao area (Núñez and Murillo, 1978), but the geology, petrography and ages have not been clearly defined yet.

The Jambaló blueschists are limited to the east by the polymetamorphic rocks of the Cajamarca Complex (Maya and González, 1995), whereas to the west the contact is tectonic with arc-related volcanic rocks, which are regionally grouped in the Quebradagrande Complex. This complex includes units of different ages, probably formed in oceanic settings (Maya and González, 1995; Nivia et al., 2006). The regional geological setting of the Jambaló blueschists is illustrated in Figure 1, and the geologic map of the study area is summarized in Figure 2.

Previous studies have considered the age of the Jambaló blueschist as Early Cretaceous (Orrego et al., 1980a; De Souza et al., 1984). This interpretation will be discussed considering new ^{40}Ar–^{39}Ar isotopic data obtained for paragonite and phengite from the blueschists.

$^{40}Ar/^{39}Ar$ METHODOLOGY

Micas from six samples of blueschist facies rocks were concentrated and analyzed by the $^{40}Ar/^{39}Ar$ method. Rarer phengite from only one sample was analyzed.

Mineral concentrates were prepared by manual separation of grains present in the 0.5–1mm fraction. Two or three grains from each sample were analyzed, although for some samples only one grain was analyzed.

$^{40}Ar/^{39}Ar$ analyses were performed at the Argon Geochronology Laboratory of the University of Michigan using a continuous laser for step-heating and a VG 1200S noble gas mass spectrometer equipped with a Daly detector operated in analog mode using the methods outlined in Streepey et al. (2000) and Keane et al. (2006). Samples were packed within pure Al foil packs and irradiated for 10.83hr at location 5C at the McMaster Nuclear reactor. Quoted ages are calculated relative to an age of 520.4Ma for hornblende standard MMHb–1. After irradiation two or three crystals were chosen from each sample for extraction and purification of argon by the step-heating method.

HIGH PRESSURE METAMORPHIC ROCKS FROM THE JAMBALÓ AREA

Orrego et al. (1980b) divided the metamorphic rocks of the Jambaló area in three units: 1) San Antonio Amphibolite, composed of metagabbro, metadiabase, metabasalt and subordinated metasedimentary rocks, all of them metamorphosed to the amphibolite facies; 2) La Mina Greenschist, which includes rocks similar to those of the San Antonio Unit, but metamorphosed to the greenschist facies, and 3) Glaucophanic Schist, formed by glaucophanic, chloritic, amphibolitic and micaceous schists associated with foliated quartzites, marbles and metaperidotites (serpentinites). This 25km-long blueschists unit was considered to be a continuous body, elongated north–northeast and parallel to the regional Andean trend (Orrego et al., 1980b; Feininger, 1982). Our field observations, however, do not support the existence of a continuous belt, but of a series of discontinuous lenses

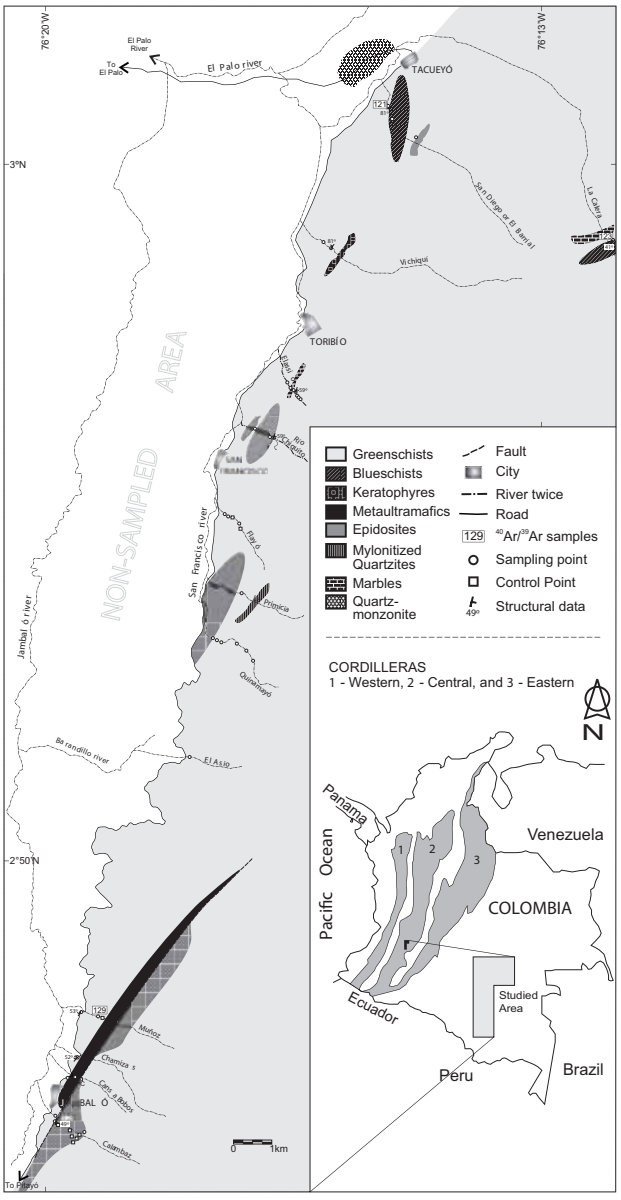

FIGURE 2 | **Simplified geologic map of the Jambaló area.**

of blueschist rocks in a greenschist matrix resultant from retrograde metamorphism to the greenschist facies, which is mainly associated with contemporaneous mylonitic foliation.

All structural data were obtained from the greenschist facies rocks. North of the Jambaló area, the strike of the foliation varies between N8ºW and N67ºE, dipping SW and NW respectively. In the middle of the studied area, near the Toribío city, the attitudes vary between N38ºE and N12ºE strongly dipping NW and SE respectively. Close to Jambaló, the foliation is approximately N28ºE, dipping NW. Although field relationships are not clearly seen, the three units could constitute tectonic blocks in a tectonic mélange (Orrego et al., 1980b), whose major tectonic implications will be discussed later.

Blueschist facies rocks from the Jambaló area are fine-grained, grey-bluish in color, strongly foliated, and occasionally folded. The main foliation is defined by white mica and glaucophane. Some samples show discontinuous greenish white bands, due to a mixture of epidote and white mica. Glaucophane crystals are slightly oriented according to foliation, but are usually randomly distributed or arranged radially in relation to the main foliation.

PETROGRAPHY

Jambaló blueschists and blueschist-facies rocks are associated with greenschists and greenschist-facies rocks, impure marbles, serpentinized peridotites, and quartzites. The relationships between the rock bodies are not well exposed, but we interpret that the greenschists are the product of retrograde metamorphism of blueschists.

The blueschist-facies rocks from the Jambaló area can be classified as mica-glaucophane schists or glaucophane-mica schists, depending on the glaucophane/white mica ratio, but due to the intense shearing all of them are mylonitic rocks. Some samples could be classified as epidote–glaucophane schists (e.g. sample 123A). More details on the petrography of these rocks are found in Bustamante (2008).

The blueschists are made up of glaucophane (30–50%), white mica (10–36%), quartz (5–12%), epidote–clinozoisite (1 to 30%), chlorite (1 to 12%) and calcite (1 to 5%). Accessory and trace minerals are albite, pyrite, ilmenite, magnetite, titanite, zircon, garnet, rutile, apatite and stilpnomelane. The mineral composition of the representative samples are summarized in Table 1 and the blastesis versus metamorphic facies are illustrated in Figure 3.

TABLE 1 | **Mineral composition of dated samples**

Sample	121B	123A	124F	124G	124J	125M	129C
Glaucophane	○	○	○	○	○	○	○
White mica	○	●	○	○	○	○	○
Quartz	○	○	○	○	○		○
Epidote–Clinozoisite	●	○		●	●	●	
Chlorite	○	●	●	●	●	○	●
Calcite	●		●	●	○		●
Albite	●	–	–	●	●	●	●
Pyrite			–	–	●		
Ilmenite	●	–	●	●		–	●
Magnetite	●	●				●	●
Titanite	●	●	●	●	●	●	
Rutile		●					●
Zircon		–			–		
Garnet					–		
Apatite	–	–	–	–	–		
Stilpnomelane	●						

○ Mineral contents varying between 10 to 50%, ● accessory minerals varying between 1 to 9% and – mineral in traces contents <1%

Glaucophane grains vary from 0.25 to 6.6mm in length and are subidioblastic and xenoblastic. Optical zoning is common and more intense in the core of the crystals. The core of glaucophane grains is also rich in inclusions of epidote–clinozoisite, opaque minerals, zircon, and locally rutile. The rims are relatively clean and commonly replaced by barroisite and/or actinolite+chlorite. Glaucophane may define a weak S_n foliation and a marked penetrative S_{n+1} mylonitic foliation, but is usually arranged radially (Fig. 4) indicating that crystallization was pre-, syn- and locally post-mylonitization. Pressure shadows of symmetrical and asymmetrical shapes possibly resulted from shearing. Polygonal arcs are also observed.

White mica grains vary from 0.05 to 0.3mm in size and are subidioblastic and continuous with foliation S_{n+1}. In most cases white mica accompanies quartzose beds. In samples with epidote–clinozoisite, mica grains are isolated. Optically this white mica is similar to phengite and/or muscovite, but X–ray diffraction analysis of several mica grains from the concentrates reveals a mixture of paragonite and phengite. Usually chlorite and epidote

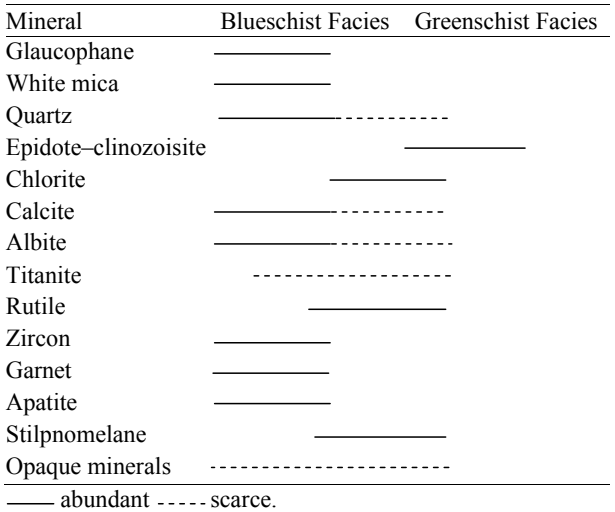

FIGURE 3 | **Mineral blastesis and metamorphic facies of representative rocks from Jambaló area.**

formed during retrograde metamorphism define the mylonitic foliation. In some samples with white mica and glaucophane defining a strong mylonitic foliation (Fig. 4), no evidence of retrograde metamorphism was detected, suggesting that shearing started in near-peak blueschist facies metamorphic conditions and continued during retrograde (i.e, exhumation-related) greenschist facies.

Quartz grains vary from 0.05 to 0.65mm in size and are generally disseminated and locally aggregated in thin lenses. Quartz also occurs as inclusions in glaucophane pressure shadows, and also in calcite, chlorite and white mica. In general, quartz constitutes xenoblastic grains with undulatory extinction. Locally polygonal texture and triple junctions are developed.

Epidote–clinozoisite grains vary from 0.05 to 0.2mm in width. They are xenoblastic to subidioblastic and occur more rarely as disseminated idioblastic crystals. These minerals are either oriented according to S_{n+1}, or have a matrix of strongly hydrothermally altered rocks.

Chlorite is disseminated and generally forms xenoblastic and subidioblastic crystals. It concentrates at rims, cleavage planes and fractures of other minerals, mainly glaucophane. Chlorite may also completely replace glaucophane, resulting in pseudomorphs ranging from 0.1 to 0.9mm in size, which are preferentially oriented along the mylonitic foliation (S_{n+1}). Chlorite with a rosette habit is also present, indicating crystallization under static or hydrothermal regimes. Calcite occurs as xenoblastic grains varying between 0.2 and 0.6mm in width, as inclusions in glaucophane or filling fractures. Some crystals show deformation lamellae. Albite (An_{2-5}) grains (up to 0.3mm in length) are subidioblastic and xenoblastic, usually associated with quartz, and systematically oriented along the mylonitic foliation.

FIGURE 4 | **Plane-polarized light microphotography of a blueschist from the Jambaló area. The mylonitic foliation is defined by glaucophane (Gln) and white mica (Wm), with some glaucophane crystals arranged radially.**

Opaque minerals are found disseminated in all rocks, and they are represented by magnetite, ilmenite and pyrite. Titanite crystals are generally subidioblastic and rarely idioblastic, varying from 0.025 to 0.075mm in size. They occur as aggregates or ribbons that follow the main foliation. Titanite inclusions in glaucophane are associated with cleavage planes and fractures.

Garnet is rare and occurs in a few samples. The crystals vary from 0.2 to 2.6mm in size, are subidioblastic and, occasionally, exhibit very well defined rims. When in contact with glaucophane, garnet grains exhibit thin rims replaced by chlorite.

Apatite, rutile, and zircon occur as small crystals up to 0.05mm in length, disseminated in the rock or as inclusions in glaucophane. Stilpnomelane was found in one sample, reaching 3% in modal proportion. Generally it is elongated according to foliation S_{n+1} and is partially replaced by chlorite.

Texturally, the rocks show lepidonematoblastic or nematolepidoblastic arrangements, depending on the amphibole/mica proportions. Porphyroblastic texture defined by glaucophane is usually observed and some of these crystals are poikiloblasts with inclusions of opaque minerals, micas, carbonate, quartz and rutile. Locally, garnet crystals develop pressure shadows indicating pre to syn-kinematic crystallization. Two metamorphic foliations associated with the generation of the high-pressure rocks were identified. The oldest is observed as a fine schistosity (S_n) observed in some glaucophane-rich rocks and a folded S_i in glaucophane crystals oriented along the mylonitic foliation. This S_i is defined mainly by fine-grained quartz and mica inclusions. The second foliation (S_{n+1}) is mylonitic and is associated with recrystallization and re-orientatation of glaucophane crystals. Usually, the development of this foliation resulted in crystallization of greenschist-facies mineral assemblages and partial to total replacement of glaucophane. In some samples, randomly oriented glaucophane suggests that it formed under near-static tectonic condition close to high-pressure metamorphic-peak conditions.

$^{40}Ar/^{39}Ar$ GEOCHRONOLOGY

Paragonite and phengite coexist in samples 123A (epidote-glaucophane schist) and 124J (mica-glaucophane schist). In other samples, white mica is represented only by paragonite.

The $^{40}Ar/^{39}Ar$ analyses resulted in consistent ages of 59–63Ma. The quality of some analyses is not good due to the low potassium contents of the paragonite and, possibly, the effect of paragonite–phengite intergrowths, as described by Boundy et al. (1997).

Mineral argon isotopic ages either indicate the time of growth, recrystallization or cooling through the blocking temperature for a given cooling rate (McDougall and Harrison, 1999). Experiments of McDougall and Harrison (1999) and Harrison et al. (2009) suggest closure temperature for the Ar–Ar system in muscovite between 325 and 375°C and 425°C, respectively. Geothermobarometric calculations of Jambaló blueschists show that the high-pressure metamorphism occurred at ca. 450°C (Bustamante, 2008), just above the estimates of muscovite closure temperatures of Harrison et al. (2009), indicating that our ages could reflect the timing of (near) peak high-pressure/low-temperature metamorphism. However, the strong deformation in a ductile shear zone and the development of mylonitic foliation defined by glaucophane and greenschist-facies mineral assemblages strongly argues for argon isotope ages corresponding to a post-peak blueschist event (i.e., beginning of exhumation) or shortly afterwards.

The Ar-Ar blocking temperature in paragonite is uncertain (Faure, 1986; Dickin, 1995). However, the concordant $^{40}Ar/^{39}Ar$ ages for Jambaló paragonite and phengite suggest that either the blocking temperature is similar, or that $^{40}Ar/^{39}Ar$ ages have been reset during recrystallization during the mylonitic event. It seems, however, that a spread in $^{40}Ar/^{39}Ar$ ages reflects differences in grain size and/or mineralogy that modulate the precise blocking temperature. Rocks that yield variable ages may relate to continuously moving crustal segments in the accretionary system/subduction channel (Ring et al., 1999).

Our data indicate:

1) The plateau age of 66.9 ±0.2Ma yielded by sample 129C (Fig. 5A), composed of glaucophane + albite + paragonite + calcite + chlorite + quartz, likely represents the age of (near-) peak blueschist-facies metamorphism.

2) Paragonite of sample 124F, consisting of glaucophane + albite + paragonite + calcite + chlorite + titanite + quartz, yielded three spectra (Figs. 5B, 5C, and 5D). The plateau ages obtained for this sample agree within error (62.9±1.0, 61.8±0.9, and 62.4±0.2Ma).

3) Paragonite of sample 124G (glaucophane + paragonite + calcite + chlorite + quartz) yielded two spectra with ages of 62.3±1.1 and 63.0±0.3Ma (Fig. 6). The first steps of one spectrum (Fig. 6A) indicate argon excess and a plateau for intermediate fractions of ^{39}Ar-released. The final steps in both spectra correspond to Ca/K ratios of ca. 4 (Fig. 6B). A third additional spectrum is characterized by Ca/K<1 (Fig. 7), resulting in an apparent age of 54.5±1.6Ma. The wide variation of Ca/K, and the saddle shape of the latter spectrum suggests that this later age is unreliable.

4) Phengite of sample 124J (phengite + glaucophane + albite + calcite + chlorite ± paragonite ± quartz) yielded a

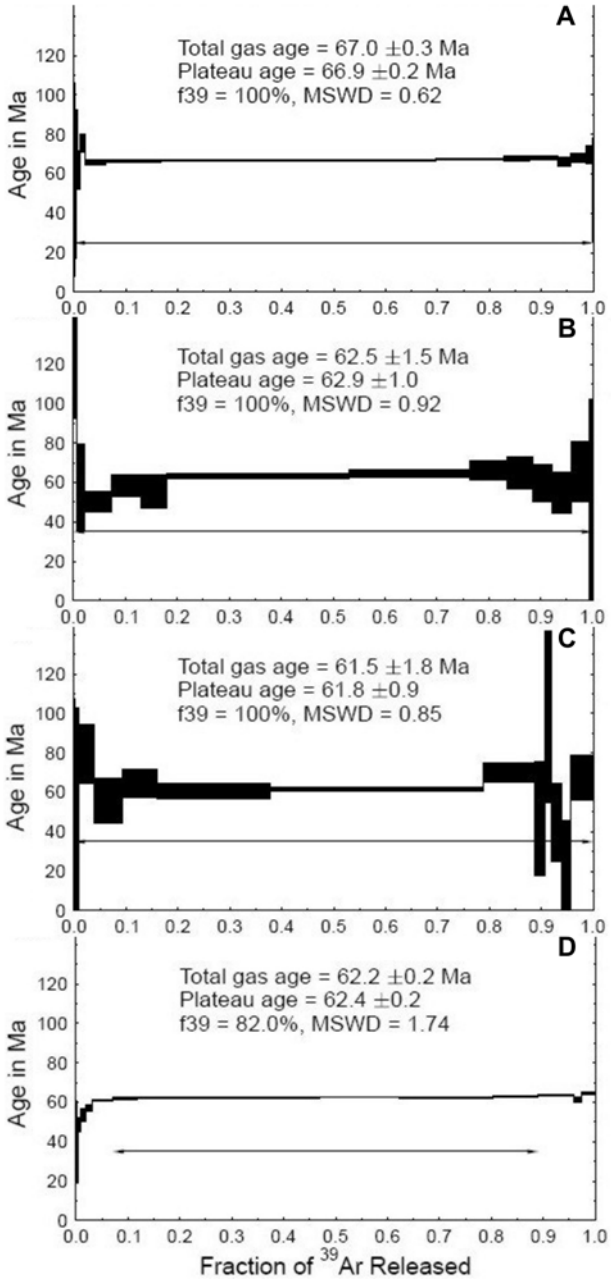

FIGURE 5 | **$^{40}Ar/^{39}Ar$ spectra obtained for sample 129C showing a plateau age of A) 66.9 ±0.2Ma, and sample 124F displaying plateau ages of B) 62.9 ±1.0,Ma C) 61.8 ±0.9Ma, and D) 62.4 ±0.2Ma.**

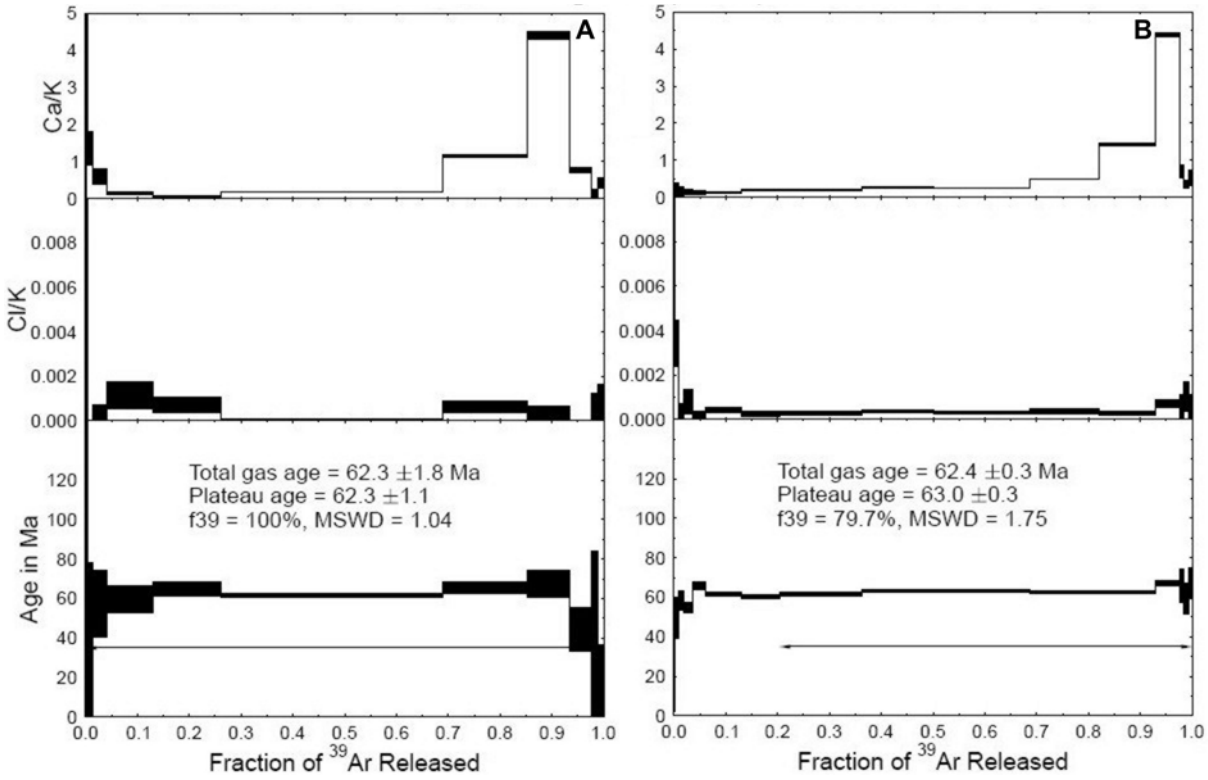

FIGURE 6 | **$^{40}Ar/^{39}Ar$ spectra obtained for sample 124G showing plateau ages of A) 62.3 ±1.1Ma, and B) 63.0 ±0.3Ma.**

spectrum with last steps characterized by Ca/K ratios close to 3 and a plateau age of 67.5±1.1Ma (Fig. 8A).

5) The spectrum of paragonite of sample 121B (glaucophane + paragonite + calcite + chlorite + quartz) yielded a plateau age of 67.8±1.1Ma (Fig. 8B).

6) Paragonite of sample 123A (glaucophane + epidote/clinozoisite + paragonite + phengite + quartz) yielded a spectrum with a Ca/K ratio near 1.5 and a plateau age of 66.0±0.7Ma (Fig. 8C) and 66.3±2.5Ma (Fig. 8D).

7) Paragonite of sample 125M (blueschist-greenschist transitional rock composed of glaucophane + albite + paragonite + calcite + chlorite) yielded a plateau age of 63.5±1.3Ma (Fig. 8E).

DISCUSSION OF THE GEOCHRONOLOGICAL RESULTS

Previous geochronological data for the Jambaló rocks were based on the K–Ar method. Orrego et al. (1980a) reported a minimum whole-rock K–Ar age for the metamorphism of 125±15Ma. Dating glaucophane by the same method De Souza et al. (1984) obtained ages of 104±14Ma and 217±10Ma, the former result being

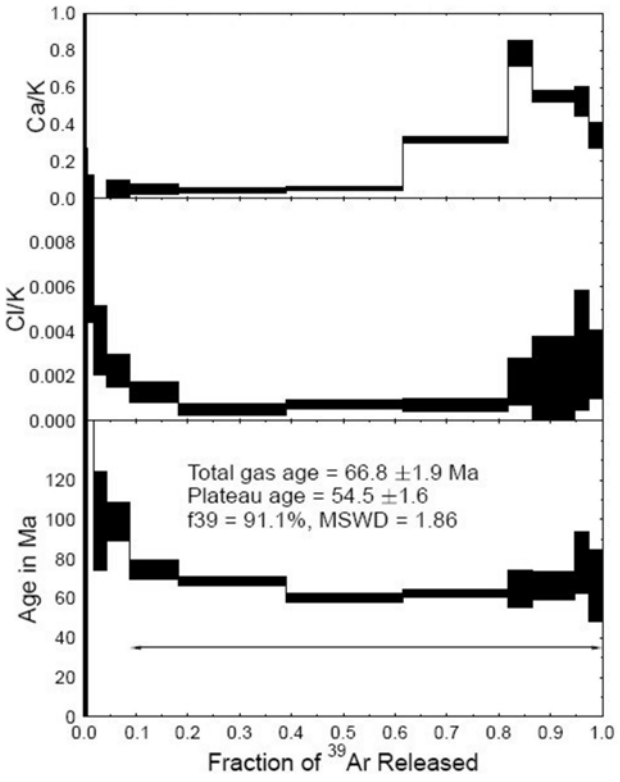

FIGURE 7 | **$^{40}Ar/^{39}Ar$ spectrum obtained for sample 124G showing a plateau age of 54.5 ±1.6Ma.**

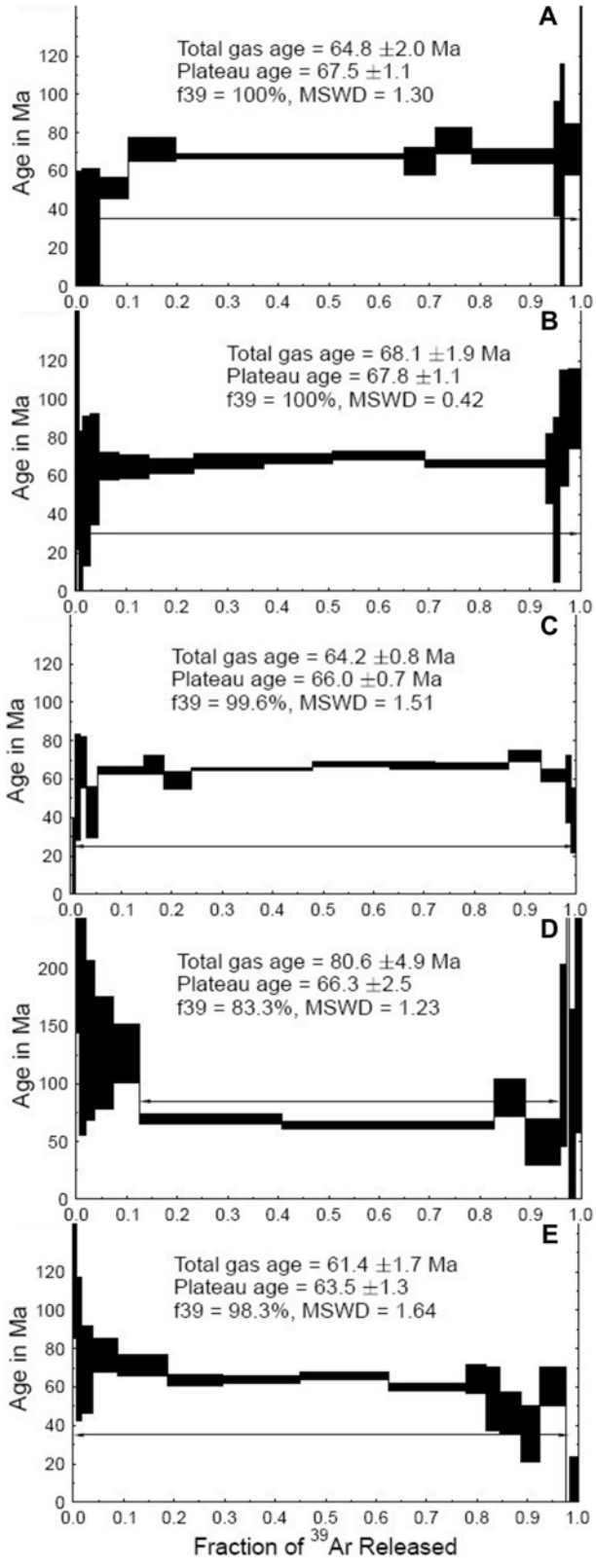

FIGURE 8 | **$^{40}Ar/^{39}Ar$ spectrum obtained for sample 124J displaying a plateau age of A) 67.5 ±1.1Ma; for sample 121B showing a plateau age of B) 67.8 ±1.1Ma; for sample 123A with plateau ages of C) 66.0 ±0.7Ma and D) 66.3 ±2.5Ma; and for sample 125M presenting a plateau age of E) 63.5 ±1.3Ma.**

interpreted as the minimum age of the blueschist-facies metamorphism and the latter as due to argon excess. However, the K–Ar method has several limitations concerning the dating of metamorphic rocks as far as argon loss or excess cannot be determined and the thermal history of minerals (i.e., white micas) cannot be discriminated (Dallmayer and Takasu, 1992; Clauer and Chauduri, 1999). Another well-known disadvantage of traditional K–Ar dating is the application of different analytical techniques for K and Ar, resulting in large propagated errors. In the case of bulk rock analyses, contributions from several K-bearing phases with different K and Ar isotope composition can render the resultant bulk age geologically meaningless (Faure, 1986; Dickin, 1995). On the other hand, the use of glaucophane K–Ar geochronology is questionable because it seldom has measurable potassium by electron microprobe and the detected potassium most likely is due to very fine inclusions of K-bearing minerals such as muscovite-phengite, stilpnomelane or barroisite. Also, ^{40}Ar in glaucophane may have not been produced after in-situ decay of ^{40}K in glaucophane, but simply after trapping of Ar diffusing through the rock (Dickin, 1995).

The $^{40}Ar/^{39}Ar$ data set presented here indicates that metamorphism of the Jambaló blueschists occurred between 67 and 61Ma (Maastritchtian–Danian). The variability in the spectra are related to variable Ca/K ratios, which most likely represent the effects of inclusions. An example of Ca-rich inclusions is illustrated by sample 123A (Fig. 8D). The high and variable Ca/K ratios most likely represent contributions from contamination by Ca-rich minerals such as epidote, calcite and/or barroisite. The high Ca/K ratio in the highest temperature steps is probably related to refractory inclusions and has nothing to do with the mica itself. From a geochronological viewpoint, there are no evidences for ages older than 68Ma.

Considering all lines of evidence, including experimental evidence for closure temperature of ca. 425ºC for muscovite-phengite (Harrison et al., 2009) and recrystallization and formation of retrograde assemblages during mylonitic blueschist-greenschist facies overprints, it is suggested that our 70–60Ma ages obtained for the Jambaló white micas record the mylonitic event responsible for the exhumation of the blueschist facies rocks.

TECTONIC IMPLICATIONS

The Jambaló blueschist-facies rocks, associated with serpentinized peridotite, metabasite and metasedimentary rocks, were affected by an intense retrograde greenschist-facies metamorphism in shear zones. This lithological association can be interpreted as a tectonic mélange bearing mixed metamafic–metaultramafic rocks of intra-oceanic

affinity and metasedimentary rocks (Bustamante, 2008) metamorphosed at different grades, being compatible with an accretionary system or subduction channel environment (see Agard et al., 2009).

It is not possible to distinguish whether the somewhat younger ages may be related to early retrogressive cooling, or to a collisional event in an arc in the western margins of the Caribbean plate. Early retrogressive cooling of paragonite would reset the paragonite ages. Or else, it could happen during a collisional event that took place during exhumation of this blueschist belt between 71–63Ma. In either case the ages would be the same and we interpret that this accretionary system/subduction channel which may be transformed into a collisional zone was actively exhumed from ca. 67Ma to 60Ma as suggested by different Ar–Ar ages that could reflect the flow of the accretionary system/subduction channel.

Late Cretaceous to Paleogene tectonics of the Northern Andes is related to the accretion of several oceanic terranes (Spadea and Espinosa, 1996; Toussaint, 1996; Kerr et al., 1997). Vestiges of these terranes extend from the western flank of the Central Cordillera and the Western Cordillera, and include several arc- and plateau-related terranes. The Jambaló blueschists are limited to the east by a major metasedimentary unit of continental affinity that probably represents a mixture of the continental margin and its older Pre-Jurassic basement (Maya and González, 1995; Vinasco et al., 2006) and to the west by major basaltic terranes of oceanic affinity.

Several models for the Colombian margin have considered that the Maastrichtian tectonic event is a consequence of the accretion of the plateau-like margins of the Caribbean plate (Kerr et al., 1997, Kerr and Tarney, 2005; Pindell and Kennan, 2009), as shown in Figure 9. Petrological constraints in southern Colombia oceanic terranes have shown that as well as this major plateau remnant, there are evidences for the existence of a Campanian intra-oceanic arc remnant in southernmost Colombia (Spadea and Espinosa, 1996). It is therefore suggested that the Jambaló blueschists are remnants of the subduction zone related to the approach of this Campanian

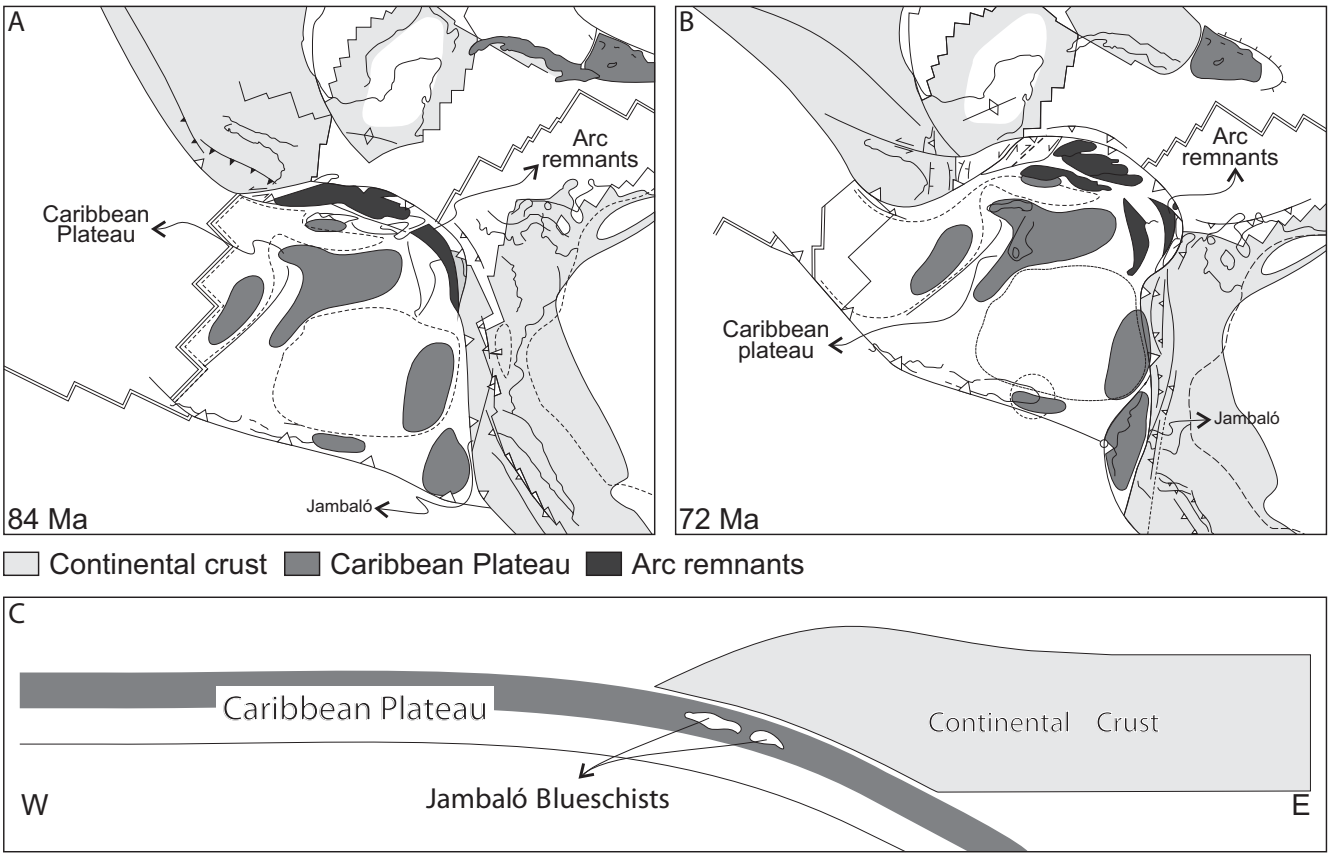

FIGURE 9 | **Model for the Caribbean-South American interactions in the Cretaceous (Pindell, 1993; Pindell et al., 2005). A) Approach of the allochthonous Caribbean arc to the Continental margin. B) Multiple arc-continent collision: in northern South America collision of the Great Caribbean arc, whereas similar contemporaneous accretion is seen along most of the Northern Andean margin. C) Cross section of the development of southwest Colombia showing the possible configuration of the Caribbean and its relationship with the Jambaló Blueschists and the Continental Crust.**

intra-oceanic arc to the continental margin (Fig. 9). Recent tectonic constraints from the Ecuadorian Andes have also shown the existence of similar Campanian arc rocks built on a Caribbean plateau-like substrate (Vallejo et al., 2006, 2009). We therefore envision a model for the southwestern Colombian Andes, with the southeastern margin of the Caribbean plate approaching South America (Pindell and Keenan, 2009). Contemporaneous accretionary events are recorded farther north in the Colombian Caribbean realm, which are related to the arc-continent collision of the Caribbean arc with the margin of northern South America (Cardona et al., 2010). This contrasts with what is seen farther south, including the Jambaló region and Ecuador, where the collision took place with the southeastern margin of the Caribbean plate, and shows the existence of multiple arc-continent collision along the eastern margin of the Caribbean plate.

REGIONAL CORRELATIONS

Barrovian and high-pressure metamorphic belts located between the Central and Western Cordillera of the Colombian Andes and groups within the Arquía Complex (Fig. 1) have been related either to Albian–Aptian metamorphism or to remnants of Pre-Triassic basement (Maya and González, 1995; Toussaint, 1996; Nivia et al., 2006).

At present there are two major ideas on the origin and evolution of the Arquía Complex. The first comprises the remobilization of a possibly Pre-Triassic basement (Maya and González, 1995; Toussaint, 1996; Nivia et al., 2006; Vinasco et al., 2006) and the second considers it as a sequence generated and evolved in Albian–Aptian times (Restrepo and Toussaint, 1976; Toussaint and Restrepo, 1978; Restrepo et al., 2009). Our geochronological data indicates that the Arquía Complex contains a heterogeneous assemblage of blocks including Pre-Triassic fragments, Albian–Aptian metamorphic blocks, and Maastrichtian–Danian rocks such as the Jambaló blueschists described here. In this sense, each one of the different blocks could be used as to decipher the history and evolution of the western South America margin.

The geochronological results presented here show that, as well as older fragments, there are also remnants of a Late Maastrichtian to Paleogene metamorphic belt. Different metamorphic complexes were assembled during the complex series of Meso-Cenozoic accretionary events and the over-imposed dispersion tectonics experienced by the margin (Toussaint, 1996). In this context it is possible to consider that "The Romeral Zone ophiolites" and their related volcanic sequences from the Central Cordillera are oceanic terranes accreted onto the continental margin before ca. 120Ma (Aspden and McCourt, 1986), whereas the Western Cordillera volcanic arc sequences (Spadea and Espinosa, 1996) are an allochtonous terrane accreted onto the continental edge ca. 65–60Ma ago (McCourt et al., 1984).

ACKNOWLEDGMENTS

This study was supported by Fundação de Amparo à Pesquisa do Estado de São Paulo (FAPESP), grant 2004/10203-7, Fundación para la Promoción de la Investigación y la Tecnología from Colombia project 1819: "Evolución geológica de los esquistos azules y rocas asociadas del area de Jambaló, Departamento de Cauca, Colombia", and National Council for Scientific and Technological Development Agency (CNPq) from Brazil. This paper has greatly benefited from a thorough review by Dr. Agustín Cardona of the Smithsonian Tropical Research Institute, and Dr. Marcela Jaramillo.

REFERENCES

Agard, P., Yamato, P., Jolivet, L., Burov, E., 2009. Exhumation of oceanic blueschists and eclogites in subduction zones: Timing and mechanisms. Earth Science Reviews, 92, 53-79.

Aspden, J.A., Bonilla, W., Duque, P., 1995. The El Oro metamorphic complex, Ecuador: geology and economic mineral deposits. Overseas Geology and Mineral Resources. Nottingham, British Geological Survey Publication, 67, 63pp.

Aspden, J.A., McCourt, W.J., 1986. Mesozoic oceanic terrane in the Central Andes of Colombia. Geology, 14, 415-418.

Avé-Lallemant, H.G., 1996. Displacement partitioning and arc-parallel extension: example from the southeastern Caribbean Plate Margin. In: Bebout, G.E., Scholl, D.W., Kirby, S.H., Platt, J.P. (eds.). Subduction top to bottom. American Geophysical Union, Geophysical Monograph, 96, 113-118.

Boundy, T.M., Hall, C.M., Essene, E.J., Halliday, A.N., Peacor, D.R., 1997. Fine-scale fluid distribution in the deep crust: A combined $^{40}Ar/^{39}Ar$ laser ablation and TEM study of single muscovites from a granulite-eclogite transition zone. Earth and Planetary Science Letters, 148, 223-242.

Bourgois, J., Toussaint, J.F., González, H., Azema, J., Calle, B., Desmet, A., Murcia, L.A., Acevedo, A.P., Parra, E., Tournon, J., 1987. Geological history of the Cretaceous ophiolitic complexes of northwestern South America (Colombian Andes). Tectonophysics, 143, 307-327.

Bowes, D.R., 1989. The encyclopedia of igneous and metamorphic petrology. USA, Van Nostrand Reinhold, 666pp.

Bustamante, A., 2008. Geotermobarometria, geoquímica, geocronologia e evolução tectônica das rochas da fácies xisto azul nas áreas de Jambaló (Cauca) e Barragán (Valle del Cauca), Colômbia. Doctoral Thesis. São Paulo, Universidade de São Paulo, 178pp. Available online since 08-25-2008 at www.teses.usp.br. Last month checked September of 2011.

Cardona, A., Valencia, V., Bustamante, C., García-Casco, A., Ojeda, G., Ruiz, J., Saldarriaga, M., Weber, M., 2010. Tectonomagmatic setting and provenance of the Santa Marta Schists, northern Colombia: Insights on the growth and approach of Cretaceous Caribbean Oceanic terranes to the South American continent. Journal of South American Earth Sciences, 29, 784-804.

Chicangana, G., 2005. The Romeral fault system: a shear and deformed extinct subduction zone between oceanic and continental lithospheres in northwestern South America. Earth Sciences Research Journal, 9, 51-66.

Clauer, N., Chauduri, S., 1999. Isotopic dating of very low-grade meta-sedimentary and meta-volcanic rocks. Methods and techniques. In: Frey, M., Robinson, D. (ed.). Low-grade metamorphism. Blackwell-Science, 202-226.

Cloos, M., 1982. Flow melanges: numerical modeling and geologic constraints on their origin in the Franciscan subduction complex, California. Geological Society of America Bulletin, 93, 330-344.

Dallmayer, R.A., Takasu, A., 1992. $^{40}Ar/^{39}Ar$ ages of detrital muscovite and whole-rock slate/phyllite, Narragansett Basin, RI-MA, USA: implications for rejuvenation during very low-grade metamorphism. Contributions to Mineralogy and Petrology, 110, 515-527.

De Souza, H.A.F., Espinosa, A., Delaloye, M., 1984. K–Ar ages of basic rocks in the Patia Valley, southwest Colombia. Tectonophysics, 107, 135-145.

Dickin, A.P., 1995. Radiogenic isotope geology. Cambridge, Cambridge University Press, 490pp.

Draper, G., Lewis, J.F., 1991. Metamorphic belts of central Hispaniola. In: Mann, P., Draper, G., Lewis, J.F. (eds.). Geologic development of the North American–Caribbean plate boundary in Hispaniola. Geological Society of America, 262 (Special Paper), 29-45.

Ernst, W.G., 1988. Tectonic history of subduction zones inferred from retrograde blueschist P–T paths. Geology, 16, 1081-1084.

Faure, G., 1986. Principles of isotope geology. United States of America, John Wiley & Sons, 589pp.

Feininger, T., 1980. Eclogite and related high-pressure regional metamorphic rocks from the Andes of Ecuador. Journal of Petrology, 21, 107-140.

Feininger, T., 1982. Glaucophane schist in the Andes at Jambaló, Colombia. The Canadian Mineralogist, 20, 41-47.

Forero-Suárez, A., 1991. Distribución de las rocas del Devónico en los Andes Colombianos. In: Suárez, R. (ed.). Trabajos presentados en la reunión del proyecto 193: Siluro–Devonian of Latin America, Bolivia. Revista Técnica de Yacimientos Petrolíferos Fiscales Bolivianos (YPFB), 12, 101-111.

Giunta, G., Beccaluva, L., Coltorti, M., Siena, F., Vaccaro, C., 2002. The southern margin of the Caribbean Plate in Venezuela: tectono–magmatic setting of the ophiolitic units and kinematic evolution. Lithos, 63, 19-40.

González, H., 1977. Conceptos de metamorfismo dinámico. Su aplicación a la Zona de Falla Romeral. Universidad Nacional, Medellín, Boletín Ciencias de la Tierra, 2, 81-106.

Harrison, T.M., Celerier, J., Aikman, A.B., Hermann, J., Heizler, M.T., 2009. Diffusion of ^{40}Ar in muscovite. Geochimica et Cosmochimica Acta, 73, 1039-1051.

Keane, S.D., Dewolf, C.P., Essene, E.J., Halliday, A.N., Hall, C.M., Cosca, M.A., 2006. Isotopic constraints on the thermal history of the Wind River Range, Wyoming: implications for Archean metamorphism. Canadian Journal of Earth Sciences, 43, 1511-1532.

Kerr, A.C., Aspden, J.A., Tarney, J., Pilatasig, L.F., 2002. The nature and provenance of accreted oceanic terranes in western Ecuador; geochemical and tectonic constraints. Journal of the Geological Society of London, 159, 577-594.

Kerr, A.C., Marriner, G.F., Tarney, J., Nivia, A., Saunders, A.D., Thirlwall, M.F., Sinton, C.W., 1997. Cretaceous basaltic terranes in western Colombia: Elemental, chronological and Sr–Nd isotopic constraints on petrogenesis. Journal of Petrology, 38, 677-702.

Kerr, A.C., Tarney, J., 2005. Tectonic evolution of the Caribbean and northwestern South America: The case for accretion of two Late Cretaceous oceanic plateaus. Geology, 33, 269-272.

Luzieux, L.D.A., Heller, F., Spikings, R., Vallejo, C.F., Winkler, W., 2006. Origin and Cretaceous tectonic history of the coastal Ecuadorian forearc between 1°N and 3°S: Paleomagnetic, radiometric and fossil evidence. Earth and Planetary Science Letters, 249, 400-414.

Maya, M., González, H., 1995. Unidades litodémicas en la Cordillera Central de Colombia. Boletín Geológico Ingeominas, 35, 43-57.

McCourt, W.J., Aspden, J.A., Brook, M., 1984. New geological and geochronological data from the Colombian Andes: continental growth by multiple accretion. Journal of the Geological Society of London, 141, 831-845.

McDougall, I., Harrison, T.M., 1999. Geochronology and thermochronology by the $^{40}Ar/^{39}Ar$ method. New York, Oxford University Press, 269pp.

Mégard, F., 1987. Cordilleran Andes and marginal Andes: a review of Andean geology north of the Arica elbow (10°S). American Geophysical Union Monograph, 18, 71-95.

Nivia, A., Marriner, G.F., Kerr, A.C., Tarney, J., 2006. The Quebradagrande Complex: A Lower Cretaceous ensialic marginal basin in the Central Cordillera of the Colombian Andes. Journal of South American Earth Sciences, 21, 423-436.

Núnez, A., Murillo, A., 1978. Esquistos de glaucofana en el municipio de Pijao, Quindio (Colombia). Bogotá, Congreso Colombiano de Geología, 2 (resúmenes), 1-18.

Orrego, A., Restrepo, J.J., Toussaint, J.F., Linares, E., 1980a. Datación de un esquisto sericítico de Jambaló, Cauca. Geología Universidad Nacional, 25 (Special Publications), 133-134.

Orrego, A., Cepeda, H., Rodríguez, G., 1980b. Esquistos glaucofánicos en el área de Jambaló, Cauca (Colombia). Geología Norandina, 1, 5-10.

Pindell, J.L., 1993. Evolution of the Gulf of Mexico and the Caribbean. In: Donovan, S.K., Jackson, T.A. (eds.).

Caribbean geology: An introduction. University of West Indies Publisher's Association, 13-39.

Pindell, J.L., Kennan, L., 2009. Tectonic evolution of the Gulf of Mexico, Caribbean and northern South America in the mantle reference frame: an update. In: James, K., Lorente, M.A., Pindell, J. (eds.). The geology and evolution of the region between North and South America. Geological Society of London, 328 (Special Publications), 1-55.

Pindell, J.L., Kennan, L., Maresch, W.V., Stasnek, K.P., Draper, G., Higgs, R., 2005. Plate kinematic and crustal dynamics of circum-Caribbean arc–continent interactions: Tectonics controls on basin development in the Proto-Caribbean margins. In: Avé-Lallemant, H.G., Sisson, V.B. (eds.). Caribbean–South American Plate Interactions, Venezuela. Geological Society of America, 394 (Special Paper), 7-52.

Ramos, V.A., 1999. Plate tectonic setting of the Andean Cordillera. Episodes, 22, 183-190.

Ramos, V.A., Alemán, A., 2000. Tectonic evolution of the Andes. In: Cordani, U.J. Milani, E.J., Thomaz Filho, A., Campos, D.A. (eds.). Tectonic evolution of South America. Rio de Janeiro, 31st International Geological Congress, 635-685.

Restrepo, J.J., 1986. Metamorfismo en el sector norte de la Cordillera Central de Colombia. Medellín (Colombia), Universidad Nacional, unpublished internal report (trabajo de promoción a profesor titular), 276pp.

Restrepo, J.J., Ordóñez-Carmona, O., Moreno-Sánchez, M., 2009. A COMMENT ON "The Quebrada Grande Complex: A Lower Cretaceous ensialic marginal basin in the Central Cordillera of the Colombian Andes" by Nivia et al. Journal of South American Earth Sciences, 28, 204-205.

Restrepo, J.J., Toussaint, J.F., 1988. Terranes and continental accretion in the Colombian Andes. Episodes, 11, 189-193.

Restrepo, J.J., Toussaint, J.F., 1982. Metamorfismos superpuestos en la Cordillera Central. Buenos Aires (Argentina), 5th Congreso Latinoamericano de Geología, 3 (Actas), 505-512.

Restrepo, J.J., Toussaint, J.F., 1976. Edades radiométricas de algunas rocas de Antioquia, Colombia. Medellín, Publicación Especial de Geología, Universidad Nacional, 6, 1-15.

Ring, U., Brandon, M.T., Willett, S.D., Lister, G.S., 1999. Exhumation processes. In: Ring, U., Brandon, M.T., Lister, G.S., Willett, S.D. (eds.). Exhumation processes: normal faulting, ductile flow and erosion. Geological Society London, 154 (Special Publications), 1-27.

Smith, C.A., Sisson, V.B., Avé-Lallemant, H.G., Copeland, P., 1999. Two contrasting pressure–temperature–time paths in the Villa de Cura blueschist belt, Venezuela: possible evidence for Late Cretaceous initiation of subduction in the Caribbean. Geological Society of America Bulletin, 111, 831-848.

Spadea, P., Espinosa, A., 1996. Petrology and chemistry of late Cretaceous volcanic rocks from the southernmost segment of the Western Cordillera of Colombia (South America). Journal of South American Earth Sciences, 9, 79-90.

Streepey, M.A., van der Pluijm, B.A., Essene, E.J., Hall, C.M., Magloughlin, J.F., 2000. Late Proterozoic (ca. 930Ma) extension in eastern Laurentia. Geological Society of America Bulletin, 112, 1522-1530.

Toussaint, J.F., 1996. Evolución Geológica de Colombia, Cretácico. Medellín, Universidad Nacional de Colombia, 142pp.

Toussaint, J.F., Restrepo, J.J., 1978. Edad cretácea de una anfibolita granatífera de Pijao, Quindío. Medellín, Publicación Especial de Geología, Universidad Nacional, 17, 1-2.

Vallejo, C., Spikings, R.A., Luzieux, L., Winkler, W., Chew, D., Page, L., 2006. The early interaction between the Caribbean Plateau and the NW South American Plate. Terra Nova, 18, 264-269.

Vallejo, C., Winkler, W., Spikings, R.A., Luzieux, L., Heller, F., Bussy, F., 2009. Mode and timing of terrane accretion in the forearc of the Andes in Ecuador. In: Kay, S.M., Ramos, V.A., Dickinson, W.R. (eds.). Backbone of the Americas: shallow subduction, plateau uplift, and ridge and terrane collision. Geological Society of America Memoirs, 204, 197-216.

Vinasco, C.J., Cordani, U.G., González, H., Weber, M., Peláez, C., 2006. Geochronological, isotopic, and geochemical data from Permo–Triassic granitic gneisses and granitoids of the Colombian Central Andes. Journal of South American Earth Sciences, 21, 355-371.

Manuscript received November 2010;
revision accepted May 2011;
published Online June 2011.

Geologica Acta, Vol.9, Nos 3-4, September-December 2011, 363-387
DOI: 10.1344/105.000001694
Available online at www.geologica-acta.com

geologica acta

Jadeitite from Guatemala: new observations and distinctions among multiple occurrences

G. E. HARLOW [1] **V. B. SISSON** [2] **S. S. SORENSEN** [3]

[1] **Department of Earth and Planetary Sciences, American Museum of Natural History**
New York, New York, USA. E-mail: gharlow@amnh.org

[2] **Department of Earth and Atmospheric Sciences, University of Houston**
Houston, TX, USA. E-mail: j_sisson@netzero.net

[3] **Department of Mineral Sciences, Smithsonian Institution**
Washington, DC, USA. E-mail: sorensen@si.edu

ABSTRACT

In Guatemala, jadeitite occurs as blocks in serpentinite mélange in distinct settings on opposite sides of the Motagua fault. Jadeitites north of the Motagua fault are associated with eclogites, blueschists, and garnet amphibolites and distributed over a 200km E-W area. Omphacitite, omphacite - taramite metabasite, albitite, and phengite rock are found with jadeitite. The assemblages indicate formation at 6-12kbar and 300-400°C, however jadeite - omphacite pairs yield T from ~200 to >500ºC for jadeite crystallization. Jadeitites south of the Motagua fault are sourced from three separate fault slices of serpentinite in Jalapa and Zacapa departments and are distinctive:

1) Jadeitite near Carrizal Grande is found in serpentinite with lawsonite eclogites, variably altered to blueschist, and rarely in schists. A large jadeite – omphacite gap and lawsonite suggests T=300-400°C, but at high P as indicated by the presence of quartz: P>12-20kbar. Lawsonite eclogites (P=20-25kbar, T=350-450°C) occur with these jadeitites.

2) At La Ceiba, jadeitites coexist with omphacite blueschists and contain late-stage veins of quartz, diopside, cymrite, actinolite, titanite and vesuvianite. A large jadeite – omphacite gap suggests 300-400°C, but at lower P as indicated by quartz + albite: P=10-14kbar.

3) At La Ensenada jade i tites occur with lawsonite-glaucophane blueschists and chloritite. It is a fine-grained jadeite-pumpellyite rock, intensely deformed and veined with grossular, omphacite, albite and titanite, but no quartz. A large jadeite–omphacite gap and pumpellyite suggest ~200-~300°C at lower P consistent with primary albite: P=6-9kbar. The silicates contain little iron.

KEYWORDS | **Jadeitite. Serpentinite. Mélange. HP–LT rock. Subduction processes.**

INTRODUCTION

The jade of the indigenous Middle American cultures of Mexico and Central America is jadeite rock (jadeitite) as well as the material from which jadeite derived its name (Foshag, 1957; Harlow et al., 2007). After knowledge of the sources was lost to the original inhabitants of Middle America, it was not until the early 1950s that workshop materials were discovered by Foshag and Leslie (1955) and then boulders by McBirney et al. (1967). These led to the eventual recognition that jadeitite was hosted in serpentinite mélanges north of the Río Motagua in central Guatemala (e.g., Hammond et al., 1979; Harlow, 1994). The river generally follows the Motagua fault zone (this zone includes many nearby parallel and sub-parallel faults within the valley), the broad boundary between the North American and Caribbean plates. The location (north versus south) is best referenced to the active strand in the Motagua fault zone, the Motagua fault, which has other names locally, such as the Cabañas fault in the central part of the valley, named for the town closest to the epicenter of the 1976 earthquake. The jadeitite-bearing region was demarked as extending between Río La Palmilla and the town of Estancia de La Virgen, a distance of about 14km (Fig. 1) and was the only described jadeitite source in Central America prior to the year 2000. A resurgence of interest and scientific recognition of a much larger areal distribution awaited the serendipitous recognition by Russell Seitz, an investigator from a 1970s jade sourcing project, of a single piece of jade (jadeitite) at a shop in Antigua Guatemala that closely resembled blue-green Olmec jade (Seitz et al., 2001; Taube et al., 2004). This discovery combined with severe flooding caused by Hurricane Mitch in 1998, which turned over the boulder fields in drainages south of the Río Motagua, led to a resurgence of interest in jadeitite sources by the authors and others. Over a few years we were shown previously undescribed sources by Guatemalan geologists and local jade hunters (jaderos), including ones traversed by Río El Tambor (Río Jalapa in Jalapa Department) and its tributaries, south of Río Motagua. In addition to the jadeitite, largely overlooked eclogite occurrences were encountered which increased the interest and potential scientific significance among the serpentinite-hosted high-pressure/low-temperature (HP–LT) rocks of the Motagua fault zone. Commercial and artisanal exploration for jade and our own field studies over the intervening years have revealed that sources north of the fault are distributed sporadically in serpentinite over at least 110km E-W and a smaller distribution of sources of 3 distinct clusters of jadeitite sources, within 11km of one another. Most recently we sampled an area of jadeitites near Rosario, east of Lago Izabal, and 203km from Saltán the most western source. Although we have mentioned some of these new sources in part in other papers (Seitz

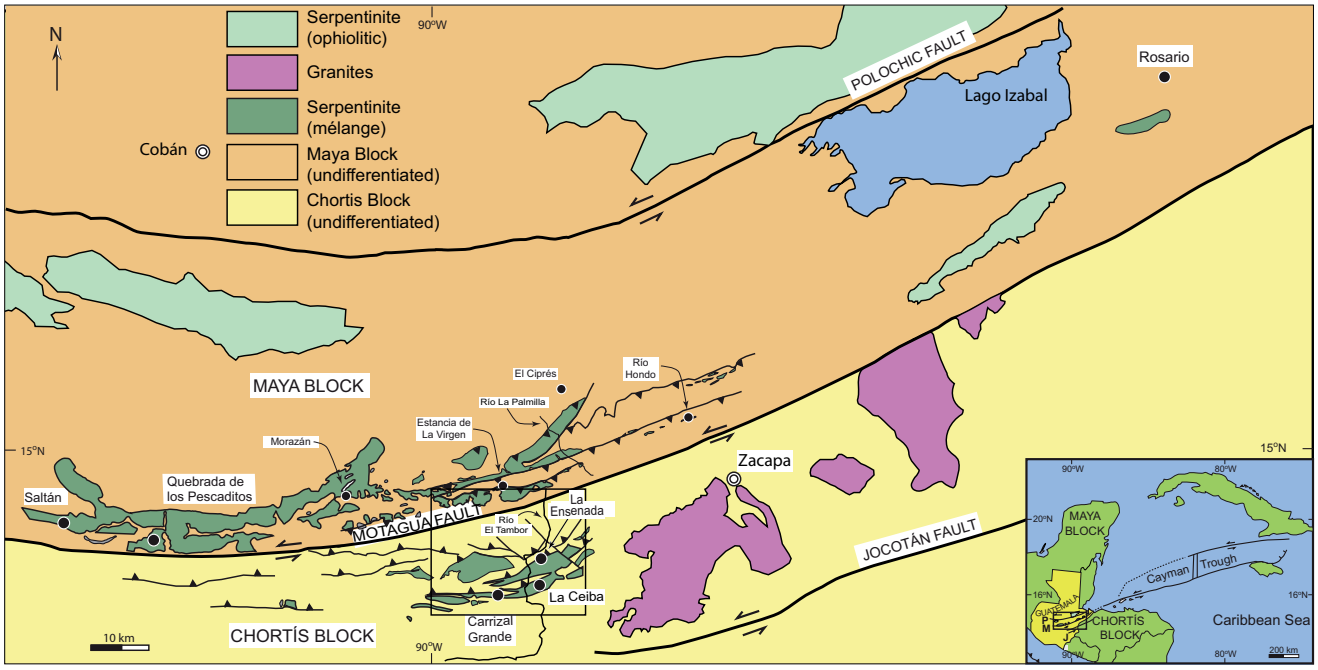

FIGURE 1 | **Regional map showing the location of jadeitite occurrences along the Motagua Valley of central Guatemala. Serpentinite bodies are differentiated between lizardite-dominant thrust blocks (ophiolitic) and antigorite-dominant HP–LT mélange. Late Cretaceous – Early Tertiary granite bodies in the Chortís block are shown with hachures. The area in Fig. 3 is defined by the outlined rectangle in lower portion of the figure. M: Motagua fault, P: Polochic fault and J: Jocotan Fault.**

et al., 2001; Harlow et al., 2004a, 2006a, 2007), here we describe these jadeitites and jade-like rocks to point out their location-distinctive appearance, mineralogy, and microtextures and inferences for origin among the HP–LT blocks in the serpentinite mélanges straddling the Motagua fault zone in Guatemala.

GEOLOGICAL SETTING

The boundary between the North American and Caribbean plates in Guatemala is defined by the Motagua fault zone, one of three left-lateral, subparallel strike-slip fault systems: Polochic (Polochic–Chixoy), Motagua, and Jocotán (Jocotán–Chamelecón); (see Fig. 1). Tectonic slices of serpentinite mélange containing HP–LT rocks occur adjacent to the Motagua fault, both north (regionally the Maya block) and south (Chortís block). These blocks are distinctly different as the basement of the Chortís block contains a significant mafic component, while the Chuacús Series of the Maya block is dominantly quartzofeldspathic. Lithologies on either side of the Motagua fault, with the exception of the serpentinites and related rocks, are completely different from each other (Francis, 2005; Alvarado et al., 2007; Martens et al., 2007a; Francis et al., in preparation), suggesting simple juxtaposition of differing terranes and/or considerable displacement along the Motagua fault. The units in the Maya block to the north include the high-metamorphic-grade Chuacús Complex (McBirney, 1963; van den Boom, 1972; Ortega-Gutiérrez et al., 2004; Martens et al., 2007b), Paleozoic sediments of the Santa Rosa Group and deformed granites. The Chortís block south of the fault contains the greenschist facies San Diego phyllite, the amphibolites facies Las Ovejas complex with felsic and mafic intrusives, and large, relatively undeformed granitoids of uncertain age. There are several granitic intrusions in the Chortís block that are of Late Cretaceous and Early Tertiary age (Donnelly et al., 1990). The block also contains the El Tambor ophiolite complex, recently dated on the basis of radiolaria to be of Late Jurassic age (Chiari et al., 2006). Both blocks are mantled with modern arc volcanics to the south and west, further complicating interpretation.

Until recently, the HP–LT belts along the Motagua fault had been assigned to a single tectonic (collisional) event in the Late Cretaceous, although all studies noted the strong lithotectonic dichotomy in these terranes (see Donnelly et al., 1990). North of the Motagua fault, serpentinite mélange hosts garnet amphibolite, omphacite-taramite metabasite, jadeitite, albitite, and, more recently reported, altered clinozoisite - amphibole - eclogite in the western reaches of the serpentinite mélange (Tsujimori et al., 2004a; Brueckner et al., 2005). These rocks span a wide range of conditions, from greenschist - blueschist at lower P (200-400°C at ≤1GPa) to moderate low-temperature eclogite facies of 500-600°C at ~2GPa. In contrast, south of the fault, assemblages include lawsonite eclogite, blueschist, and jadeitite in serpentinite matrix that record peak P-T conditions among the coldest and wettest deep subduction trajectories on Earth, to ~2.6GPa and only ~470ºC (Tsujimori et al., 2006a, b). Compounding the differences, Harlow et al. (2004a) reported disparate $^{40}Ar/^{39}Ar$ ages on the mica and amphibole from these HP–LT rocks: north of the fault ages range between 77 and 65Ma, whereas rocks south of the fault yield ages of 125-116Ma. Subsequent determinations of five Sm-Nd mineral isochrons from eclogites both north and south of the fault have yielded ages of 144-126Ma (Brueckner et al., 2009). The rarely recorded presence of jadeitite, lawsonite eclogite and a tectonic-timing conundrum represent only a small aspect of the complex geology exposed in central Guatemala related to the boundary region between the Maya and Chortís blocks, let alone the North American and Caribbean plates.

JADEITITE: OCCURRENCE AND ASSOCIATIONS

The jadeitite found north of the Motagua fault was described by Harlow (1994), so the intent here is to present new observations and interpretations, while only summarizing the generalizations in that paper. Moreover, as jadeitite from south of the Motagua fault has not been described in detail and is distinctly different from jadeitite found north of the Motagua fault, a greater portion of the attention is devoted to these. Fundamentally, most of the jadeitite occurrences were discovered by jade hunters (jaderos in Spanish) who have shown them to us. This transfer of information has resulted in the considerable growth in areal distribution presented here. The rocks studied and abbreviations for mineral names are given in Table I, Electronic Appendix, available in www.geologica-acta.com

The jadeitite occurrences along the Motagua fault zone are all sourced within serpentinite-dominant mélange (that is mélange in which serpentinite dominates both as matrix and as broken up blocks–an abundance of mixed sedimentary and HP–LT rocks is not observed). The serpentinites consist predominantly of antigorite, with lesser lizardite (no chrysotile has been observed) with interstitial magnetite, magnesite, chlorite, talc, pentlandite and low-T Ni-sulfides and occasional relict clinopyroxene, pseudomorphed orthopyroxene (bastite) or magnesiochromite (Harlow et al., 2006b; Bertrand and Vuagnat, 1976, 1980). There are subtle differences in the mineralogy of the serpentinite, as a whole, from the north to the south sides of the Motagua fault, particularly in the relative abundance of magnesite and talc, but otherwise the recorded gross differences are not large (Harlow et al., 2006b). The protolith has so far

been interpreted as dominantly harzburgite but probably ranges from dunite with rare podiform chromite through harzburgite to spinel lherzolite (Bertrand and Vuagnat, 1976, 1980; Harlow et al., 2006b); however, further analysis is required. Serpentinization in most samples is complete (no protolithic mineral or textural relics remain) with petrofabrics varying greatly between antigorite fels to highly sheared serpentine schists. Rare ultramafic relic phases include aluminous augite, chromite and pentlandite (Harlow et al., 2006b, 2010). All features are consistent with serpentinite produced at depth, presumably adjacent to a subduction channel responsible for the HP–LT blocks.

Irrespective of location relative to the Motagua fault, jadeitite occurs in small areas, typically extending no more than a few hundred meters, commonly distributed as boulders and cobbles of a dismembered larger body sitting on (and in) serpentinite (Fig. 2). Even more commonly the jadeitite occupies drainages cutting through or downstream from the serpentinite mélange. In some cases these broken blocks are dispersed with other HP–LT lithologies along alignments, which we interpret as faults within the mélanges, or in slumped fields in serpentinite downhill from such a boundary. Boulders can measure up to 5meters across (e.g., at Quebrada Seca, about 2.5km SE of Carrizal Grande, south of the Motagua fault, or in Río La Palmilla, north of the Motagua fault) although meter or smaller sizes are most common. Jadeitite rarely occurs as discrete blocks or veins with contact relationships to serpentinite. Jadeitite blocks in place (although probably with tectonic contacts) are limited to La Ceiba (S), Quebrada Seca, near Carrizal Grande (S) and El Ciprés in the Sierra de las Minas (N) (see Figs. 1 and 3), although the latter has been dismembered by jade extraction (Sorensen et al., 2005, 2010).

Occurrences North of the Motagua fault

Fields of jadeitite generally occur in what appear to be distinct fault segments or along boundaries between serpentinite and Chuacús Series basement. The distribution now extends from the westernmost occurrence, just south of the town of Saltán, Baja Verapaz department (14.9005°N, 90.5983°W), to the town of Río Hondo, Zacapa department (15.0444ºN 89.5853W), spanning a distance of 110km (Fig. 1). The newly-visited far-eastern source area is near Rosario, Izabal department (15.6866N, 88.8998W), more than 200km from Saltán. The jadeitites share many characteristics and occur with a limited assemblage of other HP–LT rocks. Most of the jadeitite is massive and whitish to pale gray or pale green (Fig. 4A) and commonly with transecting veins of coarser jadeitite or albitite-like alteration. Blocks of white-to-mauve jadeitite (Fig. 4B) have been found in a *quebrada* (dry gulch) near Saltán, the western extent to date, and have a distinctive phase assemblage as well as appearance. Mostly medium green jadeitite has been recovered from near Rosario at the eastern limit of occurrences, and this material is not distinctive in terms of phase assemblage compared to the bulk of jadeitite north of the Motagua fault. The jadeitite blocks show cataclastic to sheared textures in addition to the veins. Albitization around block margins and fractures post-dating jadeite-veining is common; complete replacement of jadeitite by albitite typically occurs toward the boundary of a block with serpentinite host, if contact relationships can be observed. The jadeitite - serpentinite contact zone consists of concentrically foliated blackwall mineralogy (actinolite + clinochlore ± talc) a few centimeters to perhaps a meter thick, penetrated by centimeter to decimeter wide bundles of acicular actinolite aligned radial to the block. Sorensen et al. (2010) have described a complete contact assemblage at El Ciprés, documenting not only the transition from jadeitite to albitite to altered ultramafic boundary to serpentinite but also the chemical transport between and through each zone. Rocks that have the same massive appearance as jadeitite but are darker green tend to be dominated by omphacite and thus are actually omphacitites. There is an intimate association of jadeitite and albitite north of the Motagua fault, which is in part due to the alteration of jadeitite to albitite, but albitite occurs as a distinct rock without apparent replacement texture (Harlow, 1994). In addition, albite-phengite rocks, phengite rocks (noticeably dense from high Ba content; Harlow, 1995), taramite-omphacite metabasite (Harlow and Donnelly, 1989), omphacitite, and garnet-clinozoisite amphibolite or clinozoisite eclogite are commonly associated with the jadeitites. Garnet amphibolite is found only in the eastern extent (as far west as Morazán) and eclogite in the west (as far east as

FIGURE 2 | **Broken jadeitite blocks sitting on serpentinite subsurface, Piedra Parada Dos Ríos, El Cimiento Quad. (9.4km NNW of the mouth of Río La Palmilla, 300m from that river). The accumulation of smaller boulders at the bases of trees were placed there by jaderos.**

Quebrada de los Pescaditos). Omphacite inclusions in garnet of garnet amphibolite indicate that some of this lithology is retrograded eclogite. Jadeitite from north of the Motagua fault is also distinctive in its mineralogy (below).

Occurrences South of the Motagua fault

Jadeitite has probably been known in this area for a considerable time by some *jaderos* and jade workshops in Antigua, Guatemala; however, study did not commence until our first visit in 2001. There are three distinct areas in the mountains of Jalapa and Zacapa departments with very small areal distributions, typically of one to several kilometers. They are near the towns of Carrizal Grande, La Ceiba, and La Ensenada (Figs. 1 and 3) and are all within 11km of one another.

In the Carrizal Grande area, further south, jadeitite occurs mostly as isolated blocks with ill-defined contacts to adjacent serpentinite or in the drainages of several *quebradas*. Up-slope and up-stream limits appear to align with minor fault traces cutting subparallel to the overall serpentinite fault boundary (see Fig. 3). Jadeitite is generally massive and often contains conspicuous phengitic muscovite (Ms) or lawsonite phenoblasts. Color is light to medium to medium dark green with occasional dark blue-green veins colored by blue omphacite (Fig. 4C; Harlow et al., 2004b). Coexisting lithologies include lawsonite eclogite, blueschist - altered eclogite, lawsonitite, glaucophane - omphacite rock, garnet - quartz - phengite schist, and graphite - bearing quartz - mica schist (Tsujimori et al., 2006a). Near La Ceiba the jadeitite is tightly confined to a 100 meter wide exposure in serpentinite (no contacts exposed) as blocks to a few meters in size. Smaller blocks litter a *quebrada* below this exposure. The jadeitite is generally medium to dark green, on occasion intensely green, and fine-grained to microcrystalline but highly fractured (Fig. 4D). In rare cases jadeitite blocks are encapsulated by a diopside-rich rock. Coexisting tectonic blocks in the area are omphacite -

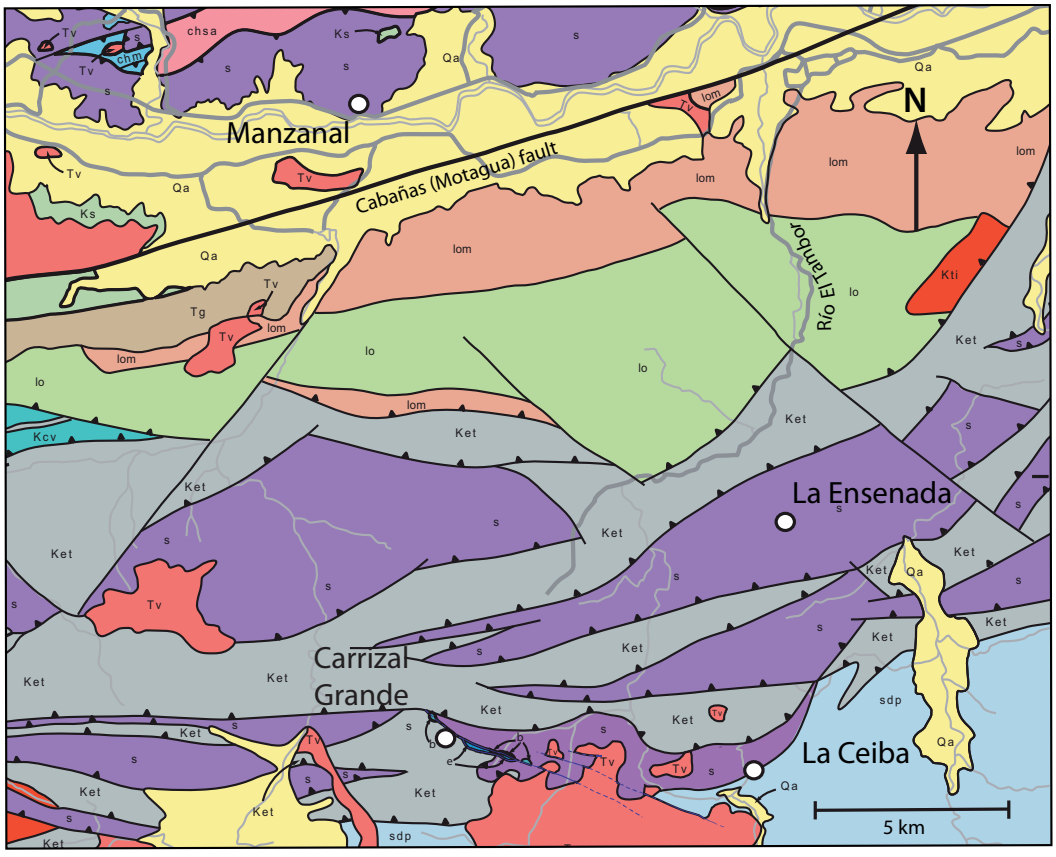

FIGURE 3 | **Geological map of area of HP–LT sources south of the Motagua fault, showing the general location of Carrizal Grande, La Ceiba, and La Ensenada; Manzanal, the first-described location north of the Motagua fault (Cabañas fault) is also shown. See the box in Fig. 1 for the location of this map. The base map is derived from a revision of an unpublished map by T. Donnelly and coworkers (Francis et al., in preparation). Formation abbreviations: chm: Chuacús marble; chsa: San Agustín formation; Kcv: Mylonitized limestone (Cerro La Virgen formation, LS tectonites); Ket: El Tambor fm.; Ks: Subinal fm.; Kti: granite plutons; lo: Las Ovejas fm. (undifferentiated); lom: Las Ovejas marble; Qa: Quaternary alluvium; s: Serpentinite; Tg: Guastatoya Fm., including mélange lithologies in most cases, but m: mélange, e: eclogite and b: blueschist shown near Carrizal Grande; sdp: San Diego phyllite; Tv: Tertiary volcanics.**

FIGURE 4 | **Photographs of jadeitite hand-samples: A) Slab of whitish coarse-grained jadeitite: MVE04-44-2, Quebrada de los Pescaditos, 2.3cm wide; B) Slab of lavender jadeitite with pumpellyite at rim: MVE07B-19-1, near Saltán, 3cm across; C) Polished slice of jadeitite w/ large phengite grains and veins of blue-green omphacite: VM02-1, Quebrada Seca, Carrizal Grande, 15cm across; D) Polished jadeitite showing mottled dark green body cut by fractures and veins of cymrite and vesuvianite + cymrite: MVE02-17-5, La Ceiba, 3cm across; E) Sawn block of pumpellyite-jadeitite cut by a vein of brown chloritite: MVE03-76-4, Quebrada La Peña, La Ensenada, sawn surface is 20cm across; F) Slab of white-green medium-grained jadeitite with zones of translucent blue-greenish microcrystalline texture: MVJ84-10-1, Manzanal, ~14cm across.**

glaucophane blueschist and epidote - amphibolite. Finally, near La Ensenada in a serpentinite slice further north, in and around an E-W trending *quebrada* are dismembered blocks (≤3m across) of a whitish gray jadeitite with green, blue, orange (grossular), and mauve streaks and spots that is a fine-grained jadeite-pumpellyite rock (this material has been sold as *jade lila* or "rainbow jade"). It occurs interlayered with a pale brown chloritite (Fig. 4E), and the associated lithologies are lawsonite blueschist and a partially amphibolitized - chloritized serpentinite. A single other occurrence of this material is found ~3km east and appears to be in the same fault slice of serpentinite.

JADEITITE: TEXTURE AND MINERALOGY

Analytical techniques

Optical and SEM/BSE petrographic and microprobe analysis of thin sections and X-ray diffraction of mineral grains were performed in this study. Electron-microprobe analysis of minerals in thin section to determine concentrations of the major constituent elements (except O) was carried out using a Cameca SX-100 microprobe at the American Museum of Natural History operated at 15kV, 10nA sample current for Na-bearing or hydrous silicates and 20kV, 15nA for oxides and sulfides, a point beam was used in all cases. Standards included natural minerals and synthetic compounds. The PAP correction scheme according to Pouchou and Pichoir (1991) was employed. Potential interferences between Ba (Lα) and Ti (Kα) were minimized by measuring X-ray counts on a PET crystal and background measured outside the window of both peaks; as long as concentrations are below ~2 wt% of either, there are no overlaps that exceed the detection limit. For all elements the detection limits are <0.01wt% but values are presented here as measured. Examination of amphiboles and micas found no detectable F or Cl, so these elements were not analyzed. No post-processing correction was made for the effect of inferred H_2O content. Estimates of Fe^{2+} and Fe^{3+} were made using an algorithm similar in concept to that of Finger (1972) to calculate Fe^{3+} from total Fe in which cation charge must sum as close as possible to twice the number of oxygen atoms plus the number of univalent anions (e.g., 6 oxygen in pyroxene), with a maximum permissible sum of cations determined by the crystal's stoichiometry (e.g., four for pyroxene as above; vacancies in large cation sites are permissible–see Harlow et al., 2006a for more details). Particularly in the case of iron-rich amphiboles, ferric-ferrous determination by the above technique may lead to poor, particularly somewhat low, totals for the C cations. Typically these totals can be improved by readjusting the FeO-Fe_2O_3 balance; but that has not been done here because the deficiencies are relatively small.

Back-scattered electron (BSE) imaging was carried out on the microprobe and on a Hitachi S-4700 Field Emission Scanning Electron Microscope (SEM). Both microprobe and SEM were equipped with either PGT-Imix (prior to April 2007) or Bruker Quantax energy-dispersive X-ray spectrometric (EDS) analyzers. X-ray diffraction identification was carried out on some powdered samples of jade using a Bragg-Brentano diffractometer or on sub-millimeter fragments and sub-millimeter areas on rock surfaces using a Rigaku DMAX/Rapid microdiffraction system employing a 100μm monocapillary collimator and monochromatized Cu Kα radiation. Patterns were interpreted with Jade 7.0 (MDI) software; although Fe fluorescence degraded the patterns in some cases, the peaks were more than sufficient for assignment of *d* values and phase identification.

Jadeite texture and mineralogy North of the Motagua fault

The macrotextures (hand samples) are generally granoblastic (grain size from 1mm to 1cm) made conspicuous in almost monomineralic masses by cleavage in blocky grains of jadeite. Weathering greatly enhances visual aspects of texture and can accentuate areas of albite and/or analcime from some combination of enhanced solubility and reduced hardness. Increased whiteness (light scattering) is common in the cores of grains or in grain clusters with grain rims more likely to be semitranslucent and greener. Although coarse grain size is typical, microcrystalline zones (Fig. 4F) and whole blocks are also found. Coarse-grained jadeitite is typically opaque while fine-grained material is more translucent. Shearing and brecciation is common, with cementation by both jadeitite and albitite assemblages (Harlow, 1994). Veins are common but not always conspicuous because of the near-monomineralic composition and lack of obvious variance in color and texture. However, very coarsely crystallized veins of jadeite exist, with walls dominated by jadeite (crystals to ~20cm) and central or interstitial white mica and/or green omphacite or late-stage alteration infilling (albitite-like), which can be decorated by black sprays of amphibole or green fingers or zones of omphacite.

Microscopic textures are highly variable, but certain features can be considered typical. Clusters of both solid and 2-phase fluid inclusions are common in the cores of jadeite grains that have survived deformational comminution. Omphacite, albite, paragonite and titanite are the most common core mineral inclusions. Moreover, in many coarse-grained jadeitites interiors of jadeite grains are dense with somewhat large solid, both mono-phase and polyphase inclusions, typically albite, analcime, paragonite, and omphacite (Fig. 5A), commonly connected

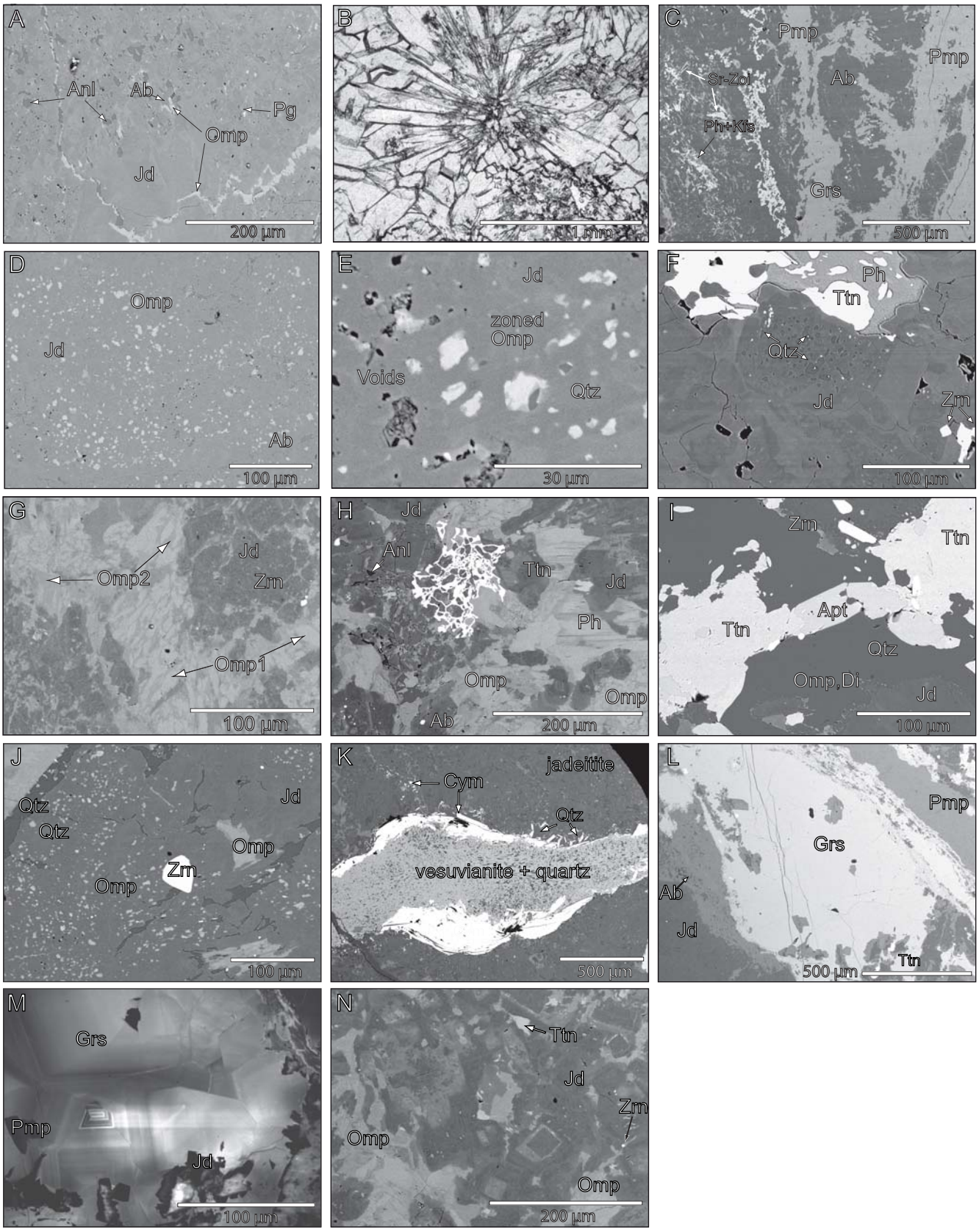
A
Anl
Ab
Pg
Omp
Jd
200 µm
B
1 mm
C
Pmp
Pmp
Sr-Zoi
Ab
Ph+Kfs
Grs
500 µm
D
Omp
Jd
Ab
100 µm
E
Jd
zoned
Omp
Voids
Qtz
30 µm
F
Ph
Ttn
Qtz
Jd
Zrn
100 µm
G
Jd
Omp2
Zrn
Omp1
100 µm
H
Jd
Anl
Ttn
Jd
Ph
Omp
Omp
Ab
200 µm
I
Zrn
Ttn
Apt
Ttn
Qtz
Omp,Di
Jd
100 µm
J
Jd
Qtz
Qtz
Omp
Zrn
Omp
100 µm
K
jadeitite
Cym
Qtz
vesuvianite + quartz
500 µm
L
Pmp
Grs
Ab
Jd
500 µm
Ttn
M
Grs
Pmp
Jd
100 µm
N
Ttn
Jd
Zrn
Omp
Omp
200 µm

by cleavage cracks. These solid inclusions commonly have associated fluid inclusions voids observed in surfaces by SEM/BSE as well as resolvable two-phase fluid inclusions via optical microscopy. These "lake district" interiors of jadeite grains typically have irregular compositional zoning and are commonly surrounded by a cleaner overgrowth of rhythmically zoned jadeite before encountering grain boundaries. Narrow boundaries between jadeite grains typically contain analcime, albite, analcime + albite or least commonly albite + nepheline; these latter two are typically in symplectitic intergrowths (Harlow, 1994). Smaller omphacite, zoisite (clinozoisite), titanite, paragonite or amphibole grains can be included in the granular boundary zone intergrowths. While not as common as the granoblastic or sheared textures, mesh and felted textures of submillimeter prismatic jadeite are found, and a few localities yield conspicuous fan-spheroidal clusters of elongate jadeite prisms relatively free of anything but two-phase fluid inclusions (Fig. 5B). In retrogressed jadeitites, inter-jadeite grain zones resemble albitite with pseudormorphing of jadeite by intergrowths of albite + omphacite ± amphibole, paragonite, preiswerkite, apatite, zoisite, titanite, banalsite, graphite, etc. (see Harlow, 1994). Sorensen et al. (2006) has shown via cathodoluminescence imaging that deformation textures plus consistent jadeite overgrowth along fracture veins are common to most jadeitite, worldwide, including those from north of the Motagua fault.

Mineralogy of samples from the originally described areas was presented in Harlow (1994); here we present mineral assemblages of samples not presented in that paper and, now, spanning the entire 200km east-west extent north of the Motagua fault (Table 1). Jadeitite exclusive of secondary veins or alteration consists fundamentally of jadeite (>90vol%, sensu stricto but more altered rocks may only be >60%) with subsidiary albite, white-to-tan mica (paragonite in most cases, with muscovite-phengite and/or phlogopite in some cases two or all three), analcime, omphacite with minor small crystals of titanite, zoisite, apatite and zircon, which all can be found as inclusions in jadeite. Rutile has only been found in one sample in the core of titanite. Veins and grain boundary alteration consist of albite + allanite or albite + nepheline, zoisite (and clinozoisite), taramitic amphibole, paragonite, phlogopite, preiswerkite, banalsite, K-feldspar, and graphite. Phengite grains can show barian overgrowths (Harlow, 1995). Zircons are generally small (<50μm long) and vary from euhedral crystals to irregular rounded ones. Their abundance correlates with K-mica abundances, and rare inclusions include holes (presumably fluid) and omphacite. As emphasized in Harlow (1994) quartz is absent from these jadeitites, not as inclusions in jadeite grains, not as a constituent phase of the rocks, nor in alterations of jadeite that retain any jadeite — jadeite + quartz is absent.

One suite of jadeitite samples north of the Motagua fault is unique for its late-stage assemblage: lavender jadeitite from near Saltán, which is the westernmost known locality (MVE07B-19). The jadeite grains form radiating prismatic clusters, although largely broken up by deformation and variably retrograded. Jadeite grains are relatively inclusion free, primarily being small (<20μm) two-phase fluid inclusions that, on occasion, have adjacent blebs of K-feldspar, and grain boundaries coated with albite ± allanite ± K-feldspar. Allanite-(Ce) with overgrowths of REE-rich clinozoisite occurs as broken prisms amidst jadeite but also with albite, so it may be either primary or an early secondary phase. Omphacite is absent and K-feldspar takes its textural place. Phengite occurs intimately with jadeite and muscovite-phengite grains are partially replaced or infiltrated by K-feldspar (variably Ba enriched) and Sr-rich zoisite-clinozoisite. Extensive albite retrogression of jadeite, which can be identified as selvages or veining through jadeite grains, contains discontinuous stringers of K-feldspar, laths of Sr-rich zoisite (sometimes overgrowing allanite), and rare crystals of pumpellyite. Isolated vesuvianite grains, graphite clusters, and boundary selvages of pumpellyite and

FIGURE 5 | **Photomicrographs: A) BSE image of jadeitite (Jd) showing cryptic-zoned grains filled with inclusions of analcime (Anl), albite (Ab), paragonite (Pg), omphacite (Omp), and now-empty fluid inclusions; rims can be relatively free of inclusions and irregular grain boundaries are decorated with the minerals found in the inclusions: MVE03-82-3, El Mapache; B) Photomicrograph (plane light, 2mm across) of radiating jadeite grains: MVE02-39-5, Pica Pica; C) BSE image of albite-pumpellyite (Pmp) selvage with grossular (Grs) stringers, Sr-zoisite (Sr-Zoi) prisms, and K-feldspar-phengite (Ph-Kfs) intergrowths on a jadeitite: MVE07B-19-1, near Saltán; D) BSE image of jadeitite showing jadeite with many blebby omphacite inclusions and a zone with more abundant fluid inclusion voids and quartz inclusions: MVE04-14-6, Quebrada Seca; E) Close-up of area with quartz (Qtz) shown in previous image; F) BSE image of jadeite grains (center) with inclusions of quartz and titanite (Ttn): MVE07-9, Carrizal Grande; G) BSE image of blue omphacite vein cutting jadeitite; jadeite exhibits cryptic zoning and overgrowth of omphacite; in vein two generations of omphacite are apparent: KT02-3, Quebrada Seca, Carrizal Grande; H) BSE image of a latticework-textured titanite typical of an association with late omphacite in jadeitite from south of the Motagua fault: JJE01-3-1, Quebrada El Silencio, Carrizal Grande; I) BSE image of titanite-apatite (Apt) intergrowth and jadeite grains surrounded by islets of omphacite plus diopside (Di) in a matrix of quartz: MVE02-15-10, Quebrada Seca, Carrizal Grande; J) BSE image of jadeite grains with small inclusions of quartz, omphacite, and fluids toward cores and small zircons (Zrn) (brightest) elsewhere and a large zircon at center: MVE02-17-5, La Ceiba; K) BSE image of a vein cutting jadeitite with quartz (dark gray) and vesuvianite (light gray) in the center and cymrite (Cym) (white) at the edges: MVE02-17-5, La Ceiba; L) BSE image of a jadeitite (dark gray) cut by vein of pumpellyite (light gray) and grossular (white): MVE04-20-1 La Ensenada; M) Cathodoluminescence (CL) image of same area as in previous image with grossular (bright), inclusions of pumpellyite (black) and jadeite (mottled bright)–subtle and sharp zoning of grossular is visible; N) BSE image of multiple stages (at least 2) of zoning from jadeite-rich-to-jadeite-poor (darker to lighter) composition of jadeite: JJE01-3-1, Quebrada El Silencio, Carrizal Grande.**

TABLE 1 | **Representative pyroxene compositions in jadeitite from north and south of the Motagua Fault**

	— NORTH —												— SOUTH —											
	West				Central				East				Carrizal Grande						La Ceiba					La Ensenada
Wt%	MVE07 B-19-4	MVE06-X-1		MVE07-1	MVE04-44-1		MVE07B-3-1		MVR07-23C		MVR07-23D		MVE04-14-6			MVE02-8-6		KT02-3	MVE02-15-6		MVE03-77-1		MVE02-15-10	MVE04-20-1	
	Jd	Jd	Omp	Aug	Jd	Omp	Jd	Omp	Jd	Omp	Jd	Omp	Jd	Jd	Omp	Jd	Omp	Omp	Jd	Omp	Jd	Omp	Di	Jd	Omp
SiO_2	59.83	59.48	56.90	54.57	59.65	56.42	57.50	59.84	59.75	56.82	59.75	56.39	59.30	58.88	54.17	59.55	57.13	56.74	58.96	56.66	57.88	54.36	55.12	58.98	56.87
TiO_2	0.07	0.08	0.30	0.69	0.03	0.03	0.05	0.05	0.10	0.05	0.04	0.08	0.03	0.03	0.14	0.02	0.15	1.86	0.08	0.11	0.26	0.05	0.14	0.47	0.09
Al_2O_3	25.30	22.47	14.12	6.89	24.31	12.26	12.38	23.83	25.21	11.98	24.18	12.24	25.13	22.17	8.34	24.48	12.03	9.81	23.67	14.01	18.69	10.06	2.54	25.31	12.84
Cr_2O_3	0.00	0.01	0.00	0.02	0.07	0.00	0.00	0.03	0.00	0.03	0.01	0.03	0.00	0.02	0.01	0.02	0.00	0.00	0.01	0.00	0.03	0.00	0.00	0.00	0.00
Fe_2O_3	0.00	0.53	3.87	9.33	0.79	4.11	2.66	0.40	0.00	1.12	0.44	5.90	0.04	0.21	9.95	0.39	2.59	1.40	0.87	1.30	3.76	5.57	1.82	0.08	0.60
FeO	0.03	1.17	1.84	0.04	0.00	0.00	0.22	0.18	0.14	2.73	0.67	10.10	0.19	1.98	6.72	0.26	0.87	2.44	0.00	0.39	1.48	3.57	4.37	0.00	0.00
MnO	0.00	0.05	0.37	0.32	0.01	0.21	0.10	0.01	0.00	0.00	0.00	0.00	0.05	0.00	0.25	0.09	0.14	0.10	0.01	0.09	0.06	0.12	0.09	0.01	0.00
MgO	0.03	1.18	5.37	8.43	0.28	7.29	8.00	0.83	0.03	7.26	0.30	3.51	0.18	0.82	2.60	0.30	7.99	8.10	0.60	7.07	1.79	6.03	12.83	0.41	9.13
CaO	0.02	1.61	7.70	12.28	0.49	10.87	11.70	1.02	0.20	12.29	0.70	2.56	0.39	2.25	9.42	0.47	11.99	11.63	0.90	10.71	3.12	12.68	20.33	0.57	12.73
BaO	0.01	0.00	0.00	0.00	0.00	0.01	0.07	0.00	0.02	0.00	0.00	0.00	0.01	0.03	0.00	0.00	0.02	0.00	0.03	0.03	0.01	0.00	0.06	0.00	0.00
Na_2O	15.40	14.20	10.06	7.47	15.39	8.91	8.46	14.80	15.23	7.89	14.96	8.93	15.06	13.82	8.89	15.04	8.16	8.12	14.75	8.85	13.09	7.41	2.72	15.17	7.79
K_2O	0.01	0.00	0.01	0.04	0.02	0.01	0.00	0.00	0.01	0.00	0.01	0.03	0.01	0.00	0.00	0.00	0.01	0.00	0.02	0.01	0.01	0.00	0.00	0.03	0.02
TOTAL	100.70	100.77	100.54	100.09	101.04	100.12	101.15	100.99	100.69	100.17	101.05	99.77	100.39	100.22	100.51	100.63	101.06	100.20	99.89	99.22	100.19	99.87	100.02	101.02	100.07
Cations per 6 O																									
Si	2.000	2.009	1.991	1.970	1.997	1.985	1.995	2.004	1.999	2.004	2.002	2.002	1.992	2.008	1.994	1.999	1.991	2.006	1.998	1.991	2.002	1.968	2.013	1.972	1.983
$^{[4]}$Al	0.000	0.000	0.009	0.030	0.003	0.015	0.005	0.000	0.001	0.000	0.000	0.000	0.008	0.000	0.005	0.000	0.009	0.000	0.002	0.009	0.000	0.032	0.000	0.028	0.017
$^{[6]}$Al	0.996	0.894	0.574	0.263	0.957	0.493	0.501	0.940	0.992	0.498	0.955	0.512	0.987	0.891	0.356	0.969	0.485	0.409	0.943	0.572	0.762	0.397	0.109	0.969	0.511
Ti	0.002	0.002	0.008	0.019	0.001	0.001	0.001	0.001	0.003	0.001	0.001	0.002	0.001	0.001	0.004	0.000	0.004	0.050	0.002	0.003	0.007	0.001	0.004	0.012	0.002
Cr	0.000	0.000	0.000	0.001	0.002	0.000	0.000	0.010	0.000	0.001	0.000	0.001	0.000	0.000	0.000	0.000	0.000	0.000	0.000	0.000	0.001	0.000	0.000	0.000	0.000
Fe^{3+}	0.000	0.014	0.102	0.254	0.020	0.109	0.070	0.005	0.000	0.030	0.011	0.094	0.001	0.005	0.276	0.010	0.068	0.037	0.022	0.035	0.098	0.152	0.050	0.002	0.016
Fe^{2+}	0.001	0.033	0.054	0.001	0.000	0.000	0.006	0.000	0.004	0.080	0.019	0.076	0.005	0.057	0.207	0.007	0.025	0.072	0.000	0.011	0.043	0.108	0.134	0.000	0.000
Mn	0.000	0.001	0.011	0.010	0.000	0.006	0.003	0.000	0.000	0.000	0.000	0.000	0.001	0.000	0.008	0.003	0.004	0.003	0.000	0.003	0.002	0.004	0.003	0.000	0.000
Mg	0.001	0.060	0.280	0.454	0.014	0.383	0.414	0.041	0.001	0.382	0.015	0.312	0.009	0.042	0.143	0.015	0.415	0.427	0.030	0.370	0.093	0.326	0.699	0.020	0.475
Ca	0.001	0.058	0.289	0.475	0.018	0.410	0.435	0.037	0.007	0.464	0.025	0.384	0.014	0.082	0.372	0.017	0.448	0.440	0.033	0.403	0.116	0.492	0.795	0.020	0.476
Ba	0.000	0.000	0.000	0.000	0.000	0.000	0.001	0.000	0.000	0.000	0.000	0.000	0.001	0.000	0.000	0.000	0.000	0.000	0.000	0.000	0.001	0.000	0.000	0.000	0.000
Na	0.998	0.929	0.682	0.523	0.999	0.608	0.569	0.961	0.988	0.540	0.972	0.615	0.981	0.914	0.635	0.979	0.551	0.557	0.969	0.603	0.877	0.520	0.193	0.983	0.527
K	0.000	0.000	0.000	0.002	0.001	0.000	0.000	0.000	0.000	0.000	0.000	0.001	0.000	0.000	0.000	0.000	0.000	0.000	0.001	0.000	0.000	0.000	0.001	0.001	0.001
Sum	4.000	4.000	4.000	4.000	4.011	4.010	4.000	4.000	3.996	4.000	4.000	4.000	4.000	4.000	4.000	4.000	4.000	4.000	4.001	4.000	4.000	4.000	4.000	4.009	4.007
		pair		vein	pair		pair		pair		pair		core	pair		pair		*	pair		pair *			pair *	
Jd (%)	99.6	89	57	25	96	48	50	94	99	50	96	51	98	89	36	97	48	41	94	57	76	37	11	95	50
Di	0.1	~4	28	44	1.4	38	41	4	0	38	1.5	31	0.6	4.2	14	1.5	41	42	3	37	9	33	70	0	46
Hd	<0.1	~2	>1	0	0	1	1.6	1	0	8	0.9	7	0	3.9	22	0.2	2.4	3	0.1	1.4	1.6	13	9	0	0
Ae	0	>1.4	10	25	2	11	7	1	0	3	1.1	9	0.1	0.5	28	1	6.7	3.7	2.2	38	10	46	5	0.2	1.6
Quad	0.2	8	34	46	1.4	40	43	4	1	46	2.9	38	1	9	36	2	44	46	3.1	3.4	12	15	81	1	46
MMF	0.6	0.64	0.81	0.98	0.98	0.98	0.99	1	0.28	0.83	0.45	0.8	0.57	0.42	0.4	0.6	0.93	0.85	0.99	0.96	0.68	0.75	0.84	0.99	1
MMF_T	0.6	0.56	0.63	0.63	0.77	0.41	0.73	0.89	0.28	0.78	0.33	0.65	0.55	0.4	0.23	0.43	0.81	0.79	0.58	0.88	0.39	0.55	0.79	0.91	0.98

MMF= $Mg/(Mg+Fe^{2+})$, $MMF_T = Mg/(Mg+Fe_{total})$; * $NaTi_{0.5}(Mg,Fe)_{0.5}Si_2O_6$ component = ~10% (KT02-3), 6.4% (Omp-MVE03-77-1), 5.6 & 3.4% (MVE04-20-1)

Ae: Aegirine, Aug: Augite, Omp: Omphacite, Di: Diopside, Hd: Hedenbergite, Jd: Jadeite, Omp: Omphacite, Quad: quadrangular components (diopside+hedenbergite+clinoenstatita+clinoferrosilite)

stringers of grossular are also associated with the late albite (Fig. 5C). This is the only recorded occurrence of pumpellyite north of the Motagua fault.

Mineral compositions

Pyroxene

Pyroxene compositions have been measured for a large number of rocks ranging from light-colored through variable green and even lavender jadeitites toward darker green mixed jadeite-omphacite jadeitites to omphacitites. Representative compositions for jadeite and omphacite (and coexisting pairs) from individual samples are presented in Table 1 (a growing database of compositions, images, and plots can be found at the senior author's research website). Figure 6A presents a sampling of compositions for clinopyroxenes in an individual jadeitite from north of the Motagua fault to demonstrate the range measured in a single sample, as well as portray the ranges among several rocks from the westernmost, central, and easternmost sources. The compositional variation is represented as broad lines where there is a continuous variation, both in jadeite and omphacite. This approach makes it easier to show the fundamental compositional variation among the four primary compositional components: jadeite - diopside – hedenbergite – aegirine. Adjacent jadeite-omphacite, either as omphacite inclusions in jadeite grains or immediate contact of omphacite overgrowths on jadeite, are shown with tie-lines. One important caveat in these data is that, although we have tried to take into account analyses that represent beam overlap between two pyroxenes which yield reasonable stoichiometry, some instances of reported compositions in plots that are actually mixtures, particularly for omphacite or diopside, cannot be ruled out without a much greater density of data than we have collected for all samples. A few characteristics of compositions and zoning are worth pointing out.

Jadeite compositions typically range from nearly pure jadeite to perhaps $Jd_{\sim 80\text{-}85}Di_{5\text{-}10}Ae_5Hd_2$, although some samples have a smaller range restricted toward pure jadeite and in others aegirine is the next most abundant component, rather than diopside. The Saltán lavender jadeite is distinctive for its very low iron content (<1wt%) consistent with enabling the Mn chromophore for the lavender color (*c.f.*, Ouyang, 2001; Nassau and Shigley, 1987), as well as minimal Ca content (diopside + hedenbergite ≤2mol%), and no coexisting omphacite.

Zoning patterns in jadeite grains vary considerably, particularly between different samples, but two general patterns are common. Most commonly grains contain relatively jadeite-rich crystal cores, with subtle cryptic

zoning and cluttered with inclusions as described above, surrounded by overgrowths richer in other components, particularly diopside. (Fig. 7A). Somewhat less common are cryptically zoned interiors of variable composition with or without an overgrowth of rhythmically zoned jadeite (Fig. 7B). Superimposed or overprinted on these patterns can be numerous "inclusions" of albite, analcime, paragonite, omphacite or some combinations of these, as described above. These observations are consistent with prior descriptions (Harlow, 1994; Sorensen et al., 2006) but different, in particular, from the recent description of jadeitite from the Sierra del Convento region, Cuba (García-Casco et al., 2009; see discussion).

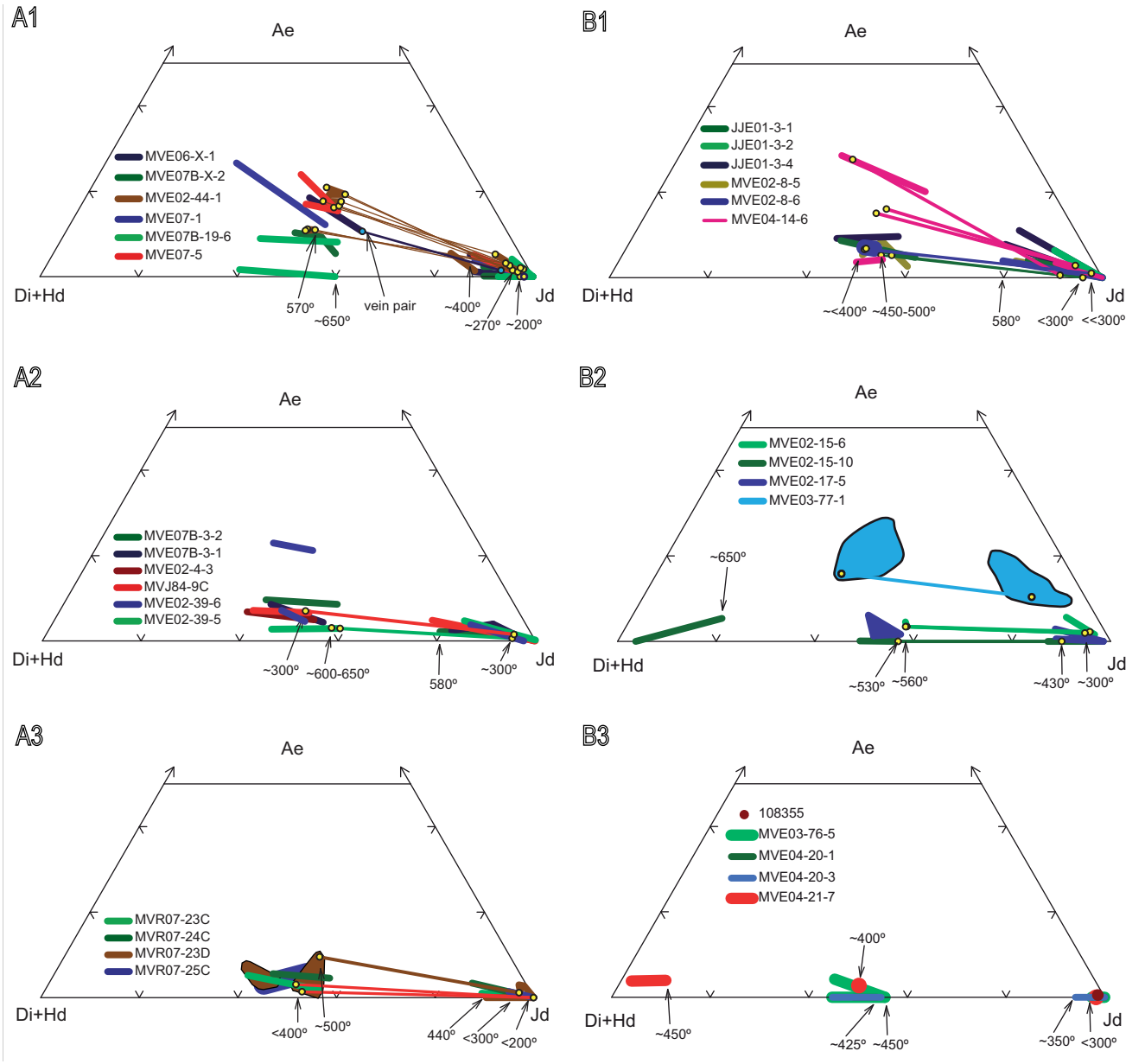

FIGURE 6 | **Plot of pyroxene compositions (molar components) in jadeitites. A) Samples north of the Motagua fault. A1: westernmost, A2: Central zone, A3: easternmost B) Samples south of the Motagua fault. B1: Carrizal Grande, B2: La Ceiba, B3: La Ensenada. Broad lines are representative of the zoning in jadeite and omphacite; individual compositions may scatter more broadly about the line but the width is indicative of the most prominent trend and the range of scatter. Samples with broader scatter (*e.g.*, MVE03-77-1 in B2) are shown with colored areas. However, where lines will obscure one another, lines have been made thinner for clarity. Fine lines and colored dots represent adjacent compositions of jadeite and omphacite. Temperature estimates are derived from pseudobinary section solvi calculations (García-Casco et al., 2009) for nearest Jd to Di_{100}, $Di_{90}Hd_5Ae_5$, $Di_{80}Hd_{10}Ae_{10}$, or $Di_{70}Hd_{15}Ae_{15}$ section. Ae: Aegirine, Di: Diopside, Hd: Hedenbergite, Jd: Jadeite.**

TABLE 2 | **Representative analyses of micas in jadeitite from north and south of the Motagua Fault**

	NORTH									SOUTH								
Wt%	MVE07-2	MVE02-39-6		MVE04	MVE07B-19-1		MVE06-X-1	MVR07-23D		MVE02-8-5			JJE01-X-3	JJE01-3-2	MVE03-77-5-1	MVE04-20-1	108355	
	Ph	Ms	Phl	Pg	Ms	Ms	Prs	Ph	Pg	Ph	Ph	Ba-Ph	Ba-Ph	Bio	Ph	Phl	Ph	Ba-Ph
SiO_2	51.79	43.79	39.26	48.55	48.38	44.67	30.91	51.06	48.30	54.25	57.24	54.71	47.31	39.09	54.77	41.07	50.34	46.27
TiO_2	0.09	0.01	0.27	0.07	0.03	0.04	0.04	0.07	0.04	0.28	0.26	0.23	0.25	0.14	0.14	0.02	0.00	0.03
Cr_2O_3	0.00	0.03	0.01	0.00	0.02	0.00	0.00	0.00	0.00	0.00	0.01	0.01	0.00	17.49	0.00	0.00	0.08	0.07
Al_2O_3	26.43	36.52	18.45	38.66	35.49	35.76	35.19	27.79	39.41	24.78	21.07	23.75	27.90	0.00	23.40	17.91	33.09	35.90
Fe_2O_3*	0.00	0.00	0.00	0.00	0.00	0.00	0.00	0.00	0.00	0.00	0.00	0.00	0.00	0.00	0.00	0.00	0.00	0.00
FeO	1.41	0.14	3.29	0.40	0.02	0.32	2.48	1.31	0.48	3.57	1.38	2.09	1.38	15.85	1.86	1.31	0.32	0.15
MnO	0.03	0.09	0.42	0.00	0.00	0.00	0.50	0.00	0.00	0.00	0.03	0.02	0.00	0.25	0.01	0.00	0.01	0.00
MgO	3.95	0.18	21.63	0.26	0.25	0.72	19.16	3.72	0.35	3.27	6.49	4.96	3.67	13.03	5.15	23.54	1.35	0.43
CaO	0.01	0.26	0.09	0.12	0.00	0.01	0.06	0.00	0.14	0.00	0.02	0.00	0.03	0.07	0.00	0.16	0.00	0.01
BaO	1.34	0.02	0.55	0.19	0.21	3.76	0.03	0.79	0.06	0.21	0.48	1.50	6.98	0.09	1.03	0.06	0.12	2.31
Na_2O	0.27	0.41	0.49	7.37	0.06	0.55	7.52	0.43	6.97	0.13	0.00	0.05	0.19	0.10	0.12	0.15	0.06	0.22
K_2O	10.13	10.36	9.67	0.50	11.43	9.50	0.09	10.73	0.86	10.16	9.72	9.15	8.66	9.36	9.64	9.97	10.27	9.97
H_2O*	4.49	4.36	4.19	4.74	4.56	4.42	4.43	4.51	4.76	4.56	4.62	4.56	4.35	4.04	4.55	4.27	4.59	4.48
Total	99.96	96.17	98.33	100.87	100.45	99.75	100.41	100.41	101.37	101.21	101.31	101.03	100.71	99.50	100.66	98.46	100.22	99.85
Cations per 20 Oxygen and 4 OH*																		
Si	6.914	6.023	5.614	6.140	6.359	6.065	4.183	6.785	6.081	7.135	7.435	7.191	6.529	5.796	7.214	5.765	6.583	6.192
$^{[4]}$Al	1.086	1.977	2.386	1.860	1.641	1.935	3.817	1.215	1.919	0.865	0.565	0.809	1.471	2.204	0.786	2.235	1.417	1.808
$^{[6]}$Al	3.072	3.943	0.723	3.903	3.856	3.787	1.795	3.137	3.929	2.976	2.659	2.869	3.066	0.852	2.846	0.729	3.684	3.854
Ti	0.010	0.001	0.029	0.007	0.003	0.004	0.004	0.007	0.004	0.027	0.025	0.022	0.026	0 .016	0.014	0.002	0.000	0.003
Cr	0.000	0.004	0.001	0.000	0.002	0.000	0.000	0.000	0.000	0.000	0.001	0.001	0.000	0.000	0.001	0.000	0.008	0.008
Fe^{3+}	0.000	0.000	0.000	0.000	0.000	0.000	0.000	0.000	0.000	0.000	0.000	0.000	0.000	0.000	0.000	0.000	0.000	0.000
Fe^{2+}	0.158	0.016	0.393	0.043	0.002	0.036	0.280	0.146	0.051	0.393	0.150	0.230	0.159	1.965	0.204	0.154	0.035	0.017
Mn	0.003	0.010	0.051	0.000	0.000	0.000	0.057	0.000	0.000	0.000	0.004	0.002	0.000	0.031	0.001	0.000	0.001	0.000
Mg	0.786	0.037	4.611	0.050	0.049	0.146	3.865	0.737	0.066	0.641	1.256	0.971	0.755	2.880	1.011	4.926	0.263	0.086
Ca	0.001	0.038	0.014	0.017	0.000	0.001	0.009	0.000	0.019	0.000	0.003	0.000	0.004	0.011	0.000	0.024	0.000	0.001
Ba	0.070	0.001	0.031	0.009	0.011	0.200	0.001	0.041	0.003	0.011	0.024	0.077	0.377	0.005	0.053	0.003	0.006	0.121
Na	0.071	0.108	0.137	1.807	0.015	0.145	1.972	0.111	1.701	0.033	0.000	0.012	0.052	0.028	0.030	0.040	0.016	0.057
K	1.725	1.819	1.765	0.081	1.916	1.645	0.016	1.819	0.138	1.705	1.610	1.535	1.524	1.770	1.619	1.785	1.714	1.702
Sum	13.896	13.977	15.753	13.916	13.855	13.965	16.001	13.997	13.911	13.786	13.733	13.721	13.965	15.559	13.780	15.663	13.727	13.850
OH *	4	4	4	4	4	4	4	4	4	4	4	4	4	4	4	4	4	4
MMF	0.83	0.7	0.92	0.54	0.96	0.8	0.93	0.83	0.56	0.62	0.89	0.81	0.83	0.59	0.83	0.97	0.88	0.84

MMF= $Mg/(Mg+Fe^{2+})$

* OH is calculated to fill univalent anion site and H_2O is back calculated from the conversion of ions to wt%

Bio: Biotite, Ba-Ph: Ba-Phengite, Ms: Muscovite, Pg: Paragonite, Ph: Phengite, Phl: Phlogopite, Prs: Preiswerkite

Omphacite is most common as overgrowths on and veins cutting through jadeite. In the former case, compositions of contacting jadeite and omphacite usually approach that of equilibrium pairs (more discussion below), but in the latter case, there is zoning across the omphacite vein (Fig. 7C) in which a portion or even all of the vein omphacite does not appear to be in equilibrium with adjacent jadeite (also discussed below). Omphacite compositions trend away from that potentially in equilibrium with jadeite toward more diopside + hedenbergite + aegirine-rich compositions. The compositions of omphacite inclusions and overgrowths generally overlap in each thin section, although some omphacite inclusion compositions are much higher in aegirine content (Fig. 6A) than is consistent with interpretations of coexisting sodic pyroxenes (Green et al., 2007). In addition, most coexisting jadeite-omphacite compositions do not follow the Green et al. (2007) solvus (see discussion below).

There is a trend displayed among the three different regional clusters of jadeitite indicating higher aegirine component in the compositions of omphacite and jadeite (trending away from the cores of jadeite grains) for the westernmost samples that decreases further eastward. In addition, there is a trend toward a smaller jadeite - omphacite compositional gap in jadeitite from the west as compared to those from further east (Fig. 6A; Table 1).

The green color of jadeite and omphacite is mostly related to iron content, although no study has been carried out to accurately evaluate the ferrous-ferric variation or its impact on color. Chromium has been shown clearly to yield the color in so-called imperial jade (see Harlow et al., 2007), and likely contributes to color in impure jadeite and omphacite (Table 1, Sorensen et al., 2006; Harlow and Olds, 1987).

Mica

Representative mica compositions are presented for only the new localities from north of the Motagua fault in Table 2, as details of mica composition were presented in Harlow (1995). Paragonite has a nearly ideal end-member composition. Phengitic muscovite is less common than paragonite in jadeitite north of the Motagua fault, with maximum Si atoms per formula

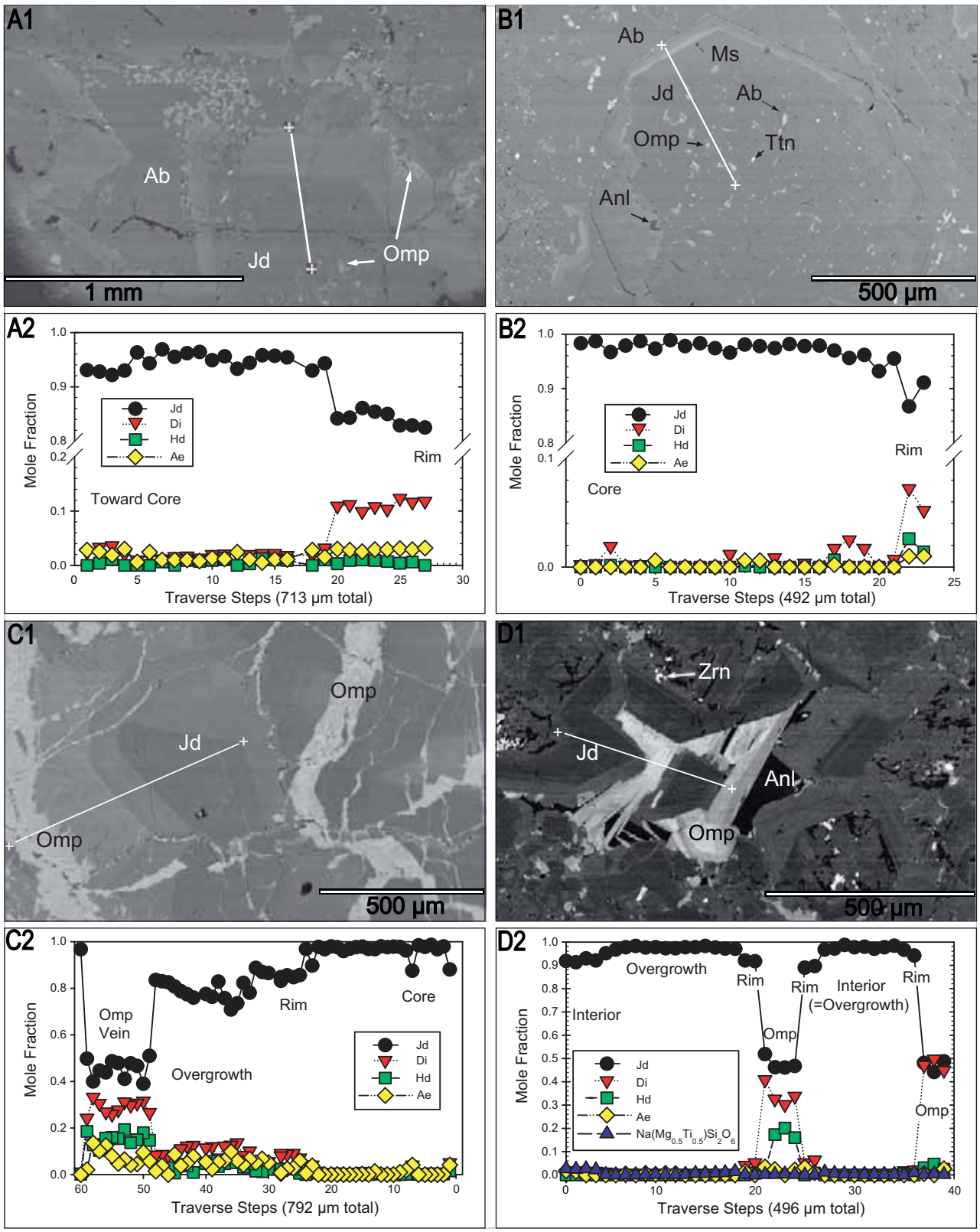

FIGURE 7 | **Plot of pyroxene components from microprobe traverses of grains, overgrowths and veins in jadeitite. BSE images show traverse (+ sign at ends) and phase labels. A) Traverse across jadeite grain with cryptically zoned interior and a more diopside-rich overgrowth: MVE04-44-1, Quebrada de los Pescaditos; B) Traverse across jadeite grain with relatively uniform interior containing inclusions toward diopsidic rim: MVR07-23C, Aldea Las Cruces; C) Traverse of a omphacite vein in a jadeitite: MVJ84-12-2, Río La Palmilla; D) Traverse of rhythmic overgrowths of jadeite-rich and jadeite-poorer compositions in MVE04-15-3, La Ceiba. Ab: Albite, Ae: Aegirine, Anl: Analcime, Di: Diopside, Hd: Hedenbergite, Jd: Jadeite, Ms: Muscovite, Omp: Omphacite, Ttn: Titanite, Zrn: Zircon.**

unit (apfu)<7 and Mg/(Mg+Fe^{2+})>0.7 (Fe^{2+} as determined by stoichiometry and charge balance). Muscovite (low Mg+Fe^{2+}) is comparatively rare as inclusions, but is most common in the latest stage of crystallization of lavender jadeitite from near Saltán; phengite occurs with jadeite in less altered areas. Phlogopite is less common than either paragonite or phengite in jadeitite but increases in abundance with that of omphacite in the jadeitite-omphacitite rocks; Mg/(Mg+Fe^{2+}) values range between 0.69 and 0.93 with variation typically limited to <0.04 in single samples. Assemblages and even interlayering of the three micas has been found in several samples (see Table I, Electronic Appendix). As described by Harlow (1994) preiswerkite occurs as a late-stage alteration of paragonite with Mg/(Mg+Fe^{2+}) varying distinctly between different rocks and even different localities, from a rare low of 0.75 to a more common 0.93-0.95.

Amphibole

Representative amphibole compositions are presented in Table 3. As also reported by Harlow (1994), all amphibole in jadeitite is late-stage taramitic amphibole, both magnesian and ferroan, which appears to reflect the composition of the late omphacite (late fluid), at least in terms of MgO/(MgO+FeO_{Total}), (Mg/(Mg+Fe_T)) as ferrous-ferric evaluation is only assessed here by stoichiometry.

Other Calcic Minerals

Grossular garnet was described in some of the taramite - omphacite rocks associated with jadeitite north of the Motagua fault (Harlow, 1994). Grossular (see above) is otherwise only found as a late phase in the lavender jadeitite from near Saltán. A single specimen of jadeitite/omphacitite near Manzanal originally collected by Zenaide Carvalho da Silva (ZC-20, see Silva, 1967, 1970) contains garnet somewhat like that of garnet amphibolites in the area but with spessartine-rich rims (Table 4). This sample is the best (and a rare) argument for metasomatic replacement of a metamorphic rock (e.g., pelitic or mafic) by jadeitite, although there is only this relict phase rather than a textural indication. Pumpellyite-Mg and vesuvianite are newly described north of the Motagua fault from Saltán jadeitite coexisting with albite, grossular, Sr-rich zoisite, allanite, K-feldspar, and phengite. Vesuvianite has recently been described by Nyunt et al. (2009) in jadeitite from the Jade Tract in Myanmar, and the compositional characteristics are very similar to that in Guatemalan jadeitite, that is, high in Ti (up to ~5wt% TiO_2) and Na (up to ~2.5wt% Na_2O; Table 4). We concur with their conclusions of composition influenced by sodic-metasomatic-HP/LT formation, however, whereas Nyunt et al. (2009) argue that vesuvianite grew in equilibrium with jadeite, textures for Guatemalan jadeitite clearly show vesuvianite to be secondary, in later veins and overgrowth selvages with the phases noted above. Pumpellyite is aluminous but still should be classified as pumpellyite-Mg. For this reason the analyses in Table 4 are normalized to 3 Si cations, which results in a ~45-50% pumpellyite-Al component, and a large cation site (Ca+Na) that contains a small proportion of vacancies (~<0.05 atoms per formula unit). Both zoisite and clinozoisite are found, generally as late stage phases as described by Harlow (1994), with Al/(Al+Fe+Mn+Cr) ranging from 0.80 to 0.99. As described in Harlow (1994) Sr can reach significant concentrations in zoisite (see Table 4), particularly in the alteration of lavender jadeitite from Saltán, and appears to be concentrated in this calcic phase among those listed above, whether by crystal-chemistry or growth stage in jadeitite evolution/alteration. Allanite–REE-rich clinozoisite/zoisite compositions require further study, but appear to be Ce-rich with ~≥20wt% total REE-oxide (0.13 apfu).

Jadeitite texture and mineralogy South of the Motagua fault

Jadeitites from this area are distinct for the three zones recognized at this time. Consequently, we describe them separately.

Carrizal Grande

This jadeitite is generally not so granoblastic, with more columnar or interfingered jadeite quasi-prisms, and massive in appearance, with smaller grain size, on average, than the jadeitite found north of the Motagua fault. Maximum grain size for jadeite is generally <2mm whereas tabular phengite grains can exceed 5mm across. Interiors of jadeite grains can contain dense clusters of small inclusions (<10μm), typically omphacite, phengite, quartz, lawsonite, 1 or 2-phase fluids as well as titanite, zircon, and apatite as crystals, clusters, or blebs. Outside of the cores jadeite grains tend to be free of inclusions (Fig. 5D-F), except near the grain boundaries. As observed in BSE images, the interiors of grains typically exhibit subtle, patchy compositional zoning, while rims are rhythmically zoned or nearly unzoned. Most grain boundaries between jadeite and other primary minerals do not show interstitial coatings or abundant veining. When jadeite rims have inclusions, they typically are enveloped as individual phengite, titanite, rutile, and/or zircon grains. Veins, when present, tend to be sharp and cross-cutting and can consist of omphacite, albite, quartz, and cymrite; quartz veins can be in direct contact with jadeite. In jadeitite from Quebrada Seca, omphacite veins are common and demonstrate several generations based on zonation across the vein (Fig. 5G) and envelopment of earlier omphacite vein

TABLE 3 | **Representative amphibole compositions in jadeitite from Guatemala**

	Tar	Tar	Ftar	Ftar	Gln	Gln	Act	Act	Act
	MVE03	MVE07	ZC-20	MVJ84	JJE01	MVE02	MVE02	MVE02	MVE03
	81-3	7	39-6	44-2	3-4	14-5	14-5	15-10	77-5-1
SiO_2	42.57	43.00	43.12	41.07	59.24	59.96	57.08	57.44	58.66
TiO_2	0.26	0.67	0.47	0.51	0.03	0.00	0.01	0.01	0.09
Cr_2O_3	0.00	0.00	–	0.00	0.00	0.03	0.00	0.02	0.08
Al_2O_3	20.17	19.34	15.28	16.34	11.61	11.88	0.31	0.26	3.37
Fe_2O_3	3.62	0.00	2.64	4.04	1.20	0.02	0.03	0.00	0.00
FeO	5.25	10.91	15.01	16.71	3.68	3.98	5.16	5.78	7.03
MnO	0.37	0.16	0.59	0.28	0.08	0.07	0.34	0.06	0.10
MgO	11.35	9.24	7.22	5.29	13.01	13.41	20.61	20.39	16.48
CaO	7.33	6.70	6.50	7.03	0.30	0.17	12.98	12.81	10.20
BaO	0.00	0.00	–	0.02	0.02	0.02	0.03	0.00	0.00
Na_2O	6.44	6.72	5.98	5.49	7.47	7.26	0.35	0.13	2.07
K_2O	0.36	0.40	0.74	0.84	0.05	0.03	0.04	0.14	0.11
H_2O*	2.10	2.06	2.01	1.98	2.22	2.24	2.14	2.15	2.18
TOTAL	99.82	99.20	99.54	99.60	98.92	99.06	99.09	99.18	100.37
Cations per 22 O + 2(OH)*									
Si	6.073	6.253	6.442	6.221	7.989	8.036	7.987	8.027	8.077
$^{[4]}Al$	1.927	1.747	1.558	1.779	0.011	0.000	0.013	0.000	0.000
$^{[6]}Al$	1.464	1.567	1.132	1.138	1.835	1.876	0.039	0.042	0.547
Ti	0.028	0.073	0.052	0.058	0.003	0.000	0.001	0.001	0.009
Cr	0.000	0.000	0.000	0.000	0.000	0.003	0.000	0.002	0.008
Fe^{3+}	0.389	0.000	0.297	0.461	0.122	0.002	0.004	0.000	0.000
Fe^{2+}	0.626	1.327	1.875	2.117	0.415	0.446	0.604	0.675	0.810
Mn	0.045	0.020	0.074	0.035	0.009	0.008	0.040	0.007	0.012
Mg	2.415	2.003	1.607	1.195	2.616	2.680	4.299	4.248	3.382
Sum C	4.966	4.990	5.037	5.004	4.999	5.015	4.986	4.975	4.769
Sum C-	0.000	0.000	0.037	0.004	0.000	0.000	0.015	0.000	0.000
Ca	1.121	1.044	1.040	1.141	0.043	1.946	0.025	1.918	1.505
Na	0.913	0.967	0.923	0.855	1.953	0.068	1.888	0.035	0.553
Sum B	2.034	2.010	2.000	2.000	1.996	2.014	1.928	1.954	2.058
Na	0.867	0.926	0.808	0.757	0.000	0.028	0.000	0.000	0.000
K	0.065	0.074	0.140	0.163	0.009	0.008	0.004	0.025	0.019
Sum A	0.932	1.001	0.948	0.920	0.009	0.036	0.004	0.025	0.019
TOTAL	15.932	16.001	15.948	15.920	15.005	15.036	14.968	14.981	14.923
OH *	2.000	2.000	2.000	2.000	2.000	2.000	2.000	2.000	2.000
MMF	0.79	0.60	0.46	0.36	0.86	0.86	0.88	0.86	0.81
MMF_T	0.70	0.60	0.43	0.32	0.83	0.86	0.88	0.86	0.81

$MMF=Mg/(Mg+Fe^{2+})$, $MMF_T=Mg/(Mg+Fe_{total})$

Act: Actinolite, Ftar: Ferrotaramite, Gln: Glaucophane, Tar: Taramite

* OH is calculated to fill the univalent anion site, and H_2O is back calculated from the conversion of ions to wt%.

fragments by later growths. These omphacite veins can color the rock an intense blue-green (desirable as "blue jade") that is correlated with relatively high TiO_2 content in the omphacite (≤2.0wt% see Table 1 and Harlow et al., 2004b). Phengite grains are typically zoned by an overgrowth of barian rims (Fig. 5G), but occasionally have a more complex pattern or cryptic internal zoning. These grains are generally free of inclusions, although titanite and zircon are most common if encountered, and phengite grain clusters can envelope jadeite and other mineral grains. Titanite grains can vary from a few microns to over 1mm across, and larger ones commonly have a small nucleus of rutile or zircon (MVE02-8-5) and can include jadeite or phengite (MVE07-9). Titanite abundance appears to be correlated with the abundance of omphacite as well as the saturation of green color of the rock. Textures of titanite vary considerably, from larger nematoblasts (to 1mm), smaller quasi-euhedral crystals, and lacework growths around other phases, such as jadeite, omphacite, phengite, etc (Fig. 5H). Zircons are generally small (<150μm long) and vary from well-defined crystals, sometimes in delicate clusters, to rounded blebs; inclusions observed to date are only cavities, presumably fluid inclusions. Zircon abundance and crystal size appears to be correlated with the abundance of phengite. Allanite has been found in several jadeitites as discrete crystals along jadeite-phengite grain boundaries to a ~75μm maximum

TABLE 4 | **Representative analyses of other calcic minerals in jadeitite north and south of the Motagua Fault**

	NORTH									SOUTH									
	MVE07B-19-1	ZC-20		MVE07B-19-4	MVE07B-19-1	MVE07B-19-4	MVE07B-19-1			MVE06-17-2		MVE04-20-1	MVE03-77-4	MVE02-17-5			MVE03-76-5	MVE04-30-1	JJE01-X-3	JJE01-6-1
Wt%		Garnet		Vesuvianite	Pumpellyite	Zoisite		Clinozoisite	Allanite	Garnet			Vesuvianite				Pumpellyite		Lawsonite	
SiO_2	39.42	36.22	36.40	34.43	37.48	38.78	38.01	34.79	30.94	37.07	37.06	39.57	36.49	37.73	37.86		38.26	37.90	38.07	37.39
TiO_2	0.30	0.07	0.15	1.55	0.22	0.28	0.27	0.09	0.27	0.37	0.09	0.17	4.51	3.92	5.89		0.03	0.01	0.05	0.89
Al_2O_3	21.84	21.13	20.27	17.95	26.44	32.43	31.22	25.96	18.29	0.03	0.00	22.32	17.86	18.61	17.62		26.36	25.95	31.50	30.67
Cr_2O_3	0.00	–	–	0.00	0.03	0.00	0.01	0.08	0.20=Y_2O_3	20.56	20.98	0.00	0.00	0.04	0.01		0.01	0.00	0.00	0.03
Fe_2O_3	0.74	1.36	1.13	–	–	0.23	0.75	5.41	26.62=LREE‡	0.58	0.49	0.03	–	1.63	1.60		–	–	0.10	0.42
FeO	0.17	17.42	22.39	1.50	2.34	–	–	–	9.55	26.84	30.39	0.00	1.87	0.00	0.00		0.52	0.13	–	–
MnO	0.48	12.55	2.98	0.00	0.08	0.00	0.00	0.10†	0.00	7.79	1.29	0.02	0.09	0.06†	0.08†		0.02	0.00	0.00	0.00
MgO	0.03	1.23	0.56	0.27	2.50	0.00	0.02	0.03	0.30	0.62	1.04	0.07	0.36	0.58	0.35		3.93	4.50	0.00	0.01
CaO	36.32	9.30	13.61	29.34	22.76	23.42	20.30	12.57	11.58	6.41	8.56	37.61	31.94	31.42	30.56		22.96	23.77	17.30	17.03
SrO	0.02	–	–	–	0.05	2.53	7.18	17.63	0.02	–	–	0.00	–	0.26	0.30		–	0.00	0.32	0.66
BaO	0.00	–	–	0.03	0.00	0.00	0.05	0.16	–	0.03	0.05	0.00	0.00	0.00	0.00		0.00	0.00	0.02	0.00
K_2O	0.01	0.01	0.01	0.00	0.50	0.02	0.02	0.00	–	0.19	0.04	0.02	2.01	2.71	3.08		0.47	0.09	0.01	0.00
Na_2O	0.00	0.06	0.01	1.05	0.04	0.00	0.00	0.03	–	0.00	0.00	0.00	0.00	0.01	0.03		0.00	0.00	0.00	0.00
H_2O*	–	–	–	3.64	6.65	1.94	1.90	1.75	1.56	–	–	–	2.53	3.18	3.18		7.19	6.84	11.41	11.21
TOTAL	99.33	99.34	97.53	89.76	99.09	99.64	99.73	98.62	99.84	100.49	99.98	99.83	97.67	100.00	100.39		99.75	99.18	98.78	98.31
Cations pe	24 O	24 O	24 O	18 Si	3 Si	25 O	25 O	25 O	25 O	24 O	24 O	24 O	18 Si	18 Si	18 Si		3 Si	3 Si	4 Si	4 Si
[4]Si	5.977	5.855	5.950	18.000	3.000	5.979	5.997	5.967	5.935	5.981	5.961	5.960	18	18	18		3	3	4	4
[4]Al	0.023	0.145	0.050	0.000	0.000	0.021	0.003	0.033	0.065	0.019	0.039	0.040	0	0	0		0	0	0	0
SumTet	6.000	6.000	6.000	18.000	3.000	6.000	6.000	6.000		6.000	6.000	6.000	18	18	18		3	3	4	4
[6]Al	3.880	3.879	3.855	11.060	2.494	5.872	5.803	5.215	4.069	3.890	3.940	3.922	10.382	10.465	9.874		2.436	2.421	3.901	3.867
Ti	0.034	0.009	0.018	0.609	0.013	0.032	0.031	0.012	0.039	0.045	0.011	0.019	1.672	1.406	2.105		0.002	0.001	0.004	0.072
Cr	0.000	–	–	0.000	0.002	0.000	0.001	0.011	0.071=Y_2O_3	0.004	0.000	0.000	0.000	0.017	0.005		0.001	0.000	0.000	0.003
Fe3+	0.085	0.165	0.140	–	–	0.027	0.089	0.698	1.829=LREE‡	0.071	0.059	0.003	–	0.587	0.574		–	–	0.008	0.034
Fe2+	0.022	2.355	3.061	0.657	0.157	–	–	–	1.532	3.620	4.089	0.000	0.769	0.000	0.000		0.034	0.008	–	–
Mn	0.061	1.718	0.413	0.000	0.005	0.000	0.000	0.014†	0.000	1.064	0.175	0.003	0.039	0.023†	0.029†		0.002	0.000	0.000	0.000
Mg	0.006	0.295	0.136	0.211	0.298	0.000	0.006	0.007	0.086	0.148	0.249	0.017	0.267	0.414	0.247		0.459	0.530	0.000	0.002
Ca	5.900	1.610	2.384	16.436	1.952	3.869	3.432	2.311	2.380	1.108	1.475	6.070	16.882	16.059	15.568		1.929	2.016	1.947	1.952
SrO	0.001	–	–	–	0.002	0.226	0.657	1.753	0.002	–	–	0.000	–	0.071	0.083		–	0.000	0.020	0.041
Ba	0.000	–	–	0.000	0.000	0.000	0.003	0.011	–	0.002	0.003	0.000	0.000	0.000	0.000		0.000	0.000	0.001	0.000
Na	0.003	0.019	0.004	1.065	0.076	0.007	0.005	0.000	–	0.060	0.011	0.007	1.924	2.509	2.837		0.073	0.013	0.003	0.000
K	0.000	0.002	0.002	0.000	0.004	0.000	0.001	0.007	–	0.000	0.000	0.000	0.000	0.007	0.017		0.000	0.000	0.000	0.000
Total	15.991	16.053	16.013	48.043	8.004	16.032	16.027	16.039	16.008	16.011	16.014	16.042	49.935	49.340	49.340		7.936	7.990	9.884	9.972
OH*	–	–	–	12.701	1.551	2	2	2	2	–	–	–	8.329	9.494	9.483		1.76	1.61	4	4
H_2O*	–	–	–	–	–	0	0	0	0	–	–	–	–	–	–		–	–	2	2
										core	rim									

* OH and H_2O calculated from stoichiometry or charge balance; H_2O wt% back calculated from stoichiometry; † Fe or Mn is recalculated as trivalent. ‡ LREE = La_2O_3 (3.33 wt%, 0.236 apfu) + Ce_2O_3 (10.47, Czo: Clinozoisite, Zo: Zoisite

dimension and surrounding/invading monazite grains of similar dimension in two samples.

Late-stage alteration is not as common as observed in jadeitites north of the Motagua fault. This is obvious from the generally greater translucency of the jadeitite due to tight grain boundaries lacking refractive-index contrast gaps or coatings. The most common grain-boundary infiltration phases, when observed, are quartz and albite, which can be accompanied by omphacite or cymrite. Quartz infiltrations have been observed in which jadeite grains, with somewhat "chewed up" rims, are separated by a quartz matrix and surrounded by blebs of omphacite and diopside (Fig. 5I).

La Ceiba

The jadeitite varies from a medium- to fine-grained, opaque, granoblastic texture to a darker translucent microcrystalline mesh texture omphacitite. However, the latter variety is cut by dense networks of fractures that render the material fragmental (and not suitable for use as gem jade). Jadeite grains have a similar texture as those in jadeitite from the Carrizal Grande area; grain interiors are decorated with blebs of omphacite, quartz and fluid inclusions. Small rounded zircon inclusions are also common in jadeite, but not generally in the areas of the previously mentioned inclusions (Fig. 5J). Zoning in jadeite grain interiors is subtle and generally patchy and cryptic, and rims are typically narrow, relatively unzoned with slightly lower jadeite content (brighter in BSE). Overgrowth of cryptically zoned core jadeite by clean rhythmic purer jadeite followed by less jadeite-rich, possibly multiple times, is observed in MVE04-15-3 (Fig. 7D). Coarser-grained omphacite, phengite, and titanite fill in around grains of jadeite in discontinuous, broken-up veins. Zoning in omphacite cores is cryptic but rims or outer regions can be rhythmically zoned. Large titanite grains (up to several mm) have an irregular shape and appear to have numerous quartz and fluid inclusions (voids in polished section). Late, light-colored veins transect the rock and typically consist of quartz, diopside, cymrite, vesuvianite (Fig. 4D; Fig. 5K) and, on occasion, pectolite. Albite appears between grain boundaries of jadeite.

La Ensenada

The jadeitite here is noted for its generally pale tan-to-grayish body color decorated by stringers of lavender, blue, emerald-green, and pink, earning it the name "rainbow jade". It consists of dense intergrowths of jadeite crystals cut by narrow pumpellyite-dominant veins, in turn cut by veins of grossular and albite. Jadeite crystals vary from lathy, generally <300μm long, to irregular to radial clusters forming a dense mat of jadeite. Veins crosscut the jadeite and mantle or infill the jadeite with blocky pumpellyite of similar but more equant grain size. The centers of the veins are occupied with grossular ± albite (Fig. 5L); however, pumpellyite + grossular ± albite is also found dispersed as small regions in the jadeitite in what appear to be late-stage veins. Pinkish grossular crystals are commonly intergrown, with individuals ranging from ~100μm to 1mm across, and cathodoluminescence reveals oscillatory zoning patterns (Fig. 5M – MVE04-20-1) not evident in BSE or in major elements. Omphacite is minor both as inclusions and overgrowths on jadeite grains. Phengite, titanite, apatite, chlorite, zircon, and celsian are other minor constituents of this rock type. Light brown chloritite veins cut through some samples and consist of Fe-poor (<1wt% FeO_T) clinochlore plus omphacite and titanite in decreasing abundance with distance from the jadeitite boundary.

Mineral compositions

Pyroxene

As with the samples from north of the Motagua fault, representative compositions are presented in Table 1, and summary plots are provided in Figure 6B, with plots for each of the three distinct source areas south of the Motagua fault. The following characteristics are noted:

1) As in the case of northern jadeitite, jadeite compositions typically range from pure jadeite to perhaps $Jd_{\sim 80\text{-}85}Di_{5\text{-}10}Ae_5Hd_2$, with some dispersion in diopside versus aegirine content. The La Ensenada jadeite, like the lavender jadeite from Saltán, is distinctive for its very low iron content (<1wt%), but does have minor coexisting omphacite and even diopside.

2) Zoning patterns in jadeite grains among individual jadeitites vary considerably, but the most common is a jadeite-rich core, either relatively homogeneous or with cryptic, patchy zoning, particularly when there are abundant inclusions, and a less jadeite-rich (more diopside + aegirine + hedenbergite) rim. In some samples, e.g., JJE01-3-1, well-formed crystals manifest coarse oscillatory zoning (from high-to-low-to-high jadeite content) usually terminated by a less jadeite-rich rim or an omphacite overgrowth (Fig. 5N).

3) The compositions of omphacite inclusions and overgrowths generally overlap in each thin section, however, the jadeite – omphacite gap tends to be larger for coexisting jadeite and omphacite at the cores of jadeite grains than at rims of those grains. And, as with samples from the North, some omphacite inclusion compositions are much higher in aegirine content (Fig. 6B; Table 1) than is consistent with the Green et al. (2007) solvus. Likewise, as with northern jadeitite, coexisting jadeite-omphacite compositions do not follow their solvus. Finally, there is the unusual Ti-rich compositions (*e.g.*, Table 1) of certain blue vein omphacite in samples from the Carrizal Grande area and even in jadeite from La Ensenada, which is best characterized by a $NaTi_{0.5}Mg_{0.5}Si_2O_6$ (rather than alumino-buffonite – $CaTi_{0.5}Mg_{0.5}AlSiO_6$) component (Table 1; Harlow et al., 2003, 2004b).

4) There are distinct differences in the pyroxene compositional arrays between the three different source areas south of the Motagua fault (Fig. 6B). In general, the range of compositions of both jadeite and omphacite are greatest for Carrizal Grande, intermediate for La Ceiba, and the smallest for La Ensenada. The most straightforward interpretation is a decrease in the maximum temperature of growth (equilibration) of jadeite and omphacite, in the order listed. Likewise, except for a single sample from La Ceiba (MVE03-77-1), the maximum aegirine content for both jadeite and omphacite varies in the same order, greatest at Carrizal Grande and least at La Ensenada. Finally, at La Ceiba and La Ensenada we found individual jadeitite samples (MVE02-15-10, MVE04-21-7) with late stage veining containing a diopside composition separated by a gap from omphacite compositions.

Mica

Representative mica compositions are presented for localities from south of the Motagua fault in Table 2. Muscovite grains analyzed are usually phengitic, with variable enrichments in Ba similar to values in muscovite north of the Motagua fault. However, Si apfu is significantly higher than in samples north of the Motagua fault, from the highest values at Carrizal Grande (≤7.5), lower at La Ceiba (≤7.2), and lowest at La Ensenada (<6.7) where mica is rare. At La Ensenada, mica is more likely to be phlogopite, but, if muscovite, it is not generally phengitic. Ba substitution for K follows the same mechanisms described by Harlow (1995) in mica north of the Motagua fault by which the predominant one ($BaAlK_{-1}Si_{-1}$) lowers Si content of the mica. Mg/(Mg+Fe) of phengite varies within and between jadeitite samples from 0.57-0.90 (MVE02-8-5) to a narrower 0.80-0.92 (JJE01-3-4), both samples from Carrizal Grande, with a similarity to those values (but perhaps slightly lower) in coexisting omphacite (jadeite cannot be well assessed for $Mg/(Mg+Fe^{2+})$ versus

$Mg/(Mg+Fe_T)$. This variability is not clear for jadeitite from La Ensenada, for lack of analyses, although $Mg/(Mg+Fe^{2+})$ of phlogopite is high 0.96-0.97 from a single sample (MVE04-20-1).

Amphibole

Representative amphibole compositions are presented in Table 3. Glaucophane is a rare late phase in jadeitite and more commonly associated with a rock composed principally of omphacite + glaucophane from the Carrizal Grande area, with composition essentially on the glaucophane – ferro - glaucophane join ($Mg/(Mg+Fe^{2+})$ 0.8-0.9 – see Table 3). Actinolite is found in veins, typically with quartz or albite and is near the tremolite-actinolite join in composition.

Other calcic minerals

Grossular garnet is common but only in the pumpellyite - jadeitite from around La Ensenada and is nearly pure end-member grossular. The zoning evident by cathodoluminescence does not manifest itself in microprobe analyses. Otherwise, a single specimen of garnet jadeitite infiltrated with quartz and lawsonite from Carrizal Grande (MVE06-17-2) contains garnet somewhat like that in eclogite in the area but with much greater spessartine content (to ~8wt% MnO, ~1.2Mn apfu: Table 4). This sample is the best (and a rare) argument for metasomatic replacement of an eclogite by jadeitite, without textural indication. If so, the high Mn content of garnet and high aegirine content (to 43mol%) and low jadeite content (4-10mol%) of minor omphacite (if relict) are not typical for local eclogite. Vesuvianite is found in late stage veins with cymrite and quartz at La Ceiba. As with compositional characteristics from the sample north of the Motagua fault, Ti is high (to >5wt% TiO_2) and Na (to ~2.5wt% Na_2O; Table 4). It also contains a small amount of SrO (0.25-0.5wt%, 0.07–0.14 Sr apfu). Pumpellyite-Mg is common in pumpellyite-jadeitite from near La Ensenada. Pumpellyite straddles the boundary between –Al and –Mg types with ~30-50% pumpellyite-Al and 40-50% pumpellyite-Mg components. Lawsonite is common in some jadeitites and omphacitites from the Carrizal Grande area, occurring in the mélange with lawsonite - eclogite. Lawsonite compositions are calculated with all iron and manganese, although minor, as trivalent cations, which still leaves the six-fold site slightly deficient when cations are normalized to 4 silicon atoms, as well as the oxide (plus calculated H_2O) and cation totals are somewhat low, even while including Sr content (typically 0.03–0.35 apfu; Table 4).

DISCUSSION

Estimates of crystallization P-T

As nearly monomineralic rocks are affected by episodes of growth and some alteration, assessing conditions of crystallization, particularly peak P-T, can be difficult. We have separated the interpretation into sections on phase assemblage and then jadeite-omphacite relationships as well as the distinctions between the tectonically distinct environments: north versus south of the Motagua fault in Guatemala.

PT conditions North of the Motagua fault

None of the jadeitites in this region contain quartz, either as inclusions in jadeite or in veins, but all contain albite, mica and usually analcime, which indicates they all formed at P lower than that of the jadeite + quartz stability field unless the phase assemblage represents a fully retrograded one, consistent with the earlier observations by Harlow (1994). The presence of zoisite/clinozoisite rather than lawsonite in the presence of paragonite suggests formation at T above the reaction lawsonite + jadeite = zoisite/clinizoisite + paragonite + albite + H_2O (Fig. 8). These constraints yield P=6-12kbar and T=300-450°C; higher temperatures are permissible if the activity of SiO_2 is much below unity (see Fig. 8 Harlow, 1994). The modest jadeite–omphacite gap (Green et al., 2007) yields temperatures from 200 to >500°C for pyroxene pairs, with indications of higher temperatures for samples from the more western localities and lower for ones from the east (see Fig. 6), except for those from Saltán. More discussion of these data are presented below.

Carpenter (1979, 1981) described antiphase domain structures <20nm in size in omphacite from a jadeitite that undoubtedly came from the central area North of the Motagua fault (presumably Manzanal). These omphacite antiphase domain textures indicate that the omphacite went through the order-disorder transformation soon after the omphacite crystallization in *C*2/*c* space group (presumably metastably). But more significantly, the very small antiphase domain size is consistent with the low-T formation of the jadeitite and a simple cooling history.

Alteration of jadeitite to the albitite assemblage, as described in Harlow (1994), involves both additional SiO_2 (as well as large ion lithophile elements (LILE)) via a fluid (see Sorensen et al., 2010), as well as a down P trajectory below the jadeite stability field, usually, into the zoisite stability field (T>350-400, see Fig. 8) and into the greenschist facies (350-450ºC at <7kbar). Moreover, the symplectitic textures of albite + analcime and albite + nepheline (also described by Tsujimori et al., 2004b) are further evidence of fluid involvement in these retrograde reactions:

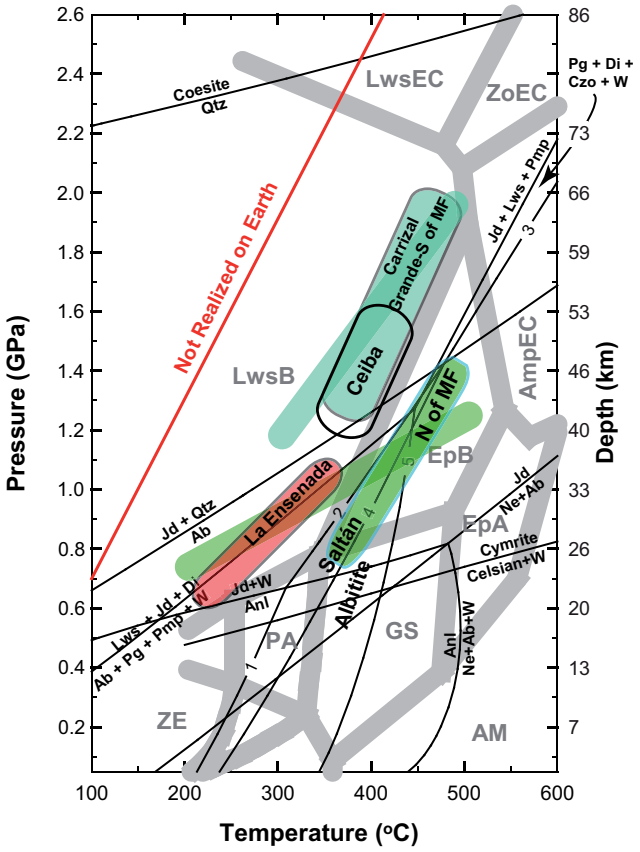

FIGURE 8 | **Plot of P-T grid with estimates for jadeitite formation. Conditions north of the fault (N of MF) are shown in green with the singular conditions at Saltán shown at the lower-left end of the distribution. Conditions south of the fault are shown in blue-green for Carrizal Grande, an outlined area for La Ceiba, and in pink for La Ensenada. Narrower colored bands show the temperature range inferred from pyroxene compositions alone in the assemblage space consistent with the mineralogy. The area around "Albitite" is the greenschist condition for the albitite/alteration of jadeitites from north of the Motagua fault. A facies grid for metabasalts that is a hybridization of Oh and Liou (1998) and Peacock (1993) is shown for reference; facies symbols are ZE: zeolite, PA: pumpellyite actinolite, GS: greenschist, AM: amphibolite, EpA: epidote amphibolite, EpB: epidote blueschist, LwsB: lawsonite blueschist, AmpEC: amphibole eclogite, ZoEC: zoisite eclogite, and LwsEC: lawsonite eclogite. Reactions are from Harlow (1994) plus pumpellyite calculations from GeoCalc (Berman et al., 1987, Berman, 1988, 1991). Reactions defined by an integer are (1) 4Lws + 2Anl = Ab + Pg + 2Czo + 8W; (2) 4Lws +2Jd = Ab + Pg + 2Czo + 6W; (3) 4Lws + Jd = Qtz + Pg + 2Czo; (4) 4Lws + Ab = 2Qtz + Pg + 2Czo + 6W; (5) 3Ab + 4 Pmp = 2 Jd + 6 Czo + Pg + 4 Di + 10 W. Ab: Albite, Anl: Analcime, Czo: Clinozoisite, Di: Diopside, Jd: Jadeite, Lws: Lawsonite, Ne: Nepheline, Pg: Paragonite, Pmp: Pumellyite, Qtz: Quartz, W: H_2O.**

Oberhänsli et al. (2007) used the method of pseudosections to calculate conditions for bulk compositions of jadeitite from Sorkhan, Iran and elsewhere, including an estimate for a sample north of the Motagua fault: R11 called Olmec-Blue containing jadeite, albite, paragonite, analcime, zoisite, titanite, and preiswerkite (Harlow, 1994). Their analysis yields T=~500ºC and P=~14kbar, at the high end of our T estimate and above our P estimate. However, this estimate is defined by the lack of omphacite and presence of zoisite, whereas jadeitites from north of the Motagua fault usually contain primary omphacite and late or alteration zoisite. The authors state that the presence of jadeite + omphacite yields *T*s below 400ºC in their calculations, more consistent with the results of Harlow (1994) and those presented here. Ultimately, their results are useful but may be difficult to apply to jadeitites North of the Motagua fault where bulk composition is strongly affected by alteration and phase assemblages must be deciphered for different stages of the rock history.

The jadeitite from Saltán is singular for samples that contain late-stage pumpellyite + grossular as well as nearly pure jadeite; however, the primary crystallization of the jadeite in these lavender-colored rocks provides little indication for initial conditions as inclusions are generally fluids and jadeite in contact with albite has rounded grain boundaries as if in reaction relationship. Omphacite is absent. Another sample from Saltán (MVE07B-19-6) contains albite and omphacite inclusions in jadeite and no pumpellyite or vesuvianite, more like other samples from the western end of the northern suite. Our conclusion is that the lavender samples represent both a different origin condition and composition (low Fe), and the alteration assemblage pumpellite + albite + grossular + zoisite/clinozoisite suggests T~350ºC at P 6-8kbar (e.g., Schiffman and Liou 1980), which is probably colder than jadeitite-albitite conditions found elsewhere North of the Motagua fault. Another distinctive aspect of these jadeitites is the late extensive enrichment in both Sr and Ba.

PT conditions South of the Motagua fault

Whereas the phase assemblages for the entire 200km span of jadeitite north of the Motagua fault (except Saltán) are remarkably consistent, those south of the Motagua fault clearly group into three distinct clusters based on geography. In jadeitites from the Carrizal Grande area, the presence of quartz inclusions in jadeite indicates P in the jadeite + quartz stability field. They are found together with lawsonite eclogites with maximum metamorphism estimated at P=20-26kbar, T=350-480°C and blueschist alteration from P≈14kbar and T≈400°C indicating a geotherm of ≈5°C/km, comparable to the coldest geotherms from subduction zones worldwide (Tsujimori et al., 2006a). Jadeitites at Carrizal Grande are consistent as a phase assemblage with the blueschist trajectory of this interpretation, but not well constrained. In this case, the results of Oberhänsli et al. (2007) may provide useful insight, as the assemblages of quartz-lawsonite-jadeite-omphacite-amphibole-paragonite have a narrow stability field from 350-425ºC and 11-16kbar (their Fig. 4A), although Carrizal Grande samples contain phengite rather than paragonite and thus have a different bulk composition.

Consequently, jadeitite formation is estimated as T<500ºC (those with lawsonite, <450ºC) and P=12-20kbar in the presence of lawsonite; without lawsonite T can only be estimated from coexisting omphacite-jadeite, which is discussed below. Jadeitites from La Ceiba also manifest quartz inclusions in jadeite but contain neither lawsonite nor zoisite/clinozoisite to further constrain the phase assemblage in PT. Compared to Carrizal Grande jadeitites, jadeite - omphacite pairs at La Ceiba suggest a somewhat lower maximum T of ~450ºC. That plus the lack of coexisting eclogite in the local mélange but presence of glaucophane blueschists argues for somewhat lower P of ~12-16?kbar. In the La Ensenada jadeitite the lack of quartz, intimate pumpellyite - jadeite textures, and a large omphacite-jadeite gap suggests maximum T=<300-350ºC at P>6kbar.

Mechanism of formation

Previous work on Guatemalan jadeitite (Harlow, 1994) and jadeitite in general (Sorensen et al., 2006; Harlow et al., 2007) has argued for crystallization from a hydrous fluid, derived from a subduction channel, in fractures in serpentinizing peridotite, presumably the hanging wall (the mantle wedge) of the channel. The fundamental arguments are 1) consistent association with serpentinite with some clear cases of contact (*e.g.*, Myanmar – see Harlow et al., 2007), 2) textural evidence for crystallization from a fluid including abundant fluid inclusions and unimpeded crystal growth into open space, 3) little evidence for metasomatic replacement of a protolith in terms of either pseudomorphic textures or relict phases from such a protolith, 4) evidence that high pressure hydrous fluids, such as those derived from the blueschist-to-eclogite transition are mostly saturated with respect to jadeite (Manning, 1998), 5) reaction zones between jadeitite and serpentinite that represent primary or secondary interactions involving a fluid (Sorensen et al., 2010; Harlow et al., 2007). This report updating jadeitite information from Guatemala reinforces these observations. Harlow et al. (2007) cite one case where metasomatic replacement has been documented – Punta Rasciassa in the Monviso serpentinite of the Western Alps, Italy (Compagnoni et al., 2007) and two cases in which jadeitite encapsulates eclogite blocks in a mélange – Kampos mélange, Syros, Cyclades, Greece (Bröcker and Keasling, 2006) and Borus mélange, Khakassia (Dobretsov, 1963). Among more than 100 jadeitite samples examined in this study only a few might be invoked to show metasomatic replacement, and these are most clearly limited to relict garnet: ZC20 and MVE06-17-2. Interestingly, both samples contain metamorphic garnets that are not likely from any eclogite or garnet amphibolite (metabasite) associated with the mélanges as the spessartine content exceeds that in the metabasites. Certainly there are ambiguous cases of jadeite nucleation around another mineral like zircon, uraninite and even albite, but the minerals are either totally exotic (uraninite) or found within the phase assemblages of jadeitite without clearly exotic compositions so metasomatism is not documented.

Pyroxene zoning, pyroxene pairs and P-T-t paths

The evaluation of the solvus in the jadeite – diopside – hedenbergite - aegirine clinopyroxene system by Green et al. (2007) has been applied to compositional data compiled on the pyroxenes in this study of jadeitite. Pressure has been uniformly set at 12kbar as a reasonable average for the pseudobinary evaluations along the (diopside + hedenbergite + aegirine) - jadeite joins, following the example of García-Casco et al. (2009). Several implications have been derived.

Firstly, only rare pairs give consistent T estimates, which is evident from Fig. 6. Omphacite consistently yields a higher T estimate than jadeite, typically by 100 to 150ºC. Whereas this could be interpreted as due to disequilibrium at low T and problems with the aegirine estimate, the consistency among many pairs from different samples and locations argues against this. Given the gentler slope of solvus for jadeite compositions and their dominance, we have used them for subsequent discussion.

The second implication is derived from the zoning of jadeite crystals with omphacite inclusions or overgrowths. The recently described jadeitites from Cuba (García Casco et al., 2009) have been interpreted with a considerably different sequence of conditions during growth than for others (Harlow et al., 2007). Cores of jadeite manifest oscillatory zoning of impure jadeite interpreted as forming at higher temperatures, ca. 640ºC, with a change to binary jadeite-omphacite crystallization (a more diopside-rich fluid) at ca. 570ºC on jadeite crystal rims. This observation led us to reexamine zoning in Guatemalan jadeite and jadeite-omphacite pairs. Jadeite-rich cores and jadeite-poor rims in most Guatemalan jadeitite are the reverse of those reported by García-Casco et al. (2009) and consistent with those previously reported (Harlow, 1994; Sorensen et al., 2006; Harlow et al., 2007). Indeed, many jadeitite samples, with few exceptions, crystallize with a jadeite-rich core (Jd_{100-95}) with an overgrowth extending to perhaps Jd_{85-80} followed by omphacite. These final jadeite compositions in equilibrium with omphacite yield T=500-580ºC based on the solvus of Green et al. (2007). Pure jadeite cores alone only demand a fluid that is saturated with respect to jadeite and presumably not saturated in other components or phases and thus cannot be used to assess T. However, in numerous samples omphacite inclusions in the interior of jadeite grains appear to be (nearly) in equilibrium with the adjacent jadeite. For these pairs, T is about

200-300ºC for P assumed to be 10-12kbar and should define roughly the initial growth conditions. Decrease in jadeite content with continued grain growth requires higher T, otherwise omphacite would form. Ultimately, jadeite grain compositions decrease to Jd_{80} followed by omphacite compositions that can, with continued crystallization along grain boundaries, evolve to diopside > jadeite and, in some cases, distinct diopside coexisting with albite. These trends suggest up-T crystallization plus increasing diopside-content of the fluid, in part contradictory to our previous interpretation (Harlow et al., 2007).

Zoning within jadeite crystals is commonly cryptic in interiors and rhythmic toward the rims. Cryptic zoning is puzzling but may combine aspects of fast crystallization and deformation as many cryptically zoned crystals have fuzzy optical extinction. Rhythmic zoning has been explained as the result of pulses of fluid entering open fractures in preexisting jadeitite that crystallizes more jadeite-rich compositions first with depletion leading to compositions higher in other components (Harlow, 1994; Sorensen et al., 2006).

Studies of jadeitites along with many other HP–LT rock P-T-t-x paths following a clockwise PT history argue that jadeitite formation should follow a down-P, down-T path during exhumation (e.g., Harlow et al., 2007; Tsujimori et al., 2006a; Sorensen et al., 2006; Harlow et al., 2003). The composition of coexisting jadeite-omphacite in the cores of jadeite crystals as compared to rims generally argue for either cold primary crystallization followed by hotter late crystallization or composition of jadeite controlled strictly by fluid composition with omphacite being in disequilibrium, perhaps encapsulated from a dismembered omphacite-bearing protolith. The lack of replacement textures (see below) and dissimilarity of omphacite compositions to any known mélange lithology make the second explanation less credible. Thus, we prefer the interpretation in which initial jadeitite crystallization is colder (ca. 300ºC) with late crystallization and omphacite veining as warmer (perhaps to 500ºC). This implies that the most jadeitite crystallizes in a chilled environment that later experiences warming while the crystallization simultaneously evolves toward more diopside (+ hedenbergite + aegirine) bulk composition. This would appear to be an improbable coincidence, but support for an alternate hypothesis is not compelling. Finally, there are a number of samples that show more than one generation of higher initial jadeite content growth followed by decreasing jadeite (e.g., MVE04-15-3 – La Ceiba: Fig. 7D; or JJE01-3-1 – Carrizal Grande Fig. 5N). Multiply zoned jadeite records a repeat of whatever sequence of events and processes responsible for zoning profiles in most jadeitites from Guatemala.

Consequently, crystallization of jadeitite probably should not be viewed as directly connected to some phase of the metamorphism of the subducted slab, such as eclogite or blueschist formation, because jadeitite most likely formed in the hanging wall, or a slice thereof, rather than in the slab. However, jadeite veins in some Lawsonite-eclogite from Carrizal Grande (Tsujimori et al., 2005, 2006a), suggest that at least a portion of jadeitite formation postdates that of eclogite and that either the jadeitite-forming fluids were active in portions of the subduction channel or eclogite had been incorporated into the serpentinizing mélange by the time of jadeitite formation. The interpreted progression of colder to warmer crystallization of jadeite unfortunately does not include any pressure information. It is unlikely that the process happens deeper than the transition from static mantle wedge to ductile where it is being dragged down with the plate, roughly at 70-80km depth (~23-26kbar; e.g., Grove et al., 2009.) So, it is not clear whether the trend tracks heating due to the exothermic serpentinization reactions (see Evans, 2004) plus aging of the contact or delamination of mantle wedge slabs via volume increase (from serpentinization) and increased traction or some other process. Cycling of this process might be explained by small scale wedge extrusion –decreasing P– with or without delamination of the overlying wedge into the subduction channel that puts colder slab and new fluids adjacent to the serpentinizing mantle. Resolution requires better control of P-T-t-x interpretation as well as modeling.

Differences between jadeitite from North and South of the Motagua fault

From the descriptions above, it is clear that jadeitite occurrences North and South of the Motagua fault vary in some very distinctive ways. The first to be considered is the tectonic context. South of the Motagua fault, eclogite and jadeitite are part of a single tectonic event (collision-exhumation) that spans eclogite crystallization from 144-132 (±~10; Sm-Nd) Ma and thermal closure (Ar-Ar) from 125-116Ma, whereas North of the Motagua fault there are clearly two events defined by mélange eclogite (131-126Ma; Sm-Nd), more or less equivalent to dates south of the Motagua fault, and thermal closure ages from 65 to 77Ma, equivalent to metamorphic ages (Ar-Ar of mica and amphibole in gneisses and Sm-Nd isochrons for eclogite enclaves, e.g., Martens et al., 2007a) from the Sierra de Las Minas, north of the mélange (Brueckner et al., 2009). Recent crystallization dates for jadeitite are limited but intriguing. U-Pb dating of zircon from a single jadeitite in the central zone north of the Motagua fault gives 95.1±3.6Ma (Yui et al., 2010) which was concluded to be a formation date on the basis of inclusions in the zircons. This age is certainly younger than the eclogite date but somewhat older than the Cretaceous event that metamorphosed the Sierra de Las Minas and

emplaced the Sierra de Santa Cruz ophiolite. A U-Pb date from a phengite jadeitite (MVE02-8-6) from south of the Motagua fault of 153.7±3.5Ma (Fu et al., 2010) was interpreted as a protolithic relic from the oceanic crust based on its being older than the eclogite ages. However, we have doubts about this interpretation: the zircon in this sample contain mineral and fluid inclusions inconsistent with an igneous origin, and being older is not a necessarily a criterion for being relict. Certainly, these dates raise a variety of interesting questions beyond the scope of this paper without more zircon dating, but it does appear that this difference between the jadeitite north and south of the Motagua fault is real. The presence or lack of albitization, albite-mica rocks, etc. may be related to both temporal and physicochemical differences in the formation events.

The next distinction is the vast areal extent of the northern jadeitite belt, more than 200km with at least three grouped areas compared to a very limited extent, ~11km, parallel to and south of the Motagua fault. All of the jadeitite north of the Motagua fault shares the extensive albitization overprint, whereas the narrow extent of jadeitite south of the Motagua fault can be readily distinguished among three fault slices by different phase assemblages and apparent P and/or T of crystallization. Moreover, quartz inclusions and veins in jadeite from two of the three occurrences south of the Motagua fault stands in contrast to the total lack of quartz in any jadeitite from north of the Motagua fault. So, clearly the different tectonic events have made a difference, but whether the lack of variability on the north side is due entirely to a possible Cretaceous overprint or to different formational events is not yet clear. If the zircon dating holds, the Cretaceous age is the crystallization date and the alteration is just part of the northern processing.

The lavender-colored jadeite in samples from Saltán, north of the Motagua fault, and La Ensenada, south of the Motagua fault, deserve special mention and attention. The jadeite in these samples has compositions among the most rich in jadeite component and lowest in iron. Likewise, coexisting omphacite (found so far only at La Ensenada), pumpellyite, and lawsonite (south only) suggest the lowest crystallization temperatures for jadeitite. The minimal iron in both pyroxene and clinochlore (La Ensenada) suggest some mechanism for keeping ferrous iron in solution during crystallization which could be related to some redox phenomenon such as that which leads to removal of iron in white bauxites during low-T diagenesis (Feenstra, 1996; see Lu et al., 2005), as well as low-T, in general, for the formation of these distinct jadeitite.

Finally, although this paper does not present rock compositions and geochemistry, an obvious difference from the mineralogy between the northern and southern jadeitite is the predominant mica. Jadeitite north of the Motagua fault predominantly features paragonite with very secondary abundance of phengite and phlogopite plus alteration preiswerkite. In contrast, paragonite (and preiswerkite) are absent in jadeitite south of the Motagua fault, whereas phengite is common to abundant. Interestingly, the late barium influx is common in all Guatemalan jadeitite occurrences by the presence of barian K-micas, cymrite, celsian, banalsite, and hyalophane. The chemically distinctive mineralogies are suspected to be attributed to the compositional characteristics of the sediments accompanying the subducted slab that sourced jadeitite-forming fluid. This would suggest a decoupling of potassium sourcing, probably from clays and continentally derived sediments, from barium, more likely coming from either oceanic seafloor sediments or carbonates. These and other geochemical issues are being taken up elsewhere.

CONCLUSION

The distribution of jadeitite in Guatemala is now known to extend for more than 200km in serpentinite mélange strung out north of the Motagua fault and in three newly described mélange slices south of the fault. All of the jadeitite from north of the Motagua fault is characterized by jadeite containing inclusions or veins of albite + omphacite ± anaclime ± paragonite ± nepheline with extensive albitization. Jadeitite from the three known sources south of the Motagua fault are distinctive by their mineralogy and associated mélange lithologies: Carrizal Grande jadeitite features jadeite with inclusions of quartz + omphacite + phengite, minor veining of quartz or albite, a substantial proportion of samples containing lawsonite, and associated lawsonite - eclogite; La Ceiba has jadeitite similar to Carrizal Grande minus any lawsonite and omphacite bearing gneisses instead of eclogite; and La Ensenada has distinctive light-colored pumpellyite - jadeitite with veins of grossular plus albite and contacts with clinochlore rock in a mélange containing lawsonite - glaucophane blueschist. All evidence points to jadeitite formation from primary crystallization of jadeite and other phases from hydrous fluid liberated from the subducted slab and introduced into peridotite/serpentinite of the overriding mantle wedge. The extent of jadeitite in Guatemala is second only to Myanmar and the complexity of the tectonic context is noteworthy: Two collisions are recorded in the HP–LT blocks from the northern and southern serpentinite mélanges, one Neocomian and the other Maastrichtian, and it appears jadeitite formed in both events.

ACKNOWLEDGMENTS

We want to thank Carlos Gonzales for field assistance and Eric Sahm and Jamie Newman for analytical and sample processing

assistance and John Cleary for sharing geological observations from mapping observations on the jade deposits near Carrizal Grande. This work was funded by EAR0309320 to GEH, and EAR0309116 to VBS. This project is part of IGCP Project 546 on Subduction Zones of the Caribbean. We appreciate constructive reviews by Walter Maresch and Tatsuki Tsujimori.

REFERENCES

Alvarado, G.E., Dengo, C., Martens, U., Bundschuh, J., Aguilar, T., Bonis, S.B., 2007. Stratigraphy and geologic history. In: Bundschuh, J., Alvarado, G.E. (eds.). Central America: Geology, Resources, and Hazards. London, Taylor and Francis Group, 345-483.

Berman, R.G., 1988. Internally-consistent thermodynamic data for minerals in the system K_2O-Na_2O-CaO-MgO-FeO-Fe_2O_3-Al_2O_3-SiO_2-TiO_2-H_2O-CO_2-O. Journal of Petrology, 29, 445-522.

Berman, R.G., 1991. Thermobarometry using multi-equilibrium calculations: a new technique, with petrological applications. Canadian Mineralogist, 29, 328-344.

Berman, R.G., Brown, T.H., Perkins, E.H., 1987. GE0-CALC Software for the calculation and display of pressure-temperature-composition phase diagrams. Vancouver, University of British Columbia.

Bertrand, J., Vuagnat, M., 1976. Etude pétrographique de diverses ultrabasites ophiolitiques du Guatémala et de leurs inclusions. Bulletin Suisse de Minéralogie et Pétrologie, 56, 527-540.

Bertrand, J., Vuagnat, M., 1980. Inclusions in the serpentinite melange of the Motagua Fault Zone, Guatemala. Société de Physique et D'Histoire Naturelle de Genève, Archives des Sciences, 33, 321-336.

Bröcker, M., Keasling, A., 2006. Ionprobe U-Pb zircon ages from the high-pressure/low-temperature melange of Syros, Greece: age diversity and the importance of pre-Eocene subduction. Journal of Metamorphic Geology, 24, 615-631.

Brueckner, H.K., Avé Lallemant, H.G., Sisson, V.B., Harlow, G.E., Hemming, S.R., Roden-Tice, M.K., Sorensen, S.S., Tsujimori, T., Francis, A.H., Gehrels, G.E., Blythe, A.E., 2009. Metamorphic reworking of a high-pressure-low temperature serpentinite-matrix mélange belt north of the Motagua fault, Guatemala: A revised record of Neocomian and Maastrichtian collisions. Earth and Planetary Science Letters, 284, 228-235.

Brueckner, H.K., Hemming, S., Sorensen, S., Harlow, G.E., 2005. Synchronous Sm-Nd mineral ages from HP Terranes on both sides of the Motagua Fault of Guatemala: convergent suture and strike slip fault? Eos Transactions American Geophysical Union, Fall Meeting Supplement, 86(52), Abstract T23D-04.

Carpenter, M.A., 1979. Omphacites from Greece, Turkey, and Guatemala: Composition limits of cation ordering. American Mineralogist, 64, 102-108.

Carpenter, M.A., 1981. Time-temperature-transformation (TTT) analysis of cation disordering in omphacite. Contributions to Mineralogy and Petrology, 78, 433-440.

Chiari, M., Dumitrica, P., Marroni, M., Padolfi, L., Principi, G., 2006. Radiolarian biostratigraphic evidence for a Late Jurassic age of the El Tambor Group Ophiolites (Guatemala). Ofioliti, 31(2), 173-182.

Compagnoni, R., Rolfo, R., Manavella, F., Salusso, F., 2007. Jadeitite in the Monviso meta-ophiolite, Piemonte Zone, Italian western Alps. Periodico di Mineralogia, 76, 79-89.

Dobretsov, N.L., 1963. Mineralogy, petrography and genesis of ultrabasic rocks, jadeitites, and albitites from the Borus Mountain Range (the West Sayan). Academia Scientifica USSR (Siberian Branch), Proceedings of the Institute of Geology and Geophysics, 15, 242-316.

Donnelly, T.W., Horne, G.S., Finch, R.C. López-Ramos, E., 1990. Northern Central America; The Maya and Chortís Blocks. In: Case, J.E., Dengo, G., (eds.). The Geology of North America, The Caribbean Region. Boulder CO, Geological Society of America, H, 37-76.

Evans, B., 2004. The serpentinite multisystem revisited: Chrysotile is metastable. International Geology Review, 46, 479-506.

Feenstra, A., 1996. An EMP and TEM-AEM study of margarite, muscovite and paragonite in polymetamorphic metabauxites of Naxos (Cyclades, Greece) and the implications of fine-scale mica interlayering and multiple mica generations. Journal of Petrology, 37, 201-233.

Finger, L.W. 1972. The uncertainty in the calculated ferric iron content of a microprobe analysis. Carnegie Institution of Washington, 71(Yearbook), 600-603.

Foshag, W.F., 1957. Mineralogical studies on Guatemalan jade. Smithsonian Miscellaneous Collections, 135(5), 60pp.

Foshag, W.F., Leslie, R., 1955. Jadeite from Manzanal, Guatemala. American Antiquity, 21, 81-83.

Francis, A.H., 2005. Deformation history of the Maya and Chortís Blocks: Insight to the Evolution of the Motagua Fault Zone, Guatemala. Doctoral Thesis. Houston, Rice University, 149pp.

Francis, A.H., Avé Lallemant, H.G., Sisson, V.B., Harlow, G.E., Donnelly, T.W., Chiquin, M., Roden-tice, M.K., Hemming, S.R., Brueckner, H.K., in preparation. Interaction of the North American and Caribbean plates in Guatemala: Part 1. Deformation history and consequences for the exhumation of HP/LT metamorphic rocks. For Geological Society of America Bulletin.

Fu, B. Valley, J.W., Kita, N.T., Spicuzza, M.J., Paton, C., Tsujimori, T., Bröcker, M., Harlow, G.E., 2010. Origin of zircons in jadeitite. Contributions to Mineralogy and Petrology, 159, 769-780. doi: 10.1007/s00410-009-0453-y

García-Casco, A., Rodríguez Vega, A., Cárdenas Párraga, J., Iturralde-Vinent, M.A., Lázaro, C., Blanco Quintero, I., Rojas Agramonte, Y., Kröner, A., Núñez Cambra, K., Millán, G., Torres-Roldán, R.L., Carrasquilla, S., 2009. A new jadeitite jade locality (Sierra del Convento, Cuba): first report and some petrological and archeological implications. Contributions to Mineralogy and Petrology, 158, 1-16. doi: 10.1007/s00410-008-0367-0

Green, E.C.R., Holland, T.J.B., Powell, R., 2007. An order-disorder model for omphacitic pyroxenes in the system jadeite-diopside-hedenbergite-acmite, with applications to eclogite rocks. American Mineralogist, 92, 1181-1189.

Grove, T.L., Till, C.B. Lev, E., Chatterjee, N., Médard, E., 2009. Kinematic variables and water transport control the formation and location of arc volcanoes. Nature, 459, 694-697.

Hammond, N., Aspinall, A., Feather, S., Hazelden, J., Gazard, T., Agrell, S., 1979. Maya Jade: Source location and analysis. In: Earle, T.K., Ericson, J.E., (eds.). Exchange Systems in Prehistory. New York, Academic Press, 3(Chapter), 35-67.

Harlow, G.E., 1994. Jadeitites, albitites and related rocks from the Motagua Fault Zone, Guatemala. Journal of Metamorphic Geology, 12, 49-68.

Harlow, G.E., 1995. Crystal chemistry of barian enrichment in micas from metasomatized inclusions in serpentinite, Motagua Valley, Guatemala. European Journal of Mineralogy, 7, 775-789.

Harlow, G.E., Brueckner, H., Sorensen, S.S., 2010. Serpentinites of the Motagua fault zone mélanges, Guatemala: An assessment. Annual Meeting, Geological Society of America, Abstracts with Programs, 42(5), Avaiable Online: http://a-c-s.confex.com/crops/2010am/webprogram/Paper181532

Harlow, G.E., Donnelly, T.W., 1989. Unusual metabasites from jadeitite-bearing serpentinite melange, Motagua Valley, Guatemala. Eos, 70 (Abstract), 505.

Harlow, G.E., Hemming, S.R., Avé Lallemant, H.G., Sisson, V.B., Sorensen, S.S., 2004a. Two high-pressure–low-temperature serpentine-matrix mélange belts, Motagua fault zone, Guatemala: A record of Aptian and Maastrichtian collisions. Geology, 32, 17-20.

Harlow, G.E., Murphy, A.R., Hozjan, D.J., de Mille, C.N., Levinson, A.A., 2006a. Pre-Columbian jadeite axes from Antigua, West Indies: Description and possible sources. Canadian Mineralogist, 44, 305-321.

Harlow, G.E., Olds, E.P., 1987. Observations on terrestrial ureyite and ureyitic pyroxene. American Mineralogist, 72, 126-136.

Harlow, G.E., Price, N.A., Tsujimori, T., 2006b. Serpentinites of the Motagua fault zone, Guatemala: A mineralogical assessment. Kobe (Japan), 19th General Meeting of the International Mineralogical Association Program & Abstracts, 223, 19-17.

Harlow, G.E., Quinn, E.P., Rossman, G.R., Rohtert, W.R., 2004b. Blue omphacite from Guatemala. Gem News International section – Gems and Gemology, 40, 68-70.

Harlow, G.E., Rossman, G.R., Matsubara, S., Miyajima, H., 2003. Blue omphacite in jadeitites from Guatemala and Japan. Seattle (Washington), 2003 Geological Society of America, Abstracts with Programs, 35(6), 620 (CD-ROM 254-1).

Harlow, G.E., Sorensen, S.S., Sisson, V.B., 2007. Jade. In: Groat, L.A. (ed.). The Geology of Gem Deposits. Quebec, Mineralogical Association of Canada, Short Course Handbook Series, 37, 207-254.

Lu, P.J., Yao, N., So, J.F., Harlow, G.E., Lu, J., Wang, G., Chaikin, P.M., 2005. Earliest use of corundum and diamond in prehistoric China. Archaeometry, 47, 1-12.

Manning, Craig E., 1998. Fluid composition at the blueschist-eclogite transition in the model system Na_2O-MgO-Al_2O_3-SiO_2-H_2O-HCl. Schweizerische Mineralogische und Petrographische Mitteilungen, 78(2), 225-242.

Martens, U., Ortega-Obregón, C., Estrada, J., Valle, M., 2007a. Metamorphism and metamorphic rocks. In: Bundschuh, J., Alvarado, G.E. (eds.). Central America: Geology, Resources, and Hazards. London, Taylor and Francis Group, 485-522.

Martens, U., Mattinson, C.G., Wooden, J., Liou, J.G., 2007b. Protolith and metamorphic ages of gneiss hosting eclogite in the Chuacús complex, Central Guatemala. Eos Transactions of the Amererican Geophysical Union, Joint Assemembly, Supplemet Abstract, 88(23), U53A-08McBirney, A.R., 1963. Geology of a part of the Central Guatemalan cordillera. University of California Publications in Geological Sciences, 38, 177-242.

McBirney, A.R., Aoki, K.-I., Bass, M., 1967. Eclogites and jadeite from the Motagua fault zone, Guatemala. American Mineralogist, 52, 908-918.

Nassau, K., Shigley, J.E., 1987. A study of the General Electric synthetic jadeite. Gems & Gemology, 23(1), 27-35.

Nyunt, T.T., Theye, T., Massonne, H.-J., 2009. Na-rich vesuvianite in jadeitite of the Tawmaw jade district, northern Myanmar. Periodico di Mineralogia, 78(3), 5-18.

Oberhänsli, R., Bousquet, R., Moinzadeh, H., Moazzen M., Arvin, M., 2007. The field of stability of blue jadeite: A new occurrence of jadeitite from Sorkhan, Iran, as a case study. The Canadian Mineralogist, 45, 1705-1713.

Oh, C.W., Liou, J.G., 1998. A petrogenetic grid for eclogite and related facies under high-pressure metamorphism. Island Arc, 7, 36-51.

Ortega-Gutiérrez, F., Solari, L.A., Solé, J., Martens, U., Gómez-Tuena, A., Morán-Ical, S., Reyes-Salas, M., Ortega-Obregón, C., 2004. Polyphase, high-temperature eclogite-facies metamorphism in the Chaucús complex, central Guatemala: Petrology geochronology and tectonic implications. International Geology Review, 46(5), 445-470.

Ouyang, Q., 2001. Characteristics of violet jadeite jade and its coloration mechanism. Baoshi He Baoshixue Zazhi, 3(1), 1-6.

Peacock, S.M., 1993. The importance of blueschist → eclogite dehydration reactions in subducting oceanic crust. Geological Society of America Bulletin, 105, 684-694.

Pouchou, J.L., Pichoir, F., 1991. Quantitative Analysis of Homogenous or Stratified Microvolumes Applying the Model "PAP". In: Heinrich, K.F.K., Newbury, D.E. (eds.). Electron Probe Quantitation. New York, Plenum Press, 31-75.

Schiffman, P., Liou, L., 1980. Synthesis and Stability Relations of Mg-Al Pumpellyite, $Ca_4Al_5MgSi_6O_{21}(OH)_7$. Journal of Petrology, 21, 441-474.

Seitz, R., Harlow, G.E., Sisson, V.B., Taube, K.E., 2001. "Olmec Blue" and Formative jade sources: new discoveries in Guatemala. Antiquity, 87, 687-688.

Silva, Z.C.G. da, 1967. Studies on jadeites and albitites from Guatemala. Master of Arts Thesis. Houston, Rice University, 21pp.

Silva, Z.C.G. da, 1970. Origin of albitites from eastern Guatemala. Boletim dos Serviços de Geologia e Minas (Brazil), 22, 23-32.

Sorensen, S., Harlow, G.E., Rumble, D., 2006. The origin of jadeitite-forming subduction zone fluids: CL-guided SIMS oxygen isotope and trace element evidence. American Mineralogist. 91, 979-996.

Sorensen, S.S., Sisson, V.B., Harlow, G.E., Avé Lallemant, H.G., 2005. Geochemistry of a jadeitite-serpentinite contact, Guatemala. Salt Lake City (Utah), Geological Society of America Annual Meeting, Abstracts with Program, 37(5), 125.

Sorensen, S.S., Sisson, V.B., Harlow, G.E., Avé Lallemant, H.G., 2010. Element transport and residence sites during subduction zone metasomatism: Evidence from a jadeitite-serpentinite contact, Guatemala. International Geology Review.

Taube, K.A., Sisson, V.B., Seitz, R., Harlow, G.E., 2004. The sourcing of Mesoamerican jade: Expanded geological reconnaissance in the Motagua Region, Guatemala. In: Taube, K.A. (ed.). Olmec Art and Dumbarton Oaks. Pre-Columbian Art at Dumbarton Oaks, Dumbarton Oaks, 2, Washington, 203-228.

Tsujimori, T., Liou, J.G., Coleman, R.G., 2004a. Comparison of two contrasting eclogites from the Motagua fault zone, Guatemala: Southern lawsonite eclogite versus northern zoisite eclogite. Denver (Colorado), Geological Society of America Annual Meeting Abstracts and Program, 36(5), 1-36.

Tsujimori, T., Liou, J.G., Coleman, R.G., 2004b. A pictorial introduction to coarse-grained symplectites in low-temperature jadeitite from Guatemala. Journal of Geological Society of Japan, 110, XVII-XVIII.

Tsujimori, T., Liou, J.G., Coleman, R.G., 2005. Coexisting retrograde jadeite and omphacite in a jadeite-bearing lawsonite eclogite from the Motagua Fault Zone, Guatemala. American Mineralogist, 90, 836-842.

Tsujimori, T., Sisson, V.B., Liou, J.G., Harlow, G.E., Sorensen, S.S., 2006a. Petrologic characterization of Guatemala lawsonite eclogite: Eclogitization of subducted oceanic crust in a cold subduction zone, In: Hacker, B.R., McClelland, W.C., Liou, J.G. (eds.). Ultrahigh pressure metamorphism: Deep continental subduction. Geological Society of America, 403 (Special Publications), 147-168.

Tsujimori, T., Sisson, V.B., Liou, J.G., Harlow, G.E., Sorensen, S.S, 2006b. Very-low-temperature record of the subduction process: A review of worldwide lawsonite eclogites. Lithos, 92(3-4), 609-624.

van den Boom, G., 1972. Petrofazielle Gliedrung des metamorphen Grudgebirges in der Sierra de Chuacús, Guatemala. Beihefte Geologisches Jahrbuch, 122, 5-49.

Yui, T-F., Maki, K., Usuki, T., Lan, C-Y., Martens, U., Wu, C-M., Wu, T-W., Liou, J.G., 2010. Genesis of Guatemala jadeitite and related fluid characteristics: Insight from zircon. Chemical Geology, 270, 45-55.

Manuscript received January 2011;
revision accepted May 2011;
published Online June 2011.

TABLE I | **Rocks studied and abbreviations for mineral names**

	Locality Name	N.Lat.	W.Long.	Description	Jd	Omp	Ab	Anl	Wm	Amp	Grt	Pmp	Zo	Lws	Apt	Rt	Ttn	Zrn	Qtz	Chl	Other
NORTH of Motagua fault. Western Region																					
MVE07B-19-1	Q nr. Saltán	14.884º	90.595º	Lavender jadeitite	x		x		Ms		Grs	x	Sr-Zo				x	x			Kfs
MVE07B-19-4	Q nr. Saltán	14.884º	90.595º	Lavender jadeitite	x		x		Ms, Ph		Grs	x	Sr-Zo				x				Ves, Kfs?
MVE07B-19-6	Q nr. Saltán	14.884º	90.595º	Jadeite metabasite?	x	x	x		Ba-Ph				Czo			?	x			x	
MVE07B-X-2	nr. Saltán	14.884º ?	90.595º ?	Pale-green jadeitite	x	x	x	x													
MVE06-X-1	Pachalum	14.884º ?	90.595º ?	White jadeitite	x	x	x		Prs	Mtar							x	x			Ne, Gph
MVE07-1	El Chol?	14.892º ?	90.549º ?	White jadeitite	x	x	x										x	x			
MVE07-5	El Chol?	14.892º ?	90.549º ?	Yellowish-green jadeitite	x	x	x		Prs				Al				x				
MVE06-4-3	Granados	14.892º	90.549º	White albitized jadeitite		?	x	?	x	Tr							x				
MVE04-44-1	Q. Los Pescaditos	14.852º	90.444º	White jadeitite w/ emerald green zones	x	x	x	x	Pg, Ph, Prs				Czo								Bnl, Ne
MVE04-44-2	Q. Los Pescaditos	14.852º	90.444º	White jadeitite	x	x	x	x	Pg				Czo				x				Ne
MVE04-44-4	Q. Los Pescaditos	14.852º	90.444º	White jadeitite	x	x	x	x	Pg,Prs				Czo				x				Bnl, Ne
NORTH of Motagua fault. Central Region																					
MVE04-30-1	CA 7, Morazán	14.904º	90.169º	White albitized jadeitite	x	x	x	?	Ba-Ph								x			x	Kfs, Cln?
MVE06-13-4	Río Comaja	14.944º	90.056º	Grayish jadeitite	x	x	x	x													
R-18	Río Comaja	14.944º	90.056º	Dark blue-green omphacitite	x	x	x		Ph	?	Sps-Grs-Alm		Al				x			x	Py, Cpy
MVE02-39-5	Pica pica	14.931º	89.961º	Greenish white jadeitite	x	x	x	x	Pg				x			x	x	x			
MVE02-39-6	Pica pica	14.931º	89.961º	Greenish white jadeitite	x	x	x	x	Phl, Ph				Czo								Ne?
MVE07-2	Pica pica	14.931º	89.961º	White jadeitite	x		x	x	Ms, Ph				Zo, Czo				x				Kfs
MVE03-81-3	El Mapache	15.008º	89.863º	Med. green jadeitite	x	x	x	x	Prs	Mtar			x				x				Unk
MVE03-82-3	El Mapache	15.007º	89.864º	Med. green jadeitite w/ veins	x	x	x	x	Pg	Mtar											
MVE04-24-4	Above Dos Rios	15.020º	89.802º	White jadeitite w/veins	x	x	x	x	Pg	Mtar			Zo								
MVE04-25-6	Piedra Parada	15.012º	89.811º	Green omphacitite		x	x		Phl								x				

DOI: 10.1344/105.000001694

TABLE I | **Continued**

	Locality Name	N.Lat.	W.Long.	Description	Jd	Omp	Ab	Anl	Wm	Amp	Grt	Pmp	Zo	Lws	Apt	Rt	Ttn	Zrn	Qtz	Chl	Other
MVE07-4	Los Vados, El Jute	14.977°	83.835°	Dark green omphacitite	x	x	x								x						
MVE07-7	Estancia de La Virgen	14.941°	89.885°	Omp-Jadeitite	x	x	x	x		Mtar							x	x			
ZC20	NW Manzanal	14.939°	89.871°	Med. green jadeitite	x	x				Ftar	Alm		Czo, Al				x				
MVJ84-3-4	Manzanal	14.942°	89.852°	White jadeitite	x		x	x													
MVE04-26-2	W Río Uyus	14.941°	89.836°	White-green jadeitite	x	x	x	x	Pg				x				x				
NHMLAC 20368	Guat. I	15°	89.8°	Green omphacitite	x	x	x		Pg, Phl								x	x		x	K-Bafs
MVJ87-8-1	Guat. I	15°	89.8°	Green Omphacitite	x	x	x	x	Ph, Pg, Phl				x		x	x	x				Kfs
MVJ87-8-2	Guat. I	15°	89.8°	Light blue-green jadeitite	x																
R-11	Guat. I	15°	89.8°	"Olmec Blue" jadeitite	x		x	x	Pg, Prs				x		x		x				
RSJ00-2	El Ciprés	15.073°	89.796°	Light green jadeitite	x	x	x		Prs?								x				
RSJ00-3	El Ciprés	15.073°	89.796°	Med. Blue-green jadeitite	x	x	x		Pg		Grs						x	x			
RSJ00-6	El Ciprés	15.073°	89.796°	Med. green jadeitite	x	x			Phl, Pg, Prs	Mtar			Czo				x				
RSJ00-7	El Ciprés	15.073°	89.796°	Med. green jadeitite	x	x	x										x	x			
RSJ01-1	El Ciprés	15.073°	89.796°	Pale green jadeitite																	
MVJ84-51-3	N. of Q. Escorpión	14.99°	89.787°	White-green jadeitite vein	x	x	x		Pg	Mtar			x				x				
RSJ01-8	nr Río La Palmilla	14.99°	89.787°	Pale green jadeitite w/ emerald green zones																	
MVJ84-9C-2	Río La Palmilla	14.99°	89.787°	Greenish white jadeitite	x	x	x	x	Pg, Prs	Mtar			Zo				x				
MVJ84-12-2	Río La Palmilla	14.99°	89.787°		x	x	x										x				
MVJ84-44-2	Río La Palmilla	14.99°	89.787°	Green omphacitite		x	x			Ftar					x		x				Cpy
MVE07-10	Río La Palmilla	14.99°	89.787°	Greenish white jadeitite	x	x	x	x													
MVJ84-29-2	Usumatlán	14.962°	89.762°	Bluish gray jadeitite	x	x	x		Pg, Phl	Mtar							x	x			Gph
MVE07B-3-1	Cerro Colorado	14.965°	89.759°	Green micaceous jadeitite	x	x	x		Phl, Ph, Pg				Czo					x			Hm, Br

TABLE I | **Continued**

	Locality Name	N.Lat.	W.Long.	Description	Jd	Omp	Ab	Anl	Wm	Amp	Grt	Pmp	Zo	Lws	Apt	Rt	Ttn	Zrn	Qtz	Chl	Other
MVE07B-3-2	Cerro Colorado	14.965º	89.759º	Light green jadeitite w/ red spots	x	x	x	x	Ph				Czo					x			Hm, Br
MVE07-8	Río Teculután	15.044º	89.748º	Dark green omphacitite	x	x	x			Ftar							x				
MVE02-2-5	Panaluya-Río Hondo	15.052º	89.59º	Green white jadeitite	x	x	x	x	Pg	Mtar					x		x	x			Bnl
MVE02-4-3	Panaluya-Río Hondo	15.032º	89.621º	Greenish white jadeitite	x	x	x	x	Pg, Bio				x								
MVE07-3	Río Hondo	15.052º	89.59º	Light green jadeitite	x	x							Czo				?	x			Bnl
NORTH of Motagua fault. Eastern Region																					
MVR07-25C	Rosario	16.182º	88.861º	Jadeitite-omphacitite	x	x	x	x	Ph, Pg								x	x	?		Gdf
MVR07-23C	Aldea Las Cruces	15.532º	88.829º	Med. green jadeitite	x	x	x	x	Pg, Ms, Phl				Czo-Zo				x				
MVR07-23D	Aldea Las Cruces	15.532º	88.829º	Med. green jadeitite	x	x	x	x	Ph, Pg								x	x			
MVR07-24C	Rosario	15.541º	88.829º	Light green jadeitite	x	x	x	x	Pg, Ph, Phl												
SOUTH of Motagua fault. Carrizal Grande																					
JJE01-3-1	S. Q. El Silencio	14.778º	89.893º	Dark-green Lws-jadeitite	x	x	x	x	Ph, Bio					x		x	x	x	x		
JJE01-3-2	S. Q. El Silencio	14.778º	89.893º	Med. green jadeitite	x	x	x	x	Ph, Bio								x	x	x	x	
JJE01-3-4	S. Q. El Silencio	14.778º	89.893º	Med. green jadeitite	x	x			Ph	Gln						x	x	x	?		
MVE02-8-5	Q. El Silencio	14.779º	89.888º	Light green Ph-jadeitite	x	x			Ph							x	x	x	x		
MVE02-8-6	Q. El Silencio	14.779º	89.888º	Light green Ph-jadeitite	x	x	x		Ph				Al			x	x	x	x		Mon
MVE07-9	Carrizal Grande	14.771º	89.886º	Light green jadeitite	x	x			Ph				x					x	x		
RSJ00-4	Q. del Mico	14.770º	89.882º	"Olmec-Blue" jadeitite	x	x	x		Ph				Czo, Al			x	x	x			Mon
MVE06-17-2	Q. del Mico	14.770º	89.882º	Grt jadeitite	x	x			Ph	Gln?	Alm		Czo	x		x	x	x	x		Gph
MVE03-80-1	Q. del Mico	14.772º	89.878º	Drk-green omphacitite		x, Di	x		Ph						x	x	x	x	?	x	Sr-Cc
MVE04-14-6	Q. Seca	14.768º	89.874º	Med. green jadeitite	x	x	x	x	Ph								x	x	x		Cym,
KT02-3b	Q. Seca	14.77º	89.873º	Blue to blue-green jadeitite	x	x							Al				x	x			Mon

TABLE I | **Continued**

	Locality Name	N.Lat.	W.Long.	Description	Jd	Omp	Ab	Anl	Wm	Amp	Grt	Pmp	Zo	Lws	Apt	Rt	Ttn	Zrn	Qtz	Chl	Other
RSJ01-X-1	Q. Seca	14.77º	89.873º	Green & blue-green omphacitite		x											x				
VM02-1	Q. Seca	14.77º	89.873º	Blue-green jadeititew/ blue vein	x	x											x				
MVE02-15-5	Q. Seca	14.77º	89.873º	Lws-omphacitite		x							x	x		x	x	x		x	Ba-Kfs
MVE02-15-6	Q. Seca	14.77º	89.873º	Dark green omphacitite	x	x	x		Ph								x	x	x		Kfs
MVE02-15-10	Q. Seca	14.77º	89.873º	Dark gray jadeitite	x	x, Di	x		Ph	Act			?		x		x	x	x		
MVE02-14-5	Q. del Mico	14.776º	89.868º	Chromian omphacite-glaucophane rock		x	x			Gln, Act											
JJE01-6-1	Río La Puerta	14.777º	89.863º	Dark-green Ph-Lws-jadeitite-omphacitite	x	x			Ph				?	x		x	x	x			
JJE01-6-2	Río La Puerta	14.777º	89.863º	Pheng-Omphacitite		x			Ph				x,al		x	x	x		x	x	Cc?
RSJ00-1	Río Jalapa	14.844	89.821	Speckled Olmec-blue	x	x	x		Ph								x				
JJE01-7-5	Río El Tambor	14.85º	89.815º	Nephrite / Diopsidite		Di				Tr	Grs		Al?								Cm, clay
JJE01-X-3	Río El Tambor	14.85º	89.815º	Med green Lws-jadeitite	x	x	x	x	Ba-Ph	Gln				x	x	x	x	x	x		
SOUTH of Motagua fault. La Ceiba																					
MVE03-77-1	La Ceiba	14.772º	89.828º	Dark green jadeite omphacitite	x	x	x		Ph				Al				x		x	x	
MVE03-77-3	La Ceiba	14.772º	89.828º	Dark green jadeite-omphacitite	x	x	x		Ph								x	x		x	Cln, Kfs
MVE03-77-4	La Ceiba	14.772º	89.828º	Dark green jadeite-omphacitite	x	x		x	Bio				Al		x				x		Cym, Hyl, Pect
MVE03-77-5-1	La Ceiba	14.772º	89.828º	Qtz jadeitite	x	x	x		Ph	Act							x		x		
MVE04-15-3	La Ceiba	14.771º	89.826º	Grn-Mauve jadeitite	x	x	x						REE-Czo		x		x	x	x		Cym, Uran
MVE02-17-5	La Ceiba	14.771º	89.826º	Med. Green jadeitite	x	x		x									x	x	x		Cym, Ves
SOUTH of Motagua fault. La Ensenada																					
MVE03-76-3a	Q. La Peña	14.822º	89.815º	brown prt/"Lila" jadeitite		x	x					x					x	x		x	
MVE03-76-3b	Q. La Peña	14.822º	89.815º	Lavender prt/"Lila" jadeitite	x	x	x		Ba-Ms		Grs	x	Zo?				x	x		x	Cln
MVE03-76-5	Q. La Peña	14.822º	89.815º	"Lila" jadeitite	x	x	x				Grs	x			x		x				
108353a	Q. La Peña	14.822º	89.815º	"Rainbow" jadeitite	x	x	x					x			x	x	x	x		x	

DOI: 10.1344/105.000001694

TABLE I | **Continued**

	Locality Name	N.Lat.	W.Long.	Description	Jd	Omp	Ab	Anl	Wm	Amp	Grt	Pmp	Zo	Lws	Apt	Rt	Ttn	Zrn	Qtz	Chl	Other
108353b	Q. La Peña	14.822º	89.815º	"Rainbow" jadeitite	x	x	x					x				x	x				
108354	Q. La Peña	14.822º	89.815º	"Rainbow" jadeitite	x	x						x					x				
108355	Q. La Peña	14.822º	89.815º	Pale green jadeitite	x		x		Ba-Ph			x					x				
MVE04-20-1	Q. La Peña	14.824º	89.814º	Mauve/orange jadeitite	x	x	x		Phl		Grs	x			x		x				
MVE04-20-3	Q. La Peña	14.824º	89.814º	White-Blue jadeitite	x		x		Ph		Grs	x	?			x	x	x			
MVE04-21-7	E of San Diego Rd	14.837º	89.79º	Wh-Or-Grn "Rainbow" jadeitite	x	x,Di	x				Grs						x		x		

JJE: Jalapa (southern) samples, MVJ: (northern) Motagua samples, RSJ: Russell Seitz jadeitite sample, R: Ridinger, Jade S.A.; Locality Guat 1 represents samples acquired from jade companies without specific location other than the central area north of the Motagua fault.

* The nomenclature of amphiboles is in transition, so we have chosen to explicitly distinguish ferro-taramite (new) from magnesiotaramite (old; actually alumino-magnesiotaramite to become taramite).

Ab: Albite, Act: Actinolite, Al: Allanite, Alm: Almandine, Amp: Amphibole, Anl: Analcime, Apt: Apatite, Bio: Biotite, Bnl: Banalsite, Cc: Chalcosite: Chl: Chlorite, Cln: Celsian, Cm: Corumdum, Cpy: Calcopyrite, Cym: Cymrite, Czo: Clinozoisite, Di: Diopside, Gln: Glaucophane, Gph: Graphite, Grt: Garnet, Grs: Grossular, Hm: Hematite, Hyl: Hyalophane, Jd: Jadeite, K-Bafs: K-Ba felspar, Kfs: K-felspar, Lws: Lawsonite, Mon: Monazite, Ms: Muscovite, Mtar: Magnesiotaramite, Ne: Nepheline, Omp: Omphacite, Pg: Paragonite, Ph: Phengite, Phl: Phlogopite, Pmp: Pumpellyite, Prs: Preiswerkite, Py: Pyrite, Qtz: Quartz, Rt: Rutile, Sps: Spessartine, Tr: Tremolite, Ttn: Titanite, Unk: Unknown, Uran: Uraninite, Ver: Vermiculite, Ves: Vesuvianite, W: H_2O, Wm: white mica, Zeo: Zeolite, Zo: Zoisite, Zrn: Zircon. –Suspected but unsubstantiated mineral due to inadequate data.

Geologica Acta, 9(3-4), 363-387 (2011)
DOI: 10.1344/105.000001694

Geologica Acta, Vol.9, Nos 3-4, September-December 2011, 389-405
DOI: 10.1344/105.000001662
Available online at www.geologica-acta.com

geologica acta

Serpentinites and serpentinites within a fossil subduction channel: La Corea mélange, eastern Cuba

I.F. BLANCO-QUINTERO [1] [*] **J.A. PROENZA** [2] **A. GARCÍA-CASCO** [1] [3] **E. TAULER** [2] **S. GALÍ** [2]

[1] **Departamento de Mineralogía y Petrología, Universidad de Granada**
Fuentenueva s/n, 18002-Granada, Spain

[2] **Departament de Cristal·lografia, Mineralogia i Dipòsits Minerals, Facultat de Geologia, Universitat de Barcelona (UB)**
Martí i Franquès s/n, 08028-Barcelona, Spain

[3] **Instituto Andaluz de Ciencias de la Tierra (CSIC-UGR)**
Fuentenueva s/n, 18002-Granada, Spain

*Corresponding author. E-mail: blanco@ugr.es. Tel.: +34 958 246 613; Fax: +34 958 243 368

ABSTRACT

A variety of metaultramafic (serpentinite) rocks in La Corea mélange, Sierra de Cristal, eastern Cuba, show differences in chemical, textural and mineralogical characteristics demonstrating a variety of protoliths. The mélange originated during the Cretaceous as part of the subduction channel associated with the Caribbean island arc. This mélange contains high pressure blocks in a serpentinite matrix and occurs at the base of the large tabular Mayarí-Cristal ophiolite. Two principal groups of serpentinites have been identified in the mélange: a) antigorite serpentinite, mainly composed of antigorite and b) antigorite-lizardite serpentinite, composed of mixtures of antigorite and lizardite and bearing distinctive porphyroblasts of diopsidic clinopyroxene. Antigorite serpentinites are closely related to tectonic blocks of amphibolite (representing subducted MORB) and constitute deep fragments of the serpentinitic subduction channel formed during hydration of the mantle wedge. The composition of the antigorite-lizardite serpentinites and the presence of clinopyroxene porphyroblasts in this type of rock suggest that abyssal lherzolite protoliths transformed into serpentinite before and during incorporation (as tectonic blocks) in the shallow part of the subduction channel. Although the studied rocks have different origin, mineralogical compositions and textures, they display similar PGE compositions, suggesting that these elements experienced no significant redistribution during metamorphism. Both types of serpentinites were exposed together in the La Corea mélange during the Late Cretaceous, during obduction of the overriding Mayarí-Baracoa ophiolitic belt that led to exhumation of the subduction channel (mélange).

KEYWORDS | **Serpentinite. Subduction Channel. La Corea Mélange. Cuba. Caribbean.**

INTRODUCTION

Ophiolite-related ultramafic rocks, commonly strongly serpentinized, appear along the margins of Caribbean Plate, being most abundant in the northern edge, principally in Cuba (Lewis et al., 2006a and references therein). These ultramafic rocks represent fragments of oceanic and sub-arc lithospheric mantle that were altered, completely or partly, to serpentinites by fluids during their evolution and accretion to the Caribbean orogenic belt. In Cuba, these ophiolitic bodies are related to serpentinite-matrix mélanges containing high-pressure (HP) blocks of different origin and composition (e.g. García-Casco et al., 2006, and references therein). These mélanges can be interpreted as the exhumed subduction channel of the Caribbean subduction zone (e.g. Gerya et al., 2002).

Two serpentinite-matrix mélanges have been documented in eastern Cuba, 100km apart (Fig. 1): La Corea and Sierra del Convento mélanges (Somin and Millán, 1981; García-Casco et al., 2006). The origin and evolution of the HP (garnet-epidote amphibolite and blueschists) blocks from both mélanges has been studied by García-Casco et al. (2006, 2008a), Lázaro and García-Casco (2008), Lázaro et al. (2009) and Blanco-Quintero et al. (2010). However, no detailed petrological and geochemical studies have been performed to characterize mélange serpentinites.

The serpentinitic rocks present in La Corea mélange have mineralogical and geochemical characteristics that indicate varied P-T conditions of formation and variable protoliths. The mélange formed during Cretaceous times in response to SW-dipping subduction beneath the northern Caribbean plate. In this paper we provide new petrological and geochemical data of representative serpentinite samples from the La Corea mélange in order to evaluate its nature, the environments of formation of serpentinites, and the implications for tectonic interactions between the Caribbean and North American plates.

GEOLOGICAL SETTING

The Cuban fold and thrust belt formed during Mesozoic to middle Eocene times in the active Caribbean-North American plate margin. It is now accreted to the southern margin of the North American plate (Fig. 1A). The Cuban orogenic belt includes several imbricated geologic complexes, including fragments of the Caribean terrane (Cangre, Pinos, Escambray and Asunción metamorphic complexes), the Bahamas platform (Cayo Coco, Remedios, Camajuaní belts), the margin of the Maya block (the Guaniguanico terrane), two different volcanic arc complexes of Cretaceous and Paleogene ages respectively, ophiolite bodies forming the northern and eastern ophiolite belts, and syn- and post-orogenic sedimentary basins (Iturralde-Vinent, 1998; Iturralde-Vinent et al., 2006, 2008; García-Casco et al., 2008b).

The most important tectonic units in northeastern Cuba are the ophiolites and the Cretaceous volcanic arc (Fig. 1B). Systematically the Cretaceous volcanic arc appears tectonically below the ophiolites. The Cretaceous volcanic arc units contain a number of basic to acid volcanic units having distinct island arc tholeiitic, boninitic and calc-alkaline signatures (Iturralde-Vinent et al., 2006; Proenza et al., 2006; Marchesi et al., 2007). The age of these formations has been paleontologically estimated to range from early Cretaceous (Aptian-Albian) to late Cretaceous (Campanian) times (Iturralde-Vinent, et al., 2006). The Purial volcanic complex, located in the southern part of the region, is metamorphosed to the greenschist and blueschist facies (Boiteau et al., 1972; Cobiella et al., 1977; Somin and Millán, 1981; Millán et al., 1985).

The ophiolite complex is represented by the Mayarí-Baracoa Ophiolitic Belt. This belt is constituted strongly deformed and faulted mafic-ultramafic thrust sheets and by the overriding Cretaceous volcanic arc and Maastrichtian-Danian olistostromic formations related to obduction (Iturralde-Vinent et al., 2006). The direction of tectonic transport is NNE (Nuñez-Cambra et al., 2004), as expected for a SW-dipping subduction zone. The Mayarí-Baracoa Ophiolitic Belt shows supra-subduction geochemical signatures (Proenza et al., 1999, 2006; Gervilla et al., 2005; Marchesi et al., 2006, 2007), and include the Mayarí-Cristal massif to the west and the Moa-Baracoa massif to the east (Fig. 1B). According to Marchesi et al. (2006) Mayarí-Baracoa Ophiolitic Belt is composed of highly depleted peridotites and cumulate gabbroic rocks. Mayarí-Baracoa Ophiolitic Belt Peridotites were highly altered (serpentinized) by seawater during the oceanic stage (Proenza et al. 2003). The Moa-Baracoa massif represents MORB-like back-arc lithosphere while Mayarí-Cristal is transitional (MORB to IAT) mantle located closer to the paleo-volcanic arc (Marchesi et al., 2006).

The Mayarí-Cristal massif is > 5km thick and is made up of harzburgite tectonite hosting minor subconcordant dunite layers and subordinate discordant microgabbro-diabase dykes. Some authors have described a sheeted-dyke complex in the northwestern part of the massif (e.g., Fonseca et al., 1985), but Marchesi et al. (2006) argue that this is a subvolcanic complex made up of massive microgabbros in tectonic contact with harzburgite tectonites. The Mayarí-Cristal harzburgites display porphyroclastic texture. They are clinopiroxene and generally have higher orthopiroxene/olivine ratios than the Moa-Baracoa harzburgites (Marchesi et al., 2006). The harzburgite tectonites show a NE–SW oriented foliation dipping NW (Marchesi et al., 2006), and the contact with the dunites is sharp.

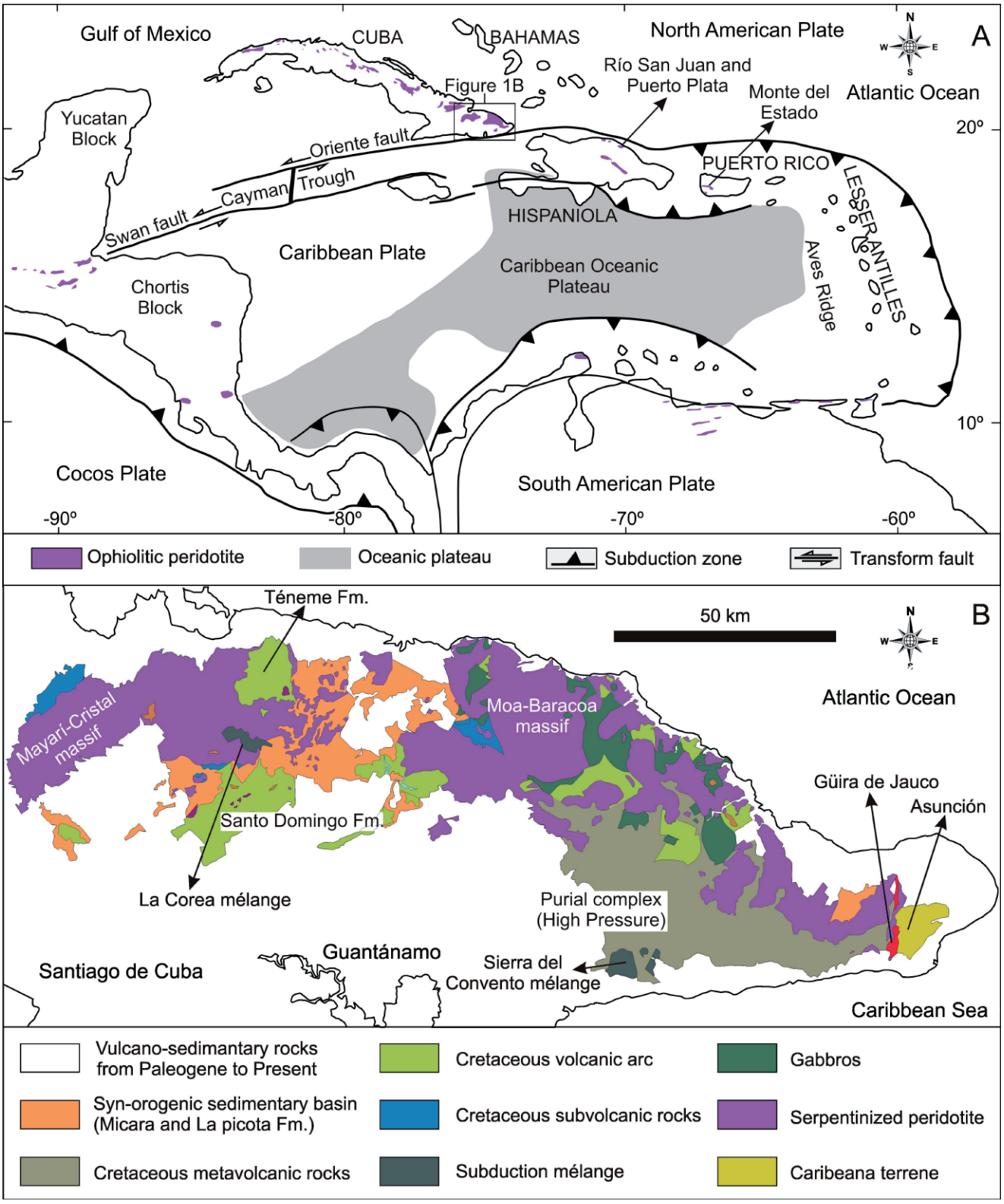

FIGURE 1 | **A) Plate tectonic configuration of the Caribbean region, including ophiolitic bodies. B) General geologic map of eastern Cuba showing the main geological units.**

The La Corea mélange, containing high pressure exotic blocks, is located in tectonic contact with ultramafic rocks of the Mayarí-Cristal massif (Fig. 1B). The tectonic position of La Corea mélange suggests that this metamorphic complex is overridden by the ophiolites, and that both override the Cretaceous volcanic arc units and the Maastrichtian-Danian olistostromic synorogenic rocks of Micara and La Picota formations. The mélange is made up of exotic blocks of diverse origin and composition (garnet-amphibolite, blueschist and greenschist are dominant) within a serpentinite matrix. Metamorphism of the amphibolites evolved under high- to medium-pressure (ca. 700ºC, 15kbar) related to a hot subduction environment from high- to low-temperature following counterclockwise P-T paths related to exhumation in the subduction channel (Blanco-Quintero et al., 2010).

The most abundant rock type is a MORB-derived epidote ± garnet amphibolite that contains a peak metamorphic assemblage made of pargasite, epidote, titanite, rutile ± quartz ± garnet ± phengite ± plagioclase and accessory apatite (Blanco-Quintero et al., 2010). The amphibolite blocks are massive to banded and of metric-size. Metaleucocratic rocks (tonalites-trondhjemites) occur as veins and blocks intimately associated with the amphibolites. The tonalites-trondhjemites are medium- to coarse-grained, including pegmatitic varieties, and are composed of quartz, albite-oligoclase, epidote, ± calcic amphibole (pargasite-actinolite) ± muscovite-phengite. These rocks formed after partial melting of subducted MORB amphibolites at 700ºC, 15kbar (Blanco-Quintero et al., 2010). Other tectonic blocks within the mélange include schists of variable composition and origin. Ultramafic rocks are mainly massive to foliated antigoritite forming the mélange matrix. Occasionally massive antigoritite blocks are included as boudins in strongly foliated antigorite rocks. In addition, blocks of serpentinite with bastite crystals are surrounded by foliated antigoritite. Masses of tremolite-actinolite rocks (composed of > 95% radial and tabular amphibole) and other metasomatic products of mafic and ultramafic composition are present.

Available isotopic data (Adamovich and Chejovich, 1964; Somin and Millán, 1981) indicates that the subduction channel mélange began to form ca. 110Ma. Final exhumation of the mélange occurred during the initial thrusting of the ophiolitic and volcanic arc units in the Late Campanian-Maastrichtian (Iturralde-Vinent et al., 2006; Lázaro et al., 2009).

In this study we characterize serpentinite rocks from the La Corea mélange, including antigorite serpentinites (5 samples: LC-G-4, LC-M-17, LC-55, LC-56 and LC-58) and antigorite-lizardite serpentinites (3 samples: LC-66, LC-88 and LC-97).

ANALYTICAL TECNIQUES

Powder X-ray diffraction (XRD) data were collected with a Panalytical X'Pert PRO MPD X-ray diffractometer with monochromatized incident Cu Kα1 radiation at 45keV and 40mA, and equipped with a x'Celerator detector of active length of 2.112º at the Serveis Cientificotècnics of the Universitat de Barcelona (Spain). The patterns were obtained by scanning powders from 4°-80° 2θ on samples crushed in an agate mortar to a particle size < 20μm. Quantitative mineral phase analyses of samples were obtained by full profile Rietveld refinement using powder diffraction data. The mineral identification software used was TOPAS V3.0.

Mineral compositions were obtained by electron microprobe using a wavelength dispersive X-ray spectometry (WDS-CAMECA SX 50) at the Serveis Cientificotècnics of the Universitat de Barcelona (Spain). Excitation voltage was 20kV and beam current 15nA. Most elements were measured with a counting time of 10s, except for Ni (30s). The chemical data for serpentine, clinopyroxene, talc and chlorite compositions were normalized to 14, 6, 22 and 28 oxygens respectively, and $Fe_{total} = Fe^{2+}$. Garnet composition was normalized to 8 cations and 12 oxygens, and Fe^{3+} was estimated by stoichiometry. The atomic concentration of elements per formula unit is abbreviated apfu. The Mg number of minerals ($Mg/(Mg+Fe^{2+})$) is expressed as Mg#. Mineral abbreviations are after Kretz (1983).

Major element compositions were determined on glass beads, made of 0.6g of powdered sample diluted in 6g of $Li_2B_4O_7$, by a PHILIPS Magix Pro (PW-2440) X-ray fluorescence (XRF) equipment (University of Granada, Centro de Instrumentación Científica, CIC). Precision was better than ±1.5% for a concentration of ≥10 wt% and ±2% for a concentration <10 wt%. Platinum-group element concentrations were determined by isotopic dilution using Inductively Coupled Plasma-Mass spectometry (ICP-MS) after nickel sulfide fire assay, in the Genalysis Laboratory Services Pty. Ltd. at Maddington (Western Australia) following the method described by Chan and Finch (2001). The detection limits were 1 ppb for Rh, and 2 ppb for Os, Ir, Ru, Pt, Pd.

PETROGRAPHY AND SERPENTINE MINERALS

On the basis of mineral assemblages and textures of metaultramafic rocks, two principal groups of serpentinite have been identified (Figs. 2 and 3): i) antigorite serpentinite and ii) antigorite-lizardite serpentinite.

Antigorite serpentinites (group I) consist mainly of antigorite (up to 94%), with minor talc-magnesite-dolomite (Fig. 2A-D, Fig. 3A). However, some samples (e.g. LC-55)

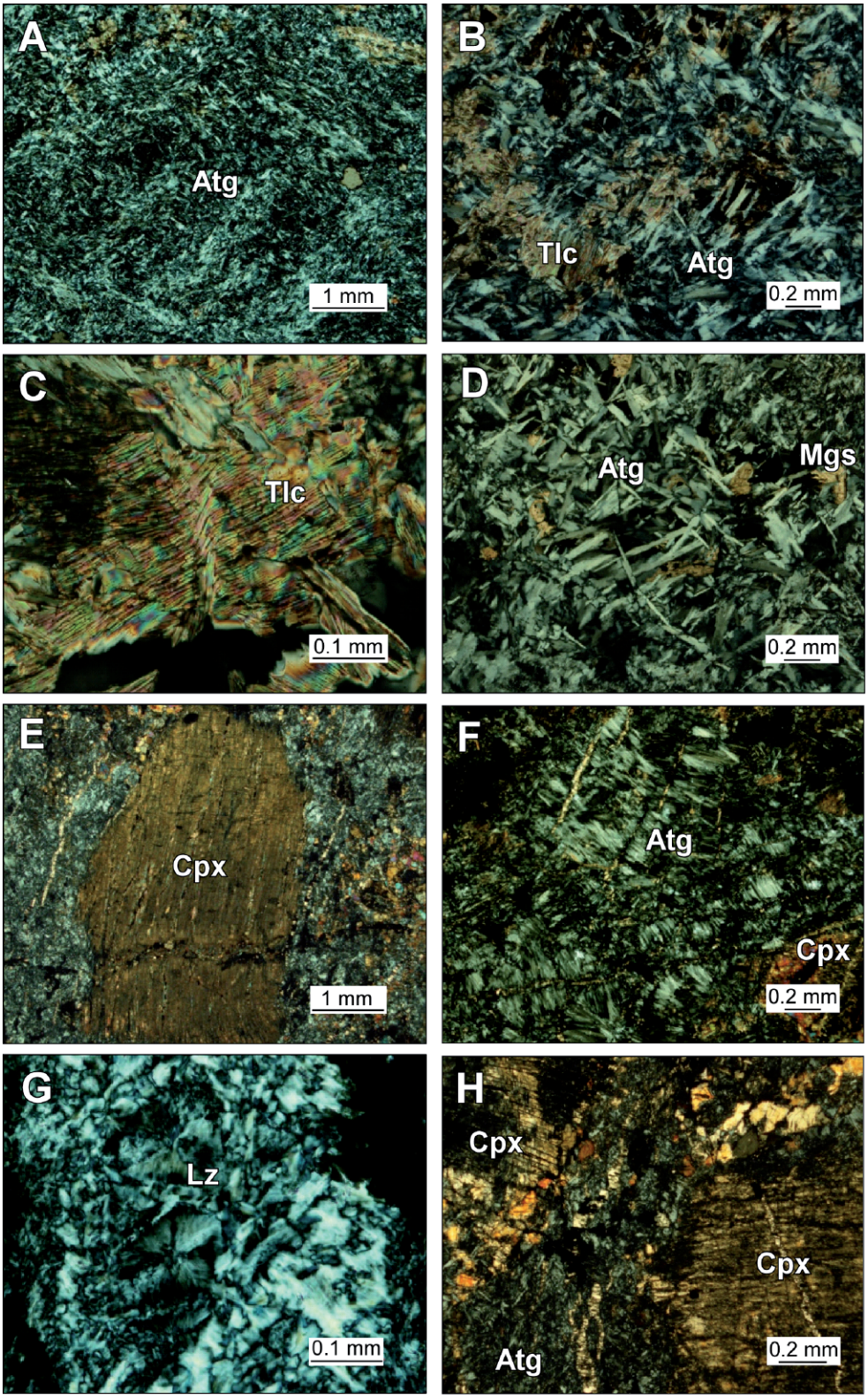

FIGURE 2 | **Cross-polarized light photographs of antigorite serpentinite (A to D) and antigorite-lizardite serpentinite (E to H). A) Nonpseudomorphic interpenetrating texture typical of antigorite. B) Talc-bearing antigorite serpentinite. Antigorite is partially replaced by talc. C) Kinking of talc in talc-bearing antigorite serpentinites. D) Detail of antigorite interpenetrating texture. Antigorite grains are partially replaced by magnesite and minor dolomite. E) Porphyroclastic texture showing clinopyroxene (diopside). F) Clinopyroxene partly replaced by ribbons of antigorite. Antigorite is a product of recrystallization of lizardite; G) Type-1 lizardite hourglass texture, showing the optical uniformity of lizardite across the mesh cell; H) Porphyroblastic and fine grained diopsidic clinopyroxene.**

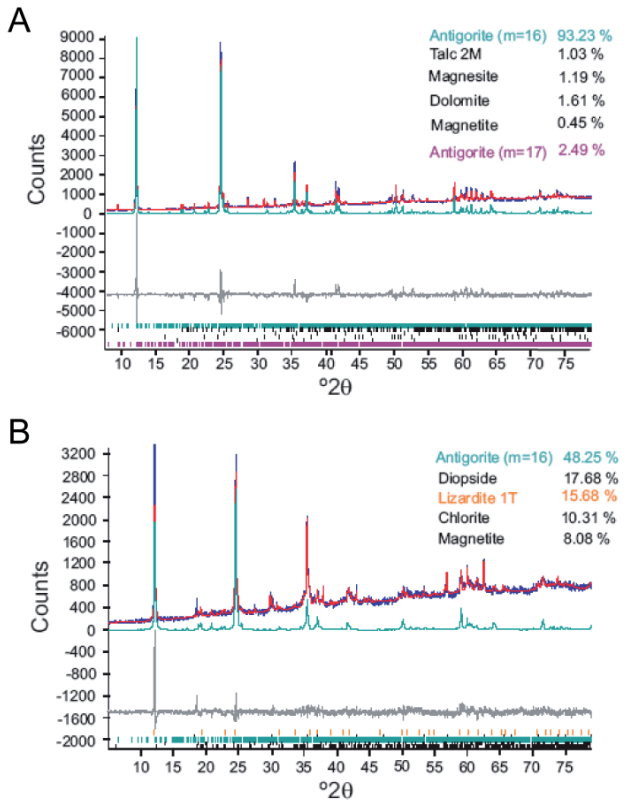

FIGURE 3 | **XRD profile refinements of representative samples of A) antigorite- (LC-58) and B) antigorite-lizardite- (LC-88) serpentinites showing experimental (blue), calculated (red), calculated antigorite (turquoise), and difference (grey) profiles. The Bragg positions for all identified mineral phases are indicated at the base of the diagram.**

contain abundant talc (Fig. 2C). Kinking of talc crystals, typical of plastic deformation (Escartín et al., 2008), is common. Antigorite grains are partially replaced by magnesite and minor dolomite (Fig. 2D). Systematically, the relicts of Cr-spinel grains are altered to ferrian chromite and magnetite, and chlorite appears forming rims around altered spinel.

Serpentinites of group I are characterized by non-pseudomorphic textures, typically showing the characteristic interpenetrating needles of antigorite (Fig. 2A, B, D; O'Hanley, 1996).

The antigorite-lizardite serpentinites (group II) contain the mineral assemblage antigorite - lizardite - diopsidic clinopyroxene - chlorite - magnetite - ferrian chromite ± brucite. They are characterized by porphyroblastic texture, showing relicts of bastitized clinopyroxene porphyroblasts up to 8mm in size (Fig. 2E). The dominant serpentine mineral is antigorite (Fig. 2F), but lizardite has been identified in thin section and by XRD (Figs 2G, 3B). Clinopyroxene porphyroblasts are partly overgrown/replaced by fine-grained clinopyroxene, antigorite, chlorite and magnetite (Fig. 2H). The hedenbergite component of clinopyroxene was oxidized to magnetite, which is mainly associated with serpentine along exfoliation planes and the rims of the grains of clinopyroxene. Primary Cr-spinels were not found; only their alteration products, ferrian chromite and newly formed magnetite, are present. In addition, chlorite forms rims around altered spinel. Andradite garnet is present in veins crosscutting the serpentine matrix. It is colourless and forms granular aggregates.

In general, antigorite-lizardite serpentinites preserve pseudomorphic textures (Wicks and Whittaker, 1977; O'Hanley, 1996): i) bastites after clinopyroxene and ii) hourglass textures (Figure 2G). Theses textures can be interpreted as the result of low grade metamorphism (i.e. ocean floor metamorphism).

Serpentine minerals

In order to identify and quantify the amount of serpentine minerals (chrysotile, lizardite and antigorite) and the lattice parameters of these structures, the observed random X-ray powder diffraction profile was simulated using several structural models of antigorite polymorphs (Rietveld method). Commonly, antigorite in serpentinites forms a polysomatic series of sheet silicates of variable structure and composition (e.g. Mellini et al., 1987). The variation of *a* parameter is expressed in terms of *m*, which is the number of SiO_4 tetrahedra seen in a projection along [010] within a full wavelength of the modulated structure.

The calculated XRD profile of group I serpentinite (sample LC-58) agrees well with two serpentine polymorphs (Fig. 3A), one with antigorite polysome m=16 with 16 tetrahedra spanning a wavelength along the *a* axis as proposed by Capitani and Mellini (2006) and the other with antigorite polysome m=17 (Capitani and Mellini, 2004). The structure with m=16 resembles that of the m=17 polysome. In both, a continuous wavy tetrahedra sheet layer (linked to brucite-like layer) reverses polarity through sixfold and eightfold tetrahedra rings. The even number of tetrahedra in m=16, leads to symmetric half-waves, a periodic *b/2* shift involving the eightfold rings, and the doubling of a parameter. The result is a C monoclinic cell.

The antigorite with polysome m=16 yields the best fit for the most abundant in group I serpentinite (93.2wt%) and the fitted lattice parameters are: a=81.878(5), b=9.264(5), c=7.248(2) Å and β = 91.409(5)°, space group C2/m. The antigorite with m=17 is scarce, 2.5wt%, and the obtained parameters are: a=43.505(6), b=9.251(1), c=7.263(1) Å and β = 91.32(1)°, space group Pm. Other mineral phases present in the sample are: talc (1.0wt%), magnesite (1.2wt%), dolomite (1.6wt%) and magnetite (0.5wt%). Mellini et al. (1987) and Li et al. (2004) suggested that

m=17 is typical for antigorite formed under greenschist-facies conditions.

In group-II serpentinites (sample LC-88) the calculated profile agrees well with the antigorite polysome m=16 and lizardite 1T (Mellini and Viti, 1994) (Fig. 3B). Antigorite is the most abundant serpentine mineral (48.3wt%) with lattice parameters a=81.551(6), b=9.247(10), c=7.266(4) Å and β = 91.00(11)°. Lizardite is also abundant (15.7wt%), with lattice parameters a=5.322(2), c= 7.295 (6) Å and space group P31m. Other phases identified in this sample are: diopside (17.7wt%), clinochlore (10.3wt%), magnetite (8.1wt%) and minor brucite.

In summary, all investigated antigorites of the La Corea mélange presents polysome values with m=16. However, the variability of the refined a parameter in these samples is too low to permit correlation with the metamorphic grade as suggested by Mellini et al. (1987) and Li et al. (2004).

MINERAL CHEMISTRY

Serpentine

Serpentine from antigorite serpentinites have Si ranging 3.94 – 4.04 apfu, Mg = 4.94 – 5.08 apfu, Fe = 0.5 – 0.59 apfu, Cr < 0.05 apfu and Ni < 0.05 apfu (Table 1). In the ternary diagram Mg-Si-Fe (molar proportions, Fig. 4) the analyzed grains of serpentinite confirm with antigorite composition following D'Antonio and Kristensen (2004) classification. The Al contents are relatively high (0.21 – 0.30 apfu). High Al and Cr could produce highest stability in temperature for antigorite (Padrón-Navarta et al., 2010). The Mg # ratios are 0.89 – 0.91.

Serpentine from antigorite-lizardite serpentinites have Si = 3.94 – 4.03 apfu, Fe = 0.19 – 0.26 apfu, Mg = 5.34 – 5.41 apfu, Cr < 0.03 apfu and Ni < 0.03 apfu, showing relative high Al = 0.17 – 0.30 apfu (Table 2). In the ternary diagram Mg-Si-Fe (Fig. 4) most point analyses represent antigorite composition, although some points with less Si content indicate lizardite and/or chrysotile composition (D'Antonio and Kristensen, 2004). The Mg# (0.95 – 0.97) is higher than in the antigorite serpentinites. These higher values do not correlate with bulk rock composition, suggesting distinct P-T conditions of growth.

Clinopyroxene

The porphyroblasts of clinopyroxene present in antigorite-lizardite serpentinites are diopside (≈ En50 Wo49-50 Fs0; Morimoto et al., 1989; Table 3), with Si contents ranging 1.97 – 1.99 apfu, Mg = 0.96 – 1.03 apfu, Ca = 0.95 – 1.01 apfu, and very low Fe contents (< 0.05 apfu).

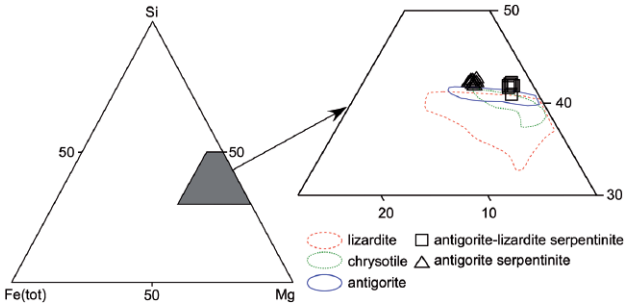

FIGURE 4 | **Ternary atomic Mg-Si-Fe diagram showing the chemical variability of serpentine minerals from La Corea mélange. The fields for lizardite, chrysotile and antigorite were compiled by D'Antonio and Kristensen (2004).**

TABLE 1 | **Representative analyses of serpentine from antigorite serpentinites (normalized to 10 O and 8 OH)**

Sample	LC-58	LC-58	LC-58	LC-58	LC-58	LC-55	LC-55	LC-55	LC-55	LC-55
SiO_2	42.81	43.01	42.46	43.16	42.46	41.84	41.58	42.04	41.54	41.91
TiO_2	0.02	0.04	0.03	0.03	0.03	0.04	0.02	0.03	0.02	0.03
Al_2O_3	1.86	2.31	2.20	2.07	1.88	2.49	2.66	2.47	2.46	2.24
Cr_2O_3	0.26	0.34	0.37	0.17	0.17	0.56	0.58	0.62	0.62	0.53
FeO_{total}	6.39	6.31	6.59	6.78	6.50	7.41	7.08	7.05	7.03	7.05
MnO	0.04	0.03	0.09	0.08	0.04	0.02	0.00	0.05	0.01	0.02
MgO	36.00	35.75	35.64	36.26	36.01	34.86	34.74	35.05	35.54	34.69
NiO	0.15	0.12	0.18	0.15	0.26	0.19	0.25	0.12	0.34	0.13
CaO	0.00	0.01	0.01	0.00	0.00	0.01	0.00	0.01	0.03	0.02
Total	87.53	87.92	87.57	88.70	87.35	87.42	86.91	87.44	87.59	86.62
Si	4.03	4.03	4.01	4.02	4.02	3.98	3.97	3.99	3.94	4.01
Ti	0.00	0.00	0.00	0.00	0.00	0.00	0.00	0.00	0.00	0.00
Al	0.21	0.26	0.24	0.23	0.21	0.28	0.30	0.28	0.27	0.25
Cr	0.02	0.03	0.03	0.01	0.01	0.04	0.04	0.05	0.05	0.04
Fe^{2+}	0.50	0.49	0.52	0.53	0.51	0.59	0.57	0.56	0.56	0.56
Mn	0.00	0.00	0.01	0.01	0.00	0.00	0.00	0.00	0.00	0.00
Mg	5.06	5.00	5.02	5.04	5.08	4.94	4.94	4.96	5.03	4.95
Ni	0.02	0.02	0.03	0.02	0.04	0.03	0.04	0.02	0.05	0.02
Ca	0.00	0.00	0.00	0.00	0.00	0.00	0.00	0.00	0.00	0.00
#Mg	0.91	0.91	0.91	0.91	0.91	0.89	0.90	0.90	0.90	0.90

TABLE 2 | **Representative analyses of serpentine from antigorite-lizardite serpentinites (normalized to 10 O and 8 OH)**

Sample	LC-88	LC-88	LC-88	LC-88	LC-66	LC-66	LC-66	LC-66
SiO_2	42.53	42.52	43.66	42.80	43.49	43.09	43.06	42.21
TiO_2	0.06	0.00	0.02	0.03	0.02	0.00	0.04	0.03
Al_2O_3	2.21	2.42	1.54	2.50	2.48	2.40	2.47	2.76
Cr_2O_3	0.31	0.29	0.18	0.25	0.38	0.45	0.35	0.07
FeO_{total}	2.95	2.75	2.83	3.23	2.80	2.50	2.49	3.34
MnO	0.14	0.07	0.10	0.06	0.09	0.14	0.19	0.07
MgO	38.86	38.47	39.23	38.67	39.10	39.41	38.72	38.43
NiO	0.07	0.12	0.20	0.17	0.16	0.12	0.13	0.00
CaO	0.01	0.33	0.00	0.01	0.00	0.02	0.01	0.29
Total	87.14	86.97	87.76	87.72	88.52	88.13	87.46	87.20
Si	3.97	3.97	4.03	3.97	3.98	3.97	3.99	3.94
Ti	0.00	0.00	0.00	0.00	0.00	0.00	0.00	0.00
Al	0.24	0.27	0.17	0.27	0.27	0.26	0.27	0.30
Cr	0.02	0.02	0.01	0.02	0.03	0.03	0.03	0.01
Fe^{2+}	0.23	0.21	0.22	0.25	0.21	0.19	0.19	0.26
Mn	0.01	0.01	0.01	0.00	0.01	0.01	0.01	0.01
Mg	5.40	5.36	5.40	5.34	5.34	5.41	5.35	5.35
Ni	0.01	0.02	0.03	0.02	0.02	0.02	0.02	0.00
Ca	0.00	0.03	0.00	0.00	0.00	0.00	0.00	0.03
#Mg	0.96	0.96	0.96	0.96	0.96	0.97	0.97	0.95

Correspondingly, Mg# is very high (0.96 – 0.97). Other elements, namely Al and Na, have very low concentration (<0.03 apfu).

Talc

Talc, present in antigorite serpentinite samples, is almost pure (Table 4), with Si = 8.00 – 8.07 apfu and Mg = 5.60 – 5.73, and low Fe = 0.17 – 0.28 apfu and Al < 0.01 apfu contents (Fig. 5). Mg# is, correspondingly, very high (0.95 – 0.97).

Chlorite

Chlorite, present in antigorite-lizardite serpentinites, has high Si (5.99 – 6.85 apfu) and Mg (9.71 – 10.27 apfu) contents, and is poor in Al (2.17 – 3.28 apfu) and Fe (0.52 – 0.87 apfu; Table 5). The contents of Cr (0.15 – 0.30 apfu) are not as high as

TABLE 3 | **Representative analyses of clinopyroxene from antigorite-lizardite serpentinites (normalized to 6 O)**

Sample	LC-97	LC-97	LC-97	LC-97	LC-97	LC-97	LC-97	LC-97	LC-97	LC-97
SiO_2	54.13	54.81	54.18	54.43	53.97	53.93	54.44	53.75	54.25	54.08
TiO_2	0.02	0.05	0.00	0.03	0.07	0.04	0.02	0.13	0.06	0.04
Al_2O_3	0.22	0.42	0.16	0.06	0.25	0.27	0.12	0.43	0.61	0.62
Cr_2O_3	0.12	0.09	0.07	0.10	0.20	0.13	0.19	0.14	0.20	0.27
Fe_2O_{3total}	1.33	1.13	1.49	1.51	1.35	1.51	1.38	1.70	1.30	1.35
MnO	0.07	0.02	0.07	0.06	0.06	0.06	0.05	0.15	0.04	0.09
MgO	18.12	18.61	17.83	17.96	18.26	18.09	18.06	18.40	18.27	18.48
CaO	25.17	24.70	25.10	25.41	24.77	24.71	25.23	24.49	24.38	24.39
Na_2O	0.14	0.28	0.21	0.11	0.20	0.18	0.15	0.18	0.27	0.23
K_2O	0.00	0.03	0.00	0.00	0.01	0.00	0.01	0.01	0.00	0.00
Sum	99.32	100.14	99.11	99.67	99.14	98.92	99.65	99.38	99.38	99.55
Si	1.97	1.98	1.98	1.98	1.97	1.97	1.98	1.96	1.97	1.97
Ti	0.00	0.00	0.00	0.00	0.00	0.00	0.00	0.00	0.00	0.00
Al	0.01	0.02	0.01	0.00	0.01	0.01	0.01	0.02	0.03	0.03
Cr	0.00	0.00	0.00	0.00	0.01	0.00	0.01	0.00	0.01	0.01
Fe^{2+}	0.04	0.03	0.04	0.04	0.04	0.04	0.04	0.05	0.04	0.04
Mn	0.00	0.00	0.00	0.00	0.00	0.00	0.00	0.01	0.00	0.00
Mg	0.99	1.00	0.97	0.97	0.99	0.99	0.98	1.00	0.99	1.00
Ca	0.98	0.96	0.98	0.99	0.97	0.97	0.98	0.96	0.95	0.95
Na	0.01	0.02	0.02	0.01	0.01	0.01	0.01	0.01	0.02	0.02
K	0.00	0.00	0.00	0.00	0.00	0.00	0.00	0.00	0.00	0.00
Sum	4.01	4.01	4.00	4.00	4.01	4.00	4.00	4.01	4.00	4.01
Wo	49.97	48.83	50.30	50.41	49.38	49.54	50.11	48.90	48.96	48.69
En	50.03	51.17	49.70	49.59	50.62	50.46	49.89	51.10	51.05	51.31
Fs	0.00	0.00	0.00	0.00	0.00	0.00	0.00	0.00	0.00	0.00

TABLE 4 | **Representative analyses of talc from antigorite-lizardite serpentinites (normalized to 20 O and 4 OH)**

Sample	LC-58	LC-58	LC-58	LC-58	LC-58	LC-58	LC-55	LC-55	LC-55	LC-55
SiO_2	62.40	62.85	62.55	63.61	62.27	61.44	62.49	62.76	61.46	62.63
TiO_2	0.05	0.04	0.00	0.02	0.02	0.04	0.02	0.05	0.05	0.01
Al_2O_3	0.04	0.02	0.04	0.03	0.00	0.01	0.01	0.04	0.00	0.01
FeO_{total}	2.49	2.34	2.20	2.12	2.10	2.33	1.61	2.41	2.60	2.11
MgO	29.54	29.54	29.70	29.88	29.82	28.63	29.61	29.54	29.38	29.57
Total	94.52	94.79	94.49	95.66	94.21	92.45	93.74	94.80	93.49	94.33
Si	8.03	8.05	8.03	8.06	8.02	8.07	8.06	8.04	8.00	8.05
Ti	0.01	0.00	0.00	0.00	0.00	0.00	0.00	0.00	0.01	0.00
Al	0.01	0.00	0.01	0.00	0.00	0.00	0.00	0.01	0.00	0.00
Fe^{2+}	0.27	0.25	0.24	0.23	0.23	0.26	0.17	0.26	0.28	0.23
Mg	5.66	5.64	5.69	5.64	5.73	5.60	5.70	5.64	5.70	5.73
Mg#	0.95	0.96	0.96	0.96	0.96	0.96	0.97	0.96	0.95	0.96

in other serpentinite bodies were chlorite formed by alteration of spinel (Jan and Windley, 1990; Proenza et al., 2004; Abu El Ela and Farahat, 2009). The high Si contents and Mg# (0.92 – 0.95) classify these chlorites as clinochlore (Bailey, 1980). Nevertheless, Al contents are lower than stoichiometric clinochlore (Fig. 5), probably as a result of intergrowth of serpentinite layers within chlorite (cf. Cressey et al., 2008).

Andradite garnet

Andradite garnet, present in antigorite-lizardite serpentinites, has Si = 2.85 – 2.93 apfu, Ca = 3.04 – 3.09 apfu, and Fe^{3+} = 1.61 – 1.88 apfu, with significant Ti contents (up to 0.32 apfu) and low concentration in Al (< 0.04 apfu), Cr (< 0.04 apfu) and Mg (< 0.06 apfu; Table 6). This type of garnet is deficient in silica as is typical of high Ti-garnets from ultramafic rocks (Müntener and Hermann, 1994 and references therein).

WHOLE ROCK GEOCHEMISTRY

Major element composition

All studied serpentinite samples have large LOI (lost on ignition) values (> 10wt%; Table 7), indicating that they are almost pure serpentinite, only sample LC-55 has higher

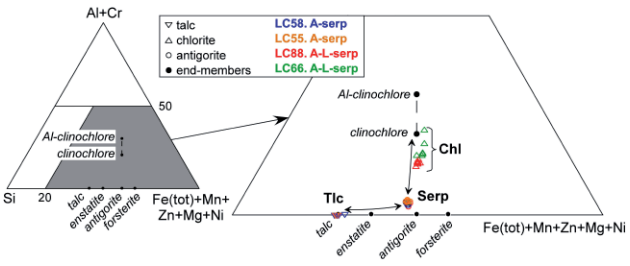

FIGURE 5 | **Atomic Si-(Al+Cr)-(Fe+Mn+Zn+Mg+Ni) diagram showing the composition of chlorite and serpentine from antigorite-lizardite serpentinites (A-L-serp) and serpentine and talc from antigorite serpentinites (A-L-serp). Representative end-members are also projected. Note that chlorites are deficient in Al.**

TABLE 5 | **Representative analyses of chlorite from antigorite-lizardite serpentinites (normalized to 20 O and 16 OH)**

Sample	LC-88	LC-88	LC-88	LC-88	LC-88	LC-88	LC-66	LC-66	LC-66	LC-66
SiO_2	34.30	34.76	34.43	34.79	34.95	36.06	31.29	32.37	32.93	34.32
TiO_2	0.03	0.02	0.01	0.02	0.00	0.00	0.07	0.05	0.01	0.05
Al_2O_3	10.57	10.64	10.95	10.57	10.06	9.67	14.55	12.95	12.36	12.50
Cr_2O_3	0.96	1.01	1.64	1.62	1.61	1.54	1.97	0.96	0.96	1.00
FeO_{total}	3.39	3.23	3.49	3.43	3.30	3.25	5.45	3.54	3.45	3.31
MnO	0.08	0.12	0.02	0.07	0.10	0.08	0.07	0.11	0.06	0.11
MgO	35.60	35.19	35.21	35.06	35.22	35.78	34.04	34.80	34.99	34.58
NiO	0.05	0.14	0.11	0.12	0.14	0.05	0.17	0.23	0.18	0.30
CaO	0.09	0.08	0.08	0.08	0.06	0.05	0.01	0.00	0.04	0.02
Total	85.07	85.19	85.94	85.76	85.44	86.48	87.62	85.01	84.98	86.19
Si	6.64	6.71	6.61	6.69	6.74	6.85	5.99	6.29	6.39	6.54
Ti	0.00	0.00	0.00	0.00	0.00	0.00	0.01	0.01	0.00	0.01
Al	2.41	2.42	2.48	2.39	2.29	2.17	3.28	2.96	2.83	2.81
Cr	0.15	0.15	0.25	0.25	0.25	0.23	0.30	0.15	0.15	0.15
Fe^{2+}	0.55	0.52	0.56	0.55	0.53	0.52	0.87	0.58	0.56	0.53
Mn	0.01	0.02	0.00	0.01	0.02	0.01	0.01	0.02	0.01	0.02
Mg	10.27	10.12	10.07	10.04	10.12	10.14	9.71	10.08	10.12	9.83
Ni	0.01	0.04	0.03	0.03	0.04	0.01	0.05	0.07	0.05	0.09
Ca	0.02	0.02	0.02	0.02	0.01	0.01	0.00	0.00	0.01	0.00
#Mg	0.95	0.95	0.95	0.95	0.95	0.95	0.92	0.95	0.95	0.95

TABLE 6 | **Representative analyses of garnet from antigorite-lizardite serpentinites (normalized to 12 O)**

Sample	LC-66	LC-66	LC-66	LC-66	LC-66	LC-66	LC-66	LC-66	LC-66
SiO_2	33.92	34.25	33.50	33.67	33.80	34.12	33.14	33.70	33.63
TiO_2	3.86	2.79	4.53	4.94	4.09	1.38	4.03	4.63	4.34
Al_2O_3	0.29	0.22	0.30	0.28	0.29	0.44	0.30	0.32	0.26
Cr_2O_3	0.27	0.05	0.08	0.40	0.42	0.54	0.37	0.29	0.34
Fe_2O_{3total}	27.02	27.59	26.17	26.12	26.55	29.21	26.89	25.52	26.36
MnO	0.07	0.04	0.02	0.08	0.13	0.05	0.09	0.06	0.07
MgO	0.33	0.33	0.46	0.41	0.32	0.14	0.36	0.39	0.38
NiO	0.00	0.00	0.00	0.00	0.00	0.00	0.00	0.00	0.17
CaO	33.25	33.27	33.41	33.30	33.45	33.26	33.13	33.77	33.70
Total	99.01	98.54	98.47	99.20	99.05	99.14	98.31	98.68	99.25
Si	2.89	2.93	2.87	2.86	2.88	2.91	2.85	2.87	2.86
Ti	0.25	0.18	0.29	0.32	0.26	0.09	0.26	0.30	0.28
Al	0.03	0.02	0.03	0.03	0.03	0.04	0.03	0.03	0.03
Cr	0.02	0.00	0.01	0.03	0.03	0.04	0.03	0.02	0.02
Fe^{3+}(*)	1.68	1.76	1.65	1.58	1.66	1.88	1.73	1.61	1.68
Fe^{2+}	0.06	0.02	0.03	0.09	0.04	0.00	0.01	0.03	0.00
Mn	0.01	0.00	0.00	0.01	0.01	0.00	0.01	0.00	0.01
Mg	0.04	0.04	0.06	0.05	0.04	0.02	0.05	0.05	0.05
Ni	0.00	0.00	0.00	0.00	0.00	0.00	0.00	0.00	0.01
Ca	3.04	3.05	3.06	3.04	3.05	3.04	3.05	3.09	3.07

(*) Calculated by stoichiometry

LOI content, suggesting alteration. Antigorite serpentinites have MgO = 35.06 – 36.32wt%, SiO_2 = 36.97 – 42.88wt%, FeO = 6.78 – 7.39wt%, Al_2O_3 = 1.49 – 2.51wt% and CaO = 0.73 – 1.93wt%. Antigorite-lizardite serpentinites have MgO = 34.72 - 37.48wt%, SiO_2 = 40.19 – 40.86wt%, FeO = 6.37 – 7.33wt%, Al_2O_3 = 2.38 – 2.93wt% and CaO = 1.12 – 3.72wt%. The Mg# in both groups is similar (89.41 – 91.00). The higher concentration of CaO in antigorite-lizardite serpentinites is in correspondence with the presence of clinopyroxene and andradite garnet in these samples while the higher Al_2O_3 is associated with the presence of chlorite.

The bulk composition of antigorite serpentinites and antigorite-lizardite serpentinites (Table 7) allow classifying the protoliths as harzburgites and lherzolites using the Ol-Opx-Cpx diagram in mole proportions (Fig. 6), and according to the fields defined by Le Maitre et al. (2002). The diagram represents the projection of bulk compositions (defined by SiO_2, Al_2O_3, FeO_{total}, MnO, MgO and CaO) in the Fo-En-Di space after projection from the exchange vectors $FeMg_{-1}$ and $FeMn_{-1}$ and the Ca-Tschermak molecule $CaAl_2SiO_6$, as calculated using software CSpace (Torres-Roldán et al., 2000). All antigorite serpentinite samples correspond to harzburgitic protoliths, while the antigorite-lizardite serpentinites suggest lherzolitic-harburgitic composition.

A comparison of the whole rock compositions of serpentinites from La Corea mélange with other regionally related ultramafic rocks are presented in Figure 7. These include the Mayari-Baracoa Ophiolite Belt (interpreted as highly refractory peridotites from an arc/back arc environment; Marchesi et al., 2006), Monte del Estado complex in Puerto Rico (interpreted as abyssal peridotite; Lewis et al., 2006b; Marchesi et al., this volume), Central Cuba serpentinites from Zaza zone and Dominican Republic serpentinites from Camú and Septentrional fault zones (interpreted as forearc peridotite; Hattori and Guillot, 2007; Saumur et al., 2010) and Dominican Republic peridotites from Río San Juan and Puerto Plata complexes (interpreted as abyssal peridotite; Saumur et al., 2010). The antigorite-lizardite serpentinite samples show compositions similar to the lherzolites of the Monte del Estado ultramafic complex and abyssal peridotites from Río San Juan and Puerto Plata complexes, Dominican Republic. Furthermore, the antigorite serpentinites have compositions similar to abyssal peridotites and with Dominican Republic serpentinites from Río San Juan and Puerto Plata complexes.

Platinum group elements composition

The studied samples have low total platinum group elements (PGE) concentrations (20-63 ppb, Table 8). The antigorite-lizardite serpentinites show similar values in all samples (35-40 ppb), while the antigorite serpentinites display somewhat larger variations (20-63 ppb). In general, all samples are characterized by poorly fractionated patters of (Os, Ir, Ru) group elements (IPGE) patterns, with relatively flat IPGE segments consistent with the

TABLE 7 | **Bulk rock chemical composition of serpentinite samples from La Corea. Group A corresponds to antigorite serpentinites and group B corresponds to antigorite-lizardite serpentinites**

Sample	LC-M-17	LC-G-4	LC55	LC56	LC58	LC66	LC88	LC97
Group	A	A	A	A	A	B	B	B
SiO_2	38.79	40.80	36.97	42.88	41.28	40.19	40.86	40.55
TiO_2	0.04	0.06	0.04	0.09	0.08	0.11	0.07	0.07
Al_2O_3	1.49	2.41	1.73	2.51	1.96	2.44	2.93	2.38
FeO_{tot}	7.03	6.96	6.78	7.39	6.98	6.82	6.37	7.33
MnO	0.11	0.11	0.16	0.10	0.09	0.13	0.13	0.14
MgO	36.32	35.52	35.06	35.31	36.00	37.48	36.17	34.72
CaO	1.20	0.68	1.93	b.d.l.	0.73	1.12	2.30	3.72
P_2O_5	0.01	0.01	0.01	0.01	0.01	0.01	0.01	0.01
LOI	13.52	12.11	17.17	10.88	12.23	11.33	10.77	10.14
Total	98.51	98.66	99.85	99.17	99.36	99.63	99.61	99.06
Mg#	0.84	0.84	0.84	0.83	0.84	0.85	0.85	0.83

LOI: Loss on ignition. b.d.l.: below detection limit

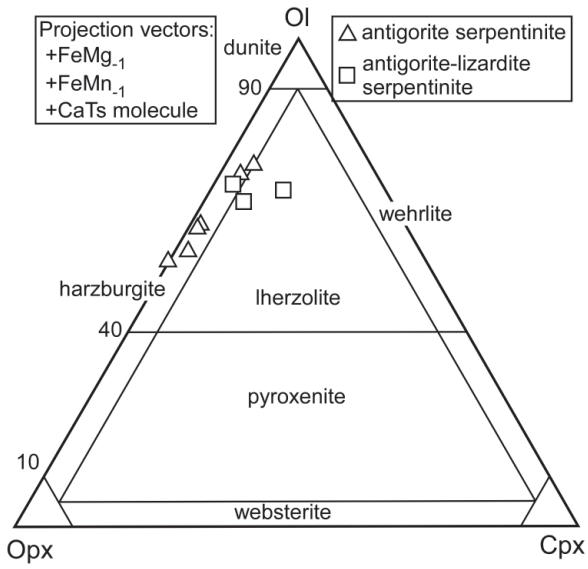

FIGURE 6 | **Calculated molar Ol-Opx-Cpx diagram for serpentinites from La Corea mélange (see text for calculation). Classification diagram from Streckeisen (1974).**

interpretation that they are all mantle residues (Fig. 8A, B). These PGE patterns are very similar to that of the primitive upper mantle (Becker et al., 2006). The composition of the studied samples are also similar to serpentinites of diverse origin (abyssal, forearc) from the Dominican Republic (Saumur et al., 2010).

In the Os versus Ir diagram (Fig. 8C) the samples show chondritic PGE abundances and weak enrichments relative to serpentinized abyssal peridotites (Snow and Reisberg, 1995; Luguet et al., 2003). The iridium contents and Ir/(Pt+Pd) ratios also indicate a mantle peridotite origin for their host protoliths (Fig. 8D). In general, the PGE distribution indicates that the PGE contents of the protoliths have not been significantly affected by metamorphism, in agreement with similar observations by Groves and Keays (1979), Prichard and Tarkian (1988), Angeli et al. (2001) and Proenza et al. (2004).

ISOCHEMICAL P-T PROJECTION

Isochemical P-T projections (pseudosections) were calculated for representative bulk-rock compositions of the two groups of serpentinites studied and the results were compared with the observed phase assemblages. The projections were computed with software PerpleX (Connolly, 2005). Thermodynamic data were taken from the internally consisted database of Holland and Powell (1998). Solid solutions considered are from Holland and Powell (1998) for olivine, from Holland and Powell (1996) for orthopyroxene and clinopyroxene, and from Holland et al. (1998) for chlorite. Talc, antigorite and tremolite were treated as ideal binary Fe-Mg solid solutions. Lizardite was not included in the calculations due to the lack of thermodynamic data for this phase. The fluid phase, assumed to be pure H_2O, is considered to be in excess. The antigorite serpentinite sample LC-58 was modeled in the CFMSH (CaO-FeO-MgO-SiO_2-H_2O) system (Fig. 9A). The bulk rock composition of this sample was slightly transformed in order to account for the Mg and Ca contents present in the carbonate phases (not considered in the calculations). The antigorite-lizardite serpentinite sample LC-97 was modeled in the system CFMASH (CaO-FeO-MgO-Al_2O_3-SiO_2-H_2O) (Fig. 9B). A small proportion of FeO_{total} was extracted to account for the presence of magnetite (not considered in the calculations).

The results of the calculations indicate a wide range of P-T conditions below ca. 500ºC for the formation of antigorite serpentinites (Fig. 9A). The predicted assemblage for these conditions is made mostly by antigorite, with minor talc, as observed in the studied samples. However, the calculated relations indicate the presence of minor tremolite, not observed in the studied samples. This is likely due to the effect of non-accounted CO_2 component and carbonate (dolomite) phases. Because these rocks are interpreted as the matrix of the subduction channel (i.e., high-T mélange formed above the subduction zone; see below), they should have followed a retrograde trajectory similar to that of the tectonic blocks of subducted oceanic material. For this reason, we have calculated mineral abundances in one point along the P-T trajectory followed by high pressure amphibolite blocks of the La Corea mélange (Blanco-Quintero et al., 2010). The results

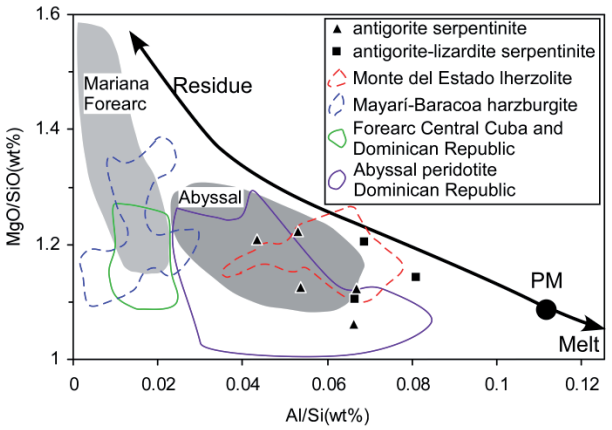

FIGURE 7 | **Weight ratios of Mg/Si versus Al/Si of serpentinite samples from La Corea mélange. Plotted for comparison are the fields of Mayarí-Baracoa harzburgites (Marchesi et al., 2006), Monte del Estado lherzolites (Marchesi et al., 2011), abyssal serpentinites from the Dominican Republic (Saumur et al., 2010), and forearc serpentinites from Central Cuba and Dominican Republic (Hattori and Guillot 2007, Saumur et al., 2010). Fields for Mariana forearc and abyssal peridotites compiled by Hattori and Guillot (2007). PM is the primitive mantle estimate of McDonough and Sun (1995).**

TABLE 8 | **Whole rock analyses of platinum group elements (PGE) of representative samples from La Corea mélange. Group A corresponds to antigorite serpentinites and group B corresponds to antigorite-lizardite serpentinites**

Samples	LC-G-4	LC-M-17	LC-55	LC-56	LC-66	LC-88	LC-97
Group	A	A	A	A	B	B	B
Ir	5	3	4	4	4	4	4
Os	4	3	4	3	3	3	4
Pd	21	7	5	7	9	13	10
Pt	18	0	10	3	5	10	10
Rh	5	2	5	2	4	3	3
Ru	10	5	10	7	10	7	9
Suma	63	20	38	26	35	40	40
IPGE	19	11	18	14	17	14	17
PPGE	44	9	20	12	18	26	23
IPGE/PPGE	0.43	1.22	0.90	1.17	0.94	0.54	0.74
Ir/(Pt+Pd)	0.13	0.43	0.27	0.40	0.29	0.17	0.20

IPGE: Os, Ir, Ru. PPGE: Rh, Pt, Pd.

indicate that the abundances of antigorite and talc are 93.63 wt% and 3.93 wt%, respectively, similar to the estimation from XRD data (see above).

The results of calculations for the antigorite-lizardite sample indicate that talc is not stable in the low temperature part of the diagram (< 600ºC; Fig 9B), as opposed to the calculations for the antigorite serpentinite sample and in agreement with observed assemblages. In addition, brucite, clinopyroxene and chlorite appear as stable phases in the low temperature field (< 400ºC), in agreement with the observed assemblages. The predicted stable coexistence of diopsidic clinopyroxene at low temperature suggests that the clinopyroxene porphyroclasts of the studied samples represent former peridotitic porphyroclasts reequilibrated during low-grade metamorphism. Since these rocks constitute tectonic blocks interpreted to have been accreted to the mélange at relatively low temperature (see below), their P-T evolution should have met the retrograde paths of the exhuming rocks of the subduction channel late during the evolution of the latter. In fact, the calculated mineral proportions at conditions appropriate for greenschist facies along the retrograde P-T path of the exotic blocks of La Corea mélange (i.e., 300ºC and 6kbar: Atg 66.46wt%, Cpx 15.20wt%, Chl 14.65wt% and Brc 3.70wt%; Fig. 9B) closely match the proportions obtained after XRD data recalculated for magnetite = 0.

DISCUSSION

The geologic setting of formation of ultramafic complexes is best determined using proxies such as the concentration of Cr, Al and Ti in Cr-spinel (Irvine, 1967; Dick and Bullen, 1984; Arai, 1992). The studied metaultramafic rocks of La Corea mélange do not preserve primary Cr-spinel, which is systematically altered to ferrian chromite or Cr-bearing magnetite. Also, no primary silicates (olivine and pyroxene) have been preserved, since diopsidic clinopyroxene of the antigorite-lizardite rocks is interpreted as metamorphic in equilibrium with antigorite. However, the fact that both types of rock have antigorite as the most abundant phase indicates a moderate temperature of serpentinization. Antigorite is the high temperature stable polymorph of the serpentine group minerals. Evans (2004) and Ulmer and Trommsdorff (1995) presented experimental results indicating antigorite stability up to 720ºC and 20kbar and 620ºC and 50kbar. These results are in agreement with formation of antigorite-bearing rocks in the subduction environment for a broad range of P-T conditions. Though the P-T conditions of formation of the studied serpentinites cannot be defined with precision, probable conditions can be deduced taking into account the dynamics of subduction channels and the evolution of high pressure exotic blocks included in the La Corea Mélange.

Dehydration of subducted altered oceanic crust and sediment from the incoming plate evolves large amounts of H_2O-fluid to the upper-plate mantle, for which models predict the possibility of partial melting at appropriate high temperature or serpentinization at low-medium temperature (e.g., Gerya et al., 2002). Subduction channels, being formed by a serpentinite matrix and HP blocks accreted from the subducting plate and/or detached from the overlying fore-arc lithosphere, may also contain exotic blocks of serpentinite formed in these environments. The strong alteration of spinel and the systematic absence of primary phases (e.g., olivine, orthopyroxene)

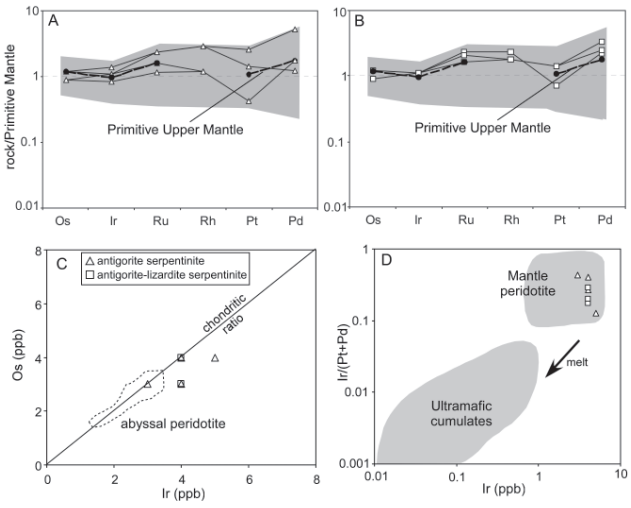

FIGURE 8 | **Primitive mantle (McDonough and Sun, 1995) normalized PGE abundances of A) antigorite serpentinite and B) antigorite-lizardite serpentinite. For reference, the composition of primitive upper mantle (PUM; Becker et al. 2006) and of abyssal and forearc serpentinites from Dominican Republic (Saumur et al., 2010) are plotted (grey fields). C) Ir versus Os diagram for samples from La Corea mélange; the field of abyssal peridotite is after compilation of Agranier et al. (2007); D) Ir versus Ir/(Pt+Pd) diagram for samples from La Corea mélange. It can be appreciated that the samples are similar to mantle peridotite and not ultramafic cumulates. The mantle peridotite and ultramafic cumulate regions (grey fields) are compiled by Hattori and Guillot (2007).**

are indications of elevated fluid fluxes and moderate temperature of formation, as indicated by the pseudosection calculations (Fig. 9). In this context, we interpret antigorite serpentinites as the deep seated serpentinitic matrix of the subduction channel formed after hydration of the boundary layer of the upper plate (harzburgitic) mantle. The bulk-rock major (Fig. 7) and PGE (Fig. 8) chemistry of this type of rock suggests a deep-seated harzburgitic protolith similar to abyssal peridotite. Harzburgites are known in abyssal and mantle wedge environments, but considering field evidence and mineralogical composition we propose that the antigorite serpentinites are derived from the hydrated mantle wedge. This interpretation implies that subduction channel serpentinites do not necessarily resemble residual harzburgites typical of fore-arcs (e.g., Mayarí-Baracoa ophiolitic complex).

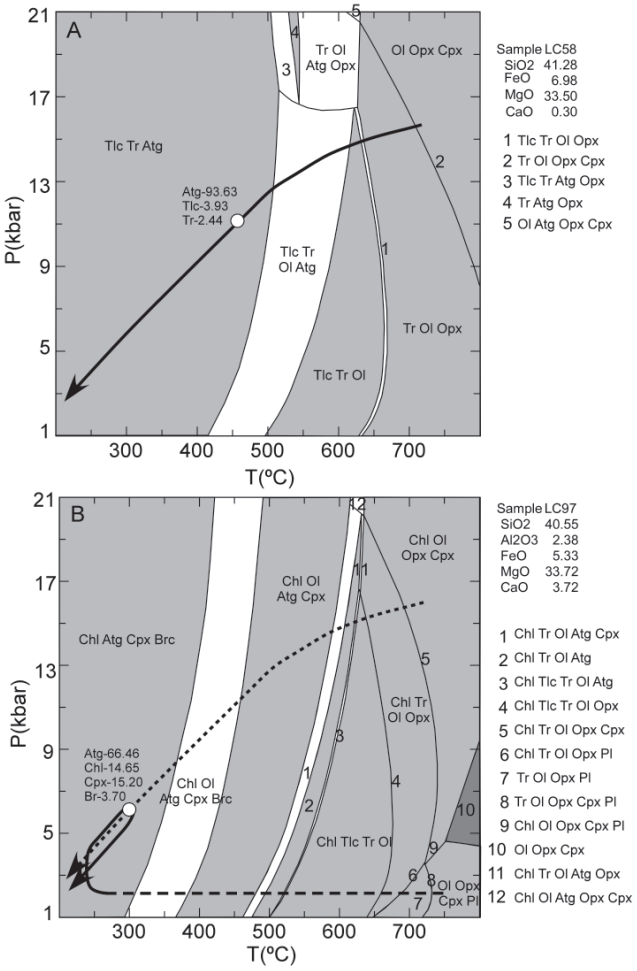

FIGURE 9 | **Isochemical P-T equilibrium phase diagram for A) antigorite serpentinite (LC58) and b) antigorite-lizardite serpentinite (LC97) calculated with Perplex. Ol: olivine, Atg: antigorite, Tlc: talc, Cpx: clinopyroxene, Opx: orthopyroxene, Chl: chlorite, Tr: tremolite, Brc: brucite. The P-T path in A) is for tectonic blocks of subducted amphibolites incorporated into the subduction channel (Blanco-Quintero et al., 2010). In B) the same P-T path is depicted with a dotted line; dashed and solid lines represent the inferred P-T paths during ocean-floor evolution of abyssal peridotites and during incorporation into the subduction channel, respectively. The calculated abundance of minerals for the inferred conditions of formation of both types of rocks is indicated.**

The antigorite serpentinites of the subduction channel would have followed a P-T path similar to that of subducted blocks accreted to the upper plate mantle. Exotic blocks of amphibolite were metamorphosed at ca. 15kbar, 700ºC, when they were accreted to the upper plate mantle (Blanco-Quintero et al., 2010). At these conditions, the calculated pseudosection for antigoritite serpentinites indicates anhydrous peridotite mineral assemblages coexisting with H_2O-fluid (i.e., hydrous peridotite; Fig. 9A). Blanco-Quintero et al. (2010) indicated that these conditions were followed by near-isobaric cooling in the accreted blocks of amphibolite, as expected after refrigeration of the subduction zone due to continued subduction (Gerya et al., 2002). Such isobaric cooling P-T path is also expected for the hydrated peridotite of the upper plate, which would hydrate (i.e., formation of tremolite and talc; Fig. 9A) due to the influx of fluids from the subducting slab. Once antigorite starts forming (ca. 650ºC, 15kbar; Fig. 9A), so does the subduction channel and rocks (both exotic tectonic blocks and hydrated metaharzburgitic matrix) begin to be exhumed. This is to be expected due to the plastic behavior of serpentinitic rocks (Gerya et al., 2002; Guillot et al., 2009) and implies that the P-T paths of the subduction channel rocks suffer an inflection, with increasing decompression upon cooling (Fig 9A). Further influx of fluids evolved from the subducting plate would allow continued hydration and the formation of almost pure antigoritite in the exhuming matrix of the subduction channel at conditions below 500ºC and 13kbar (Fig. 9A).

The lherzolitic bulk rock composition of the antigorite-lizardite serpentinites suggests a different protolith, probably an abyssal peridotite. The presence of abyssal and supra-subduction zone peridotite (protolith) rocks in subduction channels can be explained by three hypotheses. First, basaltic crust produced at slow spreading centers (Atlantic type) is normally thin or even absent, allowing abyssal peridotites to be incorporated in the subduction channel and mixed with metamafic rocks accreted from the incoming plate and hydrated ultramafic rocks of the mantle wedge. Similar rocks are described in mélanges from the Dominican Republic (Gorczyk et al., 2007, Saumur et al., 2010). Second, the preservation of abyssal-type peridotites in forearc regions has been interpreted as trapped older lithosphere that did not participate in subduction zone melting (Batanova and Sobolev, 2000). Finally, the inflow of younger abyssal lithosphere along the margins of transform-bounded trench systems is also possible, as proposed for the South Sandwich arc (Parkinson et al. 1992; Parkinson and Pearce 1998; Pearce et al. 2000).

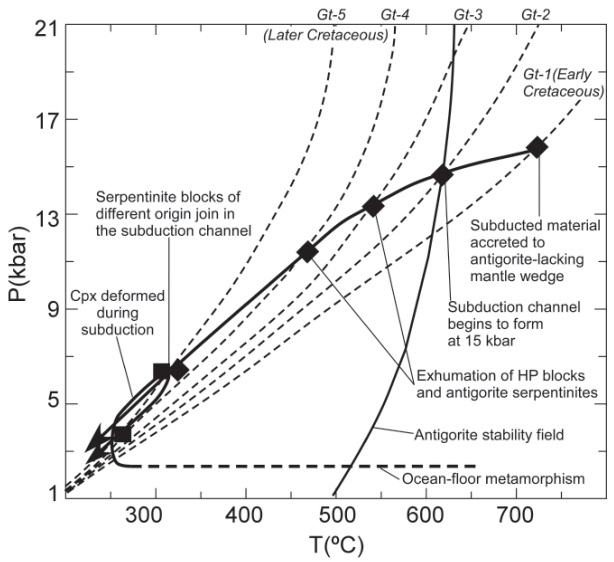

FIGURE 10 | **Schematic P-T diagram showing the model evolution of studied rocks. Dashed lines: evolving isotherms from onset of subduction to mature subduction (not scaled). Diamonds: Points along the inferred path of antigorite serpentinites (from mantle wedge to subduction channel). Squares: points along the inferred path of antigorite-lizardite serpentinites (abyssal serpentinite) during and after accretion (from the subduction channel to the mélange). The antigorite stability field corresponds to the calculation of Fig. 9A.**

The Proto-Caribbean oceanic lithosphere (Atlantic) was formed as result of breakup and disruption of Pangea during Late Jurassic - Late Cretaceous. Geological and geophysical evidence suggests a slow spreading center in the Proto-Caribbean region during the Mesozoic (e.g., Pindell et al., 2005, 2006) which may have allowed the formation of serpentinite after hydration of abyssal peridotite. Furthermore, chemical similarities among

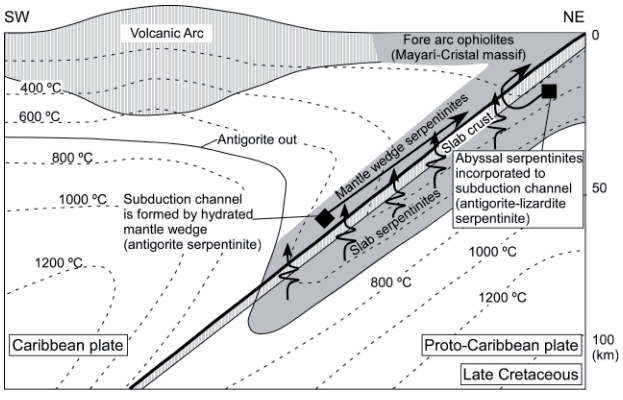

FIGURE 11 | **Schematic cross-section showing the tectonic configuration of the Caribbean region during the Cretaceous and the origin of the studied rocks. The thermal structure of the subduction zone and the stability of serpentinite is after Gerya et al. (2002; Fig. 7A) for a young plate (20Ma) after 500km of convergence.**

the antigorite-lizardite serpentinites and the Monte del Estado (Puerto Rico) ultramafic rocks (Fig. 7), interpreted as fragments of the Proto-Caribbean lithosphere (Lewis et al., 2006b; Marchesi et al., this volume), strengthen the view that the former type of rock from La Corea mélange represents fragments of the Proto-Caribbean oceanic lithosphere that escaped deep subduction. This view is consistent with the brucite, lizardite, and andradite-bearing mineral assemblages and textures of this type of rock, which suggest low temperatures of formation (Frost and Beard, 2007) in the oceanic environment and in the shallow subduction environment. Hence, the thermal evolution of this type of rocks should have encountered that of the exhuming subduction channel (mélange) at relatively low temperature and pressure. Using the P-T path of the exotic blocks of amphibolite, this should have taken place at ca. 300ºC and 5-6kbar (Fig. 9B), as indicated above.

An integrated model of evolution of serpentinites is presented in Figures 10 and 11 following the interpretations given above and those of Blanco-Quintero et al. (2010) for the exotic blocks of subducted MORB in the La Corea mélange. At the onset of subduction of young oceanic lithosphere during the Early Cretaceous (ca. 120Ma), the thermal gradient along the subduction interface was very hot. These conditions allowed the breakdown of hydrous phases from subducted hydrous oceanic lithosphere and the formation of free fluid that would flux across the mantle wedge. At relatively deep conditions, meta-MORB rocks from the incoming plate (amphibolites) were accreted to hydrous peridotitic mantle wedge. Continued subduction refrigerated the subduction system, allowing formation of hydrated metaperidotitic mantle wedge at similar depth. A serpentinitic subduction channel is formed upon reaction of liberated H_2O with the mantle wedge at conditions within the antigorite stability field (i.e., antigorite serpentinites), allowing henceforth upward flow of the rocks. This general evolution produces counter-clockwise P-T paths of accreted rocks (e.g., Wakabayashi, 1990; Gerya et al., 2002). Similar trajectories have been deduced by Krebs et al. (2008) from contemporaneous (ca. 103Ma) eclogite blocks in the Río San Juan complex (Dominican Republic), and amphibolite blocks from the Sierra del Convento mélange (115Ma; García-Casco et al., 2008a; Lázaro et al., 2009). As the subduction channel flows upward, other blocks join the mélange at shallower depths (i.e., antigorite-lizardite serpentinites). The mélange further exhumes until it is located below the forearc peridotites that could be represented by the peridotites of the Mayarí-Cristal ophiolite massif. Both the underlying forearc ophiolites and the mélange would be finally exhumed during late Cretaceous obduction, likely caused by the regional arc-platform collision event (García-Casco et al. 2008b).

CONCLUSIONS

Antigorite- and antigorite-lizardite-serpentinites in La Corea mélange (eastern Cuba) document the processes of formation of the subduction channel and accretion of abyssal peridotites. The strong alteration (i.e., serpentinization, Cr-spinel transformation) of harzburgitic and lherzolitic protholiths indicates pervasive fluid flow in all types of rock best explained if the rocks experienced hydration above a subducting plate. Antigorite serpentinites of harzburgitic protolith likely formed at depth after hydration of the mantle wedge (Caribbean lithosphere) by fluids derived from the SW-dipping subducted slab (Proto-Caribbean lithosphere). Antigorite-lizardite serpentinites of lherzolitic composition are best explained as abyssal (meta)peridotites (Proto-Caribbean lithosphere) accreted to the subduction channel developed in the Caribbean-Proto-Caribbean plate interface. Hydration of Caribbean plate mantle wedge allowed the formation and exhumation of a subduction channel during Cretaceous times until final exhumation occurred in the Late Cretaceous obduction of the supra-subduction zone Mayarí-Baracoa Ophiolite Belt and associated underlying subduction mélanges.

ACKNOWLEDGMENTS

The authors thank the constructive reviews of Robert J. Stern, Stéphane Guillot and George E. Harlow that substantially improved this paper. We appreciate financial support from Spanish MEC projects CGL2006-07384, CGL2006-08527, CGL2009-12446, CGL2009-10924 and 2009-SGR444 from the Catalan Government. This is a contribution to IGCP-546 "Subduction zones of the Caribbean". Blanco-Quintero is supported by grant AP2005-5258 from the "Programa de Formación del Profesorado Universitario" of the Spanish Ministry of Education and Science.

REFERENCES

Abu El Ela, F.F., Farahat, E.S., 2009. Neoproterozoic podiform chromitites in serpentinites of the Abu Meriewa–Hagar Dungash district, Eastern Desert, Egypt: Geotectonic implications and metamorphism. Island Arc, 19(1), 151-164. doi: 10.1111/j.1440-1738.2009.00689.x.

Adamovich, A., Chejovich, V., 1964. Principales características de la geología y de los minerales útiles de la región nordeste de la Provincia de Oriente. Revista Tecnológica, 2, 14-20.

Agranier, A., Lee, C.-T.A., Li, Z.-X.A., Leeman, W.P., 2007. Fluid-mobile element budgets in serpentinized oceanic lithospheric mantle: insights from B, As, Li, Pb, PGEs and Os isotopes in the Feather River Ophiolite, California. Chemical Geology, 245, 230-241.

Angeli, N., Fleet, M.E., Thibault, Y., Candia, M.A.F., 2001. Metamorphism and PGE-Au content of chromitite from the Ipanema mafic/ultramafic Complex, Minas Gerais, Brazil. Mineralogy and Petrology, 71, 173-194.

Arai, S., 1992. Chemistry of chromian spinel in volcanic rocks as a potential guide to magma chemistry. Mineralogical Magazine, 56, 173-784.

Bailey, S.W., 1980. Summary of recommendations of AIPEA nomenclature committee. Clay Minerals, 15, 85-93.

Batanova, V.G., Sobolev, A.V., 2000. Compositional heterogeneity in subduction-related mantle peridotites, Troodos massif, Cyprus. Geology, 28, 55-58.

Becker, H., Horan, M.F., Walker, R.J., Gao, S., Lorand, J.P., Rudnick, R.L., 2006. Highly siderophile element compositions of the Earth's primitive mantle. Geochimica et Cosmochimica Acta, 70, 4528-4550.

Blanco-Quintero, I., García-Casco, A., Rojas Agramonte, Y., Rodríguez Vega, A., Lázaro, C., Iturralde-Vinent, M.A., 2010. Metamorphic evolution of subducted hot oceanic crust, La Corea mélange, Cuba. American Journal of Science, 310, 889-915.

Boiteau, A., Michard, A., Saliot, P., 1972. Métamorphisme de haute pression dans le complexe ophiolitique du Purial (Oriente, Cuba). Comptes Rendus de l'Académie des Sciences, Série D, 274, 2137-2140.

Capitani, G., Mellini, M., 2004.The modulated crystal structure of antigorite: The m = 17 polysome. American Mineralogist, 89, 147-158.

Capitani, G., Mellini, M., 2006. The crystal structure of a second antigorite polysome (m=16), by single-crystal synchrotron diffraction. American Mineralogist, 91, 394-399.

Chan, T.K., Finch, I.J., 2001. Determination of platinum-group elements and gold by inductively coupled plasma mass spectrometry. In: Australian Platinum Conference, Perth, Western Australia.

Cobiella, J., Campos, M., Boiteau, A., Quintas, F., 1977. Geología del flanco sur de la Sierra del Purial. Revista La Minería de Cuba, 3, 54-62.

Connolly, J.A.D., 2005. Computation of phase equilibria by linear programming: a tool for geodynamic modeling and its application to subduction zone decarbonation. Earth and Planetary Science Letters, 236, 524-541.

Cressey, G., Cressey, B.A., Wicks, F.J., 2008. The significance of the aluminium content of a lizardite at the nanoscale: the role of clinochlore as an aluminium sink. Mineralogical Magazine, 72, 817-825.

D'Antonio, M.D., Kristensen, M.B., 2004. Hydrothermal alteration of oceanic crust in the West Philippine Sea Basin (Ocean Drilling Program Leg 195, Site 1201): inferences from a mineral chemistry investigation. Mineralogy and Petrology, 83(1-2), 87-112. doi: 10.1007/s00710-004-0060-6.

Dick, H.J.B., Bullen, T., 1984. Chromian spinel as a petrogenetic indicator in abyssal and alpine-type peridotites and spatially associated lavas. Contributions to Mineralogy and Petrology, 86, 54-76.

Escartín, J., Andreani, M., Hirth, G. Evans, B., 2008. Relationships between the microstructural evolution and the rheology of talc

at elevated pressures and temperatures. Earth and Planetary Science Letters, 268, 463-475.

Evans, B.W., 2004. The serpentinite multisystem revisited: Chrysotile is metastable. International Geology Review, 46, 479-506.

Fonseca, E., Zelepugin, V.N., Heredia, M., 1985. Structure of the ophiolite association of Cuba. Geotectonics, 19, 321-329.

Frost, B.R., Beard, J.S., 2007. On silica activity and serpentinization. Journal of Petrology, 48, 1351-1368.

García-Casco, A., Torres-Roldán, R.L., Iturralde-Vinent, M.A., Millán, G., Núñez Cambra, K., Lázaro, C., Rodríguez Vega, A., 2006. High pressure metamorphism of ophiolites in Cuba. Geologica Acta, 4(1-2), 63-88.

García-Casco, A., Lázaro, C., Torres-Roldán, R.L., Núñez Cambra, K., Rojas Agramonte, Y., Kröner, A., Neubauer, F., Millán, G., Blanco-Quintero, I., 2008a. Partial melting and counterclockwise P-T path of subducted oceanic crust (Sierra del Convento mélange, Cuba). Journal of Petrology, 49, 129-161.

García-Casco, A., Iturralde-Vinent, M.A., Pindell, J., 2008b. Latest Cretaceous collision/accretion between the Caribbean Plate and Caribeana: Origin of metamorphic terranes in the Greater Antilles. International Geology Review, 50, 781-809.

Gervilla, F., Proenza, J.A., Frei, R., González-Jiménez, J.M., Garrido, C.J., Melgarejo, J.C., Meibom, A., Díaz-Martinez, R., Lavaut, W., 2005. Distribution of platinum-group elements and Os isotopes in chromite ores from Mayarí-Baracoa Ophiolitic Belt (eastern Cuba). Contributions to Mineralogy and Petrology, 150, 589-607.

Gerya, T.V., Stoeckhert, B., Perchuk, A.L., 2002. Exhumation of high-pressure metamorphic rocks in a subduction channel—a numerical simulation. Tectonics, 21, 1056. doi:10.1029/2002TC001406.

Gorczyk, W., Guillot, S., Gerya, T.V., Hattori, K.H., 2007. Asthenospheric upwelling, oceanic slab retreat and exhumation of UHP mantle rocks: Insights from Greater Antilles. Geophysical Research Letters, 34, L21309, 5pp. doi: 10.1029/2007GL031059.

Groves, D.I., Keays, R.R., 1979. Mobilisation of ore-forming elements during alteration of dunites, Mt Keith-Betheno, Western Australia. The Canadian Mineralogist, 17, 373-389.

Guillot, S., Hattori, K., Agard, P., Schwartz, S., Vidal, O., 2009. Exhumation processes in oceanic and continental subduction contexts: a review. In: Lallemand, S., Funiciello F. (eds.). "Subduction Zone Dynamics". Springer-Verlag Berlin Heidelberg, 175-204. doi: 10.1007/978-3-540-87974-9.

Hattori, K.H., Guillot, S., 2007. Geochemical character of serpentinites associated with high- to ultrahigh-pressure metamorphic rocks in the Alps, Cuba, and the Himalayas: Recycling of elements in subduction zones. Geochemistry, Geophysics, Geosystems, 8, Q09010. doi:10.1029/2007GC001594.

Holland, T.J.B., Powell, R., 1996. Thermodynamics of order–disorder in minerals.2. Symmetric formalism applied to solid solutions. American Mineralogist, 81, 1425-1437.

Holland, T.J.B., Powell, R., 1998. An internally consistent thermodynamic data set for phases of petrological interest. Journal of Metamorphic Geology, 16, 309-343.

Holland, T.J.B., Baker, J., Powell, R., 1998. Mixing properties and activity-composition relationships of chlorites in the system MgO-FeO-Al_2O_3-SiO_2-H_2O. European Journal of Mineralogy, 10, 395-406.

Irvine, T.N., 1967. Chromian spinel as a petrogenetic indicator; Part II, Petrologic applications. Canadian Journal of Earth Sciences, 4, 71-103.

Iturralde-Vinent, M.A., 1998. Sinopsis de la Constitución Geológica de Cuba. Acta Geologica Hispanica, 33, 9-56.

Iturralde-Vinent, M.A., Díaz Otero, C., Rodríguez Vega, A., Díaz Martínez, R., 2006. Tectonic implications of paleontologic dating of Cretaceous-Danian sections of Eastern Cuba. Geologica Acta, 4(1-2), 89-102.

Iturralde-Vinent, M.A., Díaz Otero, C., García-Casco, A., Van Hinsbergen, D.J.J., 2008. Paleogene Foredeep Basin Deposits of North-Central Cuba: A Record of Arc-Continent Collision between the Caribbean and North American Plates. International Geology Review, 50, 863-884.

Jan, M.Q., Windley, B.F., 1990. Chromian spinel–silicate chemistry in ultramafic rocks of the Jijal Complex, Northwest Pakistan. Journal of Petrology, 31, 667-715.

Krebs, M., Maresch, W.V., Schertl, H.P., Baumann, A., Draper, G., Idleman, B., Münker, C., 2008. The dynamics of intra-oceanic subduction zones: A direct comparison between fossil petrological evidence (Rio San Juan Complex, Dominican Republic) and numerical simulation. Lithos, 103, 106-137.

Kretz, R., 1983. Symbols for rock-forming minerals. American Mineralogist, 68, 277–279.

Lázaro, C., García-Casco, A., 2008. Geochemical and Sr-Nd isotope signatures of pristine slab melts and their residues (Sierra del Convento mélange, eastern Cuba. Chemical Geology, 255, 120-133.

Lázaro, C., García-Casco, A., Neubaurer, F., Rojas-Agramonte, Y., Kröner, A., Iturralde-Vinent, M.A., 2009. Fifty-five-million-year history of oceanic subduction and exhumation at the northern edge of the Caribbean plate (Sierra del Convento mélange, Cuba. Journal of Metamorphic Geology, 27, 19-40.

Le Maitre, R.W., Streckeisen, A., Zanettin, B., Le Bas, M.J., Bonin, B., Bateman, P., Bellieni, G., Dudeck, A., Efremova, S., Keller, J., Lameyre, J., Sabine, P.A., Schmid, R., Sorensen, H., Woolley, A.R., 2002. Igneous rocks. A Classification and Glossary of Terms. Recommendations of the International Union of Geological Sciences Subcommission on the Systematics of Igneous Rocks. Cambridge, 2nd Edition, Cambridge University Press, 252pp.

Lewis, J.F., Draper, G., Proenza, J.A., Espaillat, J., Jimenez, J., 2006a. Ophiolite-Related Ultramafic Rocks (Serpentinites) in the Caribbean Region: A Review of their Occurrence, Composition, Origin, Emplacement and Ni-Laterite Soils Formation. Geologica Acta, 4(1-2), 237-263.

Lewis, J.F., Proenza, J.A., Jolly, W.T., Lidiak, E.G., 2006b. Monte del Estado (Puerto Rico) and Loma Caribe (Dominican

Republic) peridotites: A look at two different Mesozoic mantle sections within northern Caribbean region. Geophysical Research Abstracts, 8, A-08798.

Li, X.-P., Rahn, M., Bucher, K., 2004. Serpentinites of the Zermatt-Saas ophiolite complex and their texture evolution. Journal of Metamorphic Geology, 22, 159-177.

Luguet, A., Lorand, J.P., Seyler, M., 2003. Sulfide petrology and highly siderophile element geochemistry of abyssal peridotites: a coupled study of samples from the Kane Fracture Zone (45 degrees W23 degrees 20 N, MARK Area, Atlantic Ocean). Geochimica et Cosmochimica Acta, 67(8), 1553-1570.

Marchesi, C., Garrido, C.J., Godard, M., Proenza, J.A., Gervilla, F., Blanco-Moreno, J., 2006. Petrogenesis of highly depleted peridotites and gabbroic rocks from the Mayarí-Baracoa Ophiolitic Belt (eastern Cuba). Contributions to Mineralogy and Petrology, 151, 717-736.

Marchesi, C., Garrido, C.J., Bosch, D., Proenza, J.A., Gervilla, F., Monié, P., Rodríguez-Vega, A., 2007. Geochemistry of Cretaceous magmatism in eastern Cuba: recycling of North American continental sediments and implications for subduction polarity in the Greater Antilles Paleo-arc. Journal of Petrology, 48, 1813-1840.

Marchesi, C., Jolly, W.T., Lewis, J.F., Garrido, C.J., Proenza, J.A., Lidiak, E.G., 2011. Petrogenesis of fertile mantle peridotites from the Monte del Estado massif (southwest Puerto Rico): a preserved section of Proto-Caribbean lithospheric mantle? Geologica Acta, 9(3-4), 289-306.

McDonough, W.F., Sun, S.-S., 1995. The composition of the Earth. Chemical Geology, 120, 223-254.

Mellini, M., Trommsdorff, V., Compagnoni, R., 1987. Antigorite polysomatism: behaviour during progressive metamorphism. Contributions to Mineralogy and Petrology, 97, 147-155.

Mellini, M., Viti, C., 1994. Crystal structure of lizardite-1T from Elba, Italy. American Mineralogist, 79, 1194-1198.

Millán, G., Somin, M.L., Díaz, C., 1985. Nuevos datos sobre la geología del macizo montañoso de la Sierra del Purial, Cuba Oriental. Reporte de Investigación del Instituto de Geología y Paleontología, 2, 52-74.

Morimoto, N., Fabries, J., Ferguson, A.K., Ginzburg, I.V., Ross, M., Seifeit, F.A., Zussman, J., 1989. Nomenclature of pyroxenes. Canadian Mineralogist, 27, 143-156.

Müntener, O., Hermann, J., 1994. Titanian andradite in a metapyroxenite layer from the Malenco ultramafics (Italy) – implications for Ti-mobility and low-oxygen fugacity. Contributions to Mineralogy and Petrology, 116, 156-168.

Nuñez Cambra, K.E., García-Casco, A., Iturralde-Vinent, M.A., Millán, G., 2004. Emplacement of the ophiolite complex in Eastern Cuba. Florence, Proceedings of the 32nd International Geological Congress, Session G20.11, Caribbean Plate Tectonics, CD-Room.

O'Hanley, D.S., 1996. Serpentinites Records of Tectonic and Petrological History. Oxford, Oxford University Press, 290pp.

Padrón-Navarta, J.A., Hermann, J., Garrido, C.J., López Sánchez-Vizcaíno, V., Gómez-Pugnaire, M.T., 2010. An experimental investigation of antigorite dehydration in natural silica-enriched serpentinite. Contributions to Mineralogy and Petrology, 159, 25-42.

Parkinson, I.J., Pearce, J.A., 1998. Peridotites of the Izu-Bonin-Mariana forearc (ODP Leg 125) evidence for mantle melting and melt–mantle interactions in a suprasubduction zone setting. Journal of Petrology, 39, 1577-1618.

Parkinson, I.J., Pearce, J.A., Thirwall, M.F., Johnson, K.T.M., Ingram, G., 1992. Trace element geochemistry of peridotites from the Izu-Bonin-Mariana forearc, Leg 125. In: Fryer, P., Pearce, J.A., Stokking, L.B. (eds.). Proceedings of ODP science results. Ocean Drilling Program, College Station, 125, 487-506.

Pearce, J.A., Barker, P.F., Edwards, S.J., Parkinson, I.J., Leat, P.T., 2000. Geochemistry and tectonic significance of peridotites from the South Sandwich arc-basin system, south Atlantic. Contributions to Mineralogy and Petrology, 139, 36-53.

Pindell, J.L., Kennan, L., Maresch, W.V., Stanek, K.P., Draper, G., Higgs, R., 2005. Plate-kinematics and crustal dynamics of circum-Caribbean arc–continent interactions: Tectonic controls on basin development in Proto-Caribbean margins. In: Avé Lallemant, H.G., Sisson, V.B. (eds.). Caribbean–South American Plate Interactions, Venezuela. Geological Society of America, 394 (Special Papers), 7-52.

Pindell, J.L., Kennan, L., Stanek, K.P., Maresch, W.V., Draper, G., 2006. Foundations of Gulf of Mexico and Caribbean evolution: eight controversies resolved. Geologica Acta, 4(1-2), 303-341.

Prichard, H.M., Tarkian, M., 1988. Platinum and palladium minerals from two PGE-rich localities in the Shetland Ophiolite Complex. The Canadian Mineralogist, 26, 979-990.

Proenza, J., Gervilla, F., Melgarejo, J.C., Bodinier, J.L., 1999. Al- and Cr rich chromitites from the Mayarí-Baracoa Ophiolitic Belt (eastern Cuba): consequence of interaction between volatile-rich melts and peridotite in suprasubduction mantle. Economic Geology, 94, 547-566.

Proenza, J., Alfonso, J., Melgarejo, J.C., Gervilla, F., Tritlla, J., Fallick, A.E., 2003. D, O and C isotopes in podiform chromitites as fluid tracers for hydrothermal alteration processes of the Mayarí-Baracoa Ophiolitic Belt, eastern Cuba. Journal of Geochemical Exploration, 78-79, 117-122.

Proenza, J.A., Ortega-Guitiérrez, F., Camprubí, A., Tritlla, J., Elías-Herrera, M., Reyes-Salas, M., 2004. Paleozoic serpentinite-enclosed chromitites from Tehuitzingo (Acatlán) Complex, southern Mexico): a petrological and mineralogical study. Journal of South American Earth Sciences, 16, 649-666.

Proenza, J.A., Díaz-Martínez, R., Iriondo, A., Marchesi, C., Melgarejo, J.C., Gervilla, F., Garrido, C.J., Rodríguez-Vega, A., Lozano-Santacruz, R., Blanco-Moreno, J.A., 2006. Primitive Cretaceous island-arc volcanic rocks in eastern Cuba: the Téneme Formation. Geologica Acta, 4(1-2), 103-121.

Saumur, B-M., Hattori, K.H., Guillot, S., 2010. Contrasting origins of serpentinites in a subduction complex, northern

Dominican Republic. Geological Society of America Bulletin, 122, 292-304.

Snow, J.E., Reisberg, L., 1995. Os isotopic systematics of theMORB mantle: results from altered abyssal peridotites. Earth and Planetary Science Letters, 136(3-4): 723-733.

Somin, M.L., Millán, G., 1981. Geology of the Metamorphic Complexes of Cuba (in Russian). Moscow, Nauka, 219pp.

Streckeisen, A.L., 1974. Classification and Nomenclature of Plutonic Rocks. Recommendations of the IUGS Subcommission on the Systematics of Igneous Rocks. Geologische Rundschau, 63, 773-785.

Torres-Roldán, R.L., García-Casco, A., García-Sánchez, P.A., 2000. CSpace: An integrated workplace for the graphical and algebraic analysis of phase assemblages on 32-bit Wintel platforms. Computers and Geosciences, 26, 779-793.

Ulmer, P., Trommsdorff, V., 1995. Serpentine stability to mantle depths and subduction-related magmatism. Science, 268, 858-861.

Wakabayashi, J., 1990. Counterclockwise P-T-t paths from amphibolites, Franciscan Complex, California: Relics from the early stages of subduction zone metamorphism. Journal of Geology, 98, 657-680.

Wicks, F.J., Whittaker, E.J.W., 1977. Serpentine textures and serpentinization. The Canadian Mineralogist, 15, 459-488.

Manuscript received November 2010;
revision accepted January 2011;
published Online March 2011.

Geologica Acta, Vol.9, Nos 3-4, September-December 2011, 407-423
DOI: 10.1344/105.000001696
Available online at www.geologica-acta.com

geologica acta

Chromite and platinum group elements mineralization in the Santa Elena Ultramafic Nappe (Costa Rica): geodynamic implications

F. ZACCARINI [1] **G. GARUTI** [1] **J.A. PROENZA** [2] **L. CAMPOS** [3] **O.A.R. THALHAMMER** [1] **T. AIGLSPERGER** [2] **J.F. LEWIS** [4]

[1] **Department of Applied Geosciences and Geophysics, University of Leoben**
Peter Tunner Str. 5, 8700 Leoben, Austria. E-Mail: Federica.Zaccarini@unileoben.ac.at

[2] **Departament de Cristal·lografia, Mineralogia i Dipòsits Minerals, Facultat de Geologia, Universitat de Barcelona (UB)**
C/ Martí i Franquès s/n, E–08028 Barcelona, Spain

[3] **Escuela Centroamericana de Geología, University of Costa Rica**
San Pedro de Montes de Oca, 240-2060 UCR, San José, Costa Rica

[4] **Department of Earth and Environmental Sciences, The George Washington University**
2029 G St. NW, Washington, D.C. 20052, U.S.A.

ABSTRACT

Chromitites associated with strongly altered peridotite from six distinct localities in the Santa Elena ultramafic nappe (Costa Rica) have been investigated for the first time. Santa Elena chromitites commonly display a compositional variation from extremely chromiferous (Cr/(Cr+Al)=0.81) to intermediate and aluminous (Cr/(Cr+Al)=0.54). This composition varies along a continuous trend, corresponding to calculated parental liquids which may have been derived from the differentiation of a single batch of boninitic magma with Cr-rich and (Al, Ti)-poor initial composition. Fractional precipitation of chromite probably occurred during differentiation of the boninitic melt and progressive metasomatic reaction with mantle peridotite. The distribution of platinum group elements (PGE) displays the high (Os+Ir+Ru)/(Rh+Pt+Pd) ratio typical of ophiolitic chromitites and, consistently, the platinum group minerals (PGM) encountered are mainly Ru-Os-Ir sulfides and arsenides. Textural relations of most of the platinum group elements suggest crystallization at magmatic temperatures, possibly under relatively high sulfur fugacity as indicated by the apparent lack of primary Os-Ir-Ru alloys.

The chemical and mineralogical characteristics of chromitites from the Santa Elena ultramafic nappe have a strong affinity to podiform chromitites in the mantle section of supra-subduction-zone ophiolites. Calculated parental melts of the chromitites are consistent with the differentiation of arc-related magmas, and do not support the oceanic spreading center geodynamic setting previously proposed by some authors.

KEYWORDS | **Chromitite. Santa Elena Ultramafic Nappe. Costa Rica. Chromite composition. PGE-PGM. Geodynamic setting.**

INTRODUCTION

Recognition of the original geological setting of oceanic igneous complexes located along the Pacific coast of Costa Rica is at the focus of the geodynamic evolution of Central America (Fig. 1A). The northernmost of these complexes, located in Santa Elena Peninsula, has recently received contrasting interpretations, and the nature of its oceanic evolution has been a matter of debate. The Santa Elena complex may have been generated at an oceanic spreading center in a mantle plume region, analogous with the present Galapagos ridge/hot spot system (Beccaluva et al., 1999), or may represent the remnants of an inter-American proto-Caribbean ocean (Giunta et al., 2006). In contrast with these models, it has been proposed that the Santa Elena ophiolite complex was originally emplaced in a supra subduction zone, more precisely in an island arc setting (Hauff et al., 2000; Denyer et al., 2006; Gazel et al., 2006; Denyer and Gazel, 2009). Petrogenetic conditions of the ultramafic rocks of Santa Elena are difficult to determine due to the high degree of hydrothermal alteration and lateritic weathering. These processes have almost totally transformed the primary magmatic silicates into a secondary assemblage, mainly composed of serpentine, talc and chlorite, which hinder the identification of the original mantle lithology. In spite of such a deep mineralogical modification, the ultramafic block of Santa Elena contains small chromitite bodies which have visibly preserved a large part of their original magmatic character. This is due to the fact that chromian spinel is generally more resistant to alteration than mafic silicates. Although it may be transformed into secondary ferrian-chromite (Beeson and Jackson, 1969), its primary magmatic composition is usually preserved at the core of partially altered grains.

The potential of chromite (a chromian spinel with Cr_2O_3>~40wt%) as a petrogenetic indicator has been recognized for more than 40 years. Chromite composition helps to distinguish podiform chromitite associated with residual mantle in ophiolite belts (ophiolitic chromitites) from stratiform chromitite in continental layered intrusions and from chromitite segregations in Ural-Alaskan type complexes (Irvine, 1965, 1967; Thayer, 1970). In particular, the composition of chromite from podiform chromitites depends on the type of parental magma (e.g.: MORB, OIB, boninite) and the degree of depletion of its mantle source. Chromitite has become a reliable indicator of the geodynamic setting in which the minerals and their host rock have formed (Dick and Bullen, 1984; Roeder, 1994; Stowe, 1994; Zhou and Robinson, 1997; Barnes and Roeder, 2001; Kamenetsky et al., 2001; Rollinson, 2008).

Ophiolitic chromitites are carriers of PGE, although at a sub-economic level (Garuti, 2004). They are especially enriched in Os, Ir, and Ru, when compared to their country rocks, but may display different PGE compositions depending on the nature of the parent melt and the geodynamic setting of the host mantle peridotite (Zhou et al., 1998, and references therein). The mineralogical expression of the PGE content are, the PGM, occurring as micrometric minerals unevenly disseminated in the chromitite. Primary PGM representing pristine magmatic phases, trapped into crystallizing chromite at high temperatures, can be used to evaluate specific thermodynamic conditions, such as sulfur fugacity and temperature prevailing in the magmatic system during the precipitation of chromite (Augé and Johan, 1988; Garuti et al., 1999b; Brenan and Andrews, 2001).

The chromitites of Santa Elena were initially investigated by Jager-Contreras (1977) who reported the precise location of the mineralized bodies and described their morphology, size and field relations, but did not provide chemical data. Kuipjers and Jager-Contreras (1979) reported bulk chromium contents ranging from 33.1 to 61.0wt% Cr_2O_3 in 21 samples (average: 48.5wt% Cr_2O_3). Based on structural considerations, the authors concluded that the chromitites were produced by fractional crystallization of a basic magma migrating through the peridotite. This study documents the results of the first systematic investigation of chromite composition by electron-microprobe in the chromitites of Santa Elena, and provides the first data on the distribution and mineralogy of PGE within chromite grains. The data are used to identify the petrogenetic nature of the parental melt of the chromitites and, indirectly, define the tectonic setting of their emplacement. The role of the chromitites as a petrogenetic indicator represents a new approach that may contribute to resolving the geodynamic puzzle of the Santa Elena Ultramafic Nappe.

GEOLOGICAL BACKGROUND AND DESCRIPTION OF THE CHROMITITES

The Santa Elena mafic-ultramafic complex constitutes a large part of the rock exposed along the Santa Elena Peninsula on the northern Pacific coast of Costa Rica, close to the border with Nicaragua (Fig. 1B). According to Tournon (1994) and Baumgartner et al. (2008), Santa Elena Peninsula consists of three major structural units: 1) an overthrust allochthonuos unit composed of mafic-ultramafic rocks (Santa Elena Nappe), 2) a Cretaceous igneous-sedimentary sequence resting immediately below the overthrust (Santa Rosa Accretionary Complex), and 3) a volcanic sequence of pillow and massive basalts (Islas Murciélago) with IAT-affinity and $^{40}Ar/^{39}Ar$ age of 109Ma (Hauff et al., 2000). The Santa Elena Nappe is a regional SW-verging thrust over the Santa Rosa

accretionary complex (Tournon, 1994). The ultramafic rocks are composed of partially to completely serpentinized peridotite, mostly diopside-bearing harzburgite, with minor plagioclase lherzolite, dunite and orthopyroxenite. Layered gabbros and plagiogranite bodies occur along the southeastern coast, whereas dikes of pegmatitic gabbro and dolerite cut across the peridotite along its northern boundary (Gazel et al., 2006; Denyer and Gazel, 2009). The age of radiolarian cherts of the Santa Rosa accretionary complex varies from Middle Jurassic to Lower Cretaceous,

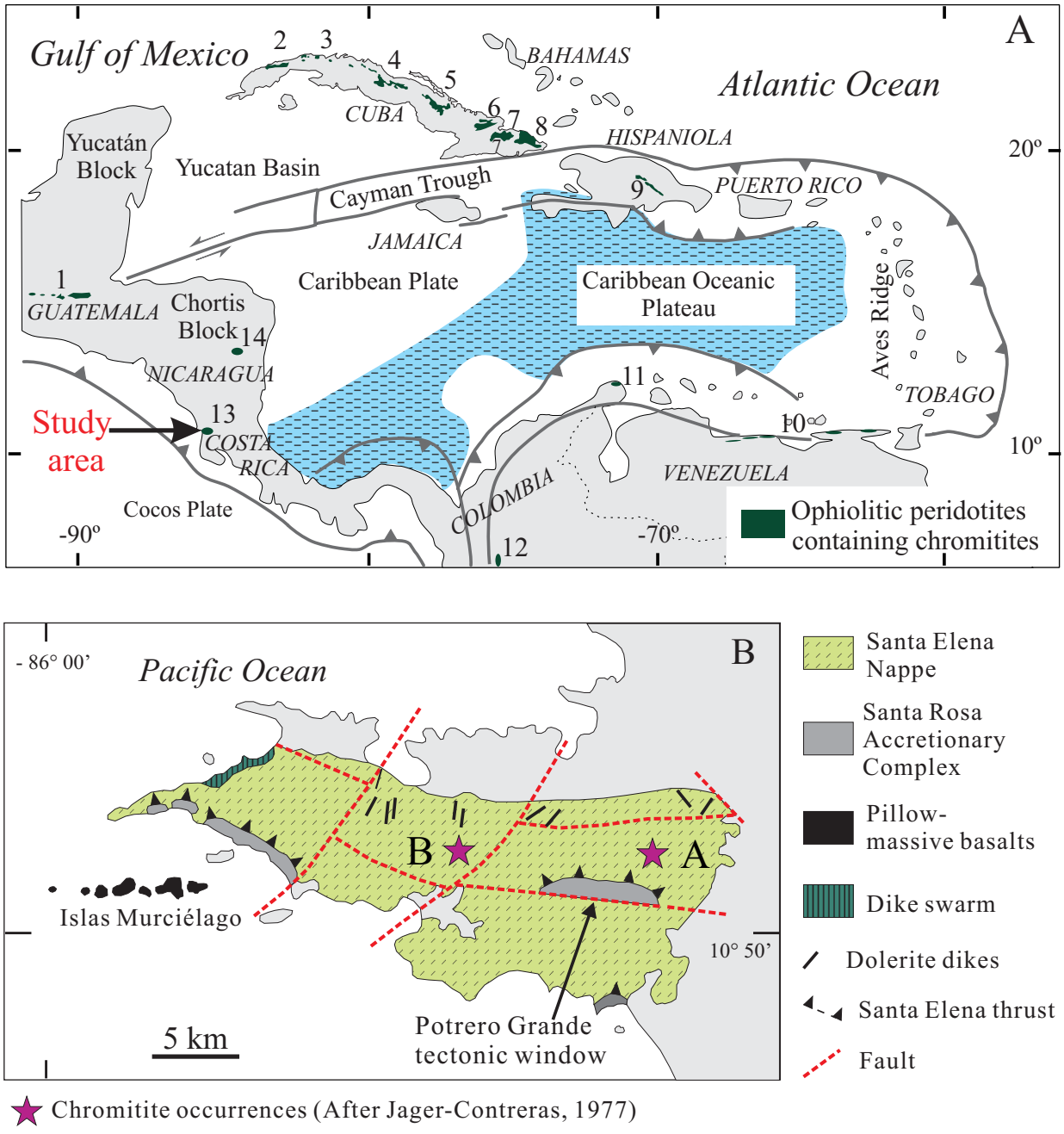

FIGURE 1 | **A) Structural sketch map showing distribution of ophiolite complexes with peridotite-host chromitite along the margin of the Caribbean plate. Locality number; 1: *Baja Verapaz*, Guatemala (Thayer, 1946); 2. to 8: *Cajálbana, Habana-Matanza, Villa Clara, Camagüey, Holguín, Mayarí-Cristal, Moa-Baracoa*, Cuba (Thayer, 1946; Proenza and Melgarejo, 1998; Proenza et al., 1999); 9: *Loma Caribe*, Dominican Republic (Proenza et al., 2007; Zaccarini et al., 2009); 10: *La Franja Costera*, Venezuela (Thayer, 1946; Rodriguez, 1986); 11: *La Guajira*, 12: *Dunita de Medellin*, Colombia (Álvarez, 1987; Buenaventura, 2001; Proenza et al., 2004); 13: *Santa Elena*, Costa Rica (Jager-Contreras, 1977; Kuipjers and Jager-Contreras, 1979; this study); 14: *Siuna*, Nicaragua (Flores et al., 2007; Baumgartner et al., 2008). B) Geological sketch map of the Santa Elena peninsula showing location of two chromitite areas (A and B) after Jager-Contreras (1977). Only chromitites from area A were investigated in this study.**

suggesting that the oceanic assemblage beneath the Santa Elena Nappe represents a discontinuous stratigraphic sequence (Baumgartner and Denyer, 2006; Baumgartner et al., 2008).

Eight chromitite bodies have been reported by Jager-Contreras (1977) and Kuipjers and Jager-Contreras (1979), occurring in two separated areas (A and B) along the central axis of the Santa Elena ultramafic body (Fig. 1B). Area A is located some kilometers north of the Potrero Grande tectonic window, and covers a surface of about 2km^2. The ore bodies occur a few ten to a few tens of meters to a few hundred off the old track leading to Cerro El Inglés. Area B is located in a remote, mountainous region currently inaccessible. Therefore only the six chromitite occurrences located in area A were sampled and studied in this work. Samples have been labeled from Jag-1 to Jag-6 according with the numeration of Jager-Contreras (1977) (Fig. 2), and are listed in Table 1 along with GPS coordinates. At the outcrop scale, the chromitites are small and irregular bodies (Figs. 3, 4) with a predominantly massive texture that locally grades into orbicular or leopard texture. It was not possible to recognize the lithology of the host ultramafic rock, in most cases, due to strong alteration. However, some of the chromitite bodies are in direct contact with partially altered dunite. Small patches of relatively fresh clinopyroxenite and gabbro (possibly dikes) occur in the peridotites from area A, away from the chromitite bodies.

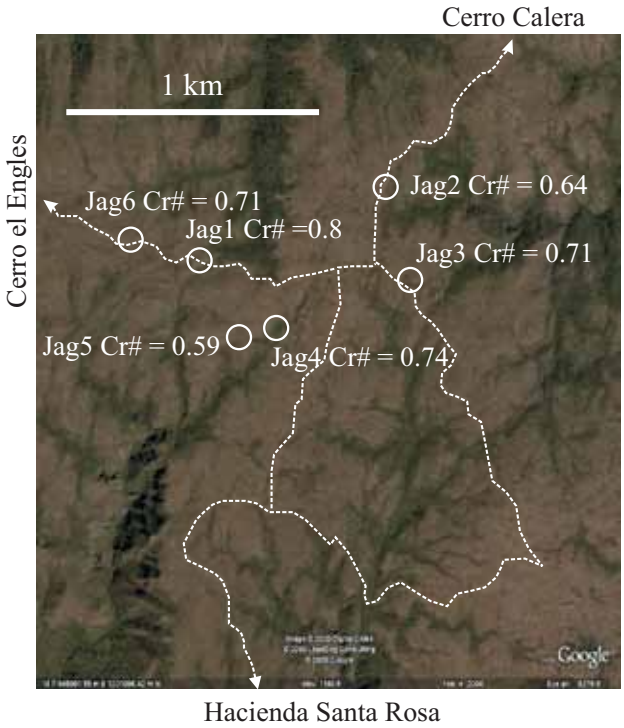

FIGURE 2 | **Google satellite view of area A with spatial distribution of the six chromitite localities investigated. Average chromium numbers, Cr#=Cr/(Cr+Al), in each chromite locality are shown (see text for discussion).**

ANALYTICAL TECHNIQUES

A total number of 24 polished sections (4 from each one of the six chromitite occurrences) were examined. Chromite and PGM were analyzed by electron microprobe with a Superprobe Jeol JXA 8200 at the Eugen F. Stumpfl Laboratory at Leoben University. Back scattered electron (BSE) images of the PGM were obtained at the Leoben laboratory as well as at the Serveis Cientificotècnics at the Universitat de Barcelona. Eleven samples of massive chromitite and two of peridotites were analyzed for PGE and Au by Inductively Coupled Plasma-Mass Spectrometry (ICP-MS) after Ni-sulfide preconcentration at Genalysis Laboratory Services Pty Ltd, Western Australia.

In order to determine the primary composition of chromite, care was taken to analyze the unaltered cores of grains. An average of 20 analysis points were obtained for each polished section. The electron microprobe was operated in the Wavelength Dispersive X-Ray Spectrometry (WDS) mode, at 15kV accelerating voltage and10nA beam current. The analysis of Mg, Al, Ti, V, Cr, Mn, Fe, Ni and Zn were carried out using the Kα lines, and were calibrated on natural chromite, rhodhonite, ilmenite and metallic V, Ni and Zn. The counting times for peak and background were 20 and 10 seconds respectively. The amount of Fe^{3+} in chromite was calculated assuming the spinel stoichiometry $R^{2+}O\ R^{3+}{}_2O_3$.

PGM were previously located by scanning polished sections under a reflected light microscope at 250-800 magnification. They were subsequently analyzed on the Electron Probe Microanalyzer in the WDS mode, at 20kV accelerating voltage and 10nA beam current, and beam diameter of about 1 micron or less. The counting time on peak and background were 15 and 5 seconds respectively. The Kα lines were used for S, As, Fe, Cu and Ni; Lα for Ir, Ru, Rh and Pt, and Mα for Os. The reference materials

TABLE 1 | **GPS coordinates of the investigated chromities from locality A, samples Jag 1-6 (Fig. 1).**

Jag 1	85°40'10.50"W	10°52'26.00"N
Jag 2	85°39'44.60"W	10°52'32.30"N
Jag 3	85°39'40.30"W	10°52'22.20"N
Jag 4	85°39'52.20"W	10°52'18.20"N
Jag 5	85°39'55.60"W	10°52'17.00"N
Jag 6	85°40'21.40"W	10°52'28.80"N

were pure metals for the six PGE (Ru, Rh, Pd, Os, Ir, Pt), synthetic NiS, natural chalcopyrite and niccolite for Ni, Fe, Cu, S and As. The following diffracting crystals were selected: PETJ for S; PETH for Ru, Os, Rh; LIF for Cu; LIFH for Ni, Ir, Pt; and TAP for As. Automatic corrections were performed for interferences involving Ru-Rh, Ir-Cu and Rh-Pd.

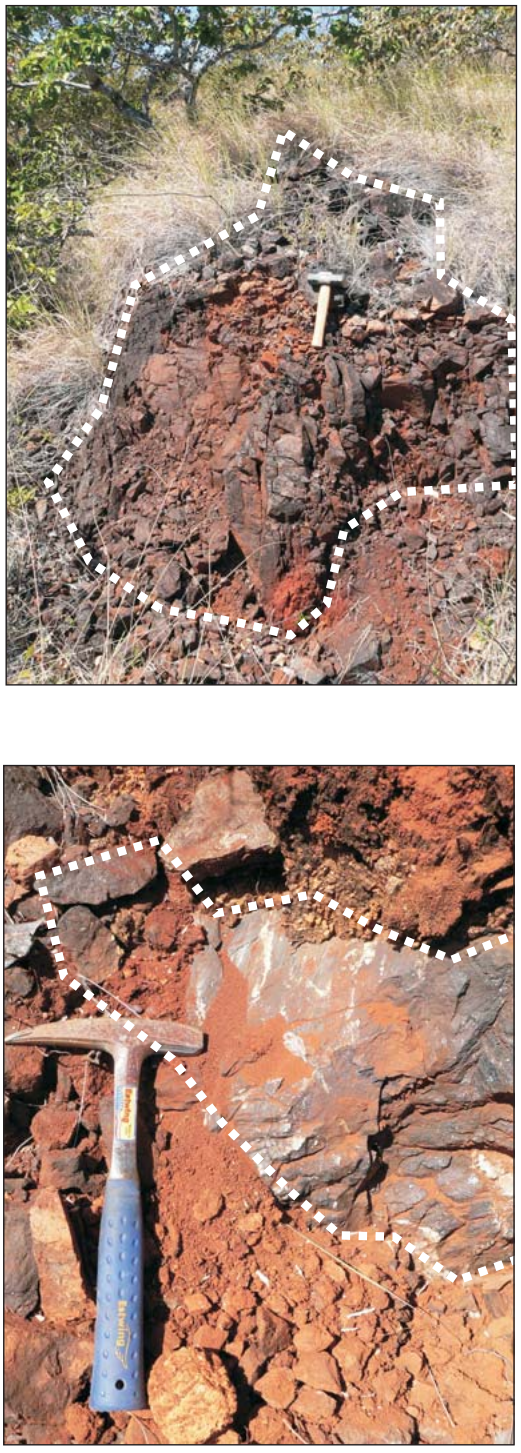

FIGURE 3 | **Field photographs of the massive chromitite and strongly lateritized peridotite host at locality Jag-1.**

RESULTS

Chromite texture and composition

Under the microscope, the chromitites of Santa Elena display a uniform massive texture (<10% interstitial silicate) interrupted by cracks, pull-apart fractures and brecciation (Fig. 5A). Chromite is usually fresh, showing the typical ferrian-chromite alteration only along grain boundaries and cracks (Fig. 5B).

Approximately 500 electron microprobe analyses were performed on 15 samples from the six chromitite occurrences, and are listed as averages in Table 2. Chromites are compositionally homogeneous or display little variation within single localities. However, substantial differences are seen from one locality to the other. The overall variation ranges of major oxides

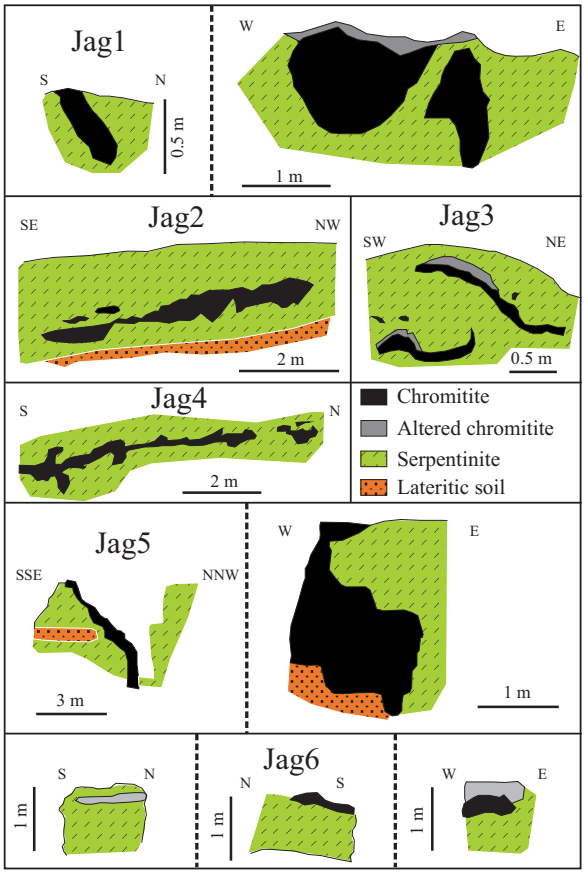

FIGURE 4 | **Oriented field sketches of chromitite bodies at the six localities in area A (redrawn and simplified after Jager-Contreras, 1977).**

(wt%) in the unaltered cores of chromite grains are: Cr_2O_3 (42.8-62.75), Al_2O_3 (7.1-24.5), MgO (9.3-14.0) and FeO (13.2-20.6). MgO and FeO display negative correlation (R=-0.76). A sharp negative correlation (R=-0.98) is also observed between Cr_2O_3 and Al_2O_3 (Fig 6A), consistent with the Al-Cr substitution predominant in podiform chromitites compared with the stratiform type (Thayer, 1970). The TiO_2 content varies between 0.1wt% and 0.35wt%, showing a well defined negative correlation with Cr_2O_3 (R=-0.91) (Fig. 6B), and positive with Al_2O_3 (R=0.88).

The calculated amount of Fe_2O_3 is usually low (<1.75wt%) and near zero in samples Jag-1 and Jag-4, which have the highest Cr contents. Maximum concentrations of 0.29wt% NiO (av.=0.05-0.19), 0.23wt% ZnO (av.=0.03-0.10), and 0.14wt% V_2O_3 (av.=0.04-0.09) have been determined. The Mn content is lower than 0.15wt% MnO, and typically below the detection limit.

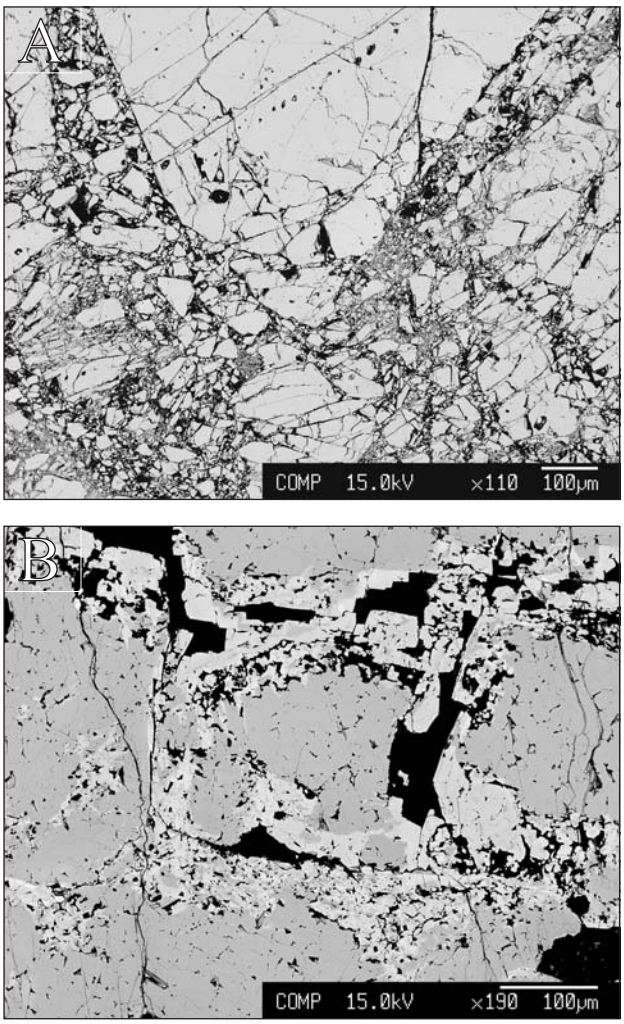

FIGURE 5 | **Back scattered electron images of polished sections from the Santa Elena chromitites. A) Coarse grained chromitite with strong brecciation controlled by shear planes. B) Ferrian chromite alteration (light grey) developed along cracks and fissures in massive chromitite.**

Santa Elena chromitites plot in the podiform field on the Cr/(Cr+Al) vs. $Fe^{2+}/(Fe^{2+}+Mg)$ binary diagram (Fig. 6C). The compositions from the various localities form a continuous trend from extremely chromiferous (av. Cr/(Cr+Al)=0.81), to intermediate and aluminous (av. Cr/(Cr+Al)=0.54), in a relatively narrow variation range in $Fe^{2+}/(Fe^{2+}+Mg)$ (0.52-0.38).

Chemical effects of alteration in Santa Elena chromitites are rather unusual compared with common chemical patterns observed in hydrothermally altered chromitites. Altered rims exhibit a consistent decrease in Al and an irregular decrease in all other analyzed elements, except Fe^{2+} and Cr that are variably enriched. Thus, the expected oxidation of Fe^{2+} to Fe^{3+} is not observed. On the contrary, a general sharp drop of Fe^{3+} occurs in the alteration rims with respect to the cores. A similar alteration pattern has been described in detrital chromian spinels from lateritic soils formed by tropical weathering of ultramafic rocks (Friedrich et al., 1980).

PGE geochemistry and mineralogy

Total PGE concentration in 11 chromitite samples ranges from 80 to 292ppb and is about 4 to 10 times higher than in serpentinized peridotites (Table 3). There is no obvious correlation between PGE abundance and chromite composition. We note, however, that the highest PGE concentrations and the lowest Pd/Ir ratios were found in the most Cr-rich chromitite from Jag-1 locality. All samples display enrichment in Ru (48-183ppb), Ir (17-81ppb) and Os (12-69ppb), with good positive correlation among the pairs Os-Ir (R^2=0.90), Ir-Ru (R^2=0.93), Os-Ru (R^2=0.88). Rh and Pd contents range from 7 to 18ppb and 3 to 5ppb, respectively. Gold and Pt are always below the detection limit, except for samples from Jag-1, which contain 3 ppb Pt.

Chondrite-normalised PGE patterns of Santa Elena chromitites display high (Os+Ir+Ru)/(Rh+Pt+Pd) ratios typical of Cr-rich chromitites formed in the mantle section of supra subduction zone ophiolites of the Balkan Peninsula (Economou-Eliopoulos, 1996; Kocks et al., 2007), Turkey (Uysal et al., 2009a, b), Urals (Melcher et al., 1997; Garuti et al., 2005), Caribbean Belt (Proenza et al., 1999), and China (Zhou et al., 1998). In most cases, PGE patterns are characterized by a consistent positive anomaly in Ru, and a negative anomaly in Pt (Fig. 7A, B). The chondrite-normalized pattern of serpentinized peridotite of Santa Elena is shifted to one order of magnitude less compared with the chromitites. However, the peridotite patterns are generally flat and have Ru and Pt anomalies

TABLE 2 | **Average compositions of chromite and calculated parental melts from 6 chromitite occurrences in the Santa Elena peridotite**

Weight % (normalized to 100%)												
Locality-Sample	N°an.	TiO_2	Al_2O_3	FeO	Fe_2O_3	MgO	MnO	Cr_2O_3	NiO	ZnO	V_2O_3	$*Al_2O_3$	$*TiO_2$
Chromite core													
Jag1-1	15	0.14	10.21	15.36	0.08	11.73	0.00	62.27	0.08	0.06	0.06	11.02	0.30
Jag1-2	18	0.12	10.36	14.67	0.00	12.09	0.03	62.48	0.13	0.05	0.07	11.09	0.26
Jag1-2 BC	20	0.12	11.60	15.48	0.00	11.62	0.05	60.91	0.11	0.05	0.06	11.68	0.26
Jag1-3	20	0.13	10.32	14.82	0.00	11.81	0.00	62.67	0.14	0.04	0.06	11.07	0.28
Jag2-1	20	0.29	18.89	15.41	0.64	12.85	0.07	51.55	0.16	0.06	0.08	14.23	0.45
Jag2-2	34	0.29	19.42	16.27	0.81	12.34	0.09	50.48	0.16	0.06	0.08	14.37	0.46
Jag2-2 BC	20	0.21	18.15	19.02	1.63	10.33	0.12	50.31	0.11	0.07	0.06	14.02	0.39
Jag2-3	20	0.31	19.49	15.43	0.97	12.88	0.12	50.48	0.19	0.05	0.07	14.39	0.47
Jag3-1	20	0.23	15.95	16.37	0.80	11.94	0.00	54.46	0.11	0.06	0.08	13.34	0.41
Jag3-1 BC	20	0.20	15.83	16.40	1.10	11.84	0.09	54.34	0.13	0.07	0.00	13.30	0.37
Jag3-2	20	0.20	14.52	17.57	1.16	10.97	0.07	55.27	0.10	0.06	0.09	12.85	0.38
Jag3-2 BC	20	0.20	15.45	18.11	1.68	10.67	0.09	53.59	0.09	0.05	0.06	13.18	0.38
Jag4-2	20	0.18	13.27	15.94	0.01	11.72	0.16	58.47	0.12	0.07	0.07	12.38	0.35
Jag4-2 BC	20	0.20	17.55	19.47	0.29	9.93	0.13	52.21	0.07	0.10	0.06	13.84	0.38
Jag4-3	30	0.19	13.68	17.07	0.43	11.20	0.12	57.09	0.10	0.05	0.07	12.54	0.37
Jag5-1	20	0.33	21.19	15.88	0.24	12.83	0.06	49.20	0.12	0.06	0.09	14.83	0.48
Jag5-2	20	0.35	23.64	15.15	0.65	13.56	0.06	46.31	0.13	0.07	0.09	15.40	0.49
Jag5-2 BC	20	0.30	22.35	17.53	1.33	11.45	0.04	46.82	0.10	0.08	0.02	15.10	0.47
Jag5-3	20	0.32	21.09	15.78	0.18	12.86	0.06	49.44	0.12	0.07	0.09	14.80	0.47
Jag6-2	30	0.20	14.96	18.96	1.05	10.11	0.08	54.41	0.07	0.10	0.07	13.01	0.38
Jag6-3	20	0.20	13.70	19.17	0.96	9.85	0.08	55.83	0.06	0.08	0.07	12.55	0.37
Altered chromite rim													
Jag1-1	6	0.10	6.82	15.92	0.00	10.36	0.00	66.66	0.06	0.03	0.04		
Jag1-2	2	0.13	10.45	14.57	0.00	12.03	0.03	62.58	0.07	0.08	0.07		
Jag2-2	26	0.16	14.71	19.11	0.99	9.99	0.04	54.79	0.06	0.06	0.09		
Jag1-3	20	0.12	6.85	15.66	0.00	10.01	0.04	67.14	0.06	0.05	0.07		
Atomic% (based on 32 Oxygens)													
Locality-Sample		Ti	Al	Fe^{2+}	Fe^{3+}	Mg	Mn	Cr	Ni	Zn	V	#Cr	$\#Fe^{2+}$
Chromite core													
Jag1-1		0.03	3.15	3.36	0.02	4.57	0.00	12.86	0.02	0.01	0.01	0.80	0.42
Jag1-2		0.02	3.55	3.36	0.00	4.50	0.01	12.51	0.02	0.01	0.01	0.78	0.43
Jag1-2 BC		0.02	3.18	3.20	0.00	4.69	0.01	12.87	0.03	0.01	0.01	0.80	0.41
Jag1-3		0.02	3.18	3.24	0.00	4.59	0.00	12.93	0.03	0.01	0.01	0.80	0.41
Jag2-1		0.05	5.57	3.22	0.12	4.79	0.02	10.19	0.03	0.01	0.01	0.65	0.40
Jag2-2		0.06	5.73	3.41	0.15	4.60	0.02	9.99	0.03	0.01	0.01	0.64	0.43
Jag2-2 BC		0.04	5.46	4.06	0.31	3.93	0.03	10.15	0.02	0.01	0.01	0.65	0.51
Jag2-3		0.06	5.73	3.22	0.18	4.79	0.03	9.95	0.04	0.01	0.01	0.63	0.40
Jag3-1		0.05	4.79	3.49	0.15	4.53	0.00	10.96	0.02	0.01	0.01	0.70	0.44
Jag3-1 BC		0.04	4.76	3.50	0.21	4.50	0.02	10.95	0.03	0.01	0.00	0.70	0.44
Jag3-2		0.04	4.41	3.79	0.23	4.22	0.02	11.27	0.02	0.01	0.01	0.72	0.47
Jag3-2 BC		0.04	4.69	3.90	0.33	4.09	0.02	10.91	0.02	0.01	0.01	0.70	0.49
Jag4-2		0.04	4.03	3.44	0.00	4.50	0.04	11.92	0.02	0.01	0.01	0.75	0.43
Jag4-2 BC		0.04	5.30	4.17	0.06	3.79	0.03	10.58	0.01	0.02	0.01	0.67	0.52
Jag4-3		0.04	4.17	3.69	0.08	4.31	0.03	11.66	0.02	0.01	0.01	0.74	0.46
Jag5-1		0.06	6.19	3.28	0.04	4.73	0.01	9.64	0.02	0.01	0.01	0.61	0.41
Jag5-2		0.06	6.80	3.09	0.12	4.93	0.01	8.94	0.03	0.01	0.01	0.57	0.39
Jag5-2 BC		0.06	6.55	3.65	0.25	4.24	0.01	9.21	0.02	0.01	0.00	0.58	0.46
Jag5-3		0.06	6.16	3.27	0.03	4.75	0.01	9.68	0.02	0.01	0.01	0.61	0.41
Jag6-2		0.04	4.57	4.10	0.21	3.90	0.02	11.14	0.01	0.02	0.01	0.71	0.51
Jag6-3		0.04	4.21	4.18	0.19	3.83	0.02	11.51	0.01	0.02	0.01	0.73	0.52
Altered chromite rim													
Jag1-1		0.02	2.15	3.57	0.00	4.13	0.00	14.11	0.01	0.01	0.01	0.87	0.46
Jag1-2		0.03	3.21	3.17	0.00	4.67	0.01	12.89	0.01	0.02	0.01	0.80	0.40
Jag2-2		0.02	2.17	3.52	0.00	4.01	0.01	14.25	0.01	0.01	0.01	0.87	0.47
Jag1-3		0.03	4.50	4.15	0.19	3.86	0.01	11.24	0.01	0.01	0.01	0.71	0.52

N°an. = number of analyses; $*TiO_2$ and $*Al_2O_3$ = calculated Silicate melt in equilibrium with chromite (see equations in Fig. 11)

#Cr = Cr/(Cr+Al)

$\#Fe^{2+} = Fe^{2+}/(Fe^{2+}+Mg)$

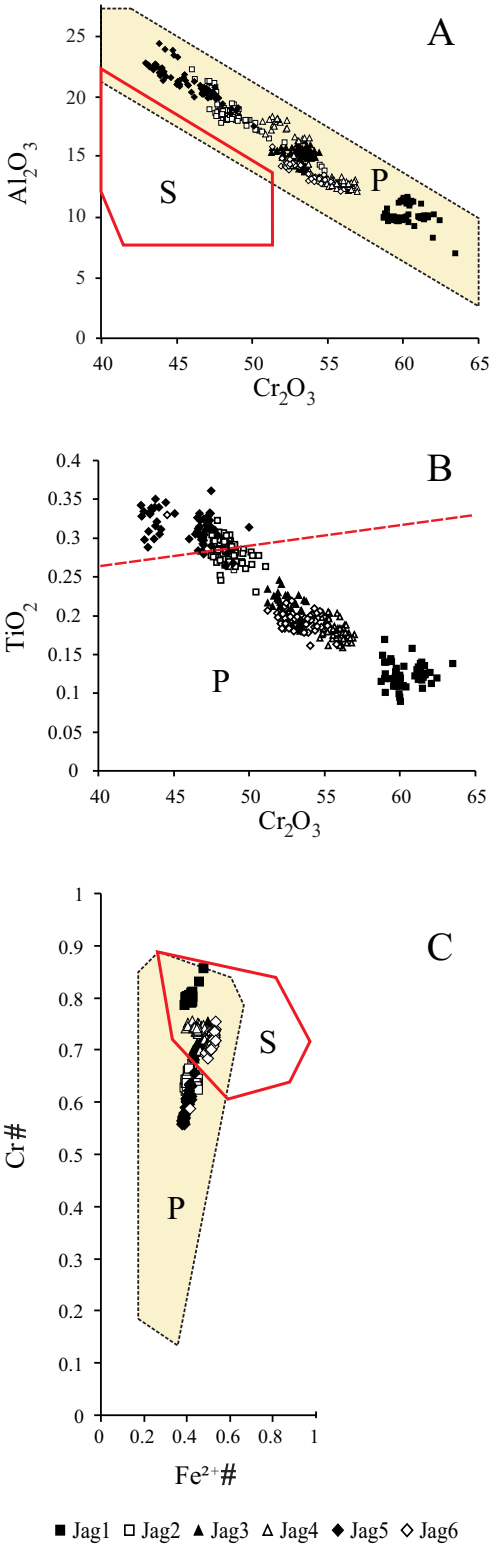

FIGURE 6 | **Composition of unaltered chromite cores in chromite from the six chromitite localities (area A) of Santa Elena. A and B) Sharp negative correlation of Al_2O_3 and TiO_2 versus Cr_2O_3. C) variation of the chromium number, Cr#=Cr/(Cr+Al), as a function of the bivalent iron number, Fe^{2+}=Fe^{2+}/(Fe^{2+}+Mg). P: field of podiform chromitites, S: field of stratiform chromitites.**

TABLE 3 | **Concentration of PGE and Au (ppb) in the Santa Elena chromitite and serpentinite**

	Os	Ir	Ru	Rh	Pt	Pd	Au	ΣPGE
d.l.	2	2	2	2	2	2	5	
Chromitite								
JAG 1-1	69	81	183	16	3	4	b.d.l.	287
JAG 1-1	68	81	180	17	3	5	b.d.l.	286
JAG 1-3	69	85	181	18	3	5	b.d.l.	292
JAG 2-1	38	32	95	9	b.d.l.	4	b.d.l.	140
JAG 3-3	12	17	48	10	b.d.l.	5	b.d.l.	80
JAG 4-1	30	41	135	14	b.d.l.	4	b.d.l.	194
JAG 4-2	15	25	79	12	b.d.l.	4	b.d.l.	120
JAG 4-3	19	30	98	12	b.d.l.	4	b.d.l.	144
JAG 5-2	42	40	119	7	b.d.l.	3	b.d.l.	169
JAG 5-3	54	48	154	8	b.d.l.	4	b.d.l.	214
JAG 6-3	17	26	48	9	b.d.l.	4	b.d.l.	87
Serpentinite								
MV-2	5	5	10	2	6	9	b.d.l.	32
MV-3	4	4	8	b.d.l.	3	6	b.d.l.	21
CC1	514	540	690	200	1020	545		

d.l. = detection limit, b.d.l. = below detection limit,
CC1 = chondrite values after Naldrett and Duke (1980)

similar to those of the chromitites, although the Pt+Pd contents are higher (Fig. 7A).

The mineralogical study of 24 polished sections resulted in finding 50 PGM grains, with a minimum frequency of at least one grain per section. The mineralogy reflects the chemical data, showing relative abundance of Ru, Ir and Os minerals, and absence of distinct Rh, Pt and Pd phases. The most abundant PGM is laurite (RuS_2), accompanied by minor erlichmanite (OsS_2) and irarsite (IrAsS). Native Os and other unidentified PGE-sulfides (Ir-Rh-S, Ir-Ni-Fe-Cu-S, Ir-Os-Ru-As-S) were also observed. Microprobe analyses (Table 4) show that minor amounts of Rh and Pd and variable amounts of Ni, Fe and Cu are carried in laurite and erlichmanite. Minor but consistent amounts of As substitute for S. Distinct arsenic minerals (i.e. irarsite) were identified, but could not be quantitatively analyzed because of their small grain size. These PGM are usually less than 10μm in size. They are euhedral and occur as inclusions either in fresh chromite (Fig. 8A, B) or in ferrian chromite (Fig. 8E), locally in contact with fractures (Fig. 8D). More rarely, they are found in a chlorite matrix filling cracks in the massive chromite (Fig. 8C). Most of the PGM form single phase grains, however some form composite inclusions with primary silicates (clinopyroxene, amphibole), or occur associated with secondary minerals (chlorite, Ni-sulfides, chalcopyrite) in the altered matrix of the chromitites. Native Os was only qualitatively identified. It was found as minute particles (<1μm in size) attached to the external border of laurite (Fig. 8E), or enclosed within NiS-CuS composite grains (Fig. 8F), the texture suggesting that osmium is a low-temperature exsolution product from laurite.

Sulfides of the laurite-erlichmanite series do not show significant compositional variations in relation to their textural association with primary magmatic (chromite, clinopyroxene, amphibole) or secondary alteration minerals (ferrian chromite, chlorite), as is common for altered laurite (Zaccarini et al., 2005). On the contrary, they have similar Ru-Os-Ir relationships regardless of their paragenetic association (Fig. 9).

DISCUSSION

Origin of chromite compositional variations at Santa Elena

Major compositional variations of chromite in Santa Elena chromitites involve sharp negative correlations of Al and Ti vs. Cr, and illustrate continuous trends between Cr-rich/Ti-poor and Al-rich/Ti-rich compositional end members.

According to theoretical predictions (Maurel and Maurel, 1982), high-Cr chromite crystallizes from less aluminous melts (picritic or boninitic basalts) than high-Al chromite (normal MORB). The coexistence of Al-rich and Cr-rich chromitites within the same ophiolite complex has been observed worldwide (e.g. Leblanc and Nicolas, 1992; Zhou and Bai, 1992; Leblanc, 1995; Melcher et al., 1997; Proenza et al., 1999; Savelieva, 2004; Kocks et al., 2007; Rollinson, 2008; Uysal et al., 2007; 2009b). In places, a clear bimodal distribution and vertical zoning are observed (Leblanc and Nicolas, 1992), the Cr-rich type being located in the deep mantle section, and the Al-rich type occurring higher in the stratigraphy, close to the Moho transition, with stratigraphic distances not less than 1-2km. This may reflect: 1) separate intrusions of magmas derived from differently depleted mantle sources (e.g.: MORB vs. boninite), during regression of the oceanic lithosphere from the MOR towards supra subduction zone regions; 2) mixing of different magmas produced by multi-stage melting of a partially re-fertilized and fluid-metasomatized residual source, in supra subduction zone regions; 3) reaction of a single parental melt (boninitic) with country-rock peridotites having variable residual character; 4) fractional precipitation during differentiation of a single melt with initial high-Cr boninitic composition in supra subduction zone regions. All mechanisms require quite a large space-time gap for the formation of Al-rich and Cr-rich chromitites coexisting within the same mantle, except for mechanism 4, which can occur in relatively short times and narrow spaces.

At Santa Elena, Cr and Al-rich chromitites occur in close vicinity, not separated by relevant faults, with estimated distances of less than 100 meters. The continuous variation from the Cr-rich to intermediate and aluminous compositions is interpreted as due to the fractionation of

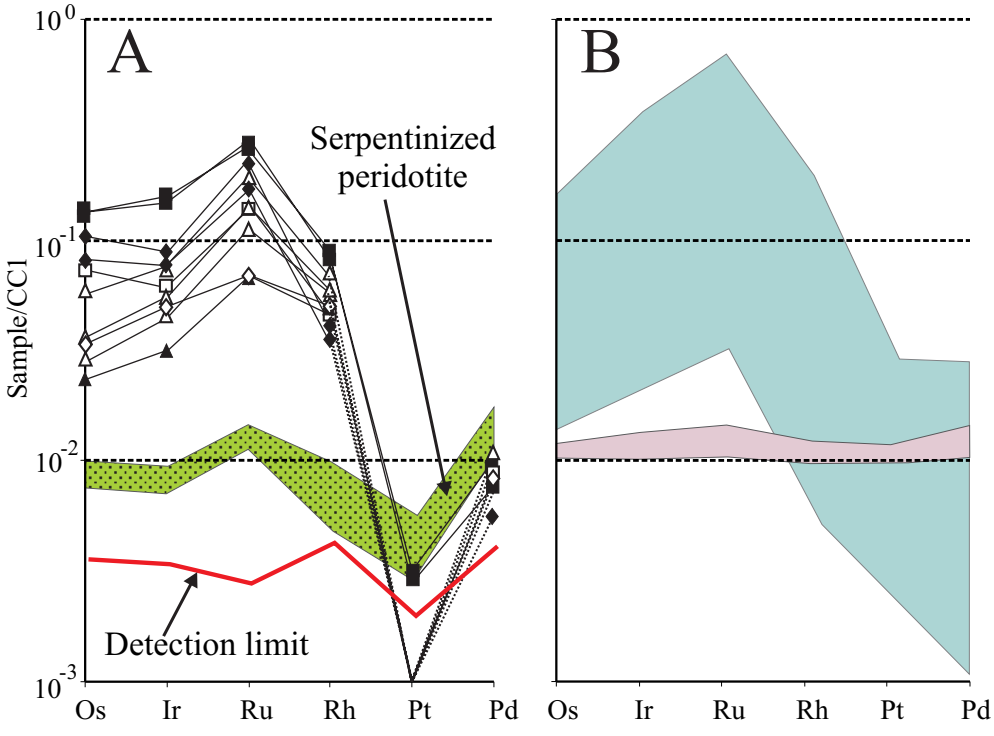

FIGURE 7 | **A) Chondrite-normalized patterns of chromi tite and partially altered peri dotite (dotted green area) from Santa Elena; normalization values from Naldrett and Duke (1980) are shown in Table 3. B) PGE chondritic patterns for Cr-rich ophiolitic chromitite from supra subduction zone setting (blue field) and host peridotite (purple field). Data source include: Economou-Eliopoulos (1996), Kocks et al. (2007), Uysal et al. (2007; 2009a, b), Melcher et al. (1998), Garuti et al. (2005), Proenza et al. (1999), and Zhou et al. (1998).**

TABLE 4 | **Representative composition of minerals of laurite-erlichmanite series in the Santa Elena chromitites**

Wt%	Os	Ir	Ru	Rh	Pt	Pd	S	As	Cu	Fe	Ni	Total
d.l.	0.8	0.1	0.02	0.01	0.1	0.02	0.01	0.05	0.04	0.02	0.04	
Enclosed in chromite												
jag2-2-3-1	2.16	9.39	43.26	3.15	b.d.l.	2.77	35.13	3.12	0.40	0.97	0.58	100.93
jag5-1-4-1	26.32	4.59	28.58	0.67	b.d.l.	1.45	32.83	1.19	0.07	2.06	2.07	99.83
jag5-2-2-3	23.61	7.40	30.92	0.65	b.d.l.	1.53	32.46	1.21	0.11	1.28	0.25	99.42
jag6-1-2-1	23.00	1.57	37.27	0.83	b.d.l.	1.88	34.20	1.47	0.13	0.80	0.13	101.28
jag6-1-2-2	22.09	1.90	37.48	0.79	b.d.l.	1.87	34.62	1.45	0.05	0.73	0.06	101.04
In contact with chlorite and ferrian chromite												
jag1-1-1-1	13.24	5.84	39.99	1.79	b.d.l.	2.12	34.11	1.68	0.04	0.78	0.15	99.74
jag4-2-2-1	10.87	4.38	41.41	4.18	b.d.l.	3.10	35.15	2.03	0.10	0.71	0.11	102.04
jag4-2-2-2	12.27	4.45	40.20	3.95	b.d.l.	2.99	34.38	1.84	0.06	0.91	0.14	101.19
jag6-3-5-1	46.47	4.28	16.13	0.59	b.d.l.	0.79	28.63	0.61	0.06	0.99	0.08	98.63
jag6-3-5-2	20.77	3.72	35.98	1.95	b.d.l.	2.09	31.16	1.75	0.09	0.92	0.06	98.49
jag1-1-3-1	20.38	10.28	30.33	1.76	b.d.l.	1.70	32.51	1.57	0.16	0.56	0.16	99.41
jag2-1-2a-1	17.14	9.04	34.19	2.27	b.d.l.	2.48	33.47	1.96	0.12	0.41	0.13	101.21
jag6-1-3-1	13.31	1.96	45.45	1.14	b.d.l.	2.35	35.82	1.85	b.d.l.	0.53	b.d.l.	102.41
jag6-1-3-2	13.03	2.13	45.45	1.12	b.d.l.	2.39	35.64	1.77	b.d.l.	0.52	0.07	102.12
jag6-1-3-3	15.98	1.60	42.80	1.11	b.d.l.	2.16	34.56	1.81	b.d.l.	0.52	0.08	100.62
At%	Os	Ir	Ru	Rh	Pt	Pd	S	As	Cu	Fe	Ni	
Enclosed in chromite												
jag2-2-3-1	0.66	2.85	24.95	1.78	b.d.l.	1.52	63.87	2.42	0.36	1.01	0.58	
jag5-1-4-1	8.77	1.51	17.92	0.41	b.d.l.	0.86	64.88	1.01	0.07	2.34	2.23	
jag5-2-2-3	8.03	2.49	19.78	0.41	b.d.l.	0.93	65.45	1.05	0.11	1.48	0.28	
jag6-1-2-1	7.43	0.50	22.65	0.49	b.d.l.	1.09	65.51	1.21	0.12	0.88	0.14	
jag6-1-2-2	7.10	0.60	22.67	0.47	b.d.l.	1.07	66.00	1.18	0.05	0.80	0.06	
In contact with chlorite and ferrian chromite												
jag1-1-1-1	4.25	1.86	24.18	1.06	b.d.l.	1.22	65.01	1.37	0.04	0.85	0.15	
jag4-2-2-1	3.36	1.34	24.12	2.39	b.d.l.	1.72	64.53	1.59	0.09	0.74	0.11	
jag4-2-2-2	3.87	1.39	23.84	2.30	b.d.l.	1.68	64.27	1.47	0.05	0.97	0.15	
jag6-3-5-1	17.96	1.64	11.73	0.42	b.d.l.	0.54	65.63	0.60	0.07	1.30	0.10	
jag6-3-5-2	7.15	1.27	22.68	1.24	b.d.l.	1.29	63.61	1.53	0.09	1.08	0.07	
jag1-1-3-1	6.94	3.46	19.44	1.11	b.d.l.	1.03	65.67	1.36	0.16	0.65	0.17	
jag2-1-2a-1	5.62	2.94	21.11	1.38	b.d.l.	1.45	65.15	1.63	0.11	0.46	0.14	
jag6-1-3-1	4.08	0.59	26.23	0.65	b.d.l.	1.29	65.16	1.44	b.d.l.	0.56	b.d.l.	
jag6-1-3-2	4.01	0.65	26.32	0.64	b.d.l.	1.31	65.07	1.38	b.d.l.	0.54	0.07	
jag6-1-3-3	5.06	0.50	25.51	0.65	b.d.l.	1.22	64.94	1.46	b.d.l.	0.56	0.08	

d.l. = detection limit, b.d.l. = below detection limit

a single batch of magma which was rapidly differentiating over short distances (mechanism 4). This model is further supported by the behavior of Ti. Santa Elena chromitites have a maximum Ti content similar to ophiolitic chromitites (<0.30wt% TiO_2, Dickey, 1975). However, Ti decreases continuously from the most aluminous samples down to the most Cr-rich ones, showing a sharp negative correlation with the Cr/Al ratio. This feature is not commonly observed in chromitite deposits of the Tethyan and Urals ophiolite belts. There, the Ti content may vary largely from Al-rich and Cr-rich chromitites, although the two types usually plot in separate fields without a clear differentiation trend (Zaccarini, 2005; Garuti et al., 2005).

Composition of the chromitite parental melt and geodynamic setting

The Cr/Al ratio in basaltic melts is a function of the degree of depletion of the mantle source, thus the ratio Cr/(Cr+Al) of chromite that crystallizes is an indirect reflection of the different geodynamic setting of magma formation (Irvine, 1967; Dick and Bullen, 1984; Roeder, 1994; Barnes and Roeder, 2001). Reciprocal variation of TiO_2 and Al_2O_3 in chromite helps to discriminate among spinels generated by MORB, OIB, and arc-related basaltic melts, as well as those from residual peridotite in supra subduction zone or MOR settings. Kamenestky et al. (2001) and Rollinson (2008) have shown that the

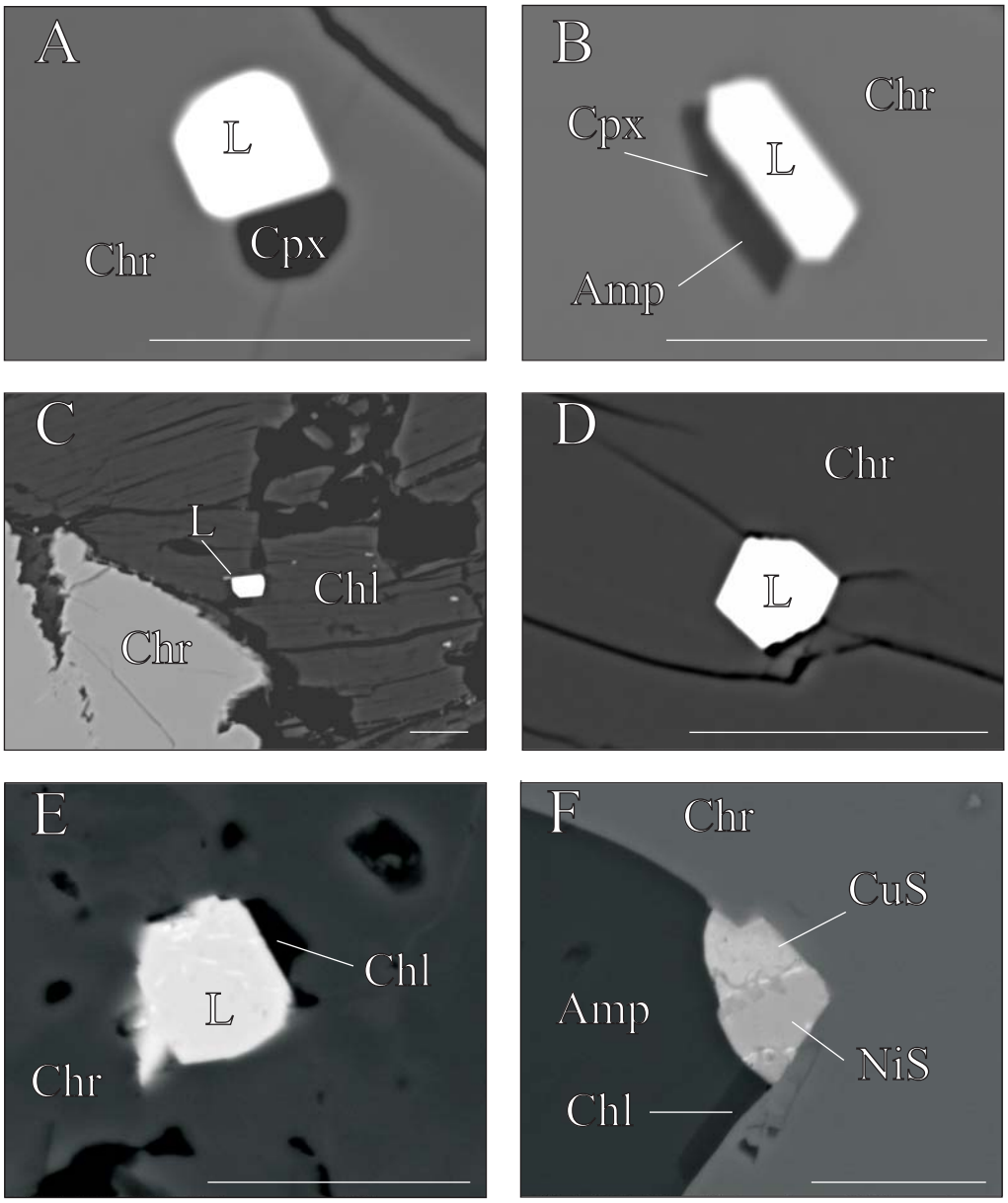

FIGURE 8 | **Back scattered electron images of Platinum-group minerals associated with the chromitites of Santa Elena. L: laurite (RuS_2). White spot visible in E and F are due to an Os bearing phase, possibly native Os. Scale bar = 10µm.**

array of MORB-type chromian spinel defines a roughly negative correlation trend in the TiO_2 vs. Al_2O_3 plot (Fig. 10). In contrast, Santa Elena chromites display a positive TiO_2-Al_2O_3 trend similar to spinels with an island arc basalt affinity and unequivocally fit the field of chromites from supra subduction zone residual peridotites, with only a few Ti- and Al-rich samples from the locality Jag-5 entering the MORB field (Fig. 10).

Using the approach of Rollinson (2008) and data from Kamenetsky et al. (2001), we have estimated the Al_2O_3 and TiO_2 contents of melts in equilibrium with the Santa Elena chromites (Table 2). Al_2O_3 and TiO_2 data for spinels and silicate melts from MOR and arc settings in Table 3 of Kamenetsky et al. (2001) were treated with the Excel Trend-Line software. They yielded best-fitting logarithmic expressions in all cases (R^2=0.68÷0.97), except for the $TiO_{2(melt)}$ vs. $TiO_{2(spinel)}$ in arc settings which show a linear regression line with R^2=0.91. When plotted on the regression lines, only samples from Jag-5 overlap the Al_2O_3 poor end of the MORB regression line, all the others lie on the arc regression line or in the transition zone (Fig. 11A). Similarly, the calculated melts of the chromitites display an arc affinity in the $TiO_{2(melt)}$ vs. $TiO_{2(spinel)}$ diagram, although the two fields largely overlap in their transition zone (Fig. 11B).

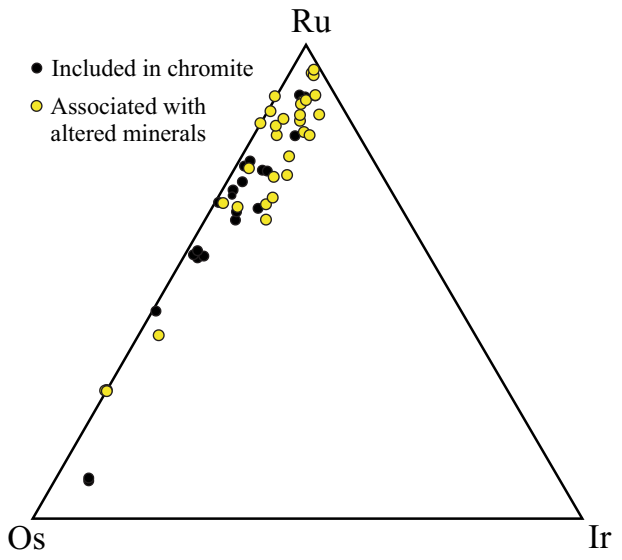

FIGURE 9 | **Electron microprobe composition (Atomic %) of Platinum-group mineral sulfides of the laurite-erlichmanite series, associated with the chromitites of Santa Elena. Both suites of PGM included in chromite or associated with altered minerals show consistent composition.**

Rollinson (2008) has shown that Al-rich and Cr-rich chromitites within the same mantle section of the Oman ophiolite complex may have derived from successive intrusions of MORB and boninitic magmas, characterized by distinct intervals of change in Al_2O_3 concentrations. In contrast, the parental melts of Santa Elena chromitites define a continuous trend from Al_2O_3-poor to relatively Al_2O_3-rich compositions (Figs. 11A and B), and suggest differentiation of a single melt with an initial composition well within the arc field.

Control on Platinum Group Elements distribution and Platinum Group Minerals mineralogy in Santa Elena chromitites

There is a general consensus that high-Cr (Cr/(Cr+Al)>0.70) podiform chromitites that crystallized from boninitic melts in supra subduction zone settings have PGE patterns characterized by high (Os+Ir+Ru)/(Rh+Pt+Pd) ratios and have very low Pd+Pt content (Economou-Eliopoulos, 1996; Zhou et al., 1998; Proenza et al., 1998, 1999; Melcher et al., 1999). Conversely, high-Al (Cr/(Cr+Al)<0.60) chromitite precipitated from MORB may be extremely depleted in PGE with respect to the Cr-rich, having overall flat, or slightly negative chondritic patterns. These variations are strictly related to sulfur saturation in the melt during chromite precipitation (Naldrett and Von Gruenewaldt, 1989; Leblanc, 1991; Garuti, 2004). Boninites are probably the most sulfur undersaturated mafic magmas, because they have formed from a severely depleted mantle source that has lost most, if not all of its original sulfide phase (Zhou et al., 1998). This implies that the condition of sulfur saturation rarely occurs during crystallization of Cr-rich chromitite within an ophiolitic mantle. In the case of low degrees of melting, the chalcophile Rh, Pt, and Pd (PPGE) are forced to remain in the melt, whereas the high-refractory and siderophile Os, Ir, and Ru (IPGE) are removed from the melt and trapped as nano-sized crystals in precipitating chromite. MORB-like tholeiitic magmas are generated by low degrees of partial melting of primitive mantle. They are believed to be sulfur saturated at the time of their formation, thereby leaving a PGE-bearing sulfide phase in the residual mantle. These melts will generate Al-rich chromitites; generally PGE depleted with slightly negative chondritic patterns (Zhou et al., 1998).

The chondrite-normalized PGE patterns of the Santa Elena chromitites are similar to those of high-Cr chromitites precipitating from boninitic melts (Zhou et al., 1998), regardless of their Cr-rich or Al-rich composition. This similarity supports the view that all the chromitites were derived from a common parental melt with a boninitic PGE signature, but also indicates that there was no apparent fractionation between IPGE and PPGE during melt differentiation and fractional precipitation of the chromitites. We suggest that this was possible if the PGE content of the invading melt precipitating chromite was continuously buffered by reaction with a depleted mantle representing an infinite reservoir of PGE, although at low concentrations, compared with the small volume of infiltrating melt. The observation that the PGE patterns of

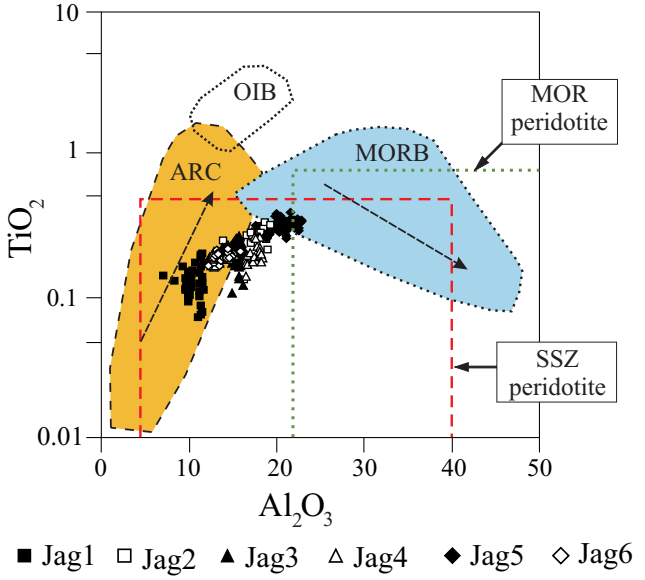

FIGURE 10 | **Al_2O_3-TiO_2 relationships in the chromitites of Santa Elena, compared with compositional fields of spinels from different types of basalts (MORB, OIB, Island Arc) and mantle peridotite in SSZ (supra subduction zone) and MOR settings. Note the contrasting trend in MORB and Island Arc basalts.**

chromitite and mantle peridotite have similar Ru and Pt anomalies strongly supports the hypothesis of melt/country rock interaction.

Mineralogy and textural relations indicate that most of the PGM in the Santa Elena chromitite have crystallized at high magmatic temperatures, prior to or concomitant with precipitation of chromite. Experimental data (Brenan and Andrews, 2001) supported by a large number of natural observations (Augé and Johan, 1988; Melcher et al., 1997; Garuti et al., 1999a, b; Uysal et al., 2007; El Ghorfi et al., 2008; Kapsiotis et al., 2009) indicate that laurite is in equilibrium with Os-Ir-(Ru) alloys at a temperature of 1300°C and relatively low sulfur fugacity. Laurite becomes progressively enriched in Os with decreasing temperature and increasing sulfur fugacity, up to the stability field of erlichmanite. At Santa Elena, the primary mineral assemblage is dominated by sulfides of the laurite-erlichmanite series, suggesting that sulfur fugacity, although well below the sulfur saturation threshold, was as high as to prevent precipitation of Os-Ir-(Ru) alloys at high temperature.

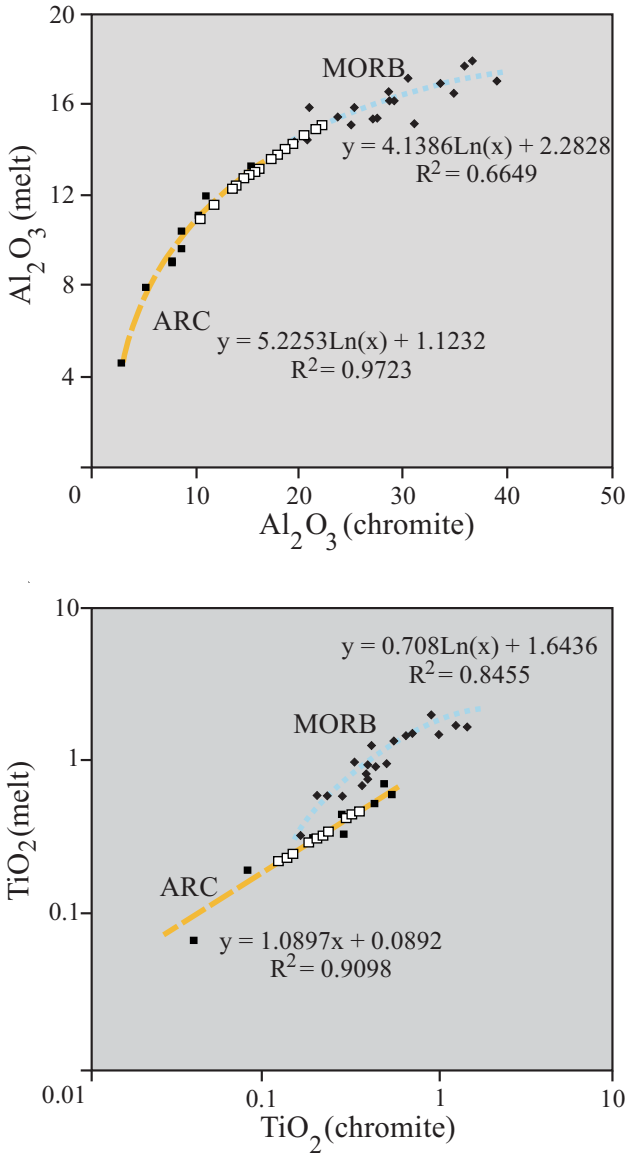

FIGURE 11 | **Graphic plots of calculated Al_2O_3-TiO_2 composition of melts in equilibrium with Santa Elena chromitite (open square, data from Table 2), compared with spinel-melt relationship for MORB (filled square) and ARC (filled diamond) lavas from Table 3, in Kamenetsky et al. (2001). Calculated equations for best fit regression lines are shown.**

This feature may not be readily reconciled with the inferred low sulfur fugacity condition of boninites. If this is the case, then addition of sulfur from an external source has to be admitted to explain the PGM assemblage dominated by sulfides observed in the chromitites of Santa Elena. We suggest that the boninitic melt might have assimilated some relic sulfide phase during interaction within the country rock mantle peridotite.

CONCLUDING REMARKS

1) Morphology and size of the ore bodies coupled with field relations (i.e. contact with peridotite) indicate that the chromitites of Santa Elena are magmatic accumulations of chromite along conduits, extending over a short stratigraphic interval in depleted harzburgitic mantle. Lago et al. (1982) described a mechanism of podiform chromitite in which mafic magmas, derived from a deep mantle source, migrate upward through narrow conduits (<50cm) precipitating chromite in relatively large magma chambers (up to 200m high and 5m thick) within the upper mantle tectonite (Fig. 12A). The thermal gradient between up-streaming melts and country rocks, generates turbulent convective cells, in which pristine chromite nuclei are kept in suspension and can agglomerate to form large chromite aggregates. Coarse chromite aggregates sink to the bottom of the chamber, causing progressive plugging of the conduit with the formation of a massive podiform chromitite body.

2) Santa Elena represents a rare example of podiform chromitites in which chromite composition varies from Cr-rich/Ti-poor to relatively rich in Al and Ti, over a short distance within the same mantle block. This feature suggests that the different chromitites might have derived from the fractional crystallization of a single batch of magma. The injected magma had an initial boninitic composition and yielded high-Cr chromite similar to sample Jag-1 (Fig. 12A). Progressive fractionation of Cr-rich chromite produced a weak Al and Ti enrichment in the residual melt that migrated upward and, by mixing with fresh injected magma, precipitated chromite with a slightly higher Al/Cr ratio and Ti content in a next chamber (Fig. 12A).

3) Important chemical variations in the boninitic melt can also be induced by reaction with the mantle country rock. At Santa Elena, the geochemical behaviour of PGE and the mineralogy of primary PGM inclusions in chromite are strong evidence supporting the influence of a melt/rock interaction process. The initial boninitic melt was sulfur depleted and probably carried significant PGE, as suspended metallic clusters (Tredoux et al., 1995). The lack of fractionation between IPGE and PPGE and the sulphide nature of the PGM indicate that small amounts of sulfur and PGE were continuously supplied to the melt by metasomatic reaction with the depleted mantle (Fig. 12A). The presence of analogous Ru and Pt-Pd anomalies in both the chromitite and the mantle peridotite supports this conclusion.

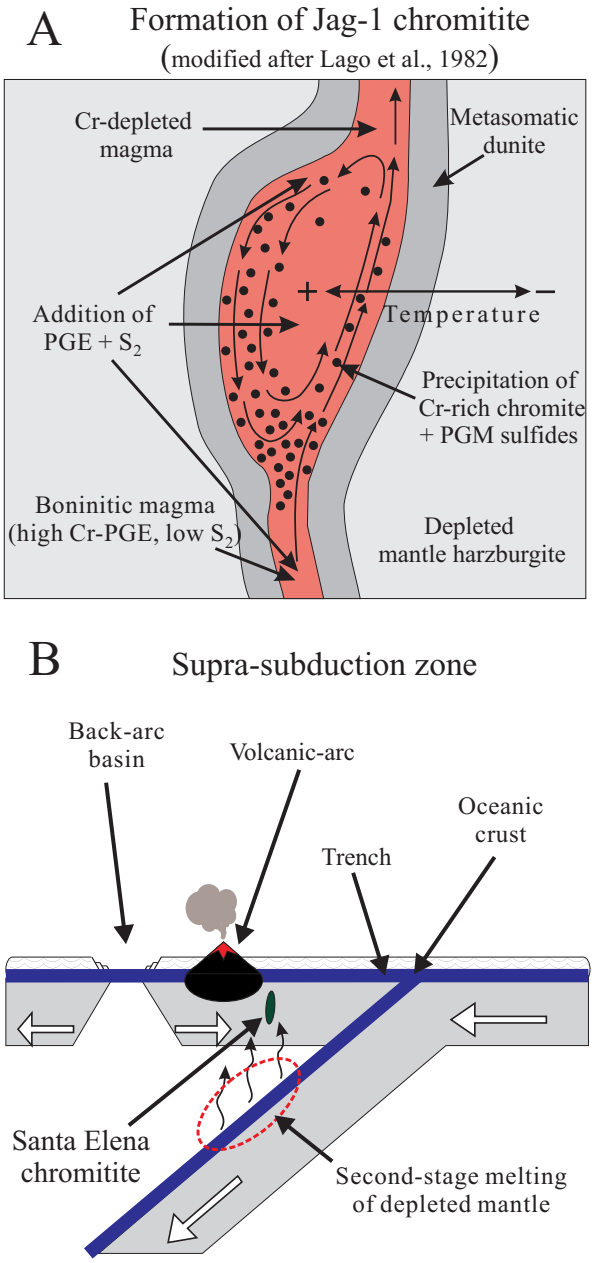

FIGURE 12 | **Synoptic cartoon illustrating A) the mechanism of formation and B) the general geodynamic setting proposed for the origin of small chromitite bodies within the depleted harzburgite mantle of Santa Elena.**

4) Santa Elena chromitites (and their calculated parent melts) have island arc signatures in terms of their TiO_2 vs. Al_2O_3 relation, and correspond to spinels from a supra subduction zone depleted mantle harzburgite, rather than to a MOR type mantle peridotite. These compositional characteristics support the proposition of Gazel et al. (2006) and Denyer and Gazel (2009) that the petrologic evolution of this portion of oceanic lithosphere largely occurred in a supra subduction zone setting (Fig. 12B), apparently independent from intra-oceanic spreading centers or mantle plumes as previously suggested (Beccaluva et al., 1999; Giunta et al., 2006).

ACKNOWLEDGMENTS

The University Centrum for Applied Geosciences (UCAG) is thanked for the access to the E. F. Stumpfl electron microprobe laboratory. Many thanks are due to H. Muehlhans for the sample preparation. We are grateful to R. Blanco and the staff of the National Park of Santa Rosa for their help during the field work. The comments of E. Gazel and T. Grammatikopoulos greatly improved the quality of the manuscript. We also thank A. García-Casco and M. Liesa for handling the manuscript. This research has been partly financed by the grant 2009-SGR444 of the Catalonian Government. This paper is a contribution to IGCP Subduction Zones of the Caribbean.

REFERENCES

Álvarez, J., 1987. Mineralogía y química de los depósitos de cromita podiforme de las dunitas de Medellín, Departamento de Antioquía, Colombia. Boletín Geológico, 33(1-3), 34-46.

Augé, T., Johan, Z., 1988. Comparative study of chromite deposits from Troodos, Vourinos, North Oman and New Caledonia ophiolites. In: Boissonas, J., Omenetto, P. (eds.). Mineral deposits within the European Comunity. Society for Geology Applied to Mineral Deposits, 6 (Special Publications), 267-288.

Barnes, S.J., Roeder, L.P., 2001. The Range of Spinel Compositions in Terrestrial Mafic and Ultramafic Rocks. Journal of Petrology, 42, 2279-2302.

Baumgartner, P.O., Denyer, P., 2006. Evidence for Middle Cretaceuos accretion at Santa Elena Peninsula (Santa Rosa Accretionary complex), Costa Rica. Geologica Acta, 4(1-2), 179-191.

Baumgartner, P.O., Flores, K., Bandini, A.N., Girault, F., Cruz, D.,

2008. Upper Triassic to Cretaceous radiolara from Nicaragua and northern Costa Rica - The Mesquito composite oceanic terrane. Ofioliti, 33, 1-19.

Beccaluva, L., Chinchilla-Chaves, A.L., Coltorti, M., Giunta, G., Siena, F., Vaccaro, C., 1999. Petrological and structural significance of the Santa Elena-Nicoya ophiolitic complex in Costa Rica and geodynamic implications. European Journal of Mineralogy, 11, 1091-1107.

Beeson, M.H., Jackson, E.J., 1969. Chemical composition of altered chromites from the Stillwater Complex, Montana. American Mineralogist, 54, 1084-1100.

Brenan, J.M., Andrews, D.R.A., 2001. High-temperature stability of laurite and Ru-Os-Ir alloys and their role in PGE fractionation in mafic magmas. The Canadian Mineralogist, 39, 341-360.

Buenaventura, J., 2001. Memoria explicativa del mapa de recursos minerales de Colombia: minerales metálicos, preciosos y energéticos a escalas 1:500.000**.** Subdirección de recursos del subsuelo. República de Colombia, Ministerio de Minas y Energía, Instituto de Investigación e Información Geocientífica, Minero Ambiental y Nuclear, Ingeominas, 64pp.

Denyer, P., Baumgartner, P.O., Gazel, E., 2006. Characterization and tectonic implications of Mesozoic-Cenozoic oceanic assemblage of Costa Rica and Western Panama. Geologica Acta, 4(1-2), 219-235.

Denyer, P., Gazel, E., 2009. The Costa Rican Jurassic to Miocene oceanic complexes: origin, tectonics and relations. Journal of South American Earth Sciences, 28, 429-442.

Dick, H.J.B., Bullen, T., 1984. Chromian spinel as a petrogentic indicator in abyssal and alpine-type peridotites and spatially associated lavas. Contributions to Mineralogy and Petrology, 86, 54-76.

Dickey, J.S.Jr., 1975. A hypothesis of origin for podiform chromite deposits. Geochimica et Cosmochimica Acta, 39, 1061-1074.

Economou-Eliopoulos, M., 1996. Platinum group element distribution in chromite ores from ophiolite complexes: implication for their exploration. Ore Geology Reviews, 11, 363-381.

El Ghorfi, M., Melcher, F., Oberthur, T., Boukhari, A.E., Maacha, L., Maddi, A., Mhaili, M., 2008. Platinum group minerals in podiform chromitites of Bou Azzer ophiolite, Anti Atlas, Central Morocco. Mineralogy and Petrology, 92, 59-80.

Flores, K., Baumgartner, P.O., Skora, S., Baumgartner, L., Muntener, O., Cosca, M., Cruz, D., 2007. The Siuna Serpentinite Melange: An Early Cretaceous Subduction/ Accretion of a Jurassic Arc. San Francisco (USA), American Geophysical Union, Fall Meeting 10-14 December 2007, abstract, T11D-03.

Friedrich, G., Brunemann, H.G., Wilcke, J., Stumpfl, E.F., 1980. Chrome spinels in lateritic soils and ultramafic source rocks, Acoje Mine, Zambales, Philippines. In: Jankovic, S., Petrasheck, W.E. (eds.). An International symposium on metallogeny of mafic and ultramafic complexes: the eastern Mediterranean-western Asian area, and its comparison with similar metallogenic environments in the world. Athens, 9-11 October 1980, UNESCO-IGCP n° 1691, 257-278.

Garuti, G. 2004. Chromite-Platinum Group Element magmatic deposits. In: De Vivo, B., Stüwe, K. (eds.). Geology, Encyclopedia of Life Support Systems (EOLSS). Oxford (United Kingdom), UNESCO, Eolss Publisher, http://www.eolss.net.

Garuti, G., Economou-Eliopoulos, M., Zaccarini, F., 1999a. Paragenesis and composition of laurite from the chromitites of Othrys (Greece): implications for Os-Ru fractionation in upper mantle of the Balkan peninsula. Mineralium Deposita, 34, 312-319.

Garuti, G., Pushkarev, E.V., Zaccarini, F., 2005. Diversity of chromite-PGE mineralization in ultramafic complexes of the Urals. In: Törmänen, T.O., Alapieti, T.T. (eds.). Platinum Group Elements – from Genesis to Benefication and Environmental Impact. Oulu (Finland), August 8-11, 10th International Platinum Symposium, extended abstracts, 341-344.

Garuti, G., Zaccarini, F., Moloshag, V., Alimov, V., 1999b. Platinum group minerals as indicator of sulfur fugacity in ophiolitic upper mantle: an example from chromitites of the Ray-Iz ultramafic complex, Polar Urals, Russia. The Canadian Mineralogist, 37, 1099-1115.

Gazel, E., Denyer, P., Baumgartner, P.O., 2006. Magmatic and geotectonic significance of Santa Elena Peninsula, Costa Rica. Geologica Acta, 4(1-2), 193-202.

Giunta, G., Beccaluva L., Siena, F., 2006. Caribbean Plate margin evolution: constraints and current problems. Geologica Acta, 4(1-2), 265-277.

Hauff, F., Hoernle, K., Bogard, van den P., 2000. Age and geochemistry of basaltic complexes in western Costa Rica: Contribution to the geotectonic evolution of Central America. Geochemistry Geophysics Geosystems, 1, doi: 1999GC000020.

Jager-Contreras, G., 1977. Geología de las mineralizaciones de cromita al Este de la Peninsula de Santa Elena, Provincia de Guanacaste, Costa Rica. In Spanish. Doctoral Thesis. San José (Costa Rica), University of Costa Rica, 136pp.

Kapsiotis, A., Grammatikopoulos, T., Tsikouras, V., Hatzipanagiotou, Zaccarini, F., Garuti, G., 2009. Chromian spinel composition and Platinum group element mineralogy of chromitites from the area of Milia, Pindos ophiolite complex, Greece. The Canadian Mineralogist, 47, 883-902.

Kamenetsky, V.S., Crawford, A.J., Meffre, S., 2001. Factors controlling chemistry of magmatic spinel: an empirical study of associated olivine, Cr-spinel and melt inclusions from primitive rocks. Journal of Petrology 42, 655-671.

Kocks, H., Melcher, F., Meisel, T., Burgath, K.-P., 2007. Diverse contributing sources to chromite petrogenesis in the Shebenik Ophiolitic Complex, Albania: evidence from new PGE- and Os-isotope data. Mineralogy and Petrology, 91, 139-170.

Kuipjers, E.P., Jager-Contreras, G., 1979. Mineralizaciones de cromita en la Península de Santa Elena, Costa Rica. In Spanish. Ciencia Técnica, 3, 99-108.

Irvine, T.N., 1965. Chromian spinel as a petrogenetic indicator. Part I. Theory. Canadian Journal of Earth Sciences, 2, 648-672.

Irvine, T.N., 1967. Chromian spinel as a petrogenetic indicator. Part II. Petrological Application. Canadian Journal of Earth Sciences, 4, 71-103.

Lago, B.L., Rabinowicz, M., Nicolas, A., 1982. Podiform chromite ore bodies: a genetic model. Journal of Petrology, 23, 103-125.

Leblanc, M., 1991. Platinum group and gold in ophiolitic complexes: Distribution and fractionation from mantle to oceanic floor. In: Peters, Tj., Nicolas, A., Coleman, R. (eds.). Ophiolite genesis and evolution of the oceanic lithosphere. Ministry of Petroleum and Minerals, Sultanate of Oman, 231-260.

Leblanc, M., 1995. Chromitite and ultramafic rock compositional zoning through a Paleotransform fault, Poum, New Caledonia. Economic Geology, 90, 2028-2039.

Leblanc, M., Nicolas, A., 1992. Ophiolitic chromitites. International Geology Review, 34(7), 653-686.

Maurel, C., Maurel, P., 1982. Étude experimental de la distribution de l'aluminium entre bain silicate basique et spinel chromifere. Implications pétrogenetiques: tenore en chrome des spinelles. Bulletin de Mineralogie, 105, 197-202.

Melcher, F., Grum, W., Simon, G., Thalhammer, T.V., Stumpfl, F.E., 1997. Petrogenesis of the ophiolitic giant chromite deposits of Kempirsai, Kazakhstan: a study of solid and fluid inclusions in chromite. Journal of Petrology, 38, 1419-1438.

Melcher, F., Grum, W., Thalhammer, T.V., Thalhammer, O.A.R., 1999. The giant chromite deposits at Kempirsai, Urals: constraints from trace element (PGE, REE) and isotope data. Mineralium Deposita, 34, 250-272.

Naldrett, A.J., Duke, J.M., 1980. Pt metals in magmatic sulfide ores. Science, 208, 1417-1424.

Naldrett, A.J., von Gruenevaldt, G., 1989. Association of platinum group elements with chromitite in layered intrusions and ophiolite complexes. Economic Geology, 84, 180-187.

Proenza, J.A., Zaccarini, F., Lewis, J.F., Longo, F., Garuti, G., 2007. Chromian spinel composition and the Platinum Group Minerals of the PGE-rich Loma Peguera chromitites, Loma Caribe peridotite, Dominican Republic. The Canadian Mineralogist, 45, 211-228.

Proenza, J.A., Melgarejo, J.C., 1998. Una introdución a la metalogenia de Cuba bajo la perspectiva de la tectónica de placas. Acta Geologica Hispanica, 33, 89-132

Proenza, J.A., Gervilla, F., Melgarejo, J.C., Reve, D., Rodríguez, Y.G., 1998. Ophiolitic chromitites from the Mercedita deposit (Cuba). Example of Al-rich chromites at the mantle-crust transition zone. Acta Geologica Hispanica, 33, 179-212.

Proenza, J.A., Gervilla, F., Melgarejo, J.C., Bodinier, J.L., 1999. Al and Cr rich chromitites from the mayari-Baracoa Ophiolitic Belt, (eastern Cuba): consequence of interaction between volatile-rich melts and peridotite in suprasubduction mantle. Economic Geology, 94, 547-566.

Proenza, J.A., Escayola, M., Ortiz, F., Pereira, E., Correa, A.M., 2004. Dunite and associated chromitites from Medellín (Colombia). Florence (Italy), 32nd International Geological Congress, Abstract volume, CD-ROM.

Rodríguez, S., 1986. Recursos Minerales de Venezuela. Caracas, Boletín del Ministerio de Energía y Minas, 15(27), 215pp.

Roeder, P.L., 1994. Chromite: from the fiery rain of chondrules to the Kilauea Iki lava lake. The Canadian Mineralogist, 32, 729-746.

Rollinson, H., 2008. The geochemistry of mantle chromitites from the northern part of the Oman ophiolite: inferred parental melt composition. Contributions to Mineralogy and Petrology, 156, 273-288.

Savelieva, G.N., 2004. Chromite of the Polar Urals. In Pecchio, M., Andrade, F.R.D., D'Agostino, L.Z., Kahn, H., Sant'Agostino, L.M., TassinarI, M.M.M.L. (eds.). Applied Mineralogy: Developments in Science and Technology. Águas de Lindoia (Brazil), 19-24 September 2004, Proceedings International Congress on Applied Mineralogy ICAM 2004, 943-945.

Stowe, C.W., 1994. Compositions and tectonic settings of chromite deposits through time. Economic Geology, 89, 528-546.

Thayer, T.P., 1946. Preliminary chemical correlation of chromite with the containing rocks. Economic Geology, 41, 202-217.

Thayer, T.P., 1970. Chromite segregations as petrogenetic indicators. The Geological Society of South Africa, 1 (Special Publications), 380-390.

Tournon, J., 1994. The Santa Elena Peninsula: an ophiolitic nappe and a sedimentary volcanic relative autochthonous. Profil, 7, 87-96.

Tredoux, M., Lindsay, N.M., Davies, G., McDonald, I., 1995. The fractionation of platinum group elements in magmatic system, with the suggestion of a novel causal mechanism. South African Journal of Geology, 98, 157-167.

Uysal, I., Zaccarini, F., Garuti, G., Meisel, T., Tarkian, M., Bernhardt, H.J., Sadiklar, M.B., 2007. Ophiolitic chromitites from the Kahramanmaras area, southeastern Turkey: their platinum group elements (PGE) geochemistry, mineralogy and Os-isotope signature. Ofioliti, 32, 151-161.

Uysal, I., Zaccarini, F., Sadiklar, M.B., Tarkian, M., Thalhammer, O.A.R., Garuti, G., 2009a. The podiform chromitites in the Dağküplü and Kavak mines Eskişeir ophiolite (NW-Turkey): Genetic implications of mineralogical and geochemical data. Geologica Acta, 7(3), 351-362.

Uysal, I., Tarkian, M., Sadiklar, M.B., Zaccarini, F., Meisel, T., Garuti, G., Heidrich, S. 2009b. Petrology of Al- and Cr-rich ophiolitic chromitites from the Muğla, SW Turkey: implications from composition of chromite, solid inclusions of platinum group mineral, silicate, and base-metal mineral, and Os-isotope geochemistry. Contributions to Mineralogy and Petrology, 158, 659-674.

Zaccarini, F., 2005. Compositions of chromitite and associated solid inclusions: a key to understanding mantle and derived magmas. In Italian. Doctoral Thesis. Italy, University of Modena and Reggio Emilia, unpublished, 76pp.

Zaccarini, F., Proenza, A.J., Ortega-Gutierrez, F., Garuti, G., 2005. Platinum group minerals in ophiolitic chromitites from Tehuitzingo (Acatlan complex, southern Mexico): implications for post-magmatic modification. Mineralogy and Petrology, 84, 147-168.

Zaccarini, F., Proenza, J.A., Rudashevsky, N.S., Cabri, L.J., Garuti, G., Rudashevsky, V.N., Melgarejo, J.C., Lewis, J.F., Longo, F., Bakker, R., Stanley, C.J., (2009). The Loma Peguera ophiolitic chromitite (Central Dominican republic): a source of new platinum group minerals (PGM) species. Neues Jahrbuch für Mineralogie Abhandlungen, 185(3), 335-349.

Zhou, M.-F., Bai, W.-J., 1992. Chromite deposits in China and their origin. Mineralium Deposita, 27, 192-199.

Zhou, M.-F., Robinson, P.T., 1997. Origin and tectonic environment of podiform chromite deposits. Economic Geology, 92, 259-262.

Zhou, M.-F., Sun, M., Keays, R.R., Kerrich, R.W., 1998. Controls on platinum group elemental distributions of podiform chromitites: A case study of high-Cr and high-Al chromitites from Chinese orogenic belts. Geochimica et Cosmochimica Acta, 62(4), 677-688.

Manuscript received November 2009;
revision accepted February 2010;
published Online June 2011.

Geologica Acta, Vol.9, Nºs 3-4, September 2011, 425-443
DOI: 10.1344/105.000001740
Available online at www.geologica-acta.com

geologica acta

Geochemistry and Geochronology of the Guajira Eclogites, northern Colombia: evidence of a metamorphosed primitive Cretaceous Caribbean Island-arc

M. WEBER [1] [*] **A. CARDONA** [2] [3] **V. VALENCIA** [4] **U. ALTENBERGER** [5] **M. LÓPEZ-MARTINEZ** [6] **M. TOBÓN** [1] **S. ZAPATA** [1] **G. ZAPATA** [1] **A.E. CONCHA** [1]

[1] **Universidad Nacional de Colombia**
Carrera 80 No. 65-223, Medellín, Colombia. Weber E-mail: mweber@unal.edu.com

[2] **Smithsonian Tropical Research Institute**
Balbóa, Ancón, Panamá. E-mail: CardonaA@si.edu

[3] **Corporación Geológica Ares**
Bogotá, Colombia

[4] **Department of Geosciences, The University of Arizona, Gould-Simpson Building**
1040 East Fourth St Tucson, Arizona, USA. E-mail: victorv@email.arizona.edu

[5] **Potsdam Universität**
Karl-Liebknecht-Str. 24; 14476 Potsdam-Golm, Germany. E-mail: uwe@geo.uni-potsdam.de

[6] **Departamento de Geología, Centro de Investigación Científica y de Educación Superior de Ensenada (CICESE)**
Carretera Ensenada Tijuana No 3918, Zona Playitas, Ensenada, Baja California, México 22860. E-mail: marlopez@cicese.mx

* Corresponding author

ABSTRACT

The chemical composition of eclogites, found as boulders in a Tertiary conglomerate from the Guajira Peninsula, Colombia suggests that these rocks are mainly metamorphosed basaltic andesites. They are depleted in LILE elements compared to MORB, have a negative Nb-anomaly and flat to enriched REE patterns, suggesting that their protoliths evolved in a subduction related tectonic setting. They show island-arc affinities and are similar to primitive island-arc rocks described in the Caribbean. The geochemical characteristics are comparable to low-grade greenschists from the nearby Etpana Terrane, which are interpreted as part of a Cretaceous intra-oceanic arc. These data support evidence that the eclogites and the Etpana terrane rocks formed from the same volcano-sedimentary sequence. Part of this sequence was accreted onto the margin and another was incorporated into the subduction channel and metamorphosed at eclogite facies conditions. ^{40}Ar-^{39}Ar ages of 79.2±1.1Ma and 82.2±2.5Ma determined on white micas, separated from two eclogite samples, are interpreted to be related to the cooling of the main metamorphic event. The formation of a common volcano-sedimentary protolith and subsequent metamorphism of these units record the ongoing Late Cretaceous continental subduction of the South American margin within the Caribbean intra-oceanic arc subduction zone. This gave way to an arc-continent collision between the Caribbean and the South American plates, where this sequence was exhumed after the Campanian.

KEYWORDS | **Eclogites. Primitive island-arc. Geochronology. Guajira Peninsula. Colombia. Caribbean.**

INTRODUCTION

High pressure rocks provide an important record of the geodynamic history of convergent margins. They enable the identification of extinct subduction zones and their tectonothermic history allows the characterization of the particular conditions of the tectonic environments of plate convergence (Ernst, 1988).

The geochemistry of eclogites can be used to constrain the tectonic setting in which the protoliths formed prior to being taken into the subduction path (Bocchio et al., 1990; Volkova et al., 2004; Unger et al., 2005), and understanding their origin can yield major insights as to the type of subduction or collisional setting (e.g. Tang et al., 2007). In addition, geochronological data can constrain the timing of the various stages of the tectonic evolution of these rocks (e.g. Stöckhert et al., 1995).

Different high-pressure metamorphosed oceanic and related continental units have been identified around the circum-Caribbean areas. They represent a record of the evolution of intra-oceanic subduction or arc-continent collision between the front of the Caribbean and the North and South American plates (e.g. Sisson et al., 1997; García-Casco et al., 2008; Krebs et al., 2008). Of these, only three locations have been identified along the southern margin of the Caribbean. These are: the Cordillera de la Costa-Margarita belt in Venezuela (Stöckhert et al., 1995; Sisson et al., 1997), the Villa de Cura belt also in Venezuela (Smith et al., 1999; Unger et al., 2005) and the Guajira boulders in a conglomerate in northern Colombia (Lockwood, 1965; Green et al., 1968; Zapata et al., 2005; Weber et al., 2007) (Fig. 1).

In this paper we present new geochemical and geochronological results from studies of the eclogites, found as clasts within proximal Miocene conglomerates, in the Colombian-southern Caribbean region, and greenschists from the nearby Etpana Terrane (Lockwood, 1965; Green et al., 1968; Zapata et al., 2005; Weber et al., 2007) (Fig. 2). Their stratigraphic and tectonic position link them

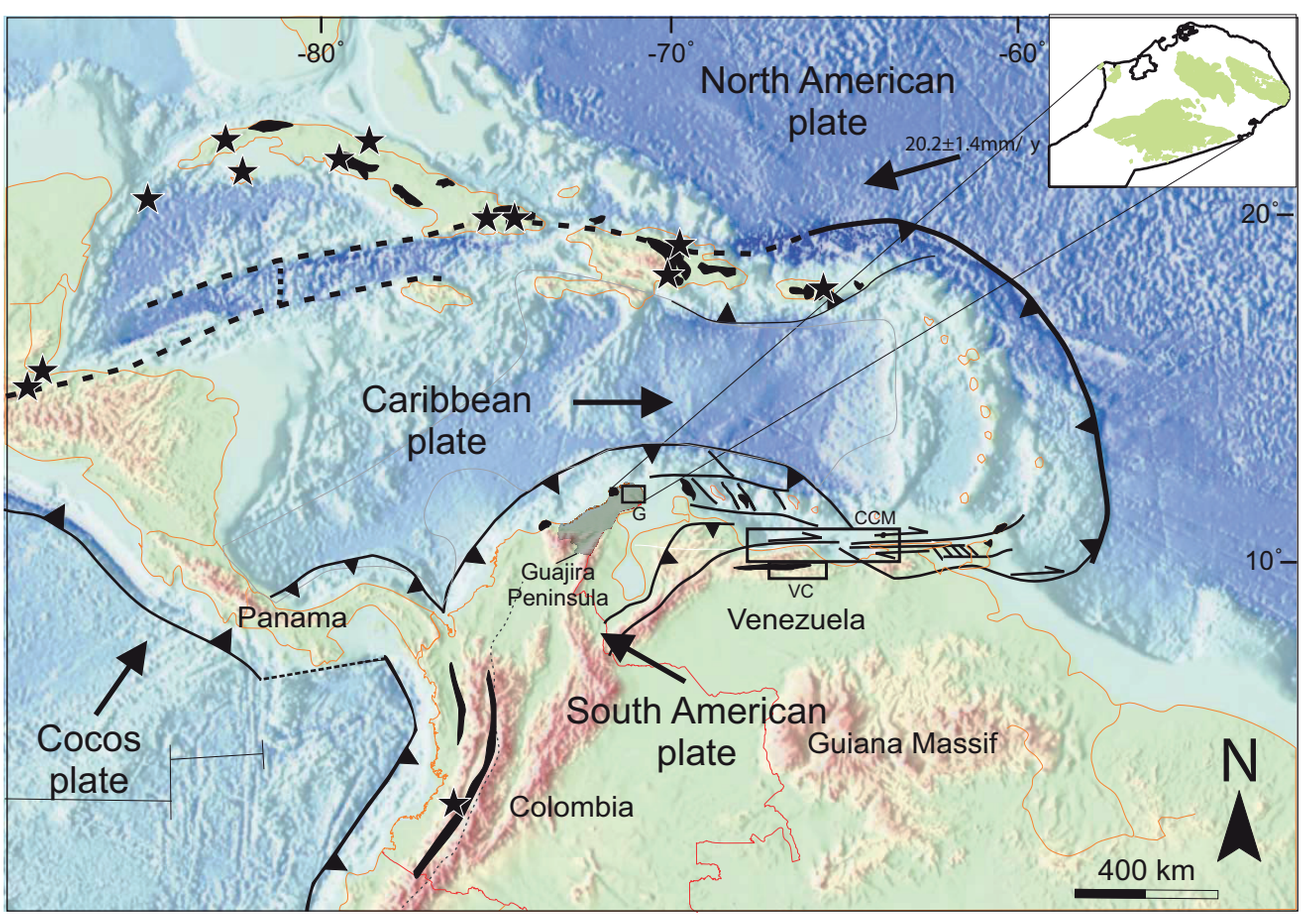

FIGURE 1 | **Present day tectonic framework of the Caribbean region and location of the Guajira Peninsula. The locations of the Cordillera de la Costa-Margarita-belt (CCM), the Villa de Cura belt (VC) and the Guajira (G) are enclosed in squares. Other high-pressure rocks localities are shown with black stars. Allochtonous basaltic provinces are shown in black. The inset shows the northern part of the Guajira Peninsula and the three Serranías. Adapted from Lidiak and Jolly (1996).**

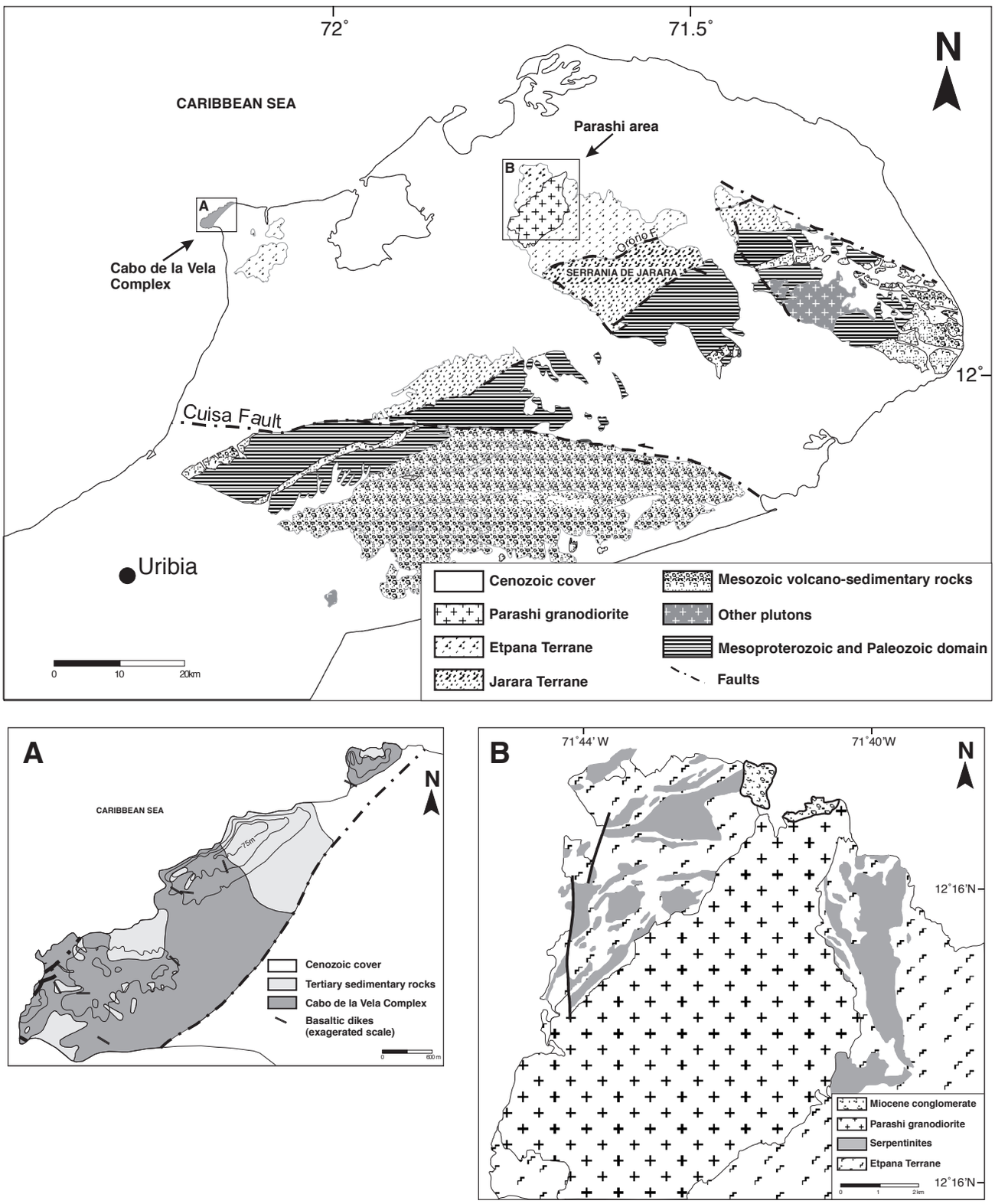

FIGURE 2 | **Simplified geological map of the northern Guajira Peninsula, showing the three main Serranías and the Cabo de la Vela area. The Serranía de Jarara is highlighted. The Parashi granodiorite lies to the northwest of the Serranía. The Etpana and Jarara Terranes and the composite Late-Mesoproterozoic and Palaeozoic metamorphic domain (see text for details) are depicted. Modified from Lockwood (1965) and Gómez et al. (2007). A) The Cabo de la Vela Complex and B) the Parashi area are shown in more detail.**

with the NW allocthonous Caribbean belt. Furthermore, similarities to other high-pressure occurrences within the Caribbean area, provide evidence as to the complexity of the convergence tectonics between the South American and Caribbean plates.

GENERAL GEOLOGY

The Guajira Peninsula, in north-easternmost Colombia (Fig. 2), is characterised by several isolated mountain ranges surrounded by broader flat lands and Cenozoic basins (Alvarez, 1967; Lockwood, 1965; MacDonald, 1964). Within these ranges, at least three main lithotectonic belts can be identified (Fig. 2). From southeast to northwest they include 1) a weakly deformed Mesozoic volcano-sedimentary belt with a typical south American passive autochthonous margin record (Villamil, 1999), 2) an older metamorphic basement, with Proterozoic and Paleozoic rocks intruded by Jurassic granitoids, whose characteristics resemble basement domains of different segments of the Northern Andes (Alvarez, 1967; Aspden et al., 1987; Cordani et al., 2005; Cardona-Molina et al., 2006) and 3) several deformed low grade meta-volcano-sedimentary units that are interpreted as intra-oceanic arcs and subduction-accretion complexes, related to the Caribbean plate evolution, that were probably accreted during the Late Cretaceous (Weber et al., 2009). The northernmost of these units is the Etpana Terrane (elsewhere called Etpana Formation) that comprises low-grade greenschists, phyllites and quartzites, and interspersed serpentinites, rodingites and gabbros (MacDonald, 1964; Lockwood, 1965; Alvarez, 1967; Zuluaga et al., 2008).

Remnants of a mafic to intermediate island-arc to back-arc are exposed immediately to the northwest in the Cabo de la Vela mafic-ultramafic complex (Fig. 2). This island-arc was active at least until ca. 77-74Ma, as indicated by K-Ar whole rock ages on basalt-andesite dikes (Weber et al., 2009). Together the Etpana Terrane and the Cabo de la Vela Complex have been interpreted as elements of the arc-continent collision between the Caribbean plate and the South American margin (Weber et al., 2009). The intrusion of the Parashi Granodiorite at ca. 50Ma defines the lower limit for metamorphism of the Etpana Terrane (Cardona et al., 2007).

Available paleomagnetic constrains have shown that the geologic units in northern South America must have undergone significant block rotation since the Late Jurassic (MacDonald and Opydike, 1974). During the eastern migration of the Caribbean plate in the Neogene, a complex strike-slip system developed in northeastern Colombia and transported tectonic fragments, including the Guajira blocks, from their original position towards the east (Macellari, 1995; Montes et al., 2005; Vence, 2008; Montes et al., 2009).

ANALYTICAL TECHNIQUES

Whole rock geochemistry

Whole rock chemical analyses were carried out at Acme Analytical Laboratories Ltd. in Vancouver, Canada. A 0.2g aliquot is weighed into a graphite crucible and mixed with 1.5g of $LiBO_2$ flux. The crucibles are placed in an oven and heated to 1050°C for 15 minutes. The molten sample is dissolved in 5% HNO_3. Calibration standards and reagent blanks are added to the sample sequence. Sample solutions are aspirated into an Inductively Coupled Plasma-Emission Spectrometer (ICP-ES) (Jarrel Ash Atom Comb 975) for determining major oxides and certain trace elements (Ba, Nb, Ni, Sr, Sc, Y & Zr) in the sample. For determination of the trace elements, including rare earth elements (REE), solutions are aspirated into an Inductively Coupled Plasma-Mass Spectrometry (ICP-MS) (Perkins-Elmer Elan 6000).

Sample EK-K2 was analysed using a Phillips PW-2400 X-ray Fluorescence (XRF) spectrometer at the GeoForschungsZentrum Potsdam (major and trace elements) and REE Inductively Coupled Plasma-Optical Emission Spectrometer (ICP-OES, VistaMPX) at the Geochemical Laboratory of the University of Potsdam.

Ar-Ar geochronology

Argon-Ar analyses were performed on two hand-picked mica samples separated from eclogite samples MJ-033 and MJ-039 at the Geochronology Laboratory of the Departamento de Geología of the Centro de Investigación Científica y de Educación Superior de Ensenada, México. The argon isotope experiments were conducted on mineral grains with a coherent Ar-ion Innova 370 laser extraction system on line with a VG5400 mass spectrometer. All the samples and irradiation monitors were irradiated in the U-enriched research reactor of the University of McMaster in Hamilton, Canada, at position 5C in capsule CIC-66 for 10hr. To block thermal neutrons, the capsule was covered with a cadmium liner during irradiation. As irradiation monitors, aliquots of standard FCT-2 sanidine (27.84±0.04Ma) were irradiated alongside the samples and distributed among them to determine the neutron flux variations. Upon irradiation the monitors were fused in one step while the samples were step-heated. The argon isotopes were corrected for blank, mass discrimination, radioactive decay of ^{37}Ar, ^{39}Ar and atmospheric contamination. For the Ca neutron interference reactions, the factors given by Masliwec (1984) were used.

In processing the data, the decay constants recommended by Steiger and Jäger (1977) were applied. The equations reported by York et al. (2004) were used in all the straight line fitting routines of the argon data reduction. The plateau age was calculated from the weighted mean of consecutive fractions that were in agreement within 1σ. The error in the plateau, and in the integrated and isochron ages includes the scatter in the irradiation monitors. The analytical precision is reported as one standard deviation (1σ). For each sample the relevant ^{40}Ar-^{39}Ar data for all the experiments is presented, and includes the results for the individual steps and the integrated ages. In the table, the fractions selected to calculate the plateau age are identified as well as the fractions ignored in the isochron age calculation. The preferred age is highlighted in bold typeface.

ECLOGITES

Various types of high-pressure rocks, including eclogites, white-mica schists and quartzites are found as rock-clasts up to 20cm in size within a Miocene conglomerate. Studies on the conglomerate have shown that the source of the clasts is proximal, possibly from the nearby Etpana Terrane (Zapata et al., 2010). Nevertheless, no in-situ outcrops of the eclogites and high-pressure metasediments have been found thus far. The eclogites were first described by Lockwood (1965) and preliminary geothermometry was undertaken by Green et al. (1968) and Weber et al. (2007). The selected samples have a variety of compositions and are similar to those described in previous studies, except for sample 2832 (J-291A) described by Green et al. (1968), which contains scapolite and calcite.

In general, all samples are different from one another in detail, but can be divided roughly into two groups: Samples that contain more than 99% omphacite + garnet + rutile (GM-2b, MJ-007B, MJ-043), and a second group of samples that, in addition to these minerals, also contain high proportions of other minerals such as clinozoisite ± kyanite ± mica ± amphibole ± quartz ± sphene (GM-2c, MJ-033, MJ-039, MJ-040, EK-K2). Folded mesoscale banding of garnet-rich and garnet-poor domains is evident in three of the samples (MJ-007B, MJ-033, MJ-039). This suggests that some of the eclogites were formed from layered gabbros. All rocks contain compositionally zoned garnet, with orange cores and lighter coloured pink rims (Fig. 3A). Garnet zonation patterns show Fe-rich cores and Mg-rich rims (Weber et al., 2007).

In the first group, two samples have a porphyroblastic texture defined by garnet crystals within an omphacite matrix (GM-2b, MJ-043), and one sample has a granoblastic texture, with garnet-rich domains interspersed with scarce pyroxene-rich domains (MJ-007B) (Fig. 3B). In all samples garnet is euhedral. Samples GM-2b and MJ-007B show weakly foliated fabrics defined by the omphacite (Fig. 3B), whereas sample MJ-043 is isotropic. Two populations of pyroxene can be identified, a larger one with zonation shown by darker green cores compared to the edges, and a smaller one, that comprises the main matrix foliation (Fig. 3A). In addition to the main minerals, sample GM-2b contains <1% of white mica within the matrix. A small degree of retrogression to green amphibole, chlorite and sphene is evident in sample MJ-007B (Fig. 3B).

Of the second group, in which additional mineral phases are present, three samples contain Ky (MJ-033, MJ-039, EK-K2) as an important part of the assemblage (Fig. 3C). Other minerals present are quartz ± clinozoisite ± white mica ± talc. In general the textures comprise porphyroblastic garnets in a weakly foliated matrix. Two samples display compositional banding (Fig. 3D): Sample MJ-039 has quartz-white mica bands intercalated with garnet + omphacite + amphibole bands (Fig. 3C), whereas sample MJ-033 has complex folded intercalations of garnet-rich, omphacite-rich, quartz-rich and kyanite-rich bands. Garnet in all samples is euhedral. Kyanite crystals are porphyroblasts, often with inclusion free cores and poikilitic rims that suggest two generations of crystal growth. Sample retrogression is evident in kyanite porphyroblasts that are almost totally replaced by a fine mass of white mica. Textures composed of white micas and quartz in sample MJ-039 suggest that they are pseudomorphs after a previous tabular mineral phase.

Sample GM-2c is a retrogressed eclogite with a heterogranular texture containing garnet + omphacite + rutile + quartz as the peak metamorphic assemblage. There is conspicuous evidence of two consecutive retrogression events. In the first event, poikilitic clinozoisite laths reaching 1.7cm along with colorless amphibole (Fig. 3E) are interpreted to have formed in the Guajira during the exhumation of these rocks (Weber et al., 2005). About 60% of the rock was replaced by this process. The second event is defined by the breakdown of garnet to form the assemblage to chlorite + white mica + amphibole + quartz, indicating that these rocks retrogressed through the amphibolite facies (Weber et al., 2005).

Sample MJ-040 is a heterogranular eclogite containing 15% of clinozoisite. Replacement textures in garnets and clinozoisite (Fig. 3F) suggest that omphacite grew after these two minerals crystallized.

$^{40}Ar/^{39}Ar$ age determinations

White micas from two eclogite samples (MJ-033 and MJ-039) were selected for ^{40}Ar-^{39}Ar step heating analyses. Results are presented in Figure 4 and Tables 1A and 1B.

White mica from sample MJ-033 yields a well-defined plateau age spectra with about 70% of the released ^{39}Ar during three steps. The calculated plateau age of 79.2±1.1Ma is consistent with the isochron age of 77.3±1.5Ma (Fig. 4A). Ca/K ratios derived from the $^{37}Ar/^{39}Ar$ show that the obtained plateau may come from a relatively homogeneous reservoir, whereas in the last steps the ages become a little younger and fall away from the plateau. The high Ca/K ratios suggest the presence of a potential Ca-bearing phase, probably inclusions of

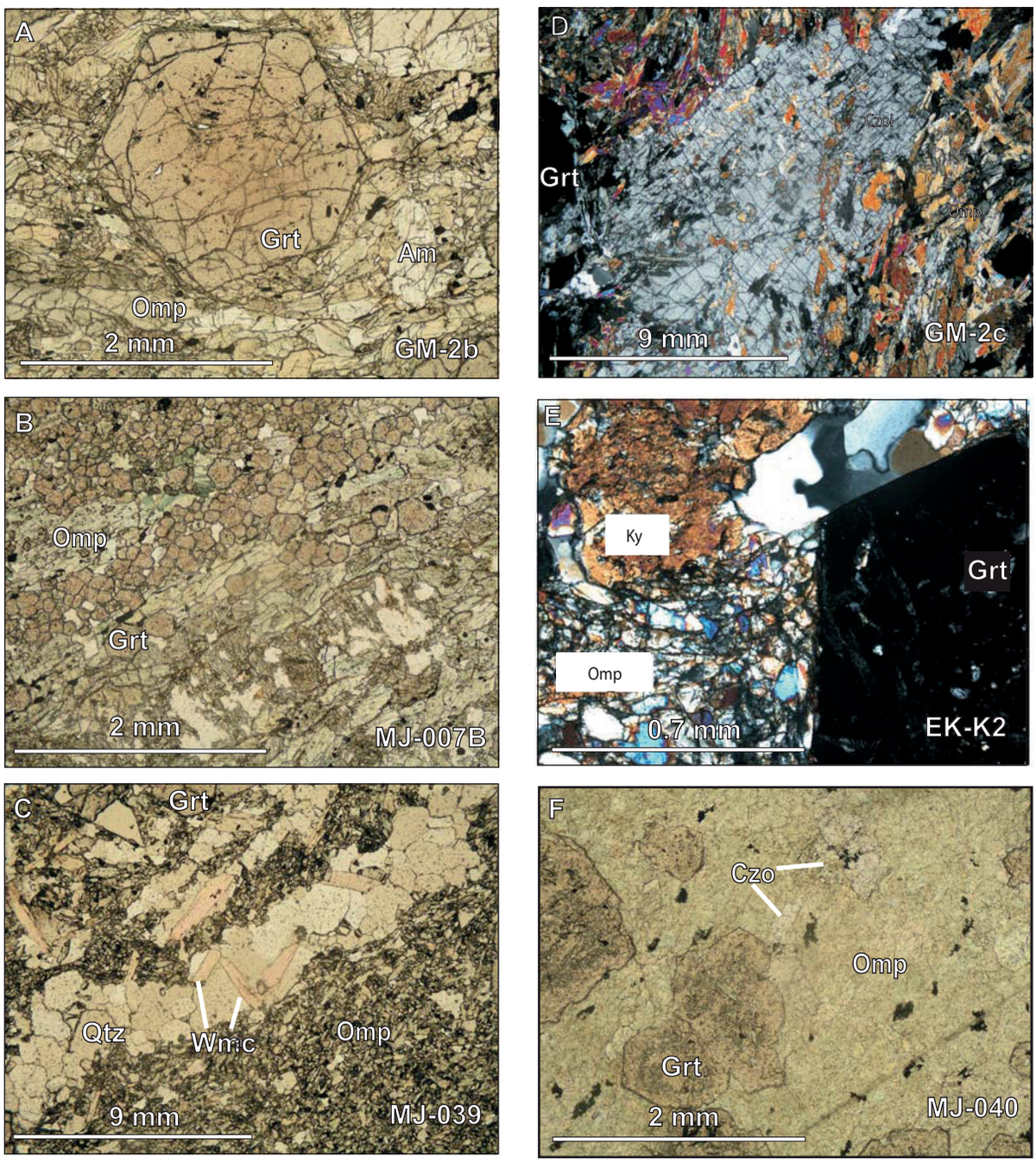

FIGURE 3 | **Microphotographs from various eclogite samples from the Guajira location. A) Garnet idioblast in a foliated omphacite matrix. Zonation is shown by garnet, and the larger omphacite crystals. PPL. B) Compositional banding defined by garnet-rich and omphacite-rich domains. PPL. C) Compositional banding defined by quartz + mica-rich domains interspersed with omphacite + garnet-rich domains. PPL. D) Clinozoisite replacement in the matrix of one of the Guajira eclogite samples. XPL. E) Kyanite-bearing eclogite with garnet idioblasts and omphacite. F) Heterogranular eclogite sample. Note the irregular edges of the garnet and particularly the clinozoisite. PPL. Abbreviations (after Kretz, 1983); Czo: clinozoisite, Grt: garnet, Omp: omphacite, Qtz: quartz, Wmca: white mica.**

minerals such as clinozoisite and sphene, which have been observed petrographically.

Muscovite from sample MJ-039 also shows an age spectra in which 85% of the ^{39}Ar was released in two intermediate stages (Fig. 4B). Ca/K ratios are also homogeneous, although in the other heating stages there is evidence of some mix with high Ca phases. The plateau age of 82.2±2.5Ma is close to the calculated isochron age of 81.6±2.7Ma (Fig. 4B).

Closure temperatures for white mica in the Ar-Ar system have conventionally been considered to lie between 325° and 375°C (McDougall and Harrison, 1999). Recent experiments have suggested that temperatures may be as high as 425°C (Harrison et al., 2009). In the case of the analysed micas from the Guajira eclogites, initial calculated temperatures are above 700°C (Weber et al., 2005), consequently the Ar-Ar ages are possibly related to the cooling of the last metamorphic event, and therefore might be linked to the exhumation path.

Geochemistry

Seven samples were analysed for major and trace element geochemistry. Analyses are presented in Table 2.

Figure 5 shows variation diagrams of selected elements versus Zr. Zirconium has been plotted against other elements as it is accepted as immobile during alteration (Humphris and Thompson, 1978; Staudigel et al., 1996). In general, elements considered as compatible are well correlated with Zr, whereas elements such as K_2O, Ba and Rb, which are considered as incompatible, show some degree of scatter. Sample MJ-043 has high Zr contents and in general plots away from the overall trend, indicating possible differences in the chemistry of the protolith.

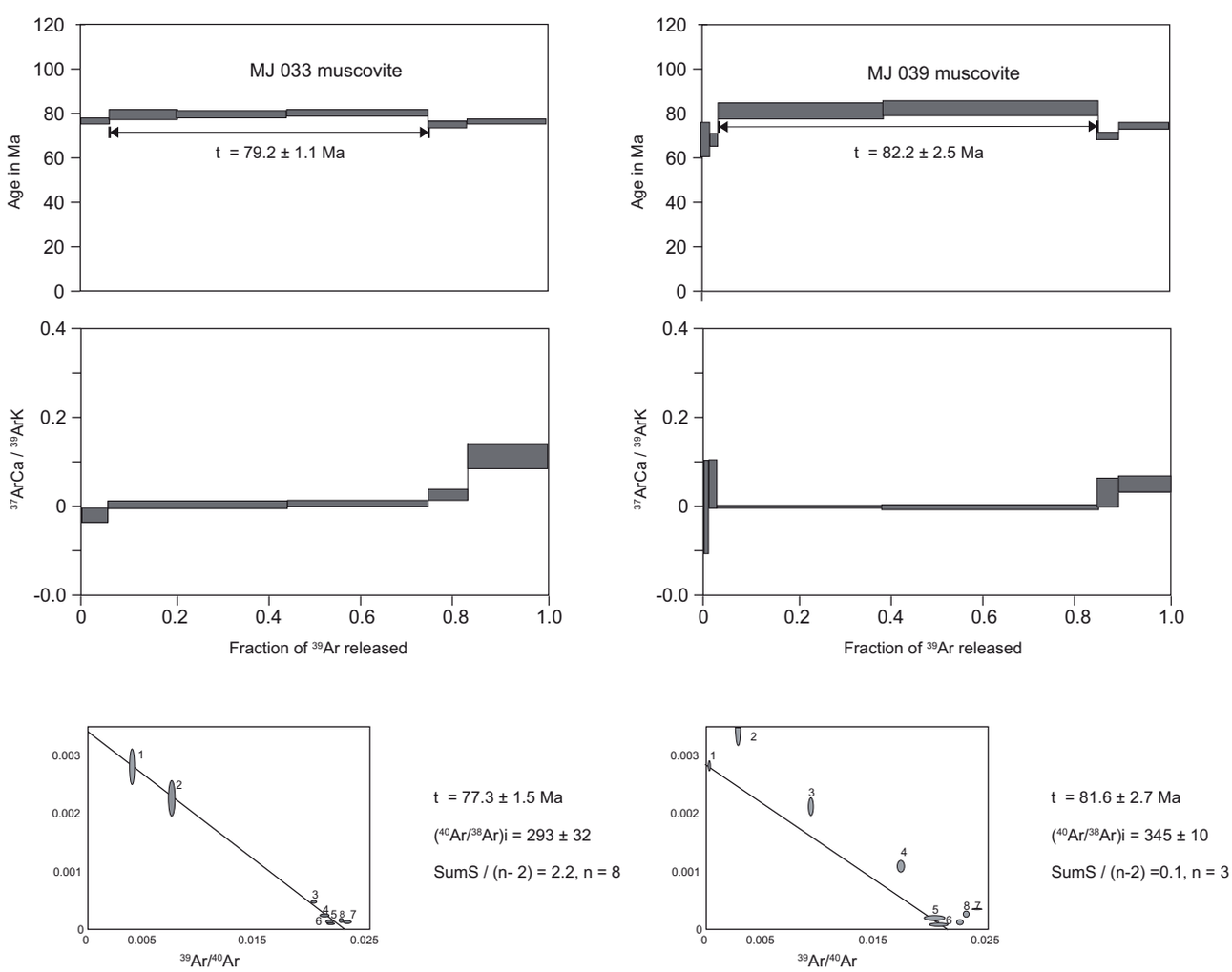

FIGURE 4 | **White mica $^{40}Ar/^{39}Ar$ incremental step heating spectra for eclogite samples MJ-033 and MJ-039 from the Guajira area.**

TABLE 1 | **Geochemical data for Guajira samples**

	Eclogite							Greenschist	
Sample	EK-K2	GM-2b	GM-2c	MJ007B	MJ033	MJ040	MJ043	GUA24A	GUA24B
SiO_2	50.4	48.08	49.16	45.35	53.84	47.15	47.17	54.77	50.51
TiO_2	1.21	1.54	1.21	1.17	1.37	0.77	3.58	0.81	1.12
Al_2O_3	14.2	14.1	17.54	14.67	15.88	15.85	15.32	13.63	16.46
Fe_2O_3	12.11	14.29	12.11	18	12.03	12.48	15.36	9.41	10.74
MnO	0.155	0.21	0.15	0.4	0.22	0.27	0.14	0.17	0.2
MgO	6.51	6.88	4.96	6.1	5.85	5.63	5.33	6.38	4.64
CaO	9.76	10.08	9.76	10.29	7.09	13.96	8.37	9.27	8.48
Na_2O	4.04	4.59	4.12	3.09	3.27	3.85	4.64	0.51	4.12
K_2O	0.03	0.04	0.34	0.02	0.13	0.01	0.01	1.05	0.42
P_2O_5	0.1	0.02	0.11	*	0.14	0.02	0.32	0.14	0.28
Cr_2O_2				0.008	0.018	0.016	0.052	0.022	
LOI	1.31	0.1	0.3	0.7	0.1	0.3	0.6	3.6	2.8
Total	99.75	100.01	100	99.78	99.77	99.74	99.73	99.79	99.82
Ba	53	72	77.8	28	36	27	11	203	57
Rb		0	8	0.6	3.5	0.6	0.5	20.3	7
Sr	37	37.2	258.8	19.3	85.6	525.7	177.2	146	152.1
Cs		0	0.4	*	*	*	*	0.4	*
Ga	14	15	17.7	10.9	16.4	13.1	20.5	14.2	15
Ta		0.2	0.1	0.3	*	*	1.9	*	*
Nb	4	3.3	1.7	5.4	2.1	0.7	24.7	1	1.4
Hf		3.9	2.2	2.8	2.2	1.2	6.2	1.5	2
Zr	67	113.2	68.3	85	72.9	42.2	232.8	44.2	67.9
Y	23	43.7	27.7	66.2	26	20.1	32.4	21.6	24.9
Th		0.9	0.4	0.9	0.5	0.8	2.4	0.5	0.9
U		0.5	0.2	0.4	0.3	0.2	0.7	0.2	0.4
La/Nb	1.05	2.3	2.82	1.04	2.62	7.14	0.91	3.3	3.93
Cr	49	*	*	*	*	*	*	*	*
Ni	103	727	1407.5	42.6	4.8	9.6	19.4	22.5	23.1
Co		38.1	39.7	23.9	34.3	30.6	42.9	23.9	29.2
Sc	46.82	32	31	48	36	41	41	32	31
V		406	334	304	371	342	318	258	273
Cu		6.9	33.7	16.5	32.1	18.3	78.9	67.9	38.3
Pb		0.2	0.5	1	0.6	1.3	0.9	1.7	0.9
Zn	68	13	8	12	11	5	14	33	55
Bi		0	0	*	*	*	*	*	*
Cd		0.1	0	*	*	*	*	0.1	*
Sn		1	1	1	*	*	2	*	*
W		0.6	0.3	*	2.8	2	2.7	*	*
Mo		0.4	0.7	*	0.7	0.9	1.2	0.2	0.3
Be		1	1	*	*	*	1	*	*
Au		0.8	0	2.4	1.6	1.3	0.9	2.8	0.6
Hg		0	0	*	*	*	*	*	*
As		0.5	1	1.1	*	*	*	*	*
Se		0	0	*	0.5	*	0.8	*	*
Sb		0.1	0.1	0.1	*	*	*	*	*
La	4.21	7.6	4.8	5.6	5.5	5	22.4	3.3	5.5
Ce	11.07	20.3	13.2	11.8	13.1	12.2	51.8	9.3	15
Pr	1.6	3.29	2.15	1.82	2.26	1.89	6.94	1.53	2.22
Nd	8.16	16.2	11.7	9	11.7	9.4	30.5	8.2	11.7
Sm	2.91	4.5	3.5	2.17	3.18	2.62	7.22	2.74	3.43
Eu	1.11	1.52	1.22	0.68	1.19	0.95	2.51	0.92	1.18
Gd	3.66	4.98	4.12	4.09	3.94	3.14	7.66	3.43	4.14
Tb	0.55	0.89	0.74	1.15	0.74	0.57	1.26	0.64	0.75
Dy	4.11	6.81	4.86	8.53	4.39	3.32	6.51	3.89	4.67
Ho	0.89	1.48	0.98	2.25	0.94	0.72	1.25	0.82	0.97
Er	2.72	4.54	2.81	8.24	2.8	2.11	3.42	2.4	2.95
Tm	0.39	0.74	0.45	1.45	0.42	0.32	0.5	0.34	0.45
Yb	2.66	4.48	2.72	10.08	2.6	2.02	2.95	2.01	2.71
Lu	0.4	0.68	0.43	1.63	0.4	0.31	0.43	0.3	0.41
La/Yb	1.58	1.7	1.76	0.56	2.12	2.48	7.59	1.64	2.03

* not analysed

Most eclogite samples from Guajira plot within the basaltic andesite field (Fig. 6) in the diagram proposed by Winchester and Floyd (1977), in a classification of volcanic rocks using less mobile (incompatible) element ratios, except for sample MJ-043, which plots in the alkali-basalts field. All the samples analysed are tholeiitic, except for sample MJ-043, which contains 3.58wt% TiO_2 and is an alkali basalt. The low to moderate MgO concentrations (4.65-6.5wt.%), the Mg# [Mg#=100Mg/(Mg+Fetot)] between 21 and 35 for SiO_2 ranging from 45.35 to 54.77wt%, as well as Ni contents lower than 40ppm, indicate that the protoliths of most of the eclogites are unlikely to be primary melts of the upper mantle and therefore represent fairly fractionated melts of basaltic to andesitic composition that cannot have been in equilibrium with a mantle peridotite. The low concentrations of Nb (<5,5ppm), Zr (<80ppm) and light rare earth elements (LREE), in most samples, are also mentioned.

On the Th-Hf-Nb representative geochemical discrimination diagram (Fig. 7A), the Guajira samples show consistent overlap, and plot within the destructive plate-margin basalt field. As expected, sample MJ-043 plots in the E-MORB or within-plate basalt field, away from the overall array.

In order to discriminate between volcanic-arc tholeiites and MOR or back-arc basin basaltic rocks, samples were plotted on the discrimination diagram of Shervais (1982) (Fig. 7B). In general The Guajira rocks fall within the MORB- back-arc basin field, and only sample MJ-043 falls within the ocean-island or alkali basalt field.

Multi-element diagrams

MORB-normalized multi-element diagrams are presented in Figure 8 (after Pearce, 1983). Eclogite samples show a similar trend (Fig. 8A) with the exception of samples MJ-043 and MJ-007B, which are plotted separately (Fig. 8B).

Some samples plotted on Figure 8A and those plotted on Figure 8B are notably depleted in Large Ion Lithophile Elements (LILE) K, Rb, Sr, and Ba, when compared to MORB. Sample MJ-043 is enriched in High Field Strength Elements when compared to MORB, whereas sample MJ-007B has a similar pattern. The LILE are scattered, possibly due to some degree of element migration during ocean floor alteration and metamorphism (Aguirre, 1988; Volkova et al., 2009). All samples have High Field Strength Elements patterns similar to N-MORB, and a strong negative Nb anomaly. Also, three of the four samples have a slightly negative Ti anomaly, the exception being sample MJ-033. La/Nb ratios range from 1.05 to 7.14. Samples MJ-007B and MJ-043 have no evident negative Nb anomaly and Y and Yb are scattered.

REE-diagrams

Chondrite normalized REE diagrams are presented in Figure 9. Eclogite samples are plotted in Figure 9A, and samples MJ-043 and MJ-007B are plotted separately, in Figure 9B. Eclogite samples from the Guajira region, except MJ-043 and MJ-007B, show a strong consistency

TABLE 2 | **^{40}Ar-^{39}Ar data for white micas from two eclogite samples. The preferred age is highlighted in bold typeface**

A, sample MJ-033 muscovite

Pwr	F ^{39}Ar	^{40}Ar*/^{39}Ar$_K$	t (Ma)		% ^{40}Ar*	^{40}Ar/^{36}Ar	^{37}Ar$_{Ca}$/^{39}Ar$_K$	t_i (Ma)	t_p (Ma)	t_c (Ma)	(^{40}Ar/^{36}Ar)$_i$	MSWD/n
0.20	0.0018	13.86 ± 6.98	77.2 ± 38.1		17.10	356.44	1.492					
0.65	0.0038	13.99 ± 3.69	78.0 ± 20.1		32.86	440.11	< 0.001					
1.00	0.0526	13.70 ± 0.26	76.4 ± 1.4		86.04	2117.44	< 0.001					
1.30	0.1457	14.12 ± 0.36	78.7 ± 1.9	§	92.98	4208.72	< 0.001					
1.50	0.2373	14.21 ± 0.23	79.2 ± 1.3	§	95.85	7127.44	< 0.001					
1.80	0.3025	14.28 ± 0.23	79.5 ± 1.2	§	96.90	9523.56	0.004					
2.10	0.0842	13.32 ± 0.27	74.3 ± 1.5		96.14	7663.45	0.024					
2.10	0.1721	13.57 ± 0.18	75.7 ± 1.0		95.55	6642.92	0.112	78.0 ± 1.4	**79.2 ± 1.1**	77.3 ± 1.5	293 ± 32	2.2 / 8

B, sample MJ-039 muscovite

Pwr	F ^{39}Ar	^{40}Ar*/^{39}Ar$_K$	t (Ma)		% ^{40}Ar*	^{40}Ar/^{36}Ar	^{37}Ar$_{Ca}$/^{39}Ar$_K$	t_i (Ma)	t_p (Ma)	t_c (Ma)	(^{40}Ar/^{36}Ar)$_i$	MSWD/n
0.20	0.0021	149.25 ± 21.83	696.5 ± 84.5		15.60	350.12	0.242					
0.41	0.0027	-4.58 ± 8.95	-26.3 ± 51.7	†	- 4.21	283.56	< 0.001					
0.80	0.0122	12.25 ± 1.40	68.4 ± 7.7	†	35.98	461.59	< 0.001					
1.10	0.0196	12.22 ± 0.55	68.3 ± 3.0	†	66.58	884.19	0.053					
1.50	0.3537	14.66 ± 0.66	81.6 ± 3.6	§	93.37	4454.26	< 0.001					
1.80	0.4607	14.87 ± 0.58	82.7 ± 3.2	§	96.82	9303.17	< 0.001					
2.00	0.0463	12.57 ± 0.23	70.2 ± 1.3	†	91.50	3475.70	0.033					
3.00	0.1026	13.43 ± 0.21	74.9 ± 1.2	†	95.03	5947.88	0.054	81.8 ± 2.3	**82.2 ± 2.5**	81.6 ± 2.7	345 ± 10	0.1 / 3

Pwr: laser power in Watts applied to release argon; t age of individual fraction, it does not include the uncertainty in J; t_i integrated age; t_p plateau age calculated with the weighted mean of the fractions selected; t_c isochron age; § fractions used to calculate the plateau age; † fractions ignored in the isochron age calculation; all errors are given to 1σ level. Corresponding J for all the samples: 0.003157 ± 0.000050. Preferred age is highlighted in bold typeface.

independent of fabric and metamorphic retrogression. REEs are largely more than 10 times that of chondrite. The samples have slightly enriched LREE patterns, with La/Yb between 1.7 and 2.48. The high heavy rare earth elements (HREE) concentrations and relatively low La/Yb ratios indicate a lack of residual garnet in the source, therefore suggesting that melting in the spinel-lherzolite stability field is more likely.

The alkali-basalt sample MJ- 043 (Fig. 9B) shows the most LREE enriched pattern with a La/Yb ratio of 7.59. HREE values overlap those of the other eclogite samples, also indicating that the source region does not contain relic garnet.

In contrast, sample MJ-007B is the only LREE depleted example, with a La/Yb ratio <1. The high chondrite-

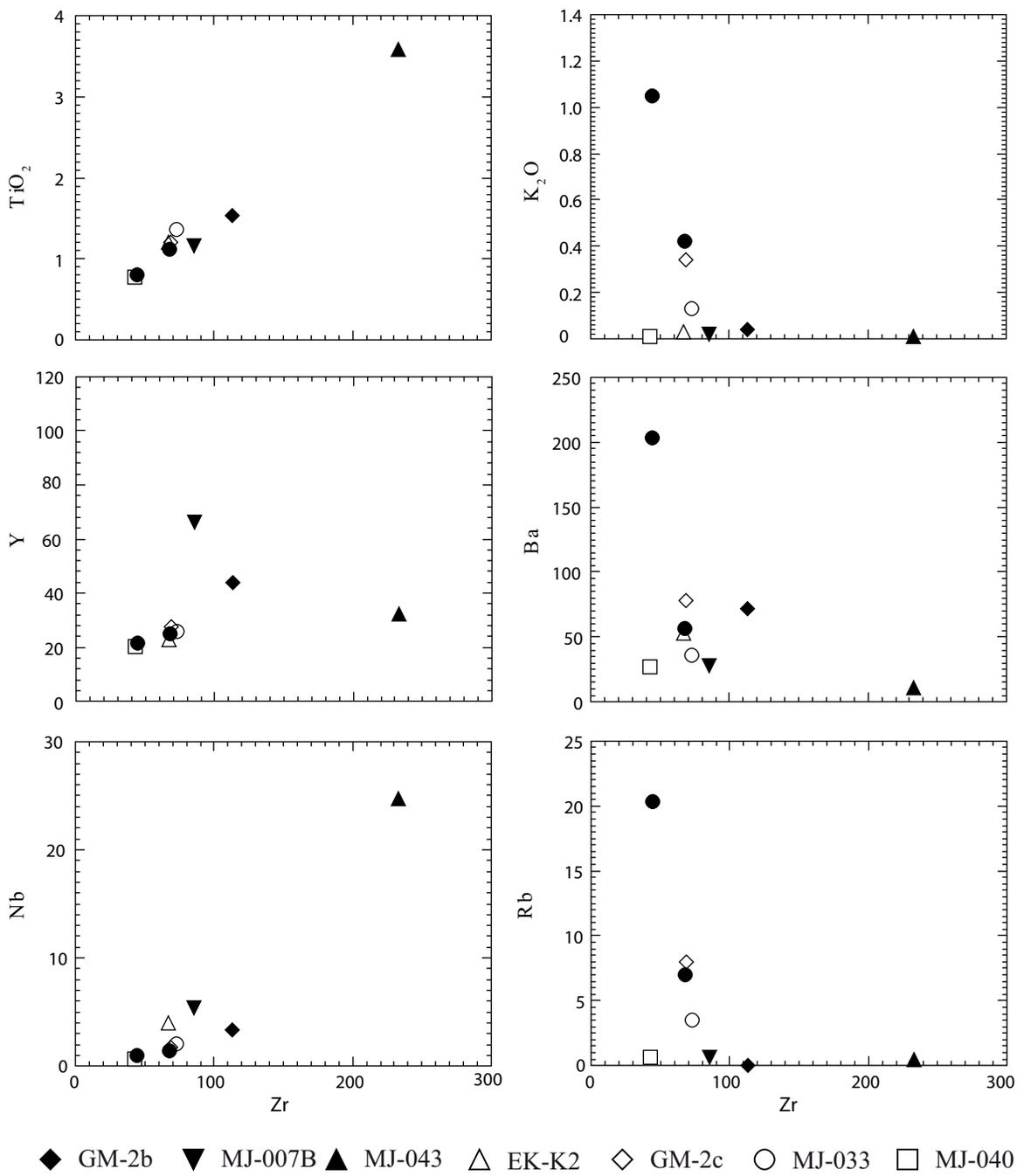

FIGURE 5 | **Zr vs. selected major and trace elements. Zr is considered to be an immobile element, unmodified by alteration. Filled symbols are Group I eclogites and white symbols are Group II eclogites.**

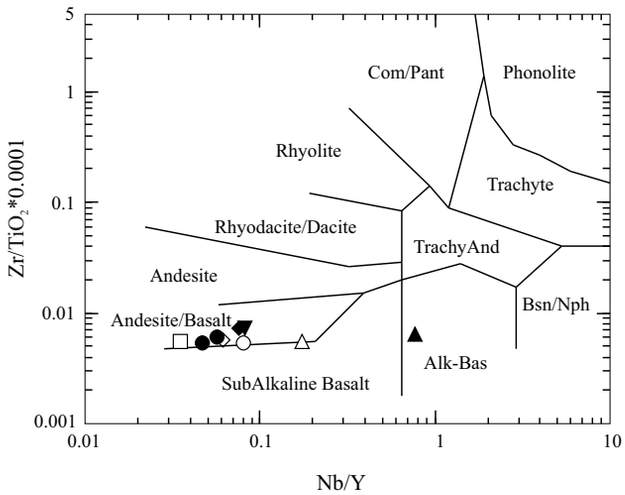

FIGURE 6 | **Nb/Y - Zr/TiO$_2$ diagram of Winchester and Floyd (1977), for the Guajira eclogite and Etpana Terrane samples. Legend as in Figure 5.**

normalized HREE concentration is possibly due to a cumulate origin within a layered magmatic protolith.

Caribbean realm

Within the Caribbean realm, metabasic rocks generally underwent various degrees of metamorphism, mainly during subduction and/or accretion processes which were driven by tectonic forces related to the west to east migration of the Caribbean during the Cretaceous, the passage of which left behind fragments accreted onto continental margins (Burke, 1988). Primary basaltic rocks within the Caribbean realm are considered to have originated from four igneous sources (Donnelly and Rogers, 1980; Donnelly et al., 1990): 1) N-MORB that formed during the North America-South America plate separation after their break-up in the Jurassic 2) Ocean plateau-type rocks which originated as part of the Colombian Caribbean Plateau in Albian-Aptian times 3) Primitive intra-oceanic island-arc or island-arc tholeiites (IAT) forming first in the Early Cretaceous and 4) More evolved calc-alkaline volcanic rocks formed as the island-arcs evolved in the Late Cretaceous (Albian-Campanian) to Early Oligocene. The two later arc building phases have been related to the growth of a single great Caribbean arc (Burke, 1988; Pindell, 1993), although this concept has been questioned recently by various authors (Iturralde-Vinent and Lidiak, 2006; Wright and Wyld, in press).

The geochemical characteristics from most of the Guajira eclogites, such as the negative Nb-Ta anomalies and LREE enrichment relative to HREE, indicate that most of these rocks are more likely to have been formed in an island-arc tectonic setting, and therefore preclude formation from N-MORB sources or the Colombian-Caribbean plateau. In addition, the concentrations of Nb below 5.5ppm, Zr below 75ppm and TiO_2 below 1.5wt% support the interpretation that these rocks are derived from an island-arc protolith (e.g. Verma, 2006).

LILE are tracers of either slab components, as they mobilize during dehydration of the subducting slab, or crustal contamination (e.g. Verma, 2006). Their slight enrichment or depletion in the Guajira rocks precludes large influence of continental contamination and slab-induced fluids. Furthermore, the depletion in LILE relative to MORB is inconsistent with a simplistic island-arc model. The subducted oceanic plate, that dehydrated and triggered magma genesis, must have been extremely depleted in LILE.

Of the Caribbean island-arc series, the calc-alkaline series basalts are characterized by the high LILE compared to High Field Strength Elements (HFSE), as well as high values of K_2O, Ba, Rb and Sr. Also present is an

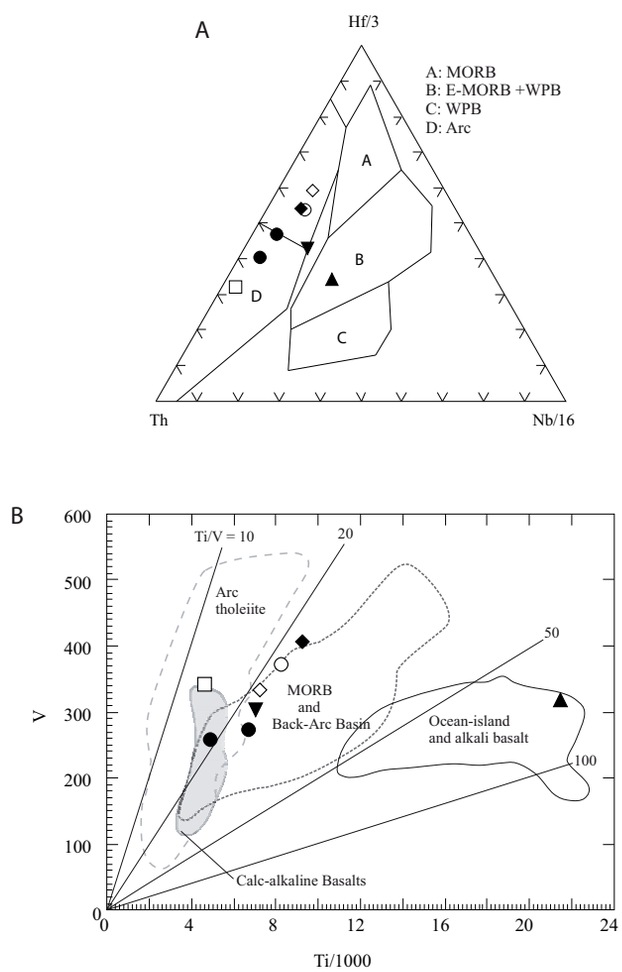

FIGURE 7 | **A) Th-Hf/3-Nb/16 discrimination diagram (Wood, 1980) for the Guajira eclogites and the Etpana Terrane rocks. B) Ti/100 vs. V discrimination diagram (Shervais, 1982) for the Guajira eclogites and the Etpana Terrane. Legend as in Figure 5.**

enrichment of LREE compared to HREE. In contrast, basalts from the Cretaceous primitive intra-oceanic island-arc series are only slightly enriched in LILE relative to high field strength elements, and the REE patterns are rather flat compared to the calc-alkaline. Figure 10A shows a comparative MORB-normalized multi-element geochemical plot between the Guajira data and the Cretaceous Washikemba Formation of Bonaire, believed to be an Aptian (~96Ma) intra-oceanic arc sequence (Beets et al., 1984; Thompson et al., 2004). Also shown is data from the Aruba Batholith (White et al., 1999), which represents a major calc-alkaline intrusion emplaced in the Late Cretaceous. The relatively flat patterns of the Guajira samples are

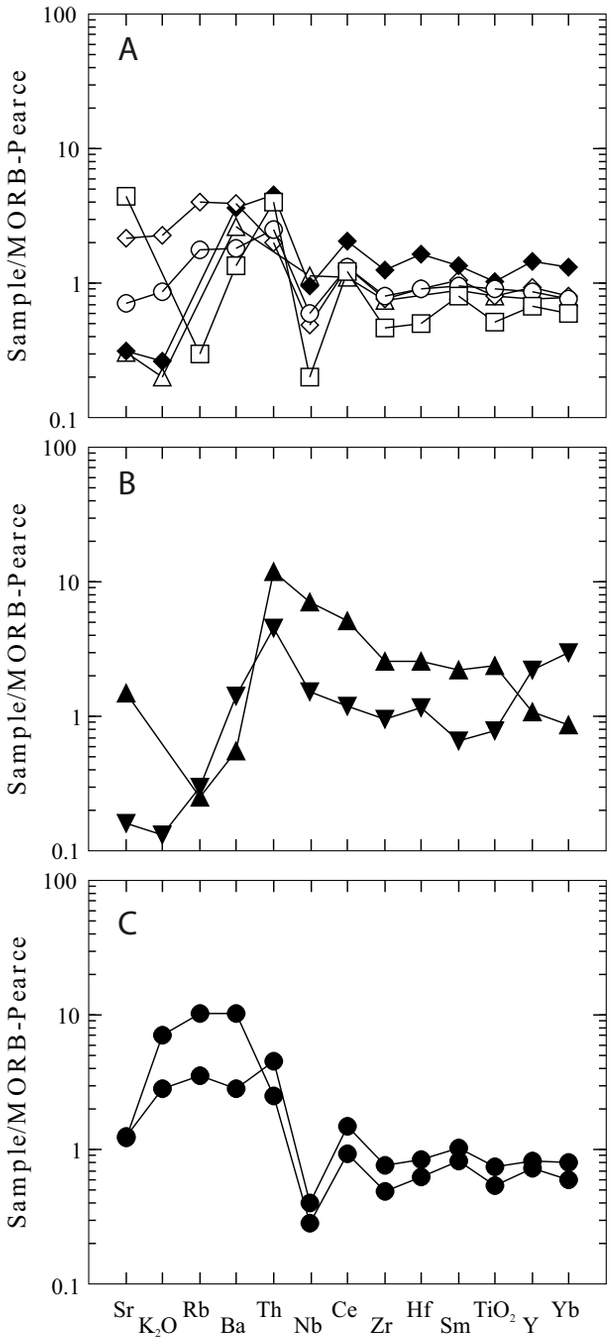

FIGURE 8 | **A) and B) Multi-element patterns normalized to MORB for Guajira Eclogites. C) Multi-element patterns normalized to MORB for Etpana Terrane greenschist-facies rocks. Legend as in Figure 5. Normalization values from Pearce.**

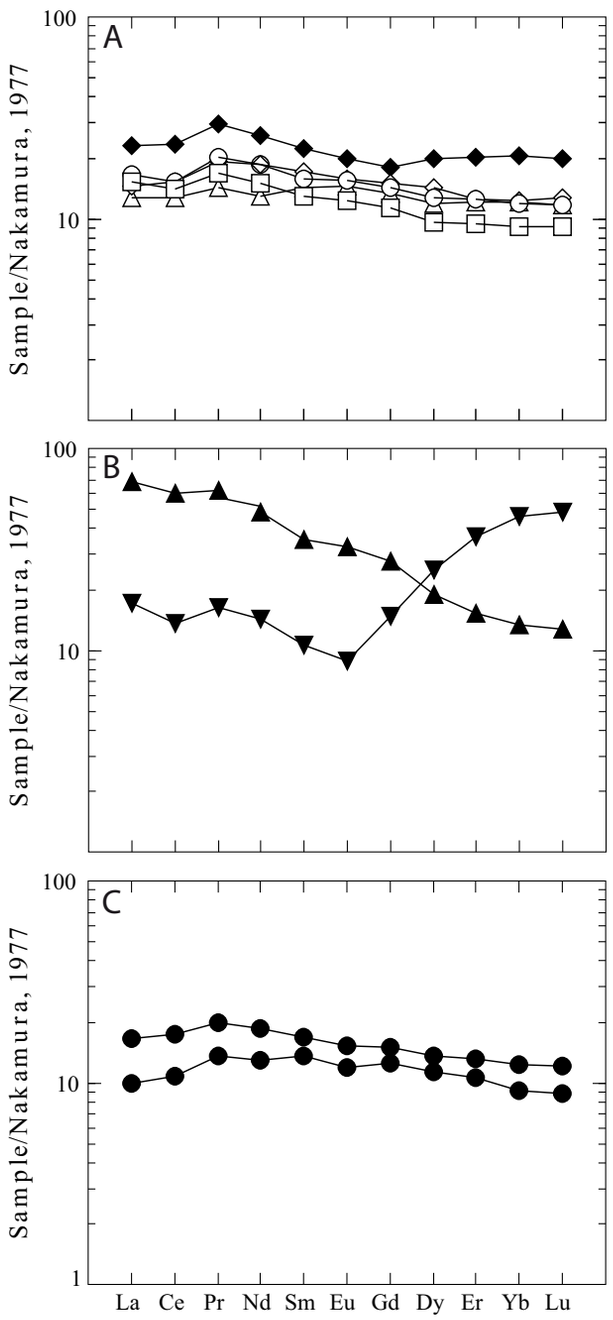

FIGURE 9 | **A) and B) REE patterns normalized to chondrite for Guajira eclogites. C) REE patterns normalized to chondrite for Etpana Terrane greenschist-facies rocks. Normalization values from Nakamura (1974).**

similar to the Washikemba Formation, whereas the Aruba Batolith rocks have a higher LREE/HREE ratio.

These considerations indicate that most of the Guajira eclogites belong to a primitive intra-oceanic island-arc type series. The primitive intra-oceanic island-arc series has been considered to have been confined to the Aptian-Albian times (Donnelly and Rogers, 1980; Donnelly et al., 1990), but it is now realised that primitive intra-oceanic island-arc rock sources were still active during most of the Cretaceous (Iturralde-Vinent and Lidiak, 2006 and references therein). Examples are the Téneme Formation in Cuba (Proenza et al., 2006), active in the Late Cretaceous, and the Cabo de la Vela rocks in the Guajira Peninsula, which have K-Ar whole rock ages of 74Ma (Weber et al., 2009). Comparison with the Cabo de la Vela samples is shown in Figure 10C, and it is evident that both have similar REE and multielement patterns, indicating that they might have formed from similar magma sources and processes, linked to comparable tectonic scenarios.

Hawkesworth et al. (1993a, b), subdivided island-arc basalts into two groups on the basis of LREE/HREE, using La-Yb ratios to discriminate between predominantly intra-oceanic arcs (La/Yb>5) and arcs developed in the proximity of continental margins (La-Yb>5). On the La-Yb variation diagram (Fig. 11) the Guajira eclogites fall within the low-LREE/Yb island-arc basalt field and are similar to the Central Puerto Rican phase I lavas (Jolly et al., 2001, Jolly et al., 2006) and the Late Cretaceous Cabo de la Vela basaltic units (Weber et al., 2009). Data from the Téneme Formation in eastern Cuba (Proenza et al., 2006) are also shown for comparison.

The different geochemical characteristics of sample MJ-043 indicate that, although the primitive intra-

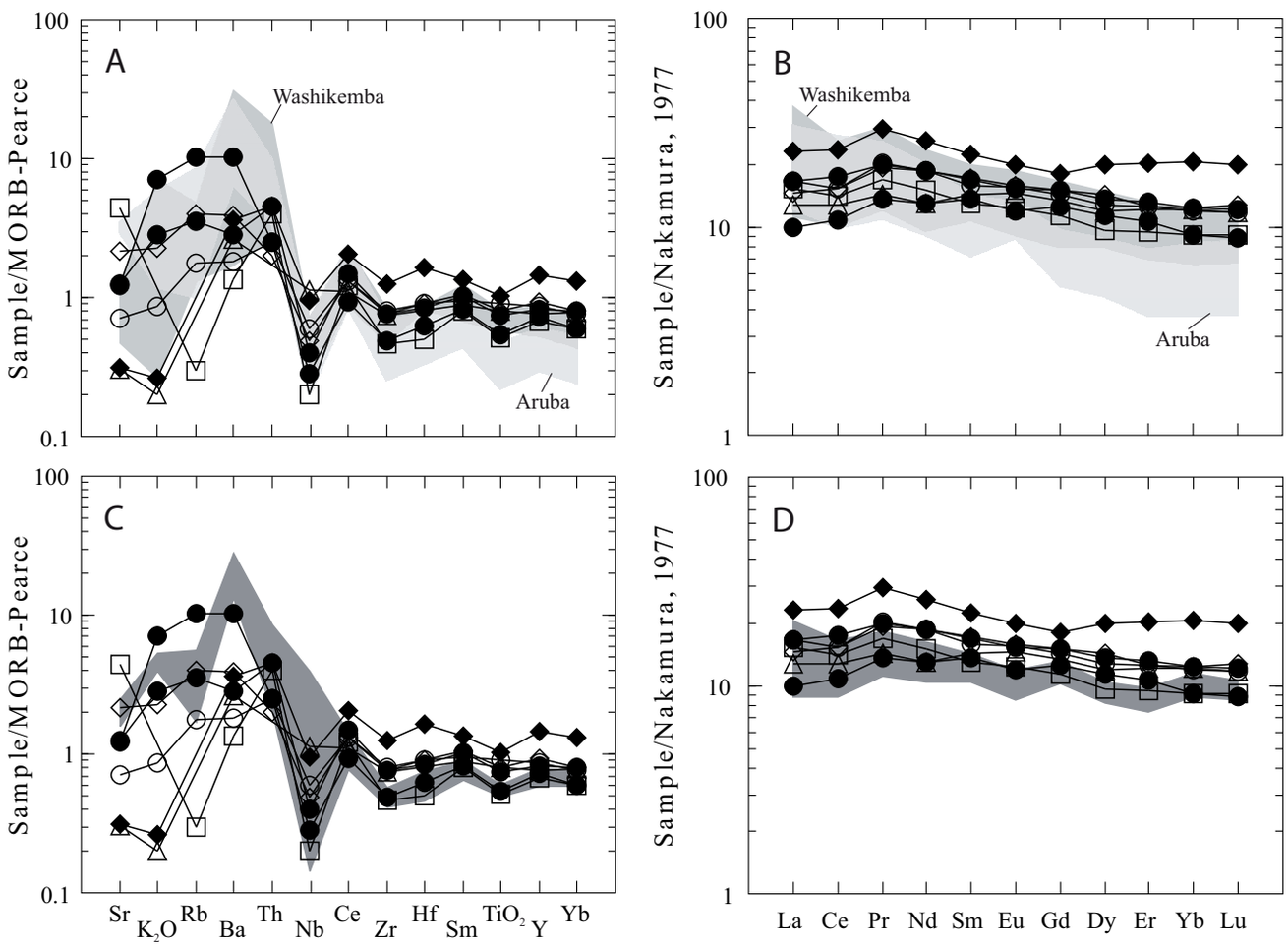

FIGURE 10 | **A) and B) Multi-element patterns normalized to MORB and REE patterns normalized to chondrite plots for the Guajira samples compared to the Washikemba Formation of Bonaire (Thompson et al., 2004) and the Aruba batholith (White et al., 1999). C) and D) Multi-element patterns normalized to MORB and REE patterns normalized to chondrite plots for the Guajira samples compared to the Cabo de la Vela intrusions (Weber et al., 2009). Sample conventions as in previous figures.**

oceanic island-arc-like source predominates in the Guajira eclogites, other mafic protoliths were also integrated into the subduction zones and underwent high-pressure metamorphism.

ETPANA TERRANE

The Cretaceous Etpana Terrane crops out on the northwestern part of the Guajira Peninsula (Fig. 2). First described as the Etpana Formation, Lockwood (1965) divided this unit into six lithologic varieties: finely laminated phyllites, coarsely laminated quartzose phyllites, coarsely bedded quartzites, albite-epidote-chlorite schists, albite-epidote-biotite schists and "complex" zones of mixed phyllite and serpentinite. Recently, this latter unit has been described as a mélange comprising a metapelite-matrix that contains exotic blocks of serpentinite and microgabbro (Zuluaga et al., 2008).

The maximum age of the Etpana Terrane is constrained by zircon provenance analyses at 116.1±7.6Ma (U-Pb in zircon) (Weber et al., 2010). The upper limit is defined by the Parashi Stock, a hornblende-biotite granodiorite intrusive that has been dated at ca. 45-48Ma (K/Ar in hornblende and biotite) (Lockwood, 1965; Cardona et al., 2007).

The assemblage of the two analysed samples of the Etpana Terrane consists of Ep+Alb+Act+Ttn. One of the samples (GUA 24A) is foliated, the schistosity being defined by actinolite and chlorite, with epidote and feldspar porphyroblasts (Fig. 12A). Inclusion trails in the porphyroclasts indicate syntectonic growth. The unfoliated sample is more albite and chlorite rich. The euhedral shape of these minerals seen in some samples suggests that they might represent phenocrystal pseudomorphs, relict from an original igneous rock (Fig. 12B).

Geochemistry

Two samples from greenschists of the Etpana Terrane were analysed for major and trace element geochemistry. Analyses are presented in Table 8. Selected elements versus Zr are plotted in Figure 5. In the compatible element diagrams, the two samples overlap in the first group of eclogites, whereas there is a considerable scatter among incompatible elements.

Figure 6 shows that both samples are classified as basaltic andesites in the Winchester and Floyd (1977) volcanic rock classification diagram, and plot within the destructive plate-margin basalt field in the Th-Hf-Nb discrimination diagram.

In the V-Ti discrimination diagram (Fig. 7B) of Shervais (1982) these samples fall in the MORB-BABB field, similar to most of the Guajira eclogites.

Multi-element diagrams

The two samples from the Etpana Terrane are plotted in a N-MORB normalized multi-element diagram (Fig. 8C). Both samples are enriched in Sr, K_2O, Rb and Ba, compared to N-MORB and have a pronounced Nb and a slightly less pronounced TiO_2 negative anomaly. The overall High Field Strength Elements pattern is similar to MORB. La/Nb ratios are 3.30 and 3.93. The Etpana Terrane pattern overlaps that of the Guajira eclogite samples, except for notable differences in the abundance of mobile elements.

REE-diagrams

The two samples from the Etpana Terrane (Fig. 9C) are somewhat LREE enriched, with La/Yb ratios of 1.64 and 2.03. Both are slightly (10 times) more enriched than chondrite, and in general have similar patterns to those shown by the Guajira eclogite samples. However, the Etpana Terrane samples exhibit a slight negative Eu-anomaly not seen in the Guajira eclogite samples, indicating probable plagioclase fractionation during the crystallization of the protolith.

Comparison between the geochemical characteristics of the geenschists from the Etpana Terrane and the eclogite boulders suggests that both have protoliths that formed in similar tectonic scenarios. There are some differences in mobile elements such as K_2O, Ba and Rb, but these can be

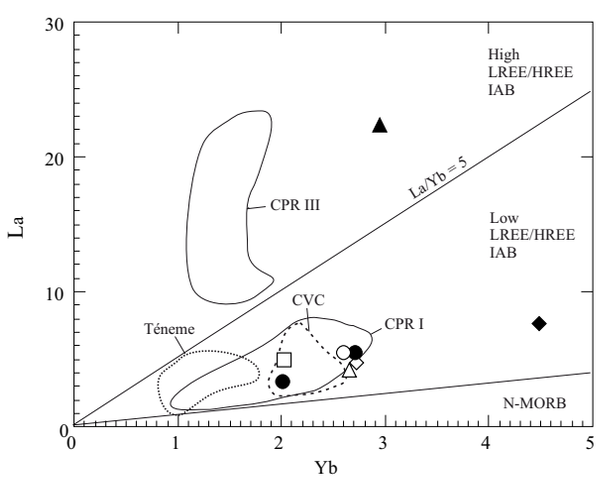

FIGURE 11 | **La vs. Yb for Guajira eclogites and Etpana Terrane rocks (SiO_2<55) in intraoceanic and continental margin settings, after Hawkesworth et al. (1993a, b). CPR indicates central Puerto Rico samples (Jolly et al., 2006). Legend as in Figure 5.**

explained by mobility during alteration and metamorphism (Aguirre, 1988; Volkova et al., 2009).

TECTONOMETAMORPHIC RECORD

Within the most accepted plate tectonic model for the evolution of the circum-Caribbean, the migration of the Caribbean during the Cretaceous took place after the Triassic-Jurassic breakup of Pangea and the formation of an oceanic rift that formed the proto-Caribbean ocean floor, between the separating North and South American plates (Pindell, 1994; Pindell et al., 2005; Pindell and Keenan, 2009). Plate motion during the mid- to Late Cretaceous resulted in the subduction of the proto-Caribbean beneath the east-west migrating Caribbean plate, and the formation of a complex island-arc setting. Parts of these island-arcs interacted with the South American continent, which resulted in the formation of subduction-accretion complexes at the Caribbean-South American and North American plate boundaries.

In the Guajira region, the distribution of high-pressure boulders is limited to the basal conglomerate of a Tertiary sedimentary sequence to the north-west of the Serranía de Jarara (Lockwood, 1965) (Fig. 2). Their eroded source has been shown to be in the adjacent Etpana Terrane (Zapata et al., 2010). This suggests that the in-situ high-pressure rocks were located towards the Caribbean plate, whereas the lower grade greenschist-facies rocks are located to the south, towards the South American continent. Farther northwest, the unmetamorphosed dikes of the ca. 77Ma Cabo de la Vela mafic-ultramafic complex have similar geochemical patterns to the Guajira eclogites and the greenschists of the Etpana Terrane. Associated with the Cabo de la Vela complex is the presence of a positive Bouguer anomaly, extending 100km offshore to the northwest and 30km, onshore to the southeast, but with no continuity into the Serranía de Jarara (Kellogg et al., 1991).

In addition, previous studies have argued that the deposition of the associated high-pressure metasedimentary rocks from within the Tertiary conglomerate and the Etpana Terrane metasediments occurred in a common paleogeographic configuration, due to the virtually identical provenance of zircon populations in their sedimentary protolith (Weber et al., 2010).

The spatial relationship between the eclogites and greenschists of the Etpana Terrane, geological and gravimetric constraints, the similarities of their geochemical characteristics and their common paleogeographic configuration are strong evidence that the volcano-sedimentary sequence that formed the Etpana Terrane also formed high-pressure rocks found in conglomerate, and that these rocks are remnants of an allocthonous island-arc of a primitive nature. This arc was partially metamorphosed to eclogite facies conditions, whereas other parts attained greenschist-facies metamorphism.

According to the models proposed, the subduction of the proto-Caribbean beneath the migrating Caribbean resulted in the formation of a multistage single volcanic arc on the front of the moving plate. However, other models suggest the existence of a multiple-arc and microplate setting in Late Cretaceous times (Iturralde-Vinent and Lidiak, 2006 and references therein), including the formation of a major arc in the southern margin of the Caribbean plate (Wright and Wyld, in press). Although it is still necessary to determine the protolith ages of the Guajira eclogites, the

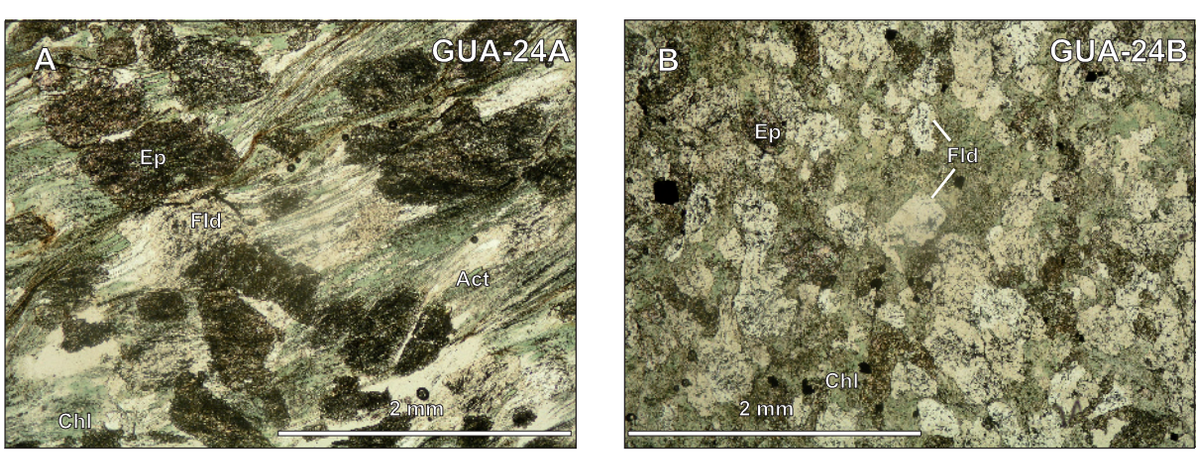

FIGURE 12 | **Microphotographs from samples of the Etpana Terrane. A) Foliated sample where the epidote and albite porphyroclasts are shown. PPL. B) Unfoliated sample, note the euhedral feldspar crystal in the centre of the photograph. PPL. Abbreviations (after Kretz, 1983); Act: actinolite, Chl: chlorite, Ep: epidote, Fld: feldspar.**

data presented here and the existence of the Cabo de La Vela in the Guajira region (Weber et al., 2009) suggest that the scenario of a multiple-arc system is very likely.

The 82.2±2.5 and 79.2±1.1Ma ages obtained from one of the Guajira eclogites, plus a 75.88±0.15Ma Ar-Ar age obtained from a high-pressure white mica schist boulder in the same conglomerate (Tobón et al., 2009), suggest that subduction was active before and during the formation of the Cabo de la Vela island-arc. Furthermore, sedimentary provenance studies of these high-pressure metasedimentary rocks and the Etpana Terrane also suggest that this arc was already approaching the continental margin, and material with South American and arc sources was deposited and continued to be incorporated into the collisional wedge until up to ~71Ma (Cardona et al., 2009; Weber et al., 2009).

The presence of Turonian to Maastrichtian fossils in the Etpana Terrane (Lockwood, 1965) also confirms that the sediments forming the accretionary wedge were deposited and metamorphosed during its advance. Throughout the convergence of this arc, it is probable that the upper plate was incorporated into the subduction zone due to subduction-erosion, and continental subduction may have started until the final continental arc collision. Due to the presence of a significant amount of continental material, the high-pressure rocks followed an alpine-type P-T-t path that indicates the involvement of a continental margin, triggering the final collision (Cloos et al., 2005; Agard et al., 2009, Guillot et al., 2009).

Other high-pressure locations in the southern Caribbean include the Villa de Cura Group and Cordillera de la Costa-Margarita high-pressure belts. The high-pressure metamorphism event of the Juan Griego Group in Margarita is constrained by the intrusion of the non-metamorphosed El Salado granite, dated at 86Ma (U-Pb in zircon). Phengites from the Juan Griego high-pressure schists that yield ages between 90-80Ma (Stöckhert et al., 1995). Ar-Ar ages of 92.4±0.5Ma in amphibole and 86.5±0.2Ma on mica were obtained by Sisson et al. (2005), which are interpreted as the Late Cretaceous cooling age for this belt. In the same study, an Ar-Ar age of 88.5Ma on white mica was obtained for the nearby low-grade Los Robles Formation.

Estimated ages range from 96.3±0.4Ma on amphibole to 79.8±0.4Ma on mica (Smith et al., 1999) in the high-pressure Villa de Cura belt, thought to represent a metamorphosed primitive intra-oceanic island-arc (Unger et al., 2005). Sisson et al. (2005) suggested that due to the similar metamorphic peak ages of both belts, the Villa de Cura and Los Robles may have formed in the same subduction system, but from different protoliths.

Although correlation between the Guajira and Venezuela occurrences remains to be determined, their timing, nature of the protolith and in some instances type of metamorphism indicate that they are all part of a regional scale convergent system that put the Caribbean arc close to the continental margin (Pindell et al., 2005). A major question that remains open is whether these high-pressure belts represent a continuous subduction zone through time, or are part of multiple subduction zones that were modified by a strike slip system during their approach to the margin (Maresch et al., 2009).

ACKNOWLEDGMENTS

Oscar Talavera is acknowledged for discussions and encouragement during field work. Continuous help from Oscar Jaramillo at the Petrography Laboratory, Universidad Nacional de Colombia is greatly appreciated. This research was supported by the Universidad Nacional de Colombia through DIME grant 30805975. This is a contribution to Project 546 of the International Geological Correlation Program "Subduction zones of the Caribbean". We are grateful to Antje Musiol (Potsdam) and Nora Groshopf (Mainz), for their assistance with the chemical analyses. M. García García assisted with the argon experiments. We would like to thank J. Lewis and J. Wright, whose careful reviews considerably improved this paper.

REFERENCES

Agard, P., Yamato, P., Jolivert, I., Burov, E., 2009. Exhumation of oceanic blueschists and eclogites in subduction zones: timing and mechanism. Earth Science Reviews, 92, 53-79.

Aguirre, L., 1988. Chemical mobility during low-grade metamorphism of a Jurassic lava flow: Río Grande Formation, Peru. Journal of South American Earth Sciences, 1, 343-361.

Alvarez, W., 1967. Geology of the Simarua and Carpintero area, Guajira Peninsula, Colombia. Doctoral Thesis. Princeton University, New Jersey, USA, 147pp.

Aspden, J.A., McCourt, W.J., Brook, M., 1987. Geometrical control of subduction related magmatism: the Mesozoic and Cenozoic plutonic history of Western Colombia. Journal of the Geological Society of London, 144, 893-905.

Beets, D.J., Maresch, W.V., Klaver, G.T., Mottana, A., Bocchio, R. Beunk, F.F., Monen, H.P., 1984. Magmatic rock series and high-pressure metamorphism as constraints on the tectonic history of the southern Caribbean. Geological Society of America Memoir, 162, 95-130.

Bocchio, R., Capitani, L., Liborio, G., Maresch, W.V., Mottana, A., 1990. The eclogite-bearing series of Isla Margarita, Venezuela: Geochemistry of metabasic lithologies in the La Rinconada and Juan Griego Groups. Lithos, 25, 55-69.

Burke, K., 1988. Tectonic evolution of the Caribbean. Annual Review of Earth and Planetary Sciences, 16, 210-230.

Cardona-Molina, A., Cordani, U., MacDonald, W., 2006. Tectonic correlations of pre-Mesozoic crust from the northern termination of the Colombian Andes, Caribbean region. Journal of South American Earth Sciences, 21, 337-354.

Cardona, A., Weber, M., Wilson, R., Cordani, U., Muñoz, C.M., Paniagua, F., 2007. Evolución tectono-magmática de las rocas máficas-ultramáficas del Cabo de La Vela y el Stock de Parashi, Península de la Guajira: registro de la evolución orogénica Cretácica-Eocena del norte de Suramérica y el Caribe. Bucaramanga, agosto 14-17, XI Congreso Colombiano de Geologia – Sesión Mineralogía y Petrología. 11p.

Cardona, A., Valencia, V., Bayona, G., Jaramillo, C., Ojeda, G., Ruiz, J., 2009. U/Pb LA-MC-ICP-MS zircon geochronology and geochemistry from a post-collisional biotite granite of the Baja Guajira basin, Colombia: Implications for Late Cretaceous and Neogene Caribbean-South America tectonics. The Journal of Geology, 117, 685-692

Cloos, M., Sapiie, B., Quarles van Ufford, A., Weiland, R.J., Warren, P.Q., McMahon, T.P., 2005. Collisional delamination in New Guinea: The geotectonics of subducting slab breakoff. Geological Society of America Special Paper, 400 (Special Paper), 48pp.

Cordani, U.G., Cardona, A., Jimenez, D., Liu, D., Nutman, A.P., 2005. Geochronology of Proterozoic basement inliers from the Colombian Andes: tectonic history of remnants from a fragmented Grenville belt. In: Vaughan, A.P.M., Leat, P.T., Pankhurst, R.J. (eds). Terrane Processes at the Margins of Gondwana. Geological Society of London, 246 (Special Publications), 329-346.

Donnelly, T.W., Rogers, J.J.W., 1978. Igneous series in island arcs. Bulletin of Volcanology, 43, 347-382.

Donnelly, T.W., Beets, D., Carr, M.J., Jackson, T., Klaver, G., Lewis, J., Maury, R., Schellenckens, H., Smith, A., Wadge, G., Westercamp, D., 1990, History and tectonic setting of Caribbean magmatism. In: Dengo, G., Case, J.(ed.). The Caribbean Region, Vol. H. The Geology of North America. Geological Society of America, 339-374.

Ernst, W.G., 1988. Tectonic history of subduction zones inferred from retrograde blueschist P-T paths. Geology, 16, 1081-1084.

García-Casco, A., Iturralde-Vinent, M.A., Pindell, J., 2008. Latest Cretaceous Collision/Accretion between the Caribbean Plate and Caribeana: Origin of Metamorphic Terranes in the Greater Antilles. International Geology Review, 50, 781-809.

Gómez, J., Nivia, A., Montes, N.E., Tejada, M.L., Jiménez, D.M., Sepúlveda, M.J., Osorio, J.A., Gaona, T., Diederix, H., Mora, M., Uribe, H., 2007. Geological Map of Colombia. Scale 1:1.000,000. INGEOMINAS. Bogotá.

Green, D.H., Lockwood, J.P., Kiss, E., 1968. Eclogite and almandine-jadeite-quartz rock from the Guajira Peninsula, Colombia, South America. American Mineralogist, 53, 1320-1335.

Guillot, S., Hattori, K., Agard, Ph., Schwartz, S., Vidal, O., 2009. Exhumation processes in oceanic and continental subduction contexts: a review. In: Lallemand, S., Funiciello, F. (eds.). Subduction zone geodynamics. Springer-Verlag Berlin Heidelberg, 175-205.

Harrison, T.M., Celerier, J., Aikman, A.B., Hermann, J., Heizler, M.T., 2009. Diffusion of ^{40}Ar in muscovite. Geochimica et Cosmochimica Acta, 73, 1039-1051.

Hawkesworth, C.J., Gallagher, K., Hergt, J.M., McDermott, F., 1993a. Mantle slab contributions in arc magmas. Annual Reviews in Earth and Planetary Science, 21, 175-204.

Hawkesworth, C.J., Gallagher, K., Hergt, J.M., McDermott, F., 1993b. Trace element fractionation processes in the generation of island arc basalts. In: Tarney, J., Pickering, K.T., Knipe, R.J., Dewey, J.F. (eds.). Melting and melt movement in the Earth. Clarendon Press/The Royal Society of London, 393-405.

Humphris, S.E., Thompson, G., 1978. Trace-element mobility during hydrothermal alteration of oceanic basalts: Geochimica et Cosmochimica Acta, 42, 127-136.

Iturralde-Vinent, M.A., Lidiak, E.G., 2006. Caribbean Tectonic, magmatic, metamorphic and stratigraphic events. Foreword. Geologica Acta, 4(1-2), 1-5.

Jolly, W.T., Lidiak, E.G., Dickin, A.P., Wu, T.W., 2001. Secular geochemistry of central Puerto Rican island arc lavas: constraints on Mesozoic tectonism in the Eastern Greater Antilles. Journal of Petrology, 42, 2197-2214.

Jolly, W.T., Lidiak, E.G., Dickin, A.P., 2006. Cretaceous to Mid-Eocene pelagic sediment budget in Puerto Rico and he Virgin Islands (northeast Antilles Island arc). Geologica Acta, 4(1-2), 35-62.

Kellogg, J.N., Godley, V.M., Ropain, C., Bermúdez, A., Aiken, C.L.V., 1991. Gravity Field of Colombia, Eastern Panama and Adjacent Marine Areas. The Geological Society of America, Map and Chart Series MCH 070, Boulder, Colorado.

Krebs, M., Maresch, W.V., Schertl, H.P., Münker,. C., Baumann, A., Draper, G., Idleman, B., Trapp, E., 2008. The dynamics of intra-oceanic subduction zones: a direct comparison between fossil petrological evidence (Rio San Juan Complex, Dominican Republic) and numerical simulation. Lithos, 103, 106-137.

Kretz, R., 1983. Symbols for rock-forming minerals. American Mineralogist, 68, 277-279.

Lockwood, J.P., 1965. Geology of the Serranía de Jarara area, Guajira Península, Colombia. Doctoral Thesis. Princeton University, New Jersey, USA, 237pp.

Macellari, C.E., 1995. Cenozoic sedimentation and tectonics of the southwestern Caribbean pull-apart basin, Venezuela and Colombia. In: Tankard, A.J., Suárez Soruco, R., Welsink, H.J. (eds.). Petroleum Basins of South America, American Association of Petroleum Geologist (AAPG) Memoir, 62, 757-780.

MacDonald, W.D., 1964. Geology of the Serranía de Macuira area, Guajira Península, Colombia. Doctoral Thesis. Princeton University, New Jersey, USA, 167pp.

MacDonald, W., Opdyke, N.D., 1974, B. Triassic Paleomagnetism of Northern South America. American Association of Petroleum Geologists (AAPG) Bulletin, 58, 208-215.

Maresch, W.V., Kluge, R., Baumann, A., Pindell, J.L., Krückhans-Lueder, G., Stanek, K., 2009. The occurrence and timing of high-pressure metamorphism on Margarita Island, Venezuela: a constraint on Caribbean-South America interaction. Geological Society of London, 328 (Special Publications), 705-741.

Masliwec, A., 1984. Applicability of the $^{40}Ar/^{39}Ar$ method to the dating of ore bodies. DoctoralThesis. University of Toronto, Canada, 159pp.

McDougall, I., Harrison, T.M., 1999. Geochronology and thermochronology by the $^{40}Ar/^{39}Ar$ method. New York, Oxford University Press, 269pp.

Montes, C., Hatcher, R.D., Restrepo-Pace, P., 2005. Tectonic reconstruction of the northern Andean blocks: Oblique convergence and rotations derived from the kinematics of the Piedras–Girardot area, Colombia. Tectonophysics, 399, 221-250.

Montes, C., Guzmán, G., Bayona, G., Cardona, A., Valencia, V. Jaramillo, C., 2010. Clockwise Rotation of the Santa Marta Massif and Simultaneous Paleogene to Neogene Deformation of the Plato-San Jorge and Cesar-Ranchería Basins. Journal of South American Earth Sciences, 29, 832-848.

Nakamura, N., 1974. Determination of REE, Ba, Fe, Mg, Na and K in carbonaceous and ordinary chondrites. Geochimica et Cosmochimica Acta, 38, 75-775.

Pearce, J.A., 1983. Role of sub-continental lithosphere in magma genesis at active continental margins. In: Hawkesworth, C.J., Norry, M.J. (eds.). Continental basalts and mantle xenoliths. Nantwich, Shiva press, 230-249.

Pindell, J.L., 1993, Regional synopsis of Gulf of Mexico and Caribbean evolution. In: Pindell, J.L., Perkins B.F. (eds.). Mesozoic and Early Cenozoic Development of the Gulf of Mexico and Caribbean Region: A Context for Hydrocarbon Exploration: Gulf Coast Section Society of Economic Paleontologists and Mineralogists Foundation, 251-274.

Pindell, J.L., 1994, Evolution of the Gulf of Mexico and the Caribbean. In: Donovan, S.K., Jackson, T.A. (eds.). Caribbean Geology: An Introduction, University of the West Indies Publisher's Association, Kingston, Jamaica, 13-39.

Pindell, J.L., Kennan, W.V., Maresch, K, Stanek, P., Draper, G., Higgs, R., 2005. Platekinematics and crustal dynamics of circum-Caribbean arc continent interactions: Tectonic controls of basin development in Proto-Caribbean margins. In: Avé Lallement, H., Sisson, V.B. (eds.). Caribbean-South American Plate Interactions, Venezuela. Geological Society of America, 394 (Special Paper), 7-52.

Pindell, J.L., Kennan, L., 2009. Tectonic evolution of the Gulf of Mexico, Caribbean and northern South America in the mantle reference frame: an update. In: James, K.H., Lorente, M.A., Pindell, J.L. (eds.). The Origin and Evolution of the Caribbean Plate. Geological Society of London, 328 (Special Publications), 1-55.

Proenza, J.A., Díaz-Martínez, R., Iriondo, A., Marchesi, C., Melgarejo, J.C., Gervilla, F., Garrido, C.J., Rodríguez-Vega, A., Lozano-Santacruz, R., Blanco-Moreno, J.A., 2006. Primitive Cretaceous island-arc volcanic rocks in Eastern Cuba: the Téneme Formation. Geologica Acta, 4(1-2), 103-121.

Shervais, J.W., 1982. Ti-V plots and the petrogenesis of modern and ophiolitic lavas. Earth and Planetary Science Letters, 59, 101-118.

Sisson, V.B., Ertan, I.E., Avé Lallemant, H.G., 1997. High-pressure (~2000 MPa) Kyanite- and glaucophane-bearing politic schist and eclogite from Cordillera de la Costa belt, Venezuela. Journal of Petrology, 33, 65-83.

Sisson, V.B., Avé Lallemant, H.G., Ostos, M., Blythe, A.E., Snee, L.W., Copeland, P., Wright, J.E., Donelick, R.A., Gruth, L.R., 2005. Overview of radiometric ages in three allochthonous belts of northern Venezuela: Old ones, new ones and their impact on regional geology. In: Avé Lallemant, J.G., Sisson, V.B. (eds.). Caribbean-South American plate interactions, Venezuela. Geological Society of America, 394 (Special Paper), 91-118.

Smith, C.A., Sisson, V.B., Avé Lallemant, H.G., Copeland, P., 1999. Two contrasting pressure-temperature-timepaths in the Villa de Cura blueschist belt, Venezuela: Possible evidence for Late Cretaceous initiation of subduction in the Caribbean. Geological Society of America Bulletin, 111, 831-848.

Staudigel, H., Plank, T., White, B., Schmincke, H.U., 1996. Geochemical fluxes during seafloor alteration of the basaltic upper oceanic crust: DSDP sites 417 and 418. In: Bebout, G.E., Scholl, D.W., Kirby, S.H., Platt, J.P. (eds.). Subduction top to bottom. American Geophysica Union Monograph, 96, 19-36.

Steiger, R.H., Jäger, E., 1977. Subcommission on Geochronology: Convention on the use of decay constants in Geo and Cosmochronology. Earth and Planetary Sciences Letters, 36, 359-362.

Stöckhert, B., Maresch, W.V., Brix, M., Kaiser, C., Toetz, A., Kluge, R., Krückhans-Lueder, G., 1995. Crustal History of Margarita Island (Venezuela) in detail: Constraint on the Caribbean plate-tectonic scenario. Geology, 23, 787-790.

Thompson, P.M.E., Kempton, P.D., White, R.V., Saunders, A.D., Kerr, A.C., Tarney, J., Pringle, M.S., 2004. Elemental, Hf – Nd isotopic and geochronological constraints on an island arc sequence associated with the Cretaceous Caribbean plateau: Bonaire, Dutch Antilles. Lithos, 74, 91-116.

Tobón, M., Weber, M., García-Casco, A., Cardona, A., Valencia, V.A., 2009. Pressure-temperature and time constraints for high pressure metasedimentary rocks from northernmost Colombia – Caribbean region. III Cuban Convention in Earth Sciences, La Havana, Cuba. Workshop "Subduction Zones of the Caribbean", 13-25.

Tang, H.F., Liu, C.Q., Nakai, S., Orishashi, Y., 2007. Geochemistry of eclogites from the Dabie–Sulu terrane, eastern China: New insights into protoliths and trace element behaviour during UHP metamorphism. Lithos, 95, 441-457.

Unger, L.M., Sisson, V.B., Avé Lallemant, H.G., 2005. Geochemical Evidence for island-arc origin of the Villa de Cura blueschist belt, Venezuela. In: Avé Lallemant,

J.G., Sisson, V.B. (eds.). Caribbean-South American plate interactions, Venezuela. Geological Society of America, 394 (Special Paper), 223-250.

Vence, E., 2008. Subsurface Structure, Stratigraphy, and Regional Tectonic Controls of the Guajira Margin of Northern Colombia. Doctoral Thesis. University of Texas, 128pp.

Verma, S.P., 2006. Extension related origin of magmas from a garnet bearing source in the Los Tuxtlas volcanic field, Mexico. International Journal of Earth Sciences, 95, 871-901.

Villamil, T., 1999. Campanian-Miocene tectonostratigraphy, depocenter evolution and basin development of Colombia and Western Venezuela. Paloegeography, Paleoclimatology, Paleoecology, 153, 239-275.

Volkova, N.I., Frenkel, A.E., Budanov, V.I., Lepezin, G.G., 2004. Geochemical signatures for eclogite protolith from Maksyutov Complex, South Urals. Journal of Asian Earth Sciences, 23, 745-759.

Volkova, N.I., Stupakov, S.I., Babin, G.A., Rudnev, S.N., Mongush, A.A., 2009. Mobility of trace elements during subduction metamorphism as exemplified by the blueschists of the Kurtushibinsky Range, Western Sayan. Geochemistry International, 47, 380-392.

White, R.N., Tarney, J., Kerr, A.C., Saunders, A.D., Kempton, R.D., Klaver, G.T., 1999. Modification of an oceanic plateau, Aruba, Dutch Caribbean: Implications for the generation of continental crust. Lithos, 46, 43-68.

Winchester, J.A, Floyd, P.A., 1977. Geochemical discrimination of different magma series and their differentiation products using immobile elements. Chemical Geology, 20, 325-343.

Weber, M., Cardona, A., Wilson, R., Gómez-Tapias, J., Zapata, G., 2007. Química mineral de las rocas de alta presión-Facies Eclogita, de la Península de la Guajira, Colombia. Boletín de Geología, 29, 31-38.

Weber, M.B.I., Cardona, A., Paniagua, F., Cordani, U., Sepúlveda, L., Wilson, R., 2009. The Cabo de la Vela mafic-ultramafic complex, Northeastern Colombian Caribbean region – A record of multi stage evolution of a Late Cretaceous intra-oceanic arc. In: James, K., Lorente, M.A., Pindell, J. (eds.). The geology and evolution of the region between North and South America. Geological Society of London, 328 (Special Publications), 549-568.

Wood, D.A., 1980. The application of the Th-Hf-Ta diagram to problems of tectonomagmatic classification and to establishing the nature of crustal contamination of basaltic lavas of the British Tertiary Volcanic Province. Earth and Planetary Science Letters, 50, 11-30.

Wright, J.E., Wyld, S.J., in press. Late Cretaceous subduction initiation on the eastern margin of the Caribbean-Colombian oceanic plateau (CCOP): One Great Arc of the Caribbean (?). Lithosphere.

York, D., Evensen, N.M., López-Martínez, M., De Basabe-Delgado, J., 2004. Unified equations for the slope, intercept, and standard errors of the best straight line. American Journal of Physics, 73, 367-375.

Zapata, G., Weber, M., Cardona, A., Jiménez, D., Gómez, J., Nivia, A., Wilson, R., 2005. Análisis petrográfico de las rocas de alta presión de la Serranía de Jarara, La Guajira y sus implicaciones tectónicas. X Congreso Colombiano de Geología – Simposio de Geología Regional, Bucaramanga, 68-69.

Zapata, S., Weber, M., Cardona, A., Valencia, V., Guzmán, G., Tobón, M., 2010. Provenance of Oligocene conglomerates and associated sandstones from the Siamaná Formation, Serrania de Jarara, Guajira, Colombia: implication on Oligocene Caribbean-South America tectonics. Boletín de Ciencias de la Tierra, 27, 7-23.

Zuluaga, C.A., Medina, P.A., Martinez, L.F., 2008. A Cretaceous Subduction Zone in Northern Colombia (southern Caribbean plate)? Geological Society of America, Joint Annual Meeting Abstract, 128-6.

Manuscript received November 2010;
revision accepted July 2011;
published Online July 2011.

Geologica Acta, Vol.9, Nos 3-4, September-December 2011, 445-466
DOI: 10.1344/105.000001739
Available online at www.geologica-acta.com

geologica acta

Transient Cenozoic tectonic stages in the southern margin of the Caribbean plate: U-Th/He thermochronological constraints from Eocene plutonic rocks in the Santa Marta massif and Serranía de Jarara, northern Colombia

A. CARDONA [1][5] **V. VALENCIA** [2] **M. WEBER** [3] **J. DUQUE** [4] **C. MONTES** [1][5] **G. OJEDA** [6] **P. REINERS** [7] **K. DOMANIK** [8] **S. NICOLESCU** [7] **D. VILLAGOMEZ** [9]

[1] **Smithsonian Tropical Research Institute.** Balboa, Ancón, Panamá

[2] **Earth and Environmental Science Department.** Washington State University, Pullman, Washington

[3] **Escuela de Geociencias y Medio Ambiente.** Universidad Nacional, Medellín, Colombia

[4] **Centro de Geociencias.** Universidad Autónoma de México, Querétaro, México

[5] **Corporación Geológica Ares.** Bogotá, Colombia

[6] **Instituto Colombiano del Petróleo-Ecopetrol.** Piedecuesta, Colombia

[7] **Department of Geosciences.** University of Arizona, Tucson, USA

[8] **Department of Planetary Sciences.** University of Arizona, Tucson, Arizona

[9] **Department of Earth Sciences.** University of Geneva, Switzerland

ABSTRACT

We use U-Th/(He) zircon and apatite thermochronology and Al in hornblende geobarometry from Eocene granitoids of the Sierra Nevada de Santa Marta and Guajira uplifted massifs in northern Colombia to elucidate the exhumation history of the northern South America continental margin and its bearing to Cenozoic Caribbean–South American plate interactions. Aluminium in hornblende geobarometry from the Eocene Santa Marta batholith yields pressures between 4.9±0.6kbar and 6.4±0.6kbar, which indicate that at least, 14.7-19.2km of unroofing took place since 56-50Ma in the northwestern Sierra Nevada de Santa Marta. In the Guajira Peninsula, calculated pressures for the Eocene Parashi stock are 2.3±0.6kbar and 3±0.6kbar. Stratigraphic considerations pertaining to Oligocene conglomerates from the Guajira area suggest that 6.9-9km of crust was lost between 50Ma and ca. 26Ma. U-Th/He zircon and apatite thermochronology from granitoids in the Sierra Nevada de Santa Marta shows the existence of major exhumation events in the Late Eocene (ca. 45-40Ma), Late Oligocene (ca. 25Ma) and Miocene (ca. 15Ma). The Guajira region records the Late Eocene to Early Oligocene (35-25Ma) event, but it lacks evidence for the Miocene exhumation phase. These differences reflect isolation of the Guajira region from the

Sierra Nevada de Santa Marta and the Andean chain due to extensive block rotation and transtensional tectonics that affected the region during post-Eocene times.
The post-Eocene events correlate in time with an increased convergence rate and the frontal approach of North and South America. It is suggested that the two major tectonic mechanisms that govern exhumation in these Caribbean massifs are: 1) subduction of the Caribbean plate, and 2) post Eocene changes in plate convergence obliquity and rates that caused the South American continental margin blocks to override the Caribbean plate. Temporal correlation with other Caribbean and Northern Andean events allows to resolve the regional Cenozoic plate tectonic reorganizations experienced by the South American, Caribbean and Pacific plates at a regional scale.

KEYWORDS | **U-Th/He thermochronology. Exhumation. Oblique convergence. Caribbean subduction.**

INTRODUCTION

Active margins characterized by multiple plate tectonic boundaries and surrounded by different oceanic plates are subjected to continuous and rapid changes in convergence relations and in the character of the accreted and/or subducted oceanic crust (Jarrard, 1986; Cross and Pilger, 1982; Cloos, 1993; Gutscher, 2002). Successive modifications of these plate configurations have magmatic, sedimentary, deformational and paleogeographic effects within the upper plate (Hall, 2002; Cawood et al., 2009). Several models have also shown that exhumation and uplift are sensitive to both plate convergence obliquity and the thickness of the subducted oceanic plate (Cloos, 1993; Thompson et al., 1997; Spotila et al., 1998; Spikings et al., 2001, 2008; Cruz et al., 2007; Espurt et al., 2008; Wipf et al., 2008; Gerya et al., 2009). Therefore, the record of exhumation explains the short-term tectonic events which, in turn, have allowed to refine tectonic models for convergent margins. This is particularly useful in regions where young tectonic overprinting or limited exposure of the associated contemporaneous rock record is scarce, or where overimposed events have erased evidence of older ones.

Plate tectonic reconstructions for the northwestern South America-Caribbean interactions suggest that the orogenic cycle began with the Late Cretaceous-Paleogene collision of the front of the oceanic Caribbean plate, which migrated from the Pacific towards an inter-American position (Burke, 1988; Pindell, 1993; Pindell et al., 1998, 2005; Spikings et al., 2000, 2001; Hughes and Pilatasig, 2002; Luzieux et al., 2006; Vallejo et al., 2006, 2009; Cardona et al., 2010a; Van der Lelij et al., in press; Weber et al., 2009, 2010). Subsequent post Eocene relative eastern migration of the Caribbean plate, Pacific subduction and collision of Panama with the northern Andean margin, as well as variations in North America–South America convergence relations, were responsible for strain partitioning and a heterogeneous geological response along the southern margin of the Caribbean plate (Muessig, 1984; Avé Lallemant, 1997; Pindell et al., 1998; Müeller et al., 1999; Spikings et al., 2000; Taboada et al., 2000; Trenkamp et al., 2002; Cortés et al., 2005; Montes et al., 2005, 2010; Pindell and Kennan, 2009). The formation of several isolated massifs surrounded by sedimentary basins in northeastern Colombia is tied to this complex tectonic scenario (Kellogg, 1984; Pindell et al., 1998; Montes et al., 2005, 2010).

Currently, the timing of uplift and the tectonic configuration that shaped these massifs is still not fully resolved (Kellogg and Bonini, 1982; Kellogg, 1984; Montes et al., 2010). In this contribution, low-temperature zircon and apatite (U-Th)/He thermochronology and geobarometric constraints from the Eocene plutonic rocks of the Sierra Nevada de Santa Marta and Serranía de Jarara uplifted massifs, in the Caribbean region of northern Colombia (Fig. 1), were integrated with published geological constraints to characterize the timing and rates of short and long term exhumation. We use these results to reconstruct the time-temperature and time-pressure paths followed by the plutonic rocks in order to understand the tectonothermal evolution of the massifs (Ring et al., 1999). Additional constraints on exhumation from the less topographically expressed Serranía de Jarara are determined with zircon and apatite U-Th/He thermochronology from Eocene granitoid clasts found in a Late Oligocene conglomerate sampled at the foothills of the Serranía de Jarara (Lockwood, 1966; Zapata et al., in press). We relate the record of Cenozoic exhumation of the two massifs to the evolution of the Caribbean–South American plate tectonic interactions and analyze the results in terms of changes in the paleogeography of the region.

TECTONIC SETTING

The Cenozoic orogenic make-up of the Northern Andes and the Caribbean is related to the interactions of multiple plate boundaries (Caribbean, Pacific and South American plates) and the collision of several oceanic terranes with

the South American margin (Pindell et al., 1998, 2005; Kellogg and Vega, 1995; Hughes and Pilatasig, 2002; Kerr et al., 2003; Vallejo et al., 2006, 2009; Jaillard et al., 2008, 2010; Pindell and Kennan, 2009). Advances in regional plate tectonic modeling have suggested that the Pacific-derived Caribbean oceanic plate drifted towards the East (relative to the Americas) during the Late Cretaceous-Cenozoic and that it obliquely collided with the continental margin during the Late Cretaceous and Paleogene (Pindell et al., 1998, 2005; Spikings et al., 2000, 2001; Kerr et al., 2003; Gómez et al., 2005; Montes et al., 2005; Vallejo et al., 2006, 2009; Cardona et al., 2010a). Continued relative eastern migration of the Caribbean plate built an array of strike-slip dominated orogenic blocks and basins linked to a composite transpressional and transtensional configuration (Muessig, 1984; Macellari, 1995; Pindell et al., 1998, 2005; Pérez de Armas, 2005; Beardsley and Avé Lallemant, 2007; Cruz et al., 2007; Montes et al., 2010).

Additional Cenozoic tectonic factors that have influenced this segment of the South American margin include: 1) changes in convergence direction and rate between North and South America and associated relative displacements of the Caribbean plate (Pindell et al., 1988; Müeller et al., 1999; Pindell and Kennan, 2009); 2) forced subduction of a thick Caribbean oceanic plate (Mauffret and Leroy, 1997; Pindell et al., 2005); 3) Early Eocene changes in convergence direction between the Pacific plates and the South American margin from N-S to WNW-ESE (Pilger, 1984; Pardo-Casas and Molnar, 1987); and 4) the collision of the trailing edge of the Caribbean oceanic plate (Panamá isthmus) with northwestern Colombia (Kellogg and Vega, 1995; Taboada et al., 2000).

The Caribbean–South America plate boundary was also marked by the formation of a Cenozoic sedimentary wedge (South Caribbean deformed belt), together with several

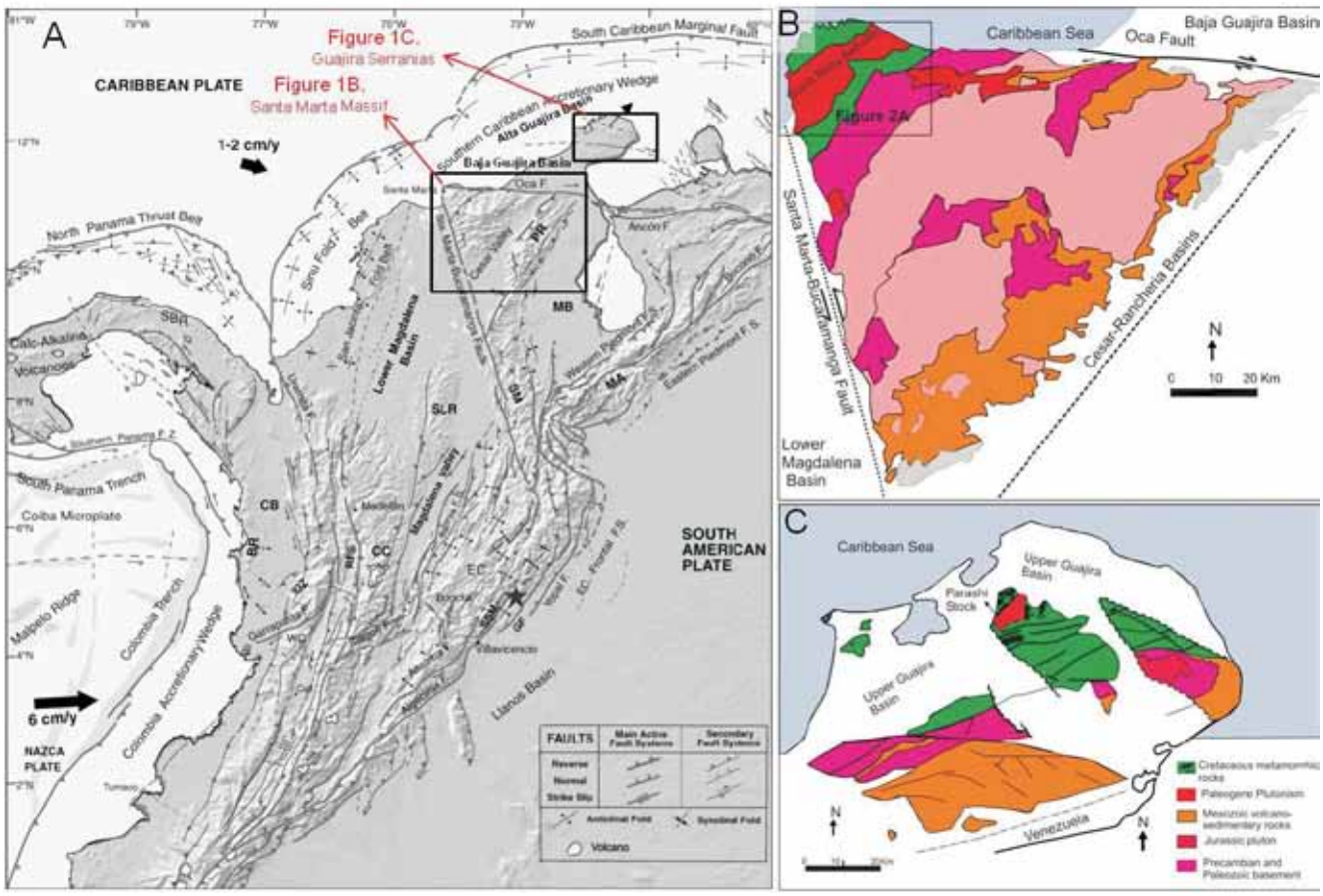

FIGURE 1 | **A) Neotectonic and digital elevation map of the Northern Andes indicating the main active fault systems (after Taboada et al., 2000; Dimate et al., 2003). The Sierra Nevada de Santa Marta, Guajira Serranías and surrounding basins are highlighted on the map. BR: Baudo Range, CB: Chocó Block, CC: Central Cordillera, EC: Eastern Cordillera, GF: Guaicaramo Fault, MA: Mérida Andes, MB: Maracaibo Block, PR: Perija Range, RFS: Romeral Fault System, SLR: San Lucas, SM: Santander Massif, SSM: Servitá–Santa María Fault, WC: Western Cordillera, SBR: San Blas Range, IDZ: Istmina deformation zone. B) and C) Geological sketch maps of the Sierra Nevada de Santa Marta massif and the Guajira region including Serranía de Jarara, respectively.**

pull-apart style basins, uplifted massifs and fold-and-thrust belts (Case et al., 1984; Duque-Caro, 1984; Kellogg, 1984; Muessig, 1984; Lugo and Mann, 1995; Avé Lallemant, 1997; Taboada et al., 2000; Gorney et al., 2007). Within this scenario the Northern Andean margin was segmented into several blocks or microplates that were displaced to the North and East towards the Caribbean realm (Kellogg, 1984; Kellogg and Vega, 1995; Montes et al., 2010).

Recent GPS measurements and stress analyses have shown an oblique East-Southeast convergence of 20±2mm/a between the Caribbean and South American plates demonstrating the North Andean block is still escaping to the northeast (Perez et al., 2001; Weber et al., 2001; Trenkamp et al., 2002; Colmenares and Zoback, 2003). Although most of the convergence is accommodated by major strike-slip zones and earthquake distribution, microseismicity studies and seismic tomographic models have suggested the existence of a slab dipping under the northern segment of the South American margin and the underthrusting of the Caribbean plate against South America (Kellogg and Bonini, 1982; Toto and Kellogg, 1992; van der Hilst and Mann, 1994; Malavé and Suarez, 1995; Miller et al., 2009).

SANTA MARTA AND GUAJIRA

In northern Colombia, the physiographic continuity of the Andean Cordillera changes to a series of isolated uplifted crystalline massifs limited by major strike-slip systems (Fig. 1), and surrounded by barely exposed Cenozoic basins filled with as much as ca. 6km of sediments (Fig. 1, reviews in Guzmán, 2007; Cerón et al., 2007; Rincón et al., 2007). Palinspastic restorations based on basement correlations and structural compatibility have suggested that these massifs were part of a continuous Andean Cordillera during the Late Cretaceous to Early Paleogene, and were later fragmented by Cenozoic Caribbean tectonics (Duque-Caro, 1979; Montes et al., 2005, 2010).

These major uplifted crystalline massifs include the Santa Marta massif and the Guajira Serranías (Simarua, Jarara and Macuira) with elevations as high as ca. 5777m and ca. 600m respectively (Fig. 1). They are both part of the Maracaibo microplate (Burke et al, 1984), which also includes other uplifted regions such as the Serranía de Perijá and the Mérida Andes of Colombia and Venezuela. It is remarkable that the ca. 5777m topography of the Santa Marta massif is characterized by a major positive gravity anomaly and an apparent high geothermal gradient, suggesting a lack of isostatic equilibrium related to recent uplift (Case and MacDonald., 1973; Cerón-Abril, 2008).

Both massifs can be divided into three roughly correlative lithological belts with a well-defined southeast-northwest younging pattern (Fig. 1B and 1C). The older southeastern segment includes ca. 1.2-1.0Ga inliers of high-grade metamorphic rocks (reviews in Tschanz et al., 1974; Cordani et al., 2005; Cardona et al., 2010b) which are intruded/covered by Jurassic to Early Cretaceous plutonic/volcanic rocks (Tschanz et al., 1974; MacDonald and Opdyke, 1972; Cardona-Molina et al., 2006). The intermediate belt is made up of amphibolites and mica schists of Paleozoic age and Permo-Carboniferous mylonitic granitoids (Tschanz et al., 1969, 1974; Cardona-Molina et al., 2006; Cardona et al., 2010c; Weber et al., 2009). The youngest belt includes an imbricate series of Cretaceous greenschist to amphibolite facies metavolcano-sedimentary units and orthogneisses in Santa Marta (Doolan, 1971; MacDonald et al., 1971; Tschanz et al., 1974; Cardona et al., 2010b), and greenschist metasediments with intercalated serpentinites and gabbros in Guajira (Lockwood; 1966; Weber et al., 2010). The three different lithostratigraphic belts are intruded by Eocene I-type plutonic bodies (Tschanz et al., 1974; Mejía et al., 2008; Cardona et al., 2008; Duque et al., 2009), such as the Santa Marta batholith, comprised of quartzdiorites, granodiorites and tonalites. In the Guajira Peninsula, Paleogene plutonism is restricted to the Eocene Parashi stock, a quartzdiorite body with associated porphyritic dikes (Lockwood, 1966; Cardona et al., 2007).

Two Cenozoic basins limit the studied massifs (Fig. 1): 1) the Late Cretaceous to Paleogene Cesar-Ranchería basin, exposed in the southeastern flank of the Santa Marta massif (Bayona et al., 2007; Ayala-Calvo et al., 2010) and 2) the Lower Magdalena and the Baja and Alta Guajira basins, limited by major strike-slip faults and characterized by an extensive post-Oligocene record (Duque-Caro, 1979; Guzmán, 2007; Rincón et al., 2007; Vence, 2008).

ANALYTICAL METHODS

U/Pb LA-MC-ICP-MS geochronology

U/Pb analyses for one granitoid clast were done at the Arizona LASERCHRON laboratory following the procedures described by Gehrels et al. (2008). Results are included in Table 1.

Zircon crystals were analyzed in polished epoxy grain mounts with a Micromass Isoprobe Multicollector Inductively Coupled Plasma-Mass Spectrometry (ICP-MS) equipped with nine Faraday collectors, an axial Daly collector, and four ion-counting channels. The Isoprobe is equipped with an ArF Excimer laser ablation system, which has an emission wavelength of 193nm. The collector

configuration allows measurement of ^{204}Pb in the ion-counting channel while ^{206}Pb, ^{207}Pb, ^{208}Pb, ^{232}Th and ^{238}U were simultaneously measured with Faraday detectors. All analyses were conducted in static mode with a laser beam diameter of 35-50μm, operated with an output energy of ~32mJ (at 23kV) and a pulse rate of 9Hz. Each analysis consisted of one 20-second integration on peaks with no laser firing and 20 one-second integrations on peaks with laser firing. Hg contribution to the ^{204}Pb mass position was removed by subtracting on-peak background values. Inter-element fractionation was monitored by analyzing an in-house zircon standard, which has a concordant Thermal Ionization Mass Spectrometry (TIMS) age of 564±4Ma (2σ). This standard was analyzed once for every five unknowns. Uranium and Th concentrations were monitored by analyzing a standard (NIST 610 Glass) with ~500ppm Th and U. The lead isotopic ratios were corrected for common Pb, using the measured ^{204}Pb, assuming an initial Pb composition according to Stacey and Kramers (1975) and respective uncertainties of 1.0, 0.3 and 2.0 for $^{206}Pb/^{204}Pb$, $^{207}Pb/^{204}Pb$ and $^{208}Pb/^{204}Pb$.

The age of the standard, calibration correction of the standard, composition of common Pb, and the decay constant uncertainty are grouped and known as the systematic error. For these samples the systematic error is of 2.1% for $^{206}Pb/^{238}U$ and $^{206}Pb/^{207}Pb$. Uranium-lead age was calculated using Isoplot (Ludwig, 2003). The final crystallization ages that we report were calculated using the TUFFZIRC algorithm. This algorithm was elaborated by Ludwig and Mundil (2003) to minimize the effect of minor inheritance or subtle Pb loss. The reported ages are one sigma level and report only analytical error. The final age error was calculated using two uncertainties: the first is derived from the uncertainty of the TUFFZIRC age calculation alone, the second represents the systematic uncertainty during that session (~1.1%). The age uncertainty is determined as the quadratic sum of the TUFFZIRC error plus the total systematic error for the set of analyses (~1.2%).

Mineral Chemistry

We analyzed the mineral chemistry of amphiboles from eight granitoid samples using a CAMECA SX-50 electron microprobe at the Department of Lunar and Planetary Sciences at the University of Arizona. Analyses were performed with a beam current of 20.0nA and an accelerating voltage of 15kV. Counting time was 10s for sodium and 20s for the rest of the elements.

TABLE 1 | **U-Pb LA-MC-ICP-MS zircon results from the granitoid conglomerate clast of the Oligocene Siamana Formation, Guajira Peninsula**

				Isotope ratios									Apparent ages (Ma)					
Analysis	U (ppm)	206Pb 204Pb	U/Th	206Pb* 207Pb*	± (%)	207Pb* 235U*	± (%)	206Pb* 238U	± (%)	error corr.	206Pb* 238U*	± (Ma)	207Pb* 235U	± (Ma)	206Pb* 207Pb*	± (Ma)	Best age (Ma)	± (Ma)
MSZH4-1	392	5058	4.7	24.1300	13.2	0.0455	13.3	0.0080	2.1	0.16	51.1	1.1	45.1	5.9	-260.3	334.7	51.1	1.1
MSZH4-2	357	7228	5.0	10.9333	2.0	0.3847	5.0	0.0305	4.5	0.91	193.7	8.6	330.5	14.0	1456.3	38.8	193.7	8.6
MSZH4-3	291	2688	8.6	21.2063	13.9	0.0487	14.5	0.0075	3.9	0.27	48.1	1.9	48.3	6.8	57.1	333.9	48.1	1.9
MSZH4-10	438	19359	1.9	16.7475	5.0	0.1478	8.1	0.0180	6.4	0.79	114.7	7.3	140.0	10.6	593.1	107.7	114.7	7.3
MSZH4-11	344	4715	3.5	21.9573	11.9	0.0496	12.1	0.0079	1.9	0.16	50.7	0.9	49.1	5.8	-26.5	289.4	50.7	0.9
MSZH4-13	521	53792	3.9	13.0216	5.1	1.0122	5.5	0.0956	2.3	0.41	588.6	12.8	710.0	28.3	1115.9	100.9	588.6	12.8
MSZH4-14	269	3595	7.9	19.5746	15.2	0.0555	15.4	0.0079	2.7	0.18	50.6	1.4	54.8	8.2	244.7	351.7	50.6	1.4
MSZH4-15	314	2842	4.0	21.0630	17.6	0.0494	17.7	0.0075	1.5	0.09	48.4	0.7	48.9	8.4	73.2	421.4	48.4	0.7
MSZH4-16	267	4683	4.3	16.6159	6.4	0.1074	11.9	0.0129	10.0	0.84	82.9	8.2	103.6	11.7	610.2	138.4	82.9	8.2
MSZH4-17	256	2006	3.3	21.0117	13.9	0.0499	14.0	0.0076	2.0	0.14	48.8	1.0	49.4	6.8	79.0	330.8	48.8	1.0
MSZH4-18	512	58450	11.6	14.6247	3.2	0.5186	7.9	0.0550	7.2	0.91	345.2	24.2	424.2	27.4	880.0	66.8	345.2	24.2
MSZH4-19	310	3241	6.3	24.5172	28.6	0.0434	##	0.0077	1.5	0.05	49.5	0.7	43.1	12.1	-300.8	743.4	49.5	0.7
MSZH4-20	378	669	2.5	25.3224	17.6	0.0407	17.8	0.0075	2.3	0.13	48.0	1.1	40.5	7.1	-384.1	461.0	48.0	1.1
MSZH4-21	341	599	4.1	19.5481	24.5	0.0519	##	0.0074	3.0	0.12	47.2	1.4	51.4	12.4	247.9	571.9	47.2	1.4
MSZH4-22	557	75226	2.2	15.3075	2.8	0.7416	7.6	0.0823	7.1	0.93	510.1	34.6	563.4	32.9	784.9	59.0	510.1	34.6
MSZH4-23	335	4176	7.4	23.7333	11.1	0.0460	11.1	0.0079	0.5	0.05	50.8	0.3	45.6	5.0	-218.4	279.6	50.8	0.3
MSZH4-25	553	20412	2.9	18.3900	1.5	0.3185	3.5	0.0425	3.2	0.91	268.2	8.4	280.7	8.7	386.7	33.7	268.2	8.4
MSZH4-26	233	511	2.2	16.7391	9.6	0.0612	9.7	0.0074	1.4	0.14	47.7	0.6	60.3	5.7	594.2	208.3	47.7	0.6
MSZH4-28	434	3161	2.1	19.6400	11.0	0.0524	11.1	0.0075	1.8	0.16	47.9	0.8	51.9	5.6	237.0	253.9	47.9	0.8
MSZH4-29	238	3826	8.5	23.1339	17.3	0.0490	17.4	0.0082	2.0	0.11	52.8	1.0	48.6	8.3	-154.5	432.5	52.8	1.0
MSZH4-30	560	6664	2.9	22.1199	5.1	0.0480	6.1	0.0077	3.4	0.56	49.5	1.7	47.6	2.9	-44.4	124.0	49.5	1.7

Microprobe analytical error varies roughly between ±0.01 and 0.04wt% (1 sigma [1σ]). Analytical results are presented in Table I (electronic appendix available in www.geologica-acta.com).

(U-Th)/He thermochronometry

Apatite and zircon concentrates were obtained through the conventional method of heavy liquid-magnetic susceptibility separation. From a non-magnetic mineral fraction, apatite and zircon crystals were hand-picked using a high-power (180x) stereozoom petrographic microscope with cross-polarization which allows inclusion screening under reflected and transmitted light. When possible, mostly transparent, inclusion-free, euhedral, unfractured grains with similar shape and size were selected (average prism width ~80±10μm, length/width ratios of less than 1.5). Uniform grain size minimizes differences in He diffusion behavior (Farley, 2000; Hourigan et al., 2005). Sizes >60-70μm require low correction factors for He ages and increases accuracy (Farley, 2002). Selected grains were digitally photographed and geometrically characterized by measuring each grain for its prism length (parallel to the c axis) and prism width in at least two different orientations (perpendicular to the c axis). Measurements were used to perform alpha ejection corrections (Ft) (Farley, 2002).

All (U-Th)/He analytical procedures were performed at the University of Arizona Radiogenic Helium Laboratory following a protocol based on methods reported for apatite (House et al., 1999, 2000; Stockli et al., 2000; Farley, 2002) and for zircon (Reiners, 2005; Farley, 2002). Helium isotopic measurements were made by degassing each sample replicate through laser heating and evaluating ^{4}He by isotope-dilution gas source mass spectrometry. Radiogenic He was analyzed using a fully-automated mass spectrometry system consisting of a Nd-YAG laser for total He laser extraction, an all-metal, ultra-high-vacuum extraction line, a precise volume aliquot system for ^{4}He standard and ^{3}He tracer for isotopes, a cryogenic gas purification system, and a Blazers Prisma QMS-200 quadrupole mass spectrometer for measuring ^{3}He/^{4}He ratios. Two single-grain aliquots per sample were prepared following the standard protocol available at the University of Arizona. Determination of U, Th, and Sm were performed on the same crystals by isotope-dilution ICP-MS on a Thermo Element 2 ICP-MS also at the University of Arizona. Mean (U-Th)/He ages were calculated on the basis of two apatite and zircon replicate analyses.

Zircon He dating

Measurements of parent and daughter nuclides in zircon grains were performed on two single-grain aliquots per sample following the protocol presented in Reiners (2005). To minimize potential zonation effects, grains without obvious inclusions were chosen. Clear, non-magnetic, tetragonal crystals with prism widths of at least 75-100μm were preferred while grains with prism widths <60μm were avoided. Morphologies most similar to a tetragonal prism with bipyramidal terminations were selected because alpha-ejection corrections entail the assumption of this characteristic grain morphology (Reiners, 2005; Hourigan et al., 2005). Irregular morphologies, elongated grains or crystals with fractured surfaces at low angles relative to the *c*-axis were rejected. Selected crystals were photographed and their dimensions measured in two perpendicular perspectives parallel to the *a*1 and *a*2 crystallographic axes. Measured dimensions and an assigned morphology were used to calculate the alpha-ejection correction following the Ft correction scheme of Farley (2002). The extraction involved placement of a single crystal into a ~1mm Nb foil packet that was then slightly closed and placed on a Cu planchet with another few dozen sample slots in a high-vacuum sample chamber connected to the He purification/measurement line. Each foil packet was directly heated using a 10μm focused laser beam of a 1064-nm Nd-YAG laser to ~1100–1250°C for 15 minute extraction intervals. All samples were then subjected to at least two re-extractions and He measurements, to assess the extent of degassing of the crystal (typical re-extracts yielded less than 0.5% of previous ^{4}He values). Helium extracted from zircons was spiked with ~0.1-1.0pmol ^{3}He, cryogenically concentrated and purified, and expanded into a small volume with a gas-source quadrupole mass spectrometer. Ratios of ^{4}He/^{3}He were measured for about ten seconds following gas release and nominal equilibration time. Measured ratios were corrected for background and interferences on mass 3 (HD+ and H3+), and compared with ^{4}He/^{3}He measured on pipetted aliquots of a manometrically calibrated ^{4}He standard processed by the same methods. ^{4}He in the unknown zircon is assumed to be the product of the ^{4}He content of the standard with ^{4}He/^{3}He ratio measurements on the unknown and the standard.

Uranium and thorium nuclides in degassed zircons were measured by isotope dilution and solution ICP-MS. The approach required spiking with isotopically distinctive U-Th spike, sample-spike equilibration, and dissolution to a final solution suitable for ICP-MS. Zircon dissolution was carried out using HF-HNO_3 mixtures which can dissolve the entire Nb foil and zircon content in Parr bombs at temperatures and pressures higher than ambient. Ratios of ^{238}U/^{233}U and ^{232}Th/^{229}Th were quantified by 2000 measurements of the average intensities in the middle 10% of peak widths in low resolution mode on an Element2 high-resolution ICP-MS. ^{238}U/^{235}U was also measured to check for Pt contamination and mass fractionation. The zircon content in U and Th was calculated from multiple determinations of isotope ratios

on pure spike and spiked normals containing 1–4ng of isotopically normal U and Th.

In zircon, He dating alpha ejection was corrected using the method of Farley et al (1996) and Farley (2002). The analyzed standard included zircons from the Fish Canyon Tuff with two standard analyses per sample batch. This standard has been routinely calibrated, yielding a (U-Th)/He age of 28.29±0.26Ma in one hundred and fourteen grains (95%; 2s external error of 2.6Ma or 9.3%, MSWD=20). Fish Canyon zircon analyses carried out during this work are included within Tables 2 and 3.

Propagated errors for zircon He ages based on the analytical uncertainty associated with U, Th, and He measurements are ~4% (2σ) for laser samples (Reiners, 2005; Farley, 2002). Nevertheless, a 6% (2σ) uncertainty for all samples is reported based on the reproducibility of replicate analyses of laboratory standard samples (Reiners, 2005). All analytical results are presented in Table 2.

Apatite He dating

Single-grain aliquots were prepared and two replicate analyses were performed for each sample. After careful optical screening, apatite crystals were placed into 0.8mm Nb packets, which were then loaded into stainless steel sample planchets. Each sample replicate was degassed via laser heating for 3 minutes utilizing a Nd-YAG laser at 1.5W to attain temperatures of ~1050°C and then analyzed for ^{4}He, followed by a second extraction (He re-extraction) to ensure complete degassing and to monitor He release from more retentive U- and Th-bearing inclusions in analyzed apatite. Helium blanks (0.05.0.1fmol ^{4}He) were determined by heating empty Nb foil packets using the same procedure. Gas extracted from samples was processed by: 1) spiking with ~4pmol of ^{3}He; 2) concentrating in a cryogenic system at 16ºK on a charcoal trap, and purification by release at 37ºK; and 3) measuring ^{4}He/^{3}He ratios (corrected for HD and H3 by monitoring H+) on a quadrupole mass spectrometer. All ratios were referenced to multiple same-day measured ratios and known volumes of ^{4}He standards processed in a similar fashion.

Once ^{4}He measurements were completed, samples were retrieved from the laser cell, placed in Teflon® vials, dissolved in ~30% HNO_3, and spiked with mixed ^{230}Th-^{235}U-^{149}Sm tracer for isotope dilution ICP-MS analysis of U, Th, and Sm. Each batch of samples was prepared with a series of acid blanks and spiked normals to monitor the purity and calibration of reagents and spikes. Spiked samples were analyzed as 0.5mL of ~1.5ppb U-Th solutions by isotope dilution on a Thermo Element 2 ICP-MS. Precision and sensitivity of the instrument allow isotopic analyses with RSD <1%. Concentrations of ^{147}Sm were close to zero for all samples. Th/U rations were used to monitor for the presence of Th rich phases such as monazite. The mean Th/U for all of the replicates combined is 0.9 and most values are below 1 so none of the analyses had to be excluded.

Alpha ejection was corrected for apatite He ages using the method of Farley et al., 1996, Farley, 2002). Durango apatite standards were run during each batch of unknown samples (every 9 unknowns) to monitor system performance and check analytical accuracy. Durango is a well-characterized apatite from Durango, México with a reference Ar-Ar age of 31.44±0.18Ma (2σ) and a (U–Th)/He age of 31.13±1.01Ma (±1 S.E.=0.21) (McDowell et al., 2005). Replicate aliquots of this standard yield an average age of 31.9Ma, with two standard deviations of 2.2Ma (6.6%), and a weighted mean age and error of 31.94±0.17Ma (95% confidence interval, with a 2s required external error of 1.9Ma or 5.9%, MSWD=5.4).

Analytical uncertainties for the University of Arizona (U-Th)/He facility are assessed ~6% (2σ), which incorporate noble gas analysis and ICP-MS uncertainties. Propagated errors for apatite He ages based on the analytical uncertainty associated with U, Th, and He measurements are 4% (2σ) for laser samples. A 6% (2σ) uncertainty for all samples is reported based on the reproducibility of replicate analysis of laboratory standard samples (Reiners, 2005). All analytical results are presented in Table 3.

SAMPLING

In order to constrain the Cenozoic exhumation history we focused on the thermochronology of the northwestern segment of the Santa Marta and the Serranía de Jarara uplifted massifs, where the younger record consists mainly of Eocene plutonic rocks (Lockwood, 1966; Tschanz et al., 1969). In the Santa Marta massif, quartzdiorite and granodiorite samples of the Eocene Santa Marta batholith and a host orthogneiss were taken along an elevation profile near the coastal region (Fig. 2A, 2B). Elevations from the sampled transect range 189m to 1609m within a horizontal distance of ca. 26km. Recent U/Pb geochronology from the Santa Marta batholith has shown an evolution with two contrasting phases of magmatism during 65-62Ma and 58-50Ma (Cardona et al., 2008; Duque et al., 2009). Recovered samples are from the youngest pulse, together with an additional orthogneiss sample that has a crystallization age of ca. 92Ma (Cardona et al., 2008). In contrast, relief in the Guajira Serranías is lower, and Paleogene plutonism is restricted to the Parashi stock, which is exposed at only ca. 100m elevation in the northwestern Serranía de Jarara (Lockwood, 1966, Fig. 2B). Unpublished

TABLE 2 | **U-Th/He zircon results from the Santa Marta batholith and Parashi stock**

	mass (ug)	U ppm	Th ppm	4He (nmol/g)	HAC	Age (Ma)	1s err (Ma)	Elevation (m)	North	E or W
Santa Marta Batholith										
EAM-18-72A	8.93	178.70	87.98	18.28	0.79	21.45	0.68	130	1713860	989845
EAM-18-72B	7.91	158.06	71.01	16.17	0.78	21.97	0.50	130	1713860	989845
EAM-11-43A	2.09	542.19	297.41	55.34	0.69	24.14	0.56	189	1728142	992387
EAM-11-43B	1.16	162.72	44.40	11.09	0.63	18.74	0.59	189	1728142	992387
EAM-11-42A	3.47	209.59	97.19	21.49	0.74	23.18	0.55	252	1726304	993827
JRG-11-15A	8.98	355.34	82.46	35.41	0.80	21.96	0.46	617	1723670	995183
JRG-11-15B	5.05	253.46	65.55	26.20	0.77	23.38	0.49	617	1723670	995183
EAM-11-50A	2.37	403.50	118.57	35.47	0.71	21.56	0.59	943	1722398	997166
EAM-11-50B	6.13	426.32	144.28	51.53	0.77	26.82	0.55	943	1722398	997166
EAM-19-66A	9.46	184.25	36.61	17.23	0.80	20.64	0.56	1430	1719467	999600
EAM-19-60A	5.30	969.79	114.18	98.68	0.74	24.73	0.67	1569	1715731	1003817
EAM-19-60B	4.05	933.69	69.91	77.67	0.75	20.33	0.37	1569	1715731	1003817
EAM-19-59A	6.02	509.65	582.56	70.10	0.77	26.19	0.49	1602	1717331	1003526
EAM-19-59B	19.94	307.86	358.18	40.20	0.84	22.50	0.42	1602	1717331	1003526
Parashi Stock										
CM-3-2A	5.21	167.33	64.50	27.56	0.77	36.51	0.73	150	12º 13' 46"	71º 41' 20.9"
CM-3-2B	3.29	207.62	77.09	34.16	0.73	38.36	0.74	150	13º 13' 46"	72º 41' 20.9"
CM-3-7A	13.21	111.46	59.98	18.88	0.83	33.40	0.68	165	12º 13' 05.2"	71º 40' 48.1"
CM-3-7B	15.24	302.02	159.63	54.46	0.83	35.58	0.63	165	13º 13' 05.2"	72º 40' 48.1"
CM-5-20A	12.48	136.25	59.70	24.53	0.82	36.77	0.74	170	12º 13' 34.8"	71º 44' 36.7"
CM-5-20B	17.40	101.76	48.84	19.44	0.84	37.79	0.72	170	13º 13' 34.8"	72º 44' 36.7"
Oligocene conglomerate										
MSZH-04A	3.90	345.74	75.28	69.28	0.74	47.36	0.98	120	12°17´13"	71°41´31"
MSZH-04B	2.92	440.96	65.63	85.95	0.72	48.69	0.96	120	12°17´13"	71°41´31"
MSZH-06A	0.71	372.43	89.28	51.60	0.55	44.58	0.94	120	12°17´18.3"	71°41´31"
MSZH-06B	1.96	570.59	155.92	105.61	0.68	47.25	0.96	120	12°17´18.3"	71°41´31"

TABLE 3 | **U-Th/He apatite results from the Santa Marta batholith and Parashi stock**

	mass (ug)	U ppm	Th ppm	Sm ppm	4He (nmol/g)	HAC	Age	1s err (Ma)	Elevation (m)	North	E or W	Weight average	MSWD
Santa Marta Batholith													
EAM-18-72A	8.75	160.36	327.63	122.69	9.36	0.79	9.21	0.19	130.00	1713860	989845	9.72	0.31
EAM-18-72B	4.12	90.48	140.83	88.67	5.47	0.75	10.89	0.28	130.00	1713860	989845		
EAM-11-43A	2.13	42.14	33.26	72.64	1.60	0.69	8.66	0.49	189.00	1728142	992387	7.6	0.8
EAM-11-43B	1.24	27.40	16.53	53.73	0.62	0.67	5.51	0.69	189.00	1728142	992387		
EAM-11-42A	0.93	18.04	23.66	147.42	0.49	0.62	6.22	1.28	252.00	1726304	993827	8.9	1.6
EAM-11-42B	1.60	14.72	29.01	136.06	0.83	0.66	10.77	1.05	252.00	1726304	993827		
JRG-11-15A	1.78	77.95	12.27	93.90	3.40	0.67	11.70	0.48	617.00	1723670	995183	14.68	5.9
JRG-11-15B	4.50	66.52	34.50	86.09	4.94	0.74	16.44	0.37	617.00	1723670	995183		
EAM-11-50A	1.28	11.41	4.15	27.35	0.55	0.64	12.87	2.40	943.00	1722398	997166	13.7	4
EAM-11-50B	1.04	11.67	0.86	49.61	0.62	0.62	15.68	3.65	943.00	1722398	997166		
EAM-19-66A	2.79	12.41	25.00	38.87	0.62	0.72	8.71	0.72	1430.00	1719467	999600	9	1.2
EAM-19-66B	2.34	9.67	1.14	22.00	0.37	0.71	9.76	1.15	1430.00	1719467	999600		
EAM-19-60A	1.08	8.68	5.11	47.55	0.45	0.63	13.26	2.96	1569.00	1715731	1003817	14.4	0.21
EAM-19-60B	0.84	19.34	5.11	121.68	1.04	0.62	15.03	2.23	1569.00	1715731	1003817		
EAM-19-59B	0.76	10.88	21.17	60.69	1.25	0.59	24.57	3.51	1602.00	1717331	1003526	24.57	7.01
Parashi Stock													
CM-5-20A	5.11	7.74	15.70	96.17	1.51	0.74	32.55	0.61	150	12º 13' 34.8"	71º 44' 36.7"		
CM-3-7A	2.87	6.27	14.27	85.75	1.01	0.72	26.54	0.66	165	12º 13' 05.2"	71º 40' 48.1"		
CM-3-2A	6.50	6.48	11.82	127.33	1.20	0.77	30.44	0.51	170	12º 13' 46"	71º 41' 20.9"		
CM-3-2B	8.16	7.32	13.80	158.88	1.41	0.79	30.73	0.61	170	13º 13' 46"	72º 41' 20.9"		
Oligocene conglomerate													
MSZH-04A	3.56	3.96	5.17	123.10	0.83	0.70	40.82	1.03	120	12°17´13"	71°41´31"		
MSZH-04B	4.69	4.13	6.67	121.02	0.93	0.76	38.82	0.80	120	12°17´13"	71°41´31"		
MSZH-06A	7.09	5.74	7.24	95.90	1.14	0.76	36.66	0.72	120	12°17´18.3"	71°41´31"		

zircon U/Pb geochronology from the Parashi stock has yielded ages between 50 and 46Ma. Three quartzdiorite samples of this granitoid (CM-5-20, CM-3-2 and CM-3-7) were selected for He zircon and apatite thermochronology.

Because of the value of conglomerate clasts to constrain older phases of exhumation (Thomson, 1994; Bernet and Spiegel, 2004; Colgan et al., 2008), we extracted complementary thermochronological information about the Serranía de Jarara from clasts recovered from a Late Oligocene–Early Miocene conglomeratic unit (Lockwood, 1966; Zapata et al., in press). Two granitoid clasts (MSZH-4 and MSZH-6) were selected from the marine fan conglomerate in the foothills of the Serranía de Jarara, near the Parashi stock. Clast counting analysis links the provenance to proximal granitoids and metamorphic rocks in the immediately adjacent Serranía de Jarara (Zapata et al., in press).

RESULTS

U-Pb Geochronology

Uranium-Pb geochronology from the Santa Marta and Jarara Paleogene granitoids has been recently constrained in detail (Cardona et al., 2008; Duque et al., 2009). Results from samples along the analyzed transect in Santa Marta show a magmatic crystallization history between 57 and 50Ma (Cardona et al., 2008), whereas for the Parashi granitoid, newly acquired U-Pb crystallization ages are between 50-46Ma. In order to further understand the origin of the sampled granitoid clasts in the conglomerate, we determined U-Pb zircon crystallization ages from one clast, by means of U-Pb LA-ICP-MS methods. This sample (MSZH-4) was subsequently analyzed for zircon and apatite helium thermochronology.

Twenty-one zircon crystals were analyzed from sample MSZH-4 (Table 1). Fifteen crystal tips yielded a mean age of $^{206}Pb/^{238}U$ of 48.8+1.5-1.1Ma (Fig. 3), calculated following Ludwig and Mundil's (2002) algorithm to minimize the effect of inheritance or subtle Pb loss. Analyses that are statistically excluded from the main cluster are shown in gray on Figure 3. We interpreted this age as the granitoid crystallization age. This age is similar to the U-Pb and hornblende K-Ar ages obtained in the Parashi stock (Cardona et al., 2007) as well as detrital zircon ages found within the conglomerate matrix (Zapata et al., in press).

Granitoid emplacement depths

When the emplacement pressures of temporally constrained granitoid rocks are transformed into paleodepths, they can be used as a valuable reference to reconstruct the denudation and exhumation record (Ring et al., 1999). Emplacement depths were estimated by Al

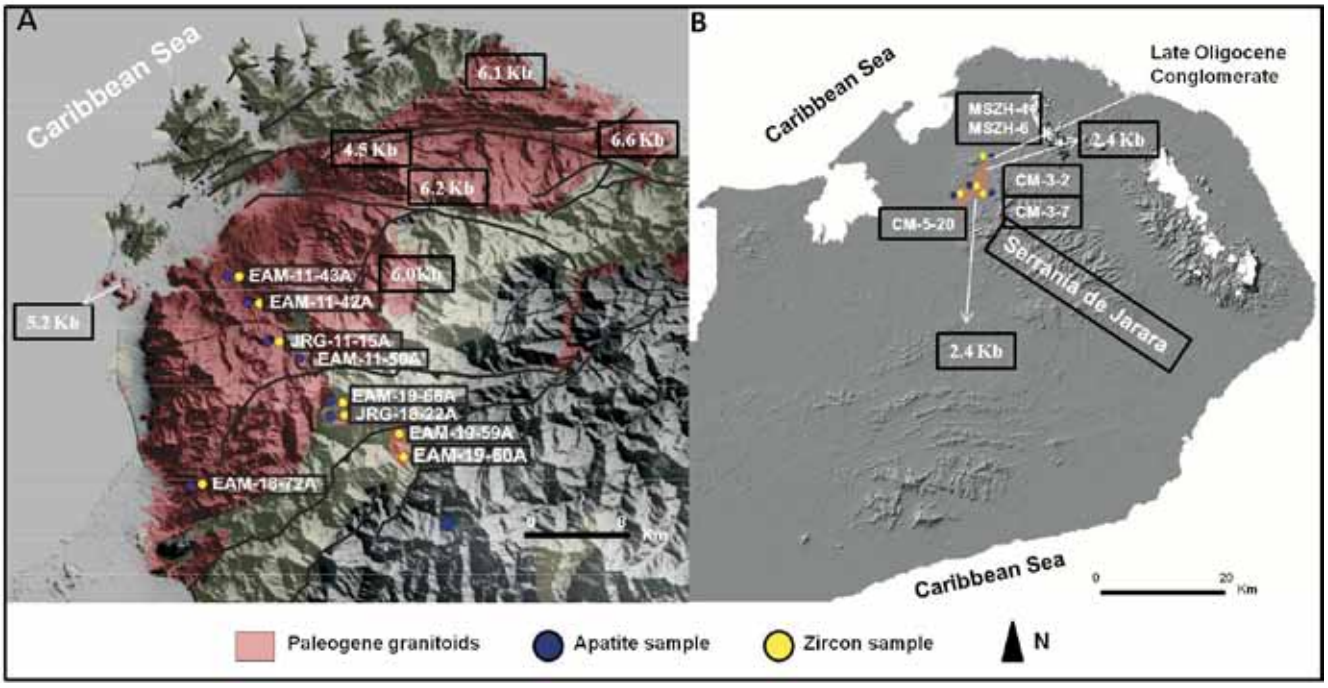

FIGURE 2 | **Digital elevation models and sample locations for A) the Santa Marta and B) Serranía de Jarara regions.**

in-amphibole content of selected granitoid samples from the Santa Marta batholith and the Parashi stock. Analyzed samples from the Santa Marta batholith include amphibole-biotite tonalites and granodiorites. They are composed of plagioclase (43-52%), K-feldspar (2.2-9.2%), quartz (14-29), hornblende (4-21.8%) and biotite (6.2-17%), with titanite, apatite and zircon as accessori. The Parashi stock is made up of granodiorite and quartzdiorite lithotypes. Compositional variations are recorded by amphibole and biotite (12-25%) as well as K-feldspar (7-10.9%). Other minerals show average values of 47.6% (plagioclase) and 22.8% (quartz).

Analytical results of hornblende and pressures calculated using the Schmidt (1992) Al in hornblende calibration are presented in Table I (electronic appendix available in www.geologica-acta.com). All the analyzed amphiboles are calcic and were classified following Leake et al. (1997) in Fig. 4. Pressures obtained from six samples of the Santa Marta batholith vary between 4.9±0.6 and 6.4±0.6kbar. For the Parashi stock, calculated pressures on two samples are lower, between 2.3±0.6 and 3±0.6kbar, and are similar to those reported by Martínez (2008) in other samples from the same stock. These pressure values are consistent with the nature of their host rocks: amphibolite facies rocks with peak pressures of 6.6±0.8kbar in the former (Bustamante et al., 2009; Cardona et al., 2009), and greenschist facies rocks in the latter (Lockwood, 1966). These pressures indicate emplacement depths of 14.7-19.2km and 6.9-9km, respectively.

U-Th/He thermochronology

Santa Marta batholith

Very old ages were discharged due to their lack of coherence and their potential relation with inclusions, which commonly yield older ages (Fitzgerald et al., 2006).

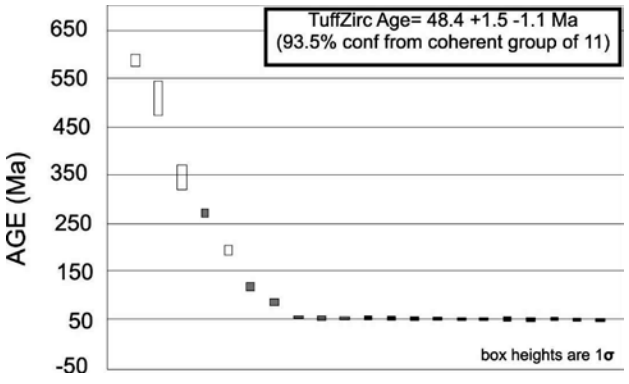

FIGURE 3 | **U-Pb zircon ages from a granitoid clast of the Oligocene conglomerate of Serranía de Jarara, Guajira Peninsula.**

Zircon ages show very poor relation with elevation. The fourteen zircon He ages from nine samples range from 18.7Ma to 26.2Ma (Table 2, Fig. 5). Some of the age variations may be related to local structural disruption. In contrast, apatite He ages extend from 24.6Ma to 5.5Ma (Table 3), showing a well-defined pattern of age increase with elevation (Table 3).

Serranía de Jarara

Elevation of the three samples collected from the Parashi stock varies between 130m and 170m. Zircon U-Th/He ages range from 33.4Ma to 38.4Ma (Table 2), and apatite helium ages are similar, ranging from 30.4Ma to 35.6Ma (Table 3). The two Eocene granitic clasts from the conglomerate yielded older zircon and apatite U-Th/He ages, 48.7-44.6Ma and 40.8-36.7Ma respectively (Tables 2 and 3).

Exhumation rates

He diffusion experiments and age comparisons with other thermochronological systems in slowly cooled rocks have suggested closure temperatures for the U-Th/He system in zircon and apatite in the range of 160-200°C and ca. 70°C respectively (reviews in Farley, 2000; Reiners et al., 2002). For mean upper crust geothermal gradients of 20 and 30°C/km, these closure temperatures give exhumation constraints for crustal levels beween 3 and 9km (Farley, 2000).

Extensive U-Pb geochronology on the magmatic rocks of the Santa Marta massif (Cardona et al., 2008; Duque et al., 2009) has shown that the magmatic episode that formed the sampled rocks in the Santa Marta region took place during the Paleocene-Eocene (ca. 58-50Ma). Similar conclusions can be drawn from the Serranía de Jarara, where the Eocene magmatic event is recorded by the 46-50Ma ages obtained in the Parashi stock (Cardona et al., 2009).

Therefore the cooling rates derived from the low-temperature thermochronometers in the in situ sampled granitoids from Santa Marta are related to unroofing. This is also in agreement with the fact that measured zircon-He and apatite-He ages are younger than pluton crystallization ages. In the case of the Jarara granitoid and clasts from the Oligocene conglomerate, it will be discussed below that their zircon-He ages may reflect fast magmatic cooling rather than unroofing or exhumation ages.

In order to estimate exhumation rates, we followed three different approaches: 1) multiple systems with different closure temperatures in single rock samples, including (U-Th)/He in zircon and apatite; 2) single (U-Th)/He ages, which yield average cooling rates between

the time of apatite He closure and the present; and 3) age-elevation profiles based on the average between the oldest and the youngest He apatite ages of the profile.

Although the effects of heat advection alter exhumation rates were calculated from very low temperature thermochronometers, such as apatite, these effects are probably not significant since the obtained exhumation rates are not high enough to promote heat advection in the upper crust (Brown and Summerfield, 1997; Mancktelow and Grasemann, 1997).

Santa Marta batholith

Actual geothermal gradients from the corner of the Santa Marta massif and surrounding sediments have been estimated by López and Ojeda (2006) from a bottom simulating reflector. Their results have yielded 20°C/km to 40°C/km geothermal gradients (Cerón-Abril, 2008). We have used these two end member values, which include the typical upper crust geothermal gradient of 30°C/km.

Figure 6A shows the pressure (depth)-time path constructed for the Santa Marta batholith, including the inferred emplacement depths for the granitoid, the assumed geothermal gradients and the associated closure-depths of the discussed thermochronological systems.

The emplacement depths of the granitoid suggest ca. 16km unroofing of the Santa Marta region since ca. 57-50Ma (Fig. 6A). Available biotite and amphibole K-Ar ages yielded values of 48.8±1.7 and 44.1±1.6 (Tschanz et al., 1974). Considering the ca. 16km emplacement level of the Santa Marta batholith, recalculated biotite K-Ar ages of ca. 41Ma after Steiger and Jaeger (1977) radioactive decay constants, and an arc gradient of ca. 30°C/km,

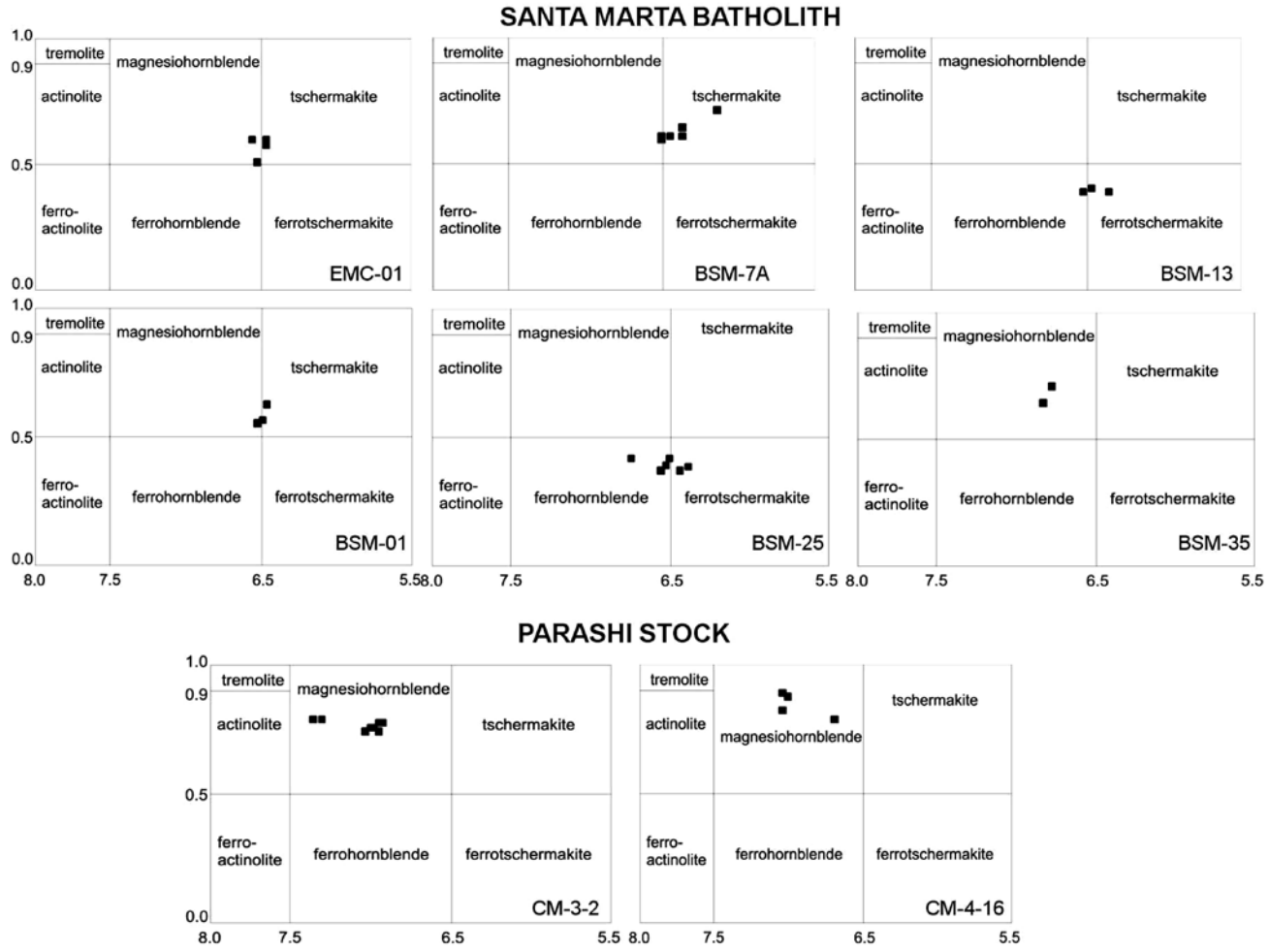

FIGURE 4 | **Composition of amphibole from the analyzed samples of the Santa Marta batholith and the Parashi stock in the amphibole classification scheme of Leake et al. (1997).**

several issues pertaining the higher temperature cooling history and associated exhumation can be reviewed. Comparing an Ar-Ar biotite closure depth of 8.3km (for ca. 250°C closure temperature; McDougall and Harrison, 1999) with the granitoid emplacement depth of ca. 16km, cooling rates between ca. 50-48Ma and 41Ma are of 0.73mm/y. Some of the Santa Marta granitoid exposures showing evidence of an overimposed deformation event in greenschist to amphibolite facies (Tschanz et al., 1969, 1974) probably relate to this exhumation event.

Following this event, between 41Ma and ca. 25Ma, long term exhumation rates seem to diminish down to the range 0.11-0.16mm/y (Fig. 6A), as determined from the biotite cooling depth to zircon-He depths (ca. 6km).

As mentioned, the emplacement depths of the Santa Marta batholith are in the range of 15-19km, which is far from the closure depth of the zircon-He system within the assumed range of geotherms. Therefore, the low temperature zircon- and apatite-He systems can be used to constrain the cooling and exhumation history. The distribution of zircon-He ages with elevation shows a weak variation between 23Ma and 26Ma (Fig. 5) that also reflects fast cooling and associated exhumation at this age. When zircon and apatite closure depths for closure temperatures of 180°C and 70°C are integrated, they vary in the 26-8Ma interval between 0.16 and 0.63mm/y. The lower rates of ca. 0.16mm/y are calculated for samples collected at lower elevation and are considered meaningless. Younger rates (ca. 10-15Ma), determined from the depth of apatite closure temperature and a surface temperature of 10°C, yielded values between 0.09 and 0.48mm/y, with the higher rates determined in samples collected at lower elevations.

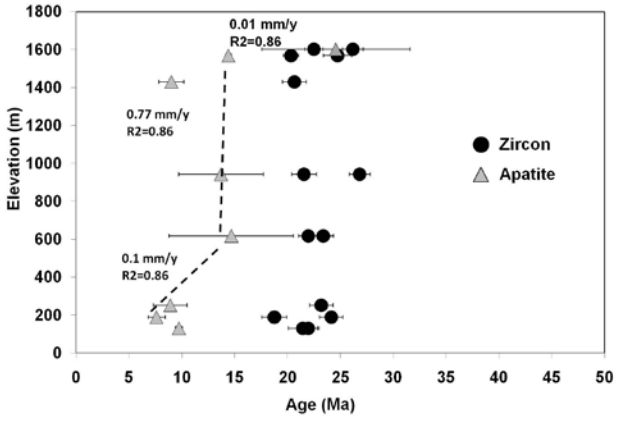

FIGURE 5 | **Santa Marta batholith zircon and apatite U-Th/He elevation profile. Apatite ages are weight average of two analyzed single grain aliquots per sample.**

Weighted average ages for each sample were calculated to construct the elevation profile. The distribution of apatite ages in the elevation profile can be divided into three different segments (Fig. 5). The lower segment, from 189m to 617m with ages between 7 and 14Ma, yields rates of ca. 0.1mm/y. The intermediate segment, from 617m to 1569m, lacks significant age variations (13-14Ma), suggesting the existence of a relatively fast cooling event with rates of 0.77mm/y. The upper segment, although marked by two samples of similar elevation (1569m and 1602m), shows a broader age variation between 14 and 23Ma and suggests very low rates (0.01mm/y).

In order to check for data consistency, we took another granitoid sample in an outcrop located at the southwest of the elevation profile. Sample EAM-18-72, collected at 139m, yielded zircon- and apatite-He ages of ca. 22Ma and 11Ma, respectively, which are similar to those determined for the elevation profile. Cooling rates between 22Ma and 11Ma extracted from this sample also yielded exhumation rates between 0.24 and 0.49mm/y between the depths of closure temperature of zircon and apatite calculated from assumed geothermal gradients of 40°C/km and 20°C/km, respectively. From the apatite data, exhumation rates after 11Ma are 0.13-0.27mm/y (Fig. 5).

In summary, the U-Th/He exhumation analysis for the Santa Marta batholith shows the existence of two relatively fast exhumation events at ca. 24Ma and ca. 15Ma.

Parashi stock

Figure 6B shows the pressure (depth)-time paths constructed for the Parashi stock assuming 20°C/km and 40°C/km geothermal gradients. Crystallization depth for the surface exposure of the Parashi stock ranges between 6.9 and 9km (Fig. 6B). This suggests that at least an equivalent amount of crust has been lost since ca. 48Ma. If stratigraphic relations with discordant Oligocene-Early Miocene conglomerates are considered, this unroofing was already accomplished by ca. 26-23Ma (Fig. 6B).

Biotite K-Ar ages for the Parashi stock granitoid have yielded ca. 45Ma (Lockwood, 1966; Cardona et al., 2007). This age is related to fast magmatic cooling, for it overlaps with hornblende K-Ar ages and are both close in time (less than 5Ma) with the U-Pb zircon crystallization ages. Also, calculated emplacement depths overlaps with zircon-He closure depths, suggesting that the zircon-He ages are related to fast magmatic cooling. On the other hand, similarities between zircon-and apatite-He ages (33.4Ma-38.3Ma and 30.4Ma-35.6Ma) suggest relatively fast cooling related to a Late Eocene exhumation event.

We have reconstructed the exhumation-cooling history of the Parashi stock using the same geothermal gradients (20-40°C/km) and zircon and apatite closure depths (for closure temperatures of 180°C and 70°C, respectively) as above for the Santa Marta region. Exhumation rates between 38Ma and 30.4Ma yielded values between 0.79 and 1.41mm/y. In addition, we considered an upper surface temperature of 10°C to constrain the cooling and exhumation rates after 30.4Ma. Stratigraphic relations with the Oligocene conglomerate suggest that this granitoid was exposed in the Late Oligocene–Early Miocene (ca. 26-23Ma). Therefore, rates between 26 and 23Ma are 0.29-0.98mm/y.

A similar approach was followed for the two conglomerate clasts. Zircon-He ages of 48–44.5Ma in the two clast overlap with the K-Ar biotite and hornblende ages (Lockwood, 1966; Cardona et al., 2007) and suggest that the zircon ages are also related to fast magmatic cooling. Exhumation rates between 48Ma to 36Ma were determined between closure He depths in zircon and apatite. Results vary between 0.51 and 1.46mm/y, which are considered maximum values for these samples, as already discussed, and probably come from the fast cooled and relatively shallow Eocene granitoid.

The younger rates between 36Ma and 23-28Ma yielded 0.13-0.40mm/y, as determined from the closure depth of He in apatite and an estimated Late Oligocene to Early Miocene deposition age for the conglomerate (Lockwood, 1966).

The integrated U-Th/He analyses of the Parashi granitoid suggest the existence of a major phase of exhumation between the Late Eocene to Oligocene (36-24Ma).

TECTONIC IMPLICATIONS

Orogeny in continuously active continental margins is influenced by collisions with arc, plateau or continental terranes, or by the nature of ocean-continent subduction geometry and dynamics (Jarrard, 1986; Silver et al., 1998; Cawood et al., 2009; DeCelles et al., 2009; Ramos, 2009). Whereas the understanding of uplift and deformation mechanisms during collisional events has improved in the last decades, mechanisms related to continuous subduction are less certain. The rate and direction of convergence and the thickness of the subducted oceanic plate have been considered as major factors for uplift and exhumation in subduction systems (Silver et al., 1998; Spikings et al., 2001, 2008; Sobolev and Babeyco, 2005; Oncken et al., 2006; DeCelles et al., 2009; Ramos, 2009; Von Houne and Ranero, 2009).

Increasingly sophisticated plate tectonic and paleogeographic reconstructions of the Circum-Caribbean region have shown that since the Late Cretaceous, the tectonic evolution of northwestern South America including the Northern Andes is linked to the interaction of the allochthonous (Pacific-derived) Caribbean oceanic plate with the South American continental margin (Pindell, 1993; Pindell et al., 1998, 2005; Spikings et al., 2000, 2001; Cortés et al., 2005; Montes et al., 2005; Vallejo et al., 2006, 2009; Jaillard et al., 2010; Kennan and Pindell, 2009; Pindell and Kennan, 2009). Although the positions

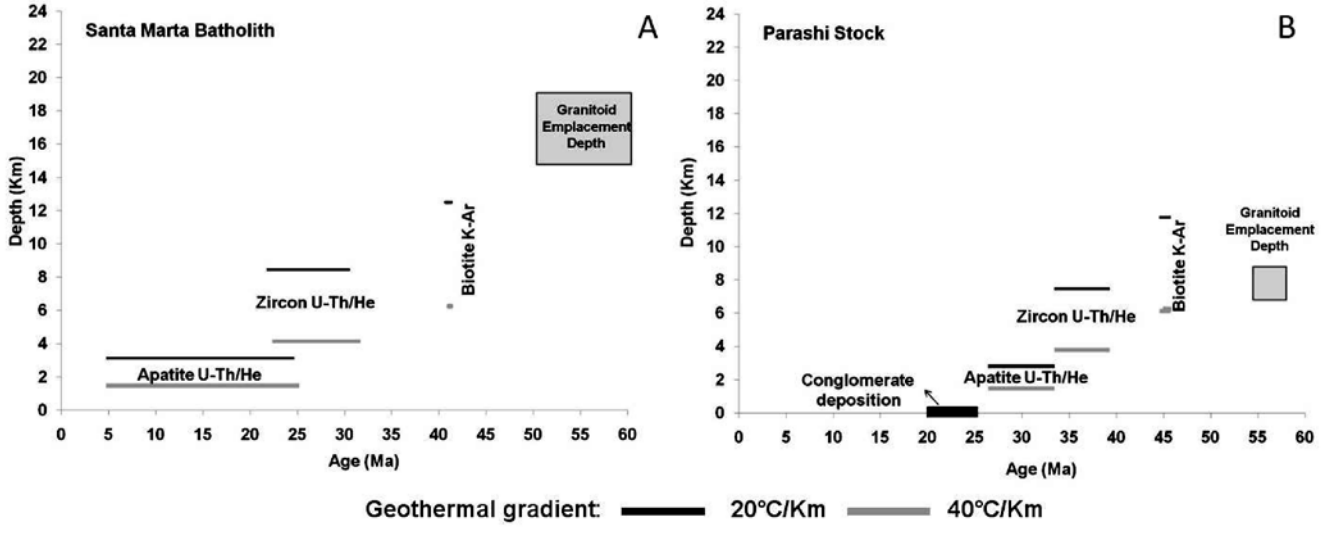

FIGURE 6 | **Depth (pressure)-time paths of A) the Santa Marta Batholith and B) the Parashi stock.**

of the Santa Marta massif and Guajira Serranías have changed throughout the Cenozoic (Muessig, 1984; Macellari, 1995; Bayona et al., 2010; Montes et al., 2010), their paleogeography since the Late Cretaceous is located near the southern margin of the Caribbean plate. Adopting these paleogeographic restrictions, we used the time and rates of exhumation of the Santa Marta batholith and the Parashi stock to test the Cenozoic tectonic scenarios of the Caribbean–South America interactions.

The U/Th-He thermochronological results presented here largely constrain post-Eocene unroofing. Paleogeographic reconstructions suggest that the Caribbean–South American interaction began in the Late Cretaceous when the thick and heterogeneous Caribbean oceanic plate approached the continental margin of South America from an allochthonous Pacific position (Burke, 1988; Pindell, 1993; Mauffet and Leroy, 1997; Pindell et al., 1998, 2005; Pindell and Kennan, 2009). This resulted in an oblique collision of several arc and oceanic plateau lithospheres from Ecuador to the western margin of the Colombian Andes (Pindell, 1993; Kerr et al., 1997; Spikings et al., 2000, 2001; Pindell et al., 2005; Vallejo et al., 2006, 2009; Jaillard et al., 2008). Although this event is not recorded by He thermochronological data, Late Maastrichtian to Paleocene metamorphic remnants that host the sampled granitoids, including high pressure metasedimentary rocks and eclogites in Guajira, are related to this major collisional event (Bustamante et al., 2009; Cardona et al., 2010a; Weber et al., 2007, 2009, 2010). Provenance constraints from Paleocene to Eocene sandstones of the Cesar-Ranchería basins located in the southeastern flank of the Santa Marta massif show major Early Paleocene changes in detrital sources that are related to the uplift of the northwestern segment of the Santa Marta massif (Bayona et al., 2007; Ayala-Calvo et al., 2010).

The Late Cretaceous-Paleogene Caribbean–South American arc-collision orogeny was followed by the eastern displacement of the Caribbean plate in between the margins of the Americas (Müeller et al., 1999; Kennan and Pindell, 2009; Pindell and Kennan, 2009). Plate tectonic reconstructions have shown that, during the Cenozoic, North and South America experienced major changes in the direction and rates of convergence that directly influence the kinematic interaction of the Caribbean and South American plates (Pindell et al., 1988; Müeller, 1999). This includes the transition from a slow and sinistral transtension regime between 83Ma and 55.9Ma that overlaps with the timing of the Late Cretaceous-Paleogene collisional event, to 6.5-1.5mm/y northeast-southwest convergence in the 55.9-38.4Ma interval. Tomographic analyses have also shown the existence of a deep slab below the Maracaibo block that includes the Santa Marta and Guajira regions (van der Hilst and Mann, 1994; Taboada et al., 2000; Miller et al., 2009). Simple plate convergence rate calculations and the current location of the slab as far as the Venezuelan Andes correlate with an inception of this slab in the Maracaibo block since the Early Paleocene, as also suggested by the existence of Late Paleocene to Eocene arc-related plutonism in Santa Marta and Guajira (Cardona et al., 2007, 2008; Duque et al., 2009).

The Santa Marta arc is characterized by a well defined crystallization record between 58-50Ma (Cardona et al., 2008; Duque et al., 2009). Fast magmatic cooling of these granitoids is suggested by a recalculated hornblende K-Ar age of ca. 45Ma from Tschanz et al. (1974) and Ar-Ar ages (Duque et al., 2009). Although fast magmatic cooling is a common feature of intermediate to shallow plutons (Glazner et al., 2004; Parada et al., 2005), the elongated character of this body and the existence of significant mineral orientations at its margins (Tschanz et al., 1969; Duque et al., 2009) suggest that its emplacement was controlled by compressional to transpressional tectonics (Saint Blanquat et al., 1998).

As already mentioned, the published biotite K-Ar ages of ca. 41Ma, in addition to the determined granitoid emplacement depth and the ca. 10Ma between the younger granitoid crystallization ages and the K-Ar cooling age, suggest another relatively fast exhumation event during the Early Eocene (ca. 50-41Ma). Evidences of local overimposed mylonitic deformation in the granitoid rocks including our field observations in the coastal zone may be related to deformation during this exhumation event (Tschanz et al., 1969, 1974).

We therefore suggest that the faster North-South approach between North and South America that ensued the onset of subduction of the Caribbean plate below South America (Pindell et al., 1988; Müeller et al., 1999) facilitated uplift and exhumation in the upper plate during the Middle Eocene (Fig. 7A; Gorczyk et al., 2008). Exhumation was probably accentuated by the effects of the subduction of a thick buoyant Caribbean plate (Cloos, 1993; Mauffret and Leroy, 1997; Spikings et al., 2001, 2008; Espurt et al., 2008; Pindell and Kennan, 2009).

Between 41 and 25Ma, long term exhumation rates on Santa Marta slowed down, contrasting with the 35-30Ma exhumation record in Guajira. Stratigraphical analysis, tectonic reconstructions and paleomagnetism suggest that block rotation in the Santa Marta massif and Guajira region took place during this time interval, forming several transtensional basins in the Guajira region (Fig. 7B, MacDonald and Opdyke, 1972; Muessig, 1984; Macellari, 1995; Vence, 2008; Bayona et al., 2010; Montes et al., 2010). Thus, we suggest that this exhumation phase in Santa Marta and Guajira

is related to the slow transcurrent configuration that characterized the Caribbean-South America interface between 38.4 and 25.8Ma (Müeller et al., 1999; Pindell and Kennan, 2009). The higher Late Eocene rates recorded by the Parashi stock, which extend until the Early Oligocene, may be the result of more severe block rotation and displacements on the Guajira Peninsula (MacDonald and Opdyke, 1972).

The Santa Marta batholith records additional exhumation phases at ca. 24 and 14Ma, contrasting with the limited exhumation record in the Parashi stock after 24Ma and the contemporaneous basin deepening in the Guajira basins (Lockwood, 1966; Vence, 2008). Between 25.8 and 9.5Ma there is evidence for an increase in convergence rates between North and South America, with values of 9.6-2.1mm/y (Müeller et al., 1999). The two periods of exhumation recorded in Santa Marta may have been triggered by this geodynamic configuration. Additional tectonic controls that favor exhumation during these periods include a Late Oligocene increase in the convergence rate between the Farallon plate and the western margin of South America (Pardo-Casas and Molnar, 1987), which was responsible for the northeastern migration of the Northern Andean blocks (including the Maracaibo block) in a fashion similar to what is seen today by GPS measurement (Trenkamp et al., 2002). Within this scenario the northern Andean blocks are pushed to the North to override the thick Caribbean plate, facilitating uplift in a way as has been argued for several segments of the Central and Southern Andes (Silver et al., 1998; Oncken et al., 2006; Kay and Coira, 2009; Ramos, 2009).

The difference in the post-Oligocene exhumation behavior between the Santa Marta and Guajira regions is also probably related to the differences between the degree of convergence obliquity. The Guajira region is apparently influenced by more oblique convergence relations than the Santa Marta region (Fig. 7C).

REGIONAL CORRELATIONS

The Santa Marta massif, the Guajira Serranías, the Perijá Range, the Venezuelan Andes and offshore and onshore bounding basins are part of the Maracaibo block (Case et al., 1984). Although previous fission track data on the adjacent Perijá range by Kohn et al. (1984) are not precise due to the acquisition technique based on the population method and the absence of track length data (reviews on Lisker et al., 2009), the correlation of the results with tectonostratigraphic analysis (Kellogg, 1984) suggest that the Sierra de Perijá experienced uplift phases during the Early and Middle Eocene, Late Oligocene and Pliocene.

Recent structural analysis of the Paleogene Ranchería basin in the southeast foothills of the Santa Marta massif also revealed the existence of a major post–50Ma shortening event (Montes et al., 2010), while apatite fission track analyses on Cretaceous sedimentary rocks of the southwestern flank of the Perijá Massif (Fig. 1A) have shown a major Miocene (ca. 12Ma) event (Hernández and Jaramillo, 2009).

The Valle Inferior of the Magdalena and Guajira basins that surround the Santa Marta and Guajira uplifted regions also record major Late Eocene–Early Oligocene, Late Oligocene–Early Miocene and Late Miocene sedimentary hiatuses (Rincón et al., 2007). Published

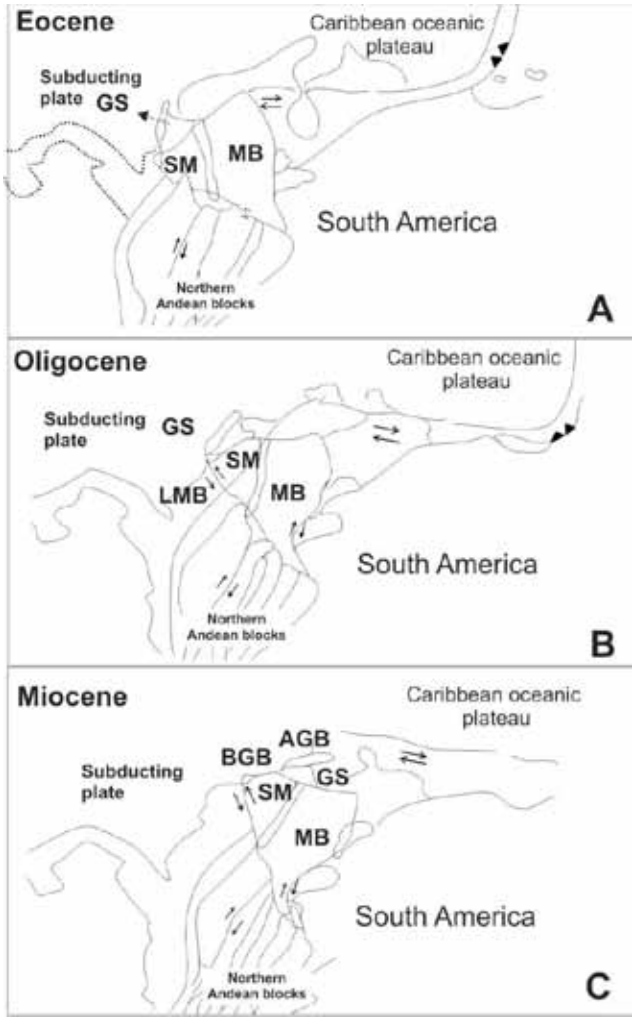

FIGURE 7 | **Cenozoic paleogeographic reconstructions of northwestern South America-Caribbean region (modified from Montes et al., 2005; 2009; Pindell and Keenan, 2009). A) Paleogene, B) Oligocene, C) Miocene-Present. See text for details. SM: Santa Marta Massif, GS: Guajira Serranía, AGB: Alta Guajira Basin, BGB: Baja Guajira Basin, LMB: Lower Magdalena Valley Basin, MB: Maracaibo Block.**

thermochronological data for the Mérida Andes of Venezuela have also shown the existence of three distinct cooling/exhumation events at ca. 2-4Ma, 6-8Ma and 17-20Ma (Kohn et al., 1984; Bermúdez et al., 2010). Similarly, the evolution of the Leeward Antilles records several phases of transtension, block rotation and a major uplift in the Late Miocene (Beardsley and Avé Lallemant, 2007; Gorney et al., 2007).

All these data indicate that the Eocene to Miocene exhumation events found in the Santa Marta and Guajira regions have affected the entire Maracaibo block. Although collision of oceanic domains with the South American margin may be responsible for some of the Late Oligocene and Miocene exhumation and deformational events of the northern Andes (Spikings et al., 2001, 2005; Parra et al., 2009; Restrepo-Moreno et al., 2009) and the Circum-Caribbean region (Sisson et al., 2008), major changes in oceanic-continent convergence relations and variations in thickness of the subducted oceanic crust seem to be the main control for exhumation and uplift in some of these orogens where evidence for collision is null (Pardo-Casas and Molnar, 1987; Silver et al., 1998; Spikings et al., 2001).

CONCLUSIONS

U-Th/He zircon and apatite thermochronological constraints and geological considerations from the Paleogene Santa Marta batholith and the Parashi stock have shown the existence of distinct Oligocene (ca. 35-24Ma) and Miocene (ca. 15-10Ma) exhumation pulses in the northern Colombian Caribbean region. Plate tectonic analysis suggests that the major controls for pre-Late Eocene events are the collision between the Caribbean plate margin and the South American continent in the Late Cretaceous–Early Paleocene and the new subduction zone that was initiated in the Early Eocene. In contrast, the post-Late Eocene events may be correlated to major changes in the rate and vector of convergence between the North and South American plates, the associated underthrusting of the buoyant Caribbean plate, and the northwestern fast overriding of the continent over the oceanic plate.

Differences in the exhumation patterns of the Eocene Santa Marta and Guajira granitoids are related to the separation of these massifs from a former continuous margin, and the formation of different transtensional basins in northeastern Colombia.

These events are temporally correlatable with other Andean and Circum-Caribbean areas and reflect the major plate tectonic reorganizations during the Cenozoic and their influence in regional orogeny.

ACKNOWLEDGMENTS

ECOPETROL-ICP, INGEOMINAS and INVEMAR are acknowledged for the support given to A. Cardona during his participation in the Sierra Nevada de Santa Marta geological project, including access to sample collections. Diego Morata and an anonymous reviewer are acknowledged for their suggestions and reviews that enormously improved the manuscript. Sergio Restrepo is acknowledged for his valuable suggestions. Field work in the Guajira Region and U-Th/He analyses received support from the Fundación para el Apoyo de la Investigación y la Cultura del Banco de la República de Colombia (project 2289), and the Universidad Nacional de Colombia DIME Grant 30805975. Funding for the LaserChron Center was provided by the NSF EAR-0443387. Scientific support by C. Jaramillo is enormously appreciated. C. Bustamante and S. Zapata are acknowledged for helping with the data organization and sample collection. A. García-Casco is acknowledged for continuous discussions and encouragement. This is a contribution to the IGCP 546: "Subduction zones of the Caribbean".

REFERENCES

Avé Lallemant, H.G., 1997. Transpression, displacement partitioning, and exhumation in the eastern Caribbean/South American plate boundary zone. Tectonics, 16, 272-289.

Ayala-Calvo, C., Bayona, G., Ojeda-Marulanda, Cardona, A., Valencia, V., Padrón, C.E., Yoris, F., Mesa-Salamanca, J., García, A., 2010. Stratigraphy and provenance of Campanian-Paleogene units in Cesar sub-basin: contributions to the regional tectonic evolution. Geología Colombiana, 34, 1-34.

Bayona, G., Lamus-Ochoa, F., Cardona, A., Jaramillo, C., Montes, C., Tchegliakova, N., 2007. Procesos orogénicos del Paleoceno para la Cuenca Ranchería (Guajira, Colombia) y áreas adyacentes definidos por análisis de procedencia. Geología Colombiana, 32, 21-46.

Bayona, G., Jimenez, G., Silva, C., Cardona, A., Montes, C., Roncancio, J., 2010. Paleomagnetic data uncovered from Mesozoic units of the Santa Marta massif: constrain for paleogeographic and paleotectonic evolution of the NW corner of the South America plate. Journal of South American Earth Sciences, 29, 817-831.

Beardsley, A.G., Avé-Lallemant, H.G., 2007. Oblique collision and accretion of the Netherlands Leeward Antilles to South America. Tectonics, 26, TC2009, 16pp. doi: 10.1029/2006TC002028

Bermúdez, M.A., Kohn, B.P., van der Beek, P.A., Bernet, M., O'Sullivan, P.B., Shagam, R., 2010. Spatial and temporal patterns of exhumation across the Venezuelan

Andes: Implications for Cenozoic Caribbean geodynamics. Tectonics, 29, TC5009. doi: 10.1029/2009TC002635

Bernet, M., Spiegel, C., 2004. Introduction: Detrital thermochronology. In: Bernet, M., Spiegel, C. (eds.). Detrital Thermochronology: Provenance analysis, Exhumation and Landscape Evolution of Mountain Belts. Geological Society of America Special Publication, 378, 1-8.

Burke, K., 1988. Tectonic evolution of the Caribbean. Annual Reviews on Earth and Planetary Science, 16, 201-230.

Burke, K., Cooper, C., Dewey, J.F., Mann, P., Pindell, J.L., 1984. Caribbean tectonics and relative motions. In: Bonini, W.E., Hargraves, R.B., Shagam, R., (eds.). The Caribbean–South American plate boundary and regional tectonics. Geological Society of America Memoir, 162, 31-63.

Bustamante, C., Cardona, A., Saldarriaga, M., García-Casco, A., Valencia, V., Weber, M., 2009. Metamorfismo de los esquistos verdes y anfibolitas pertenecientes a los Esquistos de Santa Marta, Sierra Nevada de Santa Marta (Colombia): ¿registro de la colisión entre el Arco Caribe y la margen Suramericana? Boletín de Ciencias de la Tierra, 27, 7-24.

Brown, R.W., Summerfield, M.A., 1997. Some uncertainties in the derivation of rates of denudation from thermochronologic data. Earth Surface Process and Landforms, 22, 239-248.

Cardona, A., Weber, M., Cordani, U., Wilson, R., Gomez, J., 2007. Evolución tectono-magmática de las rocas máficas-ultramáficas del Cabo de la Vela y el Stock de Parashi, Península de la Guajira: registro de la evolución orogénica Cretácica-Eocena del norte de Suramérica y el Caribe. Bucaramanga, August 14-17, XI Congreso Colombiano de Geología, CD with Abstracts, 1-7.

Cardona, A., García-Casco, A., Valencia, V., Weber, M., Pepper, M., 2009. Coastal Cretaceous Metamorphic Complexes of the Sierra Nevada de Santa Marta: a Record of Collision and Subduction. Havana (Cuba), March 13–25, Workshop "Subduction Zones of the Caribbean". Available at: http://www.ugr.es/~agcasco/igcp546/

Cardona, A., Duque, J.F., Ruiz, J., Valencia, V., Bayona, G., Jaramillo, C., Ojeda, G., Orozco, M.T., 2008. Geochronology and tectonic implications of granitoids rocks from the northwestern Sierra Nevada de Santa Marta and surrounding basins, northeastern Colombia: Late Cretaceous to Paleogene convergence, accretion and subduction interactions between the Caribbean and South American plates. 24th–28th March 2008, Santo Domingo (Dominican Republic), Abstract Volume of the 18th Caribbean Geological Conference, 24-25.

Cardona, A., Valencia, V., Bustamante, C., Garcia-Casco, A., Ojeda, G., Ruiz, J., Saldarriaga, M., Weber, M., 2010a. Tectonomagmatic setting and provenance of the Santa Marta Schists, Northern Colombia: insights on the growth and approach of Cretaceous Caribbean Oceanic Terranes to the South American continent. Journal of South American Earth Sciences, 29, 784-804.

Cardona, A., Chew, D., Valencia, V.A., Bayona, G., Miskovic, A., Ibañez-Mejia, M., 2010b. Grenvillian remnants in the Northern Andes: Rodinian and Phanerozoic paleogeographic perspectives. Journal of South American Earth Sciences, 29, 784-804.

Cardona, A., Valencia, V., Garzón, A., Montes, G., Ojeda, G., Ruiz, J., Weber, M., 2010c. Permian to Triassic I to S-type magmatic switch in the northeast Sierra Nevada de Santa Marta and adjacent regions, Colombian Caribbean: Tectonic setting and implications within Pangea paleogeography. Journal of South American Earth Sciences, 29, 772-783.

Cardona-Molina, A., Cordani, U., MacDonald, W., 2006. Tectonic correlations of pre-Mesozoic crust from the northern termination of the Colombian Andes, Caribbean region. Journal of South American Earth Sciences, 21, 337-354.

Case, I.E., MacDonald, W., 1973. Gravity Anomalies and Crustal Structure in Northern Colombia. Geological Society of America Bulletin, 84, 2905-2916.

Case, J., Holcombe, T.L., Martin, R.G., 1984. Map of geologic provinces in the Caribbean region. In: Bonini, W.E., Hargraves, R.B., Shagam, R., (eds.). The Caribbean–South American plate boundary and regional tectonics. In: Bonini, W.E., Hargraves, R.B., Shagam, R., (eds.). The Caribbean–South American plate boundary and regional tectonics. Geological Society of America Memoir, 162, 1-31.

Cawood, P.A., Kröner, A., Collins, W.J., Kusky, T.D., Mooney, W.D., Windley, B.F., 2009. Accretionary orogens through Earth history. In: Cawood, P.A., Kröner, A. (eds.). Earth accretionary systems in space and time. London, Geological Society, 318 (Special Publications), 1-36.

Cerón, J., Kellogg, J., Ojeda, G.Y., 2007. Basement configuration of the northwestern South America-Caribbean margin from recent geophysical data. Ciencia, Tecnología y Futuro, 3, 25-49.

Cerón-Abril, J., 2008. Crustal structure of the Colombian Caribbean basin and margins. University of South Carolina. PhD Thesis. 165pp.

Cloos, M., 1993. Lithospheric buoyancy and collisional orogenesis: Subduction of oceanic plateaus, continental margins, island arcs, spreading ridges, and seamounts. Geological Society of America Bulletin, 105, 715-737.

Colgan, J.P., Shuster, D.L., Reiners, P.W., 2008. Two-phase Neogene extension in the northwestern Basin and Range recorded in a single thermochronology sample. Geology, 36, 631-634.

Colmenares, L., Zoback, M.D., 2003. Stress field and seismotectonics of northern South America. Geology, 31, 721-724.

Cordani, U.G., Cardona, A., Jimenez, D., Liu, D., Nutman, A.P., 2005. Geochronology of Proterozoic basement inliers from the Colombian Andes: tectonic history of remnants from a fragmented Grenville belt. In: Vaughan, A.P.M., Leat, P.T., Pankhurst, R.J. (eds.). Terrane Processes at the Margins of Gondwana. Geological Society of London, 246 (Special Publication), 329-346.

Cortés, M., Angelier, J., Colletta, B., 2005. Paleostress evolution of the northern Andes (Eastern Cordillera of Colombia):

Implications on plate kinematics of the South Caribbean region. Tectonics, 24(1), doi: 10.1029/2003TC001551

Cross, T.A., Pilger, R.H., 1982. Controls on subduction gemetry, location of magmatic arcs, and tectonics of arc and back-arc regions. Geological Society of America Bullettin, 93, 545-562.

Cruz, L., Fayon, A., Teyssier, Ch., Weber, J., 2007. Exhumation and deformation processes in transpressional orogens: The Paria Peninsula, SE Caribbean–South American plate boundary. In: Till, A.B., Roeske, S.M., Sample, J.C., Foster, D. (eds.). Exhumation associated with strike-slip systems. Geological Society of America, 434 (Special Paper), 149-165.

DeCelles, P.G., Ducea, M.N., Kapp, P., Zandt, G., 2009. Cyclicity in Cordilleran orogenic systems. Nature Geoscience, 2, 251-257.

Doolan, B.L., 1971. Structure and metamorphism of the Santa Marta area, Colombia, South America. Ph.D. Thesis. Binghamton (New York), New York State University, 200pp.

Dimate, C., Rivera, L., Taboada, A., Delouis, B., Osorio, A., Jimenez, E., Fuenzalida, A., Cisternas, A., Gomez, I., 2003. The 19 January 1995 Tauramena (Colombia) earthquake: geometry and stress regime. Tectonophysics, 363, 159-180.

Duque, J., Orozco, M.T., Cardona, A., Ferrari, L., Solari, L., 2009. Geoquímica y geocronología (U/Pb y Ar/Ar) de las rocas Paleoceno-Eoceno en la Sierra Nevada de Santa Marta y sus relaciones con la tectónica del Caribe y el arco magmático Circum-Caribeño. Paipa, XII Colombian Geological Congress, September, CD with abstracts, 7-11.

Duque-Caro, H., 1979, Major structural elements and evolution of northwestern Colombia. In: Watkins, J.S., Montadert, L., Dickerson, P.W. (eds.). Geological and geophysical investigations of continental margins. American Association of Petroleum Geologists, 29 (Memoir), 329-351.

Duque-Caro, H., 1984. Structural Style, diapirism and accretionary episodes of the Sinu-San Jacinto terrane, southwestern Caribbean borderland. In: Bonini, W.E., Hargraves, R.B., Shagam, R., (eds.). The Caribbean–South American plate boundary and regional tectonics. Geological Society of America Memoir, 162, 303-316.

Espurt, N., Funiciello, F., Martinod, J., Guillaume, B., Regard, V., Faccenna, C., Brusset, S., 2008. Flat subduction dynamics and deformation of the South American plate: Insights from analog modeling. Tectonics, 27, TC3011. doi:10.1029/2007TC002175

Farley, K.A., Wolf, R.A., Silver, L.T., 1996. The effects of long alpha-stopping distances on (U-Th)/He ages. Geochimica et Cosmochimica Acta, 60, 4223-4229.

Farley, K.A., 2000, Helium diffusion from apatite: General behavior as illustrated by Durango fluorapatite. Journal of Geophysical Research, 105, 2903-2914. doi:10.1029/1999JB900348

Farley, K.A., 2002. (U-Th)/He dating: techniques, calibrations, and applications. Reviews in Mineral and Geochemistry, 47, 819-844.

Fitzgerald, P.G., Baldwin, S.L., Webb, L.E., O'Sullivan, P.B., 2006. Interpretation of (U-Th)/He single grain ages from slowly cooled crustal terranes: A case study from the Transantarctic Mountains of southern Victoria Land. Chemical Geology, 225, 91-120.

Gehrels, G., Valencia, V., Ruiz, J., 2008. Enhanced precision, accuracy, efficiency, and spatial resolution of U-Pb ages by laser ablation-multicollector-inductively coupled plasma mass spectrometry. Geochemistry, Geophysics, Geosystems, 9, Q03017. doi: 10.1029/2007GC001805

Gerya, T., Fossati, D., Cantieni, C., Seward, D., 2009. Dynamic effects of aseismic ridge subduction: numerical modeling. European Journal of Mineralogy, 21, 649-661.

Glazner, A.F., Bartley, J.M., Coleman, D.S., Gray, W., Taylor, R.Z., 2004. Are plutons assembled over millions of years by amalgamation from small magma chambers? GSA Today, 14, 4-11.

Gómez, E., Jordan, T., Allmendinger, R.W., Hegarty, K., Kelley, S., 2005. Syntectonic Cenozoic sedimentation in the northern middle Magdalena Valley Basin of Colombia and implications for exhumation of the Northern Andes. Geological Society of America Bulletin, 117, 547-569.

Gorney, D., Escalona, A., Mann, P., Magnani, M.B., and the BOLIVAR Study Group, 2007. Chronology of Cenozoic tectonic events in western Venezuela and the Leeward Antilles based on integration of offshore seismic reflection data and onland geology. American Association of Petroleum Geologists Bullettin, 91, 653-684.

Gorczyk, W., Willner, A.P., Gerya, T.V., Connolly, J.A.D., Burg, J.-P., 2007. Physical controls of magmatic productivity at Pacific-type convergent margins: Numerical modeling. Physics of the Earth and Planetary Interiors, 163, 209-232.

Gutsher, M-A, 2002. Andean subduction styles and their effect on thermal structure and intraplate coupling. Journal of South American Earth Sciences, 15, 3-10.

Guzmán, G., 2007, Stratigraphy and sedimentary environment and implicationsin the Plato basin and the San Jacinto belt, northwestern Colombia. Ph.D.Thesis. Belgium, University of Liège, 275pp.

Hall, R., 2002. Cenozoic geological and plate tectonic evolution of SE Asia and the SW Pacific: computer-based reconstructions, model and animations. Journal of Asian Earth Sciences, 20, 353-431.

Hernández, O., Jaramillo, J.M., 2009. Reconstrucción de la historia termal en los sectores de Luruaco y Cerro Cansona–cuenca del Sinú-San Jacinto y en el piedemonte occidental de la Serranía del Perijá entre Codazzi y la Jagua de Ibirico–cuenca de Cesar-Ranchería. Informe Final Cuenca Cesar-Ranchería. Agencia Nacional de Hidrocarburos (Bogotá), 58pp.

Hourigan, J.K., Reiners, P.W., Brandon, M.T., 2005. U-Th zonation-dependent alpha-ejection in (U-Th)/He chronometry. Geochimica et Cosmochimica Acta, 69, 3349-3365.

House, M.A., Farley, K.A., Kohn, B.P., 1999. An empirical test of helium diffusion in apatite: borehole data from the Otway Basin, Australia. Earth and Planetary Science Letters, 170, 463-474.

House, M.A, Farley, K.A., Stockli, D.F., 2000. Helium chronometry of apatite and titanite using Nd-YAG laser heating. Earth and Planetary Science Letters, 183, 365-368.

Hughes, R.A., Pilatasig, L.F., 2002. Cretaceous and Tertiary terrane accretion in the Cordillera Occidental of the Andes of Ecuador. Tectonophysics, 345, 29-48.

Jaillard, E., Bengtson, P., Ordoñez, M., Vaca, W., Dhondt, A., Suarez, J., Toro, J., 2008. Sedimentary record of terminal Cretaceous accretions in Ecuador: The Yunguilla Group in the Cuenca area. Journal of South American Earth Sciences, 25, 133-144.

Jaillard, E., Lapierre, H., Ordoñez, M., Toro Álava, J., Amórtegui, A., Vanmelle, J., 2010. Accreted oceanic terranes in Ecuador: southern edge of the Caribbean plate? In: James, K.H., Lorente, M.A., Pindell, J. (eds.). The Origin and Evolution of the Caribbean Plate. Geological Society of London, 328 (Special Publication), 469-485.

Jarrard, R.D., 1986. Relations among subduction parameters. Reviews of Geophysics, 24, 217-284.

Kay, S.M., Coira, B.L., 2009. Shallowing and steepening subduction zones, continental lithosphere loss, magmatism and crystal flow under the Central Andean Altiplano Puna Plateau. In: Kay, S.M., Ramos, V.A., Dickinson, W.D. (eds.). Backbone of the Americas: Shallow Subduction, Plateau Uplift, and Ridge and Terrane Collision. Geological Society of America, 204 (Memoir), 229-260.

Kennan, L., Pindell, J., 2009. Dextral shear, terrane accretion and basin formation in the Northen Andes: best explained by interaction with a Pacific-derived Caribbean Plate?. In: James, K.H., Lorente, M.A., Pindell, J. (eds.). The Origin and Evolution of the Caribbean Plate. Geological Society of London, 328 (Special Publication), 487-532.

Kellogg, J.N., Bonini, W.E., 1982. Subduction of the Caribbean plate and basement uplifts in the overriding South American plate. Tectonics, 1, 251-276.

Kellogg, J.N., 1984. Cenozoic tectonic history of the Sierra de Perija, Venezuela-Colombia, and adjacent basins. In: Bonini, W.E., Hargraves, R.B., Shagam, R., (eds.). The Caribbean–South American plate boundary and regional tectonics. Geological Society of America Memoir, 162, 239-261.

Kellogg, J.N., Vega, V., 1995. Tectonic development of Panama, Costa Rica, and the Colombian Andes: Constraints from Global Positioning System geodetic studies and gravity. In: Mann, P., Kolarsky, R.A. (eds.). Geologic and Tectonic Development of the Caribbean plate boundary southern Central America. Geological Society of America, 295 (Special Paper), 75-90.

Kerr, A.C., Marriner, G.F., Tarney, J., Nivia, A., Saunders, A.D., Thirlwall, M.F., Sinton, C.W., 1997. Cretaceous basaltic terranes in western Colombia: Elemental, chronological and Sr-Nd constraints on petrogenesis. Journal of Petrology, 38, 677-702.

Kerr, A.C., White, R.V., Thompson, P.M.E., Tarney, J., Saunders, A.D., 2003. No oceanic plateau–no Caribbean Plate? The seminal role of an oceanic plateau in Caribbean plate evolution. In: Bartolini, C., Buffler, R.T., Blickwede, J. (eds.). The Gulf of Mexico and Caribbean Region: Hydrocarbon Habitats, Basin Formation and Plate Tectonics. American Association of Petroleum Geologists, 79 (Memoirs), 126-168.

Kohn, B., Shagam, R., Banks, P., Burkley, L., 1984. Mesozoic–Pleistocene fission track ages on rocks of the Venezuelan Andes and their tectonic implications. In: Bonini, W.E., Hargraves, R.B., Shagam, R., (eds.). The Caribbean–South American plate boundary and regional tectonics. Geological Society of America Memoir, 162, 365-384.

Leake, B.E., Woolley, A.R., Arps, C.E.S., Birch, W.D., Gilbert, M.C., Grice, J.D., Hawthorne, F.C., Kato, A., Kisch, H.J., Krivovichev, V.G., Linthout, K., Laird, J., Mandarino, J.A., Maresch, W.V., Nickel, E.H., Rock, N.M.S., Schumacher, J.C., Smith, D.C., Stephenson, N.C.N., Ungaretti, L., Whittaker, E.J.W., Youzh, G., 1997. Nomenclature of amphiboles: report of the Subcommittee on Amphiboles of the International Mineralogical Association, Commission on New Minerals and Mineral Names. Canadian Mineralogist, 35, 219-246.

Lisker, F., Ventura, B., Glasmacher, U.A., 2009. Apatite thermochronology in modern geology. In: Lisker, F., Ventura, B., Glasmacher, U.A. (eds.). Thermochronological Methods: From Palaeotemperature Constraints to Landscape Evolution Models. Geological Society of London, 324 (Special Publications), 1-23.

Lockwood, J.P., 1966. Geology of the Serranía de Jarara area, Guajira Península, Colombia. Ph.D. Thesis. Princeton, Princeton University, 237pp.

López, C., Ojeda, G., 2006. Heat flow in the Colombian Caribbean from the bottom simulating reflector (BSR). Ciencia Tecnología &. Futuro (C.T.F.), 3, 29-39.

Ludwig, K.R., 2003, User's Manual for Isoplot 3.00. Berkeley, CA, Berkeley Geochronology Center, 70pp.

Ludwig, K.R., Mundil, R., 2003. Extracting reliable U-Pb ages and errors from complex populations of zircons from Phanerozoic tuffs. Geochimica et Cosmochimica Acta, 66, 463. doi: 10.1016/S0016-7037(01)00786-4

Lugo, J., Mann, P., 1995. Jurassic-Eocene tectonic evolution of Maracaibo Basin, Venezuela. In: Tankard, A., Suarez, R., Welsink, H. (eds.). Petroleum Basins of South America. American Association of Petroleum Geologists, 62 (Memoir), 699-725.

Luzieux, L.D.A., Heller, F., Spikings, R., Vallejo, C.F., Winkler, W., 2006. Origin and Cretaceous tectonic history of the coastal Ecuadorian forearc between 1°S-4°S: Paleomagnetic, radiometric and fossil evidence. Earth and Planetary Science Letters, 249, 400-414.

Macellari, C., 1995, Cenozoic sedimentation and tectonics of the southwestern Caribbean pull-apart basin, Venezuela and Colombia. In: Tankard, A., Suarez, S., Welsink, H. (eds.). Petroleum basins of South America. American Association of Petroleum Geologists, 62 (Memoir), 757-780.

MacDonald, W.D., Doolan, B.L., Cordani, U.G., 1971. Cretaceous–Early Tertiary metamorphic K–Ar age values from the South Caribbean. Geological Society of America Bulletin, 82, 1381-1388.

MacDonald, W., Opdyke, N.D., 1972. Tectonic rotations suggested by paleomagnetic results from northern Colombia, South America. Journal of Geophysical Research, 77, 5720-5730.

Malavé, G., Suarez, G., 1995. Intermediate-depth seismicity in northern Colombia and western Venezuela and its relationship to Caribbean Plate subduction. Tectonics, 14, 617-628.

Mancktelow, N., Grasemann, B., 1997. Time-dependent effects of heat advection and topography on cooling histories during erosion. Tectonophysics, 270, 167-195.

Martínez, L.F., 2008. Metamorfismo de contacto y emplazamiento del Stock de Parashi en la Serranía de Jarara, Alta Guajira Colombia. Degree Thesis. Sede Bogotá, Universidad Nacional, 22pp.

Mauffret, A., Leroy, S., 1997. Seismic stratigraphy and structure of the Caribbean igneous province. Tectonophysics, 283, 61-104.

McDougall, I., Harrison, T.M., 1999. Geochronology and thermochronology by the Ar/Ar method. Oxford, University Press, 269pp.

McDowell, F.W., McIntosh, W.C., Farley, K.A., 2005. A precise Ar-40-Ar-39 reference age for the Durango apatite (U-Th)/He and fission-track dating standard. Chemical Geology, 214, 249-263.

Mejía, P., Santa, M., Ordóñez, O., Pimentel., M., 2008. Consideraciones petrográficas, geoquímicas y geocronológicas de la parte occidental del Batolito de Santa Marta. Revista Dyna, 155, 223-236.

Miller, M.S., Levander, A., Niu, F., Li, A., 2009. Upper mantle structure beneath the Caribbean–South American plate boundary from surface wave tomography. Journal of Geophysical Research, 114, B01312. doi:10.1029/2007JB005507

Montes, C., Hatcher, R.D., Restrepo-Pace, P., 2005, Tectonic reconstruction of the northern Andean blocks: Oblique convergence and rotations derived from the kinematics of the Piedras-Girardot area, Colombia. Tectonophysics, 399, 221-250.

Montes, C., Guzmán, G., Bayona, G., Cardona, A., Valencia, V., 2010. Clockwise Rotation of the Santa Marta Massif and Simultaneous Paleogene to Neogene Deformation of the Plato-San Jorge and Cesar-Ranchería Basins. Journal of South American Earth Sciences, 29, 832-848.

Muessig, K.W. 1984. Structure and Cenozoic tectonics of the Falcón Basin, Venezuela, and adjacent areas. In: Bonini, W.E., Hargraves, R.B., Shagam, R. (eds.). The Caribbean–South American plate boundary and regional tectonics. Geological Society of America Memoir, 162, 217-230.

Müeller, R.D., Royer, J-Y, Cande, S.C., Roest, W.R., Maschenkov, S., 1999. New Constraints on Caribbean Plate Tectonic Evolution Caribbean Basins included in the series. Elsevier Science, Sedimentary Basins of the World, 4, 33-59.

Oncken, O., Hindle, D., Kley, J., Elger, K., Victor, P., Schemmann, K., 2006. Deformation of the central Andean plate system - Facts, fiction, and constraints for plateau models. In: Oncken, O., Chong, G., Franz, G., Giese, P., Götze, H.J., Ramos, V.A., Strecker, M.R., Wigger, P. (eds.). The Andes-Active subduction orogeny. Berlin-Heidelberg, Springer, 3-27.

Parada, M.A., Féraud, G., Fuentes, F., Aguirre, L., Morata, D., Larrondo, P., 2005. Ages and cooling history of the Early Cretaceous Caleu pluton: testimony of a switch from a rifted to a compressional continental margin in central Chile. Journal of the Geological Society of London, 205, 273-287.

Pardo-Casas, F., Molnar, P., 1987. Relative motion of the Nazca (Farallon) and South American plates since Late Cretaceous time. Tectonics, 6, 233-248.

Parra M., Mora, A., Sobel, E.R., Strecker, M.R., González, R., 2009. Episodic orogenic front migration in the northern Andes: Constraints from low-temperature thermochronology in the Eastern Cordillera, Colombia. Tectonics, 28, TC4004. doi:10.1029/2008TC002423

Perez, O.J., Bilham, R., Bendick, R., Velandia, J.R., Hernandez, N., Moncayo, C., Hoyer, M., Kozuch, M., 2001. Velocity field across the southern Caribbean plate boundary and estimates of Caribbean/South-American Plate motion using GPS geodesy 1994-2000. Geophysical Research Letters, 28, 2987-2990.

Pérez de Armas, J., 2005. Tectonic and thermal history of the western Serranía del Interior foreland fold and thrust belt and Guárico basin, north-central Venezuela: Implication of new apatite fission-track analysis and seismic interpretations. In: Avé Lallament, H.G., Sisson, V.B. (eds.). Caribbean–South American Plate Interactions, Venezuela. Geological Society of America 394 (Special Paper), 271-314.

Pilger, R.H., 1984. Cenozoic plate kinematics, subduction and magmatism: South American Andes. Journal Geological Society of London, 141, 793-802.

Pindell, J.L., 1993, Evolution of the Gulf of Mexico and the Caribbean: An Introduction. In: Donovan, S.K., Jackson, T.A. (eds.). University of the West Indies Publisher's Association Caribbean Geology, 13-39.

Pindell, J.L., Cande, S.C., Pitman, III W.C., Rowley, D.B., Dewey, J.F., LaBrecque, J., Haxby, W., 1988. A plate-kinematic framework for models of Caribbean evolution. Tectonophysics, 155, 121-138.

Pindell, J.L., Higgs, R., Dewey, J.F., 1998. Cenozoic palinspastic reconstruction, paleogeographic evolution, and hydrocarbon setting of the northern margin of South America. In: Pindell, J.L., Drake, C.L. (eds.). Paleogeographic Evolution and Non-glacial Eustasy, northern South America. Society for Sedimentary Geology (SEPM), 58 (Special Publication), 45-86.

Pindell, J., Kennan, L., Maresch, W.V., Stasnek, K.-P., Draper, G., Higgs, R., 2005. Plate kinematic and crustal dynamics of circum-Caribbean arc-continent interactions: Tectonic controls on basin development in the Proto-Caribbean margins. In: Avé Lallemant, H.G., Sisson, V.B. (eds.). Caribbean–South American plate interactions, Venezuela. Geological Society of America, 394 (Special Paper), 7-52.

Pindell, J., Kennan, L., 2009. Tectonic evolution of the Gulf of Mexico, Caribbean and northern South America in the mantle reference frame: an update. In: James, K.H., Lorente, M.A., Pindell, J. (eds.). The Origin and Evolution of the Caribbean Plate. Geological Society of London, 328 (Special Publications), 1-56.

Ramos, V.A., 2009. Anatomy and global context of the Andes: Main geologic features and the Andean orogenic cycle. In: Kay, S.M., Ramos, V.A., Dickinson, W.D. (eds.). Backbone of the Americas: Shallow Subduction, Plateau Uplift, and Ridge and Terrane Collision. Geological Society of America, 204 (Memoir), 31-66.

Reiners, P.W., 2005. Zircon (U-Th)/He Thermochronometry. In: Reiners, P.W., Ehlers, T.A. (eds.). Thermochronology. Reviews in Mineralogy and Geochemistry, 58, 151-176.

Reiners, P.W., Farley, K.A., Hickes, H.J., 2002. He diffusion and (U-Th)/He thermochronometry of zircon: Initial results from Fish Canyon Tuff and Gold Butte, Nevada. Tectonophysics, 349, 297-308.

Restrepo-Moreno, S.A., Foster D.A., Stockli, D.F., Parra-Sánchez, L-N., 2009. Long-term erosion and exhumation of the "Altiplano Antioqueño", Northern Andes (Colombia) from apatite (U-Th)/He thermochronology. Earth and Planetary Science Letters, 278, 1-2.

Rincón, D., Arenas, J.E., Cuartas, C.H., Cárdenas, A.L., Molinares, C.E., Caicedo, C., Jaramillo, C., 2007. Eocene-Pliocene planktonic foraminifera biostratigraphy from the continental margin of the southwest Caribbean. Stratigraphy, 4, 261-311.

Ring, U., Brandon, M.T., Willett, S., Lister, G., 1999. Exhumation processes. In: Ring, U., Brandon, M.T., Willett, S., Lister, G. (eds.). Exhumation Processes: Normal Faulting, Ductile Flow, and Erosion. Geological Society of London, 154 (Special Publication), 1-27.

Saint Blanquat, M., Tikoff, B., Teyssier, C., Vigneresse, J.L., 1998. Transpressional kinematics and magmatic arcs. In: Holdsworth, R.E., Strachan, R.A., Dewey, J.F., (eds.). Continental Transpressional and Transtensional Tectonics. Geological Society of London, 135 (Special Publication), 327-341.

Schmidt, M.W., 1992. Amphibole composition in tonalite as a function of pressure: An experimental calibration of the Al-in-hornblende barometer. Contributions to Mineralogy and Petrology, 110, 304-310.

Silver, P.G., Russo, R.M., Lithgow-Bertelloni, C., 1998. Coupling of South American and African plate motion and plate deformation. Science, 279, 60-63.

Sisson, V.B., Avé Lallemant, H.G., Sorensen, S.S., 2008. Correlation of Eocene-Oligocene Exhumation around the Caribbean. Venezuela, Dominican Republic, Honduras, and Guatemala, Geological Society of America, Abstracts, 292-298.

Sobolev, S.V., Babyko, A.Y., 2005. What drives orogeny in the Andes? Geology, 33, 617-620.

Spikings, R.A., Seward, D., Winkler, W., Ruiz, G., 2000. Low temperature thermochronology of the northern Cordillera Real, Ecuador: tectonic insights from zircon and apatite fission track analysis. Tectonics, 19, 649-668.

Spikings, R.A., Winkler, W., Seward, D., Handler, R., 2001. Along-strike variations in the thermal and tectonic response of the continental Ecuadorian Andes to the collision with heterogeneous oceanic crust. Earth and Planetary Science Letters, 186, 57-73.

Spikings, R.A., Winkler, W., Hughes, R.A., Handler, R., 2005. Thermochronology of Allochthonous Terranes in Ecuador: unraveling the accretionary and post-accretionary history of the Northern Andes. Tectonophysics, 399, 195-220.

Spikings, R., Dungan, M., Foeken, J., Carter, A., Page L., Stuart, F., 2008. Tectonic response of the central Chilean margin (35–38°S) to the collision and subduction of heterogeneous oceanic crust: a thermochronological study. Journal of the Geological Society of London, 165, 941-953.

Spotila, J.A., Farley, K., Sieh, K.E., 1998. Uplift and erosion of the San Bernardino Mountains associated with transpression along the San Andreas fault, California, as constrained by radiogenic helium thermochronometry. Tectonics, 17, 360-378.

Stacey, J.S., Kramers, J.D., 1975, Approximation of terrestrial lead isotope evolution by a two-stage model. Earth and Planetary Science Letters, 26, 207-221.

Steiger, R.H., Jager, E., 1977. Subcommission on geochronology: Convention on the use of decay constants in geo- and cosmochronology. Earth and Planetary Science Letters, 36(3), 359-362.

Stockli, D.F., Farley, K.A., Dumitru, T.A., 2000. Calibration of the (U-Th)/He thermochronometer on an exhumed normal fault block in the White Mountains, eastern California and western Nevada. Geology, 28, 983-986.

Taboada, A, Rivero, L., Fuenzalida, A, Cisternas, A, Philip, H., Bijwaard, H., Olaya, J, Rivera, C., 2000. Geodynamics of the northern Andes: Subduction and intracontinental deformation (Colombia). Tectonics, 19, 787-813.

Thomson, N., 1994. Fission-track analysis and provenance studies in Calabrian Arc sedimentary rocks, southern Italy. Journal of the Geological Society of London, 151, 463-471.

Thompson, A.B., Schulmann, K., Jezek, J., 1997. Thermal evolution and exhumation in obliquely convergent (transpressive) orogens. Tectonophysics, 280, 171-184.

Toto, E.A., Kellogg, J.N., 1992. Structure of the Sinu-San Jacinto fold belt-An active accretionary prism in northern Colombia. Journal of South American Earth Sciences, 5, 211-222.

Trenkamp, R., Kellogg, J.N., Freymueller, J.T., Mora, H.P., 2002. Wide plate margin deformation, southern Central America and northwestern South America, CASA GPS observations. Journal of South American Earth Sciences, 15, 157-171.

Tschanz, C.M., Jimeno, A., Vesga, C., 1969. Geology of the Sierra Nevada de Santa Marta area (Colombia). República de Colombia, Instituto de Investigaciones e Información Geocientífica, Minero–Ambiental y Nuclear, 288pp.

Tschanz, C., Marvin, R., Cruz, J., Mehnert, H., Cebula, E., 1974. Geologic evolution of the Sierra Nevada de Santa Marta. Geological Society of America Bulletin, 85, 273-284.

Vallejo, C., Spikings, R.A., Winkler, W., Luzieux, L., Chew, D., Page, L., 2006. The early interaction between the Caribbean Plateau and the NW South American plate. Terra Nova, 18, 264-269.

Vallejo, C.F., Winkler, W., Spikings, R.A., Luzieux, L.D.A., Heller, F., Bussy, F., 2009. Mode and timing of terrane accretion in the forearc of the Andes in Ecuador. In: Kay, S.M., Ramos, V.A., Dickinson, W.R. (eds.). Backbone of the Americas: Shallow Subduction, Plateau Uplift, and Ridge and Terrane Collision. Geological Society of America Memoir, 204, 197-216.

Van der Hilst, R., Mann, P., 1994. Tectonic implications of tomographic images of subducted lithosphere beneath northwestern South America. Geology, 22, 451-454.

Van der Lelij, R., Spikings, R.A., Kerr, A., Kounov, A., Cosca, M., Chew, D., Villagomez, D., in press. Thermochronology and Tectonics of the Leeward Antilles: evolution of the Southern Caribbean Plate Boundary Zone. Tectonics.

Vence, E.M., 2008. Subsurface structure, stratigraphy, and regional tectonic controls of the Guajira margin of northern Colombia. MSc. Thesis. Austin, The University of Texas, CD ROM.

Von Houne, R., Ranero, C.R., 2009. Neogene collision and deformation of convergent margins along the backbone of the Americas. In: Kay, S.M., Ramos, V.A., Dickinson, W.R., (eds.). Backbone of the Americas: Shallow Subduction, Plateau Uplift, and Ridge and Terrane Collision. Geological Society of America Memoir, 204, 67-84.

Weber, J., Dixon, T., DeMets, C., Ambeh, W., Jansma, P., Mattioli, G., Bilham, R., Saleh, J., Perez, O., 2001. A GPS Estimate of the Relative Motion between the Caribbean and South American Plates, and Geologic Implications for Trinidad and Venezuela. Geology, 29, 75-78.

Weber, M., Cardona, A., Wilson, R., Gómez-Tapias, J., Zapata, G., 2007. Química Mineral de las rocas de alta presión-Facies Eclogita, de la Península de la Guajira, Colombia. Boletín de Geología, 29, 31-39.

Weber, M.B.I., Cardona, A., Paniagua, F., Cordani, U., Sepúlveda, L, Wilson, R., 2009. The Cabo de la Vela mafic-ultramafic complex, Northeastern Colombian Caribbean region–a record of multi stage evolution of a Late Cretaceous intra-oceanic arc. In: James, K.H., Lorente, M.A., Pindell, J. (eds.). The Origin and Evolution of the Caribbean Plate. Geological Society of London, 328 (Special Publication), 549-568.

Weber, M.B., Cardona, A., Valencia, V., García-Casco, A., Tobón, M., Zapata, S., 2010. U/Pb detrital zircon provenance from Late Cretaceous metamorphic units of the Guajira Peninsula, Colombia: tectonic implications on the collision between the Caribbean arc and the South American margin. Journal of South American Earth Sciences, 29, 805-816.

Wipf, M., Zeilinger, G., Seward, D., Schlunegger, F., 2008 Focused subaerial erosion during ridge subduction: impact on the geomorphology in south-central Peru. Terra Nova, 20, 1-10.

Zapata, S., Weber, M., Cardona, A., Valencia, V., Guzmán, G., Tobón, M., in press. Provenance of Oligocene conglomerates and associated sandstone from the Siamaná Formation, Serranía de Jarara, Guajira, Colombia: Implications for Oligocene Caribbean South American Tectonics. Boletín de Ciencias de la Tierra.

Manuscript received November 2010;
revision accepted July 2011;
published Online July 2011.

ELECTRONIC APPENDIX

TABLE I | **Electron microprobe chemical data and pressure calculations from the analyzed amphiboles of the Santa Marta batholith and Parashi stock**

	Santa Marta Batholith																		
Sample	EMC-1	EMC-1	EMC-1	EMC-1	EMC-1	EMC-1	EMC-1	EMC-1	EMC-1	BSM-7A	BSM-7A	BSM-7A	BSM-7A	BSM-7A	BSM-7A	BSM-7A	BSM-7A	BSM-13	BSM-13
Analysis	1	2	3	4	5	7	8	9	10	2	3	4	5	6	7	8	9	1	2
SiO_2	42.00	43.00	43.00	43.00	43.00	44.00	43.00	43.00	42.00	42.64	42.65	43.04	43.43	43.38	41.94	43.07	42.43	44.57	43.62
TiO_2	0.53	0.72	0.85	0.56	0.69	0.88	0.48	0.55	0.98	0.71	0.96	0.95	1.10	0.93	0.92	0.69	1.07	0.99	0.88
Al_2O_3	11.21	10.37	10.66	10.79	10.36	10.45	10.55	11.00	10.58	10.81	11.20	10.83	10.53	10.65	11.52	10.75	11.00	11.33	11.42
FeO	18.54	18.13	17.68	18.28	17.88	17.94	18.04	18.33	18.12	17.85	17.81	17.91	17.49	17.66	17.62	17.74	17.57	17.84	16.95
MnO	0.73	0.74	0.72	0.72	0.73	0.75	0.73	0.71	0.74	0.62	0.59	0.57	0.60	0.60	0.63	0.62	0.64	0.50	0.48
MgO	9.03	9.88	10.18	9.53	9.70	9.79	9.97	9.46	9.68	9.83	10.19	10.16	10.00	10.44	9.55	10.00	10.23	9.90	10.40
CaO	11.70	11.59	11.60	11.52	11.72	11.38	11.61	11.63	11.48	11.81	11.73	11.75	11.66	11.65	11.63	11.52	11.58	11.28	11.69
Na_2O	1.00	1.00	1.00	1.00	1.00	1.00	1.00	1.00	2.00	0.98	1.24	1.27	1.10	1.20	0.95	1.13	1.33	1.56	1.40
K_2O	1.18	0.93	0.85	1.09	0.99	1.04	0.89	1.07	0.93	0.92	1.16	1.08	1.04	0.98	0.88	1.11	1.08	0.94	0.81
Total	95.92	96.37	96.54	96.48	96.07	97.23	96.27	96.76	96.51	95.56	98.66	98.67	98.89	97.71	94.93	97.98	98.98	99.09	98.08
Si	6.407	6.478	6.440	6.482	6.515	6.503	6.559	6.470	6.465	6.497	6.445	6.361	6.422	6.510	6.444	6.359	6.363	6.526	6.456
Al iv	1.593	1.522	1.560	1.518	1.485	1.497	1.441	1.530	1.535	1.503	1.555	1.639	1.578	1.490	1.556	1.641	1.637	1.474	1.544
Al vi	0.423	0.319	0.322	0.399	0.365	0.369	0.395	0.341	0.415	0.324	0.370	0.330	0.326	0.370	0.308	0.418	0.308	0.481	0.448
Ti	0.060	0.082	0.096	0.064	0.078	0.065	0.099	0.054	0.062	0.129	0.082	0.108	0.106	0.124	0.103	0.105	0.121	0.110	0.098
Cr	0.004	0.002	0.002	0.000	0.004	0.004	0.000	0.007	0.006	0.005	0.000	0.002	0.002	0.002	0.007	0.003	0.000	0.000	0.000
Fe^{3+}	0.696	0.826	0.866	0.769	0.667	0.749	0.725	0.868	0.746	0.570	0.735	0.766	0.707	0.607	0.797	0.783	0.773	0.616	0.637
Fe^{2+}	1.669	1.458	1.348	1.536	1.599	1.501	1.511	1.401	1.560	1.621	1.521	1.455	1.527	1.586	1.397	1.451	1.430	1.570	1.461
Mn	0.094	0.094	0.092	0.092	0.094	0.091	0.094	0.093	0.091	0.076	0.079	0.075	0.072	0.077	0.076	0.080	0.081	0.063	0.061
Mg	2.054	2.220	2.274	2.141	2.192	2.221	2.175	2.236	2.121	2.275	2.214	2.264	2.259	2.235	2.311	2.159	2.287	2.161	2.295
Ca	1.912	1.871	1.862	1.861	1.902	1.883	1.817	1.872	1.874	1.903	1.912	1.873	1.879	1.873	1.853	1.890	1.860	1.770	1.854
Na	0.296	0.292	0.290	0.292	0.294	0.293	0.289	0.292	0.292	0.337	0.286	0.358	0.367	0.319	0.345	0.278	0.386	0.443	0.403
K	0.230	0.178	0.162	0.209	0.193	0.185	0.199	0.170	0.206	0.204	0.177	0.220	0.206	0.199	0.186	0.170	0.207	0.176	0.154
Total	17.438	17.341	17.314	17.362	17.389	15.361	15.305	15.334	15.371	15.444	15.375	15.452	15.452	15.391	15.384	15.338	15.454	15.388	15.410
Na (B)	0.088	0.129	0.138	0.139	0.098	0.117	0.183	0.128	0.126	0.097	0.088	0.127	0.121	0.127	0.147	0.110	0.140	0.230	0.146
(Na+K) (A)	0.438	0.341	0.314	0.362	0.389	0.361	0.305	0.334	0.371	0.444	0.375	0.452	0.452	0.391	0.384	0.338	0.454	0.388	0.410
$Mg/(Mg+Fe^2)$	0.552	0.604	0.628	0.582	0.578	0.597	0.590	0.615	0.576	0.584	0.593	0.609	0.597	0.585	0.623	0.598	0.615	0.579	0.611
$Fe^3/(Fe^3+Alvi)$	0.622	0.722	0.729	0.658	0.646	0.670	0.647	0.718	0.643	0.638	0.665	0.699	0.684	0.621	0.721	0.652	0.715	0.561	0.587
Sum of S^2	13	13	13	13	13	13	13	13	13	13	13	13	13	13	13	13	13	13	13
P (Kb)	6.6	5.8	5.9	6.1	5.8	5.7	5.9	6.3	6.0	6.2	6.4	6.1	5.8	5.9	6.8	6.0	6.2	6.3	6.5

TABLE I | **Continued**

	Santa Marta Batholith																		
Sample	BSM-13	BSM-13	BSM-13	BSM-01	BSM-01	BSM-01	BSM-01	BSM-25	BSM-25	BSM-25	BSM-25	BSM-25	BSM-25	BSM-35A	BSM-35A	BSM-35A	BSM-35A	BSM-35A	BSM-35A
Analysis	3	5	6	1	2	3	4	1	2	3	4	5	6	1	2	3	4	5	6
SiO_2	42.40	42.12	42.38	43.22	42.09	43.45	42.72	43.15	44.18	44.42	45.67	44.21	44.92	44.31	44.38	43.91	46.91	43.81	42.35
TiO_2	0.95	0.87	0.79	1.07	1.04	0.78	1.09	0.81	1.09	1.25	1.23	1.11	1.19	1.05	1.00	1.05	0.99	1.03	0.78
Al_2O_3	11.31	11.63	11.67	10.22	11.12	10.88	10.72	9.52	8.92	9.05	8.66	9.29	8.63	9.92	9.32	9.34	8.71	9.90	9.77
FeO	17.52	17.58	17.68	18.34	18.85	17.56	18.07	16.74	17.22	17.03	16.42	17.37	16.30	15.79	16.10	16.02	15.81	16.20	16.97
MnO	0.50	0.50	0.49	0.60	0.60	0.70	0.60	0.79	0.74	0.76	0.74	0.76	0.75	0.53	0.53	0.50	0.50	0.49	0.45
MgO	9.98	9.93	9.94	9.71	9.04	10.39	9.50	11.23	11.33	11.37	12.03	11.47	11.96	10.65	11.35	10.95	12.03	10.84	10.92
CaO	11.55	11.43	11.66	11.74	11.69	11.63	11.55	11.48	11.69	11.51	11.59	11.55	11.38	11.63	11.77	11.86	11.91	11.45	11.67
Na_2O	1.52	1.58	1.42	1.20	1.32	1.16	1.12	1.39	1.13	1.39	1.52	1.29	1.38	1.23	1.16	1.29	1.23	1.59	1.28
K_2O	0.77	0.87	0.81	0.99	1.19	0.81	0.98	0.86	0.89	0.97	0.89	0.92	0.84	0.92	0.90	1.03	0.88	1.03	1.03
Total	96.91	96.94	97.43	98.04	98.85	97.82	97.33	95.48	97.58	98.04	99.17	98.31	97.77	94.58	94.58	94.58	94.58	94.58	94.58
Si	6.377	6.359	6.336	6.501	6.380	6.450	6.459	6.536	6.607	6.608	6.698	6.557	6.671	6.688	6.663	6.665	6.833	6.615	6.483
Al iv	1.623	1.641	1.664	1.499	1.620	1.550	1.541	1.464	1.393	1.392	1.302	1.443	1.329	1.312	1.337	1.335	1.167	1.385	1.517
Al vi	0.382	0.401	0.398	0.312	0.366	0.353	0.369	0.235	0.180	0.194	0.195	0.180	0.181	0.453	0.311	0.336	0.328	0.377	0.245
Ti	0.108	0.105	0.099	0.121	0.119	0.087	0.124	0.093	0.123	0.140	0.135	0.124	0.133	0.119	0.113	0.120	0.108	0.117	0.090
Cr	0.003	0.000	0.000	0.002	0.000	0.000	0.000	0.000	0.005	0.004	0.000	0.000	0.000	0.006	0.002	0.002	0.007	0.004	0.016
Fe^{3+}	0.707	0.796	0.756	0.618	0.602	0.836	0.664	0.744	0.719	0.663	0.595	0.802	0.705	0.316	0.502	0.321	0.387	0.400	0.668
Fe^{2+}	1.497	1.384	1.455	1.689	1.788	1.343	1.621	1.293	1.355	1.381	1.352	1.263	1.241	1.640	1.464	1.677	1.496	1.601	1.430
Mn	0.065	0.069	0.065	0.080	0.082	0.082	0.081	0.101	0.093	0.095	0.092	0.096	0.094	0.068	0.067	0.065	0.062	0.062	0.059
Mg	2.238	2.246	2.227	2.178	2.043	2.299	2.141	2.535	2.526	2.522	2.631	2.536	2.647	2.397	2.540	2.479	2.612	2.439	2.492
Ca	1.861	1.834	1.842	1.892	1.899	1.850	1.871	1.863	1.874	1.834	1.821	1.835	1.811	1.881	1.893	1.928	1.859	1.853	1.915
Na	0.444	0.387	0.460	0.350	0.387	0.333	0.329	0.407	0.328	0.400	0.433	0.371	0.398	0.360	0.337	0.381	0.348	0.467	0.378
K	0.149	0.180	0.168	0.190	0.230	0.154	0.191	0.167	0.170	0.184	0.166	0.174	0.159	0.177	0.172	0.199	0.164	0.198	0.201
Total	15.454	15.400	15.470	15.432	15.515	15.337	15.390	15.437	15.371	15.418	15.421	15.379	15.367	15.418	15.403	15.508	15.371	15.518	15.494
Na (B)	0.139	0.166	0.158	0.108	0.101	0.150	0.129	0.137	0.126	0.166	0.179	0.165	0.189	0.119	0.107	0.072	0.141	0.147	0.085
(Na+K) (A)	0.454	0.400	0.470	0.432	0.515	0.337	0.390	0.437	0.371	0.418	0.421	0.379	0.367	0.418	0.403	0.508	0.371	0.518	0.494
$Mg/(Mg+Fe^2)$	0.599	0.619	0.605	0.563	0.533	0.631	0.569	0.662	0.651	0.646	0.661	0.667	0.681	0.594	0.634	0.596	0.636	0.604	0.635
$Fe^3/(Fe^3+Alvi)$	0.649	0.665	0.655	0.665	0.622	0.703	0.643	0.760	0.800	0.774	0.753	0.816	0.796	0.411	0.617	0.488	0.541	0.515	0.731
Sum of S^2	13	13	13	13	13	13	13	13	13	13	13	13	13	13	13	13	13	13	13
P (Kb)	6.5	6.8	6.8	5.6	6.4	6.0	6.1	5.1	4.5	4.5	4.1	4.7	4.2	5.4	4.8	4.9	4.1	5.4	5.4

TABLE I | **Continued**

	Santa Marta Batholith				Parashi Stock								
Sample	BSM-35A	BSM-35A	BSM-35A	BSM-35A	CM-3-2	CM-3-2	CM-3-2	CM-3-2	CM-3-2	CM-3-2	CM-4-16	CM-4-16	CM-4-16
Analysis	6	7	8	9	1	2	3	4	5	6	1	2	3
SiO_2	42.35	42.53	47.52	43.25	48.24	47.68	48.00	48.21	48.11	48.43	49.36	49.23	48.68
TiO_2	0.78	1.15	1.04	1.89	0.99	1.04	1.01	0.82	0.97	0.84	1.28	1.00	1.07
Al_2O_3	9.77	10.79	9.28	10.52	6.59	7.04	6.71	6.46	6.65	6.69	6.32	5.98	5.98
FeO	16.97	15.89	15.61	15.95	13.62	13.13	13.68	13.31	13.42	13.09	11.15	11.31	12.51
MnO	0.45	0.53	0.51	0.52	0.85	0.84	0.86	0.87	0.85	0.85	0.50	0.62	0.87
MgO	10.92	11.95	12.64	8.88	14.17	14.05	14.01	14.10	13.99	14.09	16.08	16.04	14.98
CaO	11.67	11.60	11.61	11.03	12.00	11.91	12.12	12.11	12.09	12.22	11.09	11.04	11.23
Na_2O	1.28	1.22	1.22	1.38	1.00	1.10	1.06	1.03	1.01	1.01	1.42	1.40	1.27
K_2O	1.03	0.91	0.83	1.01	0.55	0.50	0.52	0.44	0.51	0.50	0.36	0.32	0.34
Total	94.58	94.58	94.58	94.58	98.00	97.28	97.97	97.33	97.59	97.72	97.56	96.94	96.93
Si	6.483	6.354	6.778	6.685	6.969	6.933	6.953	7.016	6.990	7.021	7.014	7.039	7.026
Al iv	1.517	1.646	1.222	1.315	1.031	1.067	1.047	0.984	1.010	0.979	0.986	0.961	0.974
Al vi	0.245	0.254	0.339	0.603	0.091	0.138	0.099	0.123	0.129	0.164	0.072	0.046	0.044
Ti	0.090	0.129	0.112	0.220	0.107	0.114	0.110	0.090	0.106	0.092	0.137	0.107	0.116
Cr	0.016	0.003	0.006	0.001	0.002	0.003	0.000	0.001	0.000	0.004	0.000	0.000	0.000
Fe^{3+}	0.668	0.892	0.614	0.002	0.627	0.586	0.571	0.533	0.527	0.454	0.806	0.873	0.805
Fe^{2+}	1.430	0.993	1.179	2.060	1.019	1.010	1.087	1.088	1.103	1.133	0.520	0.479	0.704
Mn	0.059	0.066	0.062	0.069	0.103	0.104	0.105	0.107	0.104	0.104	0.060	0.076	0.106
Mg	2.492	2.662	2.687	2.045	3.051	3.045	3.025	3.058	3.029	3.045	3.406	3.419	3.224
Ca	1.915	1.857	1.775	1.827	0.000	0.000	0.002	0.000	0.002	0.003	1.689	1.691	1.737
Na	0.378	0.353	0.337	0.415	1.857	1.855	1.881	1.888	1.882	1.898	0.393	0.389	0.355
K	0.201	0.173	0.152	0.200	0.280	0.311	0.298	0.290	0.284	0.284	0.066	0.058	0.063
Total	15.494	15.382	15.264	15.442	0.102	0.092	0.096	0.081	0.094	0.092	15.147	15.137	15.155
Na (B)	0.085	0.143	0.225	0.173	0.143	0.145	0.119	0.112	0.118	0.102	0.311	0.309	0.263
(Na+K) (A)	0.494	0.382	0.264	0.442	0.239	0.258	0.275	0.259	0.260	0.275	0.147	0.137	0.155
$Mg/(Mg+Fe^2)$	0.635	0.728	0.695	0.498	0.750	0.751	0.736	0.738	0.733	0.729	0.868	0.877	0.821
$Fe^3/(Fe^3+Alvi)$	0.731	0.778	0.644	0.004	0.874	0.809	0.852	0.812	0.804	0.734	0.918	0.950	0.948
Sum of S^2	13	13	13	13	13	13	13	13	13	13	13	13	13
P (Kb)	5.4	6.0	4.4	6.1	2.3	2.7	2.4	2.3	2.4	2.4	2.0	1.8	1.8

Geologica Acta, Vol.9, Nos 3-4, September-December 2011, 467-479
DOI: 10.1344/105.000001714
Available online at www.geologica-acta.com

geologica acta

Geochemistry and petrology of three granitoid rock cores from the Nicaraguan Rise, Caribbean Sea: implications for its composition, structure and tectonic evolution

J.F. LEWIS [1] **G. KYSAR MATTIETTI** [2] **M. PERFIT** [3] **G. KAMENOV** [3]

[1] **Department of Earth and Environmental Science, The George Washington University**
Washington, DC

[2] **Atmospheric, Oceanic and Earth Science Department, The George Mason University**
Fairfax, VA

[3] **Department of Geological Sciences, University of Florida**
Gainesville, Florida

ABSTRACT

The Nicaraguan Rise is a major submarine structure of poorly known origin. Its lithologies have been studied from dredge hauls and land outcrops on the Greater Antilles and Central America and its structure from geophysical data. In this paper we present the first geochemical analyses for granitoids that were recovered during the 1970s from cores drilled on the Nicaragua Rise for oil prospecting. The three Nicaraguan Rise rocks are calk-alkaline granitoids, and lie in the high-K field for Caribbean granitoids similar to the Above Rocks, Jamaica and Terre Neuve, Haiti intrusions. All of these intrusions are considered to be of Late Cretaceous – Paleocene age. Key elements abundances - K, La, Ce, Nd, Hf, Zr and Sm - indicate that the three Nicaraguan Rise rocks present more affinity with mature oceanic arc rocks similar to other granitoids from the Greater Antilles rather than mature continental arcs. The Pb, Nd and Sr isotope data show no evidence of a continental component, thus indicating that the more eastern and northern submarine area of the Northern Nicaraguan Rise is not underlain by continental crust of the Chortis block. Although of similar age, the Nicaraguan Rise samples are different from the more depleted Cuban granitoids of the Sierra Maestra, though both show strong similarities in their $^{207}Pb/^{204}Pb$ composition. We postulate that the Northern Nicaraguan Rise was most likely a Caribbean oceanic arc system that may have interacted only at its margin with the continental blocks bounding the region to the west in the area of the Northern Honduran borderland.

KEYWORDS | **Caribbean. Nicaraguan Rise. Granitoids. Geochemistry. Arc rocks.**

INTRODUCTION

The Nicaraguan Rise (or Plateau) is a major submarine crustal feature that extends northeast across the Caribbean Sea from the coast of Honduras and Nicaragua to northeast of Jamaica where it meets with the southwestern part of the Southern Peninsula of Haiti.

The Nicaraguan Rise covers an area of some 413,000 km^2 in total (Fig. 1A, 1B). Little is known about its structure and lithological composition and it is probably the least understood major crustal feature in the whole Caribbean. Information about its composition and structure has come from four main sources; 1) geophysical investigations including seismic refraction (Ewing et al., 1960; Edgar et al., 1971) seismic reflection, gravity and magnetic profiling, and more recently aeromagnetic surveys (see below); 2) studies of the compositions of the cores drilled for petroleum exploration (Arden, 1975); 3) samples dredged from the walls of the Cayman Trench (Perfit and Heezen, 1978); 4) geology of the Bay Islands, northern Honduras and Jamaica (McBirney and Bass, 1969; Arden, 1975; Lewis and Draper, 1990). Most of the work prior to 1990 was summarized by Case et al. (1990) and Holcombe et al. (1990). Except for the seismic survey by Mauffret and Leroy (1997) and some seismic work and an aeromagnetic survey on the offshore areas of Nicaragua and Honduras summarized below, there has been little work done since the drilling and seismic surveys carried out by oil companies in the 1970s.

A

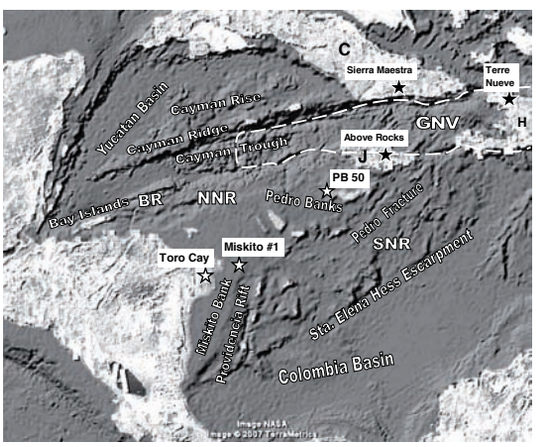

B

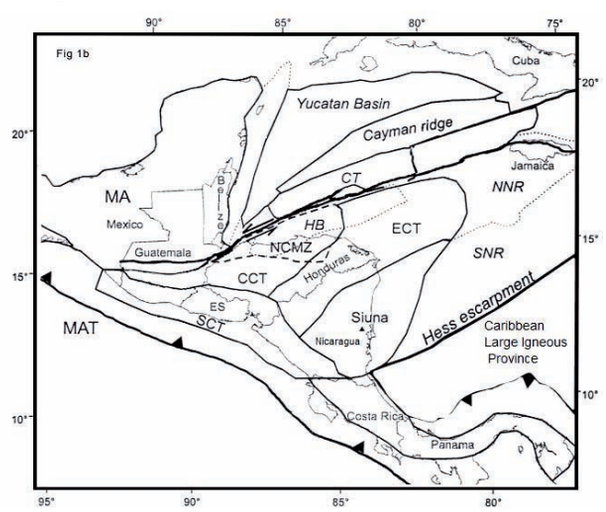

FIGURE 1 | **A) Image of the western Caribbean region, showing bathymetry and topography (base modified from Google Earth). Abbreviations for topographic features, plates, terranes and physiographic provinces are from names as given by Rogers et al. (2007); BR: Baccanao Ridge; GNV: Gonave Plate; NNR: North Nicaraguan Rise; SNR: South Nicaraguan Rise. White star represent drill core sites for the three samples. Black stars indicate the site of other Caribbean granitoid rocks referred to in text. B) Tectonic setting of northern Central America and southern Mexico showing the location and names of the terranes and physiographic provinces (adapted from Rogers et al., 2007): MA: Maya Block; MAT: Middle America Trench; YB: Yucatan Basin; NNR: Northern Nicaraguan Rise; SNR: Southern Nicaraguan Rise; MAT: Middle America Trench; ECT: Eastern Chortís Terrane; CCT: Central Chortis Terrane; HB: Honduras borderland; CB: Cuba; CT: Cayman Trough; SCT: Southern Chortís Terrane; ES: El Salvador.**

Synopses of the geology of the Nicaraguan Rise have been made by Arden (1969, 1975), Perfit and Heezen (1978) and Holcombe et al. (1990). Based on their recent compilations on the area of Honduras and Nicaragua, Rogers, Mann and colleagues (see below) and Baumgartner et al. (2008) have developed terrane models that have direct relevance as to the nature and origin of the Nicaraguan Rise. Recent models developed to account for the origin of the Nicaraguan Rise (Mann et al., 2006; Pindell and Kennan, in print) depend on the eastward movement and rotation of the Chortis block.

Three of the wells drilled in the 1970s for oil exploration along the northern Nicaraguan Rise sector (Fig. 1A) bottomed in plutonic rocks. Using up-to-date analytical techniques, we have determined the major and trace element, and Sr, Nd and Pb isotope compositions of the three granitoid rocks recovered. In this paper we show that these rocks are closely comparable in composition with those of the Above Rocks (Jamaica) pluton and the Terre Neuve (Haiti) stock but have lower amounts of the light rare earth elements (LREE), Ta and Nb. These data support the widely held view that most of the Nicaraguan Rise has evolved as island arc crust. The implication of these data as to the structure and composition of the Nicaraguan Rise are briefly discussed.

GEOLOGICAL SETTINGS

Nature and composition of the Nicaraguan Rise and relationship to Chortis Block

Fig. 1A is a map of the main topographic features of the Nicaraguan Rise and adjacent features. For more details of the topography and structural features as determined by

geophysical measurements, the reader is referred to Case et al. (1990) and the references below.

The broad shelf area of the Nicaraguan Rise to the northeast of the land areas of Honduras and Nicaragua and extending to Jamaica (the upper Nicaraguan Rise of Holcombe et al., 1990) is here termed the Northern Nicaraguan Rise (NNR of Fig. 1A). The southern boundary of the Northern Nicaraguan Rise is the Pedro Fault (or Fracture) zone. Morphologically the Northern Nicaraguan Rise is characterized by a series of carbonate banks and shelves separated by channels and basins that have evolved from a continuous carbonate "megabank" established over basement highs (Arden, 1975; Mutti et al., 2005). In essence, the submarine shelf area of the Northern Nicaraguan Rise is a topographic extension of the Precambrian-Paleozoic continental Chortis block (Dengo and Bohnenberger, 1969; Dengo, 1973; Couch and Woodcock, 1981; Donnelly et al., 1990). For this reason Meyerhof (1996) and others maintained that a considerable part of the Nicaraguan Rise must be underlain by Pre-Mesozoic continental crust. All the information, however, indicates that most of the basement rock of the Northern Nicaraguan Rise is not of continental composition but consists of island arc crust and is likely to be of similar composition to the island of Jamaica near the northern end of the Rise (Arden, 1975; Perfit and Heezen, 1978; Lewis and Draper, 1990). With the exception of the northern Honduran borderlands (HB of Fig. 1B; see below) no rocks older than Cretaceous in age are known on Jamaica or have been reported from any part of the Nicaraguan Rise.

In their review of crustal types and crustal provinces in the Caribbean, Case et al. (1990) identified three main types of crust: continental, oceanic and accretionary found in different regions of the total area of the Nicaraguan Rise. They also considered the presence of "indeterminate crust" that results "where geologic events have obscured crustal processes" (Case et al., 1990).

Based largely on a regional aeromagnetic survey of the Honduras land surface and the region off the north coast of Honduras with a compilation of geological information, isotopic dates and lead isotope data of both Honduras and Nicaragua, Rogers et al. (2007) subdivided the Chortis block into three tectonic terranes, namely the Central Chortis terrane, the Eastern Chortis terrane and the Southern Chortis terrane as shown on Figure 1B. The Central and Eastern Chortis terranes are continuous to the northeast beyond the coastline on to the submarine Northern Nicaraguan Rise. The third terrane, the Siuna terrane (Venable, 1994) is exposed in northern Nicaragua and extends northeast on to the Nicaraguan Rise (Fig. 1B). The Siuna's eastern boundary against the Southern Nicaraguan Rise is defined topographically by the Providencia Rift but its north-east trending boundary is not defined by Rogers et al. (2007) as following any topographic or geologic feature (Fig. 1). Venable (1994) concluded that the Siuna terrane consists of an Early Cretaceous island arc developed on oceanic basement that was accreted to the Chortis terrane in the Early Cretaceous.

The Southern Nicaraguan Rise (termed the lower Nicaraguan Rise by Holcombe et al., 1990) is the large block that separates the Northern Nicaraguan Rise from the Colombian Basin (Holcombe et al., 1990; Mauffret and Leroy, 1997; Fig. 1). This structure is some 200-240km wide and approximately 1200km long along its southern boundary. Its northern boundary against the Northern Nicaraguan Rise is the Pedro Escarpment (Fault or Fracture Zone). The well-defined lineament that forms the southern boundary to the Southern Nicaraguan Rise against the Colombian basin is the Saint Elena-Hess Escarpment.

Although each of the terrane segments and provinces that have been suggested has its own structural and morphological features, the divisions between the segments have not always been clear, as pointed out by Case et al. (1990). New multichannel seismic surveys and a re-evaluation of existing geophysical data have resulted in a better characterization of the three of the segments. Case et al. (1990) concluded that, like southern Central America, the Southern Nicaraguan Rise is composed of oceanic crust. Based on multichannel seismic data collected on the 1992 Casis cruise and the reprocessing of older data, using modern techniques, Mauffret and Leroy (1997) found that the Southern Nicaraguan Rise is underlain by oceanic plateau crust. The upper Layer 2V (V for volcanic plateau) is composed of a thin basaltic layer that overlies layer 2 of the original oceanic crust. This is underlain by Layer 3V which is divided into two crustal layers, an upper intrusive gabbroic layer about 6km thick that overlies a 10km thick layer of picrite and mafic cumulates. Recognition of this lithology is based on a seismic velocity of 7.2-7.4km/sec for this layer and the occurrence of picrite on Curacao with which it is correlated. If the interpretation that all of the Southern Nicaraguan Rise is composed of volcanic plateau crust is correct then this area is the largest and thickest plateau crust in the Caribbean Sea.

Unfortunately, there have been no new seismic or other geophysical measurements made across the Northern Nicaraguan Rise segment nor has there been any further drilling since the mid 1970s on the northeastern region of the Nicaraguan Rise. Seismic velocities recorded for the lower layer of the Northern Nicaraguan Rise range from 6.2 to 6.7km/s (Ewing et al., 1960), in strong contrast with the high velocities for the lower layer of the Southern Nicaraguan Rise. These lower velocities for the lower layer of the Northern Nicaraguan Rise are in agreement

with an island arc type of crust. Only a few measurements of crustal thickness (depth to the Moho) have been made in different parts of the Northern Nicaraguan Rise. Case et al. (1990) gave the thickness of the Northern Nicaraguan Rise at 20-23km. Revised thickness measurements, based on the older refraction data for the Northern Nicaraguan Rise and compiled on a regional map of the Caribbean area, range from 15 to 20km (Mauffret and LeRoy 1997, Fig. 2). Thickness measurements of the crust recorded for the area over the submarine Nicaraguan Rise between Jamaica and the mid-distance along the Rise to the coast of Central America varied from 15.3 to 18.5km (Mauffret and LeRoy, 1997). This differs decidedly from the estimates of the depth to the M-discontinuity by Case et al. (1990). These thicknesses are more typical of oceanic island arc crust, not of continental crust. Rogers et al. (2007), however, showed their Eastern Chortis terrane to extend for a considerable distance to the northeast, as part of the submerged plateau of the northern Nicaraguan Rise. In contrast, the new terrane map proposed by Baumgartner et al. (2008) shows the area of the Chortis block (underlain by definition by continental crust) to be reduced in area considerably compared with that suggested by Rogers et al. (2007) and is more in line with that proposed by Case et al. (1990).

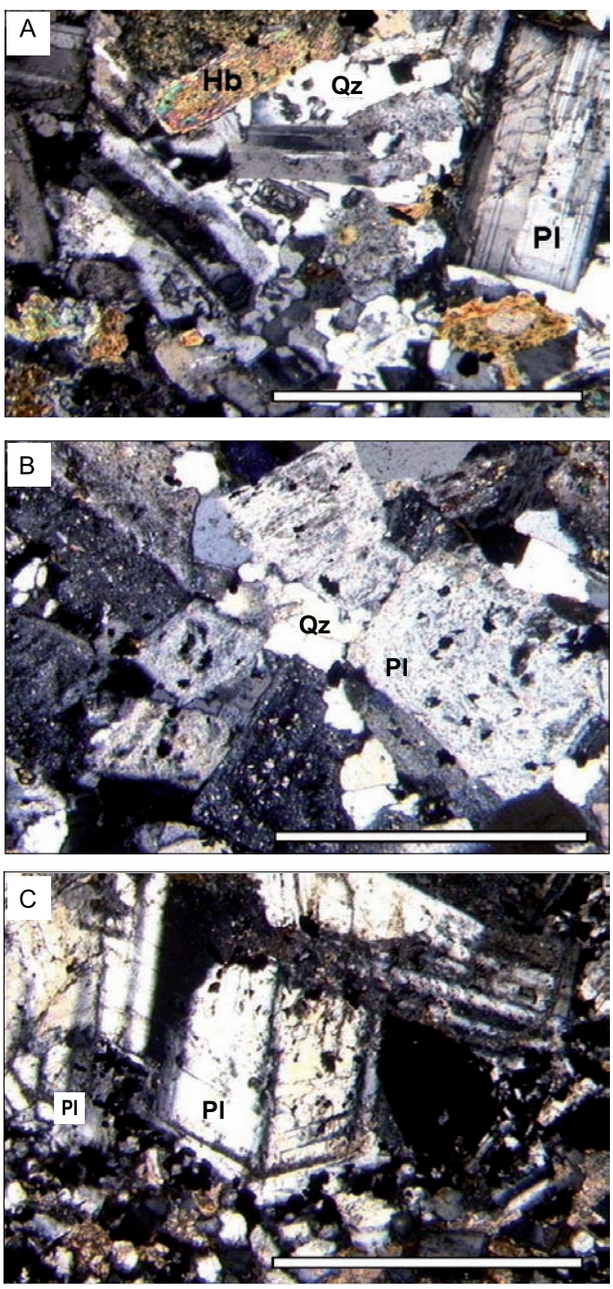

FIGURE 2 | **Thin section images of the three Nicaraguan Rise samples, White bar scale corresponds to 1mm. See text for description and discussion. A) Sample PB50. B) Sample Miskito 1. C) Sample Toro Cay.**

Baumgartner et al. (2008) have proposed a new terrane subdivision of Nicaragua and northern Costa Rica based on a detailed biostratigraphic study of Radiolaria and studies of the ultramafic and mafic rocks in the area. They identified the new terrane as the Mesquito Composite Oceanic Terrane , which includes the Siuna terrane in Nicaragua. The Mesquito Composite Oceanic Terrane extends from Guatemala in the west and forms the Southern Nicaraguan Rise (Fig. 1 and discussed above). It is considered to be underlain by accreted Pacific terranes and to extend into the "basement" units of the Greater Antilles islands of Jamaica, Hispaniola and Puerto Rico, composed essentially of island arc crust.

Northern Honduran Borderland

The one area in the northwestern part of the Nicaraguan Rise for which there is strong evidence that it is underlain by continental crust is the northern Honduran Borderland physiographic province (Fig. 1B). This is the marginal area between the Cayman Trough and the Northern Nicaraguan Rise and is the narrow offshore portion of the northernmost section of the Central Chortis terrane. It shows topographic and geological structures not seen elsewhere on the Chortis block or the Nicaraguan Rise. Swan Island, Guanaja, Utila and Roatan (the Bay Islands, Fig. 1) lie on a series of ridges that run parallel to the south wall of the Cayman Trough and are collectively known as the Bonacca Ridge. Gravity and bathymetry indicate a North and a South Bonacca Ridge separated by the Bonacca Basin (Rogers and Mann, 2007). Rocks exposed on Guanaja and Roatan islands include gabbro, pyroxene hornblendite, serpentinite, dacite and sodic granite together with a metamorphic sequence of schists, amphibolite and marble, the latter cut by the sodic granite; mudstones, chert and greywacke were reported to grade into the main metamorphic sequence (McBirney and Bass, 1969). Many structures seen in the offshore Honduran borderlands region can be traced onshore into the Cordillera Nombre de Dios and the Omoa to the southwest

(Horne et al., 1976; Holcombe et al., 1990: Rogers and Mann, 2007). The metamorphic rocks in the Bay Islands are similar to Paleozoic rocks in the Cordillera Nombre de Dios of northern Honduras. It has also been suggested that the amphibolites and associated serpentinites in the Bay Islands are the equivalent of the El Tambor amphibolites and associated serpentinised peridotites in the Motagua Valley and their emplacement may be related to the same obduction events (Donnelly et al., 1990).

Kornicker and Bryant (1969) and Pinet (1975), using single channel seismic profiling, outlined the series of elongated basins and ridges that make up the northern Honduran borderlands. Based on both multichannel and single channel seismic, together with gravity and an aeromagnetic survey and drilling, Rogers and Mann (2007) have described the structures and stratigraphy in considerable detail. They mapped 21 different basins that form a belt that narrows toward the Mid-Cayman spreading center. The four exploration wells drilled to depths of 2379-3790m together with the seismic data supported the rift interpretation of Pinet (1975) that documented "two stratigraphic sequences above an angular conformity disrupted by normal faults that form horsts and grabens filled by turbidites" (Rogers and Mann, 2007). The basement rocks penetrated in two wells consisted of black slate and quartzite and metasedimetary and volcanic rocks of Cretaceous age. These lithologies were interpreted to have an igneous source, although no intrusive or volcanic rocks were intersected. It is reasonable to assume that the basement lithologies in the wells correlate with the basement rocks exposed on Guanaja and Roatan because these islands are the exposed upper part of the ridges (Bonacca Ridge). In these wells a major unconformity separates the basement from a Middle Miocene pre-rift sequence consisting of sub-aerial redbeds to coastal or coastal shelf deposits.

SAMPLE DETAILS AND ANALYTICAL METHODS

Drill core locations and stratigraphic details of the cores of three granitoid rock samples studied here are given in Fig. 1A and Table 1. Small pieces of rock were broken off from each of the core samples and thin sectioned. Pieces of rock, free of veining and alteration, were selected and crushed to powder using a ceramic shatter box. The samples were analyzed by several methods for both major and trace elements in different laboratories and at different times, allowing an interlaboratory check to be made. Sample PB 50 was analyzed by X-ray fluorescence for major elements in the 1970's along with samples of the Above Rocks granodiorite at the University of Montreal by B.M. Gunn. Sample Toro Cay was analyzed for major elements by X-ray fluorescence at the Geological Survey of Canada. Trace elements (except for Zr and Hf) for PB 50 and Toro Cay were determined by Inductively-Coupled Plasma – Mass Spectrometry (ICP-MS) at the University of Granada, Spain. PB50 was also analyzed for trace elements on an Element2 High Resolution - Inductively-Coupled Plasma – Mass Spectrometry (HR-ICP-MS) at the Department of Geological Sciences, University of Florida. The analyses were performed in medium resolution with Re and Rh used as internal standards. Quantification of the results was done by external calibration using a combination of USGS rock standards. Major elements on samples Miskito-1 were analyzed by Inductively-Coupled Plasma – Atomic Emission spectrophotometry (ICP-AE) and trace elements by ICP-MS at ACME Laboratories, Vancouver. In the technique used at ACME Laboratories, the sample powders are fused with lithium tetraborate and taken into solution with hydrofluoric and perchloric acids and hence solution of refractory minerals such as zircon should be complete. As a further check, samples were also analyzed for Rb, Sr, Ba, Nb, Zr, Cr, and Ni by X-ray fluorescence using the pressed pellet method at Activation Laboratories, Ancaster, Canada. All these analyses have been combined with the analyses of other Caribbean granitoids to give a consistent data set for 35 elements for most samples. The new analyses for the Nicaraguan Rise rocks are presented in Table 2. Since all three samples have undergone at least some degree of alteration the most significant results are based on the most immobile elements Th, Nb, Ta, Hf, Zr, Ti, Y and REE.

In carrying out the isotope analyses Sr, Pb and Nd were separated using standard chromatographic methods in a

TABLE 1 | **Stratigraphic summary of the three cores from the Nicaraguan Rise**

Pedro Banks - Occidental - Lat. 16°56.2' N - Long. 78°48 W	
Stratigraphic position in well	Depth (meters)
Water Bottom (top Middle Eocene)	100
Top Sst-conglomerates (base Middle Eocene)	1925
Top Granodiorite (base of Sst-conglomerates)	1934
Miskito-1 - Signal/Occidental - Lat. 14°.52.4' N - Long. 81°.42.2' W	
Stratigraphic position in well	Depth (meters)
Water Bottom (top of Pleistocene)	29.7
Top Upper Miocene (base Plio-Pleistocene)	55.7
Top Middle Miocene	135.7
Top Lower Miocene	280.7
Top Oligocene (base Miocene)	740.7
Top Upper Eocene (base Oligocene)	1144.7
Top Middle Eocene	1316.7
Top Upper Cretaceous (granodiorite)	1995.7
Total Depth	2025.7
Toro Cay - Mobil Oil - Lat: 14°.20.2' - Long: 83°.06.9'	
Stratigraphic position in well	Depth (meters)
Water Bottom (Top Lower Miocene)	15.2
Top Oligocene (Base Miocene)	400.2
Top Upper Eocene (Base Oligocene)	1146.2
Top Middle Eocene (Base U Eocene)	1268.2
Top Upper Cretaceous-top of diorite (Base Eocene)	2244.2
Total depth	2265.8

TABLE 2 | **Major and trace element analyses of Nicaraguan granitoid rocks with comparisons from Above Rocks (Jamaica) and Neuve (Haiti)**

Major Elements Oxides	Toro Cay	Miskito #1	PB 50	WIR 154 Above Rocks	SK-9 Terre Neuve
SiO_2	54.31	61.38	62.87	62.92	62.77
TiO_2	0.79	0.49	0.54	0.67	0.79
Al_2O_3	19.2	16.24	17.23	16.45	15.32
Fe2O3	6.7	5.66	5.52		6.65
MnO	0.11	0.15	0.08	0.11	0.08
MgO	1.12	3.01	2.23	1.9	1.71
CaO	6.61	4.27	4.42	4.67	5.1
Na_2O	4.03	4.11	3.59	3.9	3.61
K_2O	3.15	2.15	3.41	3.69	2.9
P_2O_5	0.41	0.15	0.13	0.2	0.23
LOI	3.58	2.3	n.d	n.d.	1
TOT/C	n.d.	0.09	n.d	n.d.	0.14
TOT/S	n.d.	0.34	n.d	n.d.	0.15
Total	100.01	100.34	100.2	97.24	100.3
Trace elements ppm					
Sc	13.9	12	13.1		20.8
V	119	122	125	125	125
Cr	21.8	21	31.5	27.2	36.7
Co	13.2	11.7	14.5	12.9	16.2
Ni	5.6	7.3	8.1	5.3	6.8
Cu	53.6		41.6	905.7	1926.4
Zn	88.3	89	75.1	54.3	59.5
Ga	20.6	16.5	16.9	17.9	16.8
Rb	87	32.7	69.1	104.2	81.3
Sr	635	428.2	463	660.5	891.1
Y	19.6	18.2	14.1	19.4	15.9
Zr	132	73.7	30	143	128.9
Nb	4.1	2.7	4.9	13	15.6
Ba	626	695.3	790	1276	1009.7
La	15.9	10.9	15.2	25.2	25.6
Ce	32.8	22.2	29.4	47.2	46.5
Pr	4.6	2.83	3.8	5.8	5.48
Nd	20.1	12.6	15	22.2	21.6
Sm	4.53	3.2	3.11	4.38	3.8
Eu	1.39	0.92	0.87	1.19	1.3
Gd	4.06	3.05	2.55	3.59	3.7
Tb	0.62	0.54	0.41	0.58	0.51
Dy	3.53	2.81	2.45	3.3	3.02
Ho	0.72	0.62	0.5	0.68	0.56
Er	1.9	1.83	1.4	1.81	1.55
Tm	0.29	0.29	0.22	0.27	0.27
Yb	1.96	1.85	1.38	1.78	1.25
Lu	0.29	0.26	0.2	0.26	0.22
Hf	3.58	2.4	1.14	0.9	3.5
Ta	0.34	0.2	0.46	1.14	1
Pb	7.9	2.2	7.8	8.6	2.5
Th	5.3	1.7	5.6	9.27	3.5
U	1.3	0.6	1.8	2.61	1.4

Note: Major elements in wt %, trace elements in ppm; values not determined n.d.

clean laboratory at the Department of Geological Sciences, University of Florida. Sr isotopic compositions were determined on a Nu-Plasma Multi-Collector Inductively - Coupled Plasma – Mass Spectrometry (MC-ICP-MS) in static mode acquiring simultaneously ^{88}Sr on high-5, ^{87}Sr on high-4, ^{86}Sr on high-2, ^{85}Rb on axial and ^{84}Sr on low-2 Faraday detectors. $^{87}Sr/^{86}Sr$ ratio was corrected for mass-bias using exponential law and $^{86}Sr/^{88}Sr$=0.1194. All analyses were done by using on-peak measured zeros determined on clean 2% HNO_3 solution to correct for isobaric interferences of Kr impurities in the Ar gas. The long-term average value of NBS 987 $^{87}Sr/^{86}Sr$ is 0.71025 (+/-0.00003, 2σ). Nd isotope measurements were also conducted in static mode acquiring simultaneously ^{142}Nd on low-2, ^{143}Nd on low-1, ^{144}Nd on Axial, ^{145}Nd on high-1, ^{146}Nd on high-2, ^{147}Sm on high-3, ^{148}Nd on high-4 and ^{150}Nd on high-5 Faraday detectors. The measured ^{144}Nd, ^{148}Nd and ^{150}Nd beams were corrected for isobaric interference from Sm using $^{147}Sm/^{144}Sm = 4.88$, $^{147}Sm/^{148}Sm = 1.33$ and $^{147}Sm/^{150}Sm = 2.03$. All measured ratios were normalized to $^{146}Nd/^{144}Nd = 0.7219$ using an exponential law for mass-bias correction. Baseline was measured by electrostatic analyser (ESA) deflection of the beam. Repeated analyses of the JNdi-1 standard produced mean values of 0.512099 (+/-0.000015, 2σ). Pb isotopic analyses were also conducted on the Nu Plasma MC-ICP-MS using Tl normalization technique (Kamenov et al., 2004). The Pb isotope data are relative to the following values of NBS 981: $^{206}Pb/^{204}Pb$=16.937 (+/-0.004, 2σ), $^{207}Pb/^{204}Pb$=15.490 (+/-0.003, 2σ) and $^{208}Pb/^{204}Pb$=36.695 (+/-0.009, 2σ).

PETROGRAPHY, STRATIGRAPHY AND AGE OF THE SAMPLES

Although all three Nicaraguan Rise rock samples are medium grained grayish rocks each has a distinctive appearance and texture (Fig. 2).

Pedro Banks Drill Core - Sample: PB50 (Granodiorite)

This pale grey rock is medium-grained and consists mainly of relatively fresh plagioclase feldspar, rare potash feldspar, biotite and hornblende. In thin section the overall texture is hypidomorphic granular. Fresh subhedral plagioclase (up to about 1.2mm) is the dominant mineral. Quartz and potassium feldspar (<0.5mm) are anhedral and intersertal. Hornblende and lesser amounts of biotite are present as single grains that rarely exceed 1mm in size. Apatite and iron oxide are the main accessory minerals (Fig. 2A).

Miskito-1 Drill Core - Sample: Miskito -1 (Granodiorite)

The rock is mainly pale grayish white but has a patchy appearance due to the pale rusty color of the sericitized plagioclase feldspar in comparison with darker grey colored areas where the plagioclase is only slightly altered. Thin quartz-calcite and epidote veinlets (1-2mm across) cut the rock. In thin section subhedral and anhedral plagioclase (mainly 0.8 to 1.6mm) is altered to sericite and potash feldspar (about 0.5mm) is similarly altered. Quartz is entirely interstitial to the plagioclase feldspar. Epidote is pervasive and both hornblende and biotite are altered almost entirely to chlorite. Textural features are shown in Fig 2B.

Toro Cay Drill Core: Sample - Toro Cay (Plagioclase Porphyry)

In hand specimen this rock is darkish grey and medium-grained but on closer inspection it has a rusty appearance

due to oxidation to fine-grained hematite. The rock is best termed plagioclase diorite porphyry as it consists of abundant phenocrysts of relatively fresh plagioclase feldspar laths (up to 1.4mm in length) in a finer-grained granular matrix consisting of plagioclase, ferromagnesian minerals and hematite covered grains (Fig. 2C).

Of the 26 exploration wells drilled within the area of the Miskito Banks off the east coast of Nicaragua (Munoz et al., 1997), six wells penetrated the "economic" basement below the Cenozoic sedimentary rocks. Besides the granitoid rocks from the Miskito -1 and Toro Cay wells which were sampled, granitoid rock was reported from the Centeno-1 well located about 60km east of the coast of Nicaragua at latitude 12°N. The medium-grained texture of the three granitoids examined in this paper suggests the possibility that they are the marginal or high level facies of larger courser grained intrusions. Their intermediate compositions suggest that these samples are not high level late stage differentiates, but are part of the main intrusive phases. However there is no supporting evidence for either of these suggestions.

All three wells bottomed in the granitoid rocks interpreted in the drill core logs correspond to an igneous basement of Cretaceous age (Table 1). The granitoid rocks in the Pedro Banks, Miskito-1 and Toro Cay all uncomfortably underlie Middle Eocene sedimentary rocks. A short section of sandstone and conglomerate separates the Eocene carbonate from the granodiorite rock in the Pedro banks drill core. In the core logs there is no evidence of an intrusive contact between the granitoid rocks and the sedimentary rocks. The lower Eocene and Paleocene are missing in all three cores suggesting that this was an erosional interval or a time of no sediment deposition over a wide area with the exception of the Touché-1 well, located about 47km off the coast of Nicaragua between the Toro Cay and Miskito-I wells. There is a continuous Paleocene to Eocene section about 1,900m thick in the Touche-1 well that bottoms in calcareous shale of Paleocene age (Arden, 1975; Holcombe et al., 1990).

Only one approximate age determination of 48.6-57.4Ma (53 ± 4.4Ma) is available for the Pedro Banks sample (Meyerhof and Krieg, 1977). Because this is a K/Ar whole rock age, it is interpreted as a minimum age; still the age is consistent with the stratigraphic position in the well. Since the Pedro Banks well appears to lie along the same general arc structure as the Above Rocks intrusion in Jamaica, this age should be compared with the U/Pb age of 63 ± 3Ma (after adjustment by Harland et al., 1964) obtained on titanite from a sample of granodiorite (Chubb and Burke, 1963) and a fission track age of 60.4 ± 3.4Ma (Ahmad et al., 1987) for the Above Rocks intrusion. These determinations on the Above Rocks samples are interpreted as crystallization and minimum cooling ages respectively.

Because the Miskito-1 and Toro Cay samples appear to be from the same general stratigraphic level as the Pedro Banks sample, it is apparent that all three samples are probably of a similar age, that is, within the interval late Late Cretaceous-Paleocene. A number of the wells in the Miskito Banks area off the coast of Honduras and Nicaragua, intersected or bottomed in extrusive rocks of apparent Eocene age suggesting a significant igneous event at this time (Munoz et al., 1997; Emmet, 2008). There are no data on the nature and composition of these volcanic rocks. Greenschist rock with a thickness of 516m was penetrated in the Rama-12 hole, located about 30km off the coast of Nicaragua at latitude of 13° 12"N. This could represent an ancient imbricate subduction wedge of Cretaceous age consistent with its presence in the Siuna terrane (Munoz et al., 1997).

GEOCHEMISTRY

Major and trace element geochemistry

Major and trace element analyses for the three drill core samples from the Nicaraguan Rise are given in Table 2 along with two selected analyses of other Late Cretaceous granitoids from the Above Rocks intrusion, Jamaica (Jackson and Scott, 1994) and the Terre Neuve intrusion, Haiti (Kesler, 1971) for comparison. In terms of major elements the Toro Cay sample is slightly more basic in composition with 57% SiO_2 (volatile free) compared with the Pedro Banks and Miskito samples which are both intermediate in composition with about 63 % SiO_2 (volatile free). Samples PB50 and Miskito-1 closely match sample WIR154 from the Above Rocks and SK-9 from the Terre Neuve intrusion, Haiti (Table 2). The Toro Cay sample contains 19.20% Al_20_3 and 6.03% FeO total, but only 1.12% MgO, reflecting the high percentage of plagioclase feldspar and lack of ferromagnesian silicate minerals for a low silica rock. Most of the iron is now largely oxidized to hematite.

The three Nicaraguan rocks fall into the category of calc-alkaline granitoids according to the alkali-lime index the most widely used criterion for classifying granitoid rocks (e.g., Brown, 1982; Brown et al., 1984). With their relatively high K content they are similar to the Above Rocks and Terre Neuve intrusions, and lie in the high-K field in a K_2O-SiO_2 plot for Caribbean granitoids (Lidiak and Jolly, 1996). In this way they contrast strongly with the low-K calcic group of granitoids as found in the Cordillera Central-Massif du Nord of Hispaniola and the intrusive rocks of Paleogene age from the Sierra Maestra of Cuba (Lidiak and Jolly, 1996; Kysar Mattietti, 2001; Rojas-Agramonte, 2004).

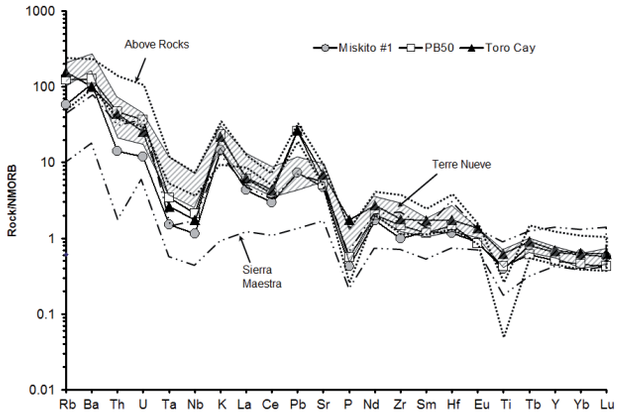

FIGURE 3 | **N-MORB- normalized trace element patterns for the three Nicaraguan granitoid rocks in comparison with granitoids from the Above Rocks and Terre Neuve plutons and intrusive rocks from the Sierra Maestra. Data for Above Rocks and Terre Neuve from unpublished data on Caribbean granitoids. Data for the Sierra Maestra from Kysar Mattietti (2001) and unpublished data.**

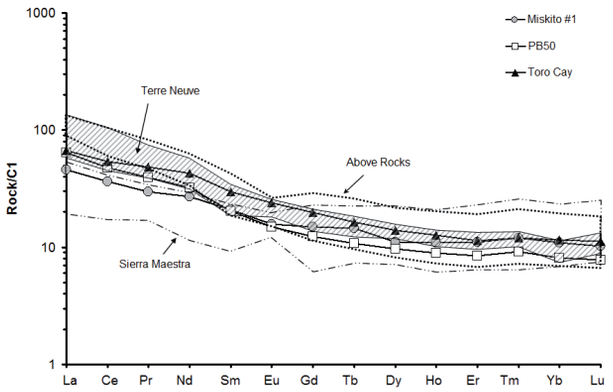

FIGURE 4 | **Chondrite-C1 normalized REE patterns for the three Nicaraguan granitoid rocks. Data for Above Rocks and Terre Neuve from unpublished data on Caribbean granitoids. Data for the Sierra Maestra from Kysar Mattietti (2001) and unpublished data.**

Trace elements for the Nicaraguan Rise samples together with the available data for the Above Rocks, Terre Neuve and Sierra Maestra intrusions have been plotted on an N-MORB normalized multi-element diagram (Fig. 3). The diagram shows the degree of subduction-derived enrichment in large ion lithophile elements (LILE) (Rb, Ba, Th, U and K) and the level above a line drawn through the high field strength elements (HFSE) (Pearce, 1983). The shapes of the patterns for all samples show similar trends with considerable enrichment in the LILE. This is less evident for the three Nicaraguan Rise samples compared with those from the Above Rocks and Terre Neuve plutons. The Sierra Maestra rocks show a more marked depletion for most elements in comparison with the other suites. This feature is typical of the more calcic or primitive type of oceanic arc Caribbean granitoid (Kysar Mattietti, 2001; Brown et al., 1984). Whereas all the samples plotted show a negative Nb -Ta anomaly with respect to Th, U and Ce, typical of subduction related rocks, the three Nicaraguan samples are all lower in Nb and Ta than the Above Rocks and Terre Neuve suites. The concentrations of Ta-Nb for the Nicaraguan samples are just above unity, that is slightly more than that of N-MORB, and the concentrations of Nd, Zr, Sm, Hf and Eu are similar and slightly higher than N-MORB for the Nicaraguan, Above Rocks and Terre Neuve suites.

The concentrations of HREE in the three suites are similar but slightly below that of typical N-MORB (Fig. 3). HREE concentrations in the Nicaraguan samples overlap with the other suites, particularly the Terre Neuve, but are lower than in many samples from the Above Rocks and Sierra Maestra.

The Nicaraguan rocks show enrichment of the LREE compared with average chondrite (Fig. 4). La/Yb in the three Nicaraguan Rise rocks ranges from 5.9 to 11, typical of the calc-alkaline group of Caribbean granitoids (Lidiak and Jolly, 1996). La values for the Nicaraguan rocks range from 10.9-15.9ppm, decidedly lower than in the Above Rocks (La = 21.33 to 31.55ppm) and Terre Neuve rocks (3.6 to 32.2ppm). Yb values for the Nicaraguan Rise rocks are in the same range as in the Terre Neuve rocks but lower than in some of the Above Rocks (Yb = 1.16 to 3.26ppm). There is only limited overlap of the LREE in the Nicaraguan rocks with those from the Sierra Maestra.

Further insight is gained by plotting the data on a multi-element mantle normalized diagram (Fig. 5) and

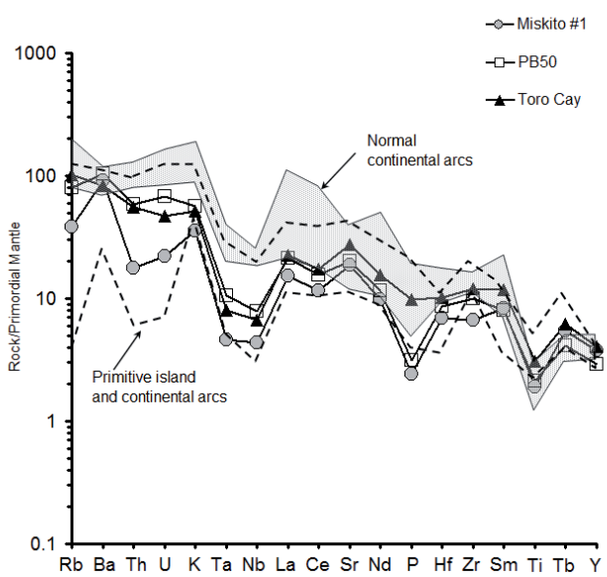

FIGURE 5 | **Primordial mantle-normalized trace element patterns for the three Nicaraguan Rise granitoid rocks in comparison with Mesozoic and Cenozoic arc granitoids. Data and terminology taken from Brown et al. (1984).**

comparing these data with two large groupings of arc-related rocks taken from the study of Brown et al. (1984). As Fig. 5 shows, there is considerable overlap, particularly for the LILE (Rb, Ba, Th, U and K) between the primitive island arc rocks and normal continental arc rocks. The normal continental arc rocks show higher concentrations of K, La, Ce, Nd, Hf and Sm than those from primitive oceanic island and continental arcs. All three Nicaraguan samples plot within the oceanic and primitive continental arc field, though there is some overlap with the normal continental arc field.

Isotope compositions

Present day $^{206}Pb/^{204}Pb$, $^{207}Pb/^{204}Pb$ and $^{208}Pb/^{204}Pb$ ratios determined for the three granitoids from the Nicaraguan Rise are listed in Table 3. The values, corrected for age to 60 Ma (common range of all ages determination available for the samples) are plotted in Figs. 6 and 7. Data for the Above Rocks and Terre Neuve plutons (unpublished) and for the Sierra Maestra intrusions (Kysar Mattietti, 2001) are plotted for comparison. The Pb isotope ratios for the samples from Toro Cay and Miskito-1 are very similar suggesting that these two rocks were derived from the same magma or at least came from the same source, consistent with their close proximity beneath the Miskito Banks. In Fig. 6 the values for the three Nicaraguan samples, the Above Rocks and Terre Neuve samples plot in a narrow band parallel to the Northern Hemisphere Reference Line (NHRL). These factors suggest a genetic link and common mantle source for these three groups of granitoid rocks. Similarly, the overlap of the Nicaraguan samples with those from the Sierra Maestra on the $^{207}Pb/^{204}Pb$ vs. $^{206}Pb/^{204}Pb$ diagram (Fig. 6) suggests a similar source for these rocks also. The close proximity of the isotopic data to the NHRL line and the overall distribution of the data on the Pb plots in Figs.6 and 7 suggest little Atlantic sediment contamination in the generation of the granitoid magmas. However, plotting of the values of $Pb\Delta^{207/204}$ and $Pb\Delta^{208/204}$ of 4.07,4.47,4.95 and 17.77,16.97,17.45, respectively, calculated for the three Nicaraguan granitoid samples (Table 3), on Figure 5 of Jolly et al. (2006), suggests an Atlantic sediment contribution of just less than 2% (Lidiak, pers. comm.). In contrast Terre Neuve has a $Pb^{\Delta 207/204}$ ratio of only 0.91.

A number of studies have shown that the lead ore samples hosted by Paleozoic and Precambrian rocks of Central America and Mexico show Pb isotopic ratios distinctive for each of the terranes from which they have been derived (Cumming et al., 1982; Kesler et al., 1990). If the granitoid magmas have assimilated any of the host rock of these continental terranes, this lead component should be reflected in the lead isotopic composition of the granitoid rocks. Such is the case for the granitoid rocks with a continental compositional affinity dredged from the northwest wall of the Cayman Trough (Fig. 7; Lewis et al., 2005; Kysar Mattietti et al., 2009). In contrast, there is no evidence of such a continental crustal component present in the granitoid rocks from the three areas of the Nicaraguan Rise studied here.

The Sr isotopic ratios for the Nicaraguan Rise samples have an average value ($^{87}Sr/^{86}Sr = 0.7041 \pm 1$) (Table 3, Fig. 8). These values are well framed within the comparative sets of Jamaica, Haiti, Southern Cuba and the Cayman Ridge. This indicates no significant contribution of isotopically

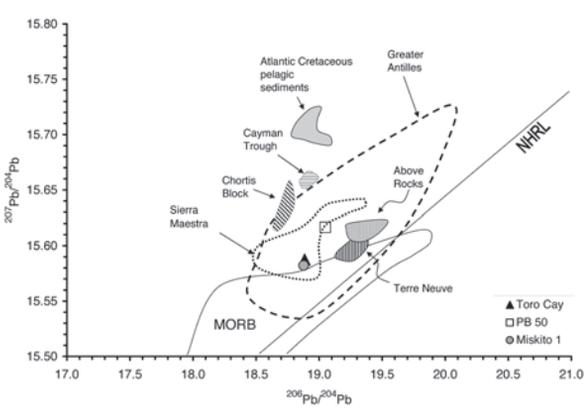

FIGURE 6 **Measured ^{207}Pb data for the Nicaraguan Rise samples. Data for Above Rocks and Terre Neuve from unpublished data on Caribbean granitoids. Data for the Sierra Maestra from Kysar Mattietti (2001) and unpublished data. Greater Antilles field drawn from GeoRoc database. Fields for|Cretaceous Atlantic pelagic sediments and MORB from Jolly and others (2006). NHRL: Northern Hemisphere Reference Line.**

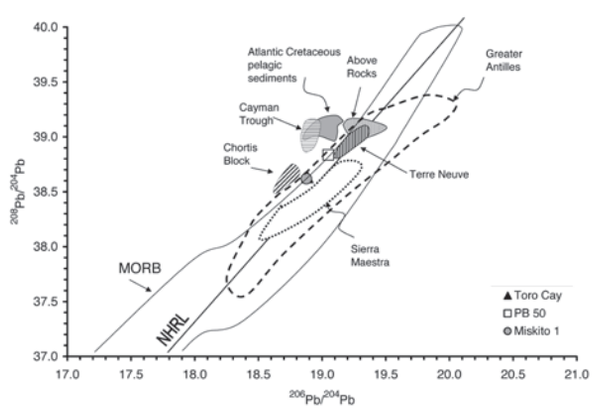

FIGURE 7 **Measured ^{208}Pb data for the Nicaraguan Rise samples with comparisons. Data source: Greater Antilles field drawn from GeoRoc database. Fields for Cretaceous Atlantic pelagic sediments and MORB from Jolly and others (2006) and from Wilson (1989). Fields for Chortis block from Cummings and others (1981) and for the Above Rocks and Cayman Ridge from unpublished data. Field from the Sierra Maestra from Kysar Mattietti (2001) and unpublished data. NHRL: Northern Hemisphere Reference Line.**

TABLE 3 | **Isotope analyses of Nicaraguan rocks**

Samples	PB50	Miskito #1	Toro Cay
SiO2	62.87	61.83	54.31
$^{206}Pb/^{204}Pb$	19.0491	18.877	18.885
$^{207}Pb/^{204}Pb$	15.6166	15.582	15.5876
$^{208}Pb/^{204}Pb$	38.8351	38.619	38.6335
Rb ppm	69.1	32.7	87
Sr ppm	463	428	635
$^{87}Rb/^{86}Sr$	0.431655	0.220971	0.39626
$^{87}Sr/^{86}Sr$	0.704249	0.704045	0.704128
ISr	0.703881	0.703857	0.70379
Sm(ppm)	3.1	3.2	4.5
Nd(ppm)	15	12.6	20.1
$^{147}Sm/^{144}Nd$	0.125394	0.153598	0.136304
$^{143}Nd/^{144}Nd$	0.512784	0.512997	0.512936
INd	0.512735	0.512883	0.512937

note: 63Ma was used to calculate Initial Sr and Initial Nd

evolved components such as older sedimentary material and/or seawater alteration across this area of the Northern Caribbean. Initial Sr isotope ratios range between 0.703790 and 0.703857 and are closest to those of the Above Rocks and Terre Neuve (Jones et al., 1979).

Nd isotope ratios for the Nicaragua Rise (Table 3, Fig. 8), in contrast, show a significant spread of values from the more radiogenic Miskito-1 sample - comparable to that of the Sierra Maestra and close to the MORB domain - to the less radiogenic Pedro Banks sample. The Toro Cay and Pedro Banks samples are similar to the Above Rocks and Terre Neuve. The Sr-Nd isotope ratios for the Nicaraguan samples plot within the field of arc related materials. Toro Cay and Miskito-1 plot in the oceanic arc field whereas PB50 plots on the margin or outside the continental arc field (Fig. 8). A more detailed discussion of this feature will be made in a future paper on the granitoids in the northwestern Caribbean. In contrast Sr-Nd ratios for the

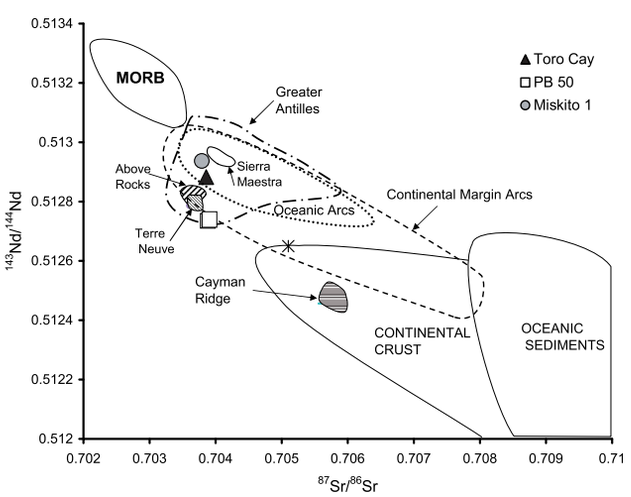

FIGURE 8 | **Measured Sr-Nd isotopic ratios for the Nicaraguan Rise samples, with comparisons. Data source: Greater Antilles field drawn from GeoRoc database; data for Cayman Trough samples unpublished. Other reference fields from Jolly and others (2006) and from Wilson (1989). Star symbol represents Bulk Earth Composition.**

granitoids dredged from the northwestern Cayman Trench (Perfit and Heezen, 1978; Lewis et al., 2005; Kysar Mattietti et al., 2009) plot well within the continental crust field consistent with their Pb isotopic composition (Figs. 6 and 7) and their origin in relation to the Chortis block as discussed above.

DISCUSSION

The Pedro Banks sample PB50 comes from the shallow bank on the median axis of the upper Nicaraguan Rise, some 90km southwest of Jamaica (Fig. 1A). The seismic and geological information clearly indicate that the Pedro Banks are the southwestern extension of the Jamaican crustal structure (Arden, 1975). The stratigraphy seen in the Pedro Banks drill core directly reflects that of Jamaica (Arden, 1975; Lewis and Draper, 1990). These are strong pieces of evidence supporting the hypothesis that the crustal rocks underlying Jamaica and the Pedro Banks are genetically related and had the same tectonic history (Arden, 1975).

The lithologies drilled at the Miskito-1 hole located north of the Pedro Fault zone on the main plateau of the upper Nicaraguan Rise are consistent with the presence, in this area, of a basement of island arc crust. The Toro Cay well is located at latitude 14° 20.2'N, about 10km off the Nicaraguan coast, immediately north of the eastward extension of the Pedro Fault zone. However, it is possible that this sample is located within the Siuna terrane, at least according to the boundary given on Fig. 1B, modified from Rogers et al., (2007). This is reasonable since this is an arc terrane and the granitoid rock is fine-grained porphyry of dioritic composition. The alternative is that the boundary between the Siuna and Eastern Chortis terrane as shown on Fig. 1B of Rogers et al. (2007) is too far to the north. If this second interpretation is correct, then this lithology represents island arc crust related to the Northern Nicaraguan Rise. The projection on Fig. 1B of the northern boundary to the Siuna terrane out into the Caribbean Sea over the Nicaraguan Rise also places the Moskito-1 drill core in the Siuna terrane. In our opinion the boundary between the Siuna terrane and the Northern Nicaraguan crust (Fig. 1A) should lie along the western Pedro Fracture zone, the eastern extension of which separates the Northern Nicaraguan Rise from the Southern Nicaraguan Rise (Fig. 1A). Based on a detailed biostratigraphic study of Radiolaria and studies of the geochemistry of mafic and ultramafic rocks in the area of Nicaragua and northern Costa Rica Baumgartner at al. (2008) identified the Mesquito Composite Oceanic Terrane, which includes the Siuna terrane, as a collage of Pacific terranes covered by Tertiary to Recent arc rocks. Both the Toro Cay and Miskito-1 well sites lie at the same latitude and the close similarity between the trace element

and isotope geochemistry of the Toro Cay and Miskito-1 samples strongly supports the view that these were derived from the same magma reservoir and belong to the same terrane.

CONCLUSIONS

The three granitoid rocks of apparent Late Cretaceous-Paleocene age from the Northern Nicaraguan Rise analyzed for this study show the same overall chemistry in terms of both major and trace elements and fall into the category of the high K calc-alkaline type for Caribbean granitoid rocks. They closely resemble in composition the Above Rocks and Terre Neuve granitoids but are lower in Ta, Nb and LREE. Like the Above Rocks and Terre Neuve intrusions, which lie within the Gonave microplate (Fig. 1A; Mann et al., 1995), the Nicaraguan intrusive rocks studied here are also apparently of Late Cretaceous-Paleocene age, considerably younger than most of the low K intrusive activity in the Cordillera Central-Massif du Nord in Hispaniola (Lewis, 1982; Kesler et al., 1991; Escuder et al., 2006) and the intrusions in central Cuba (Hall et al., 2004). This suggests that the eastern boundary to the Gonave microplate in central Hispaniola is a reactivated tectonic boundary initially formed in the Late Cretaceous that defined a distinct terrane at that time.

The Pb isotopic compositions of the three Nicaraguan granitoid rocks plot in the same general field as other plutonic rocks from the western Caribbean, suggesting that the mantle reservoir and source for the Pb components is the same. Consistent with a common depleted mantle source, the Nicaraguan Rise, Above Rocks and Terre Neuve rocks plot along the NHRL line and fall within the MORB field on Pb isotope plots.

There is no evidence from the Pb isotope data that there has been any significant contamination from the Atlantic sediments. Nor is there evidence of a Pb component in the granitoid rocks derived through contamination from Paleozoic or Precambrian crustal rocks in the Chortis block. Even at Toro Cay only 10km from the present Nicaraguan coast there is no evidence from the chemistry of the granitoid rock sampled that Paleozoic-Precambrian crust underlies the Cenozoic-Cretaceous sedimentary platform in this area. To date, no granitoid intrusive rocks nor other ”basement rocks” have been sampled and analyzed from the main area immediately offshore north of Honduras or from the Honduran borderland, both areas which are likely to be underlain by crustal rocks of the Chortis block.

We postulate that the Southern Nicaraguan Rise represents oceanic crust that was subducting below the Northern Nicaraguan Rise and was the cause of the Late Cretaceous magmatism along the Nicaraguan Rise. This subduction continued until the thick plateau crust collided with the lighter island arc crust of the Northern Nicaraguan Rise. This agrees with the conclusion of Pindell and Kennan (in press) that no more subduction was occurring by the end of the Eocene. The structure must be more complex along the Honduran borderland with the Cayman Trough, since granitoid rocks dredged from the northern wall of the Cayman Trough do show evidence of a Chortís block continental component.

ACKNOWLEDGMENTS

We express our thanks to the geologists and management of Signal, Occidental and Mobil oil companies for sending us the drill core samples of granitoid rocks recovered from three of the wells drilled along the Nicaraguan Rise. We thank Chris Harper for access to the IHS Energy database on the Nicaraguan Rise wells. Discussions with Daniel Arden of Signal Oil, when he was based in Jamaica around 1970 and his 1975 publication on the Nicaraguan Rise have proved invaluable. We acknowledge Edward Robinson and Grenville Draper for many useful discussions over the years and for sharing their knowledge of the geology of the Nicaraguan Rise and Jamaica. Our gratitude to Kenneth Flores, Peter Baumgartner, Jim Pindell, and particularly Pete Emmet and Paul Mann for discussion on their recent work and for their help by sending preprints and abstracts. Helpful reviews from Edward Lidiak and Yamirka Rojas-Agramonte improved the paper.

REFERENCES

Ahmad, R., Lal, R., Sharma, P.K., 1987. A fission-track age for the Above Rocks granodiorite, Jamaica. Caribbean Journal of Science, 23, 450-452.

Arden, D.D.Jr., 1969. Geologic history of the Nicaraguan Rise. Transactions of the Gulf Coast, Association of Geological Societies, 19, 245-309.

Arden, D.D.Jr., 1975. Geology of Jamaica and the Nicaraguan Rise. In: Nairn, A.E.M., Stehli, F.H. (eds.). The Ocean Basins and Margins. New York, Gulf of Mexico and the Caribbean Plenum Press, 3, 617-661.

Baumgartner, P.O., Flores, K., Bandini, A.N., Girault, F., Cruz, D., 2008. Upper Triassic to Cretaceous adiolaria from Nicaragua and Northern Costa Rica - The Mesquito Composite Oceanic Terrane. Ofioliti, 33(1), 1-19.

Brown, G.C., 1982. Calc-alkaline intrusive rocks; their diversity, evolution, and relation to volcanic arcs. In: Thorpe, R.S. (ed.). Orogenic Andesites and Related Rocks. New York, John Wiley & Sons, 437-461.

Brown, G.C., Thorpe, R.C., Webb, P.C., 1984. The geochemical characteristics of granitoids in contrasting arcs and comments on magma sources. London, Journal of the Geological Society, 141, 413-426.

Case, J.E., MacDonald, W.D., Fox, P.J., 1990. Caribbean crustal provinces; seismic and gravity evidence. In: Dengo, G., Case, J.E. (eds.). The Caribbean Region. The Geology of North America. Boulder (Colorado), Geological Society of America, H, 15-36.

Chubb, L.J., Burke, K., 1963. Age of the Jamaican granodiorite. Geological Magazine, 100, 524-532.

Couch, R., Woodcock, S., 1981. Gravity and structure of the continental margins of southwestern Mexico and northwestern Guatemala. Journal of Geophysical Research, 86(B3), 1829-1840.

Cumming, G.L., Kesler, S.E., Kristic, D., 1982. Source of lead in Central American and Caribbean mineralization; II, Lead isotope provinces. Earth and Planetary Science Letters, 56, 199-209.

Dengo, G., Bohnenberger, O., 1969. Structural development of northern Central América. American Association of Petroleum Geologists, 11, 203-220.

Dengo, G., 1973. Estructura geológica, historia tectónica y morfología de America Central. Guatemala City, Instituto Centroamericano de Investigación y Tecnología Industrial, 2nd edition, 52pp.

Donnelly, T.W., Horne, G.S., Finch, R.C., Lopez-Ramos, E., 1990. Northern Central America, The Maya and Chortizblocks. In: Dengo, G., Case, J.E., (eds.). The Caribbean Region. The Geology of North America. Boulder (Colorado), Geological Society of America, H, 37-76.

Edgar, N.T., Ewing, J.I., Hennion, J., 1971. Seismic refraction and reflection in the Caribbean Sea. American Association of Petroleum Geologists Bulletin, 55(6), 833-870.

Emmet, P., 2008. Discussion on drill cores from Honduras and Nicaragua. Personal communication, 5th of June 2003.

Escuder Viruete, J., Contreras, F., Stein, G., Urien, P, Joubert, M., Ullrich, T., Mortensen, J., Pérez-Estaún, A., 2006. Transpression and strain partitioning in the Caribbean island-arc: Fabric development, kinematics and Ar-Ar ages of syntectonic emplacement of the Loma Cabrera batholith, Dominican Republic. Journal of Structural Geology, 28, 1498-1519.

Ewing, J.I., Antoine, J., Ewing, M., 1960. Geophysical measurements in the western Caribbean and Gulf of Mexico. Journal of Geophysical Research, 65, 4087-4126.

Hall, C.M., Kesler, S.E., Russel, N., Piñero, E., Sánchez, R., Pérez, M., Moreira, J., Borges, M., 2004. Age and tectonic setting of the Camagüey volcanic-intrusive arc, Cuba: Late Cretaceous extension and uplift in the western Greater Antilles. The Journal of Geology, 112, 2521-2542.

Harland, W.B., Smith, A.G., Wilcock, B., (eds.), 1964. The Phanerozoic times-scale: A symposium dedicated to Professor Arthur Holmes. The Quarterly Journal of the Geological Society of London Publication, 120 (supplement), 458pp.

Holcombe, T.L., Ladd, J.W., Westbrook, G., Edgar, N.T., Bowland, C.L., 1990. Caribbean marine geology: Ridges and basins of the plate interior. In: Dengo, G., Case, J.E. (eds.). The Caribbean Region. The Geology of North America. Boulder (Colorado), The Geological Society of America, H, 231-260

Horne, G.S., Puskar, P., Shafiqullah, M., 1976. Laramide plutons on the landward continuation of the Bonacca ridge, northern Honduras. Guadeloupe, Transactions of the 7th Caribbean Geologic Conference, 583-588.

Jackson, T.A., Scott, P.W., 1994. The mineral and rock geochemistry of the Above Rocks pluton, Jamaica: new information on emplacement and petrogenesis. Caribbean Journal of Science, 40, 153-163.

Jolly, W.T., Lidiak, E.G., Dickin, A.P., 2006. Cretaceous to Mid-Eocene pelagic sediment budget in Puerto Rico and the Virgin Islands (northeast Antilles Island arc). Geologica Acta, 4(1-2), 35-62.

Jones, L.M., Kesler, S.E., Lewis, J.F., 1979. Strontium isotope geochemistry of Late Cretaceous granodiorites, Jamaica and Haiti, Greater Antilles. Earth and Planetary Science Letters, 43, 112-116.

Kamenov, G.D., Mueller, P.A., Perfit, M.R., 2004. Optimization of mixed Pb-Tl solutions for high precision isotopic analyses by MC-ICP-MS. Journal of Analytical Atomic Spectrometry, 19, 1262-1267.

Kesler, S.E., 1971. Petrology of the Terre-Neuve igneous province, northern Haiti. In: Donnelly, T.W. (ed.). Caribbean geophysical, tectonic, and petrologic studies. Geological Society of America Memoir, 130, 119-137.

Kesler, S.E., Levy, E., Martin, F.C., 1990. Metalogenetic evolution of the Caribbean region. In: Dengo, G., Case, J.E. (eds.). The Caribbean Region. The Geology of North America. Boulder (Colorado), The Geological Society of America, H, 459-482.

Kesler, S.E., Sutter, J.F., Barton, J.M., Speck, R.C., 1991. Age of intrusive rocks in northern Hispaniola. In: Mann, P., Draper G., Lewis, J.F. (eds.). Geologic and tectonic development of the North American–Caribbean plate boundary in Hispaniola. Boulder (Colorado), The Geological Society of America, 262 (Special Paper), 165-185.

Kornicker, L.S., Bryant, W.R., 1969. Sedimentation on the continental shelf of Guatemala and Honduras. In: McBirney, A.R. (ed.). Tectonic relations of northern Central America and the western Caribbean-the Bonacca Expedition. American Association of Petroleum Geologists, 11 (Memoir), 244-257.

Kysar, G., 2001. The role of Paleogene magmatism in the evolution of the northern Caribbean margin: the Sierra Maestra (southern Cuba). Unpublished Doctoral Thesis dissertation. Washington D.C., The George Washington University, 187pp.

Kysar, G., Lewis, J.F., Perfit, M.R., Kamenov, G., Mortensen, J., Ulrich, T., Friedman, R., 2009. Granitoids with a continental affinity from the NW wall of the Cayman trench: Implications for Subduction Zone magmatism in the Cayman, Sierra Maestra, N Chortis Block and Nicaraguan Rise. Third Cuban Convention of Earth Science, Geociencias 2009 "Subduction zones of the Caribbean" (16-20 of March 2009), Havana (Cuba), Proceedings Geociencias, Abstract,

website: http://www.ugr.es/~agcasco/igcp546/Cuba09/Cuba_2009_Abstracts.htm.

Lewis, J.F., 1982. Granitoid rocks in Hispaniola, in Transactions. Santo Domingo (Dominican Republic), 9th Caribbean Geological Conference (1980), 2, 391-401.

Lewis, J.F., 1980. Granitoid rocks of Hispaniola. In: Llanas, R. (eds.). Santo Domingo (Dominican Republic), Transactions of the 9th Caribbean Geological Conference, 391-403.

Lewis, J.F., Draper, G., 1990. Geology and tectonic evolution of the northern Caribbean margin. In: Dengo, G, Case, J.E. (eds.). The Caribbean Region. The Geology of North America. Boulder (Colorado), The Geological Society of America, H, 77-140.

Lewis, J.F., Perfit, M.R., Kysar, G., Aravalo, R., Mortensen, J., Ullrich, T., Friedman, R., Kamenov, G., 2005. Anomalous granitoid compositions from the northwestern Cayman Trench: Implications for the composition and evolution of the Cayman Ridge. San Juan (Puerto Rico), 17th Caribbean Geological Conference, Abstract, 49-50.

Lidiak, E., Jolly, W.T, 1996. Circum-Caribbean granitoids: characteristics and origin. International Geology Review, 38, 1098-1103.

Mann, P., Taylor, F.W., Edwards, R., Ku, T-L., 1995. Actively evolving microplate formation by oblique collision and sideways motion along strike-slip faults: An example from the northeastern Caribbean plate margin. Tectonophysics, 246, 1-69.

Mann, P., Rogers, R., Gahagan, L., 2006. Chapter 8: Overview of plate tectonic history and its unsolved tectonic problem. In: Buncdschud, J. (ed.). Central America: Geology, Resources, and Natural Hazards. The Netherlands, Balkema Publishers, 205-241.

Mauffret, A., Leroy, S., 1997. Seismic stratigraphy and structure of the Caribbean igneous province. Tectonophysics, 283(1-4), 61-104.

McBirney, A.R, Bass, M.M., 1969. Geology of the Bay Islands, Gulf of Honduras. In: McBirney, A.R. (ed.). Tectonic relations of northern Central America and the western Caribbean. American Association of Petroleum Geologists, 11 (Memoir), 229-243.

Meyerhof, A.A., 1966. Bartlett Fault System-age and offset. Transactions, Third Caribbean Geological Conference, Hope Gardens (Jamaica), Jamaica Geological Survey Publication, 95, 1-7.

Meyerhof, A.A., Kreig, E.A., 1977. Petroleum Potential of Jamaica. Division ministry of Energy and Mining (Government of Jamaica), Hope Gardens (Jamaica), Jamaica Mining and Natural Resources, 131pp.

Mutti, M., Droxler, A.W., Cunningham, A.D., 2005. Evolution of the Northern Nicaraguan Rise during the Oligocene-Miocene: Drowning by environmental factors. Sedimentary Geology, 175, 237-258.

Munoz, A., Baca, D., Artiles, V., Duarte, M., 1997. Nicaragua: Petroleum geology of the Caribbean margin. The Leading Edge, 16(12), 1799-1805.

Pearce, J.A., 1983. Role of sub-continental lithosphere in magma genesis at active continental margins. In: Hawkesworth, C.J., Norry, M.J., (eds.). Continental Basalts and Mantle Xenoliths. Nantwich, (Cheshire, United Kingdom), Shiva Publishing, 230-249.

Perfit, M.R., Heezen, B.C., 1978. The geology and evolution of the Cayman Trench. Geological Society of America Bulletin, 89, 1155-1174.

Pindell, J., Kennan, L., 2009. Tectonic evolution of the Gulf of Mexico, Caribbean and northern South America in the mantle reference frame: an update: an update. In: James, K., Lorente, M.A., Pindell, J. (eds.), 2009. The geology and evolution of the region between North and South America. Geological Society of London, Special Publications, nº328, 1-54.

Pinet, P., 1975. Structural evolution of the Honduras continental margin and the sea floor south of the western Cayman Trough. Geological Society of America Bulletin, 86, 830-838.

Rogers, R., Mann, P., 2007. Transtensional deformation of the western Caribbean-North America plate boundary zone. In: Mann, P. (ed.). Geologic and Tectonic Development of the Caribbean Plate in Northern Central America. Geological Society of America, 428 (Special Paper), 37-64.

Rogers, R., Mann, P, Emmet, P., 2007. Tectonic terranes of the Chortis block based on integration of regional aeromagnetic and geologic data. In: Mann, P. (ed.). Geologic and Tectonic Development of the Caribbean Plate in Northern Central America. Geological Society of America, 428 (Special Paper), 65-88.

Rojas-Agramonte, Y., Kröner, A., Wand, Y.S., Liu, D.Y., Garcia-Delgado, D.E., Handler, R., 2004. Geochemistry and early Paleogene SHRIMP zircon ages for island arc granitoids of the Sierra Maestra, southeastern Cuba. Chemical Geology, 213(4), 307-324.

Venable, M., 1994. A geological, tectonic, and metallogenetic evaluation of the Siuna terrane (Nicaragua). Doctoral Thesis dissertation. Tucson (Arizona), University of Arizona, 154pp.

Wilson, M., 1989. Igneous Petrogenesis: a Global Tectonic Approach. London, Unwin Hyman, Springer Editor, 466pp.

Manuscript received March 2009;
revision accepted April 2010;
published Online May 2010

Geologica Acta, Vol.9, Nos 3-4, September - December 2011, 481-498
DOI: 10.1344/105.000001742
Available online at www.geologica-acta.com

geologica acta

Geology of the Cerro Quema Au-Cu deposit (Azuero Peninsula, Panama)

I. CORRAL [1] **A. GRIERA** [1] **D. GÓMEZ-GRAS** [1] **M. CORBELLA** [1] **À. CANALS** [2] **M. PINEDA-FALCONETT** [3] **E. CARDELLACH** [1]

[1] **Departament de Geologia, Universitat Autònoma de Barcelona (UAB)**
08193 Barcelona, Spain. Corral E-mail: Isaac.Corral@uab.cat Griera E-mail: Albert.Griera@uab.es
Gómez-Gras E-mail: David.Gomez@uab.es Corbella E-mail: Merce.Corbella@uab.es Cardellach E-mail: Esteve.Cardellach@uab.es

[2] **Facultat de Geologia, Universitat de Barcelona (UAB)**
08028 Barcelona, Spain. Canals E-mail: angelscanals@ub.edu

[3] **Departamento de Geografía, Universidad de Panamá**
082304747, Chitré, Panamá. Pineda-Falconett E-mail: mpineda@ancon.up.ac.pa

ABSTRACT

The Cerro Quema district, located on the Azuero Peninsula, Panama, is part of a large regional hydrothermal system controlled by regional faults striking broadly E-W, developed within the Río Quema Formation. This formation is composed of volcanic, sedimentary and volcano-sedimentary rocks indicating a submarine depositional environment, corresponding to the fore-arc basin of a Cretaceous–Paleogene volcanic arc. The structures observed in the area and their tectono-stratigraphic relationship with the surrounding formations suggest a compressive and/or transpressive tectonic regime, at least during Late Cretaceous–Oligocene times. The igneous rocks of the Río Quema Formation plot within the calc-alkaline field with trace and rare earth element (REE) patterns of volcanic arc affinity. This volcanic arc developed on the Caribbean large igneous province during subduction of the Farallon Plate. Mineralization consists of disseminations of pyrite and enargite as well as a stockwork of pyrite and barite with minor sphalerite, galena and chalcopyrite, hosted by a subaqueous dacitic lava dome of the Río Quema Formation. Gold is present as submicroscopic grains and associated with pyrite as invisible gold. A hydrothermal alteration pattern with a core of advanced argillic alteration (vuggy silica with alunite, dickite, pyrite and enargite) and an outer zone of argillic alteration (kaolinite, smectite and illite) has been observed. Supergene oxidation overprinted the hydrothermal alteration resulting in a thick cap of residual silica and iron oxides. The ore minerals, the alteration pattern and the tectono-volcanic environment of Cerro Quema are consistent with a high sulfidation epithermal system developed in the Azuero peninsula during pre-Oligocene times.

KEYWORDS | **Panama. Cerro Quema. Au-Cu High sulfidation epithermal deposit. Fore-arc basin. Arc-magmatism.**

INTRODUCTION

Central America is a region with important mineral resources such as gold, silver, copper, lead, zinc and aluminium. Precious metals (Au and Ag) and Cu are currently attracting the interest of mining companies. A significant portion of their investment is focused on gold-bearing epithermal vein deposits (e.g. Talavera, Bonanza and La Libertad, Nicaragua; Marlín, Guatemala), on porphyry copper deposits (e.g. Petaquilla and Cerro Colorado, Panama) and on base metal skarn and replacement deposits (e.g. Mochito, Honduras) (Nelson, 2007). Compared to other Central America countries such as Honduras, Guatemala, Belize, Costa Rica and Nicaragua, our knowledge of the geology and metallogeny of Panama is still limited. Gold and copper are the most economically important metals and are mainly related to epithermal and porphyry copper deposits respectively.

In 1965 a study of the geology and metallogeny of Panama was undertaken with the objective of evaluating Panama's mineral resource potential, financed by the United Nations Development Program (UNDP). One of the regions explored during the program was the Azuero Peninsula (Del Giudice and Recchi, 1969). The main results of this program were the discovery of areas with important copper and gold anomalies that were related to porphyry copper and epithermal deposits respectively. These findings were later confirmed by Ferencic (1970, 1971) and Kesler et al. (1977). In 1988, the Compañía de Exploración Mineral SA. (CEMSA), using data collected during the program, discovered an Au-Cu deposit at Cerro Quema which was considered a potentially mineable target. Between 1990 and 1994 Cyprus Amax carried out several exploration programs including both soil geochemistry and drilling campaigns. Results were presented in three unpublished reports by Leach (1992), Horlacher and Lehmann (1993) and Torrey and Keenan (1994). These latter authors reported gold resources of 10 Million tonnes (Mt) with an average gold grade of 1.26g/t.

Unraveling the geologic evolution of the area is the first step towards understanding the processes responsible for mineralization and associated hydrothermal alteration. In order to achieve this objective, a detailed geologic study of the Cerro Quema area was carried out. Fieldwork was complemented with geochemical analyses (major, trace element and REE) of regional rocks and the mineralogical characterization of the deposit was studied from surface and drill core samples. The lack of good exposures of hypogene mineralization and its apparent relationship to dacitic domes led to a debate about the origin of the Cerro Quema deposit. It was first considered a high sulfidation epithermal system possibly related to an underlying porphyry copper deposit (Leach, 1992; Nelson, 1995; Nelson and Nietzen, 2000). More recently, it has been suggested that it is an oxidized gold and copper deposit that shares characteristics of both epithermal and volcanogenic massive sulfide deposits (Nelson, 2007). Although epithermal style mineralization, high-level porphyry systems and volcanogenic massive sulfide deposits may be end-members of a continuum (Hannington, 1997), a better understanding of these different models may have important consequences for the discovery of new deposits in geologically similar areas.

GEOLOGICAL SETTING

Panama is situated in the southern part of Central America and represents the youngest segment of the land bridge between the North and South American plates. The closure of the Caribbean-Pacific seaway, which occurred during Late Pliocene to early Pleistocene times, had profound biological, oceanographic, and climatological consequences (Duque-Caro, 1990; Coates et al., 1992).

Panama is considered to be a tectonic block that lies at the junction of four tectonic plates, namely the Caribbean, South American, Cocos, and Nazca plates (Fig. 1A). The Panama microplate is considered to be part of the Caribbean plate but new GPS data indicates a decoupling motion and relative convergence between Panama and the Caribbean plate (Trenkamp et al., 2002). The northern boundary of the Panama microplate is defined by a system of thrust and transform faults known as the North Panama Deformed Belt (Adamek et al., 1988; Silver et al., 1990). Towards the West, these faults shift to the diffuse thrust belt of the Cordillera Central of Costa Rica (Marshall et al., 2003; Denyer and Alvarado, 2007). The eastern boundary with the South American continental plate is located along the dextral shear zone of the Atrato Valley (Taboada et al., 2000; Trenkamp et al., 2002). The southern edge is characterized by the subduction of the Nazca and Cocos oceanic plates beneath the Panama microplate. The initiation of the intra-oceanic subduction and the evolution of the magmatic island arc on the Azuero Peninsula is dated as Late Cretaceous and continued until Middle Miocene time (Buchs, 2008; Buchs et al., 2009, 2010; Wörner et al., 2009). Compression along the southern border of the Panama microplate controlled the formation of the South Panama Deformed Belt. Deformation is mainly accommodated by bending of the arc and sinistral NW-SE strike-slip faults (Mann and Corrigan, 1990; Coates et al., 2004).

The morphology of the subducting oceanic plates along the Central American Isthmus has a strong influence on the tectonics of the overriding plate and the supra-subduction magmatic processes. Subduction of relatively

buoyant plates with irregular topographic highs (e.g. aseismic ridges and/or oceanic islands) causes the uplift and exposure of the fore-arc area along its margin (Fisher et al., 1998; Gardner et al., 2001; Sak et al., 2004). Such exposures provide the opportunity to study deep sections of the inner and outer fore-arc margin, which is composed of a complicated arrangement of arc-related volcanic rocks, accreted material and overlapped sequences (Buchs, 2008).

The Azuero Peninsula forms a pronounced prominence in the western Pacific coastline of Panama (Fig. 1B). The present configuration of the land bridge results from crustal mobility driven by escape tectonics and coastwise transport of fore-arc units (Krawinkel and Seyfried, 1994). The first regional mapping and stratigraphy definition was made through a joint program of the United Nations Development Program and the Dirección General de Recursos Minerales, 1976 (Del Giudice and Recchi, 1969; Metti et al., 1972; Metti and Recchi, 1976; Recchi and Miranda, 1977). The results of this work have been expanded upon in more recent contributions (Escalante, 1990; Krawinkel and Seyfried, 1994; Kolarsky and Mann, 1995; Kolarsky et al., 1995; Di Marco et al., 1995; Buchs, 2008; Buchs et al., 2009, 2010; Corral et al., 2008, and this study).

The basement of the Azuero Peninsula mainly consists of massive and pillowed basalt rocks with characteristic flat chondritic REE patterns which have been interpreted as tholeiitic basalts with plateau affinity (Hoernle et al., 2002, 2004; Hoernle and Hauff, 2007). Similar rocks have been identified in central and eastern Panama (i.e. Chagres and Darien regions) and along the Pacific onshore of Costa Rica (i.e Nicoya, Burrica and Osa Peninsula) and are interpreted as the western margin of the Caribbean large igneous province (Di Marco et al., 1995; Sinton et al., 1997; Hauff et al., 2000; Hoernle et al., 2002, Hoernle et al., 2004). Radiometric and paleontological ages range from 139 to 69Ma (Bourgois et al., 1982; Kolarsky et al., 1995; Kerr et al., 1997; Sinton et al., 1997, 1998; Revillon et al., 2000; Hauff et al., 2000; Hoernle et al., 2002, Hoernle et al., 2004; Lissinna, 2005; Buchs, 2008; Buchs et al., 2009, 2010). Although these rocks were interpreted initially as accreted oceanic terranes by Goossens et al. (1977), the current accepted interpretation is that they represent uplifted portions of the western margin of the Caribbean plate (Hauff et al., 2000; Hoernle et al., 2002, Hoernle et al., 2004).

In spite of the abundance of radiometric studies of the igneous rocks of the area (e.g. Del Giudice and Recchi, 1969; Lissinna, 2005), the age of the onset of subduction and the development of the volcanic arc remains a matter of debate. Proposed ages of arc initiation range between 88Ma (Lissinna et al., 2006) to 66Ma (Hoernle et al., 2002; Wörner et al., 2006). Recently, intermediate ages between both extremes have been proposed, (69-71Ma by Wenger et al., 2011; 84-71Ma by Pindell and Kenan, 2009). Buchs (2008) and Buchs et al. (2010) reported unusual

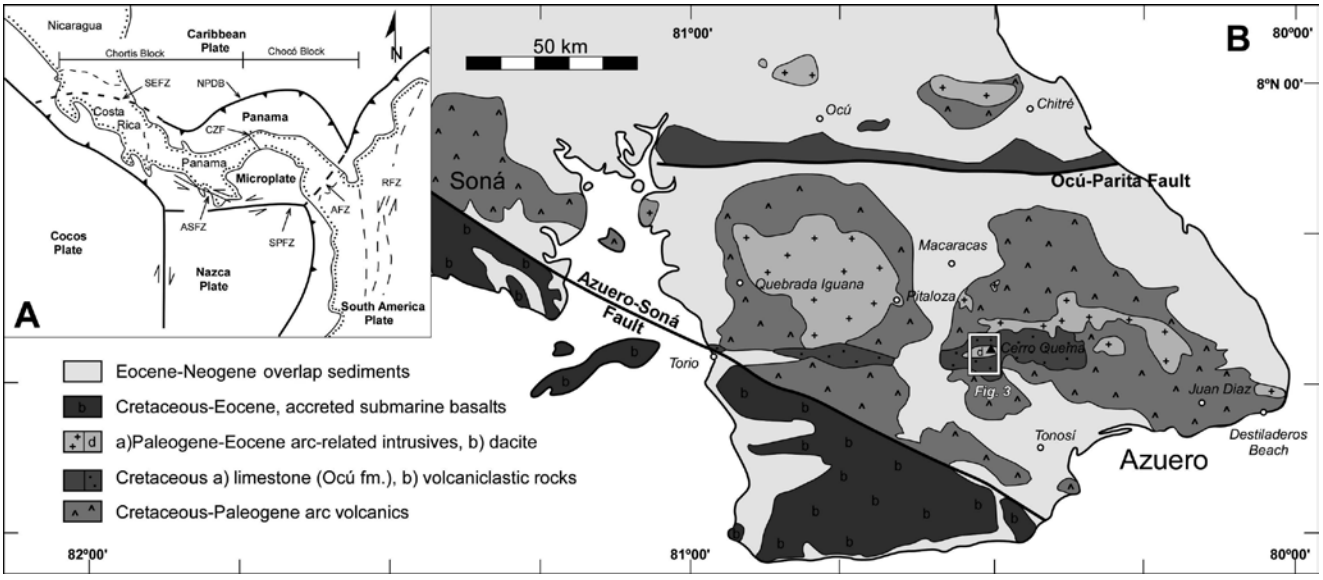

FIGURE 1 | **Present-day tectonic setting of Southern Central America and the Azuero Peninsula. A) North Panama Deformed Belt (NPDB), South Panama Fault Zone (SPFZ), Santa Elena suture (SEFZ), the Atrato Fault Zone (AFZ), Canal Fracture Zone (CFZ), Romeral Fault Zone (RFZ); (after Duque-Caro, 1990; de Boer et al., 1995; Kellogg et al., 1995; Mann and Kolarsky, 1995; Harmon, 2005). B) Geological map of Azuero Peninsula (after DGRM, 1976).**

geochemical compositions for basaltic lava flows and dikes emplaced in the Azuero basement with intermediate signatures, ranging from typical oceanic plateau to intra-oceanic island arc. These authors defined these rocks as the "Azuero Proto-arc Group" and interpreted them to have developed from early magmatism produced during the onset of subduction at 73-75Ma. These rocks are equivalent to those described by Wörner et al. (2009) as "enigmatic Caribbean large igneous province -arc rocks" and to some of the samples described by Wenger et al. (2011) as "Sona-Azuero Arc". These observations suggest a possible overlap in ages between plateau and arc magmatism during early stages of subduction.

Subsequently, arc-magmatism was developed on top of the Azuero basement and proto-arc rocks. The Azuero Arc Group (Buchs et al., 2010) is composed of an arc-related sequence of volcanic rocks and associated tuffites and volcaniclastic rocks. Their ages indicate that the arc is, at least, Maastrichtian (~71Ma) in age and expands up to ~40Ma (Del Giudice and Recchi, 1969; Maury et al., 1995; Lissinna, 2005; Lissinna et al., 2002, 2006; Wörner et al., 2005, 2006, 2009; Wegner et al., 2011). Maturation of magma sources during growth of the volcanic arc is not well constrained, although radiometric ages suggest an overlap of basic and acid igneous rocks (Buchs et al., 2010; Wörner et al., 2009).

The study area, part of the Cerro Quema district and surrounding areas, is situated in the central part of the Azuero Peninsula (see Fig. 1B) and mainly consists of andesites, dacites, limestones, basalts and turbidites, developed in a fore-arc basin environment. First studies by Del Giudice and Recchi (1969) and Weyl (1980) did not distinguish between different stratigraphic units and assigned all units to the Ocú Formation. They made this assignment because of the similarities between the limestones that occur in the Cerro Quema area and the grayish-white micritic limestones that crop out in the northern part of the Azuero Peninsula (Ocú locality, see Fig. 1B). Based on microfossil biostratigraphy and field observations, Weyl (1980) proposed a Campanian-Maastrichtian age for these rocks. Later, Horlacher and Lehmann (1993), after field mapping of the area, distinguished two units: 1) the Ocú Formation that included all limestones and volcano-sedimentary rocks, and 2) the Quema Formation, that was restricted to dacites and massive andesites.

STRATIGRAPHY

The Ocú Formation was initially described as well bedded fine-grained limestones with locally interbedded siltstones, tuffs and intermediate lava flows, deposited on top of basaltic basement rocks (Del Giudice and Recchi, 1969). The assumed age for the Ocú Formation is late Campanian-Maastrichtian on the basis of the association of planktonic foraminifera (*Globotruncana Lapparenti, Globotruncana ventricosa* and *Globotruncana contusa*) as first noted by Del Giudice and Recchi (1969), Weyl (1980) and Bourgois et al. (1982). Kolarsky et al. (1995) defined the Ocú Formation as thin to medium-bedded grayish-white limestone and calcareous siltstone, and light brown, fine grained calcareous siltstone and sandstone, mainly interbedded with basaltic rocks with 1,500m of apparent thickness. Del Giudice and Recchi (1969) and Weyl (1980) and other recent studies (Buchs, 2008; Buchs et al., 2010) describe interbedded basaltic lava flows within the Ocú Formation (e.g. Coiba Island) locally crosscut by basaltic dikes of the Azuero Proto-arc Group. The limestones of the Ocú Formation which show syn-volcanic soft deformation were dated by Buchs et al. (2010) as Late Campanian (~75-73Ma) in agreement with two limestone samples from the Ocú type locality which gave a Campanian age.

The rocks in the Cerro Quema district neither correspond with the classical definition of the Ocú Formation nor have the same genetic implications. Therefore, the rocks cropping out in the study area need to be defined and reinterpreted as a new lithostratigraphic unit. Our data, together with the work of previous authors, allow us to propose a new formation, named hereafter the Río Quema Formation, consisting of volcanic and volcaniclastic sediments interbedded with hemipelagic limestones, submarine dacite lava domes and crosscut by basaltic to andesitic dikes. The Río Quema Formation is interpreted as the infill sequence of the fore-arc basin of the Cretaceous–Paleogene volcanic arc and is integrated within the five major units of the Azuero Peninsula as follows: 1) Azuero Igneous Basement, 2) Azuero Proto-arc Group, 3) Río Quema Formation, 4) arc-related intrusive rocks, and 5) Tonosí Formation. The main characteristics of these units are described below and shown in Figure 2.

1) The Azuero Igneous Basement (Fig. 2A) is composed of massive, agglomerate and pillowed basaltic lavas, diabases, gabbros, minor occurrences of hemipelagic sediments interlayered with lavas, and basaltic dikes crosscutting all materials. Geochronological dating of the basalts indicates ages ranging from Turonian to Santonian (Lissinna, 2005) and is consistent with a Coniacian age obtained from interlayered radiolarian sediments (Kolarsky et al, 1995), recently revised by Buchs et al. (2009) who reported a Coniacian-Early Santonian age.

2) The Azuero Proto-arc Group locally overlies the Azuero Igneous Basement. In the Río Quema stratigraphical section it is composed of massive and pillowed basaltic lavas of irregular thickness (0-40m?) overlain by well bedded greenish shales, cherts and thin basaltic lava flows.

These volcanic rocks were described by Buchs (2008) and Buchs et al. (2010) as basaltic trachyandesitic lava flows and dikes, locally interbedded with hemipelagic limestones of the Ocú Formation.

3) The Río Quema Formation includes all sedimentary, volcaniclastic and extrusive volcanic units deposited in a fore-arc basin, overlying both the Azuero Igneous Basement and locally the Azuero Proto-arc Group. The total thickness of the Río Quema Formation is approximately 1,700m. The following units have been distinguished in the Cerro Quema district:

-A Lower Unit, made up of andesitic lava flows (0.20-2m thick) and well bedded crystal-rich sandstone to siltstone turbidites interbedded with hemipelagic thin limestone beds (Fig. 2B). W-SW paleocurrents were deduced from cross bedding, ripples and tool marks.

-A Limestone Unit, corresponding to a 100-150m thick light grey biomicritic hemipelagic limestone which is interlayered with well bedded cherts, thinly bedded turbidites and ash layers (Fig. 2C). The presence of planktonic foraminifera (*Globotruncana sp., Globotruncanita sp.,* and *Globotruncanella sp.*) indicates a Late Cretaceous age. The similarities with the foraminifera found in the limestones described by Del Giudice and Recchi (1969), Tournon et al. (1989), Di Marco et al. (1995) and Buchs et al. (2010) allow us to infer a late Campanian–early Maastrichtian age. Similar limestone beds have also been found in the

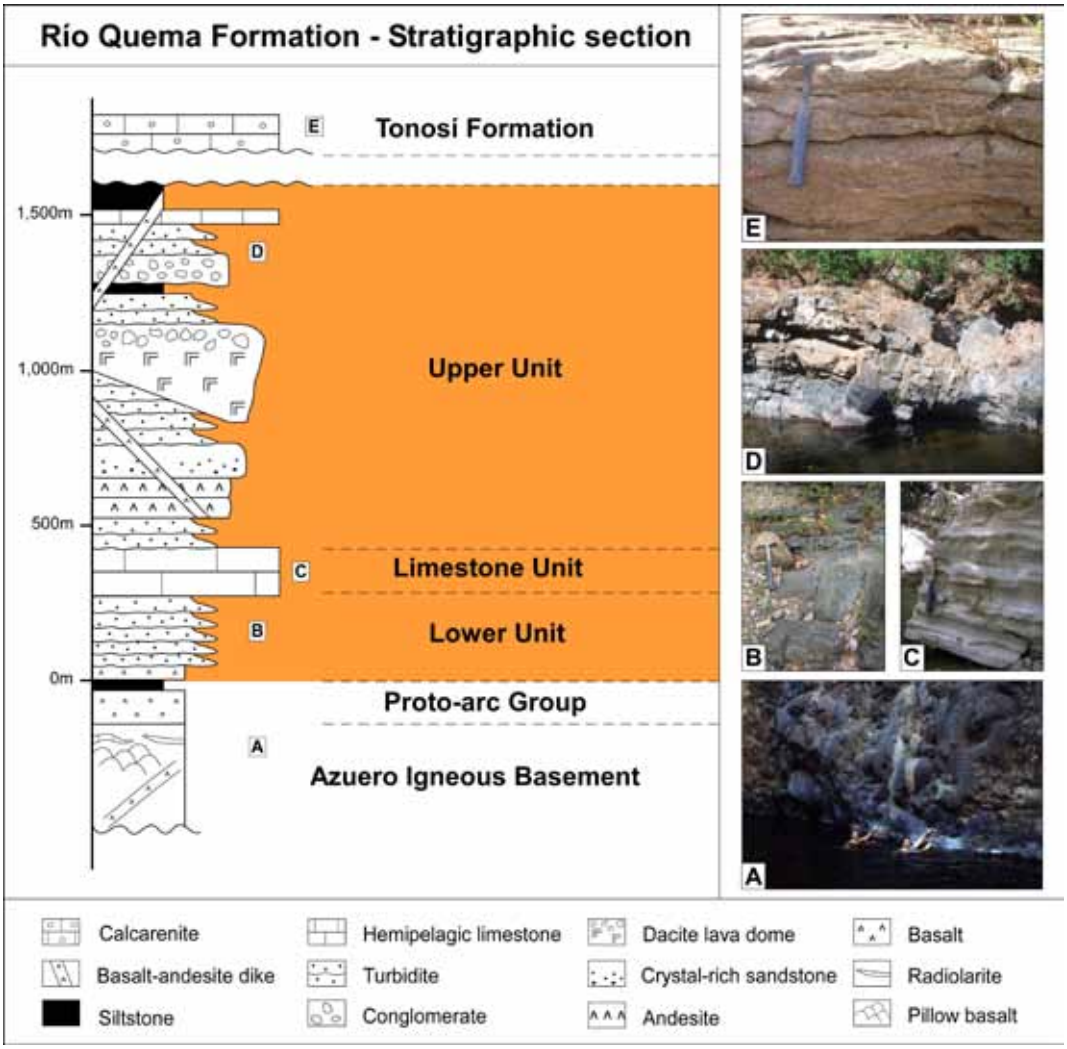

FIGURE 2 | **Idealized stratigraphic section of the Río Quema Formation. A) Pillow basalts of the Azuero Igneous Basement at Río Joaquín. B) Volcaniclastic sediments of the Río Quema Formation lower unit at Río Quema. C) Hemipelagic limestones from the Río Quema Formation limestone unit south of Río Quema. D) Volcaniclastic and hemipelagic sediments crosscut by a basaltic-andesitic dike of the Río Quema Formation upper unit north of Río Quema. E) Fossiliferous calcarenite of the Tonosí Formation at Río Güerita.**

Torio and Güera rivers, following the southernmost E-W trend fault zone of the Azuero Peninsula.

-An Upper Unit, which crops out both in the northern and southern part of the Río Quema section. The northern part is composed of volcaniclastic sediments interlayered with massive to laminar andesitic lava flows (1 to 3m thick), andesitic hyaloclastites (0.1 to 0.5m thick), and massive dacites overlain by dacite lava flows and dacitic and resedimented hyaloclastites (the latter up to 3m thick). However, in the southern part, this unit is characterized by volcaniclastic turbidites, crystal rich sandstones (up to 1m thick), siltstones and thin pelagic limestone beds (up to 0.2m). Whereas massive lava flows and extrusive rocks prevail in the northern part of the section, volcaniclastic turbidites are dominant in the southern region. W-SW paleocurrents are deduced from cross bedding. Basaltic-andesitic dikes intrude part of the series (Fig. 2D), but are more common in the northern part of the study area (Fig. 3).

4) The arc-related intrusive unit is composed of diorites, quartz-diorites and granodiorites. They are exposed as large batholiths in the central and northern part of the Azuero Peninsula, although small quartz-diorite stocks and/or dikes occur South of Cerro Quema. Ages of these igneous rocks range from 66 to 42Ma (Maury et al., 1995; Lissinna, 2005; Wörner et al., 2009; Wenger et al., 2011).

5) The Tonosí Formation consists of a sedimentary sequence unconformably overlapping all of the previous units. Recchi and Miranda (1977) defined the Tonosí Fm. as conglomerates, reefal limestones and associated calcarenites of Middle Eocene to Early Oligocene age, overlying the basaltic basement northeast of the Azuero-Soná fault zone. More recent studies (Kolarsky et al., 1995; Krawinkel and Seyfried, 1994) divided the formation into two major lithological units: 1) A lower unit composed of minor coal seams, conglomerate, coarse sandstone and reefal limestone, and 2) an upper unit composed of deeper marine interbedded sandstone, siltstone and calcarenite. Ages for the Lower unit range from Middle Eocene to Early Oligocene (~40 to 30Ma) and for the Upper unit from Late Oligocene to Early Miocene (~30 to 15Ma) (Kolarsky et al., 1995; Krawinkel and Seyfried, 1994; Krawinkel et al., 1999).

Our interpretation assumes that the Azuero Igneous Basement is equivalent to the Caribbean large igneous province described by Hauff et al. (2000), Hoernle et al. (2002, 2004), and represents the autochthonous basement of the Azuero Peninsula at the onset of subduction. At the initial stages of magmatism, a Proto-arc was developed locally on top of the Azuero Igneous Basement (Buchs, 2008; Buchs et al., 2009, 2010). Simultaneously, the deposition of the Ocú Formation took place (this formation does not crop out in the study area). The Río Quema Formation is the expression of a fore-arc basin infill submarine sequence of a more mature volcanic arc. The Lower Unit, formed by andesitic lava flows, crystal-rich sandstones and turbidites interbedded with hemipelagic limestone beds, represents a proximal depositional environment with respect to the volcanic front. The Limestone Unit records a period of time with minor volcanic activity in which autochthonous sedimentation was dominant over volcanic sedimentation. The Upper Unit records both distal and proximal depositional environments due to the presence of submarine dacite lava domes which played a paleo-barrier role in terms of sedimentation. These dacite lava domes compartmentalized the fore-arc basin, producing changes in the sedimentation. The northern slope of the dacitic domes is mainly composed of massive volcanic rocks, minor turbidites, limestone layers and abundant basaltic-andesitic dikes, suggesting a proximal depositional environment with respect to the volcanic front. In contrast, the southern slope is characterized by a large fraction of volcaniclastic sediments, turbidites, shales and siltstones and by a minor presence of andesitic lava flows, suggesting a distal depositional environment near the volcanic front. The arc-related intrusive unit represents a period of time characterized by quartz-diorite and granodiorite intrusions. These intrusions are abundant to the North of the study area, but minor quartz-diorite batholiths are also present in the southern part. The intrusions produced contact metamorphism on the Río Quema Formation close to the batholiths. Finally, the sedimentary sequence of the Tonosí Formation represents a regional transgressive event that affected the Azuero Peninsula (Kolarsky et al., 1995; Krawinkel et al., 1999).

STRUCTURE

A large network of faults can be recognized in the area. Predominant faults trend NW-SE and NE-SW, show sub-vertical dip and normal sense of offset. A left-lateral strike-slip component has been observed along faults which trend NW-SE trend. Another main tectonic structure of the area is the Río Joaquín fault zone, a 30km regional scale fault zone with a broad E-W orientation (Fig. 3). It was originally identified by Buchs (2008) combining fieldwork and interpretation of satellite images. In the Cerro Quema area, our observations indicate that the Río Joaquín fault zone maintains the general E-W orientation and does not change to a NE-SW trend as proposed by Buchs (2008). Along the Río Joaquín fault, the Azuero igneous basement is directly in contact with the upper series of the Río Quema Formation (see Fig. 3, cross section). A reverse dip-slip motion is observed at the Río Joaquín fault with the southern block uplifted with respect to the northern block. The inferred minimum vertical offset is 300-400m.

Faulting caused a strong deformation, forming cataclasites and a network of tension gashes oblique to the fault.

In addition, ENE-WSW trending folds and minor faults parallel to E-W trending lithological boundaries have also been identified in the area. All these structures are slightly oblique to the Río Joaquín fault zone and are partly cut by it. The northern part of the area is characterized by abundant decametric open folds with moderate limb dips and fold axes gently plunging to the SW. The southern area is characterized by a kilometer-scale E-W trending syncline that affects the entire fore-arc basin (see Fig. 3, cross section). All these structures are covered by the Tonosí Fm., which overlaps the Azuero

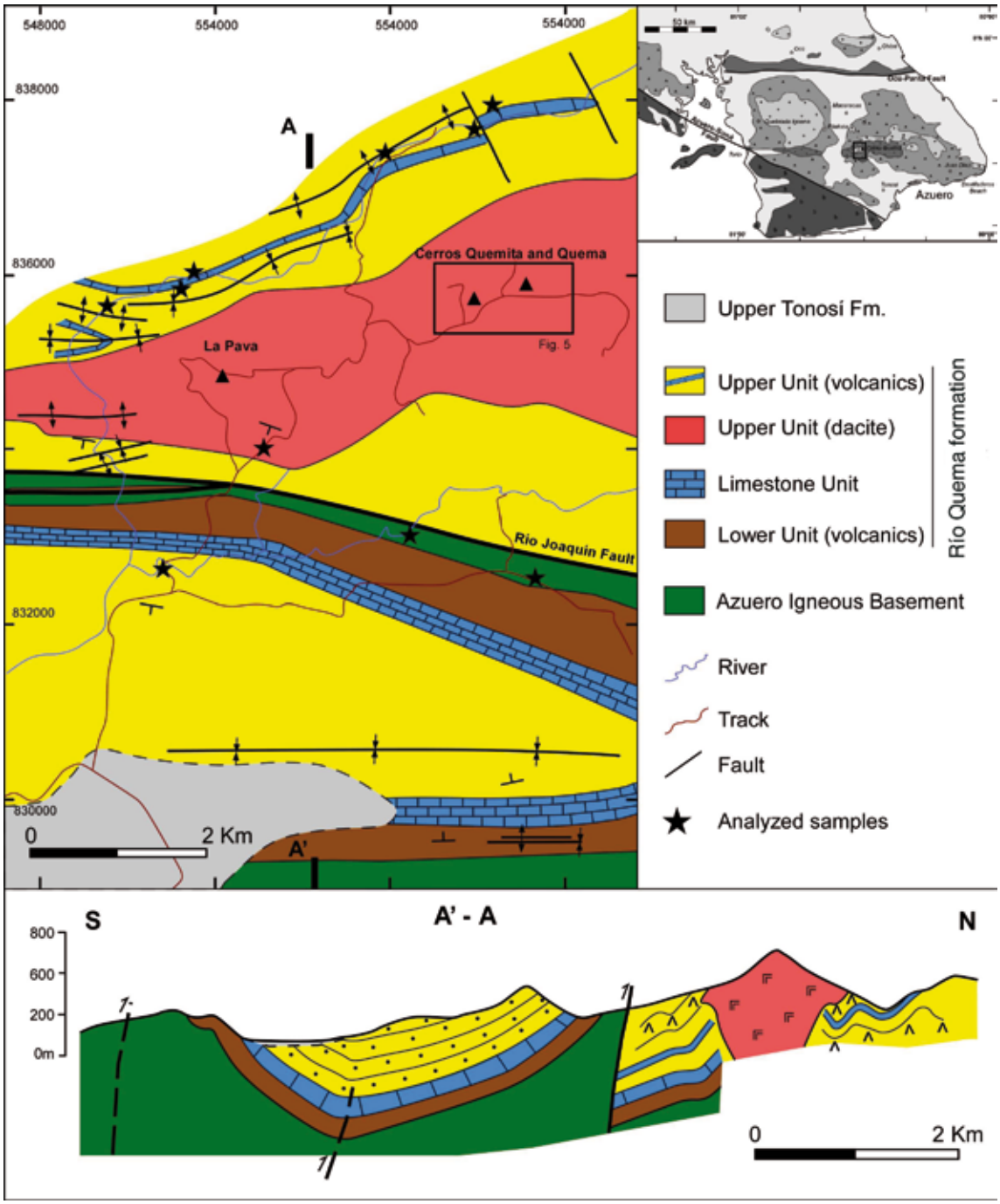

FIGURE 3 | **Geologic Map of the West Cerro Quema area.**

Igneous Basement, the Río Quema Fm. and the arc-related intrusions.

GEOCHEMISTRY

Whole rock analysis (major, trace and REE elements) was performed on 20 representative samples of unaltered igneous and volcaniclastic rocks of the Cerro Quema district and surrounding areas. Samples were cut, crushed and reduced to powder using a tungsten carbide mill. Analyses were carried out by Actlabs (Canada) using X-ray fluorescence (XRF) and inductively coupled plasma-mass spectrometry (ICP-MS). Results are presented in Table I available in www.geologica-acta.com.

As shown by the Total Alkali-Silica (TAS) diagram, the analyzed igneous rocks belong to the sub-alkaline type, spanning the entire compositional range from basalt to dacite (Fig. 4A). According to the AFM (Al_2O_3, FeO, MgO) plot, quartz-diorites from the northern part of the Cerro Quema district and volcaniclastic sediments, andesites, dacites and basaltic-andesitic dikes of the Río Quema Formation have calc-alkaline affinity whereas basalts, pillow basalts and basaltic dikes of the Azuero Igneous Basement show tholeiitic affinity (Fig. 4B).

Two distinct rock groups are recognized using the trace element and REE signatures that match up with the major element data. The first group consists of basalts, andesites and dacites of the Río Quema Formation and the quartz-diorites from the northern part of the Cerro Quema area, displaying characteristic features of rocks with volcanic arc affinities (i.e. variably enriched fluid-mobile elements and depleted in heavy REEs; Fig. 4C and 4D). The second group is represented by basalts with flat or slightly enriched trace elements (i.e. Ba, Sr and Zr) and REE patterns, compatible with compositions of oceanic plateau-like affinities as reported for the Caribbean large igneous province (Fig. 4E) and similar to the rocks of the proto-arc group described by Buchs (2008) and Buchs et al. (2010).

HYDROTHERMAL ALTERATION AND MINERALIZATION

The Río Quema Formation constitutes the most economically interesting geological formation in the Azuero Peninsula because it locally hosts Au-Cu mineralization. The mineralization crops out not only in the Cerro Quema area (e.g. Cerro Quema, Cerro Quemita, Cerro La Pava) but also further East (e.g. Juan Díaz) and West (e.g. Pitaloza and Quebrada Iguana), always to the North of the Río Joaquín fault zone. Ore minerals are rarely seen in outcrops and have been mostly studied in samples from 12 drill cores (2 from Cerro Quemita, 6 from Cerro La Pava and 4 from the area between both hills). Surface sampling and eroded cobbles accumulated in creeks were also used to complete the mineralogical study.

The Río Quema Formation is affected by regional-scale hydrothermal alteration (approximately from Torio village, West of the Azuero Peninsula to the Destiladeros Beach, East of the Azuero Peninsula, Fig. 1). The most prominent hydrothermal alteration is silicification, which is readily observed in the field.

Previous studies in the Cerro Quema area (Torrey and Keenan, 1994) described three hydrothermal alteration types: 1) Silica–pyrite, characterized at surface by highly fractured, vuggy, locally brecciated rock composed of silica and iron oxides and, at depth, by abundant pyrite (up to 35% of the rock volume). The mineral assemblage includes alunite, pyrite, dickite, quartz, pyrophyllite, barite, interlayered illite-smectite, illite, kaolinite, apatite and rutile. 2) Clay–pyrite, containing illite, kaolinite and hematite with disseminated pyrite at depth. 3) Propylitic, at the outer margins of the alteration halo and characterized by chlorite, calcite, siderite, halloysite, laumonite, hematite and illite.

The alteration zones defined by Torrey and Keenan (1994) have not been confirmed by our detailed mapping or by the analytical data from outcrop and drill-core samples. According to our observations, the alteration pattern in Cerro Quema is clearly fault controlled, following the ENE-WSW trending regional faults. Nevertheless, concentric zoning of alteration was observed (Fig. 5A), mainly within dacitic domes but also in andesites. From the microscopic study of thin and polished sections and SEM-EDS and XRD analyses of minerals, a new alteration pattern in the Cerro Quema area is proposed:

1) An inner alteration assemblage, which is characterized at surface by the presence of vuggy silica with hematite, goethite and rutile (Fig. 5B). At depth this alteration zone contains quartz, alunite-natroalunite, aluminium-phosphate-sulphate minerals (APS), dickite, barite, pyrite, enargite and rutile (Fig. 5C, D). This assemblage corresponds to an advanced argillic alteration zone.

2) An external assemblage with kaolinite, illite, smectite and interlayered illite-smectite in both surface exposures and at depth, corresponding to the argillic alteration zone (Fig. 5E). The limit between the two zones can be transitional and they locally overlap.

3) A propylitic alteration assemblage related to mineralization, containing pyrite, chlorite, calcite and siderite has only been found in some drill cores, unrelated

TABLE 1 | **Analyzed samples for major and trace elements and REE**

Sample:	RQ 9A	RQ 15AND	RQ 24	RQ 12	RQ 13	RQ 11	RQ 07	RQ 03	RQ 26	Gue 5Bis
Region:					Río Quema					Tonosí Road
Latitude	N7 34.072	N7 33.602	N7 34.702	N7 33.770	N7 33.717	N7 33.770	N7 34.245	N7 34.528	N7 34.704	N7.54121
Longitude	W80 31.959	W80 33.458	W80 31.216	W80 32.975	W80 33.030	W80 32.975	W80 31.905	W80 31.788	W80 31.121	W80.59680
Lithology:	Dacite	Andesite	Basalt	Andesite	Andesite	Andesite	Basalticandesite	Basalticandesite	Basalt	Basalt
SiO_2	64.56	57.94	54.01	58.27	57.86	55.55	55.32	51.67	45.86	48.7
Al_2O_3	14.37	14.61	16.01	13.69	14.44	15.13	15.08	18.34	14.82	13.81
Fe_2O_3(T)	5.79	7.84	8.45	8.50	7.85	10.21	10.05	8.80	11.46	12.02
MnO	0.148	0.107	0.16	0.08	0.15	0.14	0.14	0.17	0.159	0.19
MgO	1.87	4.23	4.36	5.48	5.47	4.54	4.60	4.93	6.42	7.84
CaO	4.31	6.77	7.29	1.87	2.93	7.09	7.02	4.65	12.66	10.89
Na_2O	3.65	3.1	2.89	4.04	4.12	3.16	3.12	4.43	1.99	3.03
K_2O	0.6	0.46	1.25	1.50	1.43	1.13	1.11	1.71	0.05	0.07
TiO_2	0.735	0.334	0.64	0.30	0.34	0.76	0.77	0.54	1.479	1.25
P_2O_5	0.32	0.1	0.11	0.06	0.08	0.13	0.13	0.07	0.16	0.08
LOI	4.24	4.23	4.73	4.81	5.27	2.78	2.78	4.68	5.24	2.43
Total	100.6	99.72	99.92	98.60	99.93	100.60	100.10	99.98	100.3	100.3
Cs	4.76	42.86	47.62	19.05	33.33	19.05	23.81	33.33		
Rb	18.33	15.00	38.33	43.33	26.67	20.00	25.00	33.33	10.00	6.67
Ba	44.85	27.88	71.06	123.79	50.61	68.18	68.18	72.58	13.48	7.12
Th	8.55	8.43	26.92	8.43	8.68	9.56	9.69	5.66	6.16	3.27
U	13.30	16.26	31.03	14.78	16.26	15.27	15.27	9.36	7.39	4.43
Nb	9.27	2.28	3.04	7.29	2.13	3.34	5.93	2.43	8.81	7.90
La	12.81	6.27	14.38	6.60	6.56	9.29	9.03	6.02	9.68	5.40
Ce	11.04	4.92	10.87	4.75	4.98	7.28	7.10	4.56	8.84	5.28
Pr	11.57	4.88	10.16	4.53	5.00	7.72	7.44	4.88	9.21	5.55
Nd	11.60	4.39	9.04	3.94	4.55	7.42	6.98	4.75	9.20	5.77
Sr	14.97	15.83	20.60	12.91	11.86	23.97	25.18	18.54	10.40	16.78
Sm	11.11	3.45	7.22	3.33	3.77	6.55	6.26	4.11	9.11	6.13
Zr	8.57	4.48	8.19	4.67	4.29	6.95	6.57	3.81	13.05	7.33
Hf	6.01	3.13	5.48	3.39	2.87	4.70	4.96	2.61	8.36	4.96
Ti	3.63	1.67	3.17	1.49	1.67	3.74	3.82	2.66	7.33	6.20
Eu	9.29	2.79	5.42	2.14	2.86	5.47	5.05	3.71	8.44	6.16
Gd	10.20	2.70	5.94	2.59	2.90	5.57	5.40	3.62	8.71	6.27
Tb	10.00	2.42	5.86	2.42	2.63	5.56	5.15	3.54	8.99	6.57
Dy	9.15	2.24	5.24	2.20	2.36	5.10	4.76	3.18	8.16	5.95
Ho	8.66	2.15	4.83	2.01	2.28	4.70	4.43	2.89	7.79	5.44
Y	8.14	1.86	4.65	1.63	2.09	4.42	4.42	3.02	6.98	5.12
Er	8.90	2.31	5.07	2.17	2.44	4.82	4.66	3.04	7.60	5.53
Tm	9.12	2.51	5.18	2.40	2.59	5.09	4.84	3.18	7.66	5.50
Yb	9.30	2.68	5.31	2.54	2.77	5.31	5.06	3.33	7.66	5.51
Lu	8.87	2.67	5.23	2.50	2.80	5.05	4.86	3.29	7.14	5.16

DOI: 10.1344/105.000001742

TABLE 1 | **Continued**

Sample:	PA 01	LI 01	AN 02	AN 04	TRI 01	LP 204	LP 111	PIT 02	RJ 13B	RJ 11
Region:	París	Limón	Finca AN	Finca AN	Trinidad	Cerro La Pava	Qda. Quema	Pitaloza	Río Joaquín	Río Joaquín
Latitude	N7 59.652	N8 03.452	N7 31.773	N7 31.450	N7.63192	N7 32.698	N7.5265667	N7.55377	N7 31.927	N7 31.630
Longitude	W80 31.629	W80 46.312	W80 30.676	W80 30.274	W80.66756	W80 32.543	W80.551737	W80.54827	W80 28.120	W80 28.120
Lithology:	Quartzdiorite	Quartzdiorite	Basalt	Trachyandesite	Quartzdiorite	Dacite	Andesite	Quartzdiorite	Basalt	Basalt
SiO_2	61.23	62.92	47.87	53.48	56.03	62.9	56.15	60.36	49.09	50.33
Al_2O_3	15.32	15.74	13.34	16.76	17.07	13.61	12.57	15.31	16.53	14.18
Fe_2O_3(T)	6.33	5.41	13.5	8.24	8.03	7.33	7.85	7.24	9.63	12.82
MnO	0.112	0.13	0.17	0.167	0.151	0.132	0.145	0.08	0.16	0.19
MgO	2.09	2.03	7.51	3.4	3.84	3.55	5.71	3.32	5.96	4.53
CaO	6	3.52	7.07	7.87	8.43	3.56	7.11	6.49	11.59	8.74
Na_2O	3.29	4.49	3.91	3.2	2.9	3.99	1.62	2.78	3.11	4.06
K_2O	1.01	1.82	0.1	2.13	0.82	2.91	0.53	0.84	0.28	0.09
TiO_2	0.806	0.794	1.09	0.691	0.721	0.216	0.256	0.24	1.32	2.05
P_2O_5	0.13	0.24	0.09	0.32	0.13	0.07	0.06	0.07	0.14	0.29
LOI	2.12	2.47	3.82	2.36	1.15	2.47	6.59	2.01	2.93	2.66
Total	98.43	99.56	98.49	98.61	99.27	100.7	98.59	98.75	100.70	99.95
Cs	14.29	52.38		9.52	14.29	14.29	4.76	19.05	9.52	
Rb	30.00	61.67	8.33	78.33	25.00	58.33	18.33	28.33	8.33	
Ba	62.42	98.48	9.55	155.15	53.79	96.67	25.76	29.85	20.30	5.45
Th	30.19	30.69	4.65	24.03	17.61	13.46	5.66	7.42	2.77	6.67
U	38.42	45.32	5.42	39.90	23.65	19.70	10.34	10.84	3.94	9.36
Nb	19.30	38.30	7.60	10.79	3.80	3.80	3.04	2.28	4.56	7.60
La	21.91	25.93	4.85	25.62	11.54	11.19	5.37	5.83	6.22	11.47
Ce	17.43	19.82	4.57	17.73	8.90	8.00	3.99	4.44	6.45	10.93
Pr	15.87	17.48	4.88	15.55	8.43	7.56	3.86	4.41	7.48	12.13
Nd	13.68	15.04	5.13	13.12	7.76	6.45	3.34	3.84	8.08	12.56
Sr	11.61	15.28	6.53	47.14	14.52	25.43	18.59	14.87	14.42	8.64
Sm	11.06	11.72	6.08	9.31	6.72	4.63	2.73	3.05	8.65	12.22
Zr	18.95	20.19	8.57	9.90	8.00	5.05	5.14	4.19	10.86	13.62
Hf	12.27	12.27	6.01	6.01	5.48	3.39	3.39	2.87	6.79	8.62
Ti	4.07	3.97	5.49	3.49	3.61	1.07	1.29	1.20	6.51	10.21
Eu	6.88	8.70	5.95	7.60	5.38	3.47	2.05	2.37	8.38	11.43
Gd	9.41	9.45	6.95	6.99	5.72	2.94	1.89	2.44	8.25	11.29
Tb	9.19	8.89	7.68	6.36	5.66	2.32	1.82	2.32	8.59	11.01
Dy	8.22	7.85	7.58	5.59	5.19	1.82	1.57	2.11	7.66	10.07
Ho	7.45	6.98	7.25	5.10	4.70	1.54	1.48	2.01	6.85	8.93
Y	8.37	6.98	6.98	4.88	4.65	1.63	1.16	1.40	6.74	8.60
Er	7.63	7.15	7.72	5.25	4.86	1.60	1.6	2.21	7.01	8.97
Tm	7.72	7.47	8.12	5.47	4.97	1.71	1.78	2.44	7.18	9.01
Yb	7.78	7.66	8.14	5.56	5.01	1.86	1.93	2.74	7.12	8.93
Lu	7.30	7.24	7.75	5.26	4.90	1.81	1.88	2.80	6.56	8.18

DOI: 10.1344/105.000001742

to the other alteration zones (Fig. 5F). Contrary to the reports by Torrey and Keenan (1994) it has not been observed in surface outcrops, suggesting that its extension is limited.

The intense weathering typical of tropical latitudes affects all rocks of the area. The superimposition of this supergene alteration to the hydrothermally altered terrains results in a thick cap (up to 150m) of silica and iron oxides (Fig. 5G).

In the Cerro Quema area several mineable gold deposits have been identified: La Pava in the West and Cerro Quemita and Cerro Quema in the East of the

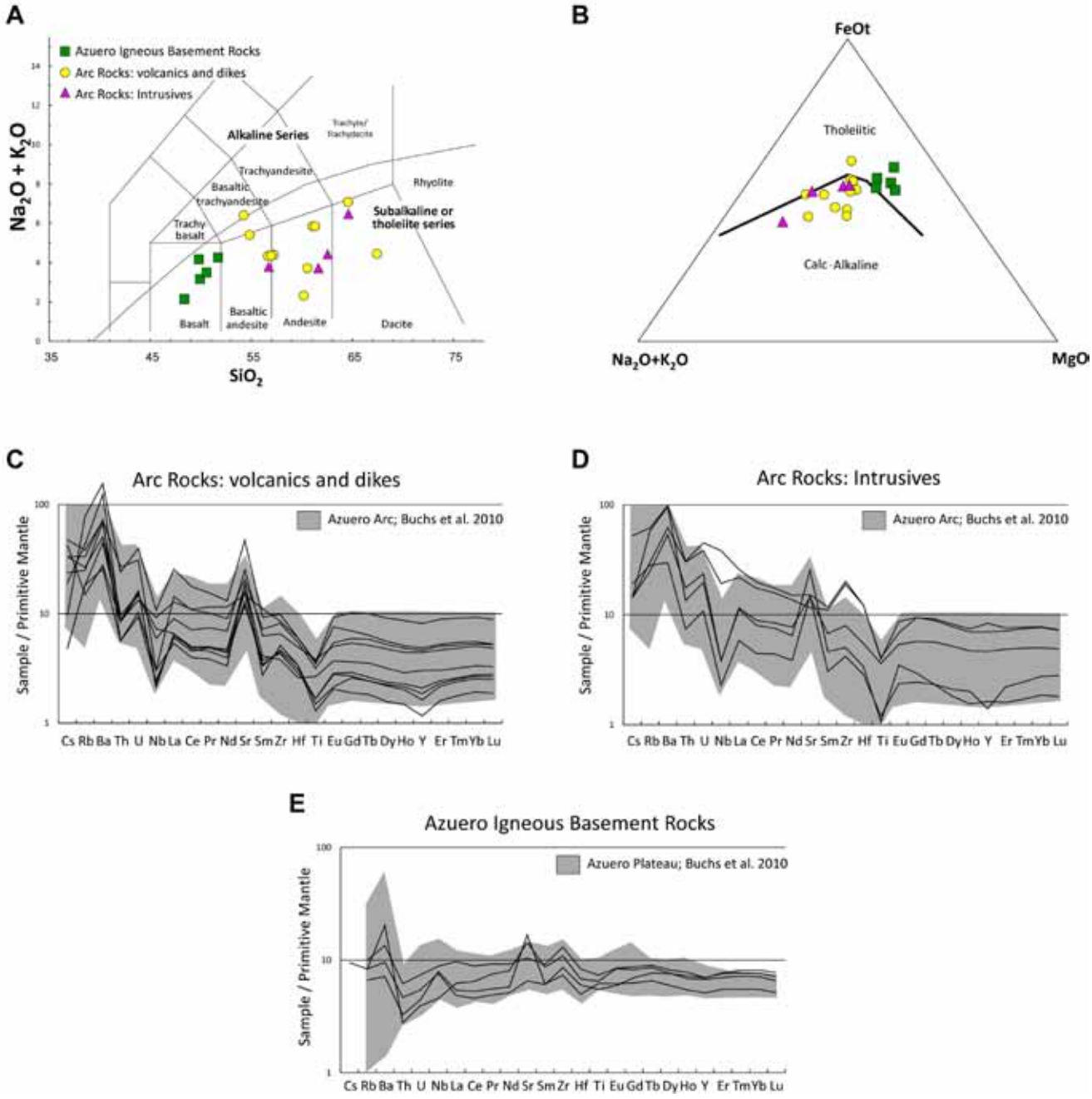

FIGURE 4 | **Major element geochemistry, chondrite-normalized (Sun and McDonough, 1989) trace element and REE concentrations of Cerro Quema area igneous rocks A) Chemical composition of igneous rocks in Total Alkali-Silica (TAS) diagram (Le Maitre et al., 1989). B) AFM diagram, Irvine and Baragar (1971). C) Arc Rocks of the RQF: Volcanic, volcaniclastic rocks and dikes. D) Arc Rocks of the RQF: Quartz-diorites and dacites. E) Azuero Igneous Basement rocks.**

area. Estimated total gold resources are 10Mt with an average gold grade of 1.26 g/T (Torrey and Keenan, 1994). The mineralization consists of disseminated pyrite, local enargite and a poorly developed stockwork of quartz, pyrite, chalcopyrite and barite with traces of galena and sphalerite. Gold occurs as disseminated submicroscopic grains and as invisible gold within the crystalline structure of pyrite (Corral, 2008), especially in the advanced argillic alteration zone. Strong supergene alteration (oxidation cap or gossan) released the gold contained in the structure of pyrite allowing the deposit to be economically profitable, as well as the mechanical transport of gold into nearby stream sediments.

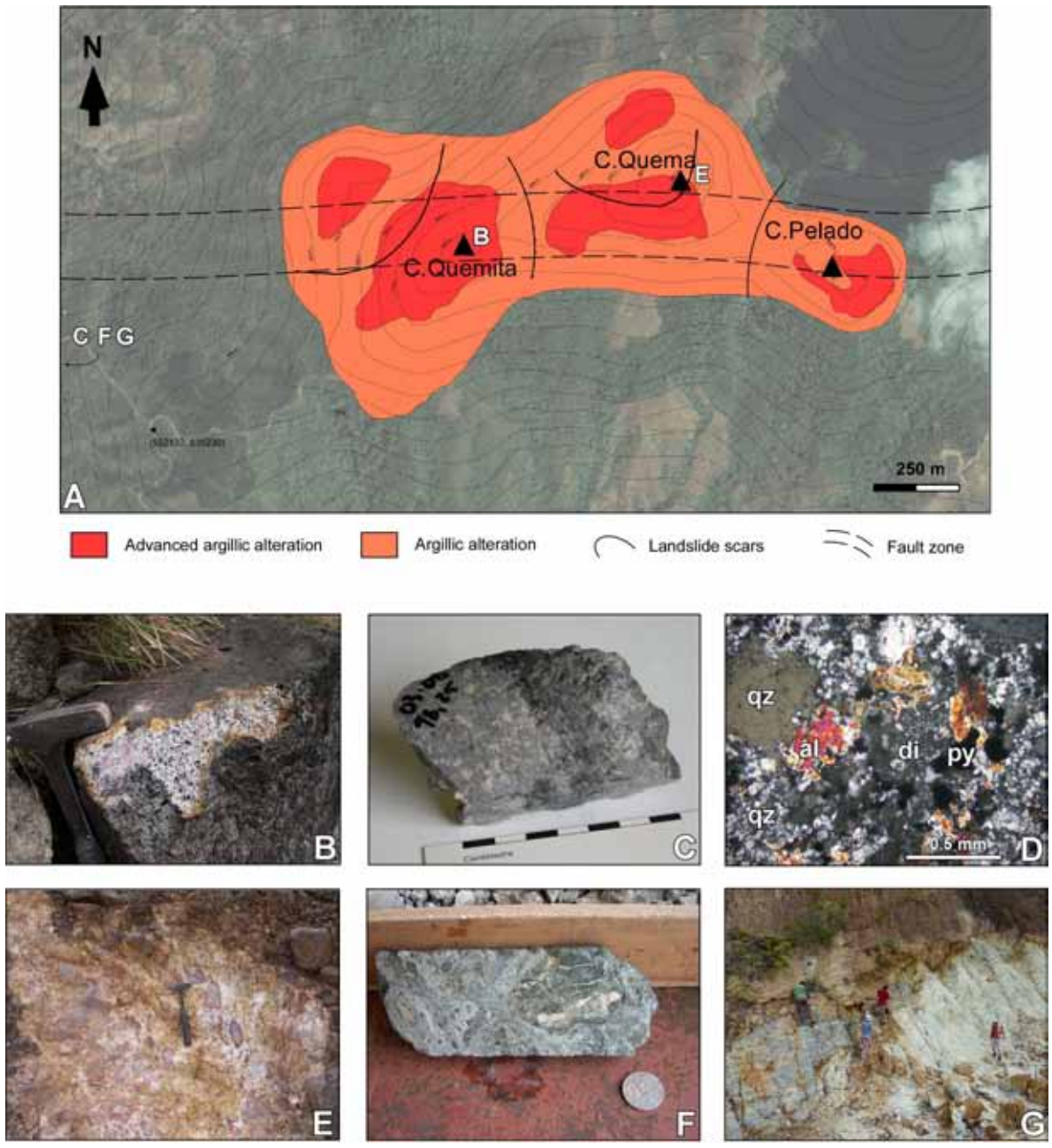

FIGURE 5 | **Alteration pattern at Cerro Quemita, Cerro Quema and Cerro Pelado. A) Hydrothermal alteration map. B) Vuggy silica at Cerro Quemita. C) Drill core sample of advanced argillic alteration, quartz-alunite-dickite crosscut by pyrite-enargite veins (dark gray). D) Thin section of the advanced argillic alteration. (py: pyrite, qz: quartz, al: alunite, di: dickite). E) Argillic alteration at Cerro Quema, kaolinite ± smectite ± illite. F) Propylitic alteration in a drill core sample, chloritized dacite with calcite veins and siderite. G) Red-ox boundary at Cerro Quemita (red-brown: oxidized zone, light gray: unoxidized zone).**

DISCUSSION

This work has focused on the study of the tectono-volcanic environment of the Cerro Quema area and on the mineralogy and spatial distribution of hydrothermal alteration related to gold and copper mineralization. Stratigraphic, petrologic and tectonic evidences suggest that the volcano-sedimentary Río Quema Formation was deposited in a submarine fore-arc basin from late Cretaceous to Eocene times. The fore-arc basin is limited to the North of Cerro Quema by arc-related intrusives of Paleogene age (Fig. 1). The southern limit is not clear, though we infer that the basin was limited by the Cretaceous subduction trench, which has not been identified in the field yet, or that it was subducted during later stages. Our geochemical data confirm that the Azuero Igneous Basement at the Cerro Quema district is chemically similar to the tholeiitic basalts of the Caribbean large igneous province (Goossens et al., 1977; Hauff et al., 2000; Hoernle et al., 2002; Hoernle et al., 2004). The less incompatible trace elements and REE show similar abundances and flat pattern tendencies to those reported for the Caribbean large igneous province (Hoernle et al., 2004; Wörner et al., 2009). Therefore, the igneous basement of the Azuero Peninsula cannot be interpreted as an accreted terrane (Goossens et al., 1977). Conversely, it represents the autochthonous basement of the upper plate, uplifted and exhumed during convergence tectonics. The recognition of the autochthonous basement of the Río Quema Formation allows us to describe the depositional environment from the onset of intra-oceanic subduction to the geochemical and geodynamic maturation of the magmatic arc.

The Proto-arc Group is interpreted to have formed at the initial stages of the magmatic arc which developed on top of the Azuero igneous basement. Its voluminous sheet flows and pillowed non-vesicular basalts and andesites associated with cherts and shales indicate extrusion/deposition in a deep marine environment proximal to the volcanic centre. Its geochemical composition is unusual and its signature is intermediate between typical oceanic plateau and intra-oceanic island arc (i.e. variably enriched in fluid-mobile elements and depleted in heavy REEs). Our interpretation of a magmatic arc on top of an oceanic plateau, such as the Caribbean large igneous province at the initial stages of subduction, would explain the presence of the so-called "enigmatic arc rocks" in the Caribbean large igneous province by Wörner et al. (2009) and some samples of the Sona-Azuero Arc described by Wegner et al. (2011). Our results are in agreement with those of Buchs (2008), Buchs et al. (2009, 2010) and Wörner et al. (2009). The Proto-arc Group rocks are true arc-related rocks, and could be associated to the initial magmatic arc generated at the onset of the Farallon plate subduction beneath the Caribbean Plate during Late Cretaceous-Paleogene times.

The classical interpretation of the Ocú formation assumes limestone deposition before the initiation of arc magmatism (Del Giudice and Recchi, 1969; Weyl, 1980; Kolarsky et al., 1995; Buchs, 2008; Buchs et al., 2010). However, in the Cerro Quema area, limestones overlie early volcanic arc rocks whose deposition followed the initiation of island arc magmatism. Therefore, the Cerro Quema limestones and equivalent calcareous layers observed at the Torio and Güera Rivers (West of Azuero; Buchs, 2008) do not belong to the Ocú Formation. Consequently, they are not indicative of the onset of subduction, being possibly a bit younger. Therefore we suggest the restriction of the so-called Ocú Formation to only the grayish foraminifera-bearing hemipelagic limestones deposited on top of basaltic basement rocks and/or interbedded with the Proto-arc Group.

The Río Quema Formation is interpreted as a fore-arc basin infill sequence accumulated during the geochemical and geodynamic maturation of the arc. The presence of andesites and dacites in the Río Quema Formation are indicative of magmatism of intermediate to acid composition. The abundance of hyaloclastites in both types of rocks, the scarcity of vesiculation and the presence of turbidites grading up into fine beds of hemipelagic sedimentary rocks indicate a submarine environment. However, the emplacement of dacites acted as a paleo-barrier to sedimentation producing the compartmentalization of the forearc basin (Fig. 6). The facies found on the northern slopes of the dacitic domes are characterized by the presence of massive volcanic rocks, minor turbidites, limestone layers with wave imprints, and abundant basaltic-andesitic dikes. These features allow us

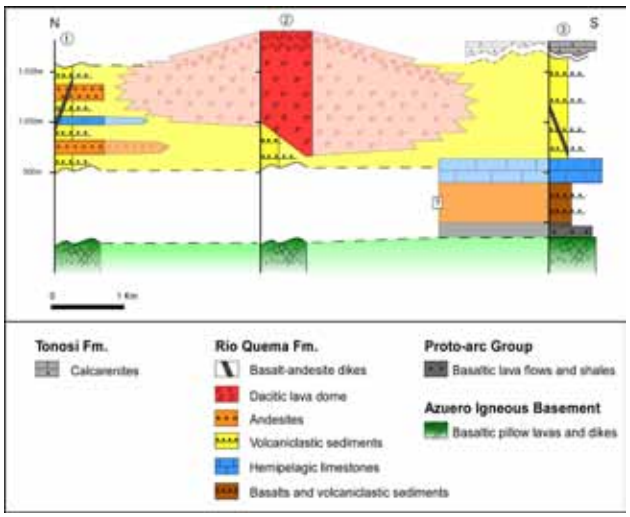

FIGURE 6 | **Schematic stratigraphic section across the Cerro Quema area. 1) North Cerro Quema area. 2) Central Cerro Quema area. 3) South Cerro Quema area.**

to interpret this part of the series as proximal to the volcanic front, so that the northern volcano-sedimentary sequence defines the inner fore-arc basin. On the other hand, the facies observed on the southern slopes of the dacitic domes with a large fraction of volcanoclastic sediments, turbidites, shales and siltstones and a small presence of andesitic lava flows are interpreted as distal and deeper facies. Hence, the southern sedimentary sequence would define the outer section of the fore-arc basin, consistent with the SW to W paleocurrents observed in turbidite sediments, indicative of axial transport in the basin.

The main tectonic structures recognized in the area are the E-W Río Joaquín fault zone, ENE-WSW folds and late sinistral NW-SE strike-slip faults. All these structures are compatible with a compressive and/or a transpressive tectonic regime. Since the Tonosí Formation unconformably overlies tectonic features and igneous rock units, we infer a minimum pre-Oligocene age for the main tectonic phase. However, additional field and geochronological data are required to better constrain the timing of tectonism.

Hydrothermal alteration has been mainly recognized in dacites, but also in andesites further East, which have a similar age to that of the Río Quema Fm. No hydrothermal alteration has been observed affecting the sediments of the Tonosí Fm. (Oligocene). Therefore, the hydrothermal event related to mineralization must have occurred between the Late Cretaceous and the Oligocene, probably associated to one or more of the magmatic events that show up in the intrusive unit rocks (diorites, quartz-diorites and granodiorites) or to a possible porphyry system associated to the intrusion of the dacitic domes.

The mineralogy and spatial distribution of hydrothermal alteration observed in Cerro Quema fit well within the classical high sulfidation epithermal gold deposits model described by Hedenquist (1987), Berger and Henley (1989), Sillitoe (1989, 1995), White (1991), Ginggenbach (1992), Rye (1993), Hedenquist and Lowenstern (1994) and Arribas et al. (1995). Hydrothermal alteration is related to the circulation of acidic fluids of magmatic origin and to the presence of a porphyry copper system at depth in a calc-alkaline volcanic arc in both, sub-aerial and submarine environment (Sillitoe et al., 1996; Herzig et al., 1998; Paulick et al., 2004; Binns et al., 2007). Despite the mineralogy, the spatial distribution and tectono-volcanic environment of the Cerro Quema deposit are in agreement with the model, the possible presence of porphyry copper at depth could not be proved. On the other hand, a model based on an oxidized gold and copper deposit that shares characteristics of both epithermal and volcanogenic massive sulfide deposits (Nelson, 2007) can be discarded, as no signs of bedded massive sulfides have been found in the alteration zones, in the vicinity of the dacitic lava domes or associated hyaloclastitic sediments.

Some of the characteristics of the Cerro Quema deposit (presence of dacitic domes, geological setting, hydrothermal alteration pattern…) are shared with the Pueblo Viejo gold deposit (Dominican Republic), the largest mineable high sulfidation epithermal gold deposit of the Caribbean (Kesler et al., 1981, 2005; Nelson, 2000; Sillitoe et al., 2006). Considering that similar hydrothermal alteration related to E-W faults has been observed towards the East and West of Cerro Quema (Juan Díaz district and Pitaloza district respectively) we can conclude that the hydrothermal flow was a large-scale structurally controlled event that affected materials of different composition. Recognition of structurally controlled high sulfidation epithermal deposits in the studied area may have important consequences for mineral exploration. Prospection should be focused at, or close to the E-W trending faults regardless of the enclosing rock type, as hydrothermal systems seem to be related to these structures situated to the North of the Río Joaquín fault.

CONCLUSIONS

The general conclusions of this study can be summarized in the following points:

1) The stratigraphy and petrology of the volcano-sedimentary rocks of the Cerro Quema area denote a submarine depositional environment. The tectonic setting corresponds to the fore-arc basin associated to a Late Cretaceous–Paleogene intra-oceanic volcanic arc.

2) A new lithostratigraphic unit, the Río Quema Formation, is proposed to describe the volcano-sedimentary sequence that crops out in the central Azuero Peninsula and corresponds to the fore-arc basin infill sequence of the Cretaceous–Paleogene volcanic arc. The igneous rocks within this formation belong to the calc-alkaline family, with trace and REE element patterns compatible with volcanic arc affinity. The volcanic arc developed on top of a tholeiitic igneous basement (Azuero Igneous Basement) and was originated by the subduction of the Farallon Plate. The Azuero Igneous Basement's geochemistry is similar to that of the Caribbean large igneous province.

3) The Río Joaquín fault zone, a major regional scale fault zone with broad E-W orientation and reverse-sense motion, has been recognized in the study area and mapped with a slightly different trend from that proposed by Buchs (2008). Along this structure, the Azuero Igneous Basement is in direct contact with the Upper Unit of the Río Quema Formation. In addition, kilometric to decametric ENE-WSW folds and late sinistral NW-SE strike-slip faults have also been identified. These structures suggest a

compressive and/or transpressive tectonic regime, at least during Late Cretaceous–Oligocene times.

4) The Cerro Quema mineral district comprises the hydrothermally altered dacite hills of Cerro Quema, Quemita and La Pava, all included in the Río Quema Formation. An inner core of advanced argillic alteration (vuggy silica, alunite-natroalunite and dickite) and an outer halo of argillic alteration (kaolinite, illite and illite-smectite) have been recognized, both in outcrops and drill core samples. A propylitic alteration zone has only been observed in a few drill core samples.

5) Mineralization at Cerro Quema consists of disseminated pyrite, chalcopyrite and locally enargite, with a poorly developed stockwork of pyrite, chalcopyrite and barite with minor galena and sphalerite. Gold is found as disseminated submicroscopic grains both alone and within the crystalline structure of pyrite (invisible gold). It is principally concentrated within vuggy silica of the advanced argillic alteration zone.

6) The mineralogy and hydrothermal alteration pattern in the Cerro Quema area as well as the tectono-volcanic environment correspond to a high sulfidation epithermal system. The Cerro Quema deposit is part of a larger hydrothermal system related to E-W trending faults that affected different lithologies further East and West of the Azuero Peninsula.

7) The exploration criteria for finding new gold deposits in the area should be focused at or close to the E-W trending regional faults, regardless of the enclosing rock type, as hydrothermal systems seem to be related to these structures which are always situated to the North of the Río Joaquín fault zone.

ACKNOWLEDGEMENTS

This study was supported by the Spanish Ministry of Science and Education (MEC) project CGL2007-62690/BTE, a pre-doctoral grant of the "Departament d'Universitats, Recerca i Societat de la Informació (Generalitat de Catalunya)". The corresponding author would like to express his gratitude to the SEG Foundation and the SEG Canada Foundation for the 2009 and 2010 student research grants (Hugh E. McKinstry) which supported part of the field and related laboratory research expenses. This study has been performed within the framework of the Ph.D. program in Geology of the Universitat Autònoma de Barcelona. We thank Bellhaven Copper and Gold Inc. for access to mine samples and drill cores used in this study. Discussions with David Buchs about the geology of the Azuero Peninsula were very fruitful. Fieldwork comments and help by Stuart Redwood and Carl Nelson are greatly appreciated. Finally, we want to show our gratitude to Mark Jessell for the final revision of the manuscript.

REFERENCES

Adamek, S., Frohlich, C., Pennington, W.D., 1988. Seismicity of the Caribbean-Nazca boundary; constraints on microplate tectonics of the Panama region. Journal of Geophysical Research, 93, 2053-2075.

Arribas, A.Jr., Hedenquist, J.W., Itaya, T., Okada, T., Concepcion, R.A., Garcia, J.S.Jr., 1995. Contemporaneous formation of adjacent porphyry and epithermal Cu-Au deposits over 300 ka in northern Luzon, Philippines. Geology, 23, 337-340.

Berger, B.R., Henley, R.W., 1989. Advances in the understanding of epithermal gold-silver deposits, with special reference to the Western United States. Economic Geology Monographs, 6, 405-423.

Binns, R.A., Barriga, F.J.A.S., Miller, D.J., 2007. Leg 193 Synthesis: Anatomy of an active felsic-hosted hydrothermal system, eastern Manus Basin, Papua New Guinea. In: Barriga, F.J.A.S., Binns, R.A., Miller, D.J., Herzig., P.M. (eds.). Proceedings of the Ocean Drilling Program, Scientific Results. Texas, College Station, Ocean Drilling Program, 193, 1-71.

Bourgois, J., Azema, J., Tournon, J., Bellon, H., Calle, B., Parra, E., Toussaint, J.F., Glacon, G., Feinberg, H., Dewever, P., Origlia, I. 1982. Ages and Structures of the Basic and Ultrabasic Complexes of the Pacific Coast between 3-Degrees-N and 12-Degrees-N (Colombia, Panama and Costa-Rica). Bulletin de La Société Géologique de France, 24, 545-554.

Buchs, D.M., 2008. Late Cretaceous to Eocene geology of the South Central American fore-arc area (southern Costa Rica and western Panama): Initiation and evolution of an intra-oceanic convergent margin. Doctoral Thesis. Switzerland, Université de Lausanne, 230pp.

Buchs, D.M., Baumgartner, P.O., Baumgartner-Mora, C., Bandini, A., Jackett, S-J., Diserens, M-O., Stucki, J., 2009. Seamount accretion and melange formation of the Osa Peninsula (southern Costa Rica): Eocene–Miocene mass wasting and tectonic processes along the Middle American Trench. In: James, K., Lorente, M.A., Pindell, J. (eds.). The geology and evolution of the region between North and South America. Geological Society of London, Special Publications, 411-456.

Buchs, D.M., Arculus, R.J., Baumgartner, P.O., Baumgartner-Mora, C., Ulianov, A., 2010. Late Cretaceous Arc Development on the SW margin of the Caribbean Plate: Insights from the Golfito (Costa Rica) and Azuero (Panama) Complexes. Geochemistry, Geophysics, Geosystems, 11(7), 35pp.

Coates, A.G., Collins, L.S., Aubry, M.-P., Berggren, W.A., 2004. The Geology of the Darien, Panama, and the late Miocene-Pliocene collision of the Panama arc with northwestern South America. Geological Society of America Bulletin, 116, 1327-1344.

Coates, A.G., Jackson, J.B.C., Collins, L.S., Cronin, T.M., Dowsett, H.J., Bybell, L.M., Jung, P., Obando, J.A., 1992. Closure of the Isthmus of Panama: The near-shore marine record of Costa Rica and western Panama. Geological Society of America Bulletin, 104, 814-828.

Corral, I., 2008. El dipòsit d'Au-Cu de "La Pava" (Península d'Azuero, Panamà): caracterització geològica i mineralògica. Master of Science. Universitat Autònoma de Barcelona, 31pp.

de Boer, J.Z., Drummond, M.S., Bordelon, M.J., Defant, M.J., Bellon, H., Maury, R.C., 1995. Cenozoic magmatic phases of the Costa Rican island arc (Cordillera de Talamanca). Geological Society of America, 295, 35-55.

Del Giudice, D., Recchi, G., 1969. Geología del área del Proyecto Minero de Azuero. Informe técnico preparado para el gobierno de la República de Panamá por las Naciones Unidas. Panamá City (Panamá), Gobierno de la República de Panamá, 48pp.

Denyer, P., Alvarado, G.E., 2007. Mapa Geológico de Costa Rica 1:400.000. Librería Francesa S.A.

Dirección General de Recursos Minerales, 1976. Panama Geologic Map (Mapa geológico de la República de Panamá), scale 1:250.000. Panama City, Panama.

Di Marco, G., Baumgartner, P.O., Channell, J.E.T., 1995. Late Cretaceous-early Tertiary paleomagnetic data and a revised tectonostratigraphic subdivision of Costa Rica and western Panama. Geological Society of America, 295, 1-27.

Duque-Caro, H., 1990. Neogene stratigraphy, paleoceanography and paleobiogeography in Northwest South America and the evolution of the Panama Seaway. Palaeogeography, Palaeoclimatology, Palaeoecology, 77, 203-234.

Escalante, G., 1990. The geology of southern Central America and western Colombia In: Dengo, G., Case, J.E. (eds.). The Caribbean Region. Boulder, Colorado, Geological Society of America, The Geology of North America, H, 201-230.

Ferencic, A., 1970. Porphyry copper mineralization in Panama. Mineralium Deposita, 5, 383-389.

Ferencic, A., 1971. Metallogenic provinces and epochs in southern Central America. Mineralium Deposita, 6, 77-88.

Fisher, D.M., Gardner, T.W., Marshall, J.S., Sak, P.B., Protti, M., 1998. Effect of subducting sea-floor roughness on fore-arc kinematics, Pacific coast, Costa Rica. Geology, 26, 467-470.

Gardner, T., Marshall, J., Merritts, D., Bee, B., Burgette, R., Burton, E., Cooke, J., Kehrwald, N., Protti, M., Fisher, D., Sak, P., 2001. Holocene fore-arc block rotation in response to seamount subduction, southeastern Peninsula de Nicoya, Costa Rica. Geology, 29, 151-154.

Giggenbach, W.F., 1992. Magma degassing and mineral deposition in hydrothermal systems along convergent plate boundaries. Economic Geology, 87, 1927-1944.

Goossens, P.J., Rose, W.I.J., Flores, D., 1977. Geochemistry of tholeiites of the Basic Igneous Complex of northwestern South America. Geological Society of America Bulletin, 88, 1711-1720.

Hannington, M.D., 1997. The Porphyry-Epithermal-VMS Transition: Lessons from the Iskut River Area, British Columbia, and Modern Island Arcs. Society of Economic Geology Newsletter, 29, 12-13.

Harmon, R.S., 2005. Geological development of Panama. Water Science and Technology Library, 52, 45-62.

Hauff, F., Hoernle, K., van den Bogaard, P., Alvarado, G., Garbe-Schoenberg, D., 2000. Age and geochemistry of basaltic complexes in western Costa Rica; contributions to the geotectonic evolution of Central America. Geochemistry Geophysics Geosystems, 1(5), 41pp.

Hedenquist, J.W., 1987. Mineralization associated with volcanic-related hydrothermal systems in the Circum-Pacific basin. Transactions of the Circum-Pacific Energy and Mineral Resources Conference, 4, 513-524.

Hedenquist, J.W., Lowenstern, J.B., 1994. The role of magmas in the formation of hydrothermal ore deposits. Nature, 370, 519-527.

Herzig, P.M., Hannington, M.D., Arribas, A.Jr., 1998. Sulfur isotopic composition of hydrothermal precipitates from the Lau back-arc: implications for magmatic contributions to seafloor hydrothermal system. Mineralium Deposita, 33, 226-237.

Hoernle, K., Hauff, F., 2007. Oceanic Igneous Complexes. Central America, geology, resources and hazards, 1, 523-548.

Hoernle, K., Hauff, F., van den Bogaard, P., 2004. 70 m.y. history (139-69 Ma) for the Caribbean large igneous province. Geology, 32, 697-700.

Hoernle, K., van den Bogaard, P., Werner, R., Lissinna, B., Hauff, F., Alvarado, G., Garbe-Schonberg, D., 2002. Missing history (16-71 Ma) of the Galapagos hotspot: Implications for the tectonic and biological evolution of the Americas. Geology, 30, 795-798.

Horlacher, C.F., Lehmann, J.H., 1993. Regional Geology, Geochemistry and Exploration potential of the central Cerro Quema concession, Panama. Unpublished report, 36pp.

Irvine, T.N., Baragar, W.R.A., 1971. A guide to the chemical classification of the common volcanic rocks. Canadian Journal of Earth Sciences, Revue Canadienne des Sciences de la Terre, 8, 523-548.

Kellogg, J.N., Vega, V., Stallings, T.C., Aiken, C.L.V., 1995. Tectonic development of Panama, Costa Rica, and the Colombian Andes; constraints from Global Positioning System geodetic studies and gravity. Geological Society of America, 295 (Special Paper), 75-90.

Kerr, A.C., Marriner, G.F., Tarney, J., Nivia, A., Saunders, A.D., Thirlwall, M.F., Sinton, C.W., 1997. Cretaceous basaltic terranes in western Colombia: Elemental, chronological and Sr-Nd isotopic constraints on petrogenesis. Journal of Petrology, 38, 677-702.

Kesler, S.E., Campbell, I.H., Smith, C.N., Hall, C.M., Allen, C.M., 2005. Age of the Pueblo Viejo Gold-Silver Deposit and its significance to models for High-Sulfidation Epithermal Mineralization. Economic Geology, 100, 253-272.

Kesler, S.E., Russell, N., Seaward, M., Rivera, J., McCurdy, K., Cumming, G.L., Sutter, J.F., 1981. Geology and geochemistry of sulfide mineralization underlying the Pueblo Viejo

gold-silver oxide deposit, Dominican Republic. Economic Geology, 76, 1096-1117.

Kesler, S.E., Sutter, J.F., Issigonis, M.J., Jones, L.M., Walker, R.L., 1977. Evolution of porphyry copper mineralization in an oceanic island arc; Panama. Economic Geology, 72, 1142-1153.

Kolarsky, R.A., Mann, P., Monechi, S., Meyerhoff-Hull, D., Pessagno, E.A., 1995. Stratigraphic development of southwestern Panama as determined from integration of marine seismic data and onshore geology. Geological Society of America Special Paper, 295, 159-200.

Kolarsky, R.A., Mann, P., 1995. Structure and neotectonics of an oblique-subduction margin, southwestern Panama. Geological Society of America Special Paper, 295, 131-157.

Krawinkel, H., Wozazek, S., Krawinkel, J., Hellmann, W., 1999. Heavy-mineral analysis and clinopyroxene geochemistry applied to provenance analysis of lithic sandstones from the Azuero-Soná Complex (NW Panama). Sedimentary Geology, 124, 149-168.

Krawinkel, J., and Seyfried, H., 1994. Struktur und Kinematik im Fore-arc der suedlichen zentralamerikanischen Landbruecke. Bonn, Terra Nostra, 2(94), 47-48.

Le Maitre, R.W., Bateman, P., Dudek, A., Keller, J., Lemeyre, J., Le Bas, M.J., Sabine, P.A., Schmid, R., Sorensen, H., Streckeisen, A., Wooley, A.R., Zanettin, B., 1989. A classification of igneous rocks and glossary of terms. Oxford, Blackwell Scientific, 193pp.

Leach, T.M., 1992. Petrological Evaluation of the High Sulphidation Systems in the La Pava and Cerro Quema Prospect Areas, Panama, for Cyprus Gold Company. Unpublished report, 55pp.

Lissinna, B., Hoernle, K., van den Bogaard, P., 2002. Northern migration of arc volcanism in western Panama: evidence for subduction erosion? Eos Transactions, American Geophysical Union, 83, 1463-1464.

Lissinna, B., 2005. A profile through the Central American Landbridge in western Panama: 115 Ma Interplay between the Galápagos Hotspot and the Central American Subduction Zone. Doctoral Thesis. Germany, Christian-Albrechts-Universität zu Kiel, 102pp.

Lissinna, B., Hoernle, F., Hauff, P., van den Bogaard, P., Sadofsky, S., 2006. The Panamanian island arc and Galápagos hotspot: A case study for the long-term evolution of arc/hotspot interaction. Geophysical Research Abstracts, 8, 05106.

Mann, P., Kolarsky, R.A., 1995. East Panama deformed belt; structure, age, and neotectonic significance. Geological Society of AAmerica, 295 (Special Paper), 111-130.

Mann, P., Corrigan, J., 1990. Model for late Neogene deformation in Panama. Geology, 18, 558-562.

Marshall, J.S., Idleman, B.D., Gardner, T.W., Fisher, D.M., 2003. Landscape evolution within a retreating volcanic arc, Costa Rica, Central America. Geology, 31(5), 419-422.

Maury, R.C., Defant, M.J., Bellon, H., De Boer, J.Z., Stewart, R.H., Coten, J., 1995. Early Tertiary arc volcanic from eastern Panama. Geological Society of America, 295 (Special Paper), 30-34.

Metti, A., Recchi, G., 1976. Geología de la Península de Sona e Isla de Coiba. Boletín de Geología Publicación Especial, 541-553.

Metti, A., Recchi, G., Esquivel, D., 1972. Mapa geológico Sona-Isla de Coiba: scale 1:250.000. Ministerio de Comercio e Industrias, Panama City (Republica de Panamá).

Nelson, C.E., 1995. Porphyry copper deposits of southern Central America. Arizona Geological Society Digest, 20, 553-565.

Nelson, C.E., 2000. Volcanic domes and gold mineralization in the Pueblo Viejo District, Dominican Republic. Mineralium Deposita, 35, 511-525.

Nelson, C.E., 2007. Metallic mineral resources. In: Bundschuh, J., Alvarado, G.E. (eds.). Central America. Geology, Resources and Hazards. The Netherlands, Taylor & Francis, 32 (Chapter), 885-915.

Nelson, C.E., Nietzen, F., 2000. Metalogenia del oro y cobre en América Central. Revista Geológica de América Central, 23, 25-41.

Paulick, H., Vanko, D.A., Yeats, C.J., 2004. Drill core-based facies reconstruction of a deep-marine felsic volcano hosting an active hydrothermal system (Pau Ridge, Papua New Guinea, ODP Leg 193). Journal of Volcanology and Geothermal Research, 130, 31-50.

Pindell, J., Kennan, L., 2009. Tectonic evolution of the Gulf of Mexico, Caribbean and northern South America in the mantle reference frame: an update. In: James, K., Lorente, M.A., Pindell, J. (eds.). The geology and evolution of the region between North and South America. Geological Society of London, 328 (Special Publications), 1-55.

Recchi, G., Miranda, R., 1977. Calizas de los Planes-Guaniquito (Tonosí). Unpublished report, Panama City, Dirección General de Recursos Minerales, 27pp.

Révillon, S., Hallot, E., Arndt, N.T., Chauvel, C., Duncan, R.A., 2000. A complex history for the Caribbean plateau: Petrology, geochemistry and geochronology of the Beata Ridge, South Hispaniola. Journal of Geology, 108, 641-661.

Rye, R.O., 1993. The evolution of magmatic fluids in the epithermal environment; the stable isotope perspective. Economic Geology, 88, 733-752.

Sak, P.B., Fisher, D.M., Gardner, T.W., 2004. Effects of subducting seafloor roughness on upper plate vertical tectonism: Osa Peninsula, Costa Rica. Tectonics, 23, 16pp.

Sillitoe, R.H., 1989. Gold deposits in western Pacific island arcs; the magmatic connection. Economic Geology Monographs, 6, 274-291.

Sillitoe, R.H., 1995. Exploration of porphyry copper lithocaps. Publication Series – Australasian. Institute of Mining and Metallurgy, 9(95), 527-532.

Sillitoe, R.H., Hannington, M.D., Thompson, J.F.H., 1996. High sulfidation deposits in the volcanogenic massive sulfide environment. Economic Geology, 91, 204-212.

Sillitoe, R.H., Hall, D.J., Redwood, S.D., Waddell, A.H., 2006. Pueblo Viejo High-sulfidation epithermal gold-silver deposit, Dominican Republic: a new mode of formation beneath barren limestone cover. Economic Geology, 101, 1427-1435.

Silver, E.A., Reed, D.L., Tagudin, J.E., Heil, D.J., 1990. Implications of the North and South Panama thrust belts for the origin of the Panama Orocline. Tectonics, 9, 261-281.

Sinton, C.W., Duncan, R.A., Denyer, P., 1997. Nicoya Peninsula, Costa Rica; a single suite of Caribbean oceanic plateau magmas. Journal of Geophysical Research, 102(B7), 15, 507-15, 520.

Sinton, C.W., Duncan, R.A., Storey, M., Lewis, J., Estrada, J.J., 1998. An oceanic flood basalt province within the Caribbean Plate. Earth and Planetary Science Letters, 155, 221-235.

Sun, S.S., McDonough, W.F., 1989. Chemical and isotopic systematics of oceanic basalts; implications for mantle composition and processes. Geological Society, 42 (Special Publications), 313-345.

Taboada, A., Rivera, L.A., Fuenzalida, A., Cisternas, A., Philip, H., Bijwaard, H., Olaya, J., Rivera, C., 2000. Geodynamics of the Northern Andes; subductions and intracontinental deformation (Colombia). Tectonics, 19, 787-813.

Torrey, C., Keenan, J., 1994. Cerro Quema Project, Panama, Prospecting in tropical and arid terrains. Toronto, Ontario, Canada, Unpublished report, 23pp.

Trenkamp, R., Kellogg, J.N., Freymueller, J.T., Mora, H.P., 2002. Wide plate margin deformation, southern Central America and northwestern South America, CASA GPS observations. Journal of South American Earth Sciences, 15, 157-171.

Tournon, J., Triboulet, C., Azéma, J., 1989. Amphibolites from Panama: anticlockwise P-T paths from a Preuper Cretaceous metamorphic basement in Istmian Central America. Journal of Metamorphic Geology, 7, 539-546.

Weyl, R., 1980. Geology of Central America. Berlin, Gebrueder Borntraeger, 2nd edition, 371pp.

White, N.C., 1991. High sulfidation epithermal gold deposits; characteristics and a model for their origin: Chishitsu Chosajo Hokoku. Report-Geological Survey of Japan, 9-20.

Wegner, W., Wörner, G., Harmon, R.S., Jicha, B.R., 2011. Magmatic history and evolution of the Central American Land Bridge in Panama since Cretaceous times. Geological Society of America Bulletin, 123, 703-724.

Wörner, G., Harmon, R.S., Wegner, W., 2009. Geochemical evolution of igneous rocks and changing magma sources during the formation and closure of the Central American land bridge of Panama: Backbone of the Americas: Shallow Subduction, Plateau Uplift, and Ridge Terrane Collision. Geological Society of America Memoir, 204, 183-196.

Wörner, G., Harmon, R.S., Hartmann, G., Simon, K., 2005. Igneous Geology and Geochemistry of the Upper Río Chagres Basin. In: Singh, V.P., Harmon, R.S. (eds.). The Río Chagres, Panama: A Multidisciplinary Profile of a Tropical Watershed. Springer, 65-81.

Wörner, G., Harmon, R.S., Wegner, W., Singer, G., 2006. Linking America's backbone: Geological development and basement rocks of central Panama. Mendoza (Argentina), 2-7 April 2006, Geological Society of America Conference "Backbone of the Americas", Boulder (Colorado), Geological Society of America, Abstrstracts with Programs, 60.

Manuscript received November 2010;
revision accepted July 2011;
published Online July 2011.